

Proceedings of the workshop

# HERA and the LHC

workshop series on the implications of HERA for LHC physics

2006 - 2008, Hamburg - Geneva

Editors: Hannes Jung, Albert De Roeck

Verlag Deutsches Elektronen-Synchrotron

# **Impressum**

## **Proceedings of the workshop HERA and the LHC**

### **2nd workshop on the implications of HERA for LHC physics 2006 - 2008, Hamburg - Geneva**

Conference homepage

<http://www.desy.de/~heralhc>

Online proceedings at

<http://www.desy.de/~heralhc/proceedings-2008/proceedings.html>

The copyright is governed by the Creative Commons agreement, which allows for free use and distribution of the articles for non-commercial activity, as long as the title, the authors' names and the place of the original are referenced.

Editors:

Hannes Jung (DESY, U. Antwerp), Albert De Roeck (CERN, U. Antwerp)

March 2009

DESY-PROC-2009-02

ISBN 978-3-935702-32-4

ISSN 1435-8077

Published by

Verlag Deutsches Elektronen-Synchrotron

Notkestraße 85

22607 Hamburg

Germany

## **Organizing Committee:**

H. Jung (DESY and U. Antwerp, chair), A. De Roeck (CERN and U. Antwerp, chair)  
G. Altarelli (CERN), J. Blümlein (DESY), M. Botje (Nikhef), J. Butterworth (UCL), K. Eggert (CERN),  
E. Gallo (INFN), T. Haas (DESY), R. Heuer (CERN), M. Klein (Liverpool), M. Mangano (CERN),  
A. Morsch (CERN), G. Polesello (INFN/CERN), O. Schneider (EPFL), C. Vallee (CPPM)

## **Conveners:**

### **Parton Density Functions:**

M. Dittmar (ETH, Zürich, CMS), S. Forte (U. Milan), A. Glazov (DESY, H1), S. Moch (DESY)

### **Multi-jet final states and energy flows:**

C. Gwenlan (UCL, ZEUS), L. Lönnblad (Lund), E. Rodrigues (LHCb), G. Zanderighi (CERN)

Contact persons: S. Banerjee (CMS), D. Traynor (H1)

### **Heavy quarks (charm and beauty):**

M. Cacciari (Paris VI & VII.), A. Dainese (INFN, ALICE), A. Geiser (DESY, ZEUS), H. Spiesberger (U. Mainz)

Contact persons: K. Lipka (U. Hamburg, H1), Ulrich Uwer (CERN)

### **Diffraction:**

M. Arneodo (U. Piemonte Orientale, Novara, INFN, CMS, ZEUS), M. Diehl (DESY), P. Newman (U. Birmingham, H1), V. A. Khoze (U. Durham)

Contact persons: A. Bruni (INFN, ZEUS), B. Cox (U. Manchester, ATLAS), R. Orava (U. Helsinki)

### **Cosmic Rays:**

C. Diaconu (DESY, CPPM, H1), Ch. Kiesling (MPI Munich, H1), T. Pierog (FZ Karlsruhe),

### **Monte Carlos and Tools:**

P. Bartalini (Taiwan, CMS), S. Chekanov (Argonne, ZEUS), F. Krauss (IPP Durham), S. Gieseke (U. Karlsruhe)

## **Advisory Committee:**

G. Altarelli (CERN), J. Bartels (Hamburg), M. Della Negra (CERN), J. Ellis (CERN), J. Engelen (CERN),  
G. Gustafson (Lund), G. Ingelman (Uppsala), P. Jenni (CERN), R. Klanner (DESY), M. Klein (DESY),  
L. McLerran (BNL), T. Nakada (CERN), D. Schlatter (CERN), F. Schrempp (DESY),  
J. Schukraft (CERN), J. Stirling (Durham), W.K. Tung (Michigan State), A. Wagner (DESY),  
R. Yoshida (ANL)

## **Supported by:**

Deutsches Elektronen-Synchrotron DESY (Hamburg)  
CERN (Geneva)

# Preface

In April 2004 the first meeting of what would become a series of HERA-LHC meetings took place at CERN. Over 250 participants joined and helped to shape the goals and objectives of this workshop. These are:

- To identify and prioritize those measurements to be made at HERA which have an impact on the physics reach of the LHC;
- to encourage and stimulate transfer of knowledge between the HERA and LHC communities and establish an ongoing interaction;
- to encourage and stimulate theory and phenomenology efforts;
- to examine and improve theoretical and experimental tools;
- to increase the quantitative understanding of the implication of HERA measurements on LHC physics;

That HERA deep inelastic scattering and photoproduction data and knowledge acquired will have an impact on the analysis of LHC data is a priori obvious. First and foremost there is the question on the structure of the proton. HERA is the first and so far only collider for lepton-proton scattering to date. The data from the 27.5 GeV electron beams scattered on the 820 (920) GeV protons have delivered an accurate picture of the Structure of the proton in a wide kinematic range. Precise predictions of cross sections at the LHC critically depend on the knowledge of the parton density functions (PDFs) in the proton. It can be the largest uncertainty in measurements, as the detector systematics will get under control to the anticipated level. The precision measurements at HERA in the last 15 years have boosted our knowledge on the parton distributions by several orders in magnitude in kinematic reach and by specific measurements of heavy flavors, such as bottom and charm quark PDFs. Final states allow to study multi-jet production, complementing the impressive LEP results by measurements in an environment with an additional important complication, namely in the presence of an object containing color: the proton. The understanding of these data will be a key to the study of LHC jet data especially at medium jet energies. Measurements of this type, together with the PDF data, allow for precision tests of QCD dynamics, e.g. to test classical approaches such as DGLAP evolution, or more sophisticated ideas, including e.g. special  $\log(1/x)$  terms, angular ordering etc. The HERA data are also instrumental in understanding double parton scattering, a phenomenon which is expected to be very important at the LHC. HERA has elevated the studies of diffraction to precision physics, and the LHC is expected to carry on that program. Finally, many tools have been developed over the last years for the analysis and understanding of HERA data, which can be adapted for future studies at the LHC.

In view of this anticipated synergy between HERA and the LHC the workshop has defined six working groups

- Parton density functions and related questions
- Multi-Jet final states and energy flows
- Heavy quarks (charm and beauty)
- Diffraction
- Cosmic Rays, HERA and the LHC
- Monte Carlo generators and tools



The *Parton Density Functions* working group had the most obvious task, namely getting to understand what the present precision - both from data and from theory- is to determine parton distributions, and what are the consequences of these uncertainties on LHC measurements. At an early stage in the workshop it became obvious that the combination of the H1 and ZEUS experiments would be very beneficial. Such lessons had been learned from LEP and are now applied at HERA. It turns out that the gain of a common analysis of the data of the two experiments on the precision of the PDFs is substantially larger than when these data-sets are used individually in fits. Benchmark test have been performed to check the systematics of the different assumptions in the QCD fit procedures, keeping certain assumptions and data sets in the fits fixed. At the start of the workshop there was some controversy on the NLO gluons at low- $x$ , being very different between different PDF fit groups. This could be resolved by measuring  $F_L$ , requiring lower energy running at HERA. The workshop has strongly supported that proposal and the last months of HERA have been used to measure  $F_L$ . First results are now being released by the experiments. Steps on getting towards common procedures to be used in the PDF fitting community and to get the most optimal PDFs are being defined and followed up in a special PDF forum called PDF4LHC, which is a spin-off of this workshop

The *Multi-Jet final states and energy flows* working group has studied in detail the novel jet algorithms, designed to be infrared and collinear safe, such as the SISCone and the (anti)- $k_T$  algorithms. Jet algorithms and performances as used in the experiments are discussed. A jet quality measure has been defined. The perturbative calculation of higher order corrections has been studied in detail and a comparison of all order analytical resummation with Monte Carlo parton shower approaches has been performed. An important issue to understand better the details of the final states in experimental data is the concept of  $k_T$  factorization. A formalism for extracting e.g. the needed unintegrated gluon distributions from fits to data is proposed. Implications for the LHC are studied e.g. on the case of gauge boson production, and boson production in association with heavy quarks. Forward so called "Mueller-Navalet" jets predictions have been made for the LHC. Very forward jet measurements opportunities e.g. using forward CASTOR detector in CMS look promising. Finally prompt photon production, high density systems and handles to multi-parton event discoveries have been discussed.

In the *Heavy Quarks (Charm and Beauty)* working group a summary of experimental results on fragmentation functions, gluon densities and charm/beauty masses from HERA has been collected. Prospects for heavy quark measurement at the LHC are discussed. In the theory area important and significant progress has been made in the understanding of heavy quark mass effects in the evolution of parton density functions. In a common contribution from members of CTEQ and MRST the progress in understanding of mass effects and its impact on the global analysis of parton density functions is reviewed and documented. In addition also progress in the calculation of fragmentation functions including mass effects is discussed. Finally the progress in calculation of higher order corrections to  $t\bar{t}$  production at the LHC is summarized.

The working group *Diffraction* brought about an important information transfer between HERA (and Tevatron) and the LHC on the experience with near beam detectors operation and calibration issues. Since the start of the workshop, there are several near beam detector projects that have been launched in the experiments. Diffractive and forward physics is now in the blood of the LHC experiments. CMS, TOTEM and ALICE present their physics program, also what can be achieved without near beam detectors by using rapidity gaps instead. Major progress has been achieved in understanding central exclusive production at  $pp$  colliders, with a tight re-evaluation of the theoretical calculations, and foremost with the exclusive measurements made at the Tevatron. Factorization in diffractive processes remains mysterious. It is known not to work between  $ep$  and  $pp$  data. Now also within  $ep$  data at HERA it is found not to work for diffractive di-jet photoproduction events. The deployment of diffractive PDFs from  $ep$  to  $pp$  data has therefore to be done with care.

In the working group *Cosmic Rays, HERA and the LHC* the impact of laboratory measurements for the understanding of the source and propagation of high energy cosmic rays has been discussed. These cosmic rays are measured mainly via air-showers and for their simulation measurements at high energy lepton hadron and hadron hadron colliders are important. The main sources of uncertainties come from cross sections (elastic and inelastic), secondary particle production and multiplicity distributions. Hadron production in the forward region especially from HERA and also the LHC can provide important constraints. On the theory side the application of perturbative QCD for the calculations, hadron production in the forward region, the relation to multi-parton interaction and non-linear effects arising at highest energies (i.e. at small

*x*) have been discussed.

The goals of working group *Monte Carlo and Tools* was to examine and improve the Monte Carlo event generators for the use at LHC, to provide a framework for tuning and to develop new tools and libraries for the analysis of data. The available Monte Carlo generators are reviewed and tools like HZtool and RIVET, tools for fitting like Professor and Proffit (in *Multi-Jet nal states and energy flows* WG) are discussed. Multiparton interaction and underlying event structures was a major issue, also in close connection with *Multi-Jet nal states and energy flows*.

The special character of this workshop was – apart from its clear charge on the connection between HERA and LHC – that it was alternative held at CERN and at DESY. Note that Tevatron was always an invited guest at the table, and its data and interpretation of the results have always been part of the input in the discussions.

The last workshop in this series was held at CERN, where the series started, and over 200 participants attended. This clearly shows that the workshop has been established to be a beacon and forum for discussions of QCD for the preparation of the LHC. With the termination of the HERA accelerator in 2007 and the turn on of the LHC, the series was terminated and the results are written up in these extensive proceedings. But clearly there is a need and community for targeted forum on LHC QCD questions, and no doubt a workshop of this kind will emerge in the near future, as soon as the first data arrive.

Finally we wish to thank all the participants of the HERA an the LHC workshops for making this series so interesting and lively. We thank especially the conveners for their enormous work in the preparation of the many meetings and finally the proceedings

Last but not least we wish to thank A. Grabowsky, D. Denise, S. Platz and L. Schmidt for their continuous help and support during all the meetings. We thank B. Liebaug for the design of the poster. We are grateful to R. Eisberg, O. Knak and S. König for recording the talks and all technical help. We thank M. Mayer, K. Sachs and M. Stein for their help in printing the proceedings. We are grateful to the CERN and DESY directorates for financial support of the workshops and for their encouragement to investigate the HERA - LHC connection in detail.

Hannes Jung and Albert De Roeck

# Contents

<b>1 WG: Parton Density Functions</b>	<b>1</b>
<b>Introduction</b>	<b>3</b>
M. Dittmar, S. Forte, A. Glazov, S. Moch G. Altarelli, J. Anderson, R. D. Ball, G. Beuf, M. Boonekamp, H. Burkhardt, F. Caola, M. Ciafaloni, D. Colferai, A. Cooper-Sarkar, A. De Roeck, L. Del Debbio, J. Feltesse, F. Gelis, J. Grebenyuk, A. Guffanti, V. Halyo, J. I. Latorre, V. Lendermann, G. Li L. Motyka, T. Petersen A. Piccione, V. Radescu, M. Rogal, J. Rojo, C. Royon, G. P. Salam, D. Šálek, A. M. Staśto, R. S. Thorne, M. Ubiali, J. A. M. Vermaseren, A. Vogt, G. Watt, C. D. White	
<b>Theoretical issues</b>	<b>8</b>
S. Moch, M. Rogal, J. A. M. Vermaseren, A. Vogt, G. Altarelli, R. D. Ball, M. Ciafaloni, D. Colferai, G. P. Salam, A. Staśto, R. S. Thorne, C. D. White, G. Beuf, F. Caola, F. Gelis, L. Motyka, Ch. Royon, D. Šálek, A. M. Staśto	
<b>Benchmarking of parton distributions and their uncertainties</b>	<b>53</b>
R. D. Ball, L. Del Debbio, J. Feltesse, S. Forte, A. Glazov, A. Guffanti, J. I. Latorre, A. Piccione, V. Radescu, J. Rojo, R. S. Thorne, M. Ubiali, G. Watt	
<b>Determination of parton distributions</b>	<b>74</b>
A. Cooper-Sarkar, A. Glazov, G. Li, J. Grebenyuk, V. Lendermann	
<b>Proton-proton luminosity, standard candles and PDFs at the LHC</b>	<b>105</b>
J. Anderson, M. Boonekamp, H. Burkhardt, M. Dittmar, V. Halyo, T. Petersen	
<b>Outlook: the PDF4LHC initiative</b>	<b>125</b>
A. De Roeck	
<b>2 WG: Multi-Jet Final States and Energy Flows</b>	<b>127</b>
<b>Introduction</b>	<b>129</b>
C.Gwenlan, . Lönnblad, E. Rodrigues, G. Zanderighi (Eds.), A. Bacchetta, A. Banfi, S. Baranov, J. Bartels, A. Bunyatyan, V. Coco, G. Corcella, M. Dasgupta, M. Deák, P.-Antoine Delsart, I.M. Dremin, F. Hautmann, S. Joseph, H. Jung, A. Knutsson, K. Kutak, A. Lipatov, G. Luisoni, S. Majhi, L. Marti, K. Müller, T. Namsoo, S. Osman, H. Perrey, G. Rodrigo, J. Rojo, Z. Rúriková, A. Sabio Vera, C. Sander, Th. Schörner-Sadenius, F. Schwennsen, G. Somogyi, G.y Soyeze, M. Strikman, M. Treccani, D. Treleani, Z. Trócsányi, B.F.L. Ward, S.A. Yost, N. Zotov	
<b>Higher-order calculations</b>	<b>132</b>
G. Zanderighi, G. Rodrigo, M. Treccani, G. Somogyi	

<b>Event shapes and resummation</b>	<b>155</b>
A. Banfi, G. Corcella, M. Dasgupta, S. Joseph G. Luisoni, S. Majhi, B.F.L. Ward, S.A. Yost	
<b>Jets and jet algorithms</b>	<b>182</b>
V. Coco, P.-Antoine D., J. Rojo, Ch. Sander, G. Soyez	
<b><math>k_{\perp}</math>-factorization and forward jets</b>	<b>205</b>
S. Baranov, J. Bartels, M. Deák, F. Hautmann, H. Jung, A. Knutsson, K. Kutak, A. Lipatov, Ch. Royon, A. Sabio Vera, F. Schwennsen, N. Zotov	
<b>HERA Results</b>	<b>240</b>
K. Müller, H. Perrey, Th. Schörner-Sadenius	
<b>Interactions at high gluon densities</b>	<b>257</b>
M. Strikman, I. M. Dremin	
<b>3 WG: Heavy Quarks (Charm and Beauty)</b>	<b>271</b>
<b>Introduction</b>	<b>272</b>
M. Cacciari, A. Dainese, A. Geiser, H. Spiesberger	
<b>Experimental study of heavy flavour production at HERA</b>	<b>274</b>
S. Boutle, J. Bracinik, A. Geiser, G. Grindhammer, A.W. Jung, P. Roloff, Z. Ruriková, M. Turcato, A. Yagües-Molina	
<b>Experimental study of heavy flavour production at RHIC and LHC</b>	<b>296</b>
M. Biasini, C. Bombonati, G.E. Bruno, E. Lytken, A. Mischke, C. Rosemann, A. Starodumov, D. Stocco, R. Wolf, M. zur Nedden	
<b>Heavy flavour production at the LHC: Theoretical Aspects</b>	<b>331</b>
Z.J. Ajaltouni, A. Banfi, S. Baranov, I. Bierenbaum, J. Blümlein, G. Corcella, M. Czakon, G. Ferrera, S. Klein, B. A. Kniehl, G. Kramer, A. Likhoded, D. A. Milstead, O. I. Piskounova, V. A. Saleev, I. Schienbein, H. Spiesberger, R.S. Thorne, W.K. Tung, G. Zanderighi, N. Zotov	
<b>4 WG: Diffraction</b>	<b>395</b>
<b>Working Group on Diffraction: Executive Summary</b>	<b>397</b>
M. Arneodo, M. Diehl, V.A. Khoze, P. Newman	
<b>Towards a Combined HERA Diffractive Deep Inelastic Scattering Measurement</b>	<b>401</b>
P. Newman, M. Ruspa	
<b>Diffractive Final States and Factorisation at HERA</b>	<b>412</b>
W. Słomiński, A. Valkárová	
<b>Leading Baryon Production at HERA</b>	<b>421</b>
W.B. Schmidke, A. Bunyatyan	
<b>Exclusive Vector Meson Production and Deeply Virtual Compton Scattering at HERA</b>	<b>427</b>
A. Bruni, X. Janssen, P. Marage	
<b>Exclusive Central Production and Diffractive W/Z Results from CDF II</b>	<b>440</b>
K. Goulianos, J. L. Pinfold	
<b>Survival probability in diffractive dijet photoproduction</b>	<b>448</b>
M. Klasen, G. Kramer	

<b>Fracture Functions at HERA and LHC</b>	<b>458</b>
F. A. Ceccopieri, L. Trentadue	
<b>Generalised parton distributions and exclusive vector meson production</b>	<b>464</b>
C. Nockles, T. Teubner	
<b>Dipole models and parton saturation in <math>ep</math> scattering</b>	<b>471</b>
L. Motyka, K. Golec-Biernat, G. Watt	
<b>Checking formalism for central exclusive production in the first LHC runs</b>	<b>482</b>
A.D. Martin, V.A. Khoze, M.G. Ryskin	
<b>Rapidity gap survival probability and total cross sections</b>	<b>488</b>
A.D. Martin, V.A. Khoze, M.G. Ryskin	
<b>Rapidity gap survival in central exclusive diffraction: Dynamical mechanisms and uncertainties</b>	<b>495</b>
M. Strikman, Ch. Weiss	
<b>Two-photon and photon-hadron interactions at the LHC</b>	<b>503</b>
J. Nystrand	
<b>Searching for the Odderon at HERA and the LHC</b>	<b>510</b>
C. Ewerz	
<b>Forward physics with CMS</b>	<b>516</b>
S. Erhan, S. Cerci, M. Grothe, J. Hollar, A. Vilela Pereira	
<b>Diffraction at TOTEM</b>	<b>527</b>
G. Antchev, P. Aspell V. Avati, M.G. Bagliesi, V. Berardi, M. Berretti, U. Bottigli, M. Bozzo, E. Brücken, A. Buzzo, F. Cafagna, M. Calicchio, M.G. Catanesi, P.L. Catastini, R. Cecchi, M.A. Ciocci, M. Deile, E. Dimovasili, K. Eggert, V. Eremin, F. Ferro, F. Garcia, S. Giani, V. Greco, J. Heino, T. Hildén, J. Kašpar, J. Kopal, V. Kandrát, K. Kurvinen, S. Lami, G. Latino, R. Lauhakangas, E. Lippmaa, M. Lokajčiček, M. Lo Vetere, F. Lucas Rodriguez, M. Macrí, G. Magazzù, M. Meucci S. Minutoli, H. Niewiadomski, E. Noschis, G. Notarnicola, E. Oliveri, F. Oljemark, R. Orava, M. Oriunno, K. Österberg, P. Palazzi, E. Pedreschi, J. Petäjäjärvi, M. Quinto, E. Radermacher, E. Radicioni, F. Ravotti, G. Rella, E. Robutti, L. Ropelewski, G. Ruggiero, A. Rummel, H. Saarikko, G. Sanguinetti, A. Santroni, A. Scribano, G. Sette, W. Snoeys, F. Spinella, P. Squillacioti, A. Ster, C. Taylor, A. Trummal, N. Turini, J. Whitmore, J. Wu	
<b>The ALFA Detector and Physics Program</b>	<b>540</b>
K. Hiller, H. Stenzel	
<b>Diffraction Physics in ALICE</b>	<b>548</b>
R. Schicker	
<b>Physics with forward FP420/FP220 tagging systems</b>	<b>557</b>
P. Bussey, P. Van Mechelen	
<b>5 WG: Cosmic Rays, HERA and the LHC</b>	<b>566</b>
<b>Introduction</b>	<b>567</b>
A. Bunyatyan, A. Cooper-Sarkar, C. Diaconu, R. Engel, C. Kiesling, K. Kutak, S. Ostapchenko, T. Pierog, T.C. Rogers, M.I. Strikman, T. Sako	

<b>Experimental results</b>	<b>582</b>
<b>Model predictions for HERA, LHC and cosmic rays</b>	<b>611</b>
<b>Summary</b>	<b>628</b>
<b>6 WG: Monte Carlo and Tools</b>	<b>630</b>
<b>Introduction to Monte Carlo models and Tools working group (WG5)</b>	<b>631</b>
P. Bartalini, S. Chekanov, S. Gieseke, F. Krauss	
<b>A multi-channel Poissonian model for multi-parton scatterings</b>	<b>635</b>
D. Treleani	
<b>Underlying events in Herwig++</b>	<b>641</b>
M. Bähr, S. Gieseke, M. H. Seymour	
<b>Multiparton Interactions at HERA</b>	<b>646</b>
H. Jung, Ll. Marti, T. Namssoo, S. Osman	
<b>Modeling the underlying event: generating predictions for the LHC</b>	<b>656</b>
A. Moares	
<b>Measurement of the Underlying Event in Jet Topologies using Charged Particle and Momentum Densities</b>	<b>663</b>
F. Ambroglini, P. Bartalini, F. Bechtel, L. Fanò, R. Field	
<b>Double-Parton-Scattering in Photon-Three-Jet Final States at the LHC</b>	<b>670</b>
F. Bechtel	
<b>Underlying Event Studies with CASTOR in the CMS Experiment</b>	<b>675</b>
Z. Rúriková, A. Bunyatyan	
<b>Direct photon production at HERA, the Tevatron and the LHC</b>	<b>681</b>
R. E. Blair, S. Chekanov, G. Heinrich, A. Lipatov, N. Zotov	
<b>Propagation of Uncertainty in a Parton Shower</b>	<b>699</b>
Ph. Stephens, A. van Hameren	
<b>Perturbative description of inclusive single hadron production at HERA</b>	<b>710</b>
S. Albino	
<b>Nonperturbative corrections from an s-channel approach</b>	<b>716</b>
F. Hautmann	
<b>Single top production in the <math>Wt</math> mode with MC@NLO</b>	<b>721</b>
Ch. White	
<b>PYTHIA 8 Status Report</b>	<b>726</b>
T. Sjöstrand	
<b>THEPEG Toolkit for High Energy Physics Event Generation</b>	<b>733</b>
L. Lönnblad	

<b>CASCADE</b>	<b>737</b>
M. Deák, H. Jung, K. Kutak	
<b>AlpGen and SHERPA in <math>Z/\gamma^* + jets</math> at LHC</b>	<b>740</b>
P. Lenzi	
<b>Generator comparison for top-pair production at CMS</b>	<b>747</b>
R. Chierici	
<b>Herwig++ Status Report</b>	<b>752</b>
M. Bähr, S. Gieseke, M.A. Gigg, D. Grellscheid, K. Hamilton, O. Latunde-Dada, S. Plätzer, P. Richardson, M.H. Seymour, A. Sherstnev, J. Tully, B.R. Webber	
<b>Forward Physics Monte Carlo (FPMC)</b>	<b>758</b>
M. Boonekamp, V. Juránek, O. Kepka, C. Royon	
<b>HEP data analysis using jHepWork and Java</b>	<b>763</b>
S. Chekanov	
<b>Tools for event generator tuning and validation</b>	<b>768</b>
A. Buckley	
<b>Prerequisites for the Validation of Experiment and Theory</b>	<b>774</b>
L. Sonnenschein	
<b>7 List of Authors</b>	<b>779</b>
<b>8 List of Participants</b>	<b>783</b>





# Chapter 1

## Working Group Parton Density Functions

### Convenors:

*M. Dittmar (ETH, Zürich, CMS),  
S. Forte (U. Milan),  
A. Glazov (DESY, H1)  
S. Moch (DESY)*



# Introduction

## CONVENERS:

*M. Dittmar*<sup>1</sup>, *S. Forte*<sup>2</sup>, *A. Glazov*<sup>3</sup>, *S. Moch*<sup>4</sup>

## CONTRIBUTING AUTHORS:

*G. Altarelli*<sup>5,6</sup>, *J. Anderson*<sup>7</sup>, *R. D. Ball*<sup>8</sup>, *G. Beuf*<sup>9</sup>, *M. Boonekamp*<sup>10</sup>, *H. Burkhardt*<sup>11</sup>,  
*F. Caola*<sup>2</sup>, *M. Ciafaloni*<sup>12</sup>, *D. Colferai*<sup>12</sup>, *A. Cooper-Sarkar*<sup>13</sup>, *A. de Roeck*<sup>14</sup>, *L. Del Debbio*<sup>8</sup>,  
*J. Feltesse*<sup>15,16</sup>, *F. Gelis*<sup>5</sup>, *J. Grebenyuk*<sup>3</sup>, *A. Guffanti*<sup>17</sup>, *V. Halyo*<sup>18</sup>, *J. I. Latorre*<sup>19</sup>,  
*V. Lendermann*<sup>20</sup>, *G. Li*<sup>21</sup>, *L. Motyka*<sup>22,23</sup>, *T. Petersen*<sup>14</sup>, *A. Piccione*<sup>2</sup>, *V. Radescu*<sup>3</sup>, *M. Rogal*<sup>4</sup>,  
*J. Rojo*<sup>2,24</sup>, *C. Royon*<sup>10</sup>, *G. P. Salam*<sup>24</sup>, *D. Šálek*<sup>25</sup>, *A. M. Staśto*<sup>26,27,28</sup>, *R. S. Thorne*<sup>29</sup>,  
*M. Ubiali*<sup>8</sup>, *J. A. M. Vermaseren*<sup>30</sup>, *A. Vogt*<sup>31</sup>, *G. Watt*<sup>29</sup>, *C. D. White*<sup>30</sup>

<sup>1</sup> Institute for Particle Physics, ETH-Zürich Hönggerberg, CH 8093 Zürich, Switzerland

<sup>2</sup> Dipartimento di Fisica, Università di Milano, INFN Sezione di Milano, Via Celoria 16, I-20133 Milan, Italy

<sup>3</sup> DESY, Notkestrasse 85, D-22603 Hamburg, Germany

<sup>4</sup> DESY, Platanenallee 6, D-15738 Zeuthen, Germany

<sup>5</sup> CERN, Department of Physics, Theory Division, CH-1211 Geneva 23, Switzerland

<sup>6</sup> Dipartimento di Fisica “E. Amaldi”, Università Roma Tre and INFN, Sezione di Roma Tre, via della Vasca Navale 84, I-00146 Rome, Italy

<sup>7</sup> School of Physics, University College Dublin, Ireland

<sup>8</sup> School of Physics, University of Edinburgh, Edinburgh EH9 3JZ, UK

<sup>9</sup> Institut de Physique Théorique, CEA-Saclay F-91191 Gif-sur-Yvette, France

<sup>10</sup> IRFU, Service de Physique des Particules, CEA-Saclay F-91191 Gif-sur-Yvette, France

<sup>11</sup> CERN-AB, CH-1211 Geneva 23, Switzerland

<sup>12</sup> Dipartimento di Fisica, Università di Firenze and INFN, Sezione di Firenze, I-50019 Sesto Fiorentino, Italy

<sup>13</sup> Department of Physics, Nuclear and Astrophysics Lab., Keble Road, Oxford, OX1 3RH, UK

<sup>14</sup> CERN-PH, CH-1211 Geneva 23, Switzerland

<sup>15</sup> IRFU, CEA-Saclay F-91191 Gif-sur-Yvette, France

<sup>16</sup> University of Hamburg, Luruper Chaussee 149, Hamburg, D-22761 Germany

<sup>17</sup> Physikalisches Institut, Albert-Ludwigs-Universität Freiburg, Hermann-Herder-Straße 3, D-79104 Freiburg i. B., Germany

<sup>18</sup> Department of Physics, Princeton University, Princeton, NJ08544, USA

<sup>19</sup> Departament d'Estructura i Constituents de la Matèria, Universitat de Barcelona, Diagonal 647, E 08028 Barcelona, Spain

<sup>20</sup> Kirchhoff-Institut für Physik, Universität Heidelberg, Im Neuenheimer Feld 227, D-69120 Heidelberg, Germany

<sup>21</sup> Laboratoire de l'Accélérateur Linéaire, Université Paris-Sud, Orsay, France

<sup>22</sup> II Institute for Theoretical Physics, University of Hamburg, Luruper Chaussee 149, Hamburg, D-22761 Germany

<sup>23</sup> Institute of Physics, Jagellonian University Reymonta 4, 30-059 Cracow, Poland

<sup>24</sup> LPTHE, UPMC – Paris 6, Paris-Diderot – Paris 7, CNRS UMR 7589, F-75005 Paris, France

<sup>25</sup> Institute of Particle and Nuclear Physics, Charles University, Prague, Czech Republic

<sup>26</sup> Physics Department, Penn State University, 104 Davey Laboratory, University Park, PA 16802, USA

<sup>27</sup> H. Niewodniczański Institute of Nuclear Physics, Polish Academy of Science, ul.Radzikowskiego 152, 31-342 Cracow, Poland

<sup>28</sup> Brookhaven National Laboratory, Upton, NY-11073, USA

<sup>29</sup> Department of Physics and Astronomy, University College, London, WC1E 6BT, UK

<sup>30</sup> NIKHEF Theory Group, Kruislaan 409, NL 1098 SJ Amsterdam, The Netherlands

<sup>31</sup> Department of Mathematical Sciences, University of Liverpool, Liverpool, L69 3BX, UK

**Abstract**

We provide an assessment of the state of the art in various issues related to experimental measurements, phenomenological methods and theoretical results relevant for the determination of parton distribution functions (PDFs) and their uncertainties, with the specific aim of providing benchmarks of different existing approaches and results in view of their application to physics at the LHC.

We discuss higher order corrections, we review and compare different approaches to small  $x$  resummation, and we assess the possible relevance of parton saturation in the determination of PDFs at HERA and its possible study in LHC processes. We provide various benchmarks of PDF fits, with the specific aim of studying issues of error propagation, non-gaussian uncertainties, choice of functional forms of PDFs, and combination of data from different experiments and different processes. We study the impact of combined HERA (ZEUS-H1) structure function data, their impact on PDF uncertainties, and their implications for the computation of standard candle processes, and we review the recent  $F_L$  determination at HERA. Finally, we compare and assess methods for luminosity measurements at the LHC and the impact of PDFs on them.

With the start of data-taking at the LHC getting closer, the importance of a detailed understanding of the physics of parton distributions (PDFs) has increased considerably, along with the awareness of the LHC community for the importance of the issues related to it. Clearly, the main reason why PDFs are important at the LHC is that at a hadron collider a detailed understanding of PDFs is needed in order to obtain accurate predictions for both signal and background processes. Indeed, for many physical processes at the LHC, PDFs are the dominant source of uncertainty. On the other hand, an accurate control of PDF uncertainties allows one to use selected processes as “standard candles”, for instance in the determination of luminosities. However, this also means that experimentation at the LHC will provide a considerable amount of new experimental information on PDFs, and it will enable us to test the adequacy of their current theoretical understanding.

The main aim of this document is to provide a state of the art assessment of our understanding of PDFs at the dawn of the LHC. Since the previous HERA-LHC workshop [1], we have witnessed several important directions of progress in the physics of PDFs. On the theoretical side there has been conclusive progress in extending the treatment of perturbative QCD beyond the current default, namely, the next-to-leading perturbative order. On the phenomenological side there has been a joint effort between experimental and theoretical groups involved in the extraction of PDFs, specifically from global fits, in agreeing on common procedures, benchmarks and standards. On the experimental side, new improved results from the HERA runs are being finalized: these include both the construction of a joint determination of structure function which combines the result of the ZEUS and H1 experiments, and the first direct measurements of the structure function  $F_L$  which have been made possible by running HERA at a reduced proton beam energy in 2007. Also, the LHC experiments (ATLAS, CMS and LHCb) are now assessing

the use of standard candle processes for luminosity measurements.

All these issues are discussed in this document. In each case, our main goal has been to provide as much as possible a joint treatment by the various groups involved, as well as a comparison of different approaches and benchmarking of results. In particular, in Sect. [2], after briefly reviewing (Sect. [3]) the current status of higher-order calculations for DIS, we provide (Sect. [4]) detailed comparisons of techniques and results of different existing approaches to small  $x$  resummation, and then we summarize (Sect. [5]) the current status of studies of parton saturation at HERA, their possible impact on current PDF extraction and the prospects of future studies at the LHC. In Sect. [6] we discuss methods and results for the benchmarking of PDF fits: with specific reference to two benchmark fits based on a common agreed set of data, we discuss issues related to error propagation and non-gaussian errors, to the choice of functional form and corresponding bias, to possible incompatibilities between different data sets. In Sect. [7] we turn to recent progress in the extraction of PDFs from HERA data, specifically the impact of combined ZEUS-H1 structure function data on PDF determination and the ensuing calculation of  $W$  and  $Z$  cross-sections (Sect. [8]) and the recent first determination of the structure function  $F_L$  (Sect. [9]). In Sect. [10] we discuss and compare luminosity measurements based on absolute proton-proton luminosity measurements to those based on the use of standard candle processes, and the impact on all of them of PDF uncertainties. Finally, in Sect. [11] we present the PDF4LHC initiative, which will provide a framework for the continuation of PDF studies for the LHC.

*Note:* Most of the contributions to this workshop are the result of collaboration between various groups. The common set of authors given for each section or subsection has read and approved the entire content of that section or subsection; however, when a subset of these authors is given for a specific part of the section or subsection, they are responsible for it.

## ACKNOWLEDGEMENTS

This work was supported in part by the following grants and agencies: the European network HEPTOOLS under contract MRTN-CT-2006-035505; ANR-05-JCJC-0046-01 (France) PRIN-2006 (Italy); MEC FIS2004-05639-C02-01; (Spain) and the Scottish Universities Physics Alliance (UK).

## References

- [1] M. Dittmar *et al.*, *Parton distributions: Summary report for the HERA - LHC workshop*. Preprint hep-ph/0511119, 2005.
- [2] S. Moch et al, *Theoretical issues*. These proceedings.
- [3] S. Moch et al, *Precision calculations for inclusive dis: an update*. These proceedings.
- [4] G. Altarelli et al, *Small  $x$  resummation*. These proceedings.
- [5] G. Beuf et al, *Parton saturation and geometric scaling*. These proceedings.
- [6] R. D. Ball et al, *Benchmarking of parton distributions and their uncertainties*. These proceedings.

- [7] A. Cooper-Sarkar et al, *Determination of parton distributions*. These proceedings.
- [8] A. Cooper-Sarkar, A. Glazov, G. Li, *Extraction of the proton pdfs from a combined fit of  $hI$  and  $zeus$  inclusive dis cross sections*. These proceedings.
- [9] J. Grebenyuk, V. Lendermann, *Measurements of the proton structure function  $f_1$  at hera*. These proceedings.
- [10] J. Anderson et al , *Proton–proton luminosity, standard candles and pdfs at the  $lhc$* . These proceedings.
- [11] A. de Roeck, *Outlook: the pdf4lhc initiative*. These proceedings.

# Theoretical issues

*S. Moch, M. Rogal, J. A. M. Vermaseren, A. Vogt, G. Altarelli, R. D. Ball, M. Ciafaloni, D. Colferai, S. Forte, G. P. Salam, A. Staśto, R. S. Thorne, C. D. White, G. Beuf, F. Caola, F. Gelis, L. Motyka, C. Royon, D. Šálek, A. M. Staśto*

## 1 Precision calculations for inclusive DIS: an update<sup>1</sup>

With high-precision data from HERA and in view of the outstanding importance of hard scattering cross sections at the LHC, a quantitative understanding of deep-inelastic processes is indispensable, necessitating calculations beyond the standard next-to-leading order of perturbative QCD.

In this contribution we briefly discuss the recent extension of the three-loop calculations for inclusive deep-inelastic scattering (DIS) [1–8] to the complete set of coefficient functions for the charged-current (CC) case. The new third-order expressions are too lengthy for this short overview. They can be found in Refs. [9, 10] together with the calculational methods and a more detailed discussion. Furthermore the reader is referred to Refs. [11, 12] for our first results on the three-loop splitting functions for the evolution of helicity-dependent parton distributions.

Structure functions in inclusive deep-inelastic scattering are among the most extensively measured observables. The combined data from fixed-target experiments and the HERA collider spans about four orders of magnitude in both Bjorken- $x$  variable and the scale  $Q^2 = -q^2$  given by the momentum  $q$  of the exchanged electroweak gauge boson [13]. Here we consider the  $W$ -exchange charged-current case, see Refs. [14–20] for recent data from neutrino DIS and HERA. With six structure functions,  $F_2^{W^\pm}$ ,  $F_3^{W^\pm}$  and  $F_L^{W^\pm}$ , this case has a far richer structure than, for example, electromagnetic DIS with only two independent observables,  $F_2$  and  $F_L$ .

Even taking into account a forthcoming combined H1/ZEUS final high- $Q^2$  data set from HERA, more detailed measurements are required to fully exploit the resulting potential, for instance at a future neutrino factory, see Ref. [21], and the LHeC, the proposed high-luminosity electron-proton collider at the LHC [22]. Already now, however, CC DIS provides important information on the parton structure of the proton, e.g., its flavour decomposition and the valence-quark distributions. Moreover, present results are also sensitive to electroweak parameters of the Standard Model such as  $\sin^2 \theta_W$ , see Ref. [23], and the space-like  $W$ -boson propagator [24]. As discussed, for example, in Refs. [25–28], a reliable determination of  $\sin^2 \theta_W$  from neutrino DIS requires a detailed understanding of non-perturbative and perturbative QCD effects.

Previous complete results on unpolarized DIS include the three-loop splitting functions [4, 5] as well as the 3-loop coefficient functions for the photon-exchange structure functions  $F_{2,L}$  [6, 7]. However, most coefficient functions for CC DIS were not fully computed to three loops so far.

For this case it is convenient to consider linear combinations of the structure functions  $F_a^{W^\pm}$  with simple properties under crossing, such as  $F_a^{\nu p \pm \bar{\nu} p}$  ( $a = 2, 3, L$ ) for neutrino DIS.

---

<sup>1</sup>Contributing authors: S. Moch, M. Rogal, J. A. M. Vermaseren, A. Vogt



For all these combinations either the even or odd moments can be calculated in Mellin- $N$  space in the framework of the operator product expansion (OPE), see Ref. [29]. The results for the third-order coefficient functions for the even- $N$  combinations  $F_{2,L}^{\nu p+\bar{\nu}p}$  can be taken over from electromagnetic DIS [6, 7]. Also the coefficient function for the odd- $N$  based charged-current structure function  $F_3^{\nu p+\bar{\nu}p}$  is completely known at three-loop accuracy, with the results only published via compact parameterizations so far [8]. For the remaining combinations  $F_{2,L}^{\nu p-\bar{\nu}p}$  and  $F_3^{\nu p-\bar{\nu}p}$ , on the other hand, only recently the first six odd or even integer moments of the respective coefficient functions have been calculated to third order in Ref. [9] following the approach of Refs. [1–3] based on the MINCER program [30, 31].

The complete results of Refs. [6–8] fix all even and odd moments  $N$ . Hence already the present knowledge of fixed Mellin moments for  $F_{2,L}^{\nu p-\bar{\nu}p}$  and  $F_3^{\nu p-\bar{\nu}p}$  is sufficient to determine also the lowest six moments of the differences of corresponding even- $N$  and odd- $N$  coefficient functions and to address a theoretical conjecture [32] for these quantities, see Ref. [10]. Furthermore these moments facilitate  $x$ -space approximations in the style of, e.g. Ref. [33] which are sufficient for most phenomenological purposes, including the determination of the third-order QCD corrections to the Paschos-Wolfenstein relation [34] used for the extraction of  $\sin^2 \theta_W$  from neutrino DIS.

The even-odd differences of the CC coefficient functions  $C_a$  for  $a = 2, 3, L$  can be defined by

$$\delta C_{2,L} = C_{2,L}^{\nu p+\bar{\nu}p} - C_{2,L}^{\nu p-\bar{\nu}p}, \quad \delta C_3 = C_3^{\nu p-\bar{\nu}p} - C_3^{\nu p+\bar{\nu}p}. \quad (1)$$

The signs are chosen such that the differences are always ‘even – odd’ in the moments  $N$  accessible by the OPE [29], and it is understood that the  $d^{abc}d_{abc}$  part of  $C_3^{\nu p+\bar{\nu}p}$  [3, 8] is removed before the difference is formed. With  $a_s = \alpha_s/(4\pi)$  these non-singlet quantities can be expanded as

$$\delta C_a = \sum_{l=2} a_s^l \delta c_a^{(l)}. \quad (2)$$

There are no first-order contributions to these differences, hence the above sums start at  $l = 2$ .

We start the illustration of these recent results by looking at the approximations for the  $\nu p - \bar{\nu}p$  odd- $N$  coefficient functions  $c_{2,L}^{(3)}(x)$  (see Ref. [10] for a detailed discussion). These are compared in Fig. 1 to their exact counterparts [6, 7] for the even- $N$  non-singlet structure functions. The dashed lines represent the uncertainty band due to the limited number of known moments. The third-order even-odd differences remain noticeable to larger values of  $x$  than at two loops, e.g., up to  $x \simeq 0.3$  for  $F_2$  and  $x \simeq 0.6$  for  $F_L$  for the four-flavour case shown in the figure. The moments  $N = 1, 3, \dots, 9$  constrain  $\delta c_{2,L}^{(3)}(x)$  very well at  $x \gtrsim 0.1$ , and approximately down to  $x \approx 10^{-2}$ .

Concerning low values of Bjorken- $x$  one should recall that the uncertainty bands shown by the dashed lines in Fig. 1 do not directly indicate the range of applicability of these approximations, since the coefficient functions enter observables only via smoothening Mellin convolutions with non-perturbative initial distributions. In Fig. 2 we therefore present the convolutions of all six third-order CC coefficient functions with a characteristic reference distribution. It turns

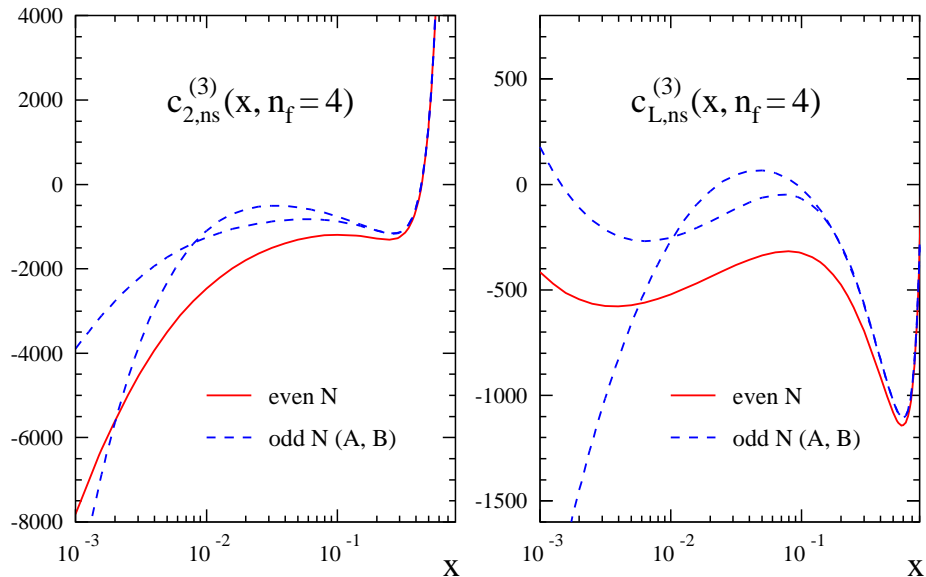


Fig. 1: The exact third-order coefficient functions of the even- $N$  structure functions  $F_{2,L}^{\nu p + \bar{\nu} p}$  for four massless flavours, and the approximate odd-moment quantities for  $\nu p - \bar{\nu} p$  combination.

out that the approximations of the previous figure can be sufficient down to values even below  $x = 10^{-3}$ , which is amply sufficient for foreseeable applications to data. The uncertainty of  $\delta c_3^{(3)}(x)$ , on the other hand, becomes relevant already at larger values,  $x \lesssim 10^{-2}$ , as the lowest calculated moment of this quantity,  $N = 2$ , has far less sensitivity to the behaviour at low  $x$ .

The three-loop corrections to the non-singlet structure functions are rather small even well below the  $x$ -values shown in the figure – recall our small expansion parameter  $\alpha_s$ : the third-order coefficient are smaller by a factor  $2.0 \cdot 10^{-3}$  if the expansion is written in powers of  $\alpha_s$ . Their sharp rise for  $x \rightarrow 1$  is understood in terms of soft-gluon effects which can be effectively resummed, if required, to next-to-next-to-next-to-leading logarithmic accuracy [35]. Our even-odd differences  $\delta c_a^{(3)}(x)$ , on the other hand, are irrelevant at  $x > 0.1$  but have a sizeable impact at smaller  $x$  in particular on the corrections for  $F_2$  and  $F_L$ . The approximate results for  $\delta c_a^{(3)}(x)$  facilitate a first assessment of the perturbative stability of the even-odd differences (1). In Fig. 3 we illustrate the known two orders for  $F_2$  and  $F_L$  for  $\alpha_s = 0.25$  and  $n_f = 4$  massless quark flavours, employing the same reference quark distribution as in Fig. 2.

Obviously our new  $\alpha_s^3$  corrections are important wherever these coefficient-function differences are non-negligible. On the other hand, our results confirm that these quantities are very small, and thus relevant only when a high accuracy is required. These conditions are fulfilled for the calculation of QCD corrections for the so-called Paschos-Wolfenstein relation. This relation is defined in terms of a ratio of neutral-current and charged-current cross sections for neutrino-nucleon DIS [34],

$$R^- = \frac{\sigma(\nu_\mu N \rightarrow \nu_\mu X) - \sigma(\bar{\nu}_\mu N \rightarrow \bar{\nu}_\mu X)}{\sigma(\nu_\mu N \rightarrow \mu^- X) - \sigma(\bar{\nu}_\mu N \rightarrow \mu^+ X)}. \quad (3)$$

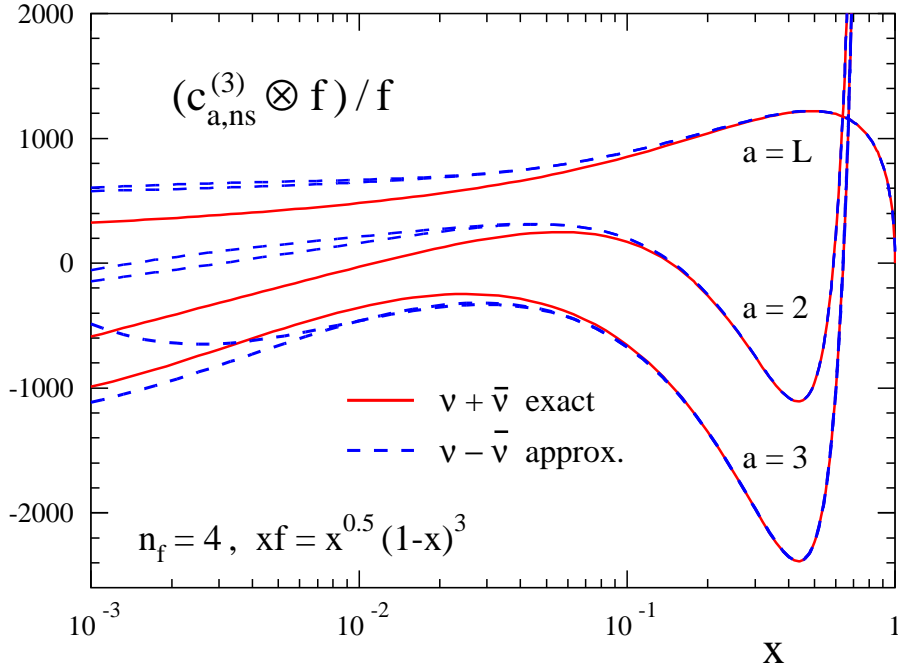


Fig. 2: Convolution of the six third-order CC coefficient functions for  $F_{2,3,L}$  in  $\nu p + \bar{\nu} p$  and  $\nu p - \bar{\nu} p$  DIS with a schematic but typical non-singlet distribution  $f$ . All results have been normalized to  $f(x)$ , suppressing the large but trivial variation of the absolute convolutions.

The asymmetry  $R^-$  directly measures  $\sin^2 \theta_W$  if the up and down valence quarks in the target carry equal momenta, and if the strange and heavy-quark sea distributions are charge symmetric. Beyond the leading order this asymmetry can be presented as an expansion in  $\alpha_s$  and inverse powers of the dominant isoscalar combination  $u^- + d^-$ , where  $q^- = \int_0^1 dx x (q(x) - \bar{q}(x))$  is the second Mellin moment of the valence quark distributions. Using the results for differences  $\delta c_a^{(3)}(x)$ ,  $a = 2, L, 3$  one can present it in a numeric form,

$$R^- = \frac{1}{2} - \sin^2 \theta_W + \frac{u^- - d^- + c^- - s^-}{u^- + d^-} \left\{ 1 - \frac{7}{3} \sin^2 \theta_W + \left( \frac{1}{2} - \sin^2 \theta_W \right) \cdot \right. \\ \left. \frac{8}{9} \frac{\alpha_s}{\pi} \left[ 1 + 1.689 \alpha_s + (3.661 \pm 0.002) \alpha_s^2 \right] \right\} + \mathcal{O}((u^- + d^-)^{-2}) + \mathcal{O}(\alpha_s^4), \quad (4)$$

where the third term in the square brackets is determined by the  $\alpha_s^3$  corrections  $\delta c_a^{(3)}(x)$ ,  $a = 2, L, 3$ . The perturbation series in the square brackets appears reasonably well convergent for relevant values of the strong coupling constant, with the known terms reading, e.g.,  $1 + 0.42 + 0.23$  for  $\alpha_s = 0.25$ . Thus the  $\alpha_s^2$  and  $\alpha_s^3$  contributions correct the NLO estimate by 65% in this case. On the other hand, due to the small prefactor of this expansion, the new third-order term increases the complete curly bracket in Eq. (4) by only about 1%, which can therefore be considered as the new uncertainty of this quantity due to the truncation of the perturbative expansion. Consequently previous NLO estimates of the effect of, for instance, the (presumably

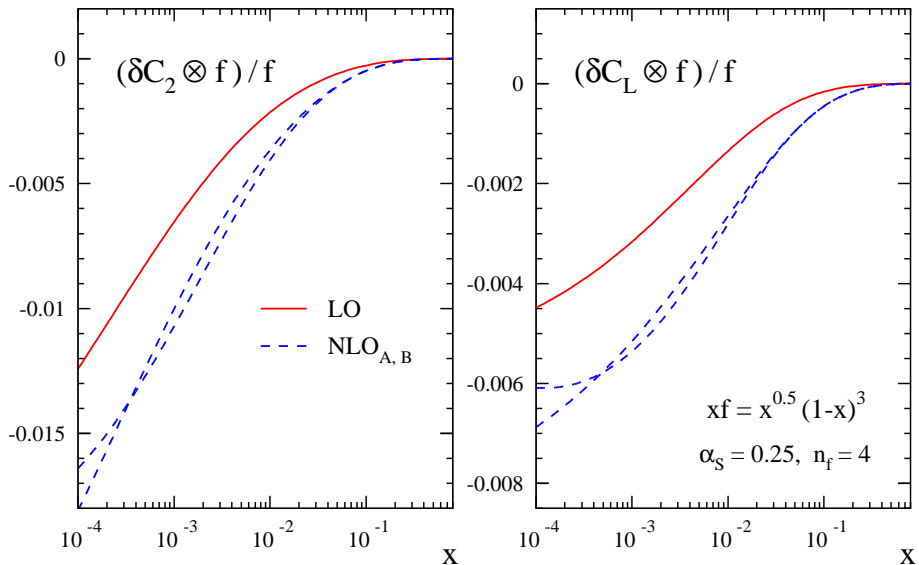


Fig. 3: The first two approximations, denoted by LO and NLO, of the differences (1) for  $F_2$  and  $F_L$  in charged-current DIS. The results are shown for representative values of  $\alpha_s$  and  $n_f$  after convolution with the reference distribution  $f(x)$  also employed in Fig. 2. The dashed curves correspond to the two approximation uncertainties for the new  $\alpha_s^3$  contributions.

mainly non-perturbative, see Refs. [36–38]) charge asymmetry of the strange sea remain practically unaffected by higher-order corrections to the coefficient functions.

To summarize, we have extended the fixed- $N$  three-loop calculations of inclusive DIS [1–3] to all charged-current cases not covered by the full (all- $N$ ) computations of Refs. [6–8]. The region of applicability of these new results is restricted to Bjorken- $x$  values above about  $10^{-3}$ , a range amply sufficiently for any fixed-target or collider measurements of those charged-current structure functions in the foreseeable future. Except for the longitudinal structure function  $F_L$ , the present coefficient functions are part of the next-to-next-to-next-to-leading order ( $N^3$ LO) approximation of massless perturbative QCD. Analyses at this order are possible outside the small- $x$  region since the corresponding four-loop splitting functions will have a very small impact here, cf. Ref. [39].

## 2 Small $x$ resummation <sup>2</sup>

The splitting functions which govern the evolution of the parton distributions (PDFs), together with the hard cross sections which relate those partons to hadronic physical observables, are potentially unstable at high energy due to logarithmically enhanced contributions. In particular, parametrizing observables such as deep-inelastic structure (DIS) functions or Drell-Yan (DY) or Higgs production cross section in hadronic collisions in terms of a dimensionful scale  $Q^2$  (photon virtuality or invariant mass of the final state in DIS and DY respectively) and a dimensionless ratio

<sup>2</sup>Contributing authors: G. Altarelli, R. D. Ball, M. Ciafaloni, D. Colferai, S. Forte, G. P. Salam, A. Stařto, R. S. Thorne, C. D. White

$x$  (the Bjorken variable or  $\frac{Q^2}{s}$  in DIS and DY respectively), when  $x \rightarrow 0$  there are logarithmically enhanced contributions to the perturbation expansion of the form  $x^{-1} \alpha_s^n(Q^2) \log^m(1/x)$  ( $n \geq m - 1$ ). When  $x$  is sufficiently small, one must resum such terms, reordering the perturbation expansion in terms of leading logarithmic (LL) terms followed by next-to-leading logarithmic (NLL) terms and so on.

The problem can be traced to ladders of  $t$ -channel gluon exchanges at LL order, with some quark mixing at NLL order and beyond. The underlying framework for the resummation procedure is the BFKL equation [40, 41], an integral equation for the unintegrated gluon  $f(k^2, Q_0^2)$  that is currently known up to full NLL order [42–44], and approximate NNLL order [45]. This has the schematic form (up to NLL):

$$Nf(k^2, Q_0^2) = Nf_I(Q_0^2) + \bar{\alpha}_S(k^2) \int dk'^2 \left[ \mathcal{K}_0(k^2, k'^2, Q_0^2) + \bar{\alpha}_S(k^2) \mathcal{K}_1(k^2, k'^2, Q_0^2) \right] f(k'^2), \quad (5)$$

where  $f_I(Q_0^2)$  is a non-perturbative initial condition at some initial scale  $Q_0$ ,  $\bar{\alpha}_S = 3\alpha_S/\pi$  and  $\mathcal{K}_{0,1}$  are the LL and NLL BFKL kernels. Different choices for the argument of the running coupling are possible, leading to accordingly modified  $\mathcal{K}_1$  [46, 47].

The solution of the BFKL equation can be used to extract leading and subleading singular contributions to singlet DGLAP splitting functions. The BFKL equation can either be solved numerically in its form given by Eq. (5), or else analytically by performing a double Mellin transform with respect to  $x$  and  $k^2$ :

$$f(\gamma, N) = \int_0^\infty (k^2)^{-\gamma-1} \int_0^1 dx x^N f(x, k^2), \quad (6)$$

whereby the BFKL equation becomes a differential equation, with kernels  $\chi_{0,1}(\gamma)$  defined respectively as the Mellin transforms of  $\mathcal{K}_{0,1}$ . Furthermore, by using the  $k_t$ -factorisation theorem [48], one may determine leading small  $x$  contributions to all orders to hard partonic cross sections for physical processes such as heavy quark electroproduction [48] and deep-inelastic scattering [49]. Approximate subleading results are also available [50, 51].

These results for splitting functions and hard partonic cross sections can then be combined with fixed-order results to obtain resummed predictions for physical observables. However, it has now been known for some time that the LL BFKL equation is unable to describe scattering data well, even when matched to a fixed order expansion. Any viable resummation procedure must then, at the very least, satisfy the following requirements:

1. Include a stable solution to the BFKL equation with running coupling up to NLL order.
2. Match to the standard DGLAP description at moderate and high  $x$  values (where this is known to describe data well).
3. Provide the complete set of splitting and coefficient functions for  $F_2$  and  $F_L$  in a well defined factorisation scheme.

Over the past few years, three approaches have emerged which, to some extent, aim at fulfilling these conditions. Here we call these the ABF [52–59], CCSS [47, 60–66] and TW [67–72] approaches. In the ABF scheme all three requirements are met, and resummed splitting functions in the singlet sector have been determined. Furthermore, a complete control of the

scheme dependence at the resummed level has been achieved, thereby allowing for a consistent determination of resummed deep-inelastic coefficient functions, and thus of resummed structure functions. However, the results obtained thus have not been fit to the data yet. In the CCSS formalism, resummed splitting functions have also been determined. However, results are given in a scheme which differs from the  $\overline{\text{MS}}$  scheme at the resummed level; furthermore, resummed coefficient functions and physical observables haven't been constructed yet. The TW approach, instead, has already been compared to the data in a global fit. However, this approach makes a number of simplifying assumptions and the ensuing resummation is thus not as complete as that which obtains in other approaches: for example, this approach does not include the full collinear resummation of the BFKL kernel.

A comparison of resummed splitting functions and solution of evolution equations determined in the ABF and CCSS approaches with  $n_f = 0$  was presented in Ref. [73]; the main features and differences of these approaches were also discussed. Here, we extend this comparison to the case of  $n_f \neq 0$  resummation, and also to the TW approach. First, we will briefly summarize the main features of each approach, and in particular we display the matrix of splitting functions determined in the ABF and CCSS approaches. Then, we will compare  $K$ -factors for physical observables determined using the ABF and TW approach.

Note that there are some difference in notations between various groups, which are retained here in order to simplify comparison to the original literature. In particular, the variable  $N$  in Eq. (6) will be referred to as  $\omega$  in the CCS approach of Section 2.2, and the variable  $\gamma$  in the same equation will be referred to as  $M$  in the ABF approach of Section 2.1.

## 2.1 The Altarelli-Ball-Forte (ABF) Approach

In the ABF approach [52–59, 74–77] one concentrates on the problem of obtaining an improved anomalous dimension (splitting function) for DIS which reduces to the ordinary perturbative result at large  $N$  (large  $x$ ), thereby automatically satisfying renormalization group constraints, while including resummed BFKL corrections at small  $N$  (small  $x$ ), determined through the renormalization-group improved (i.e. running coupling) version of the BFKL kernel. The ordinary perturbative result for the singlet anomalous dimension is given by:

$$\gamma(N, \alpha_s) = \alpha_s \gamma_0(N) + \alpha_s^2 \gamma_1(N) + \alpha_s^3 \gamma_2(N) + \dots \quad (7)$$

The BFKL corrections at small  $N$  (small  $x$ ) are determined by the BFKL kernel  $\chi(M, \alpha_s)$ :

$$\chi(M, \alpha_s) = \alpha_s \chi_0(M) + \alpha_s^2 \chi_1(M) + \dots, \quad (8)$$

which is the Mellin transform, with respect to  $t = \ln \frac{k^2}{k_0^2}$ , of the  $N \rightarrow 0$  angular averaged BFKL kernel.

The ABF construction is based on three ingredients.

1. *The duality relation* between the kernels  $\chi$  and  $\gamma$

$$\chi(\gamma(N, \alpha_s), \alpha_s) = N, \quad (9)$$

which is a consequence of the fact that at fixed coupling the solutions of the BFKL and DGLAP equations should coincide at leading twist [52, 74, 78]. By using duality, one

can use the perturbative expansions of  $\gamma$  and  $\chi$  in powers of  $\alpha_s$  to improve (resum) each other: by combining them, one obtains a "double leading" (DL) expansion which includes all leading (and subleading, at NLO) logs of  $x$  and  $Q^2$ . In particular, the DL expansion automatically resums the collinear poles of  $\chi$  at  $M = 0$ . This eliminates the alternating sign poles  $+1/M, -1/M^2, \dots$  that appear in  $\chi_0, \chi_1, \dots$ , and make the perturbative expansion of  $\chi$  unreliable. This result is a model independent consequence of momentum conservation  $\gamma(1, \alpha_s) = 0$ , whence, by duality:

$$\chi(0, \alpha_s) = 1. \quad (10)$$

2. *The symmetry of the BFKL kernel* upon gluon interchange. In Mellin space, this symmetry implies that at the fixed-coupling level the kernel  $\chi$  for evolution in  $\ln \frac{s}{k k_0}$  must satisfy  $\chi(M) = \chi(1 - M)$ . By exploiting this symmetry, one can use the collinear resummation of the region  $M \sim 0$  which was obtained using the double-leading expansion to also improve the BFKL kernel in the anti-collinear  $M \simeq 1$  region. This leads to a symmetric kernel which is an entire function for all  $M$ , and has a minimum at  $M = \frac{1}{2}$ . The symmetry is broken by the DIS choice of variables  $\ln \frac{1}{x} = \ln \frac{s}{Q^2}$  and by the running of the coupling; however these symmetry breaking contribution can be determined exactly. This then leads to a stable resummed expansion of the resummed anomalous dimension at the fixed coupling level.
3. *The running-coupling resummation* of the BFKL solution. Whereas running coupling corrections to evolution equations are automatically included when solving the DGLAP evolution equation with resummed anomalous dimensions, the duality relation Eq. (9) itself undergoes corrections when the running coupling is included in the BFKL equation (5). Running coupling corrections can then be derived order by order, and turn out to be affected by singularities in Mellin  $M$  space. This implies that after Mellin inversion the associate splitting functions is enhanced as  $x \rightarrow 0$ : their contribution grows as  $(\alpha_s \beta_0 \ln \frac{1}{x})^n$  with the perturbative order. However the series of leading enhanced contribution can be summed at all orders in closed form, because it corresponds to the asymptotic expansion in powers of  $\alpha_s$  of the solution to the running coupling BFKL equation (5) when the kernel  $\chi$  is approximated quadratically about its minimum. This exact solution can be expressed in terms of Airy functions [53, 79] when the kernel is linear in  $\alpha_s$  and in terms of Bateman [55] functions for generic kernels. Because both the exact solution and its asymptotic expansion are known, this BFKL running coupling resummation can be combined with the DGLAP anomalous dimension, already resummed at the BFKL fixed coupling level, with full control of overlap (double counting terms). Schematically, the result has the following form:

$$\begin{aligned} \gamma_{\Sigma NLO}^{rc}(\alpha_s(t), N) &= \gamma_{\Sigma NLO}^{rc, pert}(\alpha_s(t), N) + \gamma^B(\alpha_s(t), N) - \gamma_s^B(\alpha_s(t), N) \\ &\quad - \gamma_{ss}^B(\alpha_s(t), N) - \gamma_{ss,0}^B(\alpha_s(t), N) + \gamma_{\text{match}}(\alpha_s(t), N) + \gamma_{\text{mom}}(\alpha_s(t), N), \end{aligned} \quad (11)$$

where  $\gamma_{\Sigma NLO}^{rc, pert}(\alpha_s(t), N)$  contains all terms which are up to NLO in the double-leading expansion of point 1, symmetrized as discussed in point 2 above so that its dual  $\chi$  has a minimum;  $\gamma^B(\alpha_s(t), N)$  resums the series of singular running coupling corrections using the aforementioned exact BFKL solution in terms of a Bateman function;  $\gamma_s^B(\alpha_s(t), N)$ ,



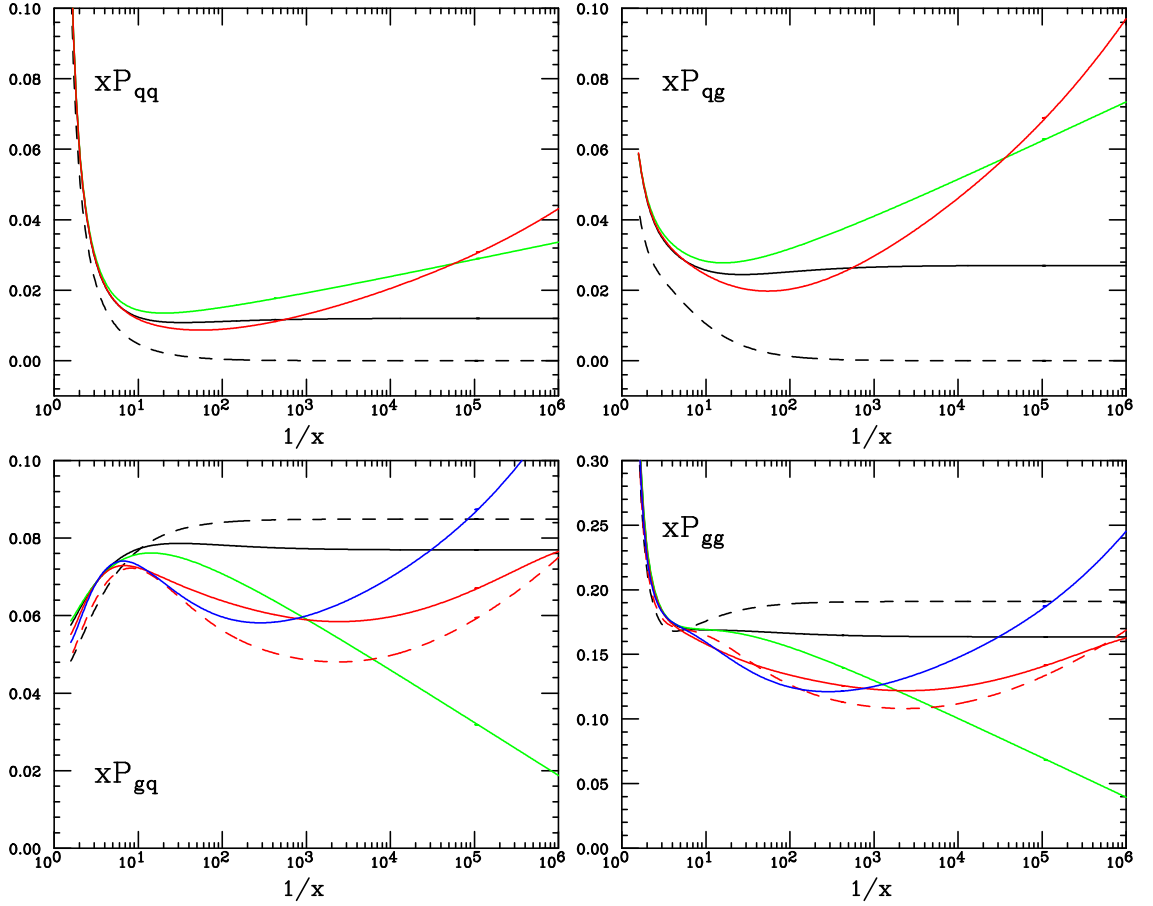


Fig. 4: The resummed splittings functions  $P_{qq}$ ,  $P_{qg}$ ,  $P_{gq}$  and  $P_{gg}$  in the ABF approach, all for  $n_f = 4$  and  $\alpha_s = 0.2$ : LO DGLAP (dashed black), NLO DGLAP (solid black), NNLO DGLAP (solid green), LO resummed (red dashed), NLO resummed in the  $Q_0\overline{\text{MS}}$  scheme (red) and in the  $\overline{\text{MS}}$  scheme (blue).

$\gamma_{ss}^B(\alpha_s(t), N)$   $\gamma_{ss,0}^B(\alpha_s(t), N)$  are double counting subtractions between the previous two contributions;  $\gamma_{\text{mom}}$  subtracts subleading terms which spoil exact momentum conservation;  $\gamma_{\text{match}}$  subtracts any contribution which deviates from NLO DGLAP and at large  $N$  doesn't drop at least as  $\frac{1}{N}$ .

The anomalous dimension obtained through this procedure has a simple pole as a leading small- $N$  (i.e. small  $x$ ) singularity, like the LO DGLAP anomalous dimension. The location of the pole is to the right of the DGLAP pole, and it depends on the value of  $\alpha_s$ . Thanks to the softening due to running of the coupling, this value is however rather smaller than that which corresponds to the leading BFKL singularity: for example, for  $\alpha_s = 0.2$ , when  $n_f = 0$  the pole is at  $N = 0.17$ .

The splitting function obtained by Mellin inversion of the anomalous dimension eq. (11)



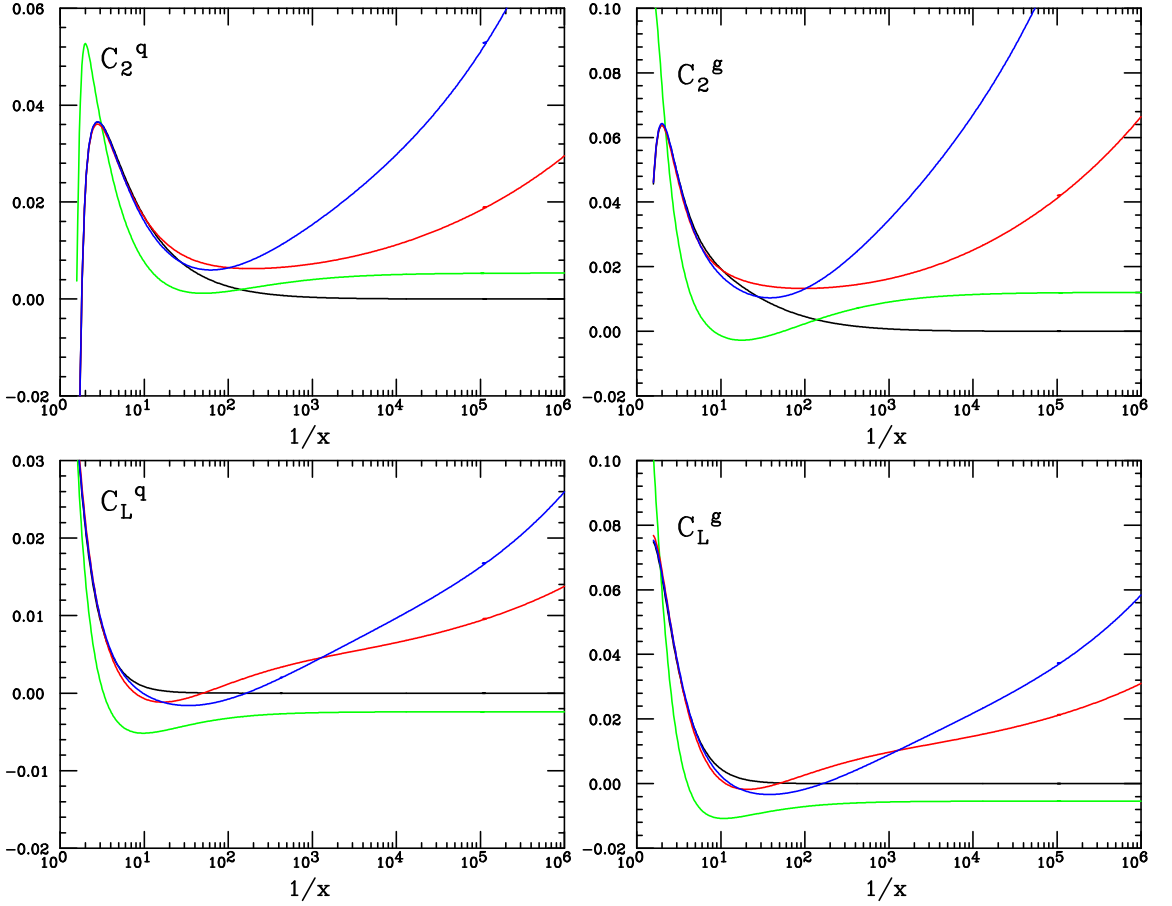


Fig. 5: The resummed DIS coefficient functions  $C_{2q}$ ,  $C_{2g}$ ,  $C_{Lq}$  and  $C_{Lg}$  in the ABF approach, all for  $n_f = 4$  and  $\alpha_s = 0.2$ . The curves are labelled as in the previous figure.

turns out to agree at the percent level to that obtained by the CCSS group by numerical resolution of the BFKL equation for all  $x \lesssim 10^{-2}$ ; for larger values of  $x$  (i.e. in the matching region) the ABF result is closer to the NLO DGLAP result.

In order to obtain a full resummation of physical observables, specifically for deep-inelastic scattering, the resummation discussed so far has to be extended to the quark sector and to hard partonic coefficients. This, on top of various technical complications, requires two main conceptual steps:

- A factorization scheme must be defined at a resummed level. Because only one of the two eigenvectors of the matrix of anomalous dimensions is affected by resummation, once a scheme is chosen, the resummation discussed above determines entirely the two-by-two matrix of splitting functions in the singlet sector. The only important requirement is that the relation of this small  $x$  scheme choice to standard large  $x$  schemes be known exactly,

since this enables one to combine resummed results with known fixed order results.

- PDFs evolved using resummed evolution equations must be combined with resummed coefficient functions. These are known, specifically for DIS [49], but are also known [80] to be affected by singularities, analogous to the running coupling singularities of the resummed anomalous dimension discussed above, which likewise must be resummed to all orders [57]. This running coupling resummation of the coefficient function significantly softens the small  $x$  growth of the coefficient function and substantially reduces its scheme dependence [58].

These steps have been accomplished in Ref. [58], where resummed anomalous dimensions (see fig. 4), coefficient functions (see fig.5) and structure functions (see section 2.4 below) have been determined. The scheme dependence of these results can be studied in detail: results have been produced and compared in both the  $\overline{\text{MS}}$  and  $\text{Q}_0\overline{\text{MS}}$  schemes, and furthermore the variation of results upon variation of factorization and renormalization scales has been studied.

Calculations of resummation corrections not only of deep inelastic processes, but also of benchmark hadronic processes such as Drell-Yan, vector boson, heavy quark and Higgs production are now possible and should be explored.

## 2.2 The Ciafaloni-Colferai-Salam-Stasto (CCSS) Approach

The Ciafaloni-Colferai-Salam-Stasto (CCSS) resummation approach proposed in a series of papers [47, 60–66] is based on the few general principles:

- We impose the so-called kinematical constraint [81–83] onto the real gluon emission terms in the BFKL kernel. The effect of this constraint is to cut out the regions of the phase space for which  $k_T'^2 \geq k_T^2/z$  where  $k_T, k_T'$  are the transverse momenta of the exchanged gluons and  $z$  is the fraction of the longitudinal momentum.
- The matching with the DGLAP anomalous dimension is done up to the next-to-leading order.
- We impose the momentum sum rule onto the resummed anomalous dimensions.
- Running coupling is included with the appropriate choice of scale. We take the argument of the running coupling to be the transverse momentum squared of the emitted gluon in the BFKL ladder in the BFKL part. For the part which multiplies the DGLAP terms in the eigenvalue equation we choose the scale to be the maximal between  $k_T^2$  and  $k_T'^2$ .
- All the calculations are performed directly in momentum space. This in particular enables easy implementation of the running of the coupling with the choice of the arguments as described above.

The implementation at the leading logarithmic level in BFKL and DGLAP (and in the single gluon channel case) works as follows. It is convenient to go to the Mellin space representation where we denote by  $\gamma$  and  $\omega$  the Mellin variables conjugated to  $\ln k_T$  and  $\ln 1/x$  respectively. The full evolution kernel can be represented as a series  $\mathcal{K} = \sum_n \alpha_s^{n+1} \mathcal{K}_n(\gamma, \omega)$ . We take the resummed kernel at the lowest order level to be

$$\mathcal{K}_0(\gamma, \omega) = \frac{2C_A}{\omega} \chi_0^\omega(\gamma) + [\gamma_0^{gg}(\omega) - \frac{2C_A}{\omega}] \chi_c^\omega(\gamma). \quad (12)$$

The terms in (12) are the following

$$\chi_0^\omega(\gamma) = 2\psi(1) - \psi(\gamma) - \psi(1 - \gamma + \omega) ,$$

is the leading logarithmic BFKL kernel eigenvalue with the kinematical constraint imposed. This is reflected by the fact that the singularities in the  $\gamma$  plane at  $\gamma = 1$  are shifted by the  $\omega$ . This ensures the compatibility with the DGLAP collinear poles, in the sense that we have only single poles in  $\gamma$ . The function  $\chi_c(\gamma)$  is the collinear part of the kernel

$$\chi_c^\omega(\gamma) = \frac{1}{\gamma} + \frac{1}{1 - \gamma + \omega} ,$$

which includes only the leading collinear poles at  $\gamma = 0$  or  $1$ . All the higher twist poles are neglected for this part of the kernel. This kernel eigenvalue is multiplied by the non-singular (in  $\omega$ ) part of the DGLAP anomalous dimension  $\gamma_0^{gg}(\omega) - 2C_A/\omega$  where  $\gamma_0^{gg}(\omega)$  is the full anomalous dimension at the leading order. The next-to-leading parts both in BFKL and DGLAP are included in the second term in the expansion, i.e. kernel  $\mathcal{K}_1$

$$\mathcal{K}_1(\gamma, \omega) = \frac{(2C_A)^2}{\omega} \tilde{\chi}_1^\omega(\gamma) + \tilde{\gamma}_1^{gg}(\omega) \chi_c^\omega(\omega) \quad (13)$$

where  $\tilde{\chi}_1^\omega(\gamma)$  is the NLL in  $x$  part of the BFKL kernel eigenvalue with subtractions. These subtractions are necessary to avoid double counting: we need to subtract the double and triple collinear poles in  $\gamma$  which are already included in the resummed expression (12) and which can be easily identified by expanding this expression in powers of  $\omega$  and using the LO relation  $\omega = \bar{\alpha}_s \chi_0(\gamma)$ . The term  $\tilde{\gamma}_1^{gg}(\omega)$  in Eq. (13) is chosen so that one obtains the correct DGLAP anomalous dimension at a fixed next-to-leading logarithmic level. The formalism described above has been proven to work successfully in the single channel case, that is for evolution of gluons only. The solution was shown to be very stable with respect to the changes of the resummation scheme.

The quarks are included in the CCSS approach by a matrix formalism. The basic assumptions in this construction are:

- Consistency with the collinear matrix factorization of the PDFs in the singlet evolution.
- Requirement that only single pole singularities in both in  $\gamma$  and  $\omega$  are present in the kernel eigenvalues. This assumption allows for the natural consistency with DGLAP and BFKL respectively. Higher order singularities can be generated at higher orders only through the subleading dependencies on these two variables.
- Ability to compute all the anomalous dimensions which can be directly compared with the DGLAP approach. This can be done by using set of recursive equations which allow to calculate the anomalous dimensions order by order from the kernel eigenvalues.
- Impose the collinear-anticollinear symmetry of the kernel matrix via the similarity transformation.
- Incorporate NLLx BFKL and DGLAP up to NLO (and possibly NNLO).

The direct solutions to the matrix equations are the quark and gluon Green's functions. These are presented in Fig. 6 for the case of the gluon-gluon and quark-gluon part. The resulting

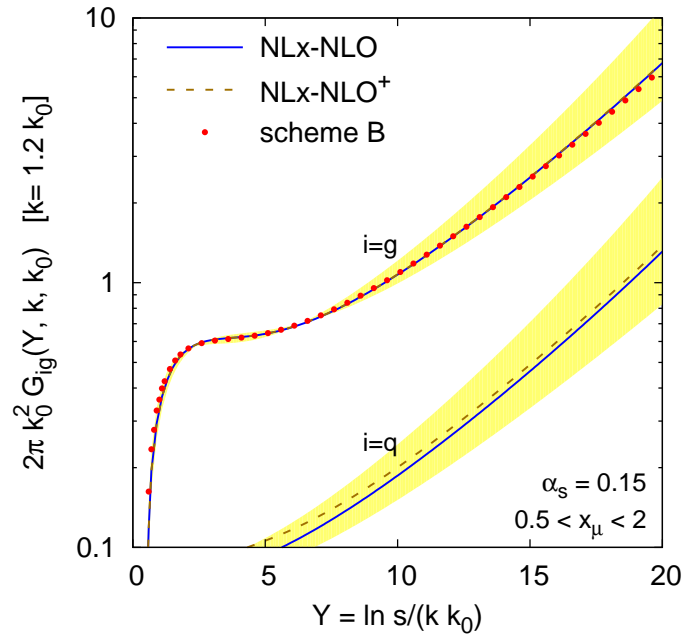


Fig. 6: Gluon-induced part of the Green function for the  $NLx\text{-}NLO$  and  $NLx\text{-}NLO^+$  models, compared to the results the single channel approach. For the models of this paper both gluon-gluon and quark-gluon Green's function are shown. The value chosen for the coupling,  $\alpha_s = 0.15$ , corresponds to  $k_0 \simeq 20 \text{ GeV}$ . The band indicates the spread in the result for the  $NLx\text{-}NLO$  model when varying the renormalization scale in the range  $0.5 < x_\mu < 2$ .

gluon-gluon part is increasing exponentially with the logarithm of energy  $\ln s$  with an effective intercept of about  $\sim 0.25$ . It is much suppressed with respect to the leading logarithmic order. We also note that the single channel results and the matrix results for the gluon-gluon Green's function are very similar to each other. In Fig. 6 we also present the quark-gluon channel which is naturally suppressed in normalization with respect to the gluon-gluon one by a factor of the strong coupling constant. This can be intuitively understood as the (singlet) quarks are radiatively generated from the gluons, and therefore this component follows the gluon density very closely. The yellow bands indicate the change of the Green's functions with respect to the change of the scale.

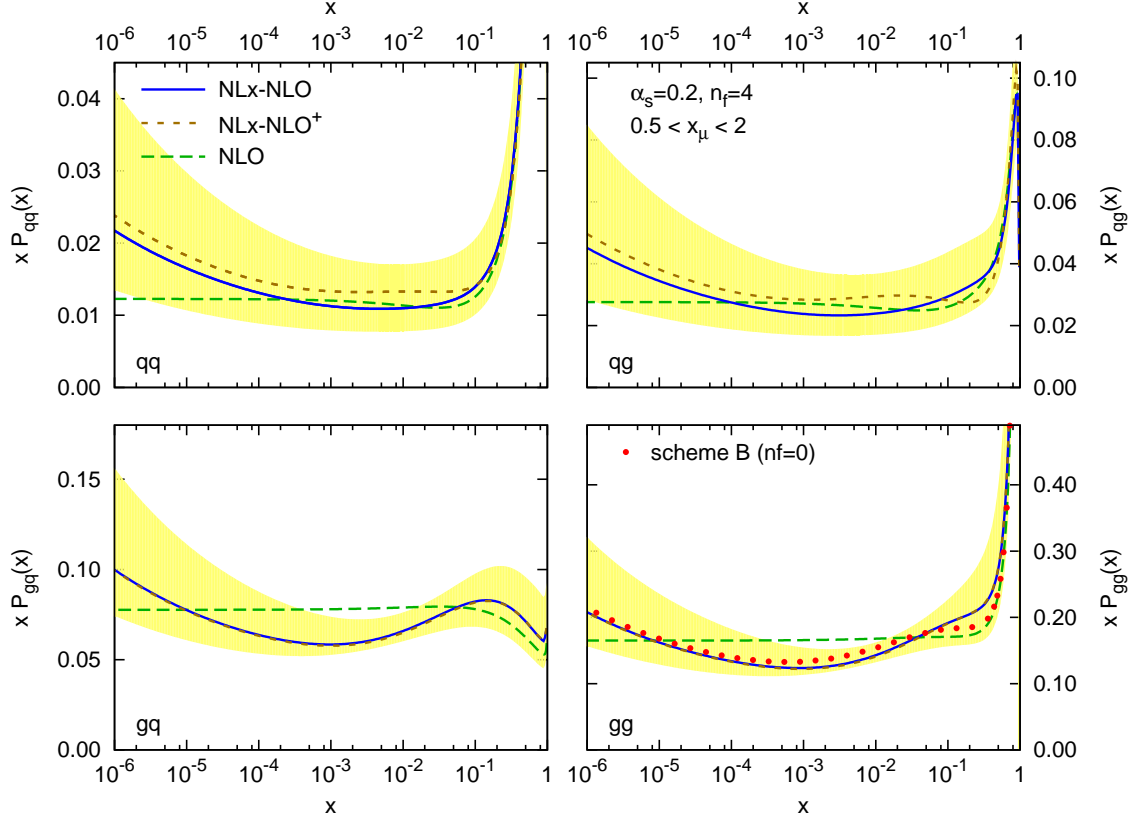


Fig. 7: The matrix of  $NLx$ -NLO (and  $NLx$ -NLO<sup>+</sup>) splitting functions together with their scale uncertainty and the NLO splitting functions for comparison. In the  $gg$  channel, we also show the old scheme B result ( $n_f = 0$ , no NLO contributions, 1-loop coupling). The band corresponds to the span of results ( $NLx$ -NLO) obtained if one chooses  $x_\mu = 0.5$  and  $x_\mu = 2.0$ .

In Fig. 7 we present all four splitting functions for fixed value of scale  $Q^2$ . Here, again the results are very close to the previous single channel approach in the case of the gluon-gluon splitting function. The gluon-quark channel is very close to the gluon-gluon one, with the characteristic dip of this function at about  $x \sim 10^{-3}$ . The dip delays the onset of rise of the splitting function only to values of  $x$  of about  $10^{-4}$ . The scale dependence grows with decreasing  $x$  but it is not larger than in the fixed NLO case. The quark-gluon and quark-quark splitting functions

tend to have slightly larger uncertainty due to the scale change but are also slightly closer to the plain NLO calculation. They also tend to have a less pronounced dip structure.

### 2.3 The Thorne-White (TW) Approach

Substituting the LO running coupling  $\bar{\alpha}_S(k^2)$  into equation (5) and performing a double Mellin transform according to equation (6), the BFKL equation 5, as mentioned in Section 2, becomes a differential equation:

$$\frac{d^2 f(\gamma, N)}{d\gamma^2} = \frac{d^2 f_I(\gamma, Q_0^2)}{d\gamma^2} - \frac{1}{\beta_0 N} \frac{d(\chi_0(\gamma) f(\gamma, N))}{d\gamma} + \frac{\pi}{3\bar{\beta}_0^2 N} \chi_1(\gamma) f(\gamma, N), \quad (14)$$

where  $\chi_{0,1}(\gamma)$  are the Mellin transforms of  $\mathcal{K}_{0,1}$ . The solution for  $f(N, \gamma)$  of Eq. (14) has the following form [61, 84]:

$$f(N, \gamma) = \exp\left(-\frac{X_1(\gamma)}{\beta_0 N}\right) \int_{\gamma}^{\infty} A(\tilde{\gamma}) \exp\left(\frac{X_1(\tilde{\gamma})}{\beta_0 N}\right) d\tilde{\gamma}. \quad (15)$$

Up to power-suppressed corrections, one may shift the lower limit of the integral  $\gamma \rightarrow 0$ , so that the gluon distribution factorises into the product of a perturbative and a non-perturbative piece. The nonperturbative piece depends on the bare input gluon distribution and an in principle calculable hard contribution. However, this latter part is rendered ambiguous by diffusion into the infrared, and in this approach is contaminated by infrared renormalon-type contributions. The perturbative piece is safe from this and is sensitive to diffusion into the ultraviolet region of weaker coupling. Substituting equation (15) into (14), one finds that the perturbative piece is given (after transforming back to momentum space):

$$\mathcal{G}_E^1(N, t) = \frac{1}{2\pi i} \int_{1/2-i\infty}^{1/2+i\infty} \frac{f^{\beta_0}}{\gamma} \exp[\gamma t - X_1(\gamma, N)/(\bar{\beta}_0 N)] d\gamma, \quad (16)$$

where:

$$X_1(\gamma, N) = \int_{\frac{1}{2}}^{\gamma} \left[ \chi_0(\tilde{\gamma}) + N \frac{\chi_1(\tilde{\gamma})}{\chi_0(\tilde{\gamma})} \right] d\tilde{\gamma}. \quad (17)$$

Structure functions  $F_i$  also factorize, and the perturbative factors have a similar form to Eq. (16), but involve an additional impact factor  $h_i(\gamma, N)$  in the integrand according to the  $k_t$ -factorisation theorem [49]. Crucially, coefficient functions and anomalous dimensions involve ratios of the above quantities, such that the non-perturbative factor cancels. Thus, once all the impact factors are known, the complete set of coefficient and splitting functions can be disentangled. Finally they can be combined with the standard NLO DGLAP results (which are known to describe data well at higher  $x$  values) using the simple prescription:

$$P^{tot.} = P^{NLL} + P^{NLO} - \left[ P^{NLL(0)} + P^{NLL(1)} \right], \quad (18)$$

where  $P$  is a splitting or coefficient function, and  $P^{NLL(i)}$  the  $\mathcal{O}(\alpha_s^i)$  contribution to the resummed result which is subtracted to avoid double-counting. It should be noted that the method

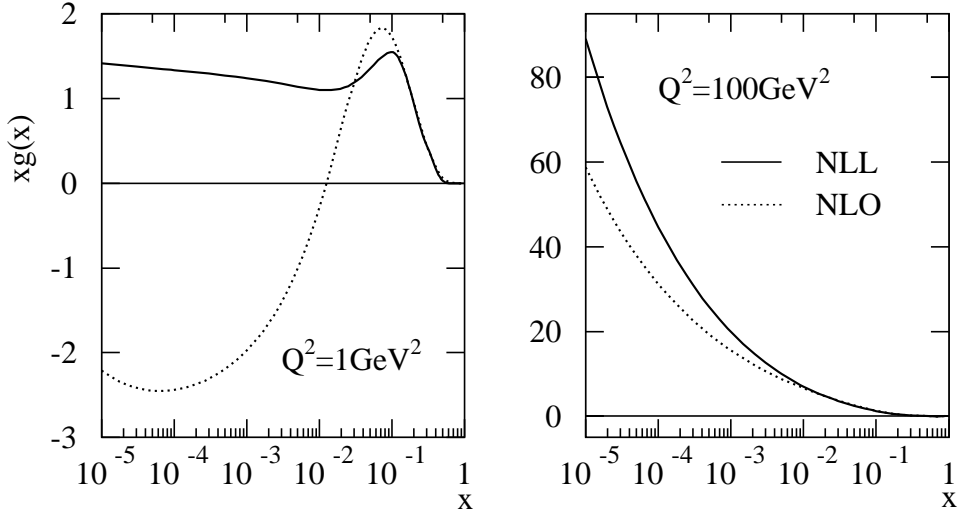


Fig. 8: Gluons arising from a global fit to scattering data including NLL small  $x$  resummations in the DIS( $\chi$ ) factorisation scheme (solid). Also shown is the result from an NLO DGLAP fit in the same scheme.

of subtraction of the resummed contribution in the matching is different to that for the ABF approach outlined after Eq. (11). For example, at NLO in the resummation the BFKL equation provides both the  $\alpha_S/N$  part of  $P_{gg}$  and the part at  $\mathcal{O}(\alpha_S)$  constant as  $N \rightarrow \infty$ . Hence we choose to keep all terms constant as  $N \rightarrow \infty$  generated by Eq. (16), with similar considerations for other splitting functions and coefficient functions, though these can contain terms  $\propto N$ . Hence, we include terms which will have some influence out to much higher  $x$  than in the ABF approach.

In the TW manner of counting orders LL is defined as the first order at which contributions appear, so while for the gluon splitting function this is for  $\bar{\alpha}_S^n \ln^m(1/x)$  for  $m = n - 1$  for impact factors this is for  $m = n - 2$ . A potential problem therefore arises in that the NLL impact factors are not known exactly. However, the LL impact factors with conservation of energy of the gluon imposed are known in cases of both massless and massive quarks [50, 51], and are known to provide a very good approximation to the full  $\mathcal{O}(\alpha_S^2)$  and  $\mathcal{O}(\alpha_S^3)$  quark-gluon splitting functions and coefficient functions [85], implying that they must contain much of the important higher-order information. These can then be used to calculate NLL coefficient and splitting functions within a particular factorisation scheme. One must also specify a general mass variable number scheme for consistent implementation of heavy quark mass effects. Such a scheme (called the DIS( $\chi$ ) scheme) has been given in [71, 72] up to NLL order in the high energy expansion, and

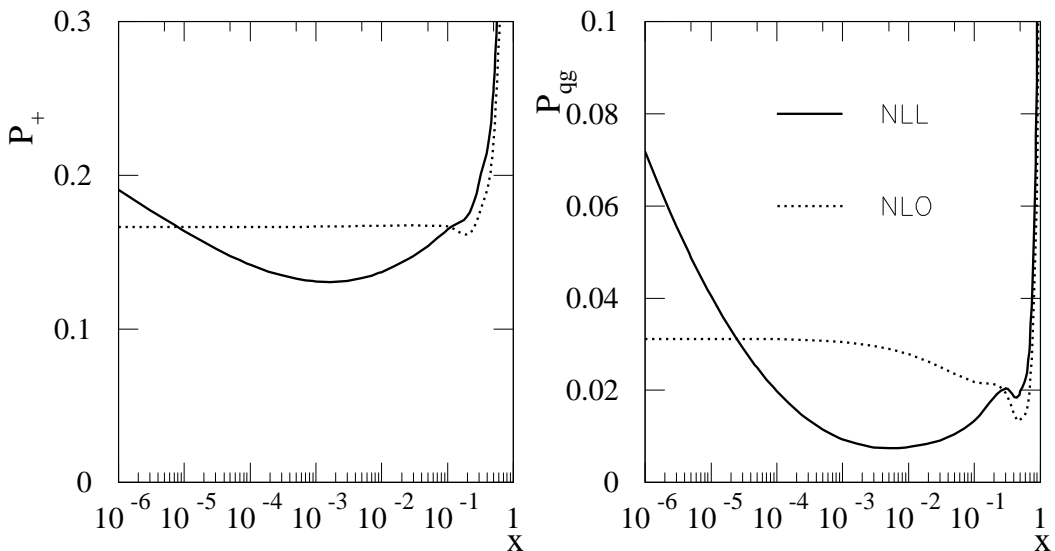


Fig. 9: The resummed splitting functions (solid)  $P_+ \approx P_{gg}$  and  $P_{qg}$  in the TW approach, both for  $n_f = 4$  and  $\alpha_s = 0.16$ , compared to the corresponding NLO forms (dotted).

NLO order in the fixed order expansion.

The form of the resummed splitting functions shown in fig. 9 are qualitatively consistent with those from the ABF approach, fig. 4, and CCSS approach fig. 7 (note however that in these plots the value of  $\alpha_s$  is a little larger, and the scheme is different). This is despite the fact that the approach does not include the explicit collinear resummation of the BFKL kernel adopted in the other two approaches. It was maintained in [69, 70] that the diffusion into the ultraviolet, effectively making the coupling weaker, hastens the perturbative convergence for splitting functions, and the kernel near  $\gamma = 0$ , making this additional resummation less necessary. There is no particular obstruction to including this resummation in the approach, it is simply cumbersome. Indeed, in Ref. [70] the effect was checked, and modifications found to be no greater than generic NNLO corrections to the resummation, so it was omitted. (Note that any process where there are two hard scales, sensitive to  $\gamma \approx 0.5$ , or attempted calculation of the hard input for the gluon distribution, sensitive to  $\gamma = 1$ , would find this resummation essential.) The main feature of the resummed splitting functions is a significant dip below the NLO DGLAP results, followed by an eventual rise at very low  $x \simeq 10^{-5}$ . This behaviour drives a qualitative change in the gluon distribution, when implemented in a fit to data.

The combined NLO+NLL splitting and coefficient functions (in the TW approach) have



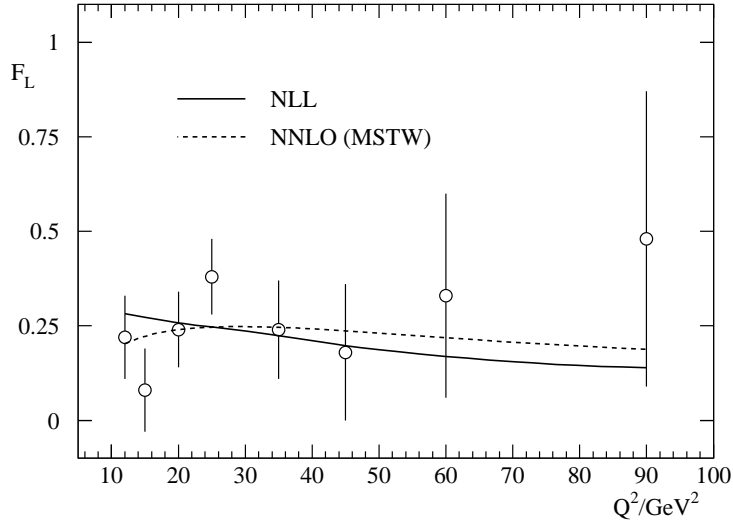


Fig. 10: Recent H1 data on the longitudinal structure function  $F_L$ , together with the NLL resummed prediction from the TW approach, and a recent NNLO result from the MSTW group.

been implemented in a global fit to DIS and related data in the  $\text{DIS}(\chi)$  scheme, thus including small  $x$  resummations in both the massless and massive quark sectors [72]. The overall fit quality was better than a standard NLO fit in the same factorisation scheme, and a similar NLO fit in the more conventional  $\overline{\text{MS}}$  factorisation scheme. The principal reason for this is the dip in the resummed evolution kernels, which allows the gluon distribution to increase at both high and low values of  $x$ . This reduces a tension that exists between the high  $x$  jet data of [86, 87] and the low  $x$  HERA data [17, 88–91]. The gluon distributions arising from the NLL and NLO fits are shown in figure 8, for the starting scale  $Q^2 = 1\text{GeV}^2$  and also for a higher value of  $Q^2$ . One sees that whilst the NLO gluon wants to be negative at low  $x$  and  $Q^2$ , the resummed gluon is positive definite and indeed growing slightly as  $x \rightarrow 0$ . The gluons agree well for higher  $x$  values (where the DGLAP description is expected to dominate), but deviate for  $x \leq 10^{-2}$ . This can therefore be thought of as the value of  $x$  below which resummation starts to become relevant.

The qualitatively different gluon from the resummed fit (together with the decreased evolution kernels w.r.t. the fixed order description) has a number of phenomenological implications:

1. The longitudinal structure function  $F_L$  is sensible at small  $x$  and  $Q^2$  values, where the standard DGLAP description shows a marked instability [92].
2. As a result of the predicted growth of  $F_L$  at small  $x$  the resummed result for the DIS reduced cross-section shows a turnover at high inelasticity  $y$ , in agreement with the HERA

data. This behaviour is not correctly predicted by some fixed order fits.

3. The heavy flavour contribution (from charm and bottom) to  $F_2$  is reduced at higher  $Q^2$  in the resummed approach, due mainly to the decreased evolution, as already noted in a full analysis in the fixed-order expansion at NNLO [93]. Nevertheless, it remains a significant fraction of the total structure function at small  $x$ .

Other resummation approaches should see similar results when confronted with data, given the qualitative (and indeed quantitative) similarities between the splitting functions. It is the decreased evolution with respect to the DGLAP description that drives the qualitative change in the gluon distribution. This is then the source of any quantitative improvement in the description of data, and also the enhanced description of the longitudinal structure function and reduced cross-section.

The resummed prediction for  $F_L$  is shown alongside the recent H1 data [94] in figure 10, and compared with an up-to-date NNLO fixed order result [95]. One sees that the data cannot yet tell apart the predictions, but that they are starting to diverge at low  $x$  and  $Q^2$ , such that data in this range may indeed be sensitive to the differences between resummed and fixed order approaches.

## 2.4 Resummed structure functions: comparison of the ABF and TW approaches

In this section, we present an application of the ABF and TW approaches to the resummed determination of the  $F_2$  and  $F_L$  deep-inelastic structure functions. The corresponding exercise for the CCSS approach has not yet been finalised. A direct comparison of the two approaches is complicated by issues of factorisation scheme dependence: whereas in the ABF approach results may be obtained in any scheme, and in particular the  $\overline{\text{MS}}$  and closely related  $Q_0$ - $\overline{\text{MS}}$  scheme, in the TW formalism splitting functions and coefficient functions beyond NLO in  $\alpha_S$  are resummed in the  $Q_0$ -DIS scheme [65, 96], which coincides with the standard DIS scheme at large  $x$  but differs from it at the resummed level; the scheme change needed in order to obtain the coefficient functions from the DIS-scheme ones is performed exactly up to NLO and approximately beyond it. Thus, without a more precise definition of the relation of this scheme to  $\overline{\text{MS}}$ , one cannot compare splitting and coefficient functions, which are factorisation scheme dependent.

A useful compromise is to present the respective results for the ratio of structure function predictions:

$$K_i = \frac{F_i^{NLL}(x, Q^2)}{F_i^{NLO}(x, Q^2)}, \quad (19)$$

where  $i \in 2, L$ , and the  $F_i$  are calculated by convoluting the relevant coefficients with PDFs obtained by perturbative evolution of a common set of partons, defined at a starting scale of  $Q_0^2 = 4\text{GeV}^2$ . The number of flavors is fixed to three, to avoid ambiguities due to heavy quark effects. The initial PDFs are assumed to be fixed (i.e., the same at the unresummed and unresummed level) in the DIS factorization scheme at the scale  $Q_0$ . Of course, in a realistic situation the data are fixed and the PDFs are determined by a fit to the data: hence they are not the same at the resummed and unresummed level (compare Fig. 8 above). However, in the DIS factorization scheme the structure function  $F_2$  is simply proportional to the quark distribution, hence by fixing the PDFs in this scheme one ensures that  $F_2$  is fixed at the starting scale.

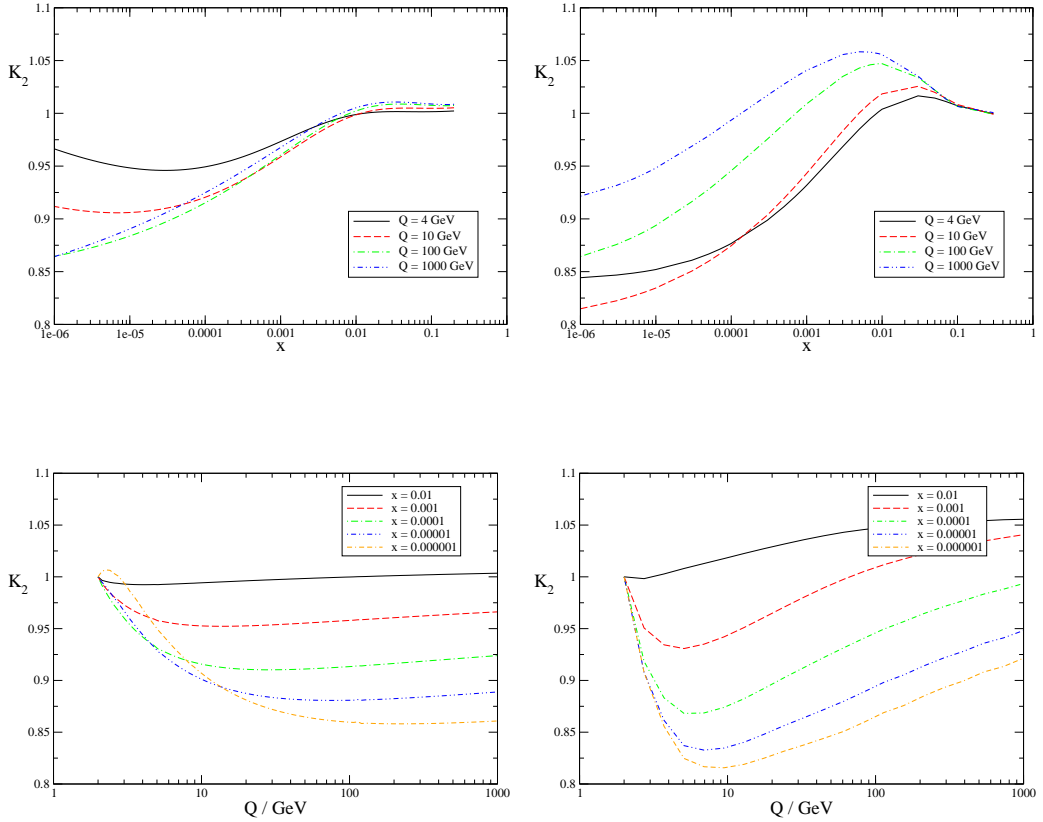


Fig. 11: The ratio  $F_2^{NLL}/F_2^{NLO}$  in the ABF approach (left) and the TW approach (right), using toy PDFs, given in eq. 20, calculated as function of  $x$  at fixed for  $Q^2$  (upper), and as a function of  $Q^2$  at fixed  $x$  (lower).

This starting PDFs are constructed as follows: the quark and gluon distributions are chosen to have the representative form also used in Ref. [58]

$$xg(x) = k_s x S(x) = k_g x^{-0.18} (1-x)^5; \quad xq_v = k_q x^{0.5} (1-x)^4, \quad (20)$$

in the  $\overline{\text{MS}}$  scheme, where  $g(x)$  is the gluon,  $S(x)$  the sea quark distribution, and  $xq_v(x)$  denotes a valence quark distribution. We choose  $k_s = 3$ , and then all other parameters are fixed by momentum and number sum rules. Note that the gluon is the same as that used in the previous comparison of Ref. [73]. The PDFs eq. (20) are then transformed to the DIS factorization scheme [97] using the NLO (unresummed) scheme change at the scale  $Q_0$ . The result is then used as a fixed boundary condition for all (unresummed and resummed, ABF and TW) calculations. In the TW approach, the DIS scheme for unresummed quantities and  $Q_0$ DIS scheme as discussed above is then used throughout. In the ABF approach, the fixed DIS-scheme boundary condition is transformed to the  $Q_0\overline{\text{MS}}$  scheme [58,98] (which at the unresummed level coincides with standard  $\overline{\text{MS}}$ ) by using the unresummed or resummed scheme change function as appropriate, and then all calculations are performed in  $Q_0\overline{\text{MS}}$ . One might hope that most of the residual scheme dependence cancels upon taking the ratio of the NLL and NLO results, at least for schemes that

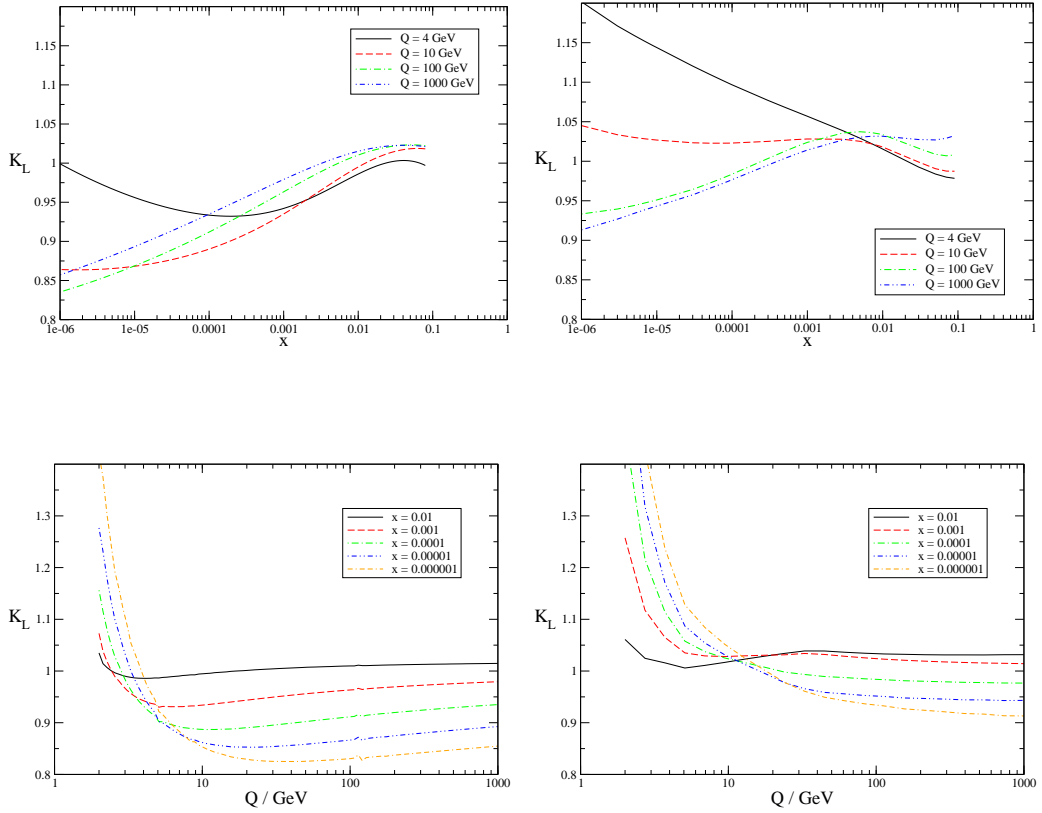


Fig. 12: The ratio  $F_L^{NLL}/F_L^{NLO}$  in the ABF approach (left) and the TW approach (right), using toy PDFs, given in eq. 20, calculated as function of  $x$  at fixed for  $Q^2$  (upper), and as a function of  $Q^2$  at fixed  $x$  (lower).

are well defined and without unphysical singularities.

The results for  $K_2$  and  $K_L$  are shown in figures 11 for  $F_2$  in the ABF and TW procedures respectively and similarly in figures 12 for  $F_L$ . One sees that for  $x$  sufficiently small, and for  $Q$  not too large, the resummed  $F_2$  is consistently lower than its fixed order counterpart in both approaches, due to the decreased evolution of the gluon, and also (in the  $\overline{\text{MS}}$  scheme) due to the fact that resummed coefficient functions are much larger than the NLO ones at small  $x$  and low  $Q^2$ . Similarly the resummed  $F_L$  is larger than the fixed order at low  $Q$  and small enough  $x$ , but falls rapidly as  $Q$  increases. However despite these superficial similarities, the two approaches differ quantitatively in several respects:

- the ABF resummed  $F_2$  matches well to the NLO for  $x \gtrsim 10^{-2}$  at all scales, while the TW  $F_2$  shows a rise around  $x \simeq 10^{-2}$ , which is largest at low  $Q$ . This may be due to the significant differences between resummed and NLO splitting functions at very high  $x$  in fig. 9. A similar mismatch may be seen at  $x \sim 0.1$  in the  $F_L$  K-factor.
- at large scales the ABF resummation stabilises, due to the running of the coupling, so the K-factors becomes rather flat: they grow only logarithmically in  $\ln Q$ . By contrast the TW  $F_2$  K-factor still shows a marked  $Q^2$  dependence. This may be related to the fact that the

TW resummation does not resum the collinear singularities in the BFKL kernel, and to the TW choice (see Sect. 2.3) not to include subtraction of terms induced by the resummation which do not drop at large  $x$ . This choice induces a change in the PDFs at higher  $x$  in the TW approach, which results in effects which persist to higher  $Q^2$  at smaller  $x$ .

- at the initial scale  $Q_0$  the TW resummed  $F_L$  grows much more strongly as  $x$  decreases than the ABF resummed  $F_L$ . This is likely to be due to the different treatment of the coefficient functions: in this respect, the fully consistent treatment of the factorization scheme, the effect of collinear resummation, and the different definitions of what is called resummed NLO used by the two groups all play a part.

## 2.5 Conclusion

The problem of understanding the small  $x$  evolution of structure functions in the domain of  $x$  and  $Q^2$  values of relevance for HERA and LHC physics has by now reached a status where all relevant physical ingredients have been identified, even though not all groups have quite reached the stage at which the formalism can be transformed into a practical tool for a direct connection with the data.

In this report we summarised the status of the three independent approaches to this problem by ABF, CCSS and TW, we discussed the differences in the adopted procedures and finally we gave some recent results. The most complete formalisms are those by ABF and CCSS while the TW approach is less comprehensive but simpler to handle, and thus has been used in fit to data. We recall that, at the level of splitting functions the ABF and CCSS have been compared in ref. [73] and found to be in very good agreement. The singlet splitting function obtained by TW was also compared with ABF and CCSS in ref. [72] and also found to be in reasonable agreement, at least at small  $x$ .

Here we have shown the results of an application to the structure functions  $F_2$  and  $F_L$  of the ABF and TW methods. The same input parton densities at the starting scale  $Q_0$  were adopted by these two groups and the  $K$ -factors for resummed versus fixed NLO perturbative structure functions were calculated using the respective methods. The results obtained are in reasonable qualitative agreement for  $F_2$ , less so for  $F_L$ . Discrepancies may in part be due to the choice of factorization scheme, but our study suggests that the following are also likely to make a quantitative difference: whether or not a resummation of collinear singularities in the BFKL kernel is performed, whether contributions from the resummation which persist at large  $x$  are subtracted and whether the factorization scheme is consistently defined in the same way at resummed and NLO levels.

## 3 Parton saturation and geometric scaling<sup>3</sup>

### 3.1 Introduction<sup>4</sup>

The degrees of freedom involved in hadronic collisions at sufficiently high energy are partons, whose density grows as the energy increases (i.e., when  $x$ , their momentum fraction, decreases). This growth of the number of gluons in the hadronic wave functions is a phenomenon which has

---

<sup>3</sup>Contributing authors: G. Beuf, F. Caola, F. Gelis, L. Motyka, C. Royon, D. Šálek, A. M. Staśto

<sup>4</sup>Contributing authors: F. Gelis, A. M. Staśto

been well established at HERA. One expects however that it should eventually “saturate” when non linear QCD effects start to play a role.

An important feature of partonic interactions is that they involve only partons with comparable rapidities. Consider the interaction between a hadron and some external probe (e.g. a virtual photon in Deep Inelastic Scattering) and consider what happens when one boosts the hadron, increasing its rapidity in successive steps. In the first step, the valence constituents become Lorentz contracted in the longitudinal direction while the time scale of their internal motions is Lorentz dilated. In addition, the boost reveals new vacuum fluctuations coupled to the boosted valence partons. Such fluctuations are not Lorentz contracted in the longitudinal direction, and represent the dynamical degrees of freedom; they are the partons that can interact with the probe. Making an additional step in rapidity would freeze these fluctuations, while making them Lorentz contracted as well. But the additional boost also produces new quantum fluctuations, which become the new dynamical variables. This argument can be repeated, and one arrives at the picture of a high-energy projectile containing a large number of frozen, Lorentz contracted partons (the valence partons, plus all the quantum fluctuations produced in the previous boosts), and partons which have a small rapidity, are not Lorentz contracted and can interact with the probe. This space-time description was developed before the advent of QCD (see for instance [99]; in Bjorken’s lectures [100], one can actually foresee the modern interpretation of parton evolution as a renormalization group evolution).

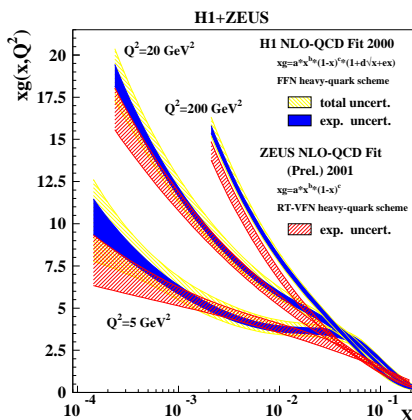


Fig. 13: The gluon structure function in a proton measured at HERA.

This space-time picture, which was deduced from rather general considerations, can now be understood in terms of QCD. In fact, shortly after QCD was established as the theory of strong interaction, quantitative equations were established, describing the phenomenon outlined above [41, 101–105]. In particular, the equation derived by Balitsky, Fadin, Kuraev and Lipatov [41, 101] describes the growth of the non-integrated gluon distribution in a hadron as it is boosted towards higher rapidities. Experimentally, an important increase of the number of gluons at small  $x$  has indeed been observed in the DIS experiments performed at HERA (see Fig. 13), down to  $x \sim 10^{-4}$ . Such a growth raises a problem: if it were to continue to arbitrarily small  $x$ , it would induce an increase of hadronic cross-sections as a power of the center of mass energy, in violation of known unitarity bounds.

However, as noticed by Gribov, Levin and Ryskin in [106], the BFKL equation includes only branching processes that increase the number of gluons ( $g \rightarrow gg$  for instance), but not the recombination processes that could reduce the number of gluons (like  $gg \rightarrow g$ ). While it may be legitimate to neglect the recombination process when the gluon density is small, this cannot remain so at arbitrarily high density: a saturation mechanism of some kind must set in. Treating the partons as ordinary particles, one can get a crude estimate

of the onset of saturation, which occurs at:

$$Q^2 = Q_s^2, \quad \text{with } Q_s^2 \sim \alpha_s(Q_s^2) \frac{xG(x, Q_s^2)}{\pi R^2}. \quad (21)$$

The momentum scale that characterizes this new regime,  $Q_s$ , is called the saturation momentum [107]. Partons with transverse momentum  $Q > Q_s$  are in a dilute regime; those with  $Q < Q_s$  are in the saturated regime. The saturation momentum increases as the gluon density increases. This comes from an increase of the gluon structure function as  $x$  decreases. The increase of the density may also come from the coherent contributions of several nucleons in a nucleus. In large nuclei, one expects  $Q_s^2 \propto A^{1/3}$ , where  $A$  is the number of nucleons in the nucleus.

Note that at saturation, naive perturbation theory breaks down, even though  $\alpha_s(Q_s)$  may be small if  $Q_s$  is large: the saturation regime is a regime of weak coupling, but large density. At saturation, the gluon occupation number is proportional to  $1/\alpha_s$ . In such conditions of large numbers of quanta, classical field approximations become relevant to describe the nuclear wavefunctions.

Once one enters the saturated regime, the evolution of the parton distributions can no longer be described by a linear equation such as the BFKL equation. The color glass condensate formalism (for a review, see [108]), which relies on the separation of the degrees of freedom in a high-energy hadron into frozen partons and dynamical fields, as discussed above, provides the non linear equations that allow us to follow the evolution of the partonic systems from the dilute regime to the dense, saturated, regime. For instance, the correlator  $\text{tr}\langle U^\dagger(\mathbf{x}_\perp)U(\mathbf{y}_\perp) \rangle$  of two Wilson lines –which enters in the discussion of DIS– evolves according to the Balitsky-Kovchegov [109, 110] equation:

$$\begin{aligned} \frac{\partial \text{tr}\langle U^\dagger(\mathbf{x}_\perp)U(\mathbf{y}_\perp) \rangle_x}{\partial \ln(1/x)} &= -\frac{\alpha_s}{2\pi^2} \int_{\mathbf{z}_\perp} \frac{(\mathbf{x}_\perp - \mathbf{y}_\perp)^2}{(\mathbf{x}_\perp - \mathbf{z}_\perp)^2(\mathbf{y}_\perp - \mathbf{z}_\perp)^2} \\ &\times \left[ N_c \text{tr}\langle U^\dagger(\mathbf{x}_\perp)U(\mathbf{y}_\perp) \rangle_x - \text{tr}\langle U^\dagger(\mathbf{x}_\perp)U(\mathbf{z}_\perp) \rangle_x \text{tr}\langle U^\dagger(\mathbf{z}_\perp)U(\mathbf{y}_\perp) \rangle_x \right]. \end{aligned} \quad (22)$$

(This equation reduces to the BFKL equation in the low density limit.)

The geometric scaling phenomenon was first introduced in the context of the dipole picture of the deep inelastic electron-proton scattering [111]. The process of the scattering of the virtual photon on a proton at very small values of  $x$  can be conveniently formulated in the dipole model. In this picture the photon fluctuates into the quark-antiquark pair (dipole) and subsequently interacts with the target. In the small  $x$  regimes these two processes factorize and they can be encoded into the dipole formula for the total  $\gamma^*p$  cross section

$$\sigma_{T,L}(x, Q^2) = \int d^2\mathbf{r} \int dz |\Psi_{T,L}(r, z, Q^2)|^2 \hat{\sigma}(x, r) \quad (23)$$

where  $\Psi_{T,L}$  is the wave function for the photon and  $\hat{\sigma}$  is the dipole cross section.  $r$  is the dipole size and  $z$  is the light-cone fraction of the longitudinal momentum carried by the quark (or antiquark). The photon wave functions  $\Psi$  are known, the dipole cross section can be expressed in terms of the correlator of Wilson lines whose evolution is driven by Eq. (22) :

$$\hat{\sigma}(x, r) = \frac{2}{N_c} \int d^2\mathbf{X} \text{tr} \left\langle 1 - U(\mathbf{X} + \frac{\mathbf{r}}{2}) U^\dagger(\mathbf{X} - \frac{\mathbf{r}}{2}) \right\rangle. \quad (24)$$



Alternatively, it can be modeled or extracted from the data. In the GBW model it was assumed that the dipole cross section has a form

$$\hat{\sigma} = \sigma_0 [1 - \exp(-r^2/R_0(x)^2)] \quad (25)$$

where  $R_0(x) = (x/x_0)^{-\lambda}$  is a saturation radius (its inverse is usually called the saturation scale  $Q_s(x)$ ) and  $\sigma_0$  a normalisation constant. One of the key properties of the model was the dependence on the dipole size and the Bjorken  $x$  through only one combined variable  $r^2 Q_s^2(x)$ . This fact, combined with the property of the dipole formula, allows to reformulate the total cross section as a function of  $Q^2/Q_s^2(x)$  only. This feature is known as the geometric scaling of the total  $\gamma^*p$  cross section. Initially postulated as a property of the GBW model, it was then shown that the experimental data do indeed exhibit the aforementioned regularity in a rather wide range of  $Q^2$  and for small values of Bjorken  $x$ .

Although it is a postulate in the GBW model, this property can be derived from the small- $x$  behavior of the solutions of Eq. (22) [112] : for a wide class of initial conditions, the BK equation drives its solution towards a function that obeys this scaling. Note also that the saturation scale, introduced by hand in the GBW model, is dynamically generated by the non linear evolution described by Eq. (22). This suggested that the regularity seen in the data could be explained by the scaling property of the solutions to the nonlinear equations in the saturated regime - and thus may provide some indirect evidence for gluon saturation.

Nevertheless, several important questions remained. One of them, is the problem of the compatibility of the DGLAP evolution with the property of the geometric scaling. It is known from the global fits that the standard DGLAP evolution works quite well for the description of the of the deep inelastic data even in the very low  $x$  and  $Q^2$  regime. That suggests that the saturation should be confined to the very tight kinematic regime, and it is therefore questionable whether the observed regularity could be attributed to the saturation at all. In the present contribution we discuss several approaches to this problem.

### 3.2 Phenomenology<sup>5</sup>

In order to compare the quality of different scaling laws, it is useful to use a quantity called *quality factor* (QF). It is also used to find the best parameters for a given scaling. In the following, this method is used to compare the scaling results for the proton structure function  $F_2$  and  $F_2^c$ , the deeply virtual Compton scattering, the diffractive structure function, and the vector meson cross section data measured at HERA.

**Quality Factor** Given a set of data points  $(Q^2, x, \sigma = \sigma(Q^2, x))$  and a parametric scaling variable  $\tau = \tau(Q^2, Y, \lambda)$  (with  $Y = \ln 1/x$ ) we want to know whether the cross-section can be parametrised as a function of the variable  $\tau$  only. Since the function of  $\tau$  that describes the data is not known, the QF has to be defined independently of the form of that function.

For a set of points  $(u_i, v_i)$ , where  $u_i$ 's are ordered and normalised between 0 and 1, we

---

<sup>5</sup>Contributing authors: C. Royon, D. Šálek



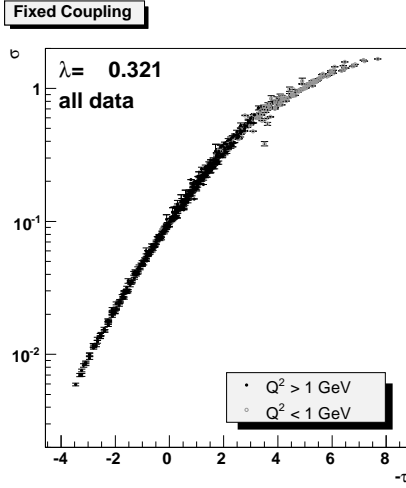


Fig. 14:  **$F_2$  data:** Scaling curve  $\sigma = \sigma(\tau)$  for “Fixed Coupling”. A  $Q^2 > 1 \text{ GeV}^2$  cut was applied to the data.

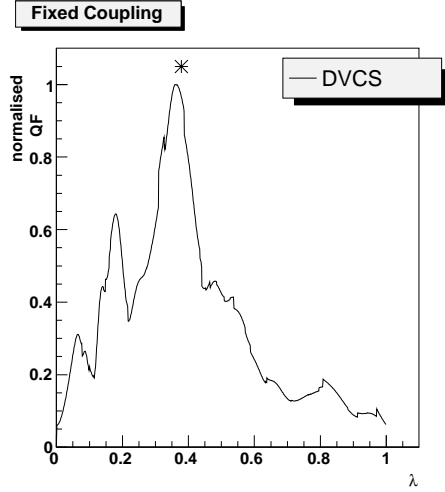


Fig. 15: **DVCS data:** Quality factor normalised to 1 plotted against the parameter  $\lambda$ . Star denotes the fit result for  $F_2$  data.

introduce  $QF$  as follows [113]

$$QF(\lambda) = \left[ \sum_i \frac{(v_i - v_{i-1})^2}{(u_i - u_{i-1})^2 + \epsilon^2} \right]^{-1}, \quad (26)$$

where  $\epsilon$  is a small constant that prevents the sum from being infinite in case of two points have the same value of  $u$ . According to this definition, the contribution to the sum in (26) is large when two successive points are close in  $u$  and far in  $v$ . Therefore, a set of points lying close to a unique curve is expected to have larger  $QF$  (smaller sum in (26)) compared to a situation where the points are more scattered.

Since the cross-section in data differs by orders of magnitude and  $\tau$  is more or less linear in  $\log(Q^2)$ , we decided to take  $u_i = \tau_i(\lambda)$  and  $v_i = \log(\sigma_i)$ . This ensures that low  $Q^2$  data points contribute to the  $QF$  with a similar weight as higher  $Q^2$  data points.

**Fits to  $F_2$  and DVCS Data** We choose to consider all available data from H1, ZEUS, NMC and E665 experiments [17, 89–91, 114–117] with  $Q^2$  in the range  $[1; 150] \text{ GeV}^2$  and  $x < 0.01^6$ . We exclude the data with  $x > 10^{-2}$  since they are dominated by the valence quark densities, and the formalism of saturation does not apply in this kinematical region. In the same way, the upper  $Q^2$  cut is introduced while the lower  $Q^2$  cut ensures that we stay away from the soft QCD domain. We will show in the following that the data points with  $Q^2 < 1 \text{ GeV}^2$  spoil the fit stability. Two kinds of fits to the scaling laws are performed, either in the full mentioned  $Q^2$  range, or in a tighter  $Q^2$  range  $[3; 150] \text{ GeV}^2$  to ensure that we are in the domain where perturbative QCD applies.

<sup>6</sup>The data in the last ZEUS paper include contributions for  $F_L$  and  $xF_3$  but those can be neglected within the kinematical domain we consider.

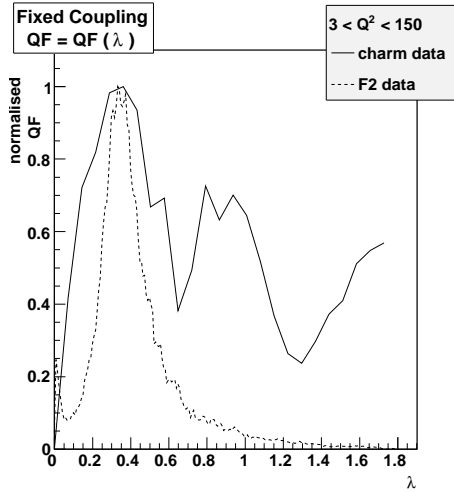


Fig. 16:  $F_2^c$  **data**: Comparison of the  $\lambda$  parameter for  $F_2$  and  $F_2^c$  data for  $Q^2 > 3 \text{ GeV}^2$ .

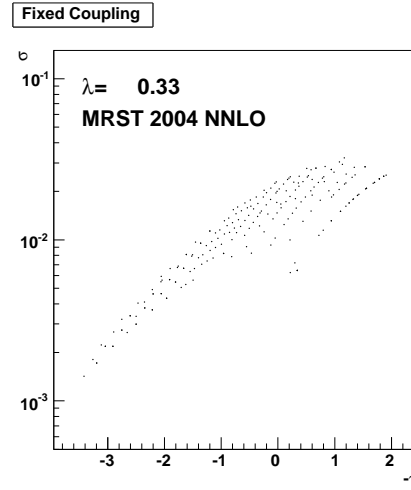


Fig. 17:  $F_2^c$  **parametrisation**: Scaling curve  $\sigma = \sigma(\tau)$  for fixed coupling using the MRST 2004 NNLO parametrisation for  $\lambda = 0.33$  as obtained in the fit to experimental data. No scaling is observed for  $Q^2 > 3 \text{ GeV}^2$ .

Figure 14 shows the scaling plot for “Fixed Coupling” in the  $Q^2$  range  $[1; 150] \text{ GeV}^2$ , which shows that the lowest  $Q^2$  points in grey have a tendency to lead to worse scaling. The QF values are similar for the “Fixed Coupling”, “Running Coupling I”, and “Running Coupling Ibis” — with a tendency to be slightly better for “Running Coupling Ibis” — and worse for diffusive scaling [118].

The amount of the DVCS data [119, 120] measured by H1 and ZEUS is smaller (34 points for H1 and ZEUS requiring  $x \leq 0.01$  as for  $F_2$  data), therefore the precision on the  $\lambda$  parameter is weaker. The kinematic coverage of the DVCS data covers smaller region in  $x$  and  $Q^2$  than  $F_2$ :  $4 < Q^2 < 25 \text{ GeV}^2$  and  $5 \cdot 10^{-4} < x < 5 \cdot 10^{-3}$ . The DVCS data lead to similar  $\lambda$  values as in the  $F_2$  data (see Fig. 15), showing the consistency of the scalings. The values of the QF show a tendency to favour “Fixed Coupling”, but all different scalings (even “Diffusive Scaling”) lead to reasonable values of QF.

**Implications for Diffraction and Vector Mesons** We used the values of the parameters obtained from the fit to  $F_2$  data to test the various scaling variables on the diffractive cross section and vector meson data [121–123]. We tested both the fixed  $\beta$  scaling behaviour in  $x_P$  and the fixed  $x_P$  scaling behaviour in  $\beta$ . At fixed  $\beta$ , we find a scaling behaviour up to  $\beta = 0.65$ . At fixed  $x_P$ , the scaling behaviour of the diffractive cross section as a function of  $\beta$  and  $Q^2$  is far less obvious. This is not a surprise, as not enough data is available in the genuine small  $\beta$  region. A sign of scaling is however observed for the  $x_P = 0.03$  bin.

Concerning  $\rho$ ,  $J/\Psi$ , and  $\phi$  production [124–126], we found a reasonable scaling behaviour for all tested scaling variables, with the hard scale  $Q^2 + M_V^2$ , borrowed from vector mesons

wave function studies. Surprisingly, the best scaling is for all three vector mesons the “Diffusive scaling”.

**Fits to  $F_2$  and  $F_2^c$  in QCD Parametrisations** First we test the scaling properties using experimental  $F_2^c$  data. The requirements on the kinematical domain remain the same as in the case of  $F_2$  studies. The lower  $Q^2 > 3 \text{ GeV}^2$  cut also allows to remove eventual charm mass effects. We use the charm  $F_2^c$  measurements from the H1 and ZEUS experiments [127–130]. Only 25 data points lie in the desired kinematical region.

Since the statistics in the data is low, the fit results are not precise. Nevertheless, they still lead to clear results that are comparable to  $F_2$  fits. The results are found similar between  $F_2$  and  $F_2^c$  (see Fig. 16). All  $\lambda$  parameters are similar for  $F_2$  and  $F_2^c$  except for “Diffusive Scaling”. As in the case of the  $F_2$  scaling analysis, “Fixed Coupling”, “Running Coupling I” and “Running Coupling II” give similar values of  $QF$ , and “Diffusive Scaling” is disfavoured.

The QCD parametrisations [131–133] of the structure function have been tested using CTEQ, MRST, GRV. The same  $Q^2$  and  $x$  points as in the experimental data were taken into account. Parametrisations of  $F_2$  are able to reproduce the scaling results seen in the experimental data. However, they are not successful in describing the scaling properties in case of  $F_2^c$ . Fig. 17 shows the scaling curve of “Fixed Coupling” in the MRST NNLO 2004 parametrisation of  $F_2^c$  where the value of  $\lambda = 0.33$  is imposed (as seen in the experimental data). The scaling curve is plotted with all the points used in the  $F_2$  study. Therefore the fact that there is not just a single scaling curve in  $F_2^c$  parametrisation is not in direct disagreement with the data — with 25 point only, the curves in parametrisation and data look similar. However the fit values of  $\lambda$  are different.

The CTEQ, MRST or GRV parametrisations are unable to reproduce the scaling properties in  $F_2^c$ . It seems a sea-like intrinsic charm component like the one used in CTEQ 6.6 C4 helps to get results closer to a single scaling curve [134]. Scaling is not present at all in the MRST or GRV parametrisations at low  $Q^2$ .

### 3.3 Geometric scaling and evolution equations with saturation<sup>7</sup>

Let us now recall how scaling properties arise from saturation, as shown in [112], using methods and results from non-linear physics (see [135, 136] for alternative demonstrations). Our discussion, independent of the precise saturation formalism, is valid *e.g.* for the JIMWLK and BK equations (see [108] and references therein), at LL, NLL or even higher order in  $\log(1/x)$ . We will discuss separately the fixed and the running  $\alpha_s$  cases, as running coupling is the main effect which can modify the discussion.

Saturation amounts to add a non-linear damping contribution to the BFKL evolution. One writes formally the evolution equation at LL for the dipole-proton cross section  $\hat{\sigma}$  (23)

$$\partial_Y \hat{\sigma}(Y, L) = \bar{\alpha} \chi(-\partial_L) \hat{\sigma}(Y, L) - \text{non-linear terms in } \hat{\sigma}(Y, L) , \quad (27)$$

where  $Y \equiv \log(1/x)$ ,  $L \equiv -\log(r^2 \Lambda_{QCD}^2)$  and  $\chi(\gamma)$  is the characteristic function of the BFKL kernel. The nonlinear damping ensures that, for any  $Y$ ,  $\hat{\sigma}(Y, L)$  grows at most as a power of

---

<sup>7</sup>Contributing author: G. Beuf

$|L|$  for  $L \rightarrow -\infty$  (i.e.  $r \rightarrow +\infty$ ). The color transparency property of the dipole cross section implies  $\hat{\sigma}(Y, L) \propto e^{-L}$  for  $L \rightarrow +\infty$ . Using a double Laplace transform with partial waves  $e^{-\gamma L + \omega Y}$ , the linear part of (27) reduces to the BFKL dispersion relation  $\omega = \bar{\alpha}\chi(\gamma)$ , which gives the partial waves solutions  $e^{-\gamma[L - \bar{\alpha}\chi(\gamma)Y/\gamma]}$ . In the relevant interval  $0 < \gamma < 1$ , the phase velocity  $\lambda(\gamma) = \bar{\alpha}\chi(\gamma)/\gamma$  has one minimum, for the critical value  $\gamma = \gamma_c \simeq 0.63$  which is the solution of  $\chi(\gamma_c) = \gamma_c \chi'(\gamma_c)$ . In the presence of saturation terms in the evolution equation, the wave with  $\gamma = \gamma_c$  is selected dynamically.

In order to understand the dynamics of the problem, let us consider an arbitrary initial condition, at some rapidity  $Y = Y_0$ . With the definition  $\gamma_{eff}(L, Y) \equiv -\partial_L \log(\hat{\sigma}(Y, L))$ ,  $\gamma_{eff}(L, Y_0)$  gives the exponential slope of the initial condition in the vicinity of  $L$ . That vicinity will then propagates for  $Y \geq Y_0$  at a velocity  $\lambda(\gamma_{eff}(L, Y)) = \bar{\alpha}\chi(\gamma_{eff}(L, Y))/\gamma_{eff}(L, Y)$ . One finds easily that, if  $\gamma_{eff}(L, Y_0)$  is a growing function of  $L$ , the regions of smaller velocity will spread during the  $Y$  evolution, and invade the regions of larger velocity. Restricting ourselves to initial conditions verifying the saturation at  $L \rightarrow -\infty$  and the color transparency at  $L \rightarrow +\infty$  as discussed previously, one obtains that  $\gamma_{eff}(L, Y_0)$  goes from 0 at low  $L$  to 1 at large  $L$ . At intermediate  $L$ ,  $\gamma_{eff}(L, Y_0)$  will cross the value  $\gamma_c$ , corresponding to the minimal velocity  $\lambda_c = \lambda(\gamma_c)$ . Hence, one conclude that, as  $Y$  grows, there is a larger and larger domain in  $L$  where  $\gamma_{eff}(L, Y) = \gamma_c$  and thus  $\lambda = \lambda_c$ . In that domain, one has  $\hat{\sigma}(Y, L) \propto e^{-\gamma_c(L - \lambda_c Y)}$ , and hence the geometric scaling  $\hat{\sigma}(Y, L) \equiv f(L - \lambda_c Y) = f(-\log(r^2 Q_s^2(x)))$ , with a saturation scale  $Q_s^2(x) = e^{\lambda_c Y} \Lambda_{QCD}^2 = x^{-\lambda_c} \Lambda_{QCD}^2$ . One finds that the geometric scaling window is limited to  $L < \lambda_c Y + \sqrt{\bar{\alpha}\chi''(\gamma_c)Y/2}$ , and separated from the region still influenced by the initial condition by a cross-over driven by BFKL diffusion. So far, we discussed only scaling properties of the dipole cross section  $\hat{\sigma}$ . As explained in the introduction, they imply similar scaling properties of the virtual photon-proton cross section, with the replacement  $r \mapsto 1/Q$ .

The mechanism of wave selection explained above happens mainly in the linear regime<sup>8</sup>, i.e. for small  $\hat{\sigma}$ , or equivalently  $r$  smaller than  $Q_s^2(x)$ . However, the geometric scaling property stays also valid in the non-linear regime, i.e. for  $r$  larger than  $Q_s^2(x)$ , which is reached after a large enough evolution in  $Y$ . The only, but decisive, role of saturation in the linear domain is to provide the following dynamical boundary condition in the IR to the linear BFKL evolution: when  $\hat{\sigma}$  is large, it should be quite flat ( $\gamma_{eff}(L) \simeq 0$ ). Indeed, one can simulate successfully the impact of saturation on the solution in the linear regime by studying the BFKL evolution in the presence of an absorptive wall [136], set at a  $Y$ -dependent and selfconsistently determined position near the saturation scale.

At NLL and higher order level, the terms different from running coupling ones do not affect the previous discussion. They just change the kernel eigenvalues  $\chi(\gamma)$  and thus shift the selected parameters  $\gamma_c$  and  $\lambda_c$ . On the contrary, going from fixed to running coupling brings important changes. As the mechanism of spreading of smaller velocity regions of the solution towards larger velocity ones is local, one expect that it holds in the running coupling case. But it selects coupling-dependent velocity and shape of the front, the coupling itself being  $L$ -dependent. Hence, the picture is the following. We still have the formation of a specific traveling wave front solution, which progressively loses memory of its initial condition. However, the selected values

<sup>8</sup>We call linear (non-linear) regime the  $(Y, L)$  domain where the explicit value of the non-linear terms in (27) is (is not) negligible compared to the value of the linear terms.

of the velocity and shape of the front drift as the front propagate towards larger  $L$  (smaller  $r$ ), due to asymptotic freedom. So far, this running coupling case has been solved analytically [112, 136] only at large  $L$  and large  $Y$ , keeping the relevant geometric scaling variable  $-\log(r^2 Q_s^2(x))$  finite. One finds that the evolution is slower than in the fixed coupling case, as the large  $Y$  behavior of the saturation scale is now  $Q_s^2(x) \sim e^{\sqrt{v_c Y/b}} \Lambda_{QCD}^2$ , with  $b \equiv (33 - 2N_f)/36$  and  $v_c \equiv 2\chi(\gamma_c)/\gamma_c$ . In addition, the geometric scaling window is narrower: asymptotically in  $Y$ , it is expected to hold only for<sup>9</sup>  $L < \sqrt{v_c Y/b} + (|\xi_1|/4) (\chi''(\gamma_c))^{1/3} Y^{1/6} / (2b\gamma_c \chi(\gamma_c))^{1/6}$ . The convergence of the selected front towards this asymptotic solution seems rather slow, which may weaken its phenomenological relevance. The whole theoretical picture is nevertheless consistent with numerical simulations [137, 138]. Both leads to a universal traveling wave front structure of the solution, implying scaling properties also subasymptotically.

In order to do phenomenological studies, one can try to extrapolate to finite  $L$  and  $Y$  the scaling behavior found asymptotically. However, this extrapolation is not unique [139]. There is indeed an infinite family of scaling variables

$$\tau_\delta \equiv \left[ 1 - \left( \frac{v_c Y}{b L^2} \right)^\delta \right] L, \quad (28)$$

parameterized by  $\delta$ , which are different from each other at finite  $L$  and  $Y$  but all converge to the same asymptotic scaling previously mentioned. The parameter  $\delta$  seems quite unconstrained, both from the theory and from the DIS data, as shown in the phenomenological section of the present contribution. We considered as benchmark points in that family two specific choices of  $\delta$ . The choice  $\delta = 1/2$  leads to the only scaling variable of the family which is a genuine geometric scaling variable, *i.e.* is equivalent to a scaling with  $r^2 Q_s^2(x)$ . It is named *running coupling I* in the phenomenological section. The choice  $\delta = 1$  leads to the scaling variable obtained by substitution of the fixed coupling by the running coupling directly in the original fixed coupling geometric scaling variable. It is called *running coupling II*.

Finally, one expects scaling properties in any case from evolution equations with saturation, both in the non-linear regime, and in a scaling window in the linear regime. In the linear regime, the solution still obey the linearized equation, and saturation play only the role of a dynamically generated boundary condition. Hence, geometric scaling there, although generated by saturation, is not a hint against the validity of PDF fits. However, geometric scaling occurs also in the non-linear regime, where the scaling function is no more a solution of the linear BFKL or DGLAP equations.

### 3.4 DGLAP evolution and the saturation boundary conditions<sup>10</sup>

One of the issues that could be studied in the context of the geometric scaling versus DGLAP evolution is the possibility of the different boundary conditions for the DGLAP evolution equations. These boundary conditions would incorporate the saturation effects and posses the scaling property. Typically, in the standard approach, to obtain the solution to the linear DGLAP evolution equations, one imposes the initial conditions onto the parton densities at fixed value of  $Q_0^2$

<sup>9</sup> $\xi_1 \simeq -2.34$  is the rightmost zero of the Airy function.

<sup>10</sup>Contributing author: A. M. Stařto

and then performs the evolution into the region of larger values of  $Q^2$ . However, in the presence of saturation these might not be the correct boundary conditions for DGLAP equations. As mentioned earlier the saturation regime is specified by the critical line, the saturation scale  $Q_s(x)$  which is a function of  $x$  Bjorken and its value increases as the Bjorken  $x$  decreases (or as we go to yet higher energies). In that case it seems legitimate to ask, what is the behavior of the DGLAP solutions when evolved from the saturation boundary  $Q^2 = Q_s^2(x)$  rather than from the fixed scale  $Q^2 = Q_0^2$ . To answer this question we imposed [140] the boundary condition for the gluon density at the saturation scale  $Q^2 = Q_s^2$  which possesses the scaling property namely  $\frac{\alpha_s}{2\pi} xg(x, Q^2 = Q_s^2(x)) = \frac{\alpha_s}{2\pi} r^0 x^{-\lambda}$  (in the fixed coupling case). The solution for the gluon density at small  $x$  (at fixed coupling) which can be derived from solving the DGLAP equations with this boundary is given by

$$\frac{\alpha_s}{2\pi} \frac{xg(x, Q^2)}{Q^2} \sim \frac{\alpha_s}{2\pi} \left( \frac{Q^2}{Q_s^2(x)} \right)^{(\alpha_s/2\pi)\gamma_{gg}(\omega_0)-1} \quad (29)$$

where  $\gamma_{gg}$  is the gluon-gluon DGLAP anomalous dimension. This solution clearly has the geometrical scaling property as it is only a function of  $Q^2/Q_s^2(x)$ . It is interesting to note that there exists a critical value of the exponent  $\lambda$  of the saturation scale which determines the existence of scaling. For example in the double leading logarithmic approximation the scaling is present for rather large values of the exponent  $\lambda \geq 4\alpha_s\pi/3$  whereas there is no scaling for smaller values of  $\lambda$ . The formula shown above is however only approximate, as in the derivation we included only the leading behavior which should be dominant at asymptotically small values of  $x$ . At any finite value of  $x$  the scaling will be mildly violated by the nonleading terms. We checked numerically that this is indeed the case, though the violation was very small. This analysis was extended for the case of the more realistic DGLAP evolution with the running coupling. As expected the presence of the scale violation due to the running coupling will lead to the violation of the scaling. In this case the geometric scaling is only approximate with the solution for the gluon density given by

$$\frac{\alpha_s(Q^2)}{2\pi} \frac{xg(x, Q^2)}{Q^2} \sim \frac{Q_s^2(x)}{Q^2} \left[ 1 + \frac{\alpha_s(Q_s^2(x))}{2\pi b} \ln[Q^2/Q_s^2(x)] \right]^{b\gamma_{gg}(\lambda)-1},$$

with  $b$  being the beta function of the QCD running coupling. The scaling here is present provided we have  $\alpha_s(Q_s(x)) \ln[Q^2/Q_s^2(x)]/(2\pi b) \ll 1$ . Thus the geometric scaling violating term can be factored out.

In summary, this analysis shows that the geometric scaling property can be build into the DGLAP initial conditions, and that the solution to the linear evolution equation which do not include the parton saturation effects can preserve the scaling even in the regime of high  $Q^2$  values, outside the saturation region.

### 3.5 Geometric scaling from DGLAP evolution<sup>11</sup>

From the DGLAP point of view there is another possible explanation for geometric scaling: the scaling behaviour can be generated by the evolution itself, rather than being a preserved boundary condition. In fact, it is possible to show [141] both analytically and numerically that in

---

<sup>11</sup>Contributing author: F. Caola



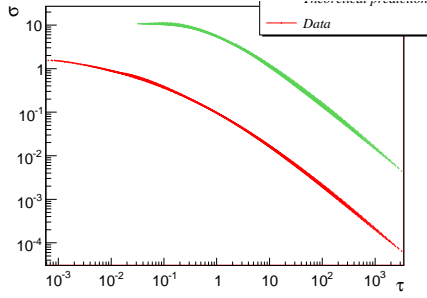


Fig. 18: Scaling plot with  $x < 0.1$ . For the theoretical DGLAP curve, only points with  $Q^2 > 1 \text{ GeV}^2$  were kept. Curves are offset for clarity.

the relevant HERA region approximate geometric scaling is a feature of the DGLAP evolution. In order to see this, one has first to rewrite the DGLAP solution as a function of  $t - \lambda(t, x) \log 1/x$  (“fixed-coupling scaling”) or  $t - \lambda(t, x) \sqrt{\log 1/x}$  (“running-coupling scaling”)<sup>12</sup>. Then from the explicit form of the DGLAP solution it follows that in the relevant kinematic region  $\lambda(t, x)$  is approximatively constant, leading to  $\sigma_{DGLAP}(t, x) \approx \sigma_{DGLAP}(t - t_s(x))$ . Hence approximate geometric scaling in the HERA region is a feature of the DGLAP evolution. Interestingly enough, this DGLAP-generated geometric scaling is expected to hold also at large  $Q^2$  and relatively large  $x$  (say  $x \lesssim 0.1$ ), in contrast with the saturation-based geometric scaling which should be a small  $x$ , small (or at least moderate)  $Q^2$  effect.

In order to make more quantitative statements, one can use the quality factor method introduced in Sec. 3.2. As a starting point, one can consider the leading-order small  $x$  DGLAP evolution of a flat boundary condition. At the level of accuracy of geometric scaling, this approximation should be accurate enough in a wide kinematic region, say  $Q^2 \gtrsim 10 \text{ GeV}^2$ ,  $x \lesssim 0.1$  at HERA. Now, a quality-factor analysis shows that in this region the leading-order small  $x$  DGLAP solution has an excellent scaling behaviour, even better than the scaling behaviour observed in HERA data. Also the DGLAP predictions for the geometric slope  $\lambda$  perfectly agree with the phenomenological values: from the DGLAP solution we obtain  $\lambda_{fix}^{DGLAP} = 0.32 \pm 0.05$  (“fixed-coupling” scaling) and  $\lambda_{run}^{DGLAP} = 1.66 \pm 0.34$  (“running-coupling” scaling), to be compared with  $\lambda_{fix}^{exp} = 0.32 \pm 0.06$ ,  $\lambda_{run}^{exp} = 1.62 \pm 0.25$ . Moreover, data exhibit geometric scaling also for larger  $x$ , larger  $Q^2$  (say  $x \lesssim 0.1$  at HERA), as predicted by the DGLAP evolution. All these results are summarized in Fig. 18, where we plot the theoretical and phenomenological<sup>13</sup> reduced cross sections in function of the “fixed-coupling” scaling variable  $\ln \tau = t - \lambda \ln 1/x$ , with  $\lambda = 0.32$ , in the HERA region with the cut  $x < 0.1$ . An analogous plot can be obtained for the “running-coupling” scaling [141]. We interpret these results as striking evidence that for  $Q^2 > 10 \text{ GeV}^2$  the geometric scaling seen at HERA is generated by the DGLAP evolution itself,

<sup>12</sup>The labels “fixed-coupling” or “running-coupling” are here a bit misleading. In fact, all the results shown here are obtained with the full running-coupling DGLAP solution. We kept this notation only for comparison with saturation-based approaches.

<sup>13</sup>In fact, in order to make a more flexible analysis, we didn’t use the actual HERA data but a neural network interpolation of world DIS data [142]. As long as one stays in the HERA region the output of the net is totally reliable.

without need of a peculiar saturation ansatz or of a suitable scaling boundary condition.

For  $Q^2 < 10 \text{ GeV}^2$  the leading-order DGLAP solution exhibits violations of geometric scaling at small  $x$ . However, in this region any fixed-order DGLAP calculation fails because it does not resum small  $x$  logarithms. If one consider the DGLAP evolution at the resummed level, geometric scaling reappears quite naturally, both in the "fixed-coupling" and "running-coupling" forms [141]. Hence, small  $x$  resummation extends the region where geometric scaling is expected to values of  $Q^2$  lower than  $10 \text{ GeV}^2$ . However at low  $Q^2$  sizeable higher twist and non perturbative effects can spoil the universal behaviour of the DGLAP solution. In this region hence the HERA scaling could still be generated by some DGLAP evolution, but, differently from the  $Q^2 > 10 \text{ GeV}^2$  region, here there is no strong evidence that this is in fact the case.

### 3.6 Saturation model and higher twists<sup>14</sup>

The QCD description of hard scattering processes within the Operator Product Expansion (OPE) approach leads to the twist expansion of matrix elements of process-dependent composite operators. Contributions of emerging local operators with the increasing twists,  $\tau$ , are suppressed by increasing inverse powers of the hard scale,  $Q^2$ . In DIS, at the lowest order (i.e. when the anomalous dimensions vanish), the twist- $\tau$  contribution to the DIS cross section scales as  $Q^{-\tau}$ . Therefore, at sufficiently large  $Q^2$  it is justified to neglect higher twist effects, and retain only the leading twist-2 contribution. This leads to the standard collinear factorisation approach with universal parton density functions evolving according to the DGLAP evolution equation. It should be kept in mind, however, that the higher twist effects do not vanish completely and that they introduce corrections to theoretical predictions based on the DGLAP approach. Thus, the higher twist corrections may affect the determination of parton density functions. The importance of these corrections depends on the level of precision required and on the kinematic domain. In particular, in the region of very small  $x$  the higher twist effects are expected to be enhanced, so that they may become significant at moderate  $Q^2$ . Thus, it should be useful to obtain reliable estimates of higher twist effects at small  $x$ . In this section we shall present higher twist corrections to  $F_T$ ,  $F_L$  and  $F_2$  structure functions following from the DGLAP improved saturation model [143]. The results presented in this section have been obtained in the course of an ongoing study [144, 145]. The method applied to perform the twist decomposition of the DGLAP improved saturation model is a generalisation of the Mellin space approach proposed in Ref. [146].

A rigorous QCD analysis of the higher twist contributions to DIS at high energies is a complex task. So far it has been performed for the  $q\bar{q}gg$  operators [147], but the evolution of twist 4 purely gluonic operators has not been resolved, — even the proper complete basis of the operators has not been found yet. The collinear evolution is known at all twists, however, for so called *quasi-partonic operators*, for which the twist index is equal to the number of partons in the  $t$ -channel [148]. Such operators should receive the strongest enhancement from the QCD evolution. At the leading logarithmic approximation the collinear evolution of quasi-partonic operators is relatively simple — it is given by pair-wise interactions between the partons in the  $t$ -channel. The interactions are described by the non-forward DGLAP kernel [148]. Within this formalism, the evolution of four-gluon quasi-partonic operators was investigated in Ref. [149,

---

<sup>14</sup>Contributing author: L. Motyka



150] in the double logarithmic approximation. At small  $x$  the scattering amplitudes are driven by exchange of gluons in the  $t$ -channel, and the quark exchanges are suppressed by powers of  $x$ . Thus we shall focus on the dominant contribution of the multi-gluon exchanges in the  $t$ -channel. In the large  $N_c$ -limit, the dominant singularities of the four gluon operator are those corresponding to states in which gluons get paired into colour singlet states. In other words, the four-gluon operator evolves like a product of two independent gluon densities. In general, for  $1/N_c \rightarrow 0$ , the  $2n$ -gluon (twist- $2n$ ) operator factorizes into the product of  $n$  twist-2 gluon densities. After suitable inclusion of the AGK cutting rules and the symmetry factors of  $1/n!$ , one arrives at the eikonal picture of  $n$ -ladder exchange between the probe and the target. This is to be contrasted with the Balitsky-Kovchegov picture of Pomeron fan diagrams, which was obtained as a result of resummation of the terms enhanced by powers of large  $\ln(1/x)$  rather than by powers of  $\ln Q^2$ .

The eikonal form of the multiple scattering was assumed in the saturation model proposed by Golec-Biernat and Wüsthoff (GBW) [151, 152]. The dipole cross-section given by Eq. 25 has a natural interpretation in terms of a resummation of multiple scattering amplitudes. The scatters are assumed to be independent of each other, and the contribution of  $n$  scatterings is proportional to  $[r^2/R_0^2(x)]^n$ . The connection of the saturation model to the QCD evolution of quasi-partonic operators is further strengthened by the DGLAP improvement of the dipole cross section [143]. In the DGLAP improved saturation model the dipole cross section depends on the collinear gluon density,

$$\hat{\sigma}(x, r) = \sigma_0 \left[ 1 - \exp \left( -\frac{\pi^2 r^2}{N_c \sigma_0} \alpha_s(\mu^2) x g(x, \mu^2) \right) \right], \quad (30)$$

where the scale  $\mu^2$  depends on the dipole size,  $\mu^2 = C/r^2$  for  $C/r^2 > \mu_0^2$ , and  $\mu^2 = \mu_0^2$  for  $C/r^2 < \mu_0^2$ . The gluon density applied has been obtained from the LO DGLAP evolution without quarks, with the input assumed at the scale  $\mu_0^2$ <sup>15</sup>. Clearly, in Eq. (30) one sees an exact matching between the power of  $r^2$  and the power of  $xg(x, \mu^2)$  suggesting a correspondence between the term  $\sim [r^2 \alpha_s(\mu^2) xg(x, \mu^2)]^n$  in the expansion of  $\hat{\sigma}(x, r)$  and the twist- $2n$  contribution to the dipole cross section. Thus, we expect that the saturation model approximately represents higher twist contributions in the deep inelastic scattering generated by the gluonic quasi-partonic operators.

The twist analysis of the DIS cross-section must include a treatment of the quark box that mediates the coupling of the virtual photon,  $\gamma^*$ , to the  $t$ -channel gluons. In the dipole model the  $\gamma^* g \rightarrow q\bar{q}$  amplitude, computed within QCD, is Fourier transformed (w.r.t. the transverse momentum of the quark) to the coordinate representation and appears as the photon wave function, compare Eq. (25). In more detail, one uses the  $\gamma^* g$  amplitude computed within the  $k_T$ -factorisation framework. This amplitude receives contributions from all twists. The twist structure of the quark box is transparent in the space of Mellin moments, and the same is true for the dipole cross-section. Thus we define,

$$\tilde{H}_{T,L}(\gamma, Q^2) = \int_0^1 dz \int_0^\infty dr^2 r^2 |\Psi_{T,L}(r, z, Q^2)|^2 r^{2(\gamma-1)}, \quad (31)$$

<sup>15</sup>In the original DGLAP-improved model [143] a different definition of the scale was adopted,  $\mu^2 = C/r^2 + \mu_0^2$ , but this choice is less convenient for the QCD analysis.

$$\tilde{\sigma}(x, \gamma) = \int_0^\infty dr^2 \hat{\sigma}(x, r^2) r^{2(\gamma-1)}. \quad (32)$$

It then follows from the Parsival formula that,

$$\sigma_{T,L}(x, Q^2) = \int_{\mathcal{C}} \frac{d\gamma}{2\pi i} \tilde{H}_{T,L}(-\gamma, Q^2) \tilde{\sigma}(x, \gamma). \quad (33)$$

For the massless quark case one has  $\tilde{H}_{T,L}(\gamma, Q^2) = \tilde{H}_{T,L}(\gamma) Q^{-2\gamma}$ . The contour of integration,  $\mathcal{C}$ , in Eq. 33 belongs to the fundamental Mellin strip,  $-1 < \text{Re } \gamma < 0$ .

In order to obtain the twist expansion of  $\sigma$ , one extends the contour  $\mathcal{C}$  in the complex  $\gamma$ -plane into a contour  $\mathcal{C}'$  closed from the left-hand side. The Mellin integral in Eq. 33 may be then decomposed into contributions coming from singularities of  $\tilde{H}_{T,L}(-\gamma, Q^2) \tilde{\sigma}(x, \gamma)$ . The function  $\tilde{H}_T(-\gamma)$  ( $\tilde{H}_L(-\gamma)$ ) has simple poles at all negative integer values of  $\gamma$ , except of  $\gamma = -2$  ( $\gamma = -1$ ), where  $\tilde{H}_T$  ( $\tilde{H}_L$ ) is regular. The singularity structure of the dipole cross section,  $\tilde{\sigma}(\gamma)$ , depends on the specific form of  $\hat{\sigma}(x, r^2)$ . For  $\hat{\sigma}(x, r^2)$  used in the GBW model, the  $\tilde{\sigma}(x, \gamma)$  has simple poles at all negative integers  $\gamma$ 's. For the DGLAP improved form of  $\hat{\sigma}$  given by (31),  $\tilde{\sigma}(x, \gamma)$  has cut singularities that extend to the left from  $\gamma = k$  where  $k = -1, -2$ , etc. The leading behaviour of  $\hat{\sigma}$  around a branch point at  $\gamma = k$  is given by  $\sim (\gamma - k)^{p(k)}$ , where the exponent  $p(k)$  is generated by the DGLAP evolution. As the cuts extend to the left from the branch points, the dominant contribution to the cross section at the given twist comes from the vicinity of the corresponding branch point.

The singularity structure of the quark box part  $\tilde{H}_{T,L}(\gamma)$  plays the crucial role in understanding the strength of the subleading twist effects. To see that one expands  $\tilde{H}_{T,L}(\gamma)$  around the singular points,  $\gamma = 1$  and  $\gamma = 2$  (recall that the argument of  $\tilde{H}_{T,L}$  is  $-\gamma$  in the Parsival formula (33)):

$$\tilde{H}_T(\gamma) = \frac{a_T^{(2)}}{\gamma - 1} + b_T^{(2)} + \mathcal{O}(\gamma - 1), \quad H_L(\gamma) = b_L^{(2)} + \mathcal{O}(\gamma - 1), \quad (34)$$

for twist-2, and

$$\tilde{H}_T(\gamma) = b_T^{(4)} + \mathcal{O}(\gamma - 2), \quad H_L(\gamma) = \frac{a_L^{(4)}}{\gamma - 2} + b_L^{(4)} + \mathcal{O}(\gamma - 2), \quad (35)$$

for twist-4. The singular  $1/(\gamma - 1)$  and  $1/(\gamma - 2)$  terms in (34) and (35) generate an additional enhancement,  $\sim \ln(Q^2)$ , of the corresponding twist-2 and twist-4 contributions to the DIS cross-section. The constant pieces, proportional to  $b_{T,L}^{(2)}$  and  $b_{T,L}^{(4)}$ , produce no new logarithms (thus they are interpreted as the next-to-leading order (NLO) QCD corrections) and the higher terms in the Laurent expansion give yet higher orders in the perturbative expansion of the  $g \rightarrow q$  splitting functions and to the coefficient functions. We summarize this discussion by displaying below the most leading contributions to  $\sigma_{T,L}$  at twist-2 ( $\sigma_{T,L}^{(2)}$ ) and at twist-4 ( $\sigma_{T,L}^{(4)}$ ) obtained in the DGLAP improved saturation model:

$$\sigma_T^{(2)} \sim \frac{a_T^{(2)}}{Q^2} \int_{\mu_0^2}^{Q^2} \frac{dQ'^2}{Q'^2} \alpha_s(Q'^2) xg(x, Q'^2), \quad \sigma_L^{(2)} \sim \frac{b_L^{(2)}}{Q^2} \alpha_s(Q^2) xg(x, Q^2), \quad (36)$$

for twist-2, and

$$\sigma_T^{(4)} \sim \frac{b_T^{(4)}}{Q^4} [\alpha_s(Q^2) x g(x, Q^2)]^2, \quad \sigma_L^{(4)} \sim \frac{a_L^{(4)}}{Q^4} \int_{\mu_0^2}^{Q^2} \frac{dQ'^2}{Q'^2} [\alpha_s(Q'^2) x g(x, Q'^2)]^2, \quad (37)$$

for twist-4. These results imply that the the relative twist-4 correction to  $F_T$  is strongly suppressed w.r.t. the twist-2 contribution, as the subleading twist-4 term in  $F_T$  appears only at the NLO. On the contrary, for  $F_L$ , the leading twist term enters only at the NLO, and the the twist-4 correction enters at the leading order. So, the relative twist-4 effects in  $F_L$  are expected to be enhanced. Note, that both in the case of  $F_T$  and  $F_L$  the twist-4 effects are enhanced w.r.t. the twist-2 contribution by an additional power of the gluon density,  $xg(x, Q^2)$ . For the structure function  $F_2 = F_T + F_L$  we expect small relative corrections from the higher twists because of the opposite sign of coefficients  $a_L^{(4)}$  and  $b_T^{(4)}$ , that leads to cancellations between the twist-4 contributions from  $F_T$  and  $F_L$  at moderate  $Q^2$ . These conclusions about the importance of the higher twist corrections are expected to be quite general, because they follow directly from the twist structure of the quark box and do not depend on the detailed form of the twist-4 gluon distribution.

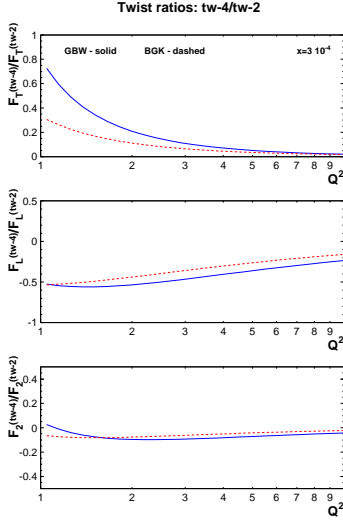


Fig. 19: The ratio of twist-4 to twist-2 components of  $F_T$ ,  $F_L$  and  $F_2$  at  $x = 3 \cdot 10^{-4}$  in the GBW model (continuous lines) and in the DGLAP improved saturation model (dashed lines).

between the twist-4 contributions to  $F_T$  and  $F_L$ , at all  $Q^2$ , down to 1 GeV<sup>2</sup>. Although an effect of this kind was expected, it still remains somewhat surprising that this cancellation works so well. We estimate that, for  $x = 3 \cdot 10^{-4}$ , the twist-4 relative correction to  $F_2$  is 2–4% at  $Q^2 = 10$  GeV<sup>2</sup>, and smaller than 10% for all  $Q^2$  down to 1 GeV<sup>2</sup>. For  $F_L$ , the relative correction is  $\sim 20\%$  at  $Q^2 = 10$  GeV<sup>2</sup>, and strongly increases with the decreasing scale, reaching  $\sim 50\%$  at  $Q^2 = 1$  GeV<sup>2</sup>. It implies that the determination of parton densities from twist-2  $F_2$  data is

We performed [144, 145] an explicit numerical evaluation of the twist-4 corrections to  $F_T$ ,  $F_L$  and  $F_2$  in the DGLAP improved saturation model, and compared the results to results obtained [146] within the GBW model without the DGLAP evolution. The parameters of the DGLAP model were fitted to describe all  $F_2$  data at small  $x$ . In the model we took into account three massless quark flavours and the massive charm quark. The twist analysis, however, has been, so far, performed only for the massless quark contribution. The obtained relative twist-4 corrections to  $F_T$ ,  $F_L$  and  $F_2$  are displayed in Fig. 3.6, as a function of  $Q^2$ , for  $x = 3 \cdot 10^{-4}$ . The continuous curves correspond to the GBW model [146], and the dashed ones have been obtained [144, 145] in the DGLAP improved saturation model. Although there are some quantitative differences between the models, the qualitative picture is quite consistent and confirms the results of the analytic analysis outlined above. Thus, the higher twist corrections are strongest in  $F_L$ , and much weaker in  $F_T$ . In  $F_2$  there occurs a rather fine cancellation between the twist-4 contributions to  $F_T$  and  $F_L$ , at all  $Q^2$ , down to 1 GeV<sup>2</sup>.

safe even at small  $x$  and moderate  $Q^2$ . On the other hand  $F_L$  at small  $x$  may provide a sensitive probe of higher twist effects and parton saturation.

### 3.7 Conclusions

There are many possible explanations for the scaling properties of HERA data, some of them based on saturation effects and some others based on pure linear evolution. In order to separate between these different explanations, it is fundamental to specify a kinematic window.

In particular, for large enough  $Q^2$  and not too small  $x$  (say  $Q^2 \gtrsim 10 \text{ GeV}^2$  in the HERA region) the observed geometric scaling is determined by the DGLAP evolution, irrespective of the boundary condition. For smaller values of  $Q^2$ , the evolution of parton densities is still linear, but is sensitive to a boundary condition. In an evolution toward smaller  $x$ , like BFKL, this boundary condition is dynamically generated by saturation, and it leads to the geometric scaling window. It is possible to take these effects into account also in a  $Q^2$  evolution, like DGLAP, by imposing as initial condition the same boundary condition. We have seen that, in this case, even the LO DGLAP equation is able to propagate geometric scaling towards larger  $Q^2$ . In that domain, although geometric scaling may arise as saturation effect, the evolution is still linear, and thus compatible with standard PDFs analysis. However, at yet lower  $Q^2$  and  $x$  standard linear evolution is no longer reliable. In particular, for  $Q^2$  smaller than a  $x$  dependent saturation scale  $Q_s(x)$ , the evolution of parton densities becomes fully nonlinear, and this spoils the actual determination of the PDFs. Results from inclusive diffraction and vector meson exclusive production at HERA, and from dA collisions at RHIC all suggest that in the kinematic accessible  $x$  region  $Q_s \sim 1 - 2 \text{ GeV}$ .

In conclusion, we can say that for large enough  $Q^2 \gtrsim 10 \text{ GeV}^2$  geometric scaling is fully compatible with linear DGLAP evolution. For smaller  $Q^2$  the situation becomes more involved. For  $Q^2 \gtrsim 5 \text{ GeV}^2$  the HERA scaling is still compatible with DGLAP, maybe with some small  $x$  resummation or some suitable boundary condition. However, other effects may be relevant in this region. For yet lower  $Q^2$  and  $x$  the linear theory becomes unreliable and saturation could be the right explanation for geometric scaling. Unfortunately at HERA we have too few data for a definitive explanation of geometric scaling in the very small  $x$  region, since many different approaches lead approximatively to the same results and it is very difficult to separate among them. For example, in the low  $x$  region both saturation and perturbative resummations lead to a decrease of the gluon and to geometric scaling. At the LHC, where higher center-of-mass energy is available, the  $x$  region is significantly extended down to very small values. Especially in the fragmentation region the typical values of  $x$  which can be probed can reach down to  $10^{-6}$  for partons with transverse momenta of about few GeV. This fact combined with the very wide rapidity coverage of the main LHC detectors opens up a completely new window for the study of parton saturation, and its relations with geometric scaling and linear evolution will possibly be clarified.

### References

- [1] S. A. Larin, T. van Ritbergen, and J. A. M. Vermaseren, Nucl. Phys. **B427**, 41 (1994).

- [2] S. A. Larin, P. Nogueira, T. van Ritbergen, and J. A. M. Vermaseren, Nucl. Phys. **B492**, 338 (1997). hep-ph/9605317.
- [3] A. Retey and J. A. M. Vermaseren, Nucl. Phys. **B604**, 281 (2001). hep-ph/0007294.
- [4] S. Moch, J. A. M. Vermaseren, and A. Vogt, Nucl. Phys. **B688**, 101 (2004). hep-ph/0403192.
- [5] A. Vogt, S. Moch, and J. A. M. Vermaseren, Nucl. Phys. **B691**, 129 (2004). hep-ph/0404111.
- [6] S. Moch, J. A. M. Vermaseren, and A. Vogt, Phys. Lett. **B606**, 123 (2005). hep-ph/0411112.
- [7] J. A. M. Vermaseren, A. Vogt, and S. Moch, Nucl. Phys. **B724**, 3 (2005). hep-ph/0504242.
- [8] A. Vogt, S. Moch, and J. Vermaseren, Nucl. Phys. Proc. Suppl. **160**, 44 (2006). hep-ph/0608307.
- [9] S. Moch and M. Rogal, Nucl. Phys. **B782**, 51 (2007). 0704.1740.
- [10] S. Moch, M. Rogal, and A. Vogt, Nucl. Phys. **B790**, 317 (2008). 0708.3731.
- [11] A. Vogt, S. Moch, M. Rogal, and J. A. M. Vermaseren, Nucl. Phys. Proc. Suppl. **183**, 155 (2008). 0807.1238.
- [12] S. Moch, M. Rogal, A. Vogt, and J. Vermaseren. In preparation.
- [13] Particle Data Group Collaboration, W. M. Yao *et al.*, J. Phys. **G33**, 1 (2006).
- [14] CCFR/NuTeV Collaboration, U.-K. Yang *et al.*, Phys. Rev. Lett. **86**, 2742 (2001). hep-ex/0009041.
- [15] NuTeV Collaboration, M. Tzanov *et al.*, Phys. Rev. **D74**, 012008 (2006). hep-ex/0509010.
- [16] CHORUS Collaboration, G. Onengut *et al.*, Phys. Lett. **B632**, 65 (2006).
- [17] H1 Collaboration, C. Adloff *et al.*, Eur. Phys. J. **C30**, 1 (2003). hep-ex/0304003.
- [18] ZEUS Collaboration, S. Chekanov *et al.*, Eur. Phys. J. **C32**, 1 (2003). hep-ex/0307043.
- [19] H1 Collaboration, A. Aktas *et al.*, Phys. Lett. **B634**, 173 (2006). hep-ex/0512060.
- [20] ZEUS Collaboration, S. Chekanov *et al.*, Phys. Lett. **B637**, 210 (2006). hep-ex/0602026.
- [21] M. L. Mangano *et al.*, *Physics at the front-end of a neutrino factory: A quantitative appraisal*. Preprint hep-ph/0105155, 2001.

- [22] J. B. Dainton, M. Klein, P. Newman, E. Perez, and F. Willeke, *JINST* **1**, P10001 (2006). [hep-ex/0603016](#).
- [23] NuTeV Collaboration, G. P. Zeller *et al.*, *Phys. Rev. Lett.* **88**, 091802 (2002). [hep-ex/0110059](#).
- [24] H1 Collaboration, A. Aktas *et al.*, *Phys. Lett.* **B632**, 35 (2006). [hep-ex/0507080](#).
- [25] S. Davidson, S. Forte, P. Gambino, N. Rius, and A. Strumia, *JHEP* **02**, 037 (2002). [hep-ph/0112302](#).
- [26] K. S. McFarland and S.-O. Moch, *Conventional physics explanations for the NuTeV  $\sin^2(\theta(W))$* . Preprint [hep-ph/0306052](#), 2003.
- [27] B. A. Dobrescu and R. K. Ellis, *Phys. Rev.* **D69**, 114014 (2004). [hep-ph/0310154](#).
- [28] S. Kretzer *et al.*, *Phys. Rev. Lett.* **93**, 041802 (2004). [hep-ph/0312322](#).
- [29] A. J. Buras, *Rev. Mod. Phys.* **52**, 199 (1980).
- [30] S. G. Gorishnii, S. A. Larin, L. R. Surguladze, and F. V. Tkachov, *Comput. Phys. Commun.* **55**, 381 (1989).
- [31] S. A. Larin, F. V. Tkachov, and J. A. M. Vermaseren. NIKHEF-H-91-18.
- [32] D. J. Broadhurst, A. L. Kataev, and C. J. Maxwell, *Phys. Lett.* **B590**, 76 (2004). [hep-ph/0403037](#).
- [33] W. L. van Neerven and A. Vogt, *Nucl. Phys.* **B603**, 42 (2001). [hep-ph/0103123](#).
- [34] E. A. Paschos and L. Wolfenstein, *Phys. Rev.* **D7**, 91 (1973).
- [35] S. Moch, J. A. M. Vermaseren, and A. Vogt, *Nucl. Phys.* **B726**, 317 (2005). [hep-ph/0506288](#).
- [36] S. Catani, D. de Florian, G. Rodrigo, and W. Vogelsang, *Phys. Rev. Lett.* **93**, 152003 (2004). [hep-ph/0404240](#).
- [37] H. L. Lai *et al.*, *JHEP* **04**, 089 (2007). [hep-ph/0702268](#).
- [38] R. S. Thorne, A. D. Martin, W. J. Stirling, and G. Watt, *Parton Distributions for the LHC*. Preprint 0706.0456, 2007.
- [39] A. Vogt (2007). [arXiv:0707.4106](#).
- [40] V. S. Fadin, E. A. Kuraev, and L. N. Lipatov, *Phys. Lett.* **B60**, 50 (1975).
- [41] I. I. Balitsky and L. N. Lipatov, *Sov. J. Nucl. Phys.* **28**, 822 (1978).
- [42] V. S. Fadin and L. N. Lipatov, *Phys. Lett.* **B429**, 127 (1998). [hep-ph/9802290](#).



- [43] G. Camici and M. Ciafaloni, Phys. Lett. **B412**, 396 (1997). hep-ph/9707390.
- [44] M. Ciafaloni and G. Camici, Phys. Lett. **B430**, 349 (1998). hep-ph/9803389.
- [45] S. Marzani, R. D. Ball, P. Falgari, and S. Forte, Nucl. Phys. **B783**, 143 (2007). 0704.2404.
- [46] M. Ciafaloni, D. Colferai, D. Colferai, G. P. Salam, and A. M. Stasto, Phys. Lett. **B576**, 143 (2003). hep-ph/0305254.
- [47] M. Ciafaloni, D. Colferai, G. P. Salam, and A. M. Stasto, Phys. Rev. **D68**, 114003 (2003). hep-ph/0307188.
- [48] S. Catani, M. Ciafaloni, and F. Hautmann, Nucl. Phys. **B366**, 135 (1991).
- [49] S. Catani and F. Hautmann, Nucl. Phys. **B427**, 475 (1994). hep-ph/9405388.
- [50] A. Bialas, H. Navelet, and R. B. Peschanski, Nucl. Phys. **B603**, 218 (2001). hep-ph/0101179.
- [51] C. D. White, R. B. Peschanski, and R. S. Thorne, Phys. Lett. **B639**, 652 (2006). hep-ph/0606169.
- [52] G. Altarelli, R. D. Ball, and S. Forte, Nucl. Phys. **B575**, 313 (2000). hep-ph/9911273.
- [53] G. Altarelli, R. D. Ball, and S. Forte, Nucl. Phys. **B621**, 359 (2002). hep-ph/0109178.
- [54] G. Altarelli, R. D. Ball, and S. Forte, Nucl. Phys. **B674**, 459 (2003). hep-ph/0306156.
- [55] G. Altarelli, R. D. Ball, and S. Forte, Nucl. Phys. **B742**, 1 (2006). hep-ph/0512237.
- [56] R. D. Ball and S. Forte, Nucl. Phys. **B742**, 158 (2006). hep-ph/0601049.
- [57] R. D. Ball, Nucl. Phys. **B796**, 137 (2008). 0708.1277.
- [58] G. Altarelli, R. D. Ball, and S. Forte, Nucl. Phys. **B799**, 199 (2008). 0802.0032.
- [59] G. Altarelli, R. D. Ball, and S. Forte, *Structure Function Resummation in small- $x$  QCD*. Preprint 0802.0968, 2007.
- [60] G. P. Salam, JHEP **07**, 019 (1998). hep-ph/9806482.
- [61] M. Ciafaloni and D. Colferai, Phys. Lett. **B452**, 372 (1999). hep-ph/9812366.
- [62] M. Ciafaloni, D. Colferai, and G. P. Salam, Phys. Rev. **D60**, 114036 (1999). hep-ph/9905566.
- [63] M. Ciafaloni, D. Colferai, and G. P. Salam, JHEP **07**, 054 (2000). hep-ph/0007240.

- [64] M. Ciafaloni and D. Colferai, JHEP **09**, 069 (2005). hep-ph/0507106.
- [65] M. Ciafaloni, D. Colferai, G. P. Salam, and A. M. Stasto, Phys. Lett. **B635**, 320 (2006). hep-ph/0601200.
- [66] M. Ciafaloni, D. Colferai, G. P. Salam, and A. M. Stasto, JHEP **08**, 046 (2007). 0707.1453.
- [67] R. S. Thorne, Phys. Rev. **D60**, 054031 (1999). hep-ph/9901331.
- [68] R. S. Thorne, Nucl. Phys. Proc. Suppl. **79**, 210 (1999). hep-ph/9906323.
- [69] R. S. Thorne, Phys. Lett. **B474**, 372 (2000). hep-ph/9912284.
- [70] R. S. Thorne, Phys. Rev. **D64**, 074005 (2001). hep-ph/0103210.
- [71] C. D. White and R. S. Thorne, Phys. Rev. **D74**, 014002 (2006). hep-ph/0603030.
- [72] C. D. White and R. S. Thorne, Phys. Rev. **D75**, 034005 (2007). hep-ph/0611204.
- [73] M. Dittmar *et al.*, *Parton distributions: Summary report for the HERA - LHC workshop*. Preprint hep-ph/0511119, 2005.
- [74] R. D. Ball and S. Forte, Phys. Lett. **B465**, 271 (1999). hep-ph/9906222.
- [75] G. Altarelli, R. D. Ball, and S. Forte, Nucl. Phys. **B599**, 383 (2001). hep-ph/0011270.
- [76] G. Altarelli, R. D. Ball, and S. Forte, *An improved splitting function for small  $x$  evolution*. Preprint hep-ph/0310016, 2003.
- [77] G. Altarelli, R. D. Ball, and S. Forte, Nucl. Phys. Proc. Suppl. **135**, 163 (2004). hep-ph/0407153.
- [78] R. D. Ball and S. Forte, Phys. Lett. **B405**, 317 (1997). hep-ph/9703417.
- [79] L. Lipatov, Sov. Phys. JETP **5**, 5 (1986).
- [80] R. D. Ball and R. K. Ellis, JHEP **05**, 053 (2001). hep-ph/0101199.
- [81] B. Andersson, G. Gustafson, H. Kharraziha, and J. Samuelsson, Z. Phys. **C71**, 613 (1996).
- [82] J. Kwiecinski, A. D. Martin, and P. J. Sutton, Z. Phys. **C71**, 585 (1996). hep-ph/9602320.
- [83] J. Kwiecinski, A. D. Martin, and A. M. Stasto, Phys. Rev. **D56**, 3991 (1997). hep-ph/9703445.
- [84] J. C. Collins and J. Kwiecinski, Nucl. Phys. **B316**, 307 (1989).



- [85] C. D. White and R. S. Thorne, Eur. Phys. J. **C45**, 179 (2006). hep-ph/0507244.
- [86] D0 Collaboration, B. Abbott *et al.*, Phys. Rev. Lett. **86**, 1707 (2001).  
hep-ex/0011036.
- [87] CDF Collaboration, T. Affolder *et al.*, Phys. Rev. **D64**, 032001 (2001).  
hep-ph/0102074.
- [88] H1 Collaboration, C. Adloff *et al.*, Eur. Phys. J. **C19**, 269 (2001). hep-ex/0012052.
- [89] H1 Collaboration, C. Adloff *et al.*, Eur. Phys. J. **C21**, 33 (2001). hep-ex/0012053.
- [90] ZEUS Collaboration, J. Breitweg *et al.*, Eur. Phys. J. **C7**, 609 (1999).  
hep-ex/9809005.
- [91] ZEUS Collaboration, S. Chekanov *et al.*, Eur. Phys. J. **C21**, 443 (2001).  
hep-ex/0105090.
- [92] A. D. Martin, W. J. Stirling, and R. S. Thorne, Phys. Lett. **B635**, 305 (2006).  
hep-ph/0601247.
- [93] R. S. Thorne, Phys. Rev. **D73**, 054019 (2006). hep-ph/0601245.
- [94] H1 Collaboration, F. D. Aaron *et al.*, Phys. Lett. **B665**, 139 (2008). 0805.2809.
- [95] A. D. Martin, W. J. Stirling, R. S. Thorne, and G. Watt, Phys. Lett. **B652**, 292 (2007).  
0706.0459.
- [96] M. Ciafaloni, Phys. Lett. **B356**, 74 (1995). hep-ph/9507307.
- [97] M. Diemoz, F. Ferroni, E. Longo, and G. Martinelli, Z. Phys. **C39**, 21 (1988).
- [98] R. D. Ball and S. Forte, Phys. Lett. **B359**, 362 (1995). hep-ph/9507321.
- [99] P. F. R. *Photon-Hadron Interactions*. Benjamin, New York, 1972.
- [100] Bjorken, J.D., Lecture Notes in Physics, **56**, Springer, Berlin (1976).
- [101] Kuraev, E.A. and Lipatov, L.N. and Fadin, V.S., Sov. Phys. JETP **45**, 199 (1977).
- [102] N. G. V. and N. L. L. Sov. J. Nucl. Phys. **15**, 438 (1972).
- [103] N. G. V. and N. L. L. Sov. J. Nucl. Phys. **15**, 675 (1972).
- [104] G. Altarelli and G. Parisi, Nucl. Phys. **B 126**, 298 (1977).
- [105] L. D. Yu. Sov. Phys. JETP **46**, 641 (1977).
- [106] Gribov, L.V. and Levin, E.M. and Ryskin, M.G., Phys. Rept. **100**, 1 (1983).
- [107] Mueller, A.H., Nucl. Phys. **B558**, 285 (1999).

- [108] E. Iancu and R. Venugopalan, *The color glass condensate and high energy scattering in QCD*. Preprint hep-ph/0303204, 2003.
- [109] Balitsky, I., Nucl. Phys. **B463**, 99 (1996).
- [110] Kovchegov, Yu.V., Phys. Rev. **D61**, 074018 (2000).
- [111] A. M. Stasto, K. J. Golec-Biernat, and J. Kwiecinski, Phys. Rev. Lett. **86**, 596 (2001). hep-ph/0007192.
- [112] S. Munier and R. Peschanski, Phys. Rev. **D69**, 034008 (2004). hep-ph/0310357.
- [113] F. Gelis, R. B. Peschanski, G. Soyez, and L. Schoeffel, Phys. Lett. **B647**, 376 (2007). hep-ph/0610435.
- [114] ZEUS Collaboration, J. Breitweg *et al.*, Phys. Lett. **B487**, 273 (2000). hep-ex/0006013.
- [115] ZEUS Collaboration, S. Chekanov *et al.*, Phys. Rev. **D70**, 052001 (2004). hep-ex/0401003.
- [116] New Muon Collaboration Collaboration, M. Arneodo *et al.*, Nucl. Phys. **B483**, 3 (1997). hep-ph/9610231.
- [117] E665 Collaboration, M. R. Adams *et al.*, Phys. Rev. **D54**, 3006 (1996).
- [118] G. Beuf, R. Peschanski, C. Royon, and D. Salek, *Systematic Analysis of Scaling Properties in Deep Inelastic Scattering*. Preprint arXiv:0803.2186 [hep-ph], 2008.
- [119] H1 Collaboration, F. D. Aaron *et al.*, Phys. Lett. **B659**, 796 (2008). 0709.4114.
- [120] H1 Collaboration, A. Aktas *et al.*, Eur. Phys. J. **C44**, 1 (2005). hep-ex/0505061.
- [121] H1 Collaboration, A. Aktas *et al.*, Eur. Phys. J. **C48**, 715 (2006). hep-ex/0606004.
- [122] ZEUS Collaboration, S. Chekanov *et al.*, Nucl. Phys. **B713**, 3 (2005). hep-ex/0501060.
- [123] ZEUS Collaboration, S. Chekanov *et al.*, Eur. Phys. J. **C38**, 43 (2004). hep-ex/0408009.
- [124] ZEUS Collaboration, S. Chekanov *et al.*, Nucl. Phys. **B718**, 3 (2005). hep-ex/0504010.
- [125] H1 Collaboration, A. Aktas *et al.*, Eur. Phys. J. **C46**, 585 (2006). hep-ex/0510016.
- [126] H1 Collaboration, C. Adloff *et al.*, Eur. Phys. J. **C13**, 371 (2000). hep-ex/9902019.
- [127] H1 Collaboration, C. Adloff *et al.*, Z. Phys. **C72**, 593 (1996). hep-ex/9607012.
- [128] H1 Collaboration, C. Adloff *et al.*, Phys. Lett. **B528**, 199 (2002). hep-ex/0108039.

- [129] ZEUS Collaboration, J. Breitweg *et al.*, Phys. Lett. **B407**, 402 (1997).  
hep-ex/9706009.
- [130] European Muon Collaboration, J. J. Aubert *et al.*, Nucl. Phys. **B213**, 31 (1983).
- [131] P. M. Nadolsky *et al.*, Phys. Rev. **D78**, 013004 (2008). 0802.0007.
- [132] A. D. Martin, R. G. Roberts, W. J. Stirling, and R. S. Thorne, Phys. Lett.  
**B604**, 61 (2004). hep-ph/0410230.
- [133] M. Gluck, E. Reya, and A. Vogt, Eur. Phys. J. **C5**, 461 (1998). hep-ph/9806404.
- [134] R. C. Beuf, G. and D. Salek, to appear.
- [135] E. Iancu, K. Itakura, and L. McLerran, Nucl. Phys. **A708**, 327 (2002).  
hep-ph/0203137.
- [136] A. H. Mueller and D. N. Triantafyllopoulos, Nucl. Phys. **B640**, 331 (2002).  
hep-ph/0205167.
- [137] E. Gardi, J. Kuokkanen, K. Rummukainen, and H. Weigert, Nucl. Phys.  
**A784**, 282 (2007). hep-ph/0609087.
- [138] J. L. Albacete and Y. V. Kovchegov, Phys. Rev. **D75**, 125021 (2007).  
arXiv:0704.0612 [hep-ph].
- [139] G. Beuf, *An alternative scaling solution for high-energy qcd saturation with running coupling*. Preprint arXiv:0803.2167 [hep-ph], 2008.
- [140] J. Kwiecinski and A. M. Stasto, Phys. Rev. **D66**, 014013 (2002). hep-ph/0203030.
- [141] F. Caola and S. Forte, Phys. Rev. Lett. **101**, 022001 (2008). 0802.1878.
- [142] NNPDF Collaboration, L. Del Debbio, S. Forte, J. I. Latorre, A. Piccione, and J. Rojo,  
JHEP **03**, 080 (2005). hep-ph/0501067.
- [143] J. Bartels, K. J. Golec-Biernat, and H. Kowalski, Phys. Rev. **D66**, 014001 (2002).  
hep-ph/0203258.
- [144] K. G.-B. J. Bartels and L. Motyka, *in preparation*.
- [145] L. Motyka, *Higher twists from the saturation model*.  
Talk at the 4th HERA and the LHC workshop, CERN, 26–30 May 2008,  
<http://indico.cern.ch/conferenceDisplay.py?confId=27458>.
- [146] J. Bartels, K. J. Golec-Biernat, and K. Peters, Eur. Phys. J. **C17**, 121 (2000).  
hep-ph/0003042.
- [147] R. K. Ellis, W. Furmanski, and R. Petronzio, Nucl. Phys. **B212**, 29 (1983).

- [148] A. P. Bukhvostov, G. V. Frolov, L. N. Lipatov, and E. A. Kuraev, Nucl. Phys. **B258**, 601 (1985).
- [149] J. Bartels and M. G. Ryskin, Z. Phys. **C60**, 751 (1993).
- [150] J. Bartels and M. G. Ryskin, Z. Phys. **C62**, 425 (1994).
- [151] K. J. Golec-Biernat and M. Wusthoff, Phys. Rev. **D59**, 014017 (1999).  
hep-ph/9807513.
- [152] K. J. Golec-Biernat and M. Wusthoff, Phys. Rev. **D60**, 114023 (1999).  
hep-ph/9903358.

# Benchmarking of parton distributions and their uncertainties

*R. D. Ball, L. Del Debbio, J. Feltesse, S. Forte, A. Glazov, A. Guffanti, J. I. Latorre, A. Piccione, V. Radescu, J. Rojo, R. S. Thorne, M. Ubiali, G. Watt*

## 1 Introduction

The proper treatment of uncertainties associated to the fit of Parton Distribution Functions (PDF) has become a subject of great interest in the last few years. A simple way of understanding differences between available approaches to parton fits is to fix some hypothesis (say, experimental data, QCD parameters, input parameterizations, error treatment), and check what is the effect of the remaining assumptions. Such studies were previously done in the framework of the first HERA–LHC workshop [1].

In the following we will discuss three benchmark fits. The first one is presented in Sect. 2. It is based on the H12000 parton fit [2], and it compares a new version of this fit, in which uncertainty bands are determined [3,4] using a Monte Carlo method, to the reference fit, where uncertainty bands are obtained using the standard Hessian method. The main motivation of this benchmark is to study the impact of possible non-Gaussian behaviour of the data and, more generally, the dependence on the error treatment.

The second benchmark is presented in Sect. 3. It is based on the study performed by S. Alekhin and R. Thorne in Ref. [1], which compared the fits by their respective groups to a common reduced set of data with common assumptions, and also to their respective reference (global) fits. This comparison is extended here in two ways. First, the comparison is extended to include an NNPDF fit to the same reduced set of data with the same assumptions, and the NNPDF1.0 reference fit [5]. Second, results are also compared to a fit based on the recent MSTW 2008 [6, 7] analysis. As in the Thorne benchmark fit, this uses slightly different data sets and assumptions; it is furthermore modified to use the same input parameterization and improved treatment of uncertainties as MSTW. The main purpose of these comparisons is to answer the questions (a) to which extent fit results from various groups obtained using different methodologies still differ from each other when common or similar assumptions and a common or similar reduced dataset are used and (b) how the fits to the reduced dataset by each group compare to the fit to the full dataset.

The third benchmark, discussed in Sect. 4, is a further elaboration on the benchmark presented in Sect. 2, extended to include the NNPDF fit, which also uses a Monte Carlo approach. The main purpose of this benchmark is to compare two fits (H1 and NNPDF) which have the same error treatment but different parton parameterizations. The inclusion in this benchmark of the NNPDF fit is also interesting because it allows a comparison of a fit based on a very consistent set of data coming from the H1 collaboration only, to fits which include all DIS data sets, which are less compatible than the H1 sets alone.

### 1.1 Settings for the H1 benchmark

This analysis is based on all the DIS inclusive data by the H1 collaboration from the HERA-I run. A kinematic cut of  $Q^2 > 3.5 \text{ GeV}^2$  is applied to avoid any higher twist effect. The data

points used in the analysis are summarized in Table 1 and Fig. 1.

Data Set	Data points	Observable	Ref.
H197mb	35	$\tilde{\sigma}^{NC,+}$	[8]
H197lowQ2	80	$\tilde{\sigma}^{NC,+}$	[8]
H197NC	130	$\tilde{\sigma}^{NC,+}$	[9]
H197CC	25	$\tilde{\sigma}^{CC,+}$	[9]
H199NC	126	$\tilde{\sigma}^{NC,-}$	[10]
H199CC	28	$\tilde{\sigma}^{CC,-}$	[10]
H199NChy	13	$\tilde{\sigma}^{NC,-}$	[10]
H100NC	147	$\tilde{\sigma}^{NC,+}$	[2]
H100CC	28	$\tilde{\sigma}^{CC,+}$	[2]
Total	612		

Table 1: Data points used in the H1 benchmark after kinematic cuts of  $Q^2 > 3.5 \text{ GeV}^2$ .

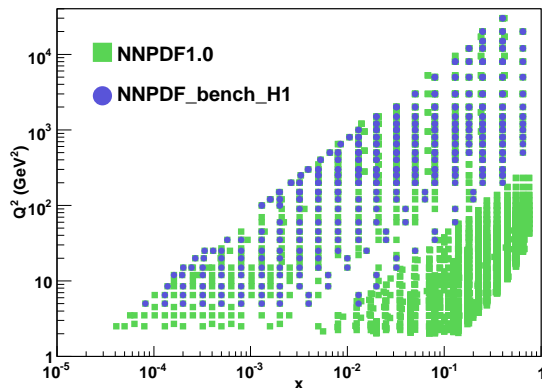


Fig. 1: The data used in the H1 benchmark and in the NNPDF reference fit.

The theoretical assumptions are:

- NLO perturbative QCD in the  $\overline{\text{MS}}$  renormalization and factorization scheme;
- zero-mass variable flavour number scheme with quark masses  $m_c = 1.4 \text{ GeV}$  and  $m_b = 4.5 \text{ GeV}$ ;
- the strong coupling fixed to  $\alpha_s(M_Z) = 0.1185$ ;
- momentum and valence sum rules enforced;
- starting scale for the evolution at  $Q_0^2 = 4 \text{ GeV}^2$ ;
- strange contribution fixed as

$$s(x, Q_0^2) = \bar{s}(x, Q_0^2) = f_s \bar{D}(x, Q_0^2) = \frac{f_s}{1 - f_s} \bar{d}(x, Q_0^2), \quad (1)$$

with  $U = u + c$  and  $D = d + s + b$  and with  $f_s = 0.33$ ;

- charm contribution fixed as

$$c(x, Q_0^2) = \bar{c}(x, Q_0^2) = f_c \bar{U}(x, Q_0^2) = \frac{f_c}{1 - f_c} \bar{u}(x, Q_0^2), \quad (2)$$

with  $f_c = 0.15$ ;

- five independent PDFs: gluon and  $U, D, \bar{U}, \bar{D}$  (see definition above);
- iterated solution for evolution (see, e.g. [11], Sect. 1.3).

Both the H1 and NNPDF methodologies are based on

- Monte Carlo method to determine uncertainties. This method will be discussed in detail in Sect. 2.2 below.

They differ in the way PDFs are parameterized:

- H1 parameterizes PDFs as

$$\begin{aligned} xg(x, Q_0^2) &= A_g x^{B_g} (1-x)^{C_g} [1 + D_g x], \\ xU(x, Q_0^2) &= A_U x^{B_U} (1-x)^{C_U} [1 + D_U x + F_U x^3], \\ xD(x, Q_0^2) &= A_D x^{B_D} (1-x)^{C_D} [1 + D_D x], \\ x\bar{U}(x, Q_0^2) &= A_{\bar{U}} x^{B_{\bar{U}}} (1-x)^{C_{\bar{U}}}, \\ x\bar{D}(x, Q_0^2) &= A_{\bar{D}} x^{B_{\bar{D}}} (1-x)^{C_{\bar{D}}}, \end{aligned} \quad (3)$$

(4)

which yields 10 free parameters after sum rules are imposed;

- NNPDF parameterizes PDFs with a 2-5-3-1 neural network, which implies 185 free parameters to be fitted.

Because of the large number of parameters, the minimum of the NNPDF fit is determined using the stopping criterion discussed in Sect. 3.2 below, while the minimum of the H1 fit is determined as the standard minimum  $\chi^2$  (or maximum likelihood) point of parameter space.

## 1.2 Settings for the HERA–LHC benchmark

This benchmark was first presented in Ref. [1], where its settings were defined. In order to have a conservative ensemble of experimental data and observables, only structure function DIS data are used. Large kinematic cuts are applied to avoid any higher twist effect. The data points used in the Alekhin analysis are summarized in Table 2 and Fig. 2.

The theoretical assumptions are:

- NLO perturbative QCD in the  $\overline{\text{MS}}$  renormalization and factorization scheme;
- zero-mass variable flavour number scheme with quark masses  $m_c = 1.5 \text{ GeV}$  and  $m_b = 4.5 \text{ GeV}$ ;
- $\alpha_s(M_Z)$  fitted: the best-fit values are  $0.1110 \pm 0.0012$  (Alekhin) and  $0.1132 \pm 0.0015$  (Thorne);
- momentum and valence sum rules imposed;

Data Set	Data points	Observable	Ref.
ZEUS97	206	$F_2^p$	[12]
H1lowx97	77	$F_2^p$	[8]
NMC	95	$F_2^p$	[13]
NMC_pd	73	$F_2^d/F_2^p$	[14]
BCDMS	322	$F_2^p$	[15]
Total	773		

Table 2: Data points used in the HERA–LHC benchmark after kinematic cuts of  $Q^2 > 9 \text{ GeV}^2$  and  $W^2 > 15 \text{ GeV}^2$  are applied.

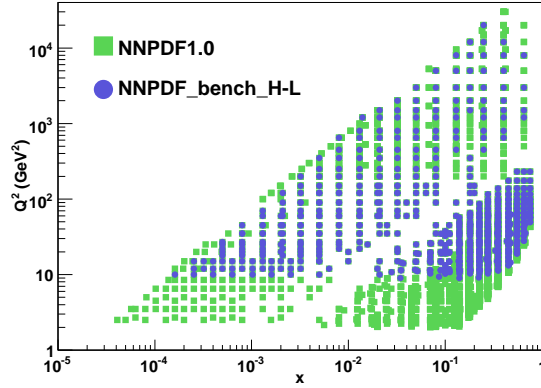


Fig. 2: The data used in the HERA–LHC benchmark and in the NNPDF reference fit.

- starting scale for evolution  $Q_0^2 = 1 \text{ GeV}^2$ ;
- four independent input PDFs ( $u$  and  $d$  valence, the sea and the gluon);
- no light sea asymmetry:  $\bar{u} = \bar{d}$ ;
- no independent strange PDF:

$$s(x, Q_0^2) + \bar{s}(x, Q_0^2) = 0.5(\bar{u}(x, Q_0^2) + \bar{d}(x, Q_0^2)); \quad (5)$$

- iterated solution of evolution equations;

The NNPDF analysis presented here is based on the same data set and theoretical assumptions, the only difference being that the strong coupling is fixed to  $\alpha_s(M_Z) = 0.112$ , i.e. the average of the fitted values of S. Alekhin and R. Thorne.

The Thorne benchmark used somewhat different data sets and assumptions. Namely:

- A somewhat different dataset is used, as displayed in Table 3. This differs from the dataset of Table 2 and Figure 2 because the NMC and BCDMS fixed-target data on  $F_2^p$  used are averaged over different beam energies, and also, HERA reduced cross sections rather than structure function data are used, resulting in an additional nine H1 points. Note that the Thorne benchmark in Ref. [1] also included the  $F_2^d$  BCDMS deuterium data.



Data Set	Data points	Observable	Ref.
ZEUS97	206	$\tilde{\sigma}^{\text{NC},+}$	[12]
H1lowx97	86	$\tilde{\sigma}^{\text{NC},+}$	[8]
NMC	67	$F_2^p$	[13]
NMC_pd	73	$F_2^d/F_2^p$	[14]
BCDMS	157	$F_2^p$	[15]
Total	589		

Table 3: Data points used in the MSTW benchmark fit after kinematic cuts of  $Q^2 > 9 \text{ GeV}^2$  and  $W^2 > 15 \text{ GeV}^2$  are applied.

- All correlations between systematics are neglected, and statistical and systematic errors are added in quadrature.
- Normalizations of individual data sets are fitted with a rescaling of uncertainties to avoid systematic bias.
- The  $F_2^d/F_2^p$  data are corrected for nuclear shadowing effects [16].

The MSTW analysis presented here makes the same choices as the Thorne benchmark, but with  $\alpha_s(M_Z) = 0.112$ , and additionally

- a global correction of  $-3.4\%$  is applied to the luminosity of the published H1 MB 97 data [8] following a luminosity reanalysis [17].
- a quartic penalty term in the  $\chi^2$  definition is given to normalizations which deviate from the central value.

## 2 Experimental Error Propagation<sup>1</sup>

### 2.1 Introduction

Standard error estimation of proton parton distribution functions (PDFs) relies on the assumption that all errors follow Gaussian (or normal) statistics. However, this assumption may not always be correct. Some systematic uncertainties such as luminosity and detector acceptance follow rather a log-normal distribution (see Section [18]). Compared to the Gaussian case, the lognormal distribution which has the same mean and root mean square (RMS), is asymmetric and has a shifted peak, as shown illustratively in Figure 3. Therefore, the non-Gaussian behaviour of the experimental uncertainties could lead to an additional uncertainty of the resulting PDFs. An alternative to the standard error propagation is a toy Monte Carlo (MC) method. Here, an implementation of the MC method is presented for estimation of the PDF uncertainties with various assumptions for the error distribution. In addition, this MC method provides an independent cross check of the standard error propagation when assuming the Gaussian error distributions.

### 2.2 Method

The Monte Carlo technique consists firstly in preparing replicas of the initial data sets which have the central value of the cross sections,  $\sigma_i$ , fluctuating within its systematic and statistical uncer-

<sup>1</sup>Contributing authors: J. Feltesse, A. Glazov, V. Radescu

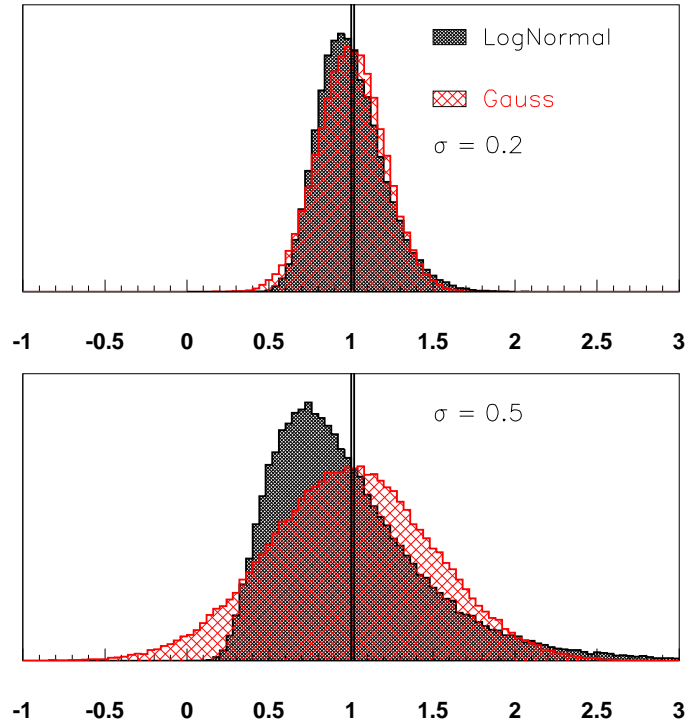


Fig. 3: Comparison of the lognormal (black, darker hatching) and Gaussian (red, lighter hatching) probability distributions. The distributions are shown with mean equal to one, and two different choices for the RMS (for both distribution):  $\sigma = 0.2$  (top) and  $\sigma = 0.5$ .

tainties taking into account all point to point correlations. Various assumptions can be considered for the error distributions. When dealing with the statistical and point to point uncorrelated errors, one could allow each data point to randomly fluctuate within its uncorrelated uncertainty assuming either Gauss, lognormal, or any other desired form of the error distribution. For example, for Gaussian errors

$$\sigma_i \longrightarrow \sigma_i (1 + \delta_i^{uncorr} \cdot R_i), \quad (6)$$

where  $\delta_i^{uncorr}$  corresponds to the uncorrelated uncertainties and  $R_i$  is a random number chosen from a normal distribution with a mean of 0 and a standard deviation of 1. Hence, the central value of each cross section point  $i$  is shifted by  $\delta_i^{uncorr} \cdot R_i$ .

For the systematic errors, the treatment is a bit more complicated than above. This is due to the correlation between data points and that, in general, the data points are sensitive to the systematic sources with a different strength  $\delta_{ij}$ , where index  $i$  ( $j$ ) runs over all the cross section points (all systematic sources). In order to take this into account, for each systematic source  $j$  a uniformly distributed *fluctuation probability*  $P_j$  is selected. Then, for each data point  $i$  the central value of cross section is shifted such that probability of this shift, which depends on  $\delta_{ij}$  and the exact form of the probability distribution function, is equal  $P_j$  (for positive  $\delta_{ij}$ ) or  $(1 - P_j)$  (for negative  $\delta_{ij}$ ). In other words, each central value of the cross section is shifted with

the same probability of the corresponding systematic shift. For example for the Gaussian errors, this procedure is equivalent to

$$\sigma_i \longrightarrow \sigma_i \left( 1 + \delta_i^{uncorr} \cdot R_i + \sum_j^{N_{sys}} \delta_{ij}^{corr} \cdot R_j \right), \quad (7)$$

where in addition to the shifts for the uncorrelated errors previously explained,  $R_j$  corresponds to another random number chosen from a normal distribution with mean of 0 and standard deviation of 1 as a fluctuation for the systematic source  $j$ . Hence, the central values of the cross sections are shifted in addition by  $\delta_{ij}^{corr} \cdot R_j$  for each systematic shift.

This preparation of the data is repeated for  $N$  times, where high statistics is desirable for more accurate results. For this study we used  $N > 100$  which proved to suffice. For each replica, a next to leading order (NLO) QCD fit is performed to extract the PDFs. The errors on the PDFs are estimated from the RMS of the spread of the  $N$  lines corresponding to the  $N$  individual fits to extract PDF.

A fit to the published H1 HERA-I data of neutral and charged current  $e^\pm p$  scattering cross sections [2] using the settings discussed in Sect. 1.1 has been performed, using the QCDNUM program [19].

### 2.3 Validation of the Method

The MC method is tested by comparing the standard error estimation of the PDF uncertainties with the MC techniques by assuming that all the errors (statistical and systematic) follow Gaussian (normal) distribution. Figure 4 shows good agreement between the methods.

### 2.4 Test of various assumptions for the error distributions

Two cases are considered which may represent most likely the error distributions: (1) the log-normal distribution for the luminosity uncertainty and the rest of the errors are set to follow the Gauss shape, (2) the lognormal distributions for all the systematic errors and the statistical errors are set to follow the Gauss distributions. The results for the first case (1) are shown in Figure 5. The results of the tests for the case when lognormal distributions for all the systematic uncertainties are assumed is shown in Figure 5. We observe that for the precise H1 HERA-1 data the effect of using lognormal distribution, which is considered for some systematic uncertainties more physical, is similar to the pure gauss distribution case.

### 2.5 Conclusions

A simple method to estimate PDF uncertainties has been built within QCD Fit framework. Assuming only gauss distribution of all errors, the results agree well with the standard error estimation. This method allows to check the effect of non- gauss assumptions for distributions of the experimental uncertainties. For the H1 data, results are similar to the gauss case when using lognormal. The method could be extended for other physical variables (i.e. cross sections) for cross checks with the standard error evaluation.

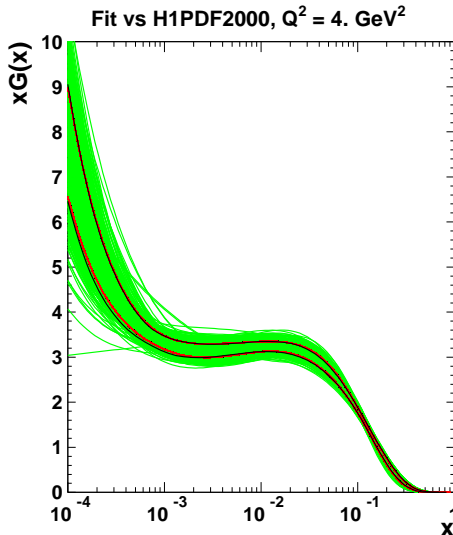


Fig. 4: Comparison between the standard error calculations and the Gauss error distribution is shown for the gluon PDF. Green lines represent the spread of Monte Carlo generated allowances for the errors, and the red lines are the RMS of this spread. The black lines correspond to the standard error calculations of the PDF errors.

### 3 HERA–LHC Benchmark

This benchmark is based on the Alekhin/Thorne benchmark of Ref. [1], whose settings has been given in Sect. 1.2. Both the Alekhin and Thorne fits had the following features:

- uncertainties determined using the Hessian method with  $\Delta\chi^2 = 1$ ;
- input PDFs are parameterized using the following functional form:

$$x f_i(x, Q_0^2) = A_i (1-x)^{b_i} (1 + \epsilon_i x^{0.5} + \gamma_i x) x^{a_i}. \quad (8)$$

with  $\epsilon_i$  and  $\gamma_i$  set to zero for the sea and gluon distributions. Hence, there were a total of 13 free PDF parameters plus  $\alpha_s(M_Z)$  after imposing sum rules.

Here, we reanalyze it within the MSTW and NNPDF approaches. First, we summarize the respective MSTW and NNPDF approaches, and especially their differences when compared to the previous HERALHC benchmark fits of Ref. [1]. Then, results for benchmark fits obtained with the various different approaches are compared to each other. Finally, we compare each benchmark fit to its counterpart based on a wider range of data, i.e. the NNPDF1.0 [5] reference and the MRST01 [20] and MSTW08 [6, 7] PDFs.

#### 3.1 MSTW approach<sup>2</sup>

The benchmark analysis is now much more closely aligned to the global analysis than was the case for the Thorne benchmark compared to the MRST global analysis. It follows the general approach taken by the MRST (or more recently, MSTW) group, and is similar to that described in Ref. [20]. There are some new features which are explained below.

<sup>2</sup>Contributing authors: R. S. Thorne, G. Watt

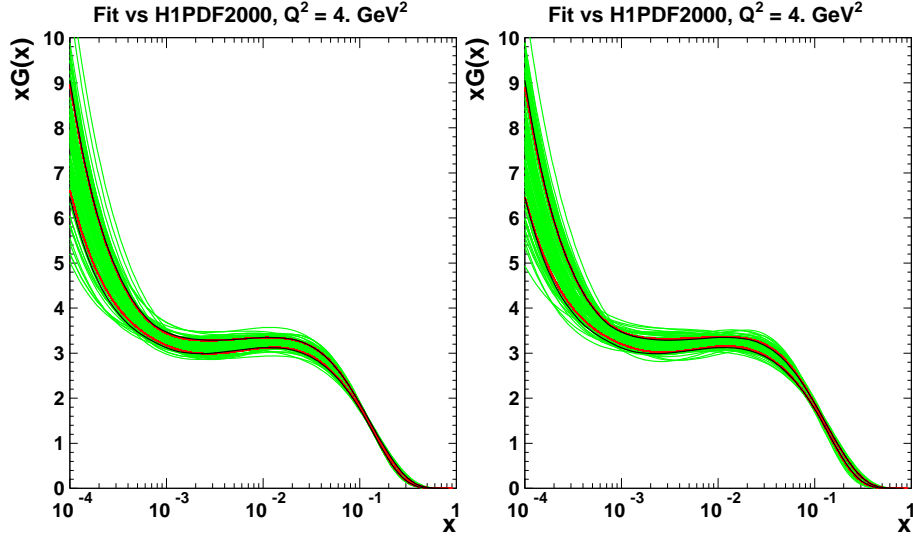


Fig. 5: Comparison between errors on PDFs obtained via standard error calculation (black) where Gauss assumption is used, and errors obtained via Monte Carlo method (red) where luminosity uncertainty is allowed to fluctuate according to lognormal distributions and all the other uncertainties follow the Gaussian distribution (left), and where all the systematic uncertainties are allowed to fluctuate according to lognormal distributions (right). Only the gluon PDF is shown, where the errors are larger. The green lines show the spread of the  $N$  individual fits.

- *Input parameterization.* We take the input PDF parameterization at  $Q_0^2 = 1 \text{ GeV}^2$  to be:

$$xu_v(x, Q_0^2) = A_u x^{\eta_1} (1-x)^{\eta_2} (1 + \epsilon_u \sqrt{x} + \gamma_u x), \quad (9)$$

$$xd_v(x, Q_0^2) = A_d x^{\eta_3} (1-x)^{\eta_4} (1 + \epsilon_d \sqrt{x} + \gamma_d x), \quad (10)$$

$$xS(x, Q_0^2) = A_S x^{\delta_S} (1-x)^{\eta_S} (1 + \epsilon_S \sqrt{x} + \gamma_S x), \quad (11)$$

$$xg(x, Q_0^2) = A_g x^{\delta_g} (1-x)^{\eta_g} (1 + \epsilon_g \sqrt{x} + \gamma_g x) + A_{g'} x^{\delta_{g'}} (1-x)^{\eta_{g'}}, \quad (12)$$

where  $S = 2(\bar{u} + \bar{d} + \bar{s})$ ,  $s = \bar{s} = 0.1 S$  and  $\bar{d} = \bar{u}$ . The parameters  $A_u$ ,  $A_d$  and  $A_g$  are fixed by sum rules, leaving potentially 19 free parameters. In practice, to reduce the number of highly correlated parameters, making linear error propagation unreliable, we determine the central value of the benchmark fit by freeing all 19 parameters, then fix 6 of those at the best-fit values when calculating the Hessian matrix used to determine the PDF uncertainties, giving a total of 13 eigenvectors. This is the same procedure as used in the MSTW 2008 global fit [6, 7], where there are an additional 3 free parameters associated with  $\bar{d} - \bar{u}$  and an additional 4 free parameters associated with strangeness, giving a total of 20 eigenvectors. Note that the parameterization used in the previous Alekhin/Thorne benchmark fits was considerably more restrictive, where the  $\epsilon_S$ ,  $\gamma_S$ ,  $\epsilon_g$  and  $\gamma_g$  parameters were set to zero, and the second (negative) gluon term was omitted entirely. In addition,  $\epsilon_u$  was held fixed for the Thorne benchmark fit, leaving a total of 12 eigenvectors. We find that the more flexible gluon parameterization, allowing it to go negative at very small  $x$ , is very highly correlated with the value obtained for  $\alpha_s$ , and a value of  $\alpha_s(M_Z) = 0.105$  is

obtained if it is allowed to go free at the same time as the other parameters, therefore we instead choose to fix it at  $\alpha_s(M_Z) = 0.112$  as in the NNPDF benchmark fit.

- *Error propagation.* Apart from the more flexible input parameterization, the other major difference in the new MSTW version of the HERA–LHC benchmark fit, with respect to the previous Thorne (MRST) version, is the choice of tolerance,  $T = \sqrt{\Delta\chi^2}$ . The MRST benchmark fit used the standard choice  $T = 1$  for one-sigma uncertainties. More precisely, the distance  $t$  along each normalized eigenvector direction was taken to be 1, and ideal quadratic behaviour about the minimum was assumed, giving  $T \approx t = 1$ . The MRST global fit used  $T = \sqrt{50}$  for a 90% confidence level (C.L.) uncertainty band; however, this is not appropriate when fitting a smaller number of data sets. Recently, a new procedure has been developed [6, 7] which enables a *dynamic* determination of the tolerance for each eigenvector direction, by demanding that each data set must be described within its one-sigma (or 90%) C.L. limits according to a hypothesis-testing criterion, after rescaling the  $\chi^2$  for each data set so that the value at the global minimum corresponds to the most probable value. Application of this procedure to the MSTW benchmark fit gives  $T \sim 3$  for one-sigma uncertainties and  $T \sim 5$  for 90% C.L. uncertainties. For the MSTW global fit, the typical values of  $T$  required are slightly larger, with more variation between different eigenvector directions. The increase in  $T$  in the global fit is mainly due to the inclusion of some less compatible data sets, while the greater variation in  $T$  between eigenvectors is due to the fact that some parameters, particularly those associated with  $s$  and  $\bar{s}$ , are constrained by far fewer data sets than others. In the MSTW fits, the data set normalizations are allowed to vary, with the aforementioned penalty term, when determining the PDF uncertainties. For global fits this automatically leads to a small increase in uncertainty compared to the MRST determinations, where data set normalisations were held fixed when calculating the Hessian matrix used for error propagation. In the MRST benchmark fit the data set normalizations were allowed to vary. To calculate the uncertainty bands from the eigenvector PDF sets, we use the formula for asymmetric errors given, for example, in Eq. (13) of Ref. [20].

### 3.2 NNPDF approach<sup>3</sup>

The NNPDF approach was proposed in Ref. [21], and it was applied there and in Ref. [22] to the parameterization of the structure function  $F_2(x, Q^2)$  with only two or more experimental data sets respectively. In Ref. [23] it was first used for the determination of a single PDF (the isotriplet quark distribution), and in Ref. [5] a full set of PDFs fit based on DIS data (NNPDF1.0) was presented. Because the method has been discussed extensively in these references, here we only summarize briefly its main features.

- *Error propagation.* We make a Monte Carlo sample of the probability distribution of the experimental data by generating an ensemble of  $N$  replicas of artificial data following a multi-gaussian distribution centered on each data point with full inclusion of the experimental covariance matrix. Each replica is used to construct a set of PDFs, thereby propagating the statistical properties of the data Monte Carlo sample to a final Monte Carlo

---

<sup>3</sup>Contributing authors: R. D. Ball, L. Del Debbio, S. Forte, A. Guffanti, J. I. Latorre, A. Piccione, J. Rojo, M. Ubiali

sample of PDFs. Here we shall take  $N = 100$ . The method is the same as discussed in Sect. 2.2, the only difference being the treatment of normalization errors: relative normalizations are fitted in the H1 approach, while they are included among the systematic errors in the Monte Carlo data generation in the NNPDF approach (see Refs. [2, 5] for details of the respective procedures).

- *Input parameterization.* Each PDF is parameterized with a functional form provided by a neural network. The architecture for the neural network is the same for all PDFs, and yields a parameterization with 37 free parameters for each PDF. This is a very redundant parameterization, it is chosen in order to avoid parameterization bias; neural networks are a particularly convenient way of dealing with redundant parameterizations. Note that sum rules are also imposed.
- *Minimization.* A redundant parameterization allows for fitting not only the underlying physical behaviour, but also statistical noise. Therefore, the minimization is stopped not at the absolute minimum of the  $\chi^2$ , but rather before one starts fitting noise. This optimal stopping point is determined as follows: the data in each replica are randomly assigned either to a training or to a validation set. The fit is performed on data of the training set only, while the validation set is used as a monitor. The fit is stopped when the quality of the fit to the training set keeps improving, but the quality of the fit to the validation set deteriorates.

### 3.3 Comparison between the Benchmark Parton Distributions

Data Set	$\chi^2_{\text{bench}}/N_{\text{data}}$	$\chi^2_{\text{global}}/N_{\text{data}}$
ZEUS97	1.09	1.18
H1lowx97	1.03	1.00
NMC	1.40	1.45
NMC <sub>pd</sub>	1.24	1.32
BCDMS	1.21	1.98
Total	1.19	1.53

Table 4: NNPDF  $\chi^2$  for the total and each single data set, both for the benchmark and global fit.

The  $\chi^2$  per data point for the NNPDF and MSTW fits are shown in Table 4 and 5 respectively. Note that in the MSTW fit statistical and systematic errors are added in quadrature, so the quantity shown is the diagonal contribution to the  $\chi^2$ . The quality of the NNPDF is seen to be uniformly good. The quality of the MSTW is also uniform, though it cannot be compared directly because of the different way systematics are treated. The comparison of each benchmark fit to the corresponding global fit will be discussed in Sect. 3.4 below.

In Fig. 6 the PDFs from the NNPDF and MSTW benchmark fits presented here are compared to those by Thorne from Ref. [1] at the same reference scale of  $Q^2 = 20 \text{ GeV}^2$  used there (denoted as MRST01 in the figure). The benchmark fit by Alekhin [1] is not shown as the PDFs are very close to the those by Thorne displayed in Fig. 6.



Data set	$\chi_{\text{bench}}^{\text{diag}^2}/N_{\text{data}}$	$\chi_{\text{global}}^{\text{diag}^2}/N_{\text{data}}$
ZEUS97	0.76	0.79
H1lowx97	0.53	0.54
NMC	1.08	1.11
NMC <sub>pd</sub>	0.78	0.89
BCDMS	0.74	1.13
Total	0.76	0.89

Table 5: MSTW  $\chi^2$  for the total and each single data set, both for the benchmark and global fit. Notice that statistical and systematic errors are added in quadrature and that relative data set normalizations are fitted.

For PDFs and kinematical regions where data are available, namely the small- $x$  gluon and sea quark and the large- $x$   $u_v$  distributions, the central values of the NNPDF fit are quite close to those of the MRST and MSTW fits, despite the differences in methodology. The central values of the PDFs are slightly different for the MRST and MSTW benchmark fits due to the use of BCDMS  $F_2^d$  data in the former, which affects mainly valence quarks. Where extrapolation is needed, such as for the  $d_v$  distribution, which is constrained only by the small amount of data on the ratio  $F_2^d/F_2^p$ , or the large- $x$  sea quark, central values are rather more different (though the Alekhin/MRST/MSTW benchmark central values are within the NNPDF error band). The exception is the smallest- $x$  gluon, where the form of the MSTW parameterization results in a very sharp turn-over. However, even here the uncertainty bands are close to overlapping.

Differences are sizeable in the estimation of uncertainties. Firstly, uncertainty bands for NNPDF benchmark are significantly larger than for the MSTW benchmark, which in turn are in general somewhat larger than those for the MRST benchmark. The difference between MRST and MSTW, which are based on similar methodology, is due to use of a dynamic tolerance and a more flexible gluon parameterization in MSTW (see Sect. 3.1). Secondly, the width of the uncertainty band for NNPDF benchmark varies rather more than that of the MRST benchmark according to the PDF and the kinematic region, though this is not quite so much the case comparing to MSTW benchmark. Indeed, the NNPDF uncertainties are quite small in the region between  $x = 0.01$  and  $x = 0.1$  (where there is the bulk of HERA and fixed-target data), while they blow up in the large- $x$  region for the sea quark or the small- $x$  gluon, where there is less or no experimental information. The smallness of the uncertainty band for MSTW for the small- $x$  valence quarks may be partially due to the lack of flexibility in the parameterization: note that because of sum rules, the size of uncertainties in the data and extrapolation region are correlated.

Finally, the MRST/MSTW central value generally falls within the NNPDF uncertainty band, but the NNPDF central value tends to fall outside the MRST/MSTW uncertainty band whenever the central values differ significantly.

### 3.4 Comparison of the Benchmark Parton Distributions and Global Fits

In Fig. 7 we compare the NNPDF benchmark fit to the NNPDF1.0 reference fit of Ref. [5] (NNPDF global, henceforth), while in Fig. 8 we compare the MSTW benchmark fit to the



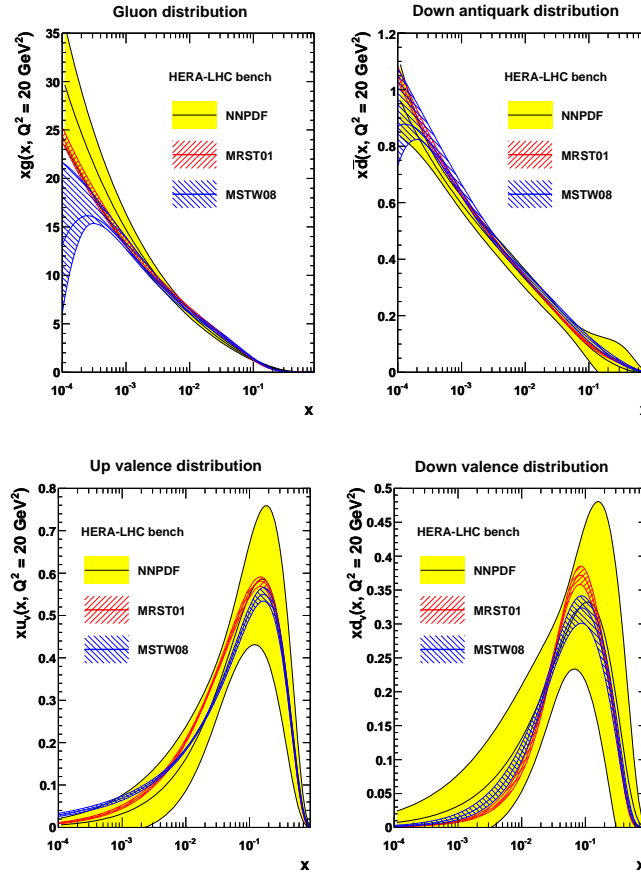


Fig. 6: Comparison of the NNPdf, MRST and MSTW benchmark fits for the gluon,  $d$ -sea,  $u$ -valence and  $d$ -valence at  $Q^2 = 20 \text{ GeV}^2$ . All uncertainties shown correspond to one- $\sigma$  bands.

MRST01 [20] (MRST global, henceforth) and MSTW08 [6, 7] global fits (MSTW global, henceforth).

The  $\chi^2$  of the NNPdf benchmark and global fits are compared in Table 4, while those of the MSTW benchmark and global fits are compared in Table 5. Note that for the NNPdf fits the  $\chi^2$  is computed using the full covariance matrix, while for the MSTW fits systematic and statistical uncertainties are added in quadrature. Note also that the MRST and MSTW global fits are carried out in a general-mass variable flavour number scheme rather than the zero-mass variable flavour number scheme used in the corresponding benchmark fits, whereas for NNPdf both global and benchmark fits are done with a zero-mass variable flavour number scheme. Comparison of the quality of each benchmark to the corresponding global fit to the same points in Table 5 shows a significant deterioration in the quality of the fit (total  $\Delta\chi^2 \gg 1$ ), especially for the BCDMS  $F_2^p$  data. All fits appear to be acceptable for all data sets: for instance, even though the  $\chi^2$  of the NNPdf global fit for the benchmark subset of data is 1.98, it is equal to 1.59 [5] for the full BCDMS set of data. However, the increase in  $\chi^2$  suggests that there might be data inconsistencies.

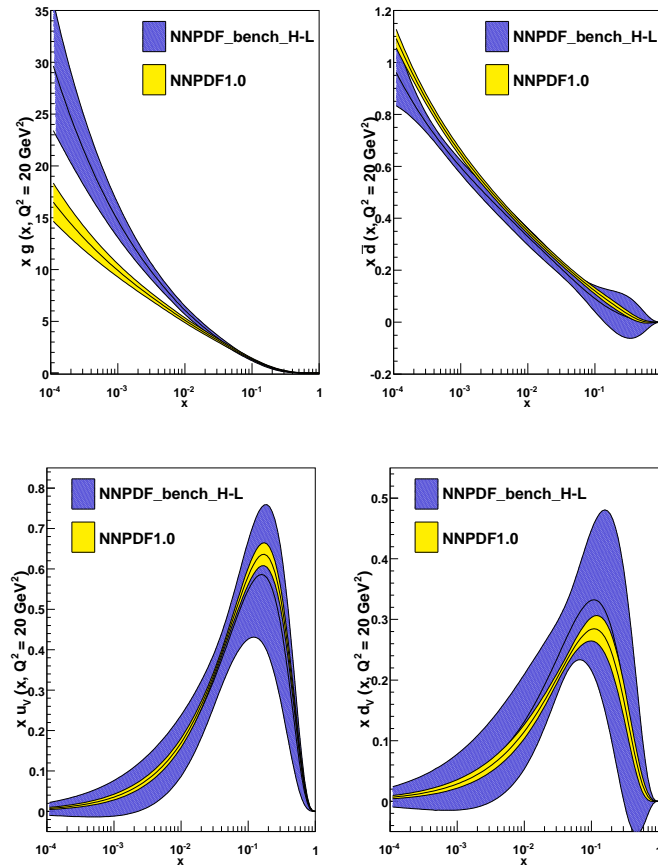


Fig. 7: Comparison of the NNPDF benchmark and reference fits for the gluon,  $d$ -sea,  $u$ -valence and  $d$ -valence at  $Q^2 = 20 \text{ GeV}^2$ .

Let us now compare each pair of benchmark and global fits. For NNPDF, the difference in central value between benchmark and reference is comparable to that found between the MRST or Alekhin global fits and their benchmark counterparts in Ref. [1]. However, the NNPDF global and benchmark fits remain compatible within their respective error bands. Indeed, the NNPDF benchmark fit has a rather larger error band than the reference, as one would expect from a fit based on a rather smaller set of (compatible) data. Such a behaviour was however not observed in the comparison between global and benchmark MRST and Alekhin fits of Ref. [1].

It is interesting to observe that the gluon shape at low  $x$  of the benchmark and global NNPDF disagree at the one  $\sigma$  level (though they agree at two  $\sigma$ ). This can be understood as a consequence of the fact that the value of  $\alpha_s$  in the two fits is sizably different ( $\alpha_s = 0.112$  vs.  $\alpha_s = 0.119$ ). Theoretical uncertainties related to the value of  $\alpha_s$  were shown in Ref. [5] to be negligible and thus not included in the NNPDF error band, but of course they become relevant if  $\alpha_s$  is varied by several standard deviations ( $3.5 \sigma$ , in this case).

Coming now to MSTW, we first notice that, as discussed in Sect. 3.3, the MSTW bench-

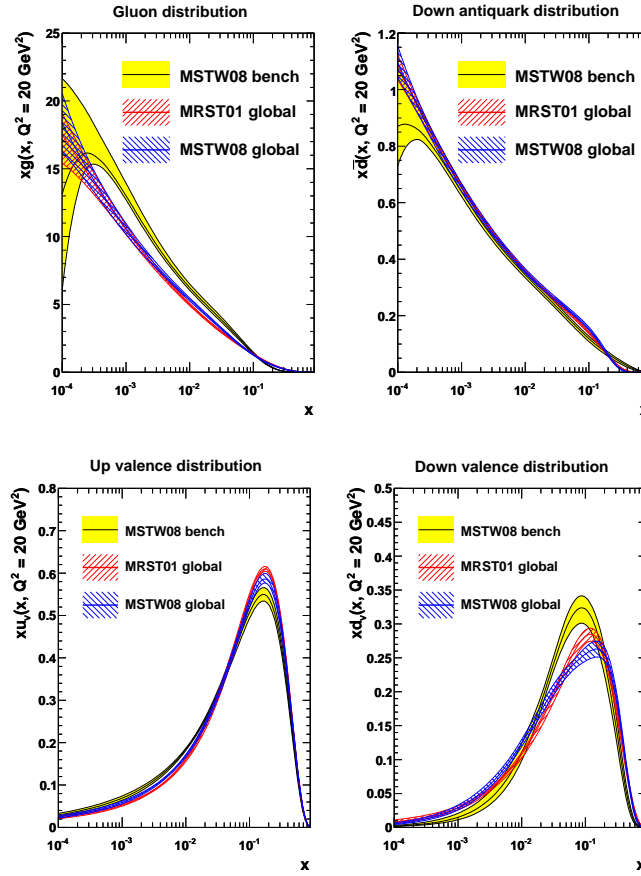


Fig. 8: Comparison of the MSTW benchmark and MRST/MSTW global fits for the gluon,  $d$ -sea,  $u$ -valence and  $d$ -valence at  $Q^2 = 20 \text{ GeV}^2$ . All uncertainties shown correspond to one- $\sigma$  bands.

mark set has somewhat larger uncertainty bands than the MRST benchmark set and thus also than each of the sets obtained from global fits. Consequently, the MSTW benchmark PDFs are generally far more consistent with the MSTW global fit sets than the corresponding comparison between MRST benchmark PDFs and global fit PDFs shown in Ref. [1], largely due to the more realistic uncertainties in the MSTW benchmark. Comparing central values we see exactly the same feature in the gluon distribution as the NNPDF group, and the explanation is likewise the same, highlighting possible difficulties in comparing PDFs obtained with different values of  $\alpha_s(M_Z)$ .

Unlike for the NNPDF group, the MSTW group sees some degree of incompatibility between the benchmark PDFs and the global fit PDFs for the valence quarks, particularly in the case of the down valence. This may be related to the assumption  $\bar{u} = \bar{d}$ , which constrains valence quarks and sea quarks in an artificial manner since there is less flexibility to alter each independently. Indeed, in the global fits there is an excess of  $\bar{d}$  over  $\bar{u}$  which maximizes at  $x = 0.1$ . Forcing equivalence of antiquark distributions might therefore lead to a deficit of down sea quarks

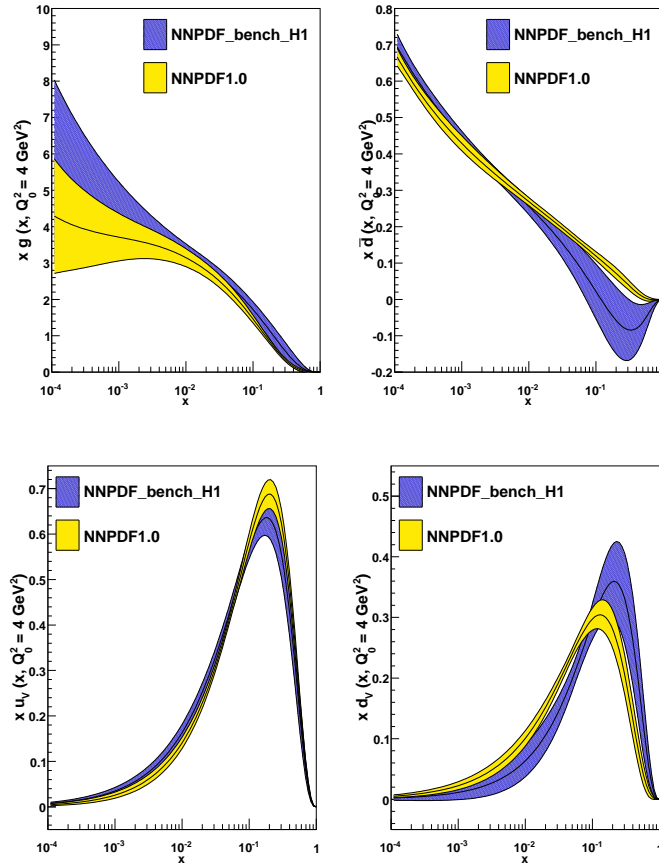


Fig. 9: Comparison of the NNPDF benchmark and reference fits for the gluon,  $d$ -sea,  $u_v$  and  $d_v$  at  $Q^2 = 4 \text{ GeV}^2$ .

and a corresponding excess of up sea quarks, and also, for the same reason, to an excess of down valence quarks. These are indeed seen both in the NNPDF and MSTW benchmark fits when compared to the respective global fits. The effect is however well within the uncertainty bands for NNPDF, which indeed do not observe any statistically significant difference between results of a fit to the reduced benchmark data set with the  $\bar{u} = \bar{d}$  assumption (as presented in Fig. 7) or without it (as presented in Ref. [5], Fig. 12).

As well as this important effect one sees that the main discrepancy at  $x = 0.1$  for down valence quarks is greater when comparing the benchmark fits to the global MSTW fit than to the global MRST fit. This is because recent new Tevatron data on  $Z$  rapidity distributions and lepton asymmetry from  $W$  decays provide a strong constraint on the down quark, and some of this new data shows considerable tension with other data sets.

## 4 H1 Benchmark

We now discuss the extension of the fit using the settings of Sect. 1.1 to also include the NNPDF approach. Results are compared both to those of the NNPDF reference fit, and to those obtained by the H1 fit of Sect. 2 to the same data. We then compare the NNPDF benchmark and reference, with the specific aim of addressing the issue of the dependence of the results on the size of the data set (H1 dataset vs. the HERA–LHC dataset of Sect. 3). Finally, the H1 and NNPDF benchmark fits are compared to each other with the purpose of understanding the impact of the respective methodologies.

### 4.1 NNPDF analysis<sup>4</sup>

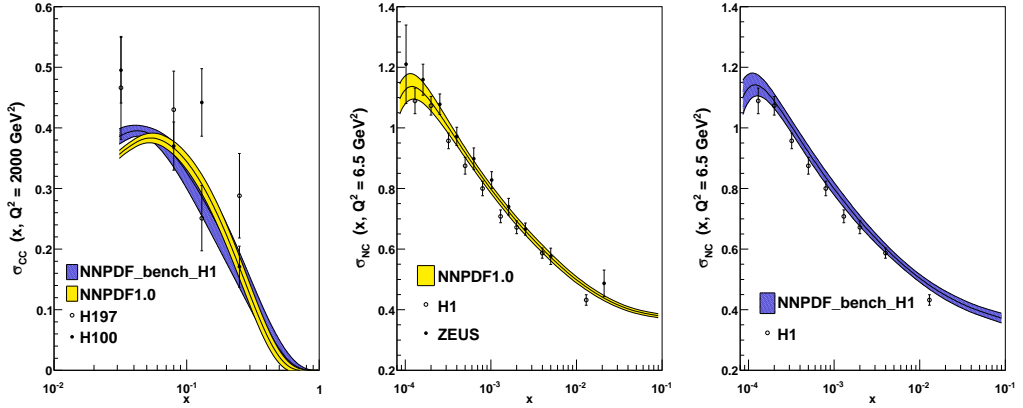


Fig. 10: Left: NNPDF benchmark and reference fits at  $\sqrt{s} = 301\text{GeV}$  compared to H1 charged current data. Center: NNPDF reference fit compared to H1 and ZEUS neutral current data. Right: NNPDF benchmark fit compared to H1 neutral current data.

The results of the NNPDF benchmark are compared to the NNPDF reference fit results in Fig. 9. The general features of the benchmark are analogous to those of the HERA–LHC benchmark discussed in Section 3.4, with some effects being more pronounced because the benchmark dataset is now even smaller. Specifically, we observe that uncertainties bands blow up when data are removed: this is very clear for instance in the  $\bar{d}$  distribution at large- $x$ , as a consequence of the fact that the benchmark dataset of Table 1 does not include deuterium data. The negative value of this PDF at large  $x$  is presumably unphysical and it would disappear if positivity of charged current cross sections were imposed, including also the (anti-)neutrino ones. The only positivity constraint in the NNPDF fit is imposed on the  $F_L$  structure function [5], because this is the only DIS observable whose positivity is not constrained by the full data set.

It is interesting to note however that this effect is not observed for the  $u_v$  distribution, where instead the benchmark and the reference fit show almost equal uncertainties. In order to

<sup>4</sup>Contributing authors R. D. Ball, L. Del Debbio, S. Forte, A. Guffanti, J. I. Latorre, A. Piccione, J. Rojo, M. Ubiali

understand this, in Fig. 10 we compare two situations with or without error shrinking, by examining the predictions obtained using the benchmark and reference fits for some observables to the corresponding data. A first plot (left) shows the shrinking of the uncertainty on the prediction for the charged-current cross section in the reference fit. This is mostly due to the CHORUS neutrino data, which are in the reference and not in the benchmark. These data are clearly consistent with the H1 data shown in the plot. The subsequent pair of plots compares (center) the prediction for the neutral-current cross section from the reference fit compared to H1 and ZEUS data (both of which are used for the reference fit), and (right) from the benchmark fit to the H1 data only (which are the only ones used in the benchmark fit). The uncertainty bands in the two fits are similar size: indeed, the ZEUS and H1 data display a systematic disagreement which is approximately the size of this uncertainty band. Hence, the (small but significant) systematic inconsistency between the ZEUS and H1 data prevents reduction of the uncertainty band when the ZEUS data are added to the fit, beyond the size of this discrepancy. Therefore, the NNPDF methodology leads to combined uncertainties for inconsistent data which are similar to those obtained with the so-called PDG (or scale-factor) method [24].

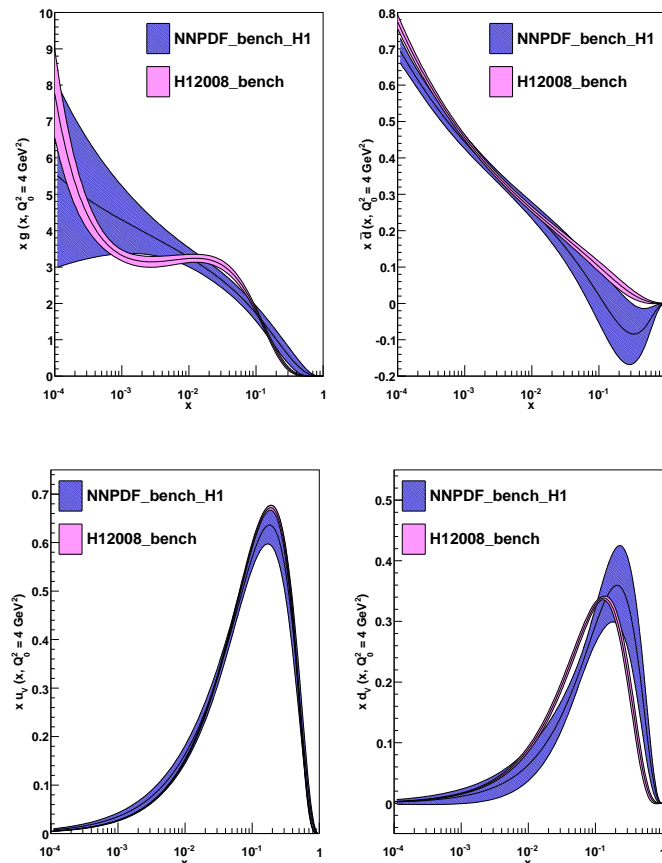


Fig. 11: Comparison of the NNPDF and H1 benchmark fit for the gluon,  $d$ -sea,  $u_v$  and  $d_v$  at  $Q^2 = 4 \text{ GeV}^2$ .

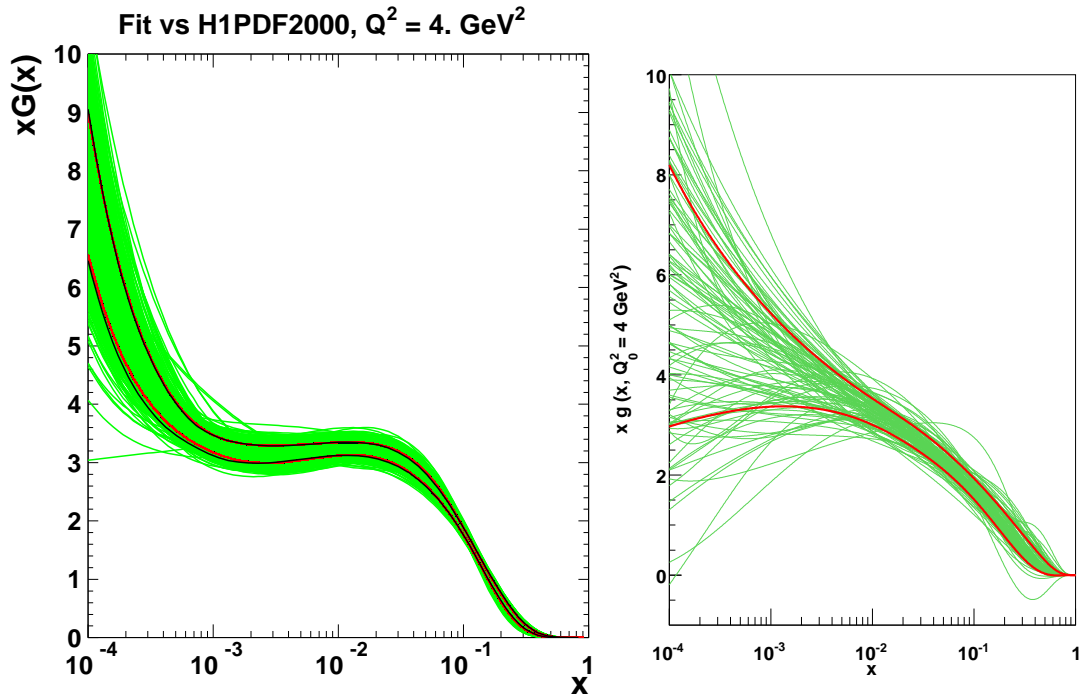


Fig. 12: The Monte Carlo set of gluon PDFs for the H1 benchmark (left, same as Fig. 4) and the NNPDF benchmark. The red lines show the one-sigma contour calculated from the Monte Carlo set, and in the H1 case the black lines show the Hessian one-sigma contour.

Data Set	$\chi^2_{\text{H1}}/N_{\text{data}}$	$\chi^2_{\text{NNPDF}}/N_{\text{data}}$
H197mb	0.83	0.82
H197lowQ2	0.90	0.87
H197NC	0.69	0.80
H197CC	0.73	0.97
H199NC	0.88	1.01
H199CC	0.62	0.84
H199NChy	0.35	0.35
H100NC	0.97	1.00
H100CC	1.07	1.38
Total	0.88	0.96

Table 6: H1 and NNPDF  $\chi^2$  for the total and each single data set. Cross correlations among data sets are neglected to evaluate the  $\chi^2$  of a single data set.

Notice that if relative normalization are fitted (as done by in the H1 approach of Sect. 2) instead of being treated simply as a source of systematics, this systematic inconsistency would be significantly reduced in the best-fit. The associate uncertainty however then appears as an

addition source of systematics. This happens when H1 and ZEUS data are combined in a single dataset (see Section [18] below). In the NNPDF approach, instead, this systematics is produced by the Monte Carlo procedure.

## 4.2 Comparison between the Benchmark Parton Distributions

The  $\chi^2$  of the H1 and NNPDF benchmarks are given in Table 6, while the corresponding PDFs are compared in Fig. 11. Furthermore, in Fig. 12 we show the respective full Monte Carlo PDF sets in the case of the gluon distribution.

The quality of the two fits is comparable, the differences in  $\chi^2$  being compatible with statistical fluctuations. In the region where experimental information is mostly concentrated, specifically for the  $u_v$  distribution over all the  $x$ -range and for the  $\bar{d}$  and the  $d_v$  distributions in the small- $x$  range, the results of the two fits are in good agreement, though the H1 uncertainty bands are generally somewhat smaller.

In the region where experimental information is scarce or missing, sizable differences are found, similar to those observed when comparing the MRST/MSTW bench and NNPDF bench to the HERA–LHC benchmark of Sect. 3.3. Specifically, in these regions NNPDF uncertainties are generally larger than H1 bands: the width of the uncertainty band for the H1 fit varies much less between the data and extrapolation regions than that of the NNPDF bench. Also, the H1 central value always falls within the NNPDF uncertainty band, but the NNPDF central value tends to fall outside the H1 uncertainty band whenever the central values differ significantly. Figure 12 suggests that this may be due to the greater flexibility of the functional form in the NNPDF fit. Specifically, the  $\bar{d}$  quark distribution at large  $x$  does not become negative in the H1 fit, because this behaviour is not allowed by the parameterization.

## References

- [1] M. Dittmar *et al.*, *Parton distributions: Summary report for the HERA - LHC workshop*. Preprint hep-ph/0511119, 2005.
- [2] H1 Collaboration, C. Adloff *et al.*, Eur. Phys. J. **C30**, 1 (2003). hep-ex/0304003.
- [3] W. T. Giele and S. Keller, Phys. Rev. **D58**, 094023 (1998). hep-ph/9803393.
- [4] W. T. Giele, S. A. Keller, and D. A. Kosower (2001). hep-ph/0104052.
- [5] NNPDF Collaboration, R. D. Ball *et al.*, Nucl. Phys. **B809**, 1 (2009). 0808.1231.
- [6] G. Watt, A. D. Martin, W. J. Stirling, and R. S. Thorne, *Recent Progress in Global PDF Analysis*. Preprint 0806.4890, 2008.
- [7] R. S. Thorne, A. D. Martin, W. J. Stirling, and G. Watt, *Parton Distributions for the LHC*. Preprint 0706.0456, 2007.
- [8] H1 Collaboration, C. Adloff *et al.*, Eur. Phys. J. **C21**, 33 (2001). hep-ex/0012053.
- [9] H1 Collaboration, C. Adloff *et al.*, Eur. Phys. J. **C13**, 609 (2000). hep-ex/9908059.



- [10] H1 Collaboration, C. Adloff *et al.*, Eur. Phys. J. **C19**, 269 (2001). hep-ex/0012052.
- [11] W. Giele *et al.*, *The QCD/SM working group: Summary report*. Preprint hep-ph/0204316, 2002.
- [12] ZEUS Collaboration, S. Chekanov *et al.*, Eur. Phys. J. **C21**, 443 (2001). hep-ex/0105090.
- [13] New Muon Collaboration Collaboration, M. Arneodo *et al.*, Nucl. Phys. **B483**, 3 (1997). hep-ph/9610231.
- [14] New Muon Collaboration Collaboration, M. Arneodo *et al.*, Nucl. Phys. **B487**, 3 (1997). hep-ex/9611022.
- [15] BCDMS Collaboration, A. C. Benvenuti *et al.*, Phys. Lett. **B223**, 485 (1989).
- [16] B. Badelek and J. Kwiecinski, Phys. Rev. **D50**, 4 (1994). hep-ph/9401314.
- [17] A. d. R. Vargas Trevino, *Measurement of the inclusive  $e p$  scattering cross section at low  $Q^2$  and  $x$  at HERA*. Prepared for 15th International Workshop on Deep-Inelastic Scattering and Related Subjects (DIS2007), Munich, Germany, 16-20 Apr 2007.
- [18] *Extraction of the proton pdfs from a combined fit of h1 and zeus inclusive dis cross sections*. These proceedings.
- [19] M. Botje, *Qcdnum16.12*. Available from <http://www.nikhef.nl/h24/qcdnum/>.
- [20] A. D. Martin, R. G. Roberts, W. J. Stirling, and R. S. Thorne, Eur. Phys. J. **C28**, 455 (2003). hep-ph/0211080.
- [21] S. Forte, L. Garrido, J. I. Latorre, and A. Piccione, JHEP **05**, 062 (2002). hep-ph/0204232.
- [22] NNPDF Collaboration, L. Del Debbio, S. Forte, J. I. Latorre, A. Piccione, and J. Rojo, JHEP **03**, 080 (2005). hep-ph/0501067.
- [23] NNPDF Collaboration, L. Del Debbio, S. Forte, J. I. Latorre, A. Piccione, and J. Rojo, JHEP **03**, 039 (2007). hep-ph/0701127.
- [24] Particle Data Group Collaboration, C. Amsler *et al.*, Phys. Lett. **B667**, 1 (2008).

# Determination of parton distributions

*A. Cooper-Sarkar, A. Glazov, G. Li, J. Grebenyuk, V. Lendermann*

## 1 Extraction of the proton PDFs from a combined fit of H1 and ZEUS inclusive DIS cross sections<sup>1</sup>

### 1.1 Introduction

The kinematics of lepton hadron scattering is described in terms of the variables  $Q^2$ , the invariant mass of the exchanged vector boson, Bjorken  $x$ , the fraction of the momentum of the incoming nucleon taken by the struck quark (in the quark-parton model), and  $y$  which measures the energy transfer between the lepton and hadron systems. The differential cross-section for the neutral current (NC) process is given in terms of the structure functions by

$$\frac{d^2\sigma(e^\pm p)}{dx dQ^2} = \frac{2\pi\alpha^2}{Q^4 x} [Y_+ F_2(x, Q^2) - y^2 F_L(x, Q^2) \mp Y_- xF_3(x, Q^2)] ,$$

where  $Y_\pm = 1 \pm (1 - y)^2$ . The structure functions  $F_2$  and  $xF_3$  are directly related to quark distributions, and their  $Q^2$  dependence, or scaling violation, is predicted by perturbative QCD. For low  $x$ ,  $x \leq 10^{-2}$ ,  $F_2$  is sea quark dominated, but its  $Q^2$  evolution is controlled by the gluon contribution, such that HERA data provide crucial information on low- $x$  sea-quark and gluon distributions. At high  $Q^2$ , the structure function  $xF_3$  becomes increasingly important, and gives information on valence quark distributions. The charged current (CC) interactions also enable us to separate the flavour of the valence distributions at high- $x$ , since their (LO) cross-sections are given by,

$$\begin{aligned} \frac{d^2\sigma(e^+p)}{dx dQ^2} &= \frac{G_F^2 M_W^4}{(Q^2 + M_W^2)^2 2\pi x} x [(\bar{u} + \bar{c}) + (1 - y)^2 (d + s)] , \\ \frac{d^2\sigma(e^-p)}{dx dQ^2} &= \frac{G_F^2 M_W^4}{(Q^2 + M_W^2)^2 2\pi x} x [(u + c) + (1 - y)^2 (\bar{d} + \bar{s})] . \end{aligned}$$

Parton Density Function (PDF) determinations are usually obtained in global NLO QCD fits [1–3], which use fixed target DIS data as well as HERA data. In such analyses, the high statistics HERA NC  $e^+p$  data have determined the low- $x$  sea and gluon distributions, whereas the fixed target data have determined the valence distributions. Now that high- $Q^2$  HERA data on NC and CC  $e^+p$  and  $e^-p$  inclusive double differential cross-sections are available, PDF fits can be made to HERA data alone, since the HERA high  $Q^2$  cross-section data can be used to determine the valence distributions. This has the advantage that it eliminates the need for heavy target corrections, which must be applied to the  $\nu$ -Fe and  $\mu D$  fixed target data. Furthermore there is no need to assume isospin symmetry, i.e. that  $d$  in the proton is the same as  $u$  in the neutron, since the  $d$  distribution can be obtained directly from CC  $e^+p$  data.

The H1 and ZEUS collaborations have both used their data to make PDF fits [3], [4]. Both of these data sets have very small statistical uncertainties, so that the contribution of systematic

---

<sup>1</sup>Contributing authors: A. Cooper-Sarkar, A. Glazov, G. Li for the H1-ZEUS combination group.

uncertainties becomes dominant and consideration of point to point correlations between systematic uncertainties is essential. The ZEUS analysis takes account of correlated experimental systematic errors by the Offset Method, whereas H1 uses the Hessian method [5]. Whereas the resulting ZEUS and H1 PDFs are compatible, the gluon PDFs have rather different shapes, see Fig 7, and the uncertainty bands spanned by these analyses are comparable to those of the global fits.

It is possible to improve on this situation since ZEUS and H1 are measuring the same physics in the same kinematic region. These data have been combined using a ‘theory-free’ Hessian fit in which the only assumption is that there is a true value of the cross-section, for each process, at each  $x, Q^2$  point [6]. Thus each experiment has been calibrated to the other. This works well because the sources of systematic uncertainty in each experiment are rather different, such that all the systematic uncertainties are re-evaluated. The resulting correlated systematic uncertainties on each of the combined data points are significantly smaller than the statistical errors. This combined data set has been used as the input to an NLO QCD PDF fit. The consistency of the input data set and its small systematic uncertainties enables us to calculate the experimental uncertainties on the PDFs using the  $\chi^2$  tolerance,  $\Delta\chi^2 = 1$ . This represents a further advantage compared to the global fit analyses where increased tolerances of  $\Delta\chi^2 = 50 - 100$  are used to account for data inconsistencies.

For the HERAPDF0.1 fit presented here, the role of correlated systematic uncertainties is no longer crucial since these uncertainties are relatively small. This ensures that similar results are obtained using either Offset or Hessian methods, or by simply combining statistical and systematic uncertainties in quadrature. The  $\chi^2$  per degree of freedom for a Hessian fit is 553/562 and for a quadrature fit it is 428/562. For our central fit we have chosen to combine the 43 systematic uncertainties which result from the separate ZEUS and H1 data sets in quadrature, and to Offset the 4 sources of uncertainty which result from the combination procedure. The  $\chi^2$  per degree of freedom for this fit is 477/562. This procedure results in the most conservative estimates on the resulting PDFs as illustrated in Fig. 1 which compares the PDFs and their experimental uncertainties as evaluated by the procedure of our central fit and as evaluated by treating the 47 systematic uncertainties by the Hessian method.

Despite this conservative procedure, the experimental uncertainties on the resulting PDFs are impressively small and a thorough consideration of further uncertainties due to model assumptions is necessary. In Section 1.2 we briefly describe the data combination procedure. In Section 1.3 we describe the NLO QCD analysis and model assumptions. In Section 1.4 we give results. In Section 1.5 we give a summary of the fit results and specifications for release of the HERAPDF0.1 to LHAPDF. In Section 1.6 we investigate the predictions of the HERAPDF0.1 for  $W$  and  $Z$  cross-sections at the LHC.

## 1.2 Data Combination

The data combination is based on assumption that the H1 and ZEUS experiments measure the same cross section at the same kinematic points. The systematic uncertainties of the measurements are separated, following the prescription given by the H1 and ZEUS, into point to point correlated sources  $\alpha_j$  and uncorrelated systematic uncertainty, which is added to the statistical uncertainty in quadrature to result in total uncorrelated uncertainty  $\sigma_i$  for each bin  $i$ . The

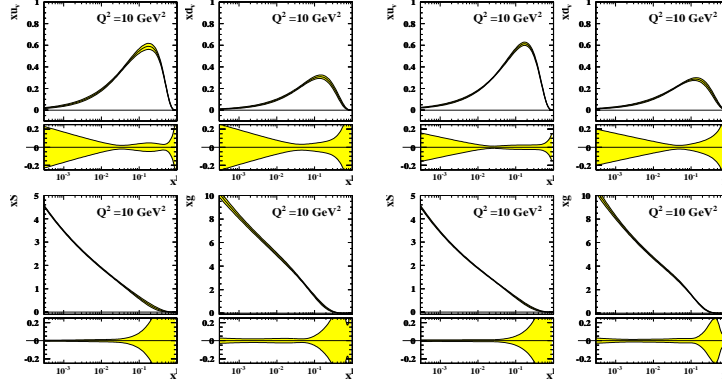


Fig. 1: HERAPDFs,  $xu_v, xd_v, xS, xg$  at  $Q^2 = 10\text{GeV}^2$ . (Left) with experimental uncertainties evaluated as for the central fit (see text) and (right) with experimental uncertainties evaluated by accounting for the 47 systematic errors by the Hessian method.

correlated systematic sources are considered to be uncorrelated between H1 and ZEUS. All uncertainties are treated as multiplicative i.e. proportional to the central values, which is a good approximation for the measurement of the cross sections.

A correlated probability distribution function for the physical cross sections  $M^{i,\text{true}}$  and systematic uncertainties  $\alpha_{j,\text{true}}$  for a single experiment corresponds to a  $\chi^2$  function:

$$\chi_{\text{exp}}^2(M^{i,\text{true}}, \alpha_{j,\text{true}}) = \sum_i \frac{\left[ M^{i,\text{true}} - \left( M^i + \sum_j \frac{\partial M^i}{\partial \alpha_j} \frac{M^{i,\text{true}}}{M^i} (\alpha_{j,\text{true}}) \right) \right]^2}{\left( \sigma_i \frac{M^{i,\text{true}}}{M^i} \right)^2} + \sum_j \frac{(\alpha_{j,\text{true}})^2}{\sigma_{\alpha_j}^2}, \quad (1)$$

where  $M^i$  are the central values measured by the experiment,  $\partial M^i / \partial \alpha_j$  are the sensitivities to the correlated systematic uncertainties and  $\sigma_{\alpha_j}$  are the uncertainties of the systematic sources. For more than one experiment, total  $\chi_{\text{tot}}^2$  can be represented as a sum of  $\chi_{\text{exp}}^2$ . The combination procedure allows to represent  $\chi_{\text{tot}}^2$  in the following form:

$$\begin{aligned} \chi_{\text{tot}}^2(M^{i,\text{true}}, \beta_{j,\text{true}}) &= \chi_0^2 + \sum_i \frac{\left[ M^{i,\text{true}} - \left( M^{i,\text{ave}} + \sum_j \frac{\partial M^{i,\text{ave}}}{\partial \beta_j} \frac{M^{i,\text{true}}}{M^{i,\text{ave}}} (\beta_{j,\text{true}}) \right) \right]^2}{\left( \sigma_{i,\text{ave}} \frac{M^{i,\text{true}}}{M^{i,\text{ave}}} \right)^2} \\ &+ \sum_j \frac{(\beta_{j,\text{true}})^2}{\sigma_{\beta_j}^2}. \end{aligned} \quad (2)$$

Here the sum runs over a union set of the cross section bins. The value of the  $\chi_{\text{tot}}^2$  at the minimum,  $\chi_0^2$ , quantifies consistency of the experiments.  $M^{i,\text{ave}}$  are the average values of the cross sections and  $\beta_j$  correspond to the new systematic sources which can be obtained from the original sources  $\alpha_j$  through the action of an orthogonal matrix. In essence, the average of several data sets allows

one to represent the total  $\chi^2$  in a form which is similar to that corresponding to a single data set, Eq. 1, but with modified systematic sources.

The combination is applied to NC and CC cross section data taken with  $e^+$  and  $e^-$  beams simultaneously to take into account correlation of the systematic uncertainties. The data taken with proton beam energies of  $E_p = 820$  GeV and  $E_p = 920$  GeV are combined together for inelasticity  $y < 0.35$ , for this a small center of mass energy correction is applied. For the combined data set there are 596 data points and 43 experimental systematic sources. The  $\chi_0^2/dof = 510/599$  is below 1, which indicates conservative estimation of the uncorrelated systematics.

Besides the experimental uncertainties, four additional sources related to the assumptions made for the systematic uncertainties are considered. Two of the extra sources deal with correlation of the H1 and ZEUS data for estimation of the photoproduction background and simulation of hadronic energy scale. These sources introduce additional  $\sim 1\%$  uncertainty for  $y > 0.6$  and  $y < 0.02$  data. The third source covers uncertainty arising from the center of mass correction by varying  $F_L = F_L^{QCD}$  to  $F_L = 0$ . The resulting uncertainty reaches few per mille level for  $y \sim 0.35$ . Finally, some of the systematic uncertainties, for example background subtraction, may not be necessary multiplicative but rather additive, independent of the cross section central values. The effect of additive assumption for the errors is evaluated by comparing the average obtained using Eq. 1 and an average in which  $M^{i,true}/M^{i,ave}$  scaling is removed for all but global normalization errors.

### 1.3 QCD Analysis

The QCD predictions for the structure functions are obtained by solving the DGLAP evolution equations [7–9] at NLO in the  $\overline{\text{MS}}$  scheme with the renormalisation and factorization scales chosen to be  $Q^2$ <sup>2</sup>. The DGLAP equations yield the PDFs at all values of  $Q^2$  provided they are input as functions of  $x$  at some input scale  $Q_0^2$ . This scale has been chosen to be  $Q_0^2 = 4\text{GeV}^2$  and variation of this choice is considered as one of the model uncertainties. The resulting PDFs are then convoluted with NLO coefficient functions to give the structure functions which enter into the expressions for the cross-sections. The choice of the heavy quark masses is,  $m_c = 1.4$ ,  $m_b = 4.75\text{GeV}$ , and variation of these choices is included in the model uncertainties. For this preliminary analysis, the heavy quark coefficient functions have been calculated in the zero-mass variable flavour number scheme. The strong coupling constant was fixed to  $\alpha_s(M_Z^2) = 0.1176$  [12], and variations in this value of  $\pm 0.002$  have also been considered.

The fit is made at leading twist. The HERA data have a minimum invariant mass of the hadronic system,  $W^2$ , of  $W_{min}^2 = 300\text{ GeV}^2$  and a maximum  $x$ ,  $x_{max} = 0.65$ , such that they are in a kinematic region where there is no sensitivity to target mass and large- $x$  higher twist contributions. However a minimum  $Q^2$  cut is imposed to remain in the kinematic region where perturbative QCD should be applicable. This has been chosen to be  $Q_{min}^2 = 3.5\text{ GeV}^2$ . Variation of this cut is included as one of the model uncertainties.

A further model uncertainty is the choice of the initial parameterization at  $Q_0^2$ . Three types of parameterization have been considered. For each of these choices the PDFs are parameterized

---

<sup>2</sup>The programme QCDNUM [10] has been used and checked against the programme QCDfit [11].

by the generic form

$$xf(x) = Ax^B(1-x)^C(1+Dx+Ex^2+Fx^3), \quad (3)$$

and the number of parameters is chosen by 'saturation of the  $\chi^2$ ', such that parameters  $D, E, F$  are only varied if this brings significant improvement to the  $\chi^2$ . Otherwise they are set to zero.

The first parameterization considered follows that used by the ZEUS collaboration. The PDFs for  $u$  valence,  $xu_v(x)$ ,  $d$  valence,  $xd_v(x)$ , total sea,  $xS(x)$ , the gluon,  $xg(x)$ , and the difference between the  $d$  and  $u$  contributions to the sea,  $x\Delta(x) = x(\bar{d} - \bar{u})$ , are parameterized.

$$\begin{aligned} xu_v(x) &= A_{uv}x^{B_{uv}}(1-x)^{C_{uv}}(1+D_{uv}x+E_{uv}x^2) \\ xd_v(x) &= A_{dv}x^{B_{dv}}(1-x)^{C_{dv}} \\ xS(x) &= A_Sx^{B_S}(1-x)^{C_S} \\ xg(x) &= A_gx^{B_g}(1-x)^{C_g}(1+D_gx) \\ x\Delta(x) &= A_\Delta x^{B_\Delta}(1-x)^{C_\Delta} \end{aligned}$$

The total sea is given by,  $xS = 2x(\bar{u} + \bar{d} + \bar{s} + \bar{c} + \bar{b})$ , where  $\bar{q} = q_{sea}$  for each flavour,  $u = u_v + u_{sea}$ ,  $d = d_v + d_{sea}$  and  $q = q_{sea}$  for all other flavours. There is no information on the shape of the  $x\Delta$  distribution in a fit to HERA data alone and so this distribution has its parameters fixed, such that its shape is consistent with Drell-Yan data and its normalization is consistent with the size of the Gottfried sum-rule violation. A suppression of the strange sea with respect to the non-strange sea of a factor of 2 at  $Q_0^2$ , is imposed consistent with neutrino induced dimuon data from NuTeV. The normalisation parameters,  $A_{uv}, A_{dv}, A_g$ , are constrained to impose the number sum-rules and momentum sum-rule. The  $B$  parameters,  $B_{uv}$  and  $B_{dv}$  are set equal, since there is no information to constrain any difference. Finally this ZEUS-style parameterization has eleven free parameters.

The second parameterization considered follows that of the H1 Collaboration. The choice of quark PDFs which are parameterized is different. The quarks are considered as  $u$ -type and  $d$ -type,  $xU = x(u_v + u_{sea} + c)$ ,  $xD = x(d_v + d_{sea} + s)$ ,  $x\bar{U} = x(\bar{u} + \bar{c})$  and  $x\bar{D} = x(\bar{d} + \bar{s})$ , assuming  $q_{sea} = \bar{q}$ , as usual. These four (anti-)quark distributions are parameterized separately.

$$\begin{aligned} xU(x) &= A_Ux^{B_U}(1-x)^{C_U}(1+D_Ux+E_Ux^2+F_Ux^3) \\ xD(x) &= A_Dx^{B_D}(1-x)^{C_D}(1+D_Dx) \\ x\bar{U}(x) &= A_{\bar{U}}x^{B_{\bar{U}}}(1-x)^{C_{\bar{U}}} \\ x\bar{D}(x) &= A_{\bar{D}}x^{B_{\bar{D}}}(1-x)^{C_{\bar{D}}} \\ xg(x) &= A_gx^{B_g}(1-x)^{C_g} \end{aligned}$$

Since the valence distributions must vanish as  $x \rightarrow 0$ , the parameters,  $A$  and  $B$  are set equal for  $xU$  and  $x\bar{U}$ ;  $A_U = A_{\bar{U}}$ ,  $B_U = B_{\bar{U}}$ ; and for  $xD$  and  $x\bar{D}$ ;  $A_D = A_{\bar{D}}$ ,  $B_D = B_{\bar{D}}$ . Since there is no information on the flavour structure of the sea it is also necessary to set  $B_{\bar{U}} = B_{\bar{D}}$ , such that there is a single  $B$  parameter for all four quark distributions. The normalisation,  $A_g$ , of the gluon

is determined from the momentum sum-rule and the parameters  $D_U$  and  $D_D$  are determined by the number sum-rules. Assuming that the strange and charm quark distributions can be expressed as  $x$  independent fractions,  $f_s = 0.33$  and  $f_c = 0.15$ , of the  $d$  and  $u$  type sea respectively, gives the further constraint  $A_{\bar{U}} = A_{\bar{D}}(1 - f_s)/(1 - f_c)$ , which ensures that  $\bar{u} = \bar{d}$  at low  $x$ . Finally this H1-style parameterization has 10 free parameters.

The third parameterization we have considered combines the best features of the previous two. It has less model dependence than the ZEUS-style parameterization in that it makes fewer assumptions on the form of sea quark asymmetry  $x\Delta$ , and it has less model dependence than the H1-style parameterization in that it does not assume equality of all  $B$  parameters. Furthermore, although all types of parameterization give acceptable  $\chi^2$  values, the third parameterization has the best  $\chi^2$  and it gives the most conservative experimental errors. This is the parameterization which we chose for our central fit. The PDFs which are parameterized are  $xu_v$ ,  $xd_v$ ,  $xg$  and  $x\bar{U}$ ,  $x\bar{D}$ .

$$xu_v(x) = A_{uv}x^{B_{uv}}(1-x)^{C_{uv}}(1 + D_{uv}x + E_{uv}x^2)$$

$$xd_v(x) = A_{dv}x^{B_{dv}}(1-x)^{C_{dv}}$$

$$x\bar{U}(x) = A_{\bar{U}}x^{B_{\bar{U}}}(1-x)^{C_{\bar{U}}}$$

$$x\bar{D}(x) = A_{\bar{D}}x^{B_{\bar{D}}}(1-x)^{C_{\bar{D}}}$$

$$xg(x) = A_gx^{B_g}(1-x)^{C_g}$$

The normalisation parameters,  $A_{uv}$ ,  $A_{dv}$ ,  $A_g$ , are constrained to impose the number sum-rules and momentum sum-rule. The  $B$  parameters,  $B_{uv}$  and  $B_{dv}$  are set equal,  $B_{uv} = B_{dv}$  and the  $B$  parameters  $B_{\bar{U}}$  and  $B_{\bar{D}}$  are also set equal,  $B_{\bar{U}} = B_{\bar{D}}$ , such that there is a single  $B$  parameter for the valence and another different single  $B$  parameter for the sea distributions. Assuming that the strange and charm quark distributions can be expressed as  $x$  independent fractions,  $f_s = 0.33$  and  $f_c = 0.15$ , of the  $d$  and  $u$  type sea, gives the further constraint  $A_{\bar{U}} = A_{\bar{D}}(1 - f_s)/(1 - f_c)$ . The value of  $f_s = 0.33$  has been chosen to be consistent with determinations of this fraction using neutrino induced di-muon production. This value has been varied to evaluate model uncertainties. The charm fraction has been set to be consistent with dynamic generation of charm from the start point of  $Q^2 = m_c^2$ , in a zero-mass-variable-flavour-number scheme. A small variation of the value of  $f_c$  is included in the model uncertainties. Finally this parameterization has 11 free parameters.

It is well known that the choice of parameterization can affect both PDF shapes and the size of the PDF uncertainties. Fig 2 compares the PDFs and their uncertainties as evaluated using these three different parameterizations. As mentioned earlier, the third parameterization results in the most conservative uncertainties.

We present results for the HERA PDFs based on the third type of parameterization, including six sources of model uncertainty as specified in Table 1. We also compare to results obtained by varying  $\alpha_s(M_Z^2)$  and by varying the choice of parameterization to those of the ZEUS and the H1 styles of parameterization.



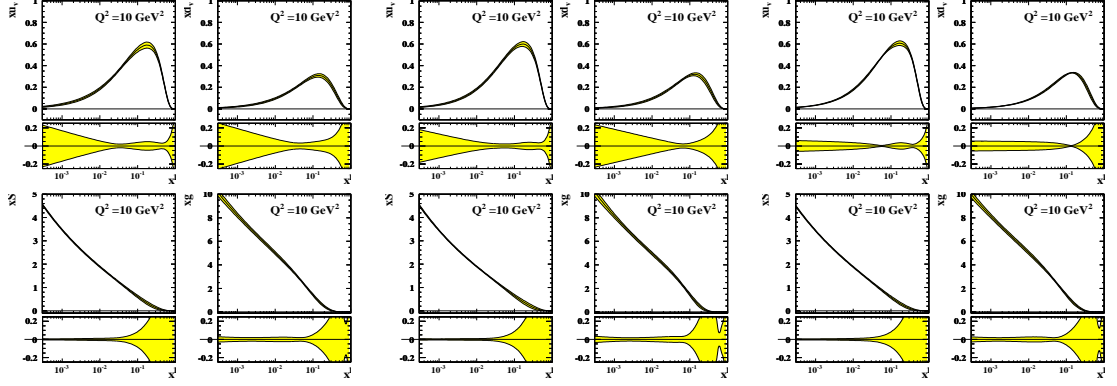


Fig. 2: HERAPDFs,  $xu_v$ ,  $xd_v$ ,  $xS$ ,  $xg$  and their uncertainties at  $Q^2 = 10\text{GeV}^2$ . (Left) for the central fit; (centre) for the ZEUS-style parameterization; (right) for the H1-style parameterization

Model variation	Standard value	Upper Limit	Lower limit
$m_c$	1.4	1.35	1.5
$m_b$	4.75	4.3	5.0
$Q_{min}^2$	3.5	2.5	5.0
$Q_0^2$	4.0	2.0	6.0
$f_s$	0.33	0.25	0.40
$f_c$	0.15	0.12	0.18

Table 1: Standard values of input parameters and cuts, and the variations considered to evaluate model uncertainty



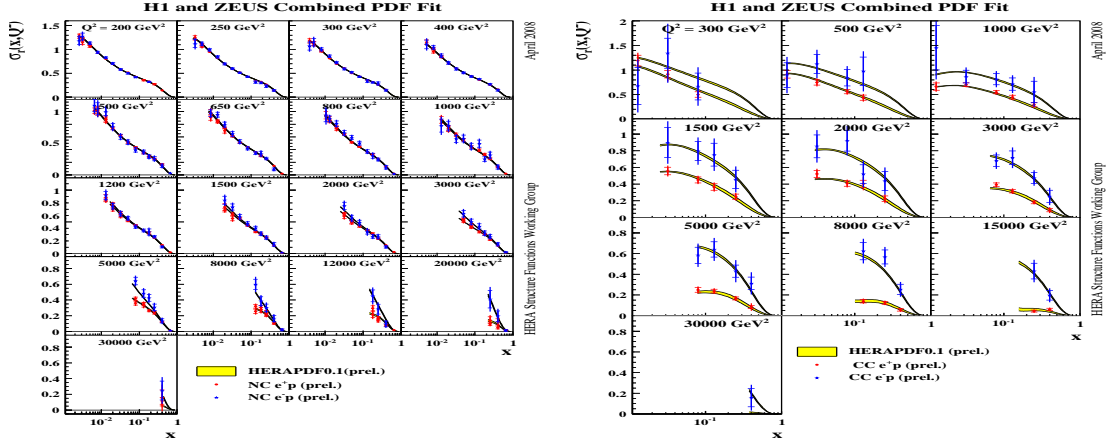


Fig. 3: HERA combined NC (left) and CC (right) data. The predictions of the HERAPDF0.1 fit are superimposed. The uncertainty bands illustrated derive from both experimental and model sources

## 1.4 Results

In Fig. 3 we show the HERAPDF0.1 superimposed on the combined data set for NC data and CC data. In Fig 4 we show the NC data at low  $Q^2$ , and we illustrate scaling violation by showing the reduced cross-section vs.  $Q^2$  for a few representative  $x$  bins. The predictions of the HERAPDF0.1 fit are superimposed, together with the predictions of the ZEUS-JETS and H1PDF2000 PDFs.

Fig. 5 shows the HERAPDF0.1 PDFs,  $xu_v, xd_v, xS, xg$ , as a function of  $x$  at the starting scale  $Q^2 = 4 \text{ GeV}^2$  and at  $Q^2 = 10 \text{ GeV}^2$ . Fig. 6 shows the same PDFs at the scales  $Q^2 = 100, 10000 \text{ GeV}^2$ . Fractional uncertainty bands are shown beneath each PDF. The experimental and model uncertainties are shown separately. As the PDFs evolve with  $Q^2$  the total uncertainty becomes impressively small.

The total uncertainty of the PDFs obtained from the HERA combined data set is much reduced compared to the PDFs extracted from the analyses of the separate H1 and ZEUS data sets, as can be seen from the summary plot Fig. 7, where these new HERAPDF0.1 PDFs are compared to the ZEUS-JETS and H1PDF2000 PDFs. It is also interesting to compare the present HERAPDF0.1 analysis of the combined HERA-I data set with an analysis of the separate data sets which uses the same parameterization and assumptions. Fig 8 makes this comparison. It is clear that it is the data combination, and not the choice of parameterization and assumptions, which has resulted in reduced uncertainties for the low- $x$  gluon and sea PDFs.

The break-up of the HERAPDFs into different flavours is illustrated in Fig. 9, where the PDFs  $xU, xD, x\bar{U}, x\bar{D}$  and  $x\bar{u}, x\bar{d}, x\bar{c}, x\bar{s}$  are shown at  $Q^2 = 10 \text{ GeV}^2$ . The model uncertainty on these PDFs from variation of  $Q_{min}^2, Q_0^2, m_c$  and  $m_b$  is modest. The model uncertainty from variation of  $f_s$  and  $f_c$  is also modest except for its obvious effect on the charm and strange quark distributions.

It is also interesting to look at the results obtained from using the ZEUS-style and H1

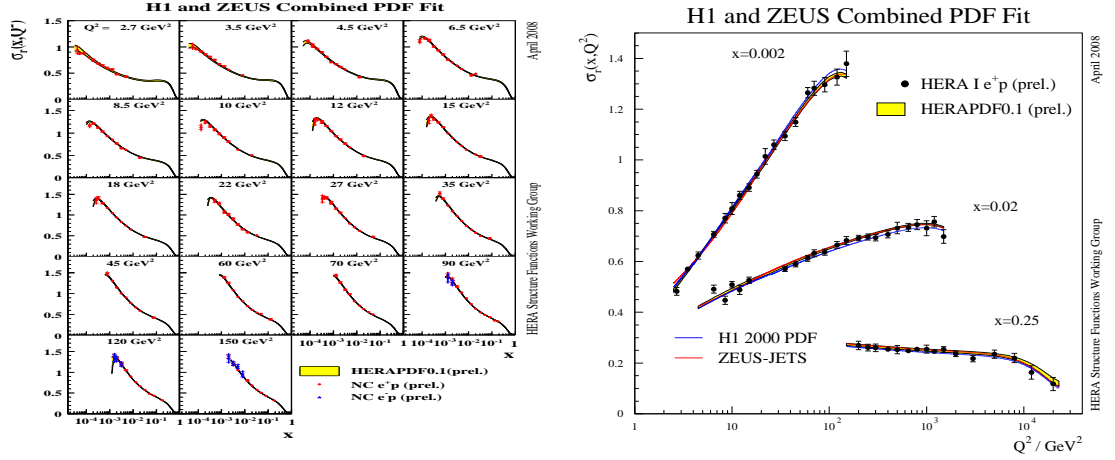


Fig. 4: Left: HERA combined NC data at low  $Q^2$ . Right: the NC reduced cross-section vs  $Q^2$  for three  $x$ -bins. The predictions of the HERAPDF0.1 fit are superimposed, together with the predictions of the ZEUS-JETS and H1PDF2000 PDFs

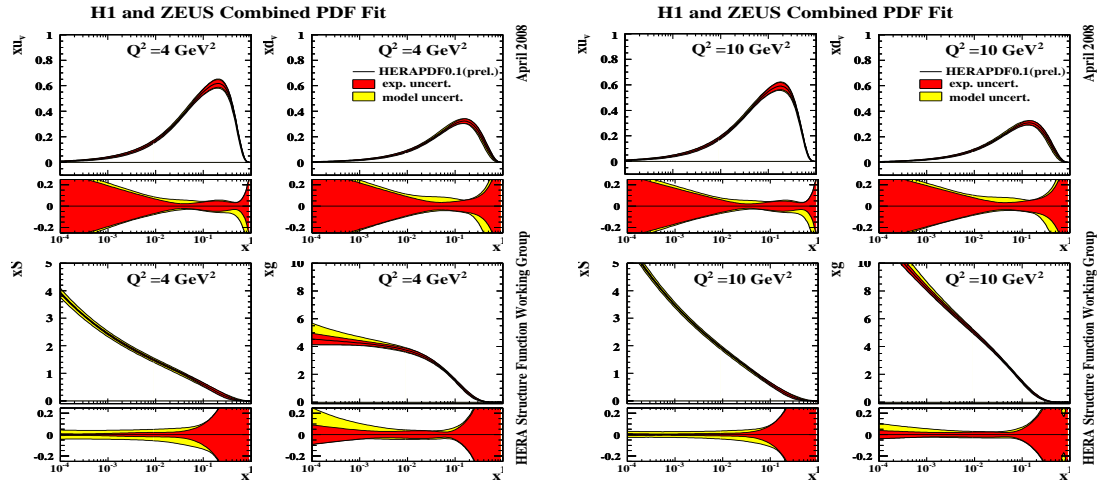


Fig. 5: HERAPDFs,  $xu_v$ ,  $xd_v$ ,  $xS$ ,  $xg$ , at (left)  $Q^2 = 4 \text{ GeV}^2$  and (right)  $Q^2 = 10 \text{ GeV}^2$ . Fractional uncertainty bands are shown beneath each PDF. The experimental and model uncertainties are shown separately as the red and yellow bands respectively

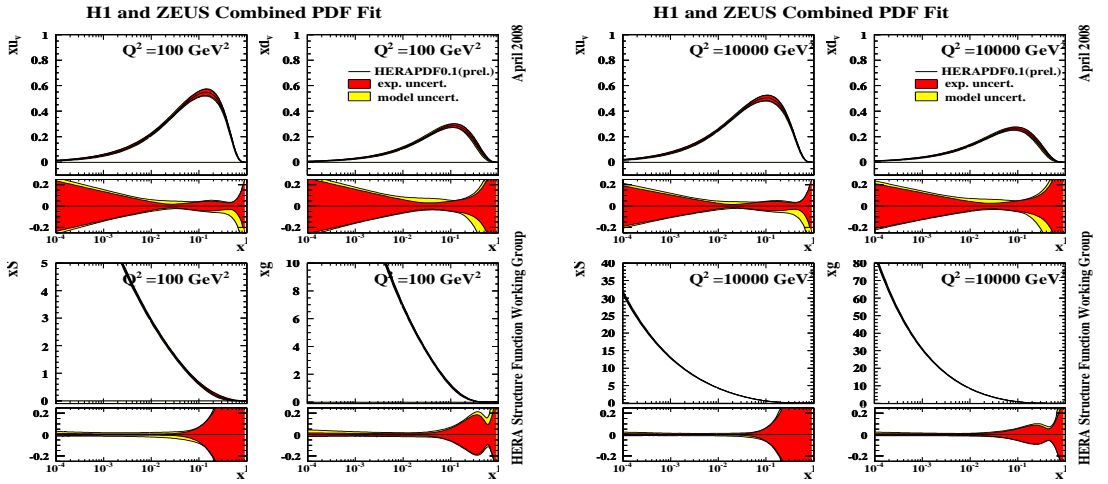


Fig. 6: HERAPDFs,  $xu_v, xd_v, xS, xg$ , at (left)  $Q^2 = 100 \text{ GeV}^2$  and (right)  $Q^2 = 10000 \text{ GeV}^2$ . Fractional uncertainty bands are shown beneath each PDF. The experimental and model uncertainties are shown separately as the red and yellow bands respectively

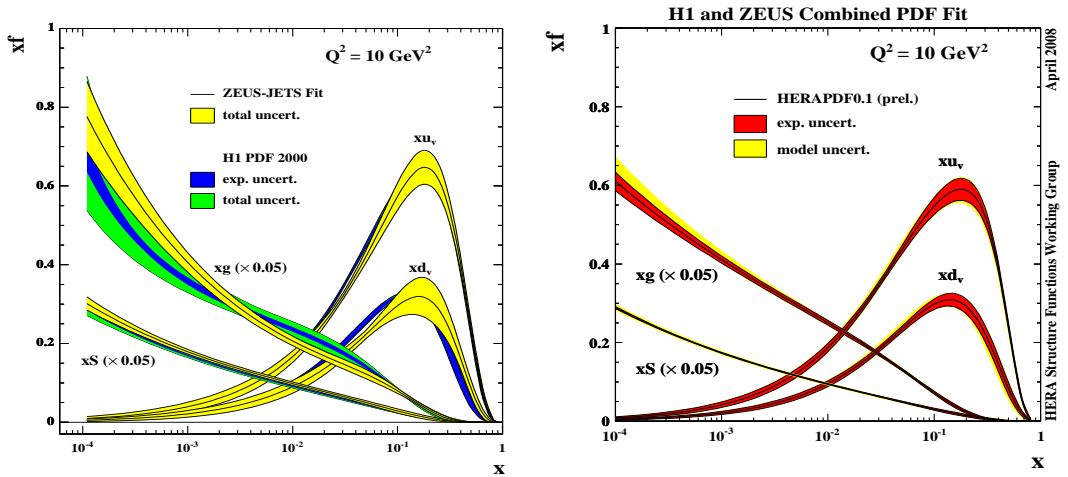


Fig. 7: Left: PDFs from the ZEUS-JETS and H1PDF2000 PDF separate analyses of ZEUS and H1. Right: HERAPDF0.1 PDFs from the analysis of the combined data set

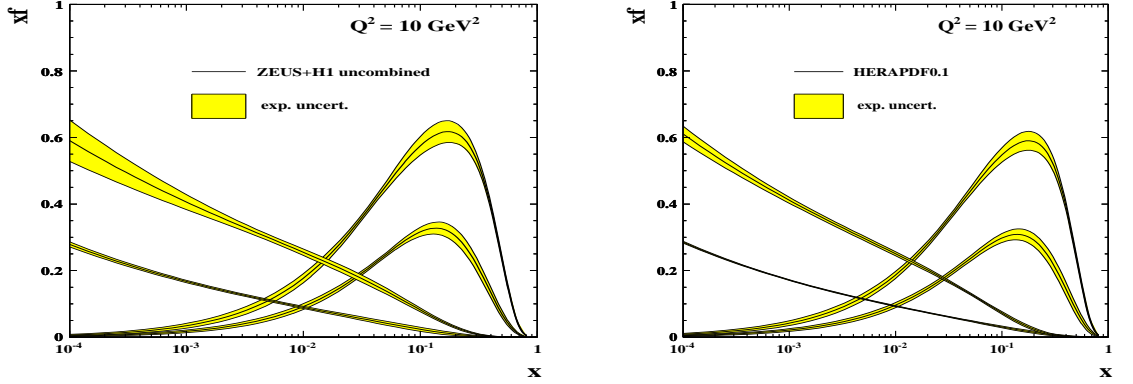


Fig. 8: Left: PDFs resulting from an analysis of the H1 and ZEUS separate data sets using the same parameterization and assumptions as HERAPDF0.1. Right: HERAPDF0.1 PDFs from the analysis of the combined data set (experimental uncertainties only)

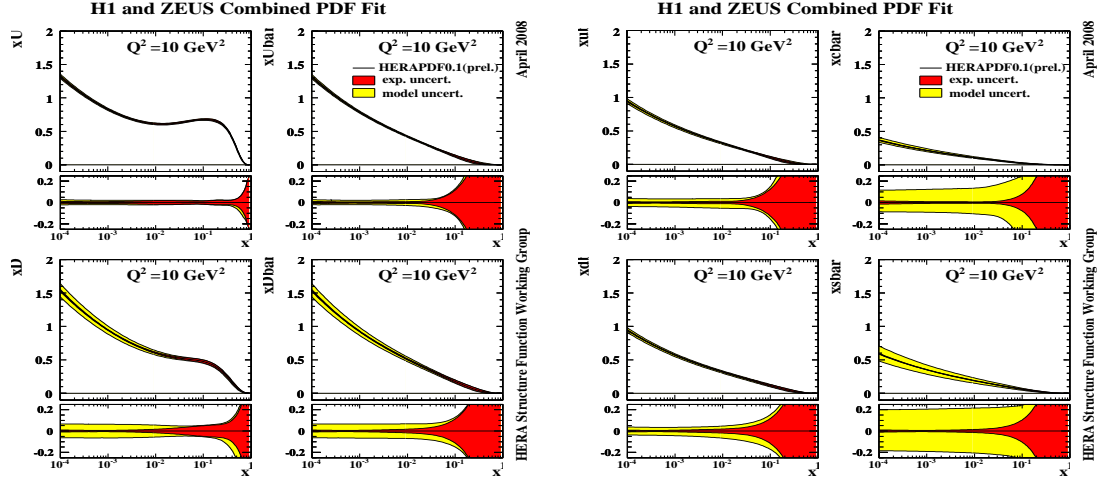


Fig. 9: HERAPDFs at  $Q^2 = 10\text{ GeV}^2$ : (left)  $xU, xD, x\bar{U}, x\bar{D}$ ; (right)  $x\bar{U}, x\bar{D}, x\bar{C}, x\bar{S}$ . Fractional uncertainty bands are shown beneath each PDF. The experimental and model uncertainties are shown separately as the red and yellow bands respectively

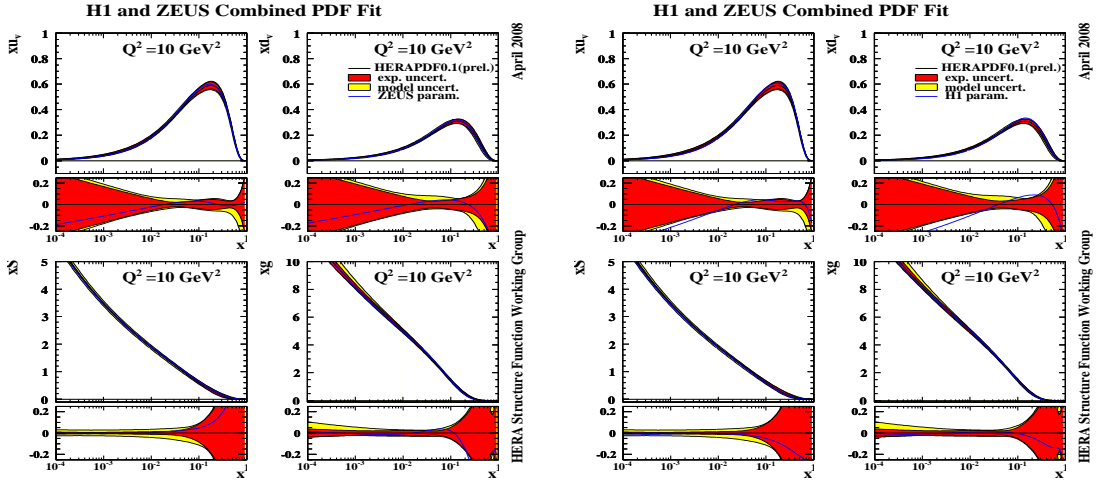


Fig. 10: HERAPDFs at  $Q^2 = 10\text{ GeV}^2$ : with the results for the ZEUS-style parameterization (left) and for the H1-style parameterization (right) superimposed as a blue line.

style parameterizations described in Section 1.3. In Fig. 10 these alternative parameterizations are shown as a blue line superimposed on the HERAPDF0.1 PDFs. These variations in parameterization produce changes in the resulting PDFs which are comparable to the experimental uncertainties in the measured kinematic range. A further variation of parameterization originates from the fact that, if the  $D$  parameter for the gluon is allowed to be non-zero, then each type of parameterization yields a double minimum in  $\chi^2$  such that the gluon may take a smooth or a 'humpy' shape. Although the lower  $\chi^2$  is obtained for the smooth shape, the  $\chi^2$  for the 'humpy' shape is still acceptable. The PDFs for the 'humpy' version of our chosen form of parameterization are compared to the standard version in Fig. 11, where they are shown as a blue line superimposed on the HERAPDF0.1 PDFs. This comparison is shown at  $Q^2 = 4\text{ GeV}^2$ , where the difference is the greatest. Nevertheless the resulting PDFs are comparable to those of the standard choice. This explains a long-standing disagreement in the shape of the gluon obtained by the separate ZEUS-JETS and H1PDF200 analyses. The ZEUS data favoured the smooth shape and the H1 data favoured the 'humpy' shape. However the precision of the combined data set results in PDFs for these shapes which are not significantly different in the measured kinematic region.

It is also interesting to compare the PDFs for the standard choice to those obtained with a different input value of  $\alpha_s(M_Z^2)$ . The uncertainty on the current PDG value of  $\alpha_s(M_Z^2)$  is  $\pm 0.002$  and thus we vary our central choice by this amount. The results are shown in Fig. 12, where we can see that this variation only affects the gluon PDF, such that the larger(smaller) value of  $\alpha_s(M_Z^2)$  results in a harder(soften) gluon as predicted by the DGLAP equations. The change is outside total uncertainty bands of the standard fit. Finally, Figs. 13 and 14 compare the HERAPDF0.1 PDFs to those of the CTEQ and the MRST/MSTW groups respectively. The uncertainty bands of the CTEQ and MRST/MSTW analyses have been scaled to represent 68% CL limits for direct comparability to the HERAPDF0.1. The HERAPDF0.1 analysis has much

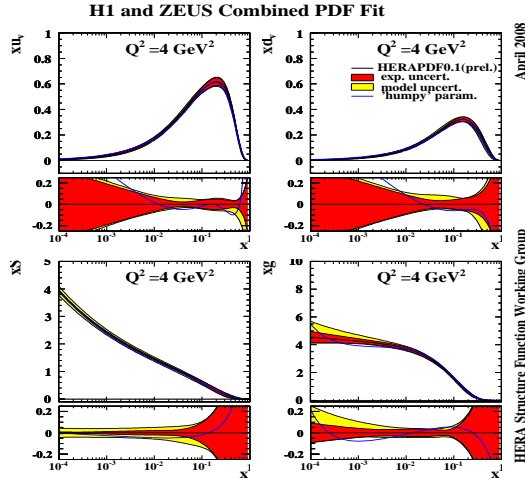


Fig. 11: HERAPDFs at  $Q^2 = 4\text{GeV}^2$ : with the results for the humpy version superimposed as a blue line.

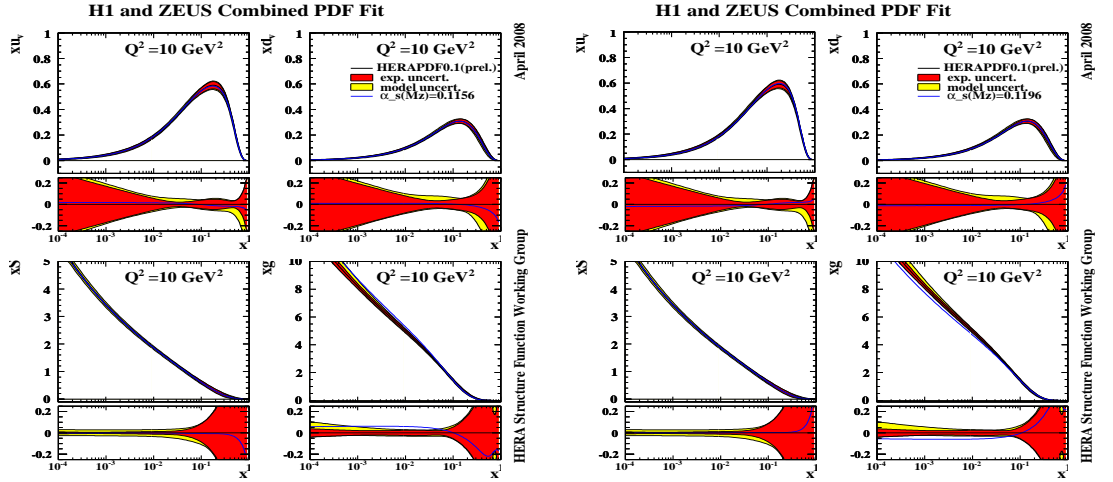


Fig. 12: HERAPDFs at  $Q^2 = 10\text{GeV}^2$ : with the results for  $\alpha_s(M_Z^2) = 0.1156$  (left) and for  $\alpha_s(M_Z^2) = 0.1196$  (right) superimposed as a blue line.

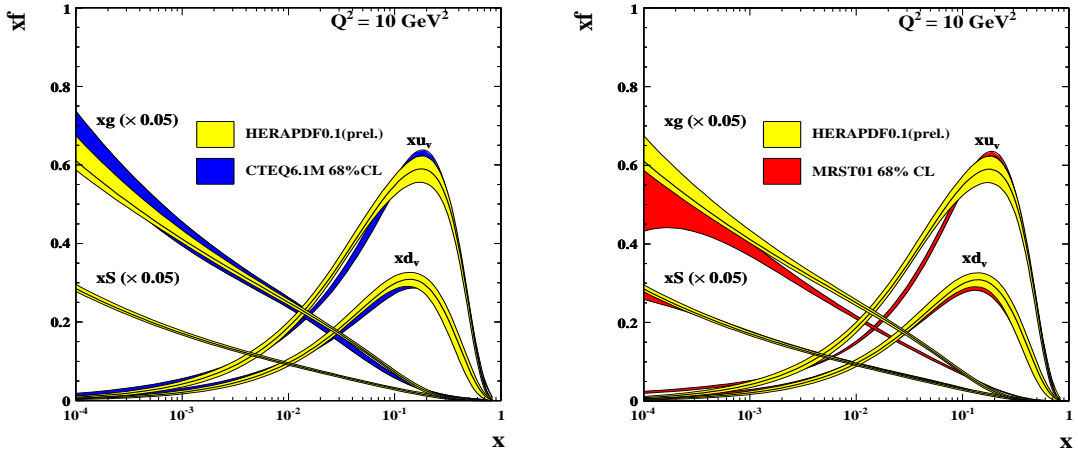


Fig. 13: HERAPDFs at  $Q^2 = 10\text{GeV}^2$  compared to the PDFs from CTEQ6.1 and MRST01

improved precision on the low- $x$  gluon.

### 1.5 Summary of HERAPDF0.1 results

Now that high- $Q^2$  HERA data on NC and CC  $e^+p$  and  $e^-p$  inclusive double differential cross-sections are available, PDF fits can be made to HERA data alone, since the HERA high  $Q^2$  cross-section data can be used to determine the valence distributions and HERA low  $Q^2$  cross-section data can be used to determine the Sea and gluon distributions. The combined HERA-I data set, of neutral and charged current inclusive cross-sections for  $e^+p$  and  $e^-p$  scattering, has been used as the sole input for an NLO QCD PDF fit in the DGLAP formalism. The consistent treatment of systematic uncertainties in the joint data set ensures that experimental uncertainties on the PDFs can be calculated without need for an increased  $\chi^2$  tolerance. This results in PDFs with greatly reduced experimental uncertainties compared to the separate analyses of the ZEUS and H1 experiments. Model uncertainties, including those arising from parameterization dependence, have also been carefully considered. The resulting HERAPDFs (called HERAPDF0.1) have improved precision at low- $x$  compared to the global fits. This will be important for predictions of the  $W$  and  $Z$  cross-sections at the LHC, as explored in the next Section.

These PDFs have been released on LHAPDF in version LHAPDF.5.6: they consist of a central value and 22 experimental eigenvectors plus 12 model alternatives. The user should sum over  $N_{\text{mem}}=1,22$  for experimental uncertainties and over  $N_{\text{mem}}=1,34$  for total uncertainties.

### 1.6 Predictions for $W$ and $Z$ cross-sections at the LHC using the HERAPDF0.1

At leading order (LO),  $W$  and  $Z$  production occur by the process,  $q\bar{q} \rightarrow W/Z$ , and the momentum fractions of the partons participating in this subprocess are given by,  $x_{1,2} = \frac{M}{\sqrt{s}} \exp(\pm y)$ , where  $M$  is the centre of mass energy of the subprocess,  $M = M_W$  or  $M_Z$ ,  $\sqrt{s}$  is the centre of mass energy of the reaction ( $\sqrt{s} = 14$  TeV at the LHC) and  $y = \frac{1}{2} \ln \frac{(E+pt)}{(E-pt)}$  gives the parton

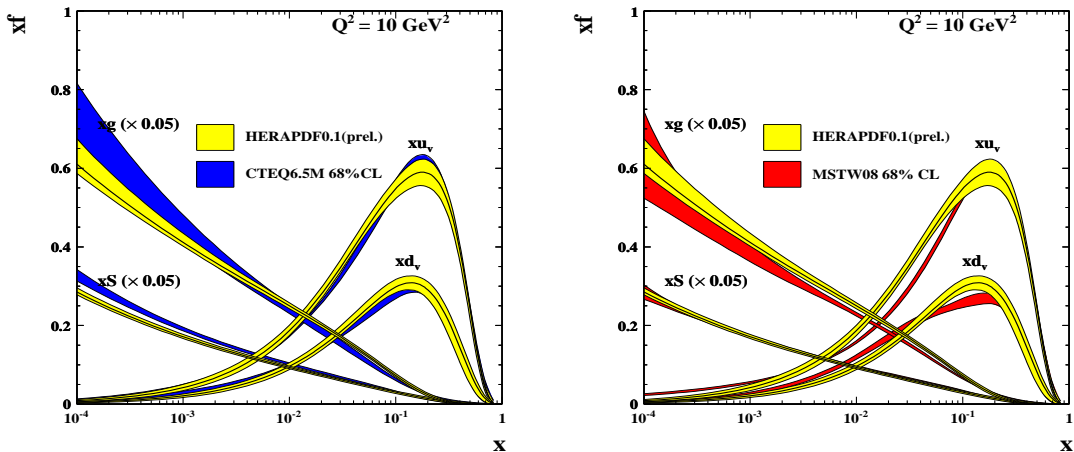


Fig. 14: HERAPDFs at  $Q^2 = 10\text{GeV}^2$  compared to the PDFs from CTEQ6.5 and MSTW08(prel.)

rapidity. The kinematic plane for LHC parton kinematics is shown in Fig. 15. Thus, at central rapidity, the participating partons have small momentum fractions,  $x \sim 0.005$ . Moving away from central rapidity sends one parton to lower  $x$  and one to higher  $x$ , but over the central rapidity range,  $|y| < 2.5$ ,  $x$  values remain in the range,  $5 \times 10^{-4} < x < 5 \times 10^{-2}$ . Thus, in contrast to the situation at the Tevatron, the scattering is happening mainly between sea quarks. Furthermore, the high scale of the process  $Q^2 = M^2 \sim 10,000 \text{ GeV}^2$  ensures that the gluon is the dominant parton, see Fig. 15, so that these sea quarks have mostly been generated by the flavour blind  $g \rightarrow q\bar{q}$  splitting process. Thus the precision of our knowledge of  $W$  and  $Z$  cross-sections at the LHC is crucially dependent on the uncertainty on the momentum distribution of the low- $x$  gluon.

HERA data have already dramatically improved our knowledge of the low- $x$  gluon, as discussed in earlier proceedings of the HERALHC workshop [13]. Now that the precision of HERA data at small- $x$  have been dramatically improved by the combination of H1 and ZEUS HERA-I data, we re-investigate the consequences for predictions of  $W, Z$  production at the LHC.

Predictions for the  $W/Z$  cross-sections, decaying to the lepton decay mode, using CTEQ, ZEUS PDFs and the HERAPDF0.1 are summarised in Table 2. Note that the uncertainties of CTEQ PDFs have been rescaled to represent 68% CL, in order to be comparable to the HERA PDF uncertainties. The precision on the predictions of the global fits (CTEQ6.1/5 and ZEUS-2002) for the total  $W/Z$  cross-sections is  $\sim 3\%$  at 68% CL. The precision of the ZEUS-2005 PDF fit prediction, which used only ZEUS data, is comparable, since information on the low- $x$  gluon is coming from HERA data alone. The increased precision of the HERAPDF0.1 low- $x$  gluon PDF results in increased precision of the  $W/Z$  cross-section predictions of  $\sim 1\%$ .

It is interesting to consider the predictions as a function of rapidity. Fig 16 shows the predictions for  $W^+, W^-, Z$  production as a function of rapidity from the HERAPDF0.1 PDF fit and compares them to the predictions from a PDF fit, using the same parameterization and assumptions, to the H1 and ZEUS data from HERA-I uncombined. The increase precision due



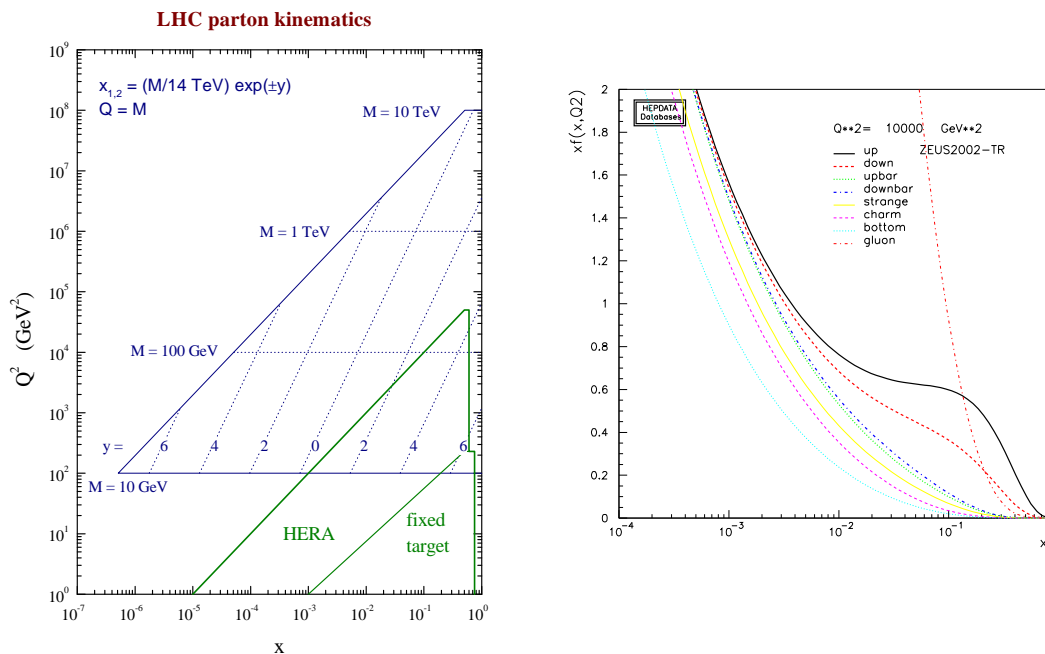


Fig. 15: Left plot: The LHC kinematic plane (thanks to James Stirling). Right plot: Typical PDF distributions at  $Q^2 = 10,000$  GeV<sup>2</sup>.

to the combination is impressive. Fig. 17 show the predictions for  $W^+$ ,  $W^-$ ,  $Z$  production as a function of rapidity from the CTEQ6.1, 6.6 and MRST01 PDF fits for comparison. The uncertainties on the CTEQ and MRST PDF predictions have been rescaled to represent 68% CL limits, for direct comparability to the HERAPDF0.1 uncertainties. At central rapidity these limits give an uncertainty on the boson cross-sections of  $\sim 5\%$ , ( $\sim 3\%$ ), ( $\sim 2\%$ ) for CTEQ6.1, (CTEQ6.6), (MRST01) compared to  $\sim 1\%$  for the HERAPDF0.1.

So far, only experimental uncertainties have been included in these evaluations. It is also necessary to include model uncertainties. Fig. 18 shows the  $W^+$ ,  $W^-$ ,  $Z$  rapidity distributions including the six sources of model uncertainty detailed in Section 1.3. These model uncertainties increase the total uncertainty at central rapidity to  $\sim 2\%$ . Further uncertainty due to the choice of  $\alpha_s(M_Z)$  is small because, although a lower (higher) choice results in a larger (smaller) gluon at low  $x$ , the rate of QCD evolution is lower (higher) and this largely compensates. Uncertainties due to the choice of parameterization also have little impact on the boson rapidity spectra in the central region as illustrated in Fig. 18 by the superimposed blue line, which represents the alternative 'humpy' gluon parameterization (see Sec. 1.4).

Since the PDF uncertainty feeding into the  $W^+$ ,  $W^-$  and  $Z$  production is mostly coming from the gluon PDF, for all three processes, there is a strong correlation in their uncertainties, which can be removed by taking ratios. Figs. 16, 17 and 18 also show the  $W$  asymmetry

$$A_W = (W^+ - W^-)/(W^+ + W^-).$$

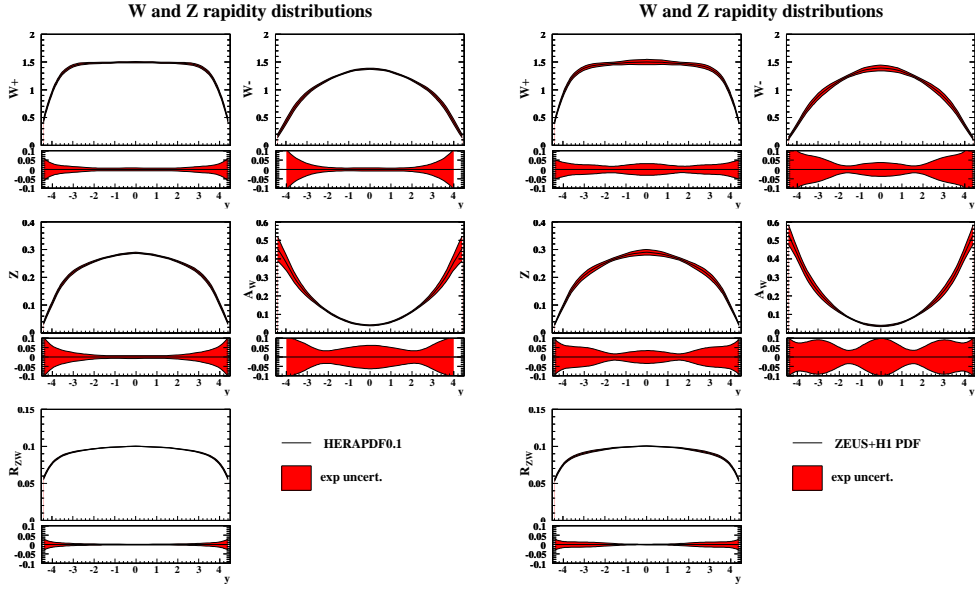


Fig. 16: The  $W^+$ ,  $W^-$ ,  $Z$  rapidity distributions,  $A_W$  and  $R_{ZW}$  (see text) and their uncertainties as predicted by (left) HERAPDF0.1 (right) a similar fit to the uncombined ZEUS and H1 data from HERA-I.

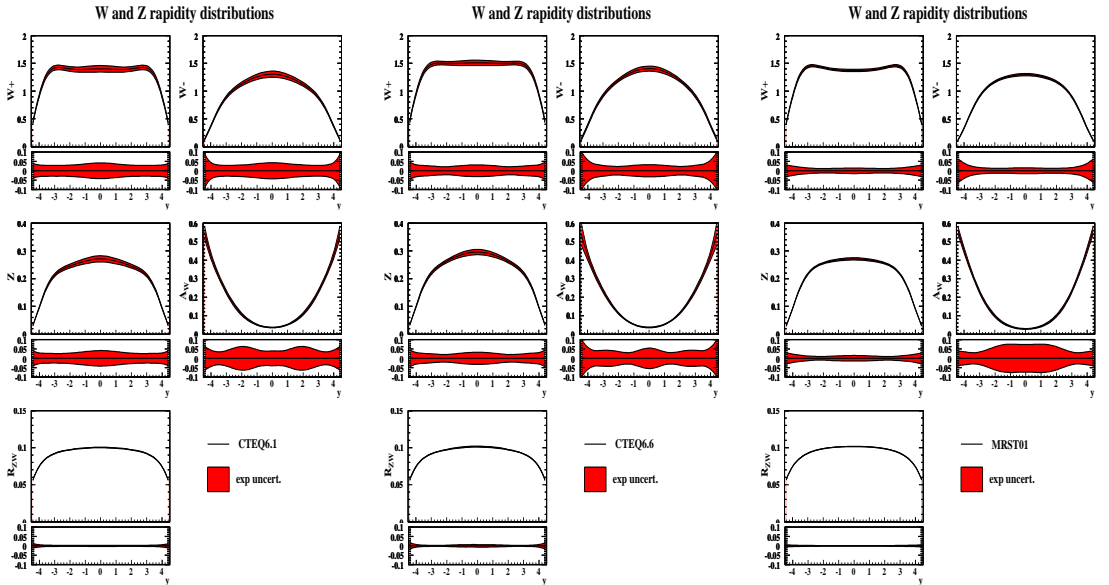


Fig. 17: The  $W^+$ ,  $W^-$ ,  $Z$  rapidity distributions,  $A_W$  and  $R_{ZW}$  (see text) and their uncertainties (scaled to 68% CL) as predicted by (left) CTEQ6.1, (middle) CTEQ6.6, right (MRST01)

PDF Set	$\sigma(W^+).B(W^+ \rightarrow l^+\nu_l)$	$\sigma(W^-).B(W^- \rightarrow l^-\bar{\nu}_l)$	$\sigma(Z).B(Z \rightarrow l^+l^-)$
CTEQ6.1	$11.61 \pm 0.34$ nb	$8.54 \pm 0.26$ nb	$1.89 \pm 0.05$ nb
CTEQ6.5	$12.47 \pm 0.28$ nb	$9.14 \pm 0.22$ nb	$2.03 \pm 0.04$ nb
ZEUS-2002	$12.07 \pm 0.41$ nb	$8.76 \pm 0.30$ nb	$1.89 \pm 0.06$ nb
ZEUS-2005	$11.87 \pm 0.45$ nb	$8.74 \pm 0.31$ nb	$1.97 \pm 0.06$ nb
HERAPDF0.1	$12.14 \pm 0.13$ nb	$9.08 \pm 0.14$ nb	$1.99 \pm 0.025$ nb

Table 2: LHC  $W/Z$  cross-sections for decay via the lepton mode, for various PDFs, with 68% CL uncertainties.

The experimental PDF uncertainty on the asymmetry is larger ( $\sim 5\%$  for both CTEQ and HERAPDFs,  $\sim 7\%$  for the MRST01 PDFs) than that on the individual distributions and the variation between PDF sets is also larger - compare the central values of the CTEQ and MRST predictions, which are almost 25% discrepant. This is because the asymmetry is sensitive to the difference in the valence PDFs,  $u_v - d_v$ , in the low- $x$  region,  $5 \times 10^{-4} < x < 5 \times 10^{-2}$ , where there is no constraint from current data. To see this consider that at LO,

$$A_W \sim (u\bar{d} - d\bar{u})/(u\bar{d} + d\bar{u} + c\bar{s} + s\bar{c})$$

and that  $\bar{d} \sim \bar{u}$  at low- $x$ . (Note that the  $c\bar{s}$  and  $s\bar{c}$  contributions cancel out in the numerator). The discrepancy between the CTEQ and MRST01 asymmetry predictions at  $y = 0$  can be quantitatively understood by considering their different valence PDFs (see Figs. 13, 14 in Sec. 1.4). In fact a measurement of the asymmetry at the LHC will provide new information to constrain these PDFs.

By contrast, the ratio

$$R_{ZW} = Z/(W^+ + W^-),$$

also shown in Figs. 16, 17 and 18, has very small PDF uncertainties (both experimental and model) and there is no significant variation between PDF sets. To understand this consider that at LO

$$R_{ZW} = (u\bar{u} + d\bar{d} + c\bar{c} + s\bar{s})/(u\bar{d} + d\bar{u} + c\bar{s} + s\bar{c})$$

(modulo electroweak couplings) and that  $\bar{d} \sim \bar{u}$  at low- $x$ <sup>3</sup>. This will be a crucial measurement for our understanding of Standard Model Physics at the LHC.

However, whereas the  $Z$  rapidity distribution can be fully reconstructed from its decay leptons, this is not possible for the  $W$  rapidity distribution, because the leptonic decay channels which we use to identify the  $W$ 's have missing neutrinos. Thus we actually measure the  $W$ 's decay lepton rapidity spectra rather than the  $W$  rapidity spectra. Fig. 18 also shows the rapidity spectra for positive and negative leptons from  $W^+$  and  $W^-$  decay, the lepton asymmetry,

$$A_l = (l^+ - l^-)/(l^+ + l^-)$$

and the ratio

$$R_{Zl} = Z/(l^+ + l^-)$$

<sup>3</sup>There is some small model dependence from the strange sea fraction accounted for in both HERAPDF0.1 and in CTEQ6.6 PDFs.

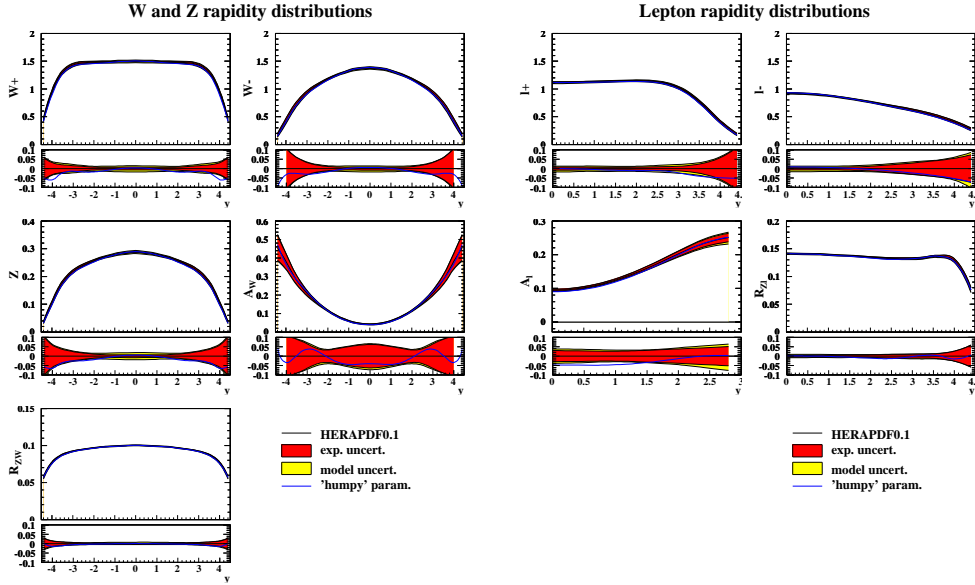


Fig. 18: Left: the  $W^+$ ,  $W^-$ ,  $Z$  rapidity distributions,  $A_W$ , and  $R_{ZW}$  (see text) and their experimental uncertainties (red) and model uncertainties (yellow). Right: the  $l^+$ ,  $l^-$  rapidity distributions,  $A_l$  and  $R_{Zl}$  (see text) and their experimental and model uncertainties. The superimposed blue line represents the results of the alternative 'humpy' gluon parameterization.

A cut of,  $p_{t\ell} > 25$  GeV, has been applied on the decay lepton, since it will not be possible to trigger on leptons with small  $p_{t\ell}$ . A particular lepton rapidity can be fed from a range of  $W$  rapidities so that the contributions of partons at different  $x$  values is smeared out in the lepton spectra, but the broad features of the  $W$  spectra remain.

In summary, these investigations indicate that PDF uncertainties, deriving from experimental error, on predictions for the  $W$ ,  $Z$  rapidity spectra in the central region, have reached a precision of  $\sim 1\%$ , due to the input of the combined HERA-I data. This level of precision is maintained when using the leptons from the  $W$  decay and gives us hope that we could use these processes as luminosity monitors<sup>4</sup>. However, model dependent uncertainties must now be considered very carefully. The current study will be repeated using a general-mass variable-flavour scheme for heavy quarks.

The predicted precision on the ratios  $R_{ZW}$ ,  $R_{Zl}$  is even better since model uncertainties are also very small giving a total uncertainty of  $\sim 1\%$ . This measurement may be used as a SM benchmark. However the  $W$  and lepton asymmetries have larger uncertainties (5 – 7%). A measurement of these quantities would give new information on valence distributions at small- $x$ .

<sup>4</sup>A caveat is that the current study has been performed using PDF sets which are extracted using NLO QCD in the DGLAP formalism. The extension to NNLO gives small corrections  $\sim 1\%$ . However, there may be much larger uncertainties in the theoretical calculations because the kinematic region involves low- $x$ . There may be a need to account for  $\ln(1/x)$  resummation or high gluon density effects.

## 2 Measurements of the Proton Structure Function $F_L$ at HERA <sup>5</sup>

### 2.1 Introduction

The inclusive deep inelastic  $ep$  scattering (DIS) cross section can at low  $Q^2$  be written in terms of the two structure functions,  $F_2$  and  $F_L$ , in reduced form as

$$\sigma_r(x, Q^2, y) \equiv \frac{d^2\sigma}{dx dQ^2} \cdot \frac{Q^4 x}{2\pi\alpha^2 Y_+} = F_2(x, Q^2) - \frac{y^2}{Y_+} \cdot F_L(x, Q^2), \quad (4)$$

where  $Q^2 = -q^2$  is the negative of the square of the four-momentum transferred between the electron<sup>6</sup> and the proton, and  $x = Q^2/2qP$  denotes the Bjorken variable, where  $P$  is the four-momentum of the proton. The two variables are related through the inelasticity of the scattering process,  $y = Q^2/sx$ , where  $s = 4E_e E_p$  is the centre-of-mass energy squared determined from the electron and proton beam energies,  $E_e$  and  $E_p$ . In eq. 4,  $\alpha$  denotes the fine structure constant and  $Y_+ = 1 + (1 - y)^2$ .

The two proton structure functions  $F_2$  and  $F_L$  are related to the cross sections of the transversely and longitudinally polarised virtual photons interacting with protons,  $\sigma_L$  and  $\sigma_T$ , according to  $F_L \propto \sigma_L$  and  $F_2 \propto (\sigma_L + \sigma_T)$ . Therefore the relation  $0 \leq F_L \leq F_2$  holds. In the Quark Parton Model (QPM),  $F_2$  is the sum of the quark and anti-quark  $x$  distributions, weighted by the square of the electric quark charges, whereas the value of  $F_L$  is zero [14]. The latter follows from the fact that a quark with spin  $\frac{1}{2}$  cannot absorb a longitudinally polarised photon.

In Quantum Chromodynamics (QCD),  $F_L$  differs from zero, receiving contributions from quarks and from gluons [15]. At low  $x$  and in the  $Q^2$  region of deep inelastic scattering the gluon contribution greatly exceeds the quark contribution. Therefore  $F_L$  is a direct measure of the gluon distribution to a very good approximation. The gluon distribution is also constrained by the scaling violations of  $F_2$  as described by the DGLAP QCD evolution equations [7–9, 16, 17]. An independent measurement of  $F_L$  at HERA, and its comparison with predictions derived from the gluon distribution extracted from the  $Q^2$  evolution of  $F_2(x, Q^2)$ , thus represents a crucial test on the validity of perturbative QCD (pQCD) at low  $x$ . Moreover, depending on the particular theoretical approach adopted, whether it be a fixed order pQCD calculation, a resummation scheme, or a color dipole ansatz, there appear to be significant differences in the predicted magnitude of  $F_L$  at low  $Q^2$ . A measurement of  $F_L$  may be able to distinguish between these approaches.

Previously the structure function  $F_L$  was extracted by the H1 collaboration from inclusive data at high  $y$  using indirect methods, as discussed in Sect. 2.2. A preliminary measurement was also presented by the ZEUS collaboration using initial state radiation (ISR) events [18], although the precision of this measurement was limited.

To make a direct measurement of  $F_L$ , reduced cross sections must be measured at the same  $x$  and  $Q^2$  but with different  $y$  values. This can be seen from eq. 4 which states that  $F_L(x, Q^2)$  is equal to the partial derivative  $\partial\sigma_r(x, Q^2, y)/\partial(y^2/Y_+)$ . Due to the relationship  $y = Q^2/xs$  this requires data to be collected at different beam-beam centre-of-mass energies, which was done in the last year of HERA running. To maximize the precision of this procedure, the measurable

<sup>5</sup>Contributing authors: J. Grebenyuk, V. Lendermann

<sup>6</sup>The term electron is used here to denote both electrons and positrons unless the charge state is specified explicitly.

range of  $y^2/Y_+$  had to be maximised for each fixed  $x$  and  $Q^2$ . This was achieved by operating HERA at the lowest attainable centre-of-mass energy and by measuring this data up to the highest possible value of  $y$ . An intermediate HERA centre-of-mass energy was also chosen, to improve the precision of  $F_L$  extraction and to act as a consistency check. More specifically, between March and June 2007, HERA was operated with proton beam energies,  $E_p = 460$  GeV and 575 GeV, compared to the previous nominal value of 920 GeV. The electron beam energy was unaltered at  $E_e = 27.6$  GeV. Thus, three data sets, referred to the high- (HER), middle- (MER) and low-energy running (LER) samples, were collected with  $\sqrt{s} = 318$  GeV, 251 GeV and 225 GeV, respectively. The integrated luminosities of the data sets used by ZEUS (H1) to measure  $F_L$  are  $32.8$  ( $21.6$ )  $\text{pb}^{-1}$  for HER,  $6$  ( $6.2$ )  $\text{pb}^{-1}$  for MER and  $14$  ( $12.4$ )  $\text{pb}^{-1}$  for LER. The specific issues of the recent H1 and ZEUS analyses are discussed in Sect. 2.3, and the results are presented in Sect. 2.4.

## 2.2 Indirect $F_L$ Extraction by H1

H1 extracted  $F_L$  from inclusive data using several indirect methods, which exploit the turn over of the reduced cross section at high  $y$  due to the  $F_L$  contribution. The basic principle is the following. First, the reduced neutral current cross section  $\sigma_r$  is measured in a  $y$  range, where the  $F_L$  contribution is negligible and thus the relation  $\sigma_r = F_2$  holds very well. Afterward, based on some theoretical assumption, the knowledge of  $F_2$  is extrapolated towards high  $y$ . Finally  $F_L$  is extracted from the difference between the prediction for  $F_2$  and the measurement of  $\sigma_r$  at high  $y$ .

In the analyses at  $Q^2 \gtrsim 10 \text{ GeV}^2$  [4, 19, 20] the “extrapolation” method is used. In this method, an NLO QCD PDF fit to H1 HERA I data is performed at  $y < 0.35$ , and the results are extrapolated to higher  $y$  using the DGLAP evolution equations.  $F_L$  is then extracted at a fixed  $y = 0.75$  and at  $Q^2$  up to  $700 \text{ GeV}^2$  using eq. 4. The extracted values are shown in Fig. 19 for the high- $Q^2$  analysis [4].

At low  $Q^2$ , extrapolations of DGLAP fits become uncertain. For  $Q^2 \lesssim 2 \text{ GeV}^2$ , as the strong coupling constant  $\alpha_s(Q^2)$  increases, the higher order corrections to the perturbative expansion become large and lead to the breakdown of the pQCD calculations. Therefore other methods are used in the H1 low- $Q^2$  data analyses.

The “shape method”, as used in the last H1 low- $Q^2$  study of HERA I data [21], exploits the shape of  $\sigma_r$  in a given  $Q^2$  bin. The  $Q^2$  dependence at high  $y$  is driven by the kinematic factor  $y^2/Y_+$  (eq. 4), and to a lesser extent by  $F_L(x, Q^2)$ . On the other hand, the gluon dominance at low  $x$  suggests that  $F_L$  may exhibit an  $x$  dependence similar to  $F_2$ . Therefore it is assumed that  $F_L$  is proportional to  $F_2$  and the coefficient of proportionality depends only on  $Q^2$ . In the extraction procedure one uses the ratio  $R$  of the cross sections of the transversely and longitudinally polarised photons

$$R = \frac{\sigma_T}{\sigma_L} = \frac{F_L}{F_2 - F_L} \quad (5)$$

which is thus assumed to depend only on  $Q^2$ . The reduced cross section is fitted by

$$\sigma_r = F_2 \left[ 1 - \frac{y^2}{Y_+} \frac{R(Q^2)}{1 + R(Q^2)} \right], \quad (6)$$

where some phenomenological model for  $F_2$  is chosen.

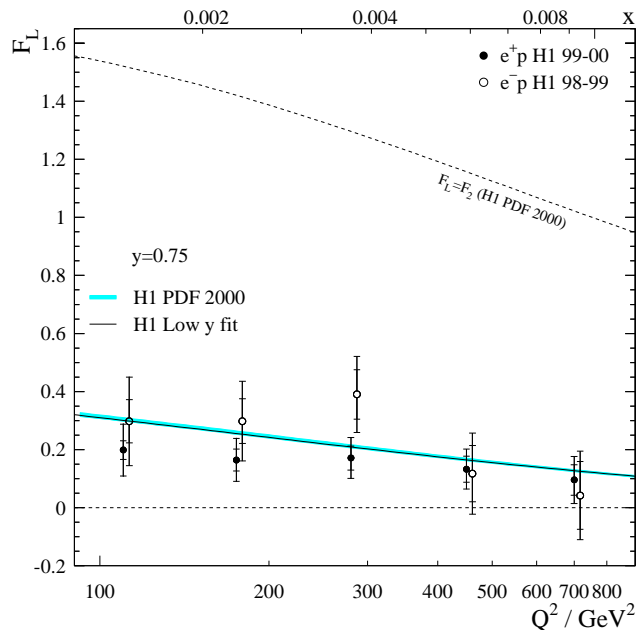


Fig. 19:  $F_L$  determined indirectly by H1 at a fixed  $y = 0.75$  and high  $Q^2$  is shown as a function of  $Q^2$  (lower scale) or equivalently  $x$  (upper scale) for  $e^+p$  (closed circles) and  $e^-p$  (open circles) data. The inner error bar represents the statistical error, and the outer error bar also includes the systematic error and the uncertainty arising from the extrapolation of  $F_2$ .

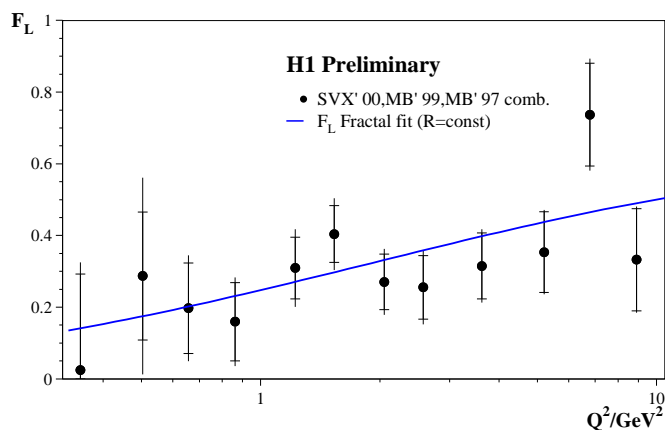


Fig. 20:  $Q^2$  dependence of  $F_L(x, Q^2)$  at fixed  $y = 0.75$ , extracted from the preliminary H1 low- $Q^2$  data. The solid line shows the prediction of the fractal fit with a constant  $R$ .

An example of such an extraction using a fractal fit for  $F_2$  [22] is shown in Fig. 20, where preliminary H1 results [21] for  $F_L$  at  $y = 0.75$  in the range of  $0.35 \leq Q^2 \leq 8.5 \text{ GeV}^2$  are presented. The data favour a positive, not small  $F_L$  at low  $Q^2$ . A drawback of this method is that it reveals a considerable dependence of  $R$  on the choice of the  $F_2$  model.

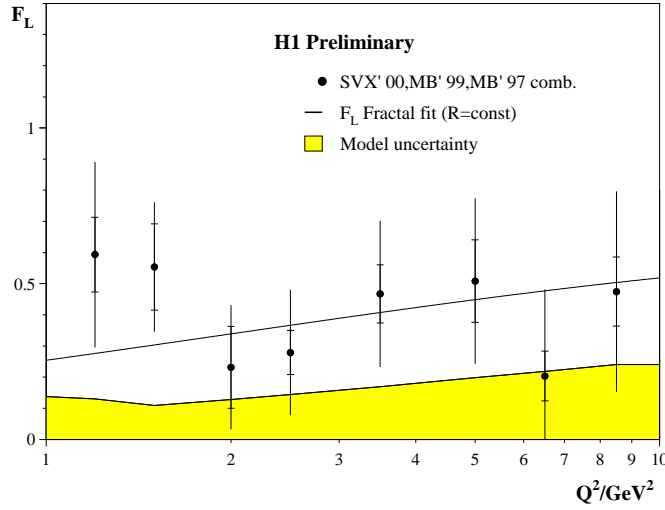


Fig. 21: Structure function  $F_L$  extracted by H1 using the derivative method. The solid line shows the prediction of the fractal fit with a constant  $R$ . The inner error bars represent statistical uncertainties, the outer error bars represent statistical and systematic uncertainties added in quadrature. The solid (yellow) band indicates the model uncertainty.

In the derivative method [20, 21],  $F_L$  is extracted from the partial derivative of the reduced cross section on  $y$  at fixed  $Q^2$

$$\left. \frac{\partial \sigma_r}{\partial \ln y} \right|_{Q^2} = -x \frac{\partial F_2}{\partial x} - \frac{2y^2(2-y)}{Y_+^2} F_L - x \frac{y^2}{Y_+} \frac{\partial F_L}{\partial x} \quad (7)$$

which is dominated by the  $F_L$ -dependent term at high  $y$ . The term proportional to  $\partial F_L / \partial x$  is negligible for moderately varying parametrisations of  $F_L$ . For low  $Q^2$  values the rise of  $F_2$  is weak. The change of the term  $x \partial F_2 / \partial x$  for the two assumptions: no rise at low  $x$ , i.e.  $\partial F_2 / \partial x = 0$ , and  $F_2 \propto x^{-\lambda}$  is numerically significantly smaller than the experimental precision for  $\partial \sigma_r / \partial \ln y$ . Therefore the derivative method provides a means for determining  $F_L$  at low  $Q^2$  with minimal phenomenological assumption. On the other hand, the errors obtained with the derivative method turn out to be significantly larger than those from the shape method.

The preliminary results of  $F_L$  extraction from H1 HERA I data [21] are presented in Fig. 21. The residual dependence of the measurement on the assumption made for  $F_2$  is estimated by a comparison with results obtained assuming an  $F_2$  which is flat in  $y$ . The lower bound on  $F_L$  obtained this way is depicted as a solid band in the figure.

### 2.3 Details of Direct $F_L$ Measurements

The H1 and ZEUS analysis procedures involve a measurement of the inclusive cross section at  $y > 0.1$ . In this range, the kinematic variables  $x$ ,  $y$  and  $Q^2$  are most accurately reconstructed using the polar angle,  $\theta_e$ , and the energy,  $E'_e$ , of the scattered electron according to

$$y = 1 - \frac{E'_e \sin^2 \theta_e}{E_e}, \quad Q^2 = \frac{E_e'^2 \sin^2 \theta_e}{1 - y}, \quad x = \frac{Q^2}{ys}. \quad (8)$$



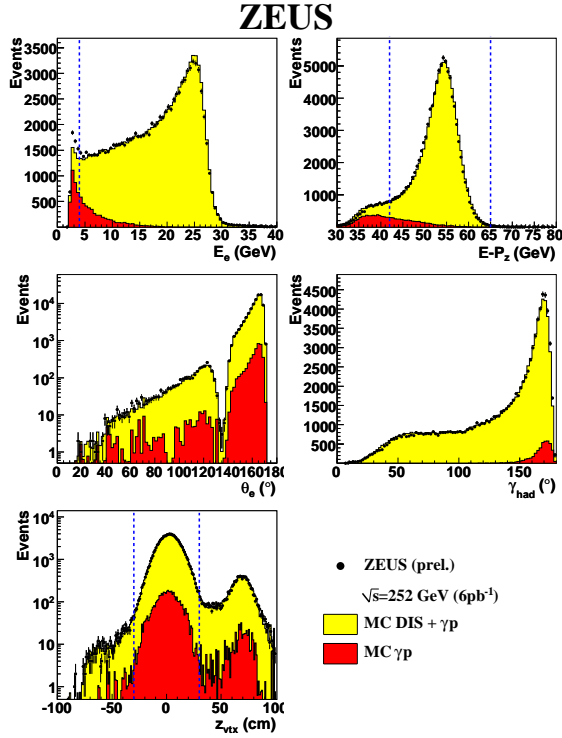


Fig. 22: Comparison of 575 GeV data with the sum of DIS and background simulations for the energy of the scattered electron, total  $E - p_z$ , theta of the scattered electron, angle of the hadronic final state and  $z$  coordinate of the vertex. The dotted lines indicate the cuts applied.

Reaching the high  $y$  values necessary for the  $F_L$  determination requires a measurement of the scattered electron with energy down to a few GeV. The electron candidate is selected as an isolated electromagnetic energy deposition (cluster) in a calorimeter. The crucial analysis issue at high- $y$  region is the identification of the scattered electron, and the estimation of the hadronic background which occurs when a particle from the hadronic final state mimics the electron signal. Most of background events are photoproduction ( $\gamma p$ ) events with  $Q^2 \approx 0$  in which the final state electron is scattered at low angles (high  $\theta$ )<sup>7</sup> and thus escapes through the beam pipe.

The  $\gamma p$  background suppression is performed in several steps. Firstly, calorimeter shower estimators are utilised which exploit the different profiles of electromagnetic and hadronic showers. Secondly, background coming from neutral particles, such as  $\pi_0$ , can be rejected by requiring a track associated to the electron candidate. Furthermore,  $\gamma p$  events are suppressed by utilising the energy-momentum conservation. For that, the variable  $E - p_z = \sum_i (E_i - p_{z,i})$  is exploited, where the sum runs over energies  $E_i$  and longitudinal momentum components  $p_{z,i}$  of all particles in the final state. The requirement  $E - p_z > 35$  (42) GeV in the H1 (ZEUS) analysis removes

<sup>7</sup>The  $z$  axis of the right-handed coordinate systems used by H1 and ZEUS is defined by the direction of the incident proton beam with the origin at the nominal  $ep$  interaction vertex. Consequently, small scattering angles of the final state particles correspond to large polar angles in the coordinate system.

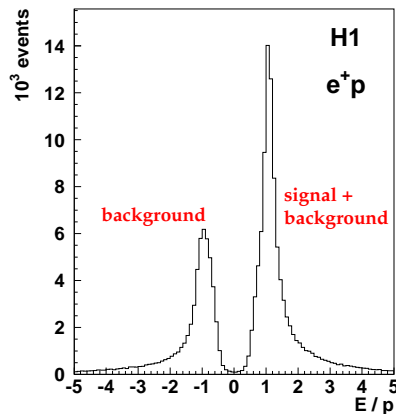


Fig. 23: Distribution of energy over momentum for tracks linked to clusters in the SpaCal with energy from 3.4 to 10 GeV that pass all the medium  $Q^2$  analysis cuts. Tracks with a negative charge are assigned a negative  $E/p$ .

events where the escaping electron carries a significant momentum. It also suppresses events with hard initial state photon radiation.

However, at low  $E'_e$  the remaining background contribution after such a selection is of a size comparable to or even exceeding the genuine DIS signal. The further analysis steps differ for the H1 and ZEUS analyses as discussed in the following.

**ZEUS Analysis Procedure** The electron candidates are selected as compact electromagnetic energy depositions in the Uranium Calorimeter (UCal). The position of the candidate is reconstructed using either the Small Angle Rear Tracking Detector (SRTD), which is a high-granularity lead-scintillator calorimeter, or with the Hadron-Electron Separator (HES), which is a silicon detector located in the electromagnetic section of the UCal. The candidates are selected such that  $E'_e > 6 \text{ GeV}$ <sup>8</sup>.

The candidates are validated using information from the tracking devices. The acceptance region for ZEUS tracking is limited to polar angles  $\theta_e \lesssim 154^\circ$ . The tracking detectors do provide some coverage beyond  $\theta_e = 154^\circ$ , up to  $\theta_e \approx 168^\circ$ , however the number of tracking layers is too sparse for full track reconstruction. The hit information from the tracking detectors can still be used. To do this, a “road” is created between the measured interaction vertex and the position of the electron candidate in the calorimeter. Hits in the tracking layers along the road are then counted and compared to the maximum possible number of hits. If too few hits are found, the candidate is assumed to be a neutral particle and it is rejected. To ensure the reliability of this method, the scattered electron is required to exit the central drift chamber at a radius  $R > 20 \text{ cm}$ . Given that  $E'_e > 6 \text{ GeV}$ , this effectively limits the maximal  $y$  to  $y < 0.8$  and the minimum  $Q^2$  achievable at low  $y$ . In the HES analysis, events are measured down to  $y = 0.2$  roughly translating to the  $Q^2$  region,  $Q^2 > 24 \text{ GeV}^2$ . No background treatment based on the charge of the candidate is performed.

<sup>8</sup>Cut of  $E'_e > 4 \text{ GeV}$  is used for the event selection, although the binning for  $F_L$  measurement is chosen such that  $E'_e > 6 \text{ GeV}$ .

The remaining  $\gamma p$  background is estimated using Monte Carlo (MC) simulations. In order to minimise the model uncertainty of the  $\gamma p$  simulation, a pure photoproduction sample is selected using an electron tagger placed close to the beam pipe about 6 meters away from the interaction point in the rear direction. It tags, with almost perfect efficiency and purity, the scattered electrons in such events which are not identified in the main detector and escape down the beam pipe. Photoproduction MC is verified against and normalised to this sample. The normalisation factor is found to be  $1 \pm 0.1$  for all data sets.

Figure 22 shows, as an example, comparisons of the 575 GeV data with simulated distributions, for the energy of the scattered electron, total  $E - p_z$ , polar angle of the scattered electron, angle of the hadronic final state and the  $z$  coordinate of the interaction vertex. A good description of the data by the simulation is observed. A similar level of agreement was found for both, HER and LER data sets.

A full set of systematic uncertainties is evaluated for the cross section measurements. The largest single contribution comes from the electron energy scale uncertainty, which is known to within  $\pm 1\%$  for  $E'_e > 10$  GeV, increasing to  $\pm 3\%$  at  $E'_e = 5$  GeV. Other significant contributions are due to the  $\pm 10\%$  uncertainty in verifying the Pythia prediction of the  $\gamma p$  cross section using the electron tagger. The systematic uncertainty due to the luminosity measurement was reduced by scaling the three cross sections relative to each other. The spread of relative normalisation factor was found to be within the expected level of uncorrelated systematic uncertainty.

**H1 Analysis Procedure** The H1 measurements of  $F_L$  are performed in separate analyses involving different detector components and thus covering different  $Q^2$  ranges. In the high- $Q^2$  analysis the electron candidate is selected as an isolated electromagnetic energy deposition in the Liquid Argon (LAr) calorimeter which covers the polar angle range  $4^\circ < \theta < 153^\circ$ . The selected cluster is further validated by a matching track reconstructed in the central tracking device (CT) with an angular acceptance of  $15^\circ < \theta < 165^\circ$ . In the medium  $Q^2$  analysis the electron candidate is selected in the backward calorimeter SpaCal covering the angular range  $153^\circ < \theta < 177.5^\circ$  and is also validated by a CT track. Lower  $Q^2$  values are expected to be accessed in the third analysis, in which the SpaCal cluster is validated by a track in the Backward Silicon Tracker reaching the highest  $\theta$ . The first measurement of  $F_L$  at medium  $Q^2$  is already published [23], and preliminary results of the combined medium-high- $Q^2$  analysis are available.

The remaining  $\gamma p$  background is subtracted on statistical basis. The method of background subtraction relies on the determination of the electric charge of the electron candidate from the curvature of the associated track.

Figure 23 shows the  $E/p$  distribution of the scattered electron candidates from  $e^+p$  interactions with the energy  $E$  measured in the SpaCal and the momentum  $p$  of the linked track determined by the CT. The good momentum resolution leads to a clear distinction between the negative and positive charge distributions. The smaller peak corresponds to tracks with negative charge and thus represents almost pure background. These tracks are termed wrong sign tracks and events with such candidates are rejected. The higher peak, due to right sign tracks, contains the genuine DIS signal superimposed on the remaining positive background. The size of the latter to first approximation equals the wrong sign background. The principal method of background

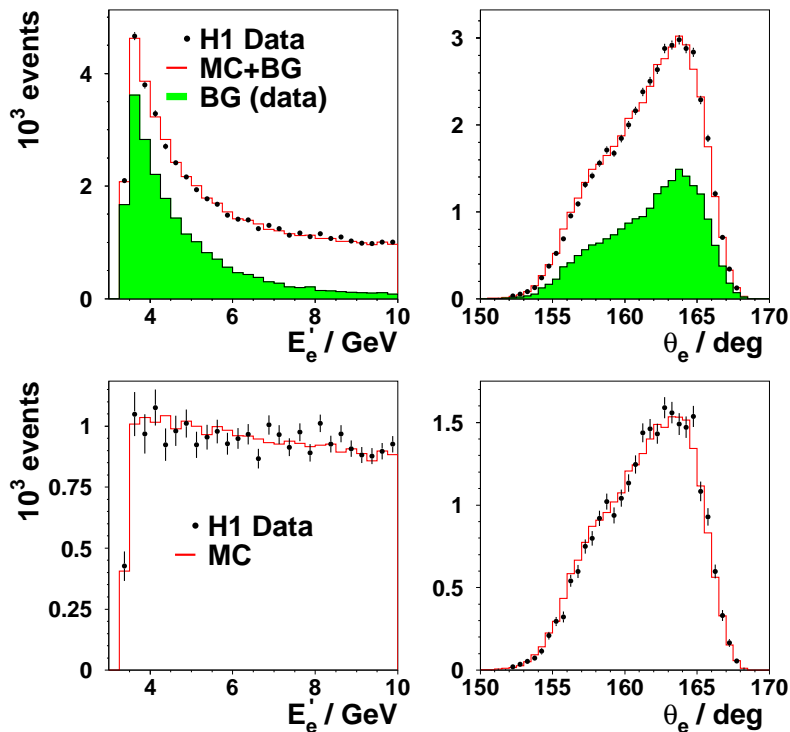


Fig. 24: Top: comparison of the correct sign data (points) with the sum (open histogram) of the DIS MC simulation and background, determined from the wrong sign data (shadowed histogram), for the energy  $E'_e$  (left) and the polar angle  $\theta_e$  (right) of the scattered electron, for the 460 GeV data with  $E'_e < 10$  GeV. Bottom: as top but after background subtraction.

subtraction, and thus of measuring the DIS cross section up to  $y \simeq 0.9$ , consists of the subtraction of the wrong sign from the right sign event distribution in each  $x, Q^2$  interval.

The background subtraction based on the charge measurement requires a correction for a small but non-negligible charge asymmetry in the negative and positive background samples, as has been observed previously by H1 [20]. The main cause for this asymmetry lies in the enhanced energy deposited by anti-protons compared to protons at low energies. The most precise measurement of the background charge asymmetry has been obtained from comparisons of samples of negative tracks in  $e^+p$  scattering with samples of positive tracks in  $e^-p$  scattering. An asymmetry ratio of negative to positive tracks of 1.06 is measured using the high statistics  $e^\pm p$  data collected by H1 in 2003-2006. This result is verified using photoproduction events with a scattered electron tagged in a subdetector of the luminosity system.

Figure 24 shows, as an example, comparisons of the 460 GeV high  $y$  data with simulated distributions, for the energy and the polar angle of the scattered electron prior to and after subtraction of the background, which is determined using wrong sign data events.

The measurement of  $F_L$  as described below relies on an accurate determination of the variation of the cross section for a given  $x$  and  $Q^2$  at different beam energies. In order to reduce

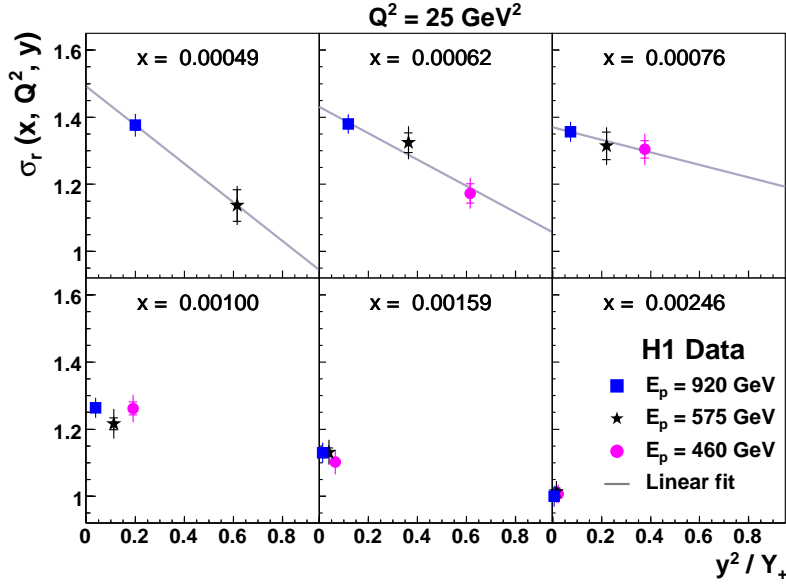


Fig. 25: The reduced inclusive DIS cross section plotted as a function of  $y^2/Y_+$  for six values of  $x$  at  $Q^2 = 25 \text{ GeV}^2$ , measured by H1 for proton beam energies of 920, 575 and 460 GeV. The inner error bars denote the statistical error, the full error bars include the systematic errors. The luminosity uncertainty is not included in the error bars. For the first three bins in  $x$ , corresponding to larger  $y$ , a straight line fit is shown, the slope of which determines  $F_L(x, Q^2)$ .

the uncertainty related to the luminosity measurement, which presently is known to 5% for each proton beam energy of the 2007 data, the three data samples are normalised relatively to each other. The renormalisation factors are determined at low  $y$ , where the cross section is determined by  $F_2$  only, apart from a small correction due to  $F_L$ . The relative normalisation is known to within 1.6%.

All correlated and uncorrelated systematic errors combined with the statistical error lead to an uncertainty on the measured cross sections at high  $y$  of 3 to 5%, excluding the common luminosity error.

## 2.4 Measurements of $F_L(x, Q^2)$ by H1 and ZEUS

The longitudinal structure function is extracted from the measurements of the reduced cross section as the slope of  $\sigma_r$  versus  $y^2/Y_+$ , as can be seen in eq. 4. This procedure is illustrated in Fig. 25. The central  $F_L$  values are determined in straight-line fits to  $\sigma_r(x, Q^2, y)$  as a function of  $y^2/Y_+$  using the statistical and uncorrelated systematic errors.

The first published H1 measurement of  $F_L(x, Q^2)$  is shown in Fig. 26, the preliminary ZEUS measurement is presented in Fig. 27. The H1 measured values of  $F_L$  are compared with the H1 PDF 2000 fit [4], while the ZEUS  $F_L$  values are compared to the ZEUS-JETS PDF fit [3]. Both measurements are consistent and show a non-zero  $F_L$ .

The H1 results were further averaged over  $x$  at fixed  $Q^2$ , as shown in the left panel of Fig. 28. The averaging is performed taking the  $x$  dependent correlations between the systematic

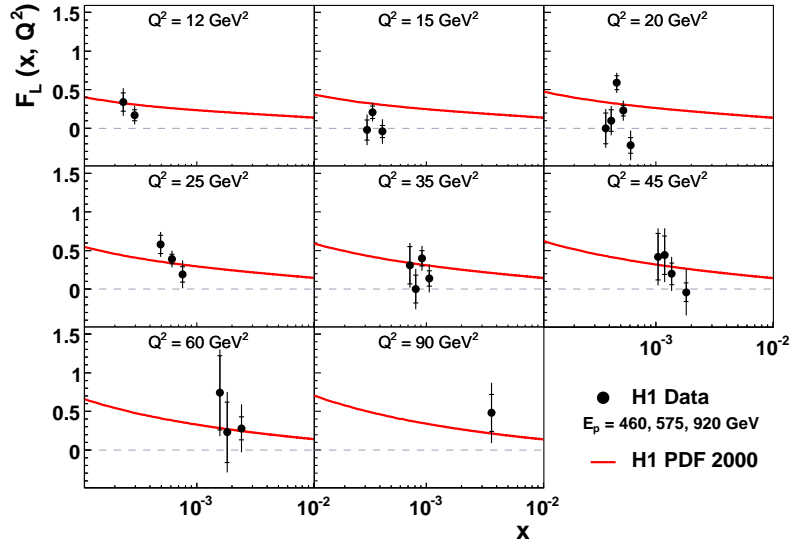


Fig. 26: The longitudinal proton structure function  $F_L(x, Q^2)$  measured by the H1 collaboration. The inner error bars denote the statistical error, the full error bars include the systematic errors. The curves represent the H1 PDF 2000 fit.

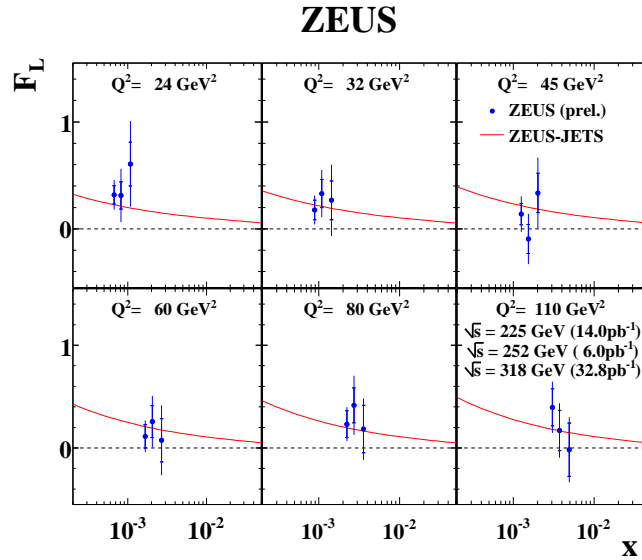


Fig. 27: The longitudinal proton structure function  $F_L(x, Q^2)$  measured by the ZEUS collaboration. The inner error bars denote the statistical error, the full error bars include the systematic errors. The curves represent the ZEUS-JETS PDF fit.

errors into account. The averaged values of  $F_L$  are compared with H1 PDF 2000 fit and with the expectations from global parton distribution fits at higher order perturbation theory performed by the MSTW [24] and the CTEQ [2, 25] groups. Within the experimental uncertainties the data are consistent with these predictions. The measurement is also consistent with previous indirect

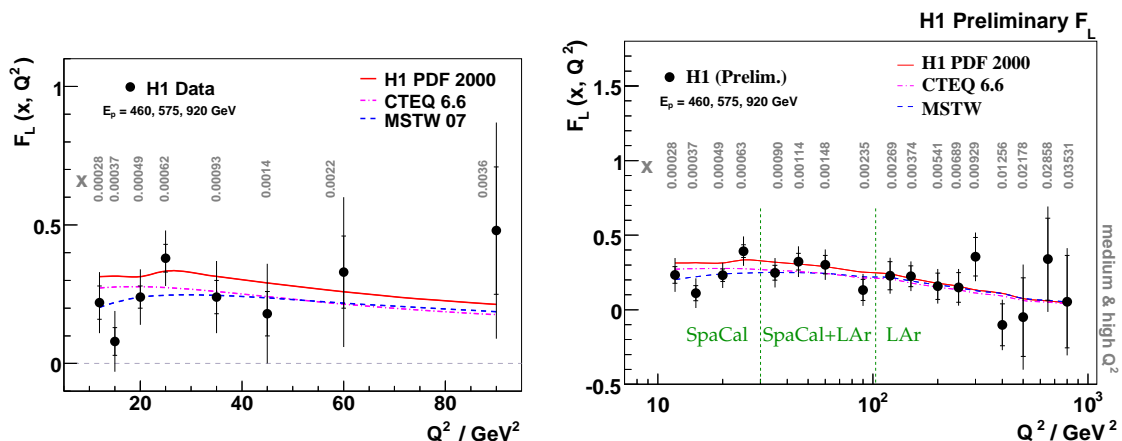


Fig. 28: The proton structure function  $F_L$  shown as a function of  $Q^2$  at the given values of  $x$ : a) first direct measurement at HERA by H1; b) preliminary H1 results combining SpaCal and LAr analyses. The inner error bars denote the statistical error, the full error bars include the systematic errors. The luminosity uncertainty is not included in the error bars. The solid curve describes the expectation on  $F_L$  from the H1 PDF 2000 fit using NLO QCD. The dashed (dashed-dotted) curve depicts the expectation of the MSTW (CTEQ) group using NNLO (NLO) QCD. The theory curves connect predictions at the given  $(x, Q^2)$  values by linear extrapolation.

determinations of  $F_L$  by H1.

In the combined medium–high  $Q^2$  analysis by H1 the  $Q^2$  range is extended up to  $Q^2 = 800 \text{ GeV}^2$ . The preliminary results are shown in the right panel of Fig. 28. In some  $Q^2$  bins there is an overlap between the SpaCal and LAr measurements which improves the precision of the  $F_L$  extraction as compared to the pure SpaCal analysis.

## 2.5 Summary

Direct measurements of the proton structure function  $F_L$  have been performed in deep inelastic  $ep$  scattering at low  $x$  at HERA. The  $F_L$  values are extracted by the H1 and ZEUS collaborations from the cross sections measured at fixed  $x$  and  $Q^2$  but different  $y$  values. This is achieved by using data sets collected with three different proton beam energies. The H1 and ZEUS results are consistent with each other and exhibit a non-zero  $F_L$ . The measurements are also consistent with the previous indirect determinations of  $F_L$  by H1. The results confirm DGLAP NLO and NNLO QCD predictions for  $F_L(x, Q^2)$ , derived from previous HERA data, which are dominated by a large gluon density at low  $x$ .

## References

- [1] A. M. et al, Eur. Phys.J C **23**, 73 (2002).
- [2] L. L. J. Pumplin, H. and K. T. W. Phys. Rev. D **75**, 054029 (2007). hep-ph/0701220.
- [3] ZEUS Collaboration, C. e. a. ZEUS Coll., S. Eur. Phys. J. C **42**, 1 (2005). hep-ph/0503274.

- [4] H1 Collaboration, C. Adloff *et al.*, Eur. Phys. J. **C30**, 1 (2003). hep-ex/0304003.
- [5] A. Cooper-Sarkar, Phys. Rev **D 67**, 012007 (2003).
- [6] ZEUS and H. Collaborations, *Combination of h1 and zeus deep inelastic  $e^+ - p$  scattering cross sections*. Preprint ZEUS-prel-07-036, H1prelim-07-007.
- [7] L. D. Yu. Sov. Phys. JETP **46**, 641 (1977).
- [8] N. G. V. and N. L. L. Sov. J. Nucl. Phys. **15**, 438 (1972).
- [9] G. Altarelli and G. Parisi, Nucl. Phys. **B 126**, 298 (1977).
- [10] M. Botje, *Qcdnum16.12*. Available from <http://www.nikhef.nl/h24/qcdnum/>.
- [11] C. Pascaud and F. Zomer, *Qcd analysis from the proton structure function  $f_2$  measurement: Issues on fitting, statistical and systematic errors*. Preprint LAL-95-05, 1995.
- [12] Particle Data Group Collaboration, C. Amsler *et al.*, Phys. Lett. **B667**, 1 (2008).
- [13] M. Dittmar *et al.*, *Parton distributions: Summary report for the HERA - LHC workshop*. Preprint hep-ph/0511119, 2005.
- [14] C. Callan and D. Gross, Phys. Rev. Lett. **22**, 156 (1969).
- [15] F. W. A. Zee and B. T. S. Phys. Rev. **D 10**, 2881 (1974);  
G. Altarelli and G. Martinelli, Phys. Lett. **B 76**, 89 (1978).
- [16] N. G. V. and N. L. L. Sov. J. Nucl. Phys. **15**, 675 (1972).
- [17] N. L. L. Sov. J. Nucl. Phys. **20**, 94 (1975).
- [18] S. C. e. a. ZEUS Coll., in *EPS 2003 conference, Aachen*. 2003.
- [19] H1 Collaboration, C. A. e. a. H1 Coll., Phys. Lett. **B 393**, 452 (1997).  
hep-ex/9611017.
- [20] H1 Collaboration, C. Adloff *et al.*, Eur. Phys. J. **C21**, 33 (2001). hep-ex/0012053.
- [21] A. V. Trevino, *Measurement of the Inclusive  $ep$  Scattering Cross Section at low  $Q^2$  and  $x$  at HERA*, in *Proceedings of the 15th International Workshop on Deep-Inelastic Scattering*. 2007.
- [22] T. Lastovicka, Eur. Phys. J. **C 24**, 529 (2002). hep-ph/0203260.
- [23] H1 Collaboration, D. A. e. a. H1 Coll., F. Phys. Lett. **B 665**, 139 (2008). 0805.2809.
- [24] W. J. S. R. S. T. A. D. Martin and G. Watt, Phys. Lett. **B 652**, 292 (2007).  
hep-ph/0706.0459.
- [25] P. M. Nadolsky *et al.*, Phys. Rev. **D78**, 013004 (2008). 0802.0007.



# Proton - proton luminosity, standard candles and PDFs at the LHC

*J. Anderson, M. Boonekamp, H. Burkhardt, M. Dittmar, V. Halyo, T. Petersen*

## 1 Introduction

The Large Hadron Collider (LHC) is expected to start colliding proton beams in 2009, and is expected to reach design parameters in energy and luminosity sometime later and deliver a few  $fb^{-1}$  per year of data at the 14 TeV collision energy.

During the past 15 years many theoretical calculations and experimental simulations have demonstrated a huge potential to perform many accurate tests of the Standard Model (SM) with LHC data, which could yield insight into new physics mechanisms.

To make these tests, the experiments identify a particular signature  $X$  and observe, using a variety of selection criteria, a certain number of events in a given data taking period. After correcting this event rate for backgrounds and the selection efficiency, the number is converted into a cross section. The cross section,  $\sigma_{pp \rightarrow X}$  can be compared with theoretical predictions<sup>1</sup> according to the formula:  $N_{corrected} = \sigma_{pp \rightarrow X} \times L_{pp}$  where  $L_{pp}$  is the recorded proton proton luminosity.

Besides the statistical errors of a measurement, the systematic error is related to the uncertainties from the  $L_{pp}$  determination, the background and efficiency corrections within the detector acceptance and from extrapolations into the uncovered very forward rapidity regions. The interpretation of an observed cross section within the SM requires further the knowledge of the theoretical cross section. Thus the uncertainties of the proton parton distribution function (PDF) have to be considered also.

In this Section we describe the status and perspectives of the ATLAS, CMS and LHCb, the three LHC pp collision detectors [1], to determine the proton proton luminosity normalization. The investigated methods are known and studied since many years and can be separated into the absolute (1) direct and (2) indirect proton proton luminosity determination. A third approach (3) tries to measure and calculate final states only relative to well understood reactions which depend on the parton-parton luminosity and are as such largely independent of the knowledge of the pp luminosity.

- Absolute, direct or indirect, proton proton luminosity normalization: If the absolute approach is used, the interpretations of a measured reaction cross section depends still on the knowledge of parton distribution function (PDF), which must be obtained from other experiments. Examples are:

---

<sup>1</sup>Alternatively, one can also apply a Monte Carlo simulation to the theoretical prediction and compare the number of background corrected events directly.

- The proton proton luminosity normalization is based on the measurements of the beam currents and shapes. While the beam currents can be accurately determined using beam transformers, the beam profiles are more difficult to determine directly and usually constitute the dominant source of uncertainty on a luminosity measurement using this technique. The use of the machine luminosity determination using beam parameter measurements [2] and [3] will be described in Section 3.1. Alternatively one can try to measure the beam profiles also within the experiments using the precision vertex detectors. A short description of this idea, currently pursued within the LHCb collaboration, is also given in Section 3.1.
  - The simultaneous measurements of a pair of cross sections that are connected with each other quadratically via the optical theorem. A well known example of this is the measurement of the total inelastic cross section and the elastic cross section at very high pseudorapidities  $|\eta| \approx 9$  and will be described in Section 3.3. So called instantaneous or real time luminosity measurements are based on “stable” high rate measurements of particular final state reactions. Once the ratio of such reactions to the pp luminosity determination has been measured, those reactions can be subsequently used as independent luminosity monitors. Some possibilities are discussed in Section 3.4.
  - The indirect absolute proton proton luminosity normalization is based on the theoretically well understood “two photon” reaction  $pp \rightarrow pp\mu\mu$  [4, 5] (Section 3.5). This reaction could perhaps be considered as the equivalent of the luminosity counting in  $e^+e^-$  experiments using forward Bhabha scattering.
- Indirect pp luminosity measurements use final states, so called “standard candles”, with well known theoretical cross sections (Section 4). Obviously, the resulting proton proton luminosity can only be as good as the theoretical and experimental knowledge of the “standard candle” reaction. The theoretically and experimentally best understood LHC reactions are the inclusive production of W and Z bosons with subsequent leptonic decays. Their large cross section combined with experimentally well defined final states, e.g. almost background free Z and W event samples can be selected over a relative large rapidity range, makes them the preferred LHC “standard candle” reaction. Other interesting candidates are the high  $p_t$  jet - boson ( $= \gamma, W$  or  $Z$ ) final states. The indirect luminosity method requires also some knowledge of the PDFs, and of course, if one follows this approach, the cross section of the “standard candle” reaction becomes an input and can not be measured anymore. Thus, only well understood reactions should be considered as candidate reactions.
  - pp luminosity independent relative rate measurements using “standard candle” reactions. In addition to the above indirect pp luminosity determinations, “standard candle” reactions allow to perform luminosity independent relative event rate calculations and measurements. This approach has already been used successfully in the past and more details were discussed during the past HERA-LHC workshop meetings [6]. For some reactions, this approach appears to be much easier and more accurate than standard cross section measurements and their interpretations. Perhaps the best known example at hadron colliders is the measurement and its interpretation of the production ratio for Z and W events,

where Tevatron experiments have reached accuracies of about 1-2% [7, 8]. Another example is related to relative branching ratio and lifetime measurements as used for b-flavored hadrons.

Furthermore the rapidity distributions of leptonic W and Z decays at the LHC are very sensitive to the PDF parameterization and, as was pointed out 10 years ago [9], one can use these reactions to determine the parton luminosity directly and very accurately over a large  $x$  (= parton momentum/proton momentum) range. In fact, W and Z production with low transverse momentum were found in this analysis to be very sensitive to  $q\bar{q}$  luminosities, and the jet-boson final states, e.g. the jet- $\gamma$ , Z, W final states at high transverse momentum are sensitive to the gluon luminosity.

In the following we attempt to describe the preparations and the status of the different luminosity measurements and their expected accuracies within ATLAS, CMS and LHCb. Obviously, all these direct and indirect methods should and will be pursued. In Section 5 we compare the advantages and disadvantages of the different methods. Even though some methods look more interesting and rewarding than others, it should be clear from the beginning that as many independent pp luminosity determinations as possible need to be performed by the experiments.

We also try to quantify the systematic accuracies which might be achieved over the next few years. As these errors depend somewhat on the overall achieved luminosity, we need in addition a hypothetical working scenario for the first 4 LHC years. We thus assume that during the first year, hopefully 2009, data at different center of mass energies can be collected by ATLAS and CMS. During the following three physics years we expect that 10 TeV will be the highest collision energy in year I and that at most  $100 \text{ pb}^{-1}$  can be collected. We assume further that during the following two years the design energy of 14 TeV can be achieved and that a luminosity of about  $1 \text{ fb}^{-1}$  and  $10 \text{ fb}^{-1}$  can be collected respectively per year. During the first few years similar numbers are expected for the LHCb experiment. However once the LHC reaches the first and second phase design luminosity of  $10^{33}/\text{cm}^2/\text{sec}$  and  $10^{34}/\text{cm}^2/\text{sec}$  it is expected that the LHCb experiment will run at an average luminosity of  $2 \times 10^{32}/\text{cm}^2/\text{sec}$  (resulting in about  $2 \text{ fb}^{-1}/\text{per year}$ ).

## 2 Luminosity relevant design of ATLAS/CMS and LHCb

In the following we give a short description of the expected performance with respect to lepton and jet identification capabilities. Especially the electron and muon measurement capabilities are important for the identification of events with leptonic decays of W and Z bosons.

Both ATLAS and CMS are large so called omni purpose experiments with a large acceptance and precision measurement capabilities for high  $p_t$  electrons, muons and photons. Currently, the simulations of both experiments show very similar performance for a large variety of LHC physics reactions with and without jets. For the purpose of this Section we focus on the possibility to identify the production of inclusive W and Z decays with subsequent decays to electrons and muons. Both experiments expect excellent trigger accuracies for isolated leptons and it is expected that electrons and muons with momenta above 20-25 GeV can be triggered with high efficiency and up to  $|\eta|$  of about 2.5. The special design of the ATLAS forward muon spectrometer should allow to detect muons with good accuracy even up to  $|\eta|$  of 2.7.

The operation of ALFA, a very far forward detector placed about 240 m down the beam line, is envisaged by the ATLAS collaboration to provide an absolute luminosity measurement, either using special optics LHC running and the use of the optical theorem or using the total cross section measurement from the dedicated TOTEM experiment installed near CMS; results from this device can be expected from 2010 and on-wards. In addition to absolute luminosity measurements from ALFA the two detectors LUCID and the Zero-Degree-Calorimeter (CDC) [10] are sensitive to the relative luminosity at time scales of single bunch crossings.

A similar approach for absolute and relative luminosity measurements is foreseen by the CMS experiment. Here it is planned that dedicated forward detectors, the Hadron Forward Calorimeter (HF) and the ZDC device provide similar results as the ones in ATLAS.

Another technique that is expected to be available early on is a luminosity-independent measurement of the  $pp$  total cross section. This will be done using a forward detector built by the TOTEM experiment [11].

The LHCb experiment [12] has been designed to search for New Physics at the LHC through precision measurements of CP violating observables and the study of rare decays in the b-quark sector. Since the  $b\bar{b}$  pairs resulting from the proton-proton collisions at the LHC will both be produced at small polar angles and in the same forward or backward cone, LHCb has been designed as a single-arm forward spectrometer covering the pseudo rapidity range  $1.9 < \eta < 4.9$ . The LHCb tracking system, which is composed of a silicon vertex detector, a warm dipole magnet and four planar tracking stations, will provide a momentum resolution of  $\delta P/P = (0.3 + 0.0014P/GeV)\%$  [13]. Muon identification is primarily achieved using a set of five planar multi-wire proportional chambers, one placed in front of the calorimeter system and four behind, and it is expected that for the momenta range 3-150 GeV/c an identification efficiency of  $\sim 98\%$  and an associated pion dis-identification rate of  $\sim 1\%$  will be achieved. The reconstruction of primary and secondary vertices, a task of crucial importance at b physics experiments, will be virtually impossible in the high particle multiplicity environment present with the nominal LHC running luminosity of  $10^{34} cm^{-2} s^{-1}$  - LHCb has therefore been designed to run at the lower luminosity of  $2 \times 10^{32} cm^{-2} s^{-1}$ .

Recent LHCb simulations have shown that leptonic W and Z decays to muons can be identified with a small background in the forward and very forward rapidity region starting from  $\eta$  of 1.9 and up to values larger than 4. As will be discussed later in more detail, the common muon acceptance region for the three LHC experiments between 1.9 and about 2.5 will allow to cross check and normalize the W and Z measurements in this region. Consequently the unique large rapidity from 2.5 to 4.9 can be used by LHCb to investigate the very low x range of the PDFs for the first time.

The absolute luminosity at LHCb will be obtained either directly, by making measurements of the beam parameters, or indirectly via a measurement of the event rate of an accurately predicted physics process.

As will be explained in the following Sections, all experiments will try to perform as many as possible direct and indirect absolute and relative luminosity measurements and will, if available, at least during the first years, also use luminosity numbers from the machine group.

## 2.1 Lepton triggering and W/Z identification.

Generally, the lepton trigger selections depend on the instantaneous luminosity and some pre-scaling might eventually be needed. However, current simulations by all experiments show that the envisaged  $|\eta|$  and  $p_T$  thresholds will not limit the measurement accuracies of leptons originating from W and Z decays.

The lepton trigger selections that are generally perceived to be used for most W and Z related analysis are very similar in ATLAS and CMS as indicated in Table 1.

Experiment	Trigger selection $e$		Trigger selection $\mu$	
	$p_T$	$ \eta $	$p_T$	$ \eta $
ATLAS	25 GeV	2.5	20 GeV	2.7
CMS	20 GeV	2.5	20 GeV	2.1
LHCb*	–	–	2.5 GeV	1.9-4.9

Table 1: For ATLAS and CMS the lepton trigger/selection  $p_T$  thresholds are given for single isolated leptons. \*For the LHCb threshold is given for the muon pair mass instead of single muons and only positive values of  $\eta$  are covered.

Trigger and reconstruction efficiencies for leptonic W and Z decays within the acceptance of the detectors have been estimated for ATLAS to be 97.7% and 80.0% for electrons and 84.3% and 95.1% for muons, respectively. The reconstruction efficiency includes the trigger efficiencies and the off-line electron and muon selections used later to identify clean inclusive W and Z event samples [14].

The current equivalent trigger and off-line efficiencies for CMS are about 85% and 77% for electrons and combined about 85% for single muons [15]. Similar efficiency numbers for muons from W and Z decays are expected within the LHCb acceptance region [16]. Current simulations show that these numbers can be determined with high accuracies, reaching perhaps 1% or better, at least for isolated leptons<sup>2</sup> which have a transverse momentum some GeV above the trigger thresholds. For lower momenta near the thresholds or for additional special trigger conditions somewhat larger systematic uncertainties can be expected.

## 3 Direct and indirect absolute pp luminosity measurements

Three different absolute proton proton luminosity measurements are discussed in this Section. (1) The machine luminosity determination using beam parameter measurements [17], (2) the luminosity independent total pp cross section measurement combined with the measurement of the elastic pp scattering rate [11] and (3) the measurement of the “two photon” reaction  $pp \rightarrow pp\mu\mu$  [4, 5]. As will be discussed in more detail in Section 5, only method (3) can be performed during the normal collision data taking. For method (1) some special methods, which take the actual detector performance during each run into account, need to be developed. Method 2 uses a two phase approach (a) a special machine optics run with low luminosity to determine the total

<sup>2</sup>As isolated high  $p_T$  photons are triggered essentially like electrons similar accuracies for both particle types can be assumed.

cross section and (b) a normalization to some high rate final state reactions which can be counted during normal physics runs.

### 3.1 Proton-proton luminosity from machine parameters<sup>3</sup>

The luminosity for colliding beams can be directly obtained from geometry and numbers of particles flowing per time unit [2]. This can be used to determine the absolute LHC luminosity from machine parameters without prior knowledge of pp scattering cross sections. The principle is briefly outlined here. More details can be found in [3].

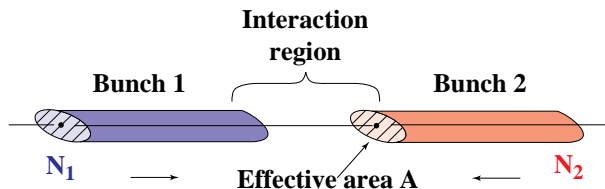


Fig. 1: Luminosity from particles flux and geometry.

For two bunches of  $N_1$  and  $N_2$  particles colliding head-on in an interaction region as sketched in Fig.1 with the frequency  $f$  the luminosity is given as

$$\mathcal{L} = \frac{N_1 N_2 f}{A_{\text{eff}}} . \quad (1)$$

$A_{\text{eff}}$  is the *effective transverse area* in which the collisions take place. For a uniform transverse particle distribution,  $A_{\text{eff}}$  would be directly equal to the transverse beam cross section. More generally, the effective area can be calculated from the overlap integral of the two transverse beam distributions  $g_1(x, y)$ ,  $g_2(x, y)$  according to

$$\frac{1}{A_{\text{eff}}} = \int g_1(x, y) g_2(x, y) dx dy . \quad (2)$$

For equal Gaussian beams

$$g_1 = g_2 = \frac{1}{2\pi\sigma_x\sigma_y} \exp \left[ -\frac{x^2}{2\sigma_x^2} - \frac{y^2}{2\sigma_y^2} \right] \quad (3)$$

we obtain for head-on collisions  $A_{\text{eff}} = 4\pi\sigma_x\sigma_y$  so that

$$\mathcal{L} = \frac{N_1 N_2 f}{4\pi\sigma_x\sigma_y} . \quad (4)$$

The collision frequency  $f$  is accurately known. The number of particles circulating in a storage ring is measured using beam current transformers to roughly 1% precision [17].

The main uncertainty in the absolute luminosity determination from machine parameters is expected to originate in the knowledge of the transverse beam dimensions. Safe operation

---

<sup>3</sup>Contributing author: H. Burkhardt

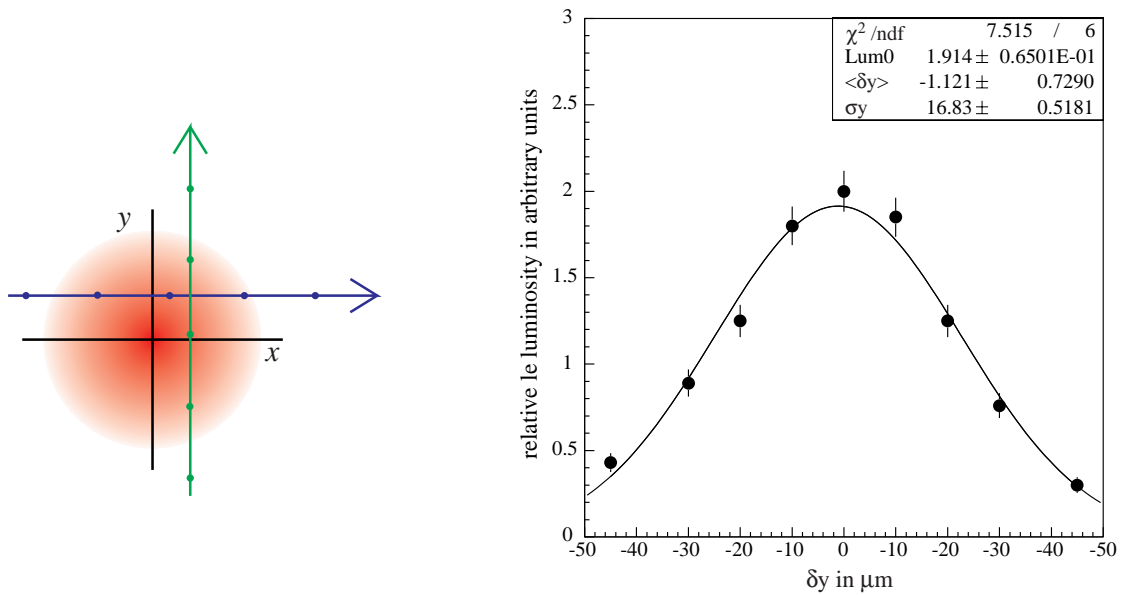


Fig. 2: Schematic view of the steps involved in an orthogonal separation scan proposed for the LHC (left) and a possible result in one direction (based on early LEP data) shown on the right.

of the LHC requires a rather good knowledge of the optics and beam sizes and we expect that this should already allow a determination of the luminosity from machine parameters to about 20 – 30 percent. A much better accuracy can be obtained when the size of the overlap region at the interaction points is determined by measuring the relative luminosity as a function of lateral beam separation, as illustrated in Fig. 2. This technique was pioneered at the ISR [18] and allowed to reduce the uncertainty to below 1%, [19, 20].

For the more complicated LHC and early operation, a 10% overall uncertainty in the absolute LHC machine luminosity calibration should be a realistic goal. The actual precision will depend on the running time and effort which is invested. A relatively small number of scans under favorable beam conditions will in principle be sufficient to obtain and verify the reproducibility in the absolute luminosity calibration. While fast scans may always be useful to optimize collisions, we assume that any dedicated, detailed luminosity scans will become obsolete when the other, cross section based luminosity determinations described in these proceedings allow for smaller uncertainties.

Optimal running conditions are moderate bunch intensities, large bunch spacings, no crossing angle and  $\beta^* = 2$  m or larger. These conditions are in fact what is proposed anyway for the initial LHC operation with 43 – 156 bunches per beam. Statistics are not expected to be a problem. For early operation at top energy (10 - 14 TeV) with 43 bunches and  $4 \times 10^{10}$  particles per bunch, before beams are squeezed. at a  $\beta^* = 11$  m, we already expect luminosities of the order of  $10^{30} \text{ cm}^{-2}\text{s}^{-1}$  resulting in event rates of  $10^4$  Hz, for a cross section of 0.01 barn as typical for the low angle luminosity monitors.

From the LHC injectors, we expect bunch by bunch variations of about 10% in intensity and 20% in emittance. For the large spacing between bunches in the operation with up to 156



bunches, there is no need for crossing angles at the interaction points. Parasitic beam-beam effects will be negligible. All bunches in each beam will follow the same equilibrium orbit and collide at the same central position.

Calibration runs require good running conditions and in particular good beam lifetimes. Bunch by bunch differences are not expected to change significantly during a scan. Storing bunch intensities at the beginning and end of a scan and using one set of timed averaged bunch intensities for a scan should be sufficient. To avoid any bias, it will be important to use the correct pairing of bunch intensities and relative luminosities in the calculation of absolute bunch luminosities according to Eq. 1, before any summing or averaging over different bunches.

We are currently preparing an on-line application for automatic luminosity scans<sup>4</sup>. Scan parameters like range, step size and duration can be set before the start of the scan. Once the parameters are defined, it is possible to launch automatic horizontal and vertical separation scans in the LHC interactions regions. For a detailed scan, we may choose a range from  $-4$  to  $+4 \sigma$  in nominal beam size in steps of  $0.5 \sigma$ , resulting in 17 equidistant points. If we wait 1 s between points to allow for the magnets to change and for 2 s integration time, the scan time would still be below a minute per plane. Details are currently being worked out in close collaboration with the experiments. Exchanging all data bunch-by-bunch at a 1 Hz rate between the machine control room (CCC) and the experiments would be rather demanding and risks to saturate current capacities.

For the initial running, it will be sufficient to exchange average values at about 1 Hz rate. It allows quality monitoring and the determination of the peak position. For the detailed off line analysis, we only have to rely on local logging and timing information synchronized to at least 1 s precision at the beginning of the scan. With fixed time interval defined and saved before the scan, this allows for off-line synchronization of the detailed data and a complete bunch by bunch analysis.

### 3.2 Direct measurements of the absolute luminosity at LHCb

LHCb plans to measure the absolute luminosity using both the Van Der Meer scan, [18], and beam-gas techniques following a more recently proposed method [21]. Here one tries to determine the transverse beam profiles at colliding beam experiments utilizing the precision vertex detectors found at modern HEP experiments to reconstruct beam gas interactions near the beams crossing point. The vertex resolution in the transverse direction at LHCb can be parameterized by the relation

$$\sigma_{x,y} = \frac{100\mu m}{\sqrt{N_{tracks}}} \quad (5)$$

where  $N_{tracks}$  is the number of tracks originating from the vertex. Since the nominal transverse bunch size at LHCb will be  $100\mu m$ , the reconstruction of beam-gas vertices's, which will have a track multiplicity of  $\sim 10$ , will enable the measurement of the colliding bunch profiles and the beam overlap integral. This method is currently under investigation by the LHCb collaboration and is expected to result in a luminosity measurement with an associated uncertainty of 3-5%.

---

<sup>4</sup>Done by Simon White, as part of his PhD thesis work on the LHC machine luminosity determination



### 3.3 Absolute pp luminosity from specialized detectors and from the total cross section measurement

ATLAS and CMS are planning to perform absolute and relative pp luminosity measurements using dedicated luminosity instruments.

Three particular luminosity instruments will operate around the ATLAS interaction point. The absolute luminosity measurement will be provided by ALFA [10] placed 240m down the beam line and due to operate in 2010. This measurement requires some special optics low luminosity running of the LHC and should be able to measure the very low angle Coulomb scattering reaction. The expected precision is of the order 3%, depending on yet unknown LHC parameters during running. The ALFA detector can also measure the absolute luminosity using the optical theorem if the Coulomb region can not be reached. Extrapolating the elastic cross section to very low momentum transfer  $t = 0$  and using the total cross section as measured by TOTEM [11] (located at the CMS interaction point) current simulations indicate that a precision of about 3% might also be reached with this method. In addition to absolute luminosity measurements from ALFA, LUCID and a Zero-Degree-Calorimeter (ZDC) [10] are sensitive to the relative single bunch crossings luminosity. LUCID and ZDC will however not give absolute measurements.

A similar approach is currently foreseen by the CMS collaboration [22].

### 3.4 Real time relative luminosity measurements

A large number of instantaneous relative luminosity measurements have been discussed during the past years by ATLAS, CMS and LHCb and more details can be found in the three presentations given during the “standard candle” session of this workshop [23]. As an example we outline in the following some ideas discussed within CMS.

Multiple techniques capable of providing suitable luminosity information in real time have been identified in CMS. One technique employs signals from the forward hadron calorimeter (HF) while another, called the Pixel Luminosity Telescope (PLT), uses a set of purpose-built particle tracking telescopes based on single-crystal diamond pixel detectors. At this writing, the PLT has not been formally approved, but is under study. The methods based on signals from the HF described are the ones being most vigorously pursued.

Two methods for extracting a real-time relative instantaneous luminosity with the HF have been studied. The first method is based on “zero counting,” in which the average fraction of empty towers is used to infer the mean number of interactions per bunch crossing. The second method called “EtSum method” exploits the linear relationship between the average transverse energy per tower and the luminosity.

Outputs of the QIE chips used to digitize the signals from the HF PMTs on a bunch-by-bunch basis are routed to a set of 36 HCAL Trigger and Readout (HTR) boards, each of which services 24 HF physical channels. In order to derive a luminosity signal from the HTR, an additional mezzanine board called the HF luminosity transmitter (HLX) is mounted on each of the HTR boards. The HLX collects channel occupancy and  $E_T$  sum data to create eight histograms: two sets of three occupancy histograms, one  $E_T$ -sum histogram, and one additional occupancy histogram. These histograms comprise about 70 KB of data, which is transmitted at a rate of approximately 1.6 Mbps to a dedicated luminosity server via an Ethernet switch that

aggregates the data from multiple HLX boards for further processing.

Although all HF channels can be read by the HLX, MC studies indicate that the best linearity is obtained using only the inner four  $\eta$  rings. The algorithm has been optimized to minimize sensitivity to pedestal drifts, gain changes and other related effects. Both “Zero Counting” and the “EtSum” method have demonstrated linearity up to LHC design luminosity. A statistical error of about 1% will be achieved at  $\text{fewtimes} \times 10^{31} \text{cm}^{-2} \text{s}^{-1}$ . Hence the dominant error on the absolute luminosity will result from the normalization of the online relative luminosity.

### 3.5 Proton-proton luminosity from the reaction $pp \rightarrow pp\mu\mu$

The QED process  $pp \rightarrow pp\mu^+\mu^-$ , where a  $\mu^+\mu^-$  pair is produced via photon-photon scattering, was first proposed for luminosity measurements at hadron colliders in [4]. At the LHC such pairs will be predominantly produced with small transverse momenta, at small polar angles and in the same forward or backward cone.

All three experiments are considering to use the well calculated  $pp \rightarrow pp\mu\mu$  process for measuring absolute luminosity. The theoretical understanding of this QED photon-photon scattering reactions is considered to be accurate to better than 1%. Consequently this final state is thus often considered to be the perfect theoretical luminosity process. However, the experimental identification of this process requires to select muon pairs with low mass and within a well understood acceptance. The measurement of this reaction at a hadron collider appears to be much more difficult than the corresponding measurements of the reaction  $ee \rightarrow ee\mu\mu$  at LEP. The systematic measurement error for example in L3 and after several years of data taking was about  $\pm 3\%$  [24]

Current simulations by the three LHC experiments indicate that the final state can be identified using straight forward criteria. For ATLAS and CMS one finds that about 1000 accepted events could at best be expected for an integrated luminosity of  $1 \text{ fb}^{-1}$ , resulting in a statistical error of about  $\pm 3\%$ .

For example the ATLAS study selects oppositely charged back-to-back muon tracks with  $p_T > 6 \text{ GeV}$  and  $|\eta| < 2.2$  with an invariant mass less than  $60 \text{ GeV}$  and a common vertex with no other tracks originating from it (isolation), yields a cross section of  $1.33 \text{ pb}$ . Thus, about 1300 events can be expected for running periods with a luminosity of  $1 \text{ fb}^{-1}$  and yielding a potential statistical error of 3%. However, backgrounds not only from pile up events will be a critical issue. Some proton tagging with high luminosity roman pots is currently investigated but this will certainly reduce the accepted cross section and introduce additional acceptance errors. Similar conclusions have been reached by simulations performed within the CMS collaboration. Consequently, both experiments expect that, during the coming years, this reaction will be mainly used as a cross check of the other methods.

The cross section for this process where both muons lie inside the LHCb acceptance and have a combined invariant mass greater than  $2.5 \text{ GeV}$  is  $\approx 88 \text{ pb}$ . The expected uncertainty is perhaps 1% or smaller and comes mainly from rescattering corrections [5], i.e. strong interactions between the interacting protons.

The feasibility of using the elastic two photon process  $pp \rightarrow p + \mu^+\mu^- + p$  to make luminosity measurements at LHCb was first explored in [25] and has recently been investigated in

more detail by members of the LHCb collaboration [26]. A variety of background processes have been studied: dimuons produced via inelastic two-photon fusion and double pomeron exchange; low mass Drell-Yan pairs; QCD processes such as  $b\bar{b} \rightarrow \mu^+\mu^- + X$ ; and the combinatoric backgrounds caused by  $K/\pi$  mis-identification. A simple offline selection has been developed that requires: the dimuon pair transverse momentum to be less than 50 MeV/c; the dimuon invariant mass to be in the range  $2.5 \text{ GeV}/c^2 < M_{\mu\mu} < 20 \text{ GeV}/c^2$ ; and a charged particle multiplicity of less than 3 (i.e. the event should contain a  $\mu^+\mu^-$  pair and no other charged particles). These criteria select  $\sim 27\%$  of the signal events that pass the trigger and are reconstructed and result in a background contamination that is  $(4.1 \pm 0.5(\text{stat.}) \pm 1.0(\text{syst.}))\%$  of the signal level with the dominant contribution due  $K/\pi$  mis-identification. Overall it is expected that  $\sim 10^4$   $pp \rightarrow p + \mu^+\mu^- + p$  events will be triggered, reconstructed and selected at LHCb during one nominal year of data taking ( $2 \text{ fb}^{-1}$ ). Systematic uncertainties on a luminosity measurement at LHCb using this channel are estimated to be  $\sim 1.31\%$  and are dominated by the uncertainty on the predicted cross section for events containing dimuons produced via double pomeron exchange, an uncertainty that is expected to be reduced in the near future. A measurement of the absolute luminosity at LHCb using this channel and a dataset of  $2 \text{ fb}^{-1}$  will therefore be possible with an associated uncertainty of  $\sim 1.5\%$ .

In summary, the accurate measurement of this theoretically well understood reaction looks like an interesting challenge for the LHC experiments. Interesting results can be expected once integrated luminosities of  $5 \text{ fb}^{-1}$  and more can be accumulated for ATLAS and CMS and about  $1 \text{ fb}^{-1}$  for LHCb. Of course, it remains to be proven, if the systematic uncertainties under real data taking conditions can indeed be reduced to the interesting 1% level.

#### 4 Indirect and relative pp luminosity measurements

The methods to measure the absolute proton proton luminosity and their limitations have been described in the previous chapter.

In this Section we will describe the possibilities to measure the luminosity indirectly using well defined processes, so called “Standard Candles” and their use to further constrain the PDFs and discuss the possibility to “measure” directly the parton-parton luminosities.

Before describing the details of these indirect approaches, a qualitative comparison of luminosity measurements at  $e^+e^-$  colliders and hadron colliders might be useful. The most important difference appears to be that in the  $e^+e^-$  case one studies point like parton parton interactions. In contrast, at hadron hadron interactions one studies the collision of protons and other hadrons made of quarks and gluons. As a result, in one case the Bhabha elastic scattering reaction  $e^+e^- \rightarrow e^+e^-$  at low  $Q^2$  reaction can be calculated to high accuracy and the observed rate can be used as a luminosity normalization tool. In contrast, the elastic proton proton scattering cross section can not be calculated at the LHC nor at any other hadron colliders. As a consequence, absolute normalization procedures depend always on the measurement accuracy of the pp total cross section. Even though it is in principle possible to determine the pp total cross section in a luminosity independent way using special forward detectors like planned by the TOTEM or the ALFA experiments, the accuracy will be limited ultimately and after a few years of LHC operation to perhaps a few %.

Furthermore, as essentially all interesting high  $Q^2$  LHC reactions are parton parton collisions, the majority of experimental results and their interpretation require the knowledge of parton distribution functions and thus the parton luminosities.

Following this reasoning, more than 10 years ago, the inclusive production of W and Z bosons with subsequent leptonic decays has been proposed as the ultimate precision parton parton luminosity monitor at the LHC [9]. The following points summarize the arguments why W and Z production are indeed the ideal “Standard Candles” at the LHC.

- The electroweak couplings of W and Z bosons to quarks and leptons are known from the LEP measurements to accuracies smaller than 1% and the large cross section of leptonic decays W and Z bosons allows that these final states can be identified over a large rapidity range with large essentially background free samples.
- Systematic, efficiency corrected counting accuracies within the detector acceptance of 1% or better might be envisioned during the early LHC running. In fact it is believed that the relative production rate of W and Z can be measured within the detector acceptance with accuracies well below 1%.
- Theoretical calculations for the W and Z resonance production are the most advanced and accurately known LHC processes. Other potentially more interesting LHC reactions, like various diboson pair production final states are expected to have always larger, either statistical or systematic, experimental and theoretical uncertainties than the W and Z production.
- The current PDF accuracies, using the latest results from HERA and other experiments demonstrate that the knowledge of the quark and anti quark accuracies are already allowing to predict the W and Z cross at 14 TeV center of mass energies to perhaps 5% or better. The measurable rapidity and  $p_t$  distributions of the Z boson and the corresponding ones for the charged leptons from W decays can be used to improve the corresponding parton luminosity functions.

Obviously, the use of W and Z bosons as a luminosity tool requires that the absolute cross section becomes an input, thus it can not be measured anymore. As a result this method has been criticized as being “a quick hack at best”. In contrast, advocates of this method point out that this would not be a noticeable loss for the LHC physics program.

#### 4.1 Using the reaction $pp \rightarrow Z \rightarrow \ell^+ \ell^-$ to measure $L_{pp}$

Very similar and straight forward selection criteria for the identification of leptonic Z decays, depending somewhat on the detector details and the acceptance region, are applied by ATLAS, CMS and LHCb. In the following the current selection strategy in ATLAS and LHCb are described.

#### 4.2 Measuring Z and W production, experimental approaches in ATLAS

The ATLAS W and Z cross section measurements are based on the following selections in the electron and muon channels:

- A typical selection of  $W \rightarrow e\nu$  requires that events with “good” electrons have to fulfill the additional kinematic acceptance criteria:

$p_T > 25 \text{ GeV}$ ,  $|\eta| < 1.37$  or  $1.52 < |\eta| < 2.4$ .

The criteria for  $W \rightarrow \mu\nu$  muons are similar where  $p_T > 25 \text{ GeV}$  and  $|\eta| < 2.5$  is required. Furthermore, in order to classify the event as a  $W$  event, the reconstructed missing transverse momentum and the transverse mass should fulfill  $E_T(\text{miss}) > 25 \text{ GeV}$  and  $m_T(W) > 40 \text{ GeV}$ .

- The selection of  $Z \rightarrow ee$  and  $Z \rightarrow \mu\mu$  requires that a pair of oppositely charged electrons or muons is found. Due to lower background the electrons should have  $p_T > 15 \text{ GeV}$  and  $|\eta| < 2.4$  and their invariant mass should be between 80-100 GeV. Similar criteria are applied for the muons with  $p_T > 15 \text{ GeV}$  and  $|\eta| < 2.5$ . The reconstructed mass should be between 71-111 GeV.

Following this selection and some standard Monte Carlo simulations, the expected number of reconstructed events per  $10 \text{ pb}^{-1}$  at  $\sqrt{s} = 14 \text{ TeV}$  are about 45000, 5500 for  $W$  and  $Z$  decays to electrons and 60000, and 5000 for the decays to muons, respectively. Thus, even with a small data sample of only  $10 \text{ pb}^{-1}$ , the statistical uncertainty for the  $Z$  counting comes close to 1% in each channel.

Systematic uncertainties from the experimental selection are dominated by the  $Z$  efficiency determination and from backgrounds in the  $W$  selection. Other sources of uncertainties originate from the knowledge of energy scale and the resolution. The lepton efficiencies are evaluated by considering  $Z \rightarrow \ell\ell$  events and using the so called “tag and probe” method, like for example described by the D0 experiment [7, 8]. The efficiency uncertainty associated with the precision of this method has been estimated for a data sample of  $50 \text{ pb}^{-1}$  ( $1 \text{ fb}^{-1}$ ) of data to be 2% (0.4%) for  $W$  and 3% (0.7%) for  $Z$  events. The backgrounds for  $W$  events are of the order 4% in the electron channel and 7% in the muon channel. The main contributions are from other  $W$  or  $Z$  decays, and are thus well understood, leading to background uncertainties of the order 4% for both channels if a sample  $50 \text{ pb}^{-1}$  is analyzed. For much larger samples it is expected that uncertainties at or below 1% can be achieved. The backgrounds for the  $Z$  decays are very small, and can be determined accurately from mass spectrum, and hence does not carry any sizable uncertainty. It has been demonstrated, that the detector scales and resolutions can be determined very accurately [14], and the associated uncertainties are therefore also close to negligible. Some detailed studies demonstrate that eventually the systematic error between 1-2% or even smaller might be achieved for the  $W$  and  $Z$  counting and within the detector acceptance up to rapidities of about 2.5.

In order to use this number for the  $pp$  luminosity determination the total inclusive  $W$  and  $Z$  cross-section at NNLO can be used. These have been calculated to be 20510 pb and 2015pb, respectively [27]. Variations in models, floating parameters, and other theoretical uncertainties lead to significant variations in the estimates. The uncertainties on these calculation are estimated to be 5% or smaller. This uncertainty appears to be currently dominated by the PDF uncertainties needed to extrapolate to the experimentally uncovered large rapidity region. More discussions about these uncertainties can be found for example at [28] and [29].

It can be assumed that the detailed studies of the rapidity distributions within the acceptance region with  $W$  and  $Z$  decays might eventually lead to further error reductions.



### 4.3 Measuring Z production, experimental approach in LHCb

The uncertainty on the predicted Z production cross section at the LHC comes from two sources: the uncertainty on the NNLO partonic cross section prediction [27], which contributes an uncertainty of  $< 1\%$ , and uncertainties in our understanding of the proton Parton Distribution Functions (PDFs) which, for the latest MSTW fit [30], contribute an uncertainty of  $\sim 3\%$  for Z bosons produced with rapidities in the range  $-5 < y < 5$ .

A measurement of the Z production rate at LHCb via the channel  $Z \rightarrow \mu^+\mu^-$ , which provides a final state that is both clean and fully reconstructible, can be achieved with high efficiency and little background contamination. In addition, since the dimuon trigger stream at LHCb [31] requires two muons with an invariant mass larger than  $2.5\text{GeV}$  and a summed transverse momentum ( $P_T^1 + P_T^2$ ) greater than  $1.4\text{GeV}$ , a high trigger efficiency of  $\sim 95\%$  is expected for these events. A variety of background sources for this channel have been investigated: other electroweak processes such as  $Z \rightarrow \tau^+\tau^-$  where both taus decay to muons and neutrinos; QCD processes such as  $b\bar{b} \rightarrow \mu^+\mu^- + X$ ; and events where two hadrons with an invariant mass near the Z mass are both mis-identified as muons. To deal with these backgrounds an off-line selection has been developed [32] that requires: the dimuon invariant mass to be within  $20\text{ GeV}$  of the Z mass; the higher and lower transverse momentum muons to be greater than  $20\text{ GeV}$  and  $15\text{ GeV}$  respectively; the impact parameter of both muons is consistent with the primary vertex; and both muons have associated hadronic energy that is less than  $50\text{ GeV}$ . For  $Z \rightarrow \mu^+\mu^-$  events that are triggered and reconstructed at LHCb, these off-line selection criteria will select  $91 \pm 1\%$  of the signal events while reducing the background to  $(3.0 \pm 2.9)\%$  of the signal level with the dominant contribution due to the combinatoric backgrounds from pion and kaon mis-identification. It is expected that these backgrounds can be well understood from real data or removed using muon isolation criteria. Overall it is expected that  $Z \rightarrow \mu^+\mu^-$  events will be triggered, reconstructed and selected at LHCb at a rate of  $\sim 190\text{evts}/\text{pb}^{-1}$ . Systematic uncertainties have also been investigated and it is expected that with as little as  $5\text{pb}^{-1}$  of data the experimental efficiency (trigger, tracking, muon identification etc.) can be measured with an uncertainty of  $\sim 1.5\%$  enabling a luminosity measurement with an uncertainty of  $\sim 3.5\%$ .

### 4.4 PDF and relative parton-parton luminosity measurements

Theoretically well understood reactions at the LHC offer the possibility to use their rapidity distributions to improve today's knowledge of PDFs. Especially the resonance production of W and Z bosons with leptonic decays with low and high transverse momentum and the production of isolated high  $p_t$   $\gamma$ -Jet events have been demonstrated to be very sensitive to the relative parton distribution functions. Simulations from ATLAS and CMS have shown that experimental errors on these rapidity regions up to  $|y|$  of about 2.5 can probably be performed with accuracies eventually reaching perhaps 1% or better. The possibility to cross-check the measurements with W and Z decays to (a) electron(s) and (b) muon(s) and between both experiments will of course help to reach the accuracy.

During the past years simulation studies from the LHCb collaboration have shown that the experiment has a unique potential to extend the acceptance region from ATLAS and CMS for muons up to rapidity values at least up to 4.5. Furthermore, the existing overlap region for y

between 1.9 and 2.5 should allow to reduce normalisation uncertainties. Obviously, these rapidity values are understood as being reasonably accurate but qualitative values and more precise values will be defined once real data will allow to define a well understood fiducial volume of the detectors.

In addition, the LHCb collaboration has investigated the possibility to identify clean samples of very low mass Drell-Yan mu-pair events. The results indicate that such pairs can be measured within their acceptance region down to masses of 5 GeV. Such a measurement would in principle allow to measure PDFs for  $x$  values approaching extremely low values of  $10^{-6}$  for the first time [33].

It should be clear that such measurements, which are known to be very sensitive to quark, antiquark and gluon relative parton luminosities will not allow an absolute PDF normalisation. Such an improvement of absolute PDF normalisation would require the accurate knowledge of the proton-proton luminosity to better than today's perhaps  $\pm 3\%$  PDF accuracy obtained from the HERA measurements over a large  $x$  range and obviously lower  $Q^2$ . The alternative approach to combine the relative parton luminosities over the larger  $x, Q^2$  range using the sum rules has, to our knowledge, so far not been studied in sufficient detail.

A more detailed analysis of the different experimental approaches to improve the PDFs are interesting but are beyond the scope of this note about the luminosity. Nevertheless we hope that the experimentalists of the three collaboration will start to combine their efforts and will pursue the PDF measurements, in direct collaboration with theorists, during the coming years.

## 5 Comparing the different pp luminosity measurements

A relatively large number of pp luminosity measurements has been proposed and the most relevant have been discussed in this note. Here we try to give a critical overview of the different methods and their potential problems. Despite these advantages and disadvantage it should be clear that it is important to perform as many as possible independent luminosity methods during the coming years.

- **The machine luminosity determination using beam parameters:**

This method will be pursued independently of the experiments and its main purpose will be to optimize the performance of the LHC and thus providing a maximum number of physics collisions for the experiments. The potential to use this number as an almost instantaneous absolute luminosity number with uncertainties of perhaps  $\pm 10\%$  (and eventually  $\pm 5\%$ ), assuming that non gaussian tails of the beam can be controlled to this accuracy will certainly be useful to the experiments. Of course the experiments would lose somewhat their “independence” and still need to combine this number with their actual active running time.

However, one should remember that the Tevatron experiments did not use this method for their measurements.

The method to determine the beam size using the LHCb precision vertex detector look very promising and it is hoped that their approach might result in a pp luminosity measurement with an associated uncertainty of 3-5%.

- **Total cross section and absolute luminosity normalisation with specialized far for-**

**ward Detectors:**

The luminosity independent total pp cross section measurement is planned by the TOTEM collaboration and by the ALFA detector. Using these numbers both ATLAS and CMS plan to obtain the pp luminosity from the counting of the pp elastic scattering counting numbers from the forward detectors which thus depend on the knowledge of the total cross section measurement. In order to obtain this number some few weeks of special optics and low luminosity LHC running are required. As all LHC experiments are very keen to obtain as quickly as possible some reasonable luminosity at 14 TeV center of mass energy it is not likely that those special LHC data taking will happen during the first year(s) of data taking. Furthermore, despite the hope that the total cross section can be determined in principle with an interesting accuracy of  $\pm 1\%$ , it remains to be demonstrated with real LHC running. In this respect it is worth remembering that the two independent measurements of the total cross section at the Tevatron differed by 12% while much smaller errors were obtained by the individual experiments. As a result the average value with an error of  $\pm 6\%$  was used for the luminosity normalisation.

- **Luminosity determination using  $Z \rightarrow \ell\ell$ :**

This method provides an accurate large statistic relative luminosity number. It will be as accurate as the theoretical cross section calculation, which is based on the absolute knowledge of the PDFs from other experiments, from unknown higher order corrections and their incomplete Monte Carlo implementation. Today's uncertainties are estimated to be about 5%. It has been estimated, assuming the experiments perform as expected, that the potential Z counting accuracy within the acceptance region including efficiency corrections might quickly reach  $\pm 1\%$ . The extrapolation to the uncovered rapidity space, mainly due to the worse knowledge of the PDFs in this region, increases the error to perhaps 3%. Taking other theoretical uncertainties into account an error of  $\pm 5\%$  is currently estimated. Of course, advocates of the Z normalisation method like to point out that the real power of this method starts once relative measurements, covering similar partons and similar ranges of the parton distribution functions will be performed with statistical errors below 5%. Examples where such a normalization procedure looks especially interesting are the relative cross section measurements of  $N(Z)/N(W)$ ,  $N(W^+)/N(W^-)$ , high mass Drell-Yan events with respect to Z events and diboson final states decaying to leptons. Of course, correlations and anticorrelations between quark and gluon dominated production rates exist and need to be carefully investigated before similar advantages for the gluon PDFs can eventually be exploited. The loss of an independent Z cross section measurement would of course be a fact of life.

- **pp luminosity from the reaction  $pp \rightarrow pp\mu\mu$ :**

A measurement of this reaction offers in principle a direct and theoretically accurate proton proton luminosity value. Unfortunately current simulations from the experiments indicate that the accepted cross section is relatively small and only a few 1000 events can be expected per  $\text{fb}^{-1}$ . The different simulation results indicate that the backgrounds can be suppressed sufficiently without increasing the experimental systematics too much. Simulation studies [34] in CMS find that in the absence of pile-up, of the order 7000 events/fb can be selected. Apart from pile-up a leading source of systematic error is the contamina-



tion of the signal with events in which one of the protons dissociates. In the absence of pile-up, the use of the Zero-Degree-Calorimeters (one on each side of IP) and the Castor calorimeter (in 2009/10 available only on one side of the IP) in veto can improve the signal to background ratio from  $\sim 1$  to  $\sim 3$ . Hence in CMS this method may provide a means of measuring the absolute luminosity in the first LHC data with a total error of below 10%. In addition, the current simulation results indicate that small systematic errors of perhaps 1-2% might eventually be achievable<sup>5</sup> once a yearly luminosity of 5-10 fb<sup>-1</sup> in ATLAS and CMS (2 fb<sup>-1</sup> for LHCb) might be recorded. It remains to be seen if muons with transverse momenta well below 20 GeV can indeed be measured as accurately as muons with transverse momenta above 25 GeV.

### 5.1 Which luminosity accuracy might be achievable and when

Of course the potential time dependent accuracy of the different luminosity methods can only be guessed today as such numbers depend obviously on the LHC machine performance during the coming years. For the purpose of this Section we are mainly interested in measurements at the 14 TeV center of mass energy and assume that the following “data samples” would define such “years”. Of course, it could be hoped that the luminosity and energy increase would go much faster resulting in “some” shorter LHC years. Thus we assume that the first 14 TeV year, currently expected to be 2010, will correspond to 0.1 fb<sup>-1</sup>, followed by a 1 fb<sup>-1</sup> year. During the third and fourth year ATLAS and CMS expect to collect about 5 fb<sup>-1</sup> and 10 fb<sup>-1</sup> while LHCb expects to collect roughly 2 fb<sup>-1</sup> per year. We assume further that the special optics low luminosity data taking periods requiring perhaps a few weeks for TOTEM and similar for ALFA will take only place during the year when more than 1 fb<sup>-1</sup> per year or more can be expected.

As a result, for the first two 14 TeV running years, realistic luminosity numbers could come from (1) the machine group and (2) from the indirect method using the inclusive production of  $Z$  events with leptonic decays.

As has been pointed out in Section 3.1 the method (1) would, without any additional efforts by the machine group, allow a first estimate with a  $\pm 20$ -30% luminosity accuracy. We assume however that, due to the delay of the real 14 TeV start to 2010, enough resources could be found that people within the machine group could carefully prepare for the necessary beam parameter measurements and that the experiments will do the corresponding efforts to correct such a machine luminosity number for real detector data taking one could hope for a 10% measurement for 2010 and a 5% accuracy for 2011.

In contrast, method (2) would by definition be an integrated part of any imaginable experimental LHC data taking period. In fact, if enough attention is put into the  $Z$  counting method, the data expected during 2010 running might already reach statistical errors of  $\pm 2\%$  per 5 pb<sup>-1</sup> periods. Thus perhaps about 10-20 such periods could be defined during the entire year and systematic errors for the lepton efficiency correction within the detector acceptance could reach similar  $\pm 2$ -3% accuracies. During the following years these errors might decrease further to 1% or better. Once the rate of any “stable” simple high rate final states and even trigger rates relative

---

<sup>5</sup>It might be interesting to study the experience from similar measurements at the experimentally ideal conditions of LEP, where uncertainties above  $\pm 3\%$  have been reported [24].

to the  $Z$  counting rate has been determined, such relative event rates can be used subsequently to track the “run” luminosity and even the real time luminosity with similar accuracy.

Theoretical limitations of the cross section knowledge, not expected to improve without LHC data taking, would limit the accuracy to about  $\pm 5\%$ . The expected detailed analysis of the 2010 rapidity distributions of  $W$ ,  $Z$  and  $\gamma$ -jet events will allow some improvements for the years 2011 and beyond. We can thus expect that appropriate ratio measurements like the cross section ratio measurements of  $Z/W^\pm$  and  $W^-/W^+$  will already reach systematic accuracies of  $\pm 1\text{--}2\%$  during 2010 and 1% or better in the following years. Measurement of  $b$  physics, either in LHCb or in ATLAS and CMS might in any case prefer to perform luminosity independent measurements and relate any of the “new” measurements to some relatively well known and measurable B-hadron decays.

It is also worth pointing out that currently no other high  $Q^2$  reaction has been envisioned, which might be measurable to a systematic precision of better than 5-10% and a luminosity of up to  $1\text{fb}^{-1}$ . In addition, most of the interesting high  $Q^2$  electroweak final states will unfortunately even be limited for the first few LHC years to statistical accuracies to 5% or more.

The prospect for the other luminosity measurements start to become at earliest interesting only once a few  $100\text{ pb}^{-1}$  can be recorded. Consequently one can expect to obtain a statistical interesting accuracy from the reaction  $pp \rightarrow pp\mu\mu$  after 2010. Similar, it looks unlikely that low luminosity special optics run will be performed before 2011. Consequently one might hope that few % accurate total cross section numbers become available before the 2012 data taking period will start.

## 6 Summary and Outlook

A large variety of potentially interesting pp luminosity measurements, proposed during the past 10-15 years, are presented in this Section.

Realistically only the machine luminosity measurement and the counting of the  $Z$  production might reach interesting accuracies of 5% before 2011. For all practical purposes it looks that both methods should be prepared in great detail before the data taking at 14 TeV collision energies will start in 2010.

We believe that a working group, consisting of interested members of the three pp collider experiments and interested theorists, should be formed to prepare the necessary Monte Carlo tools to make the best possible use of the soon expected  $W$  and  $Z$  data, not only for the pp luminosity normalization but even more for the detailed investigations of the parton parton luminosity determination and their use to predict other event rates for diboson production processes and high mass Drell-Yan events.

## References

- [1] Up to Date Performance of the ATLAS, CMS and LHCb Detectors and further detailed references can be found on the corresponding homepages <http://atlas.web.cern.ch/Atlas/index.html>, <http://cmsinfo.cern.ch/Welcome.html/> and <http://lhcb.web.cern.ch/lhcb/>.

- [2] W. Herr and B. Muratori, *Concept of luminosity*. Proceedings CAS2003, <http://doc.cern.ch/yellowrep/2006/p361.pdf> CERN-2006-002 p. 361.
- [3] H. Burkhardt and P. Grafstrom, *Absolute luminosity from machine parameters*. 2007. CERN-LHC-PROJECT-Report-1019 and <http://cdsweb.cern.ch/record/1056691>.
- [4] V. M. Budnev, I. F. Ginzburg, G. V. Meledin, and V. G. Serbo, Nucl. Phys. **B63**, 519 (1973).
- [5] V. A. Khoze, A. D. Martin, R. Orava, and M. G. Ryskin, Eur. Phys. J. **C19**, 313 (2001). [hep-ph/0010163](http://hep-ph/0010163).
- [6] M. Dittmar *et al.*, *Parton distributions: Summary report for the HERA - LHC workshop*. Preprint [hep-ph/0511119](http://hep-ph/0511119), 2005.
- [7] CDF II Collaboration, D. E. Acosta *et al.*, Phys. Rev. Lett. **94**, 091803 (2005). [hep-ex/0406078](http://hep-ex/0406078).
- [8] A. M. Bellavance, *W/Z production cross sections and asymmetries at  $E(CM) = 2\text{-TeV}$* . Preprint [hep-ex/0506025](http://hep-ex/0506025), 2005.
- [9] F. P. M. Dittmar and D. Zurcher, Phys. Rev. **D56**, 7284 (1997). [hep-ex/9705004](http://hep-ex/9705004).
- [10] J. Pinfold, *Plans for the very forward region of ATLAS: The lucid luminosity monitor*. Prepared for 9th ICATPP Conference on Astroparticle, Particle, Space Physics, Detectors and Medical Physics Applications, Villa Erba, Como, Italy, 17-21 Oct 2005.
- [11] TOTEM Collaboration, G. Anelli *et al.*, JINST **3**, S08007 (2008).
- [12] LHCb Technical Proposal, CERN-LHCC-98-004.
- [13] LHCb Technical Design Report 9 *LHCb Reoptimized Detector*, CERN-LHCC-2003-030.
- [14] ATLAS Collaboration, N. Besson, M. Boonekamp, E. Klinkby, T. Petersen, and S. Mehlhase, Eur. Phys. J. **C57**, 627 (2008). [0805.2093](http://arxiv.org/abs/0805.2093).
- [15] See CMS Collaboration CMS PAS EWK-08-005 for Electrons and CMS PAS 2007/002 for Muons.
- [16] See LHCb Technical Design Report 10, *LHCb Trigger System*, CERN-LHCC-2003-031.
- [17] H. Schmickler, *How to measure beam intensity ?* <http://indico.cern.ch/getFile.py/access?contribId=s1t18&resId=1&materialId=1&confId=a053945> given to Atlas 27 June 2005.
- [18] S. V. der Meer, *Calibration of the effective beam height in the isr*. <http://doc.cern.ch/archive/electronic/kek-scan/196800064.pdf> CERN-ISR-PO-.
- [19] K. Potter, *Luminosity measurements and calculations*. CAS 1992, CERN yellow report, <http://doc.cern.ch/yellowrep/1994/94-01/p117.pdf> p. 117 ff.

- [20] G. C. *et al.*, Nucl. Phys. **B254**, 697 (1985).
- [21] M. Ferro-Luzzi, Nucl. Instrum. Meth. **A553**, 388 (2005).
- [22] The CMS Approach using Specialized High Rate Detectors is Described in the Talk of V.Halyo during the HERA-LHC Workshop “standard candles”.
- [23] The Presentations of the “standard candle” session during the HERA LHC Workshop in May 2008 can be found at:  
[http://indico.cern.ch/conferenceOtherViews.py?view=cdsagenda\\_olist&confId=27458#18..](http://indico.cern.ch/conferenceOtherViews.py?view=cdsagenda_olist&confId=27458#18..)
- [24] L3 Collaboration, P. Achard *et al.*, Phys. Lett. **B585**, 53 (2004). [hep-ex/0402037](#).
- [25] A. G. Shamov and V. I. Telnov, Nucl. Instrum. Meth. **A494**, 51 (2002).  
[hep-ex/0207095](#).
- [26] More Details about the LHCb Approach using  $pp \rightarrow pp^{+-}$ , are given in the talk of J. Anderson at the HERA-LHC Workshop “standard candles”.
- [27] K. M. C Anastasiou, L. J. Dixon and F. Petriello, Phys. Rev. **D69**, 094008 (2004).  
[hep-ph/0312266](#).
- [28] S. A. Y. N. E. Adam, V. Halyo, JHEP **05** (2008). [0802.3251](#).
- [29] S. . Y. W. Z. N. E. Adam, V. Halyo, JHEP **09**, 13 (2008). [0808.0758](#).
- [30] R. S. Thorne, A. D. Martin, W. J. Stirling, and G. Watt, *Parton Distributions for the LHC*. Preprint 0706.0456, 2007.
- [31] LHCb Technical Design Report 10, *LHCb Trigger System*, CERN-LHCC-2003-031.
- [32] More details about the LHCb approach using  $\sigma_Z \cdot Br(Z \rightarrow \mu^+ \mu^-)$ , are given in the talk by J. Anderson at the HERA-LHC Workshop “standard candles”..
- [33] R. McNulty, *Potential PDF sensitivity at LHCb*. Preprint 0810.2550, 2008.
- [34] CMS collaboration, *Exclusive  $\gamma\gamma \rightarrow l^+ l^-$  and  $\gamma p \rightarrow \Upsilon p \rightarrow l^+ l^- p$  production*. CMS-PAS-DIF-07-001.

## Outlook: the PDF4LHC initiative

*A. De Roeck*

This document demonstrates the vast amount of progress that has taken place in the last years on pinning down the PDFs of the proton, as well as the dramatic increase in awareness of the impact of PDFs on the physics program of LHC experiments. The HERALHC workshop has acted as a regular forum for working meetings between the experiments, PDF phenomenologists and theorists. In the course of this workshop, it was realized that the momentum on the PDF studies should be kept and perhaps even focused more on the LHC, in order to continue the discussions, investigations and further work towards improving our knowledge on the PDFs.

Clearly, LHC will need the best PDFs, especially for precision measurements, setting of limits in searches, and even for discoveries. Ideally the ATLAS and CMS (and LHCb and ALICE) analyses should follow a common procedure for using PDFs and their uncertainties in their key analyses. Such a common procedure, across the experiments, is being used in other contexts, such as significance estimates in searches. Also, changing frequently the PDFs in the software of the experiments, e.g. for cross-checks or the determination of error bands, is often non-trivial (e.g. due to the inter-connection with parameter choices for underlying event modeling, showering parameters and so on) and sometimes impractical if CPU intensive detector simulations are involved. LHC studies therefore will need both good central values for the PDFs to start with, and a good estimate of the associated uncertainties.

This has triggered the so called PDF4LHC initiative. PDF4LHC offers a discussion forum for PDF studies and information exchange between all stake-holders in the field: the PDF global fitter groups, such as CTEQ and MSTW; the current experiments, such as the HERA and Tevatron ones; QCD theorists and the LHC experimental community. The PDF4LHC initiative started in 2008. More details and links to the meetings so far can be found on the PDF4LHC web site [1].

The mission statement of PDF4LHC is:

- Getting the best PDFs, including the PDF uncertainties, based on the present data.
- Devise strategies to use future LHC data to improve the PDFs.

All this needs a close collaboration between theorists and those that are preparing to make the measurements. In order to reach the first goal, the PDF4LHC forum aims to stimulate discussions and trigger further comparison exercises across the PDF community, in order to select one or a limited number of possible strategies that can be adapted to determine and use PDFs. For the second goal, PDF4LHC should also be a forum for discussions on how to include measurements from the LHC to constrain PDFs: what should be measured at LHC, and correspondingly calculated in theory. Such measurements include  $W$  and  $Z$  production and asymmetries, di-jet production, hard prompt photons, Drell-Yan production, bottom and top quark production,  $Z$ -shape fits and  $Z$ +jets measurements. One expects that some of these channels can already be studied with first data, hence we need to prepare for that well in advance.

The following issues are part of the program for in depth discussions via topical workshops, some of which took place already in 2008 [1].

- Data to be included in the PDFs. Would we get better results with a selection of data to be used? New data will become available such as  $F_L(x, Q^2)$ , and combined data from H1/ZEUS. Can we extract more from the data?

- Determination of PDF uncertainties, including the statistical treatment of the data.
- Theoretical uncertainties and regions/processes where they matter: higher-order corrections; heavy flavour treatment; low- $x$  (and high- $x$ ) resummation; other PDFs like unintegrated PDFs (and GPDs).
- PDFs for usage Monte Carlo generators.

One can expect that the LHC experiments most likely will be using for most of their studies the PDF sets and errors that are delivered by either one of the CTEQ or MSTW family. Hence it is important that the lessons learned from exercises on studies of the systematics on PDFs will be adapted by these main global PDF providers. PDF4LHC aims to advice the experiments in the use for PDFs for the LHC, based on the discussions, results and future consensus at the forum. The experience and results from HERAPDFs, and PDFs from other groups, like the Neural Net or Alekhin ones are extremely valuable in this discussion and will serve as crucial input in studies to demonstrate how well we actually know the parton distributions. Several important benchmark exercises have been already performed and are reported in section 3 of this report.

A special case are the PDFs for Monte Carlo generators. For experiments it is important that generated events be kinematically distributed close to the distribution of the real data, such that the simulated and reconstructed Monte Carlo events can be used in a straightforward way to calculate efficiencies for e.g. experimental cuts in an analysis. In case the initially generated distribution does not resemble the data close enough, the Monte Carlo samples need to be reweighted, with all its possible drawbacks. Since calculations based on LO Matrix Elements and LO PDFs are known not to describe the data well, and NLO Matrix Element based generators to date have so far only a restricted number of processes implemented, studies are ongoing on so called “improved LO” PDFs, which try to cure some of the LO PDF drawbacks. Examples are given in [2]. This is yet another part of the discussions in the PDF4LHC forum

In short, it is crucial that the work started here continues, with discussions and studies on PDFs and their uncertainties, the impact of the upcoming data on future PDF determinations and more, all with special focus on the needs for the LHC. The PDF4LHC initiative will offer a framework to do all this.

## References

- [1] The web page of the PDF4LHC forum can be found at <http://www.hep.ucl.ac.uk/pdf4lhc/>.
- [2] A. Sherstnev and R. S. Thorne, *Different PDF approximations useful for LO Monte Carlo generators*. Preprint 0807.2132, 2008.

## Chapter 2

### Working Group

### Multi-Jet Final States and Energy Flows

#### Convenors:

*C. Gwenlan (UCL, ZEUS)*

*L. Lönnblad (Lund),*

*E. Rodrigues (LHCb),*

*G. Zanderighi (CERN),*

*Contactpersons: S. Banerjee (CMS), D. Traynor (H1)*





## Working group: Multi-Jet final states and energy flows

Claire Gwenlan<sup>1</sup>, Leif Lönnblad<sup>2</sup>, Eduardo Rodrigues<sup>3</sup>, Giulia Zanderighi<sup>1</sup> (Eds.),  
Alessandro Bacchetta<sup>22</sup>, Andrea Banfi<sup>4</sup>, Sergey Baranov<sup>5</sup>, Jochen Bartels<sup>6</sup>,  
Armen Bunyatyan<sup>7,8</sup>, Victor Coco<sup>9</sup>, Gennaro Corcella<sup>10,11</sup>, Mrinal Dasgupta<sup>12</sup>, Michal Deák<sup>13</sup>,  
Pierre-Antoine Delsart<sup>9</sup>, Igor M. Dremin<sup>5</sup>, Francesco Hautmann<sup>1</sup>, S. Joseph<sup>14</sup>, Hannes Jung<sup>13</sup>,  
Albert Knutsson<sup>13</sup>, Krzysztof Kutak<sup>13</sup>, Artem Lipatov<sup>15</sup>, Gionata Luisoni<sup>16</sup>, Swapan Majhi<sup>14</sup>,  
Lluís Martí<sup>13</sup>, Katharina Müller<sup>17</sup>, Tim Namsoo<sup>13</sup>, Sakar Osman<sup>2</sup>, Hanno Perrey<sup>6</sup>,  
Germán Rodrigo<sup>18</sup>, Juan Rojo<sup>19</sup>, Zuzana Ruriková<sup>13</sup>, Agustín Sabio Vera<sup>20</sup>, Christian Sander<sup>6</sup>,  
Thomas Schörner-Sadenius<sup>6</sup>, Florian Schwennsen<sup>21</sup>, Gábor Somogyi<sup>22</sup>, Grégory Soyez<sup>23</sup>,  
Mark Strikman<sup>24</sup>, Michele Treccani<sup>25,26</sup>, Daniele Treleani<sup>27</sup>, Zoltán Trócsányi<sup>28</sup>, B.F.L. Ward<sup>14</sup>,  
S.A. Yost<sup>29</sup>, Nikolai Zotov<sup>15</sup>

<sup>1</sup> Oxford University, UK; <sup>2</sup> Lund University, Sweden; <sup>3</sup> University of Glasgow, UK; <sup>22</sup> Jefferson Lab, USA; <sup>4</sup> Università di Milano–Bicocca, Italy; <sup>5</sup> Lebedev Physical Institute, Moscow, Russia; <sup>6</sup> University of Hamburg, Germany; <sup>7</sup> MPI-K, Heidelberg Germany; <sup>8</sup> YerPhI, Yerevan, Armenia; <sup>9</sup> LAPP, Annecy, France; <sup>10</sup> Museo Storico della Fisica e Centro Studi e Ricerche E. Fermi, Italy; <sup>11</sup> Scuola Normale Superiore Italy; <sup>12</sup> University of Manchester, UK; <sup>13</sup> DESY, Hamburg, Germany; <sup>14</sup> Baylor University, Waco, USA; <sup>15</sup> Skobeltsyn Institute of Nuclear Physics, Lomonosow Moscow State University, Russia; <sup>16</sup> Universität Zürich, Switzerland; <sup>17</sup> University of Zurich, Switzerland; <sup>18</sup> IFIC, CSIC-Universitat de València, Spain; <sup>19</sup> LPTHE, Paris, France; <sup>20</sup> CERN, Geneva, Switzerland & Instituto de Física Teórica UAM/CSIC, Universidad, Autónoma de Madrid, E-28049 Madrid, Spain; <sup>21</sup> LPT Université d'Orsay, CNRS, France; <sup>22</sup> University of Zürich, Switzerland; <sup>23</sup> Brookhaven National Laboratory, USA; <sup>24</sup> Pennsylvania State University, USA; <sup>25</sup> Università di Ferrara, Italy; <sup>26</sup> Universidad de Granada, Spain; <sup>27</sup> Università di Trieste, Italy; <sup>28</sup> University of Debrecen, Hungary; <sup>29</sup> The Citadel, Charleston, USA.

### Abstract

We present a summary of the activities of the *Multi-Jet final states and energy flows* Working Group of the *HERA and the LHC workshop*, 2007-2008. Among the more specific topics considered were the status of and recent progress in higher order calculations, both in fixed perturbative expansions and in resummed approaches, recent progress in the description of jets, including the description of forward jets, new calculations performed using  $k_T$ -factorization and new determinations of unintegrated parton densities.

## 1 Introduction

*Authors: Claire Gwenlan, Leif Lönnblad, Eduardo Rodrigues, Giulia Zanderighi*

The activities of Working Group 2, *Multi-Jet Final States and Energy Flows*, have covered a broad range of topics, encompassing both theoretical and experimental advances in understanding the hadronic final state at high energies. Much of this work will be of significant benefit in preparing to fully exploit the LHC physics potential. We focus here on progress in the field since the last proceedings of this workshop [1, 2].

From a theoretical point of view, a good understanding of the Standard Model (SM) is of the utmost importance in order to be able to unravel and disentangle possible New Physics effects. In addition, the study of the Standard Model is important in its own right, especially in the QCD sector where the strong coupling in many cases prevents us from making reliable predictions. Recently, considerable progress has been made in the area of higher order calculations in perturbative QCD. Some developments are discussed in the contributions of Sec. [3]. Typically, these fixed-order calculations are sufficient to describe inclusive observables, such as cross sections or transverse momentum ( $p_t$ ) spectra at sufficiently high scales. However, more exclusive observables, such as event-shape distributions, require that one rearranges the perturbative expansion and that one resums leading and next-to-leading logarithmic terms to all orders in perturbation theory. This technology is today already well-developed both in terms of analytical calculations and in terms of numerical implementations in parton shower Monte Carlos. We report on further recent progress in the understanding and development of such resummed calculations in Sec. [4].

The development and use of jet algorithms plays a key role in the study of hadronic final states. Indeed jets are an essential tool for a variety of studies, such as top reconstruction, mass measurements and searches for Higgs and new physics. Furthermore, they are instrumental for QCD studies, e. g. for inclusive-jet measurements, which in turn constitute an important input for parton density determinations. By clustering particles into jets, jet algorithms reduce complicated multi-particle events in simple final states with few jets. This procedure and the way particles are recombined together (e.g. the  $E$ - or  $P$ -scheme) is fundamentally non-unique. This freedom can be exploited to extract information from jets. The rapid, recent development of fast, infrared- and collinear-safe cone and clustering algorithms, is discussed in Sec. [5]. Also considered are the issues of jet-finding, reconstruction and calibration currently being developed by the LHC experimental collaborations. Recent work on defining jet-quality measures, designed to quantify the performance of jet algorithms, is also presented.

In Sec. [6] we focus our attention to the  $k_T$ -factorization approach, which may be the key to fully understand the hadronic final states at the LHC. Although the standard collinear factorization should hold for the description of jets at very high scales, we expect it to break down at somewhat smaller scales and low  $x$ , and the use of  $k_T$ -factorization and unintegrated parton densities will become essential. This is an area where we have learned a lot from HERA results, and where we may learn more still from data yet to be analyzed.

A major difficulty in describing final states at high energies is the treatment of multi-parton interactions. There is no doubt that, due to the high density of small- $x$  partons, the events at the LHC will contain several semi-hard parton-parton scatterings. Indeed such events have already been studied at the Tevatron, and models including this feature are needed in order to describe e.g. the underlying events in photo-production at HERA. Although models for multi-

parton interactions exist, there are many uncertainties, and the differences in the predictions for the LHC are large. Most of the work on multi-parton interactions in the workshop was presented in joint sessions with the Monte Carlo tools working group, and the corresponding contribution to these proceedings are presented in the section of this working group [7].

In Sec. [8], reviews some recent experimental results from HERA which are of interest for future LHC studies, concentrating particularly on isolated photon and jet production, including the effects of multi-parton interactions and the underlying event.

Finally we take a look at processes at even higher parton densities, such as those occurring in heavy ion collisions. Here it is important to consider not only the productions of jets, and possible effects of gluon saturation, but also the propagation of the hard partons through a dense medium. A couple of issues related to such interactions at high densities are discussed in Sec. [9].

### Acknowledgments

G. Rodrigo acknowledges support by MICINN under Grant No. FPA2007-60323 and No. INFN08-02, and by Generalitat Valenciana under Grant No. PROMETEO/2008/069

### References

- [1] S. Alekhin *et al.* (2005), [arXiv:hep-ph/0601012](#).
- [2] S. Alekhin *et al.* (2005), [arXiv:hep-ph/0601013](#).
- [3] G. Zanderighi *et al.*, *Higher-order calculations*. These proceedings.
- [4] A. Banfi *et al.*, *Event shapes and resummation*. These proceedings.
- [5] V. Coco *et al.*, *Jets and jet algorithms*. These proceedings.
- [6] S. Baranov *et al.*,  *$k_{\perp}$ -factorization and forward jets*. These proceedings.
- [7] S. Gieseke *et al.*, *Working group summary — monte carlo tools*. These proceedings.
- [8] K. Müeller *et al.*, *Hera results*. These proceedings.
- [9] M. Strikman and I. Dremin, *Interactions at high gluon densities*. These proceedings.

## Higher-order calculations

*Giulia Zanderighi, Germán Rodrigo, Michele Treccani, Gábor Somogyi*

The start-up of the LHC will usher in a new era of discovery in high-energy physics, with the machine operating at the highest centre-of-mass energy ever attained in the laboratory. In order to fully exploit its physics potential in Higgs and beyond the Standard Model (BSM) searches, a good understanding of the Standard Model is necessary. This requires a precise theoretical understanding of QCD.

The simplest description in exact perturbative calculations is at leading order (LO) using collinear factorization. Here, partons (or particles) should be well-separated and hard so as to avoid large soft-collinear corrections. Today, these LO calculations are fully automated. However, the drawback is that they have very large scale dependencies, enhanced sensitivities to kinematical cuts and a poor modelling of the jet structure (each parton corresponding to a jet). Therefore it is currently well appreciated that accurate predictions of QCD jet cross sections require the computation of radiative corrections at least to next-to-leading order (NLO) accuracy, first for SM processes, and BSM processes at a later stage. This is simply because the QCD coupling is not small and the phase space for emitting additional partons at the LHC is large, so that NLO corrections can be numerically significant. Benefits of NLO include a reduced dependence on unphysical scales, a better modelling of jets, and a more reliable control of the normalization and shape of cross sections.

Three ingredients are needed to compute a  $2 \rightarrow N$  process at NLO: the real radiation of one parton from the  $2 + N$  parton system (tree-level  $2 + N + 1$  processes), one-loop virtual corrections to the  $2 \rightarrow N$  process and a method to cancel the divergences of real and virtual corrections before numerical integration. The calculation of tree-level amplitudes has been automated and also the cancellation of divergences is, today, well understood [1–3]. Therefore up until very recently, the bottleneck at NLO has been the calculation of virtual, loop amplitudes.

In some cases however, NLO accuracy is not yet satisfactory and one would like to be able to calculate perturbative corrections beyond NLO. The physical situations when this happens have been discussed extensively in the literature [4]. Usually NLO is insufficient when the NLO correction is comparable to, or larger than, the LO result. This may happen when a process involves very different scales, so that large logarithms of the ratio of the two scales arise, which need to be resummed. This may also happen when new channels open up (at NLO those channels are effectively LO). This is the case, for instance, for  $b$ -jet production, where gluon splitting and flavour excitation processes enter at NLO and are enhanced by large logarithms. Also, gluon dominated processes are often characterized by large corrections, both because gluons radiate on average more than quarks and because of the steeply falling parton distribution functions (PDFs) at small  $x$ . NLO might also be insufficient if very high precision is useful. This is occasionally the case, for instance, in Drell-Yan processes, top pair production, and 3-jet production in  $e^+e^-$ . Finally, since NLO provides a first reliable estimate of cross sections, only NNLO can in principle provide a reliable error estimate of those cross sections. The bottleneck at NNLO is not the calculation of virtual matrix elements, as is the case at NLO, but rather the cancellation of divergences before numerical evaluation. In the following we will report on some recent progress in higher-order perturbative QCD.

## 1 One-loop amplitudes: the gluon case

*Author: Giulia Zanderighi*

Current and upcoming collider experiments require a good understanding of Standard Model (SM) processes in order to carry out any successful search for a Higgs or beyond SM signals (BSM). Therefore, these searches will benefit from next-to-leading order predictions, for SM processes first, and BSM processes at a later stage. Traditional Feynman diagram techniques, supplemented by robust numerical methods (Passarino-Veltman decomposition, Davydychev reduction, integration by part, tensor reduction) are well developed and made it possible to develop powerful computation tools [5–8] including procedures to handle potential numerical instabilities [7, 9]. These techniques have been applied recently in a variety of  $2 \rightarrow 3$  scattering processes and pushed to their limit in few  $2 \rightarrow 4$  cases (see [10] for a recent review). The bottleneck of these approaches is the rapid increase both in the number of Feynman diagrams and in the number of terms generated during the tensors reduction. One promising alternative method is based on generalized unitarity [11]. Recent advances [12] allowed the development of analytic methods for the calculation of the full amplitude, including the rational part, using recursion relations [13, 14]. A recent computational scheme is based on unitarity in integer higher dimension [15, 16]. This allows one to reduce the calculation of *full* one-loop amplitudes to the calculation of residues and of tree-level amplitudes involving complex momenta.

Using unitarity in higher integer dimension together with Berends-Giele recursion relations, we show that it is possible to develop an algorithm of mild, polynomial complexity for the evaluation of one-loop amplitudes. As a first application, we considered here pure gluonic amplitudes. We analyze the numerical stability of the results and the time dependence of the algorithm for virtual amplitudes with up to twenty external gluons.

### 1.1 The method

We [17] implemented the methods developed in Refs. [15, 16] with some minor modifications into the **Rocket** program. These methods build upon the formalism of Ref. [18] by removing the requirement of the four dimensional spinor language, thereby allowing for the extension of the method to  $D$ -dimensional cuts. To calculate the full one-loop  $N$ -gluon amplitude, it is sufficient to be able to calculate the leading colour ordered one-loop amplitude, since from these colour ordered amplitudes the full one-loop amplitude can be constructed [11, 19]. In the following we will therefore focus on the leading colour ordered amplitudes  $A_N^{[1]}(1, 2, \dots, N)$ . We will use the (over-complete) master integral basis decomposition derived in Ref. [16]

$$\begin{aligned}
A_N^{[1]} = & - \sum_{[i_1|i_5]} \frac{(D-4)}{2} e_{i_1 i_2 i_3 i_4 i_5}^{(2,0)} I_{i_1 i_2 i_3 i_4 i_5}^{(D+2)} \\
& + \sum_{[i_1|i_4]} \left( d_{i_1 i_2 i_3 i_4}^{(0,0)} I_{i_1 i_2 i_3 i_4}^{(D)} - \frac{(D-4)}{2} d_{i_1 i_2 i_3 i_4}^{(2,0)} I_{i_1 i_2 i_3 i_4}^{(D+2)} + \frac{(D-4)(D-2)}{4} d_{i_1 i_2 i_3 i_4}^{(4,0)} I_{i_1 i_2 i_3 i_4}^{(D+4)} \right) \\
& + \sum_{[i_1|i_3]} \left( c_{i_1 i_2 i_3}^{(0,0)} I_{i_1 i_2 i_3}^{(D)} - \frac{(D-4)}{2} c_{i_1 i_2 i_3}^{(2,0)} I_{i_1 i_2 i_3}^{(D+2)} \right) \\
& + \sum_{[i_1|i_2]} \left( b_{i_1 i_2}^{(0,0)} I_{i_1 i_2}^{(D)} - \frac{(D-4)}{2} b_{i_1 i_2}^{(2,0)} I_{i_1 i_2}^{(D+2)} \right),
\end{aligned} \tag{1}$$

where we introduced the short-hand notation  $[i_1|i_n] = 1 \leq i_1 < i_2 < \dots < i_n \leq N$  and

$$I_{i_1, \dots, i_N}^D = \int \frac{d^D l}{i\pi^{D/2}} \frac{1}{d_{i_1} d_{i_2} \dots d_{i_N}}, \quad d_i = d_i(l) = (l + q_i)^2 = (l + p_1 + \dots + p_i)^2. \tag{2}$$

Because some coefficients are multiplied with a dimensional factor  $(D-4)$  they cannot be determined using four dimensional cuts, therefore we extend the dimensionality of the cut line to integer, higher dimensions, resulting in a well-defined on-shell particle after performing the cut [16]. By applying quintuple, quadruple, triple and double  $D_s$ -dimensional cuts (where  $D_s \geq D$  denotes the dimensionality of the spin-space) we can determine the coefficients of the parametric form of the one-loop amplitude. This requires the calculation of the factorized unintegrated one-loop amplitude

$$\begin{aligned}
\text{Res}_{i_1 \dots i_M}(\mathcal{A}_N^{[1]}(l)) &= \left( d_{i_1} \times \dots \times d_{i_M} \times \mathcal{A}_N^{[1]}(l) \right)_{d_{i_1} = \dots = d_{i_M} = 0} \\
&= \sum_{\{\lambda_1, \dots, \lambda_M\}=1}^{D_s-2} \left( \prod_{k=1}^M \mathcal{A}_{i_{k+1}-i_k}^{[0]}(l_{i_k}^{(\lambda_k)}, p_{i_k+1}, \dots, p_{i_{k+1}}, -l_{i_{k+1}}^{(\lambda_{k+1})}) \right), \tag{3}
\end{aligned}$$

where  $M \leq 5$  and the  $D$ -dimensional loop momentum  $l$  has to be chosen such that  $d_{i_1}(l) = \dots = d_{i_M}(l) = 0$ . To calculate these tree amplitudes we use the standard Berends-Giele recursion relation [20] which is valid in arbitrary dimension and for complex momenta. The generic solution for the loop momentum in Eq. (3) is given by

$$l_{i_1 \dots i_M}^\mu = V_{i_1 \dots i_M}^\mu + \sqrt{\frac{-V_{i_1 \dots i_M}^2}{\alpha_M^2 + \dots + \alpha_D^2}} \left( \sum_{i=M}^D \alpha_i n_i^\mu \right), \tag{4}$$

for arbitrary values of the variables  $\alpha_i$ . The vector  $V_{i_1 \dots i_m}^\mu$  is defined in the space spanned by the denominator offset momenta  $\{q_{i_1}, \dots, q_{i_m}\}$ , while the orthonormal basis vectors  $\{n_M^\mu, \dots, n_D^\mu\}$  span the space orthogonal to the space spanned by these momenta [15, 16]. Given the solution to the on-shell conditions  $l_{i_1 \dots i_M}^\mu$  in Eq. (4), the loop momenta flowing into the tree amplitudes  $l_{i_k}$  and  $l_{i_{k+1}}$  in Eq. (3) are fixed by momentum conservation (see Ref. [15]). Once all coefficients

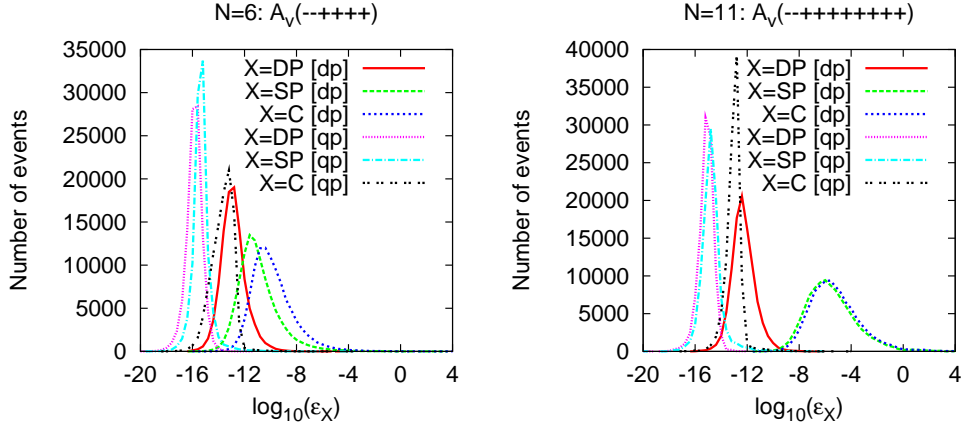


Fig. 1: Accuracy on the double pole, single pole and constant part of the maximally helicity violating (MHV) amplitude with adjacent negative helicities for 6 up to 11 external gluons. Double ([dp]) and quadrupole ([qp]) precision results for 100,000 phase space points are shown. Refer to the text for more details.

in Eq. (1) have been determined we can continue the dimensionality to the non-integer limit:  $D \rightarrow 4 - 2\epsilon$ . Neglecting terms of order  $\epsilon$  we find for the colour ordered one-loop amplitude

$$\begin{aligned}
 A_N^{[1]} = & \sum_{[i_1|i_4]} d_{i_1 i_2 i_3 i_4}^{(0,0)} I_{i_1 i_2 i_3 i_4}^{(4-2\epsilon)} + \sum_{[i_1|i_3]} c_{i_1 i_2 i_3}^{(0,0)} I_{i_1 i_2 i_3}^{(4-2\epsilon)} + \sum_{[i_1|i_2]} b_{i_1 i_2}^{(0,0)} I_{i_1 i_2}^{(4-2\epsilon)} \\
 & - \sum_{[i_1|i_4]} \frac{d_{i_1 i_2 i_3 i_4}^{(4,0)}}{6} + \sum_{[i_1|i_3]} \frac{c_{i_1 i_2 i_3}^{(2,0)}}{2} - \sum_{[i_1|i_2]} \frac{(q_{i_1} - q_{i_2})^2}{6} b_{i_1 i_2}^{(2,0)} + \mathcal{O}(\epsilon) .
 \end{aligned} \quad (5)$$

The terms in the first line give rise to the so-called cut-constructable part of the amplitude [21]. The terms in the second line can be identified with the rational part. In the approach used here the division between these two contributions is irrelevant. For the numerical evaluation of the bubble, triangle and box master integrals we use the package developed in Ref. [22].

## 1.2 Numerical results: accuracy and time dependence of the algorithm

To study the numerical accuracy of the on-shell method implemented in **Rocket** we define

$$\epsilon_C = \log_{10} \frac{|A_N^{v,\text{unit}} - A_N^{v,\text{analy}}|}{|A_N^{v,\text{analy}}|} , \quad (6)$$

where “unit” denotes the result obtained with the on-shell method and “analy” the analytical result for the constant parts of the one-loop helicity amplitudes (or in the case of  $N = 6$  the numerical results of [23]). Similarly, we denote by  $\epsilon_{\text{DP}}$  and  $\epsilon_{\text{SP}}$  the accuracy on the double and single poles, respectively.

In Fig. (1) we show the accuracy for the two adjacent minus helicity gluon MHV one-loop amplitudes,  $A_N^{[1]}(- - + \cdots +)$ , for  $N = 6$  and  $N = 11$ , which are known analytically [11,21,24].



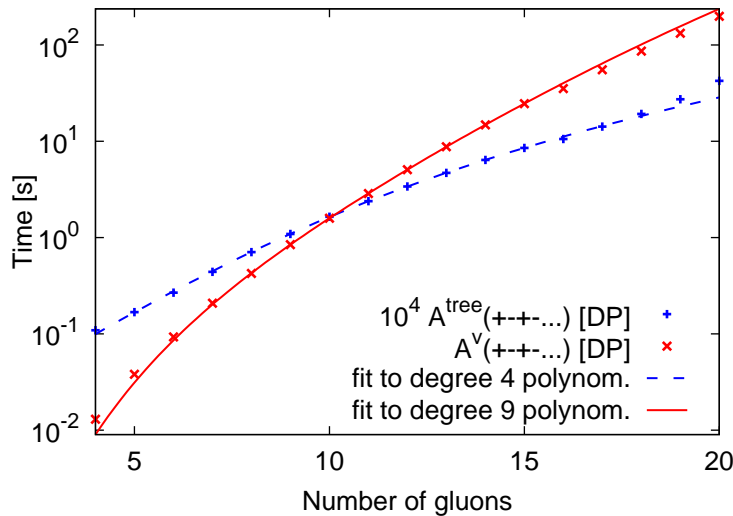


Fig. 2: Time in seconds needed to compute tree (blue, dashed) and one-loop (red, solid) ordered amplitudes with gluons of alternating helicity signs,  $A_N^{[1]}(+ - + - \dots)$ , as a function of the number of external gluons ranging between 4 to 20 using a single 2.33 GHz Xeon processor.

The 100,000 phase space points used for each multiplicity are generated uniformly in phase space using the Rambo algorithm [25] imposing minimal cuts. We plot the accuracy for the double pole ( $X = \text{DP}[\text{dp}]$ , solid, red), the single pole ( $X = \text{SP}[\text{dp}]$ , green, dot-dashed) and the constant part ( $X = \text{C}[\text{dp}]$ , blue, dotted). We see that an excellent accuracy can be reached for all contributions. The tail of the distribution reaching to large values of  $\epsilon$  contains only a very few points. This lack of agreement is due to numerical instabilities due to vanishing Gram determinants or other small intermediate denominators. Several techniques have been developed to deal with such exceptional points, such as developing systematic expansions [6, 7, 9] or interpolating across the singular regions [26]. We adopt here a more brute force approach and recur to quadrupole precision. In Fig. (1), we see three more curves marked [qp]: they correspond to the numerical accuracy on the same phase space points when the one-loop amplitude is computed in quadrupole precision. Out of 100,000 phase space points sampled, not a single one has an accuracy worse than  $10^{-4}$  and, at quadrupole precision we see no appreciable worsening of the accuracy with increasing  $N$ . Therefore up to  $N = 11$  (and probably even for more gluons) quadrupole precision is sufficient to guarantee an accuracy needed for any next-to-leading order QCD correction. If higher precision is desired one can choose to evaluate the few phase space points which have insufficient precision using some arbitrary precision package, at the cost of higher computation time. We note that while the plots here presented are for the MHV amplitudes, we performed a similar study for the finite amplitudes ( $A_N^{[1]}(+ \dots +)$ ,  $A_N^{[1]}(- + \dots +)$ ) and obtain very similar results. This indicates that the accuracy is essentially independent of the helicities of the external gluons.

A very important property of this method is that the time needed to compute one-loop amplitudes does not grow factorially with the number of external legs; indeed it is straightforward



to estimate the scaling of time with the number of gluons  $N$ . The calculation of tree-level amplitudes computed via Berends-Giele recursion relations with caching of previously computed amplitudes requires a time which grows as  $\tau_{\text{tree},N} \propto N^4$  [27]. The total number of tree amplitudes that one needs to evaluate to get a one-loop amplitudes is given by

$$n_{\text{tree}} = \{(D_{s_1} - 2)^2 + (D_{s_2} - 2)^2\} \times \left( 5 c_{5,\text{max}} \binom{N}{5} + 4 c_{4,\text{max}} \binom{N}{4} + 3 c_{3,\text{max}} \binom{N}{3} + 2 c_{2,\text{max}} \left[ \binom{N}{2} - N \right] \right), \quad (7)$$

where the first factor is due to the sum over polarization of the internal cut gluons in two integer dimensions  $D_{s_1}$  and  $D_{s_2}$ . The constants  $c_{m,\text{max}}$  denote the number of times one needs to perform a multiple cut in order to fully constrain the system of equations determining the master integral coefficients. Explicitly one has  $c_{5,\text{max}} = 1$ ,  $c_{4,\text{max}} = 5$ ,  $c_{3,\text{max}} = 10$ , and  $c_{2,\text{max}} = 10$ . The integer number in front counts the number of tree amplitudes per multiple cut, finally the binomial coefficients corresponds to the number of possible cuts (for two point functions we subtract the vanishing contributions of the external self energy graphs). It follows that the time needed to evaluate a one-loop ordered amplitude will for large  $N$  scale as

$$\tau_{\text{one-loop},N} \sim n_{\text{tree}} \cdot \tau_{\text{tree},N} \propto N^9. \quad (8)$$

In Fig. (2) we plot the time needed to compute tree (blue, dashed) and one-loop (red, solid) ordered amplitudes with alternating helicity signs for the gluons,  $A_N^{[1]}(+ - + - \dots)$ , as a function of the number of gluons in the range between four and twenty. Time estimates refer to using a 2.33 GHz Xeon processor. One can see that the times needed to compute tree and one-loop ordered amplitudes are consistent with a  $N^4$  and  $N^9$  growth respectively. When running in quadrupole precision rather than in double precision the evaluation time grows, but the scaling with  $N$  remains unchanged. Finally we remark that the time is independent on the helicities of the external gluons.

### 1.3 Discussion and outlook

The results presented here are based on  $D$ -dimensional unitarity implemented in the Fortran 90 code **Rocket**. The very mild, power-like increase in computational time and the numerical stability of the results demonstrate the power of this approach. The large number of gluons considered here demonstrates that the gluon case is fully solved as far as virtual amplitudes are concerned.

Recently this method has been applied also to other processes  $0 \rightarrow t\bar{t}ggg$  [28],  $0 \rightarrow q\bar{q}W + n$  gluons and  $0 \rightarrow q\bar{q}QQW + 1$  gluon [29]. These recent calculations demonstrate the generality of the approach and constitute first steps towards automated one-loop calculations.

## 2 Duality relation between one-loop integrals and single-cut phase-space integrals

*Author: Germán Rodrigo*

As discussed in Sec. , the physics program of the LHC requires the evaluation of multi-leg signal and background processes at next-to-leading order (NLO). In the recent years, important efforts have been devoted to the calculation of many  $2 \rightarrow 3$  processes and some  $2 \rightarrow 4$  processes (see, e.g., [10]).

We have recently proposed a method [30–32] to numerically compute multi-leg one-loop cross sections in perturbative field theories. The starting point of the method is a duality relation between one-loop integrals and phase-space integrals. The duality relation requires to properly regularize propagators by a complex Lorentz-covariant prescription, which is different from the customary  $+i0$  prescription of the Feynman propagators. This duality relation has analogies with the Feynman’s Tree Theorem (FTT) [33], but involves only single cuts of the one-loop Feynman diagrams.

The duality relation between one-loop integrals and single-cut phase-space integrals is obtained [32] by applying the Cauchy residue theorem to a generic one-loop integral  $L^{(N)}$ :

$$L^{(N)}(p_1, p_2, \dots, p_N) = \int_q \prod_{i=1}^N G(q_i) , \quad \int_q \dots \equiv -i \int \frac{d^d q}{(2\pi)^d} \dots , \quad (9)$$

where  $q_i = q + \sum_{k=1}^i p_k$  are the momenta of the internal lines, with  $q$  the loop momentum, and  $p_i$  ( $\sum_{i=1}^N p_i = 0$ ) the external (outgoing and clockwise ordered) momenta, and  $G$  is the customary Feynman propagator, which for massless internal lines is given by

$$G(q) \equiv \frac{1}{q^2 + i0} . \quad (10)$$

In the complex plane of the loop energy  $q_0$  the Feynman propagator has two poles; the pole with positive (negative) energy is slightly displaced below (above) the real axis. Hence, by using the Cauchy residue theorem in the  $q_0$  complex plane, with the integration contour closed at  $\infty$  in the lower half-plane, we obtain

$$L^{(N)}(p_1, p_2, \dots, p_N) = -2\pi i \int_q \sum \text{Res}_{\{\text{Im } q_0 < 0\}} \left[ \prod_{i=1}^N G(q_i) \right] . \quad (11)$$

The Feynman propagators produce  $N$  poles in the lower half-plane that contribute to the residues in Eq. (11). The calculation of these residues is elementary, but it involves several subtleties. We get

$$\text{Res}_{\{i^{\text{th}} \text{ pole}\}} \frac{1}{q_i^2 + i0} = \int dq_0 \delta_+(q_i^2) . \quad (12)$$

This result shows that considering the residue of the Feynman propagator of the internal line with momentum  $q_i$  is equivalent to cutting that line by including the corresponding on-shell propagator  $\delta_+(q_i^2)$ . The other propagators  $G(q_j)$ , with  $j \neq i$ , which are not singular at the value of the pole of  $G(q_i)$ , contribute as follows [32]:

$$\prod_{j \neq i} \frac{1}{q_j^2 + i0} \bigg|_{q_i^2 = -i0} = \prod_{j \neq i} \frac{1}{q_j^2 - i0 \eta(q_j - q_i)} , \quad (13)$$

where  $\eta$  is a future-like vector, i.e. a  $d$ -dimensional vector that can be either light-like ( $\eta^2 = 0$ ) or time-like ( $\eta^2 > 0$ ) with positive definite energy ( $\eta_0 \geq 0$ ). The calculation of the residue at the pole of the  $i^{\text{th}}$  internal line modifies the  $i0$  prescription of the propagators of the other

internal lines of the loop. This modified regularization is named ‘dual’  $i0$  prescription, and the corresponding propagators are named ‘dual’ propagators. The dual prescription arises from the fact that the original Feynman propagator  $1/(q_j^2 + i0)$  is evaluated at the *complex* value of the loop momentum  $q$ , which is determined by the location of the pole at  $q_i^2 + i0 = 0$ . The presence of  $\eta$  is a consequence of the fact that the residue at each of the poles is not a Lorentz-invariant quantity, because a given system of coordinates has to be specified to apply the residue theorem. Different choices of the future-like vector  $\eta$  are equivalent to different choices of the coordinate system. The Lorentz-invariance of the loop integral is, however, recovered after summing over all the residues.

Inserting the results of Eqs. (12)-(13) in Eq. (11) gives us the duality relation between one-loop integrals and single-cut phase-space integrals [32]:

$$L^{(N)} = -\tilde{L}^{(N)}, \quad (14)$$

where the explicit expression of the phase-space integral  $\tilde{L}^{(N)}$  is

$$\tilde{L}^{(N)}(p_1, p_2, \dots, p_N) = \int_q \sum_{i=1}^N \tilde{\delta}(q_i) \prod_{\substack{j=1 \\ j \neq i}}^N \frac{1}{q_j^2 - i0 \eta(q_j - q_i)}, \quad (15)$$

with  $\tilde{\delta}(q) \equiv 2\pi i \delta_+(q^2)$ . Contrary to the FTT, the duality relation involves single-cut contributions only. This result is achieved by replacing the Feynman propagators in  $L^{(N)}$  by dual propagators in  $\tilde{L}^{(N)}$ , which depend on the auxiliary vector  $\eta$ . However,  $\tilde{L}^{(N)}$  does not depend on  $\eta$ , provided it is fixed to be the same in all its contributing single-cut terms (dual integrals). The duality relation, therefore, directly expresses the one-loop integral as the phase-space integral of a tree-level quantity. In the case of the FTT, the relation between loop and tree-level quantities is more involved, since the multiple-cut contributions contain integrals of expressions that correspond to the product of  $m$  tree-level diagrams over the phase-space for different number of particles.

The FTT and the duality theorem can be directly related starting from a basic identity between dual and Feynman propagators [32]:

$$\tilde{\delta}(q) \frac{1}{2qk + k^2 - i0 \eta k} = \tilde{\delta}(q) \left[ G(q+k) + \theta(\eta k) \tilde{\delta}(q+k) \right]. \quad (16)$$

This identity applies to the dual propagators when they are inserted in a single-cut integral. The proof of equivalence of the FTT and the duality theorem is purely algebraic [32]. We explicitly illustrate it by considering the massless two-point function  $L^{(2)}(p_1, p_2)$ . Its dual representation is

$$\tilde{L}^{(2)}(p_1, p_2) = \int_q \tilde{\delta}(q) \left( \frac{1}{2qp_1 + p_1^2 - i0 \eta p_1} + (p_1 \leftrightarrow p_2) \right). \quad (17)$$

Inserting Eq. (16) in Eq. (17), we obtain

$$\tilde{L}^{(2)}(p_1, p_2) = L_{1\text{-cut}}^{(2)}(p_1, p_2) + [\theta(\eta p_1) + \theta(\eta p_2)] L_{2\text{-cut}}^{(2)}(p_1, p_2), \quad (18)$$

where the  $m$ -cut integrals  $L_{m\text{-cut}}^{(2)}$  are the contributions with precisely  $m$  delta functions:

$$L_{1\text{-cut}}^{(2)}(p_1, p_2) = \int_q \tilde{\delta}(q) (G(q + p_1) + G(q + p_2)) , \quad L_{2\text{-cut}}^{(2)}(p_1, p_2) = \int_q \tilde{\delta}(q) \tilde{\delta}(q + p_1) . \quad (19)$$

Owing to momentum conservation (namely,  $p_1 + p_2 = 0$ ),  $\theta(\eta p_1) + \theta(\eta p_2) = 1$ , and then the dual and the FTT representations of the two-point function are equivalent. The proof of equivalence in the case of higher  $N$ -point functions proceeds in a similar way [32], the key ingredient simply being the constraint of *momentum conservation*.

The extension of the duality relation to include propagators with real finite masses  $M_i$  is straightforward. The massless on-shell delta function  $\tilde{\delta}(q_i)$  is replaced by  $\tilde{\delta}(q_i; M_i) = 2\pi i \delta_+(q_i^2 - M_i^2)$  when a massive loop internal line is cut to obtain the dual representation. The  $i0$  prescription of the dual propagators is not affected by real masses. The corresponding dual propagator is

$$\frac{1}{q_j^2 - M_j^2 - i0 \eta(q_j - q_i)} . \quad (20)$$

Unstable particles, in contrast, introduce a finite imaginary contribution in their propagators. The form of the complex-mass propagators is scheme dependent, but their poles in the  $q_0$  complex plane are located at a finite imaginary distance from the real axis. Then, when complex-mass propagators are cut in the duality relation, the  $+i0$  prescription of the usual Feynman propagators can be removed.

The polarization tensor of a spin-one gauge boson has in general the form

$$d^{\mu\nu}(q) = -g^{\mu\nu} + (\zeta - 1) \ell^{\mu\nu}(q) G_G(q) . \quad (21)$$

The second term on the right-hand side is absent only in the 't Hooft–Feynman gauge ( $\zeta = 1$ ). The tensor  $\ell^{\mu\nu}(q)$ , which propagates longitudinal polarizations, has a polynomial dependence on the momentum  $q$  and, therefore, it does not interfere with the residue theorem. The factor  $G_G(q)$  ('gauge-mode' propagator), however, can introduce extra unphysical poles (i.e. in addition to the poles of the associated Feynman propagator) that will modify the duality relation. Apart from the 't Hooft–Feynman gauge, the duality relation in the form presented here, i.e. with the inclusion of the sole single-cut terms from the Feynman propagators, turns out to be valid [32] in spontaneously-broken gauge theories in the unitary gauge, and in unbroken gauge theories in physical gauges specified by a gauge vector  $n^\nu$ , *provided* the dual vector  $\eta^\mu$  is chosen such that  $n \cdot \eta = 0$ . This excludes gauges where  $n^\nu$  is time-like. In any other gauge, additional single-cut terms from the absorptive contribution of the unphysical gauge poles have to be introduced in the duality relation.

The duality relation can be applied to evaluate not only basic one-loop integrals  $L^{(N)}$  but also complete one-loop quantities  $\mathcal{A}^{(1\text{-loop})}$  (such as Green's functions and scattering amplitudes). The analogue of Eqs. (14) and (15) is the following duality relation [32]:

$$\mathcal{A}^{(1\text{-loop})} = -\tilde{\mathcal{A}}^{(1\text{-loop})} . \quad (22)$$

The expression  $\tilde{\mathcal{A}}^{(1\text{-loop})}$  on the right-hand side is obtained from  $\mathcal{A}^{(1\text{-loop})}$  in the same way as  $\tilde{L}^{(N)}$  is obtained from  $L^{(N)}$ : starting from any Feynman diagram in  $\mathcal{A}^{(1\text{-loop})}$ , and considering

all possible replacements of each Feynman propagator  $G(q_i)$  in the loop with the cut propagator  $\tilde{\delta}(q_i; M_i)$ , and then replacing the uncut Feynman propagators with dual propagators. All the other factors in the Feynman diagrams are left unchanged in going from  $\mathcal{A}^{(1\text{-loop})}$  to  $\tilde{\mathcal{A}}^{(1\text{-loop})}$ .

Equation (22) establishes a correspondence between the one-loop Feynman diagrams contributing to  $\mathcal{A}^{(1\text{-loop})}$  and the tree-level Feynman diagrams contributing to the phase-space integral in  $\tilde{\mathcal{A}}^{(1\text{-loop})}$ . How are these tree-level Feynman diagrams related to those contributing to the tree-level expression  $\mathcal{A}^{(\text{tree})}$ , i.e. the tree-level counterpart of  $\mathcal{A}^{(1\text{-loop})}$ ? The answer to this question is mainly a matter of combinatorics of Feynman diagrams. If  $\mathcal{A}^{(1\text{-loop})}$  is an off-shell Green's function, the phase-space integrand in  $\tilde{\mathcal{A}}^{(1\text{-loop})}$  is directly related to  $\mathcal{A}^{(\text{tree})}$  [32]. In a sketchy form, we can write:

$$\mathcal{A}_N^{(1\text{-loop})}(\dots) \sim \int_q \sum_P \tilde{\delta}(q; M_P) \tilde{\mathcal{A}}_{N+2}^{(\text{tree})}(q, -q, \dots), \quad (23)$$

where  $\sum_P$  denotes the sum over all the types of particles and antiparticles that can propagate in the loop internal lines, and  $\tilde{\mathcal{A}}^{(\text{tree})}$  simply differs from  $\mathcal{A}^{(\text{tree})}$  by the replacement of dual and Feynman propagators. The extension of Eq. (23) to scattering amplitudes requires a careful treatment of the on-shell limit of the corresponding Green's functions [32].

In recent years much progress [20, 34–40] has been achieved on the computation of tree-level amplitudes, including results in compact analytic form. Using the duality relation, this amount of information at the tree level can be exploited for applications to analytic calculations at the one-loop level.

The computation of cross sections at next-to-leading order (NLO) requires the separate evaluation of real and virtual radiative corrections. Real (virtual) radiative corrections are given by multi-leg tree-level (one-loop) matrix elements to be integrated over the multiparticle phase-space of the physical process. The loop–tree duality discussed here, as well as other methods that relate one-loop and phase-space integrals, have an attractive feature [30, 41–44]: they recast the virtual radiative corrections in a form that closely parallels the contribution of the real radiative corrections. This close correspondence can help to directly combine real and virtual contributions to NLO cross sections. In particular, using the duality relation, we can apply [30] mixed analytical/numerical techniques to the evaluation of the one-loop virtual contributions. The (infrared or ultraviolet) divergent part of the corresponding dual integrals can be analytically evaluated in dimensional regularization. The finite part of the dual integrals can be computed numerically, together with the finite part of the real emission contribution. Partial results along these lines are presented in Refs. [30, 31] and further work is in progress. The extension of the duality relation from one-loop to two-loop Feynman diagrams is also under investigation.

### 3 Monte Carlo simulations of $t\bar{t}$ + jets at hadron colliders

*Author: Michele Treccani*

Because of the high energy of the Tevatron and the LHC, one of the most interesting fields refers to the class of events with multiple final states, giving rise to multiple jets with complicated topologies. There exist different strategies to tackle this problem, with distinct features and points of strength. The main problem is how to consistently compose the contributions due to Matrix Element (ME) calculations with the contributions of the Monte Carlo (MC) showering codes, in

order to exploit their complementarity and avoid at the same time the so-called double counting phenomenon [45–48].

We will here focus on a particular approach which relies on a consistent leading-logarithmic (LL) accuracy in the prediction of a final state  $F$  accompanied by a varying number of extra jets. The double counting is avoided adopting a so-called *matching algorithm* for matrix elements and parton shower. We study in detail the *MLM* matching [49–51] embedded in the the ME generator ALPGEN [52] in order to describe the  $t\bar{t}$  pair production at hadron colliders. First we will address its stability with respect to its internal parameters by comparing predictions obtained with different parameters.

In a step further, we will perform detailed numerical comparison between *MLM* matching and MC program MC@NLO which is an alternative strategy to cope with double counting and reaches next-to-leading order (NLO) accuracy in the prediction [53–55].

### 3.1 Consistency studies of the matching algorithm

In this section we study the overall consistency of the matching algorithm applied to the case of  $t\bar{t}$  final states. We shall consider  $t\bar{t}$  production at the Tevatron ( $p\bar{p}$  collisions at  $\sqrt{s} = 1.96$  TeV) and at the LHC ( $pp$  collisions at  $\sqrt{s} = 14$  TeV).

The generation parameters for the light partons are defined by the following kinematical cuts: the default values for the event samples at the Tevatron (LHC) are given by:  $p_T^{min}=20$  (30) GeV and  $R_{min}=0.7$  (0.7), while they are considered only in the geometrical region defined by  $\eta \leq 4$  (5).

The top particle is assumed to be stable, and therefore all jets coming from the decay of top quarks are neglected. For the shower evolution we use HERWIG, version 6.510 [56–58]. We stopped the evolution after the perturbative phase, in order to drop down all the common systematics that could smooth out any possible discrepancy between the various simulations. For all generations we chose the parton distribution function set MRST2001J [59], with renormalization and factorization scales squared set equal to:

$$\mu_R^2 = \mu_F^2 = \sum_{i=t,\bar{t},\text{jets}} [m_i^2 + (p_T^i)^2].$$

Jet observables are built out of the partons emerging from the shower in the rapidity range  $|\eta| \leq 6$  and adopting the cone algorithm GETJET [60]. The jet cone size is set to  $R_{cone} = 0.7$  and the minimum transverse momentum to define a jet at the Tevatron(LHC) is 15(20) GeV.

To our analysis, the important feature of the whole procedure is the presence of two set of parameters: the generation cuts and the matching cuts (see [49–51]). The first set is necessary to avoid the infrared (IR) and collinear singularities:  $p_T^{min}$ , the minimum transverse momentum of the extra parton(s) to be generated, and  $R_{min}$ , the minimum separation between extra-partons in the  $(\eta, \phi)$  plane. Along with these parameters, there exist an analogous set, but with slightly different meanings: the matching cuts  $E_T^{clus}$  and  $R_{match}$ .

We choose two independent variations of the generation and of two of the matching cuts, while keeping fixed our definition of the physical objects (the jets) and of the observables. In both cases, we find that these distribution are stable against reasonable variations of the internal parameters, with relative differences confined well below few percents.

Angular observables, such as  $\Delta R$  between jets, are more sensible, since they are directly related to the matching variables, nevertheless their agreement is within 10%.

The analysis at the LHC, which will not be shown here, leads to qualitatively and quantitatively similar results.



### 3.2 Comparisons with MC@NLO

We shall now compare in detail the description of  $t\bar{t}$  events as provided by ALPGEN and MC@NLO. For consistency with the MC@NLO approach, where only the  $\mathcal{O}(\alpha_s^3)$  ME effects are included, we use ALPGEN samples obtained by stopping the ME contributions only to 1 extra-parton besides the  $t\bar{t}$  pair. This strategy allow to highlight the different features of the two alternative approaches applied to same set of contributions. It is understood that a homogeneous comparison can only be done through the introduction of a proper K-factor, determined by the ratio of the total rates of the two predictions. We adopt the same simulation setup as before, modifying only the same factorization and renormalization scale in order to match MC@NLO's default:

$$\mu_R^2 = \mu_F^2 = \sum_{i=t,\bar{t}} \frac{1}{2} [m_i^2 + (p_T^i)^2].$$

The upper two rows of plots in Fig. 3 refer to inclusive properties of the  $t\bar{t}$  system, namely the transverse momentum and rapidity of the top and anti-top quark, the transverse momentum of the  $t\bar{t}$  pair, and the azimuthal angle  $\Delta\phi^{t\bar{t}}$  between the top and anti-top quark. The overall agreement is good, once ALPGEN is corrected with the proper K-factor (1.36 for the Tevatron, and 1.51 for the LHC), and no large discrepancy is seen between the two descriptions of the chosen distributions. The most significant differences (10 to 20%) are seen in the  $p_T^{top}$  distribution, ALPGEN's one being slightly softer.

In jet-related quantities, while the  $p_T$  of leading and sub-leading jets agree, instead the rapidity of the leading jet reveals two distinct patterns: MC@NLO predictions show a dip at  $y_1 = 0$ , which is not present in ALPGEN predictions. This difference is particularly marked at the Tevatron, but is very visible also at the LHC. This is shown in the right figure of the third row in Fig. 3. Visible differences are also present in the distribution of the first and second jet separation in  $(\eta, \phi)$  space,  $\Delta R_{1,2}$ . To understand the difference in the rapidity distribution, we look in more detail in Fig. 4 at some features in the MC@NLO description of the leading jet. For the  $p_T$  of the leading jet,  $p_{T,1}$ , we plot separately the contribution from the various components of the MC@NLO generation: events in which the shower is initiated by the LO  $t\bar{t}$  hard process, and events in which the shower is initiated by a  $t\bar{t} + q(g)$  hard process. In the latter we separate the contribution of positive- and negative-weight events, where the distribution of negative events is shown in absolute value. The plots show that for MC@NLO the contribution of the  $t\bar{t} + q(g)$  hard process is almost negligible over most of the relevant range and becomes appreciable only for very large values of  $p_{T,1}$ . This hierarchy is stronger at the LHC than at the Tevatron.

Upper set of Fig. 5 shows the various contributions to the rapidity distribution  $y_1$  for different jet  $p_T$  thresholds. It appears that the  $y_1$  distribution resulting from the shower evolution of the  $t\bar{t}$  events in MC@NLO has a strong dip at  $y_1=0$ , a dip that cannot be compensated by the more central distributions of the jet from the  $t\bar{t} + q(g)$  hard process, given its marginal role in the overall jet rate.

That the dip at  $y_1=0$  is a feature typical of jet emission from the  $t\bar{t}$  state in HERWIG is shown in central set of Fig. 5, obtained from the standard HERWIG code rather than from MC@NLO. We speculate that this feature is a consequence of the dead-cone description of hard emission from heavy quarks implemented in the HERWIG shower algorithm. To complete our analysis, we show in lower set of Fig. 5 the comparison between the ALPGEN, MC@NLO and the parton-level  $y_1$  spectra, for different jet  $p_T$  thresholds. We notice that at large  $p_T$ , where the Sudakov effects that induce potential differences between the shower and the PL results have vanished, the ALP-

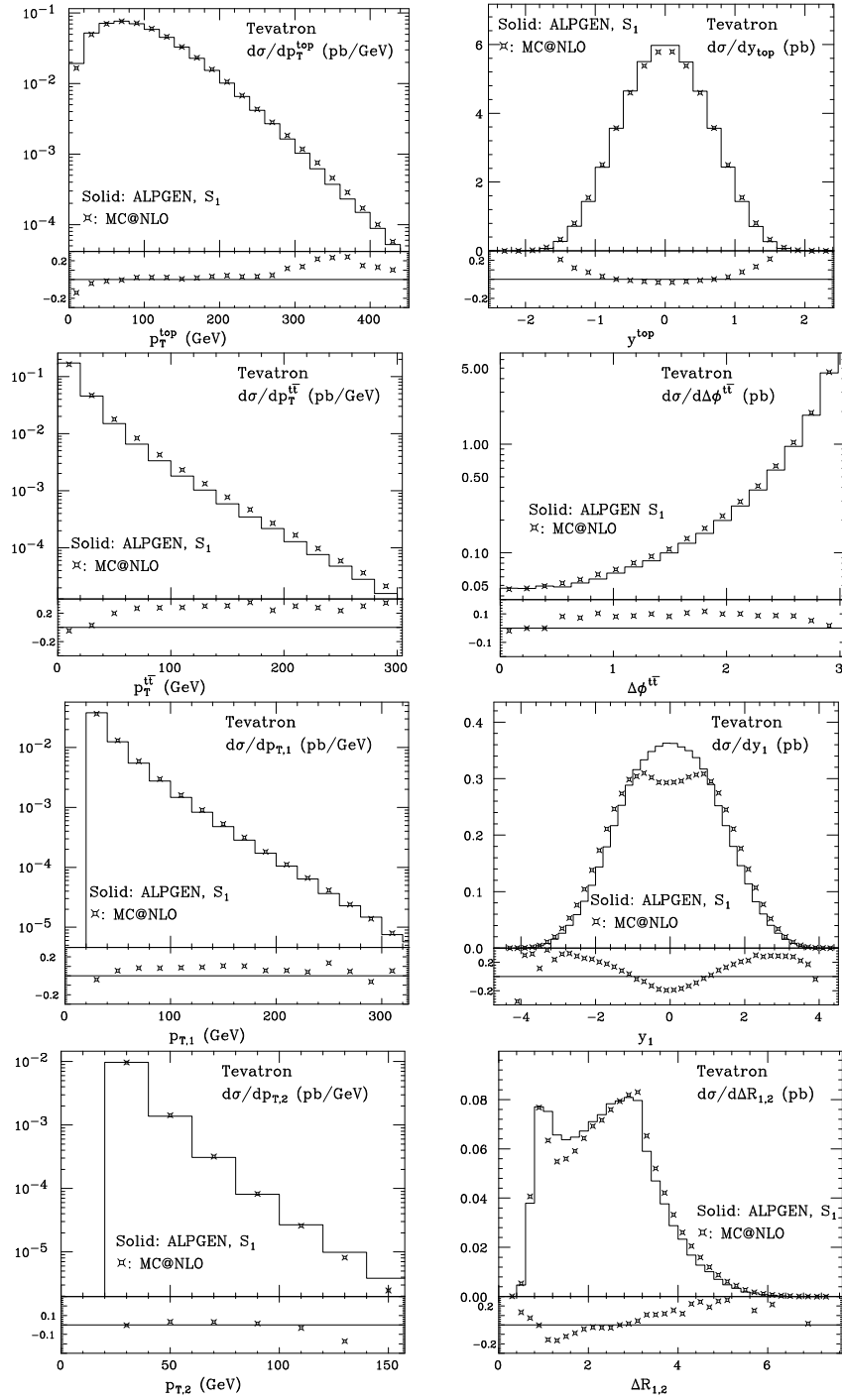


Fig. 3: Comparison of ALPGEN (histogram) and MC@NLO (plot) distributions, at the Tevatron. The ALPGEN results are rescaled to MC@NLO, using the K factor of 1.36. The relative difference  $(\text{MC@NLO} - \text{ALPGEN})/\text{ALPGEN}$  is shown at the bottom of each plot.



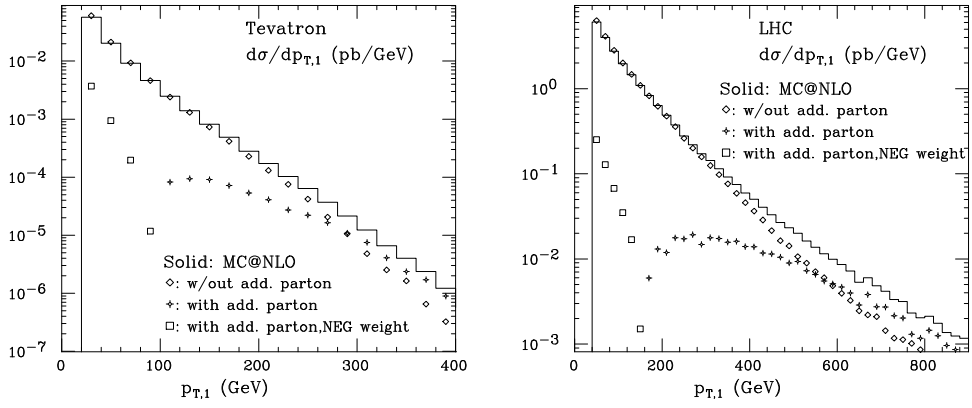


Fig. 4: Contributions to the transverse momentum of the leading jet in MC@NLO. Tevatron (left) and LHC (right).

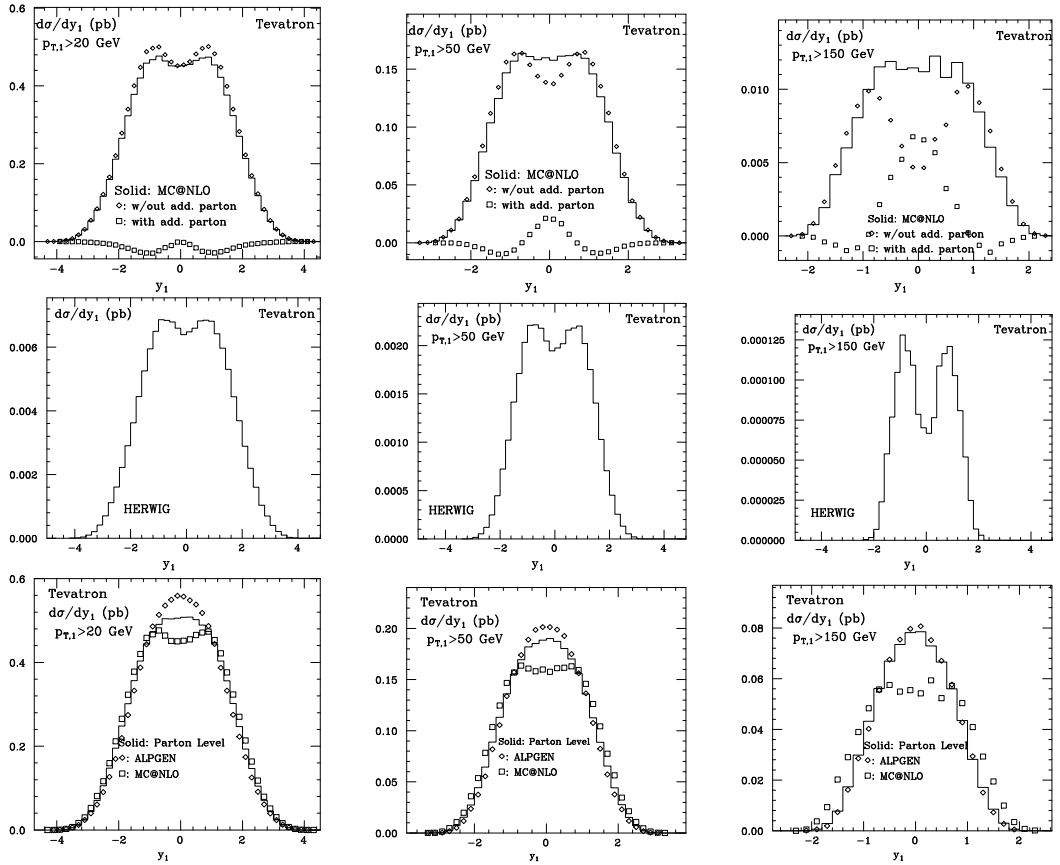


Fig. 5: Rapidity of the leading jet  $y_1$  at Tevatron for various jet  $p_T$  thresholds. Upper set: MC@NLO, with partial contributions. Central set: HERWIG. Lower set: comparison between ALPGEN, MC@NLO, and the parton level predictions

GEN result reproduces well the PL result, while still differing significantly from the MC@NLO distributions.

### 3.3 Conclusions

The analysis presented here is focused on the MC simulations of the  $t\bar{t}$ +jets process as predicted by ALPGEN and its matching algorithm. Several checks of that algorithm have shown its internal consistency, and pinpoint a mild dependence of the results on the parameters that define it. The consistency of the approach is then confirmed by the comparison with MC@NLO. In particular, inclusive variables show excellent agreement, once the NLO/LO K-factor is included.

Instead we found a rather surprising difference between the predictions of two codes for the rapidity distribution of the leading jet accompanying the  $t\bar{t}$  pair. In view of the relevance of this variable for the study at the LHC of new physics signals, it is important to further investigate the origin of this discrepancy, with independent calculations, and with a direct comparison with data. Preliminary results obtained with the new positive-weight NLO shower MC introduced in [61–63] appear to support the distributions predicted by ALPGEN.

## 4 A subtraction scheme for jet cross sections at NNLO

*Author: Gabor Somogyi*

One of the main difficulties in performing NNLO calculations is that the finite higher-order corrections are sums of several pieces which are separately infrared (IR) divergent in  $d = 4$  spacetime dimensions. To handle the IR singularities present in the intermediate stages of calculation in a general (process- and observable-independent) way is non-trivial already at NLO accuracy, where however several solutions are known [2, 3, 64–67]. It is perhaps fair to say that the most widely used is the dipole subtraction scheme of Ref. [2], which constructs a completely general and fully local approximate cross section to regularize real radiation at NLO. Setting up a general subtraction algorithm analogous to that of Ref. [2] but at NNLO accuracy has proved to be rather difficult problem. Here we give a progress report on constructing such a scheme.

### 4.1 Subtraction scheme at NNLO

In perturbative QCD the formal loop expansion for any production rate to NNLO accuracy reads

$$\sigma = \sigma^{\text{LO}} + \sigma^{\text{NLO}} + \sigma^{\text{NNLO}} + \dots \quad (24)$$

Let us consider  $e^+e^- \rightarrow m$  jet production. Then the NNLO correction may be written as

$$\sigma^{\text{NNLO}} = \int_{m+2} d\sigma_{m+2}^{\text{RR}} J_{m+2} + \int_{m+1} d\sigma_{m+1}^{\text{RV}} J_{m+1} + \int_m d\sigma_m^{\text{VV}} J_m, \quad (25)$$

*i.e.* it is the sum of a doubly-real, a real-virtual and a doubly-virtual contribution, each IR divergent in  $d = 4$  spacetime dimensions.

The general strategy of subtraction consists of the following steps: (i) we regularize all integrals in Eq. (25) by dimensional regularization then (ii) we reshuffle the singularities between the three terms by adding and subtracting suitably defined *approximate cross sections* so that finally we rewrite Eq. (25) as

$$\sigma^{\text{NNLO}} = \int_{m+2} d\sigma_{m+2}^{\text{NNLO}} + \int_{m+1} d\sigma_{m+1}^{\text{NNLO}} + \int_m d\sigma_m^{\text{NNLO}}, \quad (26)$$

where now each term on the right hand side is finite in  $d = 4$  by construction. According to Ref. [68] we have

$$d\sigma_{m+2}^{\text{NNLO}} = \left\{ d\sigma_{m+2}^{\text{RR}} J_{m+2} - d\sigma_{m+2}^{\text{RR},A_2} J_m - \left[ d\sigma_{m+2}^{\text{RR},A_1} J_{m+1} - d\sigma_{m+2}^{\text{RR},A_{12}} J_m \right] \right\}_{\varepsilon=0}, \quad (27)$$

$$d\sigma_{m+1}^{\text{NNLO}} = \left\{ \left[ d\sigma_{m+1}^{\text{RV}} + \int_1 d\sigma_{m+2}^{\text{RR},A_1} \right] J_{m+1} - \left[ d\sigma_{m+1}^{\text{RV},A_1} + \left( \int_1 d\sigma_{m+2}^{\text{RR},A_1} \right)^{A_1} \right] J_m \right\}_{\varepsilon=0} \quad (28)$$

and

$$d\sigma_m^{\text{NNLO}} = \left\{ d\sigma_m^{\text{VV}} + \int_2 \left[ d\sigma_{m+2}^{\text{RR},A_2} - d\sigma_{m+2}^{\text{RR},A_{12}} \right] + \int_1 \left[ d\sigma_{m+1}^{\text{RV},A_1} + \left( \int_1 d\sigma_{m+2}^{\text{RR},A_1} \right)^{A_1} \right] \right\}_{\varepsilon=0} J_m. \quad (29)$$

In Eq. (27) above  $d\sigma_{m+2}^{\text{RR},A_1}$  and  $d\sigma_{m+2}^{\text{RR},A_2}$  regularize the singly- and doubly-unresolved limits of  $d\sigma_{m+2}^{\text{RR}}$  respectively. The role of  $d\sigma_{m+2}^{\text{RR},A_{12}}$  is two-fold: it must regularize the singly-unresolved limits of  $d\sigma_{m+2}^{\text{RR},A_2}$  and the doubly-unresolved limits of  $d\sigma_{m+2}^{\text{RR},A_1}$  simultaneously. In Eq. (28)  $d\sigma_{m+1}^{\text{RV},A_1}$  and  $\left( \int_1 d\sigma_{m+2}^{\text{RR},A_1} \right)^{A_1}$  regularize the singly-unresolved limits of  $d\sigma_{m+1}^{\text{RV}}$  and  $\int_1 d\sigma_{m+2}^{\text{RR},A_1}$  respectively.

## 4.2 Devising approximate cross sections

Attempting to use the known (multiple) IR factorization properties of (one-loop) squared matrix elements to devise the approximate cross sections in Eqs. (27) and (28) above, we are immediately faced with two problems. First, the various limits overlap in some regions of phase space, thus care needs to be taken to avoid multiple subtraction. Second, even once the factorization formulae are written in such a way that intersecting limits are disentangled so that multiple subtraction does not occur, the resulting expressions cannot be used as true subtraction terms because they are only defined in the strict soft and/or collinear limits. Thus, constructing the approximate cross sections proceeds in two steps: (i) we write all relevant factorization formulae in such a way that their overlap structure can be disentangled (“*matching of limits*”) and (ii) we define “*extensions*” of the formulae so that they are unambiguously defined away from the IR limits.

Let us consider first the matching of limits. A single parton, say  $r$ , can become unresolved in (i) the collinear limit, when for some hard parton  $i \neq r$  we have  $p_i || p_r$  and (ii) in the soft limit, when  $p_r \rightarrow 0$ . In these limits QCD squared matrix elements obey well-known universal factorization properties [69–72], which we exhibit below at tree level for the sake of being specific<sup>1</sup>

$$\mathbf{C}_{ir} |\mathcal{M}_{m+2}^{(0)}|^2 \propto \frac{1}{s_{ir}} \langle \mathcal{M}_{m+1}^{(0)} | \hat{P}_{ir}^{(0)}(z_i, k_\perp; \varepsilon) | \mathcal{M}_{m+1}^{(0)} \rangle, \quad (30)$$

$$\mathbf{S}_r |\mathcal{M}_{m+2}^{(0)}|^2 \propto \sum_{\substack{i,k \\ i \neq k}} \frac{s_{ik}}{s_{ir} s_{kr}} \langle \mathcal{M}_{m+1}^{(0)} | \mathbf{T}_i \mathbf{T}_r | \mathcal{M}_{m+1}^{(0)} \rangle. \quad (31)$$

To write Eqs. (30) and (31) above, we used the colour-state notation of Ref. [2] and the operator notation of taking the limits introduced in Ref. [73], while  $s_{jl} = 2p_j \cdot p_l$ , ( $j, l = i, k, r$ ),  $\hat{P}_{ir}^{(0)}$

<sup>1</sup>To keep the discussion as simple as possible, we only indicate the structure of the factorization formulae.

are the tree-level Altarelli–Parisi splitting kernels and finally  $z_i$  is the momentum-fraction carried by parton  $i$  in the  $p_{ir} \rightarrow p_i + p_r$  splitting. When parton  $r$  is both soft and collinear to the hard parton  $i$ , these limits overlap. To avoid double subtraction in this region of phase space, we must identify the common soft-collinear limit of Eqs. (30) and (31), which is found to be [73]

$$\mathbf{C}_{ir}\mathbf{S}_r|\mathcal{M}_{m+2}^{(0)}|^2 \propto \frac{1}{s_{ir}} \frac{2z_i}{1-z_i} \mathbf{T}_i^2 |\mathcal{M}_{m+1}^{(0)}|^2. \quad (32)$$

Thus the formal operator

$$\mathbf{A}_1 = \sum_r \left[ \sum_{i \neq r} \frac{1}{2} \mathbf{C}_{ir} + \left( \mathbf{S}_r - \sum_{i \neq r} \mathbf{C}_{ir} \mathbf{S}_r \right) \right] \quad (33)$$

counts each singly-unresolved limit precisely once and is free of double subtractions, therefore  $\mathbf{A}_1|\mathcal{M}_{m+2}^{(0)}|^2$  has the same singly-unresolved singularity structure as  $|\mathcal{M}_{m+2}^{(0)}|^2$  itself, *i.e.* it defines a candidate subtraction term for constructing  $d\sigma_{m+2}^{\text{RR},\mathbf{A}_1}$ . Similarly, applying the formal operator  $\mathbf{A}_1$  to *e.g.*  $2\Re\langle\mathcal{M}_{m+1}^{(0)}|\mathcal{M}_{m+1}^{(1)}\rangle$  defines a candidate subtraction term for defining  $d\sigma_{m+1}^{\text{RV},\mathbf{A}_1}$ , starting from the collinear [11, 74–76] and soft [77] factorization formulae for one-loop squared matrix elements.

The matching procedure is quite a bit more elaborate when two different partons, say  $r$  and  $s$ , become unresolved, which can arise in four different limits: (i) the triple collinear limit, when for some hard parton  $i \neq r, s$  we have  $p_i||p_r||p_s$ , (ii) the doubly single collinear limit, when for two distinct hard partons  $i \neq r, s$  and  $j \neq r, s$  we have  $p_i||p_r$  and  $p_j||p_s$ , (iii) the doubly soft-collinear limit, when for  $i \neq r, s$  we have  $p_i||p_r$  and  $p_s \rightarrow 0$ , and finally (iv) the double soft limit, when  $p_r \rightarrow 0$  and  $p_s \rightarrow 0$ . The factorization formulae appropriate for each of these limits are well-known (in particular the three-parton splitting functions and the double soft  $gg$  and  $q\bar{q}$  currents are given in Refs. [78–84] and Refs. [72, 85], respectively), and their highly non-trivial overlap structure was disentangled in Ref. [73]. To identify the intersection of limits, Ref. [73] computed all common limits explicitly, which is rather cumbersome. In [86], a simple and systematic procedure was proposed that leads directly to pure soft factorization formulae at any order and thus solves the problem of matching of limits in general. Finally (using the operator notation of Ref. [73]) we find that the symbolic operator

$$\begin{aligned} \mathbf{A}_2 = & \sum_r \sum_{s \neq r} \left\{ \sum_{i \neq r, s} \left[ \frac{1}{6} \mathbf{C}_{irs} + \sum_{j \neq i, r, s} \frac{1}{8} \mathbf{C}_{ir;js} + \frac{1}{2} \mathbf{C} \mathbf{S}_{ir;s} \right] + \frac{1}{2} \mathbf{S}_{rs} - \sum_{i \neq r, s} \left[ \frac{1}{2} \mathbf{C}_{irs} \mathbf{C} \mathbf{S}_{ir;s} \right. \right. \\ & \left. \left. + \sum_{j \neq i, r, s} \frac{1}{2} \mathbf{C}_{ir;js} \mathbf{C} \mathbf{S}_{ir;s} + \frac{1}{2} \mathbf{C}_{irs} \mathbf{S}_{rs} + \mathbf{C} \mathbf{S}_{ir;s} \mathbf{S}_{rs} - \sum_{j \neq i, r, s} \frac{1}{2} \mathbf{C}_{ir;js} \mathbf{S}_{rs} - \mathbf{C}_{irs} \mathbf{C} \mathbf{S}_{ir;s} \mathbf{S}_{rs} \right] \right\} \end{aligned} \quad (34)$$

counts each doubly-unresolved limit precisely once (without overlaps). Thus  $\mathbf{A}_2|\mathcal{M}_{m+2}^{(0)}|^2$  has the same doubly-unresolved singularity structure as  $|\mathcal{M}_{m+2}^{(0)}|^2$  itself and so defines a candidate subtraction term for constructing  $d\sigma_{m+2}^{\text{RR},\mathbf{A}_2}$ .

Finally, we must address the matching of the singly- and doubly-unresolved limits of  $|\mathcal{M}_{m+2}^{(0)}|^2$  which also overlap.  $d\sigma_{m+2}^{\text{RR},\mathbf{A}_{12}}$  is introduced in Eq. (27) precisely to avoid double subtraction in the intersecting regions of phase space. However the role of this approximate cross

section is quite delicate, because (i) in the doubly-unresolved limits it must regularize  $d\sigma_{m+1}^{\text{RR},A_1}$ , while (ii) in the singly-unresolved limits, it must regularize  $d\sigma_{m+2}^{\text{RR},A_2}$  and spurious singularities that appear in  $d\sigma_{m+2}^{\text{RR},A_1}$ . It is thus a highly non-trivial statement that the correct candidate subtraction term can be obtained by applying the symbolic singly-unresolved operator  $\mathbf{A}_1$  of Eq. (33) to  $\mathbf{A}_2|\mathcal{M}_{m+2}^{(0)}|^2$  [73]. That is,

$$(\mathbf{A}_1 + \mathbf{A}_2 - \mathbf{A}_1\mathbf{A}_2)|\mathcal{M}_{m+2}^{(0)}|^2 \quad (35)$$

has the same singularity structure as  $|\mathcal{M}_{m+2}^{(0)}|^2$  itself in all singly- and doubly-unresolved limits and is free of multiple subtractions.

The second step of defining the approximate cross sections calls for an extension of the limit formulae over the full phase space. As emphasized above, the candidate subtraction terms cannot yet be used as true subtraction terms because they are only well-defined in the strict limits. In order to define suitable extensions over the full phase space, we need to define momentum mappings  $\{p\}_{m+2} \rightarrow \{\tilde{p}\}_{m+1}$  and  $\{p\}_{m+2} \rightarrow \{\tilde{p}\}_m$  that (i) implement exact momentum conservation, (ii) lead to exact phase space factorization and (iii) respect the delicate structure of cancellations among the subtraction terms in the various limits. We find it convenient to define two types of singly-unresolved ( $\{p\}_{m+2} \rightarrow \{\tilde{p}\}_{m+1}$ ) mappings and four types of doubly-unresolved ( $\{p\}_{m+2} \rightarrow \{\tilde{p}\}_m$ ) mappings, corresponding to the basic types of limits that may occur (*i.e.* we define a collinear and a soft singly-unresolved mapping). The explicit forms of these momentum mappings may be found in Ref. [68] together with the full definitions of all approximate cross sections that appear in Eq. (27). The approximate cross sections in Eq. (28) are given explicitly in Refs. [87, 88].

At the risk of belabouring the point, we note again that all our momentum mappings lead to an exact factorization of the phase space in the symbolic form

$$d\phi_{m+2} = d\phi_{m+1}[dp_1] \quad \text{and} \quad d\phi_{m+2} = d\phi_m[dp_2], \quad (36)$$

thus the singular integrals of the subtraction terms over the phase space of the unresolved parton(s) can be computed once and for all, independent of the jet function and the rest of the phase space integration.

### 4.3 Conclusions

We have set up a general (process- and observable-independent) subtraction scheme for computing QCD jet cross sections at NNLO accuracy for processes with no coloured particles in the initial state. Our scheme can naturally be viewed as the generalization of the dipole subtraction scheme of Ref. [2] to NNLO. We have defined all approximate cross sections needed to regularize the  $m+2$  and  $m+1$  parton contributions (*i.e.* all terms in Eqs. (27) and (28)) explicitly. Our subtraction terms are *fully local*, *i.e.* all colour and azimuthal correlations are properly taken into account. Thus we can check the convergence of our subtraction terms to the doubly-real, or real-virtual cross sections in any unresolved limit explicitly. In addition, we have checked that the regularized doubly-real and real-virtual contributions to  $e^+e^- \rightarrow 3$  jet production are finite by computing the first three moments of the thrust and  $C$ -parameter distributions, see Tab. 1. In order to finish the definition of the subtraction scheme, one must still compute the singly- and doubly-unresolved integrals of the approximate cross sections that appear in Eq. (29). All

n	$\langle(1-t)^n\rangle_{\text{RV}}/10^1$	$\langle C^n\rangle_{\text{RV}}/10^1$	$\langle(1-t)^n\rangle_{\text{RR}}$	$\langle C^n\rangle_{\text{RR}}$
1	$123 \pm 1$	$433 \pm 5$	$-92.7 \pm 3.4$	$-344 \pm 14$
2	$25.5 \pm 0.2$	$325 \pm 2$	$-3.07 \pm 0.43$	$-142 \pm 3$
3	$4.79 \pm 0.03$	$180 \pm 1$	$2.01 \pm 0.12$	$6.29 \pm 1.87$

Table 1: The real-virtual and doubly-real contributions to the first three moments of the thrust and  $C$ -parameter distribution in  $e^+e^- \rightarrow 3$  jets.

singly-unresolved integrals (denoted by  $\int_1$  in Eqs. (28) and (29) above) have recently been computed [87, 89–91] and we expect that the techniques applied will be flexible enough to compute the doubly-unresolved integrals (denoted by  $\int_2$  in Eq. (29)) as well. This is work in progress.

We are grateful to our collaborators: U. Aglietti, P. Bolzoni, V. Del Duca, C. Duhr and S. Moch. This work was supported in part by Hungarian Scientific Research Fund grant OTKA K-60432 and by the Swiss National Science Foundation (SNF) under contract 200020-117602.

## References

- [1] R. K. Ellis, D. A. Ross, and A. E. Terrano, Nucl. Phys. **B178**, 421 (1981).
- [2] S. Catani and M. H. Seymour, Nucl. Phys. **B485**, 291 (1997), [arXiv:hep-ph/9605323](#).
- [3] S. Frixione, Z. Kunszt, and A. Signer, Nucl. Phys. **B467**, 399 (1996), [arXiv:hep-ph/9512328](#).
- [4] E. W. N. Glover, Nucl. Phys. Proc. Suppl. **116**, 3 (2003), [arXiv:hep-ph/0211412](#).
- [5] W. T. Giele and E. W. N. Glover, JHEP **04**, 029 (2004), [arXiv:hep-ph/0402152](#).
- [6] R. K. Ellis, W. T. Giele, and G. Zanderighi, Phys. Rev. **D73**, 014027 (2006), [arXiv:hep-ph/0508308](#).
- [7] A. Denner and S. Dittmaier, Nucl. Phys. **B734**, 62 (2006), [arXiv:hep-ph/0509141](#).
- [8] T. Binoth, J. P. Guillet, G. Heinrich, E. Pilon, and T. Reiter (2008), [arXiv:0810.0992 \[hep-ph\]](#).
- [9] W. Giele, E. W. N. Glover, and G. Zanderighi, Nucl. Phys. Proc. Suppl. **135**, 275 (2004), [arXiv:hep-ph/0407016](#).
- [10] NLO Multileg Working Group Collaboration, Z. Bern *et al.* (2008), [arXiv:0803.0494 \[hep-ph\]](#).
- [11] Z. Bern, L. J. Dixon, D. C. Dunbar, and D. A. Kosower, Nucl. Phys. **B425**, 217 (1994), [arXiv:hep-ph/9403226](#).

- [12] R. Britto, F. Cachazo, and B. Feng, Nucl. Phys. **B725**, 275 (2005), arXiv:hep-th/0412103.
- [13] C. F. Berger, Z. Bern, L. J. Dixon, D. Forde, and D. A. Kosower, Phys. Rev. **D75**, 016006 (2007), arXiv:hep-ph/0607014.
- [14] C. F. Berger *et al.*, Phys. Rev. **D78**, 036003 (2008), arXiv:0803.4180 [hep-ph].
- [15] R. K. Ellis, W. T. Giele, and Z. Kunszt, JHEP **03**, 003 (2008), arXiv:0708.2398 [hep-ph].
- [16] W. T. Giele, Z. Kunszt, and K. Melnikov, JHEP **04**, 049 (2008), arXiv:0801.2237 [hep-ph].
- [17] W. T. Giele and G. Zanderighi, JHEP **06**, 038 (2008), arXiv:0805.2152 [hep-ph].
- [18] G. Ossola, C. G. Papadopoulos, and R. Pittau, Nucl. Phys. **B763**, 147 (2007), arXiv:hep-ph/0609007.
- [19] Z. Bern and D. A. Kosower, Nucl. Phys. **B362**, 389 (1991).
- [20] F. Berends and W. Giele, Nucl. Phys. **B306**, 759 (1988).
- [21] Z. Bern, L. J. Dixon, D. C. Dunbar, and D. A. Kosower, Nucl. Phys. **B435**, 59 (1995), arXiv:hep-ph/9409265.
- [22] R. K. Ellis and G. Zanderighi, JHEP **02**, 002 (2008), arXiv:0712.1851 [hep-ph].
- [23] R. K. Ellis, W. T. Giele, and G. Zanderighi, JHEP **05**, 027 (2006), arXiv:hep-ph/0602185.
- [24] D. Forde and D. A. Kosower, Phys. Rev. **D73**, 061701 (2006), arXiv:hep-ph/0509358.
- [25] R. Kleiss, W. J. Stirling, and S. D. Ellis, Comput. Phys. Commun. **40**, 359 (1986).
- [26] V. Del Duca, W. Kilgore, C. Oleari, C. Schmidt, and D. Zeppenfeld, Nucl. Phys. **B616**, 367 (2001), arXiv:hep-ph/0108030.
- [27] R. Kleiss and H. Kuijf, Nucl. Phys. **B312**, 616 (1989).
- [28] R. K. Ellis, W. T. Giele, Z. Kunszt, and K. Melnikov (2008), arXiv:0806.3467 [hep-ph].
- [29] R. K. Ellis, W. T. Giele, Z. Kunszt, K. Melnikov, and G. Zanderighi (2008), arXiv:0810.2762 [hep-ph].
- [30] S. Catani. Presented at the Workshop  $HP^2$ : High Precision for Hard Processes at the LHC, Sept. 2006, Zurich, Switzerland.
- [31] T. Gleisberg. Ph.D. Thesis, University of Dresden. .



- [32] S. Catani, T. Gleisberg, F. Krauss, G. Rodrigo, and J.-C. Winter, *JHEP* **09**, 065 (2008), [arXiv:0804.3170 \[hep-ph\]](#).
- [33] R. Feynman, *Acta Phys. Polon.* **24**, 697 (1963).
- [34] M. Mangano and S. Parke, *Phys. Rept.* **200**, 301 (1991), [arXiv:hep-th/0509223](#).
- [35] F. Caravaglios and M. Moretti, *Phys. Lett.* **B358**, 332 (1995), [arXiv:hep-ph/9507237](#).
- [36] R. K. P. Draggotis and C. Papadopoulos, *Phys. Lett.* **B439**, 157 (1998), [arXiv:hep-ph/9807207](#).
- [37] R. K. P. Draggotis and C. Papadopoulos, *Eur. Phys. J.* **C24**, 447 (2002), [arXiv:hep-ph/0202201](#).
- [38] P. S. F. Cachazo and E. Witten, *JHEP* **09**, 006 (2004), [arXiv:hep-th/0403047](#).
- [39] F. C. R. Britto and B. Feng, *Nucl. Phys.* **B715**, 499 (2005), [arXiv:hep-th/0412308](#).
- [40] B. F. R. Britto, F. Cachazo and E. Witten, *Phys. Rev. Lett.* **94**, 181602 (2005), [arXiv:hep-th/0501052](#).
- [41] D. Soper, *Phys. Rev. Lett.* **81**, 2638 (1998), [arXiv:hep-ph/9804454](#).
- [42] M. Kramer and D. E. Soper, *Phys. Rev.* **D66**, 054017 (2002), [arXiv:hep-ph/0204113](#).
- [43] T. Kleinschmidt. DESY-THESIS-2007-042.
- [44] M. Moretti, F. Piccinini, and A. D. Polosa (2008), [arXiv:0802.4171 \[hep-ph\]](#).
- [45] R. K. S. Catani, F. Krauss and B. Webber, *JHEP* **11**, 063 (2001).
- [46] L. Lonnblad, *JHEP* **05**, 046 (2002).
- [47] F. Krauss, *JHEP* **08**, 015 (2002).
- [48] S. Hoche *et al.* (2006). [hep-ph/0602031](#).
- [49] M. Mangano (2002). [www-cpd.fnal.gov/personal/mreenna/tuning/nov2002/mlm.pdf](#).
- [50] M. L. Mangano, M. Moretti, F. Piccinini, and M. Treccani, *JHEP* **01**, 013 (2007), [arXiv:hep-ph/0611129](#).
- [51] J. Alwall *et al.*, *Eur. Phys. J.* **C53**, 473 (2008).
- [52] M. L. Mangano, M. Moretti, F. Piccinini, R. Pittau, and A. D. Polosa, *JHEP* **07**, 001 (2003), [arXiv:hep-ph/0206293](#).
- [53] S. Frixione and B. R. Webber, *JHEP* **06**, 029 (2002), [hep-ph/0204244](#).



- [54] S. Frixione, P. Nason, and B. R. Webber, *JHEP* **08**, 007 (2003), [hep-ph/0305252](#).
- [55] S. Frixione and B. Webber (2006). The MC@NLO 3.2 event generator, [hep-ph/0601192](#).
- [56] G. Marchesini and B. Webber, *Nucl. Phys.* **B310**, 461 (1988).
- [57] G. Marchesini *et al.*, *Comput. Phys. Commun.* **67**, 465 (1992).
- [58] G. Corcella *et al.*, *JHEP* **01**, 010 (2001), [arXiv:hep-ph/0011363](#).
- [59] W. S. A.D. Martin, R.G. Roberts and R. Thorne, *Eur. Phys. J.* **C23**, 73 (2002).
- [60] E. Paige and S. Protopopescu. Physics of the SSC, in Snowmass, 1986, Colorado, edited by R. Donaldson and J. Marx.
- [61] P. Nason, *JHEP* **11**, 040 (2004), [hep-ph/0409146](#).
- [62] P. Nason and G. Ridolfi, *JHEP* **0608**, 077 (2006).
- [63] C. O. S. Alioli, P. Nason and E. Re, *JHEP* **07**, 060 (2008).
- [64] W. T. Giele and E. W. N. Glover, *Phys. Rev.* **D46**, 1980 (1992).
- [65] W. T. Giele, E. W. N. Glover, and D. A. Kosower, *Nucl. Phys.* **B403**, 633 (1993), [arXiv:hep-ph/9302225](#).
- [66] Z. Nagy and Z. Trócsányi, *Nucl. Phys.* **B486**, 189 (1997), [arXiv:hep-ph/9610498](#).
- [67] S. Frixione, *Nucl. Phys.* **B507**, 295 (1997), [arXiv:hep-ph/9706545](#).
- [68] G. Somogyi, Z. Trócsányi, and V. Del Duca, *JHEP* **01**, 070 (2007), [arXiv:hep-ph/0609042](#).
- [69] J. Frenkel and J. C. Taylor, *Nucl. Phys.* **B116**, 185 (1976).
- [70] D. Amati, R. Petronzio, and G. Veneziano, *Nucl. Phys.* **B146**, 29 (1978).
- [71] A. Bassetto, M. Ciafaloni, and G. Marchesini, *Phys. Rept.* **100**, 201 (1983).
- [72] S. Catani and M. Grazzini, *Nucl. Phys.* **B570**, 287 (2000), [arXiv:hep-ph/9908523](#).
- [73] G. Somogyi, Z. Trócsányi, and V. Del Duca, *JHEP* **06**, 024 (2005), [arXiv:hep-ph/0502226](#).
- [74] Z. Bern, V. Del Duca, and C. R. Schmidt, *Phys. Lett.* **B445**, 168 (1998), [arXiv:hep-ph/9810409](#).
- [75] D. A. Kosower and P. Uwer, *Nucl. Phys.* **B563**, 477 (1999), [arXiv:hep-ph/9903515](#).
- [76] Z. Bern, V. Del Duca, W. B. Kilgore, and C. R. Schmidt, *Phys. Rev.* **D60**, 116001 (1999), [arXiv:hep-ph/9903516](#).

- [77] S. Catani and M. Grazzini, Nucl. Phys. **B591**, 435 (2000), [arXiv:hep-ph/0007142](#).
- [78] A. Gehrmann-De Ridder and E. W. N. Glover, Nucl. Phys. **B517**, 269 (1998), [arXiv:hep-ph/9707224](#).
- [79] J. M. Campbell and E. W. N. Glover, Nucl. Phys. **B527**, 264 (1998), [arXiv:hep-ph/9710255](#).
- [80] S. Catani and M. Grazzini, Phys. Lett. **B446**, 143 (1999), [arXiv:hep-ph/9810389](#).
- [81] D. A. Kosower, Nucl. Phys. **B552**, 319 (1999), [arXiv:hep-ph/9901201](#).
- [82] V. Del Duca, A. Frizzo, and F. Maltoni, Nucl. Phys. **B568**, 211 (2000), [arXiv:hep-ph/9909464](#).
- [83] D. A. Kosower, Phys. Rev. **D67**, 116003 (2003), [arXiv:hep-ph/0212097](#).
- [84] D. A. Kosower, Phys. Rev. Lett. **91**, 061602 (2003), [arXiv:hep-ph/0301069](#).
- [85] F. A. Berends and W. T. Giele, Nucl. Phys. **B313**, 595 (1989).
- [86] Z. Nagy, G. Somogyi, and Z. Trócsányi (2007), [arXiv:hep-ph/0702273](#).
- [87] G. Somogyi and Z. Trócsányi, Acta Phys. Chim. Debr. **XL**, 101 (2006), [arXiv:hep-ph/0609041](#).
- [88] G. Somogyi and Z. Trócsányi, JHEP **01**, 052 (2007), [arXiv:hep-ph/0609043](#).
- [89] G. Somogyi and Z. Trócsányi, JHEP **08**, 042 (2008), [arXiv:0807.0509 \[hep-ph\]](#).
- [90] U. Aglietti, V. Del Duca, C. Duhr, G. Somogyi, and Z. Trócsányi (2008), [arXiv:0807.0514 \[hep-ph\]](#).
- [91] P. Bolzoni, S. Moch, G. Somogyi, and i. p. Trócsányi, Z. (in preparation), [arXiv:?? \[hep-ph\]](#).

# Event shapes and resummation

*Andrea Banfi, Gennaro Corcella, Mrinal Dasgupta, S. Joseph Gionata Luisoni, Swapan Majhi, B.F.L. Ward, S.A. Yost*

## 1 Event shapes and resummation

For the sake of reliable measurements at present and future colliders, the use of precise QCD calculations is mandatory. Fixed-order calculations discussed in Sec. [1] are accurate enough to predict inclusive observables, such as total cross sections or widths, whereas more exclusive quantities, such as event-shape distributions, exhibit large logarithmic enhancements, corresponding to soft- or collinear-parton radiation, which need to be resummed to all orders to improve the perturbative prediction. Analytical resummation of soft/collinear-enhanced radiation can be performed following the general method in [2–4]. Such resummations are usually based on the approximation of multiple independent emissions, implying factorization of amplitudes and phase spaces, and resulting in the exponentiation of soft/collinear single-parton radiation.

In the following we describe recent progress in the understanding and development of such resummations, including a critical comparison of analytical resummations with partons shower resummations, a discussion of non-global logarithms and recent extraction of the strong coupling using newly available NLLA+NNLO matched predictions.

## 2 Parton showers and resummations for non-global QCD observables

*Authors: Andrea Banfi, Gennaro Corcella and Mrinal Dasgupta*

Resummation of soft and collinear logarithms are usually based on the approximation of multiple independent emissions, implying factorization of amplitudes and phase spaces, and resulting in the exponentiation of soft/collinear single-parton radiation. In fact, a resummed quantity  $\Sigma(L)$ ,  $L$  being a large logarithm of soft or collinear origin, typically reads:

$$\Sigma(L) = \exp [Lg_1(\alpha_S L) + g_2(\alpha_S L) + \alpha_S g_3(L) + \dots], \quad (1)$$

where  $Lg_1$  resums the double logarithms, *i.e.* both soft and collinear,  $\mathcal{O}(\alpha_S^n L^{n+1})$ , while  $g_2$  resums single logarithms  $\mathcal{O}(\alpha_S^n L^n)$ , either soft or collinear, and so forth. Contributions  $\sim \alpha_S^n L^{n+1}$  and  $\sim \alpha_S^n L^n$  are typically classified as leading- (LL) and next-to-leading (NLL) logarithms. However, as we shall point out later on, if  $g_1$  is zero, the LLs will be the ones contained in  $g_2$ .

As an alternative tool to resum large logarithms, one can employ Monte Carlo generators, such as HERWIG [5] or PYTHIA [6], which implement parton showers in the soft/collinear approximation and include models for hadronization and the underlying event. In particular, the evolution variable for the HERWIG showers is equivalent, for soft emissions, to angular ordering [7, 8], which is a reliable approximation in the large- $N_C$  limit for azimuthally-averaged quantities. PYTHIA traditionally orders its cascades according to the virtuality of the splitting parton, with the possibility to reject non-angular-ordered showers. Lately, a new PYTHIA shower model [9] was released, ordering multiple emissions according to the transverse momentum of the radiated parton with respect to the emitter’s direction. Monte Carlo algorithms are correct

up to the double-logarithmic function  $g_1$  and in some cases they can even account for  $g_2$  (see, *e.g.*, [10] for some discussions on comparing parton showers and resummations).

In the following, we shall discuss the so-called non-global observables and compare the results of resummed calculations, with the possible inclusion of the angular-ordering approximation, with those given by Monte Carlo parton showers.

### 2.0.1 Non-global observables

It was recently found out [11] that for some quantities, called non-global observables, as they are sensitive to radiation in a limited region of the phase space, the independent-emission approximation is not sufficient any longer, even at LL level. As a case study, we consider  $e^+e^-$  annihilation into hadrons at the centre-of-mass energy  $Q$  and study the transverse-energy flow in an angular region  $\Omega$ , a limited region in rapidity  $\eta$  and azimuth  $\phi$ :

$$\Sigma(Q, Q_\Omega) = \frac{1}{\sigma} \int_0^{Q_\Omega} dE_t \frac{d\sigma}{dE_t} ; E_t = \sum_{i \in \Omega} E_{ti}. \quad (2)$$

$\Sigma$  was computed in [12] and reads:

$$\Sigma(Q, Q_\Omega) = \exp(-4C_F A_\Omega t) S(t), \quad (3)$$

with

$$A_\Omega = \int d\eta \frac{d\phi}{2\pi} ; t = \frac{1}{2\pi} \int_{Q_\Omega}^{Q/2} \frac{dk}{k} \alpha_S(k). \quad (4)$$

In Eq. (3), the contribution  $\sim \exp(-4C_F A_\Omega t)$  comes after exponentiating single-gluon radiation from the primary  $q\bar{q}$  pair, which constitutes the Born event, whereas  $S(t)$  includes non-global logarithms, due to correlated parton emission in the  $\Omega$  region. The lowest-order contribution to  $S(t)$  goes as  $\alpha_S^2 S_2 \ln^2(Q/Q_\Omega)$ , with  $S_2 \sim C_A C_F$ .  $S_2$  was calculated exactly, while the function  $S(t)$  was computed at all orders in the LL approximation and in the large- $N_C$  limit, by using the evolution algorithm presented in [11]. We point out that, for an observable like  $\Sigma$ , the function  $g_1$  in Eq. (1) is zero, hence the leading logarithms are just  $\sim \alpha_S^n L^n$ : including the non-global function  $S(t)$  is therefore necessary to fully account for LLs.

As in Ref. [13], we wish to investigate whether implementing angular ordering in the evolution algorithm of [11] still leads to acceptable results for  $\Sigma(Q, Q_\Omega)$  and  $S(t)$ . In Fig. 1 we present the leading-order non-global coefficient,  $-S_2/(C_F C_A)$ , according to the full calculation and the angular-ordering approximation, in case  $\Omega$  is a rapidity slice of width  $\Delta\eta = 2.5$ . We also show the cross section  $\Sigma(t)$  yielded by the full leading-log resummed calculation and in the angular-ordering (AO) approximation. For the sake of comparison, we also present the contribution coming from just exponentiating primary single-parton emission.

From Fig. 1 (left), we learn that for small gap sizes the full and AO results agree, while they start to differ once the gap is increased. In both cases,  $S_2$  saturates for large  $\Delta\eta$ , with the AO result being about 10% lower than the full one. As for  $\Sigma(t)$ , the AO approximation is indeed able to include significant part of the full result, whereas the primary-emission contribution lies far above the two other predictions, thus giving unreliable spectra. Considering, *e.g.*,  $t = 0.15$ , corresponding to  $Q = 100$  GeV and  $Q_\Omega = 1$  GeV, the AO and primary results are 10% and 75% above the full one, respectively. It was also shown in Ref. [13] that the results for the non-global function  $S(t)$  are roughly independent of the size of the rapidity gap.

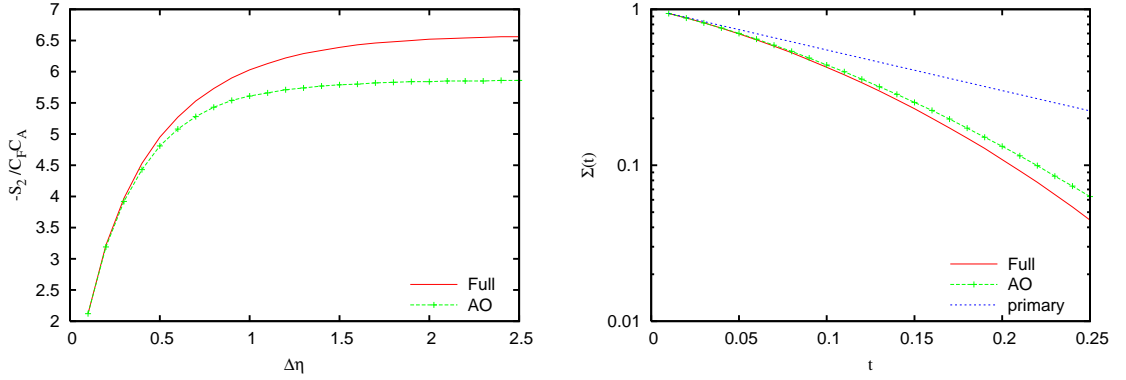


Fig. 1: Left: Function  $S(t)$  at leading-order according to the full LL calculation and in the angular-ordering approximation, in terms of the rapidity gap  $\Delta\eta$ . Right: Function  $\Sigma(t)$  according to the full resummed calculation and the angular-ordering approximation. Also shown is the result coming from the exponentiation of primary-emission contributions.

### 2.0.2 Comparison with HERWIG and PYTHIA

In this section we compare the results of the resummed calculation with the ones yielded by the Monte Carlo programs HERWIG and PYTHIA. As in [13], we study  $e^+e^-$  annihilation at the centre-of-mass energy  $Q = 10^5$  GeV. In fact, we chose such a high value of  $Q$  in order to kill subleading effects, weighted by  $\alpha_S(Q)$  or suppressed by powers of  $1/Q$ , such as subleading soft/collinear logarithms, quark mass effects, hadronization corrections. Furthermore, we checked that our results depend only on the dimensionless variable  $t$  in Eq. (4), so that our findings for a given value of  $t$  can be easily translated to any value of the centre-of-mass energy.

In Fig. 2 we present the differential cross section  $1/\sigma (d\sigma/dE_t)$  for the transverse-energy flow in a rapidity gap  $\Delta\eta = 1$ , according to the resummed result, matched to the exact NLO as in [12], and according to HERWIG and PYTHIA. In the resummation, we show the full result, the angular-ordering approximation and the primary-emission contribution. As for PYTHIA, we present the spectra obtained running the old and new models, with showers ordered in virtuality and transverse momentum, respectively. When using the old model, we shall always assume that non-AO radiation is vetoed.

As for the comparison with HERWIG, whose showers are ordered in angle, we observe good agreement with both AO and full results for  $E_t > 10$  GeV, while the primary-radiation contribution exhibit relevant discrepancies. As for PYTHIA, the new model, ordered in transverse momentum, is in good agreement with the resummation, leading to results similar to HERWIG. On the contrary, a visible disagreement is present between the old PYTHIA model and the resummed curves. In fact, as discussed in [9], evolution in transverse momentum leads to a better treatment of angular ordering with respect to virtuality ordering. Comparing the spectra at  $E_t = 10$  GeV, the discrepancies with respect to the full resummed result amount to  $-10\%$  for HERWIG,  $+7.5\%$  for the new PYTHIA model and  $-50\%$  for the old PYTHIA.

In Fig. 3 we instead compare HERWIG, PYTHIA and the resummation for a rapidity slice  $\Delta\eta = 3$ . As in Fig. 2, HERWIG is in reasonable agreement with the resummed computation for  $E_t > 10$  GeV and the old PYTHIA model lies quite far from the other curves throughout all

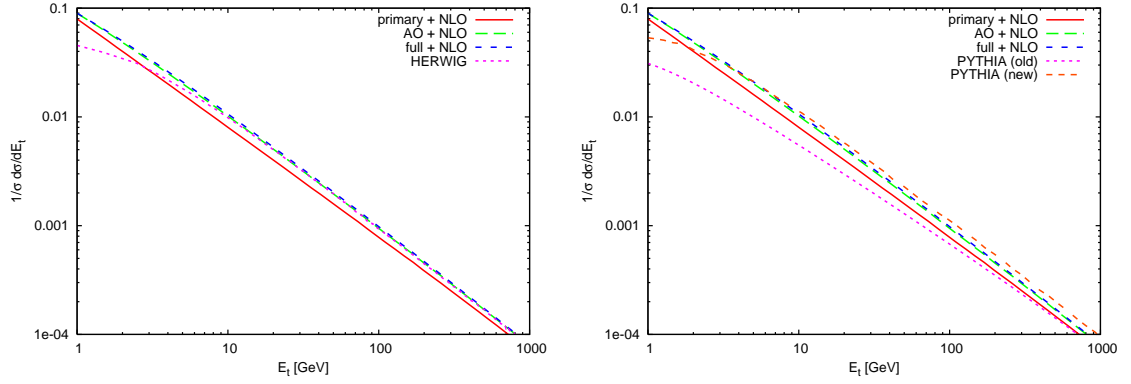


Fig. 2: Comparison of full, AO and primary resummed results with HERWIG (left) and PYTHIA (right) for  $\Delta\eta = 1$  and  $Q = 10^5$  GeV. As for PYTHIA, we show the spectra yielded by the old and new models, where parton showers are ordered in virtuality and transverse momentum, respectively.

$E_t$ -range. However, unlike the  $\Delta\eta = 1$  case, even the spectrum obtained with the new PYTHIA model exhibits a meaningful discrepancy for  $E_t > 100$  GeV, which might signal that perhaps even the new PYTHIA ordering variable is not completely adequate to describe non-global observables at large rapidity slices. A more detailed investigation of this issue is mandatory.

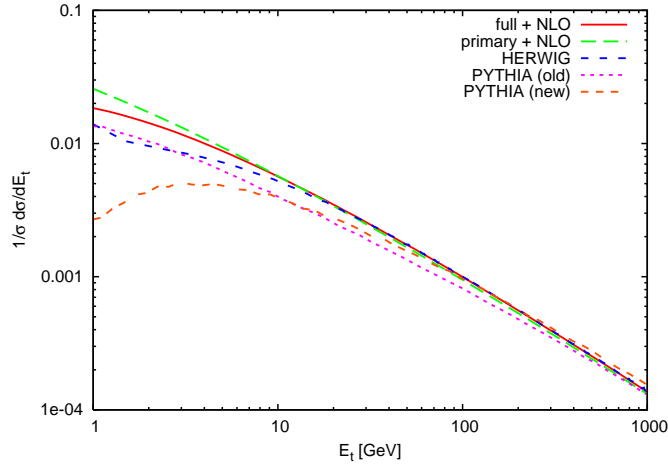


Fig. 3: Transverse-energy spectrum in a rapidity gap  $\Delta\eta = 3$ , according to the resummed calculation, HERWIG and PYTHIA (old and new models).

### 2.0.3 Conclusions

We studied non-global observables, namely the transverse-energy flow in a rapidity gap, and investigated the role played by angular ordering in the leading-logarithmic resummation. We found that the angular-ordering approximation indeed includes the bulk of the leading-logarithmic contribution, as the results are not too different with respect to the full resummed calculation.

The resummed spectra were compared with the results of the HERWIG and PYTHIA Monte Carlo generators. We found that HERWIG, whose evolution variable is equivalent to angular ordering in the soft limit, is in acceptable agreement with the resummation. As for PYTHIA, the old model, based on virtuality ordering, with an option to veto non-angular-ordered emissions, was found to be inadequate to describe non-global observables. The new model, ordered in transverse momentum and with an improved implementation of angular ordering, yields predictions qualitatively similar to HERWIG for relatively small rapidity gaps, whereas remarkable discrepancies are exhibited if the slice size is enlarged. In fact, as non-global observables are often used to tune Monte Carlo generators to data, we believe that such a discrepancy needs to be further investigated; otherwise, when fitting, *e.g.*, the old PYTHIA model to data, one would end up to include as much as 50% of perturbative leading logarithms in non-perturbative parameters, associated with hadronization or underlying event. A deeper understanding of the PYTHIA description of non-global observables, along with the application of the work here presented to hadron colliders, is in progress.

### 3 Azimuthal decorrelation between hard final state jets

*Author: Mrinal Dasgupta*

One of the most commonly measured jet observables in experimental QCD studies is the azimuthal decorrelation  $\Delta\phi$  between hard final-state jets. When compared to theory this quantity is expected to provide valuable information both on QCD parameters (strong coupling, parton distribution functions – PDFs) as well as dynamics in the near back-to-back region sensitive to multiple soft and/or collinear emissions and non-perturbative effects. To this end it has been often examined in experimental QCD studies at HERA and the Tevatron [14, 15], used for the tuning of parameters of Monte Carlo event generator models and to constrain unintegrated PDFs (uPDFs) in conjunction with HERA data [16].

In this study we aim to provide a more accurate theoretical prediction for this observable by calculating a next-to-leading logarithm (NLL) resummed result which accounts for logarithmic terms enhanced in the region where jets are back-to-back in azimuthal angle –  $\Delta\phi = \pi$ . Such a resummation has not been carried out to date, the main complication being the application of a jet algorithm to define the final state which has non-trivial implications for the standard approximations that enable NLL resummation.

To be specific one is studying here an observable that is sensitive to energy flow outside well-defined jet regions which potentially means that it and similar observables fall into the category of non-global observables [17, 18]. Since it was shown that the resummation of non-global observables is substantially more complicated than that for “global” quantities such as most event-shape variables and in any case restricted to the large  $N_c$  approximation, the most accurate theoretical predictions can be obtained only for global observables. This appears to rule out the possibility of complete NLL estimates for many interesting jet observables including the azimuthal decorrelation we study here. As far as existing predictions for jet observables are concerned, the issue of non-global logarithms was not dealt with in Ref. [19] (published prior to the discovery of non-global effects) where they would arise in threshold resummation for one of the definitions ( $M^2 = (p_1 + p_2)^2$ ) of the dijet invariant mass studied there but would be absent for the definition  $M^2 = 2p_1.p_2$ . Further we should also mention here that the non-global component has been incorrectly treated in Ref. [20] where it is mentioned that such effects will vanish with



jet radius when in fact one obtains a saturation in the small  $R$  limit.

We shall show an interplay between the potential non-global nature of the observable and the exact definition of the jet as provided by the choice of a recombination scheme. We show that in one of the resummation schemes employed in experimental studies of the azimuthal correlation the observable is in fact global and can be resummed to NLL accuracy. This may be taken as a general example of how carefully selecting the definition of the observable and the jets one may be able to render an exact NLL resummation possible, avoiding altogether the non-global issue and hence encourage future resummed studies for important regions of phase space in the context of jets.

### 3.0.4 Recombination scheme, kinematics and globalness

We wish to study the impact of two recombination schemes used to construct the angle  $\Delta\phi$  between the final-state jets in dijet production. In the first scheme the jet azimuthal angle  $\phi_j$  is given by a  $p_t$ -weighted sum over its hadronic constituents,  $\phi_j = \sum_{i \in j} p_{t,i} \phi_i / \sum_{i \in j} p_{t,i}$ , while in the second scheme one constructs the jet four-vector  $p_j = \sum_{i \in j} p_i$ , with the sum running over hadrons in the jet, and then parameterises  $p_j = p_{t,j} (\cosh \eta_j, \cos \phi_j, \sin \phi_j, \sinh \eta_j)$  to obtain the jet azimuth  $\phi_j$ . The first scheme is employed for instance by the H1 collaboration at HERA while the latter ( $E$ -scheme) is currently preferred by the Tevatron experiments.

The transverse momenta of final-state particles can be parameterised as below:<sup>1</sup>

$$\begin{aligned} \vec{p}_{t,1} &= p_{t,1}(1, 0), \\ \vec{p}_{t,2} &= p_{t,2}(\cos(\pi - \epsilon), \sin(\pi - \epsilon)), \\ &= p_{t,2}(-\cos \epsilon, \sin \epsilon), \\ \vec{k}_{t,i} &= k_{t,i}(\cos \phi_i, \sin \phi_i), \end{aligned} \quad (5)$$

where the hard final-state partons are labeled by 1 and 2 and the soft gluons by the label  $i$ . For only soft emissions the hard partons are nearly back-to-back,  $p_{t,1} = p_{t,2} = p_t$  and  $|\epsilon| \ll 1$ .

Using the above, in the scheme involving the  $p_t$ -weighted sum one obtains for  $\Delta\phi = \phi_{j1} - \phi_{j2}$ :

$$|\pi - \Delta\phi| = \left| \sum_i \frac{k_{t,i}}{p_t} (\sin \phi_i - \theta_{i1} \phi_i - \theta_{i2}(\pi - \phi_i)) \right| + \mathcal{O}(k_t^2), \quad (6)$$

where  $\theta_{ij} = 1$  if particle  $i$  is clustered to jet  $j$  and is zero otherwise. The definition above implies that the observable in question is global since it is sensitive to soft emissions in the whole phase-space, both in and outside the jets, and the dependence on soft emissions in either case is linear in  $k_t$ . This property ensures that it is possible to resum the large logarithms in the back-to-back region to next-to-leading (single) logarithmic accuracy without resorting to the large  $N_c$  approximation needed for non-global observables [17, 18].

Now turning to the  $E$ -scheme one obtains instead:

$$|\pi - \Delta\phi| = \left| \sum_{i \notin \text{jets}} \frac{k_{t,i}}{p_t} \sin \phi_i \right| + \mathcal{O}(k_t^2), \quad (7)$$

---

<sup>1</sup>Here one is looking at the projections of particle momenta in the plane perpendicular to the beam direction in hadron collisions or that perpendicular to the  $\gamma^*P$  axis in the DIS Breit or hadronic centre-of-mass (HCM) frames.



where the sum extends only over all soft particles not recombined with the hard jets. Observables sensitive to soft emissions in such delimited angular intervals are of the non-global variety [17, 18], and hence in the  $E$ -scheme definition of jets the azimuthal decorrelation is a non-global observable.

### 3.0.5 Resummed Results

Having established that the observable at hand is a global observable in the  $p_t$ -weighted recombination scheme its resummation is now straightforward. We refer the reader to Ref. [21] for the details and just quote the results below.

Taking first the case of dijets produced in DIS, the integrated cross-section ie the integral of the distribution in  $\pi - \Delta\phi$  up to some fixed value  $\Delta$  is given by an integral over “impact parameter”  $b$

$$\Sigma_a(\Delta) = \frac{1}{\pi} \int_{-\infty}^{\infty} \frac{db}{b} \sin(b\Delta) e^{-R_a(b)} f_a(x, \mu_f^2/b^2). \quad (8)$$

The index  $a$  denotes the flavour of incoming parton and the function  $R_a(b)$ , known as the radiator, embodies the soft and/or collinear single-gluon result for emission from a three hard parton system while  $f$  denotes the PDF.

For the case of hadron collisions one can write a very similar formula to the one above except that in this case one has to account for two incoming partons and hence there are two PDFs while the relevant radiator now represents soft and collinear resummation from an ensemble of four hard partons.

The result for  $R_a(\bar{b})$  for the DIS case can be expressed in terms of three pieces each with a distinct physical origin:

$$R_a(\bar{b}) = R_{\text{in}}^a(\bar{b}) + R_{\text{out}}^a(\bar{b}) - \ln S(\bar{b}, \{p\}), \quad (9)$$

with  $R_{\text{in}}^a$  and  $R_{\text{out}}^a$  being the contributions generated by emissions collinear to the incoming (excluding the set of single-logarithms already resummed in the parton densities) and outgoing legs respectively. In addition to these jet functions we have a soft function  $S(\bar{b}, \{p\})$  which resums soft emission at large angles, and which depends on the geometry of the emitting hard ensemble expressed here as a dependence on the set of hard Born momenta  $\{p\}$ .

While our results eventually include the two-loop running of the coupling which is necessary to obtain full NLL accuracy (compute the full functions  $g_1$  and  $g_2$ ), for brevity and to illustrate the main features we report our results here in a fixed coupling approximation. In this case we simply obtain:

$$\begin{aligned} R_{\text{out}}^a(\bar{b}) &= (C_1^a + C_2^a) \frac{\alpha_s}{2\pi} \left( \frac{2}{3} L^2 + \frac{4}{3} L \left( -\ln 3 - 4 \ln 2 + 3 \ln \frac{Q}{p_t} \right) \right) + \\ &\quad + \frac{4}{3} \frac{\alpha_s}{2\pi} (C_1^a B_1^a + C_2^a B_2^a) L, \end{aligned} \quad (10)$$

$$R_{\text{in}}^a = C_i^a \frac{\alpha_s}{2\pi} \left( 2L^2 + 4L \left( -\ln 2 + \ln \frac{Q}{p_t} \right) \right) + 4C_i^a \frac{\alpha_s}{2\pi} B_i^a L, \quad (11)$$

$$\ln S(\bar{b}, \{p\}) = -4L \left( 2C_F \frac{\alpha_s}{2\pi} \ln \frac{Q_{qq'}}{Q} + C_A \frac{\alpha_s}{2\pi} \ln \frac{Q_{qg} Q_{gq'}}{Q_{qq'} Q} \right), \quad (12)$$

with  $L = \ln \bar{b}$ . In the above  $C_i^a$  is the colour charge of the incoming parton in channel  $a$ , for instance  $C_i^a = C_F$  for  $a = q$ , the incoming quark channel. Likewise  $C_{1,2}^a$  are the colour charges of the partons initiating the outgoing jets 1 and 2 in channel  $a$ . The main aspect of the results for the collinear  $R_{\text{out,in}}^a$  jet functions is a leading double logarithmic behaviour, where one notes the unfamiliar coefficient  $2/3$  (different from all commonly studied event shape variables for instance) associated to the double logs on the outgoing legs, *i.e.* in the function  $R_{\text{out}}^a$ . Additionally hard collinear radiation is described by single-logarithmic terms with the coefficients  $C_\ell B_\ell$  for each leg, with the appropriate colour charge  $C_\ell$  ( $\ell = i, 1, 2$ ) and  $B_{i,1,2}$  depending on the identities (spins) of the incoming and outgoing partons such that  $B_\ell = -3/4$  for fermions and  $B_\ell = -(11C_A - 4T_{Rn_f})/(12C_A)$  for a gluon.

Finally we have the soft wide-angle single-logarithmic contribution  $\ln S$ , which depends on the geometry of the hard three-jet system via the dependence on dipole invariant masses  $Q_{ij} = 2(p_i \cdot p_j)$ . This structure is characteristic of soft inter-jet radiation for three-jet systems (see *e.g.* Ref. [22] for a detailed discussion). The result can be easily extended to the case of hadron collisions as shown in Ref. [21].

### 3.0.6 Results and Discussion

To provide a final resummed result for the  $\Delta\phi$  distribution one still needs to carry out the  $b$  integration in Eq. (8). The  $b$  integral is not well behaved at small and large  $b$ . At small  $b$  one is outside the jurisdiction of resummation and hence free to modify the small  $b$  behaviour with a prescription that does not affect the next-to-leading logarithms (see Ref. [21]). At large  $b$  one has to regulate the effect of the Landau pole in the running coupling and introduce non-perturbative corrections which procedure is described in Ref. [21].

We plot the resummed result for the  $\Delta\phi$  distribution in Fig. 4 along with the fixed order predictions for dijet production in DIS with  $Q^2 = 67 \text{ GeV}^2$  and  $x = 2.86 \cdot 10^{-3}$ . These values and other cuts on the jets have been taken from the H1 study to which we would eventually compare our results. As we can see the fixed order predictions diverge as expected near  $\Delta\phi = \pi$ . This divergence is cured by the resummation that goes to a fixed *non-zero* value at  $\Delta\phi = \pi$ . Of note here is the absence of a Sudakov peak since the Sudakov mechanism does not dominate the  $b$  integral at very small  $\Delta = |\pi - \Delta\phi|$ . The dominant mechanism to obtain back-to-back jets is thus a one-dimensional cancellation between emissions rather than a suppression of the  $k_t$  of each individual emission, leading to a washout of the Sudakov peak.

In order to obtain complete predictions which can be compared to data two further developments need to be made: matching to fixed-order NLO predictions and inclusion of non-perturbative effects. These issues will be addressed in forthcoming work.

## 4 Matching of NLLA to NNLO calculation for event shapes in $e^+e^-$

*Author: Gionata Luisoni*

Event shape distributions in  $e^+e^-$  annihilation processes are very popular hadronic observables. Their popularity is mainly due to the fact that they are well suited both for experimental measurement and for theoretical calculations because many of them are infrared and collinear safe.

The deviation from simple two-jet configurations, which are a limiting case in event shapes, is proportional to the strong coupling constant  $\alpha_s$ , so that by comparing the measured

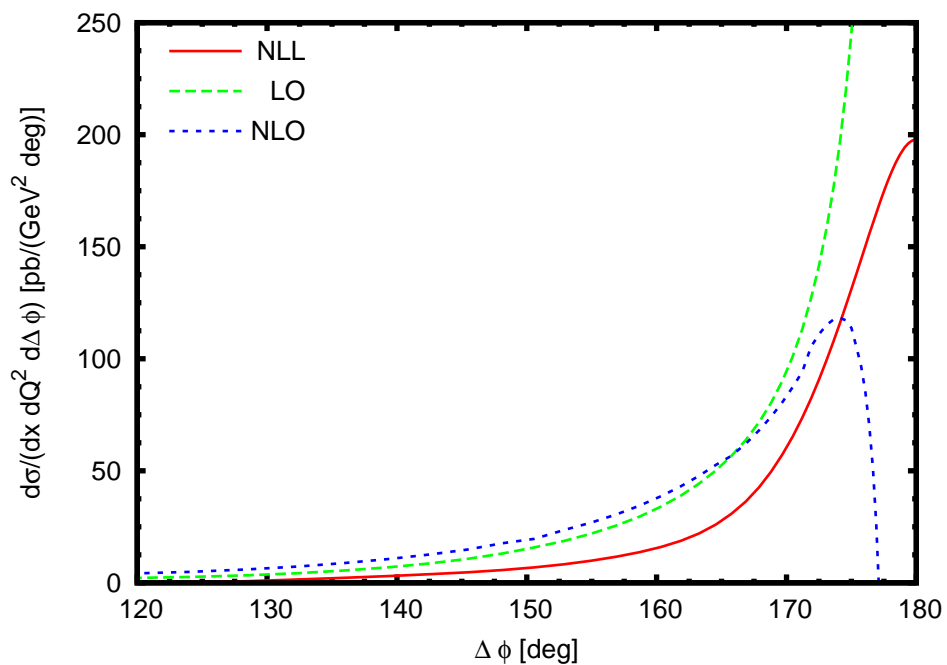


Fig. 4: The resummed  $\Delta\phi$  distribution for dijets in DIS. Also shown for comparison are the leading order (LO) and next-to-leading order (NLO) predictions from NLOJET++.

$\bar{\alpha}_s \mathcal{A}(y)$	$\bar{\alpha}_s L$	$\bar{\alpha}_s L^2$				
$\bar{\alpha}_s^2 \mathcal{B}(y, x_\mu)$	$\bar{\alpha}_s^2 L$	$\bar{\alpha}_s^2 L^2$	$\bar{\alpha}_s^2 L^3$	$\bar{\alpha}_s^2 L^4$		
$\bar{\alpha}_s^3 \mathcal{C}(y, x_\mu)$	$\bar{\alpha}_s^3 L$	$\bar{\alpha}_s^3 L^2$	$\bar{\alpha}_s^3 L^3$	$\bar{\alpha}_s^3 L^4$	$\bar{\alpha}_s^3 L^5$	$\bar{\alpha}_s^3 L^6$

Table 1: Powers of the logarithms present at different orders in perturbation theory. The colour highlights the different orders in resummation: LL (red) and NLL (blue). The terms in green are contained in the LL and NLL contributions and exponentiate trivially with them.

event shape distribution with the theoretical prediction, one can determine  $\alpha_s$  [23]. Below we will concentrate on this, using the newly available NNLO [24] and NLLA+NNLO results. At LEP, a standard set of event shapes was studied in great detail: thrust  $T$  (which is substituted here by  $\tau = 1 - T$ ), heavy jet mass  $\rho$ , wide and total jet broadening  $B_W$  and  $B_T$ ,  $C$ -parameter and two-to-three-jet transition parameter in the Durham algorithm  $Y_3$ . The definitions of these variables, which we denote collectively as  $y$  in the following, are summarized in [25]. The two-jet limit of each variable is  $y \rightarrow 0$ .

The theoretical state-of-the-art description of event shape distributions was based until very recently on the matching of the NLLA [26] onto the NLO [27–30] calculation. The newly available results of the NNLO corrections for the standard set of event shapes [24] introduced above, permits now to match them with resummed calculations, obtaining theoretical distributions at NLLA+NNLO.

At NNLO the integrated cross section

$$R(y, Q, \mu) \equiv \frac{1}{\sigma_{\text{had}}} \int_0^y \frac{d\sigma(x, Q, \mu)}{dx} dx,$$

has the following fixed-order expansion:

$$R(y, Q, \mu) = 1 + \bar{\alpha}_s(\mu) \mathcal{A}(y) + \bar{\alpha}_s^2(\mu) \mathcal{B}(y, x_\mu) + \bar{\alpha}_s^3(\mu) \mathcal{C}(y, x_\mu).$$

where  $\bar{\alpha}_s = \alpha_s/(2\pi)$  and  $x_\mu = \mu/Q$ . Approaching the two-jet region event shapes display large infrared logarithms which spoil the convergence of the series expansion. The main contribution in this case comes from the highest power of the logarithms which have to be resummed to all orders. For suitable observables resummation leads to exponentiation. At NLLA the resummed expression is given by

$$R(y, Q, \mu) = (1 + C_1 \bar{\alpha}_s) e^{(L g_1(\alpha_s L) + g_2(\alpha_s L))},$$

where the function  $g_1(\alpha_s L)$  contains all leading-logarithms (LL),  $g_2(\alpha_s L)$  all next-to-leading-logarithms (NLL) and  $\mu = Q$  is used. Terms beyond NLL have been consistently omitted. The resummation functions  $g_1(\alpha_s L)$  and  $g_2(\alpha_s L)$  can be expanded as power series in  $\bar{\alpha}_s L$

$$\begin{aligned} L g_1(\alpha_s L) &= G_{12} L^2 \bar{\alpha}_s + G_{23} L^3 \bar{\alpha}_s^2 + G_{34} L^4 \bar{\alpha}_s^3 + \dots \text{ (LL)}, \\ g_2(\alpha_s L) &= G_{11} L \bar{\alpha}_s + G_{22} L^2 \bar{\alpha}_s^2 + G_{33} L^3 \bar{\alpha}_s^3 + \dots \text{ (NLL)}. \end{aligned} \quad (13)$$

Table 1 shows the logarithmic terms present up to the third order in perturbation theory. From the expansion (13) of the exponentiated resummation functions it follows immediately, that at

the fixed-order level, the LL are terms of the form  $\alpha_s^n L^{n+1}$ , the NLL terms go like  $\alpha_s^n L^n$ , and so on.

Closed analytic forms for functions  $g_1(\alpha_s L)$ ,  $g_2(\alpha_s L)$  are available for  $\tau$  and  $\rho$  [31],  $B_W$  and  $B_T$  [32, 33],  $C$  [34, 35] and  $Y_3$  [36], and are collected in the appendix of [37]. For  $\tau$  the  $g_3(\alpha_s L)$  function is also known [38].

To obtain a reliable description of the event shape distributions over a wide range in  $y$ , it is mandatory to combine fixed-order and resummed predictions. To avoid the double counting of terms common to both, the two predictions have to be matched to each other. A number of different matching procedures have been proposed in the literature, see for example [25] for a review. We computed the matching in the so-called  $\ln R$ -matching [26] since in this particular scheme, all matching coefficients can be extracted analytically from the resummed calculation, while most other schemes require the numerical extraction of some of the matching coefficients from the distributions at fixed order. The  $\ln R$ -matching at NLO is described in detail in [26]. In the  $\ln R$ -matching scheme, the NLLA+NNLO expression is

$$\begin{aligned} \ln(R(y, \alpha_s)) = & L g_1(\alpha_s L) + g_2(\alpha_s L) + \bar{\alpha}_S (\mathcal{A}(y) - G_{11}L - G_{12}L^2) \\ & + \bar{\alpha}_S^2 \left( \mathcal{B}(y) - \frac{1}{2} \mathcal{A}^2(y) - G_{22}L^2 - G_{23}L^3 \right) \\ & + \bar{\alpha}_S^3 \left( \mathcal{C}(y) - \mathcal{A}(y) \mathcal{B}(y) + \frac{1}{3} \mathcal{A}^3(y) - G_{33}L^3 - G_{34}L^4 \right). \end{aligned} \quad (14)$$

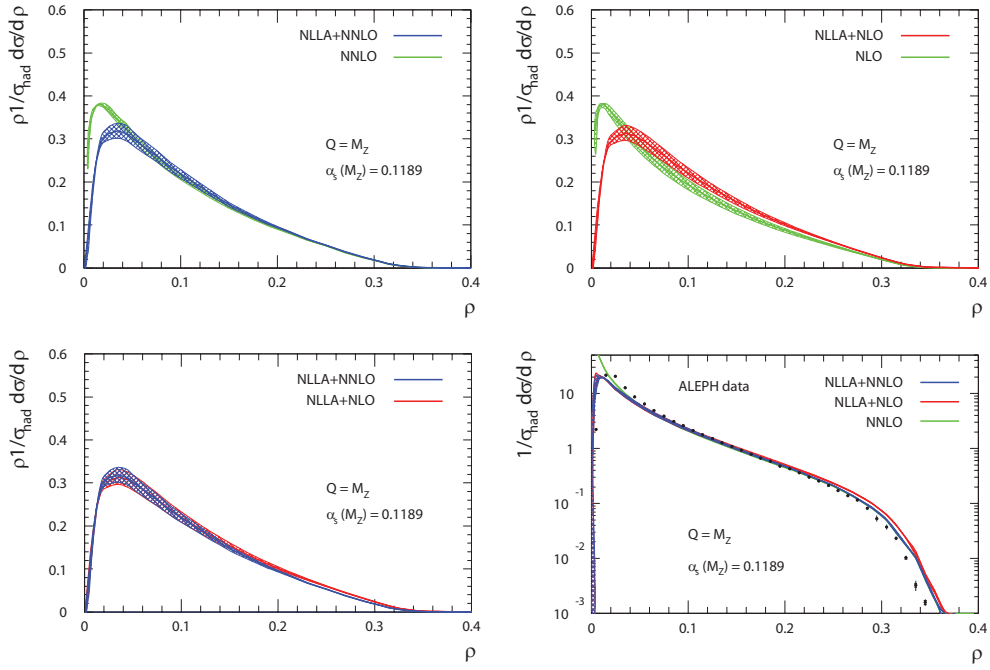
The matching coefficients appearing in this expression can be obtained from (13) and are listed in [37]. To ensure the vanishing of the matched expression at the kinematical boundary  $y_{\max}$  a further shift of the logarithm is made [25].

The full renormalisation scale dependence of (14) is given by replacing the coupling constant, the fixed-order coefficients, the resummation functions and the matching coefficients as follows:

$$\begin{aligned} \alpha_s & \rightarrow \alpha_s(\mu), \\ \mathcal{B}(y) & \rightarrow \mathcal{B}(y, \mu) = 2\beta_0 \ln x_\mu \mathcal{A}(y) + \mathcal{B}(y), \\ \mathcal{C}(y) & \rightarrow \mathcal{C}(y, \mu) = (2\beta_0 \ln x_\mu)^2 \mathcal{A}(y) + 2 \ln x_\mu [2\beta_0 \mathcal{B}(y) + 2\beta_1 \mathcal{A}(y)] + \mathcal{C}(y), \\ g_2(\alpha_s L) & \rightarrow g_2(\alpha_s L, \mu^2) = g_2(\alpha_s L) + \frac{\beta_0}{\pi} (\alpha_s L)^2 g'_1(\alpha_s L) \ln x_\mu, \\ G_{22} & \rightarrow G_{22}(\mu) = G_{22} + 2\beta_0 G_{12} \ln x_\mu, \\ G_{33} & \rightarrow G_{33}(\mu) = G_{33} + 4\beta_0 G_{23} \ln x_\mu. \end{aligned}$$

In the above,  $g'_1$  denotes the derivative of  $g_1$  with respect to its argument. The LO coefficient  $\mathcal{A}$  and the LL resummation function  $g_1$ , as well as the matching coefficients  $G_{i+1}$  remain independent of  $\mu$ .

In the two upper plots of Fig. 5 we compare the matched NLLA+NNLO predictions for the heavy jet mass with the fixed-order NNLO predictions, and the matched NLLA+NLO with fixed-order NLO. All distributions were weighted by the respective shape variables. We use  $Q = M_Z$  and fix  $x_\mu = 1$ , the strong coupling constant is taken as  $\alpha_s(M_Z) = 0.1189$ . To quantify the renormalisation scale uncertainty, we have varied  $1/2 < x_\mu < 2$ , resulting in the error

Fig. 5: Matched distributions of heavy jet mass  $\rho$ .

band on these figures. The effects visible for the heavy jet mass are common to the whole set of observables which were analyzed. The most striking observation is that the difference between NLLA+NNLO and NNLO is largely restricted to the two-jet region, while NLLA+NLO and NLO differ in normalisation throughout the full kinematical range. This behaviour may serve as a first indication for the numerical smallness of corrections beyond NNLO in the three-jet region. In the approach to the two-jet region, the NLLA+NLO and NLLA+NNLO predictions agree by construction, since the matching suppresses any fixed-order terms. On the plot in the lower left corner we observe that the difference between NLLA+NNLO and NLLA+NLO is only moderate in the three-jet region. The renormalisation scale uncertainty in the three-jet region is reduced by 20-40% between NLLA+NLO and NLLA+NNLO. Finally the lower-right plot shows the parton-level fixed NNLO and the matched NLLA+NLO and NLLA+NNLO predictions are compared to hadron-level data taken by the ALEPH experiment. The description of the hadron-level data improves between parton-level NLLA+NLO and parton-level NLLA+NNLO, especially in the three-jet region. The behavior in the two-jet region is described better by the resummed predictions than by the fixed-order NNLO, although the agreement is far from perfect. This discrepancy can in part be attributed to hadronisation corrections, which become large in the approach to the two-jet limit. A very recent study of logarithmic corrections beyond NLLA for the thrust distribution [38] also shows that subleading logarithms in the two-jet region can account for about half of this discrepancy.

With the new NNLO and NLLA+NNLO results a new extraction of  $\alpha_s$  can be performed. For this we used public ALEPH data at center-of-mass energies between 91 and 209 GeV [39]. The data are corrected to hadron level using Monte Carlo (MC) corrections and accounting for

initial- and final-state-radiation (ISR/FSR) as well as background. They are fitted by NNLO respectively NLLA+NNLO predictions, including NLO quark mass corrections, folded to hadron level by means of MC generators. Finally, after estimating the missing higher orders using the uncertainty band method [25], the fits of 8 data sets and 6 different variables are combined together [23].

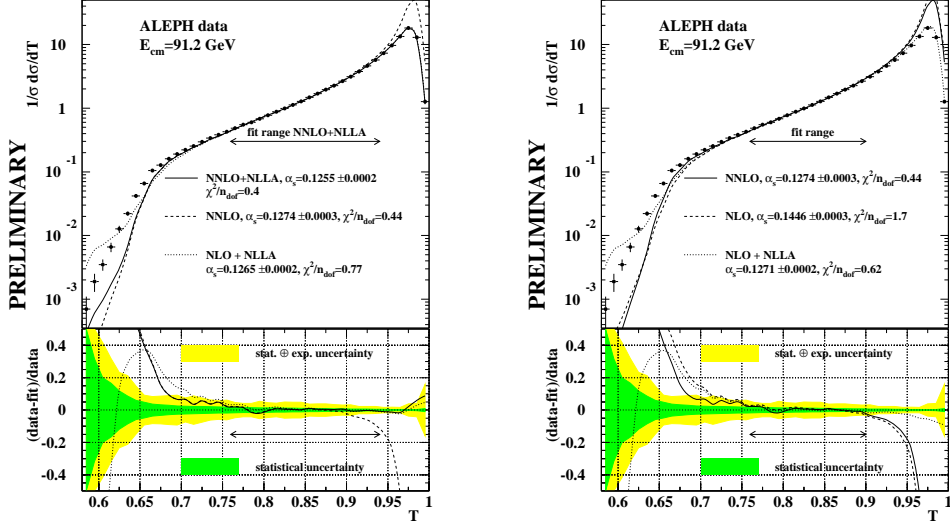


Fig. 6: Fit to ALEPH data for thrust.

The part of the distribution chosen for the fit (Fig. 6) is the one where the hadronizations and detector corrections are smaller than 25%. In the case of the NNLO distributions, the range was further reduced in the 2-jet region because of the divergence of the theoretical predictions. Only the statistical uncertainties are included in the  $\chi^2$ .

At NNLO we see a clear improvement with respect to the old NLO results. The fit is of a good quality although it still includes large statistical uncertainties of the  $C$  coefficient and in the 2-jet region the NLLA+NLO predictions still yields a better result. The improvement between NNLO and NLLA+NNLO in visible especially in the 2-jet region. The fit range is also more extended in this direction. For the resulting  $\alpha_s$  we observe that using fixed-order predictions leads basically to higher values, and that in both fixed-order and matched predictions there is a tendency for  $\alpha_s$  to decrease passing from NLO to NNLO. Finally computing the weighted average for  $\alpha_s$  from the 6 variables we obtain [23]:

$$\bar{\alpha}_s(M_Z) = 0.1240 \pm 0.0008 (\text{stat}) \pm 0.0010 (\text{exp}) \pm 0.0011 (\text{had}) \pm 0.0029 (\text{theo}).$$

From Fig. 7 it is clearly visible that the results for the different variables are coherent and the scattering is much reduced. The improvement with respect to the NLO result is also remarkable.

The combined results for the NLLA+NNLO fits are still work-in-progress, but it can be anticipated that the improvement coming from the inclusion of resummed calculation will be less

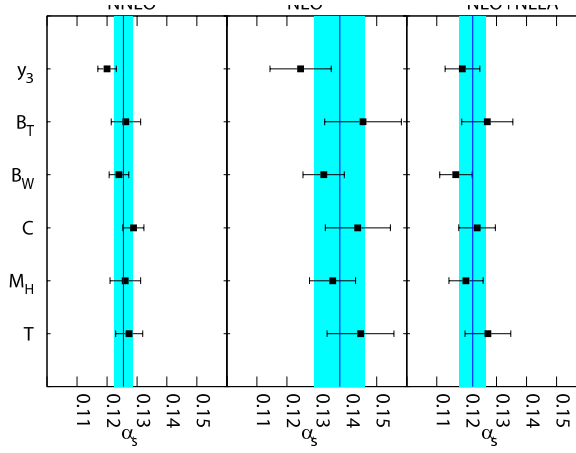


Fig. 7: Combination of  $\alpha_s$  fits at NLO, NLLA+NLO and NNLO.

dramatic than the one obtained at NLO level. The reason for this is that the compensation for the two-loop running of the coupling constant is present only in the NNLO coefficient and not in the resummed part.

These results show that there is space for further improvements, which could be obtained by resumming subleading logarithms similarly to what was done recently for thrust [38]. Improvements are also expected from the addition of electroweak corrections. Finally, a further step forward in the comparison of theoretical predictions with experimental data could be done by using modern MC tools based on NLO calculations matched with parton showers for the computation of the hadronization corrections.

## 5 Precision resummed QEDxQCD theory for LHC physics: status and update

*Authors: B.F.L. Ward, S. Joseph, Swapan Majhi, S.A. Yost*

With the advent of the LHC, we enter the era of precision QCD, by which we mean predictions for QCD processes at the total theoretical precision tag of 1% or better. The attendant requirement for this theoretical precision is control of the  $\mathcal{O}(\alpha_s^2 L^{n_1}, \alpha_s \alpha L^{n_2}, \alpha^2 L^{n_3})$ ,  $n_1 = 0, 1, 2$ ,  $n_2 = 1, 2$ ,  $n_3 = 2$  corrections in the presence of realistic parton showers, on an event-by-event basis – here,  $L$  is a generic big logarithm. This is the objective of our approach to precision QCD theory, which for example will be needed for the expected 2% experimental precision [40–42] at the LHC for processes such as  $pp \rightarrow V + m(\gamma) + n(G) + X \rightarrow \bar{\ell}\ell' + m'(\gamma) + n(G) + X$ ,  $V = W^\pm, Z$ , and  $\ell = e, \mu$ ,  $\ell' = \nu_e, \nu_\mu(e, \mu)$  for  $V = W^+(Z)$  respectively, and  $\ell = \nu_e, \nu_\mu$ ,  $\ell' = e, \mu$  respectively for  $V = W^-$ . Here, we present the elements of our approach and its recent applications in Monte Carlo (MC) event generator studies, which are still preliminary.

At such a precision as we have as our goal, issues such as the role of QED are an integral part of the discussion and we deal with this by the simultaneous resummation of QED and QCD large infrared (IR) effects,  $QED \otimes QCD$  resummation [43–49] in the presence of parton showers, to be realized on an event-by-event basis by MC methods. This is reviewed in the next section. Let us note already that in Refs. [50–55] it has been shown that QED evolution enters



at the  $\sim 0.3\%$  level for parton distributions and that in Refs. [56, 57] it has been shown that EW (large Sudakov logs, etc.) effects at LHC energies, as W's and Z's are almost massless on the TeV scale, can enter at the several percent level – such corrections must be treated systematically before any claim of 1% precision can be taken seriously. We are presenting a framework in which this can be done. The new amplitude-based resummation algebra then leads to a new scheme for calculating hard hadron-hadron scattering processes, IR-improved DGLAP-CS theory [58] for parton distributions, kernels, reduced cross sections with the appropriate shower/ME matching. This is summarized in Sec. 1.4.3. In this latter section, with an eye toward technical precision cross checks plus possible physical effects of heavy quark masses, we also deal with the issue of quark masses as collinear regulators [59–63] as an alternative [64] to the usual practice of setting all initial state quark masses to zero in calculating initial state radiation (ISR) effects in higher order QCD corrections. We also discuss in Sec. 1.4.3 the relationship between our resummation algebra and that of Refs. [65–69], as again such comparisons will be necessary in assessing the ultimate theoretical precision tag. In Sec. 1.4.4, we illustrate recent results we have obtained for the effects of our new approach on the parton showers as they are generated with the HERWIG6.5 MC [70]. Extensions of such studies to PYTHIA [71] and MC@NLO [72, 73] are in progress. Section 1.4.5 contains summary remarks.

As a point of reference, in Ref. [74] it has been argued that the current state-of-the-art theoretical precision tag on single Z production at the LHC is  $(4.1 \pm 0.3)\% = (1.51 \pm 0.75)\%(QCD) \oplus 3.79(PDF) \oplus 0.38 \pm 0.26(EW)\%$ , where the results of Refs. [72, 73, 75–86] have been used in this precision tag determination.<sup>2</sup>

### 5.0.7 $QED \otimes QCD$ Resummation

In Refs. [43–49], we have extended the YFS theory to the simultaneous exponentiation of the large IR terms in QCD and the exact IR divergent terms in QED, so that for the prototypical subprocesses  $\bar{Q}'Q \rightarrow \bar{Q}'''Q'' + m(G) + n(\gamma)$  we arrive at the new result

$$d\hat{\sigma}_{\text{exp}} = e^{\text{SUM}_{\text{IR}}(\text{QCED})} \sum_{m,n=0}^{\infty} \frac{1}{m!n!} \int \prod_{j_1=1}^m \frac{d^3 k_{j_1}}{k_{j_1}} \prod_{j_2=1}^n \frac{d^3 k'_{j_2}}{k'_{j_2}} \int \frac{d^4 y}{(2\pi)^4} e^{iy \cdot (p_1 + q_1 - p_2 - q_2 - \sum k_{j_1} - \sum k'_{j_2}) + D_{\text{QCED}}} \tilde{\beta}_{m,n}(k_1, \dots, k_m; k'_1, \dots, k'_n) \frac{d^3 p_2}{p_2^0} \frac{d^3 q_2}{q_2^0}, \quad (15)$$

where the new YFS [88–98] residuals, defined in Refs. [43–49],  $\tilde{\beta}_{m,n}(k_1, \dots, k_m; k'_1, \dots, k'_n)$ , with  $m$  hard gluons and  $n$  hard photons, represent the successive application of the YFS expansion first for QCD and subsequently for QED. The functions  $\text{SUM}_{\text{IR}}(\text{QCED})$ ,  $D_{\text{QCED}}$  are determined from their analogues  $\text{SUM}_{\text{IR}}(\text{QCD})$ ,  $D_{\text{QCD}}$  in Refs. [99–104] via the substitutions

$$\begin{aligned} B_{QCD}^{nls} &\rightarrow B_{QCD}^{nls} + B_{QED}^{nls} \equiv B_{QCED}^{nls}, \\ \tilde{B}_{QCD}^{nls} &\rightarrow \tilde{B}_{QCD}^{nls} + \tilde{B}_{QED}^{nls} \equiv \tilde{B}_{QCED}^{nls}, \\ \tilde{S}_{QCD}^{nls} &\rightarrow \tilde{S}_{QCD}^{nls} + \tilde{S}_{QED}^{nls} \equiv \tilde{S}_{QCED}^{nls} \end{aligned} \quad (16)$$

<sup>2</sup>Recently, the analogous estimate for single W production has been given in Ref. [87] – it is  $\sim 5.7\%$ .

everywhere in expressions for the latter functions given in Refs. [99–104] – see Refs. [43–49] for the details of this substitution. It can be readily established [43–49] that the QCD dominant corrections happen an order of magnitude earlier in time compared to those of QED so that the leading term  $\tilde{\beta}_{0,0}$  already gives us a good estimate of the size of the effects we study.

Important in any total theoretical prediction is knowledge of possible systematic issues associated with one’s methods. This entails the relationship between different approaches to the same classes of corrections and moves us to the relationship between our approach to QCD resummation and the more familiar approach in Refs. [65–67]. It has been shown in Ref. [105] that the latter approach is entirely equivalent to the approach in Refs. [68, 69]. Establishing the relationship between our approach and that in Refs. [65–67] will then suffice to relate all three approaches.

In Ref. [106] the more familiar resummation for soft gluons in Refs. [65–67] is applied to a general  $2 \rightarrow n$  parton process [f] at hard scale  $Q$ ,  $f_1(p_1, r_1) + f_2(p_2, r_2) \rightarrow f_3(p_3, r_3) + f_4(p_4, r_4) + \dots + f_{n+2}(p_{n+2}, r_{n+2})$ , where the  $p_i, r_i$  label 4-momenta and color indices respectively, with all parton masses set to zero to get

$$\begin{aligned} \mathcal{M}_{\{r_i\}}^{[f]} &= \sum_L^C \mathcal{M}_L^{[f]}(c_L)_{\{r_i\}} \\ &= J^{[f]} \sum_L^C S_{LI} H_I^{[f]}(c_L)_{\{r_i\}}, \end{aligned} \quad (17)$$

where repeated indices are summed,  $J^{[f]}$  is the jet function,  $S_{LI}$  is the soft function which describes the exchange of soft gluons between the external lines, and  $H_I^{[f]}$  is the hard coefficient function. The attendant IR and collinear poles are calculated to 2-loop order. To make contact with our approach, identify in  $\bar{Q}'Q \rightarrow \bar{Q}'''Q'' + m(G)$  in (15)  $f_1 = Q, \bar{Q}', f_2 = \bar{Q}', f_3 = Q'', f_4 = \bar{Q}''', \{f_5, \dots, f_{n+2}\} = \{G_1, \dots, G_m\}$  so that  $n = m+2$  here. Observe the following:

- By its definition in Eq.(2.23) of Ref. [106], the anomalous dimension of the matrix  $S_{LI}$  does not contain any of the diagonal effects described by our infrared functions  $\Sigma_{IR}(QCD)$  and  $D_{QCD}$ .
- By its definition in Eqs.(2.5) and (2.7) of Ref. [106], the jet function  $J^{[f]}$  contains the exponential of the virtual infrared function  $\alpha_s \Re B_{QCD}$ , so that we have to take care that we do not double count when we use (17) in (15) and the equations that lead thereto.

It follows that, referring to our analysis in Ref. [107], we identify  $\bar{\rho}^{(m)}$  in Eq.(73) in this latter reference in our theory as

$$\begin{aligned} \bar{\rho}^{(m)}(p_1, q_1, p_2, q_2, k_1, \dots, k_m) &= \overline{\sum_{colors, spin}} |\mathcal{M}'_{\{r_i\}}^{[f]}|^2 \\ &\equiv \sum_{spins, \{r_i\}, \{r'_i\}} \mathfrak{h}_{\{r_i\}, \{r'_i\}}^{cs} |\bar{J}^{[f]}|^2 \sum_{L=1}^C \sum_{L'=1}^C S_{LI}^{[f]} H_I^{[f]}(c_L)_{\{r_i\}} \left( S_{L'I'}^{[f]} H_{I'}^{[f]}(c_{L'})_{\{r'_i\}} \right)^\dagger, \end{aligned} \quad (18)$$

where here we defined  $\bar{J}^{[f]} = e^{-\alpha_s \Re B_{QCD}} J^{[f]}$ , and we introduced the color-spin density matrix for the initial state,  $\mathfrak{h}^{cs}$ . Here, we recall (see Refs. [58, 107], for example) that in our theory, we

have

$$d\hat{\sigma}^n = \frac{e^{2\alpha_s \text{Re} B_{QCD}}}{n!} \int \prod_{m=1}^n \frac{d^3 k_m}{(k_m^2 + \lambda^2)^{1/2}} \delta(p_1 + q_1 - p_2 - q_2 - \sum_{i=1}^n k_i) \bar{\rho}^{(n)}(p_1, q_1, p_2, q_2, k_1, \dots, k_n) \frac{d^3 p_2 d^3 q_2}{p_2^0 q_2^0}, \quad (19)$$

for  $n$ -gluon emission. It follows that we can repeat thus our usual steps (see Refs. [58, 107]) to get the QCD corrections in our formula (15), without any double counting of effects. This use of the results in Ref. [106] is in progress.

### 5.0.8 IR-Improved DGLAP-CS Theory: Applications

In Refs. [58, 107] it has been shown that application of the result (15) to all aspects of the standard formula for hard hadron-hadron scattering processes,

$$\sigma = \sum_{i,j} \int dx_1 dx_2 F_i(x_1) F_j(x_2) \hat{\sigma}(x_1 x_2 s) \quad (20)$$

where the  $\{F_i(x)\}$  and  $\hat{\sigma}$  denote the parton densities and reduced cross section, respectively, leads one to its application to the DGLAP-CS theory itself for the kernels which govern the evolution of the parton densities in addition to the implied application to the respective hard scattering reduced cross section. The result is a new set of IR-improved kernels [58],

$$P_{qq}(z) = C_F F_{YFS}(\gamma_q) e^{\frac{1}{2}\delta_q} \left[ \frac{1+z^2}{1-z} (1-z)^{\gamma_q} - f_q(\gamma_q) \delta(1-z) \right], \quad (21)$$

$$P_{Gq}(z) = C_F F_{YFS}(\gamma_q) e^{\frac{1}{2}\delta_q} \frac{1+(1-z)^2}{z} z^{\gamma_q}, \quad (22)$$

$$P_{GG}(z) = 2C_G F_{YFS}(\gamma_G) e^{\frac{1}{2}\delta_G} \left\{ \frac{1-z}{z} z^{\gamma_G} + \frac{z}{1-z} (1-z)^{\gamma_G} + \frac{1}{2} (z^{1+\gamma_G} (1-z) + z(1-z)^{1+\gamma_G}) - f_G(\gamma_G) \delta(1-z) \right\}, \quad (23)$$

$$P_{qG}(z) = F_{YFS}(\gamma_G) e^{\frac{1}{2}\delta_G} \frac{1}{2} \{ z^2 (1-z)^{\gamma_G} + (1-z)^2 z^{\gamma_G} \}. \quad (24)$$

in the standard notation, where

$$\gamma_q = C_F \frac{\alpha_s}{\pi} t = \frac{4C_F}{\beta_0} \quad (25)$$

$$\delta_q = \frac{\gamma_q}{2} + \frac{\alpha_s C_F}{\pi} \left( \frac{\pi^2}{3} - \frac{1}{2} \right) \quad (26)$$

$$\gamma_G = C_G \frac{\alpha_s}{\pi} t = \frac{4C_G}{\beta_0} \quad (27)$$

$$\delta_G = \frac{\gamma_G}{2} + \frac{\alpha_s C_G}{\pi} \left( \frac{\pi^2}{3} - \frac{1}{2} \right) \quad (28)$$

and

$$F_{YFS}(\gamma_q) = \frac{e^{-C_E \gamma_q}}{\Gamma(1 + \gamma_q)}, \quad (29)$$

so that

$$f_q(\gamma_q) = \frac{2}{\gamma_q} - \frac{2}{\gamma_q + 1} + \frac{1}{\gamma_q + 2} \quad (30)$$

$$f_G(\gamma_G) = \frac{n_f}{C_G} \frac{1}{(1 + \gamma_G)(2 + \gamma_G)(3 + \gamma_G)} + \frac{2}{\gamma_G(1 + \gamma_G)(2 + \gamma_G)} \quad (31)$$

$$+ \frac{1}{(1 + \gamma_G)(2 + \gamma_G)} + \frac{1}{2(3 + \gamma_G)(4 + \gamma_G)} \quad (32)$$

$$+ \frac{1}{(2 + \gamma_G)(3 + \gamma_G)(4 + \gamma_G)}. \quad (33)$$

Here,  $C_E = 0.5772\dots$  is Euler's constant and  $\Gamma(w)$  is the Euler Gamma function. We see that the kernels are integrable at the IR end-points and this admits a more friendly MC implementation, which is in progress.

Some observations are in order. First, we note that the connection of (24) with the higher-order kernel results in Refs. [108–117] is immediate and has been shown in Refs. [58, 107]. Second, there is no contradiction with the standard Wilson expansion, as the terms we resum are not in that expansion by its usual definition. Third, we do not change the predicted cross section: we have a new scheme such that the cross section in (20) becomes

$$\sigma = \sum_{i,j} \int dx_1 dx_2 F'_i(x_1) F'_j(x_2) \hat{\sigma}'(x_1 x_2 s) \quad (34)$$

order by order in perturbation theory, where  $\{P^{exp}\}$  factorize  $\hat{\sigma}_{\text{unfactorized}}$  to yield  $\hat{\sigma}'$  and its attendant parton densities  $\{F'_i\}$ . Fourth, when one solves for the effects of the exponentiation in (24) on the actual evolution of the parton densities from the typical reference scale of  $Q_0 \sim 2\text{GeV}$  to  $Q = 100\text{ GeV}$  one finds [58, 107] shifts of  $\sim 5\%$  for the NS  $n=2$  moment for example, which is thus of some phenomenological interest— see for example Ref. [118]. Finally, we note that we have used [43–49] the result (15) for single Z production with leptonic decay at the LHC (and at FNAL) to focus on the ISR alone, for definiteness and we find agreement with the literature in Refs. [119–123] for exact  $\mathcal{O}(\alpha)$  results and Refs. [124–126] for exact  $\mathcal{O}(\alpha_s^2)$  results, with a threshold QED effect of  $0.3\%$ , similar to that found for the parton evolution itself from QED in Refs. [50–55]. Evidently, any 1% precision tag must account for all such effects.

### 5.0.9 Shower/ME Matching

In using (15) in (34) for  $\hat{\sigma}'(x_i x_j)$ , we intend to combine our exact extended YFS calculus with HERWIG [70] and PYTHIA [71] as follows: they generate a parton shower starting from  $(x_1, x_2)$  at the factorization scale  $\mu$  after this point is provided by the  $\{F'_i\}$  and we may use [43–49] either a  $p_T$ -matching scheme or a shower-subtracted residual scheme where the respective new residuals  $\{\hat{\beta}_{n,m}(k_1, \dots, k_n; k'_1, \dots, k'_m)\}$  are obtained by expanding the shower formula and the result in (15) on product and requiring the agreement with exact results to the specified order.<sup>3</sup>

<sup>3</sup>See Ref. [127, 128] for a realization of the shower subtracted residual scheme in the context of QED parton showers.

This combination of theoretical constructs can be systematically improved with exact results order-by-order in  $\alpha_s, \alpha$ , with exact phase space.<sup>4</sup> The recently developed new parton evolution algorithms in Refs. [129, 130] may also be used here.

The issue of the non-zero quark masses in the ISR is present when one wants 1% precision, as we know that the parton densities for the heavy quarks are all different and the generic size of mass corrections for bremsstrahlung is  $\alpha_s/\pi$  for cross sections [131], so that one would like to know whether regularizing a zero-mass ISR radiation result with dimensional methods, carrying through the factorization procedure gives the same result as doing the same calculation with the physical, non-zero mass of the quark and again carrying through the factorization procedure to the accuracy  $\alpha_s^2/\pi^2$ , for example. Until the analysis in Ref. [64], this cross check was not possible because in Refs. [59–62] it was shown that there is a lack of Bloch-Nordsieck cancellation in the ISR at  $\mathcal{O}(\alpha_s^2)$  unless the radiating quarks are massless. The QCD resummation algebra, as used in (15), allows us to obviate [64] this theorem, so that now such cross checks are possible and they are in progress.

#### 5.0.10 Sample MC data: IR-Improved Kernels in HERWIG6.5

We have preliminary results on IR-improved showers in HERWIG6.5: we compare the  $z$  - distributions and the  $p_T$  of the IR-improved and usual DGLAP-CS showers in the Figs. 8-10. As we would expect, the IR-improved shower re-populates the soft region in both variables. The details of the implementation procedure and the respective new version of HERWIG6.5, HERWIG6.5-YFS, will appear elsewhere [132]. The analogous implementations in PYTHIA and MC@NLO are in progress, as are comparisons with IR-safe observables.

#### 5.0.11 Conclusions

The theory of Refs. [88, 89] extends to the joint resummation of QED and QCD with proper shower/ME matching built-in. For the simultaneous QED $\otimes$ QCD resummed theory, full MC event generator realization is open: a firm basis for the complete  $\mathcal{O}(\alpha_s^2, \alpha\alpha_s, \alpha^2)$  MC results needed for precision LHC physics has been demonstrated and all the latter are in progress – see Refs. [133–137] for new results on  $\epsilon$  expansions for the higher-order Feynman integrals needed to isolate the residuals in our approach, for example. This allows cross check between residuals isolated with the quark masses as regulators, something now allowed by the result in Ref. [64], and those isolated in dimensional regularization for the massless quark limit. Such cross checks are relevant for precision QCD theory. The first MC data have been shown with IR-improved showers in HERWIG6.5. The spectra are softer as expected. We look forward to the detailed comparison with IR-safe observables as generated with IR-improved and with the usual showers – this will appear elsewhere. [132]. Already, semi-analytical results at the  $\tilde{\beta}_{0,0}^{0,0}$  are consistent with the literature on single Z production, while a cross check for the analogous W production is near. As the QED is at 0.3% at threshold, it is needed for 1% precision.

## References

- [1] G. Zanderighi et al, *Higher-order calculations*. These proceedings.

---

<sup>4</sup>The current state of the art for such shower/ME matching is given in Refs. [72, 73], which realizes exactness at  $\mathcal{O}(\alpha_s)$ .

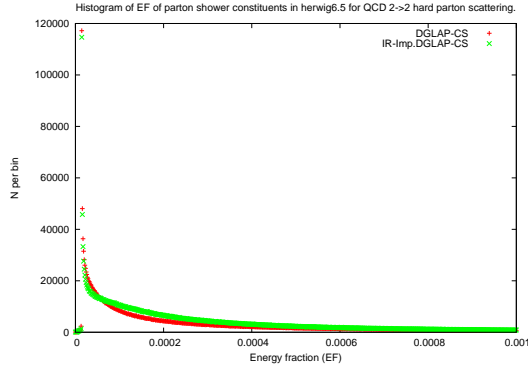


Fig. 8: The  $z$ -distribution shower comparison in HERWIG6.5 – preliminary results.

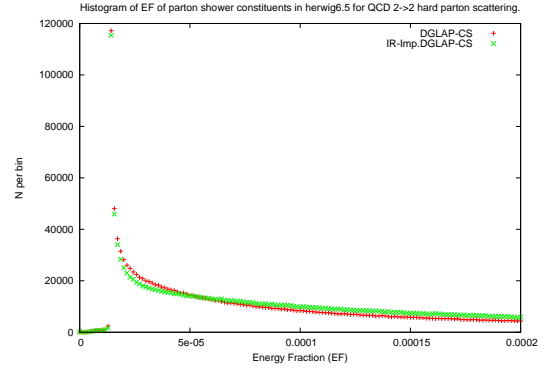


Fig. 9: The  $z$ -distribution shower comparison in HERWIG6.5 at small  $z$  – preliminary results.

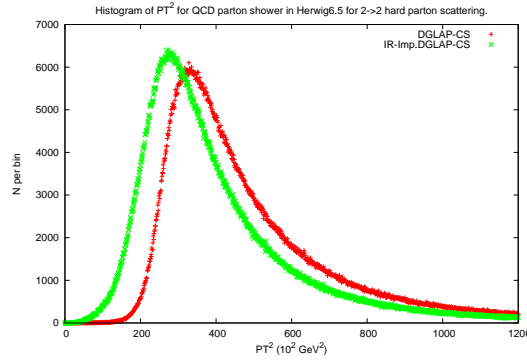


Fig. 10: The  $p_T$ -distribution shower comparison in HERWIG6.5 – preliminary results.

- [2] G. Sterman, Nucl. Phys. **281**, 310 (1987).
- [3] S. Catani and L. Trentadue, Nucl. Phys. **B 327**, 323 (1989).
- [4] G. S. A. Banfi and G. Zanderighi, JHEP **0503**, 073 (2005).
- [5] G. C. et al., JHEP **0101**, 010 (2001).
- [6] S. M. T. Sjostrand and P. Skands, JHEP **0605**, 026 (2006).
- [7] G. Marchesini and B. Webber, Nucl. Phys. **B 238**, 1 (1984).
- [8] G. Marchesini and B. Webber, Nucl. Phys. **B 310**, 461 (1988).
- [9] T. Sjostrand and P. Skands, Eur. Phys. J. **C 39**, 129 (2005).
- [10] G. M. S. Catani and B. Webber, Nucl. Phys. **B 349**, 635 (1991).

- [11] M. Dasgupta and G. Salam, Phys. Lett. **B 512**, 323 (2001).
- [12] M. Dasgupta and G. Salam, JHEP **0208**, 017 (2002).
- [13] G. C. A. Banfi and M. Dasgupta, JHEP **0703**, 050 (2007).
- [14] H1 Collaboration, A. Aktas *et al.*, Eur. Phys. J. **C33**, 477 (2004),  
arXiv:hep-ex/0310019.
- [15] D0 Collaboration, V. M. Abazov *et al.*, Phys. Rev. Lett. **94**, 221801 (2005),  
arXiv:hep-ex/0409040.
- [16] F. Hautmann and H. Jung, JHEP **10**, 113 (2008), arXiv:0805.1049 [hep-ph].
- [17] M. Dasgupta and G. P. Salam, Phys. Lett. **B512**, 323 (2001),  
arXiv:hep-ph/0104277.
- [18] M. Dasgupta and G. P. Salam, JHEP **03**, 017 (2002), arXiv:hep-ph/0203009.
- [19] N. Kidonakis, G. Oderda, and G. Sterman, Nucl. Phys. **B525**, 299 (1998),  
arXiv:hep-ph/9801268.
- [20] D. de Florian and W. Vogelsang, Phys. Rev. **D76**, 074031 (2007), arXiv:0704.1677  
[hep-ph].
- [21] A. Banfi, M. Dasgupta, and Y. Delenda, Phys. Lett. **B665**, 86 (2008),  
arXiv:0804.3786 [hep-ph].
- [22] A. Banfi, G. Marchesini, Y. L. Dokshitzer, and G. Zanderighi, JHEP **07**, 002 (2000),  
arXiv:hep-ph/0004027.
- [23] G. Dissertori *et al.*, JHEP **02**, 040 (2008), arXiv:0712.0327 [hep-ph].
- [24] A. Gehrmann-De Ridder, T. Gehrmann, E. W. N. Glover, and G. Heinrich, JHEP  
**12**, 094 (2007), arXiv:0711.4711 [hep-ph].
- [25] R. W. L. Jones, M. Ford, G. P. Salam, H. Stenzel, and D. Wicke, JHEP **12**, 007 (2003),  
arXiv:hep-ph/0312016.
- [26] S. Catani, L. Trentadue, G. Turnock, and B. R. Webber, Nucl. Phys. **B407**, 3 (1993).
- [27] R. K. Ellis, D. A. Ross, and A. E. Terrano, Nucl. Phys. **B178**, 421 (1981).
- [28] Z. Kunszt and P. Nason, CERN Yellow Report **1**, 373 (1989).
- [29] W. T. Giele and E. W. N. Glover, Phys. Rev. **D46**, 1980 (1992).
- [30] S. Catani and M. H. Seymour, Phys. Lett. **B378**, 287 (1996),  
arXiv:hep-ph/9602277.
- [31] S. Catani, G. Turnock, B. R. Webber, and L. Trentadue, Phys. Lett. **B263**, 491 (1991).



- [32] S. Catani, G. Turnock, and B. R. Webber, *Phys. Lett.* **B295**, 269 (1992).
- [33] Y. L. Dokshitzer, A. Lucenti, G. Marchesini, and G. P. Salam, *JHEP* **01**, 011 (1998), [arXiv:hep-ph/9801324](#).
- [34] S. Catani and B. R. Webber, *Phys. Lett.* **B427**, 377 (1998), [arXiv:hep-ph/9801350](#).
- [35] E. Gardi and L. Magnea, *JHEP* **08**, 030 (2003), [arXiv:hep-ph/0306094](#).
- [36] A. Banfi, G. P. Salam, and G. Zanderighi, *JHEP* **01**, 018 (2002), [arXiv:hep-ph/0112156](#).
- [37] T. Gehrmann, G. Luisoni, and H. Stenzel, *Phys. Lett.* **B664**, 265 (2008), [arXiv:0803.0695 \[hep-ph\]](#).
- [38] T. Becher and M. D. Schwartz, *JHEP* **07**, 034 (2008), [arXiv:0803.0342 \[hep-ph\]](#).
- [39] ALEPH Collaboration, A. Heister *et al.*, *Eur. Phys. J.* **C35**, 457 (2004).
- [40] M. Dittmar, F. Pauss, and D. Zurcher, *Phys. Rev.* **D56**, 7284 (1997), [arXiv:hep-ex/9705004](#).
- [41] LHC Collaboration, M. Rijssenbeek. Prepared for 14th Topical Conference on Hadron Collider Physics (HCP 2002), Karlsruhe, Germany, 29 Sep - 4 Oct 2002.
- [42] M. Dittmar. Prepared for 14th Topical Conference on Hadron Collider Physics (HCP 2002), Karlsruhe, Germany, 29 Sep - 4 Oct 2002.
- [43] C. Glosser, S. Jadach, B. F. L. Ward, and S. A. Yost, *Mod. Phys. Lett.* **A19**, 2113 (2004), [arXiv:hep-ph/0404087](#).
- [44] B. F. L. Ward, C. Glosser, S. Jadach, and S. A. Yost, *Int. J. Mod. Phys.* **A20**, 3735 (2005), [arXiv:hep-ph/0411047](#).
- [45] B. F. L. Ward, C. Glosser, S. Jadach, and S. A. Yost (2004), [arXiv:hep-ph/0410277](#).
- [46] B. F. L. Ward and S. A. Yost (2005), [arXiv:hep-ph/0509003](#).
- [47] B. F. L. Ward and S. A. Yost (2006), [arXiv:hep-ph/0610230](#).
- [48] B. F. L. Ward and S. A. Yost, *Acta Phys. Polon.* **B38**, 2395 (2007), [arXiv:0704.0294 \[hep-ph\]](#).
- [49] B. F. L. Ward and S. A. Yost, *PoS RADCOR2007*, 038 (2007), [arXiv:0802.0724 \[hep-ph\]](#).
- [50] S. Haywood *et al.* (1999), [arXiv:hep-ph/0003275](#).
- [51] H. Spiesberger, *Phys. Rev.* **D52**, 4936 (1995), [arXiv:hep-ph/9412286](#).



- [52] M. Roth and S. Weinzierl, Phys. Lett. **B590**, 190 (2004), arXiv:hep-ph/0403200.
- [53] J. Blumlein and H. Kawamura, Nucl. Phys. **B708**, 467 (2005), arXiv:hep-ph/0409289.
- [54] W. J. Stirling, A. D. Martin, R. G. Roberts, and R. S. Thorne. Prepared for 32nd International Conference on High-Energy Physics (ICHEP 04), Beijing, China, 16-22 Aug 2004.
- [55] A. D. Martin, R. G. Roberts, W. J. Stirling, and R. S. Thorne, Eur. Phys. J. **C39**, 155 (2005), arXiv:hep-ph/0411040.
- [56] M. Ciccolini, A. Denner, and S. Dittmaier, PoS **RADCOR2007**, 014 (2007), arXiv:0712.2895 [hep-ph].
- [57] A. Denner, M. Melles, and S. Pozzorini, Nucl. Phys. **B662**, 299 (2003), arXiv:hep-ph/0301241.
- [58] B. Ward, Advances in High Energy Physics, p. 682312 (2008). Article ID 682312.
- [59] C. Di’Lieto, S. Gendron, I. G. Halliday, and C. T. Sachrajda, Nucl. Phys. **B183**, 223 (1981).
- [60] R. Doria, J. Frenkel, and J. C. Taylor, Nucl. Phys. **B168**, 93 (1980).
- [61] S. Catani, M. Ciafaloni, and G. Marchesini, Nucl. Phys. **B264**, 588 (1986).
- [62] S. Catani, Z. Phys. **C37**, 357 (1988).
- [63] Particle Data Group Collaboration, W. M. Yao *et al.*, J. Phys. **G33**, 1 (2006).
- [64] B. F. L. Ward (2007), arXiv:0707.2101 [hep-ph].
- [65] G. Sterman, Nucl. Phys. **B281**, 310 (1987).
- [66] S. Catani and L. Trentadue, Nucl. Phys. **B327**, 323 (1989).
- [67] S. Catani and L. Trentadue, Nucl. Phys. **B353**, 183 (1991).
- [68] C. W. Bauer, A. V. Manohar, and M. B. Wise, Phys. Rev. Lett. **91**, 122001 (2003), arXiv:hep-ph/0212255.
- [69] C. W. Bauer, C. Lee, A. V. Manohar, and M. B. Wise, Phys. Rev. **D70**, 034014 (2004), arXiv:hep-ph/0309278.
- [70] G. Corcella *et al.* (2002), arXiv:hep-ph/0210213.
- [71] T. Sjostrand, L. Lonnblad, S. Mrenna, and P. Skands (2003), arXiv:hep-ph/0308153.
- [72] S. Frixione and B. R. Webber, JHEP **06**, 029 (2002), hep-ph/0204244.

- [73] S. Frixione, P. Nason, and B. R. Webber, *JHEP* **08**, 007 (2003), [hep-ph/0305252](#).
- [74] N. E. Adam, V. Halyo, and S. A. Yost, *JHEP* **05**, 062 (2008), [arXiv:0802.3251 \[hep-ph\]](#).
- [75] W. K. Tung *et al.*, *JHEP* **02**, 053 (2007), [arXiv:hep-ph/0611254](#).
- [76] A. D. Martin, W. J. Stirling, R. S. Thorne, and G. Watt, *Phys. Lett.* **B652**, 292 (2007), [arXiv:0706.0459 \[hep-ph\]](#).
- [77] K. Melnikov and F. Petriello, *Phys. Rev. Lett.* **96**, 231803 (2006), [arXiv:hep-ph/0603182](#).
- [78] K. Melnikov and F. Petriello, *Phys. Rev.* **D74**, 114017 (2006), [arXiv:hep-ph/0609070](#).
- [79] Q.-H. Cao and C. P. Yuan, *Phys. Rev. Lett.* **93**, 042001 (2004), [arXiv:hep-ph/0401026](#).
- [80] C. M. Carloni Calame, G. Montagna, O. Nicrosini, and M. Treccani, *Phys. Rev.* **D69**, 037301 (2004), [arXiv:hep-ph/0303102](#).
- [81] C. M. Carloni Calame, G. Montagna, O. Nicrosini, and M. Treccani, *JHEP* **05**, 019 (2005), [arXiv:hep-ph/0502218](#).
- [82] C. M. Carloni Calame, G. Montagna, O. Nicrosini, and A. Vicini, *JHEP* **12**, 016 (2006), [arXiv:hep-ph/0609170](#).
- [83] C. M. Carloni Calame, G. Montagna, O. Nicrosini, and A. Vicini, *JHEP* **10**, 109 (2007), [arXiv:0710.1722 \[hep-ph\]](#).
- [84] E. Barberio, B. van Eijk, and Z. Was, *Comput. Phys. Commun.* **66**, 115 (1991).
- [85] E. Barberio and Z. Was, *Comput. Phys. Commun.* **79**, 291 (1994).
- [86] P. Golonka and Z. Was, *Eur. Phys. J.* **C45**, 97 (2006), [arXiv:hep-ph/0506026](#).
- [87] N. E. Adam, V. Halyo, S. A. Yost, and W. Zhu (2008), [arXiv:0808.0758 \[hep-ph\]](#).
- [88] D. R. Yennie, S. C. Frautschi, and H. Suura, *Ann. Phys.* **13**, 379 (1961).
- [89] K. T. Mahanthappa, *Phys. Rev.* **126**, 329 (1962).
- [90] S. Jadach and B. F. L. Ward, *Comput. Phys. Commun.* **56**, 351 (1990).
- [91] S. Jadach, W. Placzek, E. Richter-Was, B. F. L. Ward, and Z. Was, *Comput. Phys. Commun.* **102**, 229 (1997).
- [92] S. Jadach and B. F. L. Ward, *Phys. Lett.* **B274**, 470 (1992).

- [93] S. Jadach, W. Placzek, and B. F. L. Ward, Phys. Lett. **B390**, 298 (1997), arXiv:hep-ph/9608412.
- [94] S. Jadach, M. Skrzypek, and B. F. L. Ward, Phys. Rev. **D55**, 1206 (1997).
- [95] S. Jadach, W. Placzek, and B. F. L. Ward, Phys. Rev. **D56**, 6939 (1997), arXiv:hep-ph/9705430.
- [96] S. Jadach, B. F. L. Ward, and Z. Was, Phys. Rev. **D63**, 113009 (2001), arXiv:hep-ph/0006359.
- [97] S. Jadach, B. F. L. Ward, and Z. Was, Comput. Phys. Commun. **130**, 260 (2000), arXiv:hep-ph/9912214.
- [98] S. Jadach, W. Placzek, M. Skrzypek, B. F. L. Ward, and Z. Was, Comput. Phys. Commun. **140**, 432 (2001), arXiv:hep-ph/0103163.
- [99] B. F. L. Ward and S. Jadach, Acta Phys. Polon. **B33**, 1543 (2002), arXiv:hep-ph/0205062.
- [100] B. F. L. Ward and S. Jadach (2002), arXiv:hep-ph/0210357.
- [101] B. F. L. Ward and S. Jadach, Mod. Phys. Lett. **A14**, 491 (1999).
- [102] D. DeLaney *et al.*, Mod. Phys. Lett. **A12**, 2425 (1997), arXiv:hep-ph/9506302.
- [103] D. B. DeLaney, S. Jadach, C. Shio, G. Siopsis, and B. F. L. Ward, Phys. Rev. **D52**, 108 (1995), arXiv:hep-ph/9403204.
- [104] D. B. DeLaney, S. Jadach, C. Shio, G. Siopsis, and B. F. L. Ward, Phys. Lett. **B342**, 239 (1995), arXiv:hep-ph/9304320.
- [105] C. Lee and G. Sterman, Phys. Rev. **D75**, 014022 (2007), arXiv:hep-ph/0611061.
- [106] S. Mert Aybat, L. J. Dixon, and G. Sterman, Phys. Rev. **D74**, 074004 (2006), arXiv:hep-ph/0607309.
- [107] B. F. L. Ward, Annals Phys. **323**, 2147 (2008), arXiv:0707.3424 [hep-ph].
- [108] E. G. Floratos, D. A. Ross, and C. T. Sachrajda, Nucl. Phys. **B129**, 66 (1977).
- [109] E. G. Floratos, D. A. Ross, and C. T. Sachrajda, Nucl. Phys. **B152**, 493 (1979).
- [110] A. Gonzalez-Arroyo, C. Lopez, and F. J. Yndurain, Nucl. Phys. **B153**, 161 (1979).
- [111] A. Gonzalez-Arroyo and C. Lopez, Nucl. Phys. **B166**, 429 (1980).
- [112] G. Curci, W. Furmanski, and R. Petronzio, Nucl. Phys. **B175**, 27 (1980).
- [113] W. Furmanski and R. Petronzio, Phys. Lett. **B97**, 437 (1980).

- [114] E. G. Floratos, C. Kounnas, and R. Lacaze, Nucl. Phys. **B192**, 417 (1981).
- [115] R. Hamberg and W. L. van Neerven, Nucl. Phys. **B379**, 143 (1992).
- [116] S. Moch, J. A. M. Vermaseren, and A. Vogt, Nucl. Phys. **B688**, 101 (2004), [arXiv:hep-ph/0403192](#).
- [117] A. Vogt, S. Moch, and J. A. M. Vermaseren, Nucl. Phys. **B691**, 129 (2004), [arXiv:hep-ph/0404111](#).
- [118] T. Carli, G. P. Salam, and F. Siegert (2005), [arXiv:hep-ph/0510324](#).
- [119] U. Baur, S. Keller, and W. K. Sakumoto, Phys. Rev. **D57**, 199 (1998), [arXiv:hep-ph/9707301](#).
- [120] U. Baur, S. Keller, and D. Wackeroth, Phys. Rev. **D59**, 013002 (1999), [arXiv:hep-ph/9807417](#).
- [121] U. Baur, O. Brein, W. Hollik, C. Schappacher, and D. Wackeroth, Phys. Rev. **D65**, 033007 (2002), [arXiv:hep-ph/0108274](#).
- [122] S. Dittmaier and M. Kramer, Phys. Rev. **D65**, 073007 (2002), [arXiv:hep-ph/0109062](#).
- [123] V. A. Zykunov, Eur. Phys. J. direct **C3**, 9 (2001), [arXiv:hep-ph/0107059](#).
- [124] R. Hamberg, W. L. van Neerven, and T. Matsuura, Nucl. Phys. **B359**, 343 (1991).
- [125] W. L. van Neerven and E. B. Zijlstra, Nucl. Phys. **B382**, 11 (1992).
- [126] C. Anastasiou, L. J. Dixon, K. Melnikov, and F. Petriello, Phys. Rev. **D69**, 094008 (2004), [arXiv:hep-ph/0312266](#).
- [127] G. Balossini, C. M. Carloni Calame, G. Montagna, O. Nicrosini, and F. Piccinini, Nucl. Phys. Proc. Suppl. **162**, 59 (2006), [arXiv:hep-ph/0610022](#).
- [128] G. Balossini, C. M. Carloni Calame, G. Montagna, O. Nicrosini, and F. Piccinini (2006), [arXiv:hep-ph/0609313](#).
- [129] S. Jadach and M. Skrzypek, Comput. Phys. Commun. **175**, 511 (2006), [arXiv:hep-ph/0504263](#).
- [130] P. Stephens, S. Jadach, and M. Skrzypek, Acta Phys. Polon. **B38**, 2379 (2007).
- [131] T. D. Lee and M. Nauenberg, Phys. Rev. **133**, B1549 (1964).
- [132] B. W. et al., *preprint in pre.* (unpublished). To be published.
- [133] M. Y. Kalmykov, B. F. L. Ward, and S. Yost, JHEP **02**, 040 (2007), [arXiv:hep-th/0612240](#).

- [134] M. Y. Kalmykov, B. F. L. Ward, and S. A. Yost, JHEP **10**, 048 (2007),  
arXiv:0707.3654 [hep-th].
- [135] M. Y. Kalmykov, B. F. L. Ward, and S. A. Yost, JHEP **11**, 009 (2007),  
arXiv:0708.0803 [hep-th].
- [136] S. A. Yost, M. Y. Kalmykov, and B. F. L. Ward (2008), arXiv:0808.2605  
[hep-ph].
- [137] M. Y. Kalmykov and B. A. Kniehl (2008), arXiv:0807.0567 [hep-th].

# Jets and jet algorithms

*Victor Coco, Pierre-Antoine Delsart, Juan Rojo, Christian Sander Grégory Soyez*

Jets are an important tool in hadronic physics and they will play a predominant role at the LHC. By defining jets as clusters of particles one aims at accessing, from the final-state particles, the underlying hard parton-level processes. Therefore jets are an essential tool for a variety of studies, such as top reconstruction, mass measurements, Higgs and new physics (NP) searches. Furthermore, they are instrumental for QCD studies, *e.g.* for inclusive jet measurements, which in turn constitute an important input for the determination of parton distribution functions. By clustering particles into jets, jet algorithms reduce complicated multiparticle events in simple final states with few jets. This procedure and the way particles are recombined together (*e.g.* the  $E$ - or  $P$ -scheme) is fundamentally non-unique.

In the following we will present recent progress in the description of jets, both from the phenomenological and the experimental points of view. In particular, we will focus on different aspects of the SIScone and anti- $k_t$  jet algorithms. We will also describe jet finding strategies and jet reconstruction and calibration techniques being developed by the LHC experiments ATLAS, CMS and LHCb.

Finally, a recurring question in jet studies is what the best jet definition for a given physics analysis is. We will present a proposal of a characterization of jet-finding “quality” designed to be simple, robust, physical and reasonably representative of common analysis tasks.

## 1 The SIScone and anti- $k_t$ jet algorithms

*Author: Grégory Soyez*

Two broad classes of jet definitions exist. The first one works by defining a distance between pairs of particles, performing successive recombinations of the pair of closest particles and stopping when all resulting objects are too far apart. Algorithms within this clustering class differ by the definition of the distance, frequent choices being  $d_{ij}^2 = \min(k_{t,i}^2, k_{t,j}^2)(\Delta y_{ij}^2 + \Delta \phi_{ij}^2)$  for the  $k_t$  algorithm [1,2], and  $d_{ij}^2 = (\Delta y_{ij}^2 + \Delta \phi_{ij}^2)$  for the Cambridge-Aachen algorithm [3,4].

Cone algorithms make up the second class, where jets are defined as dominant directions of energy flow. One introduces the concept of *stable cone* as a circle of fixed radius  $R$  in the  $y - \phi$  plane such that the sum of all the momenta of the particles within the cone points in the same direction as the centre of the circle. Cone algorithms attempt to identify all the stable cones. Most implementations use a seeded approach to do so: starting from a given seed *e.g.*, a given direction for the centre of the cone, one computes the contents of the cone, takes the resulting momentum as a new direction and iterates until the cone is found stable. The set of seeds can be taken as the set of initial particles (sometimes over a  $p_t$  threshold) or as the midpoints between previously-found stable cones. As we shall see, this iterative method fails to identify *all* stable cones, leading to infrared (IR) or collinear unsafety in the perturbative computations.

Cone algorithms can be split into two sub-classes according to how they deal with the fact that stable cones may overlap. On the one hand, cone algorithms with split-merge identify the

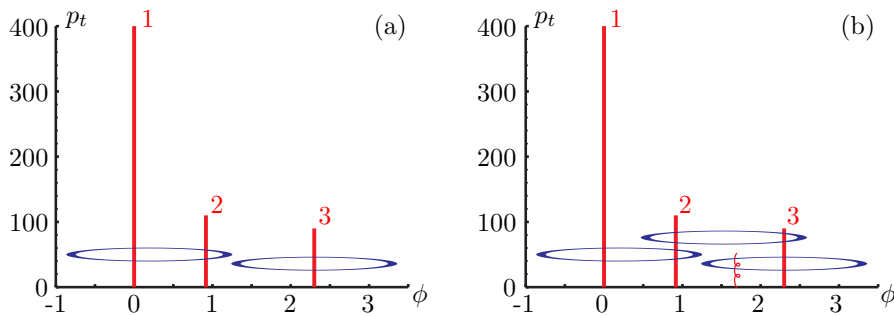


Fig. 1: Stable cones found by the midpoint algorithm for a 3-particle event (left) and for the same event with an additional infinitely soft gluon (right).

hardest overlapping pair of stable cones and merge (split) them if they share more (less) than a fraction  $f$  of the hardest cone. JetClu, midpoint and the ATLAS cone algorithms are typical representatives of that sub-class. On the other hand, cone algorithms with progressive removal start with the hardest unclustered particle, iterate from there until a stable cone is found and call it a jet. Its contents are removed and one starts again with the remaining particles. The CMS iterative cone is the typical example of this second sub-class, with the particular feature that hard jets are fully conical.

The Snowmass accords have established a series of requirements that any jet algorithm has to fulfill. These are basically that one can use the algorithm for theoretical computations, *e.g.* it gives finite perturbative results, as well as for experimental purposes, *e.g.* it runs fast enough and has small corrections from hadronisation and the underlying event.

We show in these proceedings that both the cone algorithms with split-merge and with progressive removal fail to give finite perturbative results. More precisely, we illustrate that midpoint suffers from IR unsafety and the iterative cone is collinear unsafe. We introduce SIScone and the anti- $k_t$  algorithms as infrared- and collinear-safe solutions to those problems that do not spoil the experimental usability. We conclude by discussing the importance of using these new algorithms if we want to take full advantage of jet studies at the LHC.

## 1.1 SIScone as a replacement for the midpoint algorithm

Let us consider the 3-particle event displayed in Fig. 1(a). When clustered with the midpoint algorithm, 2 stable cones are found, leading to two jets: one with particles 1 and 2 and a second one with particle 3. If one adds to that hard event an infinitely soft gluon as shown in Fig. 1(b), a third stable cone is found and the three hard particles are clustered in a single jet. This change in the jet structure upon addition of soft particles, a phenomenon which happens with infinite probability in perturbative QCD, gives rise to divergences in the perturbative expansion and proves that the midpoint algorithm is IR unsafe<sup>1</sup>. Note also that the situation is even worse with JetClu or the ATLAS cone algorithms, where the IR unsafety is already present in events with 2 particles, *i.e.* one order earlier in the perturbative expansion.

<sup>1</sup>Note that when a seed threshold is used, the midpoint algorithm becomes collinear unsafe.

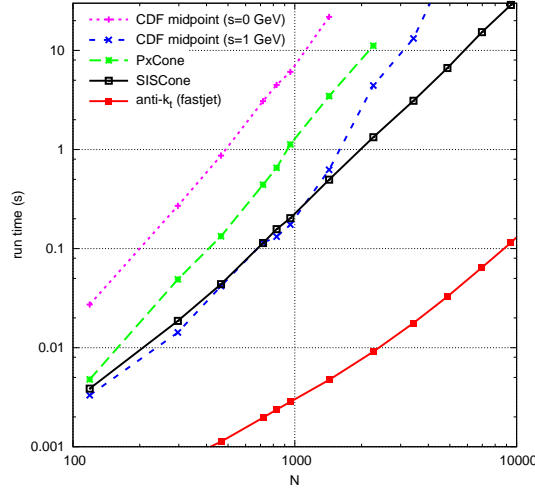


Fig. 2: Clustering time for SIScone compared to typical implementations of the midpoint and anti- $k_t$  algorithms.

This problem arises from the fact that the seeded approach misses stable cones — here the one containing particles 2 and 3 in Fig. 1(a). The workaround to restore IR safety is thus to find a seedless method that provably identifies all stable cones. This is notoriously complex: a naive approach testing the stability of all subsets of particles [5] has a complexity of order  $N \times 2^N$  for  $N$  particles which is much slower than the  $\mathcal{O}(N^3)$  complexity of the midpoint algorithm, making this solution unusable for experimental purposes.

The solution [6] is to use the geometrical observation that any enclosure in the  $y - \phi$  plane can be moved without changing its contents until it touches two points. Browsing all pairs of particles allows thus to enumerate all possible cones and to check their stability at an overall cost of  $\mathcal{O}(N^3)$ . Additional efforts to limit the amount of full stability tests to its minimum can even bring the final complexity to  $\mathcal{O}(N^2 \log(N))$ , *i.e.* faster than the midpoint algorithm. This has been implemented [6–9] in a C++ code named SIScone (Seedless Infrared Safe Cone). Fig. 2 illustrates the fact that in practice SIScone runs faster than the typical implementations of the midpoint algorithm without a seed threshold and at least as fast as when a 1 GeV seed threshold is used.

Therefore, SIScone is the first cone algorithm to satisfy the Snowmass requirements, that is to be at the same time IR and collinear safe, and to be fast enough to be used in experimental analysis.

## 1.2 Anti- $k_t$ as a replacement for the iterative cone algorithm

As for the midpoint algorithm, we start by considering an event with three hard particles (see Fig. 3(a)). When clustered with the iterative cone, iteration starts with particle 2, one stable cone containing all particles is found, resulting in a 1-jet event. If we now split the hardest particle (2) into two collinear particles (2a and 2b) — a process that also happens with an infinite probability in perturbative QCD — as shown on Fig. 3(b), clustering with the iterative cone now starts with



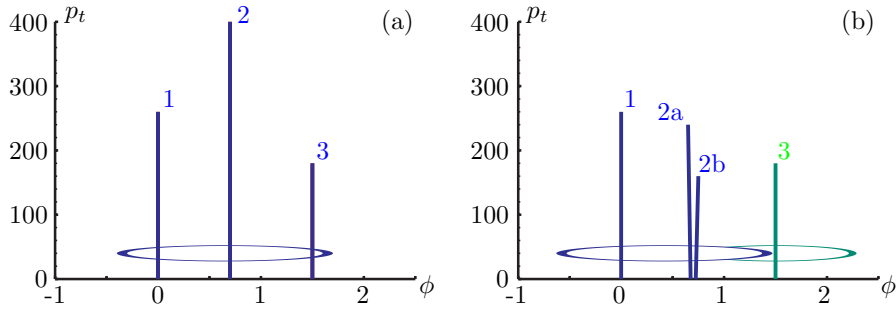


Fig. 3: Jets found by the iterative cone for a 3-particle event (left) and for the same event with a collinear splitting (right).

particle 1 which, after iteration, gives a first jet made of particle 1 plus the two collinear ones, then a second jet with particle 3. This example proves that the iterative cone algorithm is collinear unsafe.

Quite surprisingly, we can find a solution to that problem by coming back to the class of the recombination algorithms. The distance measures introduced earlier can be written as

$$d_{ij}^2 = \min(k_{t,i}^{2p}, k_{t,j}^{2p})(\Delta y_{ij}^2 + \Delta\phi_{ij}^2),$$

with  $p = 1$  for the  $k_t$  algorithm and  $p = 0$  for the Cambridge-Aachen algorithm. We can then consider a third case, the one for which  $p = -1$  and call it the *anti- $k_t$*  algorithm [10]. Obviously, this algorithm is IR and collinear safe. Furthermore, its implementation can benefit from the same geometrical observations that allowed for fast implementation of the  $k_t$  algorithm [8]. The anti- $k_t$  algorithm thus runs at a speed similar to the one of the  $k_t$  algorithm, which certainly makes it usable for experimental purposes as seen on Fig. 2.

To understand the link between the anti- $k_t$  algorithm and the iterative cone algorithm, we note from the definition of the anti- $k_t$  distance that pairs involving a hard particle will be given small distances. This means that soft particles will be recombined with hard ones before recombining among themselves. As a result, the hard jets will have a circular boundary. This soft-resilience of the anti- $k_t$  algorithm is exactly the hallmark of the iterative cone and it is in that respect that the anti- $k_t$  can be seen as its IR and collinear safe replacement.

To illustrate this property, we show in Fig. 4 the jets resulting from the clustering of an event made with a few hard particles and a large number of very soft ones uniformly dis-

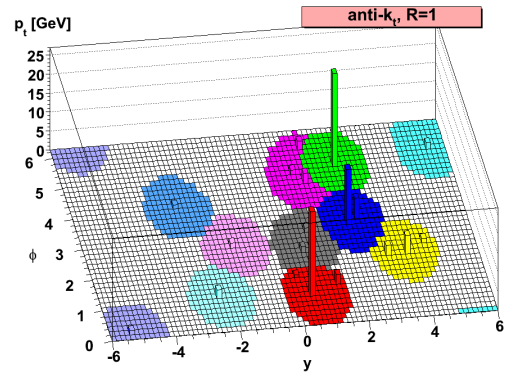
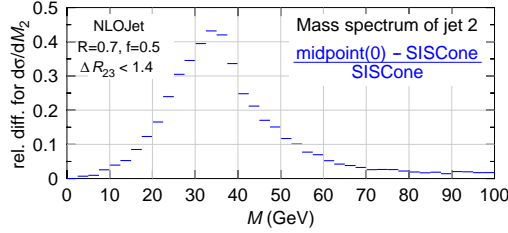


Fig. 4: Illustration of the regularity of the jets obtained with the anti- $k_t$  algorithm.

Observable	first miss cones at	Last meaningful order
Inclusive jet cross section	NNLO	NLO
$W/Z/H + 1$ jet cross section	NNLO	NLO
3 jet cross section	NLO	LO (NLO in NLOJet)
$W/Z/H + 2$ jet cross sect.	NLO	LO (NLO in MCFM)
jet masses in 3 jets	LO	<b>none</b> (LO in NLOJet)

Table 1: Perturbative level at which IR or collinear unsafety arises for various processes.

Fig. 5: Mass of the 2<sup>nd</sup> hardest jet in 3-jet events: relative difference between midpoint and SIScone. The 2<sup>nd</sup> and 3<sup>rd</sup> jets are imposed to be distant by at most  $2R$ .

tributed on a grid in the  $y - \phi$  plane. It is clear that the hardest jets are perfectly circular and that, in general, the boundaries between the jets are regular.

### 1.3 Physical impact and discussion

As we have seen, the seeded approach to stable cone search suffers from problems with respect to perturbative QCD expansion: the algorithms with split-merge are IR unsafe, while the iterative cone (with progressive removal) is collinear unsafe. We have introduced SIScone as a natural replacement of the cone algorithms with split-merge like midpoint, and the anti- $k_t$  algorithm as a candidate to replace the iterative cone. These new algorithms are both IR and collinear safe.

The question one might ask is to what extent these IR and collinear safety issues are important in real measurements. Since the unsafety arises when one has 3 particles in a common vicinity, it becomes important at the order  $\alpha_s^4$  or  $\alpha_{EW}\alpha_s^3$  of the perturbative series.

Table 1 summarises for different physical processes, the order at which seeded algorithms like midpoint of the iterative cone stop to be valid. The main message we can get from that table is that, if we do not want theoretical efforts in precise QCD computations to be done in vain, the resort of an IR and collinear safe algorithm like SIScone and the anti- $k_t$  is fundamental.

To illustrate the argument more quantitatively, Fig. 5 shows the relative difference, expected to be present at the LO of perturbative QCD, between SIScone and midpoint for the mass of the second hardest jet in 3-jet events. Differences reaching up to 40% are observed, proving that an IR and collinear safe algorithm is mandatory. The situation is even worse with JetClu or the ATLAS cone algorithm. As the infrared-unsafety problem becomes apparent at the order  $\alpha_s^3$  or  $\alpha_{EW}\alpha_s^2$ , *i.e.* one order earlier than with midpoint.

## 2 Quality measures for jet finding at the LHC

Author: *Juan Rojo*

A recurring question in jet studies is what the best jet definition for a given physics analysis is. In this contribution we propose a characterization of jet-finding “quality” designed to be simple, robust, physical and reasonably representative of common analysis tasks.

For this purpose, we require a source of quarks and gluons with well-defined energies. We will obtain these from Monte Carlo production and decay of fictitious narrow  $Z'$  and  $H$  bosons, with  $Z' \rightarrow q\bar{q}$  and  $H \rightarrow gg$  generated with Pythia 6.5 [11] with di-jet invariant masses ranging from 100 GeV to 4 TeV. For each generated event we will cluster the event into jets with about 50 different jet definitions, where a jet definition, JD, consists of the jet algorithm and the associated parameters, like the radius  $R$  [12]. The radius  $R$  will be varied between 0.3 and 1.5. For each event, we determine the invariant mass of the sum of the two hardest jets. The distribution of invariant masses should then have a peak near the heavy boson mass. We will take the sharpness of that peak to be indicative of the quality of each jet definition.

The infrared- and collinear-safe (IRC) safe jet algorithms under scrutiny are the longitudinally invariant inclusive  $k_t$  algorithm [1,2,13], the Cambridge-Aachen (C/A) algorithm [3,4], the anti- $k_t$  algorithm [10], SIScone [6] as well as C/A with filtering. The latter is C/A supplemented with a filtering procedure [14] in which, subsequent to the jet finding, each jet is unclustered down to subjets at angular scale  $x_{\text{filt}}R$  and one retains only the  $n_{\text{filt}}$  hardest of the subjets. We use  $x_{\text{filt}} = 0.5$  and  $n_{\text{filt}} = 2$ . All the jet algorithms have been used in the implementations and/or plug-ins of the `FastJet` package [8], version 2.3, with the exception of C/A with filtering, which will be made public in a forthcoming `FastJet` release.

This contribution summarizes work [15] in collaboration with M. Cacciari, G. Salam and G. Soyez, initiated in the context of the “Les Houches Physics at TeV colliders 2007” workshop [12].

### 2.1 Quality measures and effective luminosity ratio

As described in detail in [15], the merit of the jet finding is quantified by two quality measures:

1.  $Q_{f=z}^w$ : the width of the smallest (reconstructed) mass window that contains a fraction  $f = z$  of the generated massive objects,

$$f \equiv \left( \frac{\# \text{ reco. massive objects in window of width } w}{\text{Total } \# \text{ generated massive objects}} \right) = z. \quad (1)$$

2.  $Q_{w=x\sqrt{M}}^{1/f}$ : to compute this quality measure, we take a window of fixed width  $w$  and slide it over the mass distribution so as to maximise its contents. Then the figure of merit is given by

$$Q_{w=x\sqrt{M}}^{1/f} \equiv \left( \frac{\text{Max } \# \text{ reco. massive objects in window of width } w = x\sqrt{M}}{\text{Total } \# \text{ generated massive objects}} \right)^{-1}, \quad (2)$$

It is clear from its definitions that the smaller the quality measures, the better the corresponding jet definition. An illustrative example of these two measures is shown in Fig. 6. We observe that the quality measures quantify the intuitive assessment of the goodness of jet finding, represented by the sharpness of the reconstructed invariant mass peak. Note that in our approach, any matching to non-physical quantities like Monte Carlo partons is deliberately avoided.

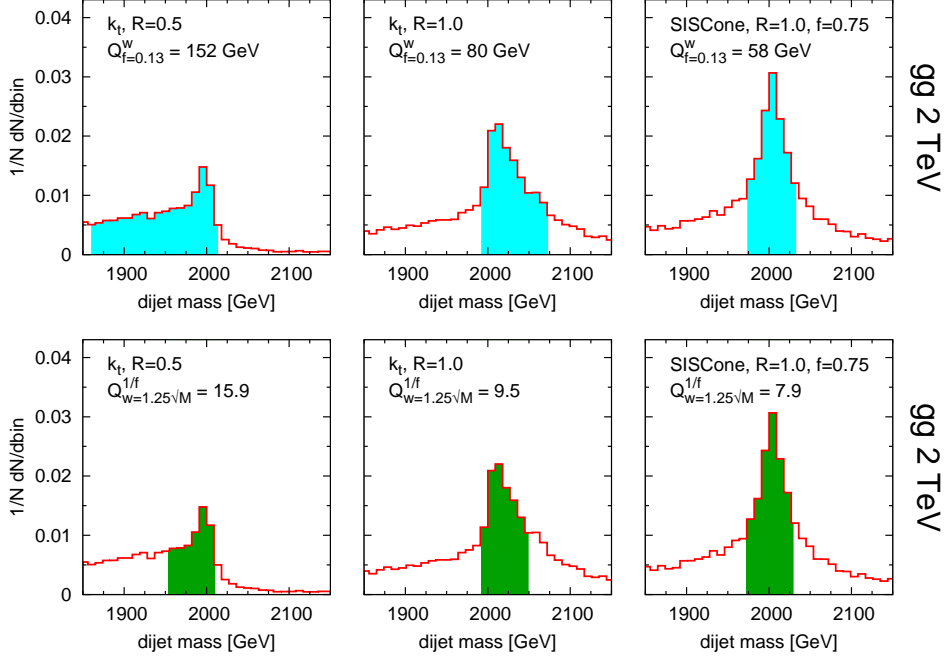


Fig. 6: Di-jet invariant mass distributions for the  $gg$  case at  $M = 2$  TeV, comparing three jet definitions for each process. The shaded bands indicate the region used when obtaining the two different quality measures.

These quality measures can be mapped to the corresponding variation of integrated luminosity needed to maintain constant signal significance. As we have seen, a larger quality measure indicates a worse jet definition. This in turn implies that a larger luminosity will be needed to obtain a given significance. It is convenient to express this in terms of an effective luminosity ratio,

$$\rho_{\mathcal{L}}(\text{JD}_2/\text{JD}_1) \equiv \frac{\mathcal{L}(\text{needed with JD}_2)}{\mathcal{L}(\text{needed with JD}_1)} = \left[ \frac{\Sigma(\text{JD}_1)}{\Sigma(\text{JD}_2)} \right]^2. \quad (3)$$

with the signal significance defined in the usual way  $\Sigma(\text{JD}) \equiv N_{\text{signal}}^{\text{JD}} / \sqrt{N_{\text{bkgd}}^{\text{JD}}}$ . Given a certain signal significance with  $\text{JD}_1$ ,  $\rho_{\mathcal{L}}(\text{JD}_2/\text{JD}_1)$  indicates the factor more luminosity needed to obtain the same significance with  $\text{JD}_2$ . For example, the expression for  $\rho_{\mathcal{L}}$  in terms of the first quality measure is

$$\rho_{\mathcal{L}}(\text{JD}_2/\text{JD}_1) = \frac{Q_{f=z}^w(\text{JD}_2)}{Q_{f=z}^w(\text{JD}_1)}. \quad (4)$$

A non-trivial check of the robustness of our analysis is that the luminosity ratios obtained with the two different quality measures are roughly consistent with each other.

## 2.2 Results

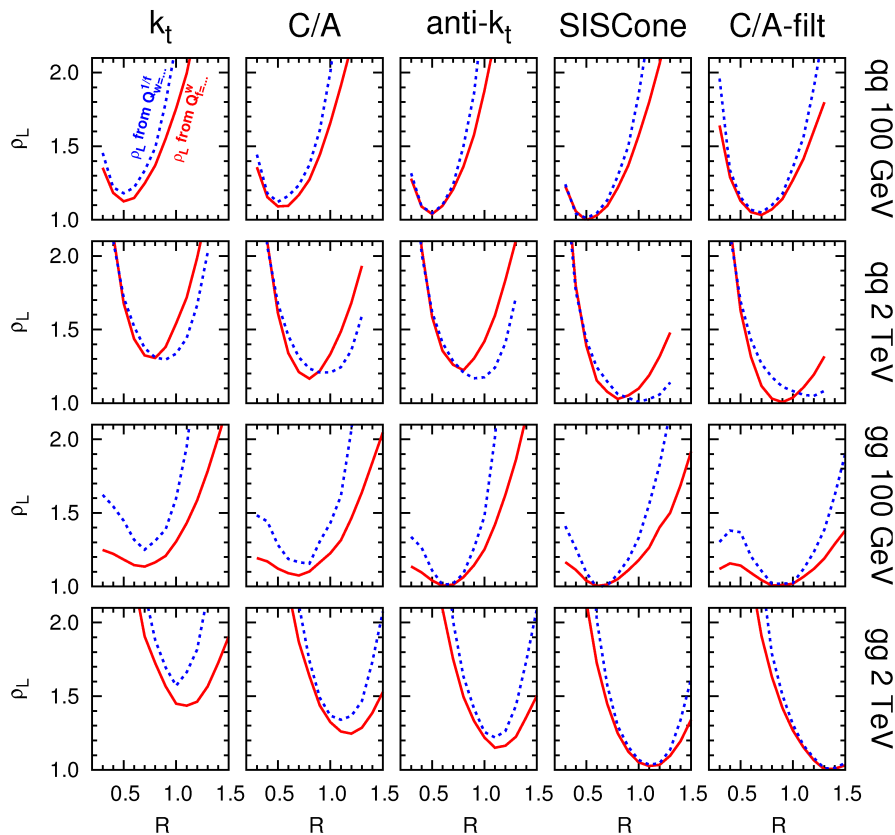


Fig. 7: The effective luminosity ratio, Eq. 3, for quark and gluon jets at 100 GeV and 2 TeV, for all algorithms studied. The two curves in each plot correspond to the value of  $\rho_L$  computed from the respective quality measure. For each process,  $\rho_L$  is normalized to the corresponding optimal jet definition.

Now we present selected results for the effective luminosity ratio for the different cases considered. We show in Fig. 7 a summary of the performance of the various jet definitions studied, for quark and gluon jets at 100 GeV and 2 TeV, without pile-up (PU). First of all, we observe a strong dependence of  $\rho_L$  with respect to  $R$ , as well as sizable differences between jet algorithms. SISCone and C/A-filt turn out to be the optimal jet algorithms in all studied processes. They achieve limited sensitivity to the Underlying Event (UE) while maintaining their perturbative reach. The optimal value of  $R$  grows with the scale of the process, specially for gluon jets, reflecting the interplay between perturbative and non-perturbative effects [16]. Our studies imply that at the TeV scale, rather large values of  $R \sim 1$  are required to obtain optimal

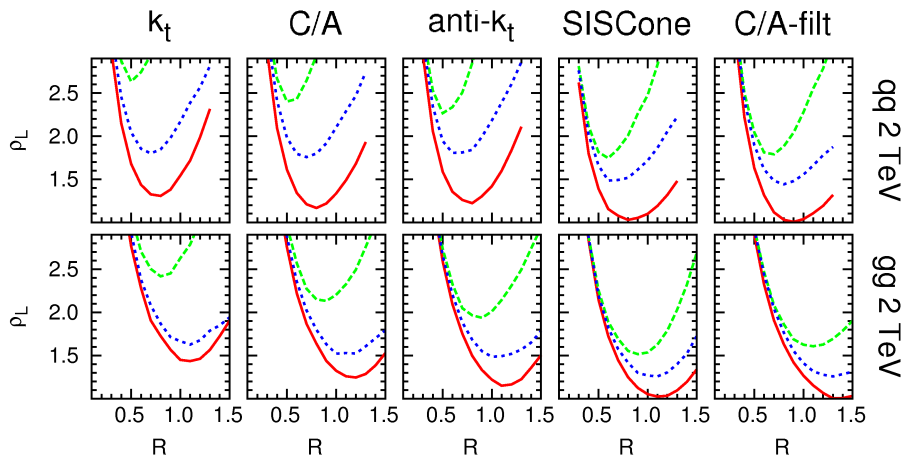


Fig. 8: The effective luminosity ratio, for quark and gluon jets at 100 GeV and 2 TeV, for all five algorithms studied. The red solid lines correspond to the no-PU case, the green dashed lines to the high luminosity PU case while the blue dotted curves correspond to high luminosity with PU subtracted as explained in the text.

resolution. LHC experiments, on the other hand, plan to use smaller radii in general, see for example Ref. [17].

From Fig. 7 one can determine how much more luminosity will be required with a less favoured jet definition compared with the optimal one. For example, we see that for the  $gg$  case at 2 TeV, if the  $k_t$  algorithm is used instead of the optimal one (SIScone), then 50% more luminosity will be required to achieve the same signal significance even at the respective optimal values of  $R$ .

These results are robust against high-luminosity PU [15] once PU is subtracted using the FastJet area method [18, 19], as can be seen in Fig. 8. This has the important consequence that for a given process, a single jet definition could be used at the LHC regardless of the machine luminosity.

As a practical application of our studies, one can consider the impact of less favoured jet definitions in LHC searches with similar signatures. For example, let us consider a particular scenario in which a di-jet invariant mass distribution is reconstructed and let us assume that the jet clustering is performed with a jet definition,  $JD_2$ , whose quality is far from the optimal one,  $JD_1$ , so that the effective luminosity ratio is large, say  $\rho_L \sim 2$ . The net effect of the choice of such non-optimal jet definition for the kinematical reconstruction can be summarized schematically in Fig. 9: the use of  $JD_1$  rather than  $JD_2$  would lead to a discovery signal with approximately only half of the machine running time required with the original jet definition.

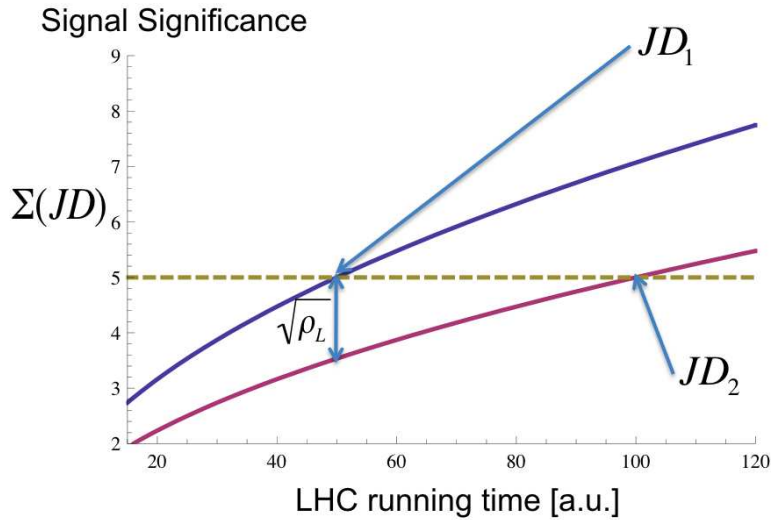


Fig. 9: Example of how optimizing the jet definition might lead to discoveries in less machine running time, compared to the non-optimal one.

### 2.3 Conclusions

Summarizing, we have proposed a technique to quantify the performance of jet algorithms for kinematic reconstructions at the LHC. To allow for more detailed studies of the results of Ref. [15], an interactive webpage has been created at <http://quality.fastjet.fr>, which allows the user to test the effects of changing and modifying various jet definitions and other inputs like PU luminosity for the process under scrutiny.

## 3 Performance of jet reconstruction at CMS

*Author: Christian Sander (on behalf of the CMS Collaboration)*

Almost every process of interest at the LHC contains quarks or gluons in the final state. The partons can not be observed directly, but fragment into stable hadrons, which can be detected in the tracking and calorimeter systems. Calorimeter jets are expected to yield a good description of both the parton-level and the hadron showers emerging from the hard interaction. For Monte Carlo (MC) events, the hadron-level is defined by applying the same clustering algorithms, which are typically formulated to accept any set of four-vectors as input to all stable particles from the MC truth record (“GenJets”). Hadron-level is also referred to as “particle-level”, and jet energy scale corrections based on MC and later on data-driven methods are derived to correct back to this detector independent level. Calorimeter jets are reconstructed using energy deposits in calorimeter towers (“CaloTowers”) as inputs: they are composed of one or more hadronic calorimeter (HCAL) cells and corresponding electromagnetic calorimeter (ECAL) crystals.

The studies presented in what follows are based on QCD di-jet and  $t\bar{t}$  MC samples without pile-up. It is often necessary to associate CaloJets with GenJets in these samples to probe how well the calorimeter-level reconstruction represents the hadron-level of the process. This



association is based on spatial separation in the  $\eta$ - $\phi$ -space between the two jet axes by requiring

$$\Delta R = \sqrt{\Delta\eta^2 + \Delta\phi^2}$$

to be less than a certain value. Besides good correspondence to the parton-level and hadron-level, a successful jet algorithm should fulfill two important requirements. Firstly, it should be collinear-safe, such that the outcome remains unchanged if *e.g.* the energy carried by a single particle is instead distributed among two collinear particles. Collinear safety is typically endangered if the jet finding is based on energetic seeds and a threshold is applied to these seeds. Secondly, it should be infrared-safe, such that the result of the jet finding is stable against the addition of soft particles. Jet algorithms which don't comply with either or both of these requirements yield ambiguous results and lead to unnecessary uncertainties when applied to calculations in perturbative theory. The performance of the following four jet clustering algorithms is discussed:

- The Iterative Cone algorithm is a simple seeded cone-based algorithm employed by CMS online in the High Level Trigger (HLT). It has a short and predictable execution time, but is neither collinear- nor infrared-safe.
- The Midpoint Cone [5] algorithm is similar to the Iterative Cone, but infrared-safety is addressed by considering the midpoints between each pair of close (proto-)jets as additional seeds. Despite its improvements to the cone-based clustering procedure, the algorithm has been shown not to be infrared-safe. This algorithm is no longer supported by CMS.
- SIScone [6] is the “Seedless Infrared-Safe Cone” jet algorithm. It is collinear- and infrared-safe to all orders of perturbative QCD (pQCD) and demands only slightly higher execution time compared to the Midpoint Cone algorithm.
- fast- $k_T$  [8] is a recent implementation of the  $k_T$  algorithm [1] which is also collinear- and infrared-safe. It has a dramatically reduced execution time with respect to previous implementations of the  $k_T$  algorithm.

The “ $E$ -Scheme” is used for all algorithms as the recombination scheme: the energy and momentum of a jet are defined as the sums of energies and momenta of its constituents. The execution time of the fast- $k_T$  algorithm is comparable to the Iterative Cone algorithm without the discussed deficiencies of the latter. The SIScone algorithm requires more CPU resources compared to the Midpoint Cone algorithm. The time spent for the jet reconstruction (0.02 s) of each event however is small compared to the total event reconstruction time (10 s): the particular jet algorithm choice does not impact the overall CPU requirements.

### 3.1 Summary of Jet Performance Study

The performance of the CMS calorimeters is known to be different in the barrel, endcaps and forward regions. Here we focus on the relative performance between different algorithms and radius parameter choices currently supported for CMS analysis. Only distributions for the barrel region are therefore shown. Further details can be found in [20].

The jet matching efficiency is defined as the ratio of the number of particle jets matched to a calorimeter jet within  $\Delta R < 0.5$  to the total number of particle jets. It represents a meaningful measure of the reconstruction efficiency of each jet algorithm, but is strongly correlated



to the position resolution and therefore depends on the  $\Delta R$  cut and the jet size parameter. However, relative comparisons between different algorithms using equivalent size parameters remain instructive. The matching efficiencies for small (left) and large (right) radius parameters as a function of the MC truth  $p_T^{\text{gen}}$  are shown in Fig. 10. The efficiencies of jets reconstructed with the fast- $k_T$  and SIScone algorithms indicate better performance than jets reconstructed with the MidpointCone and Iterative Cone algorithms.

For the jet response,  $R_{\text{jet}} = p_T/p_T^{\text{gen}}$ , very good agreement between the individual algorithms is found for all regions of the detector, indicating good correspondence between the values of  $D$  for the fast- $k_T$  algorithm and  $R$  for cone algorithms which are being compared [20].

The  $\eta$  resolutions for jets in the barrel region are shown as a function of  $p_T^{\text{gen}}$  in Fig. 11. Good agreement is found among all algorithms with comparable radius parameter, with marginal differences at low  $p_T^{\text{gen}}$ . Jets reconstructed with larger radius parameters yield slightly worse resolution. Note that the position of the primary vertex is assumed to be at  $z = 0$ , which dilutes the  $\eta$  resolution with respect to taking the correct position measured with the tracking detectors into account. The  $\phi$  resolutions can be found in [20].

Fig. 12 shows the jet energy resolutions derived from MC truth for jets in the barrel region. Jets reconstructed with fast- $k_T$  show slightly worse resolution at low  $p_T^{\text{gen}}$ , while no significant impact of the radius parameter choice is observed. The typical jet energy resolution at high  $p_T$ , 100 GeV or 1 TeV, is  $\sim 14\%$  and  $\sim 7\%$  respectively, with no significant dependence on the jet clustering algorithm.

The jet reconstruction performance in  $t\bar{t}$  events is studied by selecting events with one (“lepton+jets”) or zero (“alljets”) electron(s) or muon(s) in the final state from a  $t\bar{t}$  sample with no additional jets (“ $t\bar{t}+0$  jets”).  $t \rightarrow bq\bar{q}'$  and  $\bar{t} \rightarrow \bar{b}\bar{q}q'$  decays are identified on particle level and only events are considered for which all three decay products of one or both  $t(\bar{t})$  decay(s) can be uniquely matched to reconstructed calorimeter jets. The efficiency to select these decays indicates the performance of the respective jet algorithm in a busy multi-jet environment and its ability to correctly resolve the topology of the underlying process. The fast- $k_T$  algorithm is hereby found to fully resolve hadronic  $t(\bar{t})$  decays on calorimeter level more efficiently than any cone-based algorithm. For the selected events, the invariant two-jet ( $W$  boson) and three-jet (top quark) masses are compared on particle-level, calorimeter-level, corrected calorimeter-level, and corrected calorimeter-level with additional flavor-dependent corrections applied. The  $m_W$  and  $m_t$  distributions obtained for all correction levels are shown in Fig. 13 for jets reconstructed with fast- $k_T$   $D = 0.4$ . From the width of the obtained invariant mass distributions one can see that the impact of detector effects on the mass resolution are stronger than the algorithmic differences. A full comparison of the widths of the reconstructed  $m_W$  and  $m_t$  distributions can be found in [20].

### 3.2 Conclusion

The performance comparisons presented include jet energy response, position resolutions, energy resolutions and efficiencies in QCD di-jet samples. We find similar performance at the calorimeter level between algorithms with similar size parameter. The impact of detector effects appears to be more pronounced than the algorithmic differences studied here. The SIScone algorithm performs as well as or better than the Midpoint Cone, while known to be preferred

theoretically. Therefore it was decided to adopt SIScone as the default cone-based jet algorithm and consequently to include it in the reconstruction in the standard event processing at CMS.

The fast- $k_T$  algorithm is infrared- and collinear safe to all orders of pQCD as well and complementary to the cone-based algorithms. The execution time of fast- $k_T$  is dramatically reduced with respect to earlier implementations and it is therefore well suited for the high multiplicity environment of LHC  $pp$  collisions. We find that it performs as good or better than any other compared algorithm and strongly encourage its use as an alternative to SIScone.

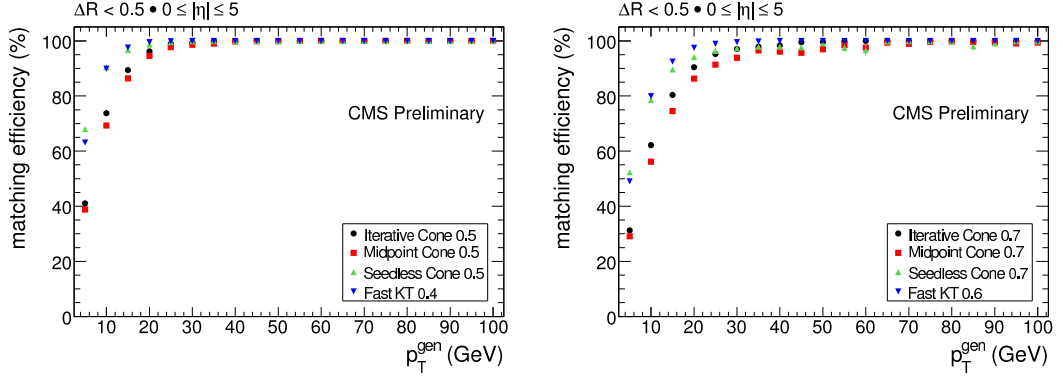


Fig. 10: Matching Efficiency versus  $p_T^{\text{gen}}$  for  $R = 0.5/D = 0.4$  (left) and  $R = 0.7/D = 0.6$  (right) jets.

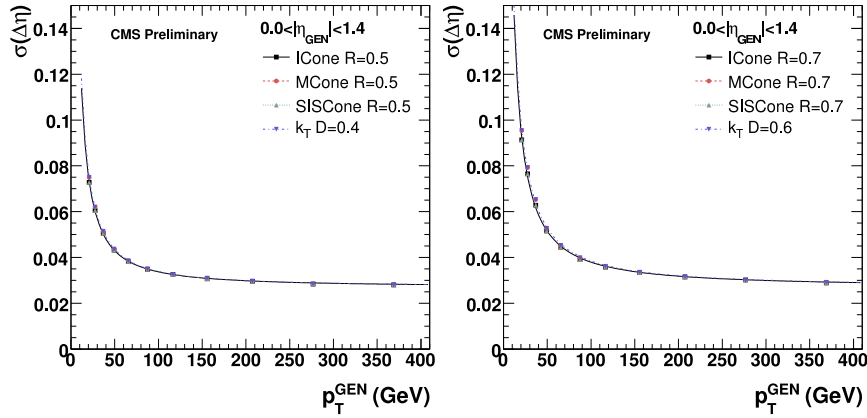


Fig. 11: The jet  $\eta$  resolutions as a function of  $p_T^{\text{gen}}$ , averaged over the Barrel region, for jets clustered with smaller (left) and larger (right) size parameters. The resolutions are derived using MC truth information.

## 4 Jet finding strategies in ATLAS

*Author: Pierre-Antoine Delsart (on behalf of the ATLAS Collaboration)*

ATLAS is a general purpose experiment at the Large Hadron Collider (LHC) [21]. Its calorimetry system, the principal tool for hadronic jet measurements, is described in detail in [21], chapter 5. Some key features of this calorimeter relevant to jet finding are its wide

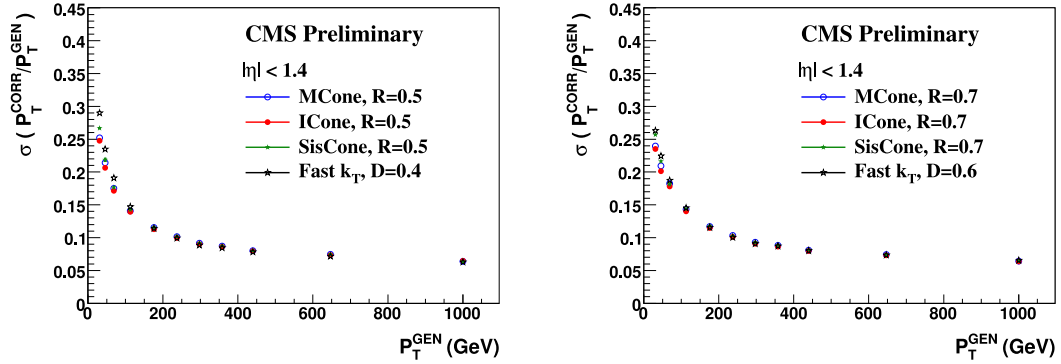


Fig. 12: Jet energy resolution derived from MC truth for Midpoint Cone, Iterative Cone, SIScone and fast- $k_T$  with  $R = 0.5/D = 0.4$  (left) and  $R = 0.7/D = 0.6$  (right) in the barrel region ( $|\eta| < 1.4$ ).

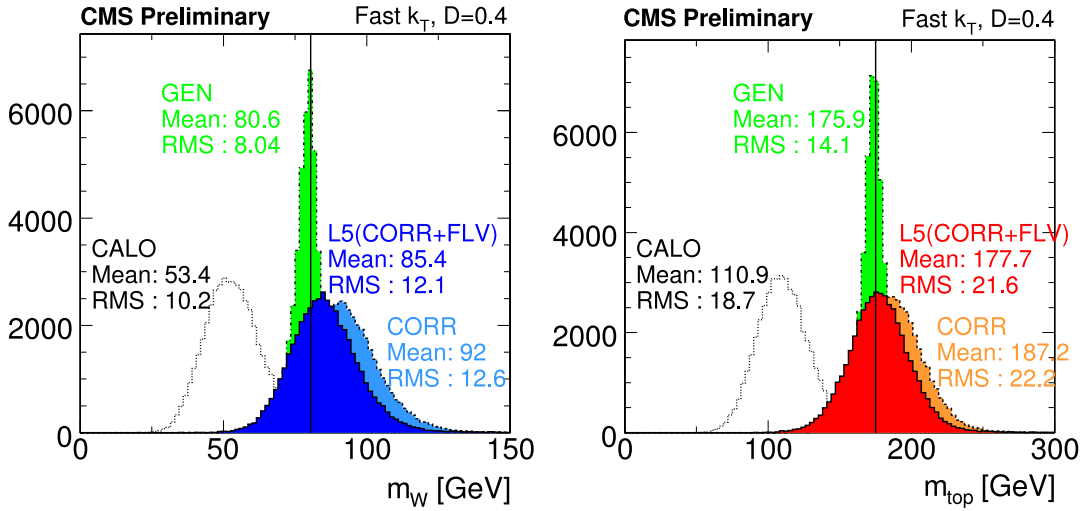


Fig. 13:  $m_W$  and  $m_t$  distributions for hadronic top decays reconstructed with the fast- $k_T$  algorithm,  $D = 0.4$ . Distributions are shown for particle-level jets (GEN), calorimeter jets (CALO), calorimeter jets corrected with “MC-Jet” corrections (CORR), and corrected calorimeter jets with an additional flavour correction applied (L5). Only jets with uncorrected  $p_T \geq 15$  GeV and  $|\eta| \leq 5$  are considered. The generated  $W$  boson (80.42 GeV) and top quark (175 GeV) masses are indicated by the black vertical lines.

acceptance (up to  $|\eta| = 4.9$  in the Forward Calorimeter) and a fine granularity (including up to 7 longitudinal segmentations). On the other hand, the calorimeter is non-compensating (ratio  $1.3 < e/\pi < 1.6$  depending on the specific sub-calorimeter) and this causes the major source of uncertainty in energy measurements because of the large fluctuations of the electromagnetic component of hadronic showers.

The other main experimental challenge will come from the LHC environment : a very large phase space for underlying event, multiple interactions per bunch crossing (23 at full luminosity). Out-of-time pile-up is also expected because of the slow response of the liquid argon calorimeter which will integrate several events before and after a given interaction.

In order to take up these challenges the ATLAS collaboration chose to adopt a flexible approach. In particular, the collaboration is studying two calibration strategies, several in-situ and data-based correction methods, and has designed a software able to cope with any jet algorithm used in physics analysis.

#### 4.1 Jet reconstruction and calibration

The ATLAS jet-related software is designed to allow any input to jet finding algorithms, provided the input is a set of valid four-momenta. This allows to run exactly the same jet finders on Monte Carlo truth simulated particles, real signal, tracks, etc. Two different calorimeter signal definitions are considered as input signal for jet finding:

- Calorimeter towers : all cells in the same projective direction (defined by a grid in the  $(\eta, \phi)$  plane) are grouped into a tower. The four-momentum is formed by the sum of the cells energies, possibly including a geometrical weight for cells larger than the tower grid size, and the direction of the tower.
- Topological clusters (“TopoClusters”). Cells are clustered together in the 3 dimensions of the calorimeter according to a nearest neighbour algorithm [21] which intrinsically performs a noise suppression.

Besides different types of input signal, ATLAS considers two approaches for the jet calibration.

**Global hadronic calibration.** Jets are built from raw calorimeter signal (towers or clusters), then a set of correction factors (weights) are applied to the energy of the constituting cells. The weights depend on the characteristics of the cells, in particular its energy density and its location in the calorimeter. They are extracted from a fit to simulated di-jet events. With this method, all calibration corrections are included in a single set of weights, hence its name “global” [22].

**Local hadronic calibration.** This second method is an attempt to have a finer, better understood calibration method for jets. It relies on hadronic calibration of topological clusters [23] : jets are built from these calibrated input signals. Then a jet energy scale correction remains to be applied. This approach is more complex but allows to decouple different corrections (non-compensation, dead material losses, energy scale) and is thus very promising.

An illustration of performance for both calibration methods is shown in Fig. 14; a detailed discussion of these performances can be found in Ref. [24];

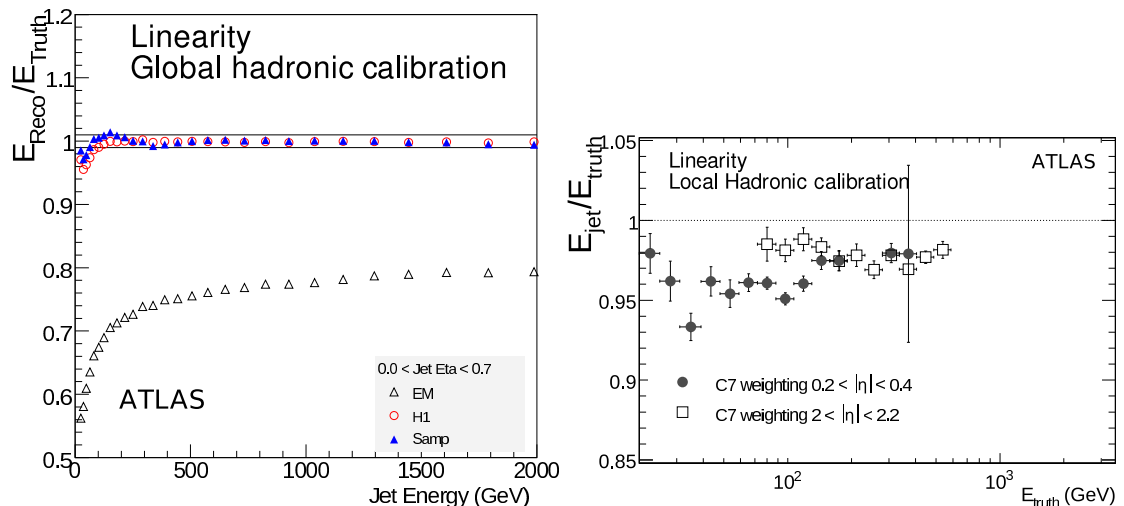


Fig. 14: Left : linearity of jet reconstruction with global calibration (QCD di-jet sample). Red and blue marks correspond to 2 alternative global calibration methods. Right: linearity with local calibration (before energy scale correction).

## 4.2 Data driven corrections

In parallel to the base-line calibrations described above, ATLAS aims to reach a precise energy scale measurement using experimental data directly. Several methods are studied:

- Momentum measurement from the tracker (P) compared to energy deposition in calorimeter (E) allows to validate the energy scale for charged pions in minimum bias events [25], studying the E/P ratio.
- QCD di-jet events can be used to uniformize the response of the calorimeter in  $\eta$  and  $\phi$  [26].
- Z+jets or  $\gamma$ +jets events will be used assuming an excellent calibration of electromagnetic objects : applying  $P_T$  balance or missing  $E_T$  projection techniques will allow to retrieve a correct jet energy scale [26].
- With QCD multi-jet events it is possible to correct high- $p_T$  jets against several lower  $p_T$  jets whose energy scale is better known thanks to previous methods [26].

In some analyses, *in-situ* methods using constraints coming from the mass of the W boson will be applied to control even better the jet energy. This is typically the case in top physics analyses where different methods are under study [27].

## 4.3 Jets algorithms, other jets studies

Several different jet algorithms are available for physics analysis. Two families of such algorithms are reconstructed by default :

- ATLAS iterative cone algorithm (described in detail in [22]), with cone radii 0.4 and 0.7;
- Kt clustering algorithm [22], setting the size parameter D to 0.3 and 0.6 .

These algorithms are officially supported and used in calibration studies. Variations of these algorithms with different jet sizes and clustering parameters can easily be configured, as appropriate in the context of a given physics analysis. In addition, other algorithms like the midpoint cone algorithm [28], the seedless infrared safe cone algorithm SIScone [6] and all flavours of recursive recombination algorithms provided in the FastJet [8] library, and the “optimal jet finder” described in [29], are available within the standard ATLAS software framework.

Various other jet-related studies are on-going in the ATLAS collaboration in order to understand better and improve jet reconstruction:

- Associating reconstructed tracks with calorimeter signals allows to obtain efficient jet energy corrections. Moreover, vertex information can help in rejecting jets coming from pile-up [24].
- Different studies are on-going in order to understand precisely the effects of pile-up, in particular in the liquid argon calorimeter.
- Jets sub-structure studies such as the use of the “y-scale” given by  $k_t$  jet algorithms [30]

#### 4.4 Conclusion

We gave a brief overview of the recent work of the ATLAS collaboration related to jets reconstruction (details in [31]). In order to deal with the great experimental challenges and to achieve an excellent measurement of hadronic jets, the collaboration has adopted a flexible approach including two main strategies for jet calibration. The collaboration is also preparing several data-based and in-situ techniques to correct and control the jet energy scale and resolution at the precision required by physics analysis as well as conducting several studies to ensure the understanding of the detector response to hadronic jets is optimal.

### 5 b-jets at LHCb

*Author: Victor Coco (on behalf of the LHCb Collaboration)*

LHCb [32] is an LHC experiment dedicated to precise measurements of CP violation and rare B-meson decays. We show that its specifications are of interest for reconstruction and identification of b-jets as well. The LHCb detector is a one-arm spectrometer. It covers the forward region of the interaction point, from 30 mrad to 300 (250) mrad in the bending (non-bending) plane. The choice of such a limited acceptance is motivated by the fact that most of the  $\approx 500 \mu\text{b}$  correlated  $b\bar{b}$  pairs are produced in this region. LHCb experiment will take data at a luminosity of  $2 \times 10^{32} \text{cm}^{-2}\text{s}^{-1}$ , where bunch crossing are dominated by single pp interactions. Good particle identification, excellent tracking and vertexing are needed for B physics measurements. Expected resolution on track momentum is about  $\delta p/p = 0.35\%$  around 10 GeV/c to  $\delta p/p = 0.55\%$  around 140 GeV/c. Impact parameter resolution is expected to be  $\sigma_{\text{IP}} = 14\mu\text{m} + 35\mu\text{m}/p_{\text{T}}$ .

#### 5.1 Reconstruction and identification of b-jets

As a textbook case, we study in the following the case of a Higgs boson decaying into  $b\bar{b}$  pairs, produced in association with a vector boson decaying leptonically. The Higgs mass is chosen

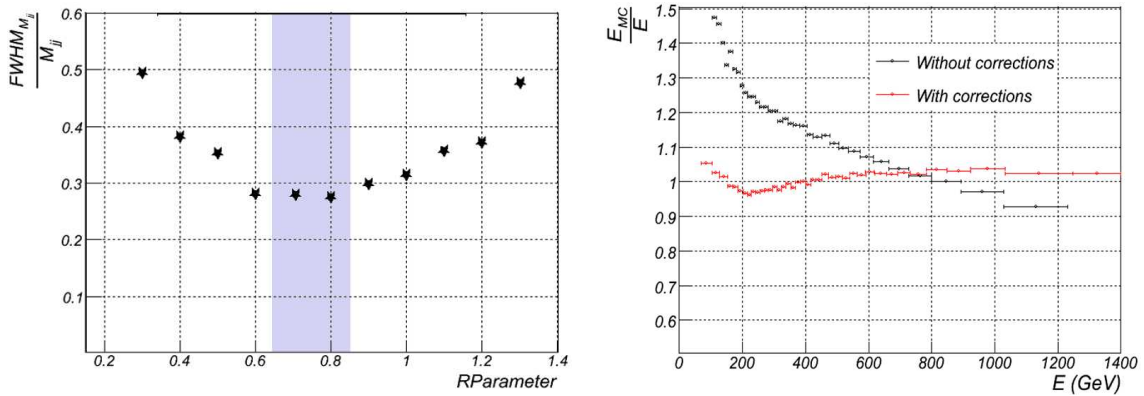


Fig. 15: Full width at half maximum (FWHM) over peak value of the di-jet mass distribution considering all particles from the generator, except neutrinos (left). True jet energy over reconstructed jet energy as a function of the reconstructed jet energy (right).

to be 120 GeV/c<sup>2</sup> and the lepton, with a transverse momentum  $p_T$  higher than 10 GeV/c, is required to be in the LHCb acceptance.

Several contributions might affect the di-jet mass resolution. In order to choose the best working point for the jet algorithm, a generator level study of the di-jet mass reconstruction is performed. The width of the di-jet mass distribution is shown in Fig. 15. At small  $R^2$ , gluon radiation and hadronisation induce a low-mass tail. This effect tends to increase the width of the distribution. For large values of  $R$ , the area of the jets is larger and the contribution of underlying event particles increases. This effect induces high-mass tails, increasing again the width of the distribution. Taking into account both effects, the optimal  $R$  value is between 0.7 and 0.9. The limited acceptance of the detector is the major restriction for jet studies at LHCb. Some jet particles arriving close to the detector border are not reconstructed. Therefore these jets need to be rejected.

Using the LHCb reconstruction framework, charged and neutral particles are separated by matching tracks and electromagnetic calorimeter clusters. In the full simulation, track measurements are used for charged particles while the energy of electromagnetic clusters is used for neutral particles. Tracks and electromagnetic clusters are calibrated objects. In a simple approach, clusters in the hadronic calorimeter are not used. The charged and neutral particles are used as input to the jet algorithm. Two ways of reconstructing and identifying b-jets are under study. The first way consists in finding tracks coming from B-decays, and use them as seed for cone-type jet finding. The second way uses a sequential recombination algorithm,  $k_t$ -jet [1], to reconstruct the jets. the  $k_t$ -jet algorithm with an  $R$  parameter of 0.75 gives on average 15 (proto-)jets for our textbook case events. Only a quarter of them has a transverse momentum higher than 5 GeV/c. The performance of b-jets reconstruction is presented below.

A primary cut is applied to remove (uninteresting) jets with  $p_T < 5$  GeV/c, less than 4 constituents and 2% of charged energy. The content of jets in particles from B-decays is

<sup>2</sup> $R$  is a generic parameter of the jet algorithm, representing in first approximation the  $(\eta, \phi)$  radius.



quantified by two weights separating b- from c- and light-jets. To construct these weights, tri-dimensional probability distribution functions have been extracted from Monte Carlo (MC) for particles that are respectively b-, light- and c-jet constituents. b-jet identification is then based on combination of these weights with several variables such as the number of constituents, the energy contained in a cone of  $R < 0.4$  around the jet axis, the charged energy percentage, etc. Taking only into account the jets that pass the primary cut, b-jet selection efficiency is about 81%, for a rejection of about 95% of light-jets and 91% of c-jets in  $t\bar{t}$  events. It is interesting to notice that the b-jets only partially inside the acceptance are rejected at more than 90% by the selection. At this level, no explicit reconstruction of vertices, nor semi-leptonic decay identification has been performed. This leaves room for future improvements.

Reconstruction of b-jets is efficient in the range of pseudorapidity  $2 < \eta < 4.2$ . For jets well contained in the acceptance, one can determine corrections to the jet energy depending on its  $p_T$  and pseudorapidity. The corrections are determined from a  $t\bar{t} \rightarrow b\bar{b} + \ell$  MC sample and applied to the b-jets of the MC Higgs sample. After correction, the energy response presents a non-linearity below 5%, see Fig. 15. In a Gaussian approximation, the di-jet mass resolution is improved from  $\sigma/\text{mean} = 24\%$  to 20%. The mass pick is still offset. The contribution due to loss of neutral hadrons will be added.

The contribution, after b-jets selection, of the remaining "partially inside the acceptance" b-jets, is shown Fig. 16. There is a 10% increase in the resolution of the corrected di-jet mass distribution due to the pollution of those jets.

## 5.2 Interesting processes for LHCb

A measurement of  $H(W, Z) \rightarrow b\bar{b} + \ell$  would be very interesting. But the level of background, especially  $t\bar{t} \rightarrow b\bar{b} + \ell$  is large and its suppression is a real challenge for LHCb. Because of the limited acceptance, global event variables (*e.g.* missing  $E_T$ , sphericity, etc.) are inaccessible. But this analysis also gives the opportunity to develop tools for b-jets studies that might be of interest for other studies involving b-jets in the forward region.

Many new physics models give rise to particles with measurable lifetime decaying into b quarks. In the following we will concentrate on feasibility of two such models.

Hidden valley is a class of phenomenological models that extends the Standard Model (SM) gauge group  $G_{SM}$  with a non-abelian group  $G_V$ . High-dimension operators at the TeV scale allow interactions between SM and new particles. Some neutral v-hadrons,  $\pi_v$ , can decay into the gauge-invariant combinations of SM-particles with observable lifetimes. An interesting process is described by M.J.Strassler and K.M.Zurek [33]. The SM Higgs, thanks to the coupling to a new scalar field, decays into two  $\pi_v$ , which decay into  $b\bar{b}$  pairs. For  $m_{\pi_v} = 45 \text{ GeV}/c^2$ , the probability of correct reconstruction of such a b-jet in LHCb is about 30% up to 50 cm flight path of the  $\pi_v$ . The di-jet mass of b-jets from  $\pi_v$  decay is shown Fig. 17.

Another interesting model was developed by L. Carpenter, D. Kaplan and E-J. Rhee [34]. They have shown that the MSSM with R-parity violation, baryon number violation and non-unified gaugino masses has a non-excluded parameter space in which a light boson decays mainly into two neutralinos. The neutralino decay length varies as the inverse square of the baryon num-



ber violation coupling constant  $\lambda''$ . The final state of such events contains six quarks, among which the probability to find b and c is large. The two vertices from the  $\tilde{\chi}^0 \rightarrow (b, c)$  sequence are reconstructed and assembled to get the  $\tilde{\chi}^0$  vertex mass. A study at generator level with vertex smearing has been performed. For  $m_{\tilde{\chi}^0} = 50 \text{ GeV}/c^2$ ,  $m_{h^0} = 115 \text{ GeV}/c^2$  and  $\lambda'' = 10^{-4}$ , about 16600 events of signal are expected. After selection of the 4 vertices per event, one gets  $\approx 6000$  events, and most of the background is rejected. The  $h^0$  mass distribution after selection, with the remaining events of  $b\bar{b}$ ,  $t\bar{t}$  and  $Z^0 W^\pm \rightarrow b\bar{b}$ , is shown on Fig. 17. Studies of vertex reconstruction and background rejection with full simulation are ongoing. Details can be found in [35].

It has been shown that LHCb can reconstruct b-jets in the forward region ( $2 < \eta < 4$ ), and reconstruct the di-jet mass with a resolution of about 20%. Selection of b-jets benefits a lot from the quality of the LHCb apparatus. Besides important B physics measurements, LHCb has the potential to observe new physics processes in the high rapidity region looking at b-jets and highly displaced vertices.

I would like to thank the LHCb Collaboration and the jets working group for stimulating discussions on the subject and for their help in the preparation of this talk.

## References

- [1] S. Catani, Y. L. Dokshitzer, M. H. Seymour, and B. R. Webber, Nucl. Phys. **B406**, 187 (1993).
- [2] S. D. Ellis and D. E. Soper, Phys. Rev. **D48**, 3160 (1993), arXiv:hep-ph/9305266.
- [3] Y. L. Dokshitzer, G. D. Leder, S. Moretti, and B. R. Webber, JHEP **08**, 001 (1997), hep-ph/9707323.
- [4] M. Wobisch and T. Wengler (1998), hep-ph/9907280.
- [5] G. C. Blazey *et al.* (2000), arXiv:hep-ex/0005012.
- [6] G. P. Salam and G. Soyez, JHEP **05**, 086 (2007), arXiv:0704.0292 [hep-ph].
- [7] G. P. Salam and G. Soyez, SISCone, <http://projects.hepforge.org/siscone>.
- [8] M. Cacciari and G. P. Salam, Phys. Lett. **B641**, 57 (2006), arXiv:hep-ph/0512210.
- [9] G. P. S. M. Cacciari and G. Soyez, [www.lpthe.jussieu.fr/~salam/fastjet](http://www.lpthe.jussieu.fr/~salam/fastjet).
- [10] M. Cacciari, G. P. Salam, and G. Soyez, JHEP **04**, 063 (2008), arXiv:0802.1189 [hep-ph].
- [11] T. Sjostrand, S. Mrenna, and P. Skands, JHEP **05**, 026 (2006), arXiv:hep-ph/0603175.
- [12] C. Buttar *et al.* (2008), arXiv:0803.0678 [hep-ph].

- [13] S. Catani, Y. L. Dokshitzer, M. Olsson, G. Turnock, and B. R. Webber, Phys. Lett. **B269**, 432 (1991).
- [14] J. M. Butterworth, A. R. Davison, M. Rubin, and G. P. Salam, Phys. Rev. Lett. **100**, 242001 (2008), [arXiv:0802.2470 \[hep-ph\]](#).
- [15] M. Cacciari, J. Rojo, G. P. Salam, and G. Soyez, JHEP **12**, 032 (2008), [arXiv:0810.1304 \[hep-ph\]](#).
- [16] M. Dasgupta, L. Magnea, and G. P. Salam, JHEP **02**, 055 (2008), [arXiv:0712.3014 \[hep-ph\]](#).
- [17] A. Bhatti *et al.* (2008), [arXiv:0807.4961 \[hep-ex\]](#).
- [18] M. Cacciari and G. P. Salam, Phys. Lett. **B659**, 119 (2008), [arXiv:0707.1378 \[hep-ph\]](#).
- [19] M. Cacciari, G. P. Salam, and G. Soyez, JHEP **04**, 005 (2008), [arXiv:0802.1188 \[hep-ph\]](#).
- [20] T. C. Collaboration, CMS PAS JME-07-003 (2008).
- [21] ATLAS Collaboration, S. Bentvelsen *et al.*, JINST **3**, S08003 (2008).
- [22] A. Collaboration, *Expected Performance of the ATLAS Experiment, Detector, Trigger and Physics – Jets and Missing Et Chapter, Jet Reconstruction Performance*, No. CERN-OPEN-2008-020. CERN, 2008, to appear.
- [23] W. e. a. Lampl, *Calorimeter Clustering Algorithms: Description and Performance*, Technical Report ATL-LARG-PUB-2008-002, CERN, Geneva, Apr 2008.
- [24] A. Collaboration, *Expected Performance of the ATLAS Experiment, Detector, Trigger and Physics – Jets and Missing Et Chapter, Detector Level Jet Corrections*, No. CERN-OPEN-2008-020. CERN, 2008, to appear.
- [25] A. Collaboration, *Expected Performance of the ATLAS Experiment, Detector, Trigger and Physics – Jets and Missing Et Chapter, E/p Performance for Charged Hadrons*, No. CERN-OPEN-2008-020. CERN, 2008, to appear.
- [26] A. Collaboration, *Expected Performance of the ATLAS Experiment, Detector, Trigger and Physics – Jets and Missing Et Chapter, In-situ Calibration Strategies*, No. CERN-OPEN-2008-020. CERN, 2008, to appear.
- [27] A. Collaboration, *Expected Performance of the ATLAS Experiment, Detector, Trigger and Physics – Top-quark Physics at ATLAS CSC Chapter*, No. CERN-OPEN-2008-020. CERN, 2008, to appear.
- [28] A. P. Cheplakov and S. Thompson, *MidPoint Algorithm for Jets Reconstruction in ATLAS Experiment*, Technical Report ATL-PHYS-PUB-2007-007, CERN, Geneva, Dec 2006.

- [29] D. Y. Grigoriev, E. Jankowski, and F. V. Tkachov, *Comput. Phys. Commun.* **155**, 42 (2003), [arXiv:hep-ph/0301226](#).
- [30] J. M. Butterworth, A. Davison, E. Ozcan, and P. Sherwood, *YSplitter: An Athena tool for studying jet substructure*, Technical Report ATL-PHYS-INT-2007-015. ATL-COM-PHYS-2007-077, CERN, Geneva, Oct 2007.
- [31] A. Collaboration, *Expected Performance of the ATLAS Experiment, Detector, Trigger and Physics*, No. CERN-OPEN-2008-020. CERN, 2008, to appear.
- [32] LHCb Collaboration, S. Amato *et al.* CERN-LHCC-98-04.
- [33] M. J. Strassler and K. M. Zurek, *Phys. Lett.* **B651**, 374 (2007), [arXiv:hep-ph/0604261](#);  
M. J. Strassler and K. M. Zurek, *Phys. Lett.* **B661**, 263 (2008), [arXiv:hep-ph/0605193](#).
- [34] D. E. Kaplan and K. Rehermann, *JHEP* **10**, 056 (2007), [arXiv:0705.3426 \[hep-ph\]](#);  
L. M. Carpenter, D. E. Kaplan, and E.-J. Rhee, *Phys. Rev. Lett.* **99**, 211801 (2007), [arXiv:hep-ph/0607204](#).
- [35] N. Gueissaz. CERN-THESIS-2007-038.

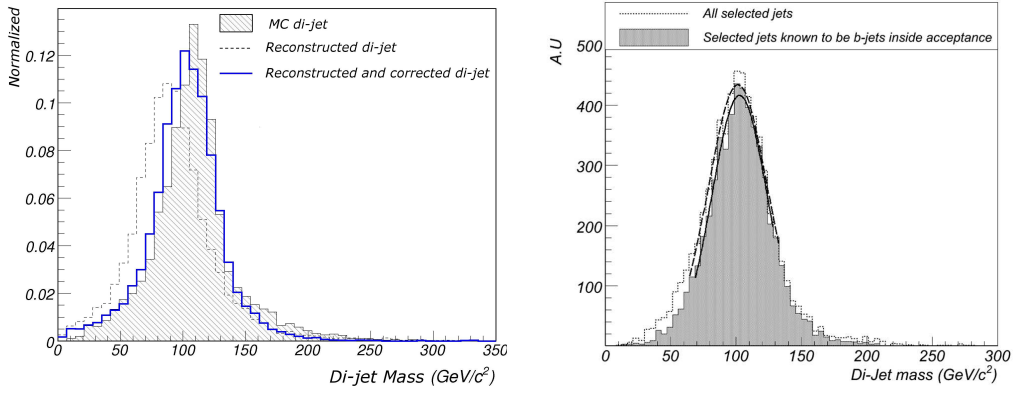


Fig. 16: Full simulation di-jet mass with and without correction, (left). Corrected di-jet mass with "inside the acceptance" b-jets only (filled grey), and all selected b-jets (dashed line), (right).

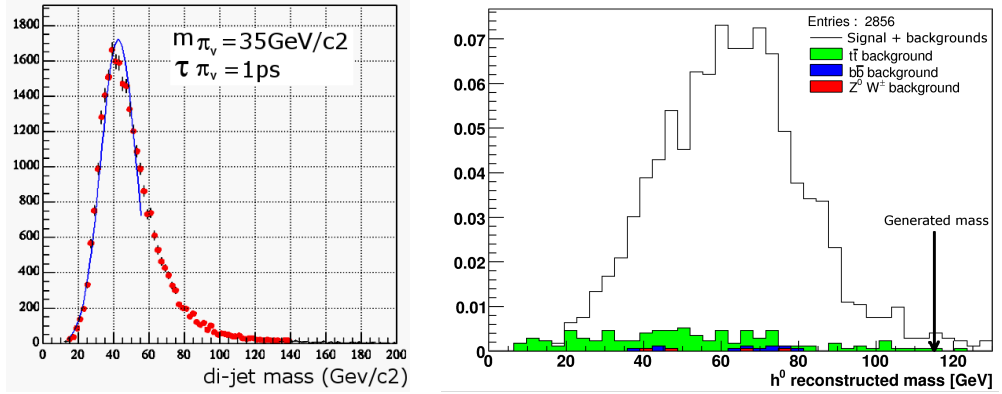


Fig. 17: Reconstructed  $\pi_v$  mass from Higgs decays with  $m_H = 120 \text{ GeV}/c^2$  in the hidden valley model (left). Higgs mass reconstructed from the two  $\tilde{\chi}^0$  vertices in MSSM with an R-parity violation model (right).

# $k_{\perp}$ -factorization and forward jets

*Sergey Baranov, Jochen Bartels, Michal Deák, Francesco Hautmann, Hannes Jung, Albert Knutsson, Krzysztof Kutak, Artem Lipatov, Christophe Royon, Augustín Sabio Vera, Florian Schwennsen, Nikolai Zotov*

Hadronic final states containing multiple jets have been investigated at the Tevatron and HERA colliders, and will play a central role in the Large Hadron Collider (LHC) physics program. The interpretation of experimental data for such final states relies both on perturbative multi-jet calculations (see [1] for a recent overview) and on realistic event simulation by parton-shower Monte Carlo generators (see e.g. [2–6]).

Owing to the complex kinematics involving multiple hard scales and the large phase space opening up at very high energies, multi-jet events are potentially sensitive to effects of QCD initial-state radiation that depend on the finite transverse-momentum tail of partonic matrix elements and distributions.

Standard shower Monte Carlos reconstructing exclusive events, such as HERWIG [7,8] and PYTHIA [9], are based on collinear evolution of the initial-state jet. Finite- $k_{\perp}$  contributions are not included, but rather correspond to corrections [10–14] to the angular or transverse-momentum ordering implemented in the parton-branching algorithms. The theoretical framework to take these corrections into account is based on using initial-state distributions unintegrated in both longitudinal and transverse momenta [12–14], coupled to hard matrix elements (ME) suitably defined off mass shell. See e.g. [15] for discussion of the Monte Carlo shower implementation of the method. Event generators based on  $k_{\perp}$ -dependent showers of this kind include [16–22].

We give a short introduction to  $k_{\perp}$ -factorization and describe the determination of unintegrated parton density functions (uPDFs). Then we discuss the calculation of new processes in the frame of  $k_{\perp}$ -factorisation and show a comparison with measurements at the Tevatron. A summary of NLO calculations for multi-jet production in  $ep$  and  $pp$  in  $k_{\perp}$ -factorisation follows. Finally, we discuss forward jet production and the azimuthal decorrelation of jets both in  $ep$  and  $pp$ , signatures which could clearly show evidence for small  $x$  parton dynamics.

## 1 Short introduction to $k_{\perp}$ -factorization and uPDFs

*Author: Francesco Hautmann, Hannes Jung*

In  $k_{\perp}$ -factorization the cross section for any process  $pp \rightarrow X$  can be written as:

$$\sigma = \int dx_1 dx_2 \int dk_{\perp 1} dk_{\perp 2} \mathcal{A}(x_1, k_{\perp 1}, q) \mathcal{A}(x_2, k_{\perp 2}, q) \hat{\sigma}(x_1, x_2, k_{\perp 1}, k_{\perp 2}, q) \quad (1)$$

with  $\mathcal{A}(x, k_{\perp}, q)$  being the un-integrated transverse momentum ( $k_{\perp}$ -dependent) parton density function (uPDF or TMD),  $q$  defines the factorization scale and  $\hat{\sigma}$  is the partonic cross section taken with off-shell initial partons. Here we concentrate on the small  $x$  region, which is described by high-energy factorization (or  $k_{\perp}$ -factorisation).

Both the uPDF and the off-shell partonic cross section can be formulated in the small  $x$  region where a gauge-invariant definition emerges from high-energy factorization [12–14]. It has

been used for studies of collider processes both by Monte Carlo (see reviews in [23–25]) and by semi-analytic resummation approaches (see [26, 27]).

To characterize a transverse momentum dependent parton distribution gauge-invariantly over the whole phase space is a nontrivial question [28, 29], currently at the center of much activity. See overview in [24].

The diagrammatic argument for gauge invariance, given in [12–14], and developed in [30, 31], is based on relating off-shell matrix elements with physical cross sections at  $x \ll 1$ , and exploits the dominance of single gluon polarization at high energies.<sup>1</sup> The main reason why a natural definition for TMD pdfs can be constructed in the high-energy limit is that one can relate directly (up to perturbative corrections) the cross section for a *physical* process, say, photoproduction of a heavy-quark pair, to an *unintegrated* gluon distribution, much as, in the conventional parton picture, one does for DIS in terms of ordinary (integrated) parton distributions. On the other hand, the difficulties in defining a TMD distribution over the whole phase space can largely be associated with the fact that it is not obvious how to determine such a relation for general kinematics.

The evolution equations obeyed by TMD distributions defined from the high-energy limit are of the type of energy evolution [32]. Factorization formulas in terms of TMD distributions [12–14] have corrections that are down by logarithms of energy rather than powers of momentum transfer. On the other hand, it is important to observe that this framework allows one to describe the ultraviolet region of arbitrarily high  $k_\perp$  and in particular re-obtain the structure of QCD logarithmic scaling violations [26, 27, 30, 31]. This ultimately justifies the use of this approach for jet physics. In particular it is the basis for using corresponding Monte Carlo implementations [15–22] to treat multi-scale hard processes at the LHC.

From both theoretical and phenomenological view-points, it is one of the appealing features of the high-energy framework for TMD distributions that one can relate its results to a well-defined summation of higher-order radiative corrections. By expanding these results to fixed order in  $\alpha_s$ , one can match the predictions thus obtained against perturbative calculations. This has been verified for a number of specific processes at next-to-leading order (see for instance [33–35] for heavy flavor production) and more recently at next-to-next-to-leading order (see for instance [36, 37]). Note that this fact also provides the basis for shower algorithms implementing this framework to be combined with fixed-order NLO calculations by using existing techniques for such matching.

## 2 Prospects and recent developments of $k_\perp$ -factorization

At HERA the  $k_\perp$ -factorization approach has been successfully applied to describe multi-jet production as well as the production of heavy quarks at small values of  $x$ , which are dominated by gluon initiated processes. The relevant off-shell matrix elements for jet and heavy quark production are known since long. The unintegrated gluon distribution has been determined using inclusive measurements at HERA. A new determination of the uPDF using also final state measurements is described in section 2.1.

---

<sup>1</sup>It is emphasized e.g. in [23, 29] that a fully worked out operator argument, on the other hand, is highly desirable but is still missing.

However to apply  $k_\perp$ -factorization to describe measurements in general in  $p\bar{p}$  or  $pp$  new and additional matrix elements for different processes need to be calculated. In the following, the calculation of new processes will be presented:

- $g^*q \rightarrow gq$  to describe jet production in the forward and backward region
- $g^*g^* \rightarrow \gamma/W/Z + q\bar{q}$  to describe the inclusive production of  $\gamma/W/Z$
- $g^*q \rightarrow \gamma q$  to describe prompt photon production

Since some of the processes are quark initiated, unintegrated quark densities need to be determined. In a simplest approach we allow only valence quarks (at large  $x$ ). The contribution of quark initiated processes is discussed in section 2.3 explicitly.

The aim of this contribution is to show the two areas, where improvements in the  $k_\perp$ -factorization approach has been made: the determination of the uPDFs and the calculation of matrix elements.

## 2.1 An approach to fast fits of the unintegrated gluon density

*Author: Alessandro Bacchetta, Albert Knutsson, Krzysztof Kutak*

In perturbative QCD the PDFs are given by solutions of integral equations, for which the initial input distributions have to be determined by fits to experimental data. It turns out that, in general it is not efficient to tune Monte Carlo event generators (MC) by sequential calls of the generator together with a minimisation program. Motivated by [38], we use an alternative fitting method, which is based on producing a grid in parameter-observable space. This allows the parameter dependence to be determined by polynomial interpolation before the fit is performed, which significantly reduces the time to do the fit itself.

Here we determine the parameters in the starting distribution of the unintegrated gluon density function by fits to deep inelastic scattering  $F_2$  structure function data from the H1 experiment [39]. This is carried out by using the CASCADE Monte Carlo event generator [16].

### *The Unintegrated Gluon Density*

The starting distribution of the unintegrated gluon density is parameterized as

$$A_0(x, k_t) = Nx^{-B}(1-x)^C(1-Dx)\exp\left[(k_t - \mu)^2/\sigma^2\right]$$

where  $x$  is the longitudinal momentum fraction of the proton carried by the gluon and  $k_t$  its transverse momentum. In this study the  $N$  (normalisation),  $B$  (low  $x$  behaviour),  $D$  are determined. The parameters  $C$ ,  $\sigma$  and  $\mu$ , are kept fixed at  $C = 4$ ,  $\sigma = 1$  and  $\mu = 0$ .

The unintegrated gluon density is determined by a convolution of the non-perturbative starting distribution  $\mathcal{A}_0(x)$  and the CCFM evolution denoted by  $\tilde{\mathcal{A}}(x, k_\perp, \bar{q})$ :

$$x\mathcal{A}(x, k_\perp, \bar{q}) = \int dx' \mathcal{A}_0(x', k_\perp) \cdot \frac{x}{x'} \tilde{\mathcal{A}}\left(\frac{x}{x'}, k_\perp, \bar{q}\right)$$



### The Fitting Method

In the first step of the fitting procedure we build up a grid of MC predictions in the parameter space  $(p_1, p_2, \dots, p_n)$  for each of the observables  $X$ . Then we use the grid to describe the parameter space analytically by a polynomial of the form

$$X(p_1, p_2, \dots, p_n) = A_0 + \sum_{i=1}^n B_i p_i + \sum_{i=1}^n C_i p_i^2 + \sum_{i=1}^{n-1} \sum_{j=i+1}^n D_{ij} p_i p_j + \text{H.O.}$$

We determine the coefficients  $A_0, B_1, \dots$  by singular value decomposition (SVD) [40], since they form an over determined system of linear equations. This is done separately for each of the MC predicted observables, which in our case corresponds to 58 experimental data points.

In order to account for correlations between parameters the form of the polynomial has to be of order higher than one. In the presented fit we use a forth order polynomial, which gives a good description of the parameter space. The  $\chi^2/n.d.f.$ , averaged over the 58 MC predicted observables, is  $\chi^2/n.d.f. = 501.7/(440 - 35) = 1.2$ , where 440 is the number of MC grid points and 35 is the number of coefficients in the polynomial of the fourth degree.

Having described with the polynomials the behavior of the MC predictions in parameter space, we can find the values of the parameters  $p_1, p_2, \dots$  for which the MC best reproduces the measurements. This is done by applying a  $\chi^2$  minimisation to

$$\chi^2 = \sum_k \frac{(X_{k,poly} - X_{k,data})^2}{\delta X_{k,poly}^2 + \delta X_{k,data}^2}$$

where the sum runs over all bins,  $k$ .  $X_{k,data}$  is the measured data, with the corresponding experimental error  $\delta X_{k,data}$ , and  $X_{k,poly}$  the polynomial prediction, with the error  $\delta X_{k,poly}$  calculated from the individual errors of the fitted coefficients by using the covariance matrix. To perform this last step we use MINUIT [41], since the dependence on the parameters  $p_1, p_2, \dots$  is non-linear.

The method turns out to be very time-efficient, in particular since the MC grid points are generated simultaneously.

### Results

The unintegrated PDF has been fitted to the proton structure function,  $F_2$ , in the kinematical range  $Q^2 > 4.5 \text{ GeV}^2$  and  $x_{Bj} < 0.005$ , where  $Q^2$  is the virtuality of the exchanged boson and  $x_{Bj}$  is the Bjorken scaling variable. In Fig. 1 the result of the fit is compared to the data [39]. The parameter values determined from the new fit are  $N = 0.221 \pm 0.011$ ,  $B = 0.201 \pm 0.007$  and  $D = -24.6 \pm 1.5$ .  $\chi^2$  profiles for these parameters are shown in Fig. 2 and confirm that this is a minimum for  $N, B$  and  $D$ . Confidence regions for these parameters are shown in Fig. 3.

The  $\chi^2/ndf$  of the new fit is 2.4 which is more than one unit better than obtained when using CASCADE together with the PDF set A0 [16]. The constraints on the parameters of the gluon could be hopefully further improved by fitting the  $k_t$ -dependent part of the gluon distribution. In Fig. 4 the new gluon distribution and set A0 are drawn as a function of  $x$  for two different values of  $k_t^2$ .



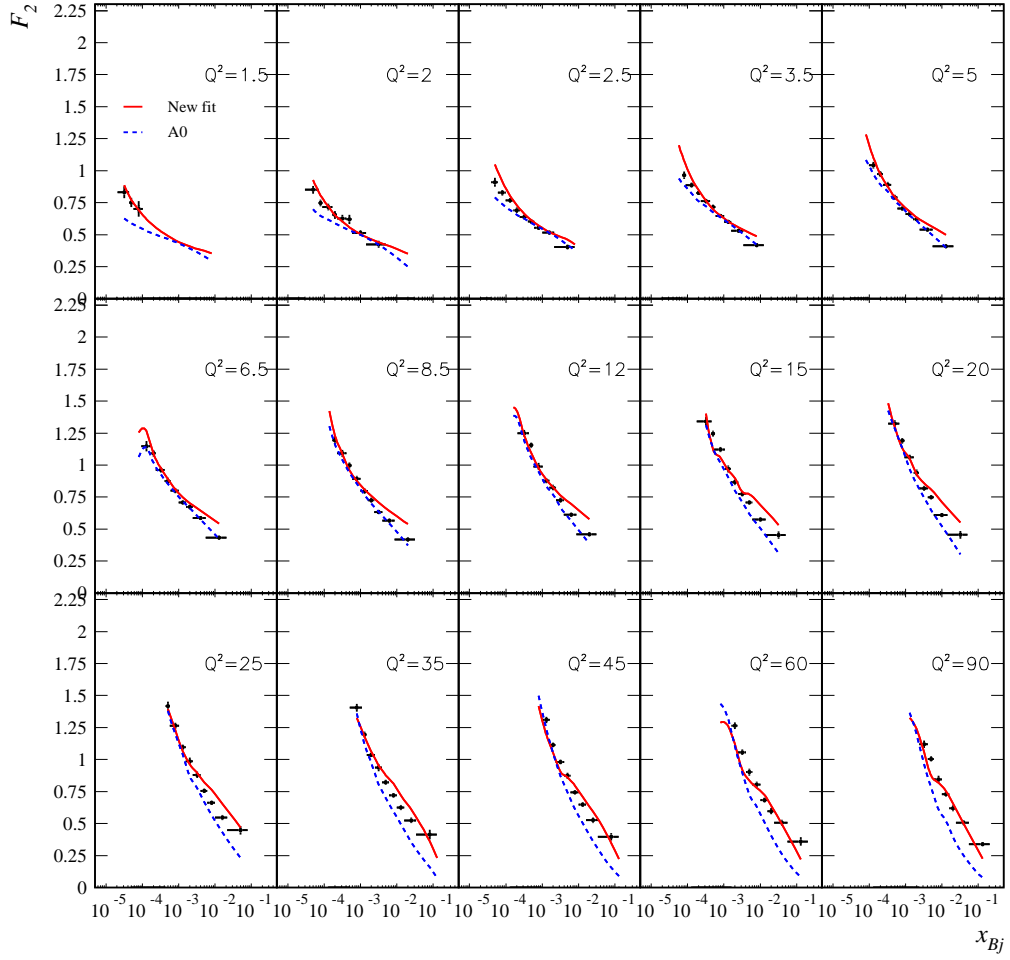
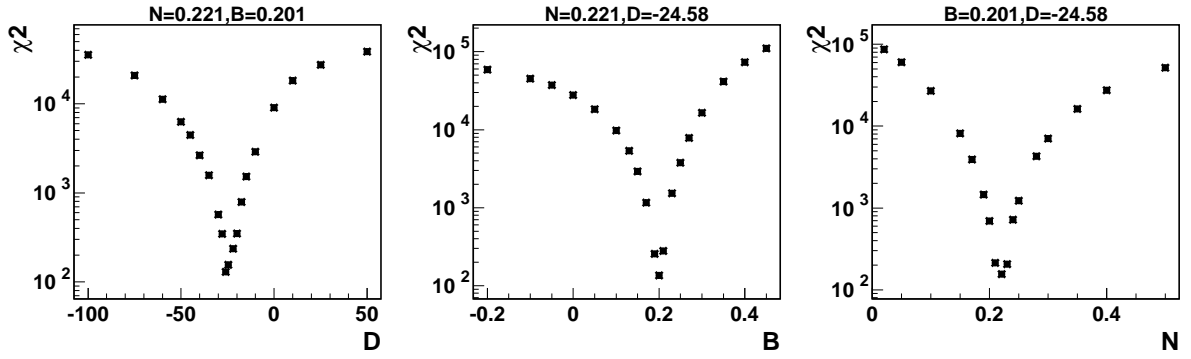
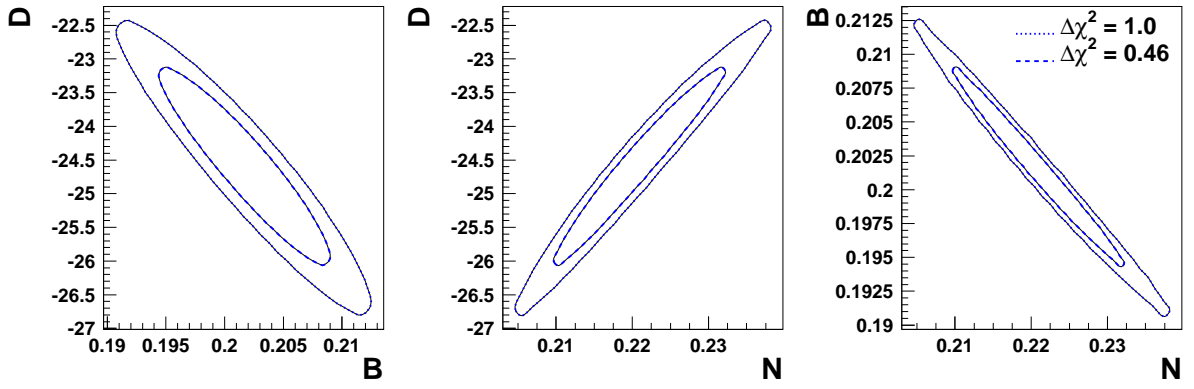


Fig. 1:  $F_2$  structure function data, as a function of  $x_{Bj}$  in  $Q^2$  bins compared to predictions from the CASCADE Monte Carlo event generator using the newly fitted PDF (continuous red line) and old PDF set A0 (blue dashed line). The new fitted PDF has been determined in the kinematic range  $Q^2 > 4.5 \text{ GeV}^2$  and  $x_{Bj} < 0.005$

Fig. 2:  $\chi^2$  as a function of the fitted parameters.Fig. 3: Confidence regions for  $N$ ,  $B$  and  $D$ 

## 2.2 Hard matrix element calculation

For jet production at high energies the following processes contribute:  $gg \rightarrow q\bar{q}$ ,  $gg \rightarrow gg$ ,  $qg \rightarrow qg$ ,  $qq \rightarrow qq$  and  $q\bar{q} \rightarrow q\bar{q}$ . In collinear factorization (with on-shell initial partons) these processes are calculated in LO ( $\mathcal{O}(\alpha_s)$ ) and also higher order corrections are known. In  $k_\perp$ -factorization the process  $gg \rightarrow q\bar{q}$  are known [13, 42]. At high energies, gluon induced processes are expected to dominate. The process  $g^*g^* \rightarrow gg$  is not yet considered, as there will be contributions of similar type from the parton branching. However, if jet production in the forward or backward region is considered, scattering a small  $x$  gluon off a large  $x$  valence quark ( $qg^* \rightarrow qg$ ) will contribute significantly. This process will be described below.

The production of  $Z/W$  is calculated to a high precision in collinear factorization, even to NNLO. However, significant effects from small  $x$  partons, which are not included in the collinear treatment could become important, as suggested by [43]. Since  $W/Z$  production is the standard candle at LHC, it is important to understand in detail any possible small  $x$  effect. The  $Z/W$  production has been calculated for the first time in the framework of  $k_\perp$ -factorization in [44, 45] for the lowest order gluon induced process  $g^*g^* \rightarrow Z/W + Q_i\bar{Q}_j$ . In [45] attempts are made to include also quark initiated processes to  $Z/W$  production.

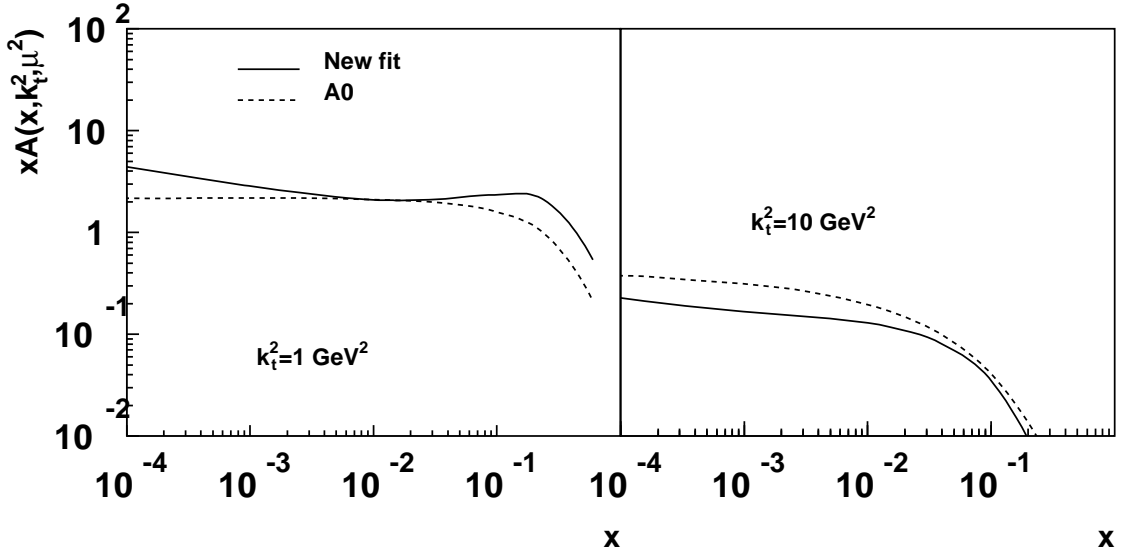


Fig. 4: The newly fitted PDF (continuous line) compared to the old PDF set A0 (dashed line), drawn as a function of  $x$  for  $k_t^2 = 1 \text{ GeV}^2$  and  $k_t^2 = 10 \text{ GeV}^2$  at a scale  $\mu^2 = 4 \text{ GeV}^2$ .

### Process $qg^* \rightarrow qg$ at the LHC

Author: Michal Deak, Krzysztof Kutak

Here we consider a very asymmetric situation in proton proton scattering in which an off-shell gluon coming from one of the protons scatters off an on-shell valence quark from the other proton. We can use small  $x$  dynamics for the gluon where the  $k_{\perp}$ -factorization formalism is justified and on the other side we use collinear large  $x$  dynamics for the valence quark. The matrix element of the hard subprocess is factorized from the unintegrated gluon density function by  $k_{\perp}$ -factorization theorem and from the valence quark uPDF.

Similar to the  $Z/W + Q_i \bar{Q}_j$  case ([44] and [45]), we will use Sudakov decomposition for the four-momenta of the initial state and final state particles.

$$k = x_g p_A + z_g p_B + k_{\perp} \quad (2)$$

$$q = x_q p_B \quad (3)$$

$$k' = x'_g p_A + z'_g p_B + k'_{\perp} \quad (4)$$

$$q' = z'_q p_A + x'_q p_B + q'_{\perp} \quad (5)$$

$$t = (k - k')^2 \quad (6)$$

The amplitude for the process  $g^* q \rightarrow gq$  consists of the diagrams in Fig. 5. The squared matrix element, after summing over colors of final and initial state particles, is calculated using the  $k_{\perp}$ -factorization prescription:

$$|\mathcal{M}|^2 = \frac{1}{4} \frac{1}{N_c(N_c^2 - 1)} \left( C_A C_F^2 A_{abelian} + C_A^2 C_F A_{nonabelian} \right) \quad (7)$$

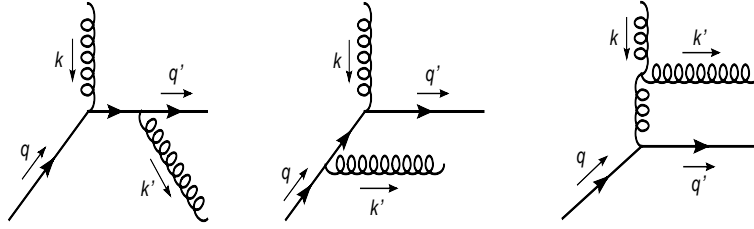


Fig. 5: Full set of diagrams of  $q g^* \rightarrow q g$  with initial state gluon off-shell required by gauge invariance. a) Diagrams similar to diagrams in collinear factorization approach, b) additional diagrams required by gauge invariance.

where

$$A_{abelian} = (4\pi\alpha_s)^2 \left( \frac{k \cdot q}{p \cdot q} \right)^2 \frac{(p \cdot q)^2 + (p \cdot q')^2}{k' \cdot q \ k' \cdot q'} \quad (8)$$

and

$$A_{nonabelian} = (4\pi\alpha_s)^2 \left( \frac{k \cdot q}{p \cdot q} \right)^2 \frac{(p \cdot q)^2 + (p \cdot q')^2}{2k' \cdot q \ k' \cdot q'} \left( \frac{2k' \cdot q' \ p \cdot q}{-t \ k' \cdot p} + \frac{2k' \cdot q \ p \cdot q'}{-t \ k' \cdot p} - 1 \right) \quad (9)$$

with  $C_A = N_c$ ,  $C_F = (N_c^2 - 1)/(2N_c)$  and  $N_c$  being the number of colours. The  $k_\perp \rightarrow 0$  can be performed and the text book result for  $qg \rightarrow qg$  is recovered.

The matrix element is singular when one of the particles in final state is collinear with the quark in initial state. To regularize the matrix element we set a cut on the transverse momenta of each of final state particles in the laboratory frame,  $|\mathbf{k}'| > p_{\perp cut}$  and  $|\mathbf{q}'| > p_{\perp cut}$ . We note that a cut on one of the transverse momenta is not enough to avoid divergencies.

### *Z and W production associated with heavy quark-antiquark pair*

The calculation of the matrix element for the process  $g^* g^* \rightarrow Z/W + Q_i \bar{Q}_j$  is described in detail in [44,45]. The calculations differ in the way the spin density of the initial state is treated. However, they are equivalent and give the same results for the matrix element of the hard subprocess. We have cross-checked the calculations numerically and found agreement of the cross sections at Tevatron and LHC energies at the 0.1 % level.

## **2.3 Implications for the LHC: Electroweak gauge boson production in hadronic collisions at high energies**

*Author: Serguei Baranov, Artem Lipatov, Nikolai Zotov*

AT HERA and the Tevatron  $k_\perp$ - factorization supplemented with the BFKL-like gluon dynamics was successfully applied to describe various measurements of heavy quark production [46, 47] (and references therein). It is important that these predictions were based on the off-shell matrix elements  $\gamma g^* \rightarrow Q \bar{Q}$  or  $g^* g^* \rightarrow Q \bar{Q}$ . In Ref. [48, 49] inclusive Higgs hadroproduction at Tevatron and LHC energies has been investigated, where the main contribution also

came from the off-shell gluon-gluon fusion. It was demonstrated that using the CCFM-evolved unintegrated gluon densities results in predictions which are very close to the NNLO pQCD ones. This encouraged us to apply the  $k_{\perp}$ -factorization approach also to the production of inclusive electroweak gauge bosons.

At leading order (LO) QCD, the  $W^{\pm}$  and  $Z^0$  bosons are produced via quark-antiquark annihilation  $q + \bar{q}' \rightarrow W/Z$ . Here, an important component of the calculations are the unintegrated quark distributions. At present, these distributions are only available in the Kimber-Martin-Ryskin (KMR) scheme [50, 51], since there are theoretical difficulties in obtaining quark distributions directly from CCFM and BFKL equations. This is in contrast to gluon-induced processes where many unintegrated gluon densities are available.

Since sea quarks can appear as a result of gluon splitting, at the price of absorbing the last gluon splitting into the hard subprocess (i.e., considering the  $2 \rightarrow 2$  and  $2 \rightarrow 3$  rather than  $2 \rightarrow 1$  matrix elements), the problem of poorly known sea quark densities can efficiently be reduced to the problem of gluon densities. However, it is not evident in advance whether the last gluon splitting dominates. This issue is addressed in Ref. [45, 52]. One of the goals of that study is to clarify, to what extent the quark contributions can be reexpressed in terms of the gluon contributions. At the same time, by considering the higher order matrix elements we take into account the terms not containing large logarithms, i.e., the terms not included in the evolution equations. Within our scheme, we get a numerical estimate of the corresponding contributions.

Our theoretical approach is the following. We start from the leading order  $\mathcal{O}(\alpha)$  subprocess  $q + \bar{q}' \rightarrow W/Z$ , and then divide it into several contributions which correspond to the interactions of valence quarks  $q_v(x, \mathbf{k}_T^2, \mu^2)$ , sea quarks appearing at the last step of the gluon evolution  $q_g(x, \mathbf{k}_T^2, \mu^2)$ , and sea quarks coming from the earlier steps  $q_s(x, \mathbf{k}_T^2, \mu^2)$ . Here we use the specific property of the KMR scheme which enables us to discriminate between the various components of the quark densities.

The KMR approach represents an approximate treatment of the parton evolution mainly based on the DGLAP equation and incorporating BFKL effects at the last step of the parton ladder only, in the form of properly defined Sudakov formfactors  $T_q(\mathbf{k}_T^2, \mu^2)$  and  $T_g(\mathbf{k}_T^2, \mu^2)$ . These formfactors already include logarithmic loop correction. Also, there are nonlogarithmic corrections which result in a K-factor on the cross section given by [53]  $K(q + \bar{q}' \rightarrow W/Z) \simeq \exp [C_F \pi \alpha_s(\mu^2)/2]$  with  $C_F = 4/3$  and  $\mu^2 = \mathbf{p}_T^{4/3} m^{2/3}$ . In this approximation, the unintegrated quark and gluon distributions are expressed by

$$f_q(x, \mathbf{k}_T^2, \mu^2) = T_q(\mathbf{k}_T^2, \mu^2) \frac{\alpha_s(\mathbf{k}_T^2)}{2\pi} \times \int_x^1 dz \left[ P_{qq}(z) \frac{x}{z} q\left(\frac{x}{z}, \mathbf{k}_T^2\right) \Theta(\Delta - z) + P_{qg}(z) \frac{x}{z} g\left(\frac{x}{z}, \mathbf{k}_T^2\right) \right], \quad (10)$$

$$f_g(x, \mathbf{k}_T^2, \mu^2) = T_g(\mathbf{k}_T^2, \mu^2) \frac{\alpha_s(\mathbf{k}_T^2)}{2\pi} \times \int_x^1 dz \left[ \sum_q P_{gq}(z) \frac{x}{z} q\left(\frac{x}{z}, \mathbf{k}_T^2\right) + P_{gg}(z) \frac{x}{z} g\left(\frac{x}{z}, \mathbf{k}_T^2\right) \Theta(\Delta - z) \right], \quad (11)$$

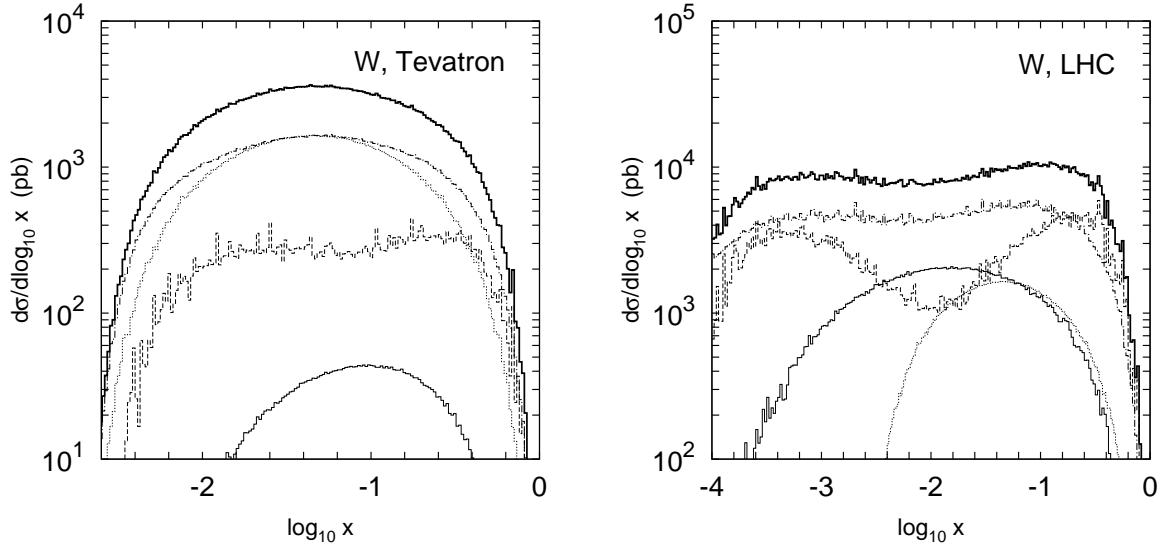


Fig. 6: Different contributions to the inclusive  $W^\pm$  boson production at the Tevatron (left panel) and LHC (right panel) conditions. The solid, dashed and dotted histograms represent the contributions from the  $g^* + g^* \rightarrow W^\pm/Z^0 + q + \bar{q}'$ ,  $q_v + g^* \rightarrow W^\pm/Z^0 + q'$  and  $q_v + \bar{q}'_v \rightarrow W^\pm/Z^0$  subprocesses, respectively. The dash-dotted histograms represent the “reduced sea” component. The thick solid histograms represent the sum of all contributions.

where  $P_{ab}(z)$  are the usual unregularised leading order DGLAP splitting functions, and  $q(x, \mu^2)$  and  $g(x, \mu^2)$  are the conventional (collinear) quark and gluon densities. The function  $f_q(x, \mathbf{k}_T^2, \mu^2)$  in Eq. (10) represents the total quark distribution. Modifying Eq. (10) in such a way that only the first term is kept and the second term omitted, we switch the last gluon splitting off, thus excluding the  $q_g(x, \mathbf{k}_T^2, \mu^2)$  component. Taking the difference between the quark and antiquark densities we extract the valence quark component  $q_v(x, \mathbf{k}_T^2, \mu^2) = f_q(x, \mathbf{k}_T^2, \mu^2) - f_{\bar{q}}(x, \mathbf{k}_T^2, \mu^2)$ .

Summing up, we consider the following partonic subprocesses: gluon-gluon fusion  $g + g \rightarrow W/Z + q + \bar{q}'$ , with which the  $q_g + \bar{q}_g$  annihilation is replaced; valence and sea quark-gluon scattering  $q_v + g \rightarrow W/Z + q$  and  $q_s + g \rightarrow W/Z + q$ , with which the  $q_v + \bar{q}_g$  and  $q_s + \bar{q}_g$  annihilation is replaced; and quark-antiquark annihilation  $q + \bar{q}' \rightarrow W/Z$  including both valence  $q_v$  and sea  $q_s$  quark components. The calculation of the matrix elements is explained in section 2.2. The basic formulas for corresponding contributions to the cross section are given in [45, 52].

Now we turn to numerical results. The solid, dashed and dotted histograms in fig. 2.3 represent the contributions from the  $g^* + g^* \rightarrow \gamma/W^\pm/Z^0 + q + \bar{q}'$ ,  $q_v + g^* \rightarrow \gamma/W^\pm/Z^0 + q'$  and  $q_v + \bar{q}'_v \rightarrow W^\pm/Z^0$  (or  $q_v + \bar{q}_v \rightarrow \gamma + g$ ) subprocesses, respectively. The dash-dotted histograms represent the sum of the contributions from the  $q_s + \bar{q}'_s \rightarrow W^\pm/Z^0$ ,  $q_s + g^* \rightarrow \gamma/W^\pm/Z^0 + q'$  and  $q_v + \bar{q}'_s \rightarrow W^\pm/Z^0$  (or  $q_s + \bar{q}_s \rightarrow \gamma + g$  and  $q_v + \bar{q}_s \rightarrow \gamma + g$ ) subprocesses. We find that the contribution from the valence quark-antiquark annihilation is important at the Tevatron but yields only about few percent at the LHC energy. The gluon-gluon fusion is unimportant at the

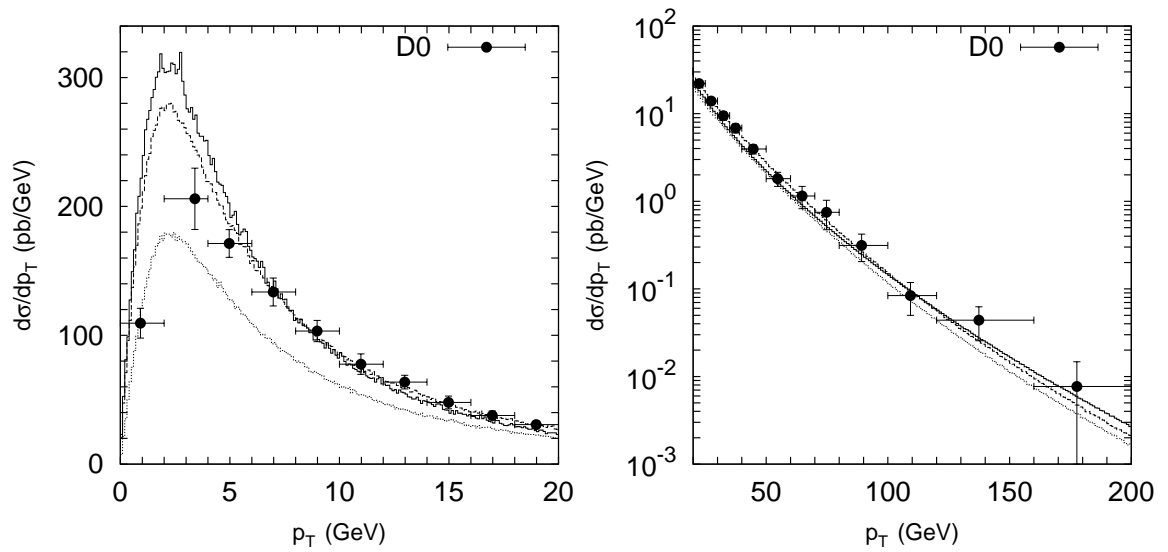


Fig. 7: Transverse momentum distribution of the  $W^{\pm}$  boson production calculated at  $\sqrt{s} = 1800$  GeV. Solid histograms represent calculations in the "decomposition" scheme where all contributions described in the text are taken into account. Dashed histograms correspond to the predictions based on the simple  $2 \rightarrow 1$  quark-antiquark annihilation subprocess with all quark components summed together. Dotted histograms correspond to the simple  $2 \rightarrow 1$  quark-antiquark annihilation subprocess without  $K$ -factor. The cross sections times branching fraction  $f(W \rightarrow l\nu)$  are shown. The experimental data are from D0.

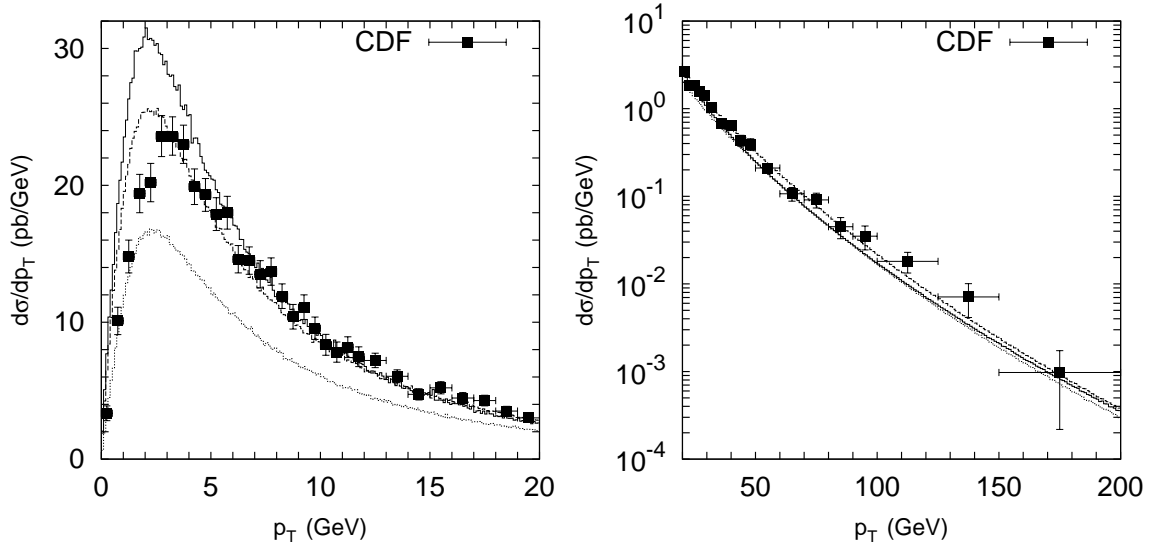


Fig. 8: Transverse momentum distribution of the  $Z^0$  boson. Notation of the histograms is as in Fig.2.3. The experimental data are from CDF.

Tevatron, but becomes important at higher energies and has to be taken into account at the LHC. Quite a significant fraction (nearly 50%) of the calculated cross section at both the Tevatron and the LHC conditions comes from the  $q_s$  quark component. The gluon-gluon fusion contributes about  $\sim 1\%$  to the total cross section at Tevatron and up to  $\sim 25\%$  at the LHC.

Figs. 2.3 and 2.3 display a comparison between the calculated differential cross sections  $d\sigma/dp_T$  and the experimental data [54–56] at low  $p_T$  ( $p_T < 20$  GeV), and in the full  $p_T$  range. For comparison, we also show the predictions based on the simple  $2 \rightarrow 1$  quark-antiquark annihilation subprocess (dotted histograms), with all quark components summed together. The difference between the results can probably be attributed to the terms not containing large logarithms. The predictions of the “subprocess decomposition” scheme lie by about a factor of 1.25 higher and show better agreement with the data.

Having considered the different partonic subprocesses we see that the dominant contribution comes from the sea quark interactions  $q_s + q_s \rightarrow W/Z$ ,  $q_s + q_v \rightarrow W/Z$  and  $q_s + g \rightarrow W/Z + q'$ . Notably, we find that these subprocesses are mainly due to the quarks emerging from the earlier steps of the parton evolution rather than from the last gluon splitting. Thus, we conclude that the quarks constitute an important component of the parton ladder, not negligible even at the LHC energies and not reducible to the gluon component. Quarks need to be directly included in the evolution equations for consistency and completeness of the latter.

The results of our calculations within the “subprocess decomposition” scheme reasonably agree with the available experimental data and show no need for an extra factor introduced in [57].



## 2.4 Implications for the LHC: Z and W associated with heavy quark pair at Tevatron and the LHC in $k_{\perp}$ -factorization

*Author: Michal Deak, Florian Schwennsen*

To calculate the cross section for  $pp \rightarrow Z/W + Q_i \bar{Q}_j$  with the hard subprocess  $g^* g^* \rightarrow Z/W + Q_i \bar{Q}_j$  at LHC energies we have to convolute the corresponding partonic off-shell cross section with gluon uPDFs. For this purpose we implemented the matrix element squared of the subprocess  $g^* g^* \rightarrow Z/W + Q_i \bar{Q}_j$  into the Monte Carlo generator CASCADE.

Our calculation of the hard matrix elements includes  $W^{\pm}$  and  $Z$  production in association with all possible quark-antiquark channels in gluon gluon fusion. Since the basic structure of all these matrix elements is very similar, we present results only for the typical case of  $Zb\bar{b}$  production at LHC energies of  $\sqrt{s} = 14\text{TeV}$ . We compare our calculation with a prediction using collinear factorization as obtained from the program MCFM [58]. For the collinear factorization calculations we use the parton densities CTEQ6L1 [59]. Since we want compare with NLO collinear calculation, which in MCFM is available only in massless quark approximation, we compare by setting the quark mass to zero in our mass dependent calculation. To emulate the quark mass effect we set a cutoff on the transversal momenta of the quarks with values  $p_{b\perp\min} = m_b = 4.62\text{ GeV}$  in our calculation and in MCFM as well.

The total cross sections are comparable in magnitude, though they differ considerably: 0.406 nb in  $k_{\perp}$ -factorization and 0.748 nb in collinear factorization.

The transverse momentum distribution of the vector boson are shown in Fig. 9. The comparison of the  $k_{\perp}$ -factorization approach to the collinear shows that they agree in transversal momentum distributions of  $Z$  at high values of this quantity. This is no surprise, since at high  $p_{Z\perp}$  the contribution from initial state gluon transverse momenta is expected to become small.

In the distribution of the azimuthal angular distance of  $Z$  and  $\max(p_{b,\perp}, p_{\bar{b},\perp})$  (Fig. 10) we observe that the region from 0 to  $\pi/2$  is forbidden within the collinear calculation due to momentum conservation, which is not the case for  $k_{\perp}$ -factorization. This is caused by the contribution from initial state gluon transversal momentum which allows the transversal momenta of  $Z$ ,  $b$  and  $\bar{b}$  to be unbalanced. A larger spread of possible configurations causes that the distribution in the  $k_{\perp}$ -factorization calculation flattens.

## 3 NLO inclusive jet production in $k_{\perp}$ -factorization

*Author: Jochen Bartels, Agustin Sabio-Vera, Florian Schwennsen*

At different high energy colliders the inclusive jet production is one of the basic measurements. Besides the very successful approach of collinear factorization, also within  $k_{\perp}$ -factorization jet production at HERA has been described [60]. There, the jet vertex has been constructed from the central hard matrix element of quark-antiquark production – connected to the unintegrated gluon and the photon being emitted from the electron. The LO calculation of the corresponding  $\gamma^* g \rightarrow q\bar{q}$  matrix element is straightforward and contains just two diagrams – one sample is shown in Fig. 11a. As it was shown in Ref. [61],  $k_{\perp}$ -factorization in the small  $x$  regime can be formulated at NLO accuracy. However, the jet production at HERA has not been calculated at NLO accuracy so far, but the building blocks are contained in the calculation of the NLO photon impact factor [62–66] including virtual corrections (like in Fig. 11b) and

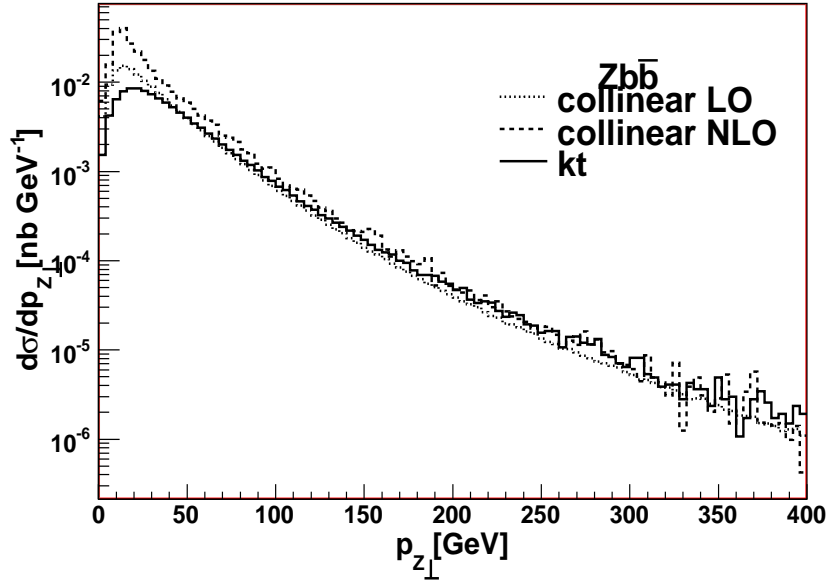


Fig. 9: Comparison of cross sections differential in transverse momentum of the produced  $Z$  gauge boson. Calculation with massless  $b$ -quarks.

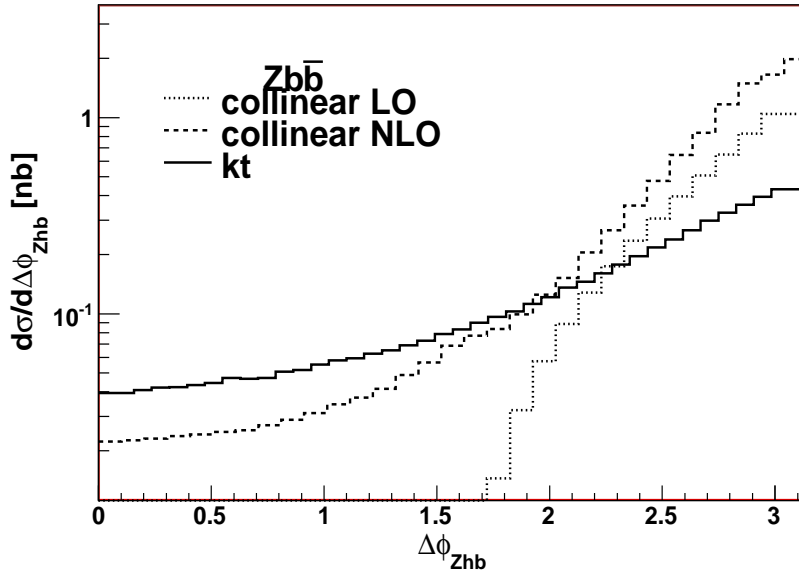


Fig. 10: Comparison of cross sections differential in distance in azimuthal angle of  $Z$  and higher  $p_{\perp} b/\bar{b}$ . Calculation with massless  $b$ -quarks.

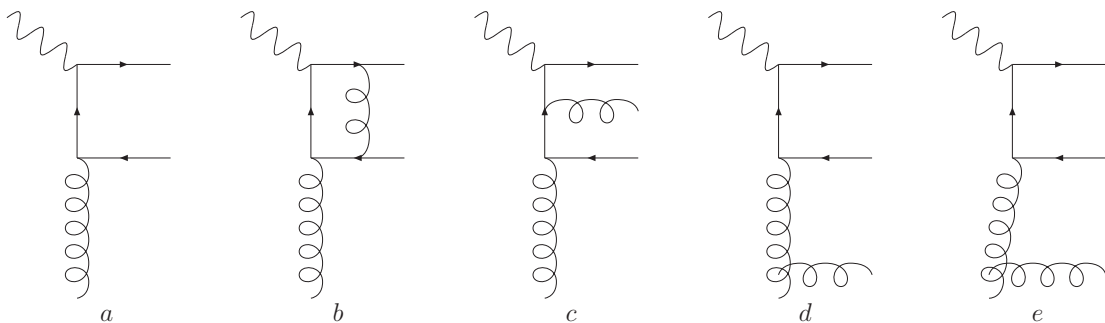


Fig. 11: sample diagrams for the dijet vertex in DIS.

corrections due to the emission of an additional gluon. For such a gluon one has to separate the case where the gluon is ‘close’ to the vertex, giving a standard real correction to the process (like in Fig. 11c), or where the gluon is ‘well separated’ from the vertex (like indicated in Fig. 11d). Another contribution (symbolically indicated in Fig. 11e) would come from the different energy scales at the jet and the proton vertices. The nature of these latter corrections will become more clear when we discuss in the following the jet vertex for hadron-hadron scattering.

In  $k_{\perp}$ -factorization of hadron-hadron collisions, the jet emission vertex can be identified with the Reggeon-Reggeon-gluon vertex (indicated in Fig. 12a). Its square is nothing else but the LO BFKL-kernel. Since the BFKL equation – from which  $k_{\perp}$ -factorization can be derived – has been formulated at NLO [67, 68] as well, it is also possible to calculate the jet emission vertex at this order [61] taking into account that at NLO also the Reggeon-Reggeon-gluon-gluon and Reggeon-Reggeon-quark-antiquark vertices enter the game. It is not sufficient to simply start from the fully integrated emission vertex as used in the NLO BFKL kernel [67, 68]. Rather, one has to carefully separate all the different contributions in their unintegrated form before one can combine them. Moreover, special care has to be taken on the correct treatment of the energy scales involved.

Instead of deriving in detail all the formulas, let us focus on the nature of the different contributions to the NLO jet vertex. In Fig. 12 we represent the different types of contributions by a symbolic diagram. At NLO virtual corrections to the vertex enter the game as shown in Fig. 12b. Since off-shell amplitudes per se are not gauge invariant, the calculation has to be performed as an embedded process. One can *e.g.* consider the process  $q + q \rightarrow q + g + q$  in multi-Regge-kinematics and extract the off-shell Reggeon-Reggeon-gluon vertex. Virtual corrections to this process then also include diagrams (like box diagrams) which do not factorize individually but only in the sum. Therefore, Fig. 12b can only be regarded as one specific example of a virtual correction.

The real corrections to the one jet production consist of two gluon and quark-antiquark production. For the quark-antiquark production one just has to distinguish two cases: either both

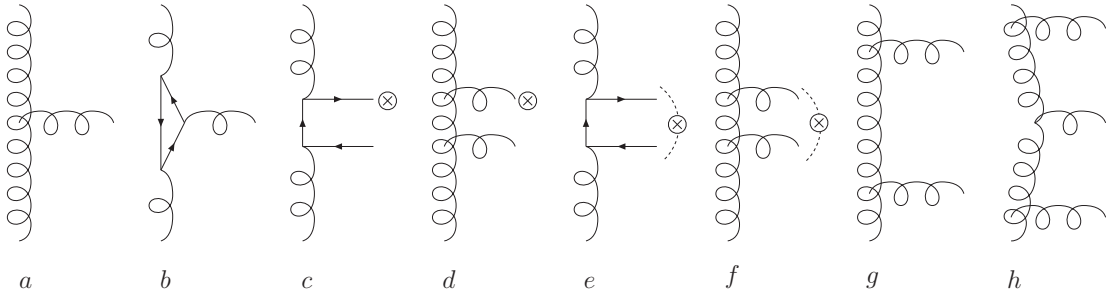


Fig. 12: sample diagrams for the jet vertex in pp.

particles are ‘well separated’ and only one forms the jet while the other contributes to the inclusive part (Fig. 12c), or they are ‘close to each other’ and form one jet (Fig. 12e). The question, whether they are ‘well separated’ or ‘close to each other’, has to be answered by a specific jet definition. The same distinction has to be made for the two gluon production (Fig. 12d and Fig. 12f).

However, the two-gluon production involves some subtleties. Even if the two gluons cannot be combined in one jet, there still remains the question whether the gluon belongs to the same emission vertex or to different ones. A more detailed study of the arrangement of diagrams in the complete framework of NLO BFKL [61, 69] reveals that a contribution from the two neighbored rungs (Fig. 12g) has to be reorganized into the NLO vertex at hand. The contributions in Fig. 12d and Fig. 12g both depend on the scale  $s_\Lambda$  which separates the multi-Regge-kinematics from the quasi-multi-Regge-kinematics. The inclusion of the contribution in Fig. 12g makes the NLO jet vertex (and the NLO BFKL kernel) – to next-to-leading accuracy – independent of  $s_\Lambda$ .

The original formulation of the BFKL approach relies on the scattering of two objects providing an intrinsic and similar hard scale. Instead, in our setting we have to deal with the evolution between the proton – at a soft scale – and the jet – at a hard scale. This imbalance ‘tilts’ the whole evolution such that in fact the BFKL evolution kernel gets a correction introducing some additional collinear evolution. In the language of BFKL this can be understood as the change from a symmetric energy scale  $s_0$  – like  $s_0 = \sqrt{Q_1 Q_2}$  for two colliding objects with scales  $Q_1$  and  $Q_2$  respectively – to an asymmetric one  $s_0 = k_{\perp, \text{Jet}}^2$ . In the end, the result does not depend on this artificial energy scale  $s_0$ , which is ensured by compensating corrections to the impact factors. With respect to the gluon ladder, our jet vertex acts as a kind of impact factor and hence receives from above and below two corrections due to this energy scale change. These complex dependencies involve a large number of concrete diagrams – we only symbolically mark by Fig. 12h that the tilted gluon evolution leads to a correction of the jet emission vertex.

The virtual corrections (Fig. 12b) themselves are infrared divergent. These divergences are canceled by the real corrections (Fig. 12c-f) after they are integrated over. To obtain a jet vertex which is explicitly free of divergences, additional effort has to be made. After identification of those terms in the real corrections which will lead to divergences, one can compensate them by an unintegrated subtraction term, while the integrated subtraction term (which in fact is added such that effectively the result is not changed) cancels the explicit divergences of the virtual

corrections. The exact form of this subtraction term as well as all other formulas which are needed can be found in Ref. [61].

#### 4 Multijet production in the multi-Regge limit: Mueller–Navelet and forward jets

*Authors: Agustín Sabio Vera, Florian Schwennsen*

In this section we briefly describe the calculations performed in [70–73] to obtain the azimuthal angle correlations in Mueller–Navelet jets [74] and forward jets at HERA using the Balitsky–Fadin–Kuraev–Lipatov (BFKL) equation in the next-to-leading (NLO) approximation [67,68] (see also [75–78]). We first comment on the normalized differential cross section for Mueller–Navelet jets. As it is quite insensitive to the parton distribution functions we can simply operate with partonic cross sections, *i.e.*

$$\frac{d\hat{\sigma}}{d^2\vec{q}_1 d^2\vec{q}_2} = \frac{\pi^2 \bar{\alpha}_s^2}{2} \frac{1}{q_1^2 q_2^2} \int \frac{d\omega}{2\pi i} e^{\omega Y} f_{\omega}(\vec{q}_1, \vec{q}_2), \quad (12)$$

where  $\bar{\alpha}_s = \alpha_s N_c / \pi$ ,  $\vec{q}_{1,2}$  are the transverse momenta of the tagged jets, and  $Y$  their relative rapidity. The Green's function carries the bulk of the  $Y$  dependence and is the solution to the NLO BFKL equation,

$$\left( \omega - \bar{\alpha}_s \hat{K}_0 - \bar{\alpha}_s^2 \hat{K}_1 \right) \hat{f}_{\omega} = \hat{1}, \quad (13)$$

which acts on the basis including the azimuthal angle, *i.e.*,

$$\langle \vec{q} | \nu, n \rangle = \frac{1}{\pi \sqrt{2}} (q^2)^{i\nu - \frac{1}{2}} e^{i n \theta}. \quad (14)$$

As  $Y$  increases the azimuthal angle dependence is controlled by the kernel and it is then reasonable to use LO jet vertices which are much simpler than the NLO ones [79,80]. The differential cross section in the azimuthal angle  $\phi = \theta_1 - \theta_2 - \pi$ , with  $\theta_i$  being the angles of the two tagged jets, reads

$$\frac{d\hat{\sigma}(\alpha_s, Y, p_{1,2}^2)}{d\phi} = \frac{\pi^2 \bar{\alpha}_s^2}{4 \sqrt{p_1^2 p_2^2}} \sum_{n=-\infty}^{\infty} e^{i n \phi} \mathcal{C}_n(Y), \quad (15)$$

where  $p_1$  and  $p_2$  are the cuts on transverse momenta and

$$\mathcal{C}_n(Y) = \frac{1}{2\pi} \int_{-\infty}^{\infty} \frac{d\nu}{\left(\frac{1}{4} + \nu^2\right)} \left( \frac{p_1^2}{p_2^2} \right)^{i\nu} e^{\chi(|n|, \frac{1}{2} + i\nu, \bar{\alpha}_s(p_1 p_2)) Y}, \quad (16)$$

and the NLO kernel can be written as

$$\chi(n, \gamma, \bar{\alpha}_s) = \bar{\alpha}_s \chi_0(n, \gamma) + \bar{\alpha}_s^2 \left( \chi_1(n, \gamma) - \frac{\beta_0}{8N_c} \frac{\chi_0(n, \gamma)}{\gamma(1-\gamma)} \right). \quad (17)$$

The eigenvalue of the LO kernel is  $\chi_0(n, \gamma) = 2\psi(1) - \psi\left(\gamma + \frac{n}{2}\right) - \psi\left(1 - \gamma + \frac{n}{2}\right)$ , with  $\psi$  the logarithmic derivative of the Euler function. The action of  $\hat{K}_1$ , in  $\overline{\text{MS}}$  scheme, can be found in [81]. The full cross section only depends on the  $n = 0$  component,

$$\hat{\sigma} = \frac{\pi^3 \bar{\alpha}_s^2}{2 \sqrt{p_1^2 p_2^2}} \mathcal{C}_0(Y). \quad (18)$$

The average of the cosine of the azimuthal angle times an integer projects out the contribution from each of these angular components:

$$\frac{\langle \cos(m\phi) \rangle}{\langle \cos(n\phi) \rangle} = \frac{\mathcal{C}_m(Y)}{\mathcal{C}_n(Y)}. \quad (19)$$

The normalized differential cross section is

$$\frac{1}{\hat{\sigma}} \frac{d\hat{\sigma}}{d\phi} = \frac{1}{2\pi} \sum_{n=-\infty}^{\infty} e^{in\phi} \frac{\mathcal{C}_n(Y)}{\mathcal{C}_0(Y)} = \frac{1}{2\pi} \left\{ 1 + 2 \sum_{n=1}^{\infty} \cos(n\phi) \langle \cos(n\phi) \rangle \right\}. \quad (20)$$

The BFKL resummation is not stable at NLO for zero conformal spin. A manifestation of this lack of convergence is what we found in the gluon–bremsstrahlung scheme where our NLO distributions have an unphysical behavior whenever the  $n = 0$  conformal spin appears in the calculation. To solve this problem we imposed compatibility with renormalization group evolution in the DIS limit following [82–84] for all conformal spins. The new kernel with collinear improvements to all orders in the coupling reads [70–73]

$$\begin{aligned} \omega = & \bar{\alpha}_s (1 + \mathcal{A}_n \bar{\alpha}_s) \left\{ 2\psi(1) - \psi\left(\gamma + \frac{|n|}{2} + \frac{\omega}{2} + \mathcal{B}_n \bar{\alpha}_s\right) \right. \\ & - \psi\left(1 - \gamma + \frac{|n|}{2} + \frac{\omega}{2} + \mathcal{B}_n \bar{\alpha}_s\right) \left. \right\} + \bar{\alpha}_s^2 \left\{ \chi_1(|n|, \gamma) - \frac{\beta_0}{8N_c} \frac{\chi_0(n, \gamma)}{\gamma(1-\gamma)} \right. \\ & - \mathcal{A}_n \chi_0(|n|, \gamma) + \left( \psi'\left(\gamma + \frac{|n|}{2}\right) + \psi'\left(1 - \gamma + \frac{|n|}{2}\right) \right) \left( \frac{\chi_0(|n|, \gamma)}{2} + \mathcal{B}_n \right) \left. \right\}, \quad (21) \end{aligned}$$

where  $\mathcal{A}_n$  and  $\mathcal{B}_n$  are collinear coefficients [70–73]. After this extra resummation our observables have a good physical behavior and are independent of the renormalization scheme. However, it is very important to stress that the asymptotic behavior of the BFKL resummation is convergent for non zero conformal spins. This is why we propose that the ideal distributions to investigate BFKL effects experimentally are those of the form  $\langle \cos(m\phi) \rangle / \langle \cos(n\phi) \rangle$  with  $m, n \neq 0$ , we will see below that in this case the difference between the predictions at LO and at higher orders results is very small.

#### 4.1 Mueller–Navelet jets at the LHC

Long ago, the  $D0$  [85] collaboration analyzed data for Mueller–Navelet jets at  $\sqrt{s} = 630$  and 1800 GeV. For the angular correlation, LO BFKL predictions were first obtained in [86, 87] and failed to describe the data since the LO results were far too decorrelated. On the other hand, a more conventional fixed order NLO analysis using JETRAD underestimated the decorrelation, while HERWIG was in agreement with the data.

In Fig. 13 we compare the Tevatron data for  $\langle \cos \phi \rangle = \mathcal{C}_1/\mathcal{C}_0$  with our LO, NLO and collinearly resummed predictions. For Tevatron’s cuts, where the lower cut off in transverse momentum for one jet is 20 GeV and for the other 50 GeV, the NLO calculation is unstable under renormalization scheme changes. The convergence of our observables is poor whenever the coefficient associated to zero conformal spin,  $\mathcal{C}_0$ , is used in the calculation. If we eliminate

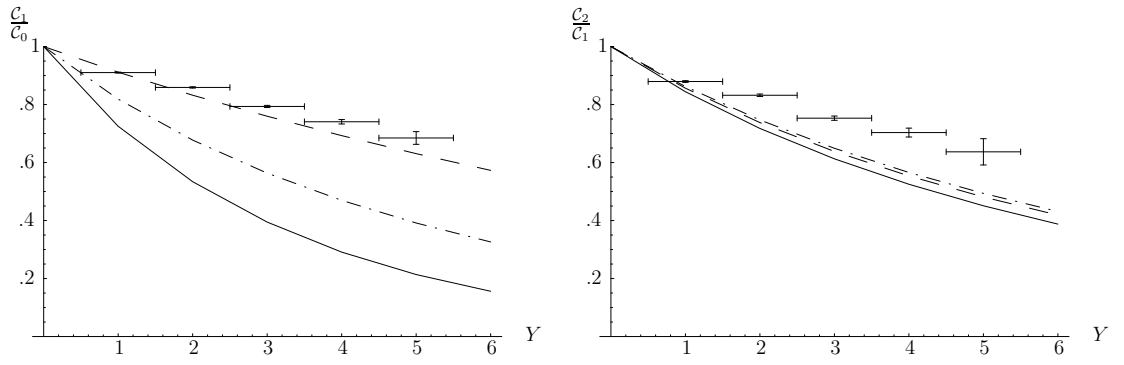


Fig. 13: Left:  $\langle \cos \phi \rangle = C_1/C_0$  and Right:  $\frac{\langle \cos 2\phi \rangle}{\langle \cos \phi \rangle} = \frac{C_2}{C_1}$ , at a  $p\bar{p}$  collider with  $\sqrt{s} = 1.8$  TeV for BFKL at LO (solid) and NLO (dashed). The results from the resummation presented in the text are shown as well (dash-dotted).

this coefficient by calculating the ratios defined in Eq. (19) then the predictions are very stable, see Fig. 13.

The full angular dependence studied at the Tevatron by the DØ collaboration was published in [85]. In Fig. 14 we compare this measurement with the predictions obtained in our approach. For the differential cross section we also make predictions for the LHC at larger  $Y$  in Fig. 15. We estimated several uncertainties in our approach which are represented by gray bands.

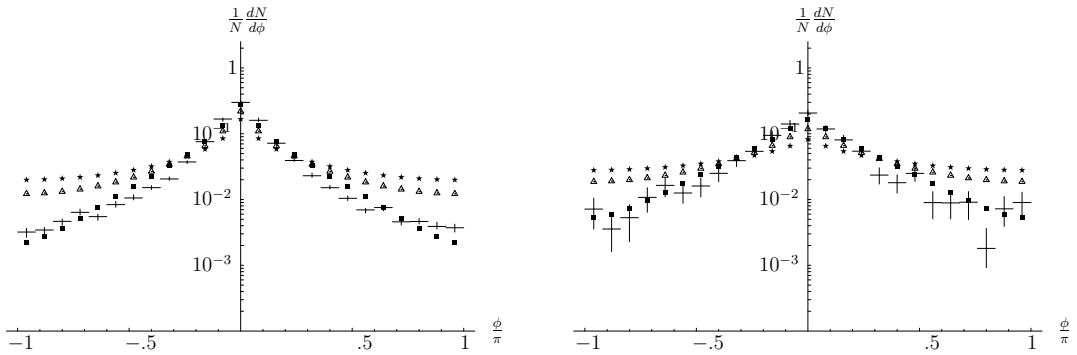


Fig. 14:  $\frac{1}{N} \frac{dN}{d\phi}$  in a  $p\bar{p}$  collider at  $\sqrt{s}=1.8$  TeV using a LO (stars), NLO (squares) and resummed (triangles) BFKL kernel. Plots are shown for  $Y = 3$  (left) and  $Y = 5$  (right).

## 4.2 Forward jets at HERA

In this section we apply the BFKL formalism to predict the decorrelation in azimuthal angle between the electron and a forward jet associated to the proton in Deep Inelastic Scattering (DIS). When the separation in rapidity space between the scattered electron and the forward jet is large and the transverse momentum of the jet is similar to the virtuality of the photon resolving the hadron, then the dominant terms are of BFKL type. This process is similar to that of Mueller–Navelet jets, the only difference being the substitution of one jet vertex by the vertex describing

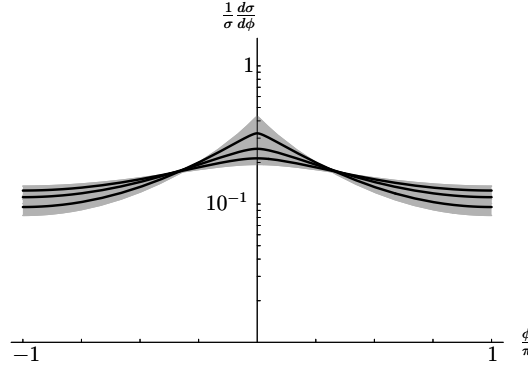


Fig. 15:  $\frac{1}{\sigma} \frac{d\sigma}{d\phi}$  in our resummation scheme for rapidities  $Y = 7, 9, 11$  from top to bottom. The gray band reflects the uncertainty in  $s_0$  and in the renormalization scale  $\mu$ .

the coupling of the electron to the BFKL gluon Green's function via a quark–antiquark pair. Azimuthal angles in forward jets were studied at LO in [88]. We improved their calculation by considering the NLO BFKL kernel and collinear improved versions of it. Fixed order calculations can be found in [89].

In the production of a forward jet in DIS it is necessary to extract a jet with a large longitudinal momentum fraction  $x_{FJ}$  from the proton. When this jet is characterized by a hard scale in the form of a large  $p_t$  it is possible to use conventional collinear factorization to describe the process and the production rate may be written as

$$\sigma(s) = \int dx_{FJ} f_{\text{eff}}(x_{FJ}, \mu_F^2) \hat{\sigma}(\hat{s}), \quad (22)$$

with  $\hat{\sigma}(\hat{s})$  denoting the partonic cross section, and the effective parton density [90] being

$$f_{\text{eff}}(x, \mu_F^2) = G(x, \mu_F^2) + \frac{4}{9} \sum_f [Q_f(x, \mu_F^2) + \bar{Q}_f(x, \mu_F^2)], \quad (23)$$

where the sum runs over all quark flavors, and  $\mu_F$  stands for the factorization scale.

The final expression for the cross section at hadronic level is of the form

$$\frac{d\sigma}{dY d\phi} = C_0(Y) + C_2(Y) \cos 2\phi, \quad (24)$$

with

$$C_n(Y) = \frac{\pi^2 \bar{\alpha}_s^2}{2} \int_{\text{cuts}} dx_{FJ} dQ^2 dy f_{\text{eff}}(x_{FJ}, Q^2) B^{(n)}(y, Q^2, Y) \delta\left(x_{FJ} - \frac{Q^2 e^Y}{ys}\right), \quad (25)$$

where the index in the integral sign refers to the cuts

$$20 \text{ GeV}^2 < Q^2 < 100 \text{ GeV}^2, \quad 0.05 < y < 0.7, \quad 5 \cdot 10^{-3} > x_{Bj} > 4 \cdot 10^{-4}. \quad (26)$$



The integration over the longitudinal momentum fraction  $x_{FJ}$  of the forward jet involves a delta function fixing the rapidity  $Y = \ln x_{FJ}/x_{Bj}$  and  $B^{(n)}$  is a complicated function which can be found in [70–73].

Since the structure of the electron vertex singles out the components with conformal spin 0 and 2, the number of observables related to the azimuthal angle dependence is limited when compared to the Mueller–Navelet case. The most relevant observable is the dependence of the average  $\langle \cos 2\phi \rangle = C_2/C_0$  with the rapidity difference between the forward jet and outgoing lepton. It is natural to expect that the forward jet will be more decorrelated from the leptonic system as the rapidity difference is larger since the phase space for further gluon emission opens up. This is indeed what we observe in our numerical results shown in Fig. 16. We find similar results to the Mueller–Navelet jets case where the most reliable calculation is that with a collinearly-improved kernel. The main effect of the higher order corrections is to increase the azimuthal angle correlation for a given rapidity difference, while keeping the decrease of the correlation as  $Y$  grows.

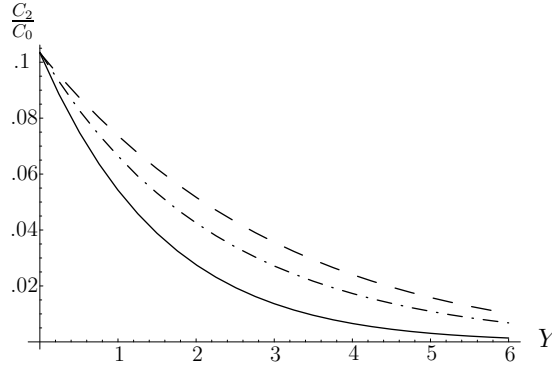


Fig. 16:  $\langle \cos 2\phi \rangle$  at the  $ep$  collider HERA at leading (solid), next to leading order (dashed), and for resummed kernel (dash-dotted).

## 5 NLL BFKL effects: Mueller-Navelet and forward jets

*Author: Christophe Royon*

### 5.1 Forward jets at HERA

Following the successful BFKL [91–93] parametrisation of the forward-jet cross-section  $d\sigma/dx$  at Leading Order (LO) at HERA [75, 94, 95], it is possible to perform a similar study using Next-to-leading (NLL) resummed BFKL kernels. This method can be used for forward jet production at HERA in particular, provided one takes into account the right two scales of the forward-jet problem, namely  $Q^2$  for the lepton and  $k_T^2$  for the jet vertex respectively. In this short report, we will only discuss the phenomenological aspects and all detailed calculations can be found in Ref. [71, 73, 76, 77] for forward jets at HERA and in Ref. [78] for Mueller-Navelet jets at the Tevatron and the LHC.

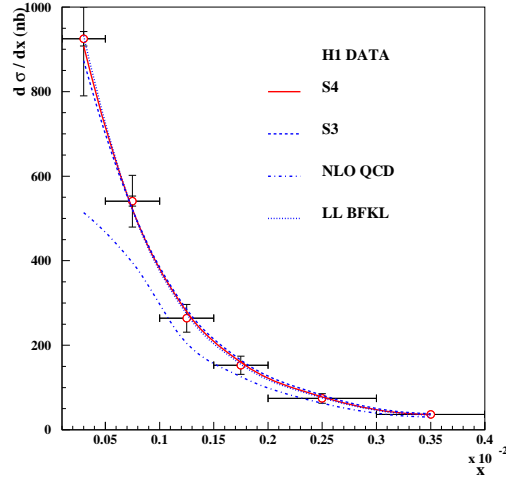


Fig. 17: Comparison between the H1  $d\sigma/dx$  measurement with predictions for BFKL-LL, BFKL-NLL (S3 and S4 schemes) and DGLAP NLO calculations (see text). S4, S3 and LL BFKL cannot be distinguished on that figure.

The BFKL NLL [67, 68, 96] longitudinal transverse cross section reads:

$$\frac{d\sigma_{T,L}^{\gamma^*p \rightarrow JX}}{dx_J dk_T^2} = \frac{\alpha_s(k_T^2)\alpha_s(Q^2)}{k_T^2 Q^2} f_{eff}(x_J, k_T^2) \int d\gamma \left(\frac{Q^2}{k_T^2}\right)^\gamma \phi_{T,L}^\gamma(\gamma) e^{\bar{\alpha}(k_T Q)\chi_{eff}[\gamma, \bar{\alpha}(k_T Q)]Y} \quad (27)$$

where the  $\chi_{eff}$  is the effective BFKL NLL kernel and the  $\phi$  are the transverse and longitudinal impact factors taken at LL. The effective kernel  $\chi_{eff}(\gamma, \bar{\alpha})$  is defined from the NLL kernel  $\chi_{NLL}(\gamma, \omega)$  by solving the implicit equation numerically

$$\chi_{eff}(\gamma, \bar{\alpha}) = \chi_{NLL}[\gamma, \bar{\alpha} \chi_{eff}(\gamma, \bar{\alpha})] . \quad (28)$$

The integration over  $\gamma$  in Eq. 27 is performed numerically. It is possible to fit directly  $d\sigma/dx$  measured [97] by the H1 collaboration using this formalism with one single parameter, the normalisation. The values of  $\chi_{NLL}$  are taken at NLL [67, 68, 96] using different resummation schemes to remove spurious singularities defined as S3 and S4 [82]. Contrary to LL BFKL, it is worth noticing that the coupling constant  $\alpha_S$  is taken using the renormalisation group equations, the only free parameter in the fit being the normalisation.

To compute  $d\sigma/dx$  in the experimental bins, we need to integrate the differential cross section on the bin size in  $Q^2$ ,  $x_J$  (the momentum fraction of the proton carried by the forward jet),  $k_T$  (the jet transverse momentum), while taking into account the experimental cuts. To simplify the numerical calculation, we perform the integration on the bin using the variables where the cross section does not change rapidly, namely  $k_T^2/Q^2$ ,  $\log 1/x_J$ , and  $1/Q^2$ . Experimental cuts are treated directly at the integral level (the cut on  $0.5 < k_T^2/Q^2 < 5$  for instance) or using a toy Monte Carlo. More detail can be found about the fitting procedure in Appendix A of Ref. [75].

The NLL fits [71, 73, 76, 77] can nicely describe the H1 data [97] for the S4 and S3 schemes [71, 73, 75–77, 94, 95] ( $\chi^2 = 0.48/5$  and  $\chi^2 = 1.15/5$  respectively per degree of

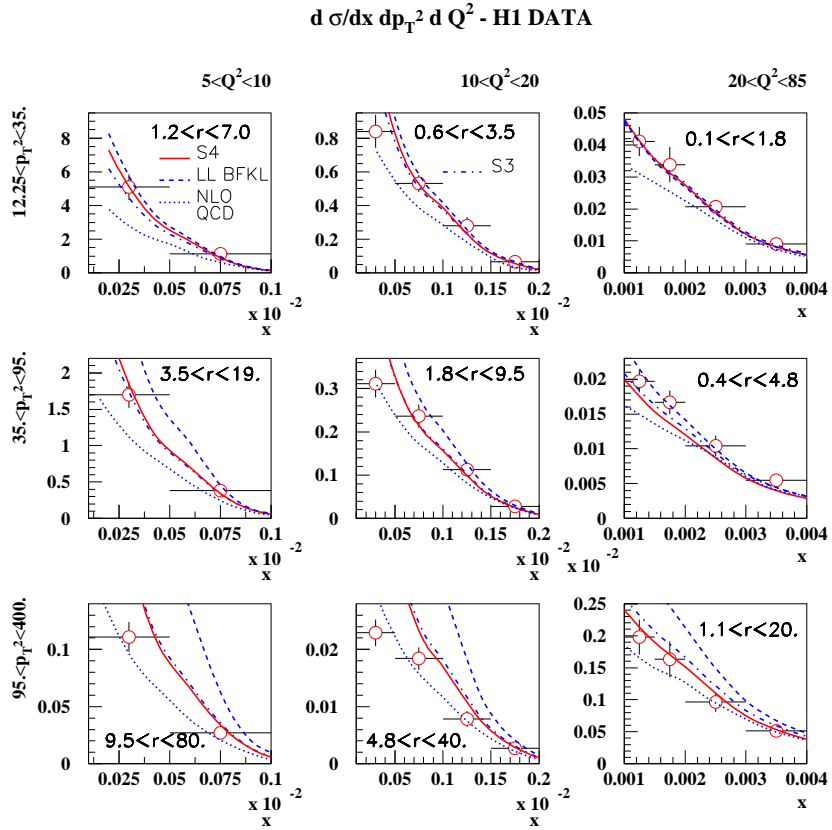


Fig. 18: Comparison between the H1 measurement of the triple differential cross section with predictions for BFKL-LL, BFKL-NLL and DGLAP NLO calculations (see text).

freedom with statistical and systematic errors added in quadrature). The curve using a LL fit is indistinguishable in Fig. 17 from the result of the BFKL-NLL fit. The DGLAP NLO calculation fails to describe the H1 data at lowest  $x$  (see Fig. 17). We also checked the effect of changing the scale in the exponential of Eq. 27 from  $k_T Q$  to  $2k_T Q$  or  $k_T Q/2$  which leads to a difference of 20% on the cross section while changing the scale to  $k_T^2$  or  $Q^2$  modifies the result by less than 5% which is due to the cut on  $0.5 < k_T^2/Q^2 < 5$ . Implementing the higher-order corrections in the impact factor due to exact gluon dynamics in the  $\gamma^* \rightarrow q\bar{q}$  transition [98] changes the result by less than 3%.

The H1 collaboration also measured the forward jet triple differential cross section [97] and the results are given in Fig. 18. We keep the same normalisation coming from the fit to  $d\sigma/dx$  to predict the triple differential cross section. The BFKL LL formalism leads to a good description of the data when  $r = k_T^2/Q^2$  is close to 1 and deviates from the data when  $r$  is further away from 1. This effect is expected since DGLAP radiation effects are supposed to occur when the ratio between the jet  $k_T$  and the virtual photon  $Q^2$  are further away from 1. The BFKL NLL calculation including the  $Q^2$  evolution via the renormalisation group equation leads to a good description of the H1 data on the full range. We note that the higher order corrections are small when  $r \sim 1$ , when the BFKL effects are supposed to dominate. By contrast, they are significant as expected when  $r$  is different from one, i.e. when DGLAP evolution becomes relevant. We notice that the DGLAP NLO calculation fails to describe the data when  $r \sim 1$ , or in the region where BFKL resummation effects are expected to appear.

In addition, we checked the dependence of our results on the scale taken in the exponential of Eq. 27. The effect is a change of the cross section of about 20% at low  $p_T$  increasing to 70% at highest  $p_T$ . Taking the correct gluon kinematics in the impact factor lead as expected to a better description of the data at high  $p_T$  [71, 73, 76, 77].

## 5.2 Mueller-Navelet jets at the Tevatron and the LHC

Mueller-Navelet jets are ideal processes to study BFKL resummation effects [74]. Two jets with a large interval in rapidity and with similar transverse momenta are considered. A typical observable to look for BFKL effects is the measurement of the azimuthal correlations between both jets. The DGLAP prediction is that this distribution should peak towards  $\pi$  - i.e. jets are back-to-back- whereas multi-gluon emission via the BFKL mechanism leads to a smoother distribution. The relevant variables to look for azimuthal correlations are the following:

$$\begin{aligned}\Delta\eta &= y_1 - y_2 \\ y &= (y_1 + y_2)/2 \\ Q &= \sqrt{k_1 k_2} \\ R &= k_2/k_1\end{aligned}$$

The azimuthal correlation for BFKL reads:

$$2\pi \frac{d\sigma}{d\Delta\eta dR d\Delta\Phi} \bigg/ \frac{d\sigma}{d\Delta\eta dR} = 1 + \frac{2}{\sigma_0(\Delta\eta, R)} \sum_{p=1}^{\infty} \sigma_p(\Delta\eta, R) \cos(p\Delta\Phi)$$

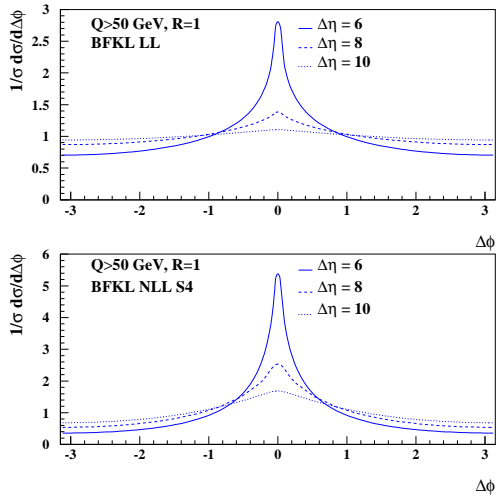


Fig. 19: The Mueller-Navelet jet  $\Delta\Phi$  distribution for LHC kinematics in the BFKL framework at LL (upper plots) and NLL-S4 (lower plots) accuracy for  $\Delta\eta = 6, 8, 10$ .

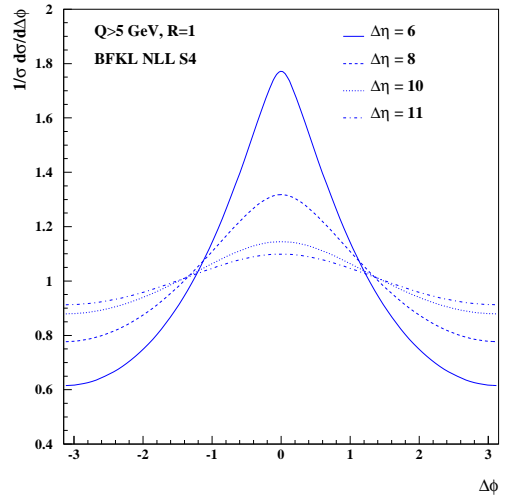


Fig. 20: Azimuthal correlations between jets with  $\Delta\eta = 6, 8, 10$  and  $p_T > 5$  GeV in the CDF acceptance. This measurement will represent a clear test of the BFKL regime.

where in the NLL BFKL framework,

$$\sigma_p = \int_{E_T}^{\infty} \frac{dQ}{Q^3} \alpha_s(Q^2/R) \alpha_s(Q^2 R) \left( \int_{y_<}^{y_>} dy x_1 f_{eff}(x_1, Q^2/R) x_2 f_{eff}(x_2, Q^2 R) \right) \int_{1/2-\infty}^{1/2+\infty} \frac{d\gamma}{2i\pi} R^{-2\gamma} e^{\bar{\alpha}(Q^2) \chi_{eff}(p, \gamma, \bar{\alpha}) \Delta\eta}$$

and  $\chi_{eff}$  is the effective resummed kernel. Computing the different  $\sigma_p$  at NLL for the resummation schemes S3 and S4 allowed us to compute the azimuthal correlations at NLL. As expected, the  $\Delta\Phi$  dependence is less flat than for BFKL LL and is closer to the DGLAP behaviour [78]. In Fig. 19, we display the observable  $1/\sigma d\sigma/d\Delta\Phi$  as a function of  $\Delta\Phi$ , for LHC kinematics. The results are displayed for different values of  $\Delta\eta$  and at both LL and NLL accuracy using the S4 resummation scheme. In general, the  $\Delta\Phi$  spectra are peaked around  $\Delta\Phi = 0$ , which is indicative of jet emissions occurring back-to-back. In addition the  $\Delta\Phi$  distribution flattens with increasing  $\Delta\eta = y_1 - y_2$ . Note the change of scale on the vertical axis which indicates the magnitude of the NLL corrections with respect to the LL-BFKL results. The NLL corrections slow down the azimuthal angle decorrelations for both increasing  $\Delta\eta$  and  $R$  deviating from 1. We also studied the  $R$  dependence of our prediction which is quite weak [78]. We also studied the scale dependence of our results by modifying the scale  $Q^2$  to either  $Q^2/2$  or  $2Q^2$  and the effect on the azimuthal distribution is of the order of 20%. The effect of the energy conservation in the BFKL equation [78] is large when  $R$  goes away from 1. The effect is to reduce the effective value of  $\Delta\eta$  between the jets and thus the decorrelation effect. However, it is worth noticing that this effect is negligible when  $R$  is close to 1 where this measurement will be performed.

A measurement of the cross-section  $d\sigma^{hh \rightarrow JXJ}/d\Delta\eta dR d\Delta\Phi$  at the Tevatron (Run 2) or

the LHC will allow for a detailed study of the BFKL QCD dynamics since the DGLAP evolution leads to much less jet angular decorrelation (jets are back-to-back when  $R$  is close to 1). In particular, measurements with values of  $\Delta\eta$  reaching 8 or 10 will be of great interest, as these could allow to distinguish between BFKL and DGLAP resummation effects and would provide important tests for the relevance of the BFKL formalism.

To illustrate this result, we give in Fig. 20 the azimuthal correlation in the CDF acceptance. The CDF collaboration installed the mini-Plugs calorimeters aiming for rapidity gap selections in the very forward regions and these detectors can be used to tag very forward jets. A measurement of jet  $p_T$  with these detectors would not be possible but their azimuthal segmentation allows a  $\phi$  measurement. In Fig. 20, we display the jet azimuthal correlations for jets with a  $p_T > 5$  GeV and  $\Delta\eta = 6, 8, 10$  and 11. For  $\Delta\eta = 11$ , we notice that the distribution is quite flat, which would be a clear test of the BFKL prediction.

## 6 Forward Jets in the CASTOR calorimeter in the CMS experiment

*Author: Albert Knutsson*

The CASTOR (Centauro and STRange Object Research) detector [99] is a Cherenkov radiation calorimeter consisting of tungsten absorber plates sandwiched with plates of quartz, used as the active material in the detector. The construction is repeated in octants in azimuthal angle, giving a full  $360^\circ$  coverage. For each octant lightguides and photomultipliers are situated on top of the plates in two columns, 14 channels deep along the beam direction. 2 of the 14 channels are designed for detection of electromagnetic particles and the rest are hadronic channels. Thus the detector consists of a total number of  $16 \times 14$  channels. CASTOR is situated 14.4 m from the interaction vertex in the CMS detector at LHC and covers the pseudorapidity range  $5.2 < \eta < 6.6$ .

Since CASTOR has no segmentation in polar angle it will not be possible to define jets according to conventional jet algorithms which use the energy, polar and azimuthal angle of particles. Here we investigate the possibility to measure jet events with CASTOR, by using only the azimuthal segmentation and energy deposition. The studies are carried out on Monte Carlo generator level. Events are generated with the ARIADNE event generator [100], with the hadron level jets defined according to the inclusive  $k_T$  algorithm. The kinematic region has been divided into 16 slices in  $\phi$ , for which the energies of all particles are summed. In Fig. 21a-b the correlations between the hadron level jet energy and different energy depositions in the CASTOR region are shown. Clearly the total energy contained in the CASTOR region is too large compared to the energy of the hadron level jet (Fig. 21a), while the energy in the  $\phi$  segment with highest energy gives a better correlation with the true jet energy (Fig. 21b). The best reconstruction of the jet energy is achieved if the energy in the most active  $\phi$  segment is summed with the two neighbouring cells (Fig. 21c). This is the method we use in the physics studies presented in the next section. In future, one can improve the jet reconstruction with more complex algorithms in order to obtain an even better correlation in jet energy. Finally, in Fig. 22 the azimuthal angle of the jet axis is plotted versus the azimuthal slice with highest energy. A good correlation is seen.

Events in which an energetic jet is produced close to the proton remnant (the forward direction) are sensitive to the higher order reactions due to the long rapidity range available for

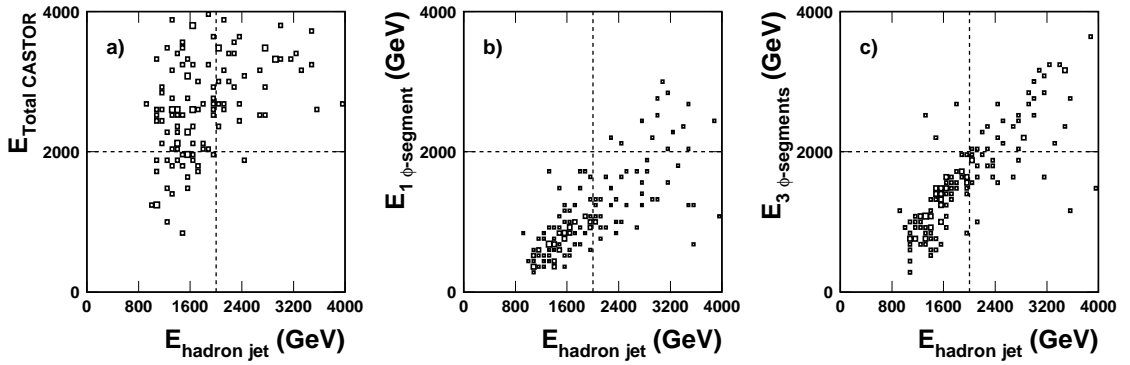


Fig. 21: Monte Carlo predictions on generator level for the hadron level jet energy vs. **a** the energy contained in the full CASTOR region, **b** the energy in the  $\phi$ -segment with the highest energy deposit and **c** the energy in the  $\phi$ -segment with the highest energy deposit summed with the energy in two neighbouring cells.

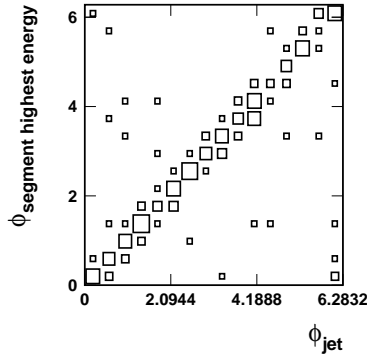


Fig. 22: Azimuthal angle of the highest energy  $\phi$ -segment vs. the azimuthal angle of the jet.

radiation between the jet and the hard scattering vertex. The longitudinal momentum fraction of the proton,  $x$ , can be related to the rapidity,  $y$ , by approximately  $x \sim e^{-y}$ , which further suggests that forward physics gives us valuable information about low  $x$  parton dynamics.

At HERA, forward jet events have been analysed [97, 101] and improved our understanding of QCD. Available fixed order calculations (next-to-leading order  $O(\alpha_s^2)$ ) as well as the higher order reactions approximated by DGLAP parton showers underestimate the HERA data by up to a factor of 2. The data can be described only if the ordering of the transverse momenta of the radiated gluons is broken in the theoretical predictions.

In events where the transverse momentum of the forward jet is close to the scale of the hard reaction the DGLAP like scenario, i.e. events with QCD radiation ordered in transverse momenta, is further suppressed. In the HERA analysis this is achieved by requiring that the square of the transverse momentum of the forward jet was in the same order as the virtuality of the exchanged photon. In the analysis presented here we instead require that two additional hard jets are produced in the central region of the detector. For the forward jets in the CASTOR region this gives up to 5 units of pseudorapidity range available for more gluon radiation.

For this study the Monte Carlo events are generated by using the full event generators PYTHIA 6.4.14 [9] and ARIADNE 1.4 [100]. PYTHIA 6.4.14 is based on LO DGLAP parton showers, which gives gluon radiation ordered in transverse momentum with respect to rapidity. In ARIADNE, parton showers are generated by the Color Dipole Model (CDM), resulting in gluon radiation without any ordering in transverse momentum with respect to rapidity. This corresponds to a BFKL like final state. PYTHIA is run with the so called tune A multiple interaction model.

The hadron level jets are defined with the inclusive  $k_t$  algorithm. Events are selected which contain a jet with a transverse momentum  $E_T > 10$  GeV and a pseudorapidity  $5.2 < \eta < 6.6$ . To further suppress events with DGLAP like dynamics, two jets with  $E_T > 10$  GeV are required in the central region,  $|\eta| < 1.5$ . The resulting cross-section is shown in Fig. 23 as a function of the forward jet energy. As can be seen, CDM is producing more jets at higher energies, while the events with gluon emissions generated according to DGLAP dynamics have a suppressed jet production. At the highest forward jet energies the difference between the models is up to two orders of magnitude.

In the following we replace the hadronic forward jet with the jet reconstruction described in the previous section. In addition we have also smeared the particle energies according to resolutions measured in the CASTOR beam test [102] and applied a noise cut at 1 GeV. Since we can no longer determine the  $E_T$  of the reconstructed forward jet, this cut is removed from the forward jet selection, but the measured range in energy is kept. The major consequence is, as expected, an increased number of jets at low energies. The predictions from PYTHIA and CDM shows that the very high sensitivity to the scheme used for the QCD radiation is still preserved (see Fig. 24).

In Fig. 25a and b we investigate the PDF uncertainties for the suggested measurement. As can be seen in Fig. 25a the predicted forward jet cross section does not distinguish between PDFs which has been fitted at leading order with LO  $\alpha_s$ , CTEQ6L, or NLO  $\alpha_s$ , CTEQ6LL. Using the CTEQ6.5 PDF however gives a lower forward jet cross section, as illustrated in Fig. 25b. Here the PDF uncertainty, based on the 40 error eigensets for CTEQ6.5, are shown for the PYTHIA prediction.

Finally, the response to multiple interactions (MI) is studied in Fig. 26. We see that the impact of MI is expected to be large in general; excluding MI lowers the cross section by roughly an order of magnitude. Except of that, the sensitivity to the different MI tunes and models are fairly small in comparison to the impact of using a CDM.

In summary a method for jet reconstruction in the CASTOR calorimeter has been suggested. We have shown that using the method to measure forward jets in CASTOR in addition to two jets in the central region may give a very large sensitivity to the dynamics of the parton shower. This is also true if PDF uncertainties and different MI models are taken into account.

## References

- [1] NLO Multileg Working Group Collaboration, Z. Bern *et al.* (2008), arXiv:0803.0494 [hep-ph].



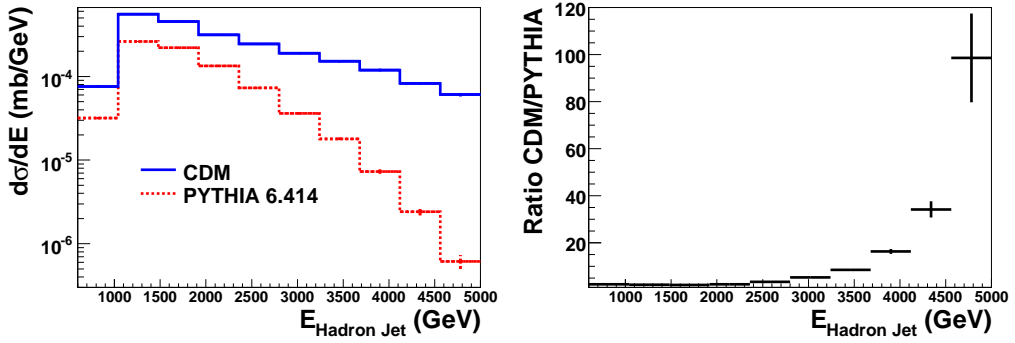


Fig. 23: Hadron level cross sections for events with two central jets and a forward jet in the pseudorapidity region of the CASTOR calorimeter. The predictions are on generator level without any assumptions about the detector.

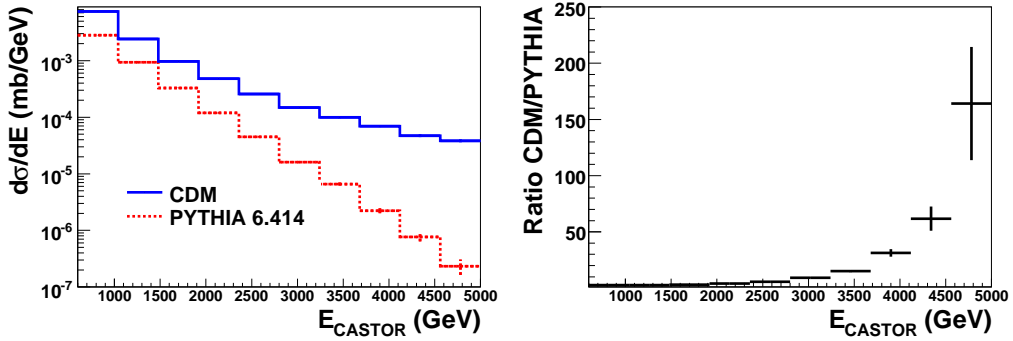


Fig. 24: Cross sections for events with two central jets and a forward jet in the pseudorapidity region of the CASTOR calorimeter. The predictions are on generator level, but here with the forward jet reconstructed as described in the text and forward particle momenta smeared according to CASTOR beam test data.

- [2] S. Hoche *et al.* (2006). hep-ph/0602031.
- [3] N. Lavesson and L. Lonnblad, JHEP **04**, 085 (2008), arXiv:0712.2966 [hep-ph].
- [4] J. Alwall *et al.*, Eur. Phys. J. **C53**, 473 (2008).
- [5] S. Alekhin *et al.* (2005), arXiv:hep-ph/0601012.
- [6] S. Alekhin *et al.* (2005), arXiv:hep-ph/0601013.
- [7] G. Corcella *et al.*, JHEP **01**, 010 (2001), arXiv:hep-ph/0011363.
- [8] G. Corcella *et al.* (2002), arXiv:hep-ph/0210213.
- [9] T. Sjostrand, S. Mrenna, and P. Skands, JHEP **05**, 026 (2006), arXiv:hep-ph/0603175.
- [10] G. Marchesini and B. R. Webber, Nucl. Phys. **B386**, 215 (1992).

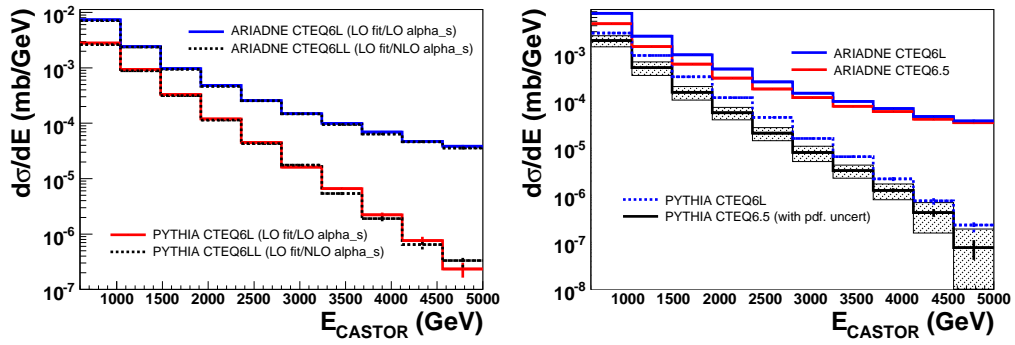


Fig. 25: The PDF uncertainties for the 2+forward jet cross section. The predictions are on generator level, but with the forward jet reconstructed as described in the text and forward particle momenta smeared according to CASTOR beam test data.

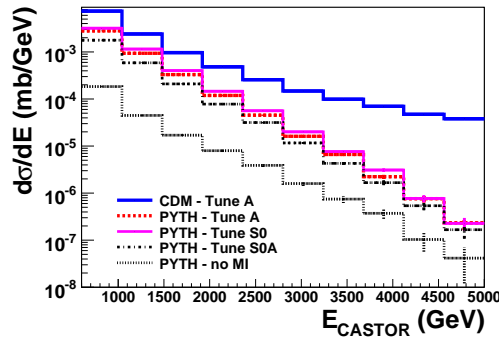


Fig. 26: Monte Carlo prediction for the 2+forward jet cross section using different MI models and tunes. The predictions are on generator level, but with the forward jet reconstructed as described in the text and forward particle momenta smeared according to CASTOR beam test data.

- [11] M. Ciafaloni, Nucl. Phys. **B296**, 49 (1988).
- [12] S. Catani, M. Ciafaloni, and F. Hautmann, Phys. Lett. **B242**, 97 (1990).
- [13] S. Catani, M. Ciafaloni, and F. Hautmann, Nucl. Phys. **B366**, 135 (1991).
- [14] S. Catani, M. Ciafaloni, and F. Hautmann, Phys. Lett. **B307**, 147 (1993).
- [15] Small x Collaboration, B. Andersson *et al.*, Eur. Phys. J. **C25**, 77 (2002), arXiv:hep-ph/0204115.
- [16] H. Jung, Comput. Phys. Commun. **143**, 100 (2002), arXiv:hep-ph/0109102.
- [17] H. Jung and G. P. Salam, Eur. Phys. J. **C19**, 351 (2001), arXiv:hep-ph/0012143.
- [18] L. Lonnblad and M. Sjodahl, JHEP **05**, 038 (2005), arXiv:hep-ph/0412111.
- [19] L. Lonnblad and M. Sjodahl, JHEP **02**, 042 (2004), arXiv:hep-ph/0311252.

- [20] G. Gustafson, L. Lonnblad, and G. Miu, JHEP **09**, 005 (2002), arXiv:hep-ph/0206195.
- [21] K. J. Golec-Biernat, S. Jadach, W. Placzek, P. Stephens, and M. Skrzypek, Acta Phys. Polon. **B38**, 3149 (2007), arXiv:hep-ph/0703317.
- [22] S. Hoche, F. Krauss, and T. Teubner, *Multijet events in the  $k_T$ -factorisation scheme*, 2007. arXiv:0705.4577 [hep-ph].
- [23] Small x Collaboration, J. R. Andersen *et al.*, Eur. Phys. J. **C35**, 67 (2004), arXiv:hep-ph/0312333.
- [24] F. Hautmann and H. Jung (2007), arXiv:0712.0568 [hep-ph].
- [25] F. Hautmann and H. Jung, JHEP **10**, 113 (2008), arXiv:0805.1049 [hep-ph].
- [26] M. Ciafaloni, PoS **RADCOR2007**, 029 (2007).
- [27] G. Altarelli, R. D. Ball, and S. Forte, PoS **RADCOR2007**, 028 (2007), arXiv:0802.0968 [hep-ph].
- [28] J. Collins, *Rapidity divergences and valid definitions of parton densities*, 2008. arXiv:0808.2665 [hep-ph].
- [29] J. C. Collins (2001), arXiv:hep-ph/0106126.
- [30] S. Catani and F. Hautmann, Nucl. Phys. **B427**, 475 (1994), arXiv:hep-ph/9405388.
- [31] S. Catani and F. Hautmann, Phys. Lett. **B315**, 157 (1993).
- [32] L. N. Lipatov, Phys. Rept. **286**, 131 (1997), arXiv:hep-ph/9610276.
- [33] M. Buza, Y. Matiounine, J. Smith, R. Migneron, and W. L. van Neerven, Nucl. Phys. **B472**, 611 (1996), arXiv:hep-ph/9601302.
- [34] S. Riemersma, J. Smith, and W. L. van Neerven, Phys. Lett. **B347**, 143 (1995), arXiv:hep-ph/9411431.
- [35] E. Laenen, S. Riemersma, J. Smith, and W. L. van Neerven, Nucl. Phys. **B392**, 162 (1993).
- [36] S. Moch, J. A. M. Vermaseren, and A. Vogt, Phys. Lett. **B606**, 123 (2005), arXiv:hep-ph/0411112.
- [37] A. Vogt, S. Moch, and J. A. M. Vermaseren, Nucl. Phys. **B691**, 129 (2004), arXiv:hep-ph/0404111.
- [38] DELPHI Collaboration, P. Abreu *et al.*, Z. Phys. **C73**, 11 (1996).
- [39] H1 Collaboration, C. Adloff *et al.*, Eur. Phys. J. **C21**, 33 (2001), hep-ex/0012053.

- [40] W. Press *et al*, *Numerical Recipes*. Cambridge University Press, 1992.
- [41] F. James and M. Roos, *Comput. Phys. Commun.* **10**, 343 (1975).
- [42] J. C. Collins and R. K. Ellis, *Nucl. Phys.* **B360**, 3 (1991).
- [43] S. Berge, P. M. Nadolsky, F. Olness, and C. P. Yuan, *Phys. Rev.* **D72**, 033015 (2005), [arXiv:hep-ph/0410375](#).
- [44] M. Deák and F. Schwennsen, *JHEP* **09**, 035 (2008), [arXiv:0805.3763 \[hep-ph\]](#).
- [45] S. P. Baranov, A. V. Lipatov, and N. P. Zotov, *Phys. Rev.* **D78**, 014025 (2008), [arXiv:0805.4821 \[hep-ph\]](#).
- [46] S. P. Baranov, A. V. Lipatov, and N. P. Zotov, *Yad. Fiz.* **67**, 856 (2004), [arXiv:hep-ph/0302171](#).
- [47] A. V. Lipatov and N. P. Zotov, *Phys. Rev.* **D75**, 014028 (2007), [arXiv:hep-ph/0611302](#).
- [48] F. Hautmann, *Phys. Lett.* **B535**, 159 (2002), [arXiv:hep-ph/0203140](#).
- [49] A. V. Lipatov and N. P. Zotov, *Eur. Phys. J.* **C44**, 559 (2005), [arXiv:hep-ph/0501172](#).
- [50] M. A. Kimber, A. D. Martin, and M. G. Ryskin, *Phys. Rev.* **D63**, 114027 (2001), [hep-ph/0101348](#).
- [51] G. Watt, A. D. Martin, and M. G. Ryskin, *Eur. Phys. J.* **C31**, 73 (2003), [arXiv:hep-ph/0306169](#).
- [52] S. P. Baranov, A. V. Lipatov, and N. P. Zotov, *Phys. Rev.* **D77**, 074024 (2008), [arXiv:0708.3560 \[hep-ph\]](#).
- [53] A. Kulesza and W. J. Stirling, *Nucl. Phys.* **B555**, 279 (1999), [arXiv:hep-ph/9902234](#).
- [54] D0 Collaboration, B. Abbott *et al.*, *Phys. Rev.* **D61**, 032004 (2000), [arXiv:hep-ex/9907009](#).
- [55] D0 Collaboration, B. Abbott *et al.*, *Phys. Lett.* **B513**, 292 (2001), [arXiv:hep-ex/0010026](#).
- [56] CDF Collaboration, A. A. Affolder *et al.*, *Phys. Rev. Lett.* **84**, 845 (2000), [arXiv:hep-ex/0001021](#).
- [57] G. Watt, A. D. Martin, and M. G. Ryskin, *Phys. Rev.* **D70**, 014012 (2004), [arXiv:hep-ph/0309096](#).

- [58] J. M. Campbell, R. K. Ellis, and D. L. Rainwater, Phys. Rev. **D68**, 094021 (2003),  
arXiv:hep-ph/0308195;  
J. M. Campbell and R. K. Ellis, Phys. Rev. **D65**, 113007 (2002),  
arXiv:hep-ph/0202176;  
J. Campbell and K. Ellis <http://mcfm.fnal.gov/>.
- [59] J. Pumplin, D. Stump, J. Huston, H. Lai, P. Nadolsky, and W. Tung, JHEP **0207**, 012 (2002). <http://www.citebase.org/abstract?id=oai:arXiv.org:hep-ph/0201195>.
- [60] S. P. Baranov and N. P. Zotov, Phys. Lett. **B491**, 111 (2000).
- [61] J. Bartels, A. Sabio Vera, and F. Schwennsen, JHEP **0611**, 051 (2006),  
hep-ph/0608154.
- [62] J. Bartels, S. Gieseke, and C. F. Qiao, Phys. Rev. **D63**, 056014 (2001),  
arXiv:hep-ph/0009102.
- [63] J. Bartels, S. Gieseke, and A. Kyrieleis, Phys. Rev. **D65**, 014006 (2002),  
arXiv:hep-ph/0107152.
- [64] J. Bartels, D. Colferai, S. Gieseke, and A. Kyrieleis, Phys. Rev. **D66**, 094017 (2002),  
arXiv:hep-ph/0208130.
- [65] J. Bartels and A. Kyrieleis, Phys. Rev. **D70**, 114003 (2004),  
arXiv:hep-ph/0407051.
- [66] G. Chachamis and J. Bartels, PoS **DIFF2006**, 026 (2006).
- [67] V. S. Fadin and L. N. Lipatov, Phys. Lett. **B429**, 127 (1998),  
arXiv:hep-ph/9802290.
- [68] M. Ciafaloni and G. Camici, Phys. Lett. **B430**, 349 (1998),  
arXiv:hep-ph/9803389.
- [69] V. S. Fadin (1998), arXiv:hep-ph/9807528.
- [70] A. Sabio Vera, Nucl. Phys. **B746**, 1 (2006), arXiv:hep-ph/0602250.
- [71] A. Sabio Vera and F. Schwennsen, Nucl. Phys. **B776**, 170 (2007),  
arXiv:hep-ph/0702158.
- [72] F. Schwennsen (2007), arXiv:hep-ph/0703198.
- [73] A. Sabio Vera and F. Schwennsen, Phys. Rev. **D77**, 014001 (2008),  
arXiv:0708.0549 [hep-ph].
- [74] A. H. Mueller and H. Navelet, Nucl. Phys. **B282**, 727 (1987).
- [75] C. Marquet and C. Royon, Nucl. Phys. **B739**, 131 (2006), arXiv:hep-ph/0510266.

- [76] O. Kepka, C. Royon, C. Marquet, and R. B. Peschanski, Phys. Lett. **B655**, 236 (2007), arXiv:hep-ph/0609299.
- [77] O. Kepka, C. Royon, C. Marquet, and R. B. Peschanski, Eur. Phys. J. **C55**, 259 (2008), arXiv:hep-ph/0612261.
- [78] C. Marquet and C. Royon (2007), arXiv:0704.3409 [hep-ph].
- [79] J. Bartels, D. Colferai, and G. P. Vacca, Eur. Phys. J. **C24**, 83 (2002), arXiv:hep-ph/0112283.
- [80] J. Bartels, D. Colferai, and G. P. Vacca, Eur. Phys. J. **C29**, 235 (2003), arXiv:hep-ph/0206290.
- [81] A. V. Kotikov and L. N. Lipatov, Nucl. Phys. **B582**, 19 (2000), arXiv:hep-ph/0004008.
- [82] G. P. Salam, JHEP **07**, 019 (1998), arXiv:hep-ph/9806482.
- [83] M. Ciafaloni, D. Colferai, G. P. Salam, and A. M. Stasto, Phys. Rev. **D68**, 114003 (2003), arXiv:hep-ph/0307188.
- [84] A. Sabio Vera, Nucl. Phys. **B722**, 65 (2005), arXiv:hep-ph/0505128.
- [85] D0 Collaboration, S. Abachi *et al.*, Phys. Rev. Lett. **77**, 595 (1996), arXiv:hep-ex/9603010.
- [86] V. Del Duca and C. R. Schmidt, Phys. Rev. **D49**, 4510 (1994), arXiv:hep-ph/9311290.
- [87] W. J. Stirling, Nucl. Phys. **B423**, 56 (1994), arXiv:hep-ph/9401266.
- [88] J. Bartels, V. Del Duca, and M. Wusthoff, Z. Phys. **C76**, 75 (1997), arXiv:hep-ph/9610450.
- [89] P. Aurenche, R. Basu, and M. Fontannaz (2008), arXiv:0807.2133 [hep-ph].
- [90] B. L. Combridge and C. J. Maxwell, Nucl. Phys. **B239**, 429 (1984).
- [91] L. N. Lipatov, Sov. J. Nucl. Phys. **23**, 338 (1976).
- [92] E. A. Kuraev, L. N. Lipatov, and V. S. Fadin, Sov. Phys. JETP **45**, 199 (1977).
- [93] I. I. Balitsky and L. N. Lipatov, Sov. J. Nucl. Phys. **28**, 822 (1978).
- [94] J. G. Contreras, R. B. Peschanski, and C. Royon, Phys. Rev. **D62**, 034006 (2000), arXiv:hep-ph/0002057.
- [95] C. Marquet, R. B. Peschanski, and C. Royon, Phys. Lett. **B599**, 236 (2004), arXiv:hep-ph/0407011.

- [96] M. Ciafaloni, Phys. Lett. **B429**, 363 (1998), `arXiv:hep-ph/9801322`.
- [97] H1 Collaboration, A. Aktas *et al.*, Eur. Phys. J. **C46**, 27 (2006), `arXiv:hep-ex/0508055`.
- [98] C. D. White, R. B. Peschanski, and R. S. Thorne, Phys. Lett. **B639**, 652 (2006), `arXiv:hep-ph/0606169`.
- [99] X. e. a. Aslanoglou, Eur. Phys. J. **C52**, 495 (2007), `arXiv:0706.2641` [`physics.ins-det`].
- [100] L. Lonnblad, Comput. Phys. Commun. **71**, 15 (1992).
- [101] ZEUS Collaboration, S. e. a. Chekanov, Phys. Lett. **B632**, 13 (2006), `arXiv:hep-ex/0502029`.
- [102] X. Aslanoglou, A. Cyz, N. Davis, D. d’Enterria, E. Gladysz-Dziadus, C. Kalfas, Y. Musienko, A. Kuznetsov, and A. D. Panagiotou (2007), `arXiv:0706.2576` [`physics.ins-det`].

# HERA Results

*Katerina Müller, Hanno Perrey, Thomas Schörner-Sadenius*

Jet production measurements at HERA allow detailed tests of our understanding of perturbative QCD. The concepts of factorization, of the perturbative expansion of the cross section and of PDF universality can all be tested. In addition, the strong coupling constant,  $\alpha_s$ , can be extracted from HERA jet production data. A further issue of particular relevance to the LHC, is the possible effects of multi-parton interactions and the underlying event. At HERA, such effects can be studied in resolved photoproduction events, since the hadronic structure of the photon means that photon-proton collisions are similar, in some respects, to hadron-hadron collisions.

The production of isolated photons, produced directly in the hard interaction, also provides a very sensitive probe of perturbative QCD, since the photons are largely insensitive to the effects of hadronisation. A good understanding of the Standard Model production mechanism of isolated photons is also important for searches of new particles decaying to photons at hadron colliders (eg.  $H \rightarrow \gamma\gamma$ ).

In this section, some recent HERA measurements of both jet production (mainly in the photoproduction regime), and of isolated photons, are reviewed. In addition, some recent measurements sensitive to the effects of multi-parton interactions and the underlying event are discussed.

## 1 HERA results on jets and prompt photons in photoproduction

*Authors: Hanno Perrey, Thomas Schörner-Sadenius*

In photoproduction at HERA, a quasi-real photon emitted from the incoming electron collides with a parton from the incoming proton. In such events, hadronic jets and also prompt (meaning: radiated by one of the outgoing quarks) photons can be produced. The photoproduction of hadronic jets can be classified into two types of processes in leading-order (LO) QCD: direct and resolved. In direct processes, the entire photon and its momentum participate in the hard scatter (left side of Fig. 1), while resolved processes involve a photon acting as a source of quarks and gluons, with only a photon momentum fraction  $x_\gamma$  participating in the hard scatter (right side of Fig. 1). It is due to the presence of resolved events that HERA data might be useful for further constraining the photon PDFs.

This contribution presents a review of some recent results on jet (and prompt photon) photoproduction at HERA. Some emphasis is placed on the prospects of using such measurements to constrain the proton and the photon PDFs. In addition, some results on multi-parton

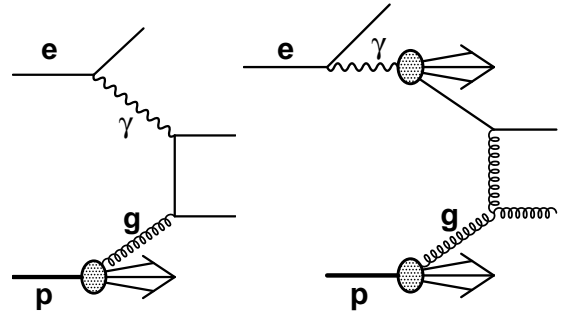


Fig. 1: Feynman diagrams of direct and resolved dijet photoproduction at leading order.



interactions and the underlying event are briefly summarised. It should be pointed out that most of these results use data only from the HERA-I data taking period, such that an improvement in statistical precision is to be expected by making use of all available data.

### 1.1 The concept of the resolved photon

Fig. 1 shows Feynman diagrams for direct (left) and resolved (right) photoproduction of dijets. Statistically, direct events are dominated by quark propagators whereas resolved events are mostly characterized by gluon propagators. This difference should lead to a distinctly different angular behaviour of the final-state jets: whereas the quark propagator (quarks being spin-1/2 particles) should lead to a distribution in the cosine of the centre-of-mass scattering angle,  $\cos \theta^*$ , like  $(1 - |\cos \theta^*|)^{-1}$ , in the gluon case a distribution like  $(1 - |\cos \theta^*|)^{-2}$  is expected. In other words, the cross section of the resolved part is expected to rise more rapidly towards higher  $\cos \theta^*$  than that of the direct part. Fig. 2 shows the experimental evidence [1]: the dijet cross section as a function of  $\cos \theta^*$  for a direct-enriched (left) and a resolved-enriched data sample (right). It is obvious that the above predictions are fulfilled, the resolved distribution rising much more rapidly than the direct one. These distributions thus form an important test of the concept of the resolved photon. Similar results have also been obtained by the ZEUS collaboration [2].

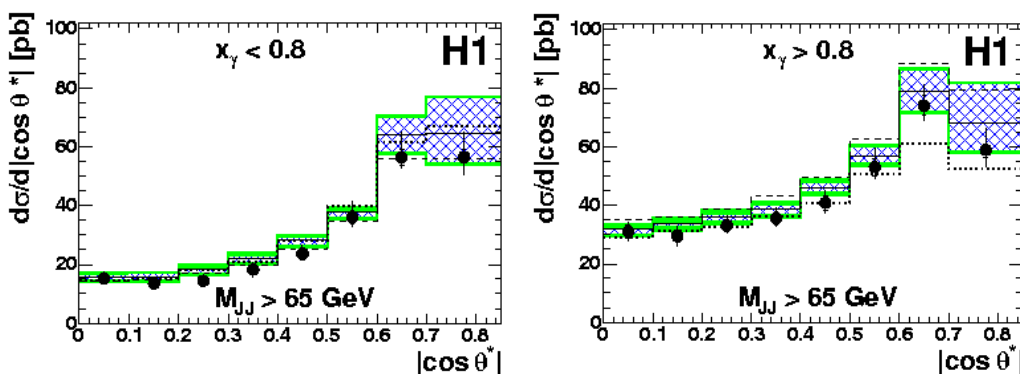


Fig. 2: Photoproduction dijet cross section as function of centre-of-mass scattering angle,  $\cos \theta^*$ , for direct- (left) and resolved-enriched (right) samples [1].

In the above discussion, the distinction between direct and resolved data samples has been made. On the theoretical side, this distinction is meaningful only at LO. On the experimental side, the distinguishing observable  $x_\gamma$  is not directly accessible but has to be reconstructed from the two final-state jets in much the same way as the proton's momentum fraction  $x_p$  entering the hard scattering,

$$x_\gamma = \frac{E_{T,1}e^{-\eta_1} + E_{T,2}e^{-\eta_2}}{2yE_e}, \quad x_p = \frac{E_{T,1}e^{+\eta_1} + E_{T,2}e^{+\eta_2}}{2E_p},$$

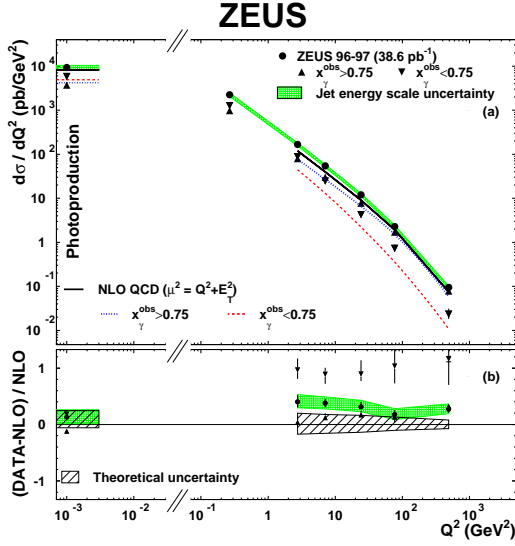


Fig. 3: Fraction of resolved events as a function of  $Q^2$  [3].

where  $E_{T,i}$  and  $\eta_i$  are the jet transverse energies and pseudorapidities,  $y$  is the inelasticity (characterizing the energy loss of the scattered electron) and  $E_e$  and  $E_p$  are the electron and proton beam energies. Typically, the resolved regime is defined to comprise values of  $x_\gamma$  between 0 and 0.75 or 0.8.

Note, however, that the phenomenon of the resolved photon is not strictly confined to the photoproduction regime. Also, the virtual photon entering into deep inelastic scattering events can exhibit a hadronic substructure, leading to a resolved contribution to DIS. The ZEUS collaboration has evaluated the fraction of resolved events in both photoproduction and DIS, measuring the fraction of dijet events with  $x_\gamma$  below and above 0.75. The results are shown in Fig. 3, as a function of the photon virtuality  $Q^2$  [3], and are compared to NLO QCD calculations. It is found that even at large  $Q^2$  values (highly virtual photons), there is a significant contribution from resolved events and that for DIS this component of the data is not correctly described by the QCD predictions (which do not include any resolved photon option). In contrast, the resolved contribution to photoproduction is well described by NLO QCD.

## 1.2 Jet cross sections in photoproduction

Numerous measurements of inclusive-jet, dijet and multijet cross sections have been performed by the HERA experiments. A very recent result [4] is presented in Fig. 4, which shows the dijet cross section as a function of the mean dijet transverse energy,  $\overline{E}_T$ , for a sample enhanced in direct and a sample enhanced in resolved events. The measurements are compared to an NLO QCD prediction using two different parameterisations of the photon PDFs.

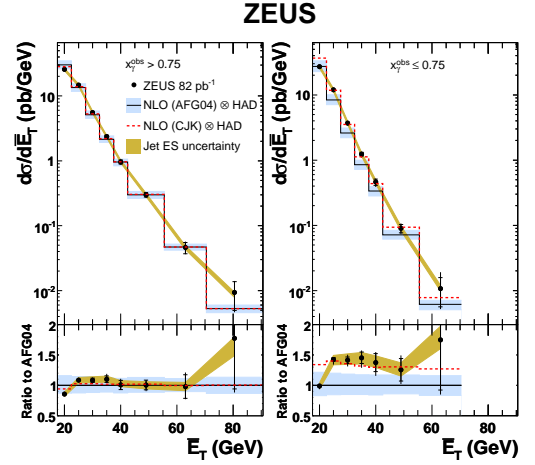


Fig. 4: Photoproduction dijet cross sections as functions of the mean transverse jet energy,  $\overline{E}_T$ , for a direct- and a resolved enriched sample [4].

The data in the direct regime are especially well described by the theory (on the level of 10% or better), as can be seen in the bottom left part of the figure, which shows the ratio of data over NLO prediction. The uncertainties here are dominated by the theoretical uncertainty which is of the order of 15%. The situation in the resolved regime is slightly more complicated and will be discussed in some more detail below.

Many more examples of photoproduction jet cross sections and their successful description by NLO QCD exist. Fig. 6 [1] shows the dijet cross section as a function of  $x_p$  in different regions of  $x_\gamma$  and jet pseudorapidity. Both the momentum fractions and the pseudorapidity distributions of the jets are sensitive to the momentum distributions of partons inside the proton, making these measurements important tests of QCD. It can be seen again that the data are very well described by NLO QCD, on the level of 10%, which are well covered by the combined uncertainties. Only for large  $x_p$  values, with both jets going forward ( $\eta_{1,2} > 1$ ), do some deviations between data and theory occur (see Fig. 6, bottom right). These differences might be explained by the large uncertainties on the proton PDFs for large momentum fractions.

Fig. 5 [4] shows, for the same data sample as in Fig. 4, the cross section as a function of the mean jet pseudorapidity,  $\bar{\eta}$ . The data are again shown separately for direct- and resolved-enhanced samples and are compared to NLO QCD predictions using different parameterisations of the photon PDFs. For the direct case, the description of the data by the theory is again excellent.

The demonstrated good performance of NLO QCD in describing photoproduction data (especially in the direct regime) gives confidence in the theory, thus rendering possible the extraction of QCD parameters like the strong coupling constant,  $\alpha_s$ , or the proton and photon PDFs from the data. One example of the former is given in [5], where a value  $\alpha_s(M_Z) = 0.1224 \pm 0.0001(\text{stat.})^{+0.0022}_{-0.0019}(\text{exp.}) \pm^{+0.0054}_{-0.0042}(\text{th.})$  was extracted from an inclusive-jet measurement in photoproduction. Many other precision extractions of  $\alpha_s$ , from jet measurements in both DIS and photoproduction, also exist. The impact of jet cross sections in constraining the PDFs is discussed in the next section.

Recently, the symmetry group underlying the strong interaction has been studied by measuring angular correlations in direct-enriched three-jet photoproduction events [6]. Fig. 7 shows the differential cross sections as functions of the angular correlations between the three jets in the final state and the proton-beam direction. The data are compared to LO calculations based on different symmetry groups, illustrating the sensitivity of the data to the colour configuration. While the measured angular correlations are consistent with the prediction of SU(3), they disfavour other symmetry groups such as SU( $N$ ) in the limit of large  $N$ . The differences between SU(3) and U(1)<sup>3</sup> were found to be smaller than the current statistical uncertainties.

### 1.3 Jets in Photoproduction and the Proton and Photon PDFs

In [4], both the theoretical uncertainties on dijet cross sections and their sensitivity to the gluon density in the photon and the proton have been investigated in great detail. As is highlighted in Fig. 8 (left), for a special choice of kinematics, there are regions in which the proton PDF uncertainty (indicated as the region between the two solid lines) is as large as, or even larger than, the combined theoretical uncertainties due to the choice of renormalization scale, factorization scale,

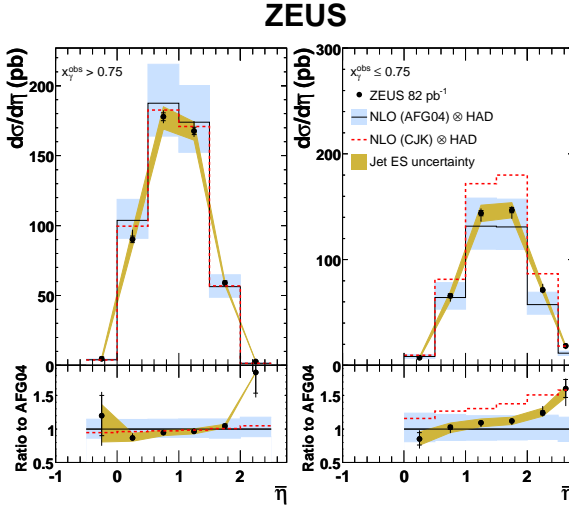


Fig. 5: Photoproduction dijet cross sections as functions of the mean jet pseudorapidity,  $\bar{\eta}$ , for a direct- and a resolved enriched sample [4].

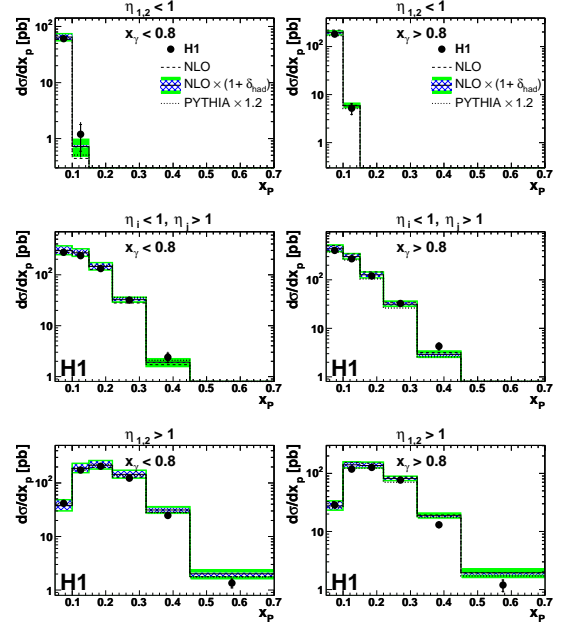


Fig. 6: Photoproduction dijet cross sections as functions of the momentum fraction  $x_p$  for a direct- and a resolved enriched sample [1].

$\alpha_s$ , and hadronisation correction. Also, the uncertainty due to the very imprecise knowledge of the photon PDF may be very large, reaching values of up to 60%, as indicated by the dashed line in the figure, which shows the difference in the cross section prediction between two different photon PDF parameterisations. Dijet data do, therefore, have the potential to further constrain both quark and gluon densities in the proton and the photon. This is indicated in Fig. 8 (right), which shows the fraction of gluon-induced events on the proton side (dark dashed line) and on the photon side according to two different photon PDF parameterisations (light dashed and solid lines). The amount of gluon-induced events can be as large as 60%, depending on the detailed kinematics under consideration.

The large discrepancies between different photon PDF parameterisations are also visible in the comparison of NLO QCD predictions with dijet cross sections in the resolved regime, like in Fig. 4 (right) or Fig. 5 (right). For example, in Fig. 4, the resolved dijet cross section can be approximately described by the NLO prediction using the CJK photon PDF parametrization, but not by the AFG04 parametrization, which is off by up to 40–50%. This difference highlights the potential of the data to further constrain the photon PDFs.

A first example of the benefit of jet photoproduction data on determinations of the proton PDFs is given in Figs. 9 and 10. Fig. 9 shows, for an older measurement of photoproduction dijet cross sections [2], the ratio of the measured cross sections over the NLO prediction. An

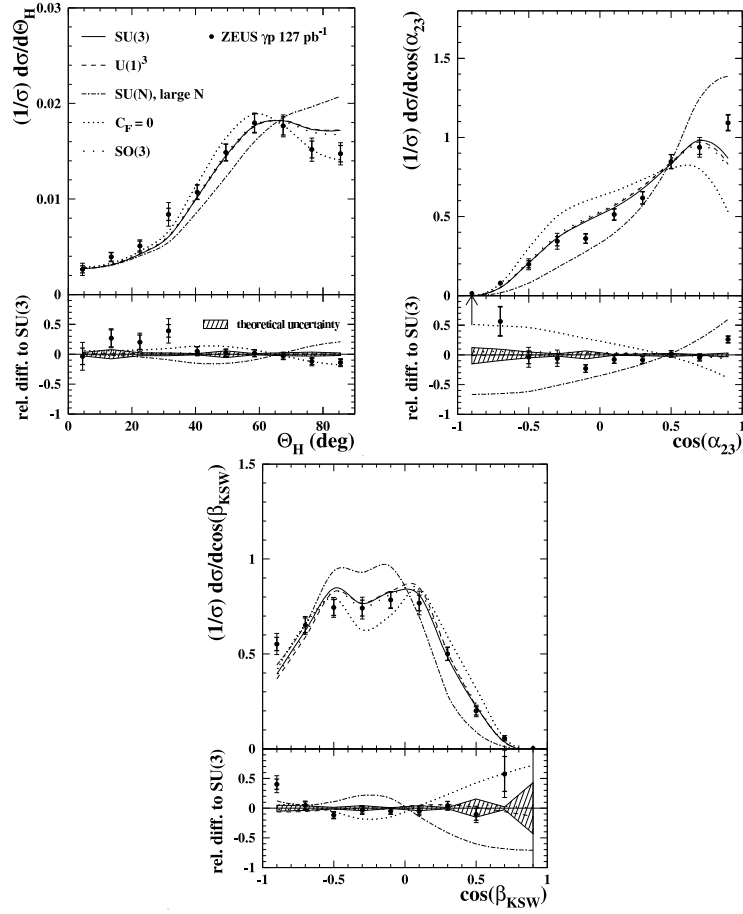


Fig. 7: Photoproduction trijet cross sections as functions of angular correlation between the jets and the proton-beam direction, for a direct enriched sample [6].

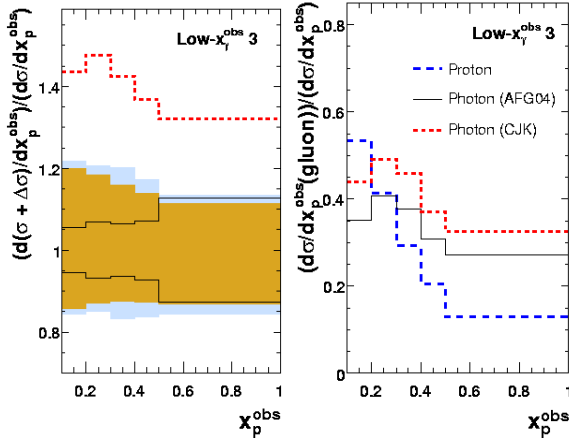


Fig. 8: Left: Theoretical uncertainties on photoproduction dijet cross sections in a special kinematic region [4]. The uncertainties are the total (outer shaded band), that from varying  $\mu_R$  (inner shaded band), the proton PDF uncertainties from the ZEUS-JETS fit (solid lines) and the difference from using the CJK photon PDF, rather than AFG04 (dashed line). Right: Gluon-induced contributions to photoproduction dijet cross sections in the same kinematic region.

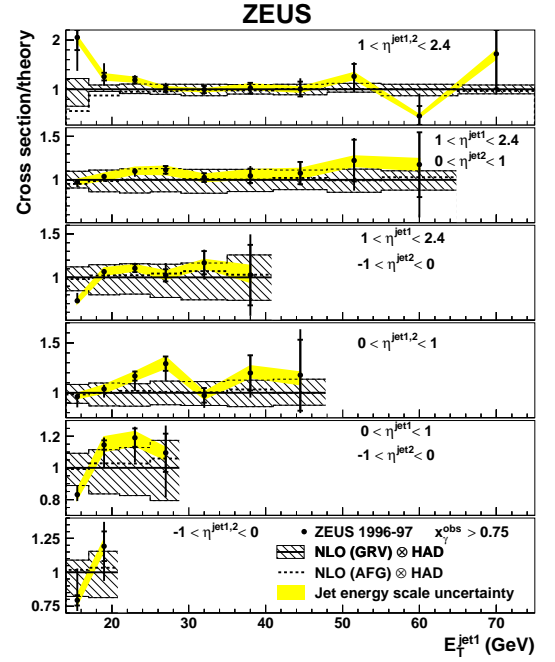


Fig. 9: Ratio of data over NLO QCD predictions for photoproduction dijet events in the direct regime as function of jet transverse energy and pseudorapidity,  $E_T$  and  $\eta$  [2].

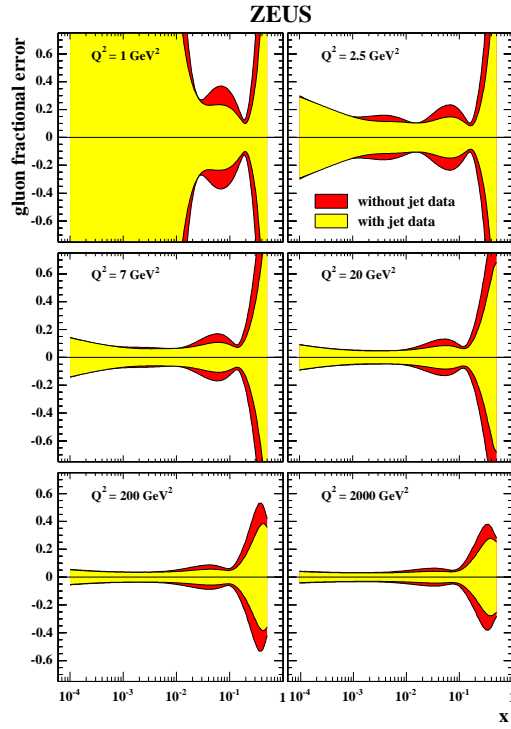


Fig. 10: Improvement of the gluon density by using jet data in NLO QCD fits of the PDFs [7].

overall good description is found, with data and theory in agreement almost everywhere within the combined theoretical and experimental uncertainties. These data (together with data from DIS jet analyses) have been used as additional inputs (besides the usual inclusive  $F_2$  data) to an NLO QCD PDF fit [7]. The success of this fit is demonstrated in Fig. 10, which shows the fractional gluon density uncertainty as a function of the proton momentum fraction  $x$  in different regions of  $Q^2$ . The uncertainty without the use of jet data is given by the dark shaded area, and the result including jet data is given by the light shaded area. An improvement in the uncertainty of up to 35% is clearly visible, especially in the region of medium-to-high- $x$  values.

The aim now is to further improve the proton PDFs (and here especially the gluon density at high values of  $x$ , since this is particularly important for LHC physics) by using more precise measurements or cross sections measured in different kinematic regions, from both photoproduction and DIS. Constraining the photon PDFs will be technically even more demanding, partly because of lack of a consistent PDF error treatment for the photon PDF, and partly because of the increased experimental and theoretical uncertainties for the resolved regime.

#### 1.4 Photoproduction of isolated photons

The production of isolated, or “prompt”, photons from the hadronic final state offers an alternative access to the QCD dynamics in  $ep$  scattering, with different systematic uncertainties and reduced effects from hadronisation. Isolated photon production has been measured by ZEUS and H1 in both photoproduction [8–10] and DIS [11, 12]. In addition to inclusive measurements of isolated photons, cross sections of photons in association with jets are also often measured, for which there are currently NLO QCD predictions available. In Sec. 2, a detailed description of the latest HERA prompt photon measurement [12] in DIS is presented. Here, only a very brief summary of a recent measurement in photoproduction is given [10].

Fig. 11 [10] shows the photon plus jet cross section, in photoproduction, as a function of  $E_T^\gamma$  and  $\eta^\gamma$ . The data are compared to NLO QCD calculations (shaded band) and to calculations based on the  $k_T$ -factorization approach and unintegrated parton densities (hatched band). The results demonstrate that the  $k_T$ -factorization approach gives the closest agreement with the data, especially in the low  $E_T^\gamma$  and forward  $\eta^\gamma$  regions. The fact that NLO QCD does not describe the data at low values of  $E_T^\gamma$  (or  $E_T^{jet}$ ) currently precludes the use of the low-transverse-energy data in constraining the PDFs or  $\alpha_s$ .

#### 1.5 The underlying event and multi-parton interactions

Resolved photon-proton interactions may, in some respects, be regarded as hadron-hadron collisions, with all the additional features with respect to direct interactions. In particular, it is possible in hadron-hadron collisions to have multiple interactions of pairs of partons (so-called ‘multi-parton interactions’ or ‘MPI’), which may populate the hadronic final state with additional soft or hard jets, or additional energy flow throughout the detector. This effect may alter the final state significantly, making it necessary to model it adequately in the Monte Carlo programs used in the analyses. There exist various MPI model implementations in standard generators, such as HERWIG and PYTHIA, which can be tested against data, or whose parameters can be adjusted to describe the data. Here, some recent examples of multi-parton interaction studies at HERA,



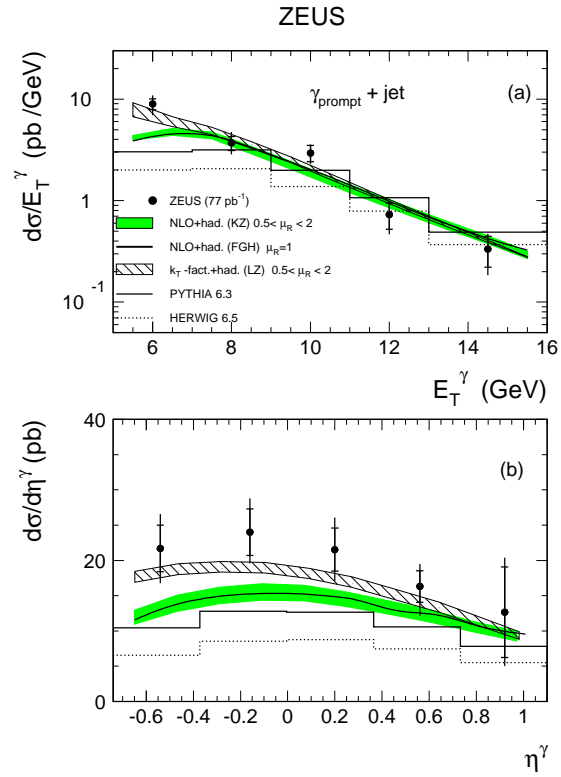


Fig. 11: The  $\gamma + \text{jet}$  differential cross sections in photoproduction as functions of  $E_T^\gamma$  and  $\eta^\gamma$  compared to theoretical QCD calculations [10].

from H1 and ZEUS, are briefly reviewed. Note that a more detailed discussion of the H1 results can be found in the WG5 section of these proceedings.

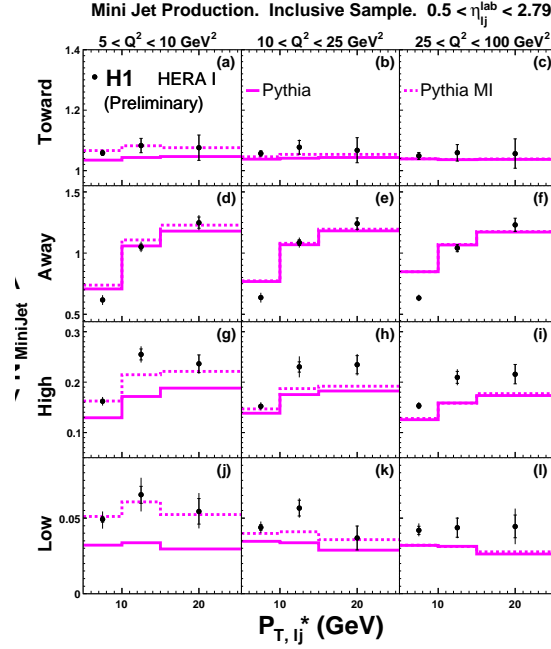


Fig. 12: Mean number of minijets as function of the leading jet  $p_T$  [13].

Fig. 12 shows the recent H1 measurement [13] of the mean number of ‘minijets’ (i.e. soft jets with transverse energies above a very low cut of 3 GeV) in DIS events, with at least one hard jet. The data are shown as a function of this leading jet’s transverse momentum,  $p_{T,lj}^*$ , in different regions of  $Q^2$ , and different regions of azimuthal angle with respect to the leading jet’s azimuth. The so-called ‘Towards’ and ‘Away’ regions are expected to be mostly populated by the results of the first and hardest parton-parton scattering in the event, and the dijet system coming from this scattering should be separated by an azimuthal angle of about  $\pi$ . In contrast, the ‘High’ and (especially) the ‘Low’ regions<sup>1</sup>, should be particularly sensitive to MPI effects which, in these regions, are not masked out by the harder energy depositions from the leading jet pair. It can be observed that the PYTHIA model with MPI effects switched on (‘PYTHIA MI’) is in rather good agreement with the data in almost all regions. In contrast, PYTHIA without MPI modelling (‘PYTHIA’) fails to describe the data in the low  $Q^2$  ‘High’ and ‘Low’ regions, consistent with the hypothesis of MPI effects dominating in these regions of phase space. Overall, the results indicate that the data strongly favour the models including MPI effects.

Another recent H1 measurement [14], this time of dijets in photoproduction, leads to similar conclusions. Fig. 13 shows the charged particle multiplicity for a resolved-enriched data sample in the ‘High’ (left) and ‘Low’ (right) regions as function of the transverse momentum

<sup>1</sup>Note that ‘High’ and ‘Low’ refer to the amount of deposited energy in the two regions.

of the leading jet. Again, PYTHIA without MPI modelling (‘PYTHIA NMI’) does not give a sufficient description of the data while PYTHIA including MPI (‘PYTHIA MI’) models the data well.

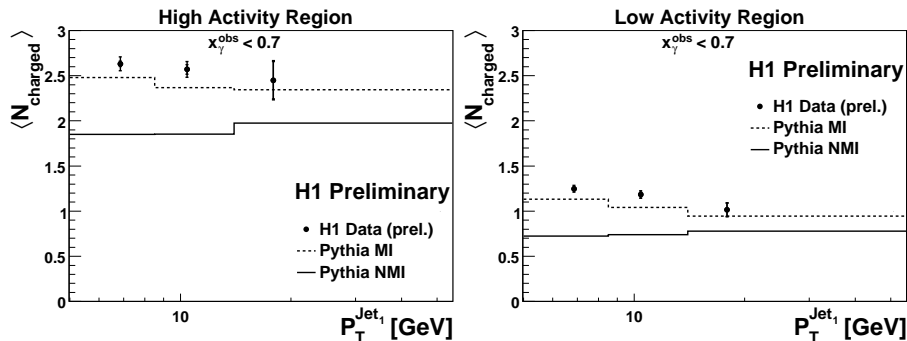


Fig. 13: Charged particle multiplicity for resolved-enriched photoproduction dijets as function of the transverse momentum of the first jet [14].

A similar statement can also be derived from a recent measurement of three- and four-jet photoproduction [15] from ZEUS. Fig. 14 shows the four-jet photoproduction cross section as a function of  $x_\gamma$ , and compares it to the predictions of HERWIG and PYTHIA, with and without the inclusion of MPI modelling. The results indicate that the two predictions including MPI effects (‘HERWIG+MPI’ and ‘PYTHIA+MPI’) are able to adequately reproduce the data, whereas the models without MPI grossly underestimate the measured cross section in the resolved-enhanced regime (i.e.  $x_\gamma < 0.8$ ). The effect is particularly drastic for low energy scales and low multijet invariant masses, a fact which is illustrated in Fig. 14, where the four-jet mass was required to be between 25 and 50 GeV. It should also be noted that the parameters of the “HERWIG+MPI” model have been tuned to these multijet data, while the “PYTHIA+MPI” parameters have not.

While the HERA measurements clearly favour models in which MPI are included, the data so far do not have the power to specify more precisely the mechanism underlying MPI effects, or to shed light on the energy evolution of MPI effects when going (for example) from TEVATRON to LHC centre-of-mass energies. The models in use so far are rather crude and will have to be replaced by more realistic models and calculations which take correctly into account features like multi-parton exchanges between photon and proton, correlations between these exchanges, etc.

## 2 Measurement of Isolated Photon Production in Deep Inelastic Scattering at HERA

*Author: Katharina Müller*

Both the H1 and ZEUS Collaborations have previously measured [8–10] prompt photon cross sections in photoproduction (see, for example, Sec. 1.4). An analysis of the isolated photon cross section in deep inelastic scattering (DIS), with  $Q^2 > 35 \text{ GeV}^2$ , has also been published by ZEUS [11]. The present contribution describes the most recent HERA measurement of isolated photon production in DIS ( $e + p \rightarrow e + \gamma + X$ ) from H1.

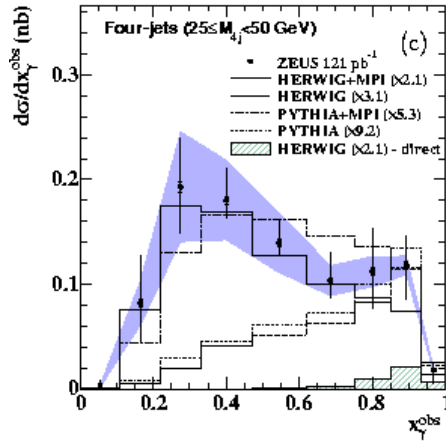


Fig. 14: Photoproduction four-jet cross section as function of  $x_\gamma$  [15].

The measurement of isolated photons in deep inelastic scattering provides a test of QCD in a kinematic range with two hard scales, the four-momentum transfer squared,  $Q^2$ , of the exchanged virtual photon and the transverse energy of the emitted photon. In DIS, the final state photon is emitted by a quark ( $QQ$  subprocess), by wide angle radiation from the lepton ( $LL$  subprocess) or by interference ( $LQ$  subprocess). The  $QQ$  contribution is dominated by the direct radiation of the photon from the quark involved in the parton level process, but also contains the contribution from quark fragmentation to a photon [16, 17]. Since the photon and the scattered electron are well separated in the present analysis, low angle QED radiation is suppressed. The  $LL$  and the more interesting  $QQ$  process can not be distinguished experimentally on event basis, but only by comparison with predictions.

The measurement of isolated photons in DIS presented here is based on a total integrated luminosity of  $227 \text{ pb}^{-1}$ . Full details of the analysis can be found in [12]. Photon candidates with transverse energy  $3 < E_T^\gamma < 10 \text{ GeV}$  and pseudorapidity  $-1.2 < \eta^\gamma < 1.8$  are selected in DIS events in the kinematic regime  $4 < Q^2 < 150 \text{ GeV}^2$ , inelasticity  $y > 0.05$  and a mass of the hadronic system  $W_X > 50 \text{ GeV}$ . The cut on  $W_X$  removes events from elastic compton scattering. The photon candidates are then used together with the other particles in the event, with the exception of the scattered electron, to reconstruct jets using the  $k_T$  algorithm [18]. The isolation of the photon is ensured by requiring that it carries at least 90% of the transverse momentum of the jet containing the photon. The isolation criteria removes a large part of the background from decay products of neutral hadrons.

Photons are separated from the remaining neutral hadrons and their decay products by a multivariate analysis of the shapes of the calorimeter energy deposits.

Jet production in events with isolated photons and no additional jet or with at least one jet is also investigated. Hadronic jets are reconstructed for  $P_T^{jet} > 2.5 \text{ GeV}$ , the pseudorapidity range is restricted to  $-1.0 < \eta^{jet} < 2.1$ . All results are compared to a leading order (LO),  $\mathcal{O}(\alpha^3 \alpha_s^0)$ , calculation [19, 20]. The cross sections for a photon plus at least one jet are further

compared to a NLO,  $\mathcal{O}(\alpha^3\alpha_s^1)$ , calculation [21].

Differential cross sections  $d\sigma/d\eta^\gamma$  and  $d\sigma/dQ^2$  for the inclusive isolated photon cross section are shown in Fig. 15. Fig. 16 shows the differential cross sections  $d\sigma/d\eta^\gamma$  for isolated photons with no additional hadronic jet (a) and with hadronic jets (b). The uncertainty on the shower description gives the dominant contribution to the systematical error. The cross sections are shown together with the predictions by the LO calculation. A comparison to a NLO calculation is possible for the photon plus jets cross section. The calculations are corrected to hadron level. The corrections amount to, at most,  $-30\%$ .

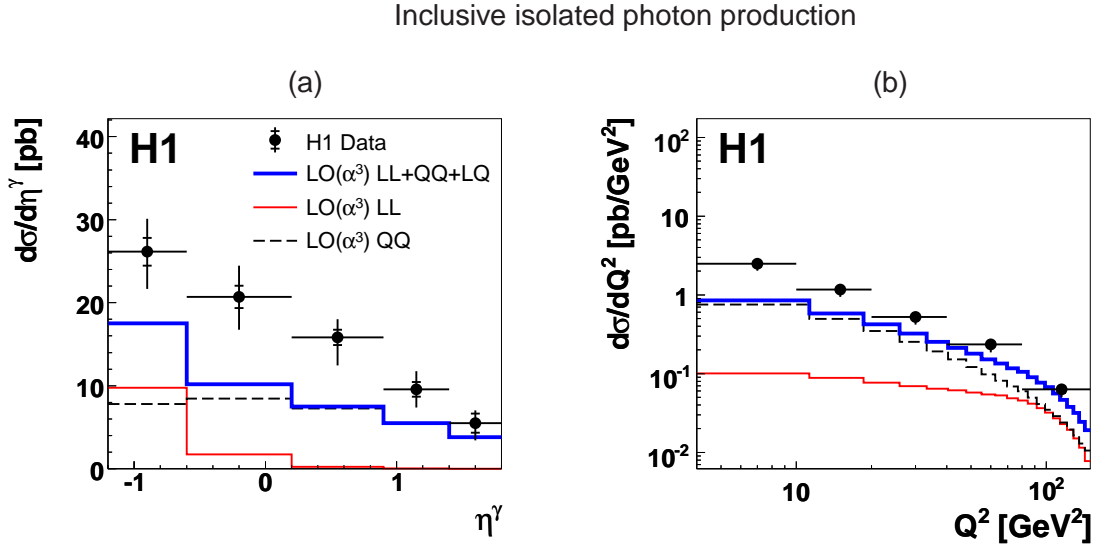


Fig. 15: Inclusive differential isolated photon cross sections  $d\sigma/d\eta^\gamma$  (a),  $d\sigma/dQ^2$  (b) for  $3 < E_T^\gamma < 10$  GeV,  $-1.2 < \eta^\gamma < 1.8$ ,  $W_X^2 > 2500$  GeV<sup>2</sup> and  $4 < Q^2 < 150$  GeV<sup>2</sup>. The inner error bars on the data points indicate the statistical error, the full error bars contain in addition the systematic errors added in quadrature. The cross sections are shown together with a leading order,  $\alpha^3\alpha_s^0$ , calculation [20] corrected for hadronisation effects, *LL* corresponding to radiation from the electron and *QQ* to radiation from the quark.

The LO  $\mathcal{O}(\alpha^3\alpha_s^0)$  calculation underestimates the inclusive cross sections by roughly a factor of two, most significantly at low  $Q^2$ . The relative contribution of radiation from the electron (*LL*) and the quark(*QQ*) depends strongly on  $\eta^\gamma$  and  $Q^2$ . At high and medium  $\eta^\gamma$  and low  $Q^2$ , radiation by the quark dominates. The shapes of the  $d\sigma/dE_T^\gamma$  and  $d\sigma/d\eta^\gamma$  distributions are described reasonably well. The comparison of data to the LO calculation in bins of  $\eta^\gamma$  show that the difference in normalisation can mainly be attributed to an underestimation of the *QQ* contribution [12].

The LO prediction also underestimates the production of isolated photons plus no hadronic jet and photons plus jets by a similar factor as for the inclusive measurement. The NLO  $\mathcal{O}(\alpha^3\alpha_s^1)$

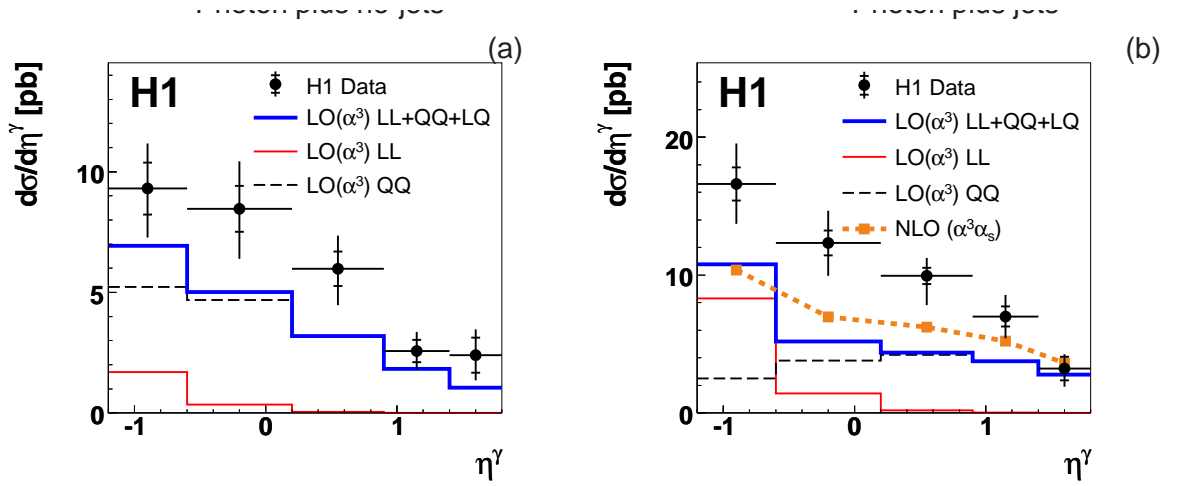


Fig. 16: Differential cross sections  $d\sigma/d\eta^\gamma$  for photon plus no-jets (a) and photon plus jets (b), with  $P_T^{jet} > 2.5$  GeV and  $-1.0 < \eta^{jet} < 2.1$ . The cross sections are compared to a leading order,  $\mathcal{O}(\alpha^3\alpha_s^0)$ , calculation [19] as in Figure 1. The photon plus jet sample is additionally compared to a NLO ( $\alpha^3\alpha_s$ ) calculation [21]. The bin averaged NLO cross sections are indicated by the squares.

prediction for photon plus jet is higher than the LO prediction, most significantly at low  $Q^2$ , but still underestimates the data. The NLO calculation describes the shapes of the differential cross sections reasonably well.

The  $LL$  contribution is largely suppressed for the sample with no additional jet due to the cut on  $W_X$ . The cross section for photon plus jet production is roughly two times higher than for photon plus no additional jet. This is in contrast to the inclusive  $ep \rightarrow eX$  cross section, where topologies with an additional jet are suppressed by  $\mathcal{O}(\alpha_s)$ . The similar cross sections for photon events with or without additional jets may be explained by the fact that both topologies correspond to the same order  $\mathcal{O}(\alpha_s^0)$  in perturbative QCD. [20] The cross section for photon plus jet production is roughly two times higher than for photon plus no-jets.

At leading order  $\mathcal{O}(\alpha_s^0)$ , the quark fragmentation contribution to the cross section enters only the sample with a photon and no hadronic jet [20]. Hence, the observed excess of the data can not solely be attributed to an underestimation of that contribution.

Further theoretical investigations are needed to understand the observed discrepancy between the measurements and the predictions, including for instance the calculation of higher order processes.

## References

- [1] H1 Collaboration, A. Aktas *et al.*, Phys. Lett. **B639**, 21 (2006), arXiv:hep-ex/0603014.

- [2] ZEUS Collaboration, S. Chekanov *et al.*, Eur. Phys. J. **C23**, 615 (2002), arXiv:hep-ex/0112029.
- [3] ZEUS Collaboration, S. Chekanov *et al.*, Eur. Phys. J. **C35**, 487 (2004), arXiv:hep-ex/0404033.
- [4] ZEUS Collaboration, S. Chekanov *et al.*, Phys. Rev. **D76**, 072011 (2007), arXiv:0706.3809 [hep-ex].
- [5] ZEUS Collaboration, S. Chekanov *et al.*, Phys. Lett. **B560**, 7 (2003), arXiv:hep-ex/0212064.
- [6] ZEUS Collaboration, . S. Chekanov (2008), arXiv:0808.3783 [hep-ex].
- [7] ZEUS Collaboration, S. Chekanov *et al.*, Eur. Phys. J. **C42**, 1 (2005), arXiv:hep-ph/0503274.
- [8] ZEUS Collaboration, J. Breitweg *et al.*, Phys. Lett. **B472**, 175 (2000), arXiv:hep-ex/9910045.
- [9] H1 Collaboration, A. Aktas *et al.*, Eur. Phys. J. **C38**, 437 (2005), arXiv:hep-ex/0407018.
- [10] ZEUS Collaboration, S. Chekanov *et al.*, Eur. Phys. J. **C49**, 511 (2007), arXiv:hep-ex/0608028.
- [11] ZEUS Collaboration, S. Chekanov *et al.*, Phys. Lett. **B595**, 86 (2004), arXiv:hep-ex/0402019.
- [12] H1 Collaboration, F. D. Aaron *et al.*, Eur. Phys. J. **C54**, 371 (2008), arXiv:0711.4578 [hep-ex].
- [13] H. Collaboration, *Minijet Production in Deep Inelastic Scattering at HERA* (unpublished). H1-PRELIM-07-032.
- [14] H. Collaboration, *Study of multiple interactions in photoproduction at HERA* (unpublished). H1-PRELIM-08-036.
- [15] ZEUS Collaboration, S. Chekanov *et al.*, Nucl. Phys. **B792**, 1 (2008), arXiv:0707.3749 [hep-ex].
- [16] K. K. *et al.*, Z. Phys. C **6**, 131 (1980).
- [17] M. Gluck, L. E. Gordon, E. Reya, and W. Vogelsang, Phys. Rev. Lett. **73**, 388 (1994).
- [18] S. D. Ellis and D. E. Soper, Phys. Rev. **D48**, 3160 (1993), arXiv:hep-ph/9305266.
- [19] A. Gehrmann-De Ridder, T. Gehrmann, and E. Poulsen, Phys. Rev. Lett. **96**, 132002 (2006), arXiv:hep-ph/0601073.

- [20] A. Gehrmann-De Ridder, T. Gehrmann, and E. Poulsen, Eur. Phys. J. **C47**, 395 (2006), [arXiv:hep-ph/0604030](#).
- [21] A. Gehrmann-De Ridder, G. Kramer, and H. Spiesberger, Nucl. Phys. **B578**, 326 (2000), [arXiv:hep-ph/0003082](#).



# Interactions at high gluon densities

Mark Strikman, Igor M. Dremin

In the previous section we mentioned the subject of gluon saturation. In this section we continue the discussion of effects due to high gluon densities. First we look at what HERA can teach us about the density of gluons in the impact parameter plane and how this will affect our understanding of processes in  $pp$  collisions at LHC. Then, in Sec. 2 we go on to heavy ion collisions and discuss effects of a dense gluon medium there, concentrating on the description of Cherenkov gluons.

## 1 HERA constrains for LHC MC generators and probing high gluon densities in $pp$ collisions using forward triggers

Author: Mark Strikman

In the high energy collisions the finite  $x$  component of the wave functions of the colliding hadrons is nearly frozen in transverse plane during the interaction process. Properties of produced final state depend strongly on whether hadrons collided at large impact parameter,  $b$  or head on. In particular for small  $b$  a chance for a parton to pass through high gluon density fields at a distance  $\rho$  from the center of the second nucleon (Fig. 1) is enhanced. The probability of multiple collisions parton collisions is enhanced as well.

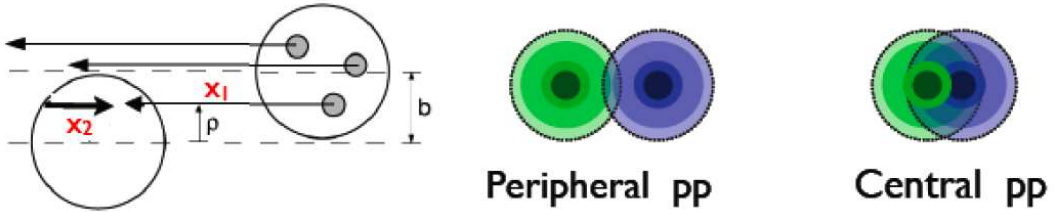


Fig. 1: Side and transverse views of  $pp$  collision.

The strength of the encountered gluon fields depends strongly on  $x$  of the parton - a parton with a given  $x_1$  and resolution  $p_t$  is sensitive to the partons in the target with  $x \geq x_2 = 4p_t^2/s_{NN}x_1$ . For fixed  $x_1$  characteristic  $x_2$  decrease  $\propto 1/s$ . For example at the LHC a parton with  $x_1 = 0.1, p_t = 2\text{GeV}/c$  resolves  $x > 10^{-6}$  while at the GZK energies such parton resolves  $x > 10^{-9}$  corresponding to huge gluon densities since a change of  $x$  by a factor of ten leads to an increase of gluon density by at least a factor of two.

Studies at HERA provided several important inputs which we discuss below: (i) transverse distribution of gluons in the nucleon, (ii) fluctuations of the strength of the gluon field in the nucleon, (iii) proximity to the black disk regime. When combined with information from the Tevatron collider they indicate also correlations of partons in the transverse plane.

These observations have a number of implications for the dynamics of  $pp$  collisions at LHC energies, which are most pronounced in the forward region. Hence we also discuss how to

trigger on central  $pp$  collisions and how to use such collisions for study of the small  $x$  dynamics at very small  $x$ .

### 1.1 Exclusive hard diffraction at HERA - implications for MC at the LHC

The QCD factorization theorem [1, 2] allow to determine the generalized gluon distribution in nucleon for small  $x$  from the DIS exclusive meson production at small  $x$  as well as from the production of onium states. The  $t$ -dependence of these distributions is connected via Fourier transform to the transverse distribution of gluons in a nucleon for a given  $x$ . The data confirm our prediction of convergence of the  $t$ -slopes for different mesons with increase of  $Q^2$  and weak dependence of the  $t$ -slope for the  $J/\psi$ -meson production on  $Q^2$ . Accordingly, this allows to determine the transverse distribution of gluons as a function of  $x$  (for review and references see [3]). It can be approximated as

$$F_g(x, \rho) = \frac{m_g^2}{2\pi} \left( \frac{m_g(x)\rho}{2} \right) K_1(m_g(x)\rho), \quad (1)$$

where  $K_1$  denotes the modified Bessel function. We find  $m_g^2(x = 0.05) \sim 1.1 \text{ GeV}^2$  which corresponds to a much more narrow transverse distribution than given by the electro-magnetic form factors. The radius of the gluon distribution grows with decrease of  $x$  reaching the value comparable to the e.m. radius for  $x \sim 10^{-4}$  ( $m_g^2 \sim 0.7 \text{ GeV}^2$ ).

Hence analysis of the HERA data suggests that the transverse gluon distribution,  $F_g(x, \rho)$ , significantly broadens with decrease of  $x$ . At the same time the current MC models of  $pp$  collisions assume that transverse parton distributions do not depend on  $x$ . Also, in the PYTHIA MC [4] it is assumed that two transverse scales are present in the  $\rho$ -dependence of  $F_g$ . It is not clear whether this assumption is consistent with Eq. (1) and correspondingly with the data on the exclusive  $J/\psi$  production.

Knowledge of  $F_g(x, \rho)$  allows to calculate the rate of the production of four jets due to double parton collisions in the  $pp$  scattering assuming that the double parton distribution is given by a product of single parton distributions. Using Eq. (1) we find the rate which is a factor of two smaller than observed in the Tevatron experiment [5, 6]. This implies presence of the transverse correlations between partons.

One of the sources of fluctuations is fluctuations of the overall size of the initial parton configurations. In the high energy scattering different initial configurations in the colliding nucleons can be considered as frozen. Studies of the soft inelastic diffraction indicate that the strength of the interaction for different configurations in nucleons fluctuates rather strongly. Presumably significant contribution to these fluctuations comes from the fluctuation of the size of these configurations. One also expects that parton distributions in different configurations should differ as well.

In ref. [7] we deduced the model-independent relation which allows one to infer the small  $x$  fluctuations of the gluon density from the observable ratio of inelastic ( $\gamma *_{L} + p \rightarrow VM + X$ ) and elastic ( $\gamma *_{L} + p \rightarrow VM + p$ ) diffractive vector meson production at  $t = 0$ :

$$\omega_g \equiv \frac{\langle G^2 \rangle - \langle G \rangle^2}{\langle G \rangle^2} = \left[ \frac{d\sigma_{\text{inel}}}{dt} \Big/ \frac{d\sigma_{\text{el}}}{dt} \right]_{t=0}^{\gamma_L^* p \rightarrow V X}. \quad (2)$$

So far there have been no dedicated experimental studies of this ratio. Overall data suggest that  $\omega_g \sim 0.2$  for  $Q^2$  of few  $\text{GeV}^2$  and  $x \leq 10^{-3}$  which corresponds to rather large fluctuations of the gluon density. We also proposed a simple model based on information on the fluctuations of the strength of the strong interaction which allows to reproduce the magnitude of  $\omega_g$ .

Correlations between fluctuations of the parton densities and the soft–interaction strength have numerous potential implications for high–energy  $pp/\bar{p}p$  collisions with hard processes. One example is the relative probability of double binary parton–parton collisions.

The QCD evolution leads to a drop of the fluctuations with an increase of virtuality. As a result in the case of double scattering configurations, the main effect for the overall rate is due to fluctuations of the size of the transverse area of the configurations. The contribution of configurations of size smaller than average is enhanced leading to a rather modest enhancement of the rate of four jet production  $\sim 10\text{--}15\%$ , which accounts for a small fraction of the remaining discrepancy with the CDF value<sup>1</sup>. However the size of configurations involved in the multijet double / triple scattering trigger is much smaller than the average size, leading to modification of the hadron product in the fragmentation region, long range fluctuations of multiplicity, etc.

Small effect from global fluctuations indicates that other dynamical mechanisms must be responsible for the enhancement of multi–parton collisions, *e.g.* local transverse correlations between partons as suggested by a “constituent quark” picture of the nucleon [3].

## 1.2 Onset of the black regime in the interaction of fast partons

Interactions of virtual photons with nucleons at HERA can be represented as superposition of the interaction of  $q\bar{q}$  dipoles of sizes given by the square of the corresponding photon wave function. The cross section of the inelastic interaction of a  $q\bar{q}$  or gluon dipole can be written as

$$\sigma^{\text{q}\bar{\text{q}}\text{--hadron}}(x, d^2) = \frac{\pi^2}{4} F^2 d^2 \alpha_s(Q_{\text{eff}}^2) x G_T(x, Q_{\text{eff}}^2). \quad (3)$$

Here  $F^2 = 4/3$  is the Casimir operator of the fundamental representation of the  $SU(3)$  gauge group. Furthermore,  $\alpha_s(Q_{\text{eff}}^2)$  is the LO running coupling constant and  $G_T(x, Q_{\text{eff}}^2)$  the LO gluon density in the target. They are evaluated at a scale  $Q_{\text{eff}}^2 \approx \lambda d^{-2}$ , where  $\lambda = 5 \div 9$  can be determined from NLO calculations or from phenomenological considerations.

Since the gluon density rapidly increases with decrease of  $x$  while the transverse radius of the nucleon grows rather slowly, one expects based on Eq. (3) that interaction should approach the black disk regime of complete absorption at sufficiently large energies. To determine the proximity to this limit it is convenient to study the amplitude of the dipole - nucleon scattering,  $A^{dp}(s, t)$  which can be inferred from analysis of the data on the total DIS cross section and data on exclusive production of vector mesons [8].

Introducing impact parameter representation of the amplitude

$$A^{dp}(s, t) = \frac{i s}{4\pi} \int d^2b e^{-i(\Delta_\perp \mathbf{b})} \Gamma^{dp}(s, b) \quad (t = -\Delta_\perp^2), \quad (4)$$

---

<sup>1</sup>Note that the CDF measurements correspond to relatively large  $x$  where the “radiative” model of the gluon density fluctuations we developed may not be applicable and where no data on the hard inelastic exclusive diffraction are available. However, if the gluon strength is larger for configurations of larger size, it would lead to reduction of already rather small enhancement of the rate of multiple collisions.

we can determine  $\Gamma^{dp}(s, b)$  which is referred to as the profile function. In the situation when elastic scattering is the “shadow” of inelastic scattering, the profile function at a given impact parameter is restricted to  $|\Gamma^{dp}(s, b)| \leq 1$ . The probability of the inelastic interaction for given  $b$

$$P_{inel}(b) = 1 - \left| 1 - \Gamma^{dp}(s, b) \right|^2, \quad (5)$$

is equal to one in the black-disc (BD) limit.

We found [8] that interaction of  $q\bar{q}$  dipoles with transverse size  $\sim 0.3$  fm corresponding to  $Q^2 \sim 4\text{GeV}^2$  is still rather far from the BD regime for the range covered by HERA even for small impact parameters,  $b$ . At the same time a much stronger interaction in the gluon channel (a factor of 9/4 larger  $F^2$  in Eq. (3)) leads to  $\Gamma_{gg}(d \sim 0.3\text{fm}, x \sim 10^{-4})$  close to one in a large range of  $b$ , see Fig. 2. Proximity of  $\Gamma_{gg}$  to one in a wide range of  $b$  for  $Q^2 \sim 4\text{GeV}^2$  naturally explains a large probability of diffraction ( $\sim 30 \div 40\%$ ) in the gluon induced hard interactions which can be inferred from the HERA DGLAP analyses of the inclusive DIS diffractive data (see discussion and references in [3]).

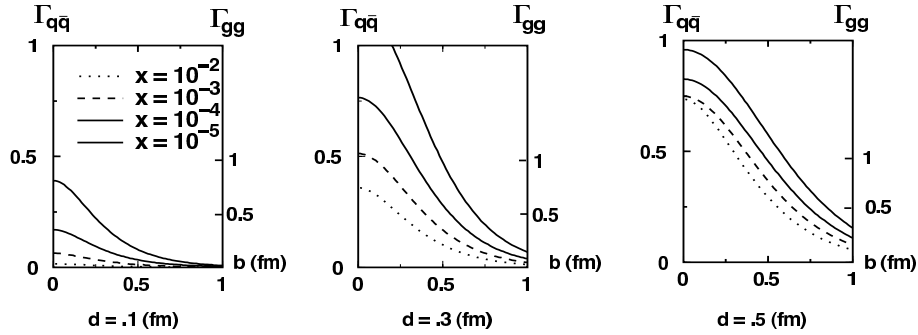


Fig. 2: The profile function of dipole-nucleon scattering,  $\Gamma^{dp}$ , as a function of the impact parameter,  $b$ , for various values of the dipole size,  $d$ , and  $x$ , as obtained from a phenomenological estimate outlined in the text. Shown are the results for  $q\bar{q}$  (left scale) and  $gg$  dipoles (right scale)

In the BD regime parton obtains transverse momenta of the order of the maximal  $p_t$  scale at which interaction remains black and also loses a substantial fraction of its longitudinal momentum (one can also think of this as a post selection of configurations in the incoming wave function with large transverse momenta; the simplest example is scattering of virtual photon in the BD regime [9]). The analysis of the data obtained by the BRAHMS [10] and STAR collaborations [11] on the leading pion production in the deuteron - gold collisions including forward - central rapidity correlations supports presence of this phenomenon for gluon densities comparable to those encountered at HERA [12].

At the LHC energies for the fragmentation region BD regime extends to quite large  $p_t$  for the leading partons (especially for gluons) up to  $\rho \sim 0.5\text{fm}$  which give important contribution to the central  $pp$  collisions (see Fig. 3 adapted from [13]).

Hence, in the  $pp$  collisions large  $x$  partons of nucleon “1” passing at small transverse distances  $\rho$  from the nucleon “2” should get large transverse momenta and also lose significant

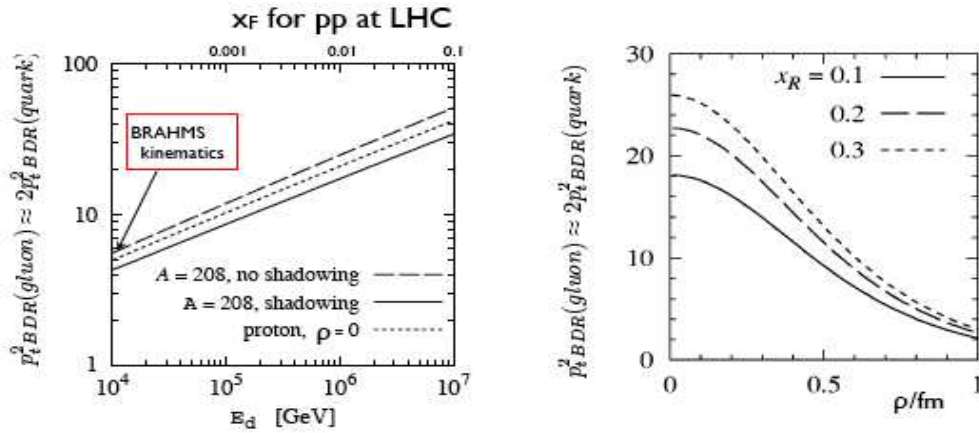


Fig. 3: Dependence of the maximum  $p_t^2$  for gluon for which interaction is close to the BD regime as a function of  $x_F$  (energy of the parton) for  $\rho = 0$  and as function of  $\rho$  for different  $x_R$  of the gluon for the LHC  $pp$  collisions.

fraction of energy. Note here that this effect is masked in many current MC event generators for  $pp$  collisions at the LHC, where a cutoff on minimal momentum transfer of the order 3 GeV is introduced.

One should note here that the necessity to tame intensity of hard collisions in  $pp$  scattering could be derived without invoking a study of the multiplicities of the produced hadrons as it is done e.g. in PYTHIA [4]. Instead, one can study the probability of inelastic interaction as a function of  $b$  which can be determined from unitarity - information on the elastic amplitude, and calculating the inelasticity due to hard parton-parton interactions. We found that for  $b \sim 1.5 fm$  (where uncertainties due to the contribution of multiparton interactions appear to be small) one needs to introduce a cutoff of the order of three GeV in order to avoid a contradiction with the S-channel unitarity [14]. The taming of the small  $x$  parton densities in the relevant  $x \geq 10^{-4}$  range for  $\rho \sim 0.7 fm$  is very small. Hence, it is not clear so far what dynamical mechanism is responsible for resolving problems with S-channel unitarity.

Modifications of the pattern of the collisions due to the large scale of BD regime for small  $\rho$  should be pronounced most prominently in the collisions at small impact parameters. Therefore they are enhanced in the processes of production of new particles which correspond to significantly smaller impact parameters than the minimum bias inelastic collisions. Among the expected effects are suppression of the leading baryon production, energy flow from forward region to smaller rapidities, larger central multiplicity, etc.

### 1.3 Centrality trigger for pp collisions

To study effects of high gluon densities it is desirable to develop a trigger for centrality in  $pp$  collisions [15]. We explore the observation that the leading nucleons are usually produced when number of "wounded" quarks,  $N_w$  is  $\leq 1$ . If  $N_w \geq 2$ , at least two quarks receive large transverse momenta they cannot combine into a leading nucleon as they fragment independently, so the spectra for  $N_w = 2$  and  $N_w = 3$  should be rather similar and shifted to much smaller  $x_F$  than in

soft interactions where the spectra of nucleons are known to be flat in  $x_F$  in a wide range of  $x_F$ .

We developed a MC event generator to quantify this observation. At the first step three quark configuration in one nucleon is generated with transverse coordinates given by the nucleon wave function. For given  $b$  we determine the gluon density encountered by each quark and if the gluon density corresponds to the BD regime, generate a transverse momentum for a quark using the model of [16] (we neglect the fractional energy losses expected in the BD regime [12]).

We implemented the fragmentation of the system produced in the first stage by constructing strings which decay using the LUND method. There are always two strings, drawn between a quark and a diquark from the interacting particles. When a quark of the diquark receives a high transverse momentum, the diquark becomes a system of two quarks and a junction. This has the nice property that one recovers the diquark when the invariant mass between the two quarks is small. The results are in good agreement with the qualitative expectation that spectra for  $N_w = 0$  and  $N_w = 1$  are similar and much harder than for  $N_w = 2, 3$  which are very similar, see Fig. 3 in Ref. [15].

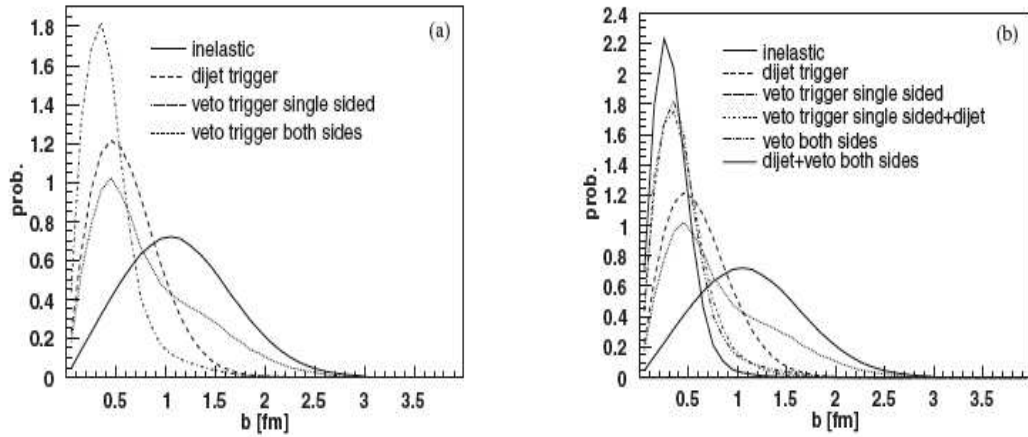


Fig. 4: (a):The combination of dijet and veto trigger gives the best constraints on central events in  $pp$ -collisions. (b):Impact parameter distributions for inelastic events, the dijet trigger and single and double sided veto-trigger (no baryon in the region  $x_F > 0.1$ ).

We find that  $N_w$  strongly depends on  $b$  with  $N_w \geq 2$  dominating for  $b \leq 0.5$  fm. A strong correlation of  $N_w$  with the multiplicity of leading baryons allows one to determine the effectiveness of a centrality trigger based on a veto for the production of leading baryons with  $x > x_{tr}$  as a function of  $x_{tr}$ . We find that an optimal value of  $x_{tr}$  is  $\sim 0.1$ . Current configurations of several LHC detectors allow to veto neutron production in this  $x$ -range. TOTEM, in addition, allows to veto production of protons with  $x_F > 0.8$ . Since neutron and proton multiplicities are similar, a one side veto for production of both charged and neutral baryons leads approximately to the same result as a two side veto for neutron production. Accordingly we will give results both for single side veto and for two side veto for both neutral and charged baryons (understanding that the full implementation of the latter option would require certain upgrades of the detectors some of which are currently under discussion). The results of the calculations are presented



in Fig. 4a together with the distribution over  $b$  for generic inelastic events and the central dijet trigger [13]. We see that the single side veto trigger leads to a centrality similar to that of a the dijet trigger, while a double side veto leads to the most narrow distribution in  $b$ . An easy way to check this expectation would be to compare other characteristics of these types of events - one expects for example a progressive increase of the central multiplicity with a decrease of average  $b$ .

The most narrow distributions can be achieved by selecting events with dijets and without leading baryons, Fig. 4b in this case we reach the limit that  $\langle \rho_{tr} \rangle = (\langle \rho^2 \rangle + \langle b^2 \rangle)^{1/2}$  becomes comparable to  $\langle \rho \rangle$  which is the smallest possible average  $\langle \rho \rangle$  for  $pp$  or DIS collisions.

## 1.4 Conclusions

Understanding of the complexity of the nucleon structure is gradually emerging from the studies of hard interactions at HERA and Tevatron collider. In addition to revealing a small transverse localization of the gluon field one finds a number of other peculiarities: presence of significant fluctuations of the transverse size of the nucleon and the strength of the gluon fields, as well as indications of a lumpy structure of nucleon at low scale (constituent quarks).

Due to proximity of BD regime for a large range of virtualities the small  $x$  physics appears to be an unavoidable component of the new particle physics production at LHC.

One of the biggest challenges is to understand the mechanism and pattern of taming of parton interactions at transverse momenta of few GeV and how it affects spectra of leading partons in the central collisions. It maybe the best to study these phenomena using centrality triggers to amplify these phenomena. Among most sensitive tools are long range correlations in rapidity - central and forward hadron production, forward - backward correlations, transverse distribution in various hard processes with centrality trigger, etc. Large rapidity coverage of ATLAS and CMS / TOTEM allows to study correlations at much larger rapidity intervals than it was possible at previous colliders.

## 2 In-medium QCD and Cherenkov gluons vs. Mach waves at LHC

*Author: Igor M. Dremin*

The properties and evolution of the medium formed in ultrarelativistic heavy-ion collisions are widely debated. At the simplest level it is assumed to consist of a set of current quarks and gluons. The collective excitation modes of the medium may, however, play a crucial role. One of the ways to gain more knowledge about the excitation modes is to consider the propagation of relativistic partons through this matter. Phenomenologically their impact would be described by the nuclear permittivity of the matter corresponding to its response to passing partons. This approach is most successful for electrodynamical processes in matter. Therefore, it is reasonable to modify the QCD equations by taking into account collective properties of the quark-gluon medium [17]. Strangely enough, this was not done earlier. For the sake of simplicity we consider here the gluodynamics only.

The classical lowest-order solution of these equations coincides with Abelian electrodynamical results up to a trivial color factor. One of the most spectacular of them is Cherenkov ra-

diation and its properties. Now, Cherenkov gluons take the place of Cherenkov photons [18–20]. Their emission in high-energy hadronic collisions is described by the same formulae but with the nuclear permittivity in place of the usual one. Actually, one considers them as quasiparticles, i.e. quanta of the medium excitations leading to shock waves with properties determined by the permittivity.

Another problem of this approach is related to the notion of the rest system of the medium. It results in some specific features of this effect at LHC energies.

To begin, let us recall the classical in-vacuum Yang-Mills equations

$$D_\mu F^{\mu\nu} = J^\nu, \quad F^{\mu\nu} = \partial^\mu A^\nu - \partial^\nu A^\mu - ig[A^\mu, A^\nu], \quad (6)$$

where  $A^\mu = iA_a^\mu T_a$ ;  $A_a(A_a^0 \equiv \Phi_a, \mathbf{A}_a)$  are the gauge field (scalar and vector) potentials, the color matrices  $T_a$  satisfy the relation  $[T_a, T_b] = if_{abc}T_c$ ,  $D_\mu = \partial_\mu - ig[A_\mu, \cdot]$ ,  $J^\nu(\rho, \mathbf{j})$  is a classical source current, and the metric is given by  $g^{\mu\nu} = \text{diag}(+, -, -, -)$ .

In the covariant gauge  $\partial_\mu A^\mu = 0$  they are written

$$\square A^\mu = J^\mu + ig[A_\nu, \partial^\nu A^\mu + F^{\mu\nu}], \quad (7)$$

where  $\square$  is the d'Alembertian operator.

The chromoelectric and chromomagnetic fields are  $E^\mu = F^{\mu 0}$ ,  $B^\mu = -\frac{1}{2}\epsilon^{\mu ij}F^{ij}$  or, as functions of the gauge potentials in vector notation,

$$\mathbf{E}_a = -\text{grad}\Phi_a - \frac{\partial \mathbf{A}_a}{\partial t} + gf_{abc}\mathbf{A}_b\Phi_c, \quad \mathbf{B}_a = \text{curl}\mathbf{A}_a - \frac{1}{2}gf_{abc}[\mathbf{A}_b\mathbf{A}_c]. \quad (8)$$

Herefrom, one easily rewrites the in-vacuum equations of motion (6) in vector form. We do not show them explicitly here (see [17]) and write down the equations of the in-medium gluon dynamics using the same method as in electrodynamics. We introduce the nuclear permittivity and denote it also by  $\epsilon$ , since this will not lead to any confusion. After that, one should replace  $\mathbf{E}_a$  by  $\epsilon\mathbf{E}_a$  and get

$$\epsilon(\text{div}\mathbf{E}_a - gf_{abc}\mathbf{A}_b\mathbf{E}_c) = \rho_a, \quad \text{curl}\mathbf{B}_a - \epsilon\frac{\partial \mathbf{E}_a}{\partial t} - gf_{abc}(\epsilon\Phi_b\mathbf{E}_c + [\mathbf{A}_b\mathbf{B}_c]) = \mathbf{j}_a. \quad (9)$$

The space-time dispersion of  $\epsilon$  is neglected here.

In terms of potentials these equations are cast in the form

$$\begin{aligned} \Delta \mathbf{A}_a - \epsilon \frac{\partial^2 \mathbf{A}_a}{\partial t^2} = & -\mathbf{j}_a - gf_{abc}(\frac{1}{2}\text{curl}[\mathbf{A}_b, \mathbf{A}_c] + \frac{\partial}{\partial t}(\mathbf{A}_b\Phi_c) + [\mathbf{A}_b\text{curl}\mathbf{A}_c] - \\ & \epsilon\Phi_b\frac{\partial \mathbf{A}_c}{\partial t} - \epsilon\Phi_b\text{grad}\Phi_c - \frac{1}{2}gf_{cmn}[\mathbf{A}_b[\mathbf{A}_m\mathbf{A}_n]] + g\epsilon f_{cmn}\Phi_b\mathbf{A}_m\Phi_n), \end{aligned} \quad (10)$$

$$\begin{aligned} \Delta \Phi_a - \epsilon \frac{\partial^2 \Phi_a}{\partial t^2} = & -\frac{\rho_a}{\epsilon} + gf_{abc}(2\mathbf{A}_c\text{grad}\Phi_b + \mathbf{A}_b\frac{\partial \mathbf{A}_c}{\partial t} + \frac{\partial \Phi_b}{\partial t}\mathbf{A}_c) - \\ & g^2 f_{amn}f_{nlb}\mathbf{A}_m\mathbf{A}_l\Phi_b. \end{aligned} \quad (11)$$



If the terms with coupling constant  $g$  are omitted, one gets the set of Abelian equations, that differ from electrodynamical equations by the color index  $a$  only. The external current is due to a parton moving fast relative to partons "at rest".

The crucial distinction between (7) and (10), (11) is that there is no radiation (the field strength is zero in the forward light-cone and no gluons are produced) in the lowest order solution of (7), and it is admitted for (10), (11), because  $\epsilon$  takes into account the collective response (color polarization) of the nuclear matter.

Cherenkov effects are especially suited for treating them by classical approach to (10), (11). Their unique feature is independence of the coherence of subsequent emissions on the time interval between these processes. The lack of balance of the phase  $\Delta\phi$  between emissions with frequency  $\omega = k/\sqrt{\epsilon}$  separated by the time interval  $\Delta t$  (or the length  $\Delta z = v\Delta t$ ) is given by

$$\Delta\phi = \omega\Delta t - k\Delta z \cos\theta = k\Delta z\left(\frac{1}{v\sqrt{\epsilon}} - \cos\theta\right) \quad (12)$$

up to terms that vanish for large distances. For Cherenkov effects the angle  $\theta$  is

$$\cos\theta = \frac{1}{v\sqrt{\epsilon}}. \quad (13)$$

The coherence condition  $\Delta\phi = 0$  is valid independent of  $\Delta z$ . This is a crucial property specific for Cherenkov radiation only. The fields  $(\Phi_a, \mathbf{A}_a)$  and the classical current for in-medium gluon dynamics can be represented by the product of the electrodynamical expressions  $(\Phi, \mathbf{A})$  and the color matrix  $T_a$ .

Let us recall the Abelian solution for the current with velocity  $\mathbf{v}$  along  $z$ -axis:

$$\mathbf{j}(\mathbf{r}, t) = \mathbf{v}\rho(\mathbf{r}, t) = 4\pi g\mathbf{v}\delta(\mathbf{r} - \mathbf{v}t). \quad (14)$$

In the lowest order the solutions for the scalar and vector potentials are related  $\mathbf{A}^{(1)}(\mathbf{r}, t) = \epsilon\mathbf{v}\Phi^{(1)}(\mathbf{r}, t)$  and

$$\Phi^{(1)}(\mathbf{r}, t) = \frac{2g}{\epsilon} \frac{\theta(vt - z - r_\perp\sqrt{\epsilon v^2 - 1})}{\sqrt{(vt - z)^2 - r_\perp^2(\epsilon v^2 - 1)}}. \quad (15)$$

Here  $r_\perp = \sqrt{x^2 + y^2}$  is the cylindrical coordinate;  $z$  symmetry axis. The cone

$$z = vt - r_\perp\sqrt{\epsilon v^2 - 1} \quad (16)$$

determines the position of the shock wave due to the  $\theta$ -function in (15). The field is localized within this cone and decreases with time as  $1/t$  at any fixed point. The gluons emission is perpendicular to the cone (16) at the Cherenkov angle (13).

Due to the antisymmetry of  $f_{abc}$ , the higher order terms ( $g^3, \dots$ ) are equal to zero for any solution multiplicative in space-time and color as seen from (10), (11).

The expression for the intensity of the radiation is given by the Tamm-Frank formula (up to Casimir operators) that leads to infinity for constant  $\epsilon$ . The  $\omega$ -dependence of  $\epsilon$  (dispersion), its imaginary part (absorption) and chromomagnetic permeability can be taken into account [17].

The attempts to calculate the nuclear permittivity from first principles are not very convincing. It can be obtained from the polarization operator. The corresponding dispersion branches have been computed in the lowest order perturbation theory [21, 22]. The properties of collective excitations have been studied in the framework of the thermal field theories (see, e.g., [23]). The results with an additional phenomenological ad hoc assumption about the role of resonances were used in a simplified model of scalar fields [20] to show that the nuclear permittivity can be larger than 1, i.e. admits Cherenkov gluons. Extensive studies were performed in [24]. No final decision about the nuclear permittivity is yet obtained from these approaches. It must be nontrivial problem because we know that, e.g., the energy dependence of the refractive index of water [25] (especially, its imaginary part) is so complicated that it is not described quantitatively in electrodynamics.

Therefore, we prefer to use the general formulae of the scattering theory to estimate the nuclear permittivity. It is related to the refractive index  $n$  of the medium  $\epsilon = n^2$  and the latter one is expressed through the real part of the forward scattering amplitude of the refracted quanta  $\text{Re}F(0^\circ, E)$  by

$$\text{Re}n(E) = 1 + \Delta n_R = 1 + \frac{6m_\pi^3\nu}{E^2}\text{Re}F(E) = 1 + \frac{3m_\pi^3\nu}{4\pi E}\sigma(E)\rho(E). \quad (17)$$

Here  $E$  denotes the energy,  $\nu$  the number of scatterers within a single nucleon,  $m_\pi$  the pion mass,  $\sigma(E)$  the cross section and  $\rho(E)$  the ratio of real to imaginary parts of the forward scattering amplitude  $F(E)$ .

Thus the emission of Cherenkov gluons is possible only for processes with positive  $\text{Re}F(E)$  or  $\rho(E)$ . Unfortunately, we are unable to calculate directly in QCD these characteristics of gluons and have to rely on analogies and our knowledge of the properties of hadrons. The only experimental facts we get for this medium are brought about by particles registered at the final stage. They have some features in common, which (one may hope!) are also relevant for gluons as the carriers of the strong forces. Those are the resonant behavior of amplitudes at rather low energies and the positive real part of the forward scattering amplitudes at very high energies for hadron-hadron and photon-hadron processes as measured from the interference of the Coulomb and hadronic parts of the amplitudes.  $\text{Re}F(0^\circ, E)$  is always positive (i.e.,  $n > 1$ ) within the low-mass wings of the Breit-Wigner resonances. This shows that the necessary condition for Cherenkov effects  $n > 1$  is satisfied at least within these two energy intervals. This fact was used to describe experimental observations at SPS, RHIC and cosmic ray energies. The asymmetry of the  $\rho$ -meson shape at SPS [26] and azimuthal correlations of in-medium jets at RHIC [27–30] were explained by emission of comparatively low-energy Cherenkov gluons [31, 32]. The parton density and intensity of the radiation were estimated. In its turn, cosmic ray data [33] at energies corresponding to LHC require very high-energy gluons to be emitted by the ultrarelativistic partons moving along the collision axis [18, 19]. Let us note the important difference from electrodynamics, where  $n < 1$  at high frequencies.

The in-medium equations are not Lorentz-invariant. There is no problem in macroscopic electrodynamics, because the rest system of the macroscopic matter is well defined and its permittivity is considered there. For collisions of two nuclei (or hadrons) it requires special discussion.

Let us consider a particular parton that radiates in the nuclear matter. It would "feel"

the surrounding medium at rest if the momenta of all other partons, with which this parton can interact, are smaller and sum to zero. In RHIC experiments the triggers, that registered the jets (created by partons), were positioned at  $90^\circ$  to the collision axis. Such partons should be produced by two initial forward-backward moving partons scattered at  $90^\circ$ . The total momentum of the other partons (medium spectators) is balanced, because for such a geometry the partons from both nuclei play the role of spectators forming the medium. Thus the center of mass system is the proper one to consider the nuclear matter at rest in this experiment. The permittivity must be defined there. The Cherenkov rings consisting of hadrons have been registered around the away-side jet, which traversed the nuclear medium. This geometry requires, however, high statistics, because the rare process of scattering at  $90^\circ$  has been chosen.

The forward (backward) moving partons are much more numerous and have higher energies. However, one cannot treat the radiation of such a primary parton in the c.m.s. in a similar way, because the momentum of the spectators is different from zero, i.e. the matter is not at rest. Now the spectators (the medium) are formed from the partons of another nucleus only. Then the rest system of the medium coincides with the rest system of that nucleus and the permittivity should refer to this system. The Cherenkov radiation of such highly energetic partons must be considered there. That is what was done for interpretation of the cosmic ray event in [18, 19]. This discussion shows that one must carefully define the rest system for other geometries of the experiment with triggers positioned at different angles.

Thus our conclusion is that the definition of  $\epsilon$  depends on the geometry of the experiment. Its corollary is that partons moving in different directions with different energies can "feel" different states of matter in the **same** collision of two nuclei because of the permittivity dispersion. The transversely scattered partons with comparatively low energies can analyze the matter with rather large permittivity corresponding to the resonance region, while the forward moving partons with high energies would "observe" a low permittivity in the same collision. This peculiar feature can help scan the  $(\ln x, Q^2)$ -plane as discussed in [34]. It explains also the different values of  $\epsilon$  needed for the description of the RHIC and cosmic ray data.

These conclusions can be checked at LHC, because both RHIC and cosmic ray geometry will become available there. The energy of the forward moving partons would exceed the thresholds above which  $n > 1$ . Then both types of experiments can be done, i.e. the  $90^\circ$ -trigger and non-trigger forward-backward partons experiments. The predicted results for  $90^\circ$ -trigger geometry are similar to those at RHIC. The non-trigger Cherenkov gluons should be emitted within the rings at polar angles of tens degrees in c.m.s. at LHC by the forward moving partons (and symmetrically by the backward ones) according to some events observed in cosmic rays [32, 33].

Let us compare the conclusions for Cherenkov and Mach shock waves. The Cherenkov gluons are described as the transverse waves while the Mach waves are longitudinal. Up to now, no experimental signatures of these features were proposed.

The most important experimental fact is the position of the maxima of humps in two-particle correlations. They are displaced from the away-side jet by 1.05-1.23 radian [35–38]. This requires rather large values of  $\text{Re}\epsilon \sim 2 - 3$  and indicates high density of the medium [32] that agrees with other conclusions. The fits of the humps with complex permittivity are in progress. The maxima due to Mach shock waves should be shifted by the smaller value 0.955 if the relativistic equation of state is used ( $\cos \theta = 1/\sqrt{3}$ ). To fit experimental values one must

consider different equation of state. In three-particle correlations, this displacement is about 1.38 [27–29].

There are some claims [27–30] that Cherenkov effect contradicts to experimental observations because it predicts the shift of these maxima to smaller angles for larger momenta. They refer to the prediction made in [20]. However, the conclusions of this paper about the momentum dependence of the refractive index can hardly be considered as quantitative ones because the oversimplified scalar  $\Phi^3$ -model with simplest resonance insertions was used for computing the refractive index. In view of difficult task of its calculation discussed above, the fits of maxima seem to be more important for our conclusions about the validity of the two schemes.

Mach waves should appear for forward moving partons at RHIC but were not found. The energy threshold of  $\epsilon$  explains this phenomenon for Cherenkov gluons.

## References

- [1] S. J. Brodsky, L. Frankfurt, J. F. Gunion, A. H. Mueller, and M. Strikman, Phys. Rev. **D50**, 3134 (1994), arXiv:hep-ph/9402283.
- [2] J. C. Collins, L. Frankfurt, and M. Strikman, Phys. Rev. **D56**, 2982 (1997), arXiv:hep-ph/9611433.
- [3] L. Frankfurt, M. Strikman, and C. Weiss, Ann. Rev. Nucl. Part. Sci. **55**, 403 (2005), arXiv:hep-ph/0507286.
- [4] T. Sjostrand, S. Mrenna, and P. Skands, JHEP **05**, 026 (2006), arXiv:hep-ph/0603175.
- [5] CDF Collaboration, F. Abe *et al.*, Phys. Rev. Lett. **79**, 584 (1997).
- [6] CDF Collaboration, F. Abe *et al.*, Phys. Rev. **D56**, 3811 (1997).
- [7] L. Frankfurt, M. Strikman, D. Treleani, and C. Weiss, Phys. Rev. Lett. **101**, 202003 (2008), arXiv:0808.0182 [hep-ph].
- [8] T. Rogers, V. Guzey, M. Strikman, and X. Zu, Phys. Rev. **D69**, 074011 (2004), arXiv:hep-ph/0309099.
- [9] L. Frankfurt, V. Guzey, M. McDermott, and M. Strikman, Phys. Rev. Lett. **87**, 192301 (2001), arXiv:hep-ph/0104154.
- [10] BRAHMS Collaboration, I. Arsene *et al.*, Phys. Rev. Lett. **93**, 242303 (2004), arXiv:nucl-ex/0403005.
- [11] STAR Collaboration, J. Adams *et al.*, Phys. Rev. Lett. **97**, 152302 (2006), arXiv:nucl-ex/0602011.
- [12] L. Frankfurt and M. Strikman, Phys. Lett. **B645**, 412 (2007).
- [13] L. Frankfurt, M. Strikman, and C. Weiss, Phys. Rev. **D69**, 114010 (2004), arXiv:hep-ph/0311231.

- [14] T. C. Rogers, A. M. Stasto, and M. I. Strikman, Phys. Rev. **D77**, 114009 (2008), arXiv:0801.0303 [hep-ph].
- [15] H. J. Drescher and M. Strikman, Phys. Rev. Lett. **100**, 152002 (2008).
- [16] D. Boer and A. Dumitru, Phys. Lett. **B556**, 33 (2003), arXiv:hep-ph/0212260.
- [17] I. M. Dremin, Eur. Phys. J. **C56**, 81 (2008), arXiv:0802.4022 [hep-ph].
- [18] I. M. Dremin, JETP Lett. **30**, 140 (1979).
- [19] I. M. Dremin, Sov. J. Nucl. Phys. **33**, 726 (1981).
- [20] V. Koch, A. Majumder, and X.-N. Wang, Phys. Rev. Lett. **96**, 172302 (2006), arXiv:nucl-th/0507063.
- [21] O. K. Kalashnikov and V. V. Klimov, Sov. J. Nucl. Phys. **31**, 699 (1980).
- [22] H. A. Weldon, Phys. Rev. **D26**, 1394 (1982).
- [23] J.-P. Blaizot and E. Iancu, Phys. Rept. **359**, 355 (2002), arXiv:hep-ph/0101103.
- [24] M. K. Djongolov, S. Pisov, and V. Rizov, J. Phys. **G30**, 425 (2004), arXiv:hep-ph/0303141.
- [25] J. D. Jackson, *Classical electrodynamics*. John Wiley and Sons, 1998.
- [26] NA60 Collaboration, R. Arnaldi *et al.*, Phys. Rev. Lett. **96**, 162302 (2006), arXiv:nucl-ex/0605007.
- [27] J. G. Ulery, PoS **LHC07**, 036 (2007), arXiv:0709.1633 [nucl-ex].
- [28] J. G. Ulery (2008), arXiv:0801.4904 [nucl-ex].
- [29] J. G. Ulery (2008), arXiv:0807.1613 [nucl-ex].
- [30] PHENIX Collaboration, N. N. Ajitanand, Nucl. Phys. **A783**, 519 (2007), arXiv:nucl-ex/0609038.
- [31] I. M. Dremin and V. A. Nechitailo (2007), arXiv:0704.1081 [hep-ph].
- [32] I. M. Dremin, Nucl. Phys. **A767**, 233 (2006), arXiv:hep-ph/0507167.
- [33] A. V. Apanasenko, N. A. Dobrotin, I. M. Dremin, and K. A. Kotelnikov, JETP Lett. **30**, 145 (1979).
- [34] I. M. Dremin, Int. J. Mod. Phys. **A22**, 3087 (2007), arXiv:0706.0596 [hep-ph].
- [35] STAR Collaboration, K. H. Ackermann *et al.*, Phys. Rev. Lett. **86**, 402 (2001), arXiv:nucl-ex/0009011.

- [36] STAR Collaboration, F. Wang, J. Phys. **G30**, S1299 (2004),  
arXiv:nucl-ex/0404010.
- [37] PHENIX Collaboration, A. Adare *et al.*, Phys. Rev. **C77**, 011901 (2008),  
arXiv:0705.3238 [nucl-ex].
- [38] PHENIX Collaboration, A. Adare *et al.*, Phys. Rev. **C78**, 014901 (2008),  
arXiv:0801.4545 [nucl-ex].

## Chapter 3

# Working Group Heavy Quarks (Charm and Beauty)

### Convenors:

*M Cacciari (Paris VI & VII.),  
A. Dainese (INFN, ALICE),  
A. Geiser (DESY, ZEUS)  
H. Spiesberger (U. Mainz),  
Contactpersons: K. Lipka (U. Hamburg, H1), Ulrich Uwer (CERN)*

# Introduction

*M. Cacciari, A. Dainese, A. Geiser, H. Spiesberger*

This document is a collection of contributions to the series of workshops, having taken place during the years 2006 – 2008 at CERN and DESY, on aspects of heavy quark physics relevant at the transition from the HERA to the LHC eras of experimentation. In three sections we review recent experimental results from HERA, describe the plans for coming analyses at the LHC and collect various reports about new results from theoretical work. The present report extends the proceedings of a previous workshop which are available online <sup>1</sup> and contain also a general theoretical review of various approaches in heavy quark production to which we refer for further reference.

The first section below reviews recent measurements of charm and beauty production in  $ep$  collisions at HERA. Heavy quark tagging methods used by the ZEUS and H1 experiments are described. Cross section results in both photoproduction and deep inelastic scattering are compared with NLO QCD predictions. In general the data are well described by the calculations. Studies of charm fragmentation yield compatibility with the assumption of universality at large transverse momenta, but illustrate some problems with this assumption in the threshold region. The DIS cross sections receive large contributions from the charm and beauty content of the proton,  $F_2^{c\bar{c}}$  and  $F_2^{b\bar{b}}$ . The corresponding most recent measurements are compared to next-to-leading order QCD predictions using different parameterisations of the theory, and of the gluon density in the proton.

The tests of the fragmentation function, the gluon density, and details of the theoretical treatment of the charm and beauty masses performed on the basis of HERA experimental data are of direct interest to corresponding applications at the LHC. In section two, after reviewing the main heavy flavour results from experiments at the Relativistic Heavy Ion Collider (RHIC), we present the expected performance for some of the most significant measurements in the heavy flavour sector at the Large Hadron Collider (LHC), for the experiments ALICE, ATLAS, and CMS.

A proper inclusion of heavy quark mass effects in parton distribution function fits has proved crucial. In the theory part of this document, we present a review of these effects in DIS and their impact on global analyses and lay out all elements of a properly defined general mass variable flavor number scheme (GM VFNS) that are shared by all modern formulations of the problem. We also report about progress in a number of theoretical problems related to exclusive measurements of heavy flavors. These topics include fragmentation functions for charmed mesons including finite mass effects, fragmentation functions including non-perturbative corrections based on an effective QCD coupling, a discussion of the status of higher-order calculations for top quark production and for polarized structure functions, heavy quark and quarkonium production in the Regge limit, double heavy baryon production, tests of time reversal and CP symmetry in  $\Lambda_b$  decays, as well as a study of the general properties of massive exotic hadrons that will be relevant for an understanding of their detection at the LHC.

---

<sup>1</sup><http://www.desy.de/~heralhc/proceedings/proceedings.html>



.

# Experimental study of heavy flavour production at HERA

*S. Boutle<sup>a</sup>, J. Bracinik<sup>b</sup>, A. Geiser<sup>c</sup>, G. Grindhammer<sup>d</sup>, A.W. Jung<sup>e</sup>, P. Roloff<sup>e,f</sup>, Z. Ruriková<sup>c</sup>, M. Turcato<sup>f</sup>, A. Yagües-Molina<sup>c</sup>*

<sup>a</sup> University College London, Gower Street, London WC1E 6BT, United Kingdom

<sup>b</sup> School of Physics and Astronomy, University of Birmingham - UK

<sup>c</sup> Deutsches Elektronen-Synchrotron DESY, Notkestraße 85, 22607 Hamburg, Germany

<sup>d</sup> Max-Planck-Institut f. Physik, Werner-Heisenberg-Institut Muenchen, Germany

<sup>e</sup> University of Heidelberg - Kirchhoff-Institute for Physics, Im Neuenheimer Feld 227, 69120 Heidelberg, Germany

<sup>f</sup> Universität Hamburg, Institut für Experimentalphysik, Luruper Chaussee 149, 22761 Hamburg, Germany

## Abstract

Recent measurements of charm and beauty production in  $ep$  collisions at HERA are reviewed. Heavy quark tagging methods used by the ZEUS and H1 experiments are described. Cross section results in both photoproduction and deep inelastic scattering (DIS) are compared with NLO QCD predictions. In general the data are well described by the calculations. Studies of charm fragmentation yield compatibility with the assumption of universality at large transverse momenta, but illustrate some problems with this assumption in the threshold region. The DIS cross sections can also be expressed in terms of the charm and beauty content of the proton,  $F_2^{c\bar{c}}$  and  $F_2^{b\bar{b}}$ . The most recent measurements are compared to next-to-leading order QCD predictions using different parameterisations of the theory, and of the gluon density in the proton. The tests of the fragmentation function, the gluon density, and details of the theoretical treatment of the charm and beauty masses are of direct interest to corresponding applications at the LHC.

*Coordinator/editor: A. Geiser*

## 1 Charm production at HERA: Experimental overview

*Author: A. Jung*

### 1.1 Introduction

Several new measurements of open charm production have been performed by the H1 collaboration

- $D^{*\pm}$  Production at low  $Q^2$  with the H1 Detector [1, 2]
- Measurement of the  $D^{*\pm}$  Production cross section in Photoproduction with the H1 Detector using HERA II data [3]
- Study of Charm Fragmentation into  $D^{*\pm}$  Mesons in Deep-Inelastic Scattering at HERA [4]

and by the ZEUS collaboration

- $D^{*\pm}$  in DIS and Measurement of  $F_2^c$  [5]
- Measurement of  $D^{*\pm}$  Meson Production in DIS ep Scattering at low  $Q^2$  [6]
- Measurement of excited charm and charm-strange mesons production at HERA [7]
- Measurement of the charm fragmentation fractions [8] and fragmentation function [9]

The details of the measurements like the visible range will not be discussed here as they are given in the literature cited for each measurement. For both experiments high statistic charm event samples are tagged by  $D^{*\pm}$  mesons reconstructed in the golden decay channel:  $D^{*\pm} \rightarrow D^0 \pi_{\text{slow}}^\pm \rightarrow K^\mp \pi^\pm \pi_{\text{slow}}^\pm$ . The well known mass difference method reduces symmetric systematic uncertainties and allows the extraction of the  $D^*$  meson signal by fits out of the background dominated data samples. Other D mesons can also be identified via their characteristic mass peaks. In addition to that method charmed mesons like  $D^+$ ,  $D_s^+$  mesons are tagged via lifetime measurements from the high resolution silicon vertex detectors used by both experiments in HERAII.

The results on the fragmentation function will be discussed in section 2.

## 1.2 Results of open charm production

The H1 photoproduction analysis [3] makes use of the H1 Fast Track Trigger (FTT) [10, 11] which enhanced the capabilities of heavy flavor measurements at H1 by a selective on-line track based event reconstruction [12]. Due to these improvements the phase space and the available statistics of the measurement has been significantly enlarged compared to the previous H1 photoproduction analysis [13].

The large statistics allows precise double differential measurements. For the H1 photoproduction measurement the data are reasonably well described except for special regions of the phase space and correlations. Especially the  $W_{\gamma P}$  dependence is not described by the NLO prediction using the FFNS. The correlation between  $\eta$  and  $p_T$  as shown in Figure 1 (right) is compared to the NLO QCD predictions in the FFNS [14] and GM-VFNS; it turns out that the NLO QCD predictions are able to describe the correlation between  $\eta$  and  $p_T$  in photoproduction. Nevertheless the NLO predictions show an increasing deficit at forward  $\eta > 0$  which is largest at high  $p_T$  where the  $D^*$  data prefer the upper edge of the error band. For the photoproduction regime the relatively large theoretical uncertainty especially at small  $p_T$  arises from the scale variation. For comparison also the double differential measurement in DIS from H1 is shown on the left side of Figure 1. The H1 DIS analysis [1] uses the full HERAII luminosity. Because of the large statistics the analysis is almost everywhere dominated by the systematic error. The use of electron and hadron quantities combined in the  $e\Sigma$  reconstruction method [15] for the reconstruction of the kinematic variables allows lower inelasticities and smaller systematic uncertainties compared to previous H1 DIS analyses [2].

The measured single and double differential  $D^*$  production cross sections are in general well described by the next-to-leading order QCD predictions in the FFNS. The theoretical uncertainty of the predictions is dominated by the mass variation of the charm quark but is in general smaller than in photoproduction because of the additional scale  $Q^2$ . The small excess in data at forward directions  $\eta > 0$  (seen previously by H1 [2]) turns out to be located at low  $p_T$  as it can be seen

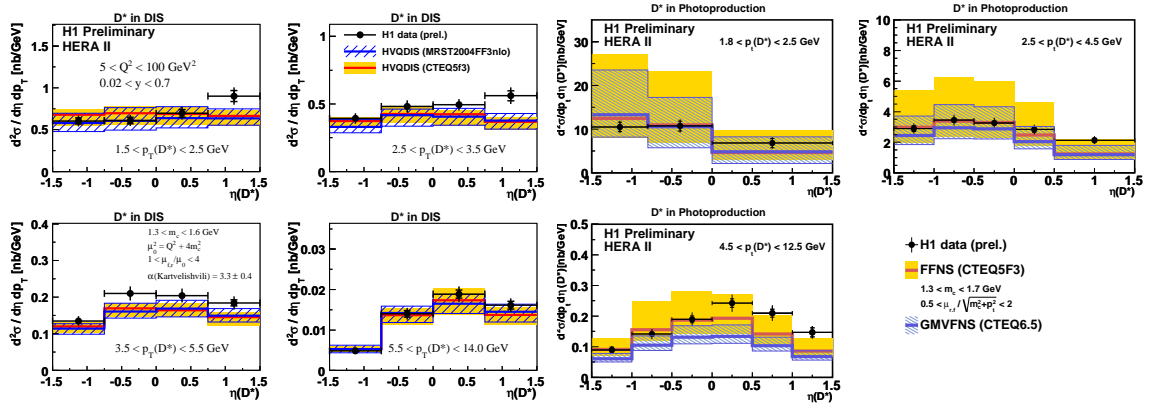


Fig. 1: The double differential cross section in  $\eta(D^*)$  and  $p_T(D^*)$  for the DIS (left) and photoproduction (right) regime compared to the NLO QCD predictions.

in comparison to the NLO prediction for the double differential distribution (see Figure 1 left). The data are above the predictions for the low  $p_T$  region at forward directions which is different to the photoproduction region where the data prefer the upper edge of the prediction at large  $p_T$ . The small discrepancy at forward directions can already be seen in the single differential  $\eta(D^*)$  distribution in comparison to the NLO QCD prediction as shown in Figure 2 left. The recent

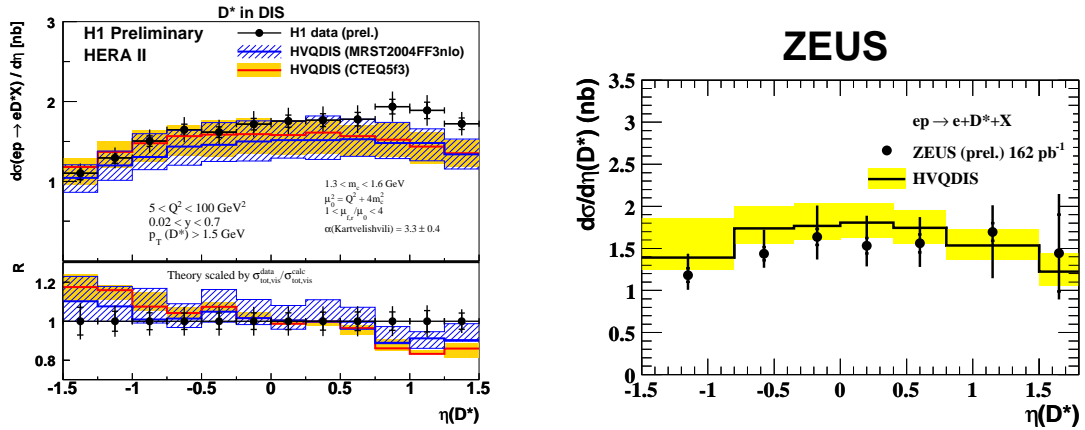


Fig. 2: The  $D^*$  cross section as a function of  $\eta(D^*)$  as measured by H1 using the luminosity of the whole HERAII data taking (left) and from ZEUS as measured using the luminosity of the years 2003 – 2005 (right).

$D^*$  measurement from the ZEUS collaboration [5] measures the same  $p_T(D^*)$  and  $y$  region but covers a slightly larger range in  $\eta(D^*)$  and goes up to larger  $Q^2$ . The ZEUS result (figure 2 right) is in good agreement with the NLO QCD predictions and in agreement with the result from H1 within errors.

A cross section measurement at very low  $Q^2$  for  $D^*$  production in DIS has been performed by ZEUS [6] using the beam pipe calorimeter. The overall  $Q^2$  range including this new measurement is shown in figure 3 (left) with a nice agreement to the NLO QCD prediction.

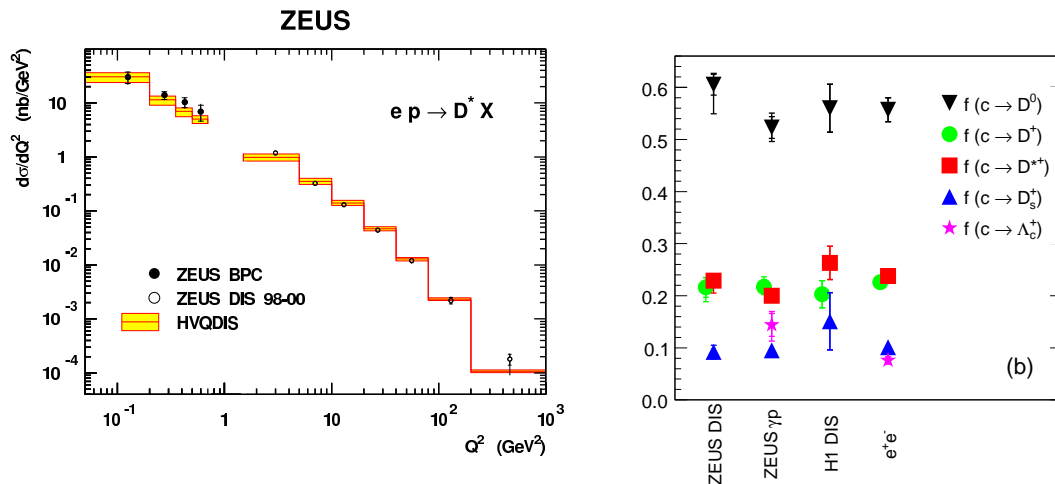


Fig. 3: The  $Q^2$  distribution including the new ZEUS measurement at very low  $Q^2$  shown right and the fragmentation fractions as measured by ZEUS and other experiment for various D mesons.

ZEUS has measured the charm production cross section of  $D^*$ ,  $D^0$ ,  $D^+$ ,  $D_s^+$  [8], in order to determine the fragmentation fractions of charm into each meson. The charm fragmentation fractions as shown in figure 3 agree with the ones extracted by H1. Because of the agreement with the fragmentation fractions from  $e^+e^-$  the conclusion is that they do not depend on the hard subprocess and are in that sense universal.

In addition to the test of the QCD predictions in differential distributions another stringent test of QCD is possible since the  $D^*$  measurement involves the gluon density which drives the  $D^*$  production via the BGF production mechanism. Several approaches exist to measure the gluon density. The well established approach to measure the charm structure function will be covered elsewhere. In order to have an impact on the fits of the gluon density it is necessary that the cross section data have the highest possible precision. At present stage H1 and ZEUS enter the precision era of charm measurements where a single differential distribution has at least some sensitivity to the proton PDF, e.g. the  $\eta(D^*)$  distribution measured by H1 shows a better compatibility to the predictions if a proton PDF is used where a gluon density providing a less steep rise towards small  $x$  is used. However, the significance of the sensitivity is diminished by the relatively large theoretical uncertainties. The available  $D^*$  cross section data can also be used to fit the gluon density directly from the differential distributions in  $\eta(D^*)$ ,  $p_T(D^*)$ ,  $z(D^*)$ ,  $x$ ,  $Q^2$  [16].

In order to further increase the data precision it is possible to combine data from H1 and ZEUS on the basis of  $(D^*)$  cross sections or at the level of  $F_2^c$  extractions. At the level of  $F_2^c$  also the combination of data within one experiment from different  $F_2^c$  measurement methods, i.e. from  $D^*$  cross sections and from lifetime measurements, provides additional information.

### 1.3 Conclusions

At the present stage H1 and ZEUS enter the precision era of charm measurements with the large statistic of about  $0.5 \text{ fb}^{-1}$  per experiment provided by the HERAII running period. These data are currently analyzed and first preliminary results with high precision are available. In general the description by the next-to-leading order QCD predictions is reasonable except for some regions of the phase space. In order to get more insights and to have a significant impact on the fits of the PDFs the cross section data must be very precise and in addition cover the largest possible phase space. New results with such improvements are still expected to come.

## 2 Study of Charm Quark Fragmentation at HERA

*Authors: J. Bracinik, G. Grindhammer, Z. Rurikova*

The inclusive cross section for the production of heavy hadrons in  $ep$  collisions can be expressed as a convolution of three terms, describing the structure of the proton, the hard subprocess and the transition of partons to colourless heavy and light hadrons. The term describing the transition of partons to hadrons, also referred to as fragmentation function (FF), contains a non-perturbative component and thus must be experimentally determined. Charm quark fragmentation has been already extensively studied in  $e^+e^-$  annihilation experiments, and the parameters of various phenomenological models (i.e. the Lund string model, independent fragmentation model), which have been developed to describe the fragmentation process, have been tuned. By studying the charm quark fragmentation function also in  $ep$  collisions one can experimentally test, if the assumed universality of fragmentation functions, i.e. their portability from the calculation of processes in  $e^+e^-$  to processes in  $ep$  or  $pp/\bar{p}$ , really holds.

Since fragmentation functions describe the longitudinal momentum fraction transferred from the parton to the hadron they cannot be measured directly. The differential cross section as a function of suitably defined observables sensitive to the FF has to be measured and used to extract the parameters of the FF by comparing the data with the prediction of a given model.

The fragmentation of charm quarks into  $D^{*\pm}$  mesons in  $ep$  collisions has been studied by the H1 [17] and ZEUS [18] collaborations in both deep-inelastic scattering (DIS) and photoproduction (PHP), respectively. A so called hemisphere and a jet observable have been used by H1 and a jet observable by ZEUS.

In case of the jet observable, the momentum of the charm quark is approximated by the momentum of the reconstructed jet, which includes a  $D^{*\pm}$  meson, leading to the definition of  $z_{\text{jet}} = (E + P_L)_{D^*} / (E + P)_{\text{jet}}$ , where the longitudinal momentum  $P_{LD^*}$  is defined with respect to the three-momentum of the jet.

In case of the hemisphere observable, the kinematics of charm production, known to proceed mainly via photon-gluon fusion, is taken into account. In the  $\gamma^*p$  rest-frame the charm and anti-charm quarks are moving in the direction of the virtual photon (see figure 4 left), hence, the contributions from initial state radiation and the proton remnant can be strongly suppressed by discarding all particles with momenta pointing to the proton direction. Furthermore, since the transverse momenta of the charm quarks are balanced in this frame, the remaining particles may be divided into two hemispheres, one containing the fragmentation products of the charm quark, and the other one those of the anti-charm quark (see figure 4 right). This division into hemi-

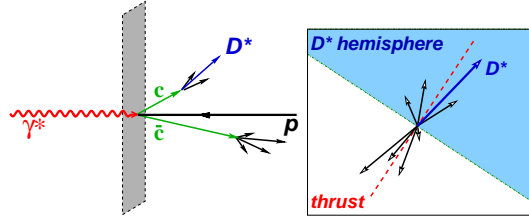


Fig. 4: Kinematics of charm/anticharm production in the  $\gamma^* p$  rest-frame as used for the definition of  $z_{\text{hem}}$ .

spheres is done by reconstructing the thrust axis in a plane perpendicular to the  $\gamma^* p$ -axis. The particles belonging to the same hemisphere as the  $D^{*\pm}$  meson are considered to be the products of the same quark and the sum of their four-momenta is used to approximate the four-momentum of the original quark, leading to this definition of  $z_{\text{hem}} = (E + P_L)_{D^*} / (E + P)_{\text{hem}}$ .

The ZEUS collaboration performed a measurement of the normalized differential cross section of  $D^{*\pm}$  meson production as a function of  $z_{\text{jet}}$  in photoproduction (kinematic range  $Q^2 < 1 \text{ GeV}^2$  and  $130 < W < 280 \text{ GeV}$ ). The  $D^{*\pm}$  mesons were reconstructed using the “golden” decay channel  $D^{*\pm} \rightarrow D^0 \pi_s^\pm \rightarrow K^\mp \pi^\pm \pi_s^\pm$ , requiring  $|\eta(D^{*\pm})| < 1.5$  and  $P_T(D^{*\pm}) > 2 \text{ GeV}$ . Jets were reconstructed using the inclusive  $k_\perp$  algorithm, requiring  $|\eta_{\text{jet}}| < 2.4$  and  $E_{T,\text{jet}} > 9 \text{ GeV}$ . Since the jets were reconstructed as massless, the jet observable reduces to  $z_{\text{jet}} = (E + P_L)_{D^*} / 2E_{\text{jet}}$ . The contribution of  $D^{*\pm}$  mesons from B-hadron decays, which amounts to about 9%, was subtracted using the prediction of the PYTHIA Monte Carlo program.

The H1 collaboration measured the normalized  $D^{*\pm}$  meson cross sections as a function of both  $z_{\text{hem}}$  and  $z_{\text{jet}}$  in DIS ( $2 < Q^2 < 100 \text{ GeV}^2$  and  $0.05 < y < 0.7$ ), using the same decay channel and requiring  $|\eta(D^{*\pm})| < 1.5$  and  $1.5 < P_T(D^{*\pm}) < 15 \text{ GeV}$ . Jets were reconstructed using the massive inclusive  $k_\perp$  algorithm in the  $\gamma^* p$  rest-frame. The measurement was performed for two event samples. In the first sample, referred to as the “ $D^{*\pm}$  jet sample”, the presence of a jet containing the  $D^{*\pm}$  with  $E_{T,\text{jet}} > 3 \text{ GeV}$  is required as a hard scale. In the second sample, the “no  $D^{*\pm}$  jet sample”, no such jet is present. The small 1 – 2% contribution of  $D^{*\pm}$  mesons originating from B-hadron decays was estimated with the RAPGAP MC and was subtracted from the data. Both measurements were corrected for detector and QED radiative effects.

The corrected data, shown in figure 5, were used to fit the parameters of fragmentation functions for two classes of QCD models: 1) the leading-order + parton shower models as implemented in the Monte Carlo programs RAPGAP (used by H1) and PYTHIA (used by ZEUS), interfaced with the Lund string model for fragmentation as implemented in PYTHIA, and 2) the next-to-leading-order (NLO) QCD calculations as implemented in HVQDIS (fixed flavor number scheme) and used by H1 for DIS, and in FMNR (variable flavor number scheme) used by ZEUS for photoproduction, with charm quarks fragmented independently to  $D^{*\pm}$  mesons. For comparison of the data with NLO calculations, hadronization corrections have been applied.

The values of the fragmentation function parameters  $\varepsilon$  and  $\alpha$  extracted for the Peterson and Kartvelishvili parametrizations respectively can be found in table 1. The optimal (at  $\chi^2_{\text{min}}$ ) fragmentation parameter value depends on the settings used for other free parameters of the PYTHIA model. With the default settings, the parameters extracted by ZEUS and H1 for the  $D^{*\pm}$  jet sam-

ple are in good agreement. When using the PYTHIA parameter settings tuned by ALEPH [19] a harder fragmentation function is needed to describe the data. This can be understood as being due to a significant fraction of  $D^{*\pm}$  mesons produced in decays of higher excited charm states, provided by the ALEPH setting in contrast to the default setting. The resulting value of the Peterson parameter, extracted by H1 using the  $D^{*\pm}$  jet event sample, is in agreement with the value  $\varepsilon = 0.040$  extracted by ALEPH from their data. This result is also consistent with the hypothesis of fragmentation universality in  $ep$  and  $e^+e^-$  processes.

For H1, in case of the HVQDIS NLO calculation, the data are well described after fitting the Kartvelishvili parametrization, while when using the Peterson one no satisfactory description of the data is achieved. In the case of ZEUS, both parametrizations are able to describe the data.

FF parametrization	ZEUS: PHP	H1: DIS		
	$z_{\text{jet}}$	$D^{*\pm}$ jet sample		No $D^{*\pm}$ jet sample
		$z_{\text{jet}}$	$z_{\text{hem}}$	$z_{\text{hem}}$
PYTHIA with default parameter setting:				
Peterson ( $\varepsilon$ )	$0.064 \pm 0.06_{-0.008}^{+0.011}$	$0.061_{-0.009}^{+0.011}$	$0.049_{-0.010}^{+0.012}$	$0.010_{-0.002}^{+0.003}$
Kartvelishvili ( $\alpha$ )	—	$3.1_{-0.3}^{+0.3}$	$3.3_{-0.4}^{+0.4}$	$7.6_{-1.1}^{+1.3}$
PYTHIA with ALEPH parameter setting [19]:				
Peterson ( $\varepsilon$ )	—	$0.035_{-0.006}^{+0.007}$	$0.029_{-0.005}^{+0.007}$	$0.006_{-0.002}^{+0.002}$
Kartvelishvili ( $\alpha$ )	—	$4.3_{-0.4}^{+0.4}$	$4.5_{-0.5}^{+0.6}$	$10.3_{-1.6}^{+1.7}$
NLO calculations FMNR (PHP) and HVQDIS (DIS):				
Peterson ( $\varepsilon$ )	$0.0721_{-0.0123}^{+0.0139}$	$0.034_{-0.004}^{+0.004}$	$0.070_{-0.013}^{+0.015}$	$0.007_{-0.001}^{+0.001}$
Kartvelishvili ( $\alpha$ )	$2.87_{-0.35}^{+0.33}$	$3.8_{-0.3}^{+0.3}$	$3.3_{-0.4}^{+0.4}$	$6.0_{-0.8}^{+1.0}$

Table 1: Extracted fragmentation function parameters.

The hemisphere observable used by H1 allows to investigate charm fragmentation also close to the kinematic threshold, by selecting events which do not contain a  $D^{*\pm}$  jet above the minimal  $E_T$  cut. The corresponding normalised  $D^{*\pm}$  meson cross sections together with the prediction of RAPGAP with the Kartvelishvili FF fitted to the data are shown in figure 5 d. The extracted fragmentation function is found to be significantly harder than the one fitted to the  $D^{*\pm}$  jet sample (the dotted line). This can be interpreted as an inadequacy of the QCD model to provide a consistent description of the full phase space down to the kinematic threshold. The NLO HVQDIS calculation fails to describe this data sample.



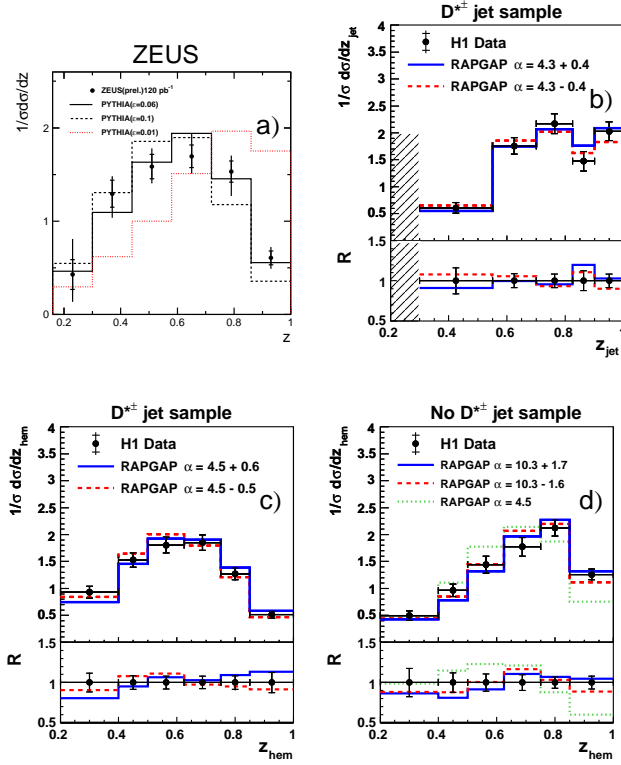


Fig. 5: Normalized  $D^{*\pm}$  meson cross sections as a function of the fragmentation observables: a)  $z_{jet}$  as measured by ZEUS, b)  $z_{jet}$  as measured by H1, c) and d)  $z_{hem}$  for the “ $D^{*\pm}$  jet” and the “no  $D^{*\pm}$  jet” samples. The full and dashed lines in the H1 sub-figures indicate a variation of  $\pm 1\sigma$  around the best fit value.

### 3 Beauty production at HERA

*Authors: S. Boutle, M. Turcato, A. Yagiies-Molina*

#### 3.1 Introduction

At HERA, beauty quarks are produced predominantly via the boson-gluon fusion process, where a photon emitted by the electron interacts with a gluon in the proton producing a  $b\bar{b}$  pair. The measurements of such interactions are directly sensitive to the gluon density in the proton. Also, perturbative calculations of these processes should be reliable since the virtuality of the exchanged photon,  $Q^2$ , in the case of deep inelastic scattering (DIS), and the large mass of the produced quark, in the case of photoproduction, provide a hard scale. Hence, the study of  $b$  quark production at HERA is a stringent test of perturbative Quantum Chromodynamics (QCD). Measurements of such processes made at HERA are relevant for the LHC since they can test the precision of the description of  $b$  quark production by theoretical calculations. They also use tagging methods and event topologies which can be used to improve experimental techniques at the LHC. In the following, recent H1 and ZEUS measurements of beauty production are presented.

#### 3.2 Measurement of beauty photoproduction using semileptonic decays into leptons.

The installation of the silicon Micro-Vertex detector [20] (MVD) in the ZEUS detector [21] during the HERA luminosity upgrade period 2000/2001 allowed the heavy flavour measurements to reach higher precision. In one such measurement, beauty quarks were tagged by identifying a muon from the  $b$  semileptonic decay. The choice of a muon provides a clean experimental signature of the events. In this measurement two variables were used to discriminate between different quark decays. The first is the relative transverse momentum,  $p_T^{\text{rel}}$ , of the muon with respect to the heavy flavour hadron which for experimental purposes is approximated to the direction of the jet associated with the muon. This variable can be used to discriminate between beauty and charm decays since the mass of the beauty quark is larger, and therefore the  $p_T^{\text{rel}}$  spectrum for muons coming from  $b$  is harder. The second variable is the signed impact parameter,  $\delta$ , of the muon track. The absolute value of  $\delta$  is given by the transverse distance of closest approach of the track to the beam spot, where the beam spot position as a function of time is evaluated as the mean position of the event vertex over a proper event range. The sign of  $\delta$  is positive if the angle between the axis of the associated jet and the line joining the beam spot to the point of closest approach of the track is less than  $90^\circ$ , and is negative otherwise. The variable  $\delta$  reflects the lifetime of the quark and hence can be used to discriminate between charm and beauty decays and the decays of light quarks. The sign allows a statistical separation of detector resolution effects from the effects of the decay lifetime of the heavy hadron.

By fitting template distributions from Monte Carlo simulations of the  $p_T^{\text{rel}}$  and  $\delta$  variables to the data, the beauty fraction in the data can be extracted and used to calculate cross sections. The distributions of the  $p_T^{\text{rel}}$  and  $\delta$  variables are shown in Fig. 6 compared to MC predictions. The data are well described by the MC simulations.

The measurement presented here is based on a data sample collected during 2005 corresponding to an integrated luminosity of  $124 \text{ pb}^{-1}$ . Photoproduction ( $Q^2 < 1 \text{ GeV}^2$ ) events with  $0.2 < y < 0.8$ , having two jets with  $p_T^{j1,j2} > 7, 6 \text{ GeV}$ ,  $|\eta^{j1,j2}| < 2.5$  and a muon with  $p_T^\mu > 2.5$

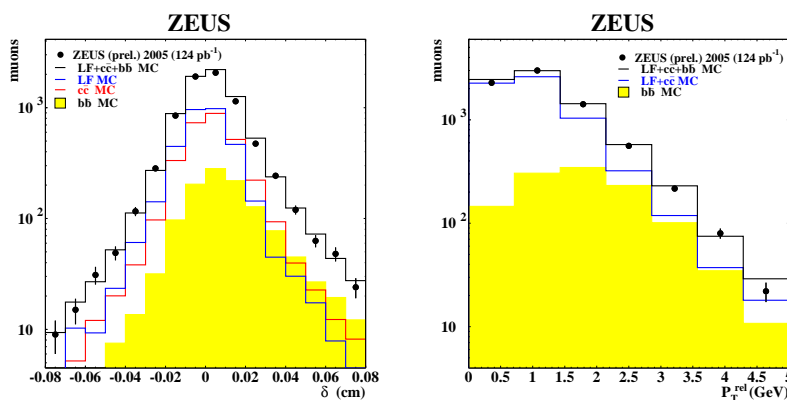


Fig. 6: Distribution of  $p_T^{\text{rel}}$  (left) and muon impact parameter  $\delta$  (right) of the data compared to the MC distributions for quarks of different flavour.

GeV and  $-1.6 < \eta^\mu < 2.3$  were selected. The event inelasticity,  $y$ , represents, in the proton rest frame, the fraction of the electron momentum which is transferred to the photon.

Figure 7 shows the distributions of the differential cross sections as a function of the muon transverse momentum,  $d\sigma/dp_T^\mu$ , and muon pseudorapidity  $d\sigma/d\eta^\mu$ . The results are compared to the ZEUS HERA-I data<sup>1</sup> [22] and to a NLO QCD prediction computed with the FMNR [14] program and corrected for hadronisation effects. The new results are in agreement with the previous measurement and compatible with NLO QCD predictions.

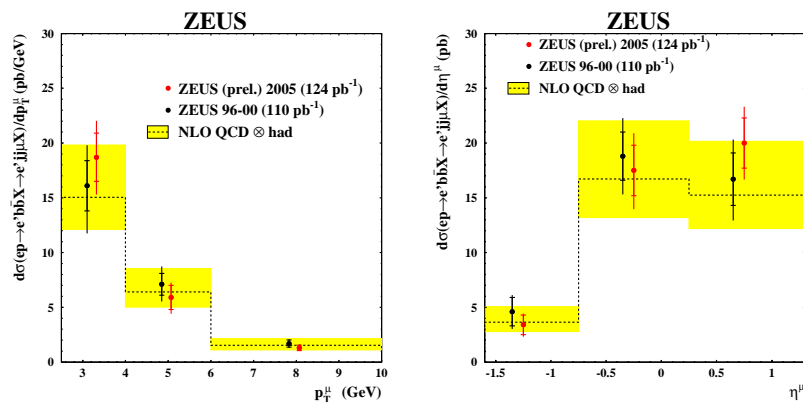


Fig. 7: Differential cross sections as a function of the muon transverse momentum,  $p_T^\mu$ , (left) and of the muon pseudorapidity,  $\eta^\mu$ , (right) for beauty photoproduction in dijet events with a muon. The measurements are compared to previous results and to NLO QCD predictions corrected for hadronisation effects.

Beauty photoproduction has been also measured using semileptonic decays to electrons or

<sup>1</sup>HERA-I refers to the data taken from 1996 to 2000 running period, previous to HERA luminosity upgrade.

positrons [23]. Tagging electrons has the advantage that lower values of the lepton transverse momentum are reachable. In this analysis, based on  $\mathcal{L} = 120 \text{ pb}^{-1}$  of HERA I data collected with the ZEUS detector from 1996 to 2000, events were selected in the photoproduction regime,  $Q^2 < 1 \text{ GeV}^2$ , having  $0.2 < y < 0.8$ , and with at least two jets with  $E_T^{j1,j2} > 7, 6 \text{ GeV}$ ,  $|\eta^{j1,j2}| < 2.5$  and an electron coming from the semileptonic  $b$  decay with  $p_T^e > 0.9 \text{ GeV}$  and  $|\eta^e| < 1.5$ . For the identification of the electrons and the extraction of the  $b$  fraction a likelihood ratio method was used combining five discriminating variables. Three of them were used mainly for the lepton identification, and are based on the ionisation energy loss of the particle in the ZEUS central drift chamber, and on other calorimeter and tracking information. The other two are the momentum of the electron candidate transverse to the jet direction,  $p_T^{\text{rel}}$ , and the azimuthal angle between the electron and the missing transverse momentum vector, which corresponds to the neutrino from the semileptonic  $b$  decay. Figure 8 shows the distributions of the differential cross sections as a function of the electron transverse momentum,  $d\sigma/dp_T^e$ , and pseudorapidity,  $d\sigma/d\eta^e$ . The data are compared with the predictions of the PYTHIA MC program, scaled by a factor 1.75, and with NLO QCD predictions from FMNR. The shape of the data is well described by both the MC and the NLO calculations. The NLO predictions describe the normalisation of the data within the large uncertainties.

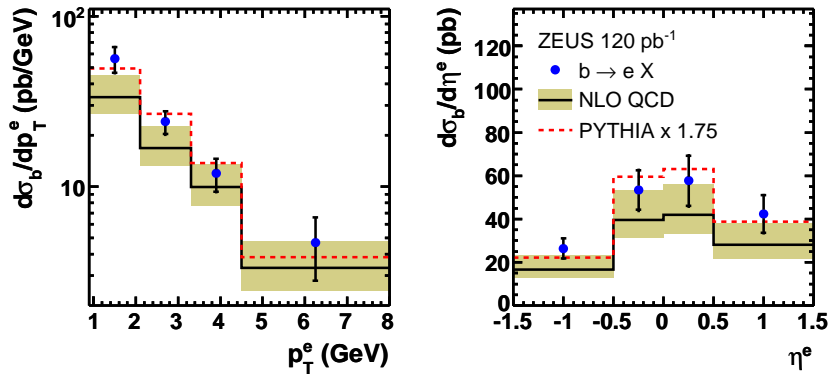


Fig. 8: Differential cross sections as a function of the transverse momentum,  $p_T^e$ , (left) and pseudorapidity,  $\eta^e$ , (right) of the electron for beauty photoproduction in dijet events with an electron. The measurements are compared to the predictions from PYTHIA as well as to NLO QCD calculations corrected for hadronisation effects.

### 3.3 Measurement of beauty dijet cross sections in photoproduction using inclusive lifetime tag.

An inclusive measurement of beauty in dijet events in the photoproduction regime [24] is presented here. The analysis is based on a sample of data collected by the H1 detector during the years 1999 and 2000 and corresponding to an integrated luminosity of  $56.8 \text{ pb}^{-1}$ . Photoproduction ( $Q^2 < 1 \text{ GeV}^2$ ) events with  $0.15 < y < 0.8$  and two jets with  $p_T^{j1,j2} > 11, 8 \text{ GeV}$  and  $-0.9 < \eta^{j1,j2} < 1.3$  were selected.

Events containing beauty quarks were distinguished from those containing only light quarks by reconstructing the signed impact parameter,  $\delta$ , of the charged tracks, i.e. their distances to the primary vertex, using precise spatial information from the H1 vertex detector. The long lifetime of  $b$  flavoured hadrons lead to larger displacements than for light quark events.

The quantities  $S_1$  and  $S_2$  are defined as the significance,  $\delta/\sigma(\delta)$ , of the track with the highest and second highest absolute significance, respectively, where  $\sigma(\delta)$  is the error on  $\delta$ . In order to reject most of the light quark background and to reduce the uncertainty due to the impact parameter resolution, the negative bins in the significance distributions were subtracted from the positive ones. To extract the beauty fraction, a simultaneous  $\chi^2$ -fit to the subtracted  $S_1$  and  $S_2$  distributions was performed (see Fig. 9). The differential cross sections as a function of  $p_T^j$  and  $\eta^j$ , shown in Fig. 10, are extracted using the scale factors obtained from the fit. The results are compared to different MC predictions and to NLO QCD calculations. The beauty cross sections are reasonably well described in shape, whereas the NLO QCD prediction seems to lie below the data.

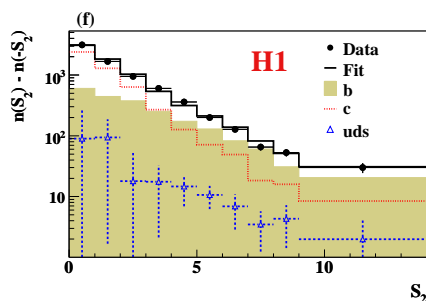


Fig. 9: Distributions of the subtracted signed significance for the sample with at least two tracks reconstructed in the Central Silicon Tracker.

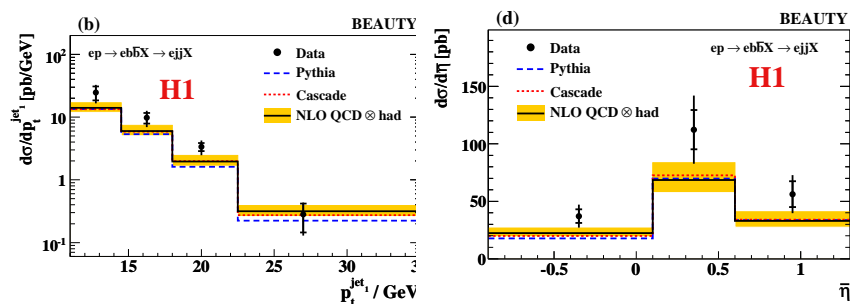


Fig. 10: Differential beauty dijet photoproduction cross sections as a function of the transverse momentum of the jet,  $d\sigma/dp_T^j$ , (left) and as a function of the jet pseudorapidity,  $d\sigma/d\eta^j$ , (right). The measurements are compared to the absolute predictions of PYTHIA and CASCADE as well as to NLO QCD calculations corrected for hadronisation effects.

### 3.4 Beauty production measurement using double tagging techniques

Beauty identification based on a single lepton tagging in dijet events is a powerful tool that allows to select a large event sample at HERA. However, the request of the presence of two jets in an event and the high background due to lighter flavour events does not allow the measurement of  $b$  quarks produced at very low transverse momenta, and therefore a total beauty cross section cannot be extracted. A way to access lower  $b$ -quark transverse momenta is to use double tagging techniques, by identifying two particles coming from the beauty decay. In this case, the cleaner event signature reduces significantly the background from non-beauty events.

An analysis [25] using this kind of approach identified beauty in events in which a  $D^*$  and a muon were found in the final state. Charm production is a background to this analysis, since a  $c\bar{c}$  pair in which one of the charm quarks hadronise into a  $D^*$  and the other produces a muon have a similar signature. However, in charm events the muon and the  $D^*$  lie in opposite hemispheres, while in the case of beauty production a muon and a  $D^*$  coming from the same  $B$  hadron lie in the same hemisphere, and in addition have opposite charges. Therefore, beauty and background can be separated by using the charge correlations and angular distributions of the muon with respect to the  $D^*$  meson.

The analysis uses a sample of  $\mathcal{L} = 114 \text{ pb}^{-1}$  of data corresponding to the full HERA I statistics collected by the ZEUS detector. The visible cross section was evaluated for unlike-sign  $D^*$ -muon events. This cross section was then extrapolated to the parton level and compared to NLO QCD predictions. No cut on the transverse momentum of the  $b$  quark,  $p_T^b$ , was imposed. The measured cross section in the kinematic region  $Q^2 < 1 \text{ GeV}^2$ ,  $\zeta^b < 1$ , where  $\zeta$  is the  $b$ -quark rapidity,  $0.05 < y < 0.85$  is

$$\sigma(ep \rightarrow b(\bar{b})X) = 11.9 \pm 2.9(\text{stat.})_{-3.3}^{+1.8}(\text{syst.}) \text{ nb}, \quad (1)$$

to be compared to a NLO QCD prediction of

$$\sigma^{NLO}(ep \rightarrow b(\bar{b})X) = 5.8_{-1.3}^{+2.1} \text{ nb}. \quad (2)$$

The measured cross section exceeds the NLO QCD prediction, but is compatible within the errors.

In another double-tagging analysis [26], events with two muons in the final state were used to study beauty production. This method has many advantages over the  $D^*\mu$  analysis. It has larger statistics due to the higher branching ratio; the kinematic region is larger allowing the extraction of the total beauty cross section with almost no extrapolation; lower background induced by charm allows  $b\bar{b}$  correlations to be measured, testing the contribution of higher orders in perturbative calculations. The analysis uses  $114 \text{ pb}^{-1}$  of HERA I data collected by the ZEUS detector. The data sample is separated into high- and low-mass (isolated and non-isolated), like- and unlike-sign muon pairs. Since beauty is the only genuine source of like-sign muon pairs and fake muon background can give rise to like- and unlike-sign pairs, the beauty contribution can be determined from the difference between the like- and unlike-sign samples.

The kinematic region for the measurement of the total cross section was kept as large as possible:  $-2.2 < \eta^\mu < 2.5$ ,  $p_T^\mu > 1.5 \text{ GeV}$  for one muon and  $p_T^\mu > 0.75 \text{ GeV}$  for the other muon, as well as  $p > 1.8 \text{ GeV}$  for  $\eta < 0.6$ , or  $(p > 2.5 \text{ GeV} \text{ or } p_T > 1.5 \text{ GeV})$  for  $\eta > 0.6$ .

Also in this case, a visible cross section was measured and then extrapolated to the total beauty cross section. DIS and photoproduction regimes were not separated. The measured total beauty cross section is

$$\sigma_{\text{tot}}(ep \rightarrow b\bar{b}X) = 13.9 \pm 1.5(\text{stat.})^{+4.0}_{-4.3}(\text{syst.}) \text{ nb.} \quad (3)$$

The NLO QCD prediction was obtained by adding the predictions from FMNR and HVQDIS [27] for the photoproduction and DIS parts, respectively:

$$\sigma_{\text{tot}}^{\text{NLO}}(ep \rightarrow b(\bar{b})X) = 7.5^{+4.5}_{-2.1} \text{ nb.} \quad (4)$$

Also in this case, the NLO QCD prediction is lower than the measured value, but compatible within the large uncertainties.

Visible differential cross sections were also measured, in the kinematic region defined by  $p_T^\mu > 1.5 \text{ GeV}$ ,  $-2.2 < \eta^\mu < 2.5$  for both the muons, in order to ensure a uniform kinematic acceptance. Figure 11 shows the the differential cross sections as a function of the muon transverse momentum,  $d\sigma/dp_T^\mu$ , and pseudorapidity,  $d\sigma/d\eta^\mu$ . The data are well described in shape by the theoretical predictions, with a tendency of the NLO QCD calculations to underestimate the normalisation of the data consistent with the observations from the total cross section.

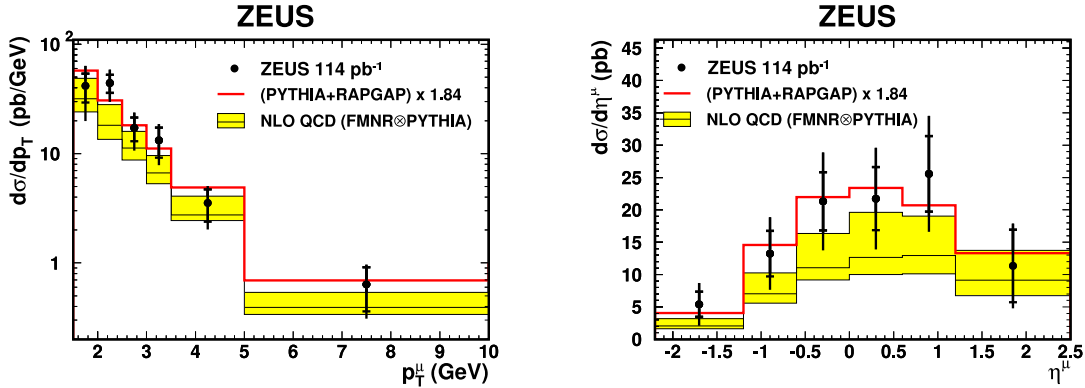


Fig. 11: Differential cross sections  $d\sigma/dp_T^\mu$  (left) and  $d\sigma/d\eta^\mu$  (right) for muons from  $b$  decays in dimuon events. The measurements (solid dots) are compared to the scaled sum of the predictions by the LO+PS generators PYTHIA and RAPGAP (histogram) and to the NLO QCD predictions from FMNR  $\otimes$  PYTHIA.

### 3.5 Conclusions

Beauty production at HERA is extensively studied using different analysis techniques. Beauty tagging with a single lepton gives a high statistics sample for the analyses, and the precision of the measurements is now comparable or better than that of the theoretical predictions. The measurements based on electron and muon tagging are affected by different systematic uncertainties, cover a slightly different kinematic region, and cross check each other. Inclusive analyses based on lifetime are also being done and will reach their full potential when the full HERAII data sample will be used. This kind of analyses are sensitive to beauty production also at large  $p_T^b$ .

For the investigation of the lower  $p_T^b$  region, double tagging techniques have been developed. In this way, the total beauty production cross section can be measured. Although these

measurements are still affected by a relatively large statistical uncertainty, they show that the difference between the observed cross sections and the theoretical predictions is not larger at lower transverse momenta.

The study of beauty production at HERA is significantly testing the precision of the perturbative QCD predictions, over a wide range in  $p_T$  and  $\eta$  of the produced  $b$  quarks. The understanding of beauty production in terms of perturbative QCD is vital for the future measurements that will be done at the large hadron collider, where a significant part of the cross section will consist on beauty.



## 4 Experimental Status of $F_2^{c\bar{c}}$ and $F_2^{b\bar{b}}$ at HERA

Authors: Philipp Roloff, Monica Turcato

### 4.1 Theoretical description

The double differential cross section versus  $x$  and  $Q^2$  for the production of a heavy quark (charm or beauty) pair,  $Q\bar{Q}$ , in deep inelastic scattering can be described by the heavy quark contributions to the proton structure functions:

$$\frac{d^2\sigma^{Q\bar{Q}}(x, Q^2)}{dx dQ^2} = \frac{2\pi\alpha^2}{Q^4 x} \left\{ [1 + (1-y)^2] F^{Q\bar{Q}}(x, Q^2) - y^2 F_L^{Q\bar{Q}}(x, Q^2) \right\}. \quad (5)$$

In the simplified picture of the quark-parton model (QPM) the electron scatters off a single quark in the proton. In this case  $x$  can be interpreted as the fraction of the proton momentum carried by the struck quark. Since heavy quarks can not exist within the proton due to their high mass, they are dominantly produced by the boson gluon fusion (BGF) process.

Heavy quark production as described above can be interpreted in two ways: on one hand it is possible to treat charm and beauty as massive quarks which are produced dynamically in the scattering process. In this case  $F_2^{c\bar{c}}$  and  $F_2^{b\bar{b}}$  provide an indirect measurement of the gluon content of the proton. On the other hand it is possible to consider the splitting of a gluon into a heavy quark pair to happen within the proton for  $Q^2 \gg (2m_Q)^2$ . Hence here  $F_2^{c\bar{c}}$  and  $F_2^{b\bar{b}}$  give the virtual charm and beauty content of the proton. As a consequence, the use of i.e.  $Z$  boson production as a luminosity monitor at the LHC requires a precise knowledge of the beauty content of the proton.

The large masses ( $m_c, m_b \gg \Lambda_{QCD}$ ) of the charm and beauty quarks provide an additional hard scale in perturbative QCD calculations. Different approaches exist to describe the multi scale problem of heavy quark production in  $ep$  collisions. In the massive or fixed flavour number scheme (FFNS) the proton contains only light quarks while charm and beauty are produced dynamically. Thus the threshold region is handled correctly, but the presence of other large scales, e.g.  $Q^2$  or the transverse momentum of the heavy quarks,  $p_T$ , can spoil the convergence of the perturbative expansion. In contrast, charm and beauty are treated as massless partons within the proton in the zero mass variable flavour number scheme (ZM-VFNS) which can improve the reliability of the calculations if one of the competing scales becomes large. An interpolation between both approaches is done in the (general mass) variable flavour number scheme (GM-VFNS) where heavy flavour production is treated as massive at low  $Q^2$  and massless at high  $Q^2$ .

While precise measurements of charm production are feasible using the large HERA II data sample, the measurements of beauty production are usually limited by the small production cross section. Since effects due to the higher beauty mass are relevant in a large part of the phase space accessible at HERA, beauty production might help to improve the understanding of mass effects for heavy quark production in deep inelastic scattering. A possible scenario is to “calibrate” theory predictions using beauty production and apply the improvements to charm for the extraction of the gluon content of the proton.

## 4.2 Experimental results on $F_2^{c\bar{c}}$

The charm contribution to the proton structure function  $F_2$ ,  $F_2^{c\bar{c}}$ , has been measured at HERA by the two Collaborations ZEUS [28–31] and H1 [32–35], in a wide kinematic region in  $x$  ( $0.00002 \lesssim x \lesssim 0.03$ ) and in the photon virtuality,  $Q^2$  ( $1 < Q^2 < 1000 \text{ GeV}^2$ ).

Charm production at HERA can be tagged in different ways. In the so-called *golden mode* a  $D^*(2010)$  meson is reconstructed through its decay  $D^{*+} \rightarrow D^0 \pi^+ \rightarrow K^- \pi^+ \pi^+$  (+c.c.). Other charmed mesons can also be reconstructed: the most copiously produced are  $D^0$ ,  $D^\pm$ ,  $D_s$ . The production cross sections of all these mesons can be measured in a defined kinematic region, and the total charm cross section can then be extracted by extrapolating the measurements to the full phase space. This extrapolated cross section is then used to evaluate  $F_2^{c\bar{c}}$ . Both the ZEUS and the H1 Collaborations have used this method to extract  $F_2^{c\bar{c}}$  from  $D$  mesons cross sections. Charm tagging with mesons gives a clean signature of charm production, but the extrapolation to the total charm cross section can be large, especially in the low  $Q^2$  region (as an example, at ZEUS typical extrapolation factors range from  $\sim 4$  in the low- $Q^2$ , low- $x$  region to 1.5 at high- $Q^2$  [28]).

An alternative method to tag charm production takes advantage of the long lifetime of the charmed particles, by reconstructing secondary vertices from  $D$ -meson decay products, or, in inclusive analyses, by identifying tracks having impact parameter,  $\delta$ , significantly displaced from the event vertex. The secondary vertex reconstruction for  $D^\pm$  and  $D^0$  mesons has been used by the ZEUS Collaboration to enhance the signal to background ratio, and therefore the statistical precision, of the measurement [31]. On the other side, fully inclusive analyses use the significance of the impact parameter of the highest impact parameter tracks to separate charm and beauty from light flavour production [33, 34], since heavy flavours show a longer tail in the positive side of this distribution. The fraction of charm and beauty in an inclusive data sample can therefore be extracted by fitting the significance distribution to the contributions from beauty, charm, and lighter quarks. This method has been used by the H1 Collaboration to obtain some of the results presented here [33–35].

The advantage of the inclusive method is that the kinematic region for the measurement of charm production is significantly enlarged, and therefore the extrapolation needed for the measurement of  $F_2^{c\bar{c}}$  is strongly reduced.

The program HVQDIS [27] is the only program which is able to provide theoretical predictions for  $D$  meson production cross sections at NLO accuracy in perturbative QCD. It was used by the ZEUS and H1 Collaborations to extrapolate the measured cross section for a particular  $D$  meson final state to  $F_2^{c\bar{c}}$ . In this program, the production of heavy flavours is performed using the fixed flavour number scheme. The ZEUS and H1 measurements of  $F_2^{c\bar{c}}$  extracted in this way should therefore be compared with NLO QCD predictions evaluated in the FFNS.

The results for  $F_2^{c\bar{c}}(x, Q^2)$  are shown in Fig. 12. In the figure the ZEUS and H1 measurements, obtained from charmed meson production, are compared with the H1 results from inclusive lifetime measurements. The agreement between the experiments is good, validating the two different analysis procedures. The data rise with increasing  $Q^2$ , with the rise becoming steeper at lower  $x$ .

The data are also compared with perturbative QCD predictions at NLO. Two different parameterisations of the proton PDFs have been used for the NLO QCD calculations, in or-

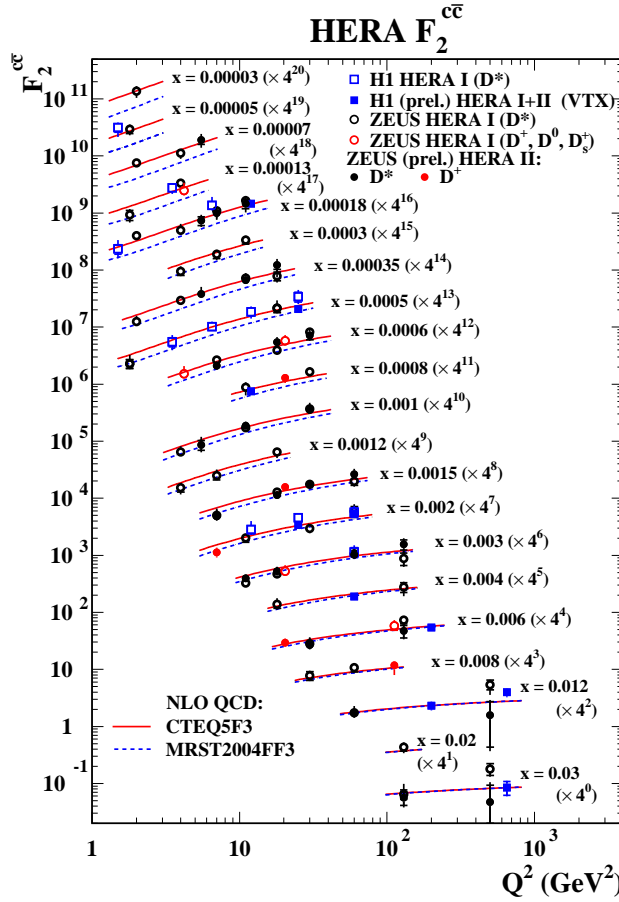


Fig. 12: The measured  $F_2^{c\bar{c}}$  at  $x$  values between 0.00003 and 0.03 as a function of  $Q^2$ . The data are shown with statistical uncertainties (inner bars) and statistical and systematic uncertainties added in quadrature (outer bars). The data are compared with next-to-leading order QCD predictions, evaluated using different proton PDFs.

der to check the sensitivity of the predictions to different gluon densities: CTEQ5F3 [36] and MRST2004FF3 [37]. The charm data are in general well described by NLO QCD: this shows that the proton PDFs, which are extracted mainly from inclusive scattering data, are also able to describe reasonably well charm production. The two PDFs show differences in the low  $x$  region, demonstrating the sensitivity of the measurement to different parameterisation of the gluon density in the proton.

### 4.3 Experimental results on $F_2^{b\bar{b}}$

The beauty contribution to the inclusive structure function  $F_2$  was measured by the ZEUS Collaboration using muons and jets and by the H1 Collaboration from lifetime information of displaced tracks.

The ZEUS Collaboration measured beauty production in events with a muon and a jet,

using a data sample of  $\mathcal{L} = 39 \text{ pb}^{-1}$ . The fraction of beauty quarks in the data was derived using the distribution of the transverse momentum of the muon relative to the axis of the associated jet,  $p_T^{\text{rel}}$  [38]. Due to the larger mass of the beauty quark, muons originating from  $b$  decays tend to higher values of  $p_T^{\text{rel}}$  compared to muons from charm and light flavour decays. The beauty contribution to  $F_2$ ,  $F_2^{bb}$ , was obtained by extrapolating the double differential cross sections as a function of  $Q^2$  and  $x$  to the full phase space using the HVQDIS program, as for the extraction of  $F_2^{c\bar{c}}$  from the visible cross sections for  $D$  meson production. Here extrapolation factors between 3 and 6 decreasing with  $Q^2$  had to be applied.

The H1 collaboration extracted  $F_2^{bb}$  in a fully inclusive analysis based on information from the Central Silicon Tracker. The impact parameter significance of tracks in the transverse plane was used in a fit to extract the (charm and) beauty fractions in the considered data sample [35]. Due to the long lifetime of the  $B$  hadrons, it is possible to distinguish the position of the decay vertices of these particles from the primary interaction vertex. As a consequence, tracks originating from beauty decays exhibit large positive impact parameters compared to tracks coming from lighter quarks. An advantage of the inclusive lifetime method is that the extrapolation to the full phase space is smaller. Recent results from the HERA II period were combined with earlier measurements [33, 34].

The results obtained by the H1 and ZEUS Collaborations are summarised in Fig. 13. The reduced cross section

$$\tilde{\sigma}^{b\bar{b}} = F_2^{b\bar{b}} - \frac{y^2}{1 + (1 - y)^2} F_L^{b\bar{b}}, \quad (6)$$

is shown as a function of  $x$  for different values of  $Q^2$ . Although very different methods have been used, the results are in agreement within the large errors.

The data are compared to NLO QCD predictions using different schemes [39]. The CTEQ5F4 [36] is done in the FFNS, while MRST04 [40], MRST NNLO [41] and CTEQ6.5 [42] implement the VFNS. At low values of  $Q^2$  and  $x$  the predictions of the CTEQ and MRST groups differ up by a factor two, but the present statistical accuracy of the data does not allow to discriminate between the different calculations. A better precision of the data is needed in order to better understand the different aspects of the theoretical calculations and to disentangle between different approaches.

#### 4.4 Conclusions and outlook

Both experiments, H1 and ZEUS, collected a data sample of about  $0.5 \text{ fb}^{-1}$ . The analysis of the full HERA I+II dataset will increase the available statistics by a factor of 2 to 10, depending on the analysis. The combination of different heavy flavour tagging methods (e.g. different  $D$  mesons for charm, different leptons for beauty, inclusive analyses) can further improve the precision of the measurements, keeping also into account the fact that the systematic uncertainties of different tagging techniques are at least partially uncorrelated. The final step is the combination of the ZEUS and H1 data into a single measurement: this will again double the available dataset.

New detector components, which allow to extend the kinematic range of the  $F_2^{c\bar{c}}$  and  $F_2^{b\bar{b}}$  measurements, were installed for the HERA II data taking period. The forward region can be studied using the ZEUS Straw Tube Tracker and Forward Microvertex Detector while the H1

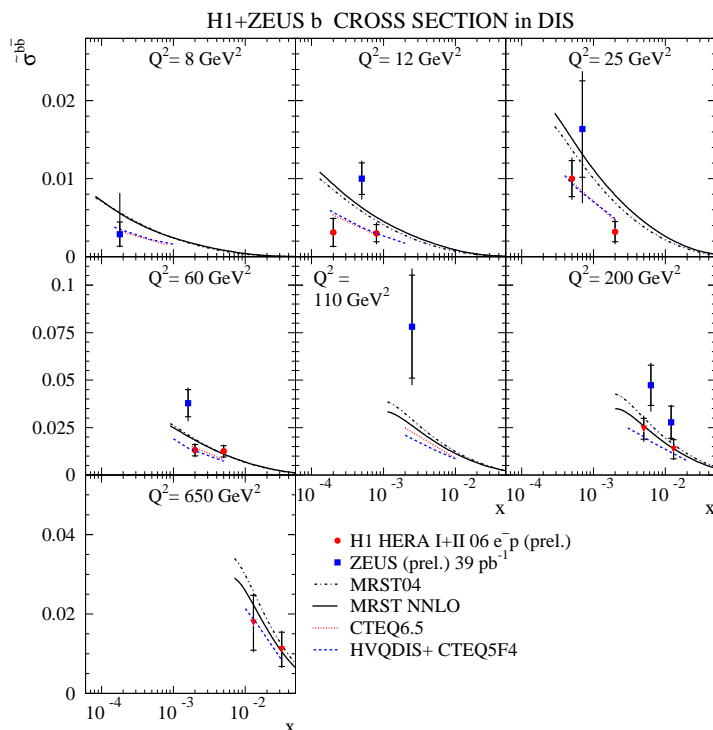


Fig. 13:  $\sigma^{b\bar{b}}$  as a function of  $x$  for different values of  $Q^2$ . The inner error bars represent the statistical uncertainties only while the outer error bars correspond to statistical and systematic uncertainties added in quadrature. Different predictions are compared to the data.

Backward Silicon Tracker gives access to the backward region.

Significant improvement in the precision of the measurements is therefore possible and will be reached by the final HERA analyses. The new beauty measurements will be of help to understand some aspects of the theory that will be then implemented for the description of charm production. A final combined ZEUS+H1 measurement of charm production could be used in the PDF fits and will hopefully help to learn something more on the gluon density in the proton.

## References

- [1] H1 Collaboration, H1prelim-08-072,  
[https://www-h1.desy.de/publications/H1preliminary.short\\_list.html#HQ](https://www-h1.desy.de/publications/H1preliminary.short_list.html#HQ), 2008.
- [2] H1 Collaboration, A. Aktas *et al.*, Eur. Phys. J. **C 51**, 271 (2007).
- [3] H1 Collaboration, H1prelim-08-073,  
[https://www-h1.desy.de/publications/H1preliminary.short\\_list.html#HQ](https://www-h1.desy.de/publications/H1preliminary.short_list.html#HQ) (2008).
- [4] H1 Collaboration, A. Aktas *et al.*, arXiv 0808.1003 (hep-ex) 2008.

- [5] ZEUS Collaboration, ZEUS-prel-07-008,  
[http://www-zeus.desy.de/physics/hfla/public/abstracts07/paper/f2charm\\_zeus\\_EPSPaper\\_106.ps](http://www-zeus.desy.de/physics/hfla/public/abstracts07/paper/f2charm_zeus_EPSPaper_106.ps), 2008.
- [6] ZEUS Collaboration, S. Chekanov et al., Phys. Lett. **B649**, 111-121 (2007).
- [7] ZEUS Collaboration, S. Chekanov et al., DESY-08-129, arXiv:0807.1290 [hep-ex] (2008).
- [8] ZEUS Collaboration, S. Chekanov et al., JHEP **0707**, 74 (2007).
- [9] ZEUS Collaboration, ZEUS-prel-07-010,  
<http://www-zeus.desy.de/physics/hfla/public/abstracts07/>, 2008.
- [10] A. Baird et al., IEEE Trans. Nucl. Sci. **48**, 1276 (2001).
- [11] A. Schöning, Nucl. Instr. and Meth. **A518**, 542 (2004).
- [12] A.W. Jung et al., *First Results from the Third Level of the H1 Fast Track Trigger*, Proc. of the 2007 IEEE NPSS RealTime Conference, Chicago, USA, 2007.
- [13] H1 Collaboration, A. Aktas et al., Eur. Phys. J. **C 50**, 251 (2006).
- [14] S. Frixione, M.L. Mangano, P. Nason and G. Ridolfi, Phys. Lett. **B 348**, 633 (1995).
- [15] U. Bassler, G. Bernardi, Nucl. Instr. and Meth. **A361**, 197 (1995).
- [16] H. Jung, PDF4MC, <http://indico.cern.ch/conferenceDisplay.py?confId=36364>, 2008.
- [17] H1 Collaboration, A Aktas et al., *Study of Charm Fragmentation into  $D^{*\pm}$  Mesons in Deep-Inelastic Scattering at HERA*, [arXiv:0808.1003], submitted to Eur. Phys. J. C
- [18] S. Fang [ZEUS Collaboration], “Charm fragmentation function and charm fragmentation fractions at ZEUS,” Proceedings DIS 2007, Munich, Germany, April 16 – 20, Eds. G. Grindhammer and K. Sachs, 10.3360/dis.2007.147
- [19] ALEPH Collaboration, S. Schael et al., Phys. Lett. **B 606**, 265 (2005); G. Rudolph [ALEPH collaboration], private communication.
- [20] E.N. Koffeman et al., Nucl. Instrum. Meth. **A 453**, 89 (2000).  
D. Dannheim et al., Nucl. Instrum. Meth. **A 505**, 663 (2003).
- [21] ZEUS Collaboration, U. Holm(ed.), *The ZEUS Detector*. Status Report (Unpublished), DESY (1993), available on  
<http://www-zeus.desy.de/bluebook/bluebook.html>
- [22] ZEUS Collaboration, S. Chekanov et al., Phys. Rev. **D 70**, 012008 (2004).
- [23] ZEUS Collaboration, S. Chekanov et al., DESY-08-056 (May 2008).
- [24] H1 Collaboration, A. Aktas et al., Eur. Phys. J. **C47**, 597-610 (2006).

- [25] ZEUS Collaboration, S. Chekanov *et al.*, Eur. Phys. J. **C50** 299-314 (2007).
- [26] ZEUS Collaboration, S. Chekanov *et al.*, DESY-08-129 (2008).
- [27] B.W. Harris and J. Smith, Phys. Rev. **D 57**, 2806 (1998).
- [28] ZEUS Collaboration, S. Chekanov *et al.*, Phys. Rev. **D 69**, 012004 (2004).
- [29] ZEUS Collaboration, S. Chekanov *et al.*, JHEP **07**, 074 (2007).
- [30] M. Turcato [ZEUS Collaboration], Proc. of the 2007 Europhysics Conference on High Energy Physics, Manchester, England, July 2007,  
[http://www.iop.org/EJ/article/1742-6596/110/2/022054/jpconf8\\_110\\_022054.pdf](http://www.iop.org/EJ/article/1742-6596/110/2/022054/jpconf8_110_022054.pdf)
- [31] D. Nicholass [ZEUS Collaboration], Proc. of 15th Int. Workshop on Deep-Inelastic Scattering and Related Subjects, Munich, April 2007, <http://dx.doi.org/10.3360/dis.2007.145>
- [32] H1 Collaboration, A. Aktas *et al.*, Phys. Lett. **B 528**, 199 (2002).
- [33] H1 Collaboration, A. Aktas *et al.*, Eur. Phys. J. **C 45**, 23 (2006).
- [34] H1 Collaboration, A. Aktas *et al.*, Eur. Phys. J. **C 40**, 349 (2005).
- [35] H1 Collaboration, *Submitted to the 23rd International Symposium on Lepton-Proton Interactions at High Energy, LP2007*, Daegu, Republic of Korea, August 13-18, 2007.
- [36] CTEQ Collaboration, Eur. Phys. J. **C 12**, 375 (2000).
- [37] A. D. Martin, W. J. Stirling and R. S. Thorne, Phys. Lett. **B 636**, 259 (2006).
- [38] B. Kahle [ZEUS Collaboration], Proc. of 15th Int. Workshop on Deep-Inelastic Scattering and Related Subjects, Munich, April 2007, <http://dx.doi.org/10.3360/dis.2007.164>
- [39] P.D. Thompson, arXiv:hep-ph/0703103v1, 2007.
- [40] A.D. Martin *et al.*, Eur. Phys. J. **D 73**, 050419 (2006).
- [41] R.S. Thorne, Phys. Rev. D **73**, 050419 (2006).
- [42] W.K. Tung *et al.*, JHEP **02**, 259 (2006).

# Experimental study of heavy flavour production at RHIC and LHC

*M. Biasini<sup>a</sup>, C. Bombonati<sup>b</sup>, G.E. Bruno<sup>c</sup>, E. Lytken<sup>d</sup>, A. Mischke<sup>e</sup>, C. Rosemann<sup>f</sup>,  
A. Starodumov<sup>g,\*</sup>, D. Stocco<sup>h</sup>, R. Wolf<sup>f</sup>, and M. zur Nedden<sup>i</sup>*

<sup>a</sup> University and INFN, Perugia, Italy

<sup>b</sup> University and INFN, Padua, Italy

<sup>c</sup> University and INFN, Bari, Italy

<sup>d</sup> CERN, Geneva, Switzerland

<sup>e</sup> Institute for Subatomic Physics, Faculty of Science, Utrecht University, Utrecht, the Netherlands

<sup>f</sup> Inst. für Experimentalphysik, Universität Hamburg and DESY, Germany

<sup>g</sup> Paul Scherrer Institut, PSI Villigen, Switzerland

<sup>h</sup> University and INFN, Torino, Italy

<sup>i</sup> Humboldt-University of Berlin, Germany

## Abstract

After reviewing the main heavy flavour results from experiments at the Relativistic Heavy Ion Collider (RHIC), we present the expected performance for some of the most significant measurements in the heavy flavour sector at the Large Hadron Collider (LHC), for the experiments ALICE, ATLAS, and CMS.

*Coordinator: A. Dainese*

## 1 Heavy flavour physics at RHIC

*Author: A. Mischke*

### 1.1 Introduction

Measurements at RHIC have revealed strong modification of the jet structure in high-energy nuclear collisions due to the interaction of hard scattered partons with the hot and dense medium created in these reactions. The study of heavy-quark (charm and bottom) production in the medium offers unique opportunities for the investigation of the properties of the Quark-Gluon Plasma (QGP). Heavy quarks are believed to be produced predominantly in hard scattering processes in the early stage of the collision, and they probe the produced medium as they propagate through it [1]. Due to their higher mass, the penetrating power is much higher for heavy quarks than for light quarks, providing a sensitive probe of the medium. The energy loss of heavy quarks in the medium is expected to be smaller compared to light quarks due to the mass dependent suppression of the gluon radiation under small angle, known as the dead-cone effect [2, 3].

---

On leave from ITEP, Moscow, Russia



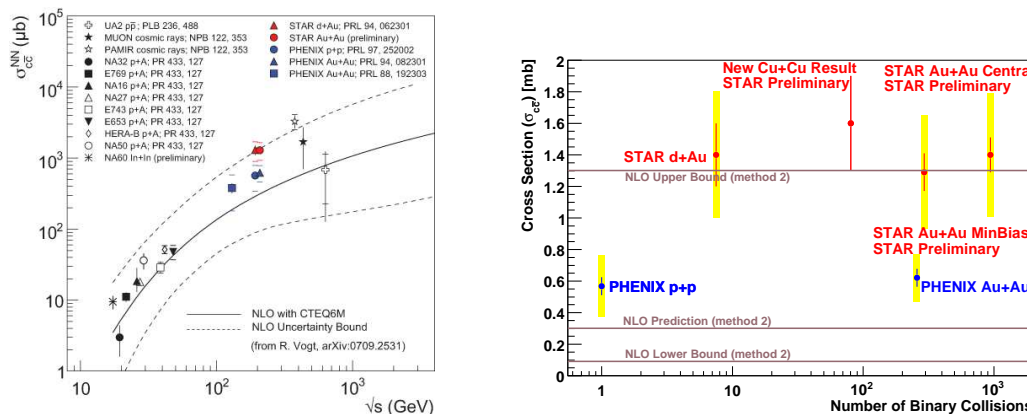


Fig. 1: (left panel) Comparison of total charm cross section measurements. The STAR (red symbols in on-line version) and PHENIX results (blue symbols in on-line version) are given as cross section per binary collisions. The dashed curves depict the uncertainty bands of the NLO calculations. (right panel) Total charm cross section divided by the number of binary collisions for different collisions systems, compared to NLO calculations (horizontal lines).

## 1.2 Total charm cross section

The total charm cross section is currently determined through basically three different measurements: direct reconstruction of  $D$  mesons, muons and electrons. Electron identification in the PHENIX experiment is based on the Ring Imaging Cherenkov detector (RICH) in conjunction with a highly granular calorimeter. The particle momentum is measured by drift and pad chambers. The subtraction of the electron background (mainly from photons,  $\pi^0$  and  $\eta$ ) is performed by the converter and the cocktail methods [4, 5], which give similar results. In the STAR experiment, electrons are identified using the  $dE/dx$  and momentum measurements from the TPC together with the Time of Flight (ToF) information at low  $p_T$  ( $< 4 - 5$  GeV/c) and energy ( $E$ ) and shower shape measurement in the electromagnetic calorimeter (EMC) at high- $p_T$  ( $> 1.5$  GeV/c). The background contribution to the electrons from photonic sources are subtracted statistically [6].

The total charm cross section is extracted from a combined fit to the measured particle spectra. The STAR data are from combined fits to hadronic and semileptonic decay data. The PHENIX data are from semileptonic decay measurements only. The total cross sections from STAR and PHENIX are compared to results at other energies and to NLO calculations [7] in Fig. 1 (left panel). The discrepancy between STAR and PHENIX is under investigation. The data agree with the NLO prediction on the total charm cross section. The large theoretical uncertainty leads to a little predictive power in the total charm cross section. Fig. 1 (right panel) depicts the charm cross section divided by the number of binary collisions for different collisions systems. Within errors, the charm cross section for the different collisions systems follows binary collisions scaling, supporting the assumption that charm is predominantly produced by hard scattering in the initial state of the collision.

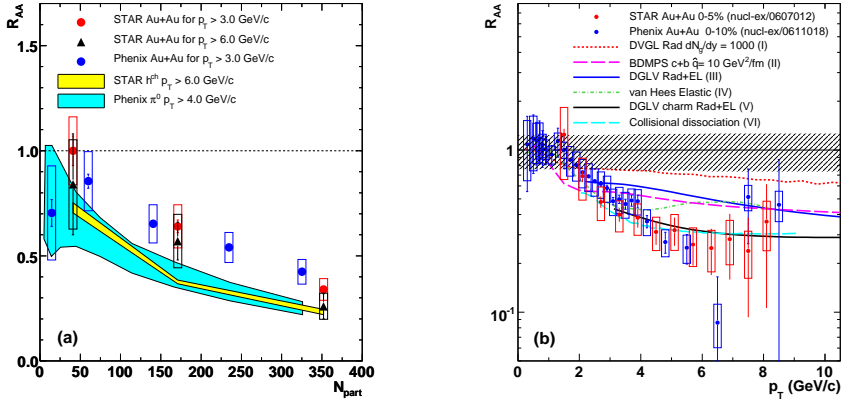


Fig. 2: Nuclear modification factor  $R_{AA}$  of non-photonic electrons in Au+Au collisions. (a)  $R_{AA}$  as a function of  $N_{part}$ . (b)  $R_{AA}$  as a function of  $p_T$  for the most central collisions.

### 1.3 Heavy-quark energy loss in hot and dense QCD matter

Nuclear effects are typically quantified using the nuclear modification factor  $R_{AA}$  where the particle yield in Au+Au collisions is divided by the yield in  $pp$  reactions scaled by the number of binary collisions.  $R_{AA} = 1$  would indicate that no nuclear effects, such as Cronin effect, shadowing or gluon saturation, are present and that nucleus-nucleus collisions can be considered as a incoherent superposition of nucleon-nucleon interactions. The average  $R_{AA}$  for high- $p_T$  non-photonic electrons as a function of participating nucleons ( $N_{part}$ ) is illustrated in Fig. 2(a). The STAR and PHENIX  $R_{AA}$  for non-photonic electrons are consistent with each other and shows an increasing suppression from peripheral to central Au+Au collisions, indicating an unexpectedly energy loss of heavy quarks in the medium in contradiction to expectations from the dead-cone effect. The suppression is similar to the one observed for light-quark hadrons, indicated by the shaded area in the figure. Fig. 2(b) shows the  $p_T$  dependence  $R_{AA}$  of non-photonic electrons in central Au+Au collisions. A strong suppression of a factor of  $\sim 5$  is observed for  $p_T > 6$  GeV/c. The  $R_{AA}$  is compared to several theoretical model calculations [4, 6]. The observed suppression is overpredicted by the models using reasonable model parameters. The data is described reasonably well if the bottom contribution to the electrons is assumed to be small. Therefore, the observed discrepancy could indicate that the  $B$  dominance over  $D$  mesons starts at higher  $p_T$ . A possible scenario for  $B$  meson suppression invokes collisional dissociation in the medium.

### 1.4 Heavy-quark azimuthal correlations

The measurement of the relative charm and bottom contributions to the non-photonic electrons is essential for the interpretation of the non-photonic electron spectra. Azimuthal angular correlations between non-photonic electrons and hadrons allow to identify the underlying production process [8]. Heavy flavours have, in general, a harder fragmentation function than gluons and light quarks, making the near-side correlation more sensitive to the decay kinematics. For the same electron transverse momentum the near-side  $e$ -hadron angular correlation from  $B$  decays is much broader than that from  $D$  decays. Fig. 3 (left panel) shows the azimuthal correlation

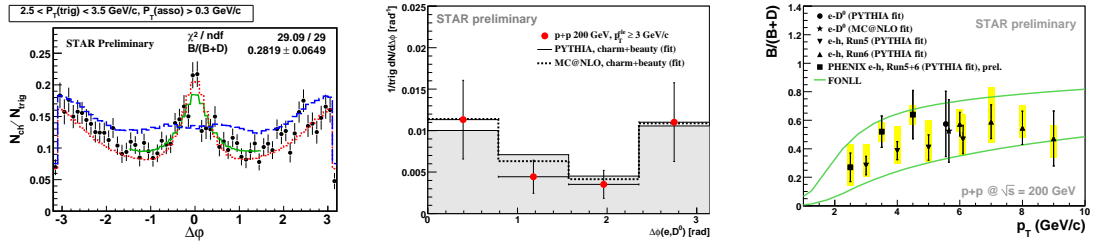


Fig. 3: (left panel)  $e$ –hadron azimuthal correlation distribution in 200 GeV  $pp$  collisions, compared to PYTHIA simulations (colored curves). (middle panel)  $e-D^0$  azimuthal correlation distribution for like-sign  $e-K$  pairs. The grey histogram (dashed line) illustrates results from PYTHIA (MC@NLO) simulations. (right panel) Relative bottom contribution to the total non-photonic electron yield derived from  $e-D^0$  and  $e$ –hadron correlations, compared to the uncertainty band from a FONLL calculation.

function of non-photonic electrons and hadrons in  $pp$  collisions at  $\sqrt{s} = 200$  GeV. The data is fitted with a linear combination of the simulated charm and bottom distribution, obtained from PYTHIA simulations, to extract the relative bottom contribution  $B/(B+D)$ . Similar studies are performed for  $e-D^0$  azimuthal correlations [8] (cf. Fig. 3, middle panel). Moreover, it has been shown that higher order sub-processes like gluon splitting may have a significant contribution to the near-side correlation. This contribution is studied by indentifying the  $D^*$  content of jets [8]. The results indicate that gluon splitting to  $c\bar{c}$  pairs contributes about 5% of the open charm production observed at RHIC, consistent with predictions from MC@NLO calculations [9].

The relative bottom contribution  $B/(B+D)$  is shown in Fig. 3 (right panel) together with predictions from FONLL calculations [10]. These data provide convincing evidence that bottom contributes significantly ( $\sim 50\%$ ) to the non-photonic electron yields at high- $p_T$ . Further studies have to show whether these findings imply substantial energy loss of bottom quarks in the produced medium.

## 1.5 Summary and conclusions

The measured total charm cross section follows binary collisions scaling as expected from the assumption that charm is produced exclusively in initial hard scattering processes. The high- $p_T$  suppression of the non-photonic electron yield in Au+Au collisions is much larger than expected. Theoretical explanations are yet inconclusive. The bottom contribution in the non-photonic electron spectrum is studied by  $e$ –hadron and  $e-D^0$  correlations. First measurements on the charm content in jets shows that the gluon splitting contribution is small at RHIC. Detailed and systematic studies will be possible with heavy flavour measurements in the ALICE experiment at the CERN-LHC [11].

### Acknowledgments

The author thanks the organizers for the stimulating atmosphere during the workshop. This work is supported by a Veni grant from the Netherlands Organization for Scientific Research (project number: 680-47-109).

## 2 Heavy flavour program of the ALICE experiment at the LHC

*Authors: C. Bombonati, G.E. Bruno, and D. Stocco*

### 2.1 Introduction

The Large Hadron Collider (LHC) will produce proton–proton, Pb–Pb, other lighter systems like Ar–Ar and proton induced nucleus collisions up to the energies corresponding to the maximum magnetic rigidity of 23,350 Tm (e.g., proton–proton and Pb–Pb collisions at centre-of-mass energy per nucleon–nucleon  $\sqrt{s_{NN}} = 14$  TeV and 5.5 TeV, respectively). ALICE [12, 13] is the dedicated heavy-ion experiment at the LHC; its main physics goal is the study of strongly-interacting matter in the conditions of high-energy density ( $> 10 \text{ GeV fm}^{-3}$ ) and high temperature ( $\gtrsim 0.2 \text{ GeV}$ ) over large volume ( $10^2\text{--}10^3 \text{ fm}^3$ ), expected to be reached in central Pb–Pb collisions. The ALICE apparatus [12, 13] has excellent capabilities for heavy-flavour measurements, for both open heavy-flavoured hadrons and quarkonia. In this paper, we shall limit the discussion to the detection of open charm and beauty in the central barrel (section 2.2) and of quarkonium states at forward rapidity (section 2.4), with an emphasis on the proton–proton collisions. Therefore only the detectors involved in these analyses are described in the following.

The ALICE central barrel covers the pseudo-rapidity region  $-0.9 < \eta < 0.9$  and is equipped with tracking detectors and particle identification systems embedded in a magnetic field  $B = 0.5 \text{ T}$ . The combined information from the central barrel detectors allows to track charged particles down to low transverse momenta (low  $p_T$  cut-off  $\approx 100 \text{ MeV}/c$ ) and provides hadron and electron identification as well as an accurate measurement of the positions of the primary (interaction) vertex and of the secondary (decay) vertices. The main tracking detector is the Time Projection Chamber (TPC) which provides track reconstruction and particle identification via  $\frac{dE}{dx}$ . The Inner Tracking System (ITS) is the innermost central barrel detector and is composed of six cylindrical layers of silicon detectors. The two layers closest to the beam pipe (at radii of  $\approx 4$  and  $7 \text{ cm}$ ) are equipped with pixel detectors, the two intermediate layers (radii  $\approx 15$  and  $24 \text{ cm}$ ) are made of drift detectors, while strip detectors are used for the two outermost layers (radii  $\approx 39$  and  $44 \text{ cm}$ ). The ITS is a key detector for open heavy-flavour studies because it allows to measure the track impact parameter (i.e. the distance of closest approach of the track to the primary vertex) with a resolution better than  $50 \mu\text{m}$  for  $p_T > 1.3 \text{ GeV}/c$ , thus providing the capability to detect the secondary vertices originating from heavy-flavour decays. Two other systems play an important role in the heavy-flavour analyses as far as particle identification is concerned. They are the Transition Radiation Detector (TRD) for high-momentum electron identification and the Time-Of-Flight (TOF) for pion, kaon and proton separation. All these four detectors have full azimuthal coverage.

The detection of heavy quarkonia in the di-muonic decay channel is performed by the ALICE Muon Spectrometer in the forward pseudo-rapidity region  $2.5 < \eta < 4$ . The detector consists of five tracking stations with two planes of Multi-Wire Proportional Chambers each, with a spatial resolution of about  $100 \mu\text{m}$ , a dipole magnet with an integral field of  $3 \text{ Tm}$  and two trigger stations of Resistive Plate Chambers placed behind an iron-wall muon filter with a thickness of about 7 interaction lengths. The system is completed by a front absorber of composite material, predominantly made of carbon and concrete, which is placed at  $90 \text{ cm}$  from the

interaction vertex to reduce the free decay length of pions and kaons, and a beam shield made of tungsten, lead and stainless steel to protect the chambers from particles and secondaries produced at large rapidities. The spectrometer can detect quarkonia down to  $p_T = 0$  and is designed to achieve an invariant-mass resolution of 70 (100) MeV/ $c^2$  at 3 (10) GeV/ $c^2$ , needed to resolve the  $J/\psi$  ( $\Upsilon$ ) resonances.

## 2.2 Open heavy flavour in the ALICE Central Barrel

Heavy flavours are produced in initial parton-parton interactions, in the early stage of the collision. Their production can be calculated to a reasonable degree of precision within pQCD and they offer the possibility to explore the properties of the medium created in the collision with probes of known mass and colour charge. The energy loss by gluon radiation, for instance, is expected to be parton-specific (stronger for gluons than for quarks due to the larger colour charge of gluons) and flavour-specific (stronger for lighter than for heavier quarks, due to the dead cone effect [14, 15]). In addition, the measurement of open heavy-flavour production is of an essential practical interest for quarkonium physics as well, both as a natural reference and B meson decays being a sizable source of non-prompt  $J/\psi$  in high energy collisions.

In figure 4 we compare schematically the ALICE  $p_T$  vs.  $\eta$  acceptance for charm (c) and beauty (b) hadrons to that of the other LHC experiments, for proton–proton collisions at  $\sqrt{s} = 14$  TeV. In this plot the high  $p_T$  reach is the one expected for one year of running at nominal luminosity (note that the value of the luminosity is different for each experiment:  $10^{34}$  cm $^{-2}$ s $^{-1}$  for ATLAS and CMS,  $2\text{--}5 \times 10^{32}$  cm $^{-2}$ s $^{-1}$  for LHCb, and  $3 \times 10^{30}$  cm $^{-2}$ s $^{-1}$  for ALICE). ATLAS and CMS have similar acceptance for beauty measurements. On one hand, their minimum accessible  $p_T$  is larger than for ALICE because of the strong magnetic fields and the larger material budget in the inner tracking detectors; on the other hand, the strong magnetic fields, together with the high luminosity, allow those experiments to cover transverse momenta up to 200–300 GeV/ $c$ . In terms of acceptance for beauty measurements, ALICE overlaps with ATLAS and CMS at central rapidity and with LHCb at forward rapidity. The moderate magnetic field allows measurements down to transverse momenta of less than 1 GeV/ $c$  for charmed and beauty hadrons in the central barrel<sup>1</sup>.

For the performance study presented here, we assume the baseline heavy-flavour production cross sections and yields presented in the ALICE Physics Performance Report, Volume II [13]. Those values are obtained from the pQCD calculations at fixed next-to-leading-order (FO NLO) implemented in the HVQMNR program [16]; note that the cross sections have a theoretical uncertainty of about a factor 2 [13].

### 2.2.1 Exclusive charm meson reconstruction

Among the most promising channels for open charm detection are the  $D^0 \rightarrow K^- \pi^+$  ( $c\tau \approx 120$   $\mu$ m, branching ratio  $\approx 3.8\%$ ) and  $D^+ \rightarrow K^- \pi^+ \pi^+$  ( $c\tau \approx 300$   $\mu$ m, branching ratio  $\approx 9.2\%$ ) decays. The detection strategy to cope with the large combinatorial background from the underlying event in Pb–Pb is based on the selection of displaced-vertex topologies [13,

---

<sup>1</sup>The study of the channel  $B \rightarrow J/\psi + X$ , discussed in section 2.3, should allow a determination of the  $p_T$  differential cross section of B hadrons down to  $p_T \approx 0$ .

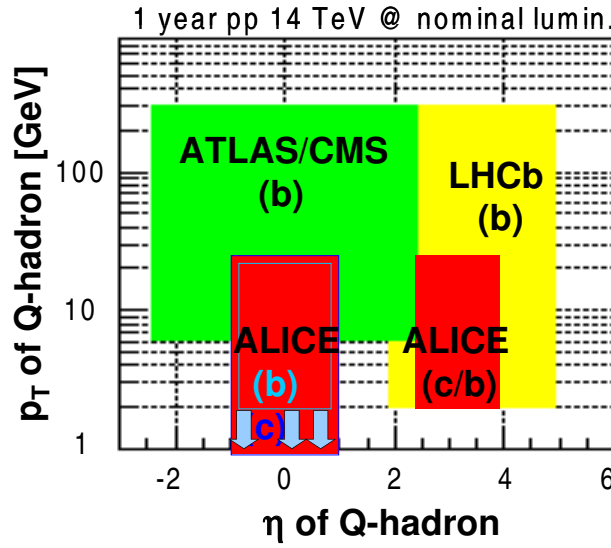


Fig. 4: Schematic acceptance in transverse momentum and pseudorapidity for open heavy flavour hadrons (indicated as Q-hadrons) in the four LHC experiments. The high- $p_T$  coverages correspond to one year (i.e. 7 months) of running at nominal luminosity.

17]. An invariant-mass analysis is used to extract the raw signal yield, to be then corrected for selection and reconstruction efficiency and for detector acceptance. As shown in figure 5 (left), the accessible  $p_T$  range for the  $D^0$  is 1–20 GeV/c in Pb–Pb and 0.5–20 GeV/c in proton–proton, with statistical errors better than 15–20% at high  $p_T$ . A similar performance is expected for the  $D^+$  (right-hand panel), though at present the statistical errors are estimated only in the range  $1 < p_T < 8$  GeV/c. The systematic errors (acceptance and efficiency corrections, centrality selection for Pb–Pb) are estimated to be smaller than 15%.

### 2.2.2 Beauty detection via displaced electrons

Beauty detection via electron-identified tracks with a displacement with respect to the primary collision vertex is favoured by the large semi-electronic branching ratio (b.r.  $\approx 11\%$  [18]) and by the significant mean proper decay length ( $c\tau \approx 500 \mu\text{m}$  [18]) of beauty hadrons. The main sources of background for the signal of beauty-decay electrons are: decays of primary D mesons, which have a branching ratio of  $\approx 10\%$  in the semi-electronic channels [18], and have an expected production yield larger by a factor about 20 with respect to B mesons ( $N^{c\bar{c}} \approx 1.6 \times 10^{-1}/\text{ev}$  and  $N^{b\bar{b}} \approx 7.2 \times 10^{-3}/\text{ev}$  [13]); di-electron decays of vector mesons ( $\rho$ ,  $\omega$ ,  $\phi$ ) and Dalitz decays of pion and  $\eta$  mesons (e.g.,  $\pi^0 \rightarrow \gamma e^+ e^-$ ); conversions of photons in the beam pipe or in the inner layers of the ITS; charged pions misidentified as electrons.

Events were generated using PYTHIA [19]. We evaluated the required statistics at about  $10^7$  proton–proton minimum-bias events at  $\sqrt{s} = 14$  TeV,  $10^6$  proton–proton events containing a

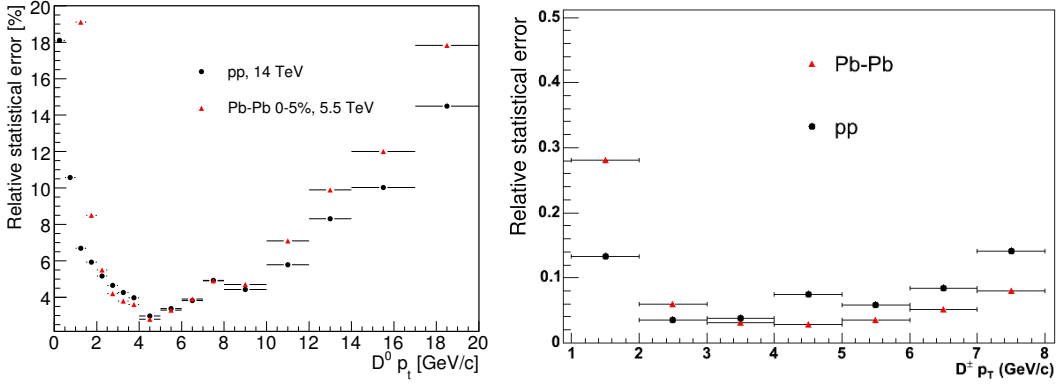


Fig. 5: Expected relative statistical errors for the measurement in ALICE of the production cross sections of  $D^0$  in the  $K^- \pi^+$  channel (left) and  $D^+$  in the  $K^- \pi^+ \pi^+$  channel (right), in 0–5% central Pb–Pb collisions and in proton–proton collisions.

$c\bar{c}$  pair and  $10^6$  proton–proton events containing a  $b\bar{b}$  pair. For the background, we used a sample of  $6 \times 10^6$  minimum-bias proton–proton events. For the proton–proton events with a heavy-quark pair, we used the same PYTHIA settings as for the minimum-bias events, without forcing heavy-flavour production, but selecting events containing a  $c\bar{c}$  or  $b\bar{b}$  pair (in order to obtain a realistic underlying-event multiplicity). Since the resulting shapes of the charm and beauty quarks  $p_T$  distributions are different from those given by NLO pQCD predictions [16] we reweighted the decay electrons in order to match the baseline shapes. The samples, for background and for proton–proton events with a heavy-quark pair, were normalized to one proton–proton event.

Figure 6 shows the distributions of the signal and of the different background sources, in impact parameter, defined in the plane transverse to the beam direction, ( $d_0$ ) and in transverse momentum ( $p_T$ ). The detection strategy is adapted from that developed for Pb–Pb collisions [20] and is based on three steps:

1. Electron identification. Electrons can be efficiently separated from hadrons by combining the PID capabilities of the TPC, and of the TRD. Here we assume for the proton–proton case the same electron PID performance as expected in Pb–Pb collisions [20]. Under the assumption of  $e_{eff}^{TRD} = 90\%$  electron identification probability, the TRD is expected to reject 99% of the charged pions ( $\pi_{eff}^{TRD} = 10^{-2}$  misidentification probability) and fully reject heavier charged hadrons, for  $p > 1$  GeV/c. Using the information from the TPC, the probability of pion misidentification can be further reduced by a factor of a hundred at low momentum. As the momentum increases and charged pions approach the Fermi plateau in  $\frac{dE}{dx}$ , the additional pion rejection from the TPC decreases and becomes marginal at  $p \simeq 10$  GeV/c.
2. Primary vertex reconstruction. Due to the TPC and SDD drift speed limitations, during LHC proton–proton runs, the luminosity at the ALICE interaction point has to be kept below  $\mathcal{L}_{max} \simeq 3 \times 10^{30} \text{ cm}^{-2} \text{ s}^{-1}$  [12]. When the LHC luminosity will be larger than this value (the design luminosity is about a factor  $10^4$  higher), the luminosity at the ALICE

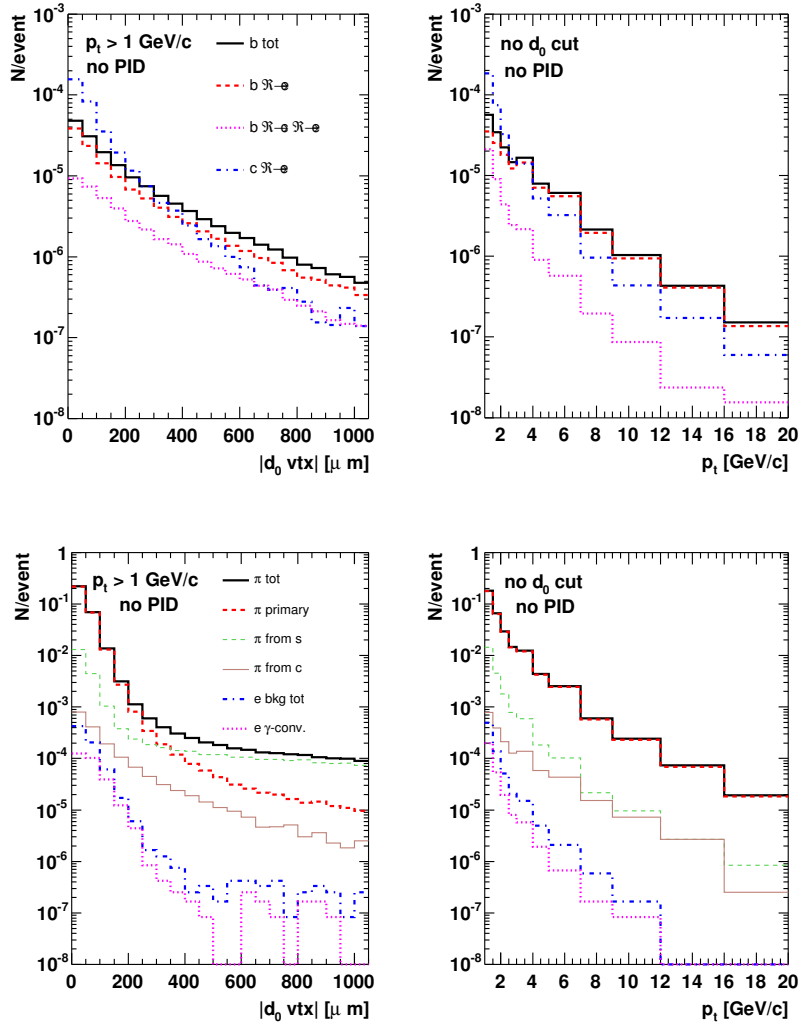


Fig. 6: Beauty and charm decay electrons (top), electrons from other sources and charged pions (bottom), as a function of  $|d_0|$  (left) and  $p_T$  (right). Here,  $|d_0|$  is calculated with respect to the true primary vertex position, known from simulation.

interaction point will have to be reduced, for instance by defocusing the beams, i.e. by enlarging their transverse size up to  $\sigma_{x,y} \sim 150 \mu\text{m}$ . The primary vertex position will be reconstructed on an event-by-event basis, using measured tracks, with an expected resolution of about  $70 \mu\text{m}$  in  $x$  and  $y$  on average [21].

3. **Impact parameter cut.** Because of the large mean proper decay length ( $\approx 500 \mu\text{m}$ ) of beauty mesons, their decay electrons have a typical impact parameter of a few hundred microns with respect to the primary vertex. A cut  $|d_0| \gtrsim 200 \mu\text{m}$  allows to reject a large fraction of the background (see Fig. 6). We have optimized the value of this cut as a



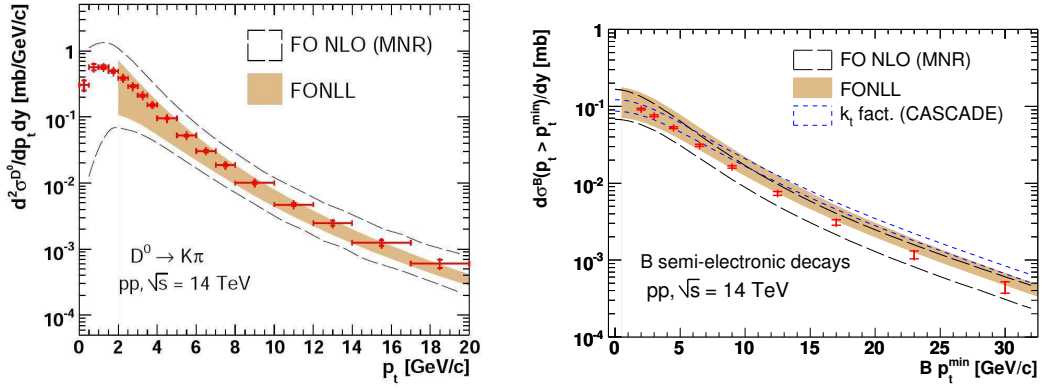


Fig. 7: Differential cross section for  $D^0$  (left) and B meson (right) production as it can be measured with  $10^9$  p–p minimum-bias events. Statistical errors (inner bars) and quadratic sum of statistical and  $p_T$ -dependent systematic errors (outer bars) are shown; the 9% normalization error is not shown. The theoretical predictions from the three pQCD calculations (see text), with their uncertainties are also shown for comparison with the expected experimental sensitivity.

function of the transverse momentum in order to minimize the total errors (statistical and systematic).

To extract the electrons cross section we first apply our cuts to the “measured” electrons. On this selected sample we subtract the residual background (estimated from the charm and pions measurements) and we apply the corrections for efficiency and acceptance. We infer the  $p_T^{\min}$ -differential cross section for beauty mesons,  $d\sigma^B(p_T > p_T^{\min})/dy$ , from the beauty electrons cross section using a procedure similar to that developed by the UA1 Collaboration [22]. The method, described in detail in Refs. [13, 20, 23], is based on Monte Carlo simulation and relies on measured B meson decay kinematics.

### 2.2.3 Results

Figure 7 presents the expected ALICE performance for the measurement of the  $p_T$ -differential cross section of  $D^0$  mesons (left) and the  $p_T^{\min}$ -differential cross section of B mesons,  $d\sigma^B(p_T > p_T^{\min})/dy$  vs.  $p_T^{\min}$  averaged in the range  $|y| < 1$ . For illustration of the sensitivity in the comparison to pQCD calculations, we report in the same figure the predictions and the theoretical uncertainty bands from three approaches [24]: collinearly-factorized FO NLO, as implemented in the HVQMNR code [16], Fixed Order Next-to-Leading Log (FONLL) [25] and  $k_t$ -factorization, as implemented in the CASCADE code [26]. It can be seen that the expected ALICE performance for  $10^9$  events will provide a meaningful comparison with pQCD predictions.

## 2.3 Beauty in the $J/\psi$ channel

Simulation studies are in progress to prepare a measurement of the fraction of  $J/\psi$  that feed-down from B decays. Such measurement can be performed by studying the separation of the dilepton

pairs in the  $J/\psi$  invariant-mass region from the main interaction vertex. The analysis should provide a measurement of the beauty  $p_T$ -differential cross section down to  $p_T \approx 0$ . The pseudo-proper decay time,  $x = L_{xy} \cdot M(J/\psi)/p_T$ , where  $L_{xy}$  is the signed projection of the  $J/\psi$  flight distance on its transverse direction,  $L_{xy} = \vec{L} \cdot \vec{p}_t(J/\psi)/|p_T|$ , can be used to separate  $J/\psi$  from the B decay products from that of prompt decays, as shown in figure 8 for proton–proton collisions. In this expression, the  $M(J/\psi)$  is taken as the known  $J/\psi$  mass [18].

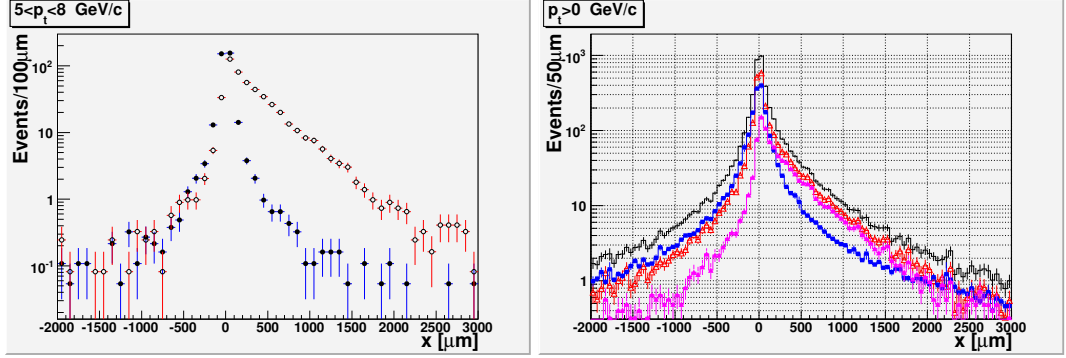


Fig. 8: Distributions of the  $x$  variable, defined in the text, for  $5 < p_T < 8$  GeV/c (left) showed for secondary (open circles) and prompt (closed circles)  $J/\psi$ , and for  $p_T > 0$  (right) showed for total  $J/\psi$  (open triangles), secondary  $J/\psi$  (closed triangles), total background (closed squares) and their sum (lines, in black).

## 2.4 Quarkonia detection in the ALICE Muon Spectrometer

The ALICE experiment will detect heavy quarkonia both at central rapidity in the di-electronic decay channel and at forward rapidity in the di-muonic one. The latter channel will be discussed here.

Quarkonia cross sections at LHC energies are provided by the Color Evaporation Model (CEM) [27]. In this model, the quarkonia cross section is the product of the  $Q\bar{Q}$  cross section times a transition probability ( $F_C$ ) which is specific to each state ( $C$ ) but independent of the energy. Ground state cross sections are the sum of direct production and feed-down from higher mass resonances below the thresholds for heavy-flavoured meson production ( $H = B$  or  $D$ ). At leading order:

$$\sigma_C^{CEM} = F_C \sum_{i,j} \int_{4m_Q^2}^{4m_H^2} d\hat{s} \int dx_1 dx_2 f_{i/A}(x_1, \mu^2) f_{j/B}(x_2, \mu^2) \hat{\sigma}_{ij}(\hat{s}) \delta(\hat{s} - x_1 x_2 s) \quad (1)$$

where  $A$  and  $B$  can be any hadron or nucleus,  $ij = q\bar{q}$  or  $gg$ ,  $\hat{\sigma}_{ij}(\hat{s})$  is the  $ij \rightarrow Q\bar{Q}$  subprocess cross section and  $f_{i/A}(x_1, \mu^2)$  is the parton density in the hadron or nucleus. The predictions for proton–proton collisions at 14 TeV are summarized in Table 1. The transverse momentum distributions are obtained by extrapolating the distributions measured by the CDF experiment at  $\sqrt{s} \sim 2$  TeV [28] at the LHC energies. The  $p_T$  and rapidity distributions of  $J/\psi$  and  $\psi(2S)$  from

	$J/\psi$	$\psi(2S)$	$\Upsilon$	$\Upsilon(2S)$	$\Upsilon(3S)$
$\sigma \times \text{BR} (\mu\text{b})$	3.18	0.057	0.028	0.007	0.0042

Table 1: CEM cross sections for quarkonia production in proton–proton collisions at 14 TeV. Cross sections include feed-down from higher mass resonances and branching ratios in lepton pairs.

the decay of B mesons are generated with PYTHIA [19]. The background, consisting in opposite sign dilepton pairs from the decay of charm, beauty, pions and kaons, is produced with PYTHIA as well.

The dimuon invariant-mass yield expected in one year of data taking in proton–proton collisions at the LHC, with a luminosity of  $3 \times 10^{30} \text{ cm}^{-2}\text{s}^{-1}$  is shown in figure 9. The left (right) panel shows the results obtained with a trigger  $p_T$  cut of 1 (2) GeV/ $c$  in the  $J/\psi$  ( $\Upsilon$ ) mass region. About  $2.8 \times 10^6$   $J/\psi$  and  $2.7 \times 10^4$   $\Upsilon$  are expected. The high statistics allows to reconstruct differential distributions with a fine binning, as illustrated in figure 10.

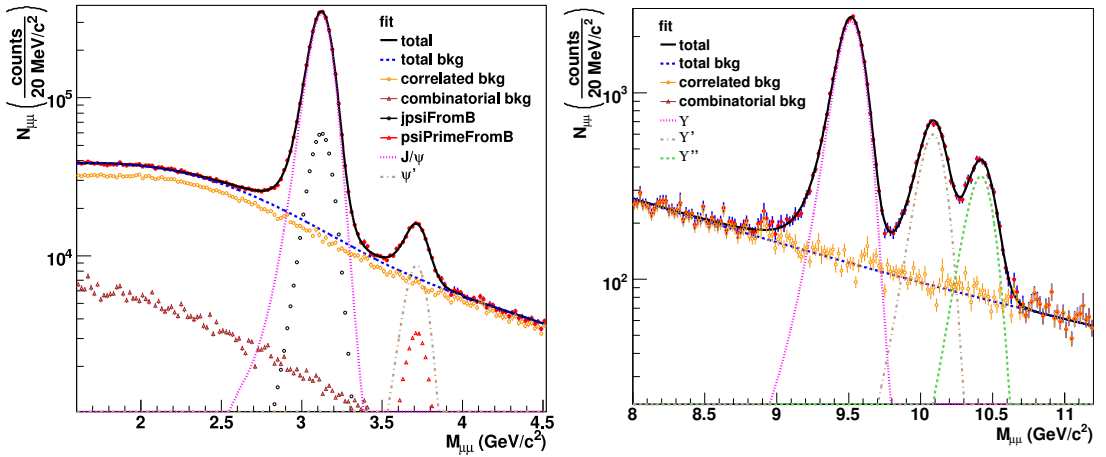


Fig. 9: Dimuon invariant-mass distribution expected in 1 year of data taking in proton–proton collisions at  $3 \times 10^{30} \text{ cm}^{-2}\text{s}^{-1}$ .

#### 2.4.1 Sensitivity to low $x$ PDFs

The choice of a hadron collider implies some uncertainties in the determination of the initial state during the collisions, which are related to the composite nature of the colliding particles. At high energies the hadrons do not interact as a whole: the scatterings takes place between the constituent quarks and gluons. An accurate knowledge of the momentum distribution of such elementary particles in the hadrons is a fundamental issue. The mapped phase space is constantly increased by taking into account data from experiments at different energies. At present, the gluon distribution are constrained by measurements down to  $x$  values higher than  $10^{-4}$ , and extrapolated down to about  $10^{-5}$ .

Leading order calculations show that in proton–proton collisions at 14 TeV, the  $J/\psi$  with a rapidity higher than 3 are produced by gluons with  $x < 10^{-5}$ . Figure 11 shows a comparison

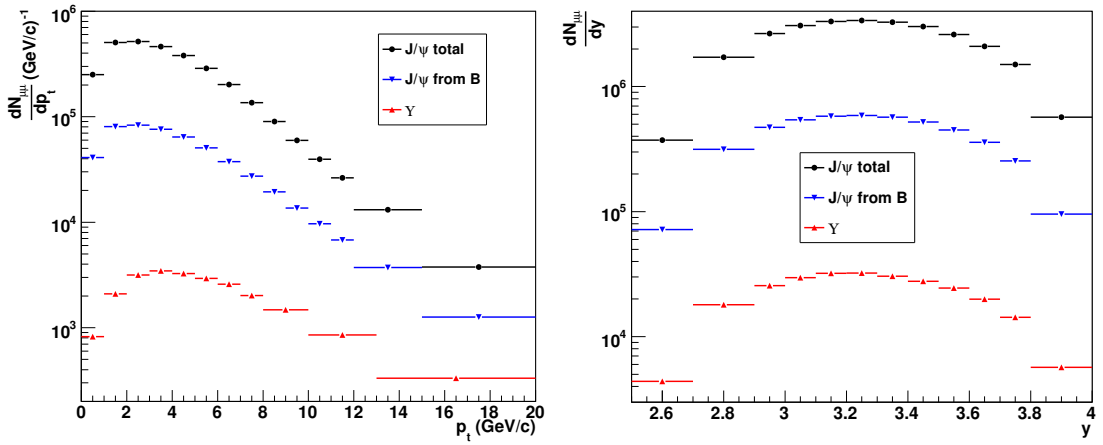


Fig. 10: Expected  $p_T$  (left panels) and rapidity (right panels) differential yields for  $J/\psi$  and  $\Upsilon$  in 1 year of data taking in proton–proton collisions at 14 TeV at the ALICE nominal luminosity of  $3 \times 10^{30} \text{ cm}^{-2} \text{ s}^{-1}$ .

among the PDF sets calculated at Leading Order by the collaborations Martin-Roberts-Stirling-Thorne (MRST98 [29] and MRST01 [30]) and the Coordinated Theoretical-Experimental Project on QCD (CTEQ5 [31] and CTEQ6 [32]) at the scale of  $J/\psi$  (left panel) and  $\Upsilon$  (right panel). For the MRST01 and CTEQ5 sets, two different extrapolations in the low  $x$  region are shown. Differently from the  $\Upsilon$  case, the  $x$ -values explored by  $J/\psi$  in the ALICE Muon Spectrometer acceptance (in yellow), partially sit on the region of extrapolation.

Performing Leading Order calculations in the framework of the Color Evaporation Model,

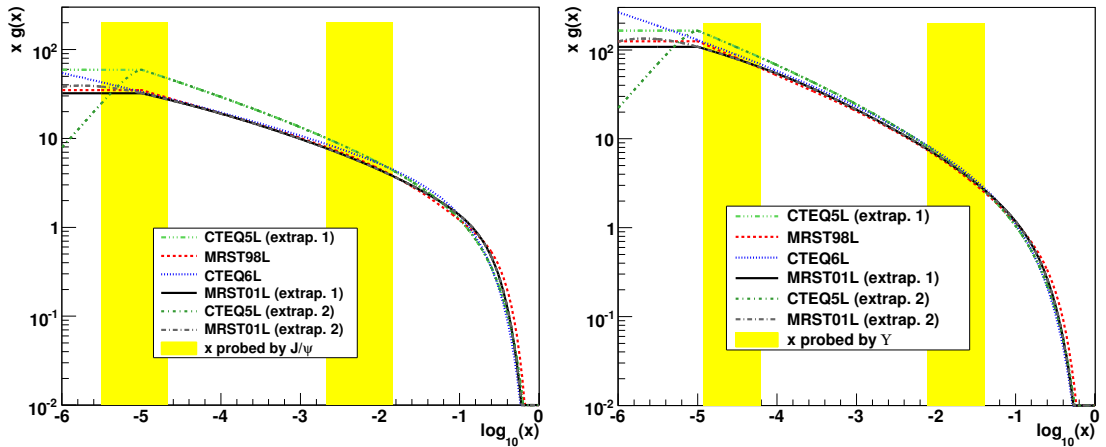


Fig. 11: Comparison of the gluon distributions from MRST and CTEQ.  $x$  regions probed by  $J/\psi$  and  $\Upsilon$  produced in proton–proton collisions at  $\sqrt{s} = 14 \text{ TeV}$  in the rapidity region  $2.5 < y < 4$  are shown.

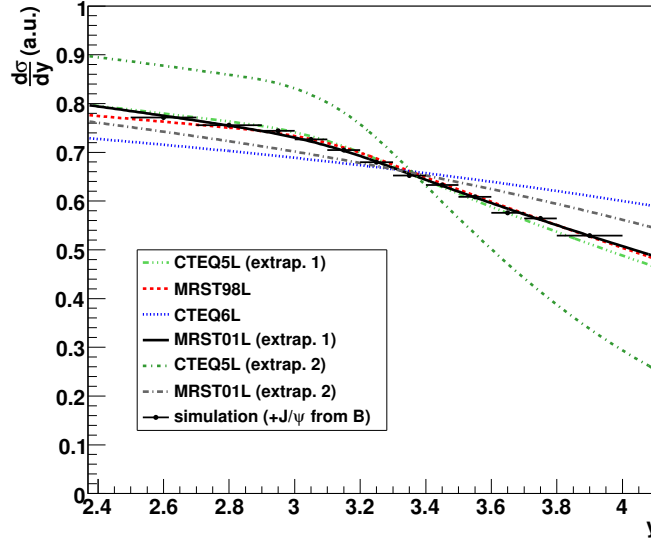


Fig. 12: Comparison between  $J/\psi$  rapidity distributions obtained with four different PDF sets (area in detector acceptance is normalized to 1). Simulation results are also shown.

it is possible to derive the  $J/\psi$  rapidity distribution:

$$\frac{d\sigma_{J/\psi}^{CEM}}{dy} = \frac{F_{J/\psi}}{s} \sum_{i,j} \int_{4m_Q^2}^{4m_H^2} d\hat{s} \hat{\sigma}_{ij}(\hat{s}) f_{i/A}(\sqrt{\frac{\hat{s}}{s}} e^y, \mu^2) f_{j/B}(\sqrt{\frac{\hat{s}}{s}} e^{-y}, \mu^2) \quad (2)$$

Figure 12 shows a comparison of the differential distributions obtained with different sets of PDFs. It is worth noting that such distributions are normalized by setting equal to unit their integral from 2.5 to 4 rapidity units. The *shape* of the distributions is clearly dependent on the behavior of the gluon functions: results obtained with MRST98L, MRST01L (extrap. 1) and CTEQ5L (extrap. 1), which were extrapolated flat in  $xg(x)$  (figure 11) are compatible among each other and are clearly different from the result obtained with CTEQ6L, and with a changed extrapolation behavior of MRST01L (extrap. 2) and CTEQ5L (extrap. 2). The results show that also a small change in the PDFs extrapolation (see MRST01L) can lead to appreciable changes in the shape of the differential distributions.

The comparison between the simulation results and the calculations (figure 12), show that, due to the high statistics, the accuracy of the data expected to be collected by the ALICE Muon Spectrometer will be good enough to allow to discriminate among different shapes of the gluon distribution functions in the region of  $x < 10^{-5}$  (at least in the frame of a leading order analysis).

## 2.5 Conclusions

We presented the expected performance of ALICE for the study of open heavy flavour and quarkonium states in nucleus–nucleus collisions at the LHC. Thanks to the good expected performance of the detectors for tracking and particle identification, and its low magnetic field in

the central barrel, the ALICE acceptance is complementary to that of other LHC experiments. This opens the possibility of measuring heavy-flavour production down to  $p_T \approx 1 \text{ GeV}/c$ , both at central and forward rapidity. Our results indicate that ALICE can provide several  $p_T$  differential measurements of charmed and beauty hadrons production with errors that are smaller or comparable to the theoretical uncertainties of pQCD calculations. The invariant-mass resolution of the muon spectrometer allows to resolve several charmonium and bottomonium resonances and the statistics expected to be collected in the first year of data taking should be enough to study in details the production of several quarkonia states. Finally, ALICE will probe the parton distribution functions down to unprecedentedly low values of the Feynman  $x$  variable.

### 3 Quarkonia and open beauty production in the ATLAS experiment at the LHC

*Authors: E. Lytken and M. zur Nedden*

#### 3.1 Introduction

ATLAS [33] is a general-purpose experiment with main emphasis on searches for new phenomena based on high  $p_T$  particles. Since most of the  $B$ -physics appears in the lower  $p_T$  range, triggering within the LHC environment on those events is a challenge. Nevertheless, ATLAS has good capabilities for a rich  $B$ -physics program, based on the dedicated and flexible trigger, the precise and flexible vertexing and tracking, the good muon identification and the high-resolution calorimetry. Furthermore, theoretical descriptions of heavy flavoured hadrons need input from the LHC, where precision measurements are already achievable after one year of data taking. The expected inclusive production cross-section for  $b\bar{b}$  pairs at LHC is estimated to be  $\sigma_{b\bar{b}} \approx 500 \mu\text{b}$  leading to more than  $10^6$  produced pairs per second at design luminosity. The experimental precision reached at ATLAS should at least allow the verification of the Standard Model (SM) prediction. In the case of the rare  $B$ -decays, clearly higher luminosity is needed to achieve sensitive upper limits for the indirect beyond the Standard Model (BSM) searches. Therefore, the most relevant part of the ATLAS  $B$ -physics program will take place in the initial phase at lower luminosities with an extension into the high luminosity phase. The envisaged measurements are extending the discovery potential for physics beyond the SM by the measurement of  $CP$  violation parameters, predicted to be small in the SM, and of rare  $B$  decays.

The exclusive  $B^+$  channel provides a clean reference signal. Due to the clear event topology and its rather large branching ratio, it can be measured during the initial luminosity phase of the LHC. The  $B^+ \rightarrow J/\psi K^+$  decay can serve as a reference channel for the measurement of the decay probability of a very rare decay channel  $B_s \rightarrow \mu^+ \mu^-$ , which is strongly suppressed in the Standard Model and therefore offers a good sensitivity to new physics. The total and differential cross-sections of the rare  $B$  decays will be measured relative to the  $B^+ \rightarrow J/\psi K^+$  cross-section allowing thus the cancellation of common systematic errors. Furthermore, it can also act as a control channel for the  $CP$  violation measurement and can be used to estimate the systematic uncertainties and efficiencies of flavour tagging algorithms. Finally, the relatively large statistics for this decay allows for initial detector performance studies.

The trigger menu for the ATLAS  $B$ -physics program has been designed to take maximum advantage of the early run phases at lower luminosities ( $\mathcal{L} < 10^{33} \text{ cm}^{-2}\text{s}^{-1}$ ). Since only 5 - 10 %

of the limited bandwidth of the ATLAS trigger system is devoted to the  $B$ -physics triggers, highly efficient and selective triggers are needed. Most  $B$ -physics triggers are based on single- and di-muon events in the final state leading to a clean signature for triggers and flavour tagging [34–36]. In the early data taking period the main  $B$ -physics triggers are expected to run without a need of prescales, allowing for low  $p_T$  muon and low  $E_T$  electron triggers (the latter will be however prescaled at  $10^{32} \text{ cm}^{-2} \text{ s}^{-1}$ ). In general, the trigger strategy is mainly based on a single muon trigger at the first level, which could be combined with certain calorimeter trigger objects at higher trigger levels to select hadronic final states ( $B_s \rightarrow D_s \pi$ ) or  $e/\gamma$  final states ( $J/\psi \rightarrow e^+ e^-$ ,  $K^* \gamma$  or  $\phi \gamma$ ). In order to not exceed the available bandwidth, in the phase of higher luminosities above  $2 \cdot 10^{33} \text{ cm}^{-2} \text{ s}^{-1}$  the main working trigger will be based on di-muons on the first level, enabling a clean measurement of rare  $B$ -decays ( $B \rightarrow \mu\mu$  or  $B \rightarrow K^{*0} \mu\mu$ ), double semi-leptonic decays and the  $B \rightarrow J/\psi(\mu\mu)$  decay channels.

### 3.2 Beauty production cross section determination

The  $b\bar{b}$  production cross-section will be measured using inclusive and exclusive methods in parallel to control the systematics. For the inclusive methods ATLAS looks at the semi-leptonic  $b \rightarrow \mu + X$  and the  $B \rightarrow J/\psi(\rightarrow \mu^+ \mu^-) + X$  decay modes. In the next section we will briefly describe the measurement of the exclusive  $B^\pm \rightarrow J/\psi K^\pm$  cross-section. The measurement of the  $J/\psi$  mass and its detection efficiency is a central task for the analysis of the first ATLAS data, providing the tools to validate the detector by extracting muon energy scale determination in the low  $p_T$  region and detector misalignments (Sect. 3.5). Finally, the mass measurement and reconstruction efficiency for  $B^+$ , the total and differential cross-sections and its lifetime measurements will be of interest for other  $B$ -physics analyses.

The main backgrounds that are competing with the signal are single-muon from  $c\bar{c}$  decays and direct  $J/\psi$ 's from  $pp \rightarrow J/\psi + X$ . In the first case, the  $p_T$  distribution of the muons is softer as compared to the muon spectrum from  $b\bar{b}$  decays while in the latter no displaced secondary vertex is expected. In consequence the following parameters are used for  $b$ -tagging:

- the signed transverse impact parameters  $d_0$  of charged particles originating from  $B$ -meson decays at a secondary vertex due to the long lifetime of  $B$ -mesons.
- the relative transverse momentum  $p_T^{\text{rel}}$  of the muon of the  $b$ -decay with respect to the axis of the associated jet.

The measurement of the  $p_T^{\text{rel}}$  distribution of the selected muons offers a good possibility to determine the  $b$ -contents fraction in the offline analysis. In the rest frame of the decaying  $B$ -meson, the muon gets a high transverse momentum, which is significantly larger than in the case of charm or light quark decays. The relative transverse muon momentum,  $p_T^{\text{rel}}$  can therefore be used to determine the  $b$ -content of a selected data sample by fitting Monte Carlo templates to data. For the  $B$ -mesons at ATLAS, generally decay lengths of the order of several mm are expected which are at the same order of magnitude as the expectation for  $D$ -mesons. The signed transverse impact parameter  $d_0$  is a boost independent quantity. For large transverse momenta ( $p_T^\mu > 10 \text{ GeV}$ )  $d_0$  is proportional to the lifetime of the decaying particle and positive values of  $d_0$  are preferable. The significance of signed impact parameter for muons with an associated  $b$ -jet and the distributions of the relative transverse momentum are shown in Fig. 13 and Fig. 14 respectively. In both cases, the selection power is clearly visible.

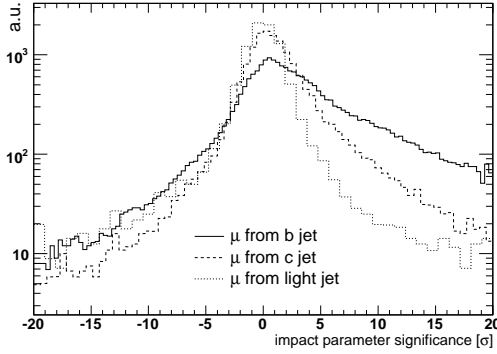


Fig. 13: The distribution of the significance of the signed impact parameter  $d_0/\sigma$

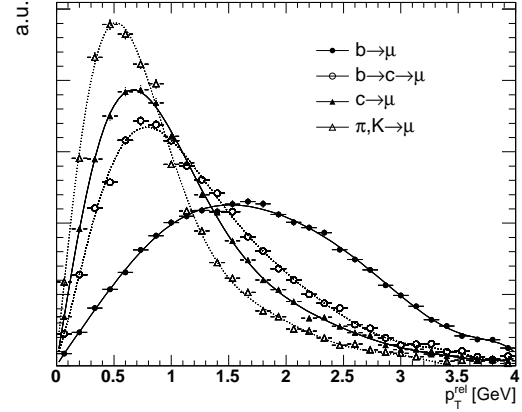


Fig. 14: The  $p_T^{\text{rel}}$  distribution for different processes considered in the  $b$ -jet selection.

The  $b\bar{b}$  production cross-section measurement based on the single-muon and jet requirements at the trigger level is then obtained according to the usual relation

$$\sigma(b\bar{b} \rightarrow \mu(p_T^\mu > 6 \text{ GeV})X) = \frac{N_b^{\text{sel}}}{\int \mathcal{L} dt} \cdot \frac{f_b}{\epsilon_b^{\text{trig}} \cdot \epsilon_b^{\text{rec}}} \quad (3)$$

where the  $b$ -trigger efficiency was found to be  $\epsilon_b^{\text{trig}} = 0.135$  and the combined muon reconstruction efficiency is  $\epsilon_b^{\text{rec}} = 0.85$ . The determination of the  $b$  content,  $f_b$ , of the selected sample is extracted by fitting the simulated  $p_T^{\text{rel}}$  distribution to the data. This can be done by a binned maximum likelihood fit taking into account the finite size of both, the data sample and the simulated Monte Carlo templates. In the signal template, the direct  $b \rightarrow \mu$  and cascade  $b \rightarrow c \rightarrow \mu$  contributions are contained, whereas all others are summarized in the background template. The distribution can be seen in Fig. 15. With this fit, a  $b$ -content of  $f_b = 0.23$  was obtained, and a corresponding background fraction of  $f_{bg} = 0.77$ . The values obtained in this study are in good agreement with the values obtained by the Tevatron experiments [37]. Combining both methods, the  $b\bar{b}$  production cross-section is expected to be measured with a statistical precision better than  $\mathcal{O}(1 \%)$  with  $\approx 100 \text{ pb}^{-1}$  of integrated luminosity. The systematic uncertainty is dominated by the luminosity measurement. It is estimated to be 10 % in the initial phase, and reduced to about 6.5 % after the first  $0.3 \text{ fb}^{-1}$ . The scale uncertainty of the NLO calculations is about 5 %, while the PDF uncertainty is estimated to be 3 %. Finally, the uncertainty originating from the muon identification is about 3 %, leading to a systematic uncertainty of 12 % and 9.2 % correspondingly in the initial and later phase .

### 3.3 $B^+$ reference channel

Negligible direct  $CP$  violation is expected in the  $B^\pm \rightarrow J/\psi K^\pm$  decay because for  $b \rightarrow c + \bar{c}s$  transitions the SM predicts that the leading and higher order diagrams are characterized by the same weak phase. The only source of asymmetry is the different interaction probability for



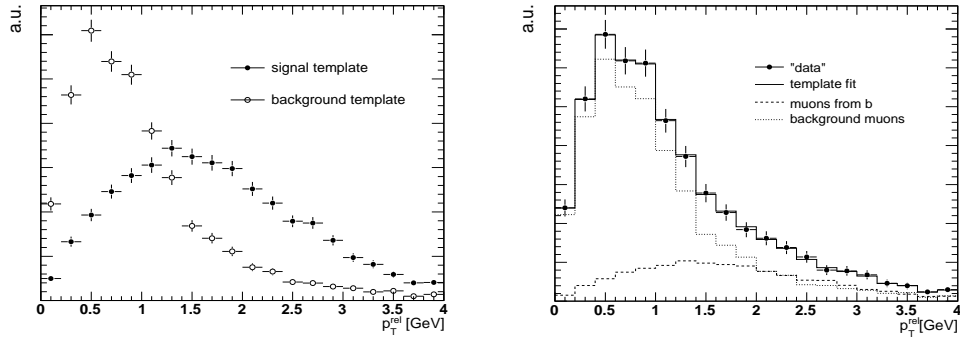


Fig. 15: The generated  $p_T^{\text{rel}}$  templates (left) and fraction of the  $b$ -content of the selected  $b$ -jet sample (right) showing comparison of the fitted to the true values from Monte Carlo.

$K^+$  and  $K^-$  with the detector material. The  $B^+$  candidates are reconstructed based on the  $J/\psi(\rightarrow \mu^+\mu^-)$  selection, and combined with  $K^+$  candidates formed from inner detector tracks.

The  $B^+$  invariant mass distribution  $M(K^+\mu^+\mu^-)$  of the candidates, fulfilling the selection cuts, is presented in Fig. 16 for signal and background with a maximum-likelihood fit, where the likelihood function is a Gaussian for the signal region and a linear function for the background ( $b\bar{b} \rightarrow J/\psi + X$ ). The mass range of the fit is taken from 5.15 GeV to 5.8 GeV in order to reduce contributions from partially reconstructed  $B$  meson decays. The background at the right of the mass peak originates from misidentified  $\pi^+$  from  $B^+ \rightarrow J/\psi\pi^+$  decays. The fit result for the  $B^+$  mass is:  $M(B^+) = (5279.3 \pm 1.1) \text{ MeV}$  with a width of  $\sigma(B^+) = (42.2 \pm 1.3) \text{ MeV}$ . The relative errors, scaled properly for an integrated luminosity of about  $10 \text{ pb}^{-1}$ , are about 0.02% and 3.5% respectively. The slight shoulder to the left of the mass distribution is due to the background shape in this mass region and has been included in the systematic uncertainties of the fit model.

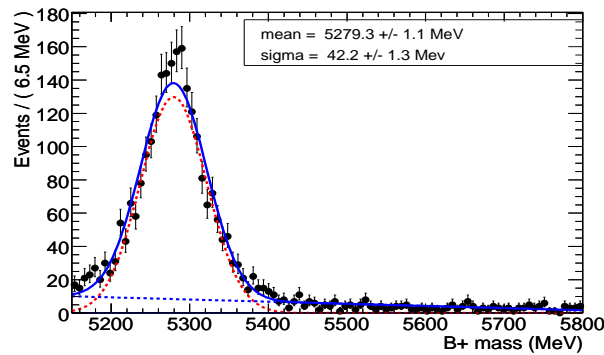


Fig. 16:  $B^+$  mass fit with the both signal (red) and background (blue) contributions shown separately.

With the first  $10 \text{ pb}^{-1}$  of LHC data a total and differential production cross-section measurement of the  $B^+ \rightarrow J/\psi K^+$  can be achieved. The differential cross-section  $d\sigma/dp_T$  can be obtained from the usual form:

$$\frac{d\sigma(B^+)}{dp_T} = \frac{N_{\text{sig}}}{\Delta p_T \cdot \mathcal{L} \cdot \mathcal{A} \cdot \text{BR}} \quad (4)$$

where  $N_{\text{sig}}$  is the number of reconstructed  $B^+$  obtained from the mass fit and the size of the  $p_T$  bin is denoted with  $\Delta p_T$ . Furthermore,  $\mathcal{L}$  is the total luminosity to which the dataset corresponds and is obtained from PYTHIA output and BR is the product of the branching ratios using the world average [38] branching ratios of  $\text{BR}(B^+ \rightarrow J/\psi K^+) = (10.0 \pm 1.0) \times 10^{-4}$  and  $\text{BR}(J/\psi \rightarrow \mu^+ \mu^-) = (5.88 \pm 0.10) \times 10^{-2}$ . The overall efficiency  $\mathcal{A}$  is calculated for each  $p_T$  range separately as the ratio of the number of signal events determined from the previous fit procedure and the number of the Monte Carlo signal events within the same  $p_T$  range. To measure the  $B^+$  total cross-section a similar procedure with that used for the calculation of the differential cross-section is followed.

The measurement of the lifetime  $\tau$  of the selected  $B^+$  candidates is a sensitive tool to confirm the beauty content in a sample, in particular the number of the reconstructed  $B^+ \rightarrow J/\psi K^+$  decays obtained in the  $b\bar{b} \rightarrow J/\psi X$  dataset. The proper decay-time is defined as  $t = \lambda/c$ . The proper decay-time distribution in the signal region  $B^+ \rightarrow J/\psi K^+$  can be parametrized as a convolution of an exponential function with a Gaussian resolution function, while the background distribution parametrization consists of two different exponential functions, where each is convoluted with a Gaussian resolution function. In the  $b\bar{b} \rightarrow J/\psi X$  no zero lifetime events are expected since there is no prompt  $J/\psi$  produced. In the realistic case, where zero lifetime events will be present, an extra Gaussian centered at zero is needed in order to properly describe those events.

The results on the lifetime measurements are shown in Fig. 17. The background can be best described with the two lifetime components ( $\tau_1$  and  $\tau_2$ ). For the events in the mass region of the signal within  $M(B^+) \in [5.15, 5.8] \text{ GeV}$  the proper decay-time found from the decay length is compared to the generated  $B^+$  lifetime. The differences are well centered at zero with a Gaussian distribution and sigma 0.088 ps. It should be noted that the resolution as well as its  $\sigma$  in  $\eta$  bins of 0.25 is found to be independent of  $\eta$ .

### 3.4 Open flavour: rare B-decays

Flavour changing neutral currents, a direct transition from  $b \rightarrow d/s$ , are forbidden at the tree level in the SM and occur at the lowest order through one loop diagrams. They are a sensitive test of the SM and its possible extension(s), providing information on the long distance QCD effects and enabling a determination of the CKM matrix elements  $|V_{td}|$  and  $|V_{ts}|$ . Furthermore, some of the rare decay channels contribute to the background for other channels, which are very sensitive to BSM effects.

An upper limit of the branching ratio  $BR(B_s^0 \rightarrow \mu^+ \mu^-) = (1 - 2) \cdot 10^{-8}$  at 90 % confidence level or of  $(2 - 3) \cdot 10^{-8}$  at  $3\sigma$  evidence based on  $N_B = 1.1$  events that can already be extracted from an integrated luminosity of  $2 \text{ fb}^{-1}$ . This is clearly better than the current CDF limit of  $4.7 \cdot 10^{-8}$  at 90 % confidence level. Already at  $1 \text{ fb}^{-1}$  ATLAS is able to collect  $\mathcal{O}(10^6)$

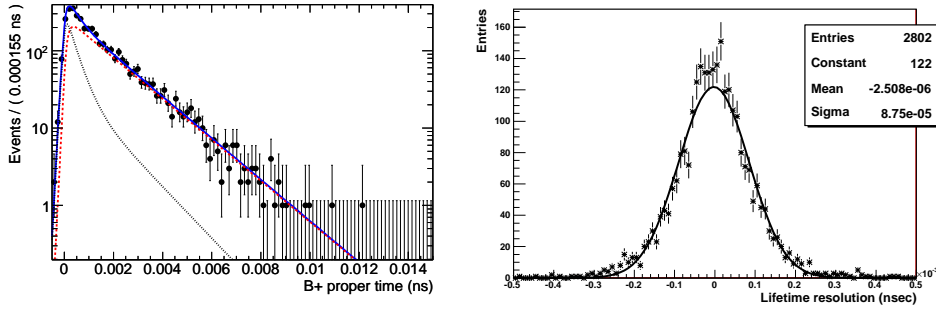


Fig. 17: The  $B^+$  lifetime fit (left) with the signal (dashed red) and the background (dashed black) contributions shown separately. The  $B^+$  lifetime resolution (right).

di-muon events in the mass window of  $4 \text{ GeV} < M(\mu^+\mu^-) < 7 \text{ GeV}$ . This is after the selection based on cuts on  $p_T$ , the invariant mass  $M_{\mu^+\mu^-}$ , the transverse decay length  $L_{xy}$  of the di-muon system, and on isolation requirements. Based on this data, an upper limit on the number of signal events,  $N_B$ , corresponding to a given confidence level will be determined. The main background sources originate from combinatorial decays as  $b\bar{b} \rightarrow \mu^+\mu^-X$ , from misidentifications ( $B_s^0 \rightarrow \pi^+\pi^-$ ,  $B_s^0 \rightarrow K^+K^-$ ,  $B_s^0 \rightarrow \pi^+K^-\nu_\mu$ ) or from other rare decays ( $B_s^0 \rightarrow \mu^+\mu^-\mu^+\nu_\mu$ ,  $B_s^0 \rightarrow \mu^+\mu^-\gamma$ ).  $N_B$  will be used to extract the upper limit on the  $B_s^0 \rightarrow \mu^+\mu^-$  branching ratio  $BR(B_s^0 \rightarrow \mu^+\mu^-)$ , using the reference channel  $B^+ \rightarrow J/\psi K^+$  as described in Sec. 3.3, since trigger and offline reconstruction efficiencies largely cancel for di-muons in these channels. In this procedure, a ratio of geometric and kinematical acceptances of the signal and the reference channel will be determined from the Monte Carlo simulations. With an integrated luminosity of  $30 \text{ fb}^{-1}$ , corresponding to three years of initial data taking, the SM predictions could be tested with a  $3 \sigma$  sensitivity. The continuation of this measurement at nominal LHC luminosities has been proved to lead to a clear statement with a  $5 \sigma$  sensitivity after already one additional year of data taking at design luminosity of  $10^{34} \text{ cm}^{-2} \text{ s}^{-1}$ .

### 3.5 Quarkonia

Understanding the production of prompt quarkonia at the LHC is an important step to understand the underlying QCD mechanisms, and one that has given rise to controversy, both with respect to the cross-section magnitude [39] and the polarization [40]. The initial discrepancy in cross-section led to the Color Octet Model [41] but more high  $p_T$  results are needed to distinguish between this and competing models.

In addition to these open questions, the narrow  $J/\psi$  and  $\Upsilon$  resonances are ideal for studies of detector performance. The expected abundant production (see Fig. 18) makes this feasible already in the very early data. Both decay channels  $J/\psi$  ( $\Upsilon$ )  $\rightarrow \mu^+\mu^-$  and  $J/\psi$  ( $\Upsilon$ )  $\rightarrow e^+e^-$  will be used as tools to test our detector performance. In the following we consider only the  $J/\psi$  and  $\Upsilon(1S)$  resonances. Quarkonia selection in ATLAS is mainly based on a di-muon trigger which requires two identified muons, both with  $p_T \geq 4 \text{ GeV}$  and within a pseudorapidity of

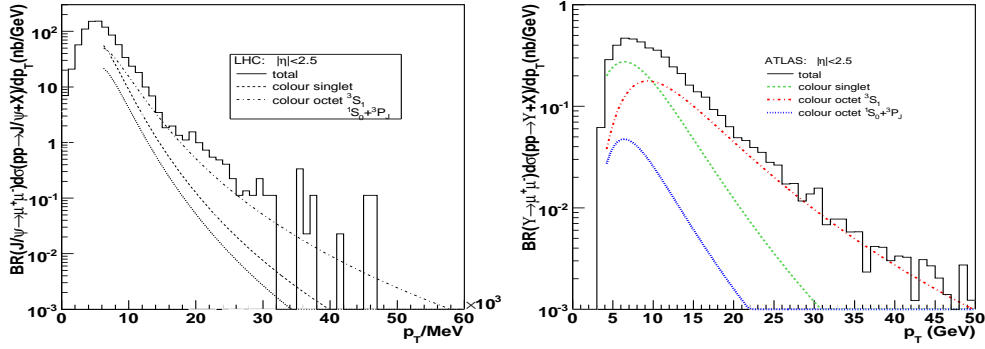


Fig. 18: Differential  $J/\psi$  and  $\Upsilon$  cross-sections as predicted from the Color Octet Model. Contributions from (singlet)  $\chi$  production is included.

$|\eta| < 2.4$ . The di-muon sample considered here has offline  $p_T$  cuts of 6 and 4 GeV applied to the two identified muons. To suppress backgrounds (decays-in-flight, heavy flavour decays) we require tracks to come from the same vertex and with a pseudo-proper time cut of  $\tau = 0.2$  ps, defined as  $\tau = \frac{M \cdot L_{xy}}{p_T(J/\psi) \cdot c}$ . In Fig. 19 (left) the resulting di-muon spectrum with background contributions is shown. We expect 15000  $J/\psi$ 's and 2500  $\Upsilon(1S)$  per  $\text{pb}^{-1}$ . The mass resolution for  $J/\psi \rightarrow \mu^+\mu^-$  is expected to be 53 MeV, and for  $\Upsilon \rightarrow \mu^+\mu^-$  we found 161 MeV on average.

We are also studying the possibility of doing performance measurements using di-electron resonances. In that case the  $E_T$  cut for both leptons is 5 GeV at trigger level and offline, and  $|\eta| < 2$ . Tight electron identification cuts are applied to reject background, including  $E/p$ , vertexing layer hit on the tracks, and the ratio of high to low threshold hits in the transition radiation tracker. We expect 2500  $J/\psi$ 's and 500  $\Upsilon \rightarrow e^+e^-$  per  $\text{pb}^{-1}$  with an instantaneous luminosity of  $10^{31} \text{ cm}^{-2} \text{ s}^{-1}$ . The mass resolution for  $J/\psi \rightarrow e^+e^-$  is expected to be about 200 MeV, see Fig. 19 right. The width is mainly constrained by bremsstrahlung due to the large amount of material in the inner detector.

In addition to cross-section measurements ATLAS will use the quarkonia di-muon decays to provide answers to the polarization puzzle and help constrain the models. Defining the polarization parameter  $\alpha$  as  $\alpha = (\sigma_T - 2\sigma_L)/(\sigma_T + 2\sigma_L)$ , we can measure this by  $\theta^*$ , the angle between  $J/\psi$  in rest frame and  $\mu^+$ , as they are related by:

$$\frac{dN}{d \cos \theta^*} = C \cdot \frac{3}{2\alpha + 6} \cdot (1 + \alpha \cos^2 \theta^*) \quad (5)$$

With the di-muon triggers we get a rather narrow  $\cos \theta^*$  distribution, with both muons having similar  $p_T$ . To access higher values of  $\cos \theta^*$  we utilize a single muon trigger where we can pair the trigger muon with a low  $p_T$  track to get large  $\Delta p_T$  and  $\cos \theta^*$  (see Fig. 20 left). For the result quoted here we used a trigger threshold of 10 GeV for the single muon trigger and the  $p_T$  requirement on the second track was 0.5 GeV. The looser cuts allow for more background but still with decent signal to background discrimination ( $S/B = 1.2$  for  $J/\psi$ ). This dataset was added (with corrections for overlaps) to complement the di-muon triggered dataset. The

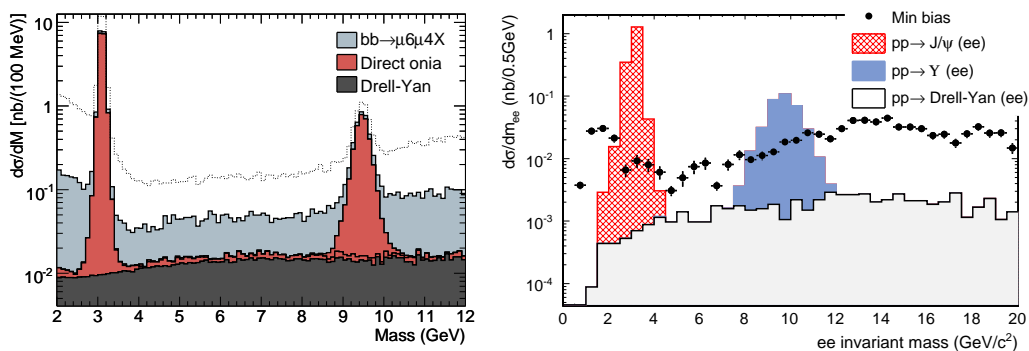


Fig. 19: Di-electron mass distributions for muons (left) and electrons (right). In the left plot the spectrum in case of no vertex cuts (top dashed line) is also shown.

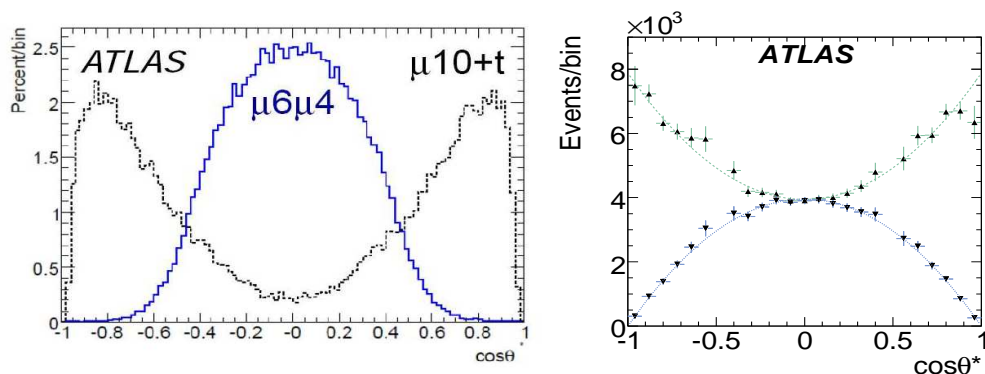


Fig. 20: Left:  $\cos \theta^*$  distributions for double and single muon triggered events. Right: Fit to combined events in  $p_T \in [12, 13]$  GeV. Top shows longitudinally polarized ( $\alpha = -1$ ) and bottom transverse polarized ( $\alpha = 1$ ) events.

combined  $\cos \theta^*$  distributions were then fitted for  $\alpha$  and  $C$  in slices of  $p_T$ . With unpolarized samples the results are given in Table 2 for  $10 \text{ pb}^{-1}$ . Similar tests have been carried out with  $\alpha = \pm 1$ . An example is shown in Fig. 20 right.

We expect to be able to measure the  $J/\psi$  polarization with the  $p_T$  of the  $J/\psi$  in the range of 10 GeV (trigger dependent) up to 50 GeV. Already with the first  $10 \text{ pb}^{-1}$  we can achieve better precision than the current Tevatron measurements - but with  $J/\psi$  at high  $p_T$ , which is what is needed to truly distinguish between models. For  $\Upsilon(1S)$  we can get the same precision with  $100 \text{ pb}^{-1}$ . In this latter case we have acceptance all the way down to  $p_T \approx 0$  for the  $\Upsilon$ , which will be a very useful region to compare with the Tevatron results.

Table 2:  $10 \text{ pb}^{-1}$ : Measured values of  $\alpha$  in  $p_T$  bins in simulated datasets with  $\alpha = 0$ .

$p_T \text{ (GeV}/c)$	9 - 12	12 - 13	13 - 15	15 - 17	17 - 21	> 21
$\alpha(J/\psi)$	0.156 $\pm 0.166$	-0.006 $\pm 0.032$	0.004 $\pm 0.029$	-0.003 $\pm 0.037$	-0.039 $\pm 0.038$	0.019 $\pm 0.057$
$\alpha(\Upsilon)$	-0.42 $\pm 0.17$	-0.38 $\pm 0.22$	-0.200 $\pm 0.20$	0.08 $\pm 0.33$	-0.15 $\pm 0.18$	0.47 $\pm 0.22$

### 3.6 Conclusions

The ATLAS experiment has a rich  $B$ -physics program [42] based on clearly defined trigger strategies for all luminosity phases of the LHC. These measurements will contribute to  $CP$  violation studies with  $B_s$ -mesons and its sensitivity to BSM as well in studies of rare  $B$  decays and quarkonia production. The precision measurement of  $B$ -physics processes are an alternative method to explore the presence of new physics at LHC in addition to the direct SUSY searches.

Two inclusive methods for beauty cross-section measurements to be used mainly at the early data taking period of ATLAS were presented. The first method is using the  $J/\psi$  signature with detached vertices, while the second one is based on semileptonic  $b \rightarrow \mu$  decays. The two methods are complementary and the plan is to apply them simultaneously since both signatures will be available with early data. The two methods rely on different trigger algorithms and different physics processes and signatures, therefore the cross-section results obtained from each one can be used for cross checking calibrations of the trigger algorithms used in the measurements. Combining these two methods, the  $b\bar{b}$  production cross-sections measurement is expected to reach a statistical precision of  $\mathcal{O}(1 \%)$  after one month of data taking, if the initial LHC luminosity will be  $\mathcal{L} = 10^{31} \text{ cm}^2\text{s}^{-1}$ , whereas a systematic uncertainty of  $\mathcal{O}(12 \%)$  is expected. Furthermore, the reference channel  $B^+ \rightarrow J/\psi K^+$  has been studied and it could be shown, that a lifetime measurement is a good tool to confirm the  $b$  content of the selected sample.

In the first data taking period ATLAS will also measure the  $J/\psi$  and  $\Upsilon$  cross-sections, taking advantage of the favorable trigger situation in the early data. A method to determine the level of polarization is also presented. We expect to measure the  $J/\psi$  polarization to within 0.02 - 0.06 in the first  $10 \text{ pb}^{-1}$ , dependent on the polarization itself.

## 4 Heavy flavour production in the CMS experiment at the LHC

*Authors: M. Biasini and A. Starodumov*

### 4.1 Introduction

There are several reasons why a general purpose detector like CMS designed for high  $p_T$  physics could be efficiently used to study heavy flavour physics. First of all, there will be about  $10^{11}$   $b\bar{b}$  pairs produced at the initial luminosity year of  $10^{32} \text{ cm}^{-2}\text{s}^{-1}$  thanks to the high  $b\bar{b}$  x-section which is  $\sigma_{b\bar{b}} \sim 500 \mu\text{b}$  at  $\sqrt{s} = 14 \text{ TeV}$ . So, very rare decays like  $B_s^0 \rightarrow \mu^+\mu^-$  and  $B_s^0 \rightarrow \gamma\mu^+\mu^-$  could be searched even with the Standard Model (SM) decay rate. In different scenarios

of New Physics (NP) the branching fraction of these decays could be enhanced by orders of magnitude, which makes the observation of these channels even more probable.

From the detector point of view heavy flavour physics is also an attractive field. Thanks to the low  $p_T$  (di)-muon triggers, precise vertex detector and efficient tracker system, the CMS detector is capable of efficiently recognizing and reconstructing specific topologies of  $b$ -decays. On the other hand, the study of  $b$ -jets provides with an important knowledge which might be crucial in searches for Higgs boson and supersymmetric particles. Also, one should not forget that  $b$ - and heavy onia-decay channels provide an excellent calibration opportunity for the vertex and tracker systems.

And finally, at the low luminosity phase there are no expectations to observe Higgs decays, but as it is mentioned above there are plenty of  $b\bar{b}$ . So, first real physics results at LHC could be obtained in the heavy flavour sector. Even at a high luminosity, thanks to efficient (di)-muon trigger, CMS is able to continue such studies.

## 4.2 The CMS detector

The complete description of the CMS detector can be found elsewhere [43]. Here only the main characteristics are mentioned. The CMS detector is a standard general purpose hadron collider detector composed of the following subsystems: vertex and tracker systems, electro-magnetic and hadron calorimeters and muon system. The full length is 22 m and outer diameter is 15 m. The total weight of the detector is 12.5 kton. All subsystems but the muon detector are placed inside a superconducting magnetic coil which is able to reach a 3.8 T-field. In the following, the most crucial subsystems for heavy flavour physics are briefly discussed.

### 4.2.1 Muon system

The CMS muon system is composed of three types of gaseous particle detectors for muon identification. Drift tubes (DT) chambers in a central barrel region and cathode strip chambers (CSC) in two end-cap regions, thanks to a high spatial resolution, are used for position and momentum measurements. Because of their fast response time, both systems are also provide the Level-1 trigger with good efficiency and high background rejection. Resistive plate chambers (RPC), which are placed in both the barrel and end-cap regions, combine an adequate spatial resolution with an excellent ( $\leq 5$  ns) time resolution. Along with the DT and CSC systems, the RPC system provides the Level-1 trigger. It also capable to identify unambiguously the relevant bunch-crossing to which a muon track is associated even in the presence of the high rate and background at a full LHC luminosity.

Muon identification efficiency in the central region ( $|\eta| < 1$ ) is above 70% for muons with  $p_T > 5$  GeV/ $c$ . In the endcap regions ( $1 < |\eta| < 2.5$ ) identification efficiency is above 70% already for muons with  $p_T > 3$  GeV/ $c$ .

### 4.2.2 Tracker system

The CMS tracker system based only on silicon detectors (220 m<sup>2</sup> of Si): micro-strip and pixel. The strip detector consists of 10 barrel layers and 9 disks positioned both forward and backward. Depending on rapidity the high  $p_T$  tracks leaves 10 to 14 hits. The hit resolution is  $\sim 50$   $\mu$ m in

$r - \phi$  direction and  $\sim 500 \mu\text{m}$  in  $z$ -direction. The pixel system is placed closer to the interaction point and consists of 3 barrel layers and 2 disks positioned both forward and backward. Since pixel dimension is  $100 \times 150 \mu\text{m}^2$  the detector provides precise 2D information. The hit resolution is  $\sim 10 \mu\text{m}$  in  $r - \phi$  direction and  $\sim 17 \mu\text{m}$  in  $z$ -direction. Momentum resolution of the CMS tracker system varies from 0.5 % in the central region to 2 % in the endcaps for tracks with  $p_T = 1 \div 10 \text{ GeV}/c$ . The primary and secondary vertex resolution is event dependent. Usually, for  $b$ -decay channels the primary vertex resolution in the transverse plane is about  $20 \mu\text{m}$  and the secondary one is  $70 \div 100 \mu\text{m}$ .

### 4.3 Trigger strategies

Triggering in CMS is done in two steps. The Level-1 trigger is based on muon and calorimetry information. It has a latency of  $3.2 \mu\text{s}$  with a goal to reduce an event rate from 40 MHz to 100 kHz. At the second step called High-Level Trigger (HLT), information from all subsystems are readout and used in the event reconstruction. The reconstruction should be fast, therefore it is done locally: topologically around Level-1 pattern. At HLT the event rate decreases from 100 kHz to 100 Hz.

B-physics events are relatively soft. Hence, Level-1 calorimetry triggers having high  $E_T$  thresholds do not 'see' such events. Only events with one or two muons in the final state can be triggered with high selection efficiency for soft  $b\bar{b}$  events (see, for example, the Level-1 trigger menu in [44]). The transverse momentum thresholds of these triggers depend on an instantaneous luminosity, but will be kept as low as possible in the range  $p_T > 7 \div 14 \text{ GeV}/c$  for single and  $p_T > 3 \div 7 \text{ GeV}/c$  for di-muon triggers. At HLT, exclusive and inclusive  $b$ -triggers, based on partial reconstruction of searched  $b$ -decay channels, are used. For the final states with two muons, a selection procedure which is used the reconstructed di-muon secondary vertex significantly improves a signal over background ratio. The detailed description of the trigger algorithms can be found in [45].

### 4.4 Physics channels

The CMS heavy flavour menu could be subdivided into two categories. The first one is approved results, which will be reported further. The second category is not finished or not yet approved by the Collaboration active studies. The last category will be only mentioned below.

#### 4.4.1 Inclusive $b$ production

Three different mechanisms contribute to the heavy flavour production at hadron colliders: gluon splitting, gluon/quark fusion and flavour excitation. Each of these production mechanism has its own final state topology. It is important to measure the B-hadron  $p_T$  spectra within a large range to be able to disentangle the contributions of those mechanisms. In CMS the measurement of the inclusive  $b$  production cross section will be done with events containing jets and at least one muon.

The measurement of the differential cross sections is studied for B-hadrons of  $p_T > 50 \text{ GeV}/c$  and within the rapidity region of  $|\eta| < 2.4$ . The event selection requires a  $b$ -tagged jet to be present in the event. B tagging is based on inclusive secondary vertex reconstruction in



jets [46]. As the Level-1 trigger, the single muon one is used with the threshold of 19 GeV/ $c$ . At HLT in addition to the muon a  $b$ -jet with  $p_T > 50$  GeV/ $c$  is required.

The signal fraction is determined from a fit to the data distribution using the simulated shapes for the signal and background. Each reconstructed muon is associated to the most energetic  $b$ -tagged jet. The average efficiency of associating the muon with the  $b$ -tagged jet is 75%. The transverse momentum of the muon with respect to the  $b$ -jet axis discriminates signal against background.

Several sources of systematic uncertainties are considered in the study [47]. The largest uncertainty arises from the 3% error on a jet energy scale which leads to a cross section error of 12% at  $p_T > 50$  GeV/ $c$ .

1.6 million  $b$ -events for 1 fb $^{-1}$  of an integrated luminosity will be collected to investigate the  $b$  production mechanism in CMS. The  $b$  purity of the selected events varies as function of the transverse momentum in a range from 70% to 55%. The  $b$  production cross-section at  $p_T = 1.2$  TeV/ $c$  can be measured with 20% uncertainty.

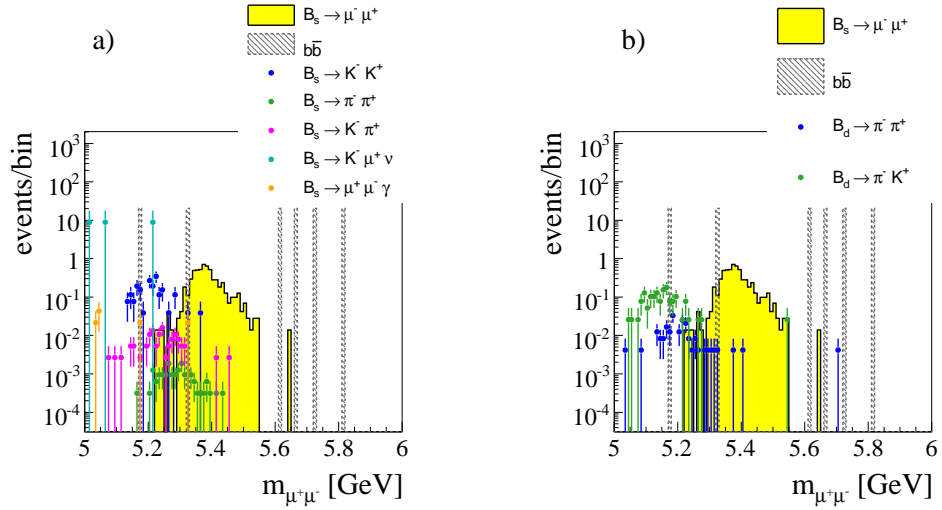


Fig. 21: Background  $m_{\mu\mu}$  distribution after the application of all selection criteria (with factorizing selection criteria) for all channels that are left: a)  $B_s$  decays, b)  $B_d$  decays.

#### 4.4.2 $B_s^0 \rightarrow \mu^+ \mu^-$

Purely leptonic  $B$ -decays are theoretically very clean, thus providing an ideal environment for seeking indirect hints of NP effects. The SM branching ratio of  $B_s^0 \rightarrow \mu^+ \mu^-$  is very small,  $(3.42 \pm 0.54) \cdot 10^{-9}$  [48], while in large- $\tan \beta$  NP models it can be enhanced by orders of magnitude [49]. Up to now only the upper limit on the branching ratio is set by the CDF Collaboration:  $4.7 \times 10^{-8}$  at the 90% C.L. [50].

The main challenge in the measurement of the  $B_s^0 \rightarrow \mu^+ \mu^-$  decay rate is background suppression. Many background sources can mimic the signal topology. First, non-resonant  $b\bar{b}$  events

Table 3: Background for  $B_s^0 \rightarrow \mu^+ \mu^-$  samples used in the analysis. The visible cross-section, and the corresponding number of events for  $10 \text{ fb}^{-1}$  is given. The visible cross-sections include fragmentation, branching fractions, and (fake) muon  $p_T$  and  $|\eta|$  selection criteria. The numbers  $N_{\mu ID}$  do not yet include any selection criteria but hadron misidentification probability.

Sample	Generator cuts/channels	$\sigma_{vis}[\text{fb}]$	$N_{\mu ID} (10 \text{ fb}^{-1})$
$b\bar{b} \rightarrow \mu^+ \mu^- + X$	$p_T^\mu > 3 \text{ GeV}/c,  \eta^\mu  < 2.4$	$1.74 \times 10^7$	$1.74 \times 10^8$
	$p_T^{\mu\mu} > 5 \text{ GeV}/c$		
	$0.3 < \Delta R(\mu\mu) < 1.8$		
	$5 < m_{\mu\mu} < 6 \text{ GeV}/c^2$		
$B_s$ decays	$B_s \rightarrow K^- K^+$	$2.74 \times 10^5$	274
	$B_s \rightarrow \pi^- \pi^+$	$9.45 \times 10^3$	3
	$B_s \rightarrow K^- \pi^+$	$3.08 \times 10^4$	16
	$B_s \rightarrow K^- \mu^+ \nu$	$2.80 \times 10^5$	$2.80 \times 10^4$
	$B_s \rightarrow \mu^+ \mu^- \gamma$	$1.29 \times 10^1$	130
$B_d$ decays	$B_d \rightarrow \pi^- \pi^+$	$8.34 \times 10^4$	21
	$B_d \rightarrow \pi^- K^+$	$3.74 \times 10^5$	187
	$B_d \rightarrow \pi^- \mu^+ \nu$	$1.25 \times 10^6$	$6.25 \times 10^4$
	$B_d \rightarrow \mu^+ \mu^- \pi_0$	$3.77 \times 10^1$	377
$B_u$ decay	$B_u \rightarrow \mu^+ \mu^- \mu^+ \nu$	$2.24 \times 10^3$	$2.24 \times 10^4$
$B_c$ decays	$B_c \rightarrow \mu^+ \mu^- \mu^+ \nu$	$2.01 \times 10^1$	201
	$B_c \rightarrow J/\psi \mu^+ \nu$	$1.89 \times 10^3$	$1.89 \times 10^4$
$\Lambda_b$ decays	$\Lambda_b \rightarrow p \pi^-$	$4.22 \times 10^3$	1
	$\Lambda_b \rightarrow p K^-$	$8.45 \times 10^3$	1
QCD hadrons	$5 < M(hh) < 6 \text{ GeV}/c^2$	$2.24 \times 10^{11}$	$1.12 \times 10^8$

with each  $b \rightarrow \mu X$  decays. Second, non-resonant QCD events, where two high  $p_T$  hadrons are misidentified as muons. And finally, rare  $B_d$ ,  $B^+$ ,  $B_s$  and  $\Lambda_b$  decays, comprising hadronic, semileptonic, and radiative decays. Some of these decays constitute a resonant background, like  $B_s \rightarrow K^+ K^-$ , others have a continuum di-muon invariant mass distribution. Potentially, the resonant background is the most dangerous one. But the contribution from such backgrounds is negligible due to the excellent mass resolution provided by the CMS detector. Fig. 21 shows background  $m_{\mu\mu}$  distribution after the application of all selection criteria for all channels that are left.

The current background simulation does not include muon samples due to hadronic in-flight decays or punch-through. It has been estimated that this hadronic component will increase the background level by about 10% (see Fig. 5.10.9 in [51]). Table 3 summarizes studied so far background samples. The probabilities for hadron misidentification used to calculate expected number of background events in CMS are found to be  $\varepsilon_\pi = 0.5\%$ ,  $\varepsilon_K = 1.0\%$ ,  $\varepsilon_p = 0.1\%$ .

As the Level-1 trigger the di-muon one with a threshold of  $p_T > 3 \text{ GeV}/c$  for each muon is used. The HLT strategy relies critically on the tracker detector for a fast and high-efficiency reconstruction of the primary and secondary vertexes, the determination of muon momenta and the mass of the muon pair. Two muons are reconstructed with only 6 hits per a track in the tracker system and required to have transverse momentum of  $p_T > 4 \text{ GeV}/c$ , to be in the central part of the detector  $|\eta| < 2.4$  and to have opposite charges. Vertexing the two muons provides a powerful handle in the rate reduction: the quality of the vertex fit must be  $\chi^2 < 20$ . The three-dimensional flight length is required to be  $l_{3D} > 150 \mu\text{m}$ . The invariant mass of the muon pair is required to be in a tight window ( $150 \text{ MeV}/c^2$ ) around the  $B_s$  meson mass.

For the offline analysis all tracks are reconstructed with full detector information. The same as above but tighter (e.g.  $\chi^2 < 1$ ) and additional selections are used to suppress background. The  $\eta\phi$  separation of the two muons  $\Delta R(\mu\mu) = \sqrt{\Delta\eta^2 + \Delta\phi^2}$  a powerful discriminator against gluon-gluon fusion background with both  $b$ -hadrons decaying semileptonically and must be in the range  $0.3 \div 1.2$ . The transverse momentum vector of the  $B_s$  candidate must be close to the displacement of the secondary vertex from the primary vertex: the cosine of the opening angle between the two vectors must fulfill  $\cos(\alpha) > 0.9985$ . The isolation  $I$  is determined from the  $B_s$  candidate transverse momentum and charged tracks with  $p_T > 0.9 \text{ GeV}/c$  in a cone with half-opening  $r = 1.0$  around the di-muon direction as follows:  $I = p_T^{\mu\mu} / (p_T^{\mu\mu} + \sum_{trk} |p_T|)$  and required to be  $I > 0.85$ . The significance of the flight length is required to be  $l_{3D}/\sigma_{3D} > 18.0$ . Mass separation between a di-muon candidate and the nominal  $B_s$  mass should not exceed  $100 \text{ MeV}/c^2$ .

For an integrated luminosity of  $10 \text{ fb}^{-1}$ , the expected number of signal events is  $n_S = 6.1 \pm 0.6_{stat} \pm 1.5_{sys}$ . The number of background events is  $n_B = (14.1)^{+22.3}_{-14.1}$ . An upper limit, extracted using the Bayesian approach, is  $Br(B_s^0 \rightarrow \mu^+ \mu^-) < 1.4 \cdot 10^{-8}$  at the 90% CL [52].

#### 4.4.3 $B_s \rightarrow J/\psi\phi$

Important properties of  $B_s^0$  system can be studied with the decay channel  $B_s^0 \rightarrow J/\psi\phi$ , such as the width and mass difference of the two weak eigenstates:  $\Delta\Gamma_s, \Delta m_s$ . In addition, the decay  $B_s^0 \rightarrow J/\psi\phi$  is a golden channel for CP violation measurements. The particular spin structure of this decay allows to express its time dependence in a particular basis, called *transversity basis*, as the sum of 6 amplitudes where physical parameters enter differently. The most important of them is the weak phase  $\phi_s$  which is at present strongly constrained by CKM fits [53] and could represent a clear hint of NP if found to be significantly different from this prediction. At present the flavour tagging tools required to extract the weak phase are not yet available in CMS and only the mixing measurement is considered here.

The Level-1 trigger is based on di-muon selection with  $p_T > 3 \text{ GeV}/c$  each. HLT is the same as the one for  $B_s^0 \rightarrow \mu^+ \mu^-$ , with additional requirement for the di-muon invariant mass to be within  $150 \text{ MeV}/c^2$  of the  $J/\psi$  mass. The  $J/\psi$  vertex is required to be  $3\sigma$  away from the primary vertex. The cosine of the angle between the transverse momentum vector and the transverse decay length vector of the  $J/\psi$  candidate is required to exceed 0.9.  $\phi$  candidates are reconstructed from all oppositely charged track pairs and all pairs with invariant mass within  $20 \text{ MeV}/c^2$  of the  $\phi$  mass are retained. All four tracks are then used for  $B_s^0$  candidates, requiring invariant mass within  $200 \text{ MeV}/c^2$  of nominal one. The transverse momentum of  $\phi$  and  $B_s^0$

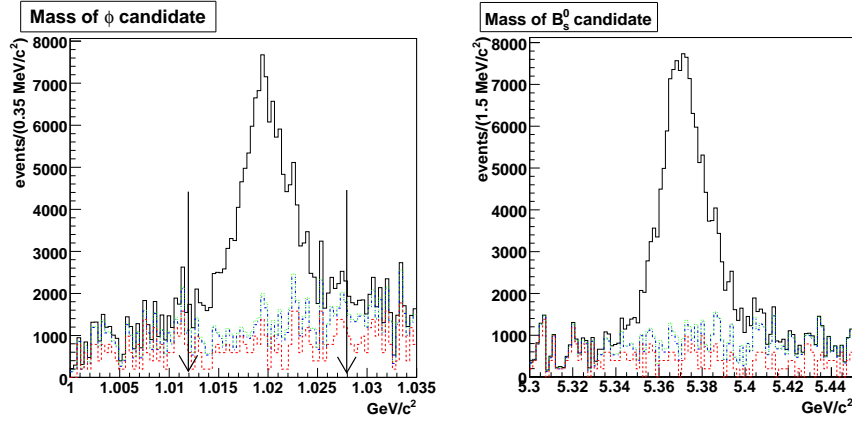


Fig. 22: Invariant mass of  $\phi$  (left) and  $B_s$  (right) candidates after all other cuts (except for the  $\phi$  mass requirement) have been applied; the selection on the  $\phi$  mass is indicated. Background is from inclusive  $b \rightarrow J/\psi X$  (red dashed line), from  $B_d^0 \rightarrow J/\psi K^{*0}$  (blue dashed-dotted line), and from combinatorial in signal events (green dotted line).

candidates are required to be greater than 1.0 and 5.0  $\text{GeV}/c$ , respectively.

The offline analysis follows the same criteria of HLT, but with complete information and tighter cuts. The main backgrounds arise from prompt  $J/\psi$  and  $B_d^0 \rightarrow J/\psi K^{*0}$  events. Fig. 22 shows invariant mass of  $\phi$  and  $B_s$  candidate distributions after all but  $\phi$  mass selections applied. From an untagged time-dependent analysis of  $B_s^0$  candidates the mixing parameters can be extracted. The result of the analysis shows that a first measurement of  $\Delta\Gamma_s/\Gamma_s$  can be made with 20% precision with an integrated luminosity of  $1.3 \text{ fb}^{-1}$ , while 5% precision can be reached with  $10 \text{ fb}^{-1}$  [54].

#### 4.4.4 $B_c^\pm \rightarrow J/\psi \pi^\pm$

The interest to the  $B_c$  meson relates to the uniqueness of the heavy-heavy quark system which carries flavour. The  $B_c$  meson has been observed at Tevatron and its mass and lifetime have been measured [55]. But available statistics does not allow to make such measurements precise enough and investigate properties of this system in details.

In CMS a feasibility study has been performed in the decay channel  $B_c^\pm \rightarrow J/\psi \pi^\pm$  [56]. First  $J/\psi$  candidates are composed by two muons with  $p_T > 4 \text{ GeV}/c$  and  $|\eta| < 2.2$  with opposite charge. The candidate invariant mass is required to be in the region from 3.0 to 3.2  $\text{GeV}/c^2$ . Then, pion candidates are selected by requiring a third track coming from the same vertex as the two muons with  $p_T > 2 \text{ GeV}/c$  and  $|\eta| < 2.4$ . The following selections are applied in addition: a proper decay length  $L_{xy}^{PDL} > 60 \text{ } \mu\text{m}$ , a significance  $L_{xy}/\sigma_{xy} > 2.5$  and an opening angle between the vector from primary to secondary vertex and the momentum vector of the reconstructed  $B_c$ :  $\cos\theta > 0.8$ .

For  $1 \text{ fb}^{-1}$  120 signal and less than 3 background events are expected. The reconstructed  $B_c$  mass is  $6.4 \text{ GeV}/c^2$  and the width of the mass peak is  $15 \text{ MeV}/c^2$ . To extract the  $B_c$  meson

lifetime a binned likelihood fit was performed, resulting in  $\tau = 460 \pm 45$  fs.

#### 4.4.5 Additional heavy flavour decays

Although the following analysis are not yet finalized, it is worth while to list them here to demonstrate a future spectrum of heavy flavour activity in CMS.

Measurements of  $b\bar{b}$  production cross-section and lifetimes of B-mesons will be done in the following decay channels:  $B^\pm \rightarrow J/\psi K^\pm \rightarrow \mu^+\mu^- K^\pm$ ,  $B \rightarrow D^0 \mu X$ ,  $b \rightarrow J/\psi + X \rightarrow \mu^+\mu^- + X$ . The correlation study of  $J/\psi$  vs  $\mu$  provides clean measurements of  $b\bar{b}$  production mechanisms. Searches for NP is also planned to be done in  $B_s \rightarrow \mu^+\mu^-\gamma$ ,  $B \rightarrow (\phi, K^*, K_s)\mu^+\mu^-$  decay channels.

### 4.5 Conclusions

While designed for high- $p_T$  physics, the CMS has a broad heavy flavour program. Main features which allow this program are 1) high  $b\bar{b}$  event rate even at a low ( $10^{32} - 10^{33}$ ) initial luminosity, 2) the efficient low  $p_T$  di-muon trigger and 3) excellent tracking that provides high momentum, mass, vertex resolution. Expected results are competitive with current B-physics experiments.

#### Acknowledgments

One of us (A.S.) would like to thank V. Ovakimian for his help in the preparation of this paper.

## 5 Top production in the CMS experiment at the LHC

*Authors: C. Rosemann and R. Wolf*

### 5.1 Top quark pair production in CMS

The LHC will provide proton proton collisions at center-of-mass energies of 14 (10) TeV with a specific luminosity of  $\approx 10 (0.1) \text{ nb}^{-1}\text{s}^{-1}$ . This will allow the inclusive production of top anti-top quark pairs at a rate of 100-(10) Hz (where the values in parenthesis are given for startup). The cross section for the production of top anti-top quark pairs in proton proton collisions at these center-of-mass energies is expected to be  $908 \pm 83 \pm 30 \text{ pb}$  ( $414 \pm 40 \pm 20 \text{ pb}$ ) [57], where the first error reflects scale uncertainties and the second error uncertainties in the choice and parametrization of parton density functions (PDFs). In the standard model (SM) top anti-top quark pair production is dominated by gluon gluon fusion (with a fraction of  $\approx 90\%$ ). As top quark production at the reached center-of-mass energies and luminosities at HERA is inaccessible the obvious impact of the HERA experiments on top production at the LHC lies in the determination of the most undefined gluon density function and thus in the reduction of the second uncertainty of the above cross section estimate. In figure 23 (left) three sets of different PDFs from the two HERA experiments H1 and ZEUS and from the CTEQ collaboration are shown at a scale of  $Q^2 = 10 \text{ GeV}^2$ . Due to kinematics and reconstruction requirements these PDFs will mostly be probed at large scales and medium to high proton momentum fraction  $x > 0.01$ , where these PDFs show smallest uncertainties and deviations.

In the beginning the emphasise will be put on the rediscovery of the top quark within the first (50-100)  $\text{pb}^{-1}$ , followed by inclusive cross section measurements based on robust selection

methods and first attempts to determine the top mass and differential cross sections with target luminosities of  $\approx 1 \text{ fb}^{-1}$ . An important aspect of top quark physics will be the capacity of top anti-top quark pair production of being a standard candle within the SM to exploit and demonstrate the detector understanding of the two major experiments ATLAS and CMS. The rediscovery of the top quark in early data taken with the CMS detector and prospects for first mass measurements in  $\approx 1 \text{ fb}^{-1}$  will be discussed in the following.

## 5.2 Rediscovery of the top quark

As an example for the rediscovery potential of the top quark within the first data a recent study in the semi-leptonic decay channel with a muon in the final state is presented [58]. It was performed for a target luminosity of  $10 \text{ pb}^{-1}$  of data at a center-of-mass energy of  $14 \text{ TeV}$  taken with the CMS detector. The conclusions may though be translated into equivalent conclusions for a luminosity of  $50 \text{ pb}^{-1}$  of data at a center-of-mass energy of  $10 \text{ TeV}$ . Focus was put on robust and simple selection methods with minimal dependency on detector components that may be least understood during startup. Main backgrounds are considered to be  $W$  or  $Z$  boson production with additional hard jets and QCD multijet production with leptons from  $b/c$  quark or in-flight decays which are mis-interpreted as originating from real  $W$  decays. Inclusive top anti-top pair production and  $W$  and  $Z$  boson production were produced with the Alpgen event generator for  $2 \rightarrow 4(5)$  processes in leading order and matched with parton showers using Pythia (values in parenthesis are given for inclusive top anti-top pair production). QCD multijet events were produced in leading order using Pythia. All events were passed through the full simulation of the

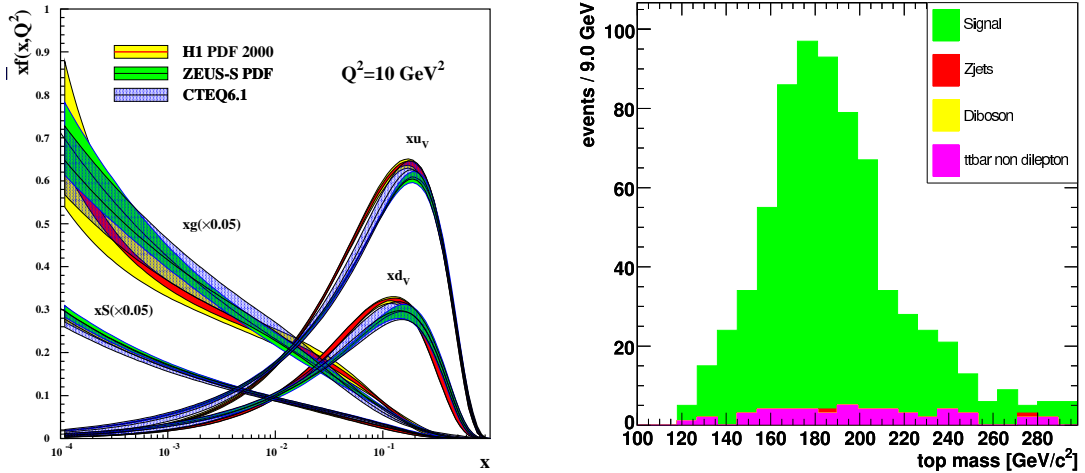


Fig. 23: (Left) Parton distribution functions (PDFs) from the HERA experiments H1 and ZEUS and from the CTEQ collaboration at a scale of  $Q^2 = 10 \text{ GeV}^2$ . Of relevance for top quark production at the LHC are the gluon density functions at values  $x > 0.01$  of the fractional proton momentum  $x$ . (Right) Top mass reconstructed from top anti-top quark pairs in the di-leptonic decay channel as expected from full simulation with the CMS detector with  $1 \text{ fb}^{-1}$  of integrated luminosity.

CMS detector including a simulation of the CMS L1 and High-Level-Trigger and mis-alignment and mis-calibration of the track detector and calorimeters as expected for the first  $10 \text{ pb}^{-1}$  were taken into account. Top events are selected by requiring a single isolated muon with transverse momentum  $p_T > 30 \text{ GeV}$  in the pseudo-rapidity range of  $|\eta| < 2.1$ , a leading jet with calibrated  $p_T > 65 \text{ GeV}$  and at least three further jets with calibrated  $p_T > 30 \text{ GeV}$  in a pseudo-rapidity range of  $|\eta| < 2.4$  in addition to the trigger criteria. With this selection the trigger efficiency is estimated to be above 90%. The muon is considered isolated if the summed  $p_T$  of all reconstructed tracks within a cone of  $\Delta R = \sqrt{\Delta\phi^2 + \Delta\eta^2} < 0.3$  in the vicinity of the muon does not exceed  $3 \text{ GeV}$  and the summed calorimeter entries in the same area do not exceed  $1 \text{ GeV}$ . Either  $b$ -tag information nor information on missing transverse energy are taken into consideration for the sake of a more robust event selection. In addition any of the selected jets is required to be separated from the isolated muon by at least  $0.3$  units in  $\Delta R$ .

This selection leads to a total of 128 events with top anti-top quark pairs in the semi-leptonic decay channel with a muon in the final state (with an estimated overall efficiency of 10%), 25 events with top anti-top pairs in other decay modes, 45  $W$ +jets events, 7  $Z$ +jets events and 11 multijet QCD events. The  $S/B$  is estimated to be  $1.5 : 1$  and the  $S/B(QCD)$  is estimated to be  $11 : 1$  with large uncertainties. As it is clear that the background from QCD multijet events will be the most difficult to control and to model methods for its estimation from data are discussed. This is a process still ongoing within the collaboration.

### 5.3 First measurements of the top mass

As an example for a measurement of the top quark mass within first data a study in the di-leptonic decay channel with  $1 \text{ fb}^{-1}$  of data taken with the CMS detector is presented [59]. Due to its clear event topology this channel is expected to have the best signal to background ratio. Main backgrounds are considered to be  $Z$  and di-boson production associated with additional hard jets and top events from other decay channels. All events were produced with the Pythia event generator in leading order and passed through the full simulation of the CMS detector including a simulation of the CMS L1 and High-Level-Trigger. Top events are selected by requiring two isolated leptons ( $e$  or  $\mu$ ) of opposite sign with transverse momentum  $p_T > 20 \text{ GeV}$ , two jets with  $p_T > 30 \text{ GeV}$  and missing transverse momentum larger than  $40 \text{ GeV}$ , in addition to the trigger criteria. Leptons are considered isolated if the summed  $p_T$  of all reconstructed tracks within a cone of  $\Delta R = \sqrt{\Delta\phi^2 + \Delta\eta^2} < 0.2$  in the vicinity of the lepton does not exceed 10% of the lepton's momentum. Electrons are identified using a likelihood method exploiting shower shape characteristics and the matching of tracks and calorimeter objects. For leptons of the same type an additional veto on the  $Z$  invariant mass is implied. The jets are required to fulfill a  $b$ -tag requirement based on the  $p_T$  and the invariant mass of the associated tracks and the result of a combined  $b$ -tag algorithm [60]. This selection is expected to provide a signal over background ratio of  $12 : 1$  for a top mass estimate between  $100$  and  $300 \text{ GeV}$  the remaining background mostly originating from other top decay channels. In fig. 23 (right) the most likely top mass determined from a parameter scan in the range of  $(100\text{-}300) \text{ GeV}$  is shown. Unknowns are reduced imposing constraints on momentum conservation in the transverse plane, the  $W$  invariant mass and the equality of the top mass in both decay branches. Remaining ambiguities are taken into account by a weighting procedure based on the SM expectation of the neutrino

momentum spectrum. The fit of a Gaussian function yields a top mass of  $m_{\text{top}}^{\text{rec}} = 178.5 \pm 1.5 \text{ (stat.)} \pm 4 \text{ (syst.) GeV}$  for an input mass of  $m_{\text{top}}^{\text{gen}} = 175 \text{ GeV}$ . Systematic uncertainties are expected to be dominated by the uncertainty of the validity of the imposed constraints in the presence of initial and final state radiation, and the uncertainty of the jet energy scale (JES). For  $10 \text{ fb}^{-1}$  the uncertainties are expected to be reduced to  $\Delta m_{\text{top}} = 0.5 \text{ (stat.)} \pm 1 \text{ (syst.) GeV}$ .

## References

- [1] Z. Lin and M. Gyulassy, Phys. Rev. **C51**, 2177 (1995).
- [2] Y. Dokshitzer and D. Kharzeev, Phys. Lett. **B519**, 199 (2001).
- [3] M. Djordjevic, M. Gyulassy, and S. Wicks, Phys. Rev. Lett. **94**, 112301 (2005).
- [4] PHENIX Collaboration, S. Adler *et al.*, Phys. Rev. Lett. **96**, 032301 (2006).
- [5] PHENIX Collaboration, A. Adare *et al.*, Phys. Rev. Lett. **98**, 172301 (2007).
- [6] STAR Collaboration, B. Abelev *et al.*, Phys. Rev. Lett. **98**, 192301 (2007).
- [7] R. Vogt, Eur. Phys. J. Special Topics **155**, 213 (2008).
- [8] STAR Collaboration, A. Mischke *et al.*, J. Phys. **G35**, 104117 (2008). ArXiv: 0804.4601.
- [9] A. Mischke, Phys. Lett. B. in press. ArXiv: 0807.1309.
- [10] M. Cacciari, P. Nason, and R. Vogt, Phys. Rev. Lett. **95**, 122001 (2005).
- [11] ALICE Collaboration, A. Dainese *et al.*, J. Phys. **G35**, 044046 (2008).
- [12] ALICE Collaboration, F. Carminati *et al.*, J. Phys. **G30**, 1517 (2005).
- [13] ALICE Collaboration, B. Alessandro *et al.*, J. Phys. **G32**, 1295 (2006).
- [14] Y. Dokshitzer and D. Kharzeev, Phys. Lett. **B519**, 199 (2001).
- [15] N. Armesto, A. Dainese, C. Salgado, and U. Wiedemann, Phys. Rev. **D71**, 054027 (2005).
- [16] M. Mangano, P. Nason, and G. Ridolfi, Nucl. Phys. **B373**, 295 (1992).
- [17] ALICE Collaboration, E. Bruna *et al.*, Preprint **nucl-ex/0703005** (2007).
- [18] S. Eidelmann and others [Particle Data Group Collaboration], Phys. Lett. **B592**, 1 (2004).
- [19] T. Sjöstrand, P. Edén, C. Friberg, L. Lönnblad, G. Miu, S. Mrenna, and E. Norrbin, Computer Phys. Commun. **135**, 238 (2001).
- [20] F. Antinori, A. Dainese, M. Lunardon, and R. Turrisi, ALICE Internal Note **033** (2006).
- [21] A. Dainese and M. Masera, ALICE Internal Note **027** (2003).
- [22] UA1 Collaboration, C. Albajar *et al.*, Phys. Lett. **B 213**, 405 (1988).



- [23] P. Crochet, R. Guernane, A. Morsch, and E. Vercellin, ALICE Internal Note **018** (2005).
- [24] J. Baines *et al.* hep-ph/0601164.
- [25] M. Cacciari, M. Greco, and P. Nason, JHEP **9805**, 007 (1998).
- [26] H. Jung, Computer Phys. Commun. **143**, 100 (2002).
- [27] M. Bedjidian *et al.* hep-ex/0311048.
- [28] CDF Collaboration, F. Acosta *et al.*, Phys. Rev. **D71**, 032001 (2005).  
hep-ex/0412071;  
CDF Collaboration, F. Acosta *et al.*, Phys. Rev. Lett. **88**, 161802 (2002).
- [29] A. D. Martin, R. G. Roberts, W. J. Stirling, and R. S. Thorne, Eur. Phys. J. **C4**, 463 (1998).  
hep-ph/9803445.
- [30] A. D. Martin, R. G. Roberts, W. J. Stirling, and R. S. Thorne, Phys. Lett.  
**B531**, 216 (2002). hep-ph/0201127.
- [31] CTEQ Collaboration, H. L. Lai *et al.*, Eur. Phys. J. **C12**, 375 (2000). hep-ph/9903282.
- [32] J. Pumplin *et al.*, JHEP **07**, 012 (2002).
- [33] ATLAS Collaboration, ATLAS TDR 15, CERN/LHCC 99-15 (1999).
- [34] D. Emeliyanov *et al.*, ATL-DAQ-CONF-2007-031 (2007).
- [35] P. Jussel *et al.*, ATL-PHYS-PUB-2007-003 (2007).
- [36] S. George, ATL-DAQ-2004-004 (2004).
- [37] CDF Collaboration, F. Acosta *et al.*, Phys. Ref. **D71**, 032001 (2005).
- [38] W. Yao *et al.*, J. of Phys. G **33**, 1 (2006).
- [39] CDF Collaboration, F. Abe *et al.*, Phys. Rev. Lett. **69**, 3704 (1992).
- [40] CDF Collaboration, F. Abulencia *et al.*, Phys. Rev. Lett. **99**, 132001 (2007).
- [41] G. Bodwin, E. Braaten, and G. Lepage, Phys. Rev. **D51**, 1125 (1995).
- [42] ATLAS Collaboration, CERN-OPEN-2008-020 (2008).
- [43] CMS Collaboration, S. Chatrchyan *et al.*, JINST **3**, S08004 (2008).
- [44] CMS Collaboration, CERN-LHCC-2006-021 (2006).
- [45] CMS Collaboration, CERN-LHCC-2002-026 (2006).
- [46] C. Weiser, CMS NOTE-2006/014 (2006).

- [47] V. Andreev, D. Cline, and S. Otwinowski, CMS NOTE-2006/120 (2006).
- [48] A. Buras, Phys. Lett. **B566**, 115 (2003).
- [49] K. Babu and C. Kolda, Phys. Rev. Lett. **84**, 228 (2000).
- [50] CDF Collaboration, T. Aaltonen *et al.*, Phys. Rev. Lett. **100**, 101802 (2008).
- [51] CMS Collaboration, J. Layter *et al.*, CERN-LHCC-1997-032 (1997).
- [52] U. Langenegger, CMS-CR-2006/071 (2006).
- [53] M. Bona *et al.*, JHEP **0610**, 081 (2006).
- [54] V. Ciulli *et al.*, CMS NOTE-2006/121 (2006).
- [55] CDF Collaboration, Phys. Rev. Lett. **96**, 082002 (2006).
- [56] X. Meng, J. Tao, and G. Chen, CMS NOTE-2006/118 (2006).
- [57] M. Cacciari *et al.*, arXiv:0804.2008.
- [58] CMS Collaboration, CMS PAS Top08-005.
- [59] CMS Collaboration, J. Phys. **G34**, 995 (2007).
- [60] R. Kinnunen and S. Lehti, CMS NOTE 2006/075.

# Heavy flavour production at the LHC: Theoretical Aspects

*Z. J. Ajaltouni<sup>a</sup>, A. Banfi<sup>b</sup>, S. Baranov<sup>c</sup>, I. Bierenbaum<sup>d</sup>, J. Blümlein<sup>e</sup>, G. Corcella<sup>f</sup>,  
M. Czakon<sup>g</sup>, G. Ferrera<sup>h</sup>, S. Klein<sup>e</sup>, B.A. Kniehl<sup>i</sup>, G. Kramer<sup>j</sup>, A. Likhoded<sup>j</sup>, D.A. Milstead<sup>k</sup>,  
O.I. Piskounova<sup>l</sup>, V.A. Saleev<sup>m</sup>, I. Schienbein<sup>n</sup>, H. Spiesberger<sup>o</sup>, R.S. Thorne<sup>p</sup>, W.K. Tung<sup>q</sup>,  
G. Zanderighi<sup>r</sup>, N. Zotov<sup>s</sup>*

<sup>a</sup> LPC, Université Blaise Pascal, F-63177 Aubière Cedex, France

<sup>b</sup> INFN, Sezione di Milano-Bicocca, Italy

<sup>c</sup> P.N. Lebedev Institute of Physics, Lenin avenue 53, Moscow 119991, Russia

<sup>d</sup> Deutsches Elektronen-Synchrotron, Platanenallee 6, D-15738 Zeuthen, Germany (now at IFIC, Universitat de València, Spain)

<sup>e</sup> Deutsches Elektronen-Synchrotron, Platanenallee 6, D-15738 Zeuthen, Germany

<sup>f</sup> Museo Storico della Fisica e Centro Studi e Ricerche ‘E. Fermi’, Roma, and Scuola Normale Superiore and INFN Sezione di Pisa, Italy

<sup>g</sup> University Würzburg, Germany

<sup>h</sup> University and INFN, Firenze, Italy

<sup>i</sup> II. Inst. für Theoretische Physik, Universität Hamburg, Germany

<sup>j</sup> Theoretical Department, Institute for High Energy Physics (IHEP), Protvino, Moscow reg., Russia

<sup>k</sup> Stockholm University, Sweden

<sup>l</sup> Lebedev Institute, Moscow, Russia

<sup>m</sup> Samara State University, Samara, Russia

<sup>n</sup> LPSC, Grenoble, France

<sup>o</sup> University Mainz, Germany

<sup>p</sup> University College London

<sup>q</sup> Michigan State U. and U. Washington, Seattle

<sup>r</sup> The Rudolf Peierls Centre for Theoretical Physics, 1 Keble Road, University of Oxford, UK

<sup>s</sup> Institute of Nuclear Physics, Moscow State University, Lenin Hills, Moscow 119991, Russia

## Abstract

A proper inclusion of heavy quark mass effects in Parton Distribution Function fits has proved crucial. We present a review these effects in DIS and their impact on global analyses and lay out all elements of a properly defined general mass variable flavor number scheme (GM VFNS) that are shared by all modern formulations of the problem. We also report about progress in a number of theoretical problems related to exclusive measurements of heavy flavors. These topics include fragmentation functions for charmed mesons including finite mass effects, fragmentation functions including non-perturbative corrections based on an effective QCD coupling, a discussion of the status of higher-order calculations for top quark production and for polarized structure functions, heavy quark and quarkonium production in the Regge limit, double heavy baryon production, tests of time reversal and CP symmetry in  $\Lambda_b$  decays, as well as a study of the general properties of massive

exotic hadrons that will be relevant for an understanding of their detection at the LHC.

*Coordinators: M. Cacciari and H. Spiesberger*

## 1 PQCD Formulations with Heavy Quark Masses and Global Analysis

*Authors: R.S. Thorne and W.K. Tung*

### 1.1 Introduction

The proper treatment of heavy flavours in global QCD analysis of parton distribution functions (PDFs) is essential for precision measurements at hadron colliders. Recent studies [1–5] show that the standard-candle cross sections for  $W/Z$  production at the LHC are sensitive to detailed features of PDFs that depend on heavy quark mass effects; and certain standard model as well as beyond standard model processes depend crucially on better knowledge of the  $c$ -quark parton density, in addition to the light parton flavors. These studies also make it clear that the consistent treatment of heavy flavours in perturbative QCD (PQCD) require theoretical considerations that go beyond the familiar textbook parton picture based on massless quarks and gluons. There are various choices, explicit and implicit, which need to be made in various stages of a proper calculation in generalised PQCD including heavy quark mass effects. In the global analysis of PDFs, these choices can affect the resulting parton distributions. Consistent choices are imperative; mistakes may result in differences that are similar to, or even greater than, the quoted uncertainties due to other sources (such as the propagation of input experimental errors). In this report, we will provide a brief, but full, review of issues related to the treatment of heavy quark masses in PQCD, embodied in the general mass variable flavor scheme (GM VFNS).

In Sec. 1.2, we describe the basic features of the modern PQCD formalism incorporating heavy quark masses. In Sec. 1.3, we first delineate the common features of GM VFNS, then identify the different (but self-consistent) choices that have been made in recent global analysis work, and compare their results. For readers interested in practical issues relating to the use (or choice) of PDFs in various physics applications, we present a series of comments in Sec. 1.4 intended as guidelines. In Sec. 1.5, we discuss the possibility of intrinsic heavy flavors.

We note that, this review on GM VFNS and global analysis is not intended to address the specific issues pertinent to heavy flavor production (especially the final state distributions). For this particular process, somewhat different considerations may favor the adoption of appropriate fixed flavor number schemes (FFNS). We shall not go into details of these considerations; but will mention the FFNS along the way, since the GM VFNS is built on a series of FFNS's. We will comment on this intimate relationship whenever appropriate.

### 1.2 General Considerations on PQCD with Heavy Flavor Quarks

The quark-parton picture is based on the factorization theorem of PQCD. The conventional proof of the factorization theorem proceeds from the zero-mass limit for all the partons—a good approximation at energy scales (generically designated by  $Q$ ) far above all quark mass thresholds

(designated by  $m_i$ ). This clearly does not hold when  $Q/m_i$  is of order 1.<sup>1</sup> It has been recognised since the mid-1980's that a consistent treatment of heavy quarks in PQCD over the full energy range from  $Q \lesssim m_i$  to  $Q \gg m_i$  can be formulated [6]. In 1998, Collins gave a general proof of the factorization theorem (order-by-order to all orders of perturbation theory) that is valid for non-zero quark masses [7]. The resulting general theoretical framework is conceptually simple: it represents a straightforward generalisation of the conventional zero-mass (ZM) modified minimal subtraction ( $\overline{\text{MS}}$ ) formalism and it contains the conventional approaches as special cases in their respective regions of applicability; thus, it provides a good basis for our discussions.

The implementation of any PQCD calculation on physical cross sections requires attention to a number of details, both kinematical and dynamical, that can affect both the reliability of the predictions. Physical considerations are important to ensure that the right choices are made between perturbatively equivalent alternatives that may produce noticeable differences in practical applications. It is important to make these considerations explicit, in order to make sense of the comparison between different calculations in the literature. This is what we shall do in this section. In subsequent sections, we shall point out the different choices that have been made in recent global analysis efforts.

Heavy quark physics at HERA involve mostly charm ( $c$ ) and bottom ( $b$ ) production; at LHC, top ( $t$ ) production, in addition, is of interest. For simplicity, we often focus the discussion of the theoretical issues on the production of a single heavy quark flavor, which we shall denote generically as  $H$ , with mass  $m_H$ . The considerations apply to all three cases,  $H = c, b, \& t$ . For global analysis, the most important process that requires precision calculation is DIS; hence, for physical predictions, we will explicitly discuss the total inclusive and semi-inclusive structure functions, generically referred to as  $F^\lambda(x, Q)$ , where  $\lambda$  represents either the conventional label (1, 2, 3) or the alternative ( $T, L, 3$ ) where  $T/L$  stands for transverse/longitudinal respectively.

### 1.2.1 The Factorization Formula

The PQCD factorization theorem for the DIS structure functions has the general form

$$F_\lambda(x, Q^2) = \sum_k f_k \otimes C_k^\lambda = \sum_k \int_\chi^1 \frac{d\xi}{\xi} f_k(\xi, \mu) C_k^\lambda \left( \frac{\chi}{\xi}, \frac{Q}{\mu}, \frac{m_i}{\mu}, \alpha_s(\mu) \right). \quad (1)$$

Here, the summation is over the active parton flavor label  $k$ ,  $f^k(x, \mu)$  are the parton distributions at the factorization scale  $\mu$ ,  $C_k^\lambda$  are the Wilson coefficients (or hard-scattering amplitudes) that can be calculated order-by-order in perturbation theory. The lower limit of the convolution integral  $\chi$  is determined by final-state phase-space constraints: in the conventional ZM parton formalism it is simply  $x = Q^2/2q \cdot p$ —the Bjorken  $x$ —but this is no longer true when heavy flavor particles are produced in the final state, cf. Sec. 1.2.4 below. The renormalization and factorization scales are jointly represented by  $\mu$ : in most applications, it is convenient to choose  $\mu = Q$ ; but there are circumstances in which a different choice becomes useful.

---

<sup>1</sup>Heavy quarks, by definition, have  $m_i \gg \Lambda_{QCD}$ . Hence we always assume  $Q, m_i \gg \Lambda_{QCD}$ . In practice,  $i = c, b, t$ .

### 1.2.2 Partons and Schemes for General Mass PQCD

In PQCD, the summation  $\sum_k$  over “parton flavor” label  $k$  in the factorization formula, Eq. (1), is determined by the *factorization scheme* chosen to *define* the Parton Distributions  $f_k(x, \mu)$ .

If mass effects of a heavy quark  $H$  are to be taken into account, the simplest scheme to adopt is the *fixed flavor number scheme* (FFNS) in which all quark flavors below  $H$  are treated as zero-mass and one sums over  $k = g, u, \bar{u}, d, \bar{d}, \dots$  up to  $n_f$  flavors of *light* (massless) quarks. The mass of  $H$ ,  $m_H$ , appears explicitly in the Wilson coefficients  $\{C_k^\lambda\}$ , as indicated in Eq. 1. For  $H = \{c, b, t\}$ ,  $n_f = \{3, 4, 5\}$  respectively. Historically, higher-order ( $\mathcal{O}(\alpha_s^2)$ ) calculations of the heavy quark production [8] were all done first in the FFNS. These calculations provide much improved results when  $\mu(Q)$  is of the order of  $m_H$  (both above and below), over those of the conventional ZM ones (corresponding to setting  $m_H = 0$ ).

Unfortunately, at any finite order in perturbative calculation, the  $n_f$ -FFNS results become increasingly unreliable as  $Q$  becomes large compared to  $m_H$ : the Wilson coefficients contain logarithmic terms of the form  $\alpha_s^n \ln^m(Q/m_H)$ , where  $m = 1 \dots n$ , at order  $n$  of the perturbative expansion, implying they are not infrared safe—higher order terms do not diminish in size compared to lower order ones—the perturbative expansion eventually breaks down. Thus, even if all  $n_f$ -flavor FFNS are mathematically equivalent, in practice, the 3-flavor scheme yields the most reliable results in the region  $Q \lesssim m_c$ , the 4-flavor scheme in  $m_c \lesssim Q \lesssim m_b$ , the 5-flavor scheme in  $m_b \lesssim Q \lesssim m_t$ , and, if needed, the 6-flavor scheme in  $m_t \lesssim Q$ . (Cf. related discussions later in this section.)

This leads naturally to the definition of the more general *variable flavor number scheme* (VFNS): it is a *composite scheme* consisting of the sequence of  $n_f$ -flavor FFNS, each in its region of validity, for  $n_f = 3, 4, \dots$  as described above; and the various  $n_f$ -flavor schemes are related to each other by perturbatively calculable transformation (finite-renormalization) matrices among the (running) coupling  $\alpha_s$ , the running masses  $\{m_H\}$ , the parton distribution functions  $\{f_k\}$ , and the Wilson coefficients  $\{C_k^\lambda\}$ . These relations ensure that there are only one set of independent renormalization constants, hence make the definition of the composite scheme precise for all energy scale  $\mu(Q)$ ; and they ensure that physical predictions are well-defined and continuous as the energy scale traverses each of the overlapping regions  $Q \sim m_H$  where both the  $n_f$ -flavor and the  $(n_f + 1)$ -flavor schemes are applicable. The theoretical foundation for this intuitively obvious scheme can be found in [6, 7], and it was first applied in detail for structure functions in [9]. Most recent work on heavy quark physics adopt this general picture, in one form or another. We shall mention some common features of this general-mass (GM) VFNS in the next few paragraphs; and defer the specifics on the implementation of this scheme, as well as the variations in the implementation allowed by the general framework until Sec. 1.3.

As mentioned above, the  $n_f$ -flavor and the  $(n_f + 1)$ -flavor schemes within the GM VFNS should be matched at some *match point*  $\mu_M$  that is of the order of  $m_H$ . In practice, the matching is commonly chosen to be exactly  $\mu_M = m_H$ , since it has been known that, in the calculational scheme appropriate for GM VFNS<sup>2</sup>, the transformation matrices vanish at this particular scale

<sup>2</sup>Technically, this means employing the CWZ subtraction scheme [10] in calculating the higher-order Feynman diagrams. CWZ subtraction is an elegant extension of the  $\overline{\text{MS}}$  subtraction scheme that ensures the decoupling of heavy quarks at high energy scales order-by-order. This is essential for factorization to be valid at each order of perturbation theory. (In the original  $\overline{\text{MS}}$  subtraction scheme, decoupling is satisfied only for the full perturbation

at NLO in the perturbative expansion [6]; thus discontinuities of the renormalized quantities are always of higher order, making practical calculations simpler in general.

Strictly speaking, once the component  $n_f$ -flavor schemes are unambiguously matched, one can still choose an independent *transition scale*,  $\mu_T$ , at which to switch from the  $n_f$ -flavor scheme to the  $(n_f + 1)$ -flavor scheme in the calculation of physical quantities in defining the GM VFNS. This scale must again be within the overlapping region, but can be different from  $\mu_M$  [1, 7]. In fact, it is commonly known that, from the physics point of view, in the region above the  $m_H$  threshold, up to  $\eta m_H$  with a reasonable-sized constant factor  $\eta$ , the most natural parton picture is that of  $n_f$ -flavor, rather than  $(n_f + 1)$ -flavor one.<sup>3</sup> For instance, the 3-flavor scheme calculation has been favored by most HERA work on charm and bottom quark production, even if the HERA DIS kinematic region mostly involves  $Q > m_c$ ; and it is also used in the dynamically generated parton approach to global analysis [11].

In practice, almost all implementations of the GM VFNS simply choose  $\mu_T = \mu_M = m_H$  (often not explicitly mentioning the conceptual distinction between  $\mu_T$  and  $\mu_M = m_H$ ). The self-consistency of the GM VFNS guarantees that physical predictions are rather insensitive to the choice of the transition point as long as it is within the overlapping region of validity of the  $n_f$ - and  $(n_f + 1)$ -flavor ones. The simple choice of  $\mu_T = m_H$  corresponds to opting for the lower end of this region for the convenience in implementation. In the following, we shall use the terms matching point and transition point interchangeably. As with all definition ambiguities in perturbative theory, the sensitivity to the choice of matching and transition points diminishes at higher orders.

### 1.2.3 Treatment of Final-state Flavors

For total inclusive structure functions, the factorization formula, Eq. (1), contains an implicit summation over all possible quark flavors in the final state. One can write,

$$C_k = \sum_j C_k^j \quad (2)$$

where “ $j$ ” denotes final state flavors, and  $\{C_k^j\}$  represent the Wilson coefficients (hard cross sections) for an incoming parton “ $k$ ” to produce a final state containing flavor “ $j$ ” calculable perturbatively from the relevant Feynman diagrams. It is important to emphasize that “ $j$ ” labels quark flavors that can be produced *physically* in the final state; it is *not* a *parton* label in the sense of initial-state parton flavors described in the previous subsection. The latter (labeled  $k$ ) is a theoretical construct and scheme-dependent (e.g. it is fixed at three for the 3-flavor scheme); whereas the final-state sum (over  $j$ ) is over *all flavors* that can be physically produced. Furthermore, the initial state parton “ $k$ ” does not have to be on the mass-shell, and is commonly treated as massless; whereas the final state particles “ $j$ ” should certainly be *on-mass-shell* in order to satisfy the correct kinematic constraints for the final state phase space and yield physically meaningful

---

series—to infinite orders.)

<sup>3</sup>Specifically, the  $n_f$ -flavor scheme should fail when  $\alpha_s(\mu) \ln(\mu/m_H) = \alpha_s(\mu) \ln(\eta)$  ceases to be a small parameter for the effective perturbation expansion. However, no theory can tell us precisely how small is acceptably “small”—hence how large  $\eta$  is permitted. Ardent FFNS advocates believe even the range of the 3-flavor scheme extends to all currently available energies, including HERA [11]. For GM VFNS, see the next paragraph.

results.<sup>4</sup> Thus, in implementing the summation over final states, the most relevant physical scale is  $W$ —the CM energy of the virtual Compton process—in contrast to the scale  $Q$  that controls the initial state summation over parton flavors.

The distinction between the two summations is absent in the simplest implementation of the conventional (i.e., textbook) zero-mass parton formalism: if all quark masses are set to zero to begin with, then all flavors can be produced in the final state. This distinction becomes blurred in the commonly used zero-mass (ZM) VFNS, where the heavy quark masses  $\{m_H\}$  implicitly enter because the number of effective parton flavors is incremented as the scale parameter  $\mu$  crosses each heavy quark threshold. This creates apparent paradoxes in the implementation of the ZM VFNS, such as: for  $\mu = Q < m_b$ ,  $b$  is not counted as a parton, the partonic process  $\gamma + g \rightarrow b\bar{b}$  would not be included in DIS calculations, yet physically this can be significant if  $W \gg 2m_b$  (small  $x$ ); whereas for  $\mu = Q > m_b$ ,  $b$  is counted as a massless parton, the contribution of  $\gamma + g \rightarrow b\bar{b}$  to DIS would be the same as that of  $\gamma + g \rightarrow d\bar{d}$ , but physically this is wrong for moderate values of  $W$ , and furthermore, it should be zero if  $W < 2m_b$  (corresponding to large  $x$ ). (We shall return to this topic in Sec. 1.3.1.)

These problems were certainly overlooked in conventional global analyses from its inception until the time when issues on mass-effects in PQCD were brought to the fore after the mid 1990's [9, 12–15]. Since then, despite its shortcomings the standard ZM VFNS continues to be used widely because of its simplicity and because NLO Wilson coefficients for most physical processes are still only available in the ZM VFNS. Most groups produce the standard ZM VFNS as either their default set or as one of the options, and they form the most common basis for comparison between groups, e.g. the “benchmark study” in [16].

It is obvious that, in a proper implementation of PQCD with mass (in any scheme), the distinction between the initial-state and final-state summation must be unambiguously, and correctly, observed. For instance, even in the 3-flavor regime (when  $c$  and  $b$  quarks are *not counted as partons*), the charm and bottom flavors still need to be counted in the final state—at tree-level via  $W^+ + d/s \rightarrow c$ , and at 1-loop level via the gluon-fusion processes such as  $W^+ + g \rightarrow \bar{s} + c$  or  $\gamma + g \rightarrow c\bar{c}$  ( $b\bar{b}$ ), provided there is enough CM energy to produce these particles.

#### 1.2.4 Phase-space Constraints and Rescaling

The above discussion points to the importance of the proper treatment of final state phase space in heavy quark calculations. Once mass effects are taken into account, kinematic constraints have a significant impact on the numerical results of the calculation; in fact, they represent the dominant factor in the threshold regions of the phase space. In DIS, with heavy flavor produced in the final state, the simplest kinematic constraint that comes to mind is

$$W - M_N > \sum_f M_f \quad (3)$$

where  $W$  is the CM energy of the vector-boson–nucleon scattering process,  $M_N$  is the nucleon mass, and the right-hand side is the sum of *all* masses in the final state.  $W$  is related to the famil-

---

<sup>4</sup>Strict kinematics would require putting the produced heavy flavor mesons or baryons on the mass shell. In the PQCD formalism, we adopt the approximation of using on-shell final state heavy quarks in the underlying partonic process.



iar kinematic variables  $(x, Q)$  by  $W^2 - M_N^2 = Q^2(1-x)/x$ , and this constraint should ideally be imposed on the right-hand side of Eq. (1). Any approach achieving this represents an improvement over the conventional ZM scheme calculations, that ignores the kinematic constraint Eq. (3) (resulting in a gross over-estimate of the corresponding cross sections). The implementation of the constraint in the most usual case of NC processes, say  $\gamma/Z + c \rightarrow c$  (or any other heavy quark) is not automatic (and is absent in some earlier definitions of a GM VFNS) because in this partonic process one must account for the existence of a *hidden heavy particle*—the  $\bar{c}$ —in the target fragment. The key observation is, heavy objects buried in the target fragment are still a part of the final state, and should be included in the phase space constraint, Eq. (3).

Early attempts to address this issue were either approximate or rather cumbersome, and could not be naturally extended to high orders.<sup>5</sup> A much better physically motivated approach is based on the idea of rescaling. The simplest example is given by charm production in the LO CC process  $W + s \rightarrow c$ . It is well-known that, when the final state charm quark is put on the mass shell, kinematics requires the momentum fraction variable for the incoming strange parton,  $\chi$  in Eq. (1) to be  $\chi = x(1 + m_c^2/Q^2)$  [17], rather than the Bjorken  $x$ . This is commonly called the *rescaling variable*. The generalization of this idea to the more prevalent case of NC processes took a long time to emerge [18, 19] which extended the simple rescaling to the more general case of  $\gamma/Z + c \rightarrow c + X$ , where  $X$  contains only light particles, it was proposed that the convolution integral in Eq. (1) should be over the momentum fraction range  $\chi_c < \xi < 1$ , where

$$\chi_c = x \left( 1 + \frac{4m_c^2}{Q^2} \right) . \quad (4)$$

In the most general case where there are any number of heavy particles in the final state, the corresponding variable is (cf. Eq. (3))

$$\chi = x \left( 1 + \frac{(\sum_f M_f)^2}{Q^2} \right) . \quad (5)$$

This rescaling prescription has been referred to as ACOT $\chi$  in the recent literature [18–20].

Rescaling shifts the momentum variable in the parton distribution function  $f^k(\xi, \mu)$  in Eq. (1) to a higher value than in the zero-mass case. For instance, at LO, the structure functions  $F_\lambda(x, Q)$  are given by some linear combination of  $f^k(x, Q)$  in the ZM formalism; but, with ACOT $\chi$  rescaling, this becomes  $f^k(\chi_c, Q)$ . In the region where  $(\sum_f M_f)^2/Q^2$  is not too small, especially when  $f(\xi, \mu)$  is a steep function of  $\xi$ , this rescaling can substantially change the numerical result of the calculation. It is straightforward to show that, when one approaches a given threshold  $(M_N + \sum_f M_f)$  from above, the corresponding rescaling variable  $\chi \rightarrow 1$ . Since generally  $f^k(\xi, \mu) \rightarrow 0$  as  $\xi \rightarrow 1$ , rescaling ensures a smoothly vanishing threshold behavior for the contribution of the heavy quark production term to all structure functions. This results in a universal<sup>6</sup>, and intuitively physical, realization of the threshold kinematic constraint for all heavy flavor production processes that is applicable to all orders of perturbation theory. For this reason, most recent global analysis efforts choose this method.

<sup>5</sup>In [9], the threshold violation was minimized by an artificial choice of the factorization scale  $\mu(m_H, Q)$ . In [14, 15] the kinematic limit was enforced exactly by requiring continuity of the slope of structure functions across the matching point, resulting in a rather complicated expression for the coefficient functions in Eq.(1).

<sup>6</sup>Since it is imposed on the (universal) parton distribution function part of the factorization formula.

### 1.2.5 Difference between $\{F_\lambda^{\text{tot}}\}$ and $\{F_\lambda^{\text{H}}\}$ Structure Functions

In PQCD, the most reliable calculations are those involving infra-red safe quantities—these are free from logarithmic factors that can become large (thereby spoiling the perturbative expansion). The total inclusive structure functions  $\{F_\lambda^{\text{tot}}\}$  defined in the GM VFNS are infrared safe, as suggested by the discussion of Sec. 1.2.2 and proven in Ref. [7].

Experimentally, the semi-inclusive DIS structure functions for producing a heavy flavor particle in the final state is also of interest. Theoretically, it is useful to note that the structure functions  $\{F_\lambda^{\text{H}}\}$  for producing heavy flavor  $H$  are not as well defined as  $F_\lambda^{\text{tot}}$ .<sup>7</sup> To see this, consider the relation between the two,

$$F_\lambda^{\text{tot}} = F_\lambda^{\text{light}} + F_\lambda^{\text{H}}, \quad (6)$$

where  $F_\lambda^{\text{light}}$  denotes the sum of terms with only light quarks in the final state, and  $F_\lambda^{\text{H}}$  consist of terms with at least one heavy quark  $H$  in the final state. Unfortunately,  $F_\lambda^{\text{H}}(x, Q, m_H)$  is, strictly speaking, *not infrared safe* beyond order  $\alpha_s$  (1-loop): they contain residual  $\ln^n(Q/m_H)$  terms at higher orders (2-loop and up). The same terms occur in  $F_\lambda^{\text{light}}$  due to contributions from virtual  $H$  loops, with the opposite sign. Only the sum of the two, i.e. the total inclusive quantities  $F_\lambda^{\text{tot}}$  are infra-red safe. This problem could be addressed properly by adopting a physically motivated, infrared-safe cut-off on the invariant mass of the heavy quark pair, corresponding to some experimental threshold [21] in the definition of  $F_\lambda^{\text{H}}$  (drawing on similar practises in jet physics). In practice, up to order  $\alpha_s^2$ , the result is numerically rather insensitive to this, and different groups adopt a variety of less sophisticated procedures, e.g. including contributions with virtual  $H$  loops within the definition of  $F_\lambda^{\text{H}}$ . Nonetheless, it is prudent to be aware that the theoretical predictions on  $F_\lambda^{\text{H}}$  are intrinsically less robust than those for  $F_\lambda^{\text{tot}}$  when comparing experimental results with theory calculations.

### 1.2.6 Conventions for “LO”, “NLO”, ... calculations

It is also useful to point out that, in PQCD, the use of familiar terms such as LO, NLO, ... is often ambiguous, depending on which type of physical quantities are under consideration, and on the convention used by the authors. This can be a source of considerable confusion when one compares the calculations of  $F_\lambda^{\text{tot}}$  and  $F_\lambda^{\text{H}}$  by different groups (cf. next section).

One common convention is to refer LO results as those derived from tree diagrams; NLO those from 1-loop calculations, ... and so on. This convention is widely used; and it is also the one used in the CTEQ papers. Another possible convention is to refer to LO results as the *first non-zero term* in the perturbative expansion; NLO as one order higher in  $\alpha_s$ , ... and so on. This convention originated in FFNS calculations of heavy quark production; and it is also used by the MRST/MSTW authors. It is a process-dependent convention, and it depends *a priori* on the knowledge of results of the calculation to the first couple of orders in  $\alpha_s$ .

---

<sup>7</sup>In the following discussion, we shall overlook logarithmic factors normally associated with fragmentation functions for simplicity. These are similar to those associated with parton distributions, but are less understood from the theoretical point of view—e.g. the general proof of factorization theorem (with mass) [7] has not yet been extended to cover fragmentation.

Whereas the two conventions coincide for quantities such as  $F_2^{\text{tot}}$ , they lead to different designations for the longitudinal structure function  $F_L^{\text{tot}}$  and the  $n_f$ -flavor  $F_2^{\text{H},n_f}$ , since the tree-level results are zero for these quantities. These designations, by themselves, are only a matter of terminology. However, mixing the two distinct terminologies in comparing results of different groups can be truly confusing. This will become obvious later.

### 1.3 Implementations of VFNS: Common Features and Differences

In this section, we provide some details of the PQCD basis for the GM VFNS, and comment on the different choices that have been made in the various versions of this general framework, implemented by two of the major groups performing global QCD analysis.

#### 1.3.1 Alternative Formulations of the ZM VFNS

As pointed out in Sec. 1.2.3, the ZM VFNS, as commonly implemented, represents an unreliable approximation to the correct PQCD in some kinematic regions because of inappropriate handling of the final-state counting and phase-space treatment, in addition to the neglect of heavy-quark mass terms in the Wilson coefficients. Whereas the latter is unavoidable to some extent, because the massive Wilson coefficients have not yet been calculated even at 1-loop level for most physical processes (except for DIS), the former (which can be more significant numerically in certain parts of phase space) can potentially be remedied by properly counting the final states and using the rescaling variables, as discussed in Secs. 1.2.3 and 1.2.4 under general considerations. Thus, alternative formulations of the ZM VFNS are possible that only involve the zero-mass approximation in the Wilson coefficient. This possibility has not yet been explicitly explored.

#### 1.3.2 Parton Distribution Functions in VFNS (ZM and GM)

In PQCD, the factorization scheme is determined by the choices made in defining the parton distribution functions (as renormalized Green functions). In a GM VFNS based on the generalized  $\overline{\text{MS}}$  subtraction (cf. footnote 2) the evolution kernel of the DGLAP equation is *mass-independent*; thus the PDFs, so defined, apply to GM VFNS calculations as they do for the ZM VFNS.

In the VFNS, the PDFs switch from the  $n_f$ -flavor FFNS ones to the  $(n_f + 1)$ -flavor FFNS ones at the matching point  $\mu = m_H$  (cf. Sec. 1.2.2); the PDFs above/below the matching point are related, order-by-order in  $\alpha_s$ , by:

$$f_j^{VF}(\mu \rightarrow m_H^+) \equiv f_j^{(n_f+1)FF} = A_{jk} \otimes f_k^{n_f FF} \equiv A_{jk} \otimes f_j^{VF}(\mu \rightarrow m_H^-), \quad (7)$$

where  $m_H^{+/-}$  indicate that the  $\mu \rightarrow m_H$  limit is taken from above/below, and we have used the shorthand VF/FF for VFNS/FFNS in the superscripts. The transition matrix elements  $A_{jk}(\mu/m_H)$ , representing a finite-renormalization between the two overlapping FFNS schemes, can be calculated order by order in  $\alpha_s$ ; they are known to NNLO, i.e.  $\mathcal{O}(\alpha_s^2)$  [12, 13]. (Note that  $A_{jk}$  is not a square matrix.) It turns out, at NLO,  $A_{jk}(\mu = m_H) = 0$  [7]; thus  $f_k^{VF}$  are continuous with this choice of matching point. There is a rather significant discontinuity in heavy quark distributions and the gluon distribution at NNLO.

With the matching conditions, Eq. 7,  $\{f_j^{VF}(\mu)\}$  are uniquely defined for all values of  $\mu$ . We shall omit the superscript VF in the following. Moreover, when there is a need to focus on  $f_j(\mu)$  in the vicinity of  $\mu = m_H$ , where there may be a discontinuity, we use  $f_j^{+/-}(\mu)$  to distinguish the above/below branch of the function. As indicated in Eq. 7,  $f_j^-$  correspond to the  $n_f$ -flavor PDFs, and  $f_j^+$  to the  $(n_f + 1)$ -flavor ones.

### 1.3.3 The Structure of a GM VFNS, Minimal Prescription and Additional Freedom

Physical quantities should be independent of the choice of scheme; hence, in a GM VFNS, we must require the theoretical expressions for the structure functions to be continuous across the matching point  $\mu = Q = m_H$  to each order of perturbative theory:

$$F(x, Q) = C_k^-(m_H/Q) \otimes f_k^-(Q) = C_j^+(m_H/Q) \otimes f_j^+(Q) \quad (8)$$

$$\equiv C_j^+(m_H/Q) \otimes A_{jk}(m_H/Q) \otimes f_k^-(Q). \quad (9)$$

where we have suppressed the structure function label ( $\lambda$ ) on  $F$ 's and  $C$ 's, and used the notation  $C_k^{+/-}$  to denote the Wilson coefficient function  $C_k(m_H/Q)$  above/below the matching point respectively. Hence, the GM VFNS coefficient functions are also, in general, discontinuous, and must satisfy the transformation formula:

$$C_k^-(m_H/Q) = C_j^+(m_H/Q) \otimes A_{jk}(m_H/Q). \quad (10)$$

order-by-order in  $\alpha_s$ . For example, at  $\mathcal{O}(\alpha_s)$ ,  $A_{Hg} = \alpha_s P_{qg}^0 \ln(Q/m_H)$ , this constraint implies,

$$C_{H,g}^{-,1}(m_H/Q) = \alpha_s C_{H,H}^{+,0}(m_H/Q) \otimes P_{qg}^0 \ln(Q/m_H) + C_{H,g}^{+,1}(m_H/Q). \quad (11)$$

where the numeral superscript (0,1) refers to the order of calculation in  $\alpha_s$  (for  $P_{jk}$ , the order is by standard convention one higher then indicated), and the suppressed second parton index on the Wilson coefficients (cf. Eq. 2) has been restored to make the content of this equation explicit. Eq. (11) was implicitly used in defining the original ACOT scheme [9]. The first term on the RHS of Eq. 11, when moved to the LHS, becomes the *subtraction term* of Ref. [9] that serves to define the Wilson coefficient  $C_{H,g}^{+,1}(m_H/Q)$  (hence the scheme) at order  $\alpha_s$ , as well as to eliminate the potentially infra-red unsafe logarithm in the gluon fusion term ( $C_{H,g}^{-,1}(m_H/Q)$ ) at high energies.

The GM VFNS as described above, consisting of the general framework of [6, 7], along with transformation matrices  $\{A_{jk}\}$  calculated to order  $\alpha_s^2$  by [12, 13], is accepted in principle by all recent work on PQCD with mass. Together, they can be regarded as the *minimal GM VFNS*.

The definition in Eq. 10 was applied to find the asymptotic limits ( $Q^2/M_H^2 \rightarrow \infty$ ) of coefficient functions in [12, 13], but it is important to observe that it does not completely define all Wilson coefficients across the matching point, hence, there are additional flexibilities in defining a specific scheme [7, 14, 15, 22]. This is because, as mentioned earlier, the transition matrix  $\{A_{jk}\}$  is not a square matrix—it is  $n_f \times (n_f + 1)$ . It is possible to swap  $\mathcal{O}(m_H/Q)$  terms between Wilson coefficients on the right-hand-side of Eq. 10 (hence redefining the scheme) without violating the general principles of a GM VFNS. For instance, one can swap  $\mathcal{O}(m_H/Q)$  terms between  $C_H^{+,0}(m_H/Q)$  and  $C_g^{+,1}(m_H/Q)$  while keeping intact the relation (11) that guarantees the

continuity of  $F(x, Q)$  according to Eq. 8. This general feature, applies to (10) to all orders. It means, in particular, that there is no need to calculate the coefficient function  $C_H^{+,i}(m_H/Q)$ , for any  $i$  – it can be chosen as a part of the definition of the scheme. Also, it is perfectly possible to define coefficient functions which do not individually satisfy the constraint in Eq. 3, since Eq. 10 guarantees ultimate cancellation of any violations between terms. However, this will not occur perfectly at any finite order so modern definitions do include the constraint explicitly, as outlined in Sec. 1.2.4.

The additional flexibility discussed above has been exploited to simplify the calculation, as well as to achieve some desirable features of the prediction of the theory by different groups. Of particular interest and usefulness is the general observation that, given a GM VFNS calculation of  $\{C_j^+\}$ , one can always switch to a simpler scheme with constant  $\{\tilde{C}_j^+\}$

$$\tilde{C}_H^+(m_H/Q) = C_H^+(0) \quad (12)$$

This is because the shift  $(C_H^+(m_H/Q) - C_H^+(0))$  vanishes in the  $m_H/Q \rightarrow 0$  limit, and can be absorbed into a redefinition of the GM scheme as mentioned above. The detailed proof are given in [7, 22]. By choosing the heavy-quark-initiated contributions to coincide with the ZM formulae, the GM VFNS calculation becomes much simplified: given the better known ZM results, we only need to know the full  $m_H$ -dependent contributions from the light-parton-initiated subprocesses; and these are exactly what is provided by the  $n_f$ -flavor FFNS calculations available in the literature. This scheme is known as the *Simplified ACOT scheme*, or SACOT [7, 22].

Further uses of the freedom to reshuffle  $\mathcal{O}(m_H/Q)$  terms between Wilson coefficients, as well as adding terms of higher order in the matching condition (without upsetting the accuracy at the given order) have been employed extensively by the MRST/MSTW group, as will be discussed in Sec. 1.3.5.

#### 1.3.4 CTEQ Implementation of the GM VFNS

The CTEQ group has always followed the general PQCD framework as formulated in [6, 7]. Up to CTEQ6.1, the default CTEQ PDF sets were obtained using the more familiar ZM Wilson coefficients, because, the vast majority of HEP applications carried out by both theorists and experimentalists use this calculational scheme. For those applications that emphasized heavy quarks, special GM VFNS PDF sets were also provided; these were named as CTEQnHQ, where  $n = 4, 5, 6$ .

The earlier CTEQ PDFs are now superseded by CTEQ6.5 [1] and CTEQ6.6 [3] PDFs; these are based on a new implementation of the general framework described in previous sections, plus using the simplifying SACOT choice of heavy quark Wilson coefficients [9, 23] specified by Eq. 12 above. There are no additional modifications of the formulae of the minimal GM VFNS, as described in previous sections. CTEQ uses the convention of designating tree-level, 1-loop, 2-loop calculations as LO, NLO, and NNLO, for all physical quantities,  $F_\lambda^{\text{tot}}$ ,  $F_\lambda^{\text{H}}$ , ... etc., cf. Sec. 1.2.6.

With these minimal choices, this implementation is extremely simple. Continuity of physical predictions across matching points in the scale variable  $\mu = Q$  is guaranteed by Eqs. 8 and 10; and continuity across physical thresholds in the physical variable  $W$ , for producing heavy

flavor final states, are guaranteed by the use of ACOT- $\chi$  rescaling variables 5, as described in Sec. 1.2.4.

For example, to examine the continuity of physical predictions to NLO in this approach, we have, for the below/above matching point calculations:

$$\begin{aligned} F_2^{-H}(x, Q^2) &= \alpha_s C_{2,Hg}^{-,1} \otimes g^{n_f} \\ F_2^{+H}(x, Q^2) &= \alpha_s C_{2,Hg}^{+,1} \otimes g^{n_f+1} + (C_{2,HH}^{+,0} + \alpha_s C_{2,HH}^{+,1}) \otimes (h + \bar{h}) \end{aligned} \quad (13)$$

where non-essential numerical factors have been absorbed into the convolution  $\otimes$ . The continuity of  $F_2^H(x, Q^2)$  in the scaling variable  $\mu = Q$  is satisfied by construction (Eq. 9) because the relation between the PDFs given by Eq. 7 and that between the Wilson coefficients given by Eq. 8 involve the same transformation matrix  $\{A_{jk}\}$  (calculated in [12, 13, 21]). In fact, to this order,  $A_{Hg} = \alpha_s P_{qg}^0 \ln(Q/m_H)$ , hence

$$\begin{aligned} h(\bar{h}) &= 0 \\ g^{n_f+1} &= g^{n_f} \\ C_{2,Hg}^{+,1} &= C_{2,Hg}^{-,1}, \end{aligned}$$

at the matching point  $\mu = Q = m_H$ . Thus, the two lines in Eq. 13 give the same result, and  $F_2^H(x, Q^2)$  is continuous. The separate issue of continuity of  $F_2^H(x, Q^2)$  in the physical variable  $W$  across the production threshold of  $W = 2m_H$  is satisfied automatically by each individual term (using the ACOT- $\chi$  prescription for the quark terms and straightforward kinematics for the gluon term).

In the CTEQ approach, all processes are treated in a uniform way; there is no need to distinguish between neutral current (NC) and charged current (CC) processes in DIS, (among others, as in MRST/MSTW). All CTEQ global analyses so far are carried out up to NLO. This is quite adequate for current phenomenology, given existing experimental and other theoretical uncertainties. Because NNLO results has been known to show signs of unstable behavior of the perturbative expansion, particularly at small- $x$ , they are being studied along with resummation effects that can stabilize the predictions. This study is still underway.

### 1.3.5 MRST/MSTW Implementation of the GM VFNS

**Prescription.** In the Thorne-Roberts (TR) heavy flavour prescriptions, described in [14, 15] the ambiguity in the definition of  $C_{2,HH}^{VF,0}(Q^2/m_H^2)$  was exploited by applying the constraint that  $(dF_2^H/d \ln Q^2)$  was continuous at the transition point (in the gluon sector). However, this becomes technically difficult at higher orders. Hence, in [20] the choice of heavy-flavour coefficient functions for  $F_2^H$  was altered to be the same as the SACOT( $\chi$ ) scheme described above. This choice of heavy-flavour coefficient functions has been used in the most recent MRST/MSTW analysis, in the first instance in [2]. To be precise the choice is

$$C_{2,HH}^{VF,n}(Q^2/m_H^2, z) = C_{2,HH}^{ZM,n}(z/x_{max}). \quad (14)$$

This is applied up to NNLO in [20] and in subsequent analyses. For the first time at this order satisfying the requirements in Eq.(10) leads to discontinuities in coefficient functions, which up

to NNLO cancel those in the parton distributions. This particular choice of coefficient functions removes one of the sources of ambiguity in defining a GM VFNS. However, there are additional ambiguities in the MRST/MSTW convention for counting LO, NLO, ... calculations (cf. Sec.1.2.6), coming about because the ordering in  $\alpha_S$  for  $F_2^H(x, Q^2)$  is different above and below matching points in Eqs. 9-11. (These complications do not arise in the minimal GM VFNS adopted by CTEQ, as already mentioned in the previous subsection.)

For the neutral current DIS  $F_2$  structure function, the above-mentioned ambiguities can be seen as follows:

	below	above
LO	$\frac{\alpha_S}{4\pi} C_{2,Hg}^{-,1} \otimes g^{n_f}$	$C_{2,HH}^{+,0} \otimes (h + \bar{h})$
NLO	$\left(\frac{\alpha_S}{4\pi}\right)^2 (C_{2,Hg}^{-,2} \otimes g^{n_f} + C_{2,Hq}^{-,2} \otimes \Sigma^{n_f})$	$\frac{\alpha_S}{4\pi} (C_{2,HH}^{+,1} \otimes (h + \bar{h}) + C_{2,Hg}^{+,1} \otimes g^{n_f+1})$
NNLO	$\left(\frac{\alpha_S}{4\pi}\right)^3$	$\sum_i C_{2,Hi}^{+,2} \otimes f_i^{n_f} \left(\frac{\alpha_S}{4\pi}\right)^2 \sum_j C_{2,Hj}^{+,2} \otimes f_j^{n_f+1},$

(15)

with obvious generalization to even higher orders. This means that switching directly from a fixed order with  $n_f$  active quarks to fixed order with  $n_f + 1$  active quarks leads to a discontinuity in  $F_2^H(x, Q^2)$ . As with the discontinuities in the ZM-VFNS already discussed this is not just a problem in principle – the discontinuity is comparable to the errors on data, particularly at small  $x$ . The TR scheme, defined in [14, 15], and all subsequent variations, try to maintain the particular ordering in each region as closely as possible. For example at LO the definition is

$$\begin{aligned}
 F_2^H(x, Q^2) &= \frac{\alpha_S(Q^2)}{4\pi} C_{2,Hg}^{-,1}(Q^2/m_H^2) \otimes g^{n_f}(Q^2) \\
 &\rightarrow \frac{\alpha_S(m_H^2)}{4\pi} C_{2,Hg}^{-,1}(1) \otimes g^{n_f}(m_H^2) + C_{2,HH}^{+,0}(Q^2/m_H^2) \otimes (h + \bar{h})(Q^2). \quad (16)
 \end{aligned}$$

The  $\mathcal{O}(\alpha_S)$  term is frozen when going upwards through  $Q^2 = m_H^2$ . This generalizes to higher orders by freezing the term with the highest power of  $\alpha_S$  in the definition for  $Q^2 < m_H^2$  when moving upwards above  $m_H^2$ . Hence, the definition of the ordering is consistent within each region, except for the addition of a constant term (which does not affect evolution) above  $Q^2 = m_H^2$  which becomes progressively less important at higher  $Q^2$ , and whose power of  $\alpha_S$  increases as the order of the perturbative expansion increases.

This definition of the ordering means that in order to define a GM VFNS at NNLO [20] one needs to use the  $\mathcal{O}(\alpha_S^3)$  heavy-flavour coefficient functions for  $Q^2 \leq m_H^2$  (and that the contribution will be frozen for  $Q^2 > m_H^2$ ). This would not be needed in a ACOT-type scheme. As mentioned above, these coefficient functions are not yet calculated. However, as explained in [20], one can model this contribution using the known leading threshold logarithms [24] and leading  $\ln(1/x)$  terms derived from the  $k_T$ -dependent impact factors [25]. This results in a significant contribution at small  $Q^2$  and  $x$  with some model dependence. However, variation in the free parameters does not lead to a large change.<sup>8</sup>

<sup>8</sup>It should be stressed that this model is only valid for the region  $Q^2 \leq m_H^2$ , and would not be useful for a NNLO

The above discussions focused on  $F_2^H$ ; but they mostly apply to  $F_L$  as well. We only need to mention that, with the adoption of the SACOT prescription for heavy-quark initiated contributions (i.e. using the ZM version of the Wilson coefficient),  $F_L^H$  vanishes at order  $\alpha_s^0$  as it does in the TR prescriptions. (This zeroth order coefficient function does appear in some older GM VFNS definitions.) According to the MRST/MSTW convention, the order  $\alpha_s^1$  term of  $F_L$  (both light and heavy flavour) counts as LO, and so on, whereas in the CTEQ convention each relative order is a power of  $\alpha_s$  lower.

The general procedure for the GM VFNS for charged-current deep inelastic scattering can work on the same principles as for neutral currents, but one can produce a *single* charm quark from a strange quark so  $\chi = x(1 + m_c^2/Q^2)$ . However, there is a complication compared to the neutral current case because the massive FFNS coefficient functions are not known at  $\mathcal{O}(\alpha_s^2)$  (only asymptotic limits [27] have been calculated). These coefficient functions are needed in a TR-type scheme at low  $Q^2$  at NLO, and for any GM VFNS at all  $Q^2$  at NNLO. This implies that we can only define the TR scheme to LO and the ACOT scheme to NLO. However, known information can be used to model the higher order coefficient functions similarly to the TR scheme definition to NNLO for neutral currents. A full explanation of the subtleties can be found in [28].

**Scheme variations.** The inclusion of the complete GM VFNS in a global fit at NNLO first appeared in [2], and led to some important changes compared a previous NNLO analysis, which had a much more approximate inclusion of heavy flavours (which was explained clearly in the Appendix of [29]). There is a general result that  $F_2^c(x, Q^2)$  is flatter in  $Q^2$  at NNLO than at NLO, as shown in Fig. 4 of [2], and also flatter than in earlier (approximate) NNLO analyses. This had an important effect on the gluon distribution. As seen in Fig. 5 of [2], it led to a larger gluon for  $x \sim 0.0001 - 0.01$ , as well as a larger value of  $\alpha_s(M_Z^2)$ , both compensating for the naturally flatter evolution, and consequently leading to more evolution of the light quark sea. Both the gluon and the light quark sea were 6 – 7% greater than in the MRST2004 set [30] for  $Q^2 = 10,000 \text{ GeV}^2$ , the increase maximising at  $x = 0.0001 - 0.001$ . As a result there was a 6% increase in the predictions for  $\sigma_W$  and  $\sigma_Z$  at the LHC. This would hold for all LHC processes sensitive to PDFs in this  $x$  range, but would be rather less for processes such as  $t\bar{t}$  pair production sensitive to  $x \geq 0.01$ . This surprisingly large change is a correction rather than a reflection of the uncertainty due to the freedom in choosing heavy flavour schemes and demonstrates that the MRST2004 NNLO distributions should now be considered to be obsolete.

To accompany the MRST 2006 NNLO parton update there is an unofficial “MRST2006 NLO” set, which is fit to exactly the same data as the MRST2006 NNLO set. By comparing to the 2004 MRST set one can check the effect on the distributions due to the change in the prescription for the GM VFNS at NLO without complicating the issue by also changing many other things in the analysis. The comparison of the up quark and gluon distributions for the “MRST2006 NLO” set and the MRST2004 NLO set, i.e. the comparable plot to Fig. 5 of [2] for NNLO, is shown in Fig. 1. As can be seen it leads to the same trend for the partons as at NNLO, i.e. an increase in the small- $x$  gluon and light quarks, but the effect is much smaller –

---

FFNS at all  $Q^2$  since it contains no information on the large  $Q^2/m_H^2$  limits of the coefficient functions. A more general approximation to the  $\mathcal{O}(\alpha_s^3)$  coefficient functions could be attempted, but full details would require first the calculation of the  $\mathcal{O}(\alpha_s^3)$  matrix element  $A_{Hg}$ . This more tractable project is being investigated at present [26].



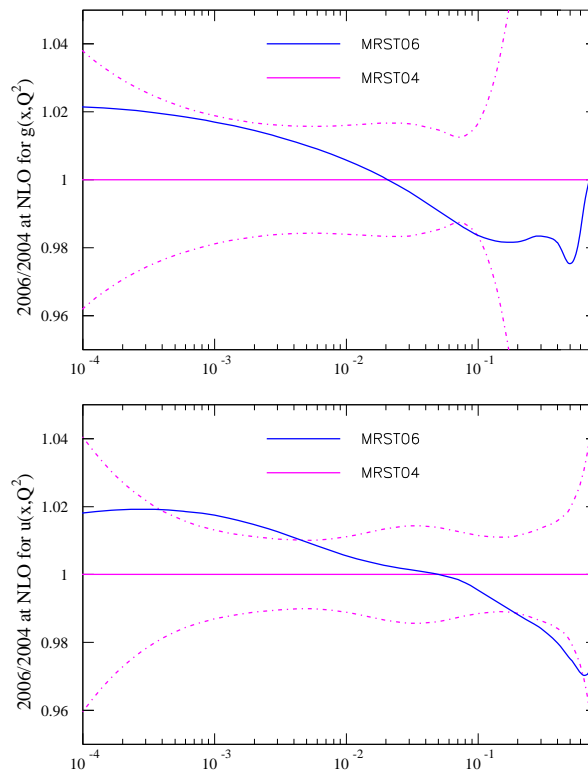


Fig. 1: A comparison of the unpublished “MRST2006 NLO” parton distributions to the MRST2004 NLO distributions. In order to illustrate the significance of the size of the differences, the uncertainty on the MRST2001 distributions is used for the 2004 distributions.

a maximum of a 2% change. Also, the value of the coupling constant increases by 0.001 from the 2004 value of  $\alpha_S(M_Z^2) = 0.120$ . From momentum conservation there must be a fixed point and this is at  $x \sim 0.05$ . Hence,  $W, Z$  and lighter particle production could be affected by up to 2 – 3%, and very high mass states by a similar amount, but final states similar in invariant mass to  $t\bar{t}$  will be largely unaffected. Hence, we can conclude that the change in our choice of the heavy-flavour coefficient function alone leads to changes in the distributions of up to 2%, and since the change is simply a freedom we have in making a definition, this is a theoretical uncertainty on the partons, much like the frequently invoked scale uncertainty. Like the latter, it should decrease as we go to higher orders.

### 1.3.6 Comparisons

We have tried to make clear that both the CTEQ and the MRST/MSTW approaches are consistent with the PQCD formalism with non-zero heavy quark masses  $\{m_H\}$ . In this sense, they are both “valid”. In addition, they both adopt certain sensible practises, such as the numerically significant rescaling-variable approach to correctly treat final-state kinematics (ACOT- $\chi$ ), and the calculationally simplifying SACOT prescription for the quark-parton initiated subprocesses. These common features ensure broad agreement in their predictions. This is borne out by the fact that global QCD analyses carried out by both groups show very good agreement with all available hard scattering data, including the high-precision DIS total inclusive cross sections and semi-inclusive heavy flavor production cross sections; and that the predictions for higher energy cross sections at LHC for the important W/Z production process agree rather well in the most recent versions of these analyses [2, 3].<sup>9</sup> Comparisons of experiment for the abundant data on total inclusive cross sections (and the associated structure functions) with theory are well documented in the CTEQ and MRST/MSTW papers. Here we only show the comparison of the recent H1 data sets on cross sections for charm and bottom production [31] to the latest CTEQ and MSTW calculations. This figure illustrates the general close agreement between the two calculations. (Also, see below.)

Because the main source of the differences between the two implementations arise from the different conventions adopted for organizing the perturbative calculation, it is impossible to make a direct (or clear-cut) comparison between the two calculations. By staying with the conventional order-by-order formulation, the CTEQ approach has all the simplicities of the minimal GM VFNS. With the alternative LO/NLO/NNLO organization, the MRST/MSTW approach includes specifically chosen higher-order terms at each stage of the calculation for different physical quantities (e.g.  $F_2^{\text{tot}}, F_L^{\text{tot}}, F_2^H$ , in Secs. 1.3.5) with their associated Wilson coefficients (e.g. Eqs. 15, 16). The choices are a matter of taste because, with the same Wilson coefficients (with heavy quark mass) available in the literature (such as [12, 13]), both analyses can be extended to the appropriate order, and they should contain the same information. So far, MRST/MSTW has carried out their analyses to one order higher than CTEQ. In practice, we have seen one comparison of the “NLO” predictions of the two approaches in Fig. 2 that shows remarkable general agreement with each other, and with experimental data. Some expected differences at small- $x$ , due to the higher order term included in the MRST/MSTW calculation are

<sup>9</sup>Some apparent worrying discrepancies in the predictions for the W/Z cross-sections at LHC between [1] and [30] have been superseded by the recent analyses.

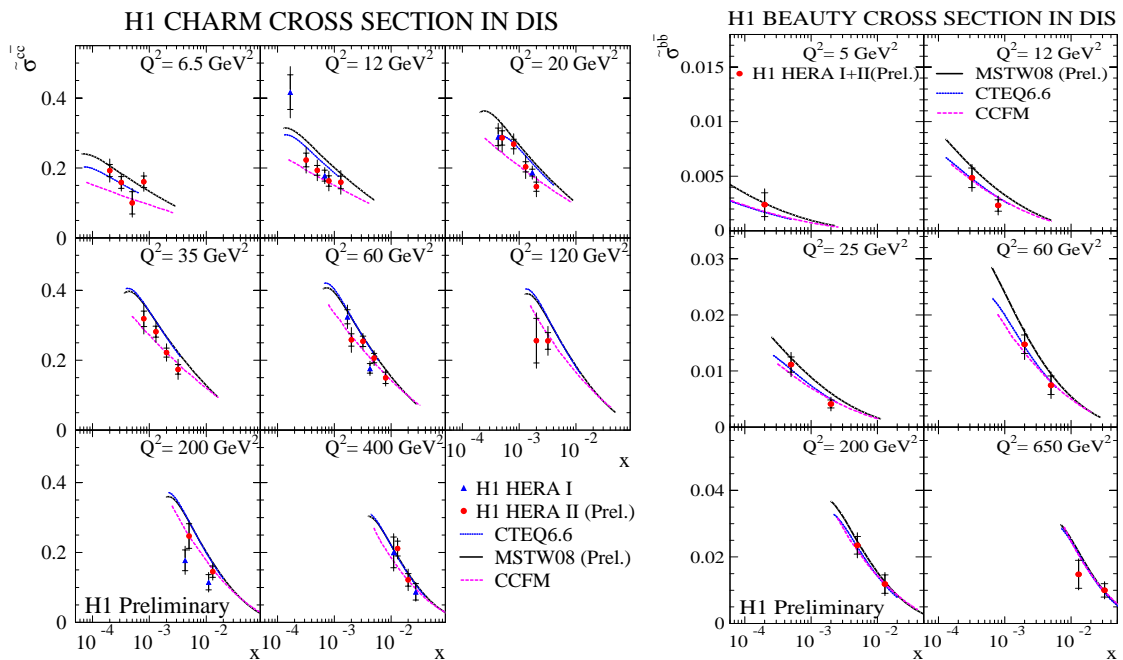


Fig. 2: Comparison of the predictions for  $\bar{\sigma}^{c\bar{c}}(x, Q^2)$  and  $\bar{\sigma}^{b\bar{b}}(x, Q^2)$  compared to preliminary data from H1.

present. Compared to experimental data, the CTEQ curves seem to give a slightly better description of data in this region of difference; but this should not be taken seriously in view of the above discussions. We intend to make a more quantitative study of the differences between the alternative formulations of a GM VFNS and ZM VFNS in a future publication.

#### 1.4 Use of Parton Distribution Functions

Some commonly asked questions in the user community for PDFs are along the lines of: (i) Which available PDF set is most appropriate for my particular calculation? and (ii) If PDF set A was obtained using scheme A (say, ZMVFNS/GMVFNs-MSTW/GMVFNs-CTEQ) do I have to use the same scheme A for my Wilson coefficients (otherwise my calculation would be inconsistent)? Whereas it is impossible to answer all such questions at once, the following observations should provide useful guidelines toward the appropriate answers. Foremost, it is important to bear in mind that in the perturbative approach, all calculations are approximate; hence the goodness of the approximation is the most (or only) relevant consideration. Any fast, or absolute, rules or prescriptions would be misguided.

\* For applications at very high energy scales, e.g. most LHC processes, it is perfectly fine to use the ZM formulae for the hard-scattering coefficient *irrespective of the choice of PDF sets* (see below), since the ZM Wilson coefficients are good approximations to the GM ones (valid to  $\mathcal{O}(M^2/Q^2)$  where  $M$  represents the typical mass in the relevant parton subprocess—heavy quarks or other produced particles), and the ZM coefficients are much simpler and *much more* readily available.

On the other hand, for applications involving physical scales  $Q \sim \mathcal{O}(M)$ , such as comparison to precision DIS data at HERA, it is important both to use GM Wilson coefficients, and to ensure that these are consistent with those adopted in generating the PDF set to be used in the calculation.

\* For the global analyses that yield the PDF sets, it matters whether the ZM VFNS or GM VFNS scheme is used in the calculation, since a substantial fraction of the input DIS data are in the region where  $Q$  is not very large compared to the heavy quark masses  $m_{c,b}$  (the top quark does not play a significant role in these analysis). Thus, the ZM-VFNS and GM VFNS PDFs can differ in some  $x$ -range, even if they agree quite well in general (cf. [1]). For example, the widely used CTEQ6.1 (ZM-VFNS) and the most recent CTEQ6.5/CTEQ6.6 (GM VFNS) PDF sets both give excellent fits to the available data, yet the differences (mainly around  $x \sim 10^{-3}$ ) are enough to lead to a 6% shift in the predictions for cross sections for  $W, Z$  and similar mass states at the LHC. Higher mass final states are much less affected.

The above differences arise from two sources: (i) the treatment of final-state counting (Sec. 1.2.3) and phase space (Sec. 1.2.4); and (ii) mass effects in the Wilson coefficients. The first is numerically significant for reasons explained in those sections, and it can potentially be removed to produce an improved ZM VFNS (Sec. 1.3.1).

\* The differences between PDFs obtained using different GM VFNS implementations, such as those by CTEQ and MSTW groups discussed in the main part of this review, are much smaller than those between the ZM and GM VFNS. This is because the treatments of final states are similar, and the differences in the Wilson coefficients are much reduced also. The current NLO predictions on  $W/Z$  cross sections at LHC by the CTEQ and MSTW groups, for instance, are within 2% [4].

\* What about single-flavor (say,  $n_f$ ) FFNS PDFs that are commonly believed to be needed for FFNS calculations, such as for heavy flavor production processes? We would like to point out, perhaps surprisingly to many readers, that: (i) with the advent of GM VFNS PDFs, *the FFNS PDFs are not in principle needed* for consistency; and (ii) the use of  $n_f$ -flavor FFNS PDFs in a  $n_f$ -flavor calculation is much *less reliable* than using the GM VFNS (if the latter is available). The reasons for these assertions are fairly easy to see, as we now explain.

First of all, as we emphasized in Sec. 1.2.2, the GM VFNS is, by definition, a composite scheme that *is* the  $n_f$ -FFNS within the region of validity of the latter. In principle one *can* use the GM VFNS PDFs in the FFNS calculations within the region where the FFNS is reliable. (In practice this range of validity (in energy scale  $\mu$ ) extends up to several times  $m_H$ , cf. second to last paragraph of Sec. 1.2.2.) Secondly, since any given  $n_f$ -FFNS has only a limited range of validity (Sec. 1.2.2), the global analysis used to determine any  $n_f$ -FFNS PDF set is inherently a compromise. This compromise is likely to be a fairly bad one for two reasons. Firstly, the limited range of validity implies that only a fraction of the data used in the global analysis can be legitimately applied. If one excludes all the data outside of the region of validity of the theory (not an easily-defined region), the constraining power of the analysis would greatly suffer. If, instead, one includes all the points in the analysis anyway, the PDFs will compensate, much like the case of the fit using the basic ZM VFNS. This can result in a good comparison to data (as in the ZM VFNS [32]), but this is potentially misleading since the compensation is caused by

the wrong physics. In either of the cases, the PDFs resulting from a fit using the FFNS will be unreliable. Secondly, Wilson coefficients in the FFNS only exist for the DIS process beyond LO, hence the ZM approximation to  $n_f$ -FFNS must be used. We note, although this second point is shared by current GM VFNS analyses, the ZM VFNS approximation to GM VFNS is a much better approximation than that of ZM FFNS to  $n_f$ -FFNS. (For instance, for collider jet data sets, the ZM 3- or 4-flavor calculation would be way-off the correct one. This is not a problem for the GM VFNS case.) These inherent problems motivated an alternative approach to FFNS PDFs in [33]: rather than performing a (imperfect) FFNS global fit, one simply generates them by fixed  $n_f$ -flavor QCD evolution from a set of initial PDFs obtained in an existing (bona fide) GM VFNS global analysis! Because of the different QCD evolution, however, the PDFs will be different from the original GM VFNS ones crossing heavy flavor thresholds; and the fits to the global data will correspondingly deteriorate, particularly for the high precision HERA data sets at higher  $Q^2$ . Thus, these PDFs deviate from truth in a different way. The relative merit between this approach and the conventional FFNS global fits is difficult to gauge because there are no objective criteria for making the assessment.

Returning to the original question that started this bullet item, we can summarize the options available to match PDFs with a FFNS calculation such as HQVDIS [34] for heavy quark production: (i) conventional FFNS PDFs (CTEQ, GRV), suitably updated if necessary [35]; (ii) PDFs generated by FFNS evolution from GM VFNS PDFs at some initial scale  $Q_0$  (MSTW [33], but also can easily be done with CTEQ); or, (iii) simply use the most up-to-date GM VFNS PDFs (MSTW, CTEQ) for all  $Q$ . For reasons discussed in the previous paragraphs, each option has its advantages and disadvantages. (i) and even (ii) are theoretically self-consistent, while (iii) is not, e.g. it opens up the awkward question of how many flavours to use in the definition of  $\alpha_s$ . However, the PDFs in (iii) are intrinsically much more accurately and precisely determined. Hence, in practical terms it is not obvious which would be most “correct”.<sup>10</sup> The choice reduces to a matter of taste, and for some, of conviction. The differences in results, obtained using these options, should not be too large, since they are mostly of one order higher in  $\alpha_s$ ; and, in an approximate manner, they define the existing theoretical uncertainty. In principle, an approach that combines the advantages of all three, hence could work the best, would be to use PDFs obtained in the GM VFNS, but with the transition scale  $\mu_T$  (Sec. 1.2.3) set at a much higher value than  $m_H$  for each heavy flavor threshold. But this option is rather cumbersome to implement (as has been hinted in Sec. 1.2.3), hence has not been done.

\* There exists another class of applications, involving multiple-scale processes, such as heavy flavor production at hadron colliders with finite transverse momentum  $p_T$  or in association with  $W/Z$  or Higgs, for which PQCD calculations are more complex than the familiar one-hard-scale case, as implicitly assumed above. Since these processes can play an important role in LHC, there has been much discussions, and controversies, in recent literature about the various approaches that may be applied [36]. Both the GM VFNS [37] and FFNS approaches have been advocated [38]. The problem is complex, generally because more than one kind of potentially large logarithms occur in these problems, and they cannot be effectively controlled all at once with some suitable choice of scheme. A detailed discussion is outside the scope of this paper,

---

<sup>10</sup>Although it is certainly better to use a current GM VFNS set of PDFs than an out-of-date FFNS set.

although our remark about the FFNS PDFs above could be helpful (and relieve some of the anxieties expressed in the literature).

All in all, for general applications, taking into account all the considerations above, the modern GM VFNS PDF sets are clearly the PDFs of choice.

## 1.5 Intrinsic Heavy Flavour

Throughout the above discussions we have made the assumption that all heavy quark flavour is generated from the gluon and lighter flavours through the perturbative QCD evolution, starting from the respective scale  $\mu = m_H$ . This is usually referred to as the *radiatively generated heavy flavor* scenario. From the theoretical point of view, this is reasonable for heavy flavors with mass scale ( $m_H$ ) very much higher than the on-set of the perturbative regime, say  $\sim 1$  GeV. Thus, while this assumption is usually not questioned for bottom and top, the case for charm is less obvious. In fact, the possibility for a non-negligible *intrinsic charm* (IC) component of the nucleon at  $\mu = Q \sim m_c$  was raised a long time ago [39]; and interests in this possibility have persisted over the years. Whereas the dynamical origin of such a component can be the subject of much debate, the phenomenological question of its existence can be answered by global QCD analysis: do current data support the IC idea, and if so, what is its size and shape? This problem has been studied recently by a CTEQ group [40], under two possible scenarios: IC is enhanced at high values of  $x$  (suggested by dynamical models such as [39]), or it is similar in shape to the light-flavor sea quarks (similar to, say, strange). They found that current data do not tightly constrain the charm distribution, but they *can* place meaningful bounds on its size. Thus, while the conventional radiatively generated charm is consistent with data, IC is allowed in both scenarios. For the model-inspired (large- $x$ ) case, the size of IC can be as large as  $\sim 3$  times that of the crude model estimates, though comparison to the EMC  $F_2^c$  data [41] imply contributions somewhat smaller [42]. If such an IC component does exist, it would have significant impact on LHC phenomenology for certain beyond SM processes. For the sea-like IC case, the bound on its size is looser (because it can be easily interchanged with the other sea quarks in the global fits); its phenomenological consequences are likewise harder to pin-point.

From a theoretical point of view, intrinsic heavy flavour and GM VFNS definitions were discussed in [43]. Allowing an intrinsic heavy quark distribution actually removes the redundancy in the definition of the coefficient functions in the GM VFNS, and two different definitions of a GM VFNS will no longer be identical if formally summed to all orders, though they will only differ by contributions depending on the intrinsic flavour. Consider using identical parton distributions, including the intrinsic heavy quarks, in two different flavour schemes. The heavy-quark coefficient functions at each order are different by  $\mathcal{O}(m_H^2/Q^2)$ . This difference has been constructed to disappear at all orders when combining the parton distributions other than the intrinsic heavy quarks, but will persist for the intrinsic contribution. The intrinsic heavy-flavour distributions are of  $\mathcal{O}(\Lambda_{QCD}^2/m_H^2)$ , and when combined with the difference in coefficient functions the mass-dependence cancels leading to a difference in structure functions of  $\mathcal{O}(\Lambda_{QCD}^2/Q^2)$ . It has been shown [7] that for a given GM VFNS the calculation of the structure functions is limited in accuracy to  $\mathcal{O}(\Lambda_{QCD}^2/Q^2)$ . Hence, when including intrinsic charm, the scheme ambiguity is of the same order as the best possible accuracy one can obtain in leading twist QCD, which is admittedly better than that obtained from ignoring the intrinsic heavy flavour (if it exists) as  $Q^2$

increases above  $m_H^2$ . It is intuitively obvious that best accuracy will be obtained from a definition of a GM VFNS where all coefficient functions respect particle kinematics. In fact, the most recent CTEQ and MSTW prescriptions would provide identical contributions to the structure functions from the same intrinsic charm parton distribution.

**Acknowledgements** We thank Matteo Cacciari for his unrelenting efforts to bring about this review on behalf of the Heavy Flavor Workshop of the HERALHC Workshop. We thank our collaborators in CTEQ and MRST/MSTW for collaborations which underlies much of the content of this paper. WKT would like especially to acknowledge the insight provided by John Collins on the theoretical foundation of PQCD with heavy quarks. We also thank Pavel Nadolsky, Fred Olness, Ingo Schienbein, Jack Smith and Paul Thompson for reading the manuscript and making useful comments that brought about improvements in the presentation of the paper.

The work of WKT is supported by the National Science Foundation (USA) under the grant PHY-0354838.

## 2 Charmed-meson fragmentation functions with finite-mass corrections

*Authors: B. A. Kniehl, G. Kramer, I. Schienbein, and H. Spiesberger*

A straight-forward and conventional approach to include heavy-quark mass effects in the theoretical predictions for the production of single heavy-flavor mesons consists in taking into account the non-zero quark mass  $m_h$  in a calculation where only light quarks and the gluon exist in the initial state and the heavy quark is pair-produced in the hard scattering process. Such a scheme is called a fixed-flavor-number scheme (FFNS) and can be implemented, presently, only at NLO. It is reliable in a kinematic region not far above production threshold. At high scales  $\mu$ , however, the presence of logarithmic terms proportional to  $\log(\mu/m_h)$  makes the predictions of a calculation in the FFNS unreliable. These logarithmic terms have to be resummed, which is conventionally done in the so-called zero-mass variable-flavor-number scheme (ZM-VFNS) where the heavy quark is treated as a parton, in addition to light quarks and the gluon. Heavy quark parton distribution functions and fragmentation functions, which are present in this scheme, can absorb the large logarithmic terms and resummation is performed with the help of the DGLAP evolution equations.

The general-mass variable-flavor-number scheme (GM-VFNS) provides a framework for the theoretical description of the inclusive production of single heavy-flavored hadrons, combining virtues of both the FFNS and the ZM-FVNS in a unified approach. It resums large logarithms by the DGLAP evolution of non-perturbative fragmentation functions, guarantees the universality of the latter as in the ZM-VFNS, and simultaneously retains the mass-dependent terms of the FFNS without additional assumptions. It was elaborated at next-to-leading order (NLO) for photo- [45] and hadroproduction [46,47] and  $e^+e^-$  annihilation [48].

Recent progress in the implementation of the GM-VFNS at NLO allowed us to extract mass-dependent FFs for  $D$ -mesons from global fits to  $e^+e^-$  annihilation data [48]. We used experimental data from the Belle, CLEO, ALEPH, and OPAL Collaborations [44]. The fits for  $D^0$ ,  $D^+$ , and  $D^{*+}$  mesons using the Bowler ansatz [49] yielded  $\chi^2/\text{d.o.f.} = 4.03, 1.99$ , and  $6.90$ , respectively. The result of the fit for  $D^+$  mesons is shown in Fig. 3.

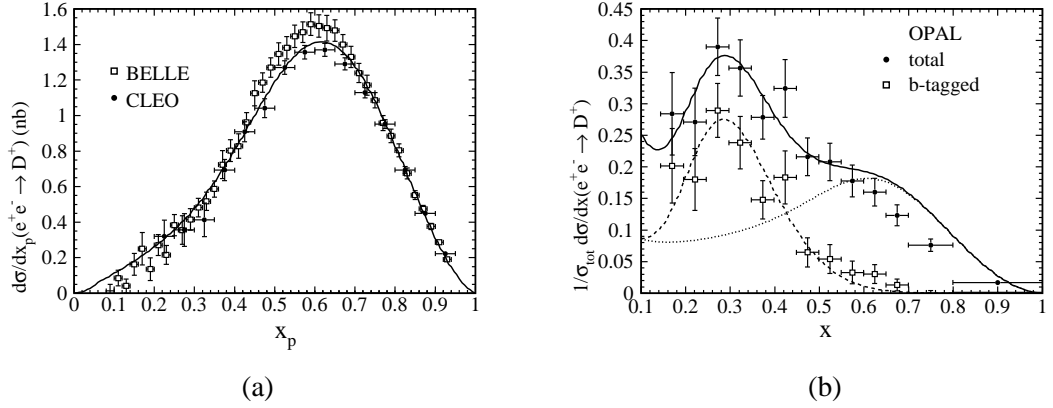


Fig. 3: Comparison of (a) Belle, CLEO, and (b) OPAL data on  $D^+$  mesons [44] with a global fit. The dotted line in panel (b) refers to the  $c$ -quark-initiated contribution.

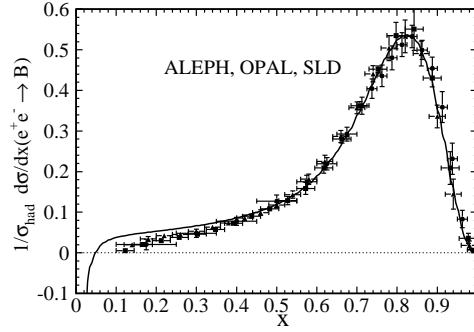


Fig. 4: Comparison of the ALEPH, OPAL, and SLD data on  $B$  meson production [50] with a fit for the  $b \rightarrow B$  FF.

The significance of finite-mass effects can be assessed through a comparison with a similar analysis in the ZM-VFNS. It turned out that for the experimental conditions at Belle and CLEO, charmed-hadron mass effects on the phase space are appreciable, while charm-quark mass effects on the partonic matrix elements are less important. In Figs. 3(a) and (b), the scaled-momentum distributions from Belle and CLEO and the normalized scaled-energy distributions from OPAL for  $D^+$  mesons are compared to the global fits. The Belle and CLEO data prefer higher values for the average  $x$  of the  $c \rightarrow D$  FFs. Due to their smaller errors they dominate the global fit, and the ALEPH and OPAL data are less well described. Charmed hadrons may also originate indirectly through the fragmentation of a  $b$  quark. Our ansatz includes non-perturbative  $b \rightarrow D$  FFs, but these are only weakly constrained by the Belle and CLEO data.

Previous fits of the  $b \rightarrow B$  FFs in the ZM-VFNS [52] were based on  $e^+e^-$  data from ALEPH, OPAL and SLD [50] and used the Kartvelishvili-Likhoded ansatz [53]. As a recent improvement we adjusted the value of  $m_b$  and the energy scale where the DGLAP evolution starts,



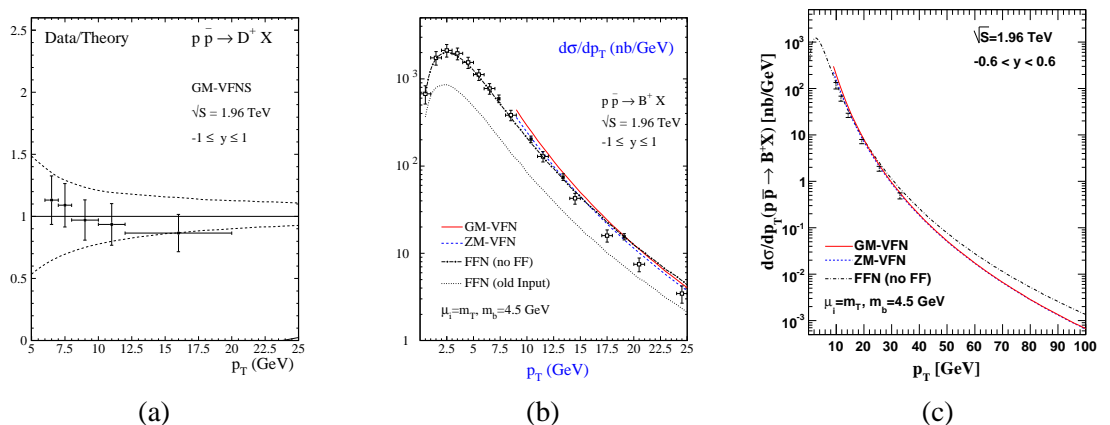


Fig. 5: (a) Comparison of CDF II data [51] on  $D^+$  mesons with the global fit.

to conform with modern PDF sets. The data are well described by the fit, with a  $\chi^2/\text{d.o.f.} = 1.495$ . The result is shown in Fig. 4.

Usage of these new FFs leads to an improved description of the CDF data for charmed-meson production [54] from run II at the Tevatron, as may be seen by comparing Fig. 5(a) in this chapter with Fig. 2(b) of Ref. [47]. Also predictions for  $B$ -meson production agree with CDF II data [51]. Comparing massless and massive calculations, we found that finite- $m_b$  effects moderately enhance the  $p_T$  distribution; the enhancement amounts to about 20% at  $p_T = 2m_b$  and rapidly decreases with increasing values of  $p_T$ , falling below 10% at  $p_T = 4m_b$  (see Fig. 5b). Such effects are thus comparable in size to the theoretical uncertainty due to the freedom of choice in the setting of the renormalization and factorization scales. At higher values of the transverse momentum,  $p_T$ , the predictions of the GM-VFNS and ZM-VFNS approach each other by construction. There, resummation of large logarithms will be important and a FFNS calculation will become inappropriate since it does not resum large logarithms. CDF data reach up to 40 GeV and preliminary data at the highest values of  $p_T$  indicate that resummation of large logarithmic terms will be necessary to obtain a reasonable description of experimental results.

### 3 Fragmentation of heavy quarks with an effective strong coupling constant

*Authors: G. Corcella and G. Ferrera*

We describe a model to include non-perturbative corrections to heavy-quark fragmentation, based on next-to-next-to-leading logarithmic threshold resummation and an effective QCD coupling constant not containing the Landau pole. Comparison with experimental data is also presented.

The hadronization of partons into hadrons cannot be calculated from first principles, but it is usually described in terms of phenomenological models, containing few parameters which need to be tuned to experimental data. In this paper we propose a different approach to describe heavy-quark (bottom and charm) fragmentation in  $e^+e^-$  processes: we use a non-perturbative model [55,56] including power corrections via an effective strong coupling constant, which does

not exhibit the Landau pole. The interesting feature of such a model is that it does not contain any extra free parameter to be fitted to the data, besides the ones entering in the parton-level calculation. In [57, 58] such a model was also employed in the framework of  $B$ -meson decays and it was found good agreement with the experimental data. Moreover, it was even possible to extract  $\alpha_S(m_Z)$  and the Cabibbo-Kobayashi-Maskawa matrix element  $|V_{ub}|$  from such data [57, 58]. In the following, we shall consider heavy-quark production in  $e^+e^-$  annihilation, in particular  $b$ - and  $c$ -quark production at LEP. In [56], charm-quark fragmentation at the  $\Upsilon(4S)$  resonance was also investigated.

The perturbative fragmentation approach [59], up to power corrections, factorizes the energy distribution of a heavy quark as the convolution of a process-dependent coefficient function, associated with the emission off a massless parton, and a process-independent perturbative fragmentation function, expressing the transition of the light parton into a heavy quark. The heavy-quark spectrum reads:

$$\frac{1}{\sigma} \frac{d\sigma}{dx}(x, Q, m_q) = C(x, Q, \mu_F) \otimes D(x, \mu_F, m_q) + \mathcal{O}((m_q/Q)). \quad (17)$$

where  $Q$  is the hard scale of the process,  $x$  is the heavy-quark energy fraction in the centre-of-mass frame, i.e.  $x = \frac{2E_q}{Q}$ , and  $\mu_F \sim Q$  is the factorization scale.

The perturbative fragmentation function follows the DGLAP evolution equations. As in [55, 56], we use coefficient function and initial condition at next-to-leading order (NLO) and solve the DGLAP equations with a NLO kernel<sup>11</sup>. This way, one resum the large mass logarithms  $\sim \ln(Q^2/m_q^2)$  in the next-to-next-to-leading logarithmic approximation [59]. Furthermore, both coefficient function and initial condition contain terms,  $\sim 1/(1-x)_+$  and  $\sim [\ln(1-x)/(1-x)]_+$ , enhanced when  $x$  approaches 1, which corresponds to soft- or collinear-gluon radiation. One needs to resum such contributions to all orders to improve the perturbative prediction (threshold resummation) [60]. In our analysis, we implement threshold resummation in the next-to-next-to-leading logarithmic (NNLL) approximation. following the general method of [61, 62].

Let us now briefly discuss the phenomenological model which includes non-perturbative power corrections through an effective QCD coupling [55–57, 63]. We start by constructing a general analytic QCD coupling  $\bar{\alpha}_S(Q^2)$  from the standard one, by means of an analyticity requirement:  $\bar{\alpha}_S(Q^2)$  is defined to have the same discontinuity as the standard coupling and no other singularity [64]. The coupling constant constructed in this way exhibits no Landau pole, which is subtracted by a power correction, while it has the same discontinuity as the standard one for  $Q^2 < 0$ , related to gluon branching. As discussed in [55], since heavy quark fragmentation is a time-like process, we have to include the absorptive parts of the gluon polarization function into the effective coupling: that amounts to a resummation of constant terms to all orders. As detailed in [55, 56], the effective time-like coupling  $\tilde{\alpha}_S(Q^2)$  is thus given by an integral over the discontinuity of the gluon propagator, with the analytic coupling  $\bar{\alpha}_S(Q^2)$  entering in the integrand function. At one-loop, for example, one obtains the following effective time-like coupling constant:

$$\tilde{\alpha}_S(Q^2) = \frac{1}{\beta_0} \left[ \frac{1}{2} - \frac{1}{\pi} \arctan \left( \frac{\log(Q^2/\Lambda^2)}{\pi} \right) \right]. \quad (18)$$

<sup>11</sup>One could go beyond such a level of accuracy and include next-to-next-to-leading order (NNLO) corrections to the coefficient function, initial condition and to the non-singlet splitting functions.

Our model simply replaces the standard  $\alpha_S(Q^2)$  with the effective time-like coupling constant. As in [55, 56],  $\tilde{\alpha}_S(Q^2)$  is evaluated up to NNLO, i.e. three-loop accuracy. We stress that, even if our model does not contain any free parameter to be fitted to data, we had to choose among possible different prescriptions, mostly concerning the low-energy behaviour of the effective coupling constant. The model presented in [55, 56] is the one which best describes the experimental data.

In Fig. 6 we compare the predictions of the effective-coupling model with experimental data from ALEPH [65], OPAL [66] and SLD [67] on  $B$ -hadron production at the  $Z^0$  pole, and from ALEPH on  $D^{*+}$  production [68]. We learn from the comparison that our model, without introducing any tunable parameter, manages to give a good description of the experimental data. As discussed in [55, 56], even the moments of the  $B$ - and  $D$ -hadron cross section are reproduced quite well.

In summary, we managed to construct a simple non-perturbative model which is able to describe data from rather different processes, namely  $B$ -decays and bottom/charm fragmentation, involving pretty different hard scales. We believe that such results are highly non trivial and that our model deserves further extension to hadron-collider physics. This is in progress.

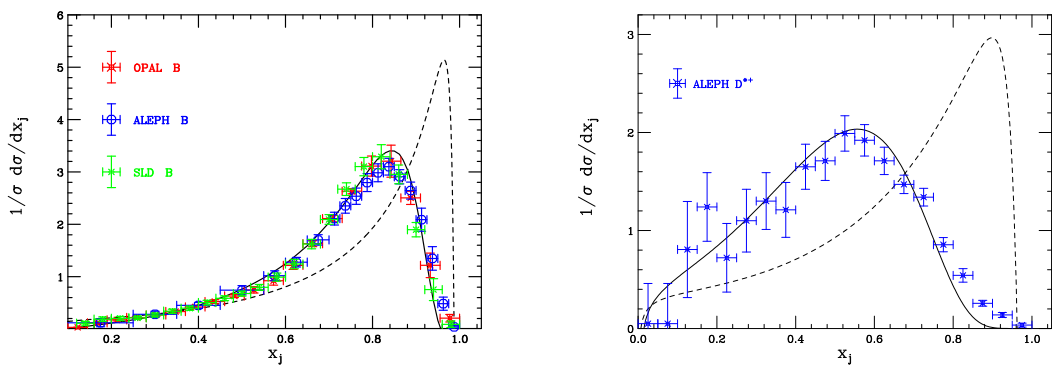


Fig. 6: Results on bottomed (left) and charmed (right) hadron production (solid line), according to the effective-coupling model, compared with the pure parton-level calculation (dashes) and with experimental data.  $x_j$  is the hadron ( $j = B, D$ ) or quark ( $j = b, c$ ) energy fraction at the  $Z^0$  pole.

## 4 Infrared safe determination of jet flavour: theory and applications

Author: A. Banfi and G. Zanderighi

### 4.1 Problems in defining the flavour of a jet

Jets are so far the best-known way to map a complicated event, characterised by a high particle multiplicity, to a simpler one made up of a small number of clusters of particles, *jets*, whose energy-momentum flow is close to that of the original event. By “close to” we mean that jets have to be infrared and collinear (IRC) safe objects, that is their momenta should not change after an extremely soft particle has been added to the event or if any of the particles in the event splits into a quasi-collinear pair. With this requirement jet cross sections can be safely computed in perturbative (PT) QCD. Furthermore, given a partonic event, any IRC safe jet algorithm, in

the soft/collinear limit, does provide a unique mapping to the underlying hard event.<sup>12</sup> It is interesting to investigate whether jet algorithms can be extended so as to define also the flavour of a jet. More precisely, suppose we have a hard event and a new event obtained from the hard event via an arbitrary number of soft emissions and/or collinear splittings. Is it possible to cluster the new event into jets, such that not only the momenta, but also the flavour of the jets, are equal to those of the particles constituting the original hard event?

Attempts to answer this questions have been performed by different experimental groups, whose definitions of jet flavour are based either on the kinematical properties [69] or on the charge of a jet [70]. Although of considerable practical usefulness, these procedures all suffer from IRC unsafety (see [71] for a discussion on this point).

To see where IRC safety problems may arise we need first to introduce our definition of jet flavour. The flavour of a jet is defined as a  $n_f$ -dimensional vector containing in the entry  $f$  the net number of quarks (number of quarks minus number of antiquarks) of flavour  $f$ . A gluon jet will have a flavour vector in which all entries are zero. A clear source of IR unsafety is gluon splitting into a quark and an antiquark that are recombined with different jets, thus changing the underlying jet flavour. At next-to-leading order (NLO), the only singular contribution occurs when the quarks are collinear. In this case, the  $q\bar{q}$  pair is always recombined in the same jet by any IRC safe jet-algorithm, and the resulting jet flavour is also IRC safe. Starting from the next perturbative order however a soft large-angle gluon splitting may produce a  $q$  and  $\bar{q}$  which are both soft but may not be collinear. Therefore the two fermions can be clustered into two different jets, thereby modifying the flavour of those hard jets. In the next section we will analyse specifically the  $k_t$  algorithm, show that its standard version is not IR safe with respect to the jet flavour, and we will see how it can be modified to achieve an IR safe jet-flavour algorithm.

## 4.2 IR safe jet-flavour algorithms at parton level

Let us see how a jet-flavour algorithm should work in the specific case of  $e^+e^-$  annihilation into hadrons. There we consider close-to-Born events with a hard  $q\bar{q}$  pair accompanied by an arbitrary number of soft/collinear partons. One of such configurations is represented in fig. 7. It contains a hard  $q\bar{q}$  pair (at the bottom of each diagram) accompanied by a soft gluon and a soft  $q\bar{q}$  pair originated by the splitting of a large-angle gluon. If one applies the  $k_t$  algorithm [72–74] to such a configuration, to all pairs of particles  $p_i, p_j$  one associates a distance

$$d_{ij} = 2(1 - \cos \theta_{ij}) \times \min\{E_i^2, E_j^2\}, \quad (19)$$

and clusters together the pair whose  $d_{ij}$  is minimum. The resulting set of distances is represented in the picture on the left hand side of fig. 7, where a thick line represents a large distance, while small distances are represented by thin lines. The only large distance obtained with the traditional  $k_t$  algorithm is that between the hard  $q\bar{q}$  pair, while all other distances are small. This is because all other pairs involve at least one soft parton and the distance in eq. (19) depends on the energy of the softest particle only. Looking in particular at the soft  $q$  and  $\bar{q}$ , they can be clustered in different jets thus giving either a couple of gluon jets or two multi-flavoured jets, i.e. not corresponding

<sup>12</sup>Beyond the soft/collinear limit, such a mapping is intrinsically ambiguous due to the presence of interference terms.

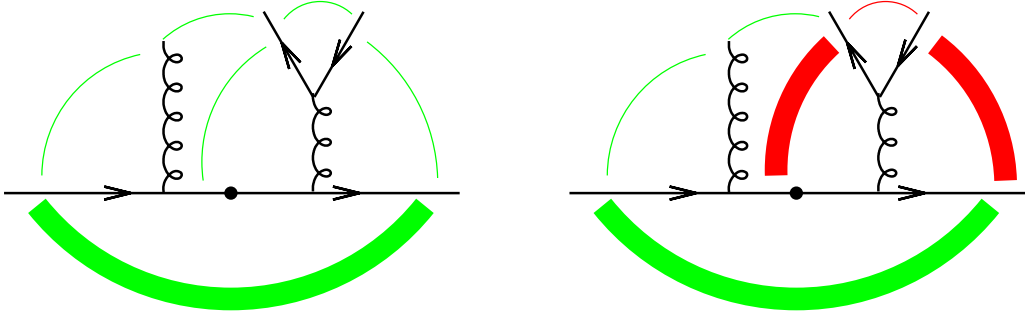


Fig. 7: Pictorial representation of recombination distances for a sample partonic final state in  $e^+e^-$  annihilation in the case of the traditional  $k_t$  algorithm (left) and a  $k_t$ -flavour algorithm (right).

to any QCD parton. The latter case can be eliminated by allowing only recombinations of  $q\bar{q}$  pairs of the same flavour, but the problem of generating fake gluon jets remains. The origin of the problem is that the distance in eq. (19) is modelled so as to compensate the soft and collinear divergence in the matrix element for gluon emission. The  $q\bar{q}$  splitting probability has no soft divergence, so that, without endangering the IRC safety of the algorithm, one could modify the distance in eq. (19) as follows:

$$d_{ij} = 2(1 - \cos \theta_{ij}) \times \begin{cases} \min\{E_i^2, E_j^2\} & \text{softer of } i, j \text{ flavourless,} \\ \max\{E_i^2, E_j^2\} & \text{softer of } i, j \text{ flavoured.} \end{cases} \quad (20)$$

What happens in this case is represented in the picture on the right-hand side of fig. 7, where the new distances are highlighted in red. There, the distance between the soft  $q\bar{q}$  pair is still small, what becomes large is the distance between either of the two and the hard  $q\bar{q}$  pair. In this way soft  $q\bar{q}$  pairs are first recombined together, and only after recombination is the resulting gluon jet recombined with other hard jets. It can be proven that with this modification the resulting flavour determination is IRC safe to all orders in perturbation theory [71].

One can generalise eq. (20) to hadron hadron collisions, defining for each pair of particles a distance parameterised by a jet radius  $R$ :

$$d_{ij} = \frac{\Delta R_{ij}^2}{R^2} \times \begin{cases} \min\{p_{t,i}^2, p_{t,j}^2\} & \text{softer of } i, j \text{ flavourless,} \\ \max\{p_{t,i}^2, p_{t,j}^2\} & \text{softer of } i, j \text{ flavoured,} \end{cases} \quad (21)$$

where  $\Delta R_{ij}^2$  is any collinear safe distance in the rapidity-azimuth  $y$ - $\phi$  plane, for instance  $(y_i - y_j)^2 + (\phi_i - \phi_j)^2$ . Furthermore, to obtain a full flavour determination, one has to add a distance between each particle and the two beams  $B$  and  $\bar{B}$  at positive and negative infinite rapidity respectively. This is achieved by introducing a rapidity dependent transverse momentum for each beam  $p_{t,B}(y)$ ,  $p_{t,\bar{B}}(y)$ , and defining

$$d_{iB} = \begin{cases} \min\{p_{t,i}^2, p_{t,B}^2(y_i)\} & i \text{ flavourless,} \\ \max\{p_{t,i}^2, p_{t,B}^2(y_i)\} & i \text{ flavoured,} \end{cases} \quad (22)$$

and analogously for  $d_{i\bar{B}}$ . The beam hard scales  $p_{t,B}(y)$  and  $p_{t,\bar{B}}(y)$  have to be constructed in such a way that emissions collinear to  $B$  or  $\bar{B}$  get recombined with the right beam, and that

$p_{t,B}(y)$  and  $p_{t,\bar{B}}(y)$  approach the hard scale of the event for central emissions. This is achieved for instance by defining

$$\begin{aligned} p_{t,B}(y) &= \sum_i p_{ti} \left( \Theta(y_i - y) + \Theta(y - y_i) e^{y_i - y} \right), \\ p_{t,\bar{B}}(y) &= \sum_i p_{ti} \left( \Theta(y_i - y) e^{y - y_i} + \Theta(y - y_i) \right). \end{aligned} \quad (23)$$

If applied at parton level, these jet-flavour algorithms have two main applications. First of all they can be used in a NLO calculation to assign each event to an underlying Born subprocess. This is needed to correctly merge real and virtual contributions when matching NLO and resummed calculations [75]. A second application of jet-flavour algorithms is the combination of parton showers and matrix elements [76, 77]. For instance, in the CKKW approach [76], the correct Sudakov form factor to be associated to each event is decided only after having clustered the event into jets. This Sudakov form factor depends on the colour charge of the hard emitters, and is therefore correctly computed only if a flavour has been properly (i.e. in a IRC safe way) assigned to each jet.

At hadron level, in general, it is not sensible to distinguish quarks and gluons. However, there is a case in which the flavour algorithm can be successfully applied also at hadron level, that is in the case of heavy flavour production. There all hadrons containing a heavy quark (of the selected flavour) are treated as flavoured, while all other hadrons are considered flavourless. As we will see in the next section, an IRC safe jet-flavour algorithm can thus be exploited to obtain accurate QCD predictions for  $b$ -jet cross sections.

### 4.3 Accurate QCD predictions for $b$ -jet cross sections

A basic measurement in  $b$  production in hadronic collisions is  $b$ -jet transverse momentum spectra. Experimentally a  $b$ -jet is defined as any jet containing at least one  $b$ -flavoured hadron [78]. It is clear that such a definition is collinear unsafe, because any jet containing a  $b\bar{b}$  pair, which should be considered a gluon jet, would be classified as a quark jet. This gives rise to collinear singular contributions if the  $b\bar{b}$  pair arise from a gluon collinear splitting. The resulting collinear singularity is regularised by the  $b$ -quark mass, giving rise to large logarithms at most of relative order  $\alpha_s^n \ln^{2n-1}(p_t/m_b)$ . These gluon splitting (GSP) processes constitute the dominant source of  $b$ -jets at the Tevatron. This is awkward since jets from GSP do not even correspond to one's physical idea of a  $b$ -jet. There are two other production channels, flavour excitation (FEX) and flavour creation (FCR). In FEX one of the constituents of a produced  $b\bar{b}$  pair is collinear to the beam, while the other builds up the  $b$ -jet. This process also contains collinear singularities, which at all orders give rise to terms  $\alpha_s^n \ln^n(p_t/m_b)$ . FCR is the process in which a  $b\bar{b}$  pair is produced directly in the hard scattering. Although, due to interference, these three processes are mixed together, they can be cleanly separated in the soft/collinear limit. All current fixed-order programs with a massive  $b$  implement only FCR at NLO [79, 80], while GSP and FEX are only LO processes. This results in  $K$ -factors (NLO/LO) and renormalisation and factorisation scale dependence that are far larger than is expected from NLO calculations, as can be seen in

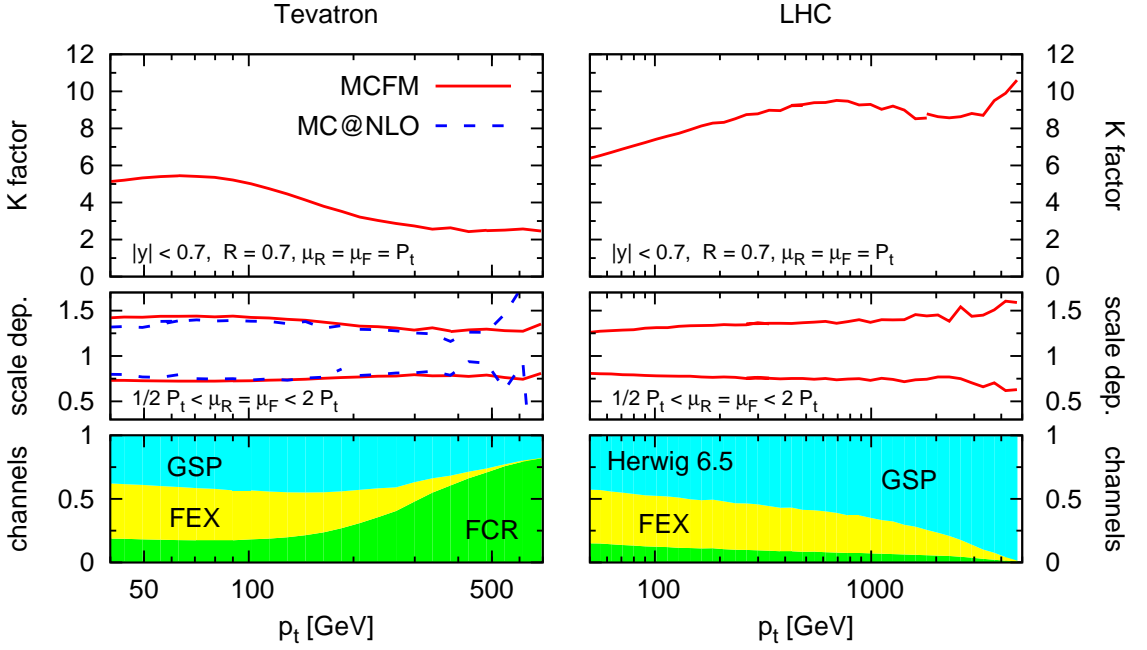


Fig. 8: Top:  $K$ -factors for inclusive  $b$ -jet spectrum as computed with MCFM, clustering particles into jets using the  $k_t$  jet-algorithm with  $R=0.7$ , and selecting jets in a central rapidity region ( $|y| < 0.7$ ). Middle: scale dependence obtained by simultaneously varying the renormalisation and factorisation scales by a factor two around  $p_t$ , the transverse momentum of the hardest jet in the event. For the Tevatron the scale uncertainty is computed also with MC@NLO. Bottom: breakdown of the HERWIG inclusive  $b$ -jet spectrum into the three major hard underlying channels contributions (for simplicity the small  $b\bar{b} \rightarrow b\bar{b}$  contribution is not shown).

fig. 8.<sup>13</sup> It is particularly instructive also to have a look at the bottom plots in the figure, which show the relevance of the various production channels as obtained from HERWIG [82]. Notice in particular how at the LHC GSP is the dominant process at any value of  $p_t$ . This is due to the fact that in  $pp$  collisions the process  $q\bar{q} \rightarrow b\bar{b}$ , the one responsible for FCR, is small also at high  $p_t$  due to the smallness of the antiquark distribution in the proton.

This situation can be significantly improved by exploiting an IRC safe definition of jet-flavour, such as the one outlined in the previous section. To overcome the experimental difficulty of discriminating  $b$  from  $\bar{b}$ , one can define a  $b$ -jet as a jet containing an odd number of  $b$ -hadrons without any risk for the IRC safety of the jet flavour [83]. In this case, the GSP contribution to  $b$ -jet production disappears immediately, because all jets with two  $b$ 's will be classified as gluon jets, and therefore will not contribute at all to  $b$ -jet cross sections. FEX contributions give rise to jets with a single  $b$ , so they cannot be eliminated by a jet-flavour algorithm. However, the FEX collinear logarithms are precisely those resummed in the  $b$  parton density, one of the ingredients of any PT calculation with massless  $b$ 's. Therefore one can compare experimental data for  $b$ -jet  $p_t$ -spectra obtained with the IRC definition of sec. 4.2 with PT predictions with massless  $b$ 's, which are available at NLO accuracy [84, 85]. Since all collinear singularities have

<sup>13</sup>Note that the addition of a parton shower as done in MC@NLO [81] does not solve the problem. This is because the underlying hard configurations remain the same as NLO, and have therefore the same collinear singularities.

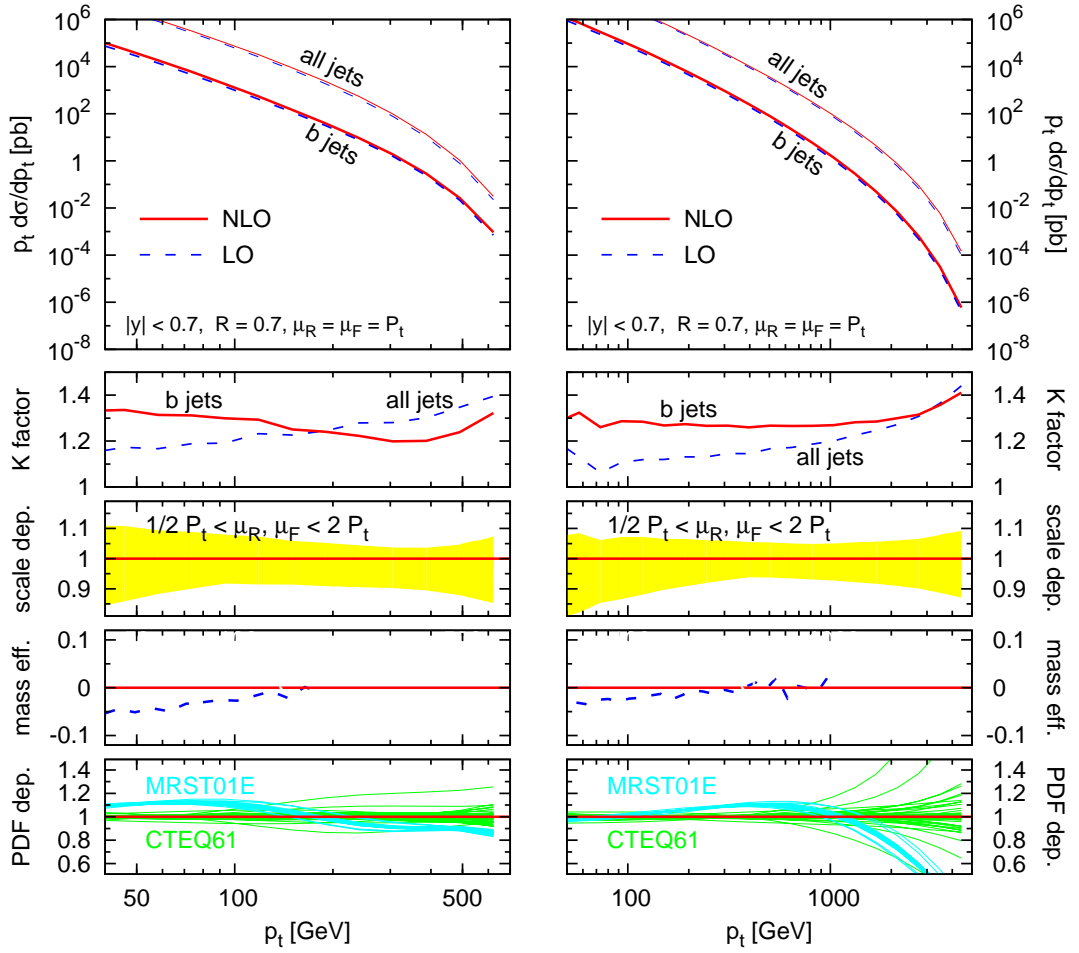


Fig. 9: The  $p_t$  spectrum for  $b$ -jets at the Tevatron (left) and at the LHC (right) obtained with NLO program NLOJET++. Below one can see, in order,  $K$ -factors for  $b$ -jets and all-flavoured inclusive jets, scale uncertainties obtained by varying *independently* renormalisation and factorisation scales by a factor of two, mass effects and PDF uncertainties.

been either eliminated or resummed, the difference between the massless and massive calculation should only involve powers of  $m_b^2/p_t^2$  (potentially enhanced by logarithms). The resulting NLO  $p_t$  spectra at the Tevatron and at the LHC are shown in fig. 9. There one can see that now the  $K$ -factors for  $b$ -jets are comparable to those for unflavoured jets, and moderate, indicating that the PT expansion is under control. Furthermore, scale uncertainties are at most 10%, and adding PDF uncertainties the overall theoretical error does not exceed 20%, except at very high  $p_t$  values at the LHC, where PDF's are less constrained. Note that mass effects are less than 5%, therefore not contributing significantly to the total uncertainty.

A technical difficulty to perform such a calculation is that no NLO program contains information on the flavour of produced partons. One is then forced to extract this information from one's favourite NLO code (in our case NLOJET++ [85]). This procedure, although not straightforward, is nevertheless far easier than writing and testing a new code from scratch. Due to the



relevance that jet-flavour algorithms can have for precision calculations we strongly encourage the authors of NLO codes to provide flavour information by default.

We remark that very similar results are obtained for charmed jet spectra. An interesting issue there is that predictions are very sensitive to possible intrinsic charm components of the proton [86], so that these observables can be exploited to set constraints on such intrinsic components.

A last remark concerns the feasibility of the experimental measurement of heavy flavour jets defined with our flavour algorithm. For a successful comparison between theory and experiment it is crucial to identify cases in which both heavy-flavoured particles are in the same jet, so as to label this jet as a gluon jet and eliminate the contribution of these configurations from the heavy-quark jet cross sections. Experimental techniques for double  $b$ -tagging in the same jet already exist [87] and steady progress is to be expected in the near future [88–90]. However one has always a limited efficiency for single  $b$  tagging, and even more for double  $b$ -tagging in the same jet. On the other hand preliminary studies indicate that one does not necessarily need high efficiencies, but what is more crucial is that one dominates the error on those efficiencies [83]. We look forward to further investigation in this direction.

**Acknowledgements.** This work has been done in collaboration with Gavin Salam.

## 5 Towards NNLO predictions for top quark production

*Author: M. Czakon*

Although discovered quite some time ago, the top quark has not been studied sufficiently to not deserve a special place in the LHC physics programme. This contribution to the workshop proceedings addresses part of the latter related to the top quark pair production cross section. While ideas of applications seem to have cristalized, there has also been progress in the evaluation of the next-to-next-to-leading order corrections. Here, I give some details of the methods.

The top quark has enjoyed a sustained attention for more than a decade since its discovery. Only this year, several theoretical studies have been published on its properties in view of the LHC. The interested reader is directed to [91]. A quantity of particular importance is the total production cross section. Without entering into a detailed discussion it is sufficient to say that one may expect a precision of measurement at the level of about 5% after a few years of LHC running, a number which on the one hand constitutes a challenge to the theory, and on the other opens the door for a few applications, of which only two will be mentioned here.

The first of the applications is indirect mass determination. Clearly, the total cross section is a decreasing function of the mass due mostly to the phase space dependence on the final states. A convenient representation of the connection between the error on the top quark mass,  $m_t$ , and the error on the total cross section,  $\sigma_{t\bar{t}}$ , is given by

$$\frac{\Delta\sigma_{t\bar{t}}}{\sigma_{t\bar{t}}} \approx 5 \frac{\Delta m_t}{m_t}, \quad (24)$$

which is valid in a broad range around the current top quark mass. Clearly, this formula points at the possibility of determining  $m_t$  with an accuracy at the one percent level, as long as the

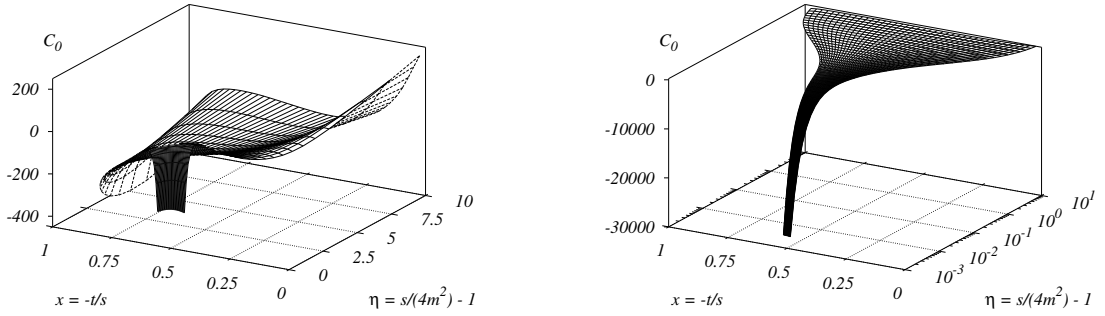


Fig. 10: Finite parts of the bosonic contributions to the two-loop amplitude in quark annihilation (most subleading color coefficient).

theory prediction of  $\sigma_{t\bar{t}}$  is not a limiting factor. This is competitive with the best results from the Tevatron, but less precise than the ambitious goals of the LHC. The question remains, therefore, of the relevance of this method. A look at the way  $m_t$  is measured at present, and the variations of the central value implied, should convince a skeptic that it is important to have an independent measurement, which is far less sensitive on the kinematic reconstruction of hadronic final states.

The second application is gluon luminosity determination, to a large extent synonymous of the gluon PDF determination. While the standard luminosity monitor process for hadron colliders, Drell-Yan gauge boson production is sensitive mostly to quark PDFs, many of the non-standard processes and also the Higgs production process are induced by gluon fusion. A recent study by CTEQ [92], has shown that one can exploit the strong correlation between those cross sections and the top quark pair production cross section to reduce the errors. A prerequisite for success is a precision of 5% on both the theory and the experimental side.

In view of the above, a precise theory prediction for  $\sigma_{t\bar{t}}$  would be more than welcome. As far as fixed order perturbation theory is concerned, the result of [93] shows an error, judged by scale dependence, in excess of 10%. Since there is a substantial enhancement of the production rate due to soft gluon emission, one might expect that the knowledge of higher order corrections in the threshold regime would reduce the final uncertainty. This is indeed the case, as shown in various studies, of which the most recent are [94–96]. In the end, it is possible to obtain a prediction with a conservative error estimate slightly below 10%. While this number is not quite satisfactory, there is a second drawback to the approach based on threshold resummations. Namely, it does not fit a Monte-Carlo generator. With the high statistics of the LHC, MC programs are indispensable. All in all, it seems that having a fixed order result with next-to-next-leading accuracy would be a perfect solution. This statement is only strengthened by the fact, that the error from scale dependence induced would then amount to only 3% [94].

An NNLO prediction for a production process at the LHC needs four ingredients: 1) the two-loop virtual corrections, 2) the one-loop squared corrections, 3) the one-loop corrections with an additional parton radiation, 4) the tree-level corrections with two additional partons radiated. Within the last one or two years, the first three points have been completed to a large extent for

the case of  $\sigma_{t\bar{t}}$  [97–102]. Clearly, point 4) is trivial as long as all the partons are distinguishable. Performing the phase space integration over the unresolved configuration in 3) and 4) is the main remaining challenge. We are not going to discuss this issue, as it is not yet solved, but rather give a few details of the solution to point 1), which is an achievement in itself.

The main problem in the determination of the two-loop virtual corrections is the integration over the virtual momenta. The method adopted in [99] is based on a numerical solution of a system of differential equations [103]. It is suitable for problems with a relatively low number of scales and relies on the fact that Feynman integrals are smooth functions when evaluated above all thresholds as is here the case. The boundaries required are obtained from a series expansion solution to the differential equations around the high energy limit of the integrals derived in [97, 98]. While the integration of the system of equations is not fast enough to fit into a Monte-Carlo program, the presence of only two kinematic variables allows to use interpolation on a grid of precalculated values. The result for the most complicated color coefficient (most subleading term) in quark annihilation is shown in Fig. 10. The appropriate color decomposition is

$$\begin{aligned} \mathcal{A}^{(0,2)} &= 2\text{Re} \langle \mathcal{M}^{(0)} | \mathcal{M}^{(2)} \rangle = 2(N^2 - 1) \\ &\times \left( N^2 A + B + \frac{1}{N^2} C + N n_l D_l + N n_h D_h + \frac{n_l}{N} E_l + \frac{n_h}{N} E_h + n_l^2 F_l + n_l n_h F_{lh} + n_h^2 F_h \right). \end{aligned} \quad (25)$$

The result for the gluon fusion channel is underway. While there are no new complications in the method itself, the number of integrals which need boundaries and have not been determined previously is about three times larger.

## 6 2- and 3-loop heavy flavor contributions to $F_2(x, Q^2)$ , $F_L(x, Q^2)$ and $g_{1,2}(x, Q^2)$

*Authors: I. Bierenbaum, J. Blümlein and S. Klein*

### 6.1 Introduction

In the case of single photon exchange, the deep-inelastic double differential scattering cross-section can be expressed in terms of the unpolarized structure functions  $F_2(x, Q^2)$  and  $F_L(x, Q^2)$ , and the polarized structure functions  $g_1(x, Q^2)$  and  $g_2(x, Q^2)$ . We are considering heavy flavor corrections to these functions. In the NLO approximation, the corrections were calculated semi-analytically in  $x$ -space for  $F_2(x, Q^2)$  and  $F_L(x, Q^2)$  in [104], with a fast implementation in Mellin  $N$ -space given in [105]. In the polarized case the NLO corrections are available only in the asymptotic case  $Q^2 \gg m^2$  [106, 107]. The  $c\bar{c}$ -contributions to these structure functions in the region of smaller values of Bjorken- $x$ , are of the order of 20-40 % and exhibit different scaling violations than the contributions due to massless partons, as shown in Figure 11. For the parameterization of the parton distribution functions we used [108]. Hence, a more precise determination of the parton distribution functions and the measurement of  $\Lambda_{\text{QCD}}$ , as reached in the non-singlet case [109], requires an extension of the heavy quark contributions to  $O(a_s^3)$ , as in the massless case, to perform the flavor-singlet analyzes consistently. This can be done by observing that for  $Q^2 \gtrsim 10 m_c^2$ ,  $F_2^{c\bar{c}}(x, Q^2)$  is very well described by its asymptotic expression in the limit  $Q^2 \gg m^2$ , [110], where one can calculate the heavy flavor Wilson coefficients, the perturbative

part of the structure functions, analytically. More precisely, the heavy flavor Wilson coefficients in the limit  $Q^2 \gg m^2$  are obtained as a convolution of the light-flavor Wilson coefficients with the corresponding massive operator matrix elements (OMEs) of flavor decomposed quarkonic and gluonic operators between massless parton states, which are obtained from the light-cone expansion. Here, we consider the level of twist-2 operators. The light Wilson coefficients are known up to three loops [111] and carry all the process dependence, whereas the OMEs, the objects to be calculated here, are universal and process-independent. Using this approximation, the heavy flavor Wilson coefficients are calculated for  $F_{2,L}^{c\bar{c}}(x, Q^2)$  to 2-loop order in [110, 112, 113] and for  $F_L^{c\bar{c}}(x, Q^2)$  to 3-loop order in [114]. First steps towards the asymptotic 3-loop corrections for  $F_2^{c\bar{c}}(x, Q^2)$  are made by the present authors by calculating the  $O(\varepsilon)$  terms of the 2-loop heavy operator matrix elements, [26, 115], contributing to the 3-loop heavy flavor Wilson coefficients via renormalization. The logarithmic contributions in  $(m^2/\mu^2)$  of the OMEs, as well as all pole terms in  $1/\varepsilon$ , are completely determined by renormalization, in this providing a check on the calculation, and containing in the single pole terms the respective contributions of the 3-loop anomalous dimensions. Furthermore, first steps towards a full 3-loop calculation of moments of the heavy flavor Wilson coefficients were undertaken. Here, the moments  $N = 2 \dots 12$  of the NNLO non-singlet (NS) and pure-singlet (PS) contributions of the OMEs were calculated. In addition, one obtains the corresponding contributions to the three-loop anomalous dimensions given in [116, 117], cf. also [118], which are confirmed in an independent calculation.

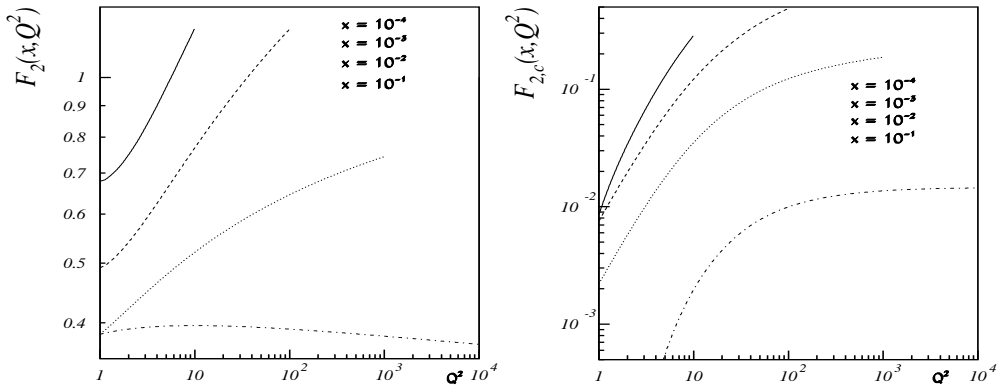


Fig. 11: The scaling violations of the light- and heavy-flavor contributions to the structure functions  $F_2^{\text{light}}$  and  $F_{2,c}$  at leading order.

## 6.2 Renormalization

Our calculation is done in Mellin space. The diagrams are of the self energy type with an additional operator insertion, which widely determines the dynamics and introduces the dependence on the Mellin variable  $N$ . The external particle is massless and on-shell. The scale is set by the mass of the heavy quark. After calculating the bare heavy flavor OMEs in  $D = 4 + \varepsilon$  dimensions and by using the Feynman-gauge, the renormalization is performed in four steps: We use the on-shell scheme [119] for mass renormalization and the  $\overline{\text{MS}}$ -scheme for the charge renor-

malization.<sup>14</sup> The remaining two types of divergences, the UV and collinear singularities, are renormalized via the operator  $Z$ -factors and by mass factorization through the transition functions  $\Gamma$ . Denoting the completely unrenormalized OMEs by a double-hat,  $\hat{\hat{A}}$ , and those for which mass and coupling renormalization have already been performed by a single hat, the operator renormalization and mass factorization proceeds via

$$\mathbf{A} = \mathbf{Z}^{-1} \hat{\mathbf{A}} \Gamma^{-1}, \quad (26)$$

which constitutes a matrix equation in the singlet case. This equation allows us to predict the pole-structure of the OMEs under consideration. The  $Z$ -factors read

$$\begin{aligned} Z_{ij}(N, a_s, \varepsilon) = & \delta_{i,j} + a_s S_\varepsilon \frac{\gamma_{ij,0}}{\varepsilon} + a_s^2 S_\varepsilon^2 \left\{ \frac{1}{\varepsilon^2} \left[ \frac{1}{2} \gamma_{im,0} \gamma_{mj,0} + \beta_0 \gamma_{ij,0} \right] + \frac{1}{2\varepsilon} \gamma_{ij,1} \right\} \\ & + a_s^3 S_\varepsilon^3 \left\{ \frac{1}{\varepsilon^3} \left[ \frac{1}{6} \gamma_{in,0} \gamma_{nm,0} \gamma_{mj,0} + \beta_0 \gamma_{im,0} \gamma_{mj,0} + \frac{4}{3} \beta_0^2 \gamma_{ij,0} \right] \right. \\ & \left. + \frac{1}{\varepsilon^2} \left[ \frac{1}{6} (\gamma_{im,1} \gamma_{mj,0} + 2 \gamma_{im,0} \gamma_{mj,1}) + \frac{2}{3} (\beta_0 \gamma_{ij,1} + \beta_1 \gamma_{ij,0}) \right] + \frac{\gamma_{ij,2}}{3\varepsilon} \right\} \quad (27) \end{aligned}$$

They are related to the anomalous dimensions of the twist-2 operators via  $\gamma = \mu \partial \ln \mathbf{Z}(\mu) / \partial \mu$ , allowing to express them in terms of the anomalous dimensions up to an arbitrary order in the strong coupling constant  $a_s := \alpha_s / (4\pi)$  (cf. [115] up to  $O(a_s^3)$ ). Additionally, we would have  $\Gamma = \mathbf{Z}^{-1}$ , if all quark lines were massless, which, however, has to be modified here since we always have at least one heavy quark line. From these equations, one can infer that for operator renormalization and mass factorization at  $O(a_s^3)$ , the anomalous dimensions up to NNLO, [116, 117], together with the 1-loop heavy OMEs up to  $O(\varepsilon^2)$  and the 2-loop heavy OMEs up to  $O(\varepsilon)$  are needed. The last two quantities enter since they multiply  $Z$ - and  $\Gamma$ -factors containing poles in  $\varepsilon$  (cf. [115]).

To see this in more detail, let us consider as an example the term  $A_{gq,Q}$ , which emerges for the first time at  $O(a_s^2)$ . By applying Eq. (26), one obtains at  $O(a_s^2)$  the renormalized OME

$$A_{gq,Q}^{(2)} = \hat{A}_{gq}^{(2)} + Z_{gq}^{-1,(2)} + \left( Z_{gg}^{-1,(1)} + \hat{A}_{gg,Q}^{(1)} \right) \Gamma_{gq}^{-1,(1)}.$$

Here, the term  $\hat{A}_{gq,Q}^{(1)}$ , cf. [120], enters through mixing. Note that since we consider only terms involving at least one heavy quark, we adopt the definition  $\hat{\gamma} := \gamma(n_f + 1) - \gamma(n_f)$  for the anomalous dimensions in order to obtain the correct color projection. Now we can predict the structure of the unrenormalized result to be

$$\hat{\hat{A}}_{gq,Q}^{(2)} = \left( \frac{m^2}{\mu^2} \right)^\varepsilon \left[ \frac{2\beta_{0,Q}}{\varepsilon^2} \gamma_{gq}^{(0)} + \frac{\hat{\gamma}_{gq}^{(1)}}{2\varepsilon} + a_{gq,Q}^{(2)} + \varepsilon \bar{a}_{gq,Q}^{(2)} \right], \quad (28)$$

where we see the LO and NLO anomalous dimensions and  $\beta_{0,Q} = -(4/3)T_F$  occurring in the pole terms. The terms which are in general not predictable are the constant and  $O(\varepsilon)$ -terms,

<sup>14</sup>For the latter we make the requirement that the heavy quark loop contributions to the gluon self-energy,  $\Pi(p^2, m^2)$ , are renormalized in such a way that  $\Pi(0, m^2) = 0$ , cf. [110, 112, 113, 115].

which, however, enter the pole and constant terms of a 3-loop OME, as mentioned above. In this particular case here, the calculation in Mellin-space in terms of Feynman-parameters is straightforward, cf. [112, 113], and a representation in Euler- $\Gamma$  functions can be obtained even to all orders in  $\varepsilon$ , where we reproduced the pole terms of Eq. (28), [121]. As a last remark, note that we consider charm quark contributions here, while for heavier quarks decoupling [122] has to be applied.

### 6.3 $O(\varepsilon)$ at 2-loops

The appearance of the constant and  $O(\varepsilon)$  terms in the renormalization process of the OMEs has been worked out in some detail in Ref. [115], [123], where we presented the  $O(\varepsilon)$  terms  $\bar{a}_{Qg}^{(2)}$ ,  $\bar{a}_{qq,Q}^{(2),\text{NS}}$  and  $\bar{a}_{Qq}^{(2),\text{PS}}$  in the unpolarized case. The term  $\bar{a}_{gg,Q}^{(2)}$  was given in [26]. The last missing 2-loop  $O(\varepsilon)$  term corresponds to the heavy OME  $A_{gg,Q}^{(2)}$ , [107, 121]. The corresponding constant contribution was calculated before in Ref. [120]. It contributes through operator mixing to the  $T_F^2$ -term of  $A_{Qq}^{(3),\text{PS}}$ , which we consider in this paper.

Since we perform our calculation in Mellin space, all results are given in terms of harmonic sums, [124, 125], the argument of which we have set equal to  $N$ . Thus, the results of the constant and  $O(\varepsilon)$ -terms of the above-mentioned  $A_{gg,Q}^{(2)}$ , for example, are given by:

$$a_{gg,Q}^{(2)} = T_F C_F \left\{ \frac{4}{3} \frac{N^2 + N + 2}{(N-1)N(N+1)} (S_2 + S_1^2 + 2\zeta_2) - \frac{8}{9} \frac{8N^3 + 13N^2 + 27N + 16}{(N-1)N(N+1)^2} S_1 + \frac{8}{27} \frac{P_1}{(N-1)N(N+1)^3} \right\}, \quad (29)$$

$$\bar{a}_{gg,Q}^{(2)} = T_F C_F \left\{ \frac{2}{9} \frac{N^2 + N + 2}{(N-1)N(N+1)} (-2S_3 - 3S_2 S_1 - S_1^3 + 4\zeta_3 - 6\zeta_2 S_1) + \frac{2}{9} \frac{8N^3 + 13N^2 + 27N + 16}{(N-1)N(N+1)^2} (2\zeta_2 + S_2 + S_1^2) - \frac{4P_1 S_1}{27(N-1)N(N+1)^3} + \frac{4P_2}{81(N-1)N(N+1)^4} \right\}, \quad (30)$$

$$P_1 = 43N^4 + 105N^3 + 224N^2 + 230N + 86.$$

$$P_2 = 248N^5 + 863N^4 + 1927N^3 + 2582N^2 + 1820N + 496.$$

The representation in Mellin-space allowed us to use various analytic and algebraic relations between harmonic sums, [126–128], to obtain a more compact result. Together with the result of Eq. (30), all 2-loop  $O(\varepsilon)$  terms of the heavy OMEs in the unpolarized case are known by now. A corresponding calculation has been performed for the polarized case up to  $O(\varepsilon)$  [107] extending the results of Ref. [106]. The contributions to the structure function  $g_2(x, Q^2)$  can be obtained using Wandzura-Wilczek relations, cf. [129, 130]. For the respective formulae we refer to the original paper.

### 6.4 Fixed moments at 3-loops

We start by calculating the diagrams for fixed even values of Mellin  $N$ . At this order, new operator vertices appear with three and four gluonic lines, for which the Feynman-rules had not yet been derived before. The necessary 3-loop diagrams are generated using QGRAF [131] and are genuinely given as tensor integrals due to the operators contracted with the light-cone vector  $\Delta$ ,  $\Delta^2 = 0$ . The calculation proceeds in the following steps: first, the contraction with the light-cone vector is made undone, which leaves tensor integrals for each diagram. For each value of Mellin  $N$  under consideration, one then constructs a projector, which, applied to the tensor integrals, projects onto the desired  $N$ . We consider  $N = 2, \dots, 12$ . The color factors of the diagrams are calculated using [132]. A generalization to higher moments is straightforward, however, the computing time increases rapidly. The diagrams are then translated into a form, which is suitable for the program MATAD [133], doing the expansion in  $\varepsilon$  for the corresponding massive three-loop tadpole-type diagrams. We have implemented all these steps into a FORM-program, cf. [134], and tested it against various two-loop results, including the result for  $\hat{A}_{gq,Q}^{(2)}$ , Eq. (28), and found agreement.

The first 3-loop objects we are investigating are the OMEs  $A_{qq,Q}^{\text{NS}}$ , cf. [121], and  $A_{Qq}^{\text{PS}}$ . All diagrams contain two inner quark loops, where the quark to which the operator insertion couples is heavy and the other one may be heavy or light. The latter two cases can be distinguished by a factor  $n_f$ , denoting the number of light flavors, in the result. From Eq. (26), we can obtain the pole structure of the  $T_F^2$  terms of the completely unrenormalized PS OME:

$$\begin{aligned} \hat{A}_{Qq}^{(3),\text{PS}} \Big|_{T_F^2} &= \left( \frac{m^2}{\mu^2} \right)^{3\varepsilon/2} \left\{ 2 \frac{n_f + 4}{3\varepsilon^3} \beta_{0,Q} \hat{\gamma}_{qg}^{(0)} \gamma_{gq}^{(0)} + \frac{1}{\varepsilon^2} \left( \frac{2 - n_f}{6} \hat{\gamma}_{qg}^{(0)} \hat{\gamma}_{gq}^{(1)} - (n_f + 1) \frac{4}{3} \beta_{0,Q} \hat{\gamma}_{\text{PS}}^{(1)} \right) \right. \\ &\quad \left. + \frac{1}{\varepsilon} \left( \frac{n_f + 1}{3} \hat{\gamma}_{\text{PS}}^{(2)} - 4(n_f + 1) \beta_{0,Q} a_{Qq}^{(2),\text{PS}} - n_f \frac{\zeta_2 \beta_{0,Q}}{4} \hat{\gamma}_{qg}^{(0)} \gamma_{gq}^{(0)} + \hat{\gamma}_{qg}^{(0)} a_{gq,Q}^{(2)} \right) + a_{Qq}^{(3),\text{PS}} \right\} \Big|_{T_F^2} \quad (31) \end{aligned}$$

The  $n_f$  dependence is written explicitly and  $\hat{\gamma}_{\text{PS}}^{(2)}$  is the term  $\propto n_f^2$  of the NNLO anomalous dimension  $\gamma_{\text{PS}}^{(2)}$ . It is not possible to factor out  $(n_f + 1)$ , not even in the triple pole term. This is due to the interplay of the prescription for coupling constant renormalization we have adopted and the fact that the transition functions  $\Gamma$  apply to sub-graphs containing massless lines only. We have calculated the above term using MATAD for  $N = 2, \dots, 12$  and all pole terms agree with Eq. (31). Detailed Tables of these results can be found in [121] and a further upcoming paper. Using Eqs. (29,31), one can obtain moments for the 3-loop anomalous dimension  $\gamma_{\text{PS}}^{(2)}|_{T_F^2}$ , see also [121] and a corresponding paper in preparation. These latter results agree with the results from [117]. Here one has to make the replacement  $n_f \rightarrow n_f(2T_F)$ , with  $T_F = 1/2$ , and to multiply by 2, to account for the different convention for the  $Z$ -factors we adopted. As an example consider the renormalized result for the second moment. Applying Eq. (26), we obtain

$$\begin{aligned} A_{Qq}^{(3),\text{PS}} \Big|_{N=2, T_F^2} &= C_F T_F^2 \left\{ -\frac{128}{81} \ln^3 \left( \frac{m^2}{\mu^2} \right) - \frac{32}{27} \ln^2 \left( \frac{m^2}{\mu^2} \right) - \frac{5344}{243} \ln \left( \frac{m^2}{\mu^2} \right) + \frac{53144}{2187} \right. \\ &\quad \left. - \frac{3584}{81} \zeta_3 + n_f \left( -\frac{128}{81} \ln^3 \left( \frac{m^2}{\mu^2} \right) + \frac{32}{27} \ln^2 \left( \frac{m^2}{\mu^2} \right) - \frac{5104}{243} \ln \left( \frac{m^2}{\mu^2} \right) - \frac{34312}{2187} + \frac{1024}{81} \zeta_3 \right) \right\} \quad (32) \end{aligned}$$

As in Eq. (32), we observe for all moments in the NS and PS case that the terms  $\propto \zeta_2$  disappear after renormalization, since the corresponding terms in the light flavor Wilson coefficients do not contain even  $\zeta$ -values. This provides us with a further check on our calculation, since it is a general observation made in many  $D = 4$  calculations.

For the  $T_F^2$ -terms of the heavy OME  $A_{qq,Q}^{(3),\text{NS}}$ , a formula similar to Eq. (31) can be derived, cf. [121]. Using again MATAD, we have calculated the first 6 non-vanishing moments of the completely unrenormalized expression. The pole terms we obtain agree with what one expects from Eq. (26) and after renormalization, we again observe that there are no  $\zeta_2$ 's left anymore. Additionally, the values for the moments of the terms  $\propto T_F$  in  $\gamma_{\text{NS}}^{(2)}$  agree with those in Refs. [116–118].

## 6.5 Conclusions and outlook

All  $O(\varepsilon)$  contributions to the unpolarized and most of the polarized heavy quark OMEs for general Mellin variable  $N$  at  $O(a_s^2)$  were calculated which are needed for the renormalization at  $O(a_s^3)$ . This part of the calculation makes significant use of the representation of Feynman-integrals in terms of generalized hypergeometric and related functions, omitting the integration-by-parts method. The solution of the sums beyond those which could be performed by `summer` [125], required new techniques and were solved using `SIGMA` [135]. Concerning the structure of the result, we find the *universal* pattern as observed in case of the massless 2-loop Wilson coefficients and related quantities in terms of harmonic sums [126, 127, 136–138]. Furthermore, we installed a program chain to calculate the corresponding 3-loop diagrams to  $O(a_s^3)$  using MATAD. As a first step, we obtained the moments of the heavy OMEs  $\hat{A}_{qq,Q}^{(3),\text{NS}}$  and  $\hat{A}_{Qq}^{(3),\text{PS}}$ , for which we found agreement with the general pole structure expected from renormalization. This provides us with a good check on the method we apply for our calculation. For the calculation of high moments we will apply `TFORM`, [139], in the future. In the same way all other contributions to the heavy quark OMEs will be calculated.

**Acknowledgments.** We would like to thank M. Steinhauser and J. Vermaseren for useful discussions and M. Steinhauser for a `FORM 3.0` compatible form of the code MATAD.

## 7 Heavy quark and quarkonium production in the Regge limit of QCD

*Author: V. Saleev*

We study production of hadrons containing charm and beauty quarks at HERA and Tevatron Colliders in the framework of the quasi-multi-Regge-kinematics approach at leading order in the strong-coupling constant  $\alpha_s$ . To describe heavy quark hadronization we use the fragmentation approach in case of  $D$ - and  $B$ -meson production, or the factorization formalism of nonrelativistic QCD at leading order in the relative velocity  $v$  of heavy quarks in quarkonia in case of heavy quarkonium production.



## 7.1 Theoretical basis

Heavy quark and quarkonium production at high energies has provided a useful laboratory for testing the perturbative quantum chromodynamics (pQCD) as well as the interplay of perturbative and nonperturbative phenomena in QCD. Also these studies are our potential for the observation of a new dynamical regime, namely the high-energy Regge limit, which is characterized by the following condition  $\sqrt{S} \gg \mu \gg \Lambda_{QCD}$ , where  $\sqrt{S}$  is the total collision energy in the center of mass reference frame,  $\Lambda_{QCD}$  is the asymptotic scale parameter of QCD,  $\mu$  is the typical energy scale of a hard interaction.

The phenomenology of strong interactions at high energies exhibits a dominant role of gluon interactions in heavy quark and quarkonium production. In the conventional parton model [140], the initial-state gluon dynamics is controlled by the Dokshitzer-Gribov-Lipatov-Altarelli-Parisi (DGLAP) evolution equations [141], in which it is assumed that  $S > \mu^2 \gg \Lambda_{QCD}^2$ . Thus, the DGLAP evolution equation takes into account only one large logarithm, namely  $\ln(\mu/\Lambda_{QCD})$  and the collinear approximation is used, in which the transverse momenta of the initial gluons ( $k_T$ ) are neglected.

In the Regge limit the summation of large logarithms  $\ln(\sqrt{S}/\mu)$  in the evolution equation can then be more important than the one of the  $\ln(\mu/\Lambda_{QCD})$  terms. In this case, the non-collinear gluon dynamics is described by the Balitsky-Fadin-Kuraev-Lipatov (BFKL) evolution equation [142]. In the region under consideration, the transverse momenta of the incoming gluons and their off-shell properties can no longer be neglected, and we deal with *Reggeized* gluons. As the theoretical framework for this kind of high-energy phenomenology, the quasi-multi-Regge-kinematics (QMRK) approach [143], which is based on the effective quantum field theory implemented with the non-abelian gauge-invariant action [144], can be used. The *Reggeization* of particles or amplitudes is the well-known effect for electrons in high-energy quantum electrodynamics (QED) [145] and for gluons and quarks in QCD [142, 146]. Roughly speaking, the *Reggeization* is a trick, which gives an opportunity to take into account efficiently large radiative corrections to the processes under Regge limit condition beyond the collinear approximation. The main ingredients of the QMRK approach are the effective vertices of Reggeon-Reggeon-Particle (RRP) or Reggeon-Particle-Particle (RPP) interactions, which can be obtained from the effective action [144].

The factorization formalism of nonrelativistic QCD (NRQCD) [147] is a theoretical framework for the description of heavy-quarkonium production and decay. The factorization hypothesis of NRQCD assumes the separation of the effects of long and short distances in heavy-quarkonium production. NRQCD is organized as a perturbative expansion in two small parameters, the strong-coupling constant  $\alpha_s$  and the relative velocity  $v$  of heavy quarks in quarkonium.

The studies of the open heavy-flavour production at high energies show that in calculations the precise implementation of the effect of heavy quark fragmentation is needed to describe data [45–47, 148]. The approach used here applies the universal fragmentation functions (FFs) [45–47], which satisfy DGLAP evolution equations and are fitted to  $e^+e^-$  annihilation data for the open heavy-flavour production from CERN LEP1.

Both models, the NRQCD and the fragmentation approach, don't depend on the choice of high-energy factorization scheme and they can be used in calculations both in the conventional

collinear parton model and in the QMRK approach.

## 7.2 Charmonium production at Tevatron and HERA

During the last decade, the CDF Collaboration at the Tevatron [149, 150] collected data on charmonium production at the energies  $\sqrt{S} = 1.8$  TeV (run I) and  $\sqrt{S} = 1.96$  TeV (run II) in the central region of pseudorapidity  $|\eta| < 0.6$ . In contrast to previous analysis in the collinear parton model [151] or the  $k_T$ -factorization approach [152–154], we perform a joint fit to the run-I and run-II CDF data [149, 150] to obtain the color-octet nonperturbative matrix elements (NMEs) for  $J/\psi$ ,  $\chi_{cJ}$ , and  $\psi'$  mesons. The run-II data include region of small  $J/\psi$  transverse momentum, which can't be described principally in the collinear parton model, but this region is important for fit procedure. Our calculations [155, 156] are based on exact analytical expressions for the relevant *Reggeized* amplitudes, which were previously unknown in the literature ( $R + R \rightarrow H$ ,  $R + R \rightarrow H + g$ , and  $R + P \rightarrow H$ , where  $H$  is  $q\bar{q}$ -pair in the fixed quantum state,  $R$  is the *Reggeized* gluon). Our fits include five experimental data sets, which come as  $p_T$  distributions of  $J/\psi$  mesons from direct production, prompt production,  $\chi_{cJ}$  decays, and  $\psi'$  decays in run I, and from prompt production in run II. In the Table I of Ref. [155, 156], we present our fit results for the relevant color-octet NMEs for three different choices of unintegrated gluon distribution function, namely JB [157], JS [158], and KMR [159]. Our fits to the Tevatron data turned out to be satisfactory, except for the one to the  $\chi_{cJ}$  sample based on the JB gluon density in the proton, where the fit result significantly exceeded the measured cross section in the small- $p_T$  region, as it is shown in Figs. 4-5 of Ref. [155, 156]. We see also that color-octet contribution in case of  $\chi_{cJ}$  production is being quite unimportant. Considering the color-octet NMEs relevant for the  $J/\psi$ ,  $\psi'$  and  $\chi_{cJ}$  production mechanisms, we can formulate the following heuristic rule for favored transitions from color-octet to color-singlet states:  $\Delta L \simeq 0$  and  $\Delta S \simeq 0$ ; *i.e.*, these transitions are doubly chromoelectric and preserve the orbital angular momentum and the spin of the heavy-quark bound state.

At HERA, the cross section of prompt  $J/\psi$  production was measured in a wide range of the kinematic variables both in photoproduction [160], at small values of photon virtuality  $Q^2$ , and deep-inelastic scattering (DIS) [161], at large values of  $Q^2$ . In the Figs. 6-9 of Ref. [155, 156], our NRQCD predictions in the high-energy factorization approach, evaluated with the NMEs from Table 1 of Ref. [155, 156], are compared with the HERA data [160, 161]. In this regime, where the contribution of  $2 \rightarrow 1$  subprocesses is suppressed, the LO NRQCD predictions in the QMRK approach are mainly due to the color-singlet channels and are therefore fairly independent of the color-octet NMEs. Thus, our results agree well with the data and with the previous calculations in the color singlet model (CSM) [162], up to minor differences in the choice of the color-singlet NMEs and the  $c$ -quark mass. Let us note that first theoretical prediction for  $J/\psi$  photoproduction in the CSM and the  $k_T$ -factorization scheme has been done 15 years ago in Ref. [163].

## 7.3 Bottomonium production at the Tevatron

The CDF Collaboration measured the  $p_T$  distributions of  $\Upsilon(1S)$ ,  $\Upsilon(2S)$ , and  $\Upsilon(3S)$  mesons in the central region of rapidity ( $y$ ),  $|y| < 0.4$ , at  $\sqrt{S} = 1.8$  TeV (run I) [164] and that of the  $\Upsilon(1S)$  meson in the rapidity regions  $|y| < 0.6$ ,  $0.6 < |y| < 1.2$ , and  $1.2 < |y| < 1.8$  at  $\sqrt{S} = 1.96$  TeV (run II) [165]. In both cases, the  $S$ -wave bottomonia were produced promptly, *i.e.*, directly or

via non-forbidden decays of higher-lying  $S$ - and  $P$ -wave bottomonium states, including cascade transitions such as  $\Upsilon(3S) \rightarrow \chi_{b1}(2P) \rightarrow \Upsilon(1S)$ .

In contrast to previous analysis in the collinear parton model [166], we perform a joint fit to the CDF data from run I [164] and run II [165] for all  $p_T$  values, including the small- $p_T$  region. Comparing the color-singlet and color-octet contributions, we observe that the latter is dominant in the  $\Upsilon(3S)$  case and in the  $\Upsilon(2S)$  case for  $p_T \geq 13$  GeV, while it is of minor importance in the  $\Upsilon(1S)$  case in the whole  $p_T$  range considered. The fits based on the KMR, JB, and JS gluons turned out to be excellent, fair, and poor, respectively. They yielded small to vanishing values for the color-octet NMEs, see Table II of Ref. [167], especially when the estimated feed-down contributions from the as-yet unobserved  $\chi_{bJ}(3P)$  states were included. The presented analysis in Ref. [167], together with the investigation of charmonium production [155, 156], suggest that the color-octet NMEs of bottomonium are more strongly suppressed than those of charmonium as expected from the velocity scaling rules of NRQCD.

Using obtained NMEs for bottomonium and charmonium states we have done predictions for the LHC Collider at the energy  $\sqrt{S} = 14$  TeV, which are presented in Figs. 14-17 of Ref. [168].

#### 7.4 Open heavy-flavour production at HERA and Tevatron

At HERA  $D$ -meson production has been studied both in the photo-production processes and in the deep inelastic scattering (DIS) processes. The data are presented by H1 and ZEUS Collaborations for different spectra, see Refs. [169, 170]. The lowest order in  $\alpha_s$  processes of heavy quark photoproduction or electroproduction in the QMRK approach in the massive  $c$ -quark scheme are the following:  $\gamma(\gamma^*) + R \rightarrow c + \bar{c}$  – direct production and  $R_\gamma + R \rightarrow c + \bar{c}$  – resolved production, where  $R$  is the *Reggeized* gluon from a proton or  $R_\gamma$  is the one from a photon.

We find approximate agreement of our results with data from HERA for  $p_T$  spectra of  $D^*$ -meson production, the pseudo-rapidity spectra are described well only at the large  $p_T \geq 6$  GeV, see Figs. 3-6 in Ref. [171]. These conclusions are true both for photoproduction and for  $D^*$  production in DIS.

Recently the CDF Collaboration measured the differential cross sections  $d\sigma/dp_T$  for the inclusive production of  $D^0$ ,  $D^+$ ,  $D^{*+}$ , and  $D_s^+$  mesons [172] in  $p\bar{p}$  collisions at the Fermilab Tevatron (run I and run II) as functions of transverse momentum ( $p_T$ ) in the central rapidity ( $y$ ) region. At the LO QMRK approach the parton subprocesses for heavy quark production in hadron collisions are:  $R + R \rightarrow c + \bar{c}$  and  $Q + \bar{Q} \rightarrow c + \bar{c}$ , where  $Q$  is the *Reggeized* quark in a proton. The squared matrix elements of all above mentioned processes, excluding last one with *Reggeized* initial quarks, are known in the literature [143, 173, 174]. The contribution of the subprocess  $Q + \bar{Q} \rightarrow c + \bar{c}$  is studied for the first time [175].

In the paper [176], we explored the usefulness of the quark-Reggeization hypothesis in the framework of the QMRK approach by studying several observables of inclusive charm production at LO, namely the charm structure function  $F_{2,c}$  of the proton measured at HERA as well as the one-particle-inclusive cross sections of  $D^{*\pm}$  and  $D_s^\pm$  photoproduction in  $ep$  collisions at HERA and of  $D^0$ ,  $D^\pm$ ,  $D^{*\pm}$ , and  $D_s^\pm$  hadroproduction in  $p\bar{p}$  collisions at the Tevatron Collider. In all three cases, we found satisfactory agreement between our default predictions and the ex-

perimental data, which is quite encouraging in view of the simplicity of our LO expressions for the partonic cross sections. By contrast, in the collinear parton model of QCD, the inclusion of NLO corrections is necessary to achieve such a degree of agreement. We thus recover the notion that the QMRK approach is a powerful tool for the theoretical description of QCD processes in the high-energy limit and automatically accommodates an important class of corrections that lie beyond the reach of the collinear parton model at LO.

The first theoretical prediction for the beauty production at Tevatron [177] based on high-energy factorization scheme and Reggeon-Reggeon effective vertices [143] for the process  $R + R \rightarrow b + \bar{b}$  has been done in Ref. [178]. It was shown that both  $p_T$ -spectra and total cross section of  $B$ -mesons can be described well with KMS unintegrated gluon distribution function [179]. We performed these calculations with KMR [159] unintegrated distribution functions and Peterson  $b$ -quark fragmentation function [180], and have found good agreement with data too. Thus, in case of  $b$ -quark production, contrary to  $c$ -quark production, theoretical description of data both for  $B$ -mesons and for bottomonia looks well grounded and more simple. The  $c$ -quark mass is not large enough and nonperturbative effects in the hadronization of  $c$ -quarks need more careful description.

## 7.5 Conclusions

Our results show that the QMRK approach is a very powerful tool in the high-energy phenomenology of heavy quark and quarkonium production. Of course, there is a number of non-solved problems yet, such as the correct description of  $J/\psi$  polarization [181] and an estimation of NLO corrections for relevant processes. At the LHC Collider the conditions of application of the QMRK approach for heavy quark production will be satisfied with higher accuracy, therefore we see many future applications of this approach in a new kinematic regime.

The author thanks B. Kniehl, D. Vasin and A. Shipilova for cooperation in study of presented results. We thank also L. Lipatov, M. Ryskin, G. Kramer, H. Spiesberger and O. Teryaev for useful discussions.

## 8 Upsilononium polarization as a touchstone in understanding the parton dynamics in QCD

*Authors: S. Baranov and N. Zotov*

Nowadays, the production of heavy quarkonium states at high energies is under intense theoretical and experimental study [182, 183]. The production mechanism involves the physics of both short and long distances, and so, appeals to both perturbative and nonperturbative methods of QCD. This feature gives rise to two competing theoretical approaches known in the literature as the color-singlet and color-octet models. According to the color-singlet approach, the formation of a colorless final state takes place already at the level of the hard partonic subprocess (which includes the emission of hard gluons when necessary). In the color-octet model, also known as nonrelativistic QCD (NRQCD), the formation of a meson starts from a color-octet  $Q\bar{Q}$  pair and proceeds via the emission of soft nonperturbative gluons.

Originally, the color-octet model was introduced to overcome the discrepancy between the large  $J/\psi$  production cross section measured in  $pp$  interactions at the Tevatron and the results of theoretical calculations based on the standard perturbative QCD. The problem was apparently

solved by attributing the discrepancy to the hypothetical contributions from the intermediate color-octet states, which must obey certain hierarchy in powers of the relative velocity of the quarks in a bound system. However, the numerical estimates of these contributions extracted from the analysis of Tevatron data are at odds with the HERA data, especially as far as the inelasticity parameter  $z = E_\psi/E_\gamma$  is concerned [184]. In the  $k_t$ -factorization approach, the values of the color-octet contributions obtained as fits of the Tevatron data appear to be substantially smaller than the ones in the collinear scheme, or even can be neglected at all [153, 155, 185, 186].

The first attempts to solve the quarkonium polarization problem within the  $k_t$ -factorization approach were made in the pioneering work [187] (see also [188]) for  $ep$  collisions and in Refs. [154, 185] for  $pp$  collisions. It was emphasised that the off-shellness of the initial gluons, the intrinsic feature of the  $k_t$ -factorization approach, has an immediate consequence in the longitudinal polarization of the final state  $J/\psi$  mesons.

The goal of this paper is to derive theoretical predictions on the polarization of  $\Upsilon$  mesons produced at the Fermilab Tevatron and CERN LHC. In the  $k_t$ -factorization approach, the cross section of a physical process is calculated as a convolution of the partonic cross section  $\hat{\sigma}$  and the unintegrated parton distribution  $\mathcal{F}_g(x, k_T^2, \mu^2)$ , which depend on both the longitudinal momentum fraction  $x$  and transverse momentum  $k_T$ :

$$\sigma_{pp} = \int \mathcal{F}_g(x_1, k_{1T}^2, \mu^2) \mathcal{F}_g(x_2, k_{2T}^2, \mu^2) \hat{\sigma}_{gg}(x_1, x_2, k_{1T}^2, k_{2T}^2, \dots) dx_1 dx_2 dk_{1T}^2 dk_{2T}^2. \quad (33)$$

In accordance with [173, 189–191], the off-shell gluon spin density matrix is taken in the form

$$\overline{\epsilon_g^\mu \epsilon_g^{*\nu}} = p_p^\mu p_p^\nu x_g^2 / |k_T|^2 = k_T^\mu k_T^\nu / |k_T|^2. \quad (34)$$

In all other respects, our calculations follow the standard Feynman rules.

In order to estimate the degree of theoretical uncertainty connected with the choice of unintegrated gluon density, we use two different parametrizations, which are known to show the largest difference with each other, namely, the ones proposed in Refs. [189, 191] and [192]. In the first case [189], the unintegrated gluon density is derived from the ordinary (collinear) density  $G(x, \mu^2)$  by differentiating it with respect to  $\mu^2$  and setting  $\mu^2 = k_T^2$ . Here we use the LO GRV set [193] as the input collinear density. In the following, this will be referred to as dGRV parametrisation. The other unintegrated gluon density [192] is obtained as a solution of leading order BFKL equation [191] in the double-logarithm approximation. Technically, it is calculated as the convolution of the ordinary gluon density with some universal weight factor. This will be referred to as JB parametrisation.

The production of  $\Upsilon$  mesons in  $pp$  collisions can proceed via either direct gluon-gluon fusion or the production of  $P$ -wave states  $\chi_b$  followed by their radiative decays  $\chi_b \rightarrow \Upsilon + \gamma$ . The direct mechanism corresponds to the partonic subprocess  $g + g \rightarrow \Upsilon + g$  which includes the emission of an additional hard gluon in the final state. The production of  $P$ -wave mesons is given by  $g + g \rightarrow \chi_b$ , and there is no emission of any additional gluons. All the other parameters are the same as in our previous paper [194].

The polarization state of a vector meson is characterized by the spin alignment parameter  $\alpha$  which is defined as a function of any kinematic variable as  $\alpha(\mathcal{P}) = (d\sigma/d\mathcal{P} - 3d\sigma_L/d\mathcal{P})/(d\sigma/d\mathcal{P} +$

$d\sigma_L/d\mathcal{P}$ ), where  $\sigma$  is the reaction cross section and  $\sigma_L$  is the part of cross section corresponding to mesons with longitudinal polarization (zero helicity state). The limiting values  $\alpha = 1$  and  $\alpha = -1$  refer to the totally transverse and totally longitudinal polarizations. We will be interested in the behavior of  $\alpha$  as a function of the  $\Upsilon$  transverse momentum:  $\mathcal{P} \equiv |\mathbf{p}_T|$ . The experimental definition of  $\alpha$  is based on measuring the angular distributions of the decay leptons  $d\Gamma(\Upsilon \rightarrow \mu^+ \mu^-)/d\cos\theta \sim 1 + \alpha \cos^2\theta$ , where  $\theta$  is the polar angle of the final state muon measured in the decaying meson rest frame.

The results of our calculations for the kinematic conditions of the Tevatron and LHC are displayed in Fig. 12. In both cases, the integration limits over rapidity were adjusted to the experimental acceptances of CDF ( $|y_\Upsilon| < 0.6$ ) at the Tevatron and ATLAS ( $|y_\Upsilon| < 2.5$ ) at the LHC. The upper panels show the predicted transverse momentum distributions. Separately shown are the contributions from the direct (dashed lines) and  $P$ -wave decay (dotted lines) mechanisms.

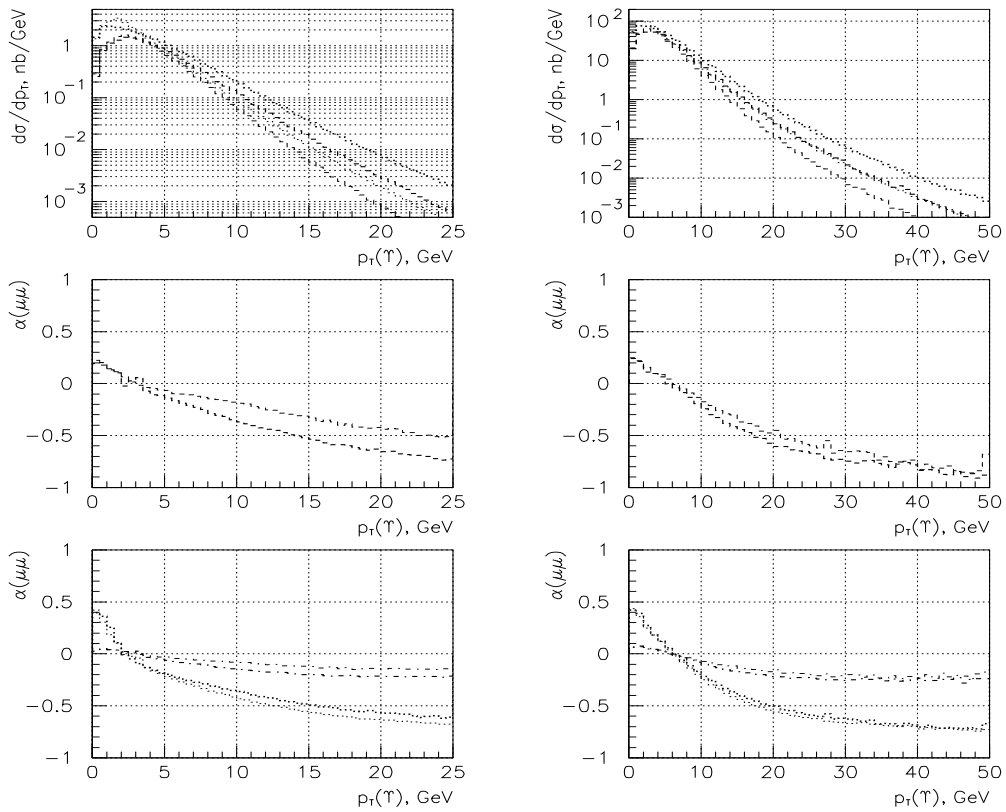


Fig. 12: Predictions on the production of  $\Upsilon$  mesons at the Tevatron (left panel) and LHC (right panel). Thick lines, JB parametrization; thin lines, dGRV parametrization. (a) Transverse momentum distribution. (b) Spin alignment parameter  $\alpha$  for the direct contribution. (c) Spin alignment parameter  $\alpha$  with feed-down from  $\chi_b$  decays taken into account. Dotted lines, the quark spin conservation hypothesis; dash-dotted lines, the full depolarization hypothesis.

As far as the decays of  $P$ -wave states are concerned, nothing is known on the polarisation

properties of these decays. If we assume that the quark spin is conserved in radiative transitions, and the emission of a photon only changes the quark orbital momentum (as it is known to be true in the electric dipole transitions in atomic physics,  $\Delta S = 0$ ,  $\Delta L = \pm 1$ ), then the predictions on  $\alpha$  appear to be similar to those made for the direct channel (lower panels in Fig. 12, dotted curves). If, on the contrary, we assume that the transition  $\chi_b \rightarrow \Upsilon + \gamma$  leads to complete depolarization, then we arrive at a more moderate behavior of the parameter  $\alpha$  (dash-dotted curves in Fig. 12).

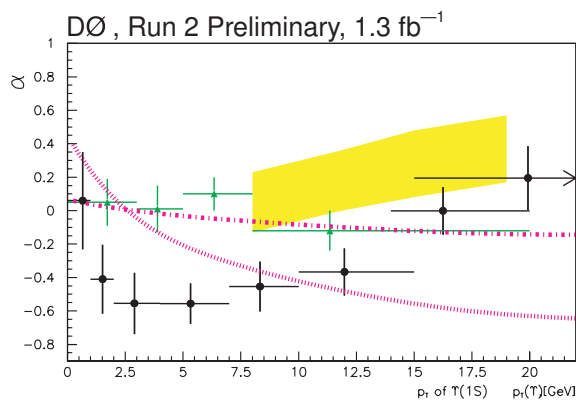


Fig. 13: Spin alignment parameter  $\alpha$  at the Tevatron. Solid curve, quark spin conservation hypothesis; dash-dotted curves, full depolarization hypothesis; yellow band, NRQCD predictions. Green and black points, D0 Run 1 and Run 2 experimental data.

The preliminary results on the  $J/\psi$  polarization at the Tevatron obtained by the collaborations E537 [195] and CDF [196] point to longitudinal polarization with the average value of spin alignment parameter  $\alpha \approx -0.2$  over the whole range of  $J/\psi$  transverse momentum  $p_T$ . In Fig. 13 our results [194] are compared with the preliminary data on the spin alignment of  $\Upsilon$  mesons obtained by the D0 collaboration [197].

A state with purely direct production mechanism in the bottomonium family is the  $\Upsilon(3S)$  meson. The calculations presented here are also valid for this state, except the lower total cross section (by an approximate factor of 1/3) because of the correspondingly lower value of the wave function

At the LHC energies, the theoretical predictions possess less sensitivity to the choice of unintegrated gluon distributions. The purest probe is provided by the polarization of  $\Upsilon(3S)$  mesons.

## 9 $B_c$ and double heavy baryon production and decays

Author: A. Likhoded

$B_c$ -meson is the heaviest of the stable under strong interaction mesons. Because of its unique properties the study of its production and decay processes can be used to check current models of quark dynamics.

There are 16 narrow  $(\bar{b}c)$  states below the threshold of  $\bar{B}D$ -pair production. In contrast to

$(c\bar{c})$  and  $(b\bar{b})$  systems there are no strong annihilation channel for  $(b\bar{c})$ -mesons, so excited states can decay only to the ground states with the emission of photons and  $\pi$ -mesons.

Experimental value for ground state mass is  $M_{B_c} = 6276.6 \pm 4 \pm 2.7 \text{ MeV}/c^2$  was measured recently by CDF collaboration in exclusive decay  $B_c \rightarrow J/\psi\pi$  [198]. It is in good agreement with theoretical predictions [199] within experimental and theoretical errors. Semileptonic decay mode was used recently by D0 and CDF collaborations to measure  $B_c$ -meson lifetime [200]

$$\tau_{B_c} = 0.448_{-0.096}^{+0.123} \pm 0.121 \text{ ps}.$$

This value is in good agreement with theoretical calculations based on operator product expansion (OPE), potential models and QCD sum rules [201]. This lifetime is caused mainly by decays of  $c$ -quark (70%), while contribution of  $b$ -quark decays and weak annihilation are 20% and 10%, respectively. It should be noted, that observed by D0 and CDF collaboration decay modes are connected with  $b$ -quark decays.

Since both constituent quarks in  $B_c$  are heavy, one can use perturbative QCD for calculation of  $B_c$  production cross section. The only nonperturbative parameter on this cross section, the value of  $B_c$  wave function at the origin, can be obtained using potential models. In this point  $B_c$ -meson production differs dramatically from production of  $B$ - and  $D$ -mesons.

In  $e^+e^-$  annihilation theory predicts usual pattern of  $b$ -quark fragmentation  $b \rightarrow B_c + X$ , with calculable fragmentation functions. In  $\gamma\gamma \rightarrow B_c + X$ ,  $\gamma g \rightarrow B_c + X$  and  $gg \rightarrow B_c + X$  processes, on the other hand, there is strong violation of fragmentation picture for large enough transverse momentum. The factorization formula

$$\frac{d\sigma}{dp_T} = \int \frac{d\hat{\sigma}(\mu, gg \rightarrow b\bar{b})}{dk_T} \Big|_{k_T=p_T/x} D^{b \rightarrow B_c+X}(x, \mu) \frac{dx}{x}$$

is valid only for very large values ( $p_T \gtrsim 40 \text{ GeV}$ ). As a result, to describe experimentally interesting values of  $B_c$  transverse momentum in these processes one needs to calculate total amplitude sets: 20 amplitudes for  $\gamma\gamma$ -, 24 for  $\gamma g$ - and 36 for  $gg$ -subprocesses [202].

A rough estimate of total contribution to  $B_c$  production cross section (including feed-down from excited states) gives the value of order  $10^{-3}$  of the cross section of  $B$ -meson production. CDF and D0 collaborations give their results on  $B_c$  production cross section ( $\sigma_{B_c}$ ) in the form of the ratio over the cross section of  $B$ -meson production ( $\sigma_B$ ):

$$R_e = \frac{\sigma_{B_c} \text{Br}(B_c \rightarrow J/\psi e^+ \nu_e)}{\sigma_B \text{Br}(B_c \rightarrow J/\psi K^\pm)} = 0.282 \pm 0.0038 \pm 0.074$$

in the kinematical region  $m_T(B) > 4.0 \text{ GeV}$  and  $|y(B)| < 1.0$ . Similar result for  $B_c \rightarrow J/\psi \mu^\pm \nu_\mu$  decay is

$$R_\mu = 0.249 \pm 0.045_{-0.076}^{+0.107}.$$

We believe that these results contradict theoretical estimates. Using known branching fractions  $Br(B \rightarrow J/\psi K^\pm) \simeq 1 \cdot 10^{-3}$  and  $Br(B_c \rightarrow J/\psi e^\pm \nu_e) \simeq 2 \cdot 10^{-3}$  one can see, that



Mode	BR, %	Mode	BR, %	Mode	BR, %
$B_c^+ \rightarrow \eta_c e^+ \nu$	0.75	$B_c^+ \rightarrow J/\psi K^+$	0.011	$B_c^+ \rightarrow B_s^0 K^+$	1.06
$B_c^+ \rightarrow \eta_c \tau^+ \nu$	0.23	$B_c \rightarrow J/\psi K^{*+}$	0.022	$B_c^+ \rightarrow B_s^{*0} K^+$	0.37
$B_c^+ \rightarrow \eta'_c e^+ \nu$	0.041	$B_c^+ \rightarrow D^+ \bar{D}^0$	0.0053	$B_c^+ \rightarrow B_s^0 K^{*+}$	–
$B_c^+ \rightarrow \eta'_c \tau^+ \nu$	0.0034	$B_c^+ \rightarrow D^+ \bar{D}^{*0}$	0.0075	$B_c^+ \rightarrow B_s^{*0} K^{*+}$	–
$B_c^+ \rightarrow J/\psi e^+ \nu$	1.9	$B_c^+ \rightarrow D^{*+} \bar{D}^0$	0.0049	$B_c^+ \rightarrow B^0 \pi^+$	1.06
$B_c^+ \rightarrow J/\psi \tau^+ \nu$	0.48	$B_c^+ \rightarrow D^{*+} \bar{D}^{*0}$	0.033	$B_c^+ \rightarrow B^0 \rho^+$	0.96
$B_c^+ \rightarrow \psi' e^+ \nu$	0.132	$B_c^+ \rightarrow D_s^+ \bar{D}^0$	0.00048	$B_c^+ \rightarrow B^{*0} \pi^+$	0.95
$B_c^+ \rightarrow \psi' \tau^+ \nu$	0.011	$B_c^+ \rightarrow D_s^{*+} \bar{D}^{*0}$	0.00071	$B_c^+ \rightarrow B^{*0} \rho^+$	2.57
$B_c^+ \rightarrow D^0 e^+ \nu$	0.004	$B_c^+ \rightarrow D_s^{*+} \bar{D}^0$	0.00045	$B_c^+ \rightarrow B^0 K^+$	0.07
$B_c^+ \rightarrow D^0 \tau^+ \nu$	0.002	$B_c^+ \rightarrow D_s^{*+} \bar{D}^{*0}$	0.0026	$B_c^+ \rightarrow B^0 K^{*+}$	0.015
$B_c^+ \rightarrow D^{*0} e^+ \nu$	0.018	$B_c^+ \rightarrow \eta_c D_s^+$	0.86	$B_c^+ \rightarrow B^{*0} K^+$	0.055
$B_c^+ \rightarrow D^{*0} \tau^+ \nu$	0.008	$B_c^+ \rightarrow \eta_c D_s^{*+}$	0.26	$B_c^+ \rightarrow B^{*0} K^{*+}$	0.058
$B_c^+ \rightarrow B_s^0 e^+ \nu$	4.03	$B_c^+ \rightarrow J/\psi D_s^+$	0.17	$B_c^+ \rightarrow B^+ \bar{K}^0$	1.98
$B_c^+ \rightarrow B_s^{*0} e^+ \nu$	5.06	$B_c^+ \rightarrow J/\psi D_s^{*+}$	1.97	$B_c^+ \rightarrow B^+ \bar{K}^{*0}$	0.43
$B_c^+ \rightarrow B^0 e^+ \nu$	0.34	$B_c^+ \rightarrow \eta_c D^+$	0.032	$B_c^+ \rightarrow B^{*+} \bar{K}^0$	1.60
$B_c^+ \rightarrow B^{*0} e^+ \nu$	0.58	$B_c^+ \rightarrow \eta_c D^{*+}$	0.010	$B_c^+ \rightarrow B^{*+} \bar{K}^{*0}$	1.67
$B_c^+ \rightarrow \eta_c \pi^+$	0.20	$B_c^+ \rightarrow J/\psi D^+$	0.009	$B_c^+ \rightarrow B^+ \pi^0$	0.037
$B_c^+ \rightarrow \eta_c \rho^+$	0.42	$B_c^+ \rightarrow J/\psi D^{*+}$	0.074	$B_c^+ \rightarrow B^+ \rho^0$	0.034
$B_c^+ \rightarrow J/\psi \pi^+$	0.13	$B_c^+ \rightarrow B_s^0 \pi^+$	16.4	$B_c^+ \rightarrow B^{*+} \pi^0$	0.033
$B_c^+ \rightarrow J/\psi \rho^+$	0.40	$B_c^+ \rightarrow B_s^0 \rho^+$	7.2	$B_c^+ \rightarrow B^{*+} \rho^0$	0.09
$B_c^+ \rightarrow \eta_c K^+$	0.013	$B_c^+ \rightarrow B_s^{*0} \pi^+$	6.5	$B_c^+ \rightarrow \tau^+ \nu_\tau$	1.6
$B_c^+ \rightarrow \eta_c K^{*+}$	0.020	$B_c^+ \rightarrow B_s^{*0} \rho^+$	20.2	$B_c^+ \rightarrow c \bar{s}$	4.9

Table 1: Branching fractions of exclusive  $B_c$  decay modes [203]

in this kinematical region the ratio

$$\frac{\sigma(B_c)}{\sigma(B)} = R_e \frac{\text{Br}(B \rightarrow J/\psi K^\pm) \text{Br}(b \rightarrow B^\pm)}{\text{Br}(B_c \rightarrow J/\psi e^\pm \nu_e)} = \frac{0.282 \cdot 10^{-3} \cdot 0.5}{2 \cdot 10^{-2}} = 0.7 \cdot 10^{-2},$$

that is about an order of magnitude higher than theoretical estimates.

Using CTEQ5L gluon distribution functions and perturbative calculation of  $gg \rightarrow B_c + X$ , we obtained about  $0.8 \mu b$  for  $B_c$ -meson production cross section at LHC. It includes contributions from  $1S_0$  ( $0.19 \mu b$ ),  $1S_1$  ( $0.47 \mu b$ ),  $2S_0$  ( $0.05 \mu b$ ) and  $2S_1$  ( $0.11 \mu b$ ) states. After summing over all spin states we can see, that the whole contribution of  $P$ -wave levels is equal to 7% of  $S$ -state cross section.

At LHC with luminosity  $\mathcal{L} = 10^{34} \text{ cm}^2 \text{ s}^{-1}$  and  $\sqrt{s} = 14 \text{ TeV}$  one can expect  $4.5 \cdot 10^{10}$   $B_c^+$  events per year. As it is clear from Table 1, branching fractions of main semileptonic and hadronic decay modes are large enough for reliable observation of  $B_c$  meson.

## 10 Testing time-reversal and CP symmetry with $\Lambda_b$ decays

Author: Z. J. Ajaltouni

## 10.1 Introduction

Time-reversal (TR) is a fundamental symmetry in many branches of Physics, principally nuclear and particle Physics. Testing its validity or, conversely, searching for its violation, is an important task similar to CP symmetry violation. Few years ago, important experimental results showing clear evidence for TR violation in  $K^0 - \bar{K}^0$  oscillations have been claimed both by CP-LEAR and K-TeV experiments [204]. Then, this research has been extended to the  $B$ -meson system by BaBar and Belle collaborations.

Another source of TR violation could be looked for in particular decays of *hyperons*, as suggested by R. Gatto after the discovery of parity violation in  $\beta$  decay [205]. If we replace the  $s$ -quark belonging to an hyperon by a  $b$ -quark, analogous tests can be performed with *beauty baryons*, like  $\Lambda_b$ ,  $\Sigma_b$ , etc. With the advent of the LHC, it is expected that 10% of the  $b\bar{b}$  pairs produced in proton-proton collisions at  $\sqrt{s} = 14$  TeV will hadronize into beauty baryons  $\mathcal{B}_b$ , and approximately 90% of the  $\mathcal{B}_b$  will be dominated by  $\Lambda_b$  or  $\bar{\Lambda}_b$ . In the framework of the LHCb experiment whose average luminosity will be  $\mathcal{L} = 2 \times 10^{32} \text{cm}^{-2} \text{s}^{-1}$ , roughly  $10^{11}$  beauty baryons will be produced each year.

## 10.2 Features of Time-Reversal

TR operator changes the sign of momentum  $\vec{p}$  and spin  $\vec{s}$  of any particle and leaves its coordinates  $\vec{r}$  invariant. Any triple product  $(\vec{v}_i \times \vec{v}_j) \cdot \vec{v}_k$  with  $\vec{v}_{i,j,k} = \vec{p}$  or  $\vec{s}$  will be *odd* under TR; a non-vanishing value of this observable being a sign of TR violation (TRV). However, an inevitable physical process as strong Final State Interactions (FSI) appears when examining hadronic decays. FSI modify particle wave-functions and generate an additional phase-shift,  $\delta_S$ , to the decay amplitude; the existence of the phase  $\delta_S$  could simulate a  $T$ -odd effect. Being aware of this issue, we developed a phenomenological model describing the decay  $\Lambda_b \rightarrow \Lambda V(1^-)$  and used it in our search for TRV supposing that FSI are negligible. Thus a non-vanishing  $T$ -odd observable will be considered as a serious sign of TRV. In the following, emphasis will be put on TR processes and, because of the delicate problem of CP study in  $\Lambda_b - \bar{\Lambda}_b$  system, only a recent reference will be mentioned [206].

## 10.3 Kinematics and Dynamics of $\Lambda_b \rightarrow \Lambda V(1^-)$ Decays

Different observables can be constructed in order to test TR; the main one being the polarization-vectors of the intermediate resonances coming from  $\Lambda_b$  decays like  $\Lambda(1/2^+)$  and  $V = \rho^0, \omega, J/\psi$ , the vector-meson  $V$  being mainly the  $J/\psi$  decaying into  $\mu^- \mu^+$ . A rigorous study of these decays requires the *helicity formalism* of Jacob-Wick-Jackson which includes the  $\Lambda_b$  initial polarization expressed by its polarization density-matrix (PDM) [207]. Full calculations permit to deduce the  $\Lambda$  angular distributions in an appropriate  $\Lambda_b$  rest-frame. It is given by:  $\frac{d\sigma}{d\Omega} = 1 + \alpha_{As}^{\Lambda_b} \vec{\mathcal{P}}^{\Lambda_b} \cdot \hat{p}$ , where  $\alpha_{As}^{\Lambda_b}$  is the decay asymmetry parameter of the  $\Lambda_b$  resonance,  $\vec{\mathcal{P}}^{\Lambda_b}$  is its polarization-vector and  $\hat{p}$  is the unit-vector parallel to  $\Lambda$  momentum.

A special dynamical model has been performed in order to compute the decay amplitude [208]. It is divided into two main parts : (i) In the framework of the *factorization hypothesis*, the Operator Product Expansion (OPE) techniques are used in order to evaluate both the *soft* (non-perturbative) contributions and the *hard* (perturbative) ones to the hadronic matrix element; the color number

$N_c$  is left *free*. (ii) The form-factors arising in the matrix element are computed by means of the Heavy Quark Effective Theory (HQET) and corrections of order  $\mathcal{O}(1/m_b)$  are performed. Finally, both tree and penguin diagrams have been taken into account in our model.

#### 10.4 Main Physical Results

- In order to test the model, the branching ratio  $BR(\Lambda_b \rightarrow \Lambda J/\psi)$  and other ones are computed according to the effective color number,  $N_c^{eff}$ , and compared to the experimental data.

$N_c^{eff}$	2	2.5	3	3.5
$\Lambda J/\psi$	$8.95 \times 10^{-4}$	$2.79 \times 10^{-4}$	$0.62 \times 10^{-4}$	$0.03 \times 10^{-4}$
$\Lambda \rho^0$	$1.62 \times 10^{-7}$	$1.89 \times 10^{-7}$	$2.2 \times 10^{-7}$	$2.4 \times 10^{-7}$
$\Lambda \omega$	$22.3 \times 10^{-7}$	$4.75 \times 10^{-7}$	$0.2 \times 10^{-7}$	$0.64 \times 10^{-7}$

Table 2: Branching ratio,  $\mathcal{BR}$ , for  $\Lambda_b \rightarrow \Lambda J/\Psi$ ,  $\Lambda_b \rightarrow \Lambda \rho^0$  and  $\Lambda_b \rightarrow \Lambda \omega$ .

The experimental value,  $BR(\Lambda_b \rightarrow \Lambda J/\psi) = (4.7 \pm 2.1 \pm 1.9) \times 10^{-4}$  (PDG 2006), favours the range of values  $2.0 \leq N_c^{eff} \leq 3.0$ .

- Other essential parameters like  $\Lambda_b$  asymmetry,  $\Lambda$  polarization and its non-diagonal matrix element, and the probability of longitudinal polarization for each vector meson can also be obtained :

Parameter	$\Lambda \rho^0 - \omega$	$\Lambda J/\psi$
$\alpha_{AS}^{\Lambda_b}$	0.194	0.490
$\mathcal{P}^\Lambda$	-0.21	-0.17
$\rho_{+-}^\Lambda$	0.31	0.25
$\rho_{00}^V$	0.79	0.66

#### 10.5 Direct Test of Time-Reversal

##### Special Angles :

We define  $\vec{n}_\Lambda$  and  $\vec{n}_V$  respectively as the unit normal vectors to  $\Lambda$  and  $V$  decay planes in the  $\Lambda_b$  rest-frame,  $\vec{e}_Z$  being the quantization axis.

$$\vec{n}_\Lambda = \frac{\vec{p}_p \times \vec{p}_\pi}{|\vec{p}_p \times \vec{p}_\pi|}, \quad \vec{n}_V = \frac{\vec{p}_{l+} \times \vec{p}_{l-}}{|\vec{p}_{l+} \times \vec{p}_{l-}|}, \quad \text{or} \quad \vec{n}_V = \frac{\vec{p}_{h+} \times \vec{p}_{h-}}{|\vec{p}_{h+} \times \vec{p}_{h-}|}$$

Those vectors are **even** under TR. But the cosine and the sine of their azimuthal angles defined by :

$$\vec{u}_i = \frac{\vec{e}_Z \times \vec{n}_i}{|\vec{e}_Z \times \vec{n}_i|}, \quad \cos \phi_{(n_i)} = \vec{e}_Y \cdot \vec{u}_i, \quad \sin \phi_{(n_i)} = \vec{e}_Z \cdot (\vec{e}_Y \times \vec{u}_i),$$

with  $\phi_{(n_i)} = \phi_{\vec{n}_\Lambda}$ ,  $\phi_{\vec{n}_V}$  are both **odd** under TR. Their distributions exhibit asymmetries which depend directly on the  $\Lambda$  azimuthal angle distribution whose analytical expression is given by:

$$d\sigma/d\phi \propto 1 + \frac{\pi}{2} \alpha_{As}^\Lambda \left( \Re e(\rho_{+-}^{\Lambda_b}) \cos \phi - \Im m(\rho_{+-}^{\Lambda_b}) \sin \phi \right).$$

The initial  $\Lambda_b$  PDM being unknown, we make the following hypothesis in our simulations :  $\mathcal{P}^{\Lambda_b} = 100\%$  and  $\Re e(\rho_{+-}^{\Lambda_b}) = -\Im m(\rho_{+-}^{\Lambda_b}) = \sqrt{2}/2$ . The following asymmetries are obtained [206] :

Asymmetries	$\Lambda\rho^0 - \omega$	$\Lambda J/\psi$
$AS(\cos \phi_{\vec{n}_\Lambda})$	$(2.4 \pm 0.3)\%$	$(5.2 \pm 0.3)\%$
$AS(\sin \phi_{\vec{n}_\Lambda})$	$-(2.7 \pm 0.3)\%$	$-(5.0 \pm 0.3)\%$

### Vector-Polarizations

In a second step, vector-polarizations have been carefully examined, mainly by considering a new frame related to each resonance  $R_i$  and defined as follows:

$$\vec{e}_L = \frac{\vec{p}}{p}, \quad \vec{e}_T = \frac{\vec{e}_Z \times \vec{e}_L}{|\vec{e}_Z \times \vec{e}_L|}, \quad \vec{e}_N = \vec{e}_T \times \vec{e}_L.$$

Each vector-polarization  $\vec{\mathcal{P}}^{(i)}$  can be expanded on the new basis by writing:  $\vec{\mathcal{P}}^{(i)} = P_L^{(i)} \vec{e}_L + P_N^{(i)} \vec{e}_N + P_T^{(i)} \vec{e}_T$ , with  $P_j^{(i)} = \vec{\mathcal{P}}^{(i)} \cdot \vec{e}_j$  and  $j = L, N, T$ . These components as well as the basis vectors  $\vec{e}_L, \vec{e}_T$  and  $\vec{e}_N$ , are studied under parity and time-reversal operations. The results are straightforward:  $P_L$  and  $P_T$  are both *Parity*–odd and *T*–even, while  $P_N$  is *Parity*–even but *T*–**odd**.

So, if the normal component  $P_N$  is not equal to zero, it would be a signal of TR violation.

### 10.6 Conclusion

The process  $\Lambda_b \rightarrow \Lambda J/\psi$  is a promising channel to look for the validity of TR symmetry at LHC energies. Complete kinematical calculations have been performed by stressing the importance of the resonance polarizations. Our dynamics model is very realistic, because it is based on the OPE formalism and completed by HQET for the computation of the form-factors. An extension of these calculations is under study in order to perform rigorous tests of both CP and TR symmetries among beauty baryons in a model-independent way [209].

## 11 Production and detection of massive exotic hadrons

*Authors: D. Milstead and O. Piskounova*

Exotic stable massive particles are proposed in many models of physics beyond the Standard Model. Understanding their interactions in matter is critical for any search. This paper outlines a model for the scattering of stable massive hadrons which is based on Regge phenomenology and the quark gluon string model.

## 11.1 Introduction

Searches for exotic stable<sup>15</sup> massive particles (SMPs) are performed at colliders as a matter of routine whenever a new collision energy is reached [210]. An additional motivation to make such searches at the LHC arises from the hierarchy problem, proposed solutions to which suggest that new physics processes may be manifest at TeV energies; indeed SMPs are predicted in a number of exotic physics models, such as supersymmetry [210]. Prior to data taking it is important to establish that LHC experiments are able both to detect and extract the quantum numbers of any SMP which may be observed. To do this, an understanding of the interactions of SMPs in matter is needed. As part of this workshop a model [211] has been developed for the scattering of hadronic SMPs (termed  $H$ -hadrons) which uses Regge phenomenology [212] and the quark gluon string model (QGSM) [213]. This work has clear implications for future searches using HERA data and the interpretation of earlier searches.

## 11.2 Interactions of $H$ -Hadrons in Matter

A qualitative picture of the scattering process can be built up [214]. The heavy exotic quark will be a spectator, and the low energy light quark system is involved in the interaction. Regge phenomenology and the QGSM are thus appropriate tools with which the interactions of exotic hadrons in matter can be explored. Fig. 14 shows the predicted cross section for the interaction of a  $H$ -meson with a stationary nucleon in a nucleus comprising equal amounts of protons and neutrons as a function of the Lorentz factor  $\gamma$  of the  $H$ -meson. Reggeon and pomeron contributions are shown separately.

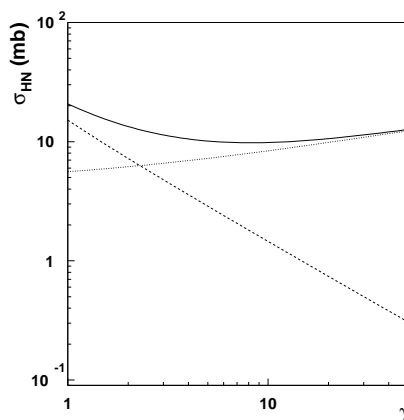


Fig. 14: Pomeron (dotted) and reggeon (dashed) contributions to the exotic-meson-nucleon cross section. The sum of the two processes is shown as a solid line.

Exotic hadrons which contain a light constituent anti-quark, eg  $H_{Q\bar{q}}$  or a  $H_{\bar{Q}q\bar{q}}$  can undergo pomeron and reggeon exchanges. Conversely, hadrons containing a light constituent quark ( $H_{\bar{Q}q}$ ,  $H_{Qqq}$ ) can only undergo pomeron exchange. Anti-baryons and baryons may undergo both

<sup>15</sup>The term stable implies a particle will not decay as it traverses a detector.

reggeon and pomeron exchange, and pomeron exchange only processes, respectively. The overall cross sections for interactions involving baryons and anti-baryons is estimated by doubling the pomeron contribution to the meson cross sections shown in Fig. 14 to take into account the extra light quark contribution. The reggeon contribution to anti-baryon interactions is set to twice the value for meson scattering together with an additional contribution from processes in which exotic anti-baryons can annihilate to exotic mesons and ordinary mesons. This latter contribution is suppressed.

### 11.3 Energy Loss

The PYTHIA [215] program was used to produce samples of stable fourth generation quark pair production events. For reasons of detector acceptance, the  $\beta$  value of the  $H$ -hadrons was restricted to be greater than 0.7 and the pseudorapidity to  $|\eta| < 2.5$  [216]. Using a Monte Carlo method, the  $H$ -hadrons were transported through iron corresponding to the material distribution of the ATLAS detector sub-systems enclosed within the muon detector system. Using a triple regge ansatz [211]  $H$ -hadron energy loss can be estimated. Fig. 15 shows the total energy loss of  $H$ -hadrons after they pass through the detector material. Distributions are presented for  $H$ -hadrons formed from different types of exotic quarks and anti-quarks with masses 200 and 1000 GeV. The distributions are normalised to the total number  $N$  of a given type of  $H$ -hadron satisfying the  $\beta$  and  $\eta$  requirements. There is little difference between them, with a peak around 5 GeV.  $H$ -hadrons containing up-like quarks typically lose more energy than those with down-like quarks owing to the greater fraction of neutral  $H$ -hadrons with down-like quarks.

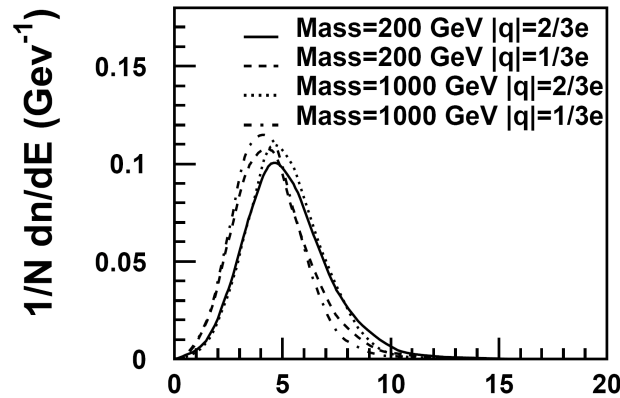


Fig. 15: Total energy loss for  $H$ -hadrons of different types and masses.

### 11.4 Acknowledgements

D. Milstead is a Royal Swedish Academy Research Fellow supported by a grant from the Knut and Alice Wallenberg Foundation.

## References

- [1] W. K. Tung *et al.*, JHEP **02**, 053 (2007). hep-ph/0611254.
- [2] A. D. Martin, W. J. Stirling, R. S. Thorne, and G. Watt, Phys. Lett. **B652**, 292 (2007). 0706.0459.
- [3] P. M. Nadolsky *et al.*, Phys. Rev. **D78**, 013004 (2008). 0802.0007.
- [4] G. Watt, A. D. Martin, W. J. Stirling, and R. S. Thorne, *Recent Progress in Global PDF Analysis*. Preprint 0806.4890, 2008.
- [5] A. D. Martin, W. J. Stirling, R. S. Thorne, and G. Watt (2009). 0901.0002.
- [6] J. C. Collins and W.-K. Tung, Nucl. Phys. **B278**, 934 (1986).
- [7] J. C. Collins, Phys. Rev. **D58**, 094002 (1998). hep-ph/9806259.
- [8] E. L. M. P. Laenen, S. Riemersma, J. Smith, and W. L. van Neerven, Nucl. Phys. **B392**, 162 (1993).
- [9] M. A. G. Aivazis, J. C. Collins, F. I. Olness, and W.-K. Tung, Phys. Rev. **D50**, 3102 (1994). hep-ph/9312319.
- [10] J. C. Collins, F. Wilczek, and A. Zee, Phys. Rev. **D18**, 242 (1978).
- [11] M. Gluck, E. Reya, and A. Vogt, Eur. Phys. J. **C5**, 461 (1998). hep-ph/9806404.
- [12] M. Buza, Y. Matiounine, J. Smith, R. Migneron, and W. L. van Neerven, Nucl. Phys. **B472**, 611 (1996). hep-ph/9601302.
- [13] M. Buza, Y. Matiounine, J. Smith, and W. L. van Neerven, Eur. Phys. J. **C1**, 301 (1998). hep-ph/9612398.
- [14] R. S. Thorne and R. G. Roberts, Phys. Lett. **B421**, 303 (1998). hep-ph/9711223.
- [15] R. S. Thorne and R. G. Roberts, Phys. Rev. **D57**, 6871 (1998). hep-ph/9709442.
- [16] M. Dittmar *et al.*, *Parton distributions: Summary report for the HERA - LHC workshop*. Preprint hep-ph/0511119, 2005.
- [17] R. M. Barnett, Phys. Rev. Lett. **36**, 1163 (1976).
- [18] W. K. Tung, S. Kretzer, and C. Schmidt, J. Phys. **G28**, 983 (2002). hep-ph/0110247.
- [19] S. Kretzer, H. L. Lai, F. I. Olness, and W. K. Tung, Phys. Rev. **D69**, 114005 (2004). hep-ph/0307022.
- [20] R. S. Thorne, Phys. Rev. **D73**, 054019 (2006). hep-ph/0601245.
- [21] A. Chuvakin, J. Smith, and W. L. van Neerven, Phys. Rev. **D61**, 096004 (2000). hep-ph/9910250.

- [22] M. Kramer, F. I. Olness, and D. E. Soper, Phys. Rev. **D62**, 096007 (2000).  
hep-ph/0003035.
- [23] S. Kretzer and I. Schienbein, Phys. Rev. **D58**, 094035 (1998). hep-ph/9805233.
- [24] E. L. M. P. Laenen and S. O. Moch, Phys. Rev. **D59**, 034027 (1999).  
hep-ph/9809550.
- [25] S. Catani, M. Ciafaloni, and F. Hautmann, Nucl. Phys. **B366**, 135 (1991).
- [26] I. Bierenbaum, J. Blümlein, and S. Klein, Acta Phys. Pol. **B39** (2008) 1531 (2008).  
0806.0451.
- [27] M. Buza and W. L. van Neerven, Nucl. Phys. **B500**, 301 (1997). hep-ph/9702242.
- [28] A. D. Martin, W. J. Stirling, R. S. Thorne, and G. Watt, *Parton distributions for the LHC*.  
Preprint in preparation, 2008.
- [29] A. D. Martin, R. G. Roberts, W. J. Stirling, and R. S. Thorne, Phys. Lett.  
**B531**, 216 (2002). hep-ph/0201127.
- [30] A. D. Martin, R. G. Roberts, W. J. Stirling, and R. S. Thorne, Phys. Lett.  
**B604**, 61 (2004). hep-ph/0410230.
- [31] H. collaboration:, *Measurement of  $F_2^{c\bar{c}}$  and  $F_2^{b\bar{b}}$  using the H1 vertex detector at HERA*.  
34th International Conference on High Energy Physics Philadelphia, 30th July - 5th  
August, 2008.
- [32] S. Alekhin, Phys. Rev. **D68**, 014002 (2003). hep-ph/0211096.
- [33] A. D. Martin, W. J. Stirling, and R. S. Thorne, Phys. Lett. **B636**, 259 (2006).  
hep-ph/0603143.
- [34] B. W. Harris and J. Smith, Nucl. Phys. **B452**, 109 (1995). hep-ph/9503484.
- [35] P. Jimenez-Delgado and E. Reya, *Dynamical NNLO parton distributions*. Preprint  
0810.4274, 2008.
- [36] J. M. Campbell, *Overview of the theory of  $W/Z + jets$  and heavy flavor*. Preprint  
0808.3517, 2008.
- [37] B. A. Kniehl, *Inclusive production of heavy-flavored hadrons at NLO in the GM-VFNS*.  
Preprint 0807.2215, 2008.
- [38] C. Buttar *et al.* (2006). hep-ph/0604120.
- [39] S. J. Brodsky, P. Hoyer, C. Peterson, and N. Sakai, Phys. Lett. **B93**, 451 (1980).
- [40] J. Pumplin, H. L. Lai, and W. K. Tung, Phys. Rev. **D75**, 054029 (2007).  
hep-ph/0701220.



- [41] European Muon Collaboration, J. J. Aubert *et al.*, Nucl. Phys. **B213**, 31 (1983).
- [42] A. D. Martin, R. G. Roberts, W. J. Stirling, and R. S. Thorne, Eur. Phys. J. **C4**, 463 (1998). hep-ph/9803445.
- [43] R. S. Thorne, J. Phys. **G25**, 1307 (1999). hep-ph/9902299.
- [44] OPAL Collaboration, G. Alexander *et al.*, Z. Phys. **C72**, 1 (1996);  
OPAL Collaboration, K. Ackerstaff *et al.*, Eur. Phys. J. **C1**, 439 (1998);  
ALEPH Collaboration, R. Barate *et al.*, Eur. Phys. J. **C16**, 597 (2000);  
CLEO Collaboration, M. Artuso *et al.*, Phys. Rev. **D70**, 112001 (2004);  
Belle Collaboration, R. Seuster *et al.*, Phys. Rev. **D73**, 032002 (2006).
- [45] G. Kramer and H. Spiesberger, Eur. Phys. J. **C22**, 289 (2001);  
G. Kramer and H. Spiesberger, Eur. Phys. J. **C28**, 495 (2003);  
G. Kramer and H. Spiesberger, Eur. Phys. J. **C38**, 309 (2004).
- [46] B. A. Kniehl, G. Kramer, I. Schienbein, and H. Spiesberger, Phys. Rev. **D71**, 014018 (2005);  
B. A. Kniehl, G. Kramer, I. Schienbein, and H. Spiesberger, Eur. Phys. J. **C41**, 199 (2005).
- [47] B. A. Kniehl, G. Kramer, I. Schienbein, and H. Spiesberger, Phys. Rev. Lett. **96**, 012001 (2006).
- [48] T. Kneesch, B. A. Kniehl, G. Kramer, and I. Schienbein, Nucl. Phys. **B799**, 34 (2008).
- [49] M. G. Bowler, Z. Phys. **C11**, 169 (1981).
- [50] SLD Collaboration, K. Abe *et al.*, Phys. Rev. Lett. **84**, 4300 (2000);  
SLD Collaboration, K. Abe *et al.*, Phys. Rev. **D65**, 092006 (2002);  
SLD Collaboration, K. Abe *et al.*, Phys. Rev. **D66**, 079905(E) (2002);  
ALEPH Collaboration, A. Heister *et al.*, Phys. Lett. **B512**, 30 (2001);  
OPAL Collaboration, G. Abbiendi *et al.*, Eur. Phys. J. **C29**, 463 (2003).
- [51] CDF Collaboration, D. Acosta *et al.*, Phys. Rev. **D71**, 021001 (2005);  
CDF Collaboration, A. Abulencia *et al.*, Phys. Rev. **D75**, 012010 (2007).
- [52] J. Binnewies, B. A. Kniehl, and G. Kramer, Phys. Rev. **D58**, 034016 (1998).
- [53] V. G. Kartvelishvili and A. K. Likhoded, Sov. J. Nucl. Phys. **42**, 823 (1985). [Yad. Fiz. **42**, 1306 (1985)].
- [54] CDF Collaboration, D. Acosta *et al.*, Phys. Rev. Lett. **91**, 241804 (2003).
- [55] U. Aglietti, G. Corcella, and G. Ferrera, Nucl. Phys. **B775**, 162 (2007).
- [56] G. Corcella and G. Ferrera, J. High Energy Phys. **12**, 029 (2007).
- [57] U. Aglietti, G. Ferrera, and G. Ricciardi, Nucl. Phys. **B768**, 85 (2007).

- [58] U. Aglietti, F. Di Lodovico, G. Ferrera, and G. Ricciardi, arXiv:0711.0860. 0711.0860.
- [59] B. Mele and P. Nason, Nucl. Phys. **B617**, 626 (1991).
- [60] M. Cacciari and S. Catani, Nucl. Phys. **B617**, 253 (2001).
- [61] G. Sterman, Nucl. Phys. **B281**, 310 (1987).
- [62] S. Catani and L. Trentadue, Nucl. Phys. **B327**, 323 (1989).
- [63] U. Aglietti and G. Ricciardi, Phys. Rev. **D70**, 114008 (2004).
- [64] D. Shirkov, Nucl. Phys. Proc. Suppl. **152**, 51 (2006).
- [65] ALEPH Collaboration, A. Heister *et al.*, Phys. Lett. **B512**, 30 (2001).
- [66] OPAL Collaboration, G. Abbiendi *et al.*, Eur. Phys. J. **C29**, 463 (2003).
- [67] SLD Collaboration, K. Abe *et al.*, Phys. Rev. Lett. **84**, 4300 (2000).
- [68] ALEPH Collaboration, R. Barate *et al.*, Eur. Phys. J. **C16**, 597 (2000).
- [69] ZEUS Collaboration, S. Chekanov *et al.*, Nucl. Phys. **B700**, 3 (2004). hep-ex/0405065.
- [70] CDF Collaboration, F. Abe *et al.*, Phys. Rev. **D60**, 072003 (1999). hep-ex/9903011.
- [71] A. Banfi, G. P. Salam, and G. Zanderighi, Eur. Phys. J. **C47**, 113 (2006). hep-ph/0601139.
- [72] S. Catani, Y. L. Dokshitzer, M. Olsson, G. Turnock, and B. R. Webber, Phys. Lett. **B269**, 432 (1991).
- [73] S. Catani, Y. L. Dokshitzer, M. H. Seymour, and B. R. Webber, Nucl. Phys. **B406**, 187 (1993).
- [74] S. D. Ellis and D. E. Soper, Phys. Rev. **D48**, 3160 (1993). hep-ph/9305266.
- [75] A. Banfi, G. P. Salam, and G. Zanderighi, JHEP **08**, 062 (2004). hep-ph/0407287.
- [76] S. Catani, F. Krauss, R. Kuhn, and B. R. Webber, JHEP **11**, 063 (2001). hep-ph/0109231.
- [77] M. L. Mangano, M. Moretti, and R. Pittau, Nucl. Phys. **B632**, 343 (2002). hep-ph/0108069.
- [78] *Measurement of the inclusive  $b$ -jet cross section in  $p\bar{p}$  collisions at  $\sqrt{s} = 1.96\text{TeV}$*  (unpublished). Note 8418.
- [79] J. M. Campbell and R. K. Ellis, Phys. Rev. **D62**, 114012 (2000). hep-ph/0006304.

- [80] M. L. Mangano, P. Nason, and G. Ridolfi, Nucl. Phys. **B373**, 295 (1992).
- [81] S. Frixione, P. Nason, and B. R. Webber, JHEP **08**, 007 (2003). hep-ph/0305252.
- [82] G. Corcella *et al.*, JHEP **01**, 010 (2001). hep-ph/0011363.
- [83] A. Banfi, G. P. Salam, and G. Zanderighi, JHEP **07**, 026 (2007). 0704.2999.
- [84] W. T. Giele, E. W. N. Glover, and D. A. Kosower, Nucl. Phys. **B403**, 633 (1993). hep-ph/9302225.
- [85] Z. Nagy, Phys. Rev. Lett. **88**, 122003 (2002). hep-ph/0110315.
- [86] J. Pumplin, H. L. Lai, and W. K. Tung, Phys. Rev. **D75**, 054029 (2007). hep-ph/0701220.
- [87] CDF Collaboration, D. E. Acosta *et al.*, Phys. Rev. **D71**, 092001 (2005). hep-ex/0412006.
- [88] C. Weiser, *A combined secondary vertex based b-tagging algorithm in CMS* (unpublished). CMS NOTE-2006/014.
- [89] M. Sapinski, *Expected performance of ATLAS for measurements of jets, b-jets, tau-jets, and  $E_{T,\text{mis}}$*  (unpublished). SN-ATLAS-2002-012, ATL-COM-CONF-2001-006.
- [90] J. Bastos, physics/0702041 (2007). physics/0702041.
- [91] W. Bernreuther, J. Phys. **G35**, 083001 (2008). 0805.1333.
- [92] P. M. Nadolsky *et al.*, Phys. Rev. **D78**, 013004 (2008). 0802.0007.
- [93] P. Nason, S. Dawson, and R. K. Ellis, Nucl. Phys. **B303**, 607 (1988).
- [94] S. Moch and P. Uwer, Phys. Rev. **D78**, 034003 (2008). 0804.1476.
- [95] M. Cacciari, S. Frixione, M. M. Mangano, P. Nason, and G. Ridolfi (2008). 0804.2800.
- [96] N. Kidonakis and R. Vogt, arXiv:0805.3844 (2008). 0805.3844.
- [97] M. Czakon, A. Mitov, and S. Moch, Phys. Lett. **B651**, 147 (2007). 0705.1975.
- [98] M. Czakon, A. Mitov, and S. Moch, Nucl. Phys. **B798**, 210 (2008). 0707.4139.
- [99] M. Czakon, Phys. Lett. **B664**, 307 (2008). 0803.1400.
- [100] J. G. Körner, Z. Merebashvili, and M. Rogal, Phys. Rev. **D73**, 034030 (2006). hep-ph/0511264.
- [101] J. G. Körner, Z. Merebashvili, and M. Rogal, Phys. Rev. **D77**, 094011 (2008). 0802.0106.

- [102] S. Dittmaier, P. Uwer, and S. Weinzierl, Phys. Rev. Lett. **98**, 262002 (2007).  
hep-ph/0703120.
- [103] M. Caffo, H. Czyz, S. Laporta, and E. Remiddi, Nuovo Cim. **A111**, 365 (1998).  
hep-th/9805118.
- [104] E. Laenen, S. Riemersma, J. Smith, and W. L. van Neerven, Nucl. Phys. **B392**, 162 (1993);  
S. Riemersma, J. Smith, and W. L. van Neerven, Phys. Lett. **B347**, 143 (1995).  
hep-ph/9411431.
- [105] S. Alekhin and J. Blümlein, Phys. Lett. **B594**, 299 (2004). hep-ph/0404034.
- [106] M. Buza, Y. Matiounine, J. Smith, and W. L. van Neerven, Nucl. Phys. **B485**, 420 (1997). hep-ph/9608342.
- [107] I. Bierenbaum, J. Blümlein, and S. Klein, in preparation.
- [108] S. Alekhin, K. Melnikov, and F. Petriello, Phys. Rev. **D74**, 054033 (2006).  
hep-ph/0606237.
- [109] Blümlein, H. J., Böttcher, and A. Guffanti, Nucl. Phys. **B774**, 182 (2007).  
hep-ph/0607200.
- [110] M. Buza, Y. Matiounine, J. Smith, R. Migneron, and W. L. van Neerven, Nucl. Phys. **B472**, 611 (1996). hep-ph/9601302.
- [111] J. A. M. Vermaseren, A. Vogt, and S. Moch, Nucl. Phys. **B724**, 3 (2005).  
hep-ph/0504242.
- [112] I. Bierenbaum, J. Blümlein, and S. Klein, Nucl. Phys. **B780**, 40 (2007).  
hep-ph/0703285.
- [113] I. Bierenbaum, J. Blümlein, and S. Klein, Phys. Lett. **B648**, 195 (2007).  
hep-ph/0702265.
- [114] J. Blümlein, A. De Freitas, W. L. van Neerven, and S. Klein, Nucl. Phys. **B755**, 272 (2006). hep-ph/0608024.
- [115] I. Bierenbaum, Blümlein, S. J., Klein, and C. Schneider, Nucl. Phys. **B803**, 1 (2008).  
0803.0273.
- [116] S. A. Larin, T. van Ritbergen, and J. A. M. Vermaseren, Nucl. Phys. **B427**, 41 (1994);  
S. A. Larin, P. Nogueira, T. van Ritbergen, and J. A. M. Vermaseren, Nucl. Phys. **B492**, 338 (1997). hep-ph/9605317;  
A. Retey and J. A. M. Vermaseren, Nucl. Phys. **B604**, 281 (2001). hep-ph/0007294;  
J. Blümlein and J. A. M. Vermaseren, Phys. Lett. **B606**, 130 (2005).  
hep-ph/0411111;  
S. Moch, J. A. M. Vermaseren, and A. Vogt, Nucl. Phys. **B688**, 101 (2004).  
hep-ph/0403192.

- [117] A. Vogt, S. Moch, and J. A. M. Vermaseren, Nucl. Phys. **B691**, 129 (2004).  
hep-ph/0404111.
- [118] J. A. Gracey, Phys. Lett. **B322**, 141 (1994). hep-ph/9401214.
- [119] N. Gray, D. J. Broadhurst, W. Grafe, and K. Schilcher, Z. Phys. **C48**, 673 (1990).
- [120] M. Buza, Y. Matiounine, J. Smith, and W. L. van Neerven, Eur. Phys. J. **C1**, 301 (1998).  
hep-ph/9612398.
- [121] I. Bierenbaum, J. Blümlein, and S. Klein, arxiv:0806.4613 [hep-ph] (2008).  
0806.4613.
- [122] B. A. Ovrut and H. J. Schnitzer, Nucl. Phys. **B179**, 381 (1981);  
B. A. Ovrut and H. J. Schnitzer, Nucl. Phys. **B189**, 509 (1981);  
W. Bernreuther and W. Wetzel, Nucl. Phys. **B197**, 228 (1982);  
W. Bernreuther, Ann. Phys. **151**, 127 (1983).
- [123] I. Bierenbaum, J. Blümlein, and S. Klein, Acta Phys. Polon. **B38**, 3543 (2007).  
0710.3348.
- [124] J. Blümlein and S. Kurth, Phys. Rev. **D60**, 014018 (1999). hep-ph/9810241.
- [125] J. A. M. Vermaseren, Int. J. Mod. Phys. **A14**, 2037 (1999). hep-ph/9806280.
- [126] J. Blümlein, Comput. Phys. Commun. **159**, 19 (2004). hep-ph/0311046.
- [127] J. Blümlein and S. Klein, arxiv:0706.2426 [hep-ph] (2007). 0706.2426.
- [128] J. Blümlein, arxiv:0807.0700 [math-ph] (2008). 0807.0700.
- [129] J. Blümlein and N. Kochelev, Phys. Lett. **B381**, 296 (1996). hep-ph/9603397.
- [130] J. Blümlein, V. Ravindran, and W. L. van Neerven, Phys. Rev. **D68**, 114004 (2003).  
hep-ph/0304292.
- [131] P. Nogueira, J. Comput. Phys. **105**, 279 (1993).
- [132] T. van Ritbergen, A. N. Schellekens, and J. A. M. Vermaseren, Int. J. Mod. Phys.  
**A14**, 41 (1999). hep-ph/9802376.
- [133] M. Steinhauser, Comput. Phys. Commun. **134**, 335 (2001). hep-ph/0009029.
- [134] J. A. M. Vermaseren, math-ph/0010025 (2000). math-ph/0010025.
- [135] C. Schneider, Ann. Comb., **9** (1) (2005) 75; Proc. ISSAC'05, (2005) pp. 285 (ACM  
Press); Proc. FPSAC'07, (2007) 1; J. Diff. Equations Appl., **11** (9) (2005) 799; J.  
Algebra Appl., **6** (3) (2007) 415; Sémin. Lothar. Combin. **56** (2007) Article B56b and  
Habilitation Thesis, JKU Linz, (2007).
- [136] J. Blümlein, DESY 08-042.

- [137] J. Blümlein and V. Ravindran, Nucl. Phys. **B716**, 128 (2005). hep-ph/0501178.
- [138] J. Blümlein and V. Ravindran, Nucl. Phys. **B749**, 1 (2006). hep-ph/0604019.
- [139] M. Tentyukov and J. A. M. Vermaseren, hep-ph/0702279 (2007). hep-ph/0702279.
- [140] CTEQ Collaboration, R. Brock *et al.*, Rev. Mod. Phys. **67**, 157 (1995).
- [141] V. N. Gribov and L. N. Lipatov, Sov. J. Nucl. Phys. **15**, 438 (1972). [Yad. Fiz. **15**, 781 (1972)];  
Y. L. Dokshitzer, Sov. Phys. JETP **46**, 641 (1977). [Zh. Eksp. Teor. Fiz. **73**, 1216 (1977)];  
G. Altarelli and G. Parisi, Nucl. Phys. **B126**, 298 (1977).
- [142] E. A. Kuraev, L. N. Lipatov, and V. S. Fadin, Sov. Phys. JETP **44**, 443 (1976). [Zh. Eksp. Teor. Fiz. **71**, 840 (1976)];  
I. I. Balitsky and L. N. Lipatov, Sov. J. Nucl. Phys. **28**, 822 (1978). [Yad. Fiz. **28**, 1597 (1978)].
- [143] V. S. Fadin and L. N. Lipatov, Nucl. Phys. **B477**, 767 (1996).
- [144] L. N. Lipatov, Nucl. Phys. **B452**, 452 (1995);  
E. N. Antonov, L. N. Lipatov, E. A. Kuraev, and I. O. Cherednikov, Nucl. Phys. **B721**, 111 (2005);  
L. N. Lipatov and M. I. Vyazovsky, Nucl. Phys. **B597**, 399 (2001).
- [145] M. Gell-Mann, M. L. Goldberger, F. E. Low, E. Marx, and F. Zachariasen, Phys. Rev. **133**, 145B (1964).
- [146] V. S. Fadin and V. E. Sherman, JETP Lett. **23**, 548 (1976);  
V. S. Fadin and V. E. Sherman, JETP **45**, 861 (1977).
- [147] G. T. Bodwin, E. Braaten, and G. P. Lepage, Phys. Rev. **D51**, 1125 (1995). Phys. Rev. **D55**, 5853E (1997).
- [148] M. Cacciari and P. Nason, JHEP **09**, 006 (2003).
- [149] CDF Collaboration, F. Abe *et al.*, Phys. Rev. Lett. **79**, 572 (1997);  
CDF Collaboration, F. Abe *et al.*, Phys. Rev. Lett. **79**, 578 (1997);  
CDF Collaboration, T. Affolder *et al.*, Phys. Rev. Lett. **85**, 2886 (2000).
- [150] CDF Collaboration, D. Acosta *et al.*, Phys. Rev. **D71**, 032001 (2005).
- [151] G. T. Bodwin, E. Braaten, and J. Lee, Phys. Rev. **D72**, 014004 (2005).
- [152] P. Hägler, R. Kirschner, A. Schäfer, L. Szymanowski, and O. V. Teryaev, Phys. Rev. **D62**, 071502 (2000);  
P. Hägler, R. Kirschner, A. Schäfer, L. Szymanowski, and O. V. Teryaev, Phys. Rev. Lett. **86**, 1446 (2001).
- [153] F. Yuan and K. T. Chao, Phys. Rev. **D63**, 034006 (2001).

- [154] F. Yuan and K. T. Chao, Phys. Rev. Lett. **87**, 022002 (2001).
- [155] B. A. Kniehl, D. V. Vasin, and V. A. Saleev, Phys. Rev. **D73**, 074022 (2006).
- [156] V. A. Saleev and D. V. Vasin, Phys. Rev. **D68**, 114013 (2003);  
V. A. Saleev and D. V. Vasin, Phys. Atom. Nucl. **68**, 94 (2005). [Yad. Fiz. **68**, 95 (2005)].
- [157] J. Blümlein, preprint (1995). DESY 95-121.
- [158] H. Jung and G. P. Salam, Eur. Phys. J. **C19**, 351 (2001).
- [159] M. A. Kimber, A. D. Martin, and M. G. Ryskin, Phys. Rev. **D63**, 114027 (2001).
- [160] ZEUS Collaboration, S. Chekanov *et al.*, Eur. Phys. J. **C27**, 173 (2003).
- [161] H1 Collaboration, C. Adloff *et al.*, Eur. Phys. J. **C25**, 41 (2002).
- [162] V. A. Saleev and D. V. Vasin, Phys. Lett. **B548**, 161 (2002);  
V. A. Saleev, Phys. Rev. **D65**, 054041 (2002).
- [163] V. A. Saleev and N. P. Zotov, Mod. Phys. Lett. **A9**, 151 (1994).
- [164] CDF Collaboration, F. Abe *et al.*, Phys. Rev. Lett. **75**, 4358 (1995);  
CDF Collaboration, D. Acosta *et al.*, Phys. Rev. Lett. **88**, 161802 (2002).
- [165] CDF Collaboration, V. M. Abazov *et al.*, Phys. Rev. Lett. **94**, 232001 (2005).
- [166] E. Braaten, S. Fleming, and A. K. Leibovich, Phys. Rev. **D63**, 094006 (2001).
- [167] B. A. Kniehl, V. A. Saleev, and D. V. Vasin, Phys. Rev. **D74**, 014024 (2006).
- [168] V. A. Saleev and D. V. Vasin, Phys. Part. Nucl. **38**, 635 (2007).
- [169] H1 Collaboration, C. Adloff *et al.*, Nucl. Phys. **B545**, 21 (1999).
- [170] ZEUS Collaboration, J. Breitweg *et al.*, Eur. Phys. J. **C6**, 67 (1999). Phys. Lett. **B481**, 213 (2000).
- [171] V. A. Saleev and D. V. Vasin, Phys. Atom. Nucl. **68**, 95 (2005).
- [172] CDF Collaboration, D. Acosta *et al.*, Phys. Rev. Lett. **91**, 241804 (2003).
- [173] J. C. Collins and R. K. Ellis, Nucl. Phys. **B360**, 3 (1991).
- [174] S. Catani, M. Ciafaloni, and F. Hautmann, Nucl. Phys. **B366**, 135 (1991).
- [175] B. A. Kniehl, A. V. Shipilova, and V. A. Saleev, to be published.
- [176] B. A. Kniehl, A. V. Shipilova, and V. A. Saleev, DESY-08-194 **2008**.  
arXiv:0812.3376[hep-ph].
- [177] CDF Collaboration, F. Abe *et al.*, Phys. Rev. **D55**, 2546 (1997).

- [178] P. Hagler *et al.*, Phys. Rev. **D62**, 071502(R) (2000).
- [179] J. Kwiecinski, A. Martin, and S. A., Phys. Rev. **D56**, 3991 (1997).
- [180] C. Peterson *et al.*, Phys. Rev. **D27**, 105 (1983).
- [181] V. A. Saleev and D. V. Vasin. [arXiv:0709.0259](#).
- [182] M. Kramer, Prog. Part. Nucl. Phys. **47**, 141 (2001). [hep-ph/0106120](#).
- [183] Quarkonium Working Group Collaboration, N. Brambilla *et al.* (2004). [hep-ph/0412158](#).
- [184] B. A. Kniehl and L. Zvirner, Nucl. Phys. **B621**, 337 (2002). [hep-ph/0112199](#).
- [185] S. P. Baranov, Phys. Rev. **D66**, 114003 (2002).
- [186] P. Hagler, R. Kirschner, A. Schafer, L. Szymanowski, and O. V. Teryaev, Phys. Rev. **D63**, 077501 (2001). [hep-ph/0008316](#).
- [187] S. P. Baranov, Phys. Lett. **B428**, 377 (1998).
- [188] S. P. Baranov, A. V. Lipatov, and N. P. Zotov (2001). [hep-ph/0106229](#).
- [189] L. V. Gribov, E. M. Levin, and M. G. Ryskin, Phys. Rept. **100**, 1 (1983).
- [190] S. Catani, M. Ciafaloni, and F. Hautmann, Phys. Lett. **B242**, 97 (1990).
- [191] E. A. Kuraev, L. N. Lipatov, and V. S. Fadin, Sov. Phys. JETP **45**, 199 (1977).
- [192] J. Blümlein, J. Phys. **G19**, 1623 (1993).
- [193] M. Gluck, E. Reya, and A. Vogt, Eur. Phys. J. **C5**, 461 (1998). [hep-ph/9806404](#).
- [194] S. P. Baranov and N. P. Zotov, JETP Lett. **86**, 435 (2007). [0707.0253](#).
- [195] C. Akerlof *et al.*, Phys. Rev. **D48**, 5067 (1993).
- [196] CDF Collaboration, A. A. Affolder *et al.*, Phys. Rev. Lett. **85**, 2886 (2000). [hep-ex/0004027](#).
- [197] D0 Collaboration, V. M. Abazov *et al.* (2008). [0804.2799](#).
- [198] V. Papadimitriou, AIP Conf. Proc. **815**, 157 (2006). [[arXiv:hep-ex/0511043](#)]; M. D. Corcoran, others (for the CDF, and D. Coll.), [arXiv:hep-ex/0506061](#).
- [199] S. S. Gershtein, V. V. Kiselev, A. K. Likhoded, and A. V. Tkabladze, Phys. Usp. **38**, 1 (1995). [[Usp. Fiz. Nauk. 165 \(1995\) 3](#), [arXiv:hep-ph/9504319](#)]; V. V. Kiselev, A. K. Likhoded, and A. V. Tkabladze, Phys. Rev. **D51**, 3613 (1995); S. N. Gupta and J. M. Johnson, Phys. Rev. **D53**, 312 (1996); D. Ebert, R. N. Faustov, and V. O. Galkin, Phys. Rev. **D67**, 014027 (2003);



- N. Brambilla, Y. Sumin, and A. Vairo, Phys. Rev. **D65**, 034001 (2002);  
 S. M. Ikhdaïr and R. Sever, Int. J. Mod. Phys. **A20**, 6509 (2005);  
 S. Godfrey, Phys. Rev. **D70**, 054017 (2004).
- [200] CDF Collaboration, A. Abulencia *et al.*, Phys. Rev. Lett. **97**, 242003 (2006);  
 D0 Collaboration, V. M. Abazov *et al.*, Phys. Rev. Lett. **97**, 021802 (2006).
- [201] I. P. Gouz, V. V. Kiselev, A. K. Likhoded, V. I. Romanovsky, and O. P. Yushchenko,  
 Phys. Atom. Nucl. **67**, 1559 (2004). [Yad. Fiz. **67**, 1581 (2004), arXiv:hep-ph/0211432];  
 V. V. Kiselev, A. E. Kovalsky, and A. K. Likhoded, Nucl. Phys. **B585**, 353 (2000);  
 C. H. Chang, Int. J. Mod. Phys. **A21**, 777 (2006);  
 V. V. Kiselev, arXiv:hep-ph/0308214.
- [202] V. V. Kiselev, A. K. Likhoded, and A. I. Onishchenko, Nucl. Phys. **B569**, 473 (2000);  
 A. V. Berezhnoi, V. V. Kiselev, and A. K. Likhoded, Z. Phys. **A356**, 79 (1996);  
 K. Kolodziej and R. Rückl, Nucl. Instrum. Meth. **A408**, 33 (1998);  
 C. H. Chang, Y. Q. Chen, G. P. Han, and H. T. Jiang, Phys. Lett. **B364**, 78 (1995).
- [203] S. S. Gershtein and A. K. Likhoded, arXiv:0706.0963.
- [204] L. Alvarez-Gaumé *et al.*, arXiv:hep-ph/9812326.
- [205] R. Gatto, Nucl. Phys. **5**, 183 (1958).
- [206] E. Conte, Thèse de Docteur de l'Université Blaise Pascal **PPCF T 0710** (2007).
- [207] Z. J. Ajaltouni *et al.*, Phys. Lett. **B614**, 165 (2005).
- [208] O. Leitner, Z. J. Ajaltouni, and E. Conte, arXiv:hep-ph/0602043;  
 Z. J. Ajaltouni *et al.*, Nucl. Phys. B Proc. Suppl. **174**, 169 (2007).
- [209] D. S. E. *et al.*, PCCF RI 0802 (2008).
- [210] M. Fairbairn *et al.*, Phys. Rept. **438**, 1 (2007). hep-ph/0611040.
- [211] Y. R. de Boer, A. B. Kaidalov, D. A. Milstead, and O. I. Piskounova, J. Phys. **G35**, 075009 (2008). 0710.3930.
- [212] P. D. B. Collins, Phys. Rept. **1**, 103 (1971);  
 P. D. B. Collins. Cambridge 1977, 445p.
- [213] A. B. Kaidalov, Phys. Lett. **B116**, 459 (1982);  
 A. B. Kaidalov and K. A. Ter-Martirosian, Phys. Lett. **B117**, 247 (1982);  
 A. B. Kaidalov and K. A. Ter-Martirosian, Sov. J. Nucl. Phys. **39**, 979 (1984);  
 A. B. Kaidalov and O. I. Piskunova, Z. Phys. **C30**, 145 (1986).
- [214] M. Drees and X. Tata, Phys. Lett. **B252**, 695 (1990);  
 A. C. Kraan, Eur. Phys. J. **C37**, 91 (2004). hep-ex/0404001.
- [215] T. Sjostrand, S. Mrenna, and P. Skands, JHEP **05**, 026 (2006). hep-ph/0603175.

- [216] A. C. Kraan, J. B. Hansen, and P. Nevski, Eur. Phys. J. **C49**, 623 (2007).  
hep-ex/0511014.

## Chapter 4

# Working Group Diffraction

### Convenors:

*M. Arneodo (U. Piemonte Orientale, Novara, INFN, CMS, ZEUS),  
M. Diehl (DESY), P. Newman (U. Birmingham, H1) V. A. Khoze (U. Durham)*

*Contactpersons: A. Bruni (INFN, ZEUS), B. Cox (ATLAS), R. Orava (U. Helsinki)*

### Working Group Members:

V. Andreev, M. Arneodo, J. Bartels, A. Bonato, K. Borras, A. Bruni, A. Bunyatyan, P. Bussey, F.A. CEC-  
copieri, S. Cerci, T. Coughlin, B. Cox, M. Diehl, S. Erhan, C. Ewerz, K. Golec-Biernat, K. Goulianos,  
M. Grothe, K. Hiller, J. Hollar, X. Janssen, M. Kapishin, J. Kaspar, V.A. Khoze, M. Klasen, G. Kramer,  
V. Kundrat, J. Łukasik, A. v. Manteuffel, P. Marage, U. Maor, I. Melzer-Pellman, A.D. Martin, L. Motyka,  
M. Mozer, P. Newman, H. Niewiadomski, C. Nockles, J. Nystrand, R. Orava, K. Österberg, A. Panagiotou,  
A. Pilkington, J.L. Pinfold, W. Plano, X. Rouby, C. Royon, M. Ruspa, P. Ryan, M.G. Ryskin, R. Schicker,  
F.-P. Schilling, W.B. Schmidke, G. Shaw, W. Słomiński, H. Stenzel, M. Strikman, M. Taševski, K. Terashi,  
T. Teubner, L. Trentadue, A. Valkárová, P. Van Mechelen, A. Vilela Pereira, G. Watt, S. Watts, C. Weiss,  
R. Wolf



# Working Group on Diffraction: Executive Summary

*M. Arneodo<sup>a</sup>, M. Diehl<sup>b</sup>, V.A. Khoze<sup>c</sup> and P. Newman<sup>d</sup>*

<sup>a</sup> Università del Piemonte Orientale, I-28100 Novara, and INFN-Torino, I-10125 Torino, Italy

<sup>b</sup> Deutsches Elektronen-Synchrotron DESY, 22603 Hamburg, Germany

<sup>c</sup> Institute for Particle Physics Phenomenology, University of Durham, DH1 3LE, UK

<sup>d</sup> School of Physics and Astronomy, University of Birmingham, B15 2TT, UK

## Abstract

We give a brief overview of the topics covered in the working group on diffraction.

## 1 Introduction

From 2006 to 2008, the working group on diffraction had 74 individual presentations, documenting the considerable activity and progress in the field. This program covered a variety of topics: the presentation and assessment of new data from HERA and the Tevatron [1–5], developments in the theory of diffraction in  $ep$  and in  $pp$  or  $p\bar{p}$  collisions [6–15], and the ongoing preparatory studies for measuring diffractive processes at the LHC [16–20]. Many presentations were related in one way or another to the prospect of seeing central exclusive production of the Higgs boson,  $p + p \rightarrow p + H + p$ , or of other new particles. Important progress has been made in this field since the first proceedings of the HERA/LHC workshop [21] appeared, both on the side of instrumentation at LHC and in the understanding of the relevant theory, with crucial input provided by new measurements from the H1, ZEUS, and CDF Collaborations. In the following we give a brief overview of the different topics presented in these proceedings and of their interrelation.

## 2 Diffraction from electron-proton to hadron-hadron collisions

A key result of the numerous studies of diffraction at HERA is that in the presence of a hard scale several diffractive channels can be understood in terms of a partonic description, which allows us to calculate important features of the process in perturbation theory. This concerns the inclusive cross section for diffractive deep inelastic scattering [1] as well as diffractive jet or heavy flavor production from a highly virtual photon [2, 9]. The increasingly precise HERA results for these channels are well described in terms of perturbatively calculated hard-scattering coefficients and of diffractive parton densities. The latter are a special case of fracture functions [6] and, just as the usual parton densities, have been fitted to data.

It has long been anticipated from theory and seen in data that such a simple factorized description is not valid in diffractive hadron-hadron collisions, and recent results from HERA and the Tevatron have corroborated this finding. Secondary interactions between partons of the colliding hadrons significantly decrease the fraction of events with large rapidity gaps, and it remains a challenge to quantitatively understand the dynamics of these interactions [7, 8] at the LHC. Let us recall that the associated physics is closely related to that of multiple parton interactions and hence of importance far beyond the context of diffractive final states [21]. Similar rescattering effects are also expected in  $ep$  collisions when the exchanged photon becomes quasi real, not

only for diffraction but also for events with an observed leading baryon [3]. The situation here seems, however, to be more complicated than initially thought due to the double nature of a real photon as a pointlike and a hadronic object. Based on the same data, the two contributions [2] and [9] to these proceedings draw conflicting conclusions about the magnitude of rescattering effects in diffractive photoproduction. The study of additional experimental observables, such as double differential distributions or certain ratios should help clarify the situation.

A wealth of information about high-energy dynamics can be gained from the detailed experimental studies of exclusive diffraction at HERA, notably of exclusive production of a vector meson or a real photon [4]. Precise data for such channels in particular provide good constraints on the generalized gluon distribution [10], which not only carries valuable information about proton structure at small momentum fractions but is also a key ingredient for calculating central exclusive production in  $pp$  or  $p\bar{p}$  collisions. Ultraperipheral collisions at LHC offer the prospect to study exclusive diffraction initiated by a real photon at energies well beyond the HERA regime [11]. Suitable exclusive channels may also provide clear signals for odderon exchange, which, although naturally arising within the QCD picture of high-energy collisions, have been conspicuously absent from data so far [12].

Finally, the combined consideration of  $ep$  data for both inclusive and exclusive diffraction and for non-diffractive events remains maybe the best strategy for clarifying the importance of parton saturation at HERA, i.e., of non-linear dynamical effects due to high parton densities [13]. To understand such dynamics at the quantitative level remains one of the great challenges in high-energy QCD, and there is hope that the huge phase space available in  $pp$  collisions at LHC can be harnessed to shed further light on this physics. This remains an ambitious enterprise, requiring measurements at forward rapidities at the LHC [16] and further development of the theory [14].

### 3 Preparing for diffraction and forward physics at LHC

The opportunities for diffractive and forward measurements at LHC cover a wide area of physics, ranging from the determination of the elastic and total  $pp$  cross section at the highest energies yet achieved in the laboratory [17, 18] to the study of both electroweak and strong interactions in  $\gamma\gamma$  and  $\gamma p$  collisions [11, 16, 19, 20]. High hopes are put into the possibility to observe central exclusive production of new particles such as a light Higgs boson, with the prospect of the precise measurement of their mass, width, and quantum numbers in a very clean environment [20]. The theoretical description of the central exclusive production mechanism involves many difficult issues, and a milestone in testing our understanding of this mechanism has been the observation of exclusive dijet production by CDF [5]. Despite this success, one must keep in mind the uncertainties inherent in extrapolating dynamics from Tevatron to LHC energies, and a number of diffractive measurements have been proposed to validate the theory at an early stage of LHC running [15].

The forward instrumentation currently available at ATLAS, CMS and ALICE will allow a rich program to be carried out in forward and diffractive physics from the very beginning of the data taking. Feasibility studies performed by CMS [16] indicate that measurements of forward jets sensitive to the low- $x$  PDFs of the proton are possible with the first  $10 \text{ pb}^{-1}$  of integrated luminosity. “Rediscovery” of hard diffraction at the LHC is possible within the first  $10\text{--}100 \text{ pb}^{-1}$ ,

via single-diffractive production of dijets and  $W$  bosons, as well as  $\Upsilon$  photoproduction [16]. In addition, exclusive dilepton production can be used for the calibration of the forward detectors and for luminosity determination [16]. TOTEM [17] plans to measure central and single diffractive cross sections, as well as high- $t$  elastic scattering and forward charged particle multiplicities with the first data. A more ambitious joint CMS-TOTEM physics program is foreseen [17] as soon as common CMS and TOTEM data taking is possible. TOTEM [17] and ATLAS [18] will also measure the total and elastic  $pp$  cross sections in dedicated runs with special beam optics. A diffractive physics program is also taking shape at ALICE [19], thanks to the particle-identification capability and good acceptance for low- $p_T$  particles of the ALICE detector, along with the lack of pile-up at the ALICE interaction point.

ATLAS and CMS will also be able to carry out a forward and diffractive physics program at the highest LHC instantaneous luminosities if the AFP and FP420 programs are approved [20]. AFP aims at instrumenting with near-beam proton detectors the regions at  $\pm 220$  and  $\pm 420$  m from the ATLAS interaction point, while FP420 at CMS aims at instrumenting the  $\pm 420$  m region to complement existing proton detectors at TOTEM. These additions to ATLAS and CMS will permit the measurement of forward protons down to values of the fractional momentum loss of the proton of  $\xi \simeq 0.002$ .

In summary, the diffractive community is looking forward to the next years, when the final analysis of HERA data and a variety of measurements at LHC will hopefully teach us valuable lessons on the physics of the strong interaction and beyond.

## References

- [1] P. Newman and M. Ruspa, *Towards a combined HERA diffractive deep inelastic scattering measurement*, these proceedings.
- [2] W. Słomiński and A. Valkárová, *Diffractive final states and factorization at HERA*, these proceedings.
- [3] W.B. Schmidke and A. Bunyatyan, *Leading baryon production at HERA*, these proceedings.
- [4] A. Bruni, X. Janssen and P. Marage, *Exclusive vector meson production and deeply virtual Compton scattering at HERA*, these proceedings.
- [5] K. Goulianos and J.L. Pinfold, *Exclusive central production and diffractive  $W/Z$  results from CDF II*, these proceedings.
- [6] F.A. Ceccopieri and L. Trentadue, *Fracture functions at HERA and LHC*, these proceedings.
- [7] A.D. Martin, V.A. Khoze and M.G. Ryskin, *Rapidity gap survival probability and total cross sections*, these proceedings.
- [8] M. Strikman and C. Weiss, *Rapidity gap survival in central exclusive diffraction: Dynamic mechanisms and uncertainties*, these proceedings.

- [9] M. Klasen and G. Kramer, *Survival probability in diffractive dijet production*, these proceedings.
- [10] C. Nockles and T. Teubner, *Generalised parton distributions and exclusive vector meson production*, these proceedings.
- [11] J. Nystrand, *Two-photon and photon-hadron interactions at the LHC*, these proceedings.
- [12] C. Ewerz, *Searching for the odderon at HERA and the LHC*, these proceedings.
- [13] L. Motyka, K. Golec-Biernat and G. Watt, *Dipole models and parton saturation in ep scattering*, these proceedings.
- [14] J. Bartels, *Searching for saturation in pp scattering: the inclusive cross section in QCD*, presentation at this workshop, CERN, May 2008.
- [15] A.D. Martin, V.A. Khoze and M.G. Ryskin, *Checking formalism for central exclusive production in the first LHC runs*, these proceedings.
- [16] S. Erhan et al., *Forward physics with CMS*, these proceedings.
- [17] G. Antchev et al., *Diffraction at TOTEM*, these proceedings.
- [18] K. Hiller and H. Stenzel, *The ALFA detector and physics program*, these proceedings.
- [19] R. Schicker, *Diffractive physics in ALICE*, these proceedings.
- [20] P. Bussey and P. Van Mechelen, *Physics with forward FP420/FP220 tagging systems*, these proceedings.
- [21] S. Alekhin et al., *HERA and the LHC – A workshop on the implications of HERA for LHC physics: Proceedings Parts A and B*, arXiv:hep-ph/0601012 and hep-ph/0601013.



# Towards a Combined HERA Diffractive Deep Inelastic Scattering Measurement

Paul Newman<sup>a</sup>, Marta Ruspa<sup>b</sup>

<sup>a</sup> School of Physics & Astronomy, University of Birmingham, B15 2TT, UK.

<sup>b</sup> Università del Piemonte Orientale, 28100 Novara, Italy.

## Abstract

The diffractive dissociation of virtual photons,  $\gamma^*p \rightarrow Xp$ , has been studied with the H1 and ZEUS detectors at HERA using various complementary techniques. Events have been selected by direct tagging of the outgoing proton or by requiring a large rapidity gap between the proton and the system  $X$ . The diffractive contribution has also been unfolded by decomposition of the inclusive hadronic final state invariant mass distribution. Here, detailed comparisons are made between diffractive cross section measurements obtained from the different methods and the two experiments, showing them to be consistent within the large uncertainties associated with the treatment of proton dissociation processes. First steps are taken towards the combination of the H1 and ZEUS results.

## 1 Introduction

In the single diffractive dissociation process in proton-proton scattering,  $pp \rightarrow Xp$ , at least one of the beam hadrons emerges intact from the collision, having lost only a small fraction of its energy and gained only a small transverse momentum. In the analogous process involving virtual photons,  $\gamma^*p \rightarrow Xp$  (figure 1) [1, 2], an exchanged photon of virtuality  $Q^2$  dissociates through its interaction with the proton at a squared four momentum transfer  $t$  to produce a hadronic system  $X$  with mass  $M_X$ . The fractional longitudinal momentum loss of the proton during the interaction is denoted  $x_{\mathbb{P}}$ , while the fraction of this momentum carried by the struck quark is denoted  $\beta$ . These variables are related to Bjorken  $x$  by  $x = \beta x_{\mathbb{P}}$ .

Diffractive interactions are often discussed in the framework of Regge phenomenology [3] in terms of the exchange of a ‘pomeron’ with vacuum quantum numbers. This interpretation in terms of a universal exchange is experimentally supported by the ‘proton vertex factorisation’, which holds to good approximation over much of the accessible kinematic range at low  $x_{\mathbb{P}}$ , whereby the dependences on variables describing the soft interaction with the proton ( $x_{\mathbb{P}}, t$ ) factorise from those related to the hard interaction with the virtual photon ( $\beta, Q^2$ ). Similar reactions, in which sub-leading Reggeon and pion trajectories are exchanged, have a negligible cross section at the smallest  $x_{\mathbb{P}}$  values.

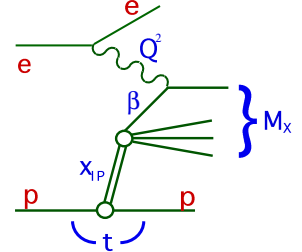


Fig. 1: Illustration of the kinematic variables describing the virtual photon dissociation process,  $\gamma^*p \rightarrow Xp$ , in  $ep$  collisions.

Significant progress has been made in understanding diffraction in terms of QCD by studying virtual photon dissociation in deep inelastic  $ep$  scattering (DIS) at HERA (for a review see [4]). As well as being sensitive to novel features of parton dynamics in the high density, low  $x$  regime, diffractive DIS cross sections are used to extract diffractive parton density functions (DPDFs) [5–9], an essential ingredient in predicting many diffractive processes at the LHC and in estimating backgrounds to more exotic processes such as central exclusive Higgs production ( $pp \rightarrow pHp$ ) [10].

Similarly to inclusive DIS, cross section measurements for the reaction  $ep \rightarrow eXp$  are conventionally expressed in terms of the reduced diffractive cross section,  $\sigma_r^{D(3)}$ , which is related to the measured cross section by

$$\frac{d\sigma^{ep \rightarrow eXp}}{d\beta dQ^2 dx_{\mathbb{P}}} = \frac{4\pi\alpha^2}{\beta Q^4} \left[ 1 - y + \frac{y^2}{2} \right] \sigma_r^{D(3)}(\beta, Q^2, x_{\mathbb{P}}). \quad (1)$$

At moderate inelasticities  $y$ ,  $\sigma_r^{D(3)}$  corresponds to the diffractive structure function  $F_2^{D(3)}$  to good approximation. In this contribution, we tackle the technical issue of compatibility between different  $\sigma_r^{D(3)}$  data sets through detailed comparisons between different measurements by the H1 and ZEUS collaborations and take the first steps towards a combined HERA data set.

## 2 Methods of selecting diffraction at HERA

Experimentally, diffractive  $ep$  scattering is characterised by the presence of a leading proton in the final state retaining most of the initial state proton energy, and by a lack of hadronic activity in the forward (outgoing proton) direction, such that the system  $X$  is cleanly separated and  $M_X$  may be measured in the central detector components. These signatures have been widely exploited at HERA to select diffractive events by tagging the outgoing proton in the H1 Forward Proton Spectrometer or the ZEUS Leading Proton Spectrometer (proton-tagging method [6, 11–14]) or by requiring the presence of a large gap in the rapidity distribution of hadronic final state particles in the forward region (LRG method [5, 8, 15, 16]). In a third approach ( $M_X$  method [16–19]), the inclusive DIS sample is decomposed into diffractive and non-diffractive contributions based on their characteristic dependences on  $M_X$ .

The kinematic coverages of the LRG and  $M_X$  methods are limited to  $x_{\mathbb{P}} \lesssim 0.05$  by the need to contain the system  $X$  in the central detector components. These two methods are equivalent for  $M_X \rightarrow 0$ , but differences are to be expected at larger  $M_X$ , where the LRG method measures the full cross section from all sources at a given  $(x_{\mathbb{P}}, \beta, Q^2)$  point, whereas the  $M_X$  method involves the subtraction of a ‘non-diffractive’ component. LPS and FPS data extend to  $x_{\mathbb{P}} \sim 0.1$  and are therefore the most sensitive to non-leading contributions, including Reggeon and pion trajectory exchanges. Apart from the proton dissociation treatment in the H1 case (see section 4.2), the cross sections measured by the proton-tagging and LRG methods are equivalent.

The methods differ substantially in their dominant sources of systematic uncertainty. In the LRG and  $M_X$  methods, the largest uncertainties arise from the admixture of low mass leading baryon systems other than protons. These include proton excitations to low mass states as well as leading neutrons produced via charge exchange reactions. All such contributions are collectively referred to here as ‘proton dissociation’,  $ep \rightarrow eXN$ , with the baryon state  $N$  having mass  $M_N$ .

Proton dissociation processes cannot always be distinguished by the LRG and  $M_X$  methods from events in which the proton is scattered elastically. Conversely, low- $x_{\mathbb{P}}$  samples selected by the proton-tagging method have little or no proton dissociation background, but are subject to large uncertainties in the proton tagging efficiency, which is strongly dependent on the proton-beam optics. Proton spectrometers also allow a measurement of  $t$ , but the statistical precision is limited by their small acceptances.

Comparing the results from the three different methods is a powerful test of the control over the systematics of the measurements. At low  $x_{\mathbb{P}}$ , the ratio of results obtained by the LRG and  $M_X$  methods to those from the proton-tagging method can also be used to quantify the proton dissociation contributions in the former samples.

### 3 Data sets

A comprehensive comparison has been carried out between recent H1 and ZEUS measurements obtained with the three different methods. The data sets used are as follows.<sup>1</sup>

- Three data sets collected with the ZEUS detector in the years 1999 and 2000. Overlapping samples have been analysed with the ZEUS Leading Proton Spectrometer (termed “**ZEUS LPS**”, based on a luminosity of  $32.6 \text{ pb}^{-1}$ ) [15], with the LRG method (“**ZEUS LRG**”,  $62.2 \text{ pb}^{-1}$ ) [15] and with the  $M_X$  method, relying on the Forward Plug Calorimeter (“**ZEUS FPC I**”,  $4.2 \text{ pb}^{-1}$  [18] and “**ZEUS FPC II**”,  $52.4 \text{ pb}^{-1}$  [19]).
- A set of data collected with the H1 Forward Proton Spectrometer (“**H1 FPS**”,  $28.4 \text{ pb}^{-1}$ ) [14] in the years 1999 and 2000.
- A set of data collected with the H1 detector in the years 1997, 1999 and 2000 and analysed with the LRG method (“**H1 LRG**”,  $2.0 \text{ pb}^{-1}$ ,  $10.6 \text{ pb}^{-1}$  and  $61.6 \text{ pb}^{-1}$  for small, intermediate and large  $Q^2$ , respectively) [8].

The H1 LRG and FPS samples are statistically independent and are only weakly correlated through systematics. The three ZEUS samples also have different dominating systematics, but are not statistically independent. About 75% of events are common to both the ZEUS LRG and ZEUS FPC II data sets and 35% of the ZEUS LPS events are also contained in the ZEUS LRG sample.

### 4 Proton dissociation background and corrections

In proton dissociation processes at the lowest  $M_N$ , the dissociative system  $N$  often escapes entirely undetected into the forward beam-pipe. As  $M_N$  increases, it becomes more likely that dissociation products are detected in the instrumentation most sensitive to forward energy flow. The LRG and  $M_X$  methods therefore do not distinguish low  $M_N$  proton dissociation events from the case in which the proton is scattered elastically. Different cross-section definitions have been adopted, in which the proton dissociation contribution is either subtracted statistically, or else the quoted results are integrated over a specific range of  $M_N$ . Since understanding the proton dissociation contributions and the corresponding corrections is fundamental to comparisons between the different measurements, a detailed discussion is presented in the following.

---

<sup>1</sup>The comparisons here are restricted to published data and do not yet include the precise H1 LRG and  $M_X$  method results obtained from 1999-2004 running [16].

In both the ZEUS LPS and the H1 FPS analyses, the contribution from proton dissociation events is negligible at small  $x_{\mathbb{P}} \lesssim 0.02$ . At the largest  $x_{\mathbb{P}}$  values, it becomes kinematically possible for the detected leading proton to be the result of a decay of an  $N^*$  or other proton excitation, the remaining decay products being unobserved. This background was estimated by ZEUS to contribute around 9% at  $x_{\mathbb{P}} = 0.1$ , using the PYTHIA Monte Carlo (MC) model [20]. In the H1 FPS analysis, using the RAPGAP [21] implementation of the DIFFVM proton dissociation model [22], it was estimated to reach 3% at  $x_{\mathbb{P}} = 0.08$ .

Proton dissociation contributions in the LRG and  $M_X$  methods can be controlled using dedicated proton dissociation simulations tuned in  $M_N$  regions where dissociating protons leave signals in the detectors, and extrapolated into the  $M_N$  regions where the dissociation products are typically not detected. In addition to this procedure, both H1 and ZEUS use standard simulations of non-diffractive processes to control the small migrations of very high  $M_N$  or  $x_{\mathbb{P}}$  events into the measurement region, which occur due to inefficiencies of the forward detectors.

#### 4.1 ZEUS LRG

In the recent ZEUS analysis, the PYTHIA simulation was tuned to proton dissociation signals. Two samples were selected by requiring activity either in the forward plug calorimeter (FPC) or at relatively low proton energy in the LPS. The samples thus include the low  $M_N$  region in which proton dissociation products are invisible to the central detector. The generated distributions were reweighted in  $M_N$ ,  $M_X$  and  $Q^2$  to best describe the energy distribution in the FPC ( $E_{\text{FPC}}$ ), and the scattered proton energy fraction distribution ( $x_L$ ) in the LPS. Figures 2a and 2b show the comparison of the reweighted PYTHIA model with the two proton dissociation samples as a function of these variables. Also shown in figures 2c-e is the resulting estimate of the fraction of proton dissociation events in the LRG sample as a function of  $Q^2$ ,  $\beta$  and  $x_{\mathbb{P}}$ . This fraction, obtained separately from the FPC and LPS samples, is constant at the level of 25%.

The ratios of cross sections extracted from the ZEUS LPS and LRG data (the latter uncorrected for proton dissociation background), are shown in figure 3. There is no significant dependence on  $Q^2$ ,  $x_{\mathbb{P}}$  or  $\beta$ , illustrating the low  $x_{\mathbb{P}}$  compatibility between the two methods. The ratio averages to  $0.76 \pm 0.01(\text{stat.})^{+0.03}_{-0.02}(\text{syst.})^{+0.08}_{-0.05}(\text{norm.})$ , the last error reflecting the normalisation uncertainty of the LPS data. The proton dissociation background fraction in the LRG data is thus  $24 \pm 1(\text{stat.})^{+2}_{-3}(\text{syst.})^{+5}_{-8}(\text{norm.})\%$ , in agreement with the result of the MC

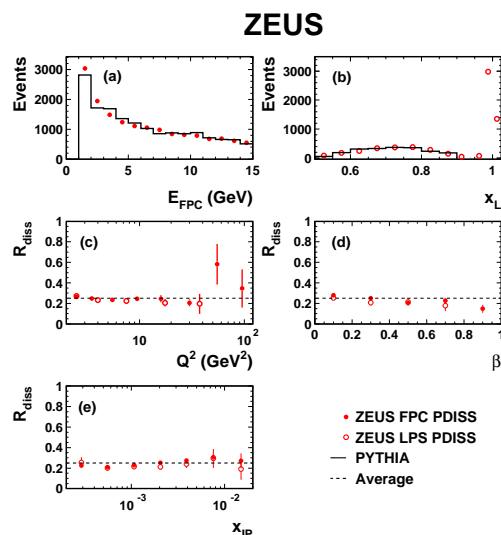


Fig. 2: (a) FPC energy and (b) LPS  $x_L$  distributions for ZEUS proton dissociation samples (see text), with data compared to the tuned PYTHIA model. (c-e) Extracted fractions of proton dissociation events in the ZEUS LRG sample as a function of  $Q^2$ ,  $\beta$  and  $x_{\mathbb{P}}$  after integration over the other variables [15].

study,  $25 \pm 1(\text{stat.}) \pm 3(\text{syst.})\%$  (figure 2). Unless stated otherwise, the ZEUS LRG data are corrected by this factor in the following and thus correspond exclusively to the truly proton-elastic process.

## 4.2 H1 LRG

The contribution from proton dissociation in the H1 LRG analysis is constrained through the DIFFVM MC [22] model, normalised using the response to large  $M_N$  events leaving signals in the forward and central detector components [8, 23].

The data are corrected using DIFFVM to  $M_N < 1.6$  GeV. The H1 LRG data are then compared with the H1 FPS measurement, in order to extract the proton dissociation cross section with  $M_N < 1.6$  GeV directly from the data. The ratio of the two measurements, after projection onto the  $Q^2$ ,  $x_{\mathbb{P}}$  and  $\beta$  axes, is shown in figure 4. There is no evidence for any dependence on any of the kinematic variables. as expected in the framework of proton vertex factorisation. The average value of the ratio is  $1.23 \pm 0.03$  (stat.)  $\pm 0.16$  (syst.), the largest uncertainty arising from the FPS efficiency. The result is in good agreement with the DIFFVM estimate of  $1.15^{+0.15}_{-0.08}$ . The data and DIFFVM ratios translate into proton dissociation background fractions of 19 % and 13 %, respectively, consistent within the uncertainties. The similarity between the proton dissociation fractions in the raw H1 and ZEUS LRG selections is to be expected given the similar forward detector acceptances of the two experiments.

## 4.3 ZEUS FPC

The proton dissociation treatment is also critical in the  $M_X$  method, where the diffractive contribution is separated from the non-diffractive component in a fit to the inclusive  $\ln M_X^2$  distribution. Proton dissociation events with sufficiently large  $M_N$  for dissociation products to reach the FPC and central detectors lead to a reconstructed  $M_X$  value which is larger than the actual photon dissociation mass. The resulting distortion of the  $\ln M_X^2$  distribution affects the diffractive contribution extracted in the fit if corrections are not made. According to the SANG MC model, the  $N$  system contaminates the  $M_X$  reconstruction for  $M_N > 2.3$  GeV on average [24], and events in this  $M_N$  range are therefore subtracted using SANG before the  $\ln M_X^2$  distribution is decomposed. The upper  $M_N$  cut in the SANG sample is defined by  $(M_N/W)^2 < 0.1$ , which leads to a variation of the subtracted fraction of events with  $W$ , the centre-of-mass energy of the photon-proton system. This contrasts with the LRG method, where MC studies confirm that the rapidity

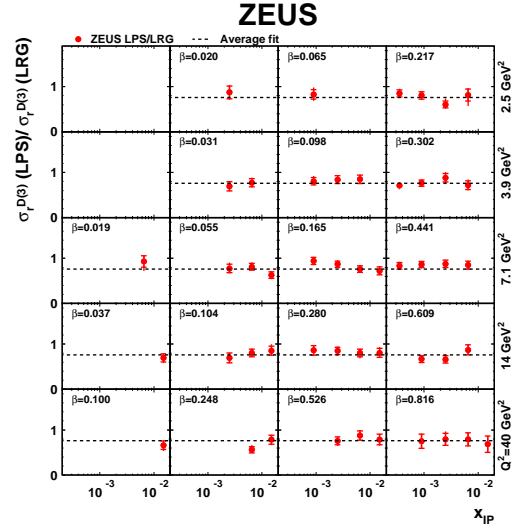


Fig. 3: The ratio of the ZEUS LPS measurement ( $M_N = m_p$ ) to the ZEUS LRG measurement before subtraction of proton dissociation background [15]. The lines represent the average value of this ratio. An overall normalisation uncertainty of  $^{+11}_{-8}\%$  is not included in the errors shown.

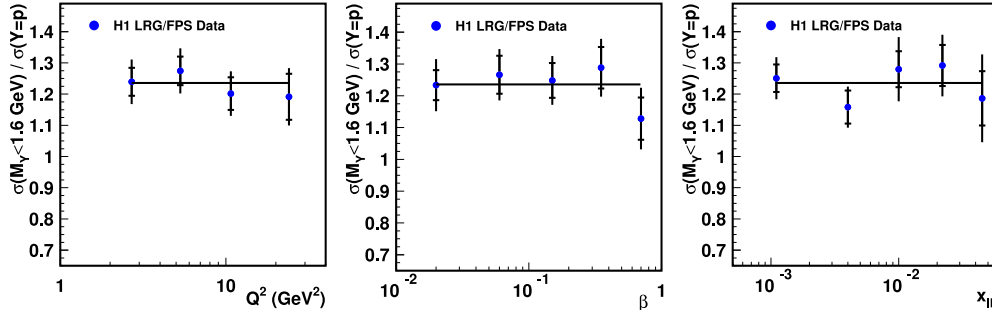


Fig. 4: The ratio of the H1 LRG measurement (corrected to  $M_N < 1.6$  GeV) to the H1 FPS measurement ( $M_N = m_p$ ), after integration over the variables not shown in each case [14]. The lines represent a fit to the data assuming no dependence on any of the variables. An overall normalisation uncertainty of 13% is not included in the errors shown.

gap requirement efficiently eliminates proton dissociation at large  $M_N$ , the remaining fractional low  $M_N$  contribution being independent of kinematics to good approximation (figures 3 and 4).

Despite these difficulties, there is acceptable agreement between the ZEUS FPC data and the ZEUS LRG measurement. A global fit comparing the normalisations of the two data sets (after correcting the LRG data to  $M_N = m_p$ ) yields a normalisation factor of  $0.83 \pm 0.04$  to be applied to the ZEUS FPC results. This factor is compatible with expectations for the residual proton dissociation contribution based on the MC studies in sections 4.1 and 4.2.

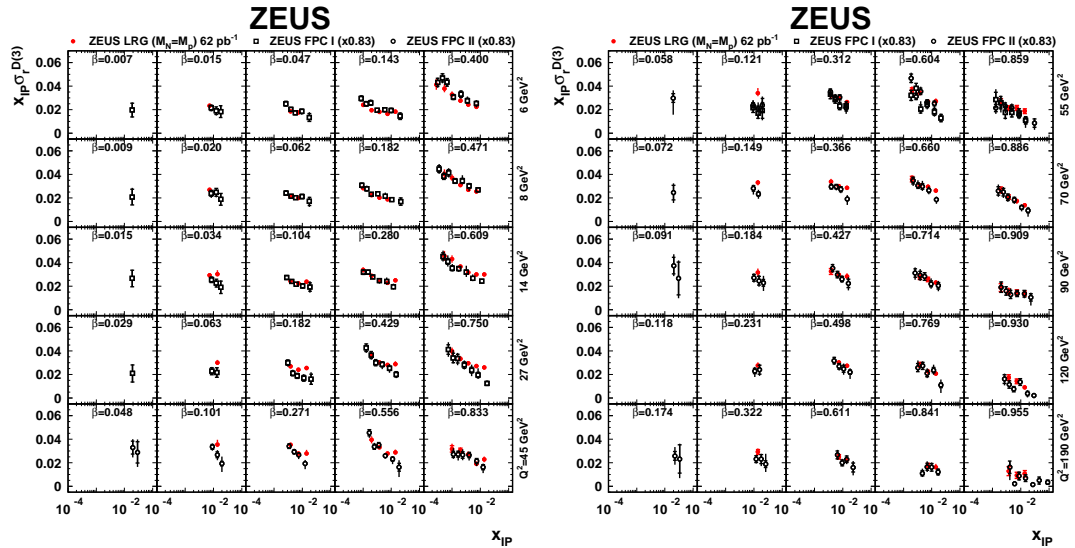


Fig. 5: Comparison between the ZEUS  $M_X$  method ('FPC I' and 'FPC II') and ZEUS LRG method data [15]. As explained in the text, the  $M_X$  method data are scaled by a constant factor of 0.83 to account for proton dissociation contributions with  $M_N < 2.3$  GeV.



## 5 Cross section comparisons

Due to their differing  $M_N$  coverages, the  $\sigma_r^{D(3)}$  measurements from the different data sets are not directly comparable. However, assuming the factorisation of the  $M_N$  dependence which is suggested in the data, varying the  $M_N$  range should introduce only global normalisation differences, which can be estimated using the proton dissociation simulations.

### 5.1 Comparison between LRG and $M_X$ methods

ZEUS cross section measurements obtained with the LRG and  $M_X$  methods are compared in figure 5. The LRG data are corrected to  $M_N = M_p$  as described in section 4.1 and the relative normalisation factor of 0.83 (section 4.3) is applied to the ZEUS FPC data to account for residual proton dissociation. The overall agreement between the two measurements is good, apart from some differences at large  $x_P \gtrsim 0.01$ . The  $Q^2$  dependence of the  $M_X$  method data is also slightly weaker than that of the LRG data.

### 5.2 Comparison between ZEUS LPS and H1 FPS measurements

The ZEUS LPS and H1 FPS data are compared in figure 6. For this comparison, the ZEUS results are extracted at the same  $\beta$  and  $Q^2$  values as H1 and are therefore not affected by extrapolation uncertainties. The shape agreement is satisfactory and the overall normalisation discrepancy of around 10% lies within the large combined normalisation uncertainty of around 14%.

### 5.3 Comparison between ZEUS and H1 LRG measurements

The ZEUS LRG data are extracted at the H1  $\beta$  and  $x_P$  values, but at different  $Q^2$  values. In order to match the  $M_N < 1.6$  GeV range of the H1 data, a global factor of  $0.91 \pm 0.07$ , estimated with PYTHIA, is applied to the ZEUS LRG data in place of the correction to an elastic proton cross section. After this procedure, the ZEUS data remain higher than those of H1 by 13% on average, as estimated with a global fit comparing the normalisations of the two data sets for  $Q^2 > 6$  GeV<sup>2</sup>. This normalisation discrepancy is similar to that between the H1 FPS and the ZEUS LPS data sets. It is in line with the errors due to the 8% uncertainty on the proton dissociation correction in the ZEUS LRG data and the 7% combined relative normalisation uncertainty between the two LRG data sets.

In figure 7, the ZEUS results are scaled by a factor  $0.91 \times 0.87$  (the factor 0.87 = 1 – 0.13 normalising the ZEUS to the H1 data) and compared with the H1 LRG measurement. An

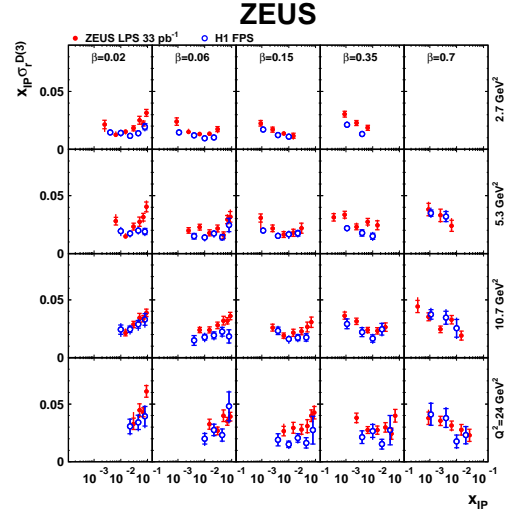


Fig. 6: Comparison between ZEUS LPS and H1 FPS measurements [15]. Normalisation uncertainties of  $\pm 10\%$  (H1) and  $+11\%$  (ZEUS) are not shown.

excellent agreement between the  $Q^2$  dependences is revealed throughout most of the phase space. There are small deviations between the  $\beta$  dependences of the two measurements at the highest and lowest  $\beta$  values. The results of the ‘H1 Fit B’ NLO QCD DPDF fit to the H1 LRG data [8] is also shown. It gives a good description of the data at large  $Q^2$ . However, the extrapolation beyond the fitted region ( $Q^2 \geq 8.5 \text{ GeV}^2$ ) undershoots the precise new ZEUS low  $Q^2$  LRG data, confirming the observation in [8] that a standard DGLAP fit to the lowest  $Q^2$  data is problematic.

## 6 A First Combination of Data Sets

For easy future consumption at the LHC and elsewhere, it is desirable to combine the various H1 and ZEUS diffractive DIS measurements into a single easily digestible HERA data set. Here we take the first steps towards this goal, by making a simple error-weighted average of the H1 and ZEUS LRG data sets, ignoring correlations between the data points due to the systematic errors. LPS and  $M_X$  method data are not considered at this stage. For the purpose of this exercise, the ZEUS normalisation is fixed to that of H1 as described in section 5.3 and shown in figure 7. The normalisation of the combined data thus has an uncertainty beyond the 10% level. Combinations can only meaningfully be made where there is basic agreement between the different measurements. Since this is not always the case at the lowest  $x_{\mathbb{P}}$  values, we restrict the averaging to the  $x_{\mathbb{P}} = 0.003$  and  $x_{\mathbb{P}} = 0.01$  data. The combinations are performed throughout the measured  $Q^2$  range, including the  $Q^2 < 8.5 \text{ GeV}^2$  region, beyond the range of the ‘H1 Fit B’ parameterisation which is compared with the data.

To account for the differences between the  $Q^2$  binning choices, H1 data points are adjusted to the ZEUS  $Q^2$  bin centres by applying small correction factors calculated using the ‘H1 Fit B’ parameterisation. Where both collaborations then have measurements at a given  $(Q^2, x_{\mathbb{P}}, \beta)$  point, a simple weighted average is taken, using the quadratic sum of statistical and systematic uncertainties for each experiment, excluding normalisation uncertainties.

The results of this averaging procedure are shown in figure 8. They are indicative of the sort of precision which is achievable through combinations, with many data points having errors at the 3 – 4% level, excluding the normalisation uncertainty. At  $x_{\mathbb{P}} = 0.01$  the combined data agree well with the ‘H1 Fit B’ DPDF results. At  $x_{\mathbb{P}} = 0.003$  the  $Q^2$  dependences are also in good agreement with the parameterisation in the  $\beta$  and  $Q^2$  region of the fit, with the exception of the highest  $\beta$  value, where the average is pulled towards the more precise ZEUS data.

More sophisticated averaging methods may be used in the future, for example that [25] developed to perform similar combinations of inclusive HERA data, with a full systematic error treatment. No attempt has yet been made to extract DPDFs from the combined data. Based on the combined  $\sigma_r^{D(3)}$  and its  $Q^2$  dependence shown here, no significant conflict is expected with the quark or gluon densities of ‘H1 Fit B’ in the bulk of the phase space. However, small modifications are likely to be necessary to the quark densities at small and large  $\beta$  values.

## 7 Summary

H1 and ZEUS diffractive DIS data obtained by various methods with very different systematics have been compared in detail. All measurements are broadly consistent in the shapes of the distributions. The comparisons between proton tagging and LRG method data internally to the



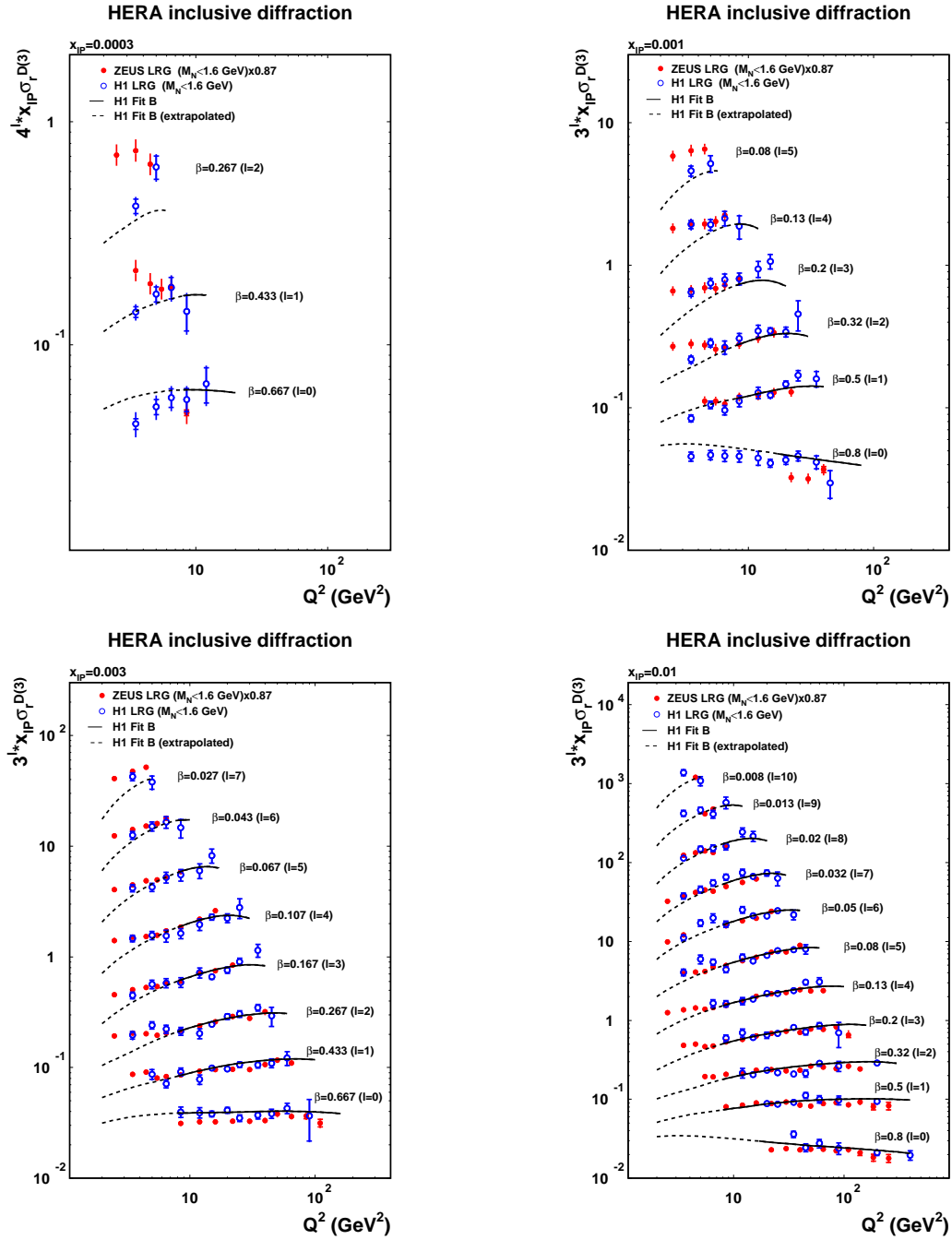


Fig. 7: Comparison between the H1 and ZEUS LRG measurements after correcting both data sets to  $M_N < 1.6$  GeV and applying a further scale factor of 0.87 (corresponding to the average normalisation difference) to the ZEUS data. The measurements are compared with the results of the 'H1 Fit B' DPDF extraction, which was based on the H1 data shown. Further H1 data at  $x_{\text{IP}} = 0.03$  are not shown.

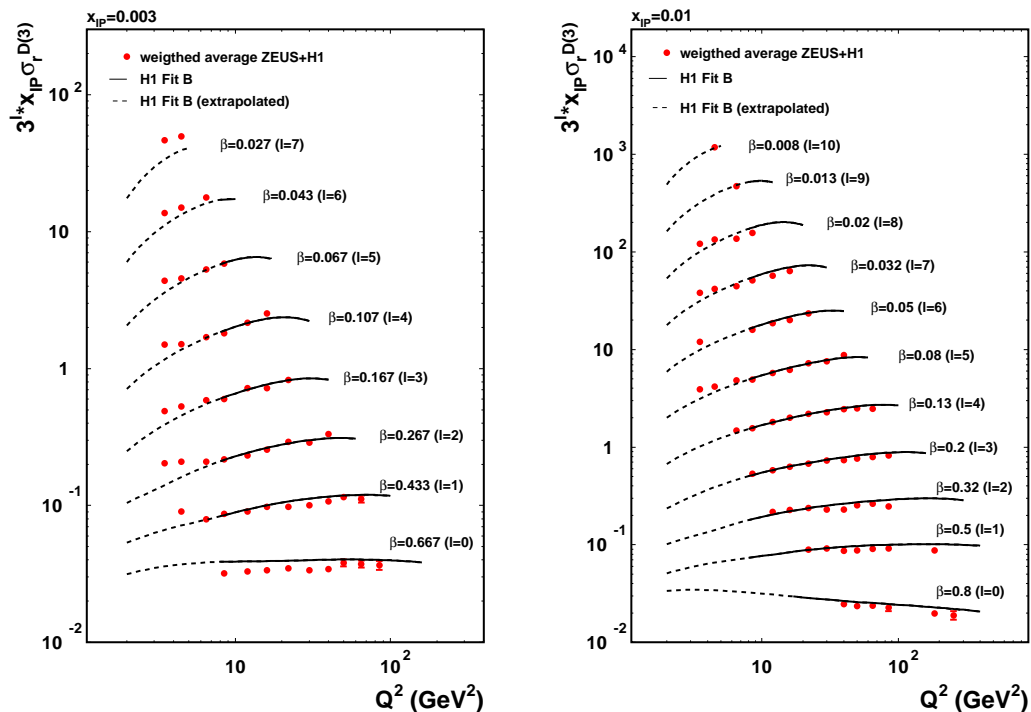


Fig. 8: Combination of the H1 and ZEUS LRG data following the procedure described in the text. The global normalisation is fixed to that of the H1 measurement, in order most easily to compare the data with the 'H1 Fit B' DPDF results.

two collaborations give compatible results on the proton dissociation contributions in the raw LRG selections. There is a global normalisation difference at the 13% level between the LRG measurements of the two experiments, which is a little beyond one standard deviation in the combined normalisation uncertainty. A similar difference is visible between the normalisations of the H1 and ZEUS proton tagged data.

A first step has been taken towards combining the two sets of LRG data, by arbitrarily fixing the normalisation to that of the H1 data set and ignoring correlations within the systematic uncertainties in obtaining weighted averages. The results hint at the precision which might be obtained in the future with a more complete procedure.

## References

- [1] ZEUS Collaboration, M. Derrick et al., Phys. Lett. **B 315**, 481 (1993).
- [2] H1 Collaboration, T. Ahmed et al., Nucl. Phys. **B 429**, 477 (1994).

- [3] P.D.B. Collins, *An Introduction to Regge Theory and High Energy Physics*. Cambridge University Press, Cambridge, 1977.
- [4] M. Arneodo and M. Diehl, Proceedings of the First HERA-LHC Workshop, eds. de Roeck, Jung, CERN-2005-014, hep-ph/0511047.
- [5] H1 Collaboration, C. Adloff et al., *Z. Phys. C* **76**, 613 (1997).
- [6] ZEUS Collaboration, S. Chekanov et al., *Eur. Phys. J. C* **38**, 43 (2004).
- [7] A. Martin, M. Ryskin, G. Watt, *Eur. Phys. J. C* **44**, 69 (2005).
- [8] H1 Collaboration, A. Aktas et al., *Eur. Phys. J. C* **48**, 715 (2006).
- [9] H1 Collaboration, A. Aktas et al., *JHEP* 0710:042 (2007).
- [10] FP420 R&D Collaboration, hep-ex/0806.0302 (2008).
- [11] ZEUS Collaboration, J. Breitweg et al., *Eur. Phys. J. C* **1**, 81 (1997).
- [12] H1 Collaboration, C. Adloff et al., *Eur. Phys. J. C* **6**, 587 (1999).
- [13] ZEUS Collaboration, S. Chekanov et al., *Eur. Phys. J. C* **25**, 169 (2002).
- [14] H1 Collaboration, A. Aktas et al., *Eur. Phys. J. C* **48**, 749 (2006).
- [15] ZEUS Collaboration, S. Chekanov et al., DESY 08-175, submitted to *Nucl. Phys. B*.
- [16] H1 Collaboration, H1prelim-06-014 (presented at DIS2006, E. Sauvan).
- [17] ZEUS Collaboration, S. Chekanov et al., *Eur. Phys. J. C* **25**, 69 (2002).
- [18] ZEUS Collaboration, S. Chekanov et al., *Nucl. Phys. B* **713**, 3 (2005).
- [19] ZEUS Collaboration, S. Chekanov et al., *Nucl. Phys. B* **800**, 1 (2008).
- [20] T. Sjöstrand, L. Lönnblad and S. Mrenna, hep-ph/0108264 (2001).
- [21] H. Jung, *Comput. Phys. Commun.* **86**, 147 (1995).
- [22] B. List and A. Mastroberardino, Proceedings of the Workshop on MC Generators for HERA Physics, p. 396 (1999).
- [23] C. Johnson, *Ph.D. Thesis, University of Birmingham*. 2002.
- [24] H. Lim, *Ph.D. Thesis, The Graduate School, Kyungpook National University, Taegu (Republic of Korea)*. Unpublished, 2002.
- [25] A. Glazov, Proceedings of DIS 2005, Madison, USA, eds Smith, Dasu, (AIP 2005).

# Diffraction Final States and Factorisation at HERA

W. Słomiński<sup>a</sup> and Alice Valkárová<sup>b</sup>

<sup>a</sup>M. Smoluchowski Institute of Physics, Jagellonian University, Kraków,

<sup>b</sup>Institute of Particle and Nuclear Physics, Faculty of Mathematics and Physics, Charles University, Praha

## Abstract

The recent experimental data from the H1 and ZEUS collaborations at HERA collider for diffractive dijet production and open charm production in deep inelastic scattering and photoproduction are presented and compared to next-to-leading order (NLO) QCD predictions. While good agreement is found for dijets in DIS and open charm production ( $D^*$ ) in both DIS and photoproduction, the dijet photoproduction data for jets with low transverse energy  $E_T$  of the leading jet are clearly overestimated by NLO predictions. The indication of the dependence of the suppression factor on  $E_T$  was found. Within large errors the same amount of suppression was observed in both direct and resolved enhanced regions.

## 1 Factorisation and diffractive parton distribution functions

Diffractive electron-proton interactions studied with the HERA collider allow us to investigate the proton diffractive structure. In this type of interactions the proton remains intact or dissociates into a low-mass state, while the photon dissociates into a hadronic state  $X$ ,  $\gamma^* p \rightarrow X p'$ . The final proton  $p'$  and the hadronic state  $X$  are separated by a large rapidity gap (LRG).<sup>1</sup> The diffractive exchange (Pomeron), with the vacuum quantum numbers, carries away a fraction  $x_P$  of the initial proton longitudinal momentum and has virtuality  $t = (p - p')^2$ . The Regge phenomenology tells us that for small  $|t|$  the diffractive cross section drops exponentially with  $t$  which allows us to integrate over  $t$  to cope with experimental setup when the final proton is not tagged.

The actual beam particles are electrons or positrons which emit photons in a wide range of virtualities  $Q^2$ . In general, the cross sections depend on both the proton and the photon structure.

For a highly virtual photon, *i.e.* the one we can consider point-like, the factorisation theorem holds [2], stating that the cross section is given in terms of the universal diffractive parton distributions (DPDFs) and hard partonic cross sections. A generic formula reads

$$\frac{d\sigma^{\gamma^* p}}{dx_P d\beta dQ^2} \propto \sum_{k=g,q,\bar{q}} f_k^{D(3)}(x_P, Q^2) \otimes \hat{\sigma}^{\gamma^* k}, \quad (1)$$

where  $\otimes$  denotes the convolution and DPDFs  $f_k^{D(3)}(x_P, z, Q^2)$  are integrated over  $t$ . In the leading log (LO) approximation Eq. (1) simplifies to

$$\frac{d\sigma^{\gamma^* p}}{dx_P d\beta dQ^2} \propto \sum_q e_q^2 f_q^{D(3)}(x_P, \beta, Q^2), \quad (2)$$

---

<sup>1</sup>For the definition of kinematics and variables see *e.g.* G. Watt's talk [1].

yielding the parton-model interpretation of  $\beta$  being fractional momentum of the quark struck by  $\gamma^*$ .

The factorisation (1) holds for the inclusive as well as non-inclusive processes provided  $Q^2$  is high enough for the photon to remain point-like and for the higher twist corrections to be neglected. Applied to the inclusive diffractive DIS it allows us to extract the proton DPDFs from the data. Both H1 and ZEUS collaborations performed such fits, assuming the Regge factorisation for DPDFs [3],

$$f_k^{D(3)}(x_P, z, Q^2) = f_P(x_P) f_k^P(z, Q^2) \quad (3)$$

with the Pomeron flux  $f_P(x_P)$  taken from the Regge phenomenology. In actual fits a small contribution from a secondary Reggeon was also taken into account — for details see [4–7].

A more elaborate approach not assuming Regge factorisation and taking into account higher twists and perturbative Pomeron contributions is discussed in [1, 8].

With DPDFs at hand, we can study some semi-inclusive processes. The topics summarized in the following include dijet and open charm ( $D^*$ ) production in both DIS and photoproduction (PHP) regimes. As already stated, if factorisation is not spoiled by higher twist contributions, it should work equally well for the above mentioned processes in the DIS regime. Thus one can extract the DPDFs from inclusive data only and use them to predict the dijet and  $D^*$  production cross sections. Comparison to the data provides us with the information on the quality of the fit and pQCD calculations. Another approach is to use inclusive as well as dijet and/or charm production data to extract DPDFs. The reason for using the semi-inclusive data is that the inclusive DIS is known to be mainly sensitive to the quark content of the proton, *cf.* (2). Gluons enter the cross section only via scaling violations and higher order QCD corrections, resulting in a quite high uncertainty in the extracted  $f_g$  [6]. Both dijet and charm production are directly sensitive to  $f_g$  and can be used to better establish the diffractive gluon distribution. A combined fit using inclusive and dijet data is discussed in detail in [7, 9–11], while the one using inclusive and  $D^*$  production data is presented in [5].

The photoproduction regime is qualitatively different. Here the photon is (nearly) real and reveals its hadronic structure. The  $\gamma p$  interaction has components analogous to the hadron-hadron scattering, at LO ascribed to the ‘resolved’ photon. In this case there is no theoretical reason for the factorisation and experimentally it is known to be badly broken in the  $p\bar{p}$  diffractive dijet production [12]. This factorisation breaking is phenomenologically understood in terms of the rescattering (screening) effects [13, 14], which lead to a suppression of the cross section calculated assuming that both proton and photon PDFs factorise.

In order to investigate the amount of this suppression the NLO QCD calculations using factorisation assumption are confronted with the experimental results. In general the observed suppression is much smaller than in the  $p\bar{p}$  case, which qualitatively agrees with theoretical expectations [13, 14]. For a small suppression (up to ca. 50%, as observed at HERA) the accuracy of theoretical predictions becomes an important factor. The actual uncertainties can easily reach the order of the measured effect.

The uncertainty inherent in the perturbative QCD calculations, is the amount of higher order contributions. A common method to qualify it, is to look at the renormalisation/factorisation

scale dependence (there should be none in the complete result). As shown in the figures below this scale dependence is strong, telling us that the higher order corrections are important<sup>2</sup>. The only way to resolve this issue is to go to higher pQCD orders (NNLO,...). There are, however, other uncertainties which are not shown in the plots. Let us discuss them briefly.

The fits to the inclusive DIS data are performed using the Fixed Flavour Number Scheme (FFNS) with three massless quarks and heavy charm and bottom treated as massive particles, not partons. On the contrary, the NLO calculations of the dijet production cross section take all flavours massless, as in the Variable Flavour Number Scheme. The both flavour schemes differ in the heavy quarks treatment and in the amount of gluons.

Gluon content of the Pomeron is poorly established by a fit to the inclusive DIS data only and both dijet and open charm production are very sensitive to gluons. In photoproduction about 80% of the cross section comes from  $\gamma g$  subprocesses [15]. This ambiguity is, of course, smaller in the case of combined fits [5, 9].

All the above mentioned uncertainties, present in the assumed model of Regge factorisation and non-perturbative Pomeron, should be kept in mind when looking at experimental data compared to the NLO QCD predictions.

For a discussion on theoretical aspects of diffractive dijet photoproduction see the contribution of M. Klasen and G. Kramer to these proceedings.

## 2 Diffractive Dijet Production

Diffractive dijet production in DIS was analysed by both H1 and ZEUS collaborations in [9, 16, 17] and presented in [10, 11, 15, 18–20]. The data was taken during the HERA running periods 1996/97 and 1999/00. The kinematic range of the photon virtuality was  $4 < Q^2 < 80 \text{ GeV}^2$  (H1) and  $5 < Q^2 < 100 \text{ GeV}^2$  (ZEUS). The photon-proton CMS energy  $W$  was above 100 GeV. Diffractive events were selected with the help of criteria of large rapidity gap (LRG) and the jets were identified using the longitudinally invariant inclusive  $k_T$  cluster algorithm [21] in the Breit frame. The transverse energies for leading and subleading jets were required to be  $E_{T1}^* > 5 \text{ GeV}$  ( $E_{T1}^* > 5.5 \text{ GeV}$  in [9]) and  $E_{T2}^* > 4 \text{ GeV}$ .

The experimental results are compared to the NLO predictions obtained with the DISENT [22] and NLOJET++ [23] codes using several DPDFs. The cross sections vs.  $x_{\mathbb{P}}$  and  $E_{T1}^*$  depicted in Figure 1, show that the NLO predictions agree within errors with the data. We can conclude that the QCD factorisation for diffractive dijets holds as expected. Note, however, that the ZEUS data tend to lie about (10–20)% below the NLO predictions.

The diffractive photoproduction (DPHP) of dijets was analysed by both H1 [16] and ZEUS [24] collaborations. The H1 experiment analysed the data with tagged electron in the running period 1996/97. The kinematic region was taken the same as for the DIS dijets (except  $Q^2 < 0.01 \text{ GeV}^2$ ) with the purpose to study the double ratio of photoproduction/DIS cross sections. The ZEUS analysis of dijets in DPHP covers somewhat different kinematic region, main difference being higher transverse energies of leading and subleading jets satisfying  $E_{T1} > 7.5 \text{ GeV}$ ,  $E_{T2} > 6.5 \text{ GeV}$ . In both experiments the jets were identified using

---

<sup>2</sup>Note that very small or no scale dependence is not a proof that the result is correct.

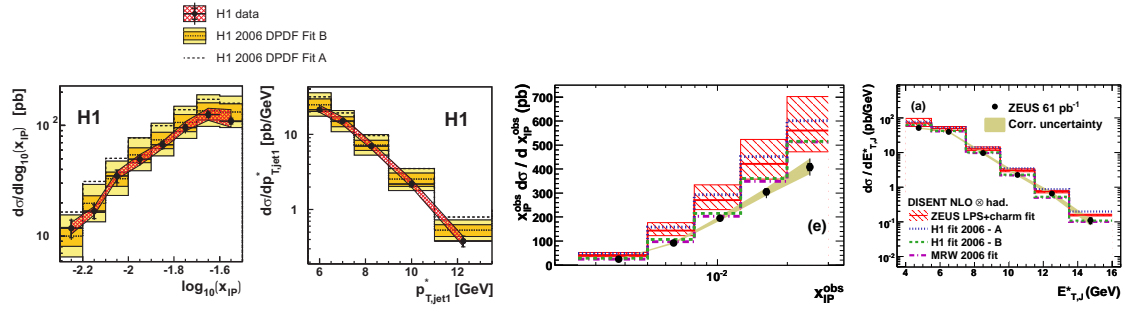


Fig. 1: Differential cross section for the diffractive production of dijets vs.  $x_{IP}$  and  $E_{T1}^*$  as measured by H1 [9] (two left plots) and ZEUS [17] (two right plots). NLO predictions for several DPDFs parametrizations are also shown. The shaded bands show the uncertainty resulting from the variation of renormalization scale by factors 1/2 and 2.

the inclusive  $k_T$  cluster algorithm in the laboratory frame. For detailed discussion of the results see [10, 11, 15, 18, 19].

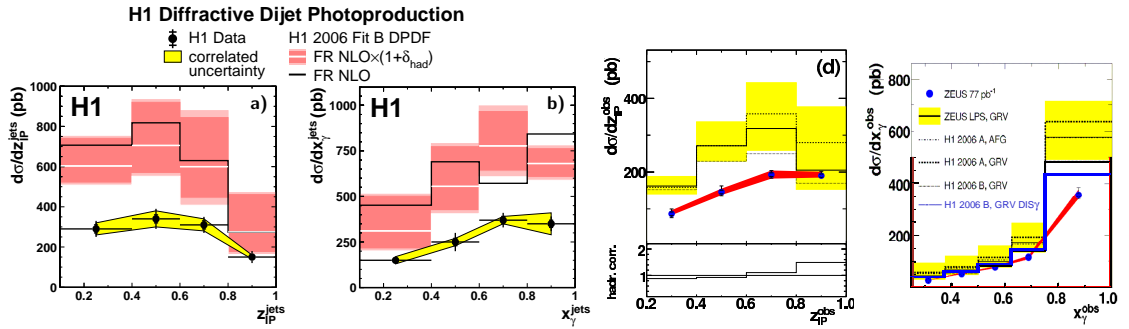


Fig. 2: Differential cross section for the diffractive photoproduction of dijets vs.  $z_{IP}$  and  $x_{\gamma}$  as measured by H1 [16] (two left plots) and ZEUS [24] (two right plots). NLO predictions for several DPDFs parametrizations are also shown. The shaded bands show the uncertainty resulting from the variation of renormalization scale by factors 1/2 and 2.

The cross sections vs.  $z_{IP}$  and  $x_{\gamma}$  are shown in Figure 2. The NLO QCD predictions were obtained using several DPDFs and photon PDFs parametrizations, and with two independent computer codes, one by Frixione and Ridolfi [25] and the other by Klasen and Kramer [26]. It was checked that both codes give the same results.

The H1 experiment observes a global suppression of NLO QCD predictions by factor 0.5. The ZEUS data are compatible with no suppression — the level of agreement with the NLO predictions is similar to the DIS case. However, 10–20% suppression is not excluded. Both experiments observe that the approach when only resolved photon part of the cross section is suppressed ( $x_{\gamma} \lesssim 0.8$ ) is clearly disfavoured by data in contradiction with theoretical expectation of [14].

The difference between kinematic regions of both experiments lead us to a hypothesis that the suppression may depend on the  $E_T$  range of the jets [27]. Indeed, the cross section double ratio of data and NLO prediction for the diffractive PHP and DIS as a function of transverse

momentum  $E_T$  of the leading jet measured by H1, and the ratio of the ZEUS data cross section over the NLO predictions, indicate the rise with increasing  $E_T$ , as shown in Figure 3<sup>3</sup>.

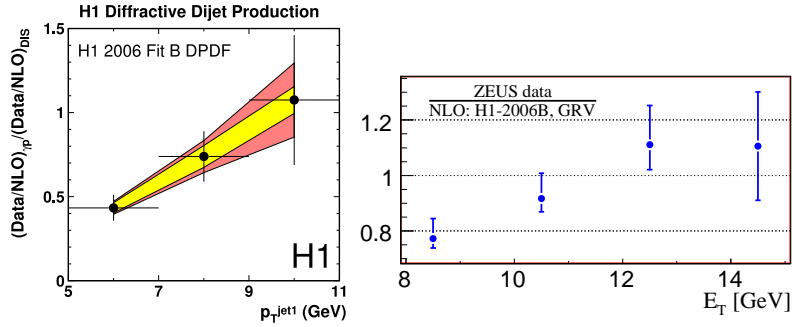


Fig. 3: Cross section double ratio of data to NLO prediction for photoproduction and DIS as a function of transverse momentum of the leading jet measured by H1 (left plot) and cross section ratio of data and NLO for the diffractive photoproduction of dijets vs.  $E_T$  of the leading jet as measured by ZEUS (right plot).

A detailed study of this issue was performed in the new H1 analysis of dijets in photoproduction [28]. The study was performed in two cut schemes. The first one identical to [16] with  $E_{T1} > 5$  GeV, to crosscheck results of previous analysis. The second one with all cuts as close as possible to the cuts used by ZEUS [24],  $E_{T1} > 7.5$  GeV, to check for a possible dependence of suppression on  $E_T$  of the jets. The results were compared to NLO calculations using three H1 DPDFs — fits A,B and Jets. The best agreement of the shapes of measured cross sections was obtained with NLO predictions using fit B and scaled by factor 0.53 for low  $E_T$  cut scenario, and by factor 0.61 for high  $E_T$  cut scenario [28].

This measurement of the suppression factor together with the ZEUS results of 0.8–1 factor seem to support the idea of the  $E_T$ -dependent suppression.

As in the previous analyses no dependence of suppression on measured  $x_\gamma$  was observed, indicating that there is no evidence for the suppression of the resolved part only.

### 3 Open charm production in diffraction

Another semi-inclusive process analysed at HERA is the diffractive production of open charm observed in the reactions with  $D^*$  mesons production. Both DIS and PHP regimes have been studied and discussed during the workshop [18–20, 29, 30].

If QCD factorisation is fulfilled, NLO QCD calculations based on DPDFs measured in inclusive processes should be able to predict the production rates of such processes in shape and normalization.

The data from the HERA running period 1998–2000 were analysed by both H1 [31] and ZEUS [32] collaborations. The charm quark was tagged by the reconstruction of  $D^{*\pm}(2010)$  meson in diffractive DIS and PHP regimes. H1 used also another method — based on the measurement of the displacement of tracks from primary vertex — to identify the  $D^*$  production in the sample of DIS events only.

<sup>3</sup>left plot derived from [16], thanks to S.Schaetzel



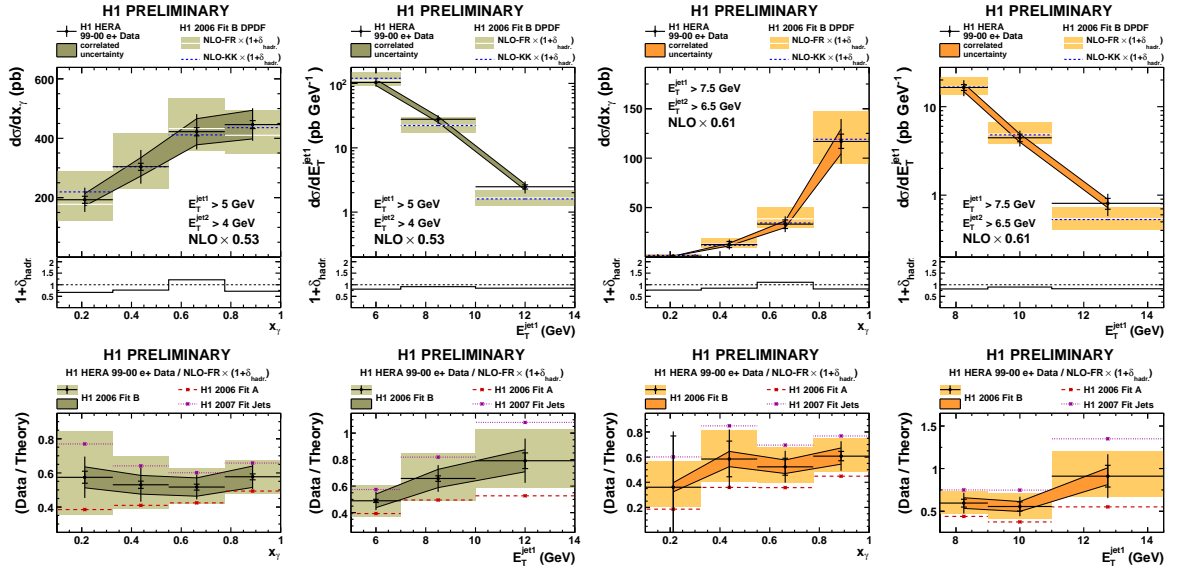


Fig. 4: Differential cross section for the diffractive photoproduction of dijets as a function of  $x_T$  and  $E_{T1}$  for the lower  $E_T$  cut scenario (two left plots) and for the higher  $E_T$  cut scenario (two right plots), compared to NLO scaled calculations (upper plots). The lower plots show the corresponding ratios of the data to NLO calculated cross sections.

The measurements were compared to the NLO QCD predictions using DPDFs from H1 and ZEUS fits. The calculations were performed using HVQDIS [33] for DIS and FMNR [34] for PHP. In Figure 5 the H1 results for the cross sections vs.  $x_P$  and  $z_P$  are shown. The recent ZEUS results for the diffractive  $D^{*\pm}(2010)$  photoproduction are presented in Figure 6.

Within large errors a good agreement is observed, which supports the validity of QCD factorisation in both diffractive DIS and PHP. In particular no sizable suppression of the open charm photoproduction is seen, in contrast to the diffractive dijet case. A plausible explanation of this difference is that the resolved photon contribution to the  $D^*$  production is ca. 10% as compared to about 50% for the dijet diffractive PHP.

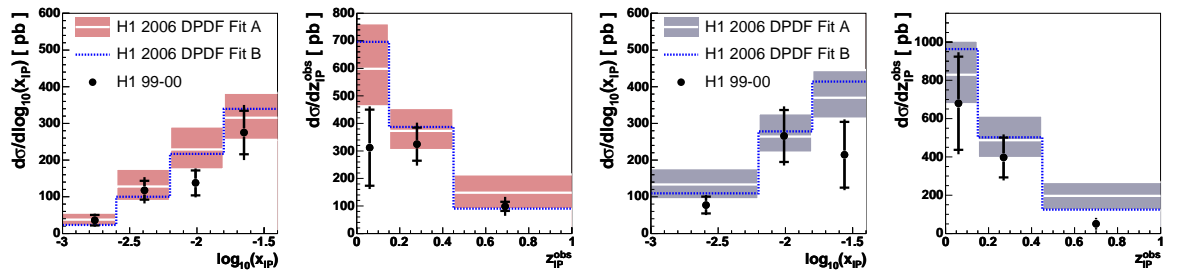


Fig. 5: Differential cross sections for diffractive  $D^*$  meson production as a function of  $x_P$  and  $z_P$  in DIS (two left plots) and photoproduction (two right plots).

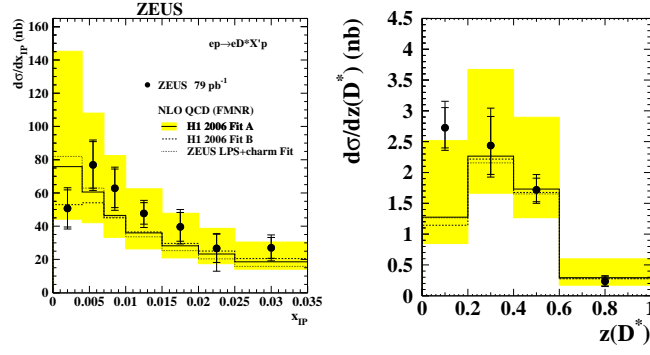


Fig. 6: Differential cross section for the diffractive photoproduction of  $D^{*\pm}(2010)$  as a function of  $x_P$  and  $z(D^*)$  compared to NLO predictions.

## 4 Summary

The factorisation issues were analyzed by H1 and ZEUS experiments studying the production of dijets and open charm in diffractive DIS and photoproduction. The factorisation was found to hold in the case of  $D^*$  production and dijet production in DIS. In dijet photoproduction factorisation breaking was observed. The indication was found that the suppression of the dijet photoproduction depends on the transverse momentum  $E_T$  of the leading jet. On the other hand, no dependence on measured  $x_\gamma$  was observed indicating the same order of suppression in the direct and resolved enhanced regions.

## References

- [1] G. Watt, *Theoretical uncertainties in diffractive parton densities*, in *2nd HERA and the LHC workshop*. 2006, available on <http://indico.cern.ch/conferenceDisplay.py?confId=1862>.
- [2] J.C. Collins, Phys. Rev. **D57**, 3051 (1998). Erratum: *ibid.* **D61**, 019902 (2000).
- [3] G. Ingelman and P.E. Schlein, Phys. Lett. **B152**, 256 (1985).
- [4] H1 Coll., A. Aktas et al., Eur. Phys. J. **C48**, 715 (2006).
- [5] ZEUS Coll., S. Chekanov et al., Eur. Phys. J. **C38**, 43 (2004).
- [6] P. Newman, *H1 2006 diffractive parton densities*, in *3rd HERA and the LHC workshop*. 2007, available on <http://indico.cern.ch/conferenceDisplay.py?confId=11784>.
- [7] M. Ruspa, *Inclusive diffraction in DIS*, in *4th HERA and the LHC workshop*. 2008, available on <http://indico.cern.ch/conferenceDisplay.py?confId=27458>.
- [8] A.D. Martin, M.G. Ryskin and G. Watt, Eur. Phys. J. **C37**, 285 (2004).

- [9] H1 Coll., A. Aktas et al., JHEP **10**, 042 (2007).
- [10] M. Mozer, *Recent H1 results on jet production in diffractive DIS and photoproduction*, in *3rd HERA and the LHC workshop*. 2007, available on <http://indico.cern.ch/conferenceDisplay.py?confId=11784>.
- [11] A. Valkarova, *Diffractive dijets at HERA*, in *4th HERA and the LHC workshop*. 2008, available on <http://indico.cern.ch/conferenceDisplay.py?confId=27458>.
- [12] CDF Coll., A.A. Affolder et al., Phys. Rev. Lett. **84**, 5043 (2000).
- [13] A. Bialas, Acta Phys. Polon. **B33**, 2635 (2002).
- [14] A.B. Kaidalov, V.A. Khoze, A.D. Martin and M.G. Ryskin, Phys. Lett. **B567**, 61 (2003).
- [15] W. Slominski, *Dijets in diffractive DIS and photoproduction*, in *XVI International Workshop on Deep Inelastic Scattering, DIS 2008*. April 2008, London, available on <http://indico.cern.ch/conferenceDisplay.py?confId=24657>. To be published in proceedings.
- [16] H1 Coll., A. Aktas et al., Eur. Phys. J. **C51**, 549 (2007).
- [17] ZEUS Coll., S. Chekanov et al., Eur. Phys. J. **C52**, 813 (2007).
- [18] A. Bonato, *Diffractive final states at ZEUS*, in *2nd HERA and the LHC workshop*. 2006, available on <http://indico.cern.ch/conferenceDisplay.py?confId=1862>.
- [19] R. Wolf, *Diffractive jets, charm and factorisation tests at H1*, in *2nd HERA and the LHC workshop*. 2006, available on <http://indico.cern.ch/conferenceDisplay.py?confId=1862>.
- [20] I.-A. Melzer-Pellmann, *Diffractive dijet and  $D^*$  production at ZEUS*, in *3rd HERA and the LHC workshop*. 2007, available on <http://indico.cern.ch/conferenceDisplay.py?confId=11784>.
- [21] S.D. Ellis and D.E. Soper, Phys. Rev. **D48**, 3160 (1993).
- [22] S. Catani and M.H. Seymour, Nucl. Phys. **B485**, 291 (1997). Erratum: *ibid.* **B510**, 503 (1998).
- [23] Z. Nagy and Z. Trocsanyi, Phys. Rev. Lett. **87**, 082001 (2001).
- [24] ZEUS Coll., S. Chekanov et al., Eur. Phys. J. **C55**, 177 (2008).
- [25] S. Frixione, Z. Kunszt and A. Signer, Nucl. Phys. **B467**, 399 (1996).
- [26] M. Klasen and G. Kramer, Eur. Phys. J. **C38**, 93 (2004).

- [27] Y. Yamazaki, *Dijet production in diffractive DIS and photoproduction at ZEUS*, in *XV International Workshop on Deep Inelastic Scattering, DIS 2007*. 2007.  
Doi:10.3360/dis.2007.112.
- [28] K. Cerny, *Dijets in diffractive photoproduction*, in *XVI International Workshop on Deep Inelastic Scattering, DIS 2008*. April 2008, London, available on  
<http://indico.cern.ch/conferenceDisplay.py?confId=24657>. To be published in proceedings.
- [29] R. Wolf, *Diffractive open charm production at HERA*, in *3rd HERA and the LHC workshop*. 2007, available on  
<http://indico.cern.ch/conferenceDisplay.py?confId=11784>.
- [30] A.W. Jung, *D\* production in DIS and photoproduction at H1*, in *4th HERA and the LHC workshop*. 2008, available on  
<http://indico.cern.ch/conferenceDisplay.py?confId=27458>.
- [31] H1 Coll., A. Aktas et al., *Eur. Phys. J.* **C50**, 1 (2007).
- [32] ZEUS Coll., S. Chekanov et al., *Nucl. Phys.* **B672**, 3 (2003);  
ZEUS Coll., S. Chekanov et al., *Eur. Phys. J.* **C51**, 301 (2007).
- [33] B.W. Harris and J. Smith, *Nucl. Phys.* **B452**, 109 (1995);  
L. Alvero, J.C. Collins and J.J. Whitmore, *Tests of factorization in diffractive charm production and double pomeron exchange*. Preprint hep-ph/9806340, 1998.
- [34] S. Frixione, M.L. Mangano, P. Nason and G. Ridolfi, *Phys. Lett.* **B348**, 633 (1995);  
S. Frixione, P. Nason and G. Ridolfi, *Nucl. Phys.* **B454**, 3 (1995).

# Leading Baryon Production at HERA

William B. Schmidke<sup>1</sup> and Armen Bunyatyan<sup>2</sup> (on behalf of the H1 and ZEUS collaborations)

<sup>1</sup>MPI, Munich, <sup>2</sup>MPI, Heidelberg and Yerevan Physics Institute, Yerevan, Armenia

## Abstract

Data from leading baryon production at HERA are presented and compared to models. Standard string fragmentation models alone do not describe the data; models including also baryon production via virtual meson exchange give a good description of the data. Exchange models accounting for absorption describe the  $Q^2$  evolution of the data. In the exchange picture, leading neutron data are used to extract the pion structure function.

## 1 Introduction

Events with a baryon carrying a large fraction of the proton beam energy have been observed in  $ep$  scattering at HERA [1]. The dynamical mechanisms for their production are not completely understood. They may be the result of hadronization of the proton remnant, conserving baryon number in the final state. Exchange of virtual particles is also expected to contribute. In this picture, the target proton fluctuates into a virtual meson-baryon state. The virtual meson scatters with the projectile lepton, leaving the fast forward baryon in the final state. Leading neutron (LN) production occurs through the exchange of isovector particles, notably the  $\pi^+$  meson. For leading proton (LP) production isoscalar exchange also contributes, including diffraction mediated by Pomeron exchange. In the exchange picture, the cross section for some process in  $ep$  scattering with e.g. LN production factorizes:

$$\sigma_{ep \rightarrow enX} = f_{\pi/p}(x_L, t) \cdot \sigma_{e\pi \rightarrow eX}.$$

Here  $f_{\pi/p}$  is the flux of virtual pions in the proton,  $x_L = E_n/E_p$  is the fraction of the proton beam energy carried by the neutron, and  $t$  is the virtuality of the exchanged pion.

The H1 and ZEUS experiments at HERA measured leading baryons in deep inelastic scattering and photoproduction events. Leading protons were measured with position sensitive detectors placed along the proton beam downstream of the interaction point. Leading neutrons were measured with lead-scintillator calorimeters at the zero-degree point after the proton beam was bent vertically; magnet apertures limited neutron detection to scattering angles less than 0.75 mrad.

## 2 Leading neutron production and models

Figure 1 shows the LN  $x_L$  distribution (left) and  $p_T^2$  distributions in bins of  $x_L$  (right). The  $x_L$  distribution rises from lowest  $x_L$  because of the increasing  $p_T^2$  range due to the angle limit, and then falls to zero at the kinematic limit  $x_L = 1$ . The  $p_T^2$  distributions are well described by exponentials; thus the parameterization  $d^2\sigma/dx_L dp_T^2 \propto a(x_L) \exp(-b(x_L)p_T^2)$  fully characterizes the two dimensional distribution.

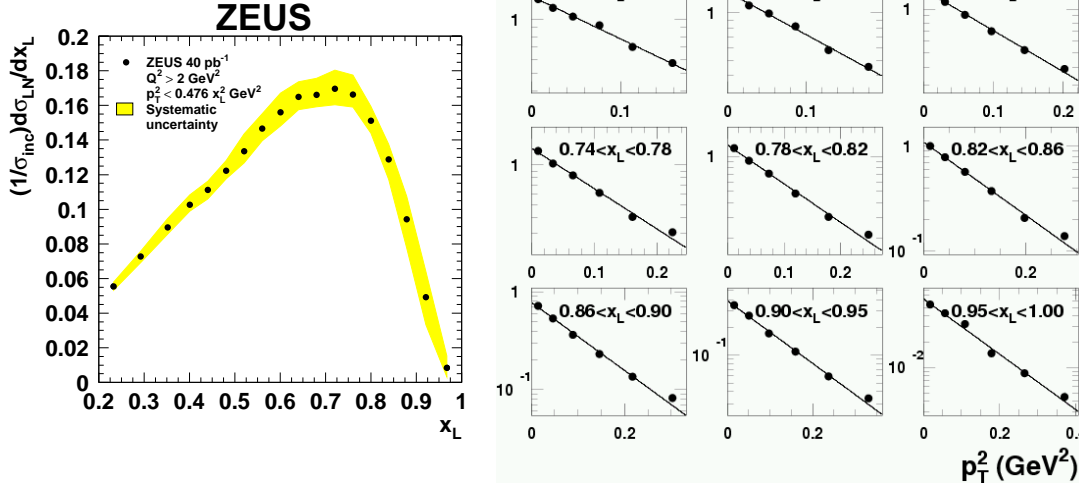


Fig. 1: Left: LN  $x_L$  distribution. Right: LN  $p_T^2$  distributions in bins of  $x_L$ . The lines are the result of exponential fits.

The left side of Fig. 2 shows the LN  $x_L$ , intercept  $a$  and slope  $b$  distributions compared to several models. The standard fragmentation models implemented in RAPGAP and LEPTO do not describe the data, predicting too few neutrons, concentrated at lower  $x_L$ , and slopes too small and independent of  $x_L$ . The LEPTO model with soft color interactions gives a fair description of the  $x_L$  distribution and overall rate, but also fails to describe the slopes. The RAPGAP model mixing standard fragmentation and pion exchange gives a better description of the shape of the  $x_L$  distribution, and also predicts the rise of the slopes with  $x_L$ , although both with too high values. The right side of Fig. 2 shows the  $x_L$  distribution with an optimized mixture of standard fragmentation and pion exchange; the agreement with the data is very good.

### 3 Leading proton production and models

Figure 3 shows the  $x_L$  distribution for leading protons and neutrons in the same  $p_T$  range. If LP production proceeded only through isovector exchange, as LN production must, there should be half as many LP and LN. The data instead has approximately twice as many LP as LN. Thus, exchanges of particles with different isospins such as isoscalars must be invoked for LP production.

The left side of Fig. 4 shows a comparison of the LP  $x_L$  distributions and  $p_T^2$  exponential slopes  $b$  to the DJANGO and RAPGAP Monte Carlo models incorporating standard fragmentation or soft color interactions, none of which describe the data. The right side of Fig. 4 shows a comparison to a model including exchange of both isovector and isoscalar particles, including the Pomeron for diffraction [2]. These exchanges combine to give a good description of the  $x_L$  distribution and slopes.

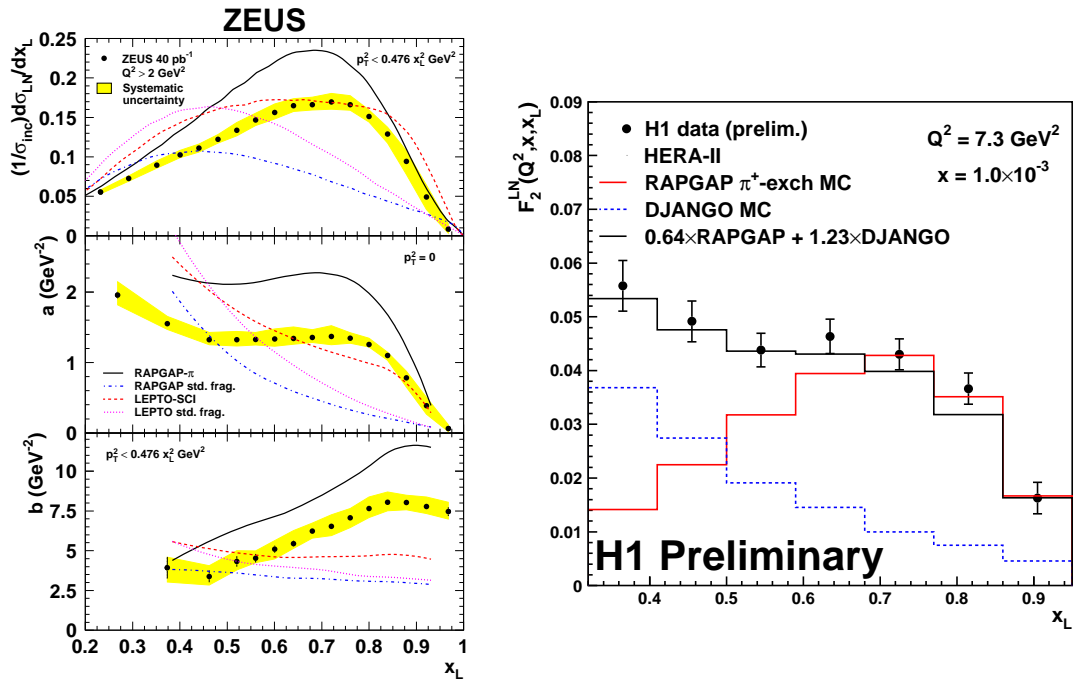


Fig. 2: Left: LN  $x_L$  intercept and slope distributions compared to models. Right: LN  $x_L$  distribution with an optimized mixture of exchange and fragmentation models.

#### 4 Absorption of leading neutrons

The evidence for particle exchange in leading baryon production motivates further investigation of the model. One refinement of the simple picture described in the introduction is absorption, or rescattering [3]. In this process, the virtual baryon also scatters with the projectile lepton. The baryon may migrate to lower  $x_L$  or higher  $p_T$  such that it is outside of the detector acceptance, resulting in a relative depletion of observed forward baryons. The probability of this should increase with the size of the exchanged photon. The size of the photon is inversely related to its virtuality  $Q^2$ , so the amount of absorption should increase with decreasing  $Q^2$ .

The left side of Fig. 5 shows the LN  $x_L$  spectra for photoproduction ( $Q^2 \sim 0$ ) and three bins of increasing  $Q^2$ . The yield of LN increases monotonically with  $Q^2$ , in agreement with the expectation of the decrease of loss through absorption as  $Q^2$  rises. The right side of Fig. 5 shows photoproduction data with two predictions from models of exchange with absorption [4]. The dashed curve model incorporates pion exchange with absorption, accounting also for the migration in  $x_L$  and  $p_T$  of the neutron. The solid curve model include the same effects, adding also exchange of  $\rho$  and  $a_2$  mesons. Both models give a good description of the large depletion of LN in photoproduction relative to DIS seen in the left side of the figure.

#### 5 Pion structure function

Analogous to the inclusive proton structure function  $F_2(Q^2, x)$ , one can define an LN tagged semi-inclusive structure function  $F_2^{LN}(Q^2, x, x_L)$ , including also the dependence on the LN

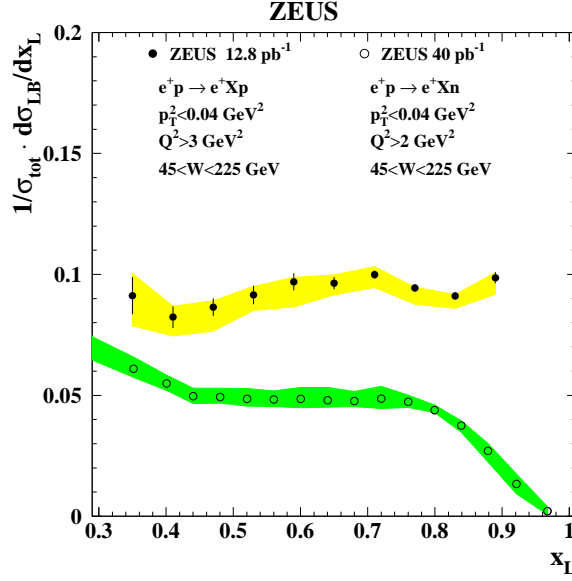


Fig. 3: LP and LN  $x_L$  distributions for  $p_T^2 < 0.04 \text{ GeV}^2$ .

energy. The left side of Fig. 6 shows the ratios  $F_2^{LN}/F_2$  as a function of  $Q^2$  in bins of  $x$  and  $x_L$ . Here  $F_2^{LN}$  are the measured values from LN production in DIS and the values of  $F_2$  are obtained from the H1-2000 parameterization [5]. For fixed  $x_L$  the ratios are almost flat for all  $(x, Q^2)$  implying that  $F_2^{LN}$  and  $F_2$  have a similar  $(x, Q^2)$  behavior. This result suggests the validity of factorization, i.e. independence of the photon and the proton vertices. The statistical precision of the data precludes sensitivity to absorptive effects as discussed in the previous section.

Based on the assumption that at high  $x_L$  LN production is dominated by the pion exchange mechanism, the measurement of  $F_2^{LN}$  can provide important information about the pion structure. The quark and gluon distributions of the pion have previously been constrained using Drell–Yan and direct photon production data obtained by  $\pi p$  scattering experiments and are limited to high  $x$  values  $x > 0.1$ .

Using the measurement of  $F_2^{LN(3)}$  for  $0.68 < x_L < 0.77$ , and the integral over  $t$  of the pion flux factor at the center of this  $x_L$  range,  $\Gamma_\pi = \int f_{\pi/p} dt = 0.131$ , one can estimate the pion structure function at low Bjorken- $x$ . Assuming that the Regge model of leading neutron production is valid, the quantity  $F_2^{LN(3)}/\Gamma_\pi$  can be associated to the structure function of the pion. The right side of Fig. 6 shows  $F_2^{LN(3)}/\Gamma_\pi$  as a function of  $\beta = x/(1 - x_L)$  for fixed values of  $Q^2$ . The results are consistent with a previous ZEUS measurement [6], where two extreme choices of the pion flux were used to extract  $F_2^\pi$ . The data are compared to predictions of parameterizations of the pion structure function [7]. The measurements are also compared to the H1-2000 parameterization of the proton structure function [5] which is multiplied by the factor  $2/3$  according to naive expectation based on the number of valence quarks in the pion and proton respectively. The distributions show a steep rise with decreasing  $\beta$ , in accordance with the



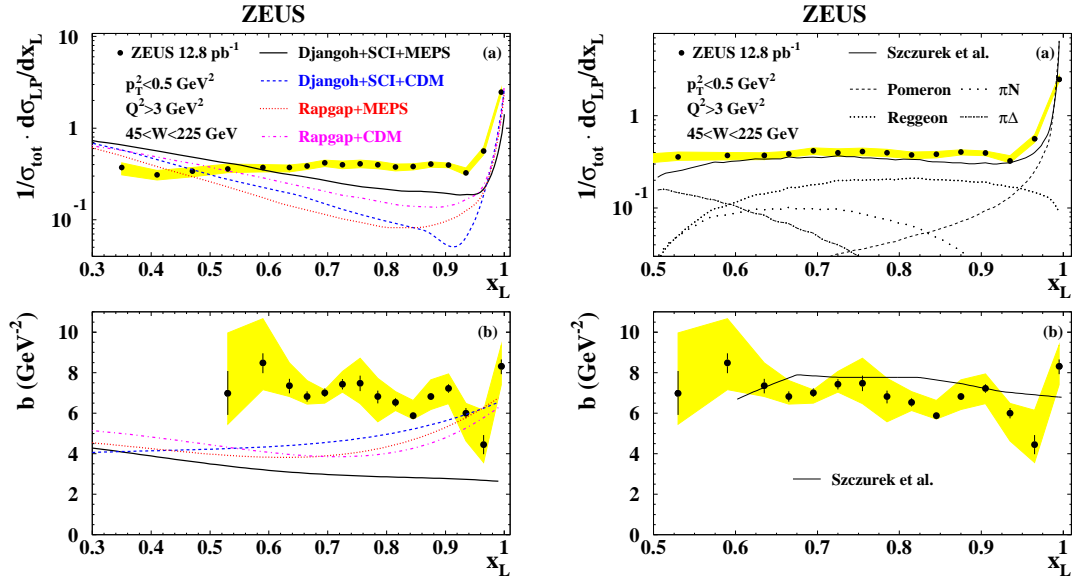


Fig. 4: Left: LP  $x_L$  distribution and exponential slopes compared to standard fragmentation models. Right: LP  $x_L$  distribution and exponential slopes compared to a model incorporating isoscalar and isovector exchanges.

pion and the proton structure function parameterizations. The scaled proton structure function gives the best description of the data. In absolute values, the presented data are slightly below the expectations, suggesting that additional phenomena, like absorption, may play a role.

## References

- [1] ZEUS Coll., S. Chekanov et al., Nucl. Phys. **B 776**, 1 (2007);  
H1 Coll., contribution to ICHEP-08, H1prelim-08-111;  
ZEUS Coll., *Leading proton production in deep inelastic scattering at HERA*, to be published;  
and references cited therein.
- [2] A. Szczurek, N.N. Nikolaev and J. Speth, Phys. Lett. **B 428**, 383 (1998).
- [3] N.N. Nikolaev, J. Speth and B.G. Zakharov, Preprint KFA-IKP(TH)-1997-17 (hep-ph/9708290) (1997);  
U. D'Alesio and H.J. Pirner, Eur. Phys. J. **A 7**, 109 (2000).
- [4] V.A. Khoze, A.D. Martin and M.G. Ryskin, Eur. Phys. J. **C 48**, 797 (2006).
- [5] H1 Coll., C. Adloff et al., Eur. Phys. J. **C 21**, 33 (2001).
- [6] ZEUS Coll., S. Chekanov et al., Nucl. Phys. **B 637**, 3 (2002).
- [7] P. Aurenche et al., Phys. Lett. **B 233**, 517 (1989);  
M. Glück, E. Reya and I. Schienbein, Eur. Phys. J. **C 10**, 313 (1999).

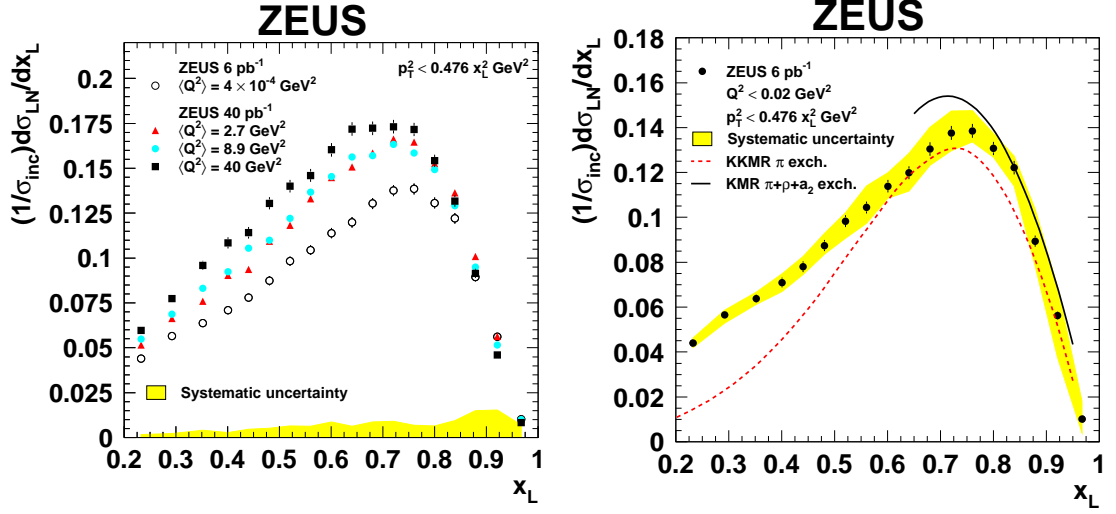


Fig. 5: Left: LN  $x_L$  distributions for photoproduction and three bins of  $Q^2$  in DIS. Right: LN  $x_L$  distributions for photoproduction compared to exchange models including absorptive effects.

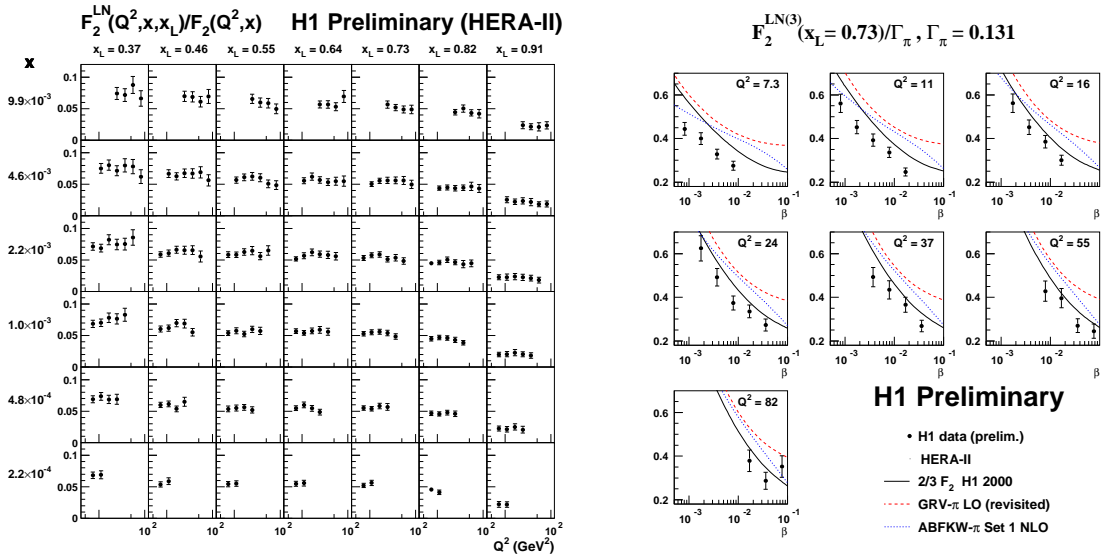


Fig. 6: Left: Ratio of semi-inclusive LN to inclusive structure functions as a function of  $Q^2$  in bins of  $x$  and  $x_L$ . Right: Extracted pion structure function as a function of  $\beta = x/(1 - x_L)$  in bins of  $Q^2$ . The curves are the proton structure function scaled by 2/3 and two parameterizations based on Drell-Yan and direct photon production data.

# Exclusive Vector Meson Production and Deeply Virtual Compton Scattering at HERA

Alessia Bruni<sup>1</sup>, Xavier Janssen<sup>2</sup>, Pierre Marage<sup>2</sup>

<sup>1</sup> Istituto Nazionale di Fisica Nucleare, Via Innerio 46, I-40126 Bologna, Italy

<sup>2</sup> Faculty of Science, Université Libre de Bruxelles, Bd. du Triomphe, B-1040 Brussels, Belgium

## Abstract

Exclusive vector meson production and deeply virtual Compton scattering are ideally suited reactions for studying the structure of the proton and the transition from soft to hard processes. The main experimental data obtained at HERA are summarised and presented in the light of QCD approaches.

## 1 Introduction

The two processes which are the object of the present report, the exclusive production of a vector meson (VM) of mass  $M_V$ ,  $e+p \rightarrow e+VM+Y$ , and deeply virtual Compton scattering (DVCS),  $e+p \rightarrow e+\gamma+Y$ , where  $Y$  is a proton (elastic scattering) or a diffractively excited system (proton dissociation), are characterised in Fig. 1. The kinematical variables are  $Q^2$ , the negative square of the photon four-momentum,  $W$  the photon-proton centre of mass energy ( $W^2 \simeq Q^2 (1/x - 1)$ ,  $x$  being the Bjorken scaling variable) and  $t$ , the square of the four-momentum transfer at the proton vertex.

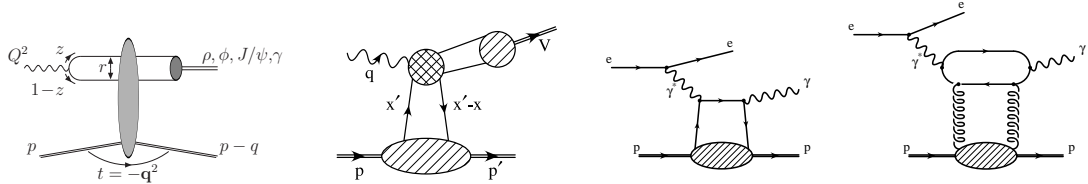


Fig. 1: (from left to right) Representative diagrams of a) low  $x$  dipole approach and b) GPD approach, for VM production; c) LO scattering and d) two gluon exchange, for the DVCS process.

The H1 and ZEUS collaborations at HERA have studied the elastic and proton dissociative production of  $\rho$  [1–4],  $\omega$  [5],  $\phi$  [3,6],  $J/\psi$  [7,8],  $\psi(2s)$  [9] and  $\Upsilon$  [10,11] mesons, and the DVCS process in the elastic channel [12,13]. The measurements are performed in the low  $x$ , large  $W$  domain  $10^{-4} \lesssim x \lesssim 10^{-2}$ ,  $30 \leq W \leq 300$  GeV. They cover photoproduction ( $Q^2 \simeq 0$ ), with  $|t|$  values up to  $30 \text{ GeV}^2$ , and electroproduction in the deep inelastic (DIS) domain ( $2 \leq Q^2 \leq 90 \text{ GeV}^2$ ) with  $|t| \lesssim 2 \text{ GeV}^2$ . The cross sections, expressed in terms of  $\gamma^*p$  scattering, are measured differentially in  $Q^2$ ,  $W$  and  $t$ . The measurement of angular distributions gives access to spin density matrix elements and polarised amplitudes.

## 1.1 Production mechanisms

Within the QCD formalism, two main complementary approaches are used to describe VM production and DVCS: dipole factorisation and collinear factorisation.

**Dipole approach of VM production** At high energy, i.e. small  $x$ , VM production can be described in the proton rest frame with three factorising contributions [14] (see Fig. 1a): the fluctuation of the virtual photon into a  $q\bar{q}$  colour dipole, the elastic or proton dissociative dipole–proton scattering, and the  $q\bar{q}$  recombination into the final state VM. The dipole–proton cross section is expected to be flavour independent and governed by the transverse size of the dipole. Light VM photoproduction is dominated by large dipoles, leading to large interaction cross sections with the incoming proton, similar to soft hadron–hadron interactions. In contrast, heavy VM production and large  $Q^2$  processes are dominated by small dipoles, with smaller cross sections implied in QCD by colour transparency, the quark and the antiquark separated by a small distance tending to screen each other’s colour.

The cross section for VM production can be computed at small  $x$  and for all  $Q^2$  values through models [15–17] using universal dipole–proton cross sections measured in inclusive processes, possibly including saturation effects [18] (see also [19]). This formalism thus connects the inclusive and diffractive cross sections, also in the absence of a hard scale.

In the presence of a hard scale (large quark mass or  $Q$ ), the dipole–proton scattering is modelled in perturbative QCD (pQCD) as the exchange of a colour singlet system consisting of a gluon pair (at lowest order) or a BFKL ladder (at leading logarithm approximation, LL  $1/x$ ). At these approximations, the cross sections are proportional to the square of the gluon density  $|xG(x)|^2$  in the proton [20]. The pQCD calculations [21–24] use  $k_t$ -unintegrated gluon distributions (see also [25]). The typical interaction scale is  $\mu^2 \simeq z(1-z)(Q^2 + M_V^2)$ , where  $z$  is the fraction of the photon longitudinal momentum carried by the quark. For heavy VM (in the non-relativistic wave function (WF) approximation) and for light VM production from longitudinally polarised photons,  $z \simeq 1/2$  and the cross sections are expected to scale with the variable  $\mu^2 = (Q^2 + M_V^2)/4$ . In contrast, for light VM production by transversely polarised photons, contributions with  $z \rightarrow 0, 1$  result in the presence of large dipoles and the damping of the scale  $\mu$ , thus introducing non-perturbative features even for non-small  $Q^2$ .

**Collinear factorisation and GPD** In a complementary approach (see Fig. 1b), a collinear factorisation theorem [26] has been proven in QCD for longitudinal amplitudes in the DIS domain, which does not require low  $x$  values. This allows separating contributions from different scales, a large scale at the photon vertex, provided by the photon virtuality  $Q$  (or the quark mass), and a small scale for the proton structure. The latter is described by Generalised Parton Distributions (GPD – see e.g. the reviews [27]), which take into account the distribution of transverse momenta of partons with respect to the proton direction and longitudinal momentum correlations between partons. They account for “off-diagonal” or “skewing” effects arising from the kinematic matching between the initial state (virtual) photon and the final state, VM or real photon for DVCS. GPD calculations have been performed for light VM electroproduction [28]. NLO corrections to light VM electroproduction and to heavy VM photoproduction have been computed [29].

**DVCS** Following collinear factorisation, the DVCS process is described at LO by Fig. 1c, where the virtual photon couples directly to a quark in the proton. QCD calculations at the scale  $\mu^2 = Q^2$  involve GPD distributions [30, 31]. At higher order, two gluon exchange as in Fig. 1d gives also an important contribution at HERA. Joint fits to DVCS and inclusive structure functions data have been used to extract GPD distributions [32].

**Large  $|t|$  production** Calculations for VM production at large  $|t|$  have been performed both in a DGLAP and in a BFKL approach (see section 6).

## 1.2 Measurements at HERA

Vector mesons are identified by H1 and ZEUS via their decay to two oppositely charged particles  $\rho \rightarrow \pi^+\pi^-$ ,  $\phi \rightarrow K^+K^-$ ,  $J/\psi \rightarrow e^+e^-$ ,  $\mu^+\mu^-$  and  $\Upsilon \rightarrow \mu^+\mu^-$ . The kinematic variables are reconstructed from the scattered electron and decay particle measurements. Forward calorimeters and taggers at small angles are generally used to separate elastic and proton dissociative events. The scattered proton is also measured in forward proton spectrometers, with an acceptance of a few %, allowing the selection of a purely elastic sample and the direct measurement of the  $t$  variable.

VM production has been investigated mainly using the HERA I data, collected between 1992 and 2000 and corresponding to an integrated luminosity of  $\simeq 150 \text{ pb}^{-1}$  for both collaborations. The integrated luminosity of  $500 \text{ pb}^{-1}$  collected at HERA II (2003-2007) has been analysed so far for DVCS [13] and  $\Upsilon$  [11]. For HERA II, ZEUS has installed a microvertex detector but has removed the small angle detectors: the leading proton spectrometer and the forward and rear calorimeters, compromising the precise analysis of diffractive data. The HERA II analyses of H1 will benefit of the fast track trigger installed in 2002 and, for general diffraction studies, of the very forward proton spectrometer VFPS installed in 2003, which however has very limited acceptance for VM.

## 2 From soft to hard diffraction: $t$ dependences and the size of the interaction

The  $t$  dependences of DVCS and VM production provide information on the size and the dynamics of the processes and on the scales relevant for the dominance of perturbative, hard effects. Whereas total cross sections ( $F_2$  measurements) are related, through the optical theorem, to the scattering amplitudes in the forward direction, diffractive final states provide a unique opportunity to study the region of non-zero momentum transfer  $t$ . This gives indirect information on the variable conjugate to  $t$ , the transverse size of the interaction.

For  $|t| \lesssim 1 - 2 \text{ GeV}^2$ , the  $|t|$  distributions are exponentially falling with slopes  $b$ :  $d\sigma/dt \propto e^{-b|t|}$ . In an optical model approach, the diffractive  $b$  slope is given by the convolution of the transverse sizes of the interacting objects:  $b = b_{q\bar{q}} + b_Y + b_{\mathbb{P}}$ , with contributions of the  $q\bar{q}$  dipole, of the diffractively scattered system (the proton or the excited system  $Y$ ) and of the exchange (“Pomeron”) system. Neglecting effects related to differences in the WF, universal  $b$  slopes are thus expected for all VM with the same  $q\bar{q}$  dipole sizes, i.e. with the same values of the scale  $\mu^2 = (Q^2 + M_V^2)/4$ . Conversely, elastic and proton dissociative slopes are expected to differ for all VM production at the same scale by the same amount,  $b_p - b_Y$ . Measurements of elastic and

proton dissociative  $b$  slopes for DVCS and VM production are presented in Fig. 2 as a function of the scale  $\mu^1$ .

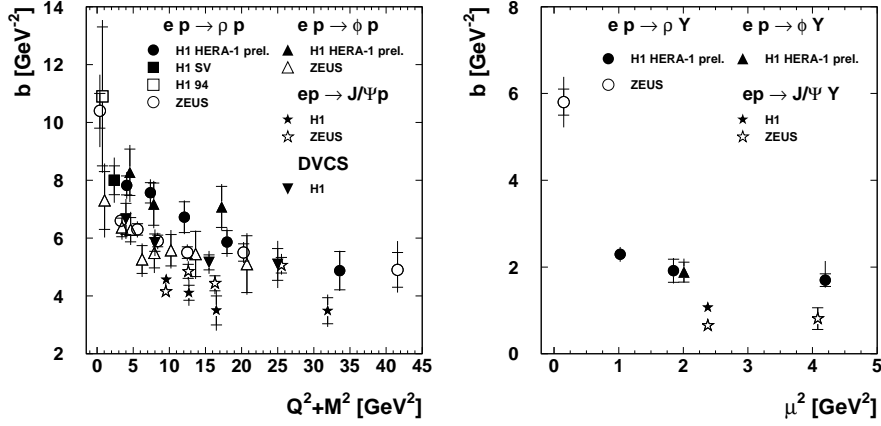


Fig. 2: Measurement of (left) the elastic and (right) the proton dissociative slopes  $b$  of the exponential  $t$  distributions, as a function of the scale  $\mu^2 = (Q^2 + M_V^2)/4$  for VM production and  $\mu^2 = Q^2$  for DVCS.

For  $J/\psi$  elastic production, the  $b$  slope is  $\lesssim 4.5 \text{ GeV}^{-2}$ , with no visible  $Q^2$  dependence. This value may be related to the proton form factor [16]. For proton dissociation, the  $b$  slope is below  $1 \text{ GeV}^{-2}$ , putting an upper limit to the transverse size of the exchange (with the assumption that  $b_Y \simeq 0$  for proton dissociation).

At variance with  $J/\psi$  production, which is understood as a hard process already in photoproduction, a strong decrease of  $b$  slopes for increasing values of  $\mu^2 = (Q^2 + M_V^2)/4$  is observed for light VM production, both in elastic and proton dissociative scattering. A similar scale dependence is observed for DVCS. This is consistent with a shrinkage of the size of the initial state object with increasing  $Q^2$ , i.e. in the VM case a shrinkage of the colour dipole. It should however be noted that, both in elastic and proton dissociative scatterings,  $b$  slopes for light VM remain larger than for  $J/\psi$  when compared at the same values of the scale  $(Q^2 + M_V^2)/4$  up to  $\gtrsim 5 \text{ GeV}^2$ . The purely perturbative domain may thus require larger scale values.

### 3 From soft to hard diffraction: $W$ dependences vs. mass and $Q^2$

Figure 3-left presents measurements as a function of  $W$  of the total photoproduction cross section and of the exclusive photoproduction cross sections of several VM;  $\rho$  electroproduction cross sections for several values of  $Q^2$  are shown in Fig. 3-right. As expected for decreasing dipole sizes, the cross sections at fixed values of  $W$  decrease significantly with increasing VM mass or  $Q^2$ . In

<sup>1</sup>Differences between the H1 and ZEUS measurements for elastic scattering are due to differences in background subtraction. The major effect is due to the subtraction of  $\rho'$  production by H1, a contribution evaluated to be negligible by ZEUS. Another difference concerns the values used for the  $b$  slopes of the proton dissociative contamination.

addition, different reactions exhibit strongly different  $W$  dependences. The total photoproduction cross section and the photoproduction of light VM show weak energy dependences, typical of soft, hadron–hadron processes. In contrast, increasingly steep  $W$  dependences are observed with increasing mass or  $Q^2$ . In detail, the  $W$  dependences are investigated using a parameterisation inspired by Regge theory, in the form of a power law with a linear parameterisation of the effective trajectory

$$\sigma \propto W^\delta, \quad \delta = 4(\alpha_P - 1), \quad \alpha_P(t) = \alpha_P(0) + \alpha' \cdot t. \quad (1)$$

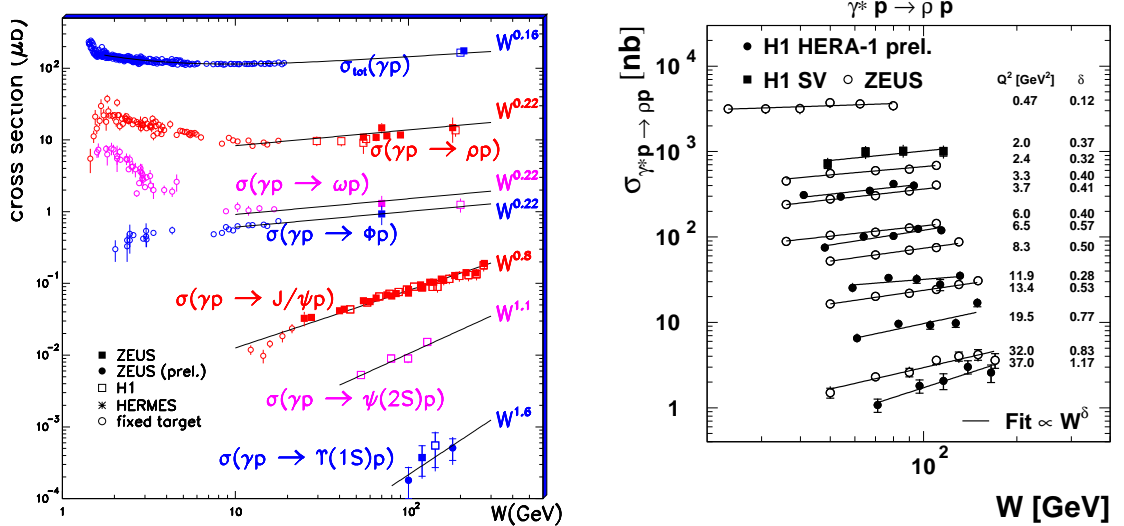


Fig. 3:  $W$  dependences of (left) total and VM photoproduction cross sections; (right)  $\rho$  electroproduction for several values of  $Q^2$ . The lines show fits to the form  $W^\delta$ .

The intercept  $\alpha_P(0)$  of the effective trajectory quantifies the energy dependence of the reaction for  $t = 0$ . The evolution of  $\alpha_P(0)$  with  $\mu^2$  is shown in Fig. 4-left. Light VM production at small  $\mu^2$  gives values of  $\alpha_P(0) \lesssim 1.1$ , similar to those measured for soft hadron–hadron interactions [33]. In contrast larger values,  $\alpha_P(0) \gtrsim 1.2$ , are observed for DVCS, for light VM at large  $Q^2$  and for heavy VM at all  $Q^2$ . This increase is related to the large parton densities in the proton at small  $x$ , which are resolved in the presence of a hard scale: the  $W$  dependences of the cross section is governed by the hard  $x^{-\lambda}$  evolution of the gluon distribution, with  $\lambda \simeq 0.2$  for  $Q^2 \simeq M_{J/\psi}^2$ . The  $W$  dependences of VM cross sections, measured for different  $Q^2$  values, are reasonably well described by pQCD models (not shown). In detail these are however sensitive to assumptions on the input gluon densities in the domain  $10^{-4} \lesssim x \lesssim 10^{-2}$  which is poorly constrained by inclusive data [25, 34].

The slope  $\alpha'$  in eq. (1) describes the correlation between the  $t$  and  $W$  dependences of the cross section. The measurement of the evolution with  $t$  of the  $\delta$  exponent can be parameterised as a  $W$  dependence of the  $b$  slopes, with  $b = b_0 + 4\alpha' \ln W/W_0$ . In hadron–hadron scattering,

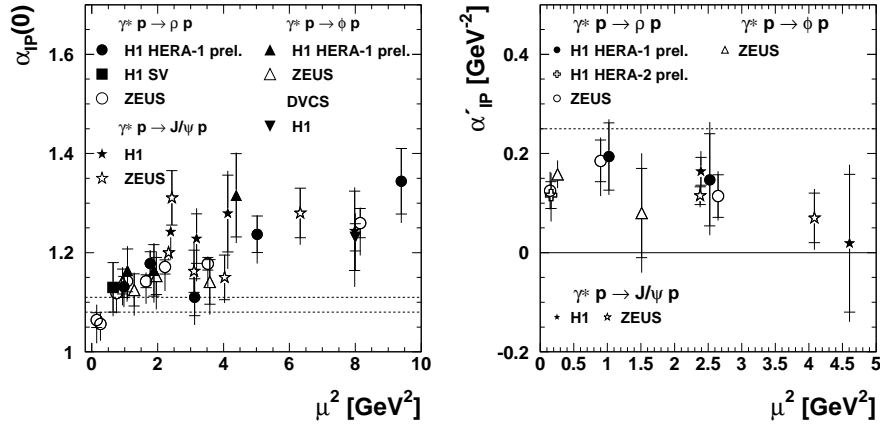


Fig. 4: Values of (left) the intercept  $\alpha_P(0)$  and (right) the slope  $\alpha'_P$  of the effective Pomeron trajectory, obtained from fits of the  $W$  cross section dependences to the form  $d\sigma/dt \propto W^{4(\alpha_P(0) + \alpha'_P \cdot t - 1)}$ . The scales are  $\mu^2 = Q^2$  for DVCS and  $\mu^2 = (Q^2 + M_V^2)/4$  for VM production. The dotted lines represent typical values for hadron–hadron scattering.

positive values of  $\alpha'_P$  are measured, with  $\alpha'_P \simeq 0.25 \text{ GeV}^{-2}$  [35]. This shrinkage of the diffractive peak indicates the expansion with energy of the size of the interacting system, i.e. the expansion of the gluon cloud in the periphery of the interaction. HERA measurements are presented in Fig. 4-right. The values of  $\alpha'_P$  are positive and appear smaller than in hadron–hadron interactions, also for  $\rho$  photoproduction. This suggests a limited expansion of the systems considered here on the relevant interaction time scale. In a BFKL approach,  $\alpha'_P$  is related to the average  $k_t$  of gluons around the ladder in their random walk, and is expected to be small [36].

## 4 $Q^2$ dependences in DVCS and VM production

The description of the  $Q^2$  dependences of the cross sections is a challenge, in view of the presence of higher order corrections and of non-perturbative effects, especially for transverse VM production.

### 4.1 DVCS

The DVCS cross section depends on the proton GPD distributions. To investigate the dynamical effects due to QCD evolution, the  $Q^2$  dependence has been measured and studied [13] as a function of the dimensionless scaled variable  $S$ ,

$$S = \sqrt{\sigma_{DVCS} Q^4 b(Q^2) / (1 + \rho^2)},$$

which removes the effects of the photon propagator and of the  $Q^2$  dependence of the  $b$  slope, and of the ratio  $R$  of the imaginary parts of the DVCS and DIS amplitudes,

$$R = \frac{\text{Im}A(\gamma^*p \rightarrow \gamma p)_{t=0}}{\text{Im}A(\gamma^*p \rightarrow \gamma^*p)_{t=0}} = 4 \frac{\sqrt{\pi \sigma_{DVCS} b(Q^2)}}{\sigma_T(\gamma^*p \rightarrow X)} \sqrt{1 + \rho^2},$$



with  $\sigma_T(\gamma^*p \rightarrow X) = 4\pi^2\alpha_{EM}F_T(x, Q^2)/Q^2$ ,  $F_T = F_2 - F_L$  and  $\rho = \mathcal{R}eA/\mathcal{I}m A$  determined from dispersion relations [31].

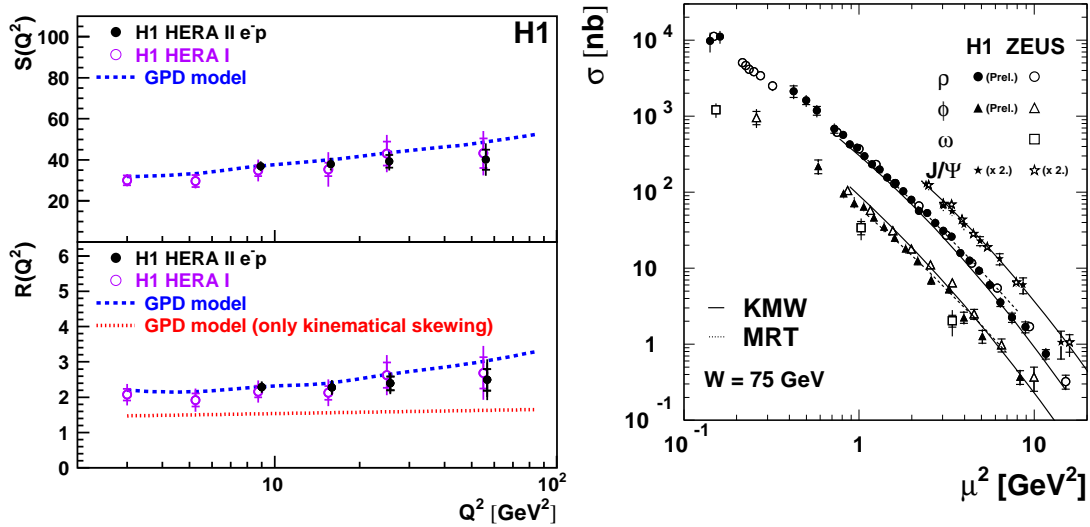


Fig. 5: (left)  $Q^2$  dependences of the observables  $S$  and  $R$  for DVCS (see text); (right)  $\rho$ ,  $\omega$ ,  $\phi$  and  $J/\psi$  elastic production cross sections, as a function of the scale  $\mu^2 = (Q^2 + M_V^2)/4$ ; for readability of the figure, the  $J/\psi$  cross sections have been multiplied by a factor 2. The curves are predictions of the KMW [16] and MRT [23] models.

Figure 5-upper-left shows a weak rise of  $S$  with  $Q^2$ , which is reasonably well described by the GPD model [30] using the CTEQ PDF parameterisation [37]. The large effect of skewing is visible in Fig. 5-lower-left, where the variable  $R$  takes values around 2, instead of 1 in the absence of skewing. GPD calculations [30] compare well with measurements, whereas the same figure shows that it is not sufficient to include only the kinematic contribution to skewing, and that the  $Q^2$  evolution of the GPD must also be taken into account.

## 4.2 Vector mesons

The elastic production cross sections  $\rho$ ,  $\omega$ ,  $\phi$  and  $J/\psi$  are shown in Fig. 5-right, as a function of the scaling variable  $(Q^2 + M_V^2)/4$  (for readability, the  $J/\psi$  cross sections have been multiplied by 2)<sup>2</sup>. It is striking that, whereas light VM and  $J/\psi$  production cross sections for the same value of  $Q^2$  differ by orders of magnitude (see Fig. 3-left for  $Q^2 = 0$ ), they are close when plotted as a function of the scaling variable  $(Q^2 + M_V^2)/4$ , up to the factors accounting for the VM charge

<sup>2</sup>Whereas the H1 and ZEUS measurements for  $\rho$  agree well,  $\phi$  measurements of ZEUS are a factor 1.20 above H1. When an improved estimation of the proton-dissociation background, investigated for the latest ZEUS  $\rho$  production study [2], is used to subtract this background in their  $\phi$  analysis, the cross section ratio of the two experiments is reduced to 1.06, which is within experimental errors.

content ( $\rho : \phi : J/\psi = 9 : 2 : 8$ )<sup>3</sup>. This supports the dipole approach of VM production at high energy.

The cross sections are roughly described by power laws  $1/(Q^2 + M_V^2)^n$ , with  $n \simeq 2.2 - 2.5$ . The simple  $n = 3$  dependence expected in a two-gluon approach for the dominant longitudinal cross sections is modified not only by an additional factor  $1/Q^2$  in the transverse amplitudes, but also by the  $Q^2$  dependence of the gluon distribution at small  $x$ , described by the DGLAP evolution equations. Calculations using the  $k_t$ -unintegrated gluon distribution model of MRT [23] or the GPD model [28] (not shown) give reasonable descriptions of the  $(Q^2 + M_V^2)$  dependences. However, in detail, a good description necessitates the precise modelisation of the  $Q^2$  dependence of the longitudinal to transverse cross section ratio  $R$ , with non-perturbative effects affecting  $\sigma_T$ . Dipole models using different saturation and WF parameterisations, e.g. the FSS [15], KMW [16] and DF [17] models, attempt at describing VM production over the full  $Q^2$  range, including photoproduction, with reasonable success.

## 5 Matrix elements and $\sigma_L/\sigma_T$

Measurements of the VM production and decay angular distributions give access to spin density matrix elements, which are related to the helicity amplitudes  $T_{\lambda_V \lambda_\gamma}$  [38]. Analyses of  $\rho$ ,  $\phi$  and  $J/\psi$  photo- and electroproduction indicate the dominance of the two  $s$ -channel helicity conserving (SCHC) amplitudes, the transverse  $T_{11}$  and the longitudinal  $T_{00}$  amplitudes. In the accessible  $Q^2$  ranges,  $J/\psi$  production is mostly transverse, whereas for light VM electroproduction the longitudinal amplitude  $T_{00}$  dominates (see Fig. 6a and Fig. 7a). In  $\rho$  and  $\phi$  electroproduction, a significant contribution of the transverse to longitudinal helicity flip amplitude  $T_{01}$  is observed. The amplitude ratio  $T_{01}/T_{00}$  decreases with  $Q^2$  (Fig. 6b) and increases with  $|t|$  (Fig. 6d), as expected (see e.g. [24]); the SCHC amplitude ratio  $T_{11}/T_{00}$  decreases with  $|t|$  (Fig. 6c).

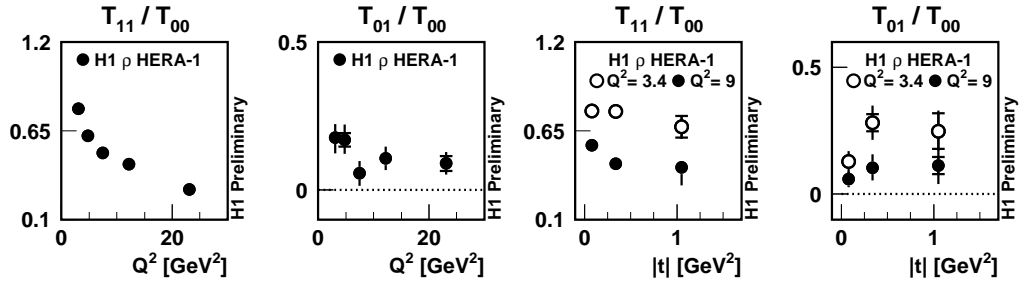


Fig. 6: Amplitude ratios  $T_{11}/T_{00}$  and  $T_{01}/T_{00}$  as a function of  $Q^2$  and  $|t|$  (for two bins in  $Q^2$ ), for  $\rho$  electroproduction. The dotted lines represent the SCHC approximation.

Figure 7 presents measurements of the longitudinal to transverse cross ratio  $R = \sigma_L/\sigma_T \simeq |T_{00}|^2/|T_{11}|^2$  (in the SCHC approximation). The behaviour  $R \propto Q^2/M_V^2$  predicted for two-gluon exchange is qualitatively verified for all VM production, in fixed target and HERA ex-

<sup>3</sup>For detailed comparisons, modifications due to WF effects, as observed in VM electronic decay widths, may need to be taken into account.

periments. This is shown in Fig. 7-left, where  $R$  is plotted as a function of the scaled variable  $Q^2 \cdot M_\rho^2/M_V^2$ . However, the  $Q^2$  dependence is tamed at large values of  $Q^2$ , a feature which is expected and relatively well described by pQCD based calculations, e.g. the GPD model [28], the  $k_t$ -unintegrated models [23, 24] or the dipole model [16].

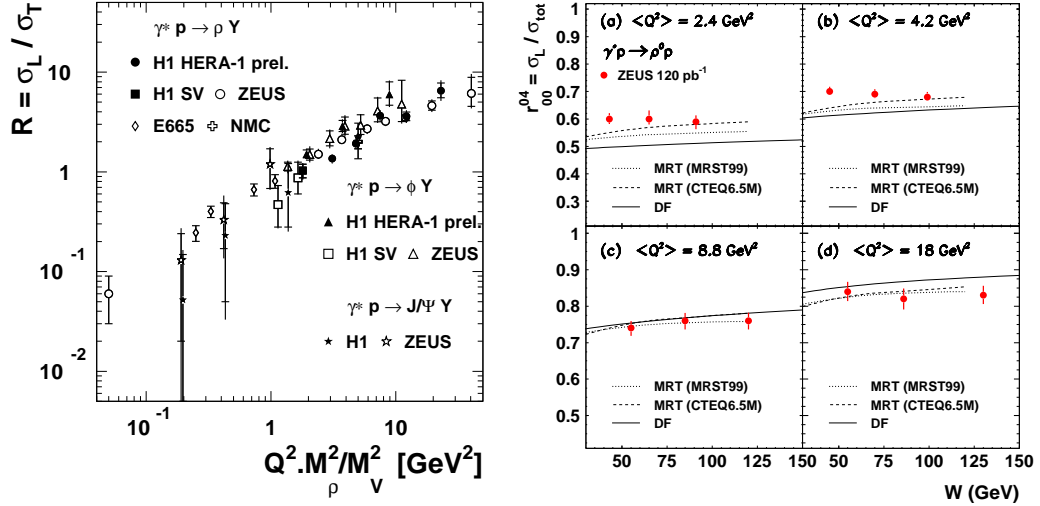


Fig. 7: Cross section ratio  $R = \sigma_L/\sigma_T$  as a function of (left) the scaling variable  $Q^2 \cdot M_\rho^2/M_V^2$  for different VM; (right) the centre of mass energy  $W$  in several  $Q^2$  bins for  $\rho$  electroproduction, compared to model predictions.

The cross section ratio  $R$  for  $\rho$  electroproduction is also found to depend very significantly on the dipion mass  $M_{\pi\pi}$  (not shown), in line with the  $Q^2/M_V^2$  dependence if the relevant mass is the dipion mass rather than the nominal  $\rho$  resonance mass. Following the MRT model approach [23], this suggests a limited influence of the WF on VM production.

Figure 7-right shows that no strong dependence of  $R$  with  $W$  is observed. Since transverse amplitudes are expected to include significant contributions of large dipoles, with a soft energy dependence, this suggests that large dipoles are also present in longitudinal amplitudes, due to finite size effects, i.e. a smearing of  $z$  away from  $z = 1/2$ . On the other hand, in the domain  $Q^2 \gtrsim 10 - 20 \text{ GeV}^2$ , no strong dependence of  $R$  with  $W$  is expected from models. It should also be noted that a significant phase difference is observed between the two dominant amplitudes,  $T_{00}$  and  $T_{11}$  [3]. This indicates a difference between the ratios of the real to imaginary parts of the forward amplitudes. Since these ratios are given by  $\log 1/x$  derivatives of the amplitudes, the phase difference is an indication of different  $W$  dependences.

## 6 Large $|t|$ ; BFKL evolution

Large values of the momentum transfer  $|t|$  provide a hard scale for diffractive processes in QCD, with the dominance of the proton dissociative channel for  $|t| \gtrsim 1 \text{ GeV}^2$ . It should be noted that for large  $|t|$  production, a hard scale is present at both ends of the exchanged gluon ladder. No

strong  $k_t$  ordering is thus expected, which is typical for BFKL evolutions for sufficiently high  $|t|$  values. This is at variance with large  $Q^2$  VM production at low  $|t|$ , where a large scale is present at the upper (photon) end of the ladder and a small scale at the proton end, implying that these processes are expected to be described by DGLAP evolutions, with strong  $k_t$  ordering along the ladder.

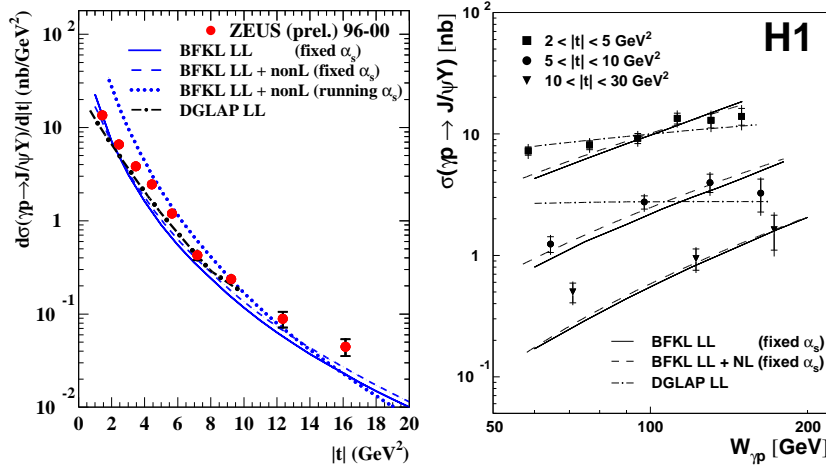


Fig. 8:  $t$  (left) and  $W$  (right) dependences of  $J/\psi$  production with  $|t| > 2 \text{ GeV}^2$ , with comparisons to pQCD model predictions.

For  $|t|$  larger than a few  $\text{GeV}^2$ , the  $t$  dependences of the cross sections follow power laws, both for  $\rho$  [4] and  $J/\psi$  [8] photoproduction. As shown by Fig. 8-left, they are well described by pQCD calculations based on the BFKL equations with fixed  $\alpha_s$  [39]; predictions using the DGLAP evolution [40] also describe the  $J/\psi$  data for  $|t| \lesssim m_\psi^2$ . BFKL calculations describe the  $W$  evolution (Fig. 8-right), at variance with DGLAP, but do not describe well the spin density matrix elements. For  $\rho$ ,  $\phi$  and  $J/\psi$  photoproduction with  $|t| \gtrsim 2 \text{ GeV}^2$ , the slope  $\alpha'$  of the effective Regge trajectory tends to be slightly negative, but are compatible with 0.

## 7 Conclusions

In conclusion, studies of VM production and DVCS at HERA provide a rich and varied field for the understanding of QCD and the testing of perturbative calculations over a large kinematical domain, covering the transition from the non-perturbative to the perturbative domain. Whereas soft diffraction, similar to hadronic interactions, dominates light VM photoproduction, typical features of hard diffraction, in particular hard  $W$  dependences, show up with the developments of hard scales provided by  $Q^2$ , the quark mass or  $|t|$ . The size of the interaction is accessed through the  $t$  dependences. Calculations based on pQCD, notably using  $k_t$ -unintegrated gluon distributions and GPD approaches, and predictions based on models invoking universal dipole–proton cross sections describe the data relatively well. The measurement of spin density matrix

elements gives a detailed access to the polarisation amplitudes, which is also understood in QCD. Large  $|t|$  VM production supports BFKL calculations.

## Acknowledgements

It is a pleasure to thank the numerous colleagues from H1 and ZEUS who contributed to the extraction of the beautiful data presented here, and to thank the theorist teams whose efforts led to a continuous increase in the understanding of diffraction in terms of QCD, the theory of strong interactions. Special thanks are due to L. Motyka, T. Teubner and G. Watt for providing calculations used for the present review and to J.-R. Cudell and L. Favart for useful discussions and comments. It is also a pleasure to thank the organisers of the HERA-LHC Workshop for the lively discussions and the pleasant atmosphere of the workshop.

## References

- [1] H1 Coll., S. Aid et al., Nucl. Phys. **B 463**, 3 (1996);  
 ZEUS Coll., M. Derrick et al., Z. Phys. **C 73**, 253 (1997);  
 ZEUS Coll., J. Breitweg et al., Eur. Phys. J. **C 2**, 247 (1998);  
 H1 Coll., "A new Measurement of Exclusive  $\rho^0$  Meson Photoproduction at HERA", XIV Int. Workshop on DIS, Tsukuba, Japan (2006);  
 ZEUS Coll., J. Breitweg et al., Eur. Phys. J. **C 6**, 603 (1999);  
 ZEUS Coll., J. Breitweg et al., Eur. Phys. J. **C 12**, 393 (2000);  
 H1 Coll., C. Adloff et al., Eur. Phys. J. **C 13**, 371 (2000);  
 H1 Coll., C. Adloff et al., Phys. Lett. **B 539**, 25 (2002).
- [2] ZEUS Coll., S. Chekanov et al., PMC Phys. **A 1**, 6 (2007).
- [3] H1 Coll., X. Janssen, "Diffractive  $\rho$  and  $\phi$  production in DIS", XVI Int. Workshop on DIS, London, UK (2008);  
 H1 Coll., "Diffractive electroproduction of  $\rho$  and  $\phi$  mesons at HERA", to be publ.
- [4] ZEUS Coll., S. Chekanov et al., Eur. Phys. J. **C 26**, 389 (2003);  
 H1 Coll., A. Aktas et al., Phys. Lett. **B 638**, 422 (2006).
- [5] ZEUS Coll., M. Derrick et al., Z. Phys. **C 73**, 73 (1996);  
 ZEUS Coll., J. Breitweg et al., Phys. Lett. **B 487**, 273 (2000).
- [6] ZEUS Coll., M. Derrick et al., Phys. Lett. **B 377**, 259 (1996);  
 H1 Coll., C. Adloff et al., Phys. Lett. **B 483**, 360 (2000);  
 ZEUS Coll., S. Chekanov et al., Nucl. Phys. **B 718**, 3 (2005).
- [7] ZEUS Coll., S. Chekanov et al., Eur. Phys. J. **C 24**, 345 (2002);  
 ZEUS Coll., S. Chekanov et al., Nucl. Phys. **B 695**, 3 (2004);  
 H1 Coll., A. Aktas et al., Eur. Phys. J. **C 46**, 585 (2006).
- [8] H1 Coll., A. Aktas et al., Phys. Lett. **B 568**, 205 (2003);  
 ZEUS Coll., "Diffractive photoproduction of  $J/\psi$  mesons with large momentum transfer at HERA", subm. to XXXIII ICHEP, Moscow (2006).

- [9] H1 Coll., C. Adloff et al., Phys. Lett. **B 541**, 251 (2002).
- [10] ZEUS Coll., J. Breitweg et al., Phys. Lett. **B 437**, 432 (1998);  
H1 Coll., C. Adloff et al., Phys. Lett. **B 483**, 23 (2000).
- [11] ZEUS Coll., "Exclusive photoproduction of  $\Upsilon$  mesons at HERA", submitted to the 2007 EPS Conference, Manchester (2007).
- [12] ZEUS Coll., S. Chekanov et al., Phys. Lett. **B 573**, 46 (2003);  
H1 Coll., A. Aktas et al., Eur. Phys. J. **C 44**, 1 (2005).
- [13] H1 Coll., F. D. Aaron et al., Phys. Lett. **B 659**, 796 (2008).
- [14] A.H. Mueller, Nucl. Phys. **B 335**, 115 (1990);  
N.N. Nikolaev and B.G. Zakharov, Z. Phys. **C 49**, 607 (1991).
- [15] J.R. Forshaw, R. Sandapen and G. Shaw, Phys. Rev. **D 69**, 094013 (2004).
- [16] H. Kowalski, L. Motyka and G. Watt, Phys. Rev. **D 74**, 074016 (2006).
- [17] H.G. Dosch and E. Ferreira, Eur. Phys. J. **C 51**, 83 (2007).
- [18] K.J. Golec-Biernat and M. Wusthoff, Phys. Rev. **D 59**, 014017 (1999);  
K.J. Golec-Biernat and M. Wusthoff, Phys. Rev. **D 60**, 114023 (1999);  
S. Munier, A.M. Stasto and A.H. Mueller, Nucl. Phys. **B 603**, 427 (2001);  
E. Iancu, K. Itakura and S. Munier, Phys. Lett. **B 590**, 199 (2004).
- [19] L. Motyka, these proceedings.
- [20] M.G. Ryskin, Z. Phys. **C 57**, 89 (1993);  
J.S. Brodsky et al., Phys. Rev. **D 50**, 3134 (1994).
- [21] L. Frankfurt, W. Koepf and M. Strikman, Phys. Rev. **D 54**, 3194 (1996).
- [22] I.P. Ivanov, N.N. Nikolaev and A.A. Savin, Phys. Part. Nucl. **37**, 1 (2006).
- [23] A.D. Martin, M.G. Ryskin and T. Teubner, Phys. Rev. **D 55**, 4329 (1997).
- [24] D. Yu. Ivanov and R. Kirschner, Phys. Rev. **D 58**, 114026 (1998).
- [25] T. Teubner, these proceedings.
- [26] J. Collins, L. Frankfurt and M. Strikman, Phys. Rev. **D 56**, 2982 (1997).
- [27] M. Diehl, Phys. Rep. **388**, 41 (2003);  
A.V. Belitsky and A.V. Radyushkin, Phys. Rep. **418**, 1 (2005).
- [28] S.V. Goloskokov and P. Kroll, Eur. Phys. J. **C 53**, 367 (2008).

- [29] D. Yu. Ivanov, L. Szymanowski and G. Krasnikov, JETP Lett. **80**, 226 (2004);  
D. Yu. Ivanov, A. Schafer, L. Szymanowski and G. Krasnikov, Eur. Phys. J. **C 34**, 297 (2004);  
D. Yu. Ivanov, Blois Conference on Forward Physics and QCD, Hamburg (2007).
- [30] A. Freund, Phys. Rev. **D 68**, 096006 (2003).
- [31] L. Favart and M. V. T. Machado, Eur. Phys. J. **C 29**, 365 (2003).
- [32] K. Kumericki, D. Mueller and K. Passek-Kumericki, Nucl. Phys. **B 794**, 244 (2008).
- [33] A. Donnachie and P.V. Landshoff, Phys. Lett. **B 296**, 227 (1992);  
J.-R. Cudell, K. Kang and S. Kim, Phys. Lett. **B 395**, 311 (1997).
- [34] A. D. Martin, C. Nockles, M. G. Ryskin and T. Teubner, Phys. Lett. **B 662**, 252 (2008).
- [35] G.A. Jaroszkiewicz and P.V. Landshoff, Phys. Rev. **D 10**, 170 (1974).
- [36] S. J. Brodsky et al., JETP Lett. **70**, 155 (1999).
- [37] J. Pumplin et al., JHEP **07**, 012 (2002).
- [38] K. Schilling and G. Wolf, Nucl. Phys. **B 61**, 381 (1973).
- [39] R. Enberg, L. Motyka and G. Poludniowski, Eur. Phys. J. **C 26**, 219 (2002).
- [40] E. Gotsman, E. Levin, U. Maor and E. Naftali, Phys. Lett. **B 532**, 37 (2002).

# Exclusive Central Production and Diffractive W/Z Results from CDF II

*Konstantin Goulianos<sup>1</sup> and James L. Pinfold<sup>2</sup>*

<sup>1</sup>The Rockefeller University  
1230 York Avenue, New York, NY 10065, USA

<sup>2</sup>The University of Alberta  
Centre for Particle Physics, Edmonton, Alberta T6G2N6, CANADA

## Abstract

We report recently published results on central exclusive production of di-jets and di-photons, and exclusive QED production of  $e^+e^-$  pairs. In addition, we discuss preliminary results on exclusive photoproduction of charmonium and bottomonium, exclusive QED production of  $\mu^+\mu^-$  pairs, and single diffractive W/Z production. All the presented results were extracted from data collected by the CDF II detector from  $p\bar{p}$  collisions at  $\sqrt{s}=1.96$  TeV. The implications of these results for the Large Hadron Collider (LHC) are briefly examined.

## 1 Introduction

We present results obtained by CDF II at the Tevatron <sup>1</sup> in two broad areas: inclusive diffraction and exclusive production. The main goal of the Run II inclusive diffractive program of CDF has been to understand the QCD nature of the Pomeron <sup>2</sup> ( $\mathbb{P}$ ) by measuring the diffractive structure function [3]  $F^{D4}(Q^2, x_{Bj}, \xi, t)$ , where  $\xi$  is the fractional momentum loss of the diffracted nucleon, for different diffractive production processes. In addition, the possibility of a composite Pomeron is being investigated by studies of very forward jets with a rapidity gap between the jets. Important results are the observation of a breakdown of QCD factorization in hard diffractive processes, expressed as a suppression by a factor of  $\mathcal{O}(10)$  of the production cross section relative to theoretical expectations, and the breakdown of Regge factorization in soft diffraction by a factor of the same magnitude [3]. Combined, these two results support the hypothesis that

---

<sup>1</sup>The presented results are from the CDF diffractive and exclusive physics program of Run II. This program relies on a system of special forward detectors, which include: a Roman Pot Spectrometer (RPS) equipped with scintillation counters and a fiber tracker to detect and measure the angle and momentum of leading anti-protons, a system of Beam Shower Counters (BSCs) [1] covering the pseudorapidity range  $5.5 < |\eta| < 7.5$  used to select diffractive events by identifying forward rapidity gaps and reducing non-diffractive background on the trigger level, and two very forward ( $3.5 < |\eta| < 5.1$ ) MiniPlug (MP) calorimeters [2], designed to measure energy and lateral position of both electromagnetic and hadronic showers. The ability to measure the event energy flow in the very forward rapidity region is vital for the identification of diffractive events in the high luminosity environment of Run II.

<sup>2</sup>Diffractive reactions are characterized by the exchange of a spin 1 quark/gluon construct with the quantum numbers of the vacuum. In Regge theory, this exchange is the vacuum trajectory traditionally referred to as the Pomeron ( $\mathbb{P}$ ). Because the exchange is colorless, a large region in pseudorapidity space is left empty of particles (this region is called a “rapidity gap”). In perturbative QCD, the lowest order prototype of the Pomeron is the color neutral system of two gluons.



the breakdown of factorization is due to a saturation of the rapidity gap formation probability by an exchange of a color-neutral construct of the underlying parton distribution function (PDF) of the proton [4]. Historically, such an exchange is referred to as the Pomeron. Renormalizing the “gap probability” to unity over all  $(\xi, t)$  phase space corrects for the unphysical effect of overlapping diffractive rapidity gaps and leads to agreement between theory and experiment (see [4]).

Central exclusive production in  $p\bar{p}$  collisions is a process in which the  $p$  and  $\bar{p}$  remain intact and an exclusive state  $X_{excl}$  is centrally produced:  $p + \bar{p} \rightarrow p + X_{excl} + \bar{p}$ . The primary motivation for studying exclusive physics at the Tevatron is to test the feasibility of using exclusive production to search for and study the Higgs boson as well search for other new physics at the LHC [5]. In leading order QCD, exclusive production occurs through gluon-gluon fusion, while an additional soft gluon screens the color charge allowing the protons to remain intact [6]. This mechanism, historically termed Double Pomeron Exchange (DPE), enables exclusive production of di-jets [3],  $\gamma\gamma$  [7], and the  $\chi_c^0$  [8] at the Tevatron, whereas at the LHC, where central masses up to several hundred GeV are attainable, new central exclusive channels open up, as for example  $W^+W^-$  and  $Z^0Z^0$ . While the main effort at the LHC is directed toward searches for inclusively produced Higgs bosons, an intense interest is developing in exclusive Higgs production,  $p + \bar{p} \rightarrow p + H + \bar{p}$ . This production channel presents several advantages, as for example the production of clean events in an environment of suppressed QCD background for the main Higgs decay mode of  $H \rightarrow b_{jet} + \bar{b}_{jet}$  due to the  $J_z = 0$  selection rule [5]. Exclusive production can also occur through photoproduction ( $\mathbb{P} - \gamma$  fusion), yielding charmonium and bottomonium. The same tagging technique can also be utilized to select  $\gamma p$ , or  $\gamma q$  and  $\gamma g$  interactions at the LHC, for which the energy reach and the effective luminosity are higher than for  $\gamma\gamma$  interactions.

Additionally, exclusive production of central lepton pairs,  $\gamma\gamma \rightarrow l^+l^-$  ( $l = e, \mu, \tau$ ), via two-photon exchange has been observed at CDF [9]. Tagging two-photon production offers a significant extension of the LHC physics program.<sup>3</sup> Particularly exciting is the possibility of detecting two-photon exclusive  $W^+W^-$ ,  $Z^0Z^0$ , Higgs boson and new physics production at the LHC [10]. The deployment of forward proton detectors at 200 m and 420 m (FP420 project) from the interaction point of ATLAS and CMS, in order to exploit the above mentioned forward physics scenarios, is currently under consideration [11]. Two-photon exclusive production of lepton pairs will provide an excellent monitoring tool of the tagging efficiency and energy scale of the detectors of the FP420 project. These events can also be used for several systematic studies, including luminosity normalization and contributions from inelastic production or accidental tagging.

## 2 Central Exclusive Production

Exclusive production is hampered by expected low production rates [5]. As rate calculations are model dependent and generally involve non-perturbative suppression factors, it is sensible to calibrate them against processes involving the same suppression factors but have high enough production rates to be measurable at the Tevatron. The leading order diagrams relating to the

---

<sup>3</sup>The effective luminosity of high-energy  $\gamma\gamma$  collisions reaches  $\sim 1\%$  of the  $pp$  luminosity, so that the standard detector techniques used for measuring very forward proton scattering should allow for a reliable extraction of  $\gamma\gamma$  results.

exclusive central production processes discussed in this paper are summarized in Fig. 1.

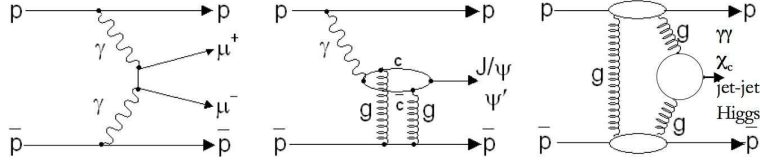


Fig. 1: Leading order diagrams for three types of exclusive process:  $\gamma\gamma$  interactions (left),  $\gamma P$  fusion or photoproduction (middle), and  $gg$   $t$ -channel color-singlet two-gluon exchange (right). Higgs boson production proceeds via the  $gg$  diagram.

## 2.1 Exclusive Di-jet Production

The process of exclusive di-jet production, which has been observed by CDF in Run II data [12], proceeds through the same mechanism as  $\gamma\gamma$ ,  $\chi_c^0$ , and Higgs production, as shown in Fig. 1. The analysis strategy developed to search for exclusive di-jet production is based on measuring the di-jet mass fraction,  $R_{jj}$ , defined as the di-jet invariant mass  $M_{jj}$  divided by the total mass of the central system:  $R_{jj} = M_{jj}/M_X$ .<sup>4</sup> The POMWIG MC [13] generator along with a detector simulation are used to simulate the DPE di-jets. The signal from exclusive di-jets is expected to appear at high values of  $R_{jj}$ , smeared by resolution and gluon radiation effects. Events from the inclusive DPE production process  $p + \bar{p} \rightarrow p + \text{gap} + [X + jj] + \text{gap}$  (the leading  $p$  is not observed in CDF II) are expected to contribute to the entire  $R_{jj}$  region. Any such events within the exclusive  $R_{jj}$  range contribute to background and must be subtracted when evaluating exclusive production rates.

The process of exclusive di-jet production is important for testing and/or calibrating models for exclusive Higgs production at the LHC. The CDF II collaboration has made the first observation of this process and the main final result is presented in Fig. 2. Details can be found in Ref. [12]. This result favours the model of Ref. [6], which is implemented in the MC simulation ExHuME [14].

## 2.2 Exclusive $e^+e^-$ Production

The CDF II collaboration has reported the first observation of exclusive  $e^+e^-$  production in  $p\bar{p}$  collisions [9] using  $532 \text{ pb}^{-1}$   $p\bar{p}$  data collected at  $\sqrt{s} = 1.96 \text{ TeV}$  by CDF II at the Fermilab Tevatron. The definition of exclusivity used requires the absence of any particle signatures in the detector in the pseudorapidity region  $|\eta| < 7.4$ , except for an electron and a positron candidate each with transverse energy of  $E_T \geq 5 \text{ GeV}$  and within the pseudorapidity  $|\eta| \leq 2$ . With these criteria, 16 events were observed. The dominant background is due to events with unobserved proton dissociation ( $1.6 \pm 0.3$  events). The total background expectation is  $1.9 \pm 0.3$  events.

<sup>4</sup>The mass  $M_X$  is obtained from all calorimeter towers with energy above the thresholds used to calculate  $\xi_p^X$ , while  $M_{jj}$  is calculated from calorimeter tower energies inside jet cones of  $R=0.7$ , where  $R=\sqrt{\Delta\phi^2 + \Delta\eta^2}$ . The exclusive signal is extracted by comparing the  $R_{jj}$  distribution shapes of DPE di-jet data and simulated di-jet events obtained from a Monte Carlo (MC) simulation that does not contain exclusive di-jet production.

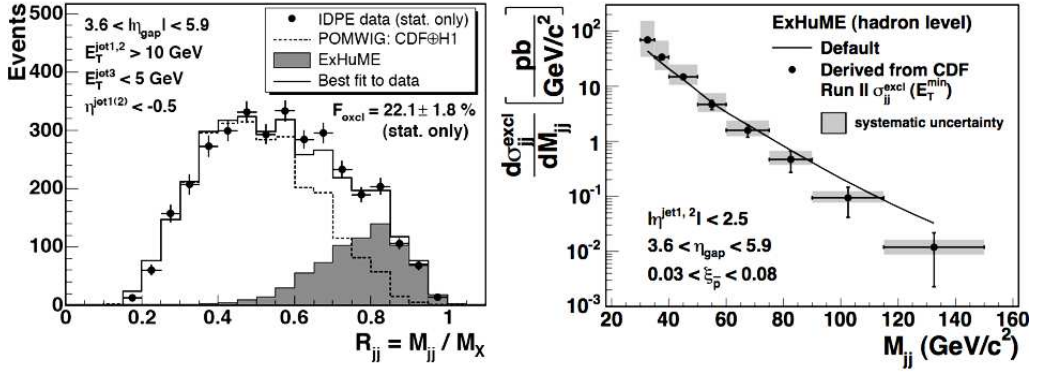


Fig. 2: (Left) The di-jet mass fraction in DPE data (points) and best fit (solid histogram) to a simulated di-jet mass fraction obtained from POMWIG MC events (dashed histogram) and ExHuME di-jet MC events (shaded histogram). (Right) The ExHuME [14] exclusive di-jet differential cross section at the hadron level vs. di-jet mass  $M_{jj}$  normalized to measured  $\sigma_{jj}^{excl}$  values. The curve is the cross section predicted by ExHuME.

The observed events are consistent in cross section and properties with the QED process  $p\bar{p} \rightarrow p + (e^+e^-) + \bar{p}$  through two-photon exchange. The measured cross section is  $1.6^{+0.5}_{-0.3}(stat) \pm 0.3(syst)$  pb. This agrees with the theoretical prediction of  $1.71 \pm 0.01$  pb obtained using the LPAIR MC generator [15] and a GEANT based detector simulation, CDFSim [16]. Details on the observation of the exclusive  $e^+e^-$  signal are reported in reference [9].

### 2.3 Exclusive $\gamma\gamma$ Production

An exclusive  $\gamma\gamma$  event can be produced via  $gg \rightarrow \gamma\gamma$  ( $g$  = gluon) through a quark loop, with an additional “screening” gluon exchanged to cancel the color of the interacting gluons and so allow the leading hadrons to stay intact. This process is closely related [7, 17] to exclusive Higgs production at the LHC,  $p\bar{p} \rightarrow p + H + \bar{p}$ , where the production mechanism of the Higgs boson is gg-fusion through a top quark loop. These processes can also be described as resulting from DPE.

A search has been performed for exclusive  $\gamma\gamma$  production in  $p\bar{p}$  collisions at  $\sqrt{s} = 1.96$  TeV, using  $532 \text{ pb}^{-1}$  of integrated luminosity data taken by CDF II at Fermilab. The event signature requires two electromagnetic showers, each with transverse energy  $E_T \geq 5$  GeV and pseudorapidity  $|\eta| \leq 1.0$ , with no other particles detected. Three candidate events were observed. Each candidate can be interpreted as either a  $\gamma\gamma$  or a  $\pi^0\pi^0/\eta\eta$  final state with overlapping photons that satisfy the  $\gamma\gamma$  selection criteria and thus form a background. The probability that processes other than these fluctuate to  $\geq 3$  events is  $1.7 \times 10^{-4}$ . Two events clearly favor the  $\gamma\gamma$  hypothesis and the third event favors the  $\pi^0\pi^0$  hypothesis. On the assumption that two of the three candidates are  $\gamma\gamma$  events we obtain a cross section  $\sigma(p\bar{p} \rightarrow p + \gamma\gamma + \bar{p}) = 90^{+120}_{-30}(stat) \pm 16(syst)$  fb, for  $E_T \geq 5$  GeV and  $|\eta| \leq 1.0$ , compatible within the theoretical uncertainties with the prediction of 40 fb of Ref. [5]. A comparison between the predictions of the ExHuMe MC and the data shows good agreement both in normalization and in the shapes of the kinematic distributions.

Although two of the candidates are most likely to arise from  $\gamma\gamma$  production, the  $\pi^0\pi^0$  hypotheses cannot be excluded. A 95% C.L. upper limit is obtained on the exclusive  $\gamma\gamma$  production cross section ( $E_T \geq 5$  GeV,  $|\eta| \leq 1.0$ ) of 410 fb, which is about ten times higher than the prediction of Ref. [7]. This result may be used to constrain calculations of exclusive Higgs boson production at the LHC. Additional CDF data, collected with a lower  $E_T$  threshold, are being analysed. Exclusive  $\gamma\gamma$  production has not previously been observed in hadron-hadron collisions. This work is described in more detail in Ref. [18].

## 2.4 Exclusive $\mu^+\mu^-$ Production

**Low Mass Exclusive  $\mu^+\mu^-$  Production.** The CDF II collaboration has performed a search for exclusive low mass  $\mu^+\mu^-$  final states resulting from three processes:  $\gamma\gamma \rightarrow$  non-resonant  $\mu^+\mu^-$  “continuum” events, and  $J/\psi \rightarrow \mu^+\mu^-$  &  $\psi' \rightarrow \mu^+\mu^-$  events arising from  $IP - \gamma$  fusion (photoproduction). In addition, evidence for exclusive  $\chi_c^0$  production was sought arising from the decay channel  $\chi_c^0 \rightarrow J/\psi(\rightarrow \mu^+\mu^-) + \gamma$ . The invariant mass distribution of the exclusive di-muon events obtained from 1.48 fb $^{-1}$  of data is shown in Fig. 3. The  $J/\psi$  and  $\psi'$  peaks can be clearly seen above the  $\mu^+\mu^-$  continuum.<sup>5</sup> Continuum  $\mu^+\mu^-$  production arises from  $\gamma\gamma$

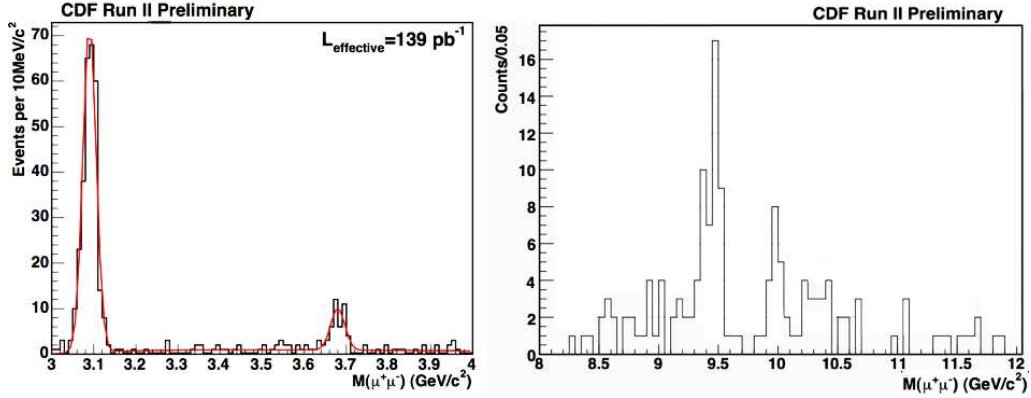


Fig. 3: (Left) The invariant mass distribution obtained from the exclusive  $\mu^+\mu^-$  data; the  $J/\psi$  peak (left) and the smaller  $\psi'$  peak (right) can be clearly seen above the continuum of muon-pair production. (Right) The invariant mass distribution obtained from the exclusive higher mass  $\mu^+\mu^-$  data: the  $\Upsilon$  (1S) peak (middle-left) and the smaller  $\Upsilon$  (2S) (middle) peaks can be clearly seen above the continuum, while the  $\Upsilon$  (3S) peak (middle-right) is only barely discernible with these statistics.

interactions. These interactions are simulated by the LPAIR [15] and STARlight MCs [19]. Both give a very good description of the data in shape and in normalization. The events in the  $J/\psi$  and  $\psi'$  peak of Figure 3, from the process  $p\bar{p} \rightarrow p + J/\psi(J/\psi') + \bar{p}$ , are mainly produced via  $IP - \gamma$  fusion. The STARLight MC is used to simulate the photoproduction of the  $J/\psi$  and the  $\psi'$ .

<sup>5</sup>The offline cuts applied to the muon-pair data are the same as those applied in the  $e^+e^-$  case: there should be no activity in the event in the region  $|\eta| < 7.4$ , and the final state must have two identified muons of  $P_T > 1.4$  GeV/c within  $|\eta| < 0.6$ .

A  $J/\psi$  in the final state can arise from exclusive  $\chi_c^0$  production,  $p\bar{p} \rightarrow p + (\chi_c^0) + \bar{p}$  with  $\chi_c^0 \rightarrow J/\psi(J/\psi \rightarrow \mu^+\mu^-) + \gamma$ . The photon in the  $\chi_c^0$  decay is soft and consequently may not be reconstructed and form a “background” to exclusive  $J/\psi$  production via  $\mathbb{P} - \gamma$  fusion. The  $\chi_c^0$  contributes to the exclusive  $J/\psi$  peak when the soft photon from its decay survives the exclusivity cut. By fitting the shapes of the  $E_T$  and  $\Delta\phi$  distributions of the di-muon pair of the events in the  $J/\psi$  peak of the data with MC generated distributions of  $J/\psi$  from photoproduction and  $\chi_c^0$  production, CDF II estimates the  $\chi_c^0$  contribution to the exclusive  $J/\psi$  photoproduction peak to be  $\approx 10\%$ .

**Higher Mass Exclusive  $\mu^+\mu^-$  Production.** The basis of the study of high exclusive muon pairs is somewhat different in that it does not rely on the “standard” exclusivity cuts applied to the low mass data. In this case, one looks for muon pairs that form a vertex with no additional tracks. It is also required that the muons be consistent with  $\Delta\phi \approx 0$  and with  $P_T$ -sum approximately zero. For  $890 \text{ pb}^{-1}$  of data (2.3M events), with  $\Delta\phi > 120^\circ$  and a  $P_T$ -sum of the two muon tracks less than  $7 \text{ GeV}/c$ , the mass plot shown in Fig. 3 was obtained. One can clearly discern the  $\Upsilon(1S)$  and  $\Upsilon(2)$  peaks in this plot. The high mass exclusive muon pair data, with enhanced statistics, is currently under study.

### 3 Diffractive W/Z Production

Studies of diffractively produced W/Z boson are important for understanding the structure of the Pomeron. The production of intermediate vector bosons is due to the annihilation of quark-antiquark pairs and thus is a probe of the quark content of the Pomeron. In leading order, the W/Z is produced by a quark in the Pomeron, while production by a gluon is suppressed by a factor of  $\alpha_S$  and can be distinguished from quark production by an associated jet [20]. Diffractive dijet production at the Tevatron was found to be suppressed by a factor of  $\mathcal{O}(10)$  compared to expectations from the Diffractive Structure Function (DSF) extracted from diffractive deep inelastic scattering (DDIS) at the DESY  $ep$  Collider HERA. A more direct comparison could be made by measuring the DSF in diffractive  $W$  production at the Tevatron, which is dominated by a  $q\bar{q}$  exchange, as in DDIS. In Run I, only the overall diffractive  $W$  fraction was measured by CDF [20]. In Run II, both the  $W$  and  $Z$  diffractive fractions and the DSF are measured.

The CDF Run II analysis is based on events with RPS tracking from a data sample of  $\sim 0.6 \text{ fb}^{-1}$ . In addition to the  $W/Z$  selection requirements<sup>6</sup>, a hit in the RPS trigger counters and a RPS reconstructed track with  $0.03 < \xi < 0.1$  and  $|t| < 1$  are required. A novel feature of the analysis is the determination of the full kinematics of the  $W \rightarrow e\nu/\mu\nu$  decay using the neutrino  $E_T^\nu$  obtained from the missing  $E_T$ , as usual, and  $\eta_\nu$  from the formula  $\xi^{\text{RPS}} - \xi^{\text{cal}} = (E_T/\sqrt{s}) \exp[-\eta_\nu]$ , where  $\xi^{\text{cal}} = \sum_{\text{towers}} (E_T/\sqrt{s}) \exp[-\eta]$ . The extracted value of  $M_W^{\text{exp}} = 80.9 \pm 0.7 \text{ GeV}$  is in good agreement with the world average  $W$  mass of  $M_W^{\text{PDG}} = 80.403 \pm 0.029 \text{ GeV}$  [21]. After applying corrections accounting for the RPS acceptance,  $A_{\text{RPS}} \approx 80\%$ , the trigger counter efficiency,  $\epsilon_{\text{RPS}^{\text{trig}}} \approx 75\%$ , the track reconstruction

<sup>6</sup>The CDF  $W/Z$  selection requirements are:  $E_T^{e,\mu} > 25 \text{ GeV}$ ,  $40 < M_T^W < 120 \text{ GeV}$ ,  $66 < M^Z < 116 \text{ GeV}$ , and vertex  $z$ -coordinate  $|z_{vtx}| < 60 \text{ cm}$ . In the  $W$  case, the requirement of  $\xi^{\text{RPS}} > \xi^{\text{cal}}$  is very effective in removing the overlap events in the region of  $\xi^{\text{cal}} < 0.1$ , while a mass cut of  $50 < M_W < 120 \text{ GeV}$  has the same effect. In the  $Z$  case, we use the  $\xi^{\text{cal}}$  distribution of all  $Z$  events normalized to the RP-track distribution in the region of  $-1 < \log \xi^{\text{cal}} < -0.4$  ( $0.1 < \xi^{\text{cal}} < 0.4$ ) to obtain the ND background in the diffractive region of  $\xi^{\text{cal}} < 0.1$ .

efficiency,  $\epsilon_{\text{RPStrk}} \approx 87\%$ , multiplying by 2 to include production by  $p\bar{p} \rightarrow W/Z + p$ , and correcting the ND event number for the effect of overlaps due to multiple interactions by multiplying by the factor  $f_{1-\text{int}} \approx 0.25$ , the diffractive fraction of  $W/Z$  events was obtained as  $R_{W/Z} = 2 \cdot N_{SD}/A_{\text{RPS}}/\epsilon_{\text{RPStrig}}/\epsilon_{\text{RPStrk}}/(N_{\text{ND}} \cdot f_{1-\text{int}})$ :

$$R_W(0.03 < \xi < 0.10, |t| < 0.1) = [0.97 \pm 0.05 (\text{stat}) \pm 0.11 (\text{syst})]\% \quad (1)$$

$$R_Z(0.03 < \xi < 0.10, |t| < 0.1) = [0.85 \pm 0.20 (\text{stat}) \pm 0.11 (\text{syst})]\% \quad (2)$$

The  $R_W$  value is consistent with the Run I result of  $R_W(0.03 < \xi < 0.10, |t| < 0.1) = [0.97 \pm 0.47]$  obtained from the published value of  $R^W(\xi < 0.1) = [0.15 \pm 0.51 (\text{stat}) \pm 0.20 (\text{syst})]\%$  [20] multiplied by a factor of 0.85 that accounts for the reduced  $(\xi-t)$  range in Run II.

## 4 Conclusion

We present recent results on exclusive central production of di-jets, di-leptons, and di-photons reported by the CDF II collaboration, obtained from Run II data collected at the Tevatron  $p\bar{p}$  collider at  $\sqrt{s} = 1.96$  TeV. The results are compared with theoretical expectations, and implications for the possible observation of exclusive Higgs boson production and other interesting new physics processes at the Large Hadron Collider are discussed.

## References

- [1] M. Gallinaro (for the CDF Collaboration), arXiv:hep-ph/0407255, p. 1 (2004).
- [2] K. Goulios *et al.*, Nucl. Instrum. Meth. **A 518**, 42-44 (2004).
- [3] T. Affolder *et al.*, Phys. Rev. Lett. **84**, 5043 (2000).
- [4] K. Goulios, in Proceedings of *La Thuile 2004*, arXiv:hep-ph/0407035 .
- [5] V. A. Khoze, A. Kaidalov, A. D. Martin, M. G. Ryskin, W. J. Stirling, World Scientific (Gribov Memorial Volume), arXiv:hep-ph/0507040, p. 1 (2005).
- [6] V. A. Khoze, A. D. Martin, M. G. Ryskin, Eur. Phys. J. **C 14**, 525 (2000).
- [7] V.A. Khoze, A.D. Martin, M.G. Ryskin, W.J. Stirling, Eur. Phys. J. **C 38**, 475 (2005).
- [8] V.A. Khoze, A.D. Martin, M.G. Ryskin and W.J. Stirling, Eur. Phys. J. **C 35**, 211 (2004).
- [9] A. Abulencia *et al.*, Phys.Rev.Lett. **98**, 112001 (2007).
- [10] K. Piotrkowski, Phys. Rev. **D 63**, 071502 (2001).
- [11] M. Albrow *et al.*, arXiv:0806.0302 [hep-ex], FERMILAB-FN-0825-E, p. 1 (2008).
- [12] T. Aaltonen *et al.*, Phys. Rev. **D 77**, 052004 (2008).
- [13] B. Cox and J. Forshaw, Compu. Phys. Commun. **144**, 104 (2002).

- [14] J. Monk and A. Pilkington, *Comput. Phys. Commun.* **175**, 232 (2006).
- [15] S. P Baranov, O. Duenger, H. Shooshtari, J. A. M. Vermaseren, Hamburg 1991, in *Proceedings of Physics at HERA* **3**, 1478 (1991).
- [16] E. Gerchtein and M. Paulini, *Computing in High Energy and Nuclear Physics*, p. 1 (2003).
- [17] M. Albrow *et al.*, arXiv:hep-ex/0511057, p. 1 (2005).
- [18] T. Aaltonen *et al.*, *Phys. Rev. Lett.* **99**, 242002 (2007).
- [19] S. Klein and J. Nystrand, *Phys. Rev. C* **60**, 014903 (1999).
- [20] K. Abe *et al.*, *Phys. Rev. Lett.* **78**, 2698 (1997).
- [21] W.-M. Yao *et al.*, *Journ. Phys. G* **33**, 1 (2006).

# Survival probability in diffractive dijet photoproduction

Michael Klasen<sup>1</sup> and Gustav Kramer<sup>2</sup>

<sup>1</sup> Laboratoire de Physique Subatomique et de Cosmologie, Université Joseph Fourier / CNRS-IN2P3 / INPG, 53 Avenue des Martyrs, F-38026 Grenoble, France

<sup>2</sup> II. Institut für Theoretische Physik, Universität Hamburg, Luruper Chaussee 149, D-22761 Hamburg, Germany

## Abstract

We confront the latest H1 and ZEUS data on diffractive dijet photoproduction with next-to-leading order QCD predictions in order to determine whether a rapidity gap survival probability of less than one is supported by the data. We find evidence for this hypothesis when assuming global factorization breaking for both the direct and resolved photon contributions, in which case the survival probability would have to be  $E_T^{jet}$ -dependent, and for the resolved or in addition the related direct initial-state singular contribution only, where it would be independent of  $E_T^{jet}$ .

## 1 Introduction

The central problem for hard diffractive scattering processes, characterized by a large rapidity gap in high-energy collisions, is whether they can be factorized into non-perturbative diffractive parton density functions (PDFs) of a colorless object (e.g. a pomeron) and perturbatively calculable partonic cross sections. This concept is believed to hold for the scattering of point-like electromagnetic probes off a hadronic target, such as deep-inelastic scattering (DIS) or direct photoproduction [1], but has been shown to fail for purely hadronic collisions [1, 2]. Factorization is thus expected to fail also in resolved photoproduction, where the photon first dissolves into partonic constituents, before these scatter off the hadronic target. The separation of the two types of photoproduction processes is, however, a leading order (LO) concept. At next-to-leading order (NLO) of perturbative QCD, they are closely connected by an initial-state (IS) singularity originating from the splitting  $\gamma \rightarrow q\bar{q}$  (for a review see [3]), which may play a role in the way factorization breaks down in diffractive photoproduction [4]. The breaking of the resolved photoproduction component only leads to a dependence of the predicted cross section on the factorization scale  $M_\gamma$  [4]. Since this  $M_\gamma$ -dependence is unphysical, it must be remedied also for the factorization breaking of the resolved part of the cross section, e.g. by modifying the IS singular direct part. A proposal how to achieve this has been worked out in [4] and has been reviewed already in the proceedings of the workshop on *HERA and the LHC* of 2004-2005 [5] (see also [6]). Since from a theoretical point of view only the suppression of the resolved or in addition the IS singular direct component [4] is viable, it is an interesting question whether the diffractive dijet photoproduction data show breaking of the factorization, how large the suppression in comparison to no breaking will be, and whether the breaking occurs in all components or just in the resolved plus direct IS component. The value of the suppression factor or survival probability can then be compared to theoretical predictions [7] and to the survival probability



observed in jet production in  $p\bar{p}$  collisions at the Tevatron [2] and will be of interest for similar diffractive processes at the LHC.

Since 2005 no further developments occurred on the theoretical side. On the experimental side, however, the final diffractive PDFs (DPDFs), which have been determined from the inclusive measurements of the diffractive structure function  $F_2^D$  by the H1 collaboration, have been published [8]. Also both collaborations at HERA, H1 and ZEUS, have now published their final experimental data of the cross sections for diffractive dijet photoproduction [9, 10]. Whereas H1 confirm in [9] their earlier findings based on the analysis of preliminary data and preliminary DPDFs, the authors of the ZEUS analysis [10] reached somewhat different conclusions from their analysis. Specifically, the H1 collaboration [9] obtained a global suppression of their measured cross sections as compared to the NLO calculations. In this comparison [9], the survival probability is  $R = 0.5$ , independent of the DPDFs fit used, i.e. fit A or B in Ref. [8]. In addition they concluded that the assumption that the direct cross section obeys factorization is strongly disfavored by their analysis. The ZEUS collaboration, on the other hand, concluded from their analysis [10], that, within the large uncertainties of the NLO calculations, their data are compatible with the QCD calculations, i.e. that no suppression would be present.

Due to these somewhat inconsistent results we made a new effort [11] to analyze the H1 [9] and the ZEUS [10] data, following more or less the same strategy as in our earlier work [12, 13] on the basis of the NLO program of [12, 13] and the new DPDFs sets of Ref. [8]. The H1 and the ZEUS dijet data cannot be compared directly, since they have different kinematic cuts. In particular, in the H1 measurements [9]  $E_T^{jet1(2)} > 5$  (4) GeV and  $x_{\mathbb{P}} < 0.03$ , and in the ZEUS measurements [10]  $E_T^{jet1(2)} > 7.5$  (6.5) GeV and  $x_{\mathbb{P}} < 0.025$  (these and all other variables used in this review are defined in [11–13] and in the corresponding experimental contribution in these proceedings). It is clear that in order to establish a global suppression, i.e. an equal suppression of the direct and the resolved cross section, the absolute normalization and not so much the shape of the measured cross section is very important. This normalization depends on the applied kinematic cuts. Of course, the same cuts must be applied to the NLO cross section calculation. In case of a resolved suppression only, the suppression depends on the normalization of the cross sections, but also on the shape of some (in particular the  $x_{\gamma}^{obs}$ ,  $E_T^{jet1}$ ,  $M_{12}$ , and  $\bar{\eta}^{jets}$ ) distributions, and will automatically be smaller at large  $E_T^{jet1}$  [3]. Distributions in  $x_{\mathbb{P}}$  and  $y$  (or  $W$ ) are not sensitive to the suppression mechanism. The distribution in  $z_{\mathbb{P}}$ , on the other hand, is sensitive to the functional behavior of the DPDFs, in particular of the gluon at large fractional momenta.

In the meantime, the H1 collaboration made an effort to put more light into the somewhat contradictory conclusions of the H1 [9] and ZEUS [10] collaborations by performing a new analysis of their data, now with increased luminosity, with the same kinematic cuts as in [9], i.e. the low- $E_T^{jet1}$  cut, and the high- $E_T^{jet1}$  cut as in the ZEUS analysis [10]. The results have been presented at DIS 2008 [14] and will be published soon. We have performed a new study of these H1 [14] and ZEUS data [10] to show more clearly the differences between the three data sets [15]. In this contribution we shall show a selection of these comparisons. The emphasis in these comparisons will be, how large the survival probability of the diffractive dijet cross section will be globally and whether the model with resolved suppression only will also describe the data in a satisfactory way. In section 2 we show the comparison with the H1 data [14] and in section

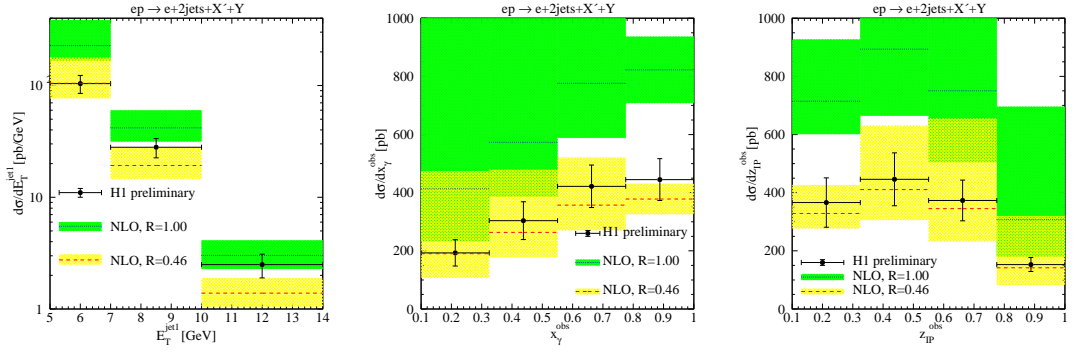


Fig. 1: Differential cross sections for diffractive dijet photoproduction as measured by H1 with low- $E_T^{jet}$  cuts and compared to NLO QCD without ( $R = 1$ ) and with ( $R = 0.46$ ) global suppression (color online).

3 with the ZEUS data [10]. Section 4 contains our conclusions.

## 2 Comparison with recent H1 data

The recent H1 data for diffractive photoproduction of dijets [14] have several advantages as compared to the earlier H1 [9] and ZEUS [10] analyses. First, the integrated luminosity is three times higher than in the previous H1 analysis [9] comparable to the luminosity in the ZEUS analysis [10]. Second, H1 took data with low- $E_T^{jet}$  and high- $E_T^{jet}$  cuts, which allows for a comparison of [9] with [10]. The exact two kinematic ranges are given in [14]. The ranges for the low- $E_T^{jet}$  cuts are as in the previous H1 analysis [9] and for the high- $E_T^{jet}$  cuts are chosen as in the ZEUS analysis with two exceptions. In the ZEUS analysis the maximal cut on  $Q^2$  is larger and the data are taken in an extended  $y$ -range. The definition of the various variables can be found in the H1 and ZEUS publications [9, 10]. Very important is the cut on  $x_P$ . It is kept small in both analyses in order for the pomeron exchange to be dominant. In the experimental analysis as well as in the NLO calculations, jets are defined with the inclusive  $k_T$ -cluster algorithm [16, 17] in the laboratory frame. At least two jets are required with the respective cuts on  $E_T^{jet1}$  and  $E_T^{jet2}$ , where  $E_T^{jet1(2)}$  refers to the jet with the largest (second largest)  $E_T^{jet}$ .

Before we confront the calculated cross sections with the experimental data, we correct them for hadronization effects. The hadronization corrections are calculated by means of the LO RAPGAP Monte Carlo generator. The factors for the transformation of jets made up of stable hadrons to parton jets were supplied by the H1 collaboration [14]. Our calculations are done with the ‘H1 2006 fit B’ [8] DPDFs, since they give smaller diffractive dijet cross sections than with the ‘H1 2006 fit A’. We then take  $n_f = 4$  with  $\Lambda_{\overline{\text{MS}}}^{(4)} = 0.347$  GeV, which corresponds to the value used in the DPDFs ‘H1 2006 fit A, B’ [8]. For the photon PDFs we have chosen the NLO GRV parameterization transformed to the  $\overline{\text{MS}}$  scheme [18].

As it is clear from the discussion of the various preliminary analyses of the H1 and ZEUS collaborations, there are two questions which we would like to answer from the comparison with the recent H1 and the ZEUS data. The first question is whether a suppression factor, which differs substantially from one, is needed to describe the data. The second question is whether the data

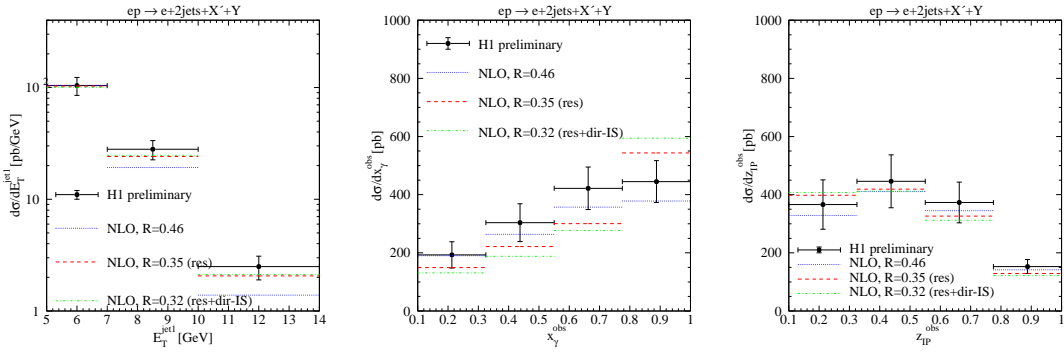


Fig. 2: Differential cross sections for diffractive dijet photoproduction as measured by H1 with low- $E_T^{jet}$  cuts and compared to NLO QCD with global, resolved, and resolved/direct-IS suppression.

are also consistent with a suppression factor applied to the resolved cross section only. For both suppression models it is also of interest whether the resulting suppression factors are universal, i.e. whether they are independent of the kinematic variables of the process. To give an answer to these two questions we calculated first the cross sections with no suppression factor ( $R = 1$  in the following figures) with a theoretical error obtained from varying the common scale of renormalization and factorization by factors of 0.5 and 2 around the default value (highest  $E_T^{jet}$ ). In a second step we show the results for the same differential cross sections with a global suppression factor, adjusted to  $d\sigma/dE_T^{jet1}$  at the smallest  $E_T^{jet1}$ -bin. As in the experimental analysis [14], we consider the differential cross sections in the variables  $x_\gamma^{obs}$ ,  $z_{IP}^{obs}$ ,  $\log_{10}(x_{IP})$ ,  $E_T^{jet1}$ ,  $M_X$ ,  $M_{12}$ ,  $\bar{\eta}^{jets}$ ,  $|\Delta\eta^{jets}|$  and  $W$  [15]. Here we show only a selection, i.e. the cross sections as a function of  $E_T^{jet1}$ ,  $x_\gamma^{obs}$  and  $z_{IP}^{obs}$ . For the low- $E_T^{jet}$  cuts, the resulting suppression factor is  $R = 0.46 \pm 0.14$ , which gives in the lowest  $E_T^{jet1}$ -bin a cross section equal to the experimental data point. The error comes from the combined experimental statistical and systematic error. The theoretical error due to the scale variation is taken into account when comparing to the three distributions. The results of this comparison are shown in Figs. 1a-c. With the exception of Fig. 1a, where the comparison of  $d\sigma/dE_T^{jet1}$  is shown, the other two plots are such that the data points lie outside the error band based on the scale variation for the unsuppressed case. However, the predictions with suppression  $R = 0.46$  agree nicely with the data inside the error bands from the scale variation. Most of the data points even agree with the  $R = 0.46$  predictions inside the much smaller experimental errors. In  $d\sigma/dE_T^{jet1}$  (see Fig. 1a) the predictions for the second and third bins lie outside the data points with their errors. For  $R = 1$  and  $R = 0.46$  this cross sections falls off stronger with increasing  $E_T^{jet1}$  than the data, the normalization being of course about two times larger for  $R = 1$ . In particular, the third data point agrees with the  $R = 1$  prediction. This means that the suppression decreases with increasing  $E_T^{jet1}$  (see also Fig. 5 below). This behavior was already apparent when we analyzed the first preliminary H1 data [12, 13]. Such a behavior points in the direction that a suppression of the resolved cross section only would give better agreement with the data, as we shall see below. The survival probability  $R = 0.46 \pm 0.14$  agrees with the result in [14], which quotes  $R = 0.51 \pm 0.01$  (stat.)  $\pm 0.10$  (syst.), determined by fitting the integrated cross section. From our comparison we conclude that the low- $E_T^{jet}$  data show a global

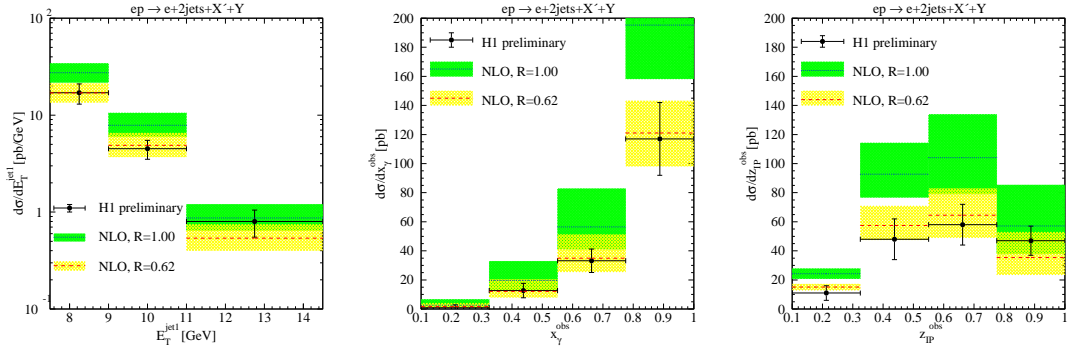


Fig. 3: Differential cross sections for diffractive dijet photoproduction as measured by H1 with high- $E_T^{jet}$  cuts and compared to NLO QCD without ( $R = 1$ ) and with ( $R = 0.62$ ) global suppression (color online).

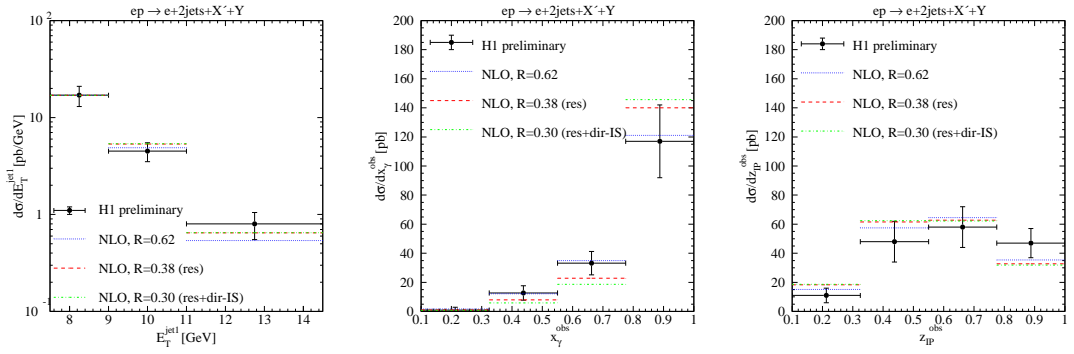


Fig. 4: Differential cross sections for diffractive dijet photoproduction as measured by H1 with high- $E_T^{jet}$  cuts and compared to NLO QCD with global, resolved, and resolved/direct-IS suppression.

suppression of the order of two in complete agreement with the results [12, 13] and [9] based on earlier preliminary and final H1 data [9].

Next we want to answer the second question, whether the data could be consistent with a suppression of the resolved component only. For this purpose we have calculated the cross sections in two additional versions: (i) suppression of the resolved cross section and (ii) suppression of the resolved cross section plus the NLO direct part which depends on the factorization scale at the photon vertex [4]. The suppression factors needed for the two versions will, of course, be different. We determine them again by fitting the measured  $d\sigma/dE_T^{jet1}$  for the lowest  $E_T^{jet1}$ -bin (see Fig. 2a). Then, the suppression factor for version (i) is  $R = 0.35$  (denoted *res* in the figures), and for version (ii) it is  $R = 0.32$  (denoted *res+dir-IS*). The results for  $d\sigma/dE_T^{jet1}$ ,  $d\sigma/dx_\gamma^{obs}$  and  $d\sigma/dz_{IP}^{obs}$  are shown in Figs. 2a-c, while the six other distributions can be found in [15]. We also show the global (direct and resolved) suppression prediction with  $R = 0.46$  already shown in Figs. 1a-c. For the cross section as a function of  $z_{IP}^{obs}$ , the agreement with the global suppression ( $R = 0.46$ ) and the resolved suppression ( $R = 0.35$  or  $R = 0.32$ ) is comparable. For  $d\sigma/dE_T^{jet1}$ , the agreement improves considerably for the resolved suppression only

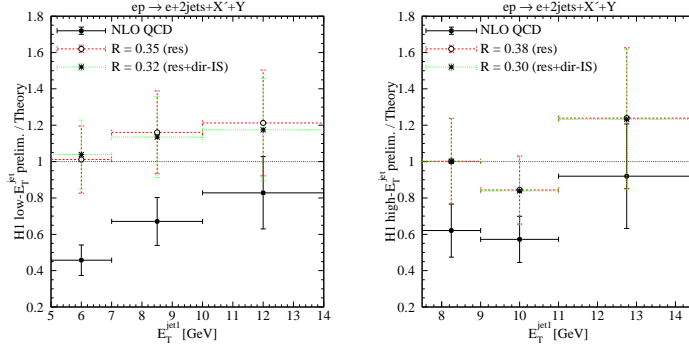


Fig. 5: Ratio of the  $E_T^{jet1}$ -distribution as measured by H1 with low- $E_T^{jet}$  (left) and high- $E_T^{jet}$  cuts (right) to the NLO QCD prediction without (full), with resolved-only (dashed), and with additional direct IS suppression (dotted).

(note the logarithmic scale in Fig. 2a). The global suppression factor could, of course, be  $E_T$ -dependent, although we see no theoretical reason for such a dependence. For  $d\sigma/dx_\gamma^{obs}$ , which is usually considered as the characteristic distribution for distinguishing global versus resolved suppression, the agreement with resolved suppression does not improve. Unfortunately, this cross section has the largest hadronic corrections of the order of  $(25 - 30)\%$  [14]. Second, also for the usual photoproduction of dijets the comparison between data and theoretical results has similar problems in the large  $x_\gamma^{obs}$ -bin [19], although the  $E_T^{jet}$ -cut is much larger there. In total, we are tempted to conclude from the comparisons in Figs. 2a-c that the predictions with a resolved-only (or resolved+direct-IS) suppression are consistent with the new low- $E_T^{jet}$  H1 data [14] and the survival probability is  $R = 0.35$  (only resolved suppression) and  $R = 0.32$  (resolved plus direct-IS suppression), respectively.

The same comparison of the high- $E_T^{jet}$  data of H1 [14] with the various theoretical predictions is shown in the following figures. The global suppression factor is obtained again from a fit to the smallest  $E_T^{jet1}$ -bin. It is equal to  $R = 0.62 \pm 0.16$ , again in agreement with the H1 result  $R = 0.62 \pm 0.03$  (stat.)  $\pm 0.14$  (syst.) [14]. The same cross sections as for the low- $E_T^{jet}$  comparison are shown in Figs. 3a-c for the two cases  $R = 1$  (no suppression) and  $R = 0.62$  (global suppression), while the six others can again be found in [15]. As before with the exception of  $d\sigma/dE_T^{jet1}$  and  $d\sigma/dM_{12}$  (not shown), most of the data points lie outside the  $R = 1$  results with their error bands and agree with the suppressed prediction with  $R = 0.62$  inside the respective errors. However, compared to the results in Figs. 1a-c the distinction between the  $R = 1$  band and the  $R = 0.62$  band and the data is somewhat less pronounced, which is due to the larger suppression factor. We also tested the prediction for the resolved (resolved+direct-IS) suppression, which is shown in Figs. 4a-c. The suppression factor fitted to the smallest bin came out as  $R = 0.38$  (res) and  $R = 0.30$  (res+dir-IS), which are almost equal to the corresponding suppression factors derived from the low- $E_T^{jet}$  data. In most of the comparisons it is hard to observe any preference for the global against the pure resolved (resolved plus direct-IS) suppression. We remark that the suppression factor for the global suppression is increased by 35%, if we go from the low- $E_T^{jet}$  to the high- $E_T^{jet}$  data, whereas for the resolved suppression this increase is only 9%. Under the assumption that the suppression factor should not depend on  $E_T^{jet1}$ , we would

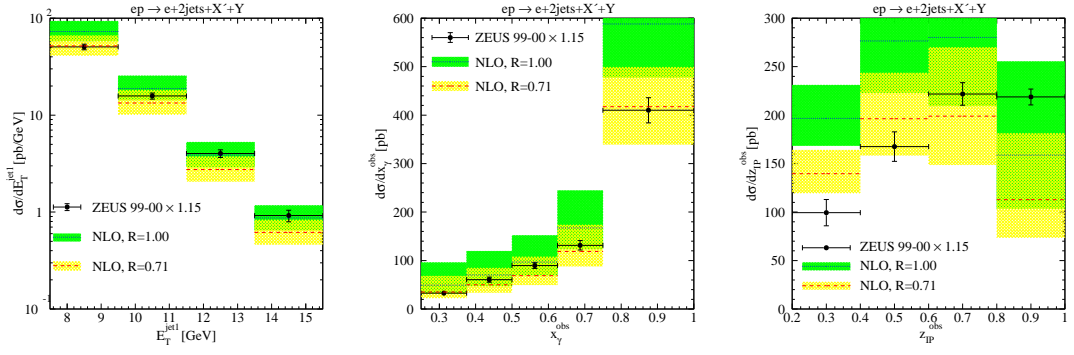


Fig. 6: Differential cross sections for diffractive dijet photoproduction as measured by ZEUS and compared to NLO QCD without ( $R = 1$ ) and with ( $R = 0.71$ ) global suppression (color online).

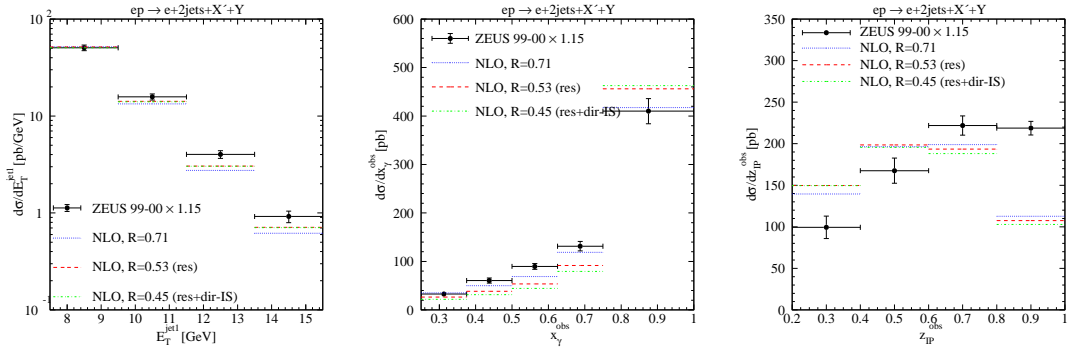


Fig. 7: Differential cross sections for diffractive dijet photoproduction as measured by ZEUS and compared to NLO QCD with global, resolved, and resolved/direct-IS suppression.

conclude that the resolved suppression would be preferred, as can also be seen from Fig. 5. A global suppression is definitely observed also in the high- $E_T^{jet}$  data and the version with resolved suppression explains the data almost as well as with the global suppression.

In Fig. 5 we show the ratio of the  $E_T^{jet1}$ -distribution as measured by H1 to the NLO QCD prediction without (full), with resolved-only (dashed), and with additional direct IS suppression (dotted). Within the experimental errors, obviously only the former, but not the latter are  $E_T^{jet}$ -dependent.

### 3 Comparison with ZEUS data

In this section we shall compare our predictions with the final analysis of the ZEUS data, which was published this year [10], in order to see whether they are consistent with the large- $E_T^{jet}$  data of H1. The kinematic cuts [10] are almost the same as in the high- $E_T^{jet}$  H1 measurements. The only major difference to the H1 cuts is the larger range in the variable  $y$ . Therefore the ZEUS cross sections will be larger than the corresponding H1 cross sections. The constraint on  $M_Y$  is

not explicitly given in the ZEUS publication [10]. They give the cross section for the case that the diffractive final state consists only of the proton. For this they correct their measured cross section by subtracting in all bins the estimated contribution of a proton-dissociative background of 16%. When comparing to the theoretical predictions they multiply the cross section with the factor 0.87 in order to correct for the proton-dissociative contributions, which are contained in the DPDFs ‘H1 2006 fit A’ and ‘H1 2006 fit B’ by requiring  $M_Y < 1.6$  GeV. We do not follow this procedure. Instead we leave the theoretical cross sections unchanged, i.e. they contain a proton-dissociative contribution with  $M_Y < 1.6$  GeV and multiply the ZEUS cross sections by 1.15 to include the proton-dissociative contribution. This means that the so multiplied ZEUS cross sections have the same proton dissociative contribution as is in the DPDF fits of H1 [8]. Since the ZEUS collaboration did measurements only for the high- $E_T^{jet}$  cuts,  $E_T^{jet(2)} > 7.5$  (6.5) GeV, we can only compare to those. In this comparison we shall follow the same strategy as before. We first compared to the predictions with no suppression ( $R = 1$ ) and then determine a suppression factor by fitting  $d\sigma/dE_T^{jet1}$  to the smallest  $E_T^{jet1}$ -bin. Then we compared to the cross sections as a function of the seven observables  $x_\gamma^{obs}$ ,  $z_P^{obs}$ ,  $x_P$ ,  $E_T^{jet1}$ ,  $y$ ,  $M_X$  and  $\eta^{jet1}$  instead of the nine variables in the H1 analysis. The distribution in  $y$  is equivalent to the  $W$ -distribution in [14]. The theoretical predictions for these differential cross sections with no suppression factor ( $R = 1$ ) are shown in Figs. 6a-g of [11], together with their scale errors and compared to the ZEUS data points, and a selection is shown in Fig. 6. Except for the  $x_\gamma^{obs}$ - and  $E_T^{jet1}$ -distributions, most of the data points lie outside the theoretical error bands for  $R = 1$ . In particular, in Figs. 6b, c, e, f and g, most of the points lie outside. This means that most of the data points disagree with the unsuppressed prediction. Next, we determine the suppression factor from the measured  $d\sigma/dE_T^{jet1}$  at the lowest  $E_T^{jet1}$ -bin,  $7.5 \text{ GeV} < E_T^{jet1} < 9.5 \text{ GeV}$ , and obtain  $R = 0.71$ . This factor is larger by a factor of 1.15 than the suppression factor from the analysis of the high- $E_T^{jet}$  data from H1. Curiously, this factor is exactly equal to the correction factor we had to apply to restore the dissociative proton contribution. Taking the total experimental error of  $\pm 7\%$  from the experimental cross section  $d\sigma/dE_T^{jet1}$  in the first bin into account, the ZEUS suppression factor is  $0.71 \pm 0.05$  to be compared to  $0.62 \pm 0.14$  in the H1 analysis [14], so that both suppression factors agree inside the experimental errors.

If we now check how the predictions for  $R = 0.71$  compare to the data points inside the theoretical errors, we observe from Figs. 6a-g of Ref. [11] that, with the exception of  $d\sigma/dz_P^{obs}$  and  $d\sigma/dE_T^{jet1}$ , most of the data points agree with the predictions. This is quite consistent with the H1 analysis (see above) and leads to the conclusion that also the ZEUS data agree much better with the suppressed predictions than with the unsuppressed prediction. In particular, the global suppression factor agrees with the global suppression factor obtained from the analysis of the H1 data inside the experimental error.

Similarly as in the previous section we compared the ZEUS data also with the assumption that the suppression results only from the resolved cross section. Here, we consider again (i) only resolved suppression (res) and (ii) resolved plus direct suppression of the initial-state singular part (res+dir-IS). For these two models we obtain the suppression factors  $R = 0.53$  and  $R = 0.45$ , respectively, where these suppression factors are again obtained by fitting the data point at the first bin of  $d\sigma/dE_T^{jet1}$ . The comparison to the global suppression with  $R = 0.71$  and to the data is shown in Figs. 7a-g of [11] and a selection in Fig. 7. In general, we observe that the difference

between global suppression and resolved suppression is small, i.e. the data points agree with the resolved suppression as well as with the global suppression.

## 4 Conclusion

In conclusion, we found that most of the data points of diffractive dijet photoproduction in the latest H1 analyses with low- and high- $E_T^{jet}$  cuts and in the final ZEUS analysis with the same high- $E_T^{jet}$  cuts disagree with NLO QCD predictions within experimental and theoretical errors. When global factorization breaking is assumed in both the direct and resolved contributions, the resulting suppression factor would have to be  $E_T^{jet}$ -dependent, although we see no theoretical motivation for this assumption. Suppressing only the resolved or in addition the direct initial-state singular contribution by about a factor of three, as motivated by the proof of factorization in point-like photon-hadron scattering and predicted by absorptive models [7], the agreement between theory and data is at least as good as for global suppression, and no  $E_T^{jet}$ -dependence of the survival probability is needed.

## References

- [1] Collins, J.C., Phys. Rev. **D57**, 3051 (1998).
- [2] Affolder, A.A. *et al.*, Phys. Rev. Lett. **84**, 5043 (2000).
- [3] Klasen, M., Rev. Mod. Phys. **74**, 1221 (2002).
- [4] Klasen, M. and Kramer, G., J. Phys. **G31**, 1391 (2005).
- [5] Bruni, A., Klasen, M., Kramer, G., and Schaetzel, S. Prepared for the Workshop on the Implications of HERA for LHC Physics, CERN, Geneva, Switzerland, 26-27 Mar 2004.
- [6] Klasen, M. and Kramer, G., AIP Conf. Proc. **792**, 444 (2005).
- [7] Kaidalov, A.B., Khoze, V.A., Martin, A.D., and Ryskin, M.G., Phys. Lett. **B567**, 61 (2003).
- [8] Aktas, A. *et al.*, Eur. Phys. J. **C48**, 715 (2006).
- [9] Aktas, A. *et al.*, Eur. Phys. J. **C51**, 549 (2007).
- [10] Chekanov, S. *et al.*, Eur. Phys. J. **C55**, 177 (2008).
- [11] Klasen, M. and Kramer, G., Mod. Phys. Lett. **A23**, 1885 (2008).
- [12] Klasen, M. and Kramer, G. Prepared for 12th Int. Workshop on Deep Inelastic Scattering, Strbske Pleso, Slovakia, 14-18 Apr 2004.
- [13] Klasen, M. and Kramer, G., Eur. Phys. J. **C38**, 93 (2004).
- [14] Aktas, A. *et al.* Prepared for 16th Int. Workshop on Deep Inelastic Scattering, London, England, 7-11 Apr 2008.



- [15] Klasen, M. and Kramer, G. DESY 08-109, LPSC 08-113, to be published.
- [16] Ellis, S.D. and Soper, D.E., Phys. Rev. **D48**, 3160 (1993).
- [17] Catani, S., Dokshitzer, Y.L., Seymour, M.H., and Webber, B. R., Nucl. Phys. **B406**, 187 (1993).
- [18] Glueck, M., Reya, E., and Vogt, A., Phys. Rev. **D46**, 1973 (1992).
- [19] Aktas, A. *et al.*, Phys. Lett. **B639**, 21 (2006).

# Fracture Functions at HERA and LHC

*Federico Alberto Ceccopieri, Luca Trentadue*  
Dipartimento di Fisica, Università degli Studi di Parma  
INFN Gruppo Collegato di Parma, Italy

## Abstract

Developments of the fracture functions formalism in the context of DIS jet cross-sections and Semi-Inclusive Drell-Yan process at hadron colliders are briefly presented.

Fracture functions were introduced in Ref. [1] in order to give a QCD-based description of semi-inclusive Deep Inelastic Scattering in the target fragmentation region. The first analyses of HERA data [2] revealed a non-negligible contributions to the DIS cross-sections of events characterized by absence of hadronic activity in the remnant direction. Recent analyses of diffractive data collected by H1 and ZEUS collaborations have now confirmed substantial contributions of perturbative QCD effects in diffractive DIS cross-sections [3]. This experimental evidence strengthens the idea itself of fracture functions. These non-perturbative distributions, hereafter indicated by  $M_{h/P}^i(x, z, Q^2)$ , give the conditional probability of finding at a given scale  $Q^2$  a parton  $i$  with momentum fraction  $x$  of the incoming hadron momentum  $P$  while a hadron  $h$ , with momentum fraction  $z$ , is detected in the target fragmentation region of  $P$ . In Ref. [4] it was shown within a fixed order  $\mathcal{O}(\alpha_s)$  calculation that the additional collinear singularities occurring in the remnant direction can be properly renormalized only introducing fracture functions. An all-order proof of collinear and soft singularities factorization into  $M_{h/P}^i(x, z, Q^2)$  was finally given in Refs. [5] and [6], respectively. This theoretical background offers the basis for an accurate analysis of diffractive data and the possibility to fully exploit factorization in order to extract diffractive parton distributions, *i.e.* fracture functions. In this brief contribution we will report on recent developments in this topic. In particular we will focus on the extension of fracture functions in the context of DIS jet cross-section and their possible applications to hadronic collisions.

As is well known, hadrons resulting from a hard interaction are often collimated in a definite portion of momentum space. Hadron jets are the highlighting signature of the dominant collinear branching of pQCD dynamics. For this reason jet cross-sections are the natural and, possibly, the most effective representation of hadronic final state. While jet cross-sections with a given, in general low, number of partons in the final state are calculable within pQCD, a description of the beam-jet in terms of pQCD is however precluded by its intrinsic soft and kinematical nature. It results from the fragmentation of the spectator partons of the hadron remnants plus, eventually, semi-hard radiation coming from the evolution of the active parton at low momentum transfer. Since at the forthcoming hadron collider topics as minimum bias and underlying event will play a central role and will probably plague the extraction of hard scattering events signals, we have proposed and introduced in Ref. [7] a new semi-inclusive jet-like distribution, here after indicated with  $\mathcal{M}_{\triangleleft}^i(x, Q^2, z, t)$ , referring to it as to a jet-like fracture function.  $\mathcal{M}_{\triangleleft}^i(x, Q^2, z, t)$  expresses the probability of finding a parton  $i$  with fractional momentum  $x$  of the incoming

hadron and virtuality  $Q^2$ , while a cluster of hadrons  $h_i$  is detected in a portion of phase space  $\mathcal{R}$  specified by two variables,  $z$  and  $t$ . The region  $\mathcal{R}$  is limited by the constraint

$$\mathcal{R} : t_i = -(P - h_i)^2 < t, \quad t_0 \leq t \ll Q^2, \quad (1)$$

where the value of  $t$  is arbitrary chosen and can be conceived as the analogous of the clustering variable used in ordinary jet-algorithms. Once the clustering procedure is performed, the variable  $z$  is obtained by summing the fractional longitudinal momenta of all hadrons  $h_i$  satisfying the constraint in eq. (1):

$$z = \sum_i z_i, \quad h_i \in \mathcal{R}. \quad (2)$$

In analogy with the standard inclusive DIS, which makes use of parton distributions functions, we may write the beam-jet DIS cross-section as

$$\frac{1}{\sigma_{tot}} \frac{d\sigma^{\mathcal{R},jet}}{dx dQ^2 dz dt} \propto x \sum_{i=q,\bar{q}} e_i^2 \mathcal{M}_{\triangleleft}^i(x, Q^2, z, t). \quad (3)$$

In this framework, the parton initiating the space-like cascade is specified by the initial state radiation itself, *i.e.* the closest in rapidity to the hadron remnant. It has a fractional momentum  $1 - z$ , where  $z$  is overall fractional momentum taken away by the hadrons with  $t_i \leq t$  and has the highest allowed virtuality,  $t$ , according to strong ordering. When  $t$  is chosen in the perturbative region, as shown in Ref. [7], jet-like fracture functions obey a standard DGLAP evolution equations:

$$Q^2 \frac{\partial}{\partial Q^2} \mathcal{M}_{\triangleleft}^i(x, Q^2, z, t) = \frac{\alpha_s(Q^2)}{2\pi} \int_{\frac{x}{1-z}}^1 \frac{du}{u} P_j^i(u) \mathcal{M}_{\triangleleft}^j(x/u, Q^2, z, t). \quad (4)$$

This equation describes how the virtual photon resolves the distributions  $\mathcal{M}_{\triangleleft}^i$  when the virtuality of the latter is varied. In particular it resums potentially large collinear logarithms of the type  $\alpha_s^n \log^n(Q^2/t)$ . In real processes, strong  $t$ -ordering is only partially realized and one could in principle improve the theoretical description including higher order and coherence effects. As discussed in Ref. [7], the introduction of  $\mathcal{M}_{\triangleleft}^i$  allows one to include the beam remnants jet in the perturbative treatment of DIS jet cross-sections. Moreover jet-like fracture functions could find applications also in hard diffractive processes. In events characterized by the absence of hadron activity in the remnant direction, this absence can be conceived as the *shadow* in the detector of the propagation of the exchanged object in the  $t$ -channel. The rapidity gap can then be considered as a *missing jet*. It can be defined in terms of a jet-like fracture functions specified by the value  $t$  of the measured particle at the edge of the gap, *i.e.* the one with the highest rapidity (a part from the proton itself). The study of *gap topology* might be important to investigate diffractive phenomena and jet-like fracture functions could be a useful tool in this context.

The knowledge acquired at HERA on Deep Inelastic process in the target fragmentation region is expected to be essential in the LHC diffractive physics program. Dedicated experiments as TOTEM will measure leading baryon production, while combined CMS-TOTEM measurements will trigger on a wide class of diffractive processes characterized by a large momentum

transfer [8]. The fundamental step in transporting information from diffractive Deep Inelastic Scattering at HERA to LHC is to assume factorization to hold in hard diffractive hadron-hadron reactions. The Tevatron analysis has put, however, serious doubts on such an hypothesis. A non universality of diffractive parton distributions, as extracted from diffractive DIS, emerged when these distributions were used to predict hard scattering events cross-sections [9]. In such a reactions, at variance with diffractive DIS where factorization has been shown to hold in Ref. [6], theoretical arguments has been given such that the detection of particle in the target fragmentation region leads to a factorization breaking effect [6, 10]. For this reasons our understanding of the dynamics of diffractive processes is strongly correlated with the understanding of factorization.

Hard diffractive processes can be approached with pQCD techniques and the Drell-Yan process plays indeed a central role in this context. In particular it is the only hadrons-induced process for which factorization has been shown to hold at soft and collinear level [11]. Furthermore QCD corrections to this process have been calculated for inclusive and differential distributions in such a way that it constitutes a fundamental testing process of QCD at the hadron collider. For this reasons we have performed in Ref. [12] a pQCD analysis of the Semi-Inclusive Drell-Yan process

$$P_1 + P_2 \rightarrow \gamma^* + h + X. \quad (5)$$

In eq. (5)  $P_1$  and  $P_2$  stands for the incoming hadrons,  $\gamma^*$  the virtual photon of invariant mass  $Q^2$  and  $h$  the additional hadron measured in the final state. If  $Q^2$  is large enough so that perturbation theory applies, the factorization property of the considered cross-section should depend on the region of phase space in which the final hadron  $h$  is detected. In particular, if  $h$  is produced at sufficiently high transverse momentum,  $p_{h\perp}^2$ , then the relative cross-sections can be predicted by pQCD. On the contrary, if  $h$  is produced at low  $p_{h\perp}^2$  and thus detected in the target fragmentation region, arguments against factorization have been already given in Refs. [6, 10]. The formalism of fracture functions allows one to performed a next-to-leading order QCD analysis of the Semi-Inclusive Drell-Yan process without introducing unphysical scale in order to separate the dominant production mechanisms in each region of phase space. The first step in order to perform consistently such a calculation is to provide a parton model formula for the considered process. Since in zero-th order QCD initial state radiation is absent, we assume the hadron  $h$  is "non-perturbatively" produced in the target fragmentation region of  $P_1$  ( $\mathcal{R}_{T_1}$ ) or  $P_2$  ( $\mathcal{R}_{T_2}$ ) by means of a "bare" (in the renormalization sense) fracture function  $M_{h/P}^i(x, z)$ . In the following we will consider the differential cross-sections for producing a lepton pair of invariant mass  $Q^2 \gg \Lambda_{QCD}^2$ , accompanied by an additional hadron  $h$  with fractional energy  $z = 2E_h/\sqrt{S}$  (defined in the hadronic center of mass frame) and integrated over its transverse momentum,  $p_{h\perp}^2$ . By defining the combination  $M_q^h(x, z) = M_q^{h/P_1}(x, z) + M_q^{h/P_2}(x, z)$ , the parton model formula for the semi-inclusive Drell-Yan cross-sections reads:

$$\frac{d\sigma^{DY}(\tau)}{dQ^2 dz} = \frac{4\pi\alpha^2}{9SQ^2} \int_{\tau}^{1-z} \frac{dx_1}{x_1} \int_{\frac{\tau}{x_1}}^1 \frac{dx_2}{x_2} \sum_q e_q^2 \left[ M_q^h(x_1, z) f_{\bar{q}}(x_2) + (x_1 \leftrightarrow x_2) \right] \delta\left(1 - \frac{\tau}{x_1 x_2}\right). \quad (6)$$

A pictorial representation of this formula is drawn in Fig. (1). In the following we will restrict ourselves to the discussion of NLO corrections to the  $q\bar{q}$  channel. The corrections to eq. (6) have

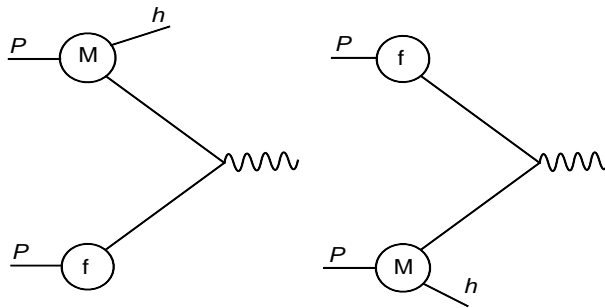


Fig. 1: A pictorial representation of the parton model formula for Semi-Inclusive Drell-Yan process, eq. (6).

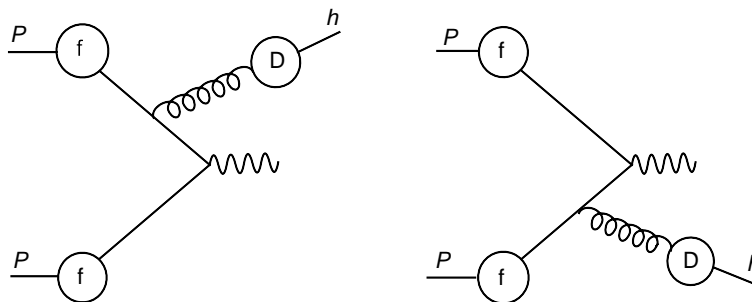


Fig. 2: A pictorial representation of the second term on r.h.s. in eq. (7). The observed hadron  $h$  results from the hadronization of initial state radiation (gluon).

the following formal structure

$$d\sigma_{q\bar{q}}^{DY,(1)} \simeq M_q^h \otimes f_{\bar{q}} \otimes \left[ 1 + \frac{\alpha_s}{2\pi} C_{q\bar{q}} \right] + \frac{\alpha_s}{2\pi} f_q \otimes f_{\bar{q}} \otimes D_g^h \otimes K_{q\bar{q}}^g, \quad (7)$$

where the symbol  $\otimes$  stands for the convolution on the momentum fraction of the participating partons. The more involved part of the calculation does consist in evaluating next-to-leading order diagrams in which the final state parton hadronize into the observed hadron  $h$ . These diagrams are at the origin of the second term on the right hand side of eq. (7). An example of such a diagram is shown in Fig. (2). The coefficient functions  $C_{q\bar{q}}$  and  $K_{q\bar{q}}^g$  at this level still present poles due to collinear singularities. It is however possible to show, see Ref. [12] for details, that all collinear singularities can be subtracted from the coefficient functions by the same factorization procedure firstly used in Ref. [4] in the context of Deep Inelastic Scattering. We consider this result as a direct evidence of collinear factorization for the Semi-Inclusive Drell-Yan cross-sections. The present QCD-based calculation deals however only with standard soft gluon exchange between active partons but it is blind to soft gluon exchange between spectators. Since our findings support factorization at the collinear level, we implicitly confirm the general widespread idea indicating soft exchanges between spectators partons as responsible for factorization breaking in semi-inclusive hadronic collisions. When diffractive parton distribution, as obtained from HERA data, are used in the present calculation, the resulting predictions would

be valid only in the case that factorization hypothesis holds. As a consequence, any deviation observed in the data not accounted for by the present NLO calculation, could be interpreted as a manifestation of factorization breaking. A comparison with data would also establish whether a factorization breaking shows up only in a diffractive kinematic regime or if it manifests itself also in processes with a gapless final state containing, as well, a single hadron in the target fragmentation region. At the same time it would be interesting to study, within the proposed approach, light mesons production which is sensitive to the soft, high multiplicity, fragmentation process. For this reason, in Ref. [12], we address the Semi-Inclusive Drell-Yan process as a prototype of *factorization analyzer*. Since we expect that the factorizing properties of the cross-sections to be extremely sensible to the  $p_{h\perp}^2$  of the measured hadron  $h$ , we guess that a more efficient observable in this context would be the triple-differential cross-sections:

$$\frac{d\sigma^{DY}}{dQ^2 dp_{h\perp}^2 dz}, \quad (8)$$

for which an analog of the present calculation is still not available. The possible identification of an intermediate scale or range of scales at which the factorization breaking effects start to manifest themselves would constitute an important insight into the dynamics of the factorization mechanism.

Let us conclude by listing some further possible developments of the formalism. The present work can be generalized to double hadron production. The evaluation of a double hadron production cross-section needs a full  $\mathcal{O}(\alpha_s^2)$  QCD calculation. However, as discussed in Ref. [12], an approximate result could be obtained if one considers the production of two hadrons at low  $p_{h\perp}^2$  observed in opposite fragmentation regions with respect to the incoming hadrons. In this case higher order corrections for this process should be the same as for inclusive Drell-Yan process, when the proper kinematics is taken into account. Finally we are thinking to a generalization of the present approach to include gluon initiated hard processes [13] whose relevance in diffractive Higgs production was first suggested in Ref. [14].

## References

- [1] L. Trentadue, G. Veneziano, Phys. Lett. **B 323**, 201 (1994) .
- [2] ZEUS Collaboration, Phys. Lett. **B 315**, 481 (1993);  
H1 Collaboration Nucl. Phys. **B 435**, 3 (1995) .
- [3] S. Chekanov & al., ZEUS Collaboration, Nucl. Phys. **B 713**, 3 (2005);  
A. Aktas & al., H1 Collaboration, Eur. Phys. J. **C 48**, 715 (2006) .
- [4] D. Graudenz, Nucl. Phys. **B 432**, 351 (1994) .
- [5] M. Grazzini, L. Trentadue, G. Veneziano, Nucl. Phys. **B 519**, 394 (1998) .
- [6] J.C. Collins, Phys. Rev. **D 57**, 3051 (1998) .
- [7] F.A. Ceccopieri, L. Trentadue, Phys. Lett. **B 665**, 15 (2007) .

- [8] M. Albrow et al., CERN-LHCC-2006-039, CERN-LHCC-G-124, CERN-CMS-NOTE-2007-002 .
- [9] CDF Collaboration, Phys. Rev. Lett. **84**, 5043 (2000) .
- [10] J. C. Collins, L. Frankfurt, M. Strikman, Phys. Lett. **B 307**, 161 (1993);  
A. Berera, D. E. Soper, Phys. Rev. **D 50**, 4328 (1994) .
- [11] W.W. Lindsay, D.A. Ross, C.T. Sachrajda, Phys. Lett. **B 117**, 105 (1982);  
Nucl. Phys. **B 214**, 61 (1983); Nucl. Phys. **B 222**, 189 (1983);  
J.C. Collins, D.E. Soper, G. Sterman, Phys. Lett. **B 134**, 263 (1984);  
Nucl. Phys. **B 261**, 104 (1985);  
G. T. Bodwin, Phys. Rev. **D 31**, 2616 (1985); Erratum-ibid. **D 34**, 3932 (1986) .
- [12] F.A. Ceccopieri, L. Trentadue, Phys. Lett. **B 668**, 319 (2008) .
- [13] S. Chekanov *et al.* [ZEUS Collaboration], Eur. Phys. J. C **52**, 813 (2007);  
A. Aktas *et al.* [H1 Collaboration], JHEP **0710**, 042 (2007);  
A. A. Affolder *et al.* [CDF Collaboration], Phys. Rev. Lett. **88**, 151802 (2002) .
- [14] D. Graudenz, G. Veneziano, Phys. Lett. **B 365**, 302 (1996) .

# Generalised parton distributions and exclusive vector meson production

C. Nockles and T. Teubner

Department of Mathematical Sciences, University of Liverpool, Liverpool L69 3BX, U.K.

## Abstract

We briefly review recent developments in the description of exclusive vector meson production in terms of generalised parton distributions. The determination of the gluon distribution at small  $x$  from HERA data on diffractive  $J/\psi$  production is discussed.

## 1 Introduction

Contrary to normal DIS, processes like deeply virtual Compton scattering (DVCS) or the diffractive production of (di-) jets, heavy quarks or vector mesons (VMs), cannot be described accurately with the diagonal (normal) parton distribution functions (PDFs). This can be seen from Fig. 1, where the leading order diagram for DVCS (left) and  $J/\psi$  vector meson production (right figure) are shown. While DVCS is mainly testing the quark distribution, the amplitude for exclusive vector meson production is, to leading order, directly probing the gluon PDF. The momentum fractions  $x$  and  $x'$  of the two partons are in general different, resulting in a deviation from the diagonal limit for the distribution function of the respective parton. In this instance, a generalised parton distribution (GPD) must be used to describe the process.

Unlike the diagonal parton distributions, which represent a probability distribution, generalised distributions are defined by matrix elements of quark and gluon light-cone operators  $\hat{\mathcal{O}}$  for different initial and final states of the proton,  $\langle p' | \hat{\mathcal{O}} | p \rangle$ . They encode richer information about the distribution of partons inside the hadron and have no direct probabilistic interpretation. One may express the parton momentum fractions in a GPD in a symmetric manner, with the introduction of a skewing parameter  $\xi$  and a symmetric  $\tilde{x}$ :  $x = \tilde{x} - \xi$ ,  $x' = \tilde{x} + \xi$ . In the forward limit  $\xi, t \rightarrow 0$ , the generalised partons reduce to the conventional diagonal partons, where  $t$  is the square of the momentum transfer between initial and final protons. In the following we will briefly discuss

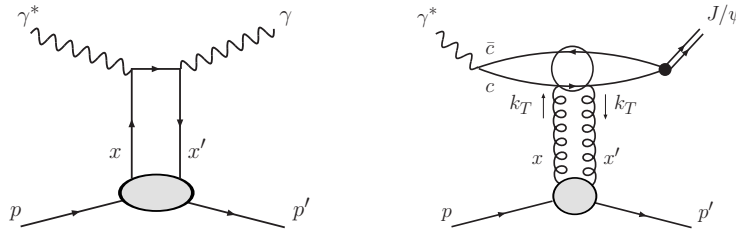


Fig. 1: Left: DVCS  $\gamma^* p \rightarrow \gamma p'$  and right: elastic  $J/\psi$  production  $\gamma^* p \rightarrow J/\psi p'$ . The two partons entering the scattering have different momentum fractions  $x, x'$ .



selected recent work on the prediction of diffractive production of vector mesons based on generalised parton distributions, both in the framework of collinear and  $k_T$  factorisation, and the determination of the small  $x$  gluon from diffractive  $J/\psi$  data in the latter framework.

## 2 Predictions for diffractive vector meson production

In the last years a lot of work has been done on dipole and saturation models. For a review of these topics in these proceedings we refer to [1]. Calculations in the framework of dipole cross sections often do not attempt at including the effect of non-forwardness. However, in [2] the skewedness is treated as in [3] discussed below.

### 2.1 Predictions based on collinear factorisation

Kroll and Goloskokov have described electroproduction of light vector mesons using collinear factorisation on the proton side [4–6]. In the limit of large photon virtuality  $Q^2$  the production amplitude factorises into a perturbatively calculable hard scattering amplitude (coefficient function), a generalised PDF and the wave function of the VM. This is similar to DVCS, where the term ‘handbag factorisation’ is used which is particularly suitable in the case of initial quarks relevant at lower c.m. energies. The transverse momentum  $p_T$  of the quarks forming the vector meson is retained, and a corresponding meson light-cone wave function  $\psi_{VM}(\tau, p_T)$  (with  $p_T$  the intrinsic transverse momentum and  $\tau$  the fraction of the light-cone plus component of the meson’s momentum carried by the quark) is used. In addition a Sudakov factor  $\exp[-S(\tau, p_T, Q^2)]$  is applied at next-to-leading-logarithmic accuracy. This suppresses gluon radiation in the regime between a soft cut-off and a factorisation scale related to the quark-antiquark separation. Softer gluons are included in the VM wave function while harder ones are part of the hard, perturbative scattering amplitude. This so-called ‘modified perturbative approach’ cures the end-point singularities stemming from configurations with large transverse quark-antiquark separation which otherwise would prevent a prediction of the cross section for transversely polarised mesons. The generalised parton distributions are derived using the ansatz of double distributions following the work of Radyushkin [7] and using global PDFs as input for the diagonal limit.<sup>1</sup> The evolution is approximated by the evolution of the diagonal input. With their approach Kroll and Goloskokov find fair agreement with electroproduction data from COMPASS, HERMES, E665, ZEUS and H1, see [4–6] and Fig. 2 for an example of their longitudinal cross section predictions for  $\phi$  and  $\rho$  electroproduction. The extension to contributions from transverse photons is discussed in [6].

While the approach of Kroll and Goloskokov is not restricted by the high energy approximation adopted in other calculations, the hard, perturbative scattering kernel used in [4–6] is leading order (LO) only. Next-to-leading order (NLO) corrections in the framework of collinear factorisation have been calculated by Ivanov et al. [8] and were found to be large generally. In their recent work Diehl and Kugler [9] have made use of these results to further study the impact

---

<sup>1</sup>Double distributions offer a way to parameterise the hadronic matrix elements defining generalised distributions [7]. They are defined through Fourier transforms of these matrix elements. Such double distributions guarantee the required symmetry properties and the polynomiality ( $N$ th moments of GPDs are  $N$ th degree polynomials in the skewing parameter  $\xi$ ) of the derived generalised distributions. However their physical interpretation is different (and maybe less apparent) as they are not directly dependent on  $\xi$ .

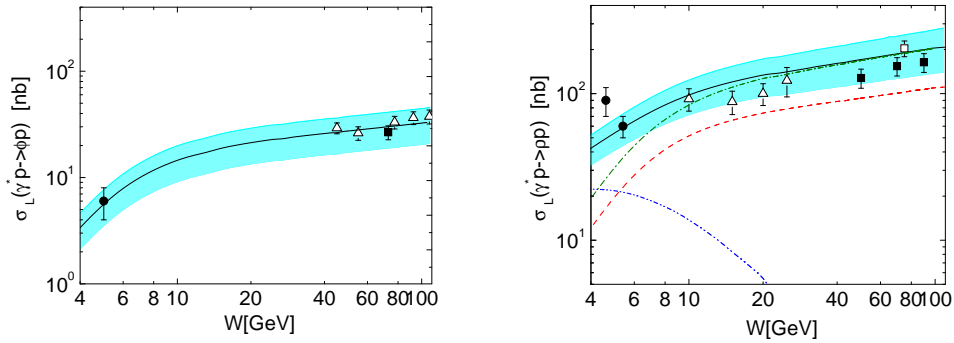


Fig. 2: Predictions from [5] for the longitudinal cross section of  $\phi$  electroproduction for  $Q^2 = 3.8 \text{ GeV}^2$  (left) and  $\rho$  electroproduction for  $Q^2 = 4 \text{ GeV}^2$  (right).  $\phi$  production data are from HERMES (solid circle), ZEUS (open triangles) and H1 (solid square), and  $\rho$  production data are from HERMES (solid circles), E665 (open triangles), ZEUS (open square) and H1 (solid square), see [5] for references. The dashed (dash-dotted) line represents the gluon (gluon+sea) contribution. The dash-dot-dotted line represents the sum of the interference between the valance and (gluon+sea) contributions and the valance contribution. The solid line is the sum of all contributions.

of the NLO corrections to exclusive meson production. They use collinear factorisation, neglecting the transverse momenta of the partons entering the hard scattering both on the proton and on the meson side. For the evolution of the generalised partons they use the leading order evolution code of Vinnikov [10] which uses an optimised fourth order Runge-Kutta method to solve the LO kernels as given in [11]. The input GPDs are again estimated via the double distribution method, and with diagonal input from the global PDF fit CTEQ6M [12]. Diehl and Kugler observe large NLO corrections leading to a strong suppression of the LO result in the small  $x$  regime, but no gain from LO to NLO in the stability w.r.t. the scale variation. In Fig. 3 this is shown for the case of  $\rho$  electroproduction in different kinematic regimes. Unfortunately such large corrections, which can partly be traced back to BFKL type logarithms (see [13] for first predictions including resummation effects), limit the applicability of the fixed-order collinear approach to describe data for elastic VM production.

## 2.2 Vector meson production in $k_T$ factorization

Traditionally,  $k_T$  (or ‘high energy’) factorisation has been introduced for the description of heavy quark production in the high energy regime. Recently it has also been applied to various other processes including Higgs production at hadron colliders. Martin et al. have used it for the calculation of diffractive production of light and heavy vector mesons at HERA [14, 15]. The relevant amplitude is shown in Fig. 1 (right diagram). Their predictions involve the integration over the transverse momentum  $k_T$  of the exchanged gluons, so the input parton distributions need to be unintegrated w.r.t.  $k_T$ . This involves the application of a Sudakov factor, see [15] for details. Additional contributions from the real part of the amplitude are calculated based on dispersive methods. This approach goes beyond the leading  $\log Q^2$  approximation while also capturing certain contributions beyond the leading high energy (BFKL) limit. Of course NLO corrections also arise from additional loops, for example gluonic one-loop corrections to the

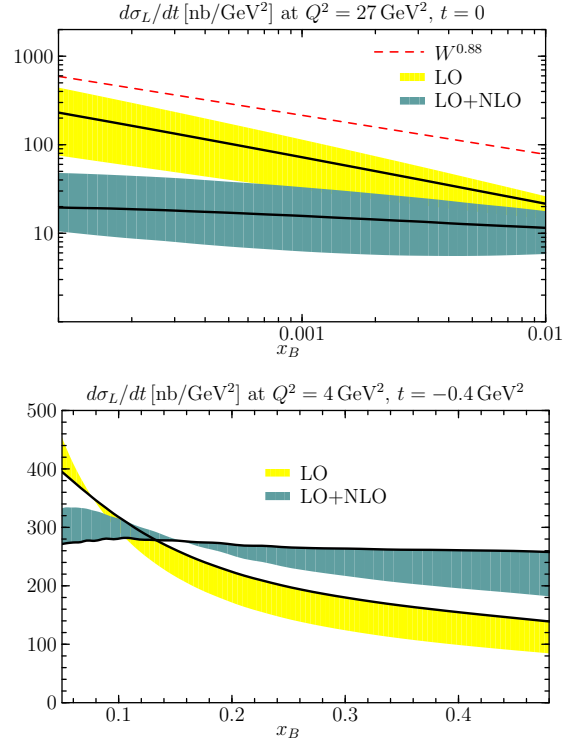


Fig. 3: Longitudinal cross section predictions for  $\rho$  electroproduction from [9] for  $Q^2$ ,  $t$  and  $x$  as indicated on the plots. The bands are generated from the ranges  $Q/2 < \mu < 2Q$  (left) and  $2 < \mu < 4 \text{ GeV}^2$  (right), where  $\mu$  is the renormalisation and factorisation scale. The solid lines correspond to  $\mu = Q$ . The dashed line in the left panel shows the power-law behaviour  $\sigma \propto W^{0.88}$  (with arbitrary normalisation) obtained from a fit by the ZEUS Collaboration to data in the range  $x_B = 0.001 \dots 0.005$ .

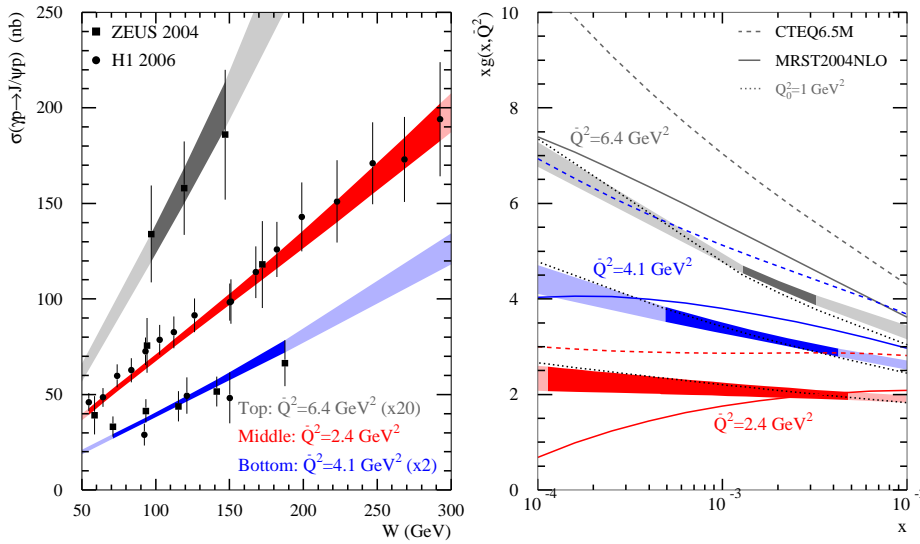


Fig. 4: ‘NLO’ fit of elastic  $J/\psi$  data from HERA [19] as done in [3]. Left: cross section compared to some of the H1 and ZEUS data for three different values of the effective scale  $\hat{Q}^2 = (Q^2 + M_{J/\psi}^2)/(W^2 + M_{J/\psi}^2)$ . Right: Fitted diagonal gluon compared to global gluons for scales as indicated. The width of the bands displays the uncertainty of the cross section predictions and the fitted gluon, whereas darker shaded areas indicate the region of available data.

two-gluon quark-antiquark vertex, or when the two gluon system couples via a quark loop to the proton. While such quark contributions are suppressed in the high energy regime, the former class of corrections leads to a genuine  $K$  factor which was calculated by Ivanov et al. [8] in collinear factorisation but which is not known in the case of  $k_T$  factorisation. Work is in progress to calculate these corrections.

Skewing corrections are taken into account via the Shuvaev transform [16] which, in the case of small  $x$  and  $\xi$ , allows to calculate the GPDs from the forward PDFs.<sup>2</sup> In this regime, with the assumption of a pure power behaviour of the diagonal PDF  $\sim x^{-\lambda}$ , the skewing correction is well approximated by a simple factor,  $R = \frac{2^{2\lambda+3}}{\sqrt{\pi}} \frac{\Gamma(\lambda+5/2)}{\Gamma(\lambda+3+p)}$  ( $p = 1$  for gluons, 0 for quarks), which only depends on the anomalous dimension  $\lambda$ .

### 3 Determination of the gluon from diffractive $J/\psi$ data

While a good description of many data from HERA and other experiments has been achieved, the predictions show a large dependence on the gluon parametrisations used as input, in the regime of small  $x$  and semi-hard scales where they are only poorly known. However, Martin et al. have turned the game around and used their theoretical approach as described above together with exclusive  $J/\psi$  data from HERA [19] to determine the gluon distribution in the small  $x$  and low-scale regime [3]. Note that whereas in [14, 15] VM production was described via parton-hadron

<sup>2</sup>The use of the Shuvaev transform has become subject of some criticism [17], but see [18] for the justification of its applicability in the regime under consideration here.

duality by integrating over open quark-antiquark production in a suitably chosen mass regime, for the gluon fits in [3] the non-relativistic limit for the  $J/\psi$  wave function was adopted. While this is a sufficient approximation w.r.t. the other theoretical and experimental uncertainties, it also allows for the prediction of the normalisation which is not well controlled in the parton-hadron duality approach. With the use of a simple three-parameter ansatz for the gluon,  $xg(x, \mu^2) = Nx^{-\lambda}$ , with  $\lambda = a + b \ln \ln(\mu^2/\Lambda_{\text{QCD}}^2)$ , a fit (with  $\chi_{\text{min}}^2/d.o.f. = 0.8$ ) gives the results  $N = 1.55 \pm 0.18$ ,  $a = -0.50 \pm 0.06$ ,  $b = 0.46 \pm 0.03$ . In Fig. 4, both the results for the emerging cross section predictions (left) and the fitted gluon distribution (right panel) are shown for different scales and compared to the gluon PDFs of global fits from CTEQ [20] and MRST [21].

## 4 Conclusions

We have briefly reviewed recent work on the description of exclusive vector meson production in  $ep$  collisions based on generalised parton distributions. While it has been known for a long time that this process is particularly interesting due to its quadratic sensitivity on the input partons, the complexity of the full amplitudes makes systematic higher order predictions difficult. Different approaches as presented above have been discussed at the recent HERA-LHC workshops. Clearly we have gained a much better understanding of exclusive VM production, though the quantitative predictions have not yet achieved the desired accuracy. Nevertheless, a lot of progress has been made in predicting these processes and first results on extracting the gluon at small  $x$  from HERA data have been reported. The situation will be even more complicated at the LHC, and with the wider kinematic range accessible, the future will be very interesting.

## References

- [1] L. Motyka, K. Golec-Biernat and G. Watt, in these proceedings.
- [2] H. Kowalski, L. Motyka and G. Watt, Phys. Rev. **D 74**, 074016 (2006).
- [3] A.D. Martin, C.J. Nockles, M.G. Ryskin and T. Teubner, Phys. Lett. **B 662**, 252 (2008).
- [4] S.V. Goloskokov and P. Kroll, Eur. Phys. J. **C 42**, 281 (2005).
- [5] S.V. Goloskokov and P. Kroll, Eur. Phys. J. **C 50**, 829 (2007).
- [6] S.V. Goloskokov and P. Kroll, Eur. Phys. J. **C 53**, 367 (2008).
- [7] A.V. Radyushkin, Phys. Lett. **B 449**, 81 (1999);  
I.V. Musatov and A.V. Radyushkin, Phys. Rev. **D 61**, 074027 (2000).
- [8] D.Yu. Ivanov, L. Szymanowski and G. Krasnikov, JETP Lett. **80**, 226 (2004);  
D.Yu. Ivanov, A. Schäfer, L. Szymanowski and G. Krasnikov, Eur. Phys. J. **C 34**, 297 (2004);  
D.Yu. Ivanov, M.I. Kotsky and A. Papa, Eur. Phys. J. **C 38**, 195 (2004).
- [9] M. Diehl and W. Kugler, Eur. Phys. J. **C 52**, 933 (2007).

- [10] A.V. Vinnikov, *Code for prompt numerical computation of the leading order gpd evolution*. Preprint `arXiv:hep-ph/0604248`.
- [11] J. Blümlein, B. Geyer and D. Robaschik, Nucl. Phys. **B 560**, 283 (1999).
- [12] CTEQ Collaboration, J. Pumplin et al., JHEP **0207**, 012 (2002).
- [13] D.Yu. Ivanov, *Exclusive vector meson electroproduction*. Preprint `arXiv:0712.3193 [hep-ph]`.
- [14] A.D. Martin, M.G. Ryskin and T. Teubner, Phys. Lett. **B 454**, 339 (1999).
- [15] A.D. Martin, M.G. Ryskin and T. Teubner, Phys. Rev. **D 62**, 014022 (2000).
- [16] A. Shuvaev, Phys. Rev. **D 60**, 116005 (1999);  
A.G. Shuvaev, K.J. Golec-Biernat, A.D. Martin and M.G. Ryskin, Phys. Rev. **D 60**, 014015 (1999).
- [17] M. Diehl and W. Kugler, Phys. Lett. **B 660**, 202 (2008).
- [18] A.D. Martin, C.J. Nockles, M.G. Ryskin, A.G. Shuvaev and T. Teubner. To appear.
- [19] H1 Collaboration, A. Aktas et al., Eur. Phys. J. **C 46**, 585 (2006);  
ZEUS Collaboration, S. Chekanov et al., Nucl. Phys. **B 695**, 3 (2004);  
ZEUS Collaboration, J. Breitweg et al., Z. Phys. **C 75**, 215 (1997);  
ZEUS Collaboration, J. Breitweg et al., Eur. Phys. J. **C 6**, 603 (1999).
- [20] CTEQ Collaboration, W.-K. Tung et al., JHEP **0702**, 053 (2007).
- [21] A.D. Martin, R.G. Roberts, W.J. Stirling and R.S. Thorne, Phys. Lett. **B 604**, 61 (2004).

# Dipole models and parton saturation in $ep$ scattering

*L. Motyka*<sup>1,2</sup>, *K. Golec-Biernat*<sup>3,4</sup> and *G. Watt*<sup>5</sup>

<sup>1</sup> II Institute for Theoretical Physics, Luruper Chaussee 149, 22761 Hamburg, Germany

<sup>2</sup> Institute of Physics, Jagellonian University, Reymonta 4, 30-059 Kraków, Poland

<sup>3</sup> Institute of Nuclear Physics, Polish Academy of Sciences, Kraków, Poland

<sup>4</sup> Institute of Physics, University of Rzeszów, Rzeszów, Poland

<sup>5</sup> Department of Physics & Astronomy, University College London, WC1E 6BT, UK

## Abstract

In this contribution we briefly review the current status of the dipole models and parton saturation on the basis of results presented at the HERA–LHC workshops in the years 2006–2008. The problem of foundations of the dipole models is addressed within the QCD formalism. Some limitations of the models and open problems are pointed out. Furthermore, we review and compare the currently used dipole models and summarise the applications to describe various sets of HERA data. Finally we outline some of the theoretical approaches to the problem of multiple scattering and saturation.

## 1 Introduction

Dipole models [1–3] represent a QCD motivated framework that has been successfully applied to describe a variety of gluon mediated scattering cross sections at high energies. In particular, they provide a transparent and intuitive picture of scattering processes. Their main strength is a combination of universality, simplicity and efficiency. The dipole models are capable of simultaneously describing all  $F_2$ ,  $F_L$  and heavy quark production  $ep$  data at small  $x$ , the inclusive diffractive data, the bulk of measurements for exclusive diffractive vector meson production, deeply virtual Compton scattering (DVCS), and even nuclear shadowing [4–13]. This unified description is achieved using only a few parameters with a transparent physical meaning, such as the normalisation of the gluon distribution at a low scale, the quark mass or the proton size. At the same time, the dipole models provide a phenomenological insight into important aspects of high energy scattering, like the relative importance of multiple scattering or higher twist contributions. This importance may be quantified in terms of a *saturation scale*,  $Q_S$ , the scale of the process at which the unitarity corrections become large [4]. Up to now, the dipole models applied to HERA data offer one of the most convincing arguments for the dependence of this scale on the scattering energy and provide one of the best quantitative estimates of the saturation scale [4–6, 11, 12]. This shows the complementarity of dipole models to the rigorous framework of collinear factorisation, within which the description of multiple scattering, although possible in principle, is quite inefficient. It is not only very demanding from the technical side (for instance, even the basis of twist-four operators is not fully understood yet), but it would also require introducing a set of new unknown functions parameterising the expectation values of higher twist operators at the low (input) scale. In dipole models this problem is bypassed by simply fitting the (implicitly) resummed multiple scattering cross section together with the nonperturbative contribution with constraints imposed by the unitarity of the scattering matrix.

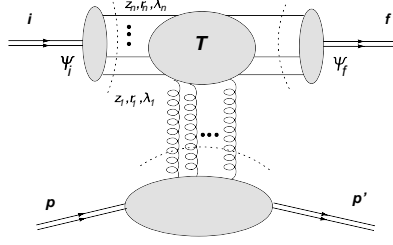


Fig. 1: High energy scattering in the dipole representation.

## 2 Foundations and limitations of dipole models

Let us consider a  $2 \rightarrow 2$  scattering amplitude of  $i + p \rightarrow f + p$ , where the strongly interacting projectile  $i$  hits a hadronic target  $p$  and undergoes a transition to a state  $f$ , while the target scatters elastically. At HERA the projectile is always a virtual photon,  $\gamma^*$ , with a four-momentum  $q$  and virtuality  $q^2 = -Q^2$ , and the target is a proton, with initial momentum  $p$  and final momentum  $p'$ . The final states considered are virtual and real photon states, vector meson states and diffractive states. The states  $i$  and  $f$  carry a typical scale  $\bar{Q}^2$ ; for  $i = f = \gamma^*(Q^2)$ ,  $\bar{Q}^2 = Q^2$ . The invariant collision energy  $s = (p + q)^2$  is assumed to be large,  $s \gg \bar{Q}^2$  and  $s \gg |t|$ , where  $t = (p - p')^2$  is the momentum transfer. We shall also use the variable  $x = \bar{Q}^2/s$ , that reduces to the Bjorken  $x$  for the case of deeply inelastic scattering (DIS).

The key idea behind dipole models is a separation (factorisation) of a high energy scattering amplitude,  $\mathcal{A}^{i p \rightarrow f p}$ , into an initial ( $\Psi_i$ ) and final ( $\Psi_f$ ) state wave function of the projectile  $i$  and the outgoing state  $f$ , and a (diagonal) universal scattering amplitude of a multi-parton Fock state,  $\mathcal{F}_n$ , off a target  $p$ ; see Fig. 1. The scattering operator,  $T$ , is assumed to be diagonal in the basis of states that consist of a definite number of partons,  $n$ , with fixed longitudinal momentum fractions,  $z_k$  ( $k = 1, \dots, n$ ), of the projectile, definite helicities,  $\lambda_k$ , and transverse positions,  $\mathbf{r}_k$ . One may write symbolically (see e.g. [14]):

$$\mathcal{A}^{i p \rightarrow f p} = \sum_{n, \mathcal{F}_n, \{\lambda_k\}} \int [d^{2n} \mathbf{r}_k] \int [d^n z_k] \Psi_f^*(n, \{z_k, \mathbf{r}_k, \lambda_k\}) T(\mathcal{F}_n) \Psi_i(n, \{z_k, \mathbf{r}_k, \lambda_k\}). \quad (1)$$

In most practical applications one takes into account only the lowest Fock states, composed of a quark–antiquark ( $q\bar{q}$ ) pair and, possibly, one additional gluon ( $q\bar{q}g$ ). In the limit of a large number of colours,  $N_c \rightarrow \infty$ , flavourless scattering states,  $i$  and  $f$ , may be represented as a collection of colour dipoles [2]. For the simplest case of  $q\bar{q}$  scattering, the intermediate state  $\mathcal{F}_2$  is defined by the quark and antiquark helicities, the longitudinal momentum fraction,  $z$ , of the projectile carried by the quark, the dipole vector,  $\mathbf{r} = \mathbf{r}_2 - \mathbf{r}_1$ , and the impact parameter vector,  $\mathbf{b} = z\mathbf{r}_1 + (1 - z)\mathbf{r}_2$ . It is convenient to define the imaginary part of the dipole scattering amplitude (assuming independence of the azimuthal angles),  $\mathcal{N}(x, \mathbf{r}, \mathbf{b}) \equiv \text{Im } T(\mathcal{F}_2)$ , and the  $b$ -dependent dipole–target cross-section

$$\frac{d\sigma_{q\bar{q}}}{d^2\mathbf{b}} = 2 \mathcal{N}(x, \mathbf{r}, \mathbf{b}). \quad (2)$$



The picture encoded in (1) may be motivated within perturbative QCD. In the high energy limit of QCD [15, 16], the dominant contribution to scattering amplitudes comes from vector boson (gluon) exchanges, that lead to cross-sections constant with energy (modulo quantum corrections that may generate an additional enhancement). For each spin-1/2 fermion (quark) exchange in the  $t$ -channel the amplitude is power suppressed by a factor of  $1/s^{1/2}$ . In consequence, the high energy scattering amplitude may be factorised into the amplitude describing slow (in the target frame) gluon fields and the amplitude of fast parton fields of the projectile moving in the gluon field of the target. This is, in fact, the basic assumption of the  $k_T$ - (high energy) factorisation [16, 17]. In the high energy limit, the vertex describing the coupling of the fast  $s$ -channel parton (quark or gluon) to a gluon exchanged in the  $t$ -channel is *eikonal*: the large light-cone component of the longitudinal parton momentum and the parton helicity are conserved. Also, up to subleading terms in the collision energy, the fast parton does not change its transverse position in the scattering process. These properties of high energy amplitudes in QCD were used to derive the dipole model for hard processes. In more detail, the scattering amplitudes in the dipole model follow from the QCD scattering amplitudes obtained within the  $k_T$ -factorisation scheme, in the high energy limit and at the leading logarithmic (LL)  $\ln(1/x)$  approximation [1].

The fact that the QCD dipole model follows from the  $k_T$ -factorisation approximation implies that the model, up to subleading terms in  $1/s$ , is also consistent with the leading order (LO) collinear approximation [17]. In addition, as in the case of the  $k_T$ -factorisation framework, the dipole model incorporates an exact treatment of the quark transverse momentum in the box diagram. These kinematic effects, when analysed within the collinear approximations, manifest themselves as higher order corrections to the coefficient functions [17]. Although the implicit resummation of the collinear higher order terms in the dipole model is only partial, it should still be viewed as an improvement of the LO collinear approximation.

Practical use of dipole models is not restricted to hard processes, where precise predictions can be obtained within the collinear factorisation framework. On the contrary, one of the most successful applications of the dipole model (the saturation model [4]) provides an efficient and simple description of the transition from the perturbative single scattering regime (the colour transparency regime) to the multiple scattering regime as a function of the process scale and scattering energy (or  $\bar{Q}^2$  and  $x$ ). In this transition region scattering amplitudes are expected to receive contributions both of the nonperturbative nature and from perturbatively calculable multiple scattering effects. The nonperturbative effects in high energy scattering are currently not computable with theoretical methods and have to be modelled. The multiple scattering effects enter the scattering amplitudes e.g. as higher twist contributions [18]<sup>1</sup>, that are suppressed by inverse powers of the hard scale,  $\bar{Q}^2$ , and additional powers of  $\alpha_s$ . Nevertheless, the higher twist effects may be quite sizable at small  $x$  and at moderately large  $\bar{Q}^2$  [18]. This originates from a rapid growth of the multi-gluon density with decreasing  $x$ : assuming the large  $N_c$  limit, the  $n$ -gluon density evolves approximately as the single gluon density to power  $n$  [19, 20]. Thus, at decreasing  $x$  the multiple scattering effects are increasingly enhanced and may eventually become competitive with the single scattering contribution.

Thus far we discussed the dipole model from the perspective of perturbative QCD. An interesting attempt to provide foundations of the model in a general (i.e. non-perturbative) frame-

---

<sup>1</sup>Multiple scattering effects that occur at low scales are absorbed into the input gluon density at the initial scale.

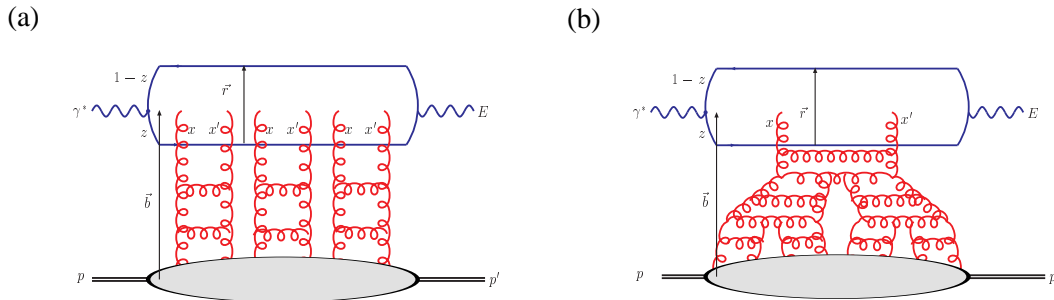


Fig. 2: The  $\gamma^*p$  scattering amplitude with unitarisation achieved via (a) *eikonal* diagrams or (b) *fan* diagrams. For exclusive diffractive processes, such as vector meson production ( $E = V = \Upsilon, J/\psi, \phi, \rho$ ) or DVCS ( $E = \gamma$ ), we have  $x' \ll x \ll 1$  and  $t = (p - p')^2$ . For inclusive DIS, we have  $E = \gamma^*$ ,  $x = x' \ll 1$  and  $p = p'$ .

work was recently put forward [21, 22]. The scattering amplitudes were written in terms of skeleton diagrams and the QCD path-integral. Approximations and assumptions necessary to recover the dipole model amplitudes were identified. To a large extent the conclusions from that analysis confirm those obtained within the perturbative framework: the dipole model accuracy is not theoretically guaranteed when higher twist and higher order corrections are large. An interesting point raised in Refs. [22, 23] is the dependence of the dipole cross section,  $\sigma_{q\bar{q}}$ , on the dipole–target collision energy,  $\sqrt{s}$ . In most models one assumes that  $\sigma_{q\bar{q}}$  depends on  $s$  through  $x = \bar{Q}^2/s$ . The scale, however, is part of the wave functions and it is not obvious that the dipole cross section should depend on  $\bar{Q}^2$  rather than on the dipole variables, like e.g. the dipole scale,  $1/r^2$ . Interestingly, assuming the dependence of  $\sigma_{q\bar{q}}$  on a combined variable  $s r^2$  was shown to create some tension between the HERA data on  $F_2$  and  $F_L$  and the dipole model, irrespective of the detailed functional form of  $\sigma_{q\bar{q}}$ . Some insight may be gained from inspecting the issue in the  $k_T$ -factorisation approach. Then, the energy dependence enters through  $x_g$  of the gluon, that essentially depends on the external state virtuality, the scattered quarks’ transverse momenta and the distribution of the quark longitudinal momentum. So, the proposed replacement of  $\bar{Q}^2$  by  $1/r^2$  might be somewhat oversimplified. On the other hand, within the LL( $1/x$ ) approximation the standard choice of  $x_g \simeq \bar{Q}^2/s$  is justified. To sum up, the choice of the optimal dimensionless variable that would carry the energy dependence of the dipole cross-section remains an open and interesting problem.

### 3 Phenomenology of dipole models

Implementations of multiple scattering in colour dipole models are based on two main approaches, that adopt different approximations. The Glauber–Mueller (GM) *eikonal* approach [24] is used in the family of models that evolved from the Golec-Biernat–Wüsthoff (GBW) model [4]. One assumes in this approach that multiple colour dipole scatters are independent of each other, see Fig. 2a. This assumption may be supported (although it was not yet explicitly derived) with properties of the collinear evolution of quasi-partonic operators describing the multi-gluon density in the proton, and in the large  $N_c$  limit [18–20]. Assuming in addition a factorised  $b$ -dependence of the gluon distribution, one postulates the dipole–proton scattering amplitude of

the form:

$$\mathcal{N}(x, r, b) = 1 - \exp \left( -\frac{\pi^2}{2N_c} r^2 \alpha_s(\mu^2) x g(x, \mu^2) T(b) \right), \quad (3)$$

where the scale  $\mu^2 = C/r^2 + \mu_0^2$  with  $\mu_0 \sim 1$  GeV. HERA data on exclusive vector meson production imply a Gaussian form of the proton shape in the transverse plane,  $T(b)$ , with  $\sqrt{\langle b^2 \rangle} = 0.56$  fm. The corresponding quantity determined from the proton charge radius (0.87 fm) is somewhat larger,  $\sqrt{\langle b^2 \rangle} = 0.66$  fm, implying that gluons are more concentrated in the centre of the proton than quarks. The form (3) is denoted by the “b-Sat” model [6, 11]. It can be considered to be an improvement on a previous model [5] where  $T(b) \propto \Theta(R_p - b)$  was assumed, and also on the original GBW model [4] where additionally the scale dependence of the gluon distribution was neglected, that is,  $xg(x, \mu^2) \propto x^{-\lambda}$  was assumed for a fixed power  $\lambda \sim 0.3$ . Note that in the GBW model large saturation effects were needed to get from the hard Pomeron behaviour ( $\sim r^2 x^{-0.3}$ ) at small dipole sizes to soft Pomeron behaviour ( $\sim x^{-0.1}$ ) at large dipole sizes. On the other hand, in Refs. [5, 6, 11] this transition can alternatively be achieved with DGLAP evolution, therefore saturation effects are correspondingly smaller.

In the alternative approach one exploits solutions of the Balitsky–Kovchegov (BK) equation [25]. It was derived for scattering of a small colour dipole off a large nucleus, composed of  $A$  nucleons. The LL BK equation rigorously resums contributions of BFKL Pomeron *fan* diagrams (Fig. 2b), that are leading in  $A$ ,  $1/N_c$  and in the  $\ln 1/x$  approximation (properties of solutions of the next-to-LL BK equation are not known yet and so cannot be used in the dipole models). A colour glass condensate (CGC) dipole model parameterisation [8] was constructed from an approximate solution of the BK equation:

$$\mathcal{N}(x, r, b) = T(b) \mathcal{N}(x, r) = \Theta(R_p - b) \begin{cases} \mathcal{N}_0 \left( \frac{rQ_s}{2} \right)^{2\left(\gamma_s + \frac{\ln(2/rQ_s)}{9.9\lambda \ln(1/x)}\right)} & : rQ_s \leq 2 \\ 1 - e^{-A \ln^2(BrQ_s)} & : rQ_s > 2 \end{cases}, \quad (4)$$

where  $Q_s = (x_0/x)^{\lambda/2}$  is a saturation scale.<sup>2</sup> The original analysis [8] neglected the charm quark contribution to  $F_2$ . The inclusion of charm was later found [11] to significantly lower the saturation scale when the anomalous dimension  $\gamma_s$  was fixed at the LO BFKL value of 0.63. By letting  $\gamma_s$  go free, a solution was subsequently found with  $\gamma_s = 0.74$  which included heavy quarks but had a large saturation scale [9]. (This model has been modified to include a  $t$  dependence in the saturation scale allowing the description of exclusive diffractive processes [10].) However, the HERA data do not show a strong preference for the solution with  $\gamma_s = 0.74$ , and a secondary solution with  $\gamma_s = 0.61$  and a much smaller saturation scale also describes the data well [12]. The CGC model (4) assumes a factorised  $b$  dependence which is not supported by HERA diffractive data, where one finds a significantly non-zero effective Pomeron slope  $\alpha'_{\mathbb{P}}$ , indicating correlation between the  $b$  and  $x$  dependence of the dipole scattering amplitude. A more realistic impact parameter dependence was included by introducing a Gaussian  $b$  dependence into the saturation scale  $Q_s$ , denoted by the “b-CGC” model [11, 12]. It was not possible to obtain a good fit to HERA data with a fixed  $\gamma_s = 0.63$  [11], but on freeing this parameter, a good fit was obtained

<sup>2</sup>In what follows we shall use  $Q_s$  (with a lower-case  $s$ ) to denote the saturation scale defined in a model-dependent way.

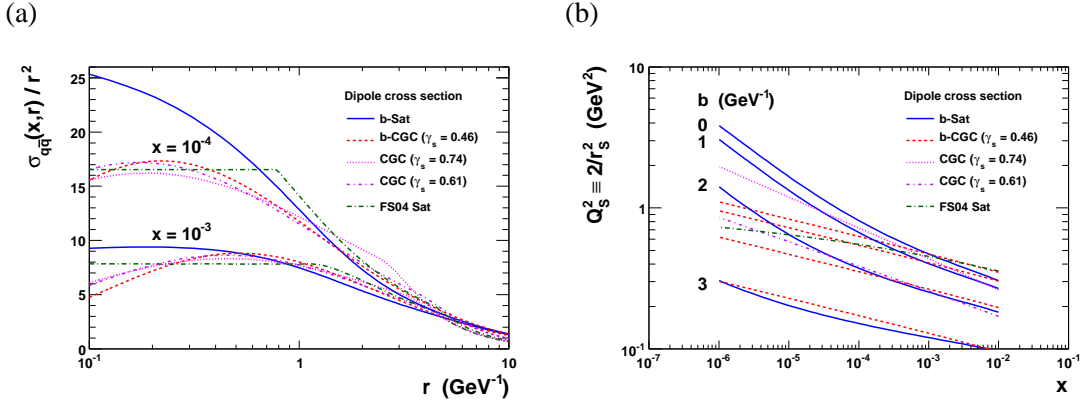


Fig. 3: (a) The  $b$ -integrated dipole–proton cross sections divided by  $r^2$  and (b) the saturation scale  $Q_s^2 \equiv 2/r_s^2$ .

with a value of  $\gamma_s = 0.46$  [12], close to the value of  $\gamma_s \simeq 0.44$  obtained from numerical solution of the BK equation [26]. However, the value of  $\lambda = 0.119$  obtained from the “b-CGC” fit [12] is lower than the perturbatively calculated value of  $\lambda \sim 0.3$  [27].

In both the approaches to unitarisation one neglects multi-gluon correlations in the target. Thus, the key difference between the eikonal and the BK approaches is that in the latter one resums the leading logarithms of  $1/x$  while in the former one aims at keeping a reasonable representation of leading logarithms of  $\bar{Q}^2$ . Both dipole model realisations have built in saturation of the black disc limit of the colour dipole scattering amplitude. This means that the absolute value of the  $T$ -matrix elements tends to unity for large dipoles or as  $x \rightarrow 0$ . It is curious that the choice of approximation has a striking consequence in how the unitarity (the black disc) limit is approached. In the GM case unitarisation happens because of cancellations between contributions of non-saturating multiple gluon exchanges, while in the BK case multiple scattering effects are contained in the single gluon density that saturates at a certain small value of  $x$ . These differences in the mechanism of unitarisation do not affect, however, the crucial qualitative feature of the dipole cross-section: the transition from a power-like growth with decreasing  $x$  in the colour transparency regime to a flat (possibly  $\sim \ln(1/x)$ ) behaviour in the black disc limit. Thus, the necessary modelling of the dipole cross section for large dipole sizes is strongly constrained.

A third type of parameterisation for the dipole cross section does not assume any mechanism for unitarisation. It is a two-component Regge model (FS04 Sat) [7], which uses hard Pomeron behaviour ( $\sim r^2 x^{-0.3}$ ) for small dipole sizes  $r < r_0$  and soft Pomeron behaviour ( $\sim x^{-0.1}$ ) for large dipole sizes  $r > r_1$ , with linear interpolation between the two regions. Again, a factorising impact parameter dependence is assumed. Saturation effects are modelled by allowing  $r_0$  to move to lower values with decreasing  $x$ . This feature was found to be preferred by the HERA data, whereas the two-component Regge model with a fixed  $r_0$  was disfavoured [7].

We compare the dipole model parameterisations in Fig. 3a, where the  $b$ -integrated dipole cross sections have been divided by the trivial factor  $r^2$  in order to emphasise the differences at small  $r$ . We restrict attention to dipole model parameterisations which have been shown to give a good fit (with charm quarks included) to recent HERA inclusive structure function data, meaning a  $\chi^2$  per data point of  $\sim 1$ . This excludes, for example, the original GBW parameterisation [4]

and the unsaturated two-component Regge model [7]. All parameterisations shown in Fig. 3a are similar at intermediate dipole sizes where they are most constrained by HERA data. At very small dipole sizes the b-Sat model deviates from the other parameterisations, as it is the only one which incorporates explicit DGLAP evolution. The b-Sat model was found to be preferred over the b-CGC model for observables sensitive to relatively small dipole sizes [12]. There are also differences between the parameterisations in the approach to the unitarity limit at large dipole sizes. For example, the b-Sat and b-CGC dipole cross sections tend to a constant at large  $r$  only for a fixed  $b$ , but not when integrating over all impact parameters.

In order to compare the magnitude of unitarity corrections between various models it is customary to define a model-independent saturation scale  $Q_S^2$ , that is, the momentum scale at which the dipole–proton scattering amplitude  $\mathcal{N}$  becomes sizable. There is no unique definition of  $Q_S^2$  and various choices are used in the literature. We define the saturation scale  $Q_S^2 \equiv 2/r_S^2$ , where the saturation radius  $r_S$  is the dipole size where the scattering amplitude

$$\mathcal{N}(x, r_S[b]) = 1 - e^{-\frac{1}{2}} \simeq 0.4, \quad (5)$$

chosen to match the corresponding quantity,  $Q_s$ , in the GBW model [4]. Note that this “saturation scale” is still far from the unitarity limit where  $\mathcal{N} = 1$ . The model-independent saturation scale  $Q_S^2$  is shown in Fig. 3b: it is generally less than  $0.5 \text{ GeV}^2$  in the HERA kinematic regime for the most relevant impact parameters  $b \sim 2\text{--}3 \text{ GeV}^{-1}$  [11, 12]. It should be remembered, however, that any observable will depend on integration over a range of dipole sizes, therefore even at high  $Q^2$  there will be some contribution from large dipole sizes  $r > r_S$ . Moreover, dipole models incorporating saturation fitted to HERA data may be extrapolated to very low  $x$  and to predict cross sections for nuclear collisions where the saturation scale is enhanced by  $A^{1/3}$  [13]. In these situations, multi-Pomeron exchange may become important and extrapolation based on single-Pomeron exchange would be unreliable.

#### 4 Theory outlook: saturation beyond the BK equation in a statistical picture

The BK equation describes unitarity corrections in the asymmetric configuration, when the target is extended and dense and the projectile is small and dilute. In a more symmetric situation, like  $\gamma^*(Q^2)p$  scattering at low  $Q^2$ , the BK approximation is no longer sufficient. In the diagrammatic formulation, besides the fan diagram one should then take into account diagrams with closed Pomeron loops. To construct a fully reliable and practical theoretical treatment of this complex case has turned out to be a prohibitively difficult task so far. Fortunately, the key properties of solutions of the BK equation in the low momentum region follow from its universal features and do not rely on the details of the equation.

In the Kovchegov derivation of the BK equation [25] one uses the Mueller dipole cascade picture [2] of the small  $x$  QCD evolution. The equation expressed in terms of the dipole scattering amplitude,  $N_{uv}(Y) \equiv \mathcal{N}(x, \mathbf{r}, \mathbf{b})$ , with  $Y = \ln(1/x)$ , reads

$$\frac{\partial N_{uv}}{\partial Y} = \frac{\bar{\alpha}_s}{2\pi} \int d^2\mathbf{w} \frac{(\mathbf{u} - \mathbf{v})^2}{(\mathbf{u} - \mathbf{w})^2(\mathbf{w} - \mathbf{v})^2} [N_{uw} + N_{vw} - N_{uv} - N_{uw}N_{vw}] \quad (6)$$

where  $\mathbf{u} = \mathbf{b} - \mathbf{r}/2$ , and  $\mathbf{v} = \mathbf{b} + \mathbf{r}/2$  (assuming  $z=1/2$  in the definition of  $\mathbf{b}$ , cf. Sec. 2). The equation has two fixed points: the repulsive one,  $N_{uv} = 0$ , from which the solution is

driven out by the linear term, and the attractive one,  $N_{uv} = 1$ , where the linear and nonlinear term compensate each other. This scenario of linear growth of the amplitude tamed by nonlinear rescattering effects is common to all existing approaches to the saturation phenomenon. In the uniform case, when  $N$  does not depend on the impact parameter,  $b$ , this combination of growth and nonlinearity was shown to lead to a *geometric scaling* property [28] of the solutions,  $N_{uv}(Y) = N(|\mathbf{u} - \mathbf{v}|^2 Q_s^2(Y))$  for  $Y \gg 1$ , irrespective of the initial conditions [29]. For the  $\gamma^*p$  cross section, geometric scaling implies that  $\sigma^{\gamma^*p}(x, Q^2) = \sigma^{\gamma^*p}(Q_s^2/Q^2)$ , which was observed in HERA data [28].

Interestingly enough, the geometric scaling property of the BK equation does not depend on the details of either the linear or the non-linear term. Therefore the scaling is a robust and universal phenomenon. In particular, the BK equation belongs to the same universality class as a simpler and well understood Fisher–Kolmogorov–Petrovsky–Piscounov (FKPP) equation [29],  $\partial_t u(x, t) = \partial_{xx}^2 u + u - u^2$ , where the rapidity is mapped onto the time  $t$  and the logarithm of the dipole size onto the real variable  $x$ . Employing this connection it was proved that, indeed, both the emergence of geometric scaling and the rapidity evolution of the saturation scale are universal phenomena and do not depend on the details of the BK equation, provided that the initial condition is uniform in the impact parameter space.

The statistical framework implied by the Mueller dipole model may also be used to provide some qualitative insight into the effect of “Pomeron loops” in the scattering amplitudes [30, 31]. This effect corresponds to a stochastic term added to the FKPP equation [31],

$$\partial_t u(x, t) = \partial_{xx}^2 u + u - u^2 + \sqrt{u(1-u)} \eta \quad (7)$$

where  $\eta$  is the white noise. The origin of stochasticity can be traced back to the discreteness of the colour dipoles in the Mueller cascade model. The BK equation is derived in the mean field approximation when the density of colour dipoles in the projectile is large enough ( $n \gg 1$ ) that statistical fluctuations in the number of dipoles can be neglected. In this case,  $N_{uv}$  is an averaged dipole scattering amplitude. At the edge of the dense regime of the dipole distribution, however, the dipole occupation number is small,  $n \sim 1$ , so the statistical fluctuations play an important rôle. It was realised in Ref. [30] and subsequently developed in Ref. [31] that these fluctuations get enhanced in the  $Y$ -evolution and affect the global properties of the amplitude. In this approach the saturation scale becomes a stochastic variable that fluctuates from one scattering event to another, with a lognormal distribution with the variance  $\sigma^2 = DY$ , where  $D \sim \alpha_s / \ln^3(1/\alpha_s^2)$  [32]. The most important result of fluctuations is a new scaling of the physical amplitude, called *diffusive scaling* [31]. Namely, the dipole scattering amplitude  $N_{uv}(Y)$ , should depend only on one variable,  $\xi = (\ln(r^2) + \langle \ln Q_s^2 \rangle) / \sqrt{DY}$ . Note that the factor  $\sqrt{DY}$  in the denominator which spoils the geometric scaling is of the diffusive origin. A first attempt to trace the diffusive scaling in the HERA data on  $F_2$  was presented in Ref. [33] with a negative result. This would suggest that Pomeron loops introduce only a small effect in the HERA data.

The results presented here neglect the impact parameter dependence of the scattering amplitudes, assuming that the high energy QCD evolution is local in the transverse coordinate space. Thus the local evolutions at different  $b$ 's are uncorrelated. Recent numerical studies [34] suggest that this is a quite accurate picture of high energy scattering if the dipole size is significantly smaller than the target size.

Recently, an interesting attempt was made [35] to explicitly model the colour dipole cascade taking into account effects related to Pomeron loops. In more detail, subleading effects in the  $1/N_c$  expansion were phenomenologically incorporated that lead to a possibility of colour dipole reconnections in the dipole wave function. The resulting dipole–dipole scattering amplitudes were shown to respect with good accuracy the symmetry between the target and the projectile, which does not hold in the absence of the colour reconnection. The approach employs Monte-Carlo methods and was shown to be quite successful in describing total cross-sections and many diffractive observables.

## 5 Concluding remarks

The dipole models applied to HERA data on inclusive and diffractive processes provide a successful unified description of most observables. These analyses provide significant evidence for sizable unitarity (rescattering) corrections to the single scattering approximation, that is used in the linear QCD evolution equations, in both DGLAP and BFKL. These corrections become strong below the saturation scale,  $Q_S(x)$ . The determination of the saturation scale within different dipole models yields consistently that  $Q_S < 1$  GeV, over the HERA kinematic range.  $Q_S$  is found to increase with  $1/x$ , approximately as  $Q_S^2(x) \sim (1/x)^{\lambda_S}$  with  $\lambda_S \simeq 0.12-0.2$ , depending on the model. Both these properties of  $Q_S$  suggest that the onset of perturbative saturation is probed at HERA, and that non-perturbative effects may still be significant around  $Q_S$ . Fortunately, the key results on the saturation phenomenon obtained within perturbative QCD are universal and should remain valid despite a possible non-perturbative contamination.

## Acknowledgements

K. G.-B. and L. M. acknowledge a support of grant of Polish Ministry of Education No. N N202 249235. L. M. is supported by the DFG grant SFB 676. G. W. acknowledges the UK Science and Technology Facilities Council for the award of a Responsive Research Associate position.

## References

- [1] N. N. Nikolaev and B. G. Zakharov, Z. Phys. **C49**, 607 (1991);  
N. N. Nikolaev and B. G. Zakharov, Z. Phys. **C53**, 331 (1992).
- [2] A. H. Mueller, Nucl. Phys. **B415**, 373 (1994);  
A. H. Mueller and B. Patel, Nucl. Phys. **B425**, 471 (1994).
- [3] K. J. Golec-Biernat, *Review on parton saturation*.  
Talk at the 4th HERA and the LHC workshop, CERN, 26–30 May 2008,  
<http://indico.cern.ch/conferenceDisplay.py?confId=27458>.
- [4] K. J. Golec-Biernat and M. Wüsthoff, Phys. Rev. **D59**, 014017 (1999);  
K. J. Golec-Biernat and M. Wüsthoff, Phys. Rev. **D60**, 114023 (1999).
- [5] J. Bartels, K. J. Golec-Biernat and H. Kowalski, Phys. Rev. **D66**, 014001 (2002);  
K. J. Golec-Biernat and S. Sapeta, Phys. Rev. **D74**, 054032 (2006).

- [6] H. Kowalski and D. Teaney, Phys. Rev. **D68**, 114005 (2003).
- [7] J. R. Forshaw and G. Shaw, JHEP **12**, 052 (2004);  
J. R. Forshaw, R. Sandapen and G. Shaw, JHEP **11**, 025 (2006);  
G. Shaw, *Saturation and the colour dipole model*.  
Talk at the 3rd HERA and the LHC workshop, DESY, 12–16 March 2007,  
<http://indico.cern.ch/conferenceDisplay.py?confId=11784>.
- [8] E. Iancu, K. Itakura and S. Munier, Phys. Lett. **B590**, 199 (2004).
- [9] G. Soyez, Phys. Lett. **B655**, 32 (2007).
- [10] C. Marquet, R. B. Peschanski and G. Soyez, Phys. Rev. **D76**, 034011 (2007).
- [11] H. Kowalski, L. Motyka and G. Watt, Phys. Rev. **D74**, 074016 (2006).
- [12] G. Watt and H. Kowalski, Phys. Rev. **D78**, 014016 (2008);  
G. Watt, *Exclusive diffractive processes within the dipole picture*.  
Talk at the 4th HERA and the LHC workshop, CERN, 26–30 May 2008,  
<http://indico.cern.ch/conferenceDisplay.py?confId=27458>.
- [13] H. Kowalski, T. Lappi and R. Venugopalan, Phys. Rev. Lett. **100**, 022303 (2008);  
H. Kowalski, T. Lappi, C. Marquet and R. Venugopalan, arXiv:0805.4071  
[hep-ph].
- [14] J. Bartels and L. Motyka, Eur. Phys. J. **C55**, 65 (2008).
- [15] P. Lepage and S. Brodsky, Phys. Rev. **D22**, 2157 (1980).
- [16] L. V. Gribov, E. M. Levin and M. G. Ryskin, Phys. Rept. **100**, 1 (1983).
- [17] S. Catani, M. Ciafaloni and F. Hautmann, Nucl. Phys. **B366**, 135 (1991);  
S. Catani and F. Hautmann, Nucl. Phys. **B427**, 475 (1994).
- [18] J. Bartels, K. J. Golec-Biernat and K. Peters, Eur. Phys. J. **C17**, 121 (2000);  
L. Motyka, *Higher twists from the saturation model*.  
Talk at the 4th HERA and the LHC workshop, CERN, 26–30 May 2008,  
<http://indico.cern.ch/conferenceDisplay.py?confId=27458>.
- [19] A. P. Bukhvostov, G. V. Frolov, L. N. Lipatov and E. A. Kuraev, Nucl. Phys. **B258**, 601 (1985).
- [20] J. Bartels and M. Ryskin, Z. Phys. **C60**, 751 (1993).
- [21] C. Ewerz and O. Nachtmann, Annals Phys. **322**, 1635 (2007);  
C. Ewerz and O. Nachtmann, Annals Phys. **322**, 1670 (2007).
- [22] A. von Manteuffel, *Bounds on DIS observables from the colour dipole picture*.  
Talk at the 3rd HERA and the LHC workshop, DESY, 12–16 March 2007,  
<http://indico.cern.ch/conferenceDisplay.py?confId=11784>.



- [23] C. Ewerz, A. von Manteuffel and O. Nachtmann, Phys. Rev. **D77**, 074022 (2008).
- [24] R. J. Glauber, Phys. Rev. **99**, 1515 (1955);  
A. H. Mueller, Nucl. Phys. **B335**, 115 (1990).
- [25] I. Balitsky, Nucl. Phys. **B463**, 99 (1996);  
Y. V. Kovchegov, Phys. Rev. **D60**, 034008 (1999);  
Y. V. Kovchegov, Phys. Rev. **D61**, 074018 (2000).
- [26] D. Boer, A. Utermann and E. Wessels, Phys. Rev. **D75**, 094022 (2007).
- [27] D. N. Triantafyllopoulos, Nucl. Phys. **B648**, 293 (2003).
- [28] A. M. Staśto, K. Golec-Biernat and J. Kwieciński, Phys. Rev. Lett. **86**, 596 (2001).
- [29] S. Munier and R. Peschanski, Phys. Rev. Lett. **91**, 232001 (2003);  
S. Munier and R. Peschanski, Phys. Rev. **D69**, 034008 (2004);  
S. Munier and R. Peschanski, Phys. Rev. **D70**, 077503 (2004).
- [30] A. H. Mueller and A. Shoshi, Nucl. Phys. **B692**, 175 (2004).
- [31] S. Munier, Nucl. Phys. **A755**, 622 (2005);  
E. Iancu, A. Mueller and S. Munier, Phys. Lett. **B606**, 342 (2005).
- [32] C. Marquet, G. Soyez and Bo-Wen Xiao, Phys. Lett. **B639**, 635 (2006);  
R. Enberg, K. Golec-Biernat and S. Munier, Phys. Rev. **D72**, 074021 (2005).
- [33] E. Basso, M. B. Gay Ducati, E. G. de Oliveira and J. T. de Santana Amaral,  
[arXiv:0807.1556](https://arxiv.org/abs/0807.1556) [hep-ph].
- [34] S. Munier, G. P. Salam, and G. Soyez, [arXiv:0807.2870](https://arxiv.org/abs/0807.2870) [hep-ph].
- [35] E. Avsar, G. Gustafson and L. Lönnblad, JHEP **07**, 062 (2005);  
E. Avsar, G. Gustafson and L. Lönnblad, JHEP **01**, 012 (2007);  
E. Avsar, G. Gustafson and L. Lönnblad, JHEP **12**, 012 (2007);  
C. Flensburg, G. Gustafson and L. Lönnblad, [arXiv:0807.0325](https://arxiv.org/abs/0807.0325) [hep-ph];  
E. Avsar, *Small- $x$  physics and an improved dipole model*.  
Talk at the 3rd HERA and the LHC workshop, DESY, 12–16 March 2007,  
<http://indico.cern.ch/conferenceDisplay.py?confId=11784>.

# Checking formalism for central exclusive production in the first LHC runs

A.D. Martin, V.A. Khoze and M.G. Ryskin

Institute for Particle Physics Phenomenology, University of Durham, DH1 3LE, UK

## Abstract

We discuss how the early LHC data runs can provide crucial tests of the formalism used to predict the cross sections of central exclusive production.

## 1 Introduction

The physics potential of forward proton tagging at the LHC has attracted much attention in the last years, for instance, [1–5]. The combined detection of both outgoing protons and the centrally produced system gives access to a unique rich programme of studies in QCD, electroweak and BSM physics. Importantly, these measurements will provide valuable information on the Higgs sector of MSSM and other popular BSM scenarios, see [6–9].

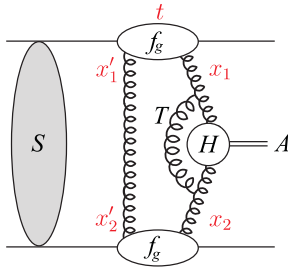


Fig. 1: A symbolic diagram for the CEP of a system  $A$ .

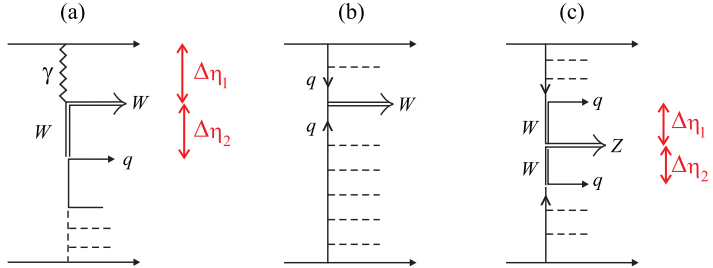


Fig. 2: (a)  $W$  production with 2 gaps, (b) Inclusive  $W$  production, (c)  $Z$  production with 2 gaps.

The theoretical formalism [10–12] for the description of a central exclusive production (CEP) process contains quite distinct parts, shown symbolically in Fig. 1. We first have to calculate the  $gg \rightarrow A$  subprocess,  $H$ , convoluted with the gluon distributions  $f_g$ . Next, we must account for the QCD corrections which reflect the absence of additional radiation in the hard subprocess – that is, for the Sudakov factor  $T$ . Finally, we must enter soft physics to calculate the survival probability  $S^2$  of the rapidity gaps (RG).

The uncertainties of the CEP predictions are potentially not small. Therefore, it is important to perform checks using processes that will be accessible in the first LHC runs [13]. We first

consider measurements which do not rely on proton tagging and can be performed through the detection of RG.

The main uncertainties of the CEP predictions are associated with

- (i) the probability  $S^2$  that additional secondaries will not populate the gaps;
- (ii) the probability to find the appropriate gluons, that are given by generalized, unintegrated distributions  $f_g(x, x', Q_t^2)$ ;
- (iii) the higher order QCD corrections to the hard subprocess, in particular, the Sudakov suppression;
- (iv) the so-called semi-enhanced absorptive corrections (see [14, 15]) and other effects, which may violate the soft-hard factorization.

## 2 Gap survival factor $S^2$

Usually, the gap survival is calculated within a multichannel eikonal approach [16]. The probability  $S^2$  of elastic  $pp$  rescattering, shown symbolically by  $S$  in Fig. 1 can be evaluated in a model independent way once the elastic cross section  $d\sigma_{el}/dt$  is measured at the LHC. However, there may be excited states between the blob  $S$  and the amplitude on the r.h.s of Fig. 1. The presence of such states enlarges absorption. To check experimentally the role of this effect, we need a process with a bare cross section that can be reliably calculated. Good candidates are the production of  $W$  or  $Z$  bosons with RGs [13]. In the case of ‘ $W$ +gaps’ production the main contribution comes from the diagram of Fig. 2(a) [17]. One gap,  $\Delta\eta_1$ , is associated with photon exchange, while the other,  $\Delta\eta_2$ , is associated with the  $W$ . In the early LHC data runs the ratio ( $W$ +gaps/ $W$  inclusive) will be measured first. This measurement is a useful check of the models for soft rescattering [13].

A good way to study the low impact parameter ( $b_t$ ) region is to observe  $Z$  boson production via  $WW$  fusion, see Fig. 2(c). Here, both gaps originate from  $W$ -exchange, and the corresponding  $b_t$  region is similar to that for exclusive Higgs production. The expected  $Z$ +gaps cross section is of the order of 0.2 pb, and  $S^2=0.3$  for  $\Delta\eta_{1,2} > 3$  and for quark jets with  $E_T > 50$  GeV [18].

## 3 Generalized, unintegrated gluon distribution $f_g$

The cross section for the CEP of a system  $A$  essentially has the form [10]

$$\sigma(pp \rightarrow p+A+p) \simeq \frac{S^2}{B^2} \left| \frac{\pi}{8} \int \frac{dQ_t^2}{Q_t^4} f_g(x_1, x'_1, Q_t^2, \mu^2) f_g(x_2, x'_2, Q_t^2, \mu^2) \right|^2 \hat{\sigma}(gg \rightarrow A). \quad (1)$$

Here the factor  $1/B^2$  arises from the integration over the proton transverse momentum. Also,  $f_g$  denotes the generalized, unintegrated gluon distribution. In our case the distribution  $f_g$  can be obtained from the conventional gluon distribution,  $g$ , known from the global parton analyses. The main uncertainty here comes from the lack of knowledge of the integrated gluon distribution

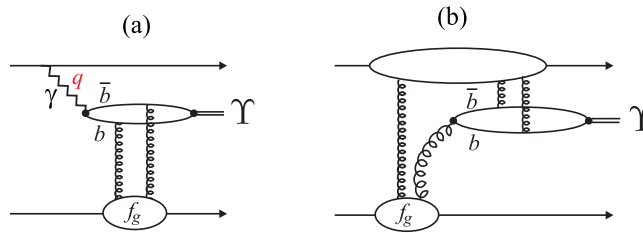


Fig. 3: Exclusive  $\Upsilon$  production via (a) photon exchange, and (b) via odderon exchange.

$g(x, Q_t^2)$  at low  $x$  and small scales. For example, taking  $Q_t^2 = 4 \text{ GeV}^2$  we find [13]  $xg = (3 - 3.8)$  for  $x = 10^{-2}$  and  $xg = (3.4 - 4.5)$  for  $x = 10^{-3}$ . These are big uncertainties bearing in mind that the CEP cross section depends on  $(xg)^4$ . To reduce the uncertainty associated with  $f_g$  we can measure exclusive  $\Upsilon$  production. The process is shown in Fig. 3(a). The cross section for  $\gamma p \rightarrow \Upsilon p$  is given in terms of the same unintegrated gluon distribution  $f_g$  that occurs in Fig. 1. There may be competition between production via photon exchange, Fig. 3(a), and via odderon exchange, see Fig. 3(b). A lowest-order calculation (e.g. [19]) indicates that the odderon process (b) may be comparable to the photon-initiated process (a). If the upper proton is tagged, it will be straightforward to separate the two mechanisms.

#### 4 Three-jet events as a probe of the Sudakov factor

The search for the exclusive dijets at the Tevatron,  $p\bar{p} \rightarrow p + jj + \bar{p}$ , is performed [20] by plotting the cross section in terms of the variable  $R_{jj} = M_{jj}/M_A$ , where  $M_A$  is the mass of the whole central system. However, the  $R_{jj}$  distribution is smeared out by QCD radiation, hadronization, the jet algorithm and other experimental effects [20,21]. To weaken the smearing it was proposed in Ref. [21] to study the dijets in terms of a variable  $R_j = 2E_T (\cosh \eta^*)/M_A$ , where only the transverse energy and the rapidity  $\eta$  of the jet with the *largest*  $E_T$  enter. Here  $\eta^* = \eta - y_A$ , where  $y_A$  is the rapidity of the central system. Clearly, the largest  $E_T$  jet is less affected by the smearing. As shown in [13], it is sufficient to consider the emission of a third jet, when we take all three jets to lie in a specified rapidity interval  $\delta\eta$ . The cross section  $d\sigma/dR_j$ , as a function of  $R_j$ , for the production of a pair of high  $E_T$  dijets accompanied by a third jet is discussed in [13,21]. It is shown that the measurements of the exclusive two- and three-jet cross sections *as a function of*  $E_T$  of the highest jet allow a detailed check of the Sudakov physics; with much more information coming from the  $\delta\eta$  dependence study. A clear way to observe the Sudakov suppression is just to measure the  $E_T$  dependence of exclusive dijet production. On dimensional grounds we would expect  $d\sigma/dE_T^2 \propto 1/E_T^4$ . This behaviour is modified by the gluon anomalous dimension and by a stronger Sudakov suppression with increasing  $E_T$ . Already the existing CDF dijet data [20] exclude predictions which omit the Sudakov effect.

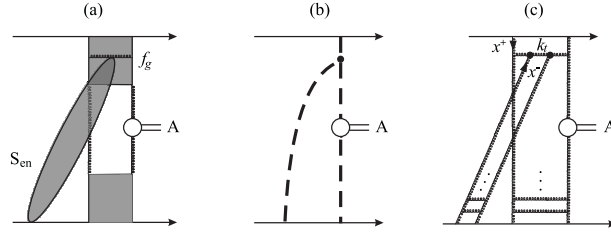


Fig. 4: (a) A typical enhanced diagram, where the shaded boxes denote  $f_g$ , and the soft rescattering is on an intermediate parton, giving rise to a survival factor  $S_{\text{en}}$ ; (b) and (c) are the Reggeon and QCD representations, respectively.

## 5 Soft-hard factorization: enhanced absorptive effects

The soft-hard factorization implied by Fig. 1 could be violated by the so-called enhanced Reggeon diagrams, see Fig. 4(a). The contribution of the first Pomeron loop, Fig. 4(b) was calculated in pQCD in Ref. [15]. A typical diagram is shown in Fig. 4(c). For LHC energies it was found that such effect may be numerically large. The reason is that the gluon density grows at low  $x$  and, for low  $k_t$  partons, approaches the saturation limit. However, as discussed in [13], the enhanced diagram should affect mainly the very beginning of the QCD evolution – the region that cannot be described perturbatively and which, in [11, 12], is already included phenomenologically.

Experimentally, we can study the role of semi-enhanced absorption by measuring the ratio  $R$  of diffractive event rate for  $W$  (or  $\Upsilon$  or dijet) as compared to the inclusive process [13]. That is

$$R = \frac{\text{no. of } (A + \text{gap}) \text{ events}}{\text{no. of (inclusive } A) \text{ events}} = \frac{a^{\text{diff}}(x_{\mathbb{P}}, \beta, \mu^2)}{a^{\text{incl}}(x = \beta x_{\mathbb{P}}, \mu^2)} \langle S^2 S_{\text{en}}^2 \rangle_{\text{over } b_t}, \quad (2)$$

where  $a^{\text{incl}}$  and  $a^{\text{diff}}$  are the parton densities determined from the global analyses of inclusive and diffractive DIS data, respectively. We can measure a double distribution  $d^2\sigma^{\text{diff}}/dx_{\mathbb{P}}dy_A$ , and form the ratio  $R$  using the inclusive cross section,  $d\sigma^{\text{incl}}/dy_A$ . If we neglect the enhanced absorption, it is quite straightforward to calculate the ratio  $R$  of (2). The results for a dijet case are shown by the dashed curves in Fig. 5 as a function of the rapidity  $y_A$  of the dijet system. The enhanced rescattering reduce the ratios and lead to steeper  $y_A$  distributions, as illustrated by the continuous curves. Perhaps the most informative probe of  $S_{\text{en}}^2$  is to observe the ratio  $R$  for dijet production in the region  $E_T \sim 15 - 30$  GeV. For example, for  $E_T \sim 15$  GeV we expect  $S_{\text{en}}^2 \sim 0.25, 0.4$  and  $0.8$  at  $y_A = -2, 0$  and  $2$  respectively.

## 6 Conclusion

The addition of forward proton detectors to LHC experiments will add unique capabilities to the existing LHC experimental programme. For certain BSM scenarios, the tagged-proton mode may even be the discovery channel. There is also a rich QCD, electroweak, and more exotic physics, menu.

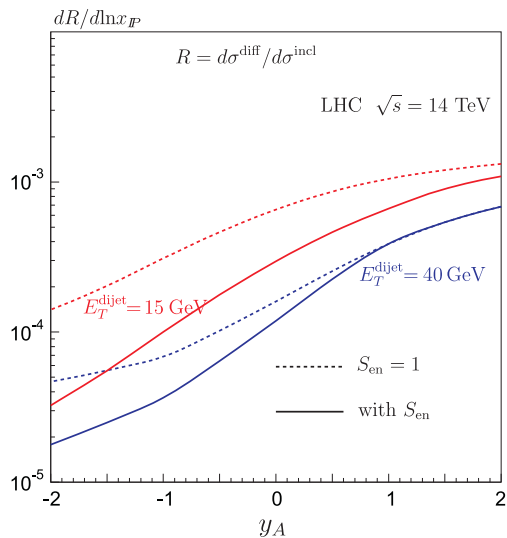


Fig. 5: The predictions of the ratio  $R$  of (2) for the production of a pair of high  $E_T$  jets.

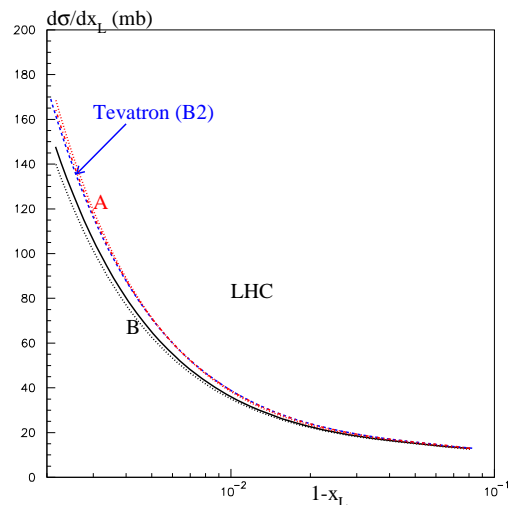


Fig. 6: The cross section  $d\sigma_{SD}/dx_L$  for single dissociation integrated over  $t$  at the LHC energy.

The uncertainties in the prediction of the CEP processes are potentially not small. Therefore, it is crucial to perform checks of the theoretical formalism using reactions that will be experimentally accessible in the first LHC runs [13].

Most of the measurements discussed above can be performed, without detecting the protons, by taking advantage of the relatively low luminosity in the early LHC runs. When the forward proton detectors are operating much more can be done. First, it is possible to measure directly the cross section  $d^2\sigma_{SD}/dtdM_X^2$  for single diffractive dissociation and also the cross section  $d^2\sigma_{DPE}/dy_1dy_2$  for soft central diffractive production. These measurements will strongly constrain the models used to describe diffractive processes and the effects of soft rescattering. The recent predictions can be found in [12]. For illustration we show in Fig. 6 the expectation for  $d\sigma_{SD}/dx_L$ , see for details [12]. Next, a study of the transverse momentum distributions of both of the tagged protons, and the correlations between their momenta, is able to scan the proton optical density [17, 22].

## References

- [1] V.A. Khoze, A.D. Martin and M.G. Ryskin, *Eur. Phys. J.* **C23**, 311 (2002).
- [2] A. De Roeck *et al.*, *Eur. Phys. J.* **C25**, 391(2002).
- [3] J. Forshaw and A. Pilkington, In *\*Hamburg 2007, Blois07, Forward physics and QCD\** 130-136.
- [4] M. G. Albrow *et al.* [FP420 R and D Collaboration], arXiv:0806.0302 [hep-ex].

- [5] P. J. Bussey, arXiv:0809.1335 [hep-ex].
- [6] A.B. Kaidalov *et al.*, *Eur. Phys. J. C***33**, 261 (2004).
- [7] S. Heinemeyer *et al.*, *Eur. Phys. J. C***53**, 231 (2008).
- [8] B. Cox, F. Loebinger and A. Pilkington, *JHEP* **0710**, 090 (2007).
- [9] J. R. Forshaw *et al.*, *JHEP* **0804**, 090 (2008).
- [10] V.A. Khoze, A.D. Martin and M.G. Ryskin, *Eur. Phys. J. C***14**, 525 (2000).
- [11] V.A. Khoze, A.D. Martin and M.G. Ryskin, *Eur. Phys. J. C***18**, 167 (2000).
- [12] M.G. Ryskin, A.D. Martin and V.A. Khoze, *Eur. Phys. J. C***54**, 199 (2008); E.G.S. Luna *et al.*, arXiv:0807.4115 [hep-ph].
- [13] V.A. Khoze, A.D. Martin and M.G. Ryskin, *Eur. Phys. J. C* **55**, 363 (2008).
- [14] A.B. Kaidalov *et al.*, *Eur. Phys. J. C***21**, 521 (2001).
- [15] J. Bartels *et al.*, *Phys. Rev. D***73**, 093004 (2006).
- [16] For a review see: E. Gotsman *et al.*, arXiv:hep-ph/0511060.
- [17] V.A. Khoze, A.D. Martin and M.G. Ryskin, *Eur. Phys. J. C***24**, 459 (2002).
- [18] V.A. Khoze *et al.*, *Eur. Phys. J. C***26**, 429 (2003).
- [19] A. Bzdak *et al.*, *Phys. Rev. D***75**, 094023 (2007).
- [20] T. Aaltonen *et al.* [CDF Run II Collaboration], *Phys. Rev. D* **77**, 052004 (2008).
- [21] V.A. Khoze, A.D. Martin and M.G. Ryskin, *Eur. Phys. J. C***48**, 467 (2006).
- [22] V.A. Khoze, A.D. Martin and M.G. Ryskin, *Eur. Phys. J. C***24**, 581 (2002).

# Rapidity gap survival probability and total cross sections

A.D. Martin, V.A. Khoze and M.G. Ryskin

Institute for Particle Physics Phenomenology, University of Durham, DH1 3LE, UK

## Abstract

We discuss recent calculations of the survival probability of the large rapidity gaps in exclusive processes of the type  $pp \rightarrow p + A + p$  at high energies. Absorptive or screening effects are important, and one consequence is that the total cross section at the LHC is predicted to be only about 90 mb.

At the LHC, the observation of an exclusive process of the type  $pp \rightarrow p + A + p$ , where a produced new heavy object  $A$  is separated from the outgoing protons by large rapidity gaps (LRG), will provide very good experimental conditions to study the properties of object  $A$  [1–3]. The process is sketched in Fig. 1. The case of  $A = H \rightarrow b\bar{b}$  is particularly interesting. The cross is usually written in the form

$$\sigma \sim \frac{\langle S^2 \rangle}{B^2} \left| N \int \frac{dQ_t^2}{Q_t^4} f_g(x_1, x'_1, Q_t^2, \mu^2) f_g(x_2, x'_2, Q_t^2, \mu^2) \right|^2 \quad (1)$$

where  $B/2$  is the  $t$ -slope of the proton-Pomeron vertex, and the constant  $N$  is known in terms of the  $A \rightarrow gg$  decay width. The amplitude-squared factor,  $|\dots|^2$ , can be calculated in perturbative QCD, since the dominant contribution to the integral comes from the region  $\Lambda_{QCD}^2 \ll Q_t^2 \ll M_A^2$ , for the large values of  $M_A^2$  of interest. The probability amplitudes,  $f_g$ , to find the appropriate pairs of  $t$ -channel gluons  $(x_1, x'_1)$  and  $(x_2, x'_2)$  of Fig. 1, are given by skewed unintegrated gluon densities at a hard scale  $\mu \sim M_A/2$ . To evaluate the cross section of such an exclusive processes it is important to know the probability,  $\langle S^2 \rangle$ , that the LRG survive and will not be filled by secondaries from eikonal and enhanced rescattering effects. The main effect comes from the rescattering of soft partons, since they have the largest absorptive cross sections. Therefore, we need a realistic model to describe soft interactions at the LHC energy, and to predict the total cross section at LHC. The model must account for (i) elastic rescattering (with two protons in intermediate state), (ii) the probability of the low-mass proton excitations (with an intermediate proton replaced by the N(1400), N(1700), etc. resonances), and (iii) the screening corrections due to high-mass proton dissociation.

The effect of elastic rescattering may be evaluated in a model independent way once the elastic  $pp$ -amplitude is known. The effect of the low-mass dissociation is usually calculated in the framework of the Good-Walker formalism [4], that is, by introducing diffractive eigenstates,  $\phi_i$  with  $i = 1, \dots, n$ , which only undergo ‘elastic’ scattering. The resulting  $n$ -channel eikonal  $\Omega_{ik}(s, b)$  depends on the energy and the impact parameter of the  $pp$  interaction. The parameters



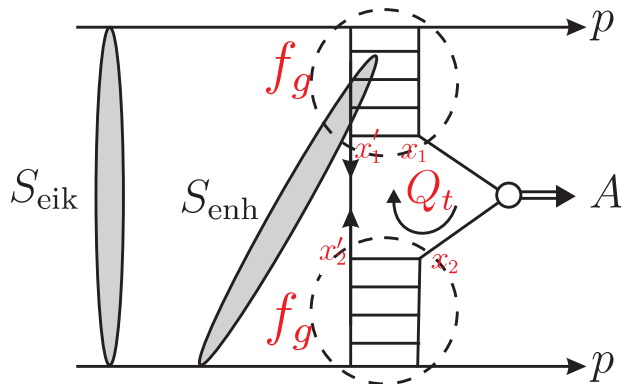


Fig. 1: The mechanism for the exclusive process  $pp \rightarrow p + A + p$ , with the eikonal and enhanced survival factors shown symbolically.

of the model are chosen to reproduce the available (fixed-target and CERN-ISR) data on the cross section of low-mass diffractive dissociation. Usually either a two- or three-channel eikonal is used. Finally, high-mass dissociation is described in terms of Reggeon diagram technique [5]. A symbolic representation of these soft scattering effects is shown in Fig. 2. The latest calculations along these lines are described in Refs. [6, 7]. In Ref. [6] the authors account only for the triple-Pomeron vertex, and, moreover, sum up only the specific subset<sup>1</sup> of multi-Pomeron diagrams that were considered in Ref. [8], which is called the MPSI approximation. In Ref. [7] all possible multi-Pomeron vertices were included under a reasonable assumption about the form of the  $n \rightarrow m$  multi-Pomeron vertices,  $g_m^n$ . The assumption corresponds to the hypothesis that the screening of the  $s$ -channel parton  $c$  during the evolution is given by the usual absorption factor  $\exp(-\Omega_{ic}(b) - \Omega_{ck}(b))$ , where  $\Omega_{ic}(b)$  ( $\Omega_{ck}(b)$ ) is the value of the opacity of the beam (target) proton at impact parameter  $b$  with respect to the parton  $c$ .

Since the absorptive corrections increase with energy, the cross section grows more slowly than the simple power ( $\sigma \propto s^\Delta$ ) parametrisation [9]. In spite of the fact that the models of [6] and [7] are quite different to each other, after the parameters are fixed to describe the data on the total, elastic and single dissociation cross sections ( $\sigma_{\text{tot}}$ ,  $d\sigma_{\text{el}}/dt$  and  $d\sigma_{\text{SD}}/dM^2$ ) within the CERN-ISR – Tevatron energy range, the latest versions of the Tel-Aviv and Durham models predict almost the same total cross section at the LHC, namely  $\sigma_{\text{tot}} \sim 90$  mb. Correspondingly, both models predict practically the same gap survival probability  $\langle S_{\text{eik}}^2 \rangle \sim 0.02$  with respect to the eikonal (including the elastic and low-mass proton excitation) rescattering, for the exclusive production of a Higgs boson.

A more delicate problem is the absorptive correction to exclusive cross sections caused by the so-called enhanced diagrams, that is by the interaction with the intermediate partons, see

<sup>1</sup>For example, the third, but not the second, term on the right-hand side of the expression for  $\Omega_{ik}/2$  in Fig. 2 is included; neither are multi-Pomeron terms, like the last term, included.

$$T_{ik} = 1 - e^{-\Omega_{ik}/2} = \sum \text{diagrams} \quad \Omega_{ik}/2 = \text{diagrams} + \dots$$

Fig. 2: The multi-channel eikonal form of the amplitude, where  $i, k$  are diffractive (Good-Walker) eigenstates. Low-mass proton dissociation is included by the differences of the Pomeron couplings to one or another Good-Walker state (i) in the first diagram, while the remaining (multi-Pomeron) diagrams on the right-hand side of the expression for  $\Omega_{ik}/2$  include the high-mass dissociation.

Fig. 1. This rescattering violates ‘soft-hard’ factorisation, since the probability of such an interaction depends both on the transverse momentum and on the impact parameter of the intermediate parton.

The contribution of the first enhanced diagram was evaluated in [10] in the framework of the perturbative QCD. It turns out to be quite large. On the other hand, such an effect is not seen experimentally. The absorptive correction due to enhanced screening must increase with energy. This was not observed in the present data (see [11] for a more detailed discussion).

Several possible reasons are given below.

(a) We have to sum up the series of the multi-loop Pomeron diagrams. The higher-loop contributions partly compensate the correction caused by the first-loop graph.

(b) There should be a “threshold”, since Pomeron vertices must be separated by a non-zero rapidity interval [12]. That is, at present energies, the kinematical space available for the position of a multi-Pomeron vertex in an enhanced diagram is small, and the enhanced contribution is much less than that obtained in leading logarithmic (LL) approximation.

(c) The factor  $S_{\text{eik}}^2$  already absorbs almost all the contribution from the center of the disk. The parton only survives eikonal rescattering on the periphery, that is at large  $b$ . On the other hand, on the periphery the parton density is rather small, and the probability of *enhanced* absorption is not large. This fact can be seen in Ref. [13]. There, the momentum,  $Q_s$ , below which we may approach saturation, was extracted from HERA data in the framework of the dipole model. Already at  $b = 0.6$  fm the value of  $Q_s^2 < 0.3 \text{ GeV}^2$  for  $x < 10^{-6}$ . See also [14] where the value of  $Q_s$  was evaluated using LO DGLAP evolution.

Point (c) is relevant to the calculation of  $S_{\text{enh}}^2$  described in [6]. First, note that the  $b$  dependence of the beginning of ‘saturation caused by enhanced graphs’ is not accounted for in the MPSI approximation used in [6]. In this model, we have the same two-particle irreducible amplitude (which sums up the enhanced diagrams) at any value of  $b$ . Therefore, the enhanced

screening effect does not depend on the initial parton density at a particular impact parameter point  $b$ . For this reason the suppression due to enhanced screening corrections  $\langle S_{\text{enh}}^2 \rangle = 0.063$  claimed in [6] is much too strong<sup>2</sup>.

The survival factor  $\langle S_{\text{enh}}^2 \rangle$  has also been calculated in the new version of the Durham model [16]. The model includes 3 components of the Pomeron, with the different transverse momenta  $k_t$  of the partons in each Pomeron component, in order to mimic BFKL diffusion in  $\ln k_t$ . In this way we obtain a more realistic estimate of the ‘enhanced screening’ in exclusive diffractive Higgs boson production at the LHC. The model predicts  $\langle S_{\text{enh}}^2 \rangle \sim 1/3$ . However the CDF data on exclusive  $\gamma\gamma$  and  $\chi_c$  production indicate that this suppression is not so strong.

Note, that comparing the values of the survival factors in this way is too simplistic. The problem is that, with enhanced screening on intermediate partons, we no longer have exact factorisation between the hard and soft parts of the process. Thus, before computing the effect of soft absorption we must fix what is included in the bare exclusive amplitude calculated in terms of perturbative QCD.

The first observation is that the bare amplitude is calculated as a convolution of two generalised (skewed) gluon distributions with the hard subprocess matrix element, see (1). These gluon distributions are determined from integrated gluon distributions of a global parton analysis of mainly deep inelastic scattering data. Now, the phenomenological integrated parton distributions already include the interactions of the intermediate partons with the parent proton. Thus calculations of  $S_{\text{enh}}$  should keep only contributions which embrace the hard matrix element of the type shown in Fig. 1.

The second observation is that the phenomenologically determined generalised gluon distributions,  $f_g$ , are usually taken at  $p_t = 0$  and then the observed ‘total’ cross section is calculated by integrating over  $p_t$  of the recoil protons assuming the an exponential behaviour  $e^{-Bp_t^2}$ ; that is

$$\int dp_t^2 e^{-Bp_t^2} = 1/B = \langle p_t^2 \rangle. \quad (2)$$

However, the total soft absorptive effect changes the  $p_t$  distribution in comparison to that for the bare cross section determined from perturbative QCD. Thus the additional factor introduced by the soft interactions is not just the gap survival  $S^2$ , but rather the factor  $S^2/B^2$  [17], which strictly speaking has the form  $S^2\langle p_t^2 \rangle^2$ .

In order to compare determinations of the suppression due to absorptive effects we should compare only the values of the complete cross section for  $pp \rightarrow p + A + p$ . However a comparison is usually made by reducing the cross section to a factorized form. If this is done, as in (1), then

---

<sup>2</sup>Moreover, since the irreducible amplitude approaches saturation at some fixed energy (rapidity), independent of the value of  $b$ , the approximation gives  $\sigma_{\text{tot}}(s \rightarrow \infty) \rightarrow \text{constant}$ . On the other hand, a theory with an asymptotically constant cross section can only be self-consistent in the so-called ‘weak coupling’ regime for which the triple-Pomeron vertex vanishes for zero momentum transfer [15]. The vertex used in [6] does not vanish. This indicates that the MPSI approximation cannot be used at asymptotically high energies, and the region of its validity must be studied in more detail.

the Durham predictions for the survival factor to eikonal and enhanced screening of the exclusive production of a 120 GeV Higgs at the LHC are  $\langle S^2 \rangle = 0.008, 0.017, 0.030$  where enhanced screening is only permitted outside a threshold rapidity gap  $\Delta y = 0, 1.5, 2.3$  respectively. The values correspond to  $B = 4 \text{ GeV}^{-2}$ .

Let us discuss the survival factors claimed by Frankfurt et al. [18]. They use another approach. Within the eikonal formalism, they account for elastic rescattering only. The possibility of proton diffractive excitation is included in terms of parton-parton correlations, for both low- and high-mass dissociation. At a qualitative level, it is possible to consider all the effects discussed above in terms of such a language. On the other hand, to the best of our knowledge, they did not describe the available data on  $\sigma_{\text{tot}}$ ,  $d\sigma_{\text{el}}/dt$ ,  $M^2 d\sigma_{\text{SD}}/dM^2$ . Also, the energy (i.e.  $1/x$ ) dependence of the parton densities was evaluated using simple LO DGLAP evolution. This is grossly inadequate for the low values of  $x$  sampled,  $x \sim 10^{-5}$ . Thus, it is difficult to judge the accuracy of their numerical predictions. Moreover, part of the Sudakov-like suppression, which above was calculated using perturbative QCD, is here treated as parton correlations and included in the value of  $S_{\text{enh}}^2$ .<sup>3</sup> Therefore, one cannot compare literally the predictions for the gap survival factors  $S^2 = \langle S_{\text{eik}}^2(b) S_{\text{enh}}^2(b) \rangle$  given by [18] and by the Durham, Tel-Aviv and Petrov et al. [19] models<sup>4</sup>. The only possibility is to compare the predictions for the final exclusive cross section. Unfortunately, such a prediction is not available in [18].

Next, we comment on another recent calculation [20] along the lines of eq. (1). They claim very large uncertainties in the predictions arising mainly from the freedom in the choice of limits of integration in the Sudakov form factor which is embedded in  $f_g$ . However, this is not the case. In fact, the Sudakov factors have been calculated to *single* log accuracy. The collinear single logarithms are summed up using the DGLAP equation. To account for the ‘soft’ logarithms (corresponding to the emission of low energy gluons) the one-loop virtual correction to the  $gg \rightarrow A$  vertex was calculated explicitly, and then the scale  $\mu = 0.62 M_A$  was chosen so that double log expression for the Sudakov form factor reproduces the result of the explicit calculation. Similarly, the lower limit  $k_t^2 = Q_t^2$  was verified to give the one-loop result. It is sufficient to calculate just the one-loop correction since it is known that the effect of ‘soft’ gluon emission exponentiates. Thus double log expression, with  $\mu = 0.62 M_A$ , gives the Sudakov factor to single log accuracy. Also the form used for  $f_g$ ’s in Ref. [20] contradicts the known leading  $\log(1/x)$  asymptotic behaviour.

Finally, we discuss a very recent calculation [21] based on the dipole approach. A new development is that instead of using a multi-channel eikonal with a fixed number of diffractive eigenstates, the authors consider an explicit wave function of a fast hadron (proton, pion) and have a continuous integration over the size of the quark-quark dipoles. In this model the incoming

---

<sup>3</sup>In general, one may include the absence of QCD radiation in the large rapidity gap in the “soft” survival factors, but to make comparisons we must define precisely in which part of the calculation each effect is included. Note also that in [18] the DL expression for Sudakov  $T$ -factor is used, which grossly overestimates the suppression.

<sup>4</sup>The last group calculated  $S^2$  within their own eikonal model and fitted the parameters in a Regge-type expression for  $f_g$  to describe HERA data. The final prediction is again rather close to that by the Durham group.

hadron wave function is approximated by a simple Gaussian. The parameters are fitted so as to describe the data on  $\sigma_{\text{tot}}$ ,  $\sigma_{\text{el}}$  and  $F_2$  at low  $x$ . A shortcoming is that high-mass dissociation is calculated separately. Its contribution is not included in the proton dipole opacity  $\Omega(r, b)$ , for which a simplified asymptotic solution of the BFKL equation was used. Moreover, to calculate the gap survival probability,  $S^2(b)$ , the  $b$  dependence is considered, but the dependence of the “hard subprocess” cross section on the dipole size was not accounted for. That is, again, the correlation between the saturation momentum  $Q_s$  and  $b$  is lost. Nevertheless, the model confirms the observation that the energy dependence of  $S^2$  is not too steep;  $S^2$  at the LHC for central exclusive production is only reduced by a factor of about 2.5 to that at the Tevatron. Thus, Tevatron data serve as a reliable probe of the theoretical model predictions of these production rates.

In summary, we have briefly discussed various recent calculations of the exclusive process  $pp \rightarrow p + A + p$  at high energy. The value of the cross section when  $A = (H \rightarrow b\bar{b})$  is important for the feasibility of using tagged protons to study the Higgs sector via this process at the LHC. We have paid special attention to the survival factors of the large rapidity gaps. We see no reason to doubt the claimed value, or accuracy, of the existing predictions of the Durham model. Recall that these predictions have been checked in many places by comparing with the available experimental data on exclusive  $\gamma\gamma$  and high  $E_T$  dijet production at the Tevatron and on exclusive diffractive  $J/\psi$  production at HERA (see [22, 23] for more details). Since all the factors, which enter the calculations, depend rather weakly (logarithmically) on the initial energy, there is no reason to expect that the model, which describes the data at the Tevatron energy, will be too far from reality at the LHC.

## References

- [1] V. A. Khoze, A. D. Martin and M. G. Ryskin, *Eur. Phys. J. C* **23**, 311 (2002).
- [2] A. De Roeck, V. A. Khoze, A. D. Martin, R. Orava and M. G. Ryskin, *Eur. Phys. J. C* **25**, 391 (2002).
- [3] V. A. Khoze, A. D. Martin and M. G. Ryskin, arXiv:0705.2314 [hep-ph].
- [4] M.L. Good and W.D. Walker, *Phys. Rev.* **120** (1960) 1857.
- [5] V.N. Gribov, *Sov. Phys. JETP* **26** (1968) 414.
- [6] E. Gotsman, E. Levin, U. Maor and J. S. Miller, arXiv:0805.2799 [hep-ph].
- [7] M. G. Ryskin, A. D. Martin and V. A. Khoze, *Eur. Phys. J. C* **54**, 199 (2008)
- [8] A. H. Mueller and B. Patel, *Nucl. Phys.* **B425**, 471 (1994); A. H. Mueller and G. P. Salam, *Nucl. Phys.* **B475**, 293 (1996); G. P. Salam, *Nucl. Phys.* **B461**, 512 (1996); E. Iancu and A. H. Mueller, *Nucl. Phys.* **A730** (2004) 460, 494.

- [9] A. Donnachie and P.V. Landshoff, Phys. Lett. **B296** 227 (1992).
- [10] J. Bartels, S. Bondarenko, K. Kutak and L. Motyka, Phys. Rev. D **73**, 093004 (2006).
- [11] V. A. Khoze, A. D. Martin and M. G. Ryskin, JHEP **0605**, 036 (2006).
- [12] A. B. Kaidalov, V. A. Khoze, A. D. Martin and M. G. Ryskin, Eur. Phys. J. C **21**, 521 (2001).
- [13] G. Watt, arXiv:0712.2670v1 [hep-ph]; arXiv:0807.4464 [hep-ph].
- [14] T. Rogers, V. Guzey, M. Strikman and X. Zu, Phys. Rev. D **69**, 074011 (2004).
- [15] V.N. Gribov and A.A. Migdal, Sov. J. Nucl.Phys. **8** (1969).
- [16] M. G. Ryskin, A. D. Martin and V. A. Khoze, to be published.
- [17] V. A. Khoze, A. D. Martin, M. G. Ryskin and W. J. Stirling, Eur. Phys. J. C **35**, 211 (2004).
- [18] L. Frankfurt et al., arXiv:07102942; arXiv:0808.0182 [hep-ph].
- [19] V. A. Petrov and R. A. Ryutin, J. Phys. G **35**, 065004 (2008), and references therein.
- [20] J. R. Cudell, A. Dechambre, O. F. Hernandez and I. P. Ivanov, arXiv:0807.0600 [hep-ph].
- [21] A. Kormilitzin and E. Levin, arXiv:0809.3886.
- [22] V. A. Khoze et al., arXiv:hep-ph/0507040.
- [23] V. A. Khoze, A. D. Martin and M. G. Ryskin, Eur. Phys. J. C **55**, 363 (2008).

# Rapidity gap survival in central exclusive diffraction: Dynamical mechanisms and uncertainties\*

Mark Strikman<sup>a</sup>, Christian Weiss<sup>b</sup>

<sup>a</sup> Department of Physics, Pennsylvania State University, University Park, PA 16802, USA

<sup>b</sup> Theory Center, Jefferson Lab, Newport News, VA 23606, USA

## Abstract

We summarize our understanding of the dynamical mechanisms governing rapidity gap survival in central exclusive diffraction,  $pp \rightarrow p + H + p$  ( $H$  = high-mass system), and discuss the uncertainties in present estimates of the survival probability. The main suppression of diffractive scattering is due to inelastic soft spectator interactions at small  $pp$  impact parameters and can be described in a mean-field approximation (independent hard and soft interactions). Moderate extra suppression results from fluctuations of the partonic configurations of the colliding protons. At LHC energies absorptive interactions of hard spectator partons associated with the  $gg \rightarrow H$  process reach the black-disk regime and cause substantial additional suppression, pushing the survival probability below 0.01.

## 1 Strong interaction dynamics in rapidity gap survival

Calculation of the cross section of central exclusive diffraction,  $pp \rightarrow p + H + p$  ( $H$  = dijet, heavy quarkonium, Higgs boson, *etc.*) presents a major challenge for strong interaction physics. It involves treating the hard dynamics in the elementary  $gg \rightarrow H$  subprocess, and calculating the probability that no other interactions leading to hadron production occur during the  $pp$  collision. The latter determines the suppression of diffractive relative to non-diffractive events with the same hard process, referred to as the rapidity gap survival (RGS) probability. In this article we summarize our understanding of the dynamical mechanisms determining the RGS probability, their phenomenological description, and the uncertainties in present numerical predictions.

RGS in central exclusive diffraction has extensively been discussed in an approach where soft interactions are modeled by eikonalized pomeron exchange; see Ref. [1] for a summary. More recently a partonic description was proposed, which allows for a model-independent formulation of the interplay of hard and soft interactions and reveals the essential role of the “transverse geometry” of the  $pp$  collision [2]. In the mean-field approximation, where hard and soft interactions are considered as independent aside from their common dependence on the impact parameter, we derived a simple “factorized” expression for the RGS probability, using closure of the partonic states to take into account inelastic diffractive intermediate states. The resulting RGS probability is smaller than in the models of Refs. [1, 3] without inelastic diffraction,

---

\* Notice: Authored by Jefferson Science Associates, LLC under U.S. DOE Contract No. DE-AC05-06OR23177. The U.S. Government retains a non-exclusive, paid-up, irrevocable, world-wide license to publish or reproduce this manuscript for U.S. Government purposes.

but comparable to the some of the versions of those models with multichannel diffraction. Our partonic description also permits us to go beyond the mean-field approximation and incorporate various types of correlations between the hard scattering process and spectator interactions. Here we discuss two such effects: (a) quantum fluctuations of the partonic configurations of the colliding protons, which somewhat reduce the survival probabilities at RHIC and Tevatron energies; (b) absorptive interactions of high-virtuality spectator partons ( $k^2 \sim \text{few GeV}^2$ ) associated with the hard scattering process, related to the onset of the black-disk regime (BDR) in hard interactions at LHC energies; this new effect substantially reduces the RGS probability compared to previously published estimates.

## 2 Soft spectator interactions in the mean-field approximation

A simple picture of RGS is obtained in the impact parameter representation. On one hand, to produce the heavy system  $H$  two hard gluons from each of the two protons need to collide in the same space-time point (actually, an area of transverse size  $\sim 1/\langle k_T^2 \rangle$  in the hard process); because such gluons are concentrated around the transverse centers of the protons this is most likely when the protons collide at a small impact parameters,  $b \lesssim 1 \text{ fm}$ . On the other hand, soft inelastic spectator interactions are strongest at small  $b$  and would favor collisions at  $b \gg 1 \text{ fm}$  for diffractive scattering. These different preferences limit diffraction to an intermediate range of impact parameters and ensure that its cross section is substantially suppressed compared to non-diffractive scattering. More precisely, the RGS probability is given by [2]

$$S^2 = \int d^2b P_{\text{hard}}(b) |1 - \Gamma(b)|^2, \quad b \equiv |\mathbf{b}|. \quad (1)$$

Here  $P_{\text{hard}}(b)$  is the probability for two gluons to collide at the same transverse point as a function of the  $pp$  impact parameter, given by the convolution of the transverse spatial distributions of the gluons in the colliding protons, normalized to  $\int d^2b P_{\text{hard}}(b) = 1$  (see Fig. 1a). The factor  $|1 - \Gamma(b)|^2$  is the probability for the two protons not to interact inelastically in a collision at the given impact parameter, calculable in terms of the profile function of the  $pp$  elastic amplitude,  $\Gamma(b)$ . Figure 1b shows the  $b$ -dependence of the two factors as well as their product, illustrating the interplay described above. While we have motivated Eq. (1) by probabilistic arguments, it actually can be derived (as well as the expression for the differential cross section) in the partonic description of Ref. [2] within the mean-field approximation, where one assumes no correlation between the presence of the gluons involved in the hard interaction (with the particular  $x$ ) and the strength of the soft spectator interactions. In this approximation one can use closure to sum over the different diffractive intermediate states, and thus effectively include the contribution of inelastic diffraction.<sup>1</sup> The numerical values of the RGS probability obtained from Eq. (1) are of the order  $S^2 \sim 0.03$  for  $M_H = 100 \text{ GeV}$  and  $\sqrt{s} = 14 \text{ TeV}$ ; see Ref. [2] for details.

It is worthwhile to discuss the uncertainty in the numerical predictions for  $S^2$  in the mean-field approximation, Eq. (1), resulting from our imperfect knowledge of the functions in the

<sup>1</sup>In principle there is also a contribution from excitation of a diffractive state by soft spectator interactions and subsequent transition back to the proton via the nondiagonal gluon GPD; however, it is strongly suppressed because the typical excitation masses in hard and soft diffraction are very different in the kinematics of Higgs production at the LHC ( $10^{-8} \leq x_P \leq 0.1$  for generic  $pp$  diffraction and  $10^{-2} \leq x_P \leq 0.1$  for the GPD); see Section IV C of Ref. [2].



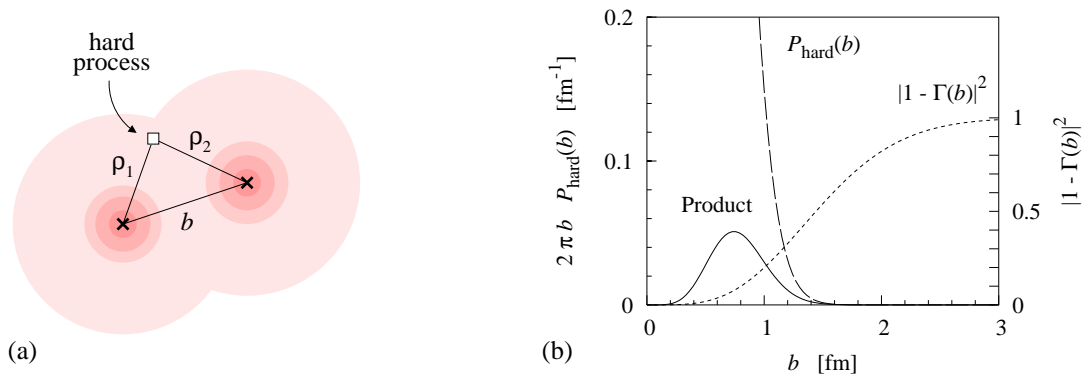


Fig. 1: (a) Transverse geometry of hard diffractive  $pp$  scattering. (b) RGS probability in the impact parameter representation *cf.* Eq. (1), for  $\sqrt{s} = 14$  TeV,  $M_H \sim 100$  GeV [2]. Dashed line: Probability for hard scattering process  $P_{\text{hard}}(b)$  (left vertical axis). Dotted line: Probability for no inelastic interactions between the protons,  $|1 - \Gamma(b)|^2$  (right vertical axis). Solid line: Product  $P_{\text{hard}}(b)|1 - \Gamma(b)|^2$  (left vertical axis). The RGS probability Eq. (1) is given by the area under this curve.

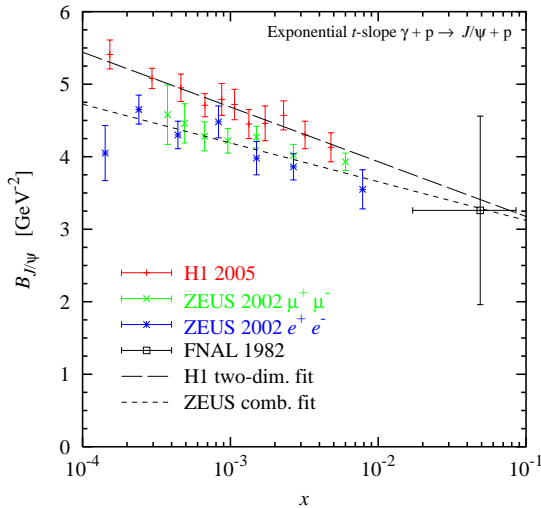


Fig. 2: The exponential  $t$ -slope,  $B_{J/\psi}$ , of exclusive  $J/\psi$  photoproduction, extracted from fits to the FNAL E401/E458 [4], HERA H1 [5], and ZEUS [6] data. The long-dashed and short-dashed lines represent fits to the  $x$ -dependence of the H1 and ZEUS  $t$ -slopes [5, 6], *cf.* Eq. (2). The  $t$ -slope of the gluon GPD,  $B_g$ , is obtained from  $B_{J/\psi}$  after applying a small correction for the finite size of the  $J/\psi$  [7].

integrand. We first consider the transverse spatial distribution of gluons entering in  $P_{\text{hard}}(b)$ . The latter is obtained as the Fourier transform of the  $t$ -dependence (more precisely, transverse momentum dependence) of the gluon generalized parton distribution (GPD) measured in hard exclusive vector meson production. Extensive studies at HERA have shown that exclusive  $J/\psi$  photoproduction,  $\gamma p \rightarrow J/\psi + p$ , provides an effective means for probing the  $t$ -dependence of the gluon GPD at small and intermediate  $x$  (a small correction for the finite transverse size of the  $J/\psi$  is applied) [7]. Figure 2 summarizes the results for the exponential  $t$ -slope of this process,  $B_{J/\psi}$ , from HERA H1 [5] and ZEUS [6] and the FNAL E401/E458 experiment [4], as well as fits to the  $x$ -dependence of the H1 and ZEUS results of the form (here  $x = M_{c\bar{c}}^2/W^2$ )

$$B_{J/\psi}(x) = B_{J/\psi}(x_0) + 2\alpha'_{J/\psi} \ln(x_0/x). \quad (2)$$

There is a systematic difference between the H1 and ZEUS results due to different analysis methods [5, 6]; however, the fits to both sets agree well with the FNAL point when extrapolated to larger  $x$ . In diffractive production of a system with  $M_H = 100 \text{ GeV}$  at  $\sqrt{s} = 14 \text{ TeV}$  at zero rapidity the gluons coupling to the heavy system  $H$  have momentum fractions  $x_{1,2} = M_H/\sqrt{s} = 0.007$ . Assuming exponential  $t$ -dependence of the gluon GPD, we can estimate the uncertainty in the transverse spatial distribution of gluons at such  $x$  by evaluating the fits to the HERA data within the error bands quoted for  $B_{J/\psi}(x_0)$  and  $\alpha'_{J/\psi}$  [5, 6]. We find a 15-20% uncertainty of  $B_{J/\psi}$  at  $x = 0.007$  in this way, translating into a 20–30% uncertainty in the mean-field RGS probability, Eq. (1). We note that there is at least a comparable uncertainty in  $S^2$  from the uncertainty of the shape of the  $t$ -dependence; this is seen from Fig. 10 of Ref. [2], where the exponential is compared with a theoretically motivated dipole form which also describes the FNAL data. Altogether, we estimate that our imperfect knowledge of the spatial distribution of gluons results in an uncertainty of the mean-field result for  $S^2$  by a factor  $\sim 2$ . Dedicated analysis of the remaining HERA exclusive data, and particularly precision measurements with a future electron–ion collider (EIC), could substantially improve our knowledge of the transverse spatial distribution of gluons.

We now turn to the uncertainty in  $S^2$  arising from the  $pp$  elastic amplitude,  $\Gamma(b)$ . Most phenomenological analyses of  $pp$  elastic and total cross section data find that for TeV energies  $|1 - \Gamma(b)| \leq 0.05$  at  $b = 0$ , corresponding to near-unit probability of inelastic interactions at small impact parameters (BDR). This is supported by theoretical studies in the QCD dipole model, which show that the large- $x$  partons with virtualities of up to several  $\text{GeV}^2$  experience “black” interactions with the small- $x$  gluon field in the other proton when passing through the other proton at transverse distances  $\rho \leq 0.5 \text{ fm}$ , and receive transverse momenta  $k_T \geq 1 \text{ GeV}$  (see Ref. [7] for a summary). At  $pp$  impact parameter  $b = 0$  the chance that none of the leading partons in the protons receive such a kick is extremely small, implying that  $|1 - \Gamma(b)| \sim 0$  [8]. For the RGS probability in the mean-field approximation, Eq. (1), the fact that  $|1 - \Gamma(b)|^2$  is small at  $b = 0$  is essential, as this eliminates the contribution from small  $b$  in the integral (see Fig. 1b) and stabilizes the numerical predictions. However, present theoretical arguments and data analysis cannot exclude a small non-zero value of  $|1 - \Gamma(b)|$  at  $b = 0$ ; a recent analysis finds  $|1 - \Gamma(b)| \sim 0.1$  [9]. To investigate the potential implications for the RGS probability, we evaluate Eq. (1) with the Gaussian parametrization of  $\Gamma(b)$  of Ref. [2], Eq. (12), but with  $\Gamma(b = 0) = 1 - \epsilon$ . We find that a value of  $\epsilon = 0.1$ , corresponding to  $|1 - \Gamma(b)|^2 = 0.01$ , increases

the mean-field result for  $S^2$  by a factor  $\sim 1.8$ , indicating significant uncertainty of the mean-field result. However, as explained in Sec. 4 below, hard spectator interactions associated with the  $gg \rightarrow H$  process lead to an additional suppression of diffraction at small  $b$  (not contained in the soft RGS probability), which mitigates the impact of this uncertainty on the overall diffractive cross section.

### 3 Fluctuations of parton densities and soft-interaction strength

Corrections to the mean-field picture of RGS arise from fluctuations of the interacting configurations in the colliding protons. This concept is known well in soft diffraction, where fluctuations of the strength of interaction between the colliding hadrons give rise to inelastic diffraction. In hard diffraction, one expects that also the gluon density fluctuates; *e.g.* because the color fields are screened in configurations of small size [10]. In fact, the variance of the gluon density fluctuations can be directly related to the ratio of inelastic and elastic diffraction in processes such as  $\gamma_L^* + p \rightarrow \text{“vector meson”} + X$ ,

$$\omega_g \equiv \frac{\langle G^2 \rangle - \langle G \rangle^2}{\langle G \rangle^2} = \frac{d\sigma_{\text{inel}}}{dt} \bigg/ \frac{d\sigma_{\text{el}}}{dt} \bigg|_{t=0}. \quad (3)$$

The HERA data are consistent with the dynamical model estimate of  $\omega_g \sim 0.15 - 0.2$  for  $Q^2 = 3 \text{ GeV}^2$  and  $x \sim 10^{-4} - 10^{-3}$  [10]; unfortunately, the limited  $Q^2$  range and the lack of dedicated studies do not allow for a more precise extraction of this fundamental quantity.

In central exclusive diffraction, correlated fluctuations of the soft-interaction strength and the gluon density lower the RGS probability, because small-size configurations which experience little absorption have a lower gluon density. This effect can be modeled by a generalization of the mean-field expression (1), in which both the gluon GPDs in  $P_{\text{hard}}$  and the profile function fluctuate as a function of an external parameter controlling the overall size of the configurations [10]. Numerical studies find a reduction of the RGS probability by a factor  $\sim 0.82$  (0.74) for a system with mass  $M_H = 100 \text{ GeV}$  produced at zero rapidity at  $\sqrt{s} = 2$  (14) TeV. The dynamical model used in this estimate does not include fluctuations of the gluon density at larger  $x$  ( $\sim 0.05 - 0.1$ ), which could increase the suppression.

We emphasize again that inelastic diffraction *per se* is included in the partonic approach of Ref. [2] through the closure of partonic states. The effect discussed in this section is specifically related to correlations between the fluctuations of the parton densities and the soft-interaction strength; in the limit of zero correlations (independent fluctuations) we recover the mean-field result described above [10].

### 4 Black-disk regime in hard spectator interactions

Substantial changes in the mechanism of diffractive scattering are brought about by the onset of the BDR in hard interactions at LHC energies, where even highly virtual partons ( $k^2 \sim \text{few GeV}^2$ ) with  $x \gtrsim 10^{-2}$  experience “black” interactions with the small- $x$  gluons in the other proton. This new effect modifies the amplitude of central exclusive diffraction in several ways: (a) absorption of the “parent” partons of the gluons attached to the high-mass system; (b) absorption of the hard gluons attached to the high-mass system; (c) absorption due to local interactions

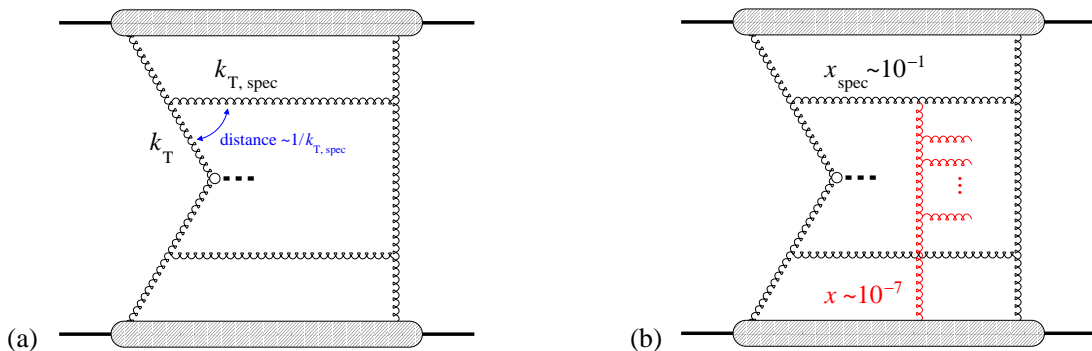


Fig. 3: (a) QCD evolution-induced correlation between hard partons. The transverse distance between the active parton and the spectator is  $\sim 1/k_{T, \text{spec}}$ . (b) Absorptive interaction of the hard spectator with small- $x$  gluons in the other proton.

within the partonic ladder. Such absorptive hard interactions cause additional suppression of diffractive scattering, not included in the traditional soft-interaction RGS probability [2]. Because of the generic nature of “black” interactions, we can estimate this effect by a certain modification of the mean-field picture in the impact parameter representation. Here we focus on mechanism (a) and show that it causes substantial suppression; the other mechanisms may result in further suppression.

According to Ref. [11] (and references therein) the dominant contribution to the hard amplitude of Higgs production at the LHC ( $M_H = 100 \text{ GeV}$ ,  $x_{1,2} \sim 10^{-2}$ ) originates from gluons with transverse momenta of the order  $k_T \sim 2 \text{ GeV}$ . Such gluons are typically generated by DGLAP evolution starting from the initial scale,  $Q_0^2$ , in which spectator partons, mostly gluons, are emitted (see Fig.3a). In the leading-log approximation  $Q_0 \ll k_{T, \text{spec}} \ll k_T$ , and thus the transverse distance between the active and spectator parton is  $\sim 1/k_{T, \text{spec}} \ll R_{\text{proton}}$ , amounting to short-range correlations between partons. If the interactions of the spectator parton with the small- $x$  gluons in the other proton become significant (see Fig.3b), the basic assumption of the mean-field approximation — that the spectator interactions are independent of the hard process — is violated, and the interactions of that parton need to be treated separately. Indeed, studies within the QCD dipole model show that at the LHC energy spectator gluons with  $k_{T, \text{spec}} \sim 1 \text{ GeV}$  and  $x_{\text{spec}} \sim 10^{-1}$  “see” gluons with momentum fractions  $x \sim 10^{-7}$  in the other proton, and are absorbed with near-unit probability if their impact parameters with the other proton are less than  $\sim 1 \text{ fm}$  [2].<sup>2</sup> For  $pp$  impact parameters  $b < 1 \text{ fm}$  about 90% of the strength in  $P_{\text{hard}}(b)$  comes from parton-proton impact parameters  $\rho_{1,2} < 1 \text{ fm}$  (*cf.* Fig. 1a), so that this effect practically eliminates diffraction at  $b < 1 \text{ fm}$ . Since  $b < 1 \text{ fm}$  accounts for 2/3 of the cross section (see Fig. 1b), and the remaining contributions at  $b > 1 \text{ fm}$  are also reduced by absorption, we estimate that absorptive interactions of hard spectators in the BDR reduce the RGS probability at LHC to about 20% of its mean-field value. Much less suppression is expected

<sup>2</sup>The cross section of “gluonic” (88) dipoles is larger than that of the quark-antiquark ( $\bar{3}3$ ) dipoles in  $\gamma^*p$  scattering [12] by a factor 9/4. A summary plot of the profile function for gluon-proton scattering is given in Fig. 13 of Ref. [7] (right  $y$ -axis). Note that  $\Gamma^{\text{gluon-proton}} = 0.5$  already corresponds to a significant absorption probability of  $1 - |1 - \Gamma^{\text{gluon-proton}}|^2 = 0.75$ .

at the Tevatron energy, where hard spectator interactions only marginally reach the BDR.

In the above argument one must also allow for the possibility of trajectories with no gluon emission, which correspond to the Sudakov form factor-suppressed  $\delta(1-x)$ -term in the evolution kernel. While such trajectories are not affected by absorption, their contributions are small both because of the Sudakov suppression, and because they effectively probe the gluon density at a low scale,  $Q_0^2 \sim 1 \text{ GeV}^2$ , where evolution-induced correlations between partons can be neglected. We estimate that the contribution of such trajectories to the cross section is suppressed compared to those with emissions by a factor  $R = [S_G^2 G(x, Q^2)/G(x, Q_0^2)]^2 \sim 1/10$ , where  $S_G^2 = \exp[-(3\alpha_s/\pi) \ln^2(Q^2/Q_0^2)]$  is the square of the Sudakov form factor, and  $Q^2 \sim 4 \text{ GeV}^2$ . Their net contribution is thus comparable to that of the trajectories with emissions, because the latter are strongly suppressed by the absorption effect described above. Combining the two, we obtain an overall suppression by a factor of the order  $\sim 0.3$ . More accurate estimates would need to take into account fluctuations in the number of emissions; in particular, trajectories on which only one of the partons did not emit gluons are suppressed only by  $\sqrt{R}$  and may make significant contributions.

The absorptive hard spectator interactions described here “push” diffractive  $pp$  scattering to even larger impact parameters than would be allowed by the soft spectator interactions included in the mean-field RGS probability, Eq. (1) (except for the Sudakov-suppressed contribution). One interesting consequence of this is that it makes the uncertainty in the mean-field prediction arising from  $\Gamma(0) \neq 1$  (see Sec. 2) largely irrelevant, as the region of small impact parameters is now practically eliminated by the hard spectator interactions. Another consequence is that the final-state proton transverse momentum distribution is shifted to smaller values; this could in principle be observed in  $p_T$ -dependent measurements of diffraction. We note that the estimates of hard spectator interactions reported here are based on the assumption that DGLAP evolution reasonably well describes the gluon density down to  $x \sim 10^{-6}$ ; the details (but not the basic picture) may change if small- $x$  resummation corrections were to significantly modify the gluon density at such values of  $x$  (see Ref. [13] and references therein).

## 5 Summary

The approach to the BDR in the interaction of hard spectator partons, caused by the increase of the gluon density at small  $x$ , has profound implications for central exclusive diffraction at LHC: *No saturation without disintegration!* The RGS probability is likely to be much smaller (by a factor of  $\sim 1/3$  or less) than predicted by the mean-field approximation or corresponding models which neglect correlations of partons in the transverse plane. Diffractive scattering is relegated either to very large impact parameters ( $b > 1 \text{ fm}$ ) or to Sudakov-suppressed trajectories without gluon radiation. We estimate that the overall RGS probability at LHC is  $S^2 < 0.01$ . Extrapolation of the Tevatron results may be misleading because interactions of hard spectators are generally far from “black” at that energy. The new effects described here call for detailed MC-based studies of possible histories of the hard scattering process and their associated spectator interactions.

## References

- [1] Khoze, V. A. and Martin, A. D. and Ryskin, M. G., Eur. Phys. J. **C55**, 363 (2008).
- [2] Frankfurt, L. and Hyde, C. E. and Strikman, M. and Weiss, C., Phys. Rev. **D75**, 054009 (2007).
- [3] Gotsman, E. and Levin, E. and Maor, U. and Miller, J. S. (2008).
- [4] Binkley, M. and others, Phys. Rev. Lett. **48**, 73 (1982).
- [5] Aktas, A. and others, Eur. Phys. J. **C46**, 585 (2006).
- [6] Chekanov, S. and others, Nucl. Phys. **B695**, 3 (2004).
- [7] Frankfurt, L. and Strikman, M. and Weiss, C., Ann. Rev. Nucl. Part. Sci. **55**, 403 (2005).
- [8] Frankfurt, L. and Strikman, M. and Zhalov, M., Phys. Lett. **B616**, 59 (2005).
- [9] Luna, E. G. S. and Khoze, V. A. and Martin, A. D. and Ryskin, M. G. (2008).
- [10] Frankfurt, L. and Strikman, M. and Treleani, D. and Weiss, C., Phys. Rev. Lett. **101**, 202003 (2008).
- [11] Khoze, Valery A. and Martin, Alan D. and Ryskin, M. G., Eur. Phys. J. **C14**, 525 (2000).
- [12] Rogers, T. and Guzey, V. and Strikman, M. and Zu, X., Phys. Rev. **D69**, 074011 (2004).
- [13] Ciafaloni, M. and Colferai, D. and Salam, G. P. and Stasto, A. M., JHEP **08**, 046 (2007).

# Two-photon and photon-hadron interactions at the LHC

*Joakim Nystrand*

Department of Physics and Technology,  
University of Bergen, Bergen, Norway

## **Abstract**

The possibilities to extend the results from HERA by using the strong flux of equivalent photons associated with the proton and nuclear beams at the LHC are reviewed.

## **1 Introduction**

Much of the focus of this workshop has been on how the parton distribution functions determined at HERA will be an integral part of the interpretation of the results from the LHC. We wish to point out, however, that the LHC offers an opportunity to directly extend the results from HERA on photoproduction, by using the strong flux of photons associated with the proton and nuclear beams.

Charged particles moving with relativistic velocities are surrounded by a cloud of virtual photons. For point particles, the energy of the virtual photons can in principle be as high as the energy of the charged particle itself. For extended objects, like protons and nuclei, the maximum photon energy is highly suppressed for energies above a fraction of the charged particle's energy because of the form factor. At the extreme energies of the LHC, this is not a serious limitation, however, and it will be possible to probe photon-induced interactions at energies much higher than at HERA both in proton-proton and nucleus-nucleus collisions. Photon-induced interactions can be studied in ultra-peripheral collisions where the impact parameter is larger than the sum of the projectile radii and no hadronic interactions occur. This is illustrated in Fig. 1.

The photon-induced interactions can be divided into two categories: exclusive interactions, where a certain final state is produced, while both beam particles remain intact; and inclusive interactions, where a certain final state is produced but where the photon target breaks up and additional particles may be produced. Exclusive interactions include two-photon and photon-Pomeron interactions. Inclusive interactions include, but are not limited to, direct photon-parton interactions. These two types of processes will be discussed in the following two sections. For two longer reviews of photon interactions at hadron colliders, see [1, 2].

## **2 Exclusive Production**

The study of photon-induced interactions at hadron colliders has so far focused mainly on exclusive production, where both protons or nuclei remain intact. The cross sections for exclusive production are normally lower than for the corresponding inclusive reaction channel. The advantage is, however, that the exclusive events have a much clearer event topology, with rapidity gaps on both sides of the produced state, which makes it easy to separate them from background and hadronic processes.

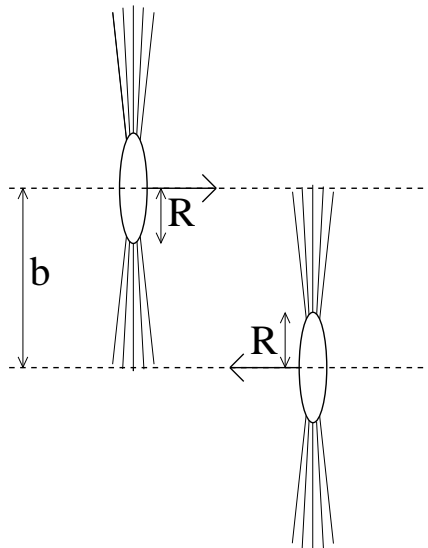


Fig. 1: An ultra-peripheral collision with impact parameter  $b$  much larger than the sum of the projectile radii,  $R$ . The solid lines indicate the Lorentz contracted electric fields.

The early theoretical studies of electromagnetic processes at hadron colliders were concentrated on two-photon interactions. It was later discovered that exclusive production of vector mesons through photon-Pomeron fusion had much larger cross sections [3]. Exclusive photoproduction of vector mesons and two-photon interactions will be discussed in the following two subsections. One should note, however, that exclusive production of vector mesons can occur also through the hadronic process Odderon-Pomeron fusion; this possibility has attracted an increased interest recently [4].

## 2.1 Photon-hadron interactions

According to the Vector Meson Dominance model, the bulk of the photon-hadron cross section can be explained by the photon first fluctuating to a vector meson, with the same quantum numbers as the photon. While in the vector meson state, the photon will interact hadronically with the target. This interaction can be elastic or inelastic. In elastic scattering enough momentum can be transferred for the virtual vector meson to become real; this is the basis for exclusive photoproduction of vector mesons.

The cross section for exclusive production of the lightest vector meson,  $\rho^0$ , is very high in collisions with heavy ions, such as Au or Pb, reaching 50% of the total inelastic hadronic cross sections at the energies of the LHC [3]. At the Relativistic Heavy-Ion Collider (RHIC), the measured exclusive  $\rho^0$  cross section in Au+Au collisions at  $\sqrt{s_{NN}} = 200$  GeV is  $530 \pm 19(\text{stat}) \pm 57(\text{syst})$ , roughly 10% of the total inelastic cross section [5].

The momentum transfer from each projectile is limited by the form factor, and the vector meson production is therefore typically centered around mid-rapidity; the exact shape of the



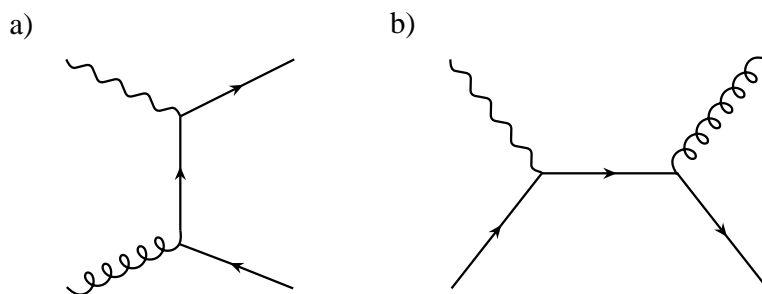


Fig. 2: Feynman diagrams for direct photoproduction of jets in ultra-peripheral collisions through photon-gluon fusion,  $\gamma + g \rightarrow q + \bar{q}$ , and the QCD Compton process,  $\gamma + q \rightarrow g + q$ . Direct photoproduction of heavy quarks is described by the diagram in a).

rapidity distribution varies somewhat with collision energy and vector meson mass.

Exclusive vector mesons have been studied by the STAR [5] and PHENIX [6] collaborations at RHIC, and by the CDF collaboration at the Tevatron [7].

The STAR collaboration at RHIC has studied exclusive photoproduction of  $\rho^0$  mesons in Au+Au collisions at  $\sqrt{s_{NN}} = 200$  GeV. The energy range probed by STAR,  $7.6 \leq W_{\gamma p} \leq 20.6$  GeV, includes energies larger than have been studied in fixed target experiments with lepton beams on heavy nuclear targets. The measured cross sections are found to be in good agreement with models that include a Weizsäcker-Williams photon spectrum and Glauber-like models for the photonuclear cross section.

The PHENIX collaboration has studied exclusive production of  $J/\Psi$  in Au+Au collisions in coincidence with Coulomb break-up of at least one of the nuclei. Coulomb break-up means that an additional, soft photon is exchanged in the interaction, leading to the break up of the “target” nucleus. The  $J/\Psi$ s have been studied around mid-rapidity in the  $e^+e^-$  decay channel.

The CDF collaboration has studied exclusive  $J/\Psi$  and  $\Psi'$  production in the  $\mu^+\mu^-$  decay channel in  $p\bar{p}$  collisions at the Tevatron [7]. CDF has also seen hints of  $\Upsilon$  mesons.

The outlook for studying exclusive vector meson production at the LHC is promising. The rates are very high. The  $J/\Psi$  cross section, for example, increases by about a factor 100 from Au+Au collisions at RHIC to Pb+Pb collisions at the LHC. There are plans to study this reaction channel in both the CMS and ALICE experiments, in pp as well as in PbPb collisions.

## 2.2 Two-photon interactions

The cross section for two-photon production of lepton pairs scales as  $Z^4$ , where  $Z$  is the charge of the projectile. The total cross section for producing an  $e^+e^-$ -pair is several orders of magnitude larger than the total hadronic cross section in heavy-ion interactions at RHIC and the LHC. Most of these electrons/positrons are produced with very low invariant masses, however, and are emitted with small angles relative to the beam axis.

The pairs can be produced as free pairs or as bound-free pairs, where the electron (or the positron with anti-proton beams) binds to the beam particle. When a bound-free pair is produced, the rigidity of the capturing beam nucleus or proton changes and it is lost from the beam. This is the leading source of beam loss at high energy heavy-ion colliders such as RHIC and the LHC. Moreover, the projectile that has captured the electron will hit the wall of the beam pipe at a well-defined spot downstream from the interaction point. At the LHC, the resulting heat deposition could induce quenching of the superconducting magnets. The impact of copper ions with a captured electron about 140 m downstream from the interaction point has recently been observed at RHIC [8]. Bound-free pair production where the positron binds to the anti-proton has been used to observe anti-hydrogen at the Tevatron [9].

Free pair production has been studied in fixed target heavy-ion interactions, in Au+Au collisions at RHIC [6, 10], and, recently, by the CDF Collaboration in  $p\bar{p}$  collisions at the Tevatron [11]. The results have generally been found to be in good agreement with lowest order perturbation theory. The limit on invariant mass used by the CDF Collaboration ( $> 10$  GeV) is unfortunate, however, since it falls almost on top of the mass of the  $\Upsilon(2S)$  meson. The yield from heavy vector mesons produced by photon-Pomeron fusion and decaying to di-lepton pairs is comparable or larger than the one from two-photon production over the relevant invariant mass range.

Two-photon production of mesons, e.g. at  $e^+e^-$  colliders, is a useful tool in meson spectroscopy. In principle, such studies could be performed also at hadron colliders, but backgrounds from coherent photonuclear interactions pose a problem. A two-photon “standard candle” like the  $f_2(1270)$  is likely to be obscured by continuum production of  $\pi^+\pi^-$  through photon-Pomeron fusion. No results on two-photon production of mesons at hadron colliders have been reported.

Finally, it has been suggested to search for the Higgs boson in two-photon interactions at the LHC. Despite the enhancement by a factor  $Z^4$  in heavy-ion collisions, the cross section for a standard model Higgs with mass around 100 GeV appears too low, only about 10 pb in Pb+Pb collisions, corresponding to an event rate of only  $10^{-9} \text{ s}^{-1}$  [12]. With Ca beams the situation is a bit better because of the higher luminosity, but the event rate is not more than about  $10^{-6} \text{ s}^{-1}$ .

### 3 Inclusive Production

The bulk of the photonuclear particle production stems from events where the photon first fluctuates to a hadronic state, which then interact with the target nucleus or proton. Since the energy of the photon typically is much lower than that of the beam particle, these events resemble fixed target interactions. The photon can, however, also interact as a “bare” photon with one of the partons in the target nucleus or proton. The focus of this section will be on photon-parton interactions in nucleus-nucleus collisions. Direct processes that can be calculated using perturbative QCD include photoproduction of jets and heavy quarks. None of these processes have been investigated at RHIC or the Tevatron, but the prospects should be good at the LHC, particularly because of the strong increase in the cross sections with energy.

### 3.1 Photoproduction of jets

The Feynman diagrams for the two leading-order direct contributions to the jet yield,  $\gamma + g \rightarrow q + \bar{q}$  and  $\gamma + q \rightarrow g + g$ , are shown in Fig. 2. The corresponding differential cross section can be written as a convolution of the equivalent photon flux with the parton distribution functions and the partonic cross sections

$$s^2 \frac{d^2\sigma}{dt du} = 2 \int_{k_{min}}^{\infty} n(k) dk \int_{x_{2min}}^1 \frac{dx_2}{x_2} \left[ \sum_{i=q,\bar{q},g} F_i(x_2, Q^2) s'^2 \frac{d^2\sigma_{\gamma i}}{dt' du'} \right]. \quad (1)$$

Here,  $n(k)$  is the number of equivalent photons with energy  $k$ .  $F_i(x_2, Q^2)$  is the parton density for parton  $i$  at scale  $Q^2$  and  $x_2$  is the Bjorken- $x$  of the parton in the target nucleus. The unprimed Mandelstam variables,  $s, t, u$ , refer to the hadronic system, whereas the primed variables,  $s', t', u'$ , refer to the partonic system. The minimum  $x_2$  is given by  $x_{2min} = -u/(s+t)$  and  $k_{min}$  is the minimum photon energy needed to produce the final state.

The cross section for photonuclear jet production is high at the LHC. The cross section to produce a jet with  $p_T > 50$  GeV/c and rapidity  $|y| < 1$  in Pb+Pb collisions is for example larger than  $1 \mu\text{b}$  [13]. As can be seen from Eq. 1, the jet cross section is sensitive to the nuclear parton distributions. Calculations show that nuclear shadowing (and anti-shadowing) affects the yield by up to 10%, while the differences between individual parameterizations of shadowing differ by a few percent. It has also been noted that there is a significant contribution to the jet yield from resolved interactions, where a parton in the target interacts with a parton in the resolved photon; the resolved contribution is expected to be the leading production mechanism in certain regions of phase space, particularly for low  $p_T < 50$  GeV/c [13].

### 3.2 Photoproduction of heavy quarks

For the production of heavy quarks, only the diagram in Fig. 2 a) contributes. The production cross section is thus a less ambiguous probe of the proton or nuclear gluon distribution. The cross sections are very high at the LHC, as can be seen in Table 3.2 (from [14] with updated numbers from [1]). Calculations are shown for two different parameterizations of the nuclear gluon shadowing and without shadowing. Shadowing has an enhanced effect on the cross section for  $c\bar{c}$  pairs, where lower values of  $x$  are probed. In Pb+Pb collisions, the two parameterizations correspond to reductions by 16% and 32%, respectively. For  $b\bar{b}$  pairs, the effect of shadowing is smaller, 4% and 10% in the two cases.

The resolved contribution is smaller than for jet production. It is largest for  $c\bar{c}$  pairs, but does not contribute more than 15-20 % to the total cross section.

The cross section for producing pairs of top quarks is too low for observation with the design LHC Pb+Pb luminosity. It might be possible with lighter ions or with protons.

## 4 Summary

The feasibility of studying at least a few reaction channels in ultra-peripheral collisions at collider energies has been shown by experiments at RHIC and the Tevatron. The measured cross sections have been found to be in general agreement with expectations, but the statistics have so far been

	flavor	$\sigma$ [mb]	$\sigma$ [mb]	$\sigma$ [mb]
		No shadowing	EKS98	FGS
Ar+Ar	$c\bar{c}$	16.3	14.3	12.3
	$b\bar{b}$	0.073	0.070	0.066
Pb+Pb	$c\bar{c}$	1250	1050	850
	$b\bar{b}$	4.9	4.7	4.4

Table 1: Cross sections for  $q\bar{q}$  photoproduction through direct photon-gluon fusion in Ar+Ar and Pb+Pb interactions at the LHC. The numbers in column 3 and 4 include nuclear gluon shadowing from the parameterizations by Eskola, Kolhinen, and Ruuskanen (EKS98) and Frankfurt, Guzey, and Strikman (FGS), respectively.

low. There are plans to study photon-induced processes in at least 3 of the 4 LHC experiments, although it is not the main focus of any of them. There is an overwhelming number of reaction channels that can be investigated at the LHC in “ordinary” hadronic interactions. Including photon-induced processes leads to an even greater number. It seems unlikely that all these will be investigated during the life-time of the LHC. It will be up to the experiments to judge which are the most interesting and to which the necessary trigger resources and bandwidths should be allocated. In this talk, we have tried to argue that at least some photon-induced processes should meet the criteria for feasibility and interest.

## References

- [1] A.J. Baltz et al., Phys. Rep. **458**, 1 (2008).
- [2] C.A. Bertulani, S.R. Klein, J. Nystrand, Ann. Rev. Nucl. Part. Sci. **55**, 271 (2005).
- [3] S.R. Klein, J. Nystrand, Phys. Rev. **C60**, 014903 (1999).
- [4] A. Bzdak, L. Motyka, L. Szymanowski, J.R. Cudde, Phys. Rev. **D75**, 094023 (2007).
- [5] STAR Coll., B.I. Abelev et al., Phys. Rev. **C77**, 034910 (2008).
- [6] PHENIX Coll., D. d’Enterria et al., *Coherent photoproduction of J/Psi and high-mass  $e+e^-$  pairs in ultra-peripheral Au+Au collisions at  $\sqrt{s_{NN}} = 200$  GeV* (unpublished). Nucl-ex/0601001.
- [7] J. Pinfold, *presentation at this workshop*.
- [8] R. Bruce et al., Phys. Rev. Lett. **99**, 144801 (2007).
- [9] G. Blanford et al., Phys. Rev. Lett. **80**, 3037 (1998).
- [10] STAR Coll., J. Adams et al., Phys. Rev. **C70**, 031902 (2004).
- [11] CDF Coll., A. Abulencia et al., Phys. Rev. Lett. **98**, 112001 (2007).
- [12] CMS Coll., G. Baur et al., Eur. Phys. J. **C32**, s69 (2003).

- [13] M. Strikman, R. Vogt, S. White, Phys. Rev. Lett. **96**, 082001 (2006);  
R. Vogt, *Jet Photoproduction in Peripheral Heavy-Ion Collisions* (unpublished).  
Hep-ph/0407298.
- [14] S.R. Klein, J. Nystrand, R. Vogt, Phys. Rev. **C66**, 044906 (2002).

# Searching for the Odderon at HERA and the LHC

*Carlo Ewerz*

Institut für Theoretische Physik, Universität Heidelberg  
Philosophenweg 16, D-69120 Heidelberg, Germany

## Abstract

We review the present status of the odderon, focusing in particular on searches at HERA and the prospects for finding the odderon in exclusive processes at the LHC.

## 1 The odderon

The odderon is the negative charge parity ( $C = -1$ ) partner of the well-known pomeron. Therefore, it is the  $t$ -channel exchange that gives rise to the difference between a particle-particle scattering cross section and the corresponding particle-antiparticle cross section at high center-of-mass energy  $\sqrt{s}$ . The concept of the odderon was introduced and its existence conjectured in [1] in the context of Regge theory. It was subsequently realized that in QCD a colorless exchange in the  $t$ -channel with negative  $C$ -parity can be constructed from three gluons in a symmetric color state. In recent years considerable progress in understanding the odderon has been made in particular in perturbative QCD. The nonperturbative odderon, on the other hand, remains poorly understood.

In perturbative QCD the odderon is described by the Bartels-Kwieciński-Praszałowicz (BKP) equation [2] which resums the leading logarithms of  $\sqrt{s}$ , corresponding to the pairwise interaction of the three gluons exchanged in the  $t$ -channel. One finds that also compound states of more than three gluons with odderon quantum numbers can be constructed, which are also described by the BKP equation. The BKP equation exhibits interesting mathematical properties like conformal invariance in impact parameter space and holomorphic separability [3], and even turns out to be an integrable system [4]. Two explicit solutions to the BKP equation have been found, one with intercept  $\alpha_0 = 1$  [5] and one with a slightly smaller intercept [6], giving rise to a high-energy behavior of the cross section  $\sim s^{\alpha_0-1}$ . The main difference of the two solutions lies in their different coupling to external particles rather than in their intercepts which for all practical purposes can be considered equal.

While the perturbative odderon is at least theoretically rather well understood, our picture of the odderon in the nonperturbative regime is not at all satisfying. The main reason is the lack of experimental data which does not even allow us to test models of nonperturbative odderon exchange. This is in strong contrast to the nonperturbative pomeron which is theoretically equally hard to describe, but for the pomeron a rather clear picture has emerged at least on the phenomenological level from the study of a variety of high energy scattering data.

In the following we discuss some aspects of the odderon which are particularly relevant for HERA and LHC. A detailed review of the odderon and further references can be found in [7].

## 2 Experimental evidence

It would seem natural to expect that odderon exchange is suppressed relative to pomeron (two-gluon) exchange only by a power of  $\alpha_s$  due to the requirement to couple an additional gluon to the external particles. And at moderately low momenta  $\alpha_s$  is not too small, such that – given the ubiquitous pomeron – one expects odderon exchange to appear in many processes. Surprisingly, the contrary is true.

So far the only experimental evidence for the odderon has been found in a small difference in the differential cross sections for elastic proton-proton and proton-antiproton scattering at  $\sqrt{s} = 53 \text{ GeV}$ . Figure 1 shows the data taken at the CERN ISR in the dip region around  $t = -1.3 \text{ GeV}^2$ . The proton-proton data have a dip-like structure, while the proton-antiproton data

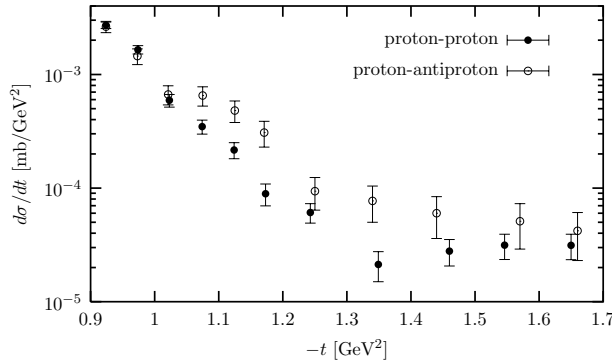


Fig. 1: Differential cross section for elastic  $pp$  and  $p\bar{p}$  scattering in the dip region for  $\sqrt{s} = 53 \text{ GeV}$ ; data from [8]

only level off at the same  $|t|$ . This difference between the two data sets can only be explained by invoking an odderon exchange. However, the difference relies on just a few data points with comparatively large error bars.

The data at various energies are well described by models that take into account the various relevant exchanges between the elastically scattering particles [9], [10]. Both of these models involve of the order of twenty parameters that need to be fitted. The structure in the region around  $|t| = 1 - 2 \text{ GeV}^2$  is the result of a delicate interference between different contributions to the scattering amplitude including the odderon. Therefore it is rather difficult to extract the odderon contribution unambiguously. In fact it turns out that the two odderon contributions obtained in [9] and [10], respectively, are not fully compatible with each other [11] (see also [7]). In [12] it was shown that assuming a perturbative odderon (three gluon exchange) in the context of the model of [9] requires to choose a very small coupling of the odderon to the proton. This small coupling can be either due to a small relevant value of  $\alpha_s \simeq 0.3$  or due to a small average distance of two of the constituent quarks in the proton corresponding to a diquark-like structure.

Unfortunately,  $\sqrt{s} = 53 \text{ GeV}$  is the only energy for which data for both reactions are available. The comparison of data taken at different energies rather strongly relies on theoretical models. Given the large number of parameters in these models it is not possible to arrive at firm conclusions about the odderon on the basis of the presently available data.

### 3 Odderon searches at HERA

The cross section for elastic  $pp$  and  $p\bar{p}$  scattering is a typical example in which the odderon exchange is only one of many contributions to the scattering amplitude. It was recently realized that the chances for a clean identification of the odderon should be better in exclusive processes in which the odderon is the only exchange (usually besides the well-understood photon) that can give rise to the final state to be studied. This strategy was chosen at HERA.

Searches for the odderon at HERA have concentrated on the exclusive diffractive production of pseudoscalar mesons ( $M_{PS}$ ) as depicted in Figure 2. In addition to that diagram only the exchange of a photon instead of the odderon is possible at high energies. (Similarly also tensor mesons can be produced only by odderon and photon exchange.) This process had been suggested in [13]. The photon exchange contribution is rather well understood and is expected

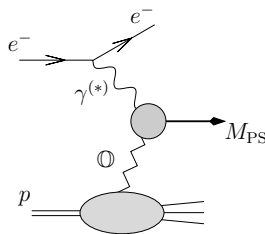


Fig. 2: Diffractive production of a pseudoscalar meson in  $ep$  scattering

to have a much steeper  $t$ -dependence than the odderon exchange.

The process which has been studied in most detail experimentally is the exclusive diffractive production of a single neutral pion,  $\gamma^{(*)}p \rightarrow \pi^0 X$ . Early theoretical considerations [14] had led to an estimate of the total photoproduction cross section for that process of  $\sigma(\gamma p \rightarrow \pi^0 X) \simeq 300$  nb, with a possible uncertainty of a factor of about two. The experimental search for that process, however, was not successful and resulted in an upper limit of  $\sigma(\gamma p \rightarrow \pi^0 X) < 49$  nb [15], obviously ruling out the prediction of [14]. The smallness of the cross section is a striking result since of all processes at HERA in which hadrons are diffractively produced this is the one with the largest phase space. Therefore a strong suppression mechanism must be at work here. One possibility is again a potentially small coupling of the odderon to the proton. Further possible causes for the failure of the prediction of [14] were discussed in [16]. The most important among them is probably the suppression of pion production due to approximate chiral symmetry, as has been discussed in detail in [17]. In fact it turns out that the odderon contribution to the amplitude for diffractive single-pion production vanishes exactly in the chiral limit. This suppression had not been taken into account properly in [14].

Also searches for similar processes in which instead of the pion some other pseudoscalar or tensor meson is produced diffractively have been performed, although only on a preliminary basis [18]. Again, no evidence for the odderon was found. However, for these processes the experimental bounds are closer to the theoretical estimates of [14], and hence the situation is less clear.



#### 4 Prospects for the LHC

At the LHC one can in analogy to the ISR try to look for the odderon in elastic  $pp$  scattering. The measured differential cross section can be compared to models which are fitted to the differential cross section at lower energies and extrapolated to LHC energies, see for example [19]. Although these models involve a large number of fit parameters and some uncertainty in the extrapolation to a new energy range it is argued in [19] that there is a chance to see evidence of the odderon. Also the spin dependence of elastic scattering is sensitive to the odderon and can be used to search for it, see [20]. In both cases the odderon is again one of several contributions to the scattering amplitude, which makes an unambiguous identification unlikely.

Recent proposals for odderon searches at the LHC (and analogously at the Tevatron) have therefore again focussed on exclusive processes in which the odderon is (except for the photon) the only contribution to the cross section. Here the mere observation of the process can already be sufficient to confirm odderon exchange. The most prominent of these exclusive processes at LHC is the double-diffractive production of a vector meson  $M_V$  in pomeron-odderon fusion, that is  $p + p \rightarrow X + M_V + Y$  with the vector meson separated from the forward hadronic systems  $X$  and  $Y$  by rapidity gaps, see Figure 3. This process was first proposed and discussed in the

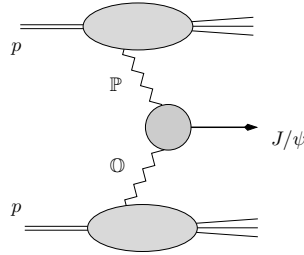


Fig. 3: Pomeron-odderon fusion mechanism for double-diffractive  $J/\psi$  production in  $p\bar{p}$  scattering

framework of Regge theory in [21]. In particular heavy vector mesons,  $M_V = J/\psi, \Upsilon$ , are well suited for odderon searches since here the reggeon exchange contribution (in place of the odderon) is suppressed by Zweig's rule. (In the production of  $\phi$  mesons that contribution could still be relevant – especially if the odderon contribution is small.) At the LHC in particular the ALICE detector appears to be best suited for the observation of centrally produced  $J/\psi$  or  $\Upsilon$  mesons and can in addition identify rapidity gap events [22].

In [23] a detailed study of this process has been performed in perturbation theory. The leading perturbative diagram contains the fusion of two of the three gluons in the odderon with one from the two in the pomeron to the  $J/\psi$  or  $\Upsilon$ , and an additional ('spectator') gluon exchange between the two protons. There are two important uncertainties in the calculation of this process. One is again the coupling of the odderon to the proton which might be small. The other main uncertainty is the survival probability for the rapidity gaps in the final state. Presently, a full understanding of the gap survival is still lacking. In hadronic collisions the gap survival is very different from  $ep$  scattering, and extrapolations from Tevatron energies to the LHC energy contain a considerable uncertainty. Depending on the assumptions about these uncertainties the expected

cross sections  $d\sigma/dy|_{y=0}$  at mid-rapidity  $y$  for  $J/\psi$  production are between 0.3 and 4 nb at the LHC. For the  $\Upsilon$  one expects 1.7 – 21 pb. One has to keep in mind that also photon instead of odderon exchange can give rise to the same final state. A possibility to separate the two contributions is to impose a cut on the squared transverse momentum  $p_T^2$  of the vector meson. The photon dominates at small  $p_T^2$  but then falls rapidly towards higher  $p_T^2$ . The odderon contribution does not fall so quickly and for the  $J/\psi$  dominates above  $p_T^2 \simeq 0.3 \text{ GeV}^2$ .

It is possible that the negative result of all odderon searches to date is caused by a small coupling of the odderon to the proton. If that coupling is indeed so small also the process just described will not be observable at the LHC. A possibility to find the odderon nevertheless might then be to look for the production of two heavy vector mesons in triple-diffractive events,  $p + p \rightarrow X + M_V + M_V + Y$  (with the  $+$ -signs indicating rapidity gaps), as suggested in [7]. This process is shown in Figure 4. For small odderon-proton coupling the right hand diagram can be neglected.

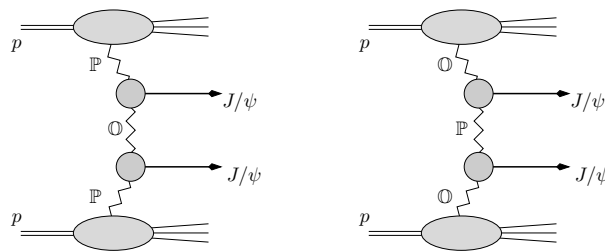


Fig. 4: Diagrams contributing to the triple-diffractive production of two  $J/\psi$  mesons in  $p\bar{p}$  scattering

In the left hand diagram – which does not involve the  $\mathbb{O}p$  coupling – the middle rapidity gap can only be produced by odderon (or photon) exchange and the mere observation of the process could finally establish the existence of the odderon.

## 5 Summary

The existence of the odderon is a firm prediction of perturbative QCD. But also in the nonperturbative regime we do not have good reasons to expect the absence of the odderon. A possible obstacle in finding it might be its potentially small coupling to the proton. As we have pointed out there are exclusive processes that can give a clear indication of the odderon at the LHC – including some which do not involve the potentially small odderon-proton coupling. If the odderon remains elusive also in these processes we might have to reconsider our picture of QCD at high energies.

## References

- [1] Lukaszuk, L. and Nicolescu, B., *Nuovo Cim. Lett.* **8**, 405 (1973);  
Joynson, David and Leader, Elliot and Nicolescu, Basarab and Lopez, Cayetano, *Nuovo Cim.* **A30**, 345 (1975).

- [2] Bartels, Jochen, Nucl. Phys. **B175**, 365 (1980);  
Kwiecinski, J. and Praszalowicz, M., Phys. Lett. **B94**, 413 (1980).
- [3] Lipatov, L. N., Phys. Lett. **B251**, 284 (1990).
- [4] Lipatov, L. N. (1993);  
Lipatov, L. N., JETP Lett. **59**, 596 (1994);  
Faddeev, L. D. and Korchemsky, G. P., Phys. Lett. **B342**, 311 (1995).
- [5] Bartels, Jochen and Lipatov, L. N. and Vacca, G. P., Phys. Lett. **B477**, 178 (2000).
- [6] Janik, R. A. and Wosiek, J., Phys. Rev. Lett. **82**, 1092 (1999).
- [7] Ewerz, Carlo (2003).
- [8] Breakstone, A. and others, Phys. Rev. Lett. **54**, 2180 (1985).
- [9] Donnachie, A. and Landshoff, P. V., Nucl. Phys. **B267**, 690 (1986).
- [10] Gauron, Pierre and Nicolescu, Basarab and Leader, Elliot, Phys. Lett. **B238**, 406 (1990).
- [11] Schatz, Volker (2003).
- [12] Dosch, Hans Günter and Ewerz, Carlo and Schatz, Volker, Eur. Phys. J. **C24**, 561 (2002).
- [13] Schäfer, A. and Mankiewicz, L. and Nachtmann, O. In Proc. of the Workshop *Physics at HERA*, DESY Hamburg 1991, vol. 1, p. 243;  
Barakovsky, V. V. and Zhitnitsky, I. R. and Shelkovenko, A. N., Phys. Lett. **B267**, 532 (1991);  
Kilian, W. and Nachtmann, O., Eur. Phys. J. **C5**, 317 (1998).
- [14] Berger, E. R. and others, Eur. Phys. J. **C9**, 491 (1999).
- [15] Adloff, C. and others, Phys. Lett. **B544**, 35 (2002).
- [16] Donnachie, A. and Dosch, H. G. and Nachtmann, O., Eur. Phys. J. **C45**, 771 (2006).
- [17] Ewerz, Carlo and Nachtmann, Otto, Eur. Phys. J. **C49**, 685 (2007).
- [18] Olsson, J. (2001).
- [19] Avila, Regina and Gauron, Pierre and Nicolescu, Basarab, Eur. Phys. J. **C49**, 581 (2007).
- [20] Trueman, T. L., Phys. Rev. **D77**, 054005 (2008).
- [21] Schäfer, A. and Mankiewicz, L. and Nachtmann, O., Phys. Lett. **B272**, 419 (1991).
- [22] Schicker, R. (2008).
- [23] Bzdak, A. and Motyka, L. and Szymanowski, L. and Cudell, J. -R., Phys. Rev. **D75**, 094023 (2007).

# Forward physics with CMS

*Samim Erhan<sup>1</sup>, Salim Cerci<sup>2</sup>, Monika Grothe<sup>3</sup>, Jonathan Hollar<sup>4</sup>, Antonio Vilela Pereira<sup>5</sup>  
on behalf of the CMS collaboration*

<sup>1</sup>University of California, Los Angeles, Los Angeles, California, USA

<sup>2</sup>Cukurova University, Adana, Turkey

<sup>3</sup>University of Wisconsin, Madison, Wisconsin, USA

<sup>4</sup>Lawrence Livermore National Laboratory, Livermore, California, USA

<sup>5</sup>Universita di Torino e Sezione dell' INFN, Torino, Italy

## Abstract

We describe several example analyses of the CMS forward physics program: A feasibility study for observing  $W$  production in single diffractive dissociation, the analysis of exclusive  $\mu\mu$  production and the measurement of very low- $x$  parton distributions and search for evidence of BFKL dynamics with forward jets.

## 1 Introduction

The CMS Experiment has a rich and broad forward physics program with measurements that can be realized from the start of the LHC [1–6]. The CMS detectors in the forward region allow an experimental program to be carried out that reaches beyond the traditional forward gap physics, such as soft and hard single diffraction and double Pomeron exchange physics, and also includes the study of  $\gamma\gamma$  and  $\gamma p$  interactions, energy and particle flow measurements relevant for understanding multi-parton interactions for tuning of Monte Carlo event generators, jet-gap-jet events to understand the origin of these event topologies, and forward jets and forward Drell-Yan processes at 14 TeV center-of-mass energies. Topics of soft and hard diffraction include but are not limited to:

1. Dependence of the diffractive cross sections on  $\xi$ ,  $t$  and  $M_x$  as fundamental quantities of non-perturbative QCD.
2. Gap survival dynamics and multi-gap event topologies.
3. Production of jets,  $W$ ,  $J/\psi$ ,  $b$  and  $t$  quarks, hard photons in hard diffraction.
4. Double Pomeron Exchange events as gluon factory.
5. Central exclusive Higgs boson production.
6. SUSY and other low mass exotics in exclusive processes.
7. Proton light cone studies.

CMS shares its interaction point (IP) with the TOTEM experiment [7]. The two experiments plan [8] to join their resources and use common trigger and data acquisition systems to increase their forward physics potential.

The studies presented in the following assume no event pile-up, i.e. are analyses to be carried out during the low pile-up, start-up phase of the LHC. In addition, CMS is studying a proposal to install tracking and time-of-flight detectors at 420 m from the IP [9], which has the

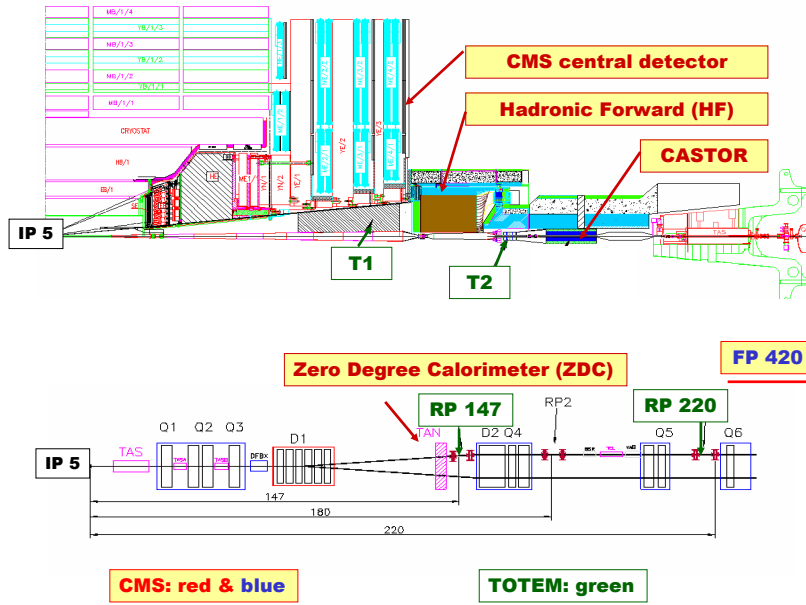


Fig. 1: Layout of the forward detectors around the CMS interaction point.

potential of adding discovery physics, notably central exclusive Higgs production, to the forward physics program of CMS.

For space limitations, in this paper, we describe only three processes as examples of the CMS forward physics program. After a brief description of the forward detector instrumentation around the CMS IP, section III covers a feasibility study on observing  $W$  production in single diffractive dissociation. The analysis of exclusive  $\mu\mu$  production is discussed in Section IV and the possibility of measuring very low- $x$  parton distributions and of looking for evidence of BFKL signatures with forward jets is described in Section V.

## 2 Forward detectors around the CMS interaction point

Forward physics at the LHC covers a wide range of diverse physics subjects that have in common that particles produced at small polar angles,  $\theta$ , and hence large values of rapidity provide a defining characteristic. At the Large-Hadron-Collider (LHC), where proton-proton collisions occur at center-of-mass energies of 14 TeV, the maximal possible rapidity is  $y_{max} = \ln \frac{\sqrt{s}}{m_\pi} \sim 11.5$ . The central components of CMS are optimized for efficient detection of processes with large polar angles and hence high transverse momentum,  $p_T$ . They extend down to about  $|\theta| = 1^\circ$  from the beam axis or  $|\eta| = 5$ , where  $\eta = -\ln [\tan (\theta/2)]$  is the pseudorapidity. In the forward region, the central CMS components are complemented by several CMS [10] and TOTEM subdetectors with coverage beyond  $|\eta| = 5$ , see figure 1. TOTEM is an approved experiment at the LHC for precision measurements of the  $pp$  elastic and total cross sections. The combined CMS and TOTEM

apparatus comprises two suites of calorimeters with tracking detectors in front plus near-beam proton taggers. The CMS Hadron Forward (HF) calorimeter with the TOTEM telescope T1 in front covers the region  $3 < |\eta| < 5$ , the CMS CASTOR calorimeter with the TOTEM telescope T2 in front covers  $5.2 < |\eta| < 6.6$ . The CMS ZDC calorimeters are installed at the end of the straight LHC beam-line section, at a distance of  $\pm 140$  m from the IP. Near-beam proton taggers will be installed by TOTEM at  $\pm 147$  m and  $\pm 220$  m from the IP. The kinematic coverage of the combined CMS and TOTEM apparatus is unprecedented at a hadron collider. The CMS and TOTEM collaborations have described the considerable physics potential of joint data taking in a report to the LHCC [8]. Further near-beam proton taggers in combination with very fast timing detectors to be installed at  $\pm 420$  m from the IP (FP420) are in the proposal stage in CMS. FP420 would give access to possible discovery processes in forward physics at the LHC [9].

## 2.1 The CMS forward calorimeters HF, CASTOR, ZDC

The forward part of the hadron calorimeter, HF, is located 11.2 m from the interaction point. It consists of steel absorbers and embedded radiation hard quartz fibers, which provide a fast collection of Cherenkov light. Each HF module is constructed of 18 wedges in a nonprojective geometry with the quartz fibers running parallel to the beam axis along the length of the iron absorbers. Long (1.65 m) and short (1.43 m) quartz fibers are placed alternately with a separation of 5 mm. These fibers are bundled at the back of the detector and are read out separately with phototubes.

The CASTOR calorimeters are octagonal cylinders located at  $\sim 14$  m from the IP. They are sampling calorimeters with tungsten plates as absorbers and fused silica quartz plates as active medium. The plates are inclined by  $45^\circ$  with respect to the beam axis. Particles passing through the quartz emit Cherenkov photons which are transmitted to photomultiplier tubes through aircore lightguides. The electromagnetic section is 22 radiation lengths  $X_0$  deep with 2 tungsten-quartz sandwiches, the hadronic section consists of 12 tungsten-quartz sandwiches. The total depth is 10.3 interaction lengths  $\lambda_I$ . The calorimeters are read out segmented azimuthally in 16 segments and longitudinally in 14 segments. They do not have any segmentation in  $\eta$ . The CASTOR coverage of  $5.2 < |\eta| < 6.6$  closes hermetically the CMS calorimetric pseudorapidity range over 13 units. Currently, funding is available only for a CASTOR calorimeter on one side of the IP. Installation is foreseen for 2009.

The CMS Zero Degree Calorimeters, ZDC, are located inside the TAN absorbers at the ends of the straight section of the LHC beamline, between the LHC beampipes, at  $\pm 140$  m distance on each side of the IP. They are very radiation-hard sampling calorimeters with tungsten plates as absorbers and as active medium quartz fibers read out via aircore light guides and photomultiplier tubes. The electromagnetic part,  $19X_0$  deep, is segmented into 5 units horizontally, the hadronic part into 4 units in depth. The total depth is  $6.5 \lambda_I$ . The ZDC calorimeters have 100% acceptance for neutral particles with  $|\eta| > 8.4$  and can measure 50 GeV photons with an energy resolution of about 10%. The ZDC calorimeters are already installed and will be operational in 2009.

## 2.2 The TOTEM T1 and T2 telescopes

The TOTEM T1 telescope consists of two arms symmetrically installed around the CMS IP in the endcaps of the CMS magnet, right in front of the CMS HF calorimeters and with  $\eta$  coverage similar to HF. Each arm consists of 5 planes of Cathod Strip Chambers (CSC) which measure 3 projections per plane, resulting in a spatial resolution of 0.36 mm in the radial and 0.62 mm in the azimuthal coordinate in test beam measurements. The two arms of the TOTEM T2 telescope are mounted right in front of the CASTOR calorimeters, with similar  $\eta$  coverage. Each arm consists of 10 planes of 20 semi-circular modules of Gas Electron Multipliers (GEMs). The detector read-out is organized in strips and pads, a resolution of 115  $\mu\text{m}$  for the radial coordinate and of 16  $\mu\text{rad}$  in azimuthal angle were reached in prototype test beam measurements. A more detailed description can be found in [11].

## 2.3 Near-beam proton taggers

The LHC beamline with its magnets is essentially a spectrometer in which protons slightly off the beam momentum are bent sufficiently to be detectable by means of detectors inserted into the beam-pipe. At high luminosity at the LHC, proton tagging is the only means of detecting diffractive and  $\gamma$  mediated processes because areas of low or no hadronic activity in the detector are filled in by particles from overlaid pile-up events.

The TOTEM proton taggers at  $\pm 220$  m at nominal LHC optics have acceptance for scattered protons from the IP for  $0.02 < \xi < 0.2$ . Smaller values of  $\xi$ ,  $0.002 < \xi < 0.02$ , can be achieved with proton taggers at  $\pm 420$  m. The FP420 proposal [9] foresees employing 3-D Silicon, an extremely radiation hard novel Silicon technology, for the proton taggers, and additional fast timing Cherenkov detectors for the rejection of protons from pile-up events. The proposal is currently under consideration in CMS. If approved, installation could proceed in 2010, after the LHC start-up.

Forward proton tagging capabilities enhance the physics potential of CMS. They would render possible a precise measurement of the mass and quantum numbers of the Higgs boson should it be discovered by traditional searches. They also augment the CMS discovery reach for Higgs production in the minimal supersymmetric extension (MSSM) of the Standard Model (SM) and for physics beyond the SM in  $\gamma p$  and  $\gamma\gamma$  interactions. The proposed FP420 detectors and their physics potential are discussed in [12].

## 3 Observation of single-diffractive $W$ production with CMS: a feasibility study

The single-diffractive (SD) reaction  $pp \rightarrow Xp$ , where  $X$  includes a  $W$  boson (Fig. 2) is studied to demonstrate the feasibility of observing SD  $W$  production at CMS given an integrated effective luminosity for single interactions of  $100 \text{ pb}^{-1}$ . Only  $W \rightarrow \mu\nu$  decay mode is considered in this analysis [2].

The analysis relies on the extended forward coverage of the CMS forward calorimeters, that cover the pseudo-rapidity range of  $3 < |\eta| < 5$ . Additional coverage at  $-6.6 < \eta < -5.2$  is assumed by means of the CASTOR calorimeter.

Single diffractive  $W$  production was simulated by using the POMWIG generator [13], version v2.0 beta. For the diffractive PDFs and the Pomeron flux, the result of the NLO H1 2006

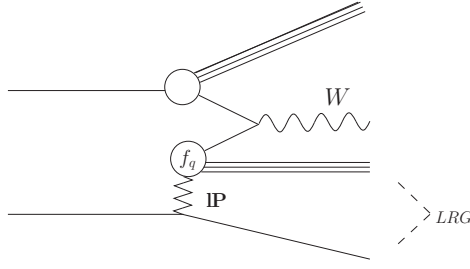


Fig. 2: Sketch of the single-diffractive reaction  $pp \rightarrow Xp$  in which  $X$  includes a  $W$  boson. The symbol  $IP$  indicates the exchange with the vacuum quantum numbers (Pomeron). The large rapidity gap (LRG) is also shown.

fit B [14] was used. A rapidity gap survival probability of 0.05, as predicted in Ref. [15], is assumed. For non-diffractive  $W$  production, the PYTHIA generator [16] was used. With the assumed numbers for the cross sections, the ratio of diffractive to inclusive yields is around 0.3%.

### 3.1 Event Selection and Observation of SD $W$ Production

#### 3.1.1 $W \rightarrow \mu\nu$ selection

The selection of the events with a candidate  $W$  decaying to  $\mu\nu$  is the same as that used in Ref. [17]. Events with a candidate muon in the pseudo-rapidity range  $|\eta| > 2.0$  and transverse momentum  $p_T < 25$  GeV were rejected, as were events with at least two muons with  $p_T > 20$  GeV. Muon isolation was imposed by requiring  $\sum p_T < 3$  GeV in a cone with  $\Delta R < 0.3$ . The transverse mass was required to be  $M_T > 50$  GeV. The contribution from top events containing muons was reduced by rejecting events with more than 3 jets with  $E_T > 40$  GeV (selected with a cone algorithm with radius of 0.5) and requiring that the acoplanarity ( $\zeta = \pi - \Delta\phi$ ) between the muon and the direction associated to  $E_T^{\text{miss}}$  be less than 1 rad. Approximately 2,400 SD  $W$  events and 600,000 non-diffractive  $W$  events per  $100 \text{ pb}^{-1}$  are expected to pass these cuts.

#### 3.1.2 Diffractive selection and Evidence for SD $W$ Production

Diffractive events have, on average, lower multiplicity both in the central region (lower underlying event activity) and in the hemisphere that contains the scattered proton, the so-called “gap side”, than non-diffractive events.

The gap side was selected as that with lower energy sum in the HF. A cut was then placed on the multiplicity of tracks with  $p_T > 900$  MeV and  $|\eta| < 2$ . For the events passing this cut, multiplicity distributions in the HF and CASTOR calorimeters in the gap side were studied, from which a diffractive sample can be extracted.

Figure 3 shows the HF tower multiplicity vs the CASTOR  $\phi$  sector multiplicity for events with central track multiplicity  $N_{\text{track}} \leq 5$ . Since CASTOR will be installed at first on the negative side of the interaction point, only events with the gap on that side (as determined with the procedure discussed above) were considered. The CMS software chain available for this study did not include simulation/reconstruction code for CASTOR; therefore, the multiplicity of generated hadrons with energy above a 10 GeV threshold in each of the CASTOR azimuthal



sectors was used.

The top left and top right plots show the distributions expected for the diffractive  $W$  events with generated gap in the positive and negative  $Z$  direction, respectively. The few events in the top left plot are those for which the gap-side determination was incorrect. The non-diffractive  $W$  events have on average higher multiplicities, as shown in the bottom left plot. Finally, the bottom right plot shows the sum of the POMWIG and PYTHIA distributions – this is the type of distribution expected from the data.

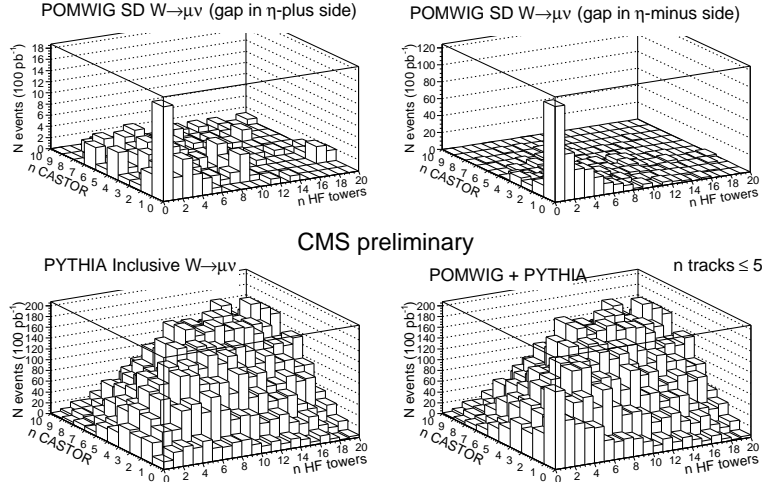


Fig. 3: HF tower multiplicity vs CASTOR sector multiplicity distribution for events with track multiplicity in the central tracker  $N_{\text{track}} \leq 5$ .

A simple way to isolate a sample of diffractive events from these plots is to use the zero-multiplicity bins, where the diffractive events cluster and the non-diffractive background is small.

The HF plus CASTOR combination yields the best signal to background ratio. When an integrated effective luminosity for single interactions of  $100 \text{ pb}^{-1}$  becomes available, SD  $W \rightarrow \mu\nu$  production can then be observed with  $\mathcal{O}(100)$  signal events. The situation is even more favorable for SD dijet production where a recently completed study [3] arrives at  $\mathcal{O}(300)$  SD dijet events per  $10 \text{ pb}^{-1}$  of integrated effective luminosity for single interactions. With an observation of a number of signal events of this size, it should be possible to exclude values of rapidity gap survival probability at the lower end of the spectrum of theoretical predictions. A method to establish that the observed population of the zero-multiplicity bins is indeed indicative of the presence of SD events in the data is described in [3]. The method is based on the observation that the size of the SD signal in the zero-multiplicity bins can be controlled in a predictable way when the cuts for enhancing the SD signal are modified.

The main background other than non-diffractive  $W$  production consists of SD  $W$  production with proton-dissociation,  $pp \rightarrow XN$ , where  $X$  contains a  $W$  boson and  $N$  is a low-mass state into which the proton has diffractively dissociated. A study of proton-dissociation has been carried out in Ref. [4], where it has been shown that about 50% of the proton-dissociative background can be rejected by vetoing events with activity in the CMS Zero Degree Calorimeter

(ZDC), which provides coverage for neutral particles for  $|\eta| > 8.1$ . The net effect is to enhance the diffractive signal in the zero multiplicity bin of Fig. 3 by about 30%.

#### 4 Exclusive $\gamma\gamma \rightarrow \ell^+\ell^-$ and $\gamma p \rightarrow \Upsilon p \rightarrow \ell^+\ell^-p$

Exclusive dilepton production in  $pp$  collisions at CMS can occur through the processes  $\gamma\gamma \rightarrow \ell^+\ell^-$  and  $\gamma p \rightarrow \Upsilon p \rightarrow \ell^+\ell^-p$ . The first is a QED process, making it an ideal sample for luminosity calibration at the LHC. The second will allow studies of vector meson photoproduction at energies significantly higher than previous experiments. Zero pileup is assumed for this study [4]. Both signal processes are characterized by the presence of two same-flavor opposite-sign leptons back-to-back in  $\Delta\phi$ , and with equal  $|p_T|$ . In the no-pileup startup scenario assumed here, the signal is also distinguished by having no calorimeter activity that is not associated with the leptons, and no charged tracks in addition to the two signal leptons. This exclusivity requirement is implemented by requiring that there be no more than 5 “extra” calorimeter towers with  $E > 5$  GeV, where extra towers are defined as those separated from either of the lepton candidates by  $\Delta R > 0.3$  in the  $\eta - \phi$  plane. The track multiplicity is required to be  $< 3$ . The dominant inelastic photon-exchange background is reduced by requiring no activity in the CASTOR calorimeter (covering  $5.2 < \eta < 6.6$ ) or the Zero Degree Calorimeter (covering  $|\eta| > 8.2$ ). The residual background from non-photon exchange processes is estimated from an exponential fit to the sideband of the extra calorimeter towers distribution, resulting in a background estimate of approximately 39 events in  $100 \text{ pb}^{-1}$ , which is small compared to the inelastic background.

The expected  $\gamma\gamma \rightarrow \mu^+\mu^-$  signal yields in  $100 \text{ pb}^{-1}$  are  $N_{\text{elastic}}(\gamma\gamma \rightarrow \mu^+\mu^-) = 709 \pm 27$ , and  $N_{\text{inelastic}}(\gamma\gamma \rightarrow \mu^+\mu^-) = 223 \pm 15 \pm 42(\text{model})$ . Without the ZDC and Castor vetoes, the singly inelastic contribution would be significantly larger:  $N_{\text{inelastic}}(\gamma\gamma \rightarrow \mu^+\mu^-) = 636 \pm 25 \pm 121(\text{model})$ . In the  $\gamma\gamma \rightarrow e^+e^-$  channel, the expected yields are significantly smaller. After all trigger and selection criteria are applied the expected elastic signal yields in  $100 \text{ pb}^{-1}$  are:  $N_{\text{elastic}}(\gamma\gamma \rightarrow e^+e^-) = 67 \pm 8$ , and  $N_{\text{inelastic}}(\gamma\gamma \rightarrow e^+e^-) = 31 \pm 6 \pm 6(\text{model})$ .

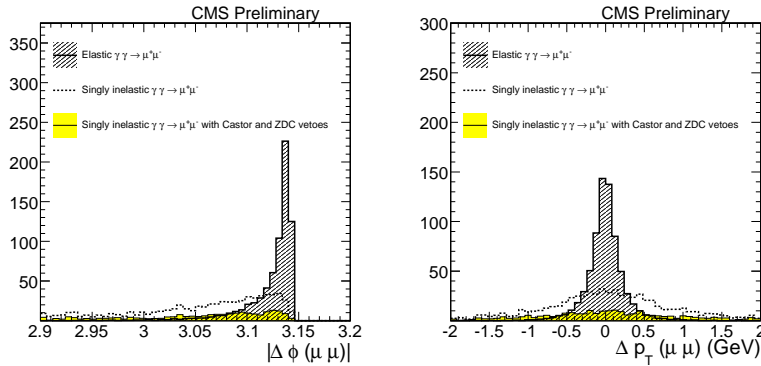


Fig. 4: Distributions of  $|\Delta\phi(\mu^+\mu^-)|$  (left) and  $|\Delta p_T(\mu^+\mu^-)|$  (right) for  $\gamma\gamma \rightarrow \mu^+\mu^-$  events passing all selection requirements. The elastic signal is denoted by the open histogram, the inelastic background is shown with no CASTOR/ZDC vetoes (dashed line), and with the vetoes described in the text (solid histogram).

Without the ZDC and Castor vetoes, the singly inelastic contribution would be:  $N_{inelastic}(\gamma\gamma \rightarrow e^+e^-) = 82 \pm 9 \pm 15(model)$ . The elastic  $\gamma\gamma \rightarrow \mu^+\mu^-$  signal can be separated from the inelastic background for luminosity measurements using the  $\Delta\phi$  and  $\Delta p_T$  distributions (Figure 4), while the  $\Upsilon$  photoproduction signal can be further distinguished by performing a fit to the dimuon invariant mass distribution (Figure 5).

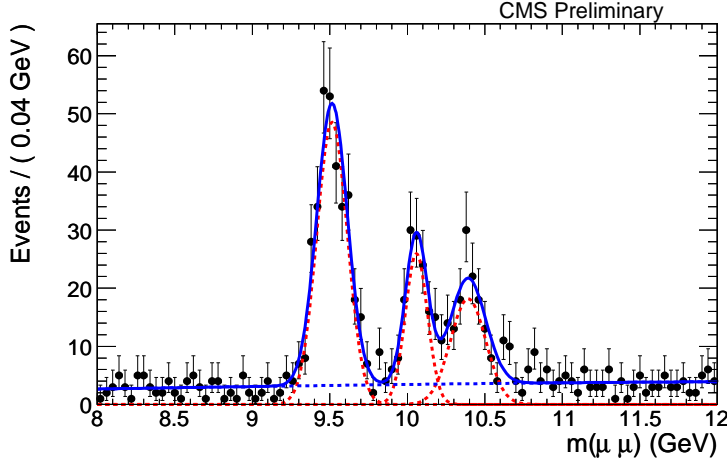


Fig. 5: Dimuon invariant mass in the range  $8 < m(\mu^+\mu^-) < 12$  GeV. The lines show the result of a fit, where the dashed line is the  $\Upsilon$  component, the dotted line is the two-photon continuum, and the solid line is the sum of the two.

We conclude that with  $100pb^{-1}$  of integrated luminosity, a large sample of  $\gamma\gamma \rightarrow \mu^+\mu^-$  and  $\gamma p \rightarrow \Upsilon p \rightarrow \mu^+\mu^-p$  events can be triggered and reconstructed in the CMS detector, using a common selection for both samples. With minimal pileup these events can be cleanly distinguished from the dominant backgrounds. The  $\Upsilon$  sample will allow measurements of cross-sections and production dynamics at significantly higher energies than previous experiments, while the  $\gamma\gamma \rightarrow \ell^+\ell^-$  sample will serve as a calibration sample for luminosity studies.

## 5 Forward jets reconstruction in HF

### 5.1 Introduction

The parton distribution functions (PDFs) in the proton have been studied in detail in deep-inelastic-scattering (DIS)  $ep$  collisions at HERA [18]. For decreasing parton momentum fraction  $x = p_{parton}/p_{hadron}$ , the gluon density is observed to grow rapidly as  $xg(x, Q^2) \propto x^{-\lambda(Q^2)}$ , with  $\lambda \approx 0.1-0.3$  rising logarithmically with  $Q^2$ . As long as the densities are not too high, this growth is described by the Dokshitzer-Gribov-Lipatov-Altarelli-Parisi (DGLAP) [19] or by the Balitski-Fadin-Kuraev-Lipatov (BFKL) [20] evolution equations which govern, respectively, parton radiation in  $Q^2$  and  $x$ . Experimentally, direct information on the parton structure and evolution can be obtained in hadron-hadron collisions from the perturbative production of e.g. jets or prompt  $\gamma$ 's, which are directly coupled to the parton-parton scattering vertex. The measurement of jets with transverse momentum  $p_T \approx 20$  GeV in the CMS forward calorimeters (HF,  $3 < |\eta| < 5$  and CASTOR,  $5.1 < |\eta| < 6.6$ ) will allow one to probe  $x$  values as low as  $x_2 \approx 10^{-5}$ .

Figure 6 (right) shows the actual  $\log(x_{1,2})$  distribution for two-parton scattering in p-p collisions at 14 TeV producing at least one jet above 20 GeV in the HF and CASTOR acceptances. Full detector simulation and reconstruction packages were used in obtaining these results.

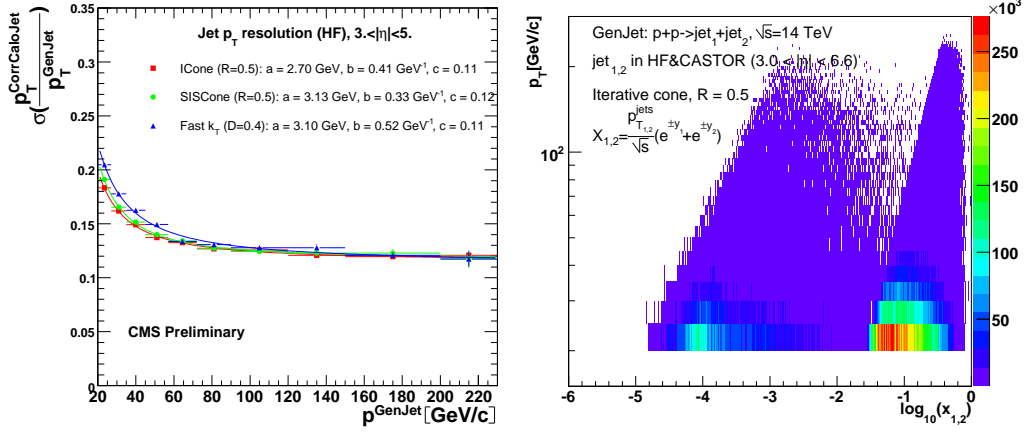


Fig. 6: Energy resolution as a function of  $p_T$  for the I Cone, SiS Cone (with cone sizes  $R = 0.5$ ) and FastKt ( $D = 0.4$ ) algorithms for jets reconstructed in HF ( $3. < |\eta| < 5.$ ). The resolutions are fitted to  $f(p_T) = \sqrt{\left(\frac{a}{p_T^{g_{en}}}\right)^2 + \left(\frac{b}{\sqrt{p_T^{g_{en}}}}\right)^2 + c^2}$  with the parameters quoted in the legend (Left).  $\log(x_{1,2})$  distribution of two partons producing at least one jet above  $p_T = 20$  GeV within HF ( $3 < |\eta| < 5$ ) and CASTOR ( $5.1 < |\eta| < 6.6$ ) in p-p collisions at  $\sqrt{s} = 14$  TeV (Right).

## 5.2 Forward jets reconstruction in HF

Jets in CMS are reconstructed at the generator- and calorimeter-level using 3 different jet algorithms [5]: iterative cone [10] with radius of  $\mathcal{R} = 0.5$  in  $(\eta, \phi)$ , SiS Cone [22] ( $\mathcal{R} = 0.5$ ), and the Fast- $k_T$  [23] ( $E_{seed} = 3$  GeV and  $E_{thres} = 20$  GeV). The  $p_T$  resolutions for the three different algorithms are very similar:  $\sim 18\%$  at  $p_T \sim 20$  GeV decreasing to  $\sim 12\%$  for  $p_T \gtrsim 100$  GeV (Fig. 6, Left). The position  $(\eta, \phi)$  resolutions (not shown here) for jets in HF are also very good:  $\sigma_{\phi, \eta} = 0.045$  at  $p_T = 20$  GeV, improving to  $\sigma_{\phi, \eta} \sim 0.02$  above 100 GeV.

## 5.3 Single inclusive jet $p_T$ spectrum in HF

In this section, we present the reconstructed forward jet yields as a function of  $p_T$  for  $1 \text{ pb}^{-1}$  integrated luminosity. Figure 7 (left) shows reconstructed (and corrected for energy resolution smearing) single inclusive forward jet spectrum in HF in p-p collisions at 14 TeV for a total integrated luminosity of  $1 \text{ pb}^{-1}$  compared to fastNLO jet predictions [24] using various PDFs (MRST03 and CTEQ6.1M). Figure 7 (right) shows percent differences between the reconstructed forward jet  $p_T$  spectrum and two fastNLO predictions (CTEQ6.1M and MRST03 PDFs). The error bars include the statistical and the energy-resolution smearing errors. The solid curves indicate the propagated uncertainty due to the jet-energy scale (JES) error for “intermediate”

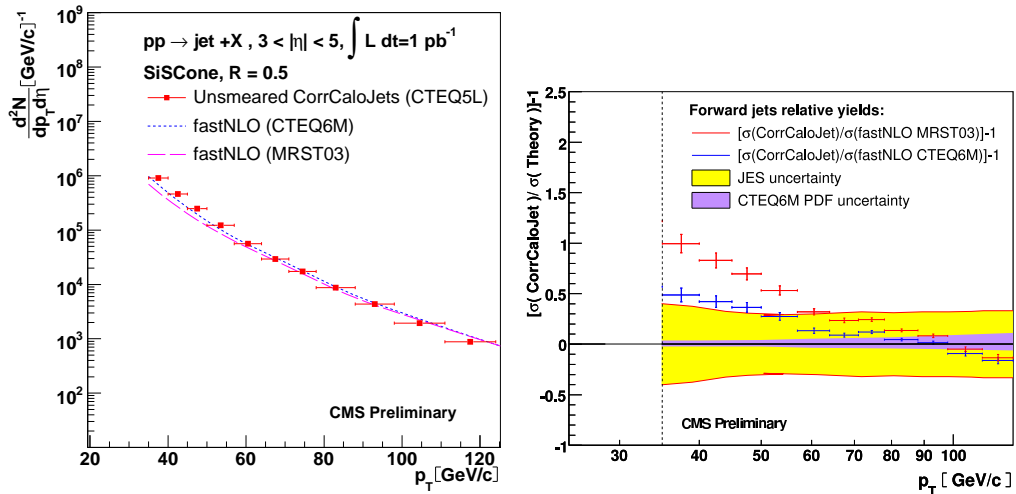


Fig. 7: Left: The forward jet yields for a total integrated luminosity of  $1 \text{ pb}^{-1}$ . Right: Percent differences between the reconstructed forward jet  $p_T$  spectrum and two fastNLO predictions (CTEQ6.1M and MRST03 PDFs). The solid curves indicate the propagated uncertainty due to the jet-energy scale (JES) error for “intermediate” 10% decreasing to a constant 5% for  $p_T > 50 \text{ GeV/c}$  conditions.

(10% decreasing to a constant 5% for  $p_T > 50 \text{ GeV/c}$ ) conditions. If the JES can be improved below 10% (such as in the “intermediate” scenario considered), our measurement will be more sensitive to the underlying PDF. The main conclusion of this part of the study is that the use of the forward jet measurement in HF to constrain the proton PDFs in the low- $x$  range will require careful studies of the HF jet calibration.

## References

- [1] CERN-LHCC-2006-021 (2006).
- [2] CMS Collaboration, CMS PAS DIF-07-002 (2007).
- [3] CMS Collaboration, CMS PAS FWD-08-002 (2008).
- [4] CMS Collaboration, CMS PAS DIF-07-001 (2007).
- [5] CMS Collaboration, CMS PAS FWD-08-001 (2008).
- [6] M. Grothe, in proceedings of the workshop on high-energy photon collisions at the LHC, D. D’Enterria *et al.* (eds), CERN, Geneva, Switzerland, 2008.
- [7] TOTEM Collaboration: Letter of Intent, CERN-LHCC 97-49; Technical Proposal, CERN-LHCC 99-7; Technical Design Report, CERN-LHCC-2004-002.
- [8] M. Albrow *et al.* [CMS and TOTEM Collaborations], CERN/LHCC 2006-039/G-124.

- [9] FP420 Collaboration, arXiv:0806.0302, [hep-ex].
- [10] CMS Collaboration, CERN-LHCC-2006-001 (2006).
- [11] TOTEM Collaboration, these proceedings.
- [12] P. Bussey, these proceedings.
- [13] B. E. Cox and J. R. Forshaw, Comput. Phys. Commun. **144** (2002) 104.
- [14] A. Aktas *et al.*, [H1 Collaboration], Eur. Phys. J. C **48** (2006) 715.
- [15] V. A. Khoze, A. D. Martin and M. G. Ryskin, Phys. Lett. B **643** (2006) 93.
- [16] T. Sjostrand, S. Mrenna and P. Skands, JHEP **0605** (2006) 026.
- [17] CMS Collaboration, CMS PAS EWK-07-002 (2007).
- [18] M. Klein and R. Yoshida, arXiv:0805.3334 [hep-ex].
- [19] V.N. Gribov and L.N. Lipatov, Sov. Journ. Nucl. Phys. **15** (1972) 438; G. Altarelli and G. Parisi, Nucl. Phys. **B126** (1977) 298; Yu. L. Dokshitzer, Sov. Phys. JETP **46** (1977) 641.
- [20] L.N. Lipatov, Sov. J. Nucl. Phys. **23** (1976) 338; E.A. Kuraev, L.N. Lipatov and V.S. Fadin, Zh. Eksp. Teor. Fiz **72**, (1977) 3; I.I. Balitsky, L.N. Lipatov, Sov. J. Nucl. Phys. **28** (1978) 822.
- [21] CMS Physics TDR, Volume 1, CERN-LHCC-2006-001, 2 February 2006
- [22] G. P. Salam and G.Soyez, JHEP05 (2007) 086
- [23] M.Cacciari and G. P. Salam, Phys. Lett. B **641** (2006) 57.
- [24] T. Kluge, K. Rabbertz, M. Wobisch, arXiv:hep-ph/0609285; K. Rabbertz, private communication.

# Diffraction at TOTEM

*G. Antchev<sup>1</sup>, P. Aspell<sup>1</sup>, V. Avati<sup>1,9</sup>, M.G. Bagliesi<sup>5</sup>, V. Berardi<sup>4</sup>, M. Berretti<sup>5</sup>, U. Bottigli<sup>5</sup>, M. Bozzo<sup>2</sup>, E. Brücken<sup>6</sup>, A. Buzzo<sup>2</sup>, F. Cafagna<sup>4</sup>, M. Calicchio<sup>4</sup>, M.G. Catanest<sup>4</sup>, P.L. Catastini<sup>5</sup>, R. Cecchi<sup>5</sup>, M.A. Ciocchi<sup>5</sup>, M. Deile<sup>1</sup>, E. Dimovasili<sup>1,9</sup>, K. Eggert<sup>9</sup>, V. Eremin<sup>\*\*</sup>, F. Ferro<sup>2</sup>, F. Garcia<sup>6</sup>, S. Giani<sup>1</sup>, V. Greco<sup>5</sup>, J. Heino<sup>6</sup>, T. Hildén<sup>6</sup>, J. Kašpar<sup>1,7</sup>, J. Kopal<sup>1,7</sup>, V. Kundrát<sup>7</sup>, K. Kurvinen<sup>6</sup>, S. Lami<sup>5</sup>, G. Latino<sup>5</sup>, R. Lauhakangas<sup>6</sup>, E. Lippmaa<sup>8</sup>, M. Lokajčiek<sup>7</sup>, M. Lo Vetere<sup>2</sup>, F. Lucas Rodriguez<sup>1</sup>, M. Macri<sup>2</sup>, G. Magazzù<sup>5</sup>, M. Meucci<sup>5</sup>, S. Minutoli<sup>2</sup>, H. Niewiadomski<sup>1,9</sup>, E. Noschis<sup>1</sup>, G. Notarnicola<sup>4</sup>, E. Oliveri<sup>5</sup>, F. Oljemark<sup>6</sup>, R. Orava<sup>6</sup>, M. Oriunno<sup>1</sup>, K. Österberg<sup>6,‡</sup>, P. Palazzi<sup>1</sup>, E. Pedreschi<sup>5</sup>, J. Petäjäjärvi<sup>6</sup>, M. Quinto<sup>4</sup>, E. Radermacher<sup>1</sup>, E. Radicioni<sup>4</sup>, F. Ravotti<sup>1</sup>, G. Rella<sup>4</sup>, E. Robutti<sup>2</sup>, L. Ropelewski<sup>1</sup>, G. Ruggiero<sup>1</sup>, A. Rummel<sup>8</sup>, H. Saarikko<sup>6</sup>, G. Sanguinetti<sup>5</sup>, A. Santroni<sup>2</sup>, A. Scribano<sup>5</sup>, G. Sette<sup>2</sup>, W. Snoeys<sup>1</sup>, F. Spinella<sup>5</sup>, P. Squillacioti<sup>5</sup>, A. Ster<sup>\*</sup>, C. Taylor<sup>3</sup>, A. Trummal<sup>8</sup>, N. Turini<sup>5</sup>, J. Whitmore<sup>9</sup>, J. Wu<sup>1</sup>*

<sup>1</sup>CERN, Genève, Switzerland,

<sup>2</sup>Università di Genova and Sezione INFN, Genova, Italy,

<sup>3</sup>Case Western Reserve University, Dept. of Physics, Cleveland, OH, USA,

<sup>4</sup>INFN Sezione di Bari and Politecnico di Bari, Bari, Italy,

<sup>5</sup>INFN Sezione di Pisa and Università di Siena, Italy,

<sup>6</sup>Helsinki Institute of Physics and Department of Physics, University of Helsinki, Finland,

<sup>7</sup>Institute of Physics of the Academy of Sciences of the Czech Republic, Praha, Czech Republic,

<sup>8</sup>National Institute of Chemical Physics and Biophysics NICPB, Tallinn, Estonia.

<sup>9</sup>Penn State University, Dept. of Physics, University Park, PA, USA.

<sup>\*</sup>Individual participant from MTA KFKI RMKI, Budapest, Hungary.

<sup>\*\*</sup>On leave from Ioffe Physico-Technical Institute, Polytechnicheskaya Str. 26, 194021 St-Petersburg, Russian Federation.

## Abstract

The TOTEM experiment at the LHC measures the total proton-proton cross section with the luminosity-independent method and the elastic proton-proton cross-section over a wide  $|t|$ -range. It also performs a comprehensive study of diffraction, spanning from cross-section measurements of individual diffractive processes to the analysis of their event topologies. Hard diffraction will be studied in collaboration with CMS taking advantage of the large common rapidity coverage for charged and neutral particle detection and the large variety of trigger possibilities even at large luminosities. TOTEM will take data under all LHC beam conditions including standard high luminosity runs to maximize its physics reach. This contribution describes the main features of the TOTEM physics programme including measurements to be made in the early LHC runs. In addition, a novel scheme to extend the diffractive proton acceptance for high luminosity runs by installing proton detectors at IP3 is described.

---

<sup>‡</sup> corresponding author: Kenneth Österberg (kenneth.osterberg@helsinki.fi)

## 1 Introduction

The TOTEM experiment [1] is dedicated to the total proton-proton ( $pp$ ) cross-section measurement using the luminosity-independent method, which requires a detailed measurement of the elastic scattering rate down to a squared four-momentum transfer of  $-t \sim p^2\Theta^2 \sim 10^{-3} \text{ GeV}^2$  together with the measurements of the total inelastic and elastic rates. Furthermore, by studying elastic scattering with momentum transfers up to  $10 \text{ GeV}^2$ , and via a comprehensive study of diffractive processes – partly in cooperation with CMS [2], located at the same interaction point, TOTEM’s physics programme aims at a deeper understanding of the proton structure. To perform these measurements, TOTEM requires a good acceptance for particles produced at small and even tiny angles with respect to the beams. TOTEM’s coverage in the pseudo-rapidity range of  $3.1 \leq |\eta| \leq 6.5$  ( $\eta = -\ln \tan \frac{\theta}{2}$ ) on both sides of the interaction point (IP) is accomplished by two telescopes, T1 and T2 (Figure 1, top), for the detection of charged particles with emission angles between a few and about hundred milliradians. This is complemented by detectors in special movable beam-pipe insertions – so called Roman Pots (RP) – placed at about 147 m and 220 m from the IP, designed to detect elastically or diffractively scattered protons at merely a few millimeter from the beam center corresponding to emission angles down to a few microradians (Figure 1, bottom).

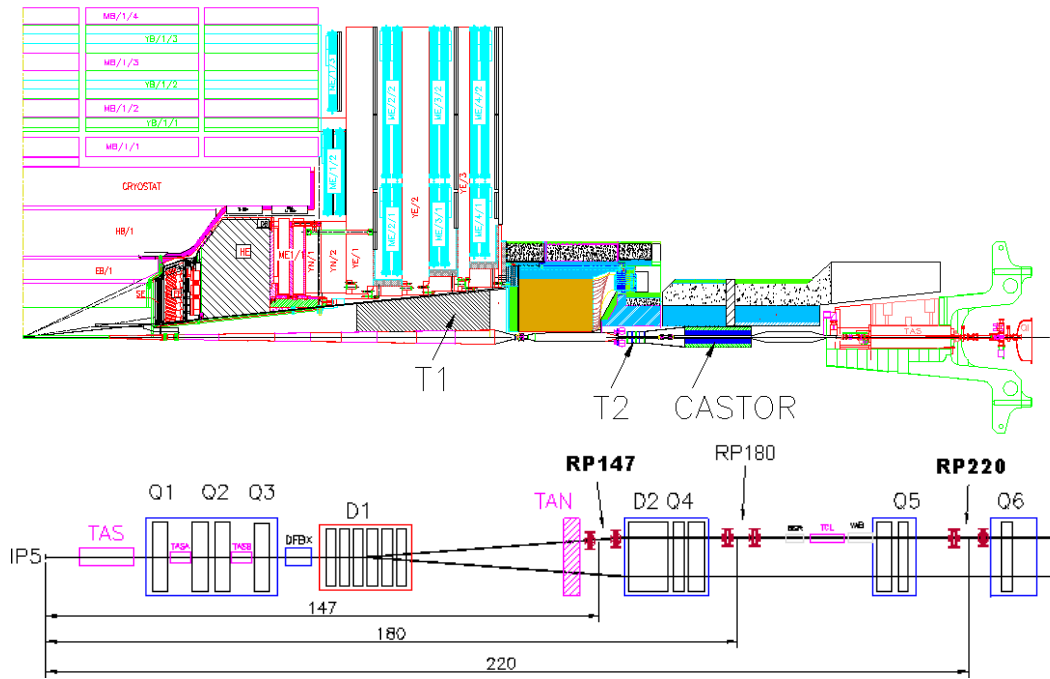


Fig. 1: Top: TOTEM forward telescopes T1 and T2 embedded in the CMS experiment together with the CMS forward calorimeter CASTOR. Bottom: LHC beam line on one side of interaction point IP5 and TOTEM Roman Pot stations at distances of about 147 m (RP147) and 220 m (RP220). RP180 at 180 m is another possible location but presently not equipped.



For the luminosity-independent total cross-section measurement, TOTEM has to reach the lowest possible  $|t|$  values in elastic  $pp$  scattering. Elastically scattered protons close to the beam can be detected downstream on either side of the IP if the displacement at the detector location is large enough and if the beam divergence at the IP is small compared to the scattering angle. To achieve these conditions special LHC optics with high beta value at the IP ( $\beta^*$ ) are required: the larger the  $\beta^*$ , the smaller the beam divergence ( $\sim 1/\sqrt{\beta^*}$ ) will be. Two optics are proposed: an ultimate one with  $\beta^* = 1540$  m and another one, possibly foreseen for 2009, with  $\beta^* = 90$  m. The latter uses the standard injection optics ( $\beta^* = 11$  m) and beam conditions typical for early LHC running: zero degree crossing-angle and consequently at most 156 bunches together with a low number of protons per bunch.

The versatile physics programme of TOTEM requires different running scenarios that have to be adapted to the LHC commissioning and operation in the first years. A flexible trigger can be provided by the two telescopes and the Roman Pot detectors. TOTEM will take data under all optics conditions, adjusting the trigger schemes to the luminosity. The DAQ will allow trigger rates up to a few kHz without involving a higher level trigger. The high- $\beta^*$  runs (Table 1) with 156 bunches, zero degree crossing-angle and maximum luminosity between  $10^{29}$  and  $10^{30} \text{ cm}^{-2}\text{s}^{-1}$ , will concentrate on low- $|t|$  elastic scattering, total cross-section, minimum bias physics and soft diffraction. A large fraction of forward protons will be detected even at the lowest  $\xi$  values. Low- $\beta^*$  runs (Table 1) with more bunches and higher luminosity ( $10^{32} - 10^{34} \text{ cm}^{-2}\text{s}^{-1}$ ) will be used for large- $|t|$  elastic scattering and diffractive studies with  $\xi > 0.02$ . Hard diffractive events come within reach. In addition, early low  $\beta^*$  runs will provide first opportunities for measurements of soft diffraction at LHC energies and for studies of forward charged multiplicity.

$\beta^*$ [m]	$k$	$N/10^{11}$	$\mathcal{L} [\text{cm}^{-2}\text{s}^{-1}]$	$ t $ -range [ $\text{GeV}^2$ ] @ $\xi = 0$	$\xi$ -range
1540	$43 \div 156$	$0.6 \div 1.15$	$10^{28} \div 2 \cdot 10^{29}$	$0.002 \div 1.5$	$< 0.2$
90	156	$0.1 \div 1.15$	$2 \cdot 10^{28} \div 3 \cdot 10^{30}$	$0.03 \div 10$	$< 0.2$
11	$43 \div 2808$	$0.1 \div 1.15$	$\sim 10^{30} \div 5 \cdot 10^{32}$	$0.6 \div 8$	$0.02 \div 0.2$
$0.5 \div 3$	$43 \div 2808$	$0.1 \div 1.15$	$\sim 10^{30} \div 10^{34}$	$2 \div 10$	$0.02 \div 0.2$

Table 1: Running scenarios at different LHC optics ( $k$ : number of bunches,  $N$ : number of particles per bunch,  $\mathcal{L}$ : estimated luminosity). The  $|t|$  ranges for elastically scattered protons correspond to the  $\geq 50\%$  combined RP147 and RP220 acceptance.

In the following, after a brief description of the TOTEM detectors and the principles of proton detection, the main features of the TOTEM physics programme will be given. This will be followed by a description of the early physics programme. Finally the novel idea of proton detection at IP3 will be presented. A detailed technical description of the TOTEM experiment can be found in Ref. [3].

## 2 TOTEM detectors and performance

### 2.1 Inelastic detectors

The measurement of the inelastic rate requires identification of all beam-beam events with detectors capable to trigger and reconstruct the interaction vertex. The main requirements of these

detectors are:

- to provide a fully inclusive trigger for minimum bias and diffractive events, with minimal losses at a level of a few percent of the inelastic rate;
- to enable the reconstruction of the primary vertex of an event, in order to disentangle beam-beam events from the background via a partial event reconstruction.

These requirements are fulfilled by the T1 telescope (centered at  $z = 9$  m), consisting of Cathode Strip Chambers (CSC) and T2 telescope (centered at  $z = 13.5$  m) exploiting Gas Electron Multipliers (GEM). The  $\eta$  coverage of T1 and T2 is  $3.1 \leq |\eta| \leq 4.7$  and  $5.3 \leq |\eta| \leq 6.5$ , respectively. Each T1 telescope arm consists of five planes made up of six trapezoidal formed CSC's with a spatial resolution of  $\sim 1$  mm. Each T2 telescope arm consists of 20 semicircular shaped triple-GEM detectors with a spatial resolution of  $\sim 100$   $\mu\text{m}$  in the radial direction and a inner radius that matches the beam-pipe. Ten aligned detectors mounted back-to-back are combined to form one T2 half arm on each side of the beam-pipe. For charged particles with momenta typical of particles produced within the detector acceptances in inelastic events, the particle  $\eta$  can be determined with a precision that increases with  $|\eta|$  and is between 0.02 and 0.06 in T1 and between 0.04 and 0.1 in T2. The corresponding azimuthal angle resolution for both detectors is  $\sim 1^\circ$ . The magnetic field at the detector locations is too weak to allow for a momentum determination for the charged particles. The primary vertex can be reconstructed with a precision of  $\sim 1.5$  cm in the radial direction and  $\sim 20$  cm in the beam direction in presence of the CMS magnetic field. Vertex resolutions one order of magnitude better can be achieved running with the CMS magnetic field switched off.

## 2.2 Proton detectors

To measure elastically and diffractively scattered protons with high acceptance requires the reconstruction of the protons tracks by "trigger capable" detectors moved as close as  $\sim 1$  mm from the center of the outgoing beam. This is obtained with two RP stations installed, symmetrically on both sides of IP5, at a distance of  $\sim 147$  m and  $\sim 220$  m from IP5. These positions are given by an interplay between the development of the special TOTEM optics and the constraints given by the LHC accelerator elements. Each RP station is composed of two units at a distance of several meters. This large lever arm allows local track reconstruction and a fast trigger selection based on the track angle. Each unit consists of three pots, two approaching the beam vertically from the top and the bottom and one horizontally to complete the acceptance for diffractively scattered protons, in particular for the low  $\beta^*$  optics. Furthermore, the overlap of the detector acceptance in the horizontal and vertical pots is vital for the relative alignment of the three pots via common particle tracks. The position of the pots with respect to the beam is given by Beam Position Monitors mechanically fixed to all three pots in one unit. Each pot contains a stack of 10 planes of silicon strip "edgeless" detectors with half with their strips oriented at an angle of  $+45^\circ$  and half at an angle of  $-45^\circ$  with respect to the edge facing the beam. These detectors, designed by TOTEM with the objective of reducing the insensitive area at the edge facing the beam to only a few tens of microns, have a spatial resolution of  $\sim 20$   $\mu\text{m}$ . High efficiency up to the physical detector border is essential in view of maximizing the elastic and diffractive proton acceptances. For the same reason, the pots' stainless steel bottom foil that faces the beam has been reduced to a thickness of 150  $\mu\text{m}$ .

### 2.3 Proton detection

The transverse displacement  $(x(s), y(s))$  of an elastically or diffractively scattered proton at a distance  $s$  from the IP is related to its origin  $(x^*, y^*, 0)$ , scattering angles  $\Theta_{x,y}^*$  and fractional momentum loss  $\xi$  ( $= \Delta p/p$ ) value at the IP via the optical functions  $L$  and  $v$ , and the dispersion  $D$ :

$$x(s) = v_x(s) \cdot x^* + L_x(s) \cdot \Theta_x^* + \xi \cdot D(s) \quad \text{and} \quad y(s) = v_y(s) \cdot y^* + L_y(s) \cdot \Theta_y^* \quad (1)$$

$L$ ,  $v$  and  $D$  determining the explicit path of the proton through the LHC elements, depend mainly on the position along the beam line i.e. on all the elements traversed before reaching that position and their settings, which is a optics dependent repetition, and hence the RP acceptance for leading protons will depend on the optics. The allowed minimum distance of a RP to the beam center on one hand being proportional to the beam size  $((10 - 15) \cdot \sigma_{x(y)}(s))$  as well as constraints imposed by the beam-pipe or beam screen size on the other hand will determine the proton acceptance of a RP station.

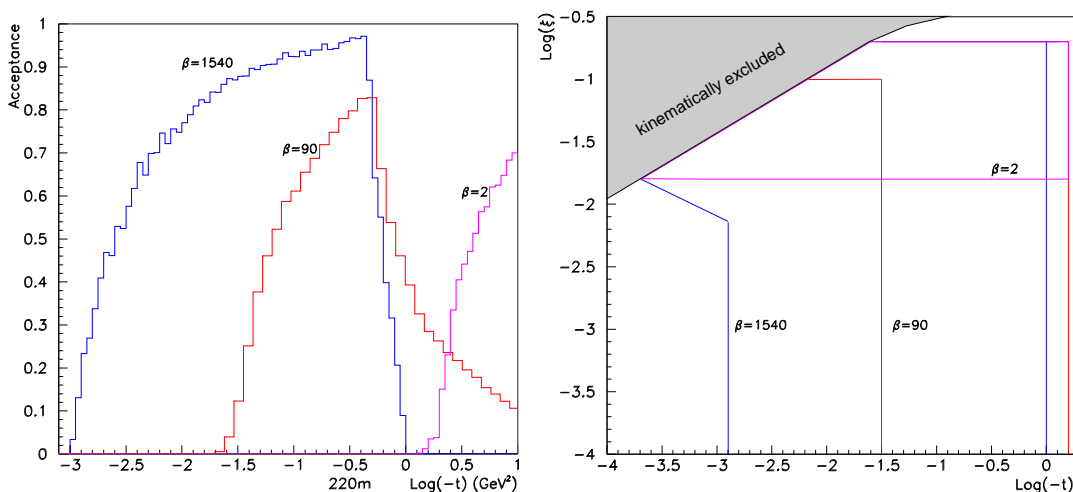


Fig. 2: Left: RP220  $\log_{10} |t|$  acceptance for elastically scattered protons at different optics configurations. Right: contour lines of 10 % acceptance for RP220 in  $\log_{10} |t|$  and  $\log_{10} \xi$  for diffractively scattered protons at different optics configurations.

The complementarity of the acceptances for different optics configurations is shown in Figure 2. The TOTEM-specific optics with  $\beta^* = 1540$  m (blue graphs in Figure 2) is particularly optimized for accepting protons down to very low  $|t|$ -values. For the diffractive case all kinematically allowed values of  $\xi$  are accepted. With the  $\beta^* = 90$  m optics (red graphs in Figure 2), diffractive scattered protons are still accepted independently of their  $\xi$ -value, but the  $t$ -acceptance is reduced compared to  $\beta^* = 1540$  m optics. With the standard high luminosity optics ( $\beta^* = 0.5 \div 3$  m, magenta graphs in Figure 2) elastically scattered protons can only be detected at very large  $|t|$  and diffractively scattered protons are accepted independently of their  $t$  value in the horizontal pots for  $\xi$  values above 2 %.

	$\beta^* = 0.5 - 3 \text{ m}$	$\beta^* = 90 \text{ m}$	$\beta^* = 1540 \text{ m}$
$\sigma(\xi)$	$0.001 \div 0.006$	$\sim 0.0015$ (w CMS vtx) $\sim 0.006$ (w/o CMS vtx)	$0.002 \div 0.006^{\ddagger}$
$\sigma(t) [\text{GeV}^2]$	$(0.3 \div 0.45) \sqrt{ t }$	$\sigma(t_y) \sim 0.04 \sqrt{ t_y }$	$\sim 0.005 \sqrt{ t }$
$\sigma(M) [\text{GeV}]$ in central diffraction	$(0.02 \div 0.05) M$	$< 18$ for $R > 0.6$ (w CMS vtx) $< 80$ for $R > 0.6$ (w/o CMS vtx)	$\sim 20 M^b$ $^{\ddagger}$ $b = 0.17$ for $R = 0.5 \div 1$

Table 2: Summary of resolutions for the RP220 proton reconstruction at different optics configurations. “w CMS vtx” and “w/o CMS vtx” refers to whether vertex position information from CMS is available or not (relevant for  $\beta^* = 90 \text{ m}$ ),  $R = \xi_{\text{lower}}/\xi_{\text{higher}}$  to the momentum loss symmetry between the two outgoing protons and “ $\ddagger$ ” to reconstruction using also RP147.

The reconstruction of the proton kinematics is optics dependent. The main resolutions are given in Table 2. More details can be found in Ref. [4]. A feature of the  $\beta^* = 90 \text{ m}$  optics is that  $L_y \gg L_x$  and hence  $t_y$  is determined with almost an order of magnitude better precision than  $t_x$ . For central diffraction, the diffractive mass can be reconstructed from the  $\xi$  measurements of the two protons according to

$$M^2 = \xi_1 \xi_2 s. \quad (2)$$

The mass resolution for central diffractive events at different optics is also quoted in Table 2. If the scattering vertex is determined with high precision ( $\sim 30 \mu\text{m}$ ) with the CMS tracking detectors during common data taking, a substantial improvement in the  $\xi$  and  $M$  measurement is achieved at  $\beta^* = 90 \text{ m}$ .

### 3 TOTEM physics programme

Given its unique coverage for charged particles at high rapidities, TOTEM is ideal for studies of forward phenomena, including elastic and diffractive scattering. Its main physics goals, precise measurements of the total cross-section and of elastic scattering over a large range in  $|t|$ , are of primary importance for distinguishing between different models of soft  $pp$  interactions. Furthermore, as energy flow and particle multiplicity of inelastic events peak in the forward region, the large rapidity coverage and proton detection on both sides allow the study of a wide range of processes in inelastic and diffractive interactions.

#### 3.1 Elastic scattering and diffraction

Much of the interest in large-impact-parameter collisions centers on elastic scattering and soft inelastic diffraction. The differential cross-section of elastic  $pp$  interactions at  $14 \text{ TeV}$ , as predicted by different models [5–8], is given in Figure 3 (left). Increasing  $|t|$  means looking deeper into the proton at smaller distances. Several  $|t|$ -regions with different behavior (at  $\sqrt{s} = 14 \text{ TeV}$ ) can be distinguished:

- $|t| < 6.5 \cdot 10^{-4} \text{ GeV}^2$ : The Coulomb region dominated by photon exchange:  $d\sigma/dt \sim 1/t^2$ .
- $10^{-3} \text{ GeV}^2 < |t| < 0.5 \text{ GeV}^2$ : The nuclear region, described in a simplified way by “single-Pomeron exchange”:  $d\sigma/dt \sim e^{-Bt}$ , is crucial for the extrapolation of the differ-

ential counting-rate  $dN_{el}/dt$  to  $t = 0$ , needed for the luminosity-independent total cross-section measurement.

- $0.5 \text{ GeV}^2 < |t| < 1 \text{ GeV}^2$ : A region exhibiting the diffractive structure of the proton.
- $|t| > 1 \text{ GeV}^2$ : Domain of central elastic collisions, described by perturbative QCD, e.g. via triple-gluon exchange with a predicted cross-section  $\propto |t|^{-8}$ . The model dependence of the predictions being very pronounced in this region, measurements will test the validity of different models.

TOTEM will cover the full elastic  $|t|$ -range from 0.002 up to  $10 \text{ GeV}^2$  by combining data from runs at several optics configurations as indicated in Figure 3 (left). With typical expected LHC machine cycle times of  $10^4 - 10^5 \text{ s}$ , enough statistics at low  $|t|$  values can be accumulated in one run. This statistics is also sufficient for track-based alignment of the RP detectors. The overlap between the acceptances of the different optics configurations will allow for cross-checks of the measurements.

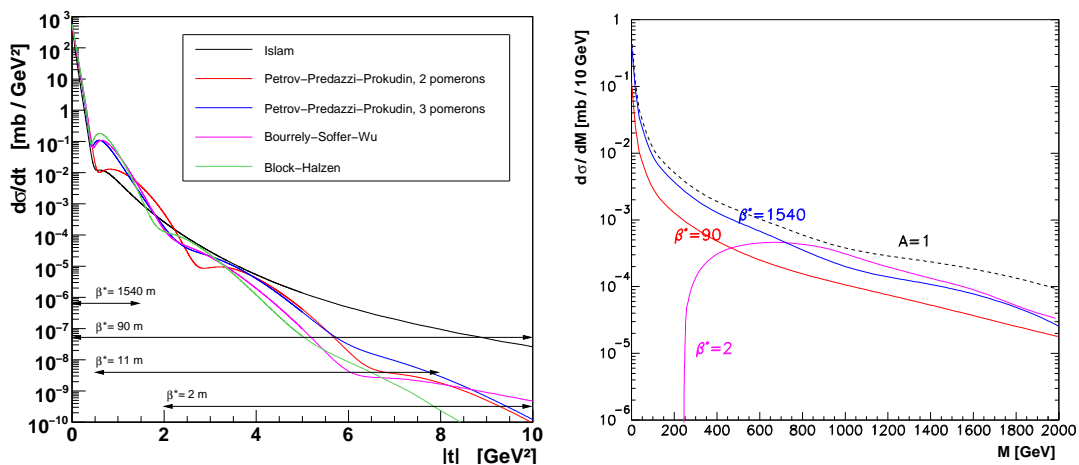


Fig. 3: Left: differential cross-section of elastic scattering at  $\sqrt{s} = 14 \text{ TeV}$  as predicted by various models together with the  $t$ -acceptance ranges of different optics configurations. Right: predicted differential cross-section of central diffraction at  $\sqrt{s} = 14 \text{ TeV}$  with (solid) and without (dashed) taking the proton acceptance into account for different optics configurations.

Diffractive scattering comprises single diffraction, double diffraction, central diffraction (a.k.a. “double Pomeron exchange”), and higher order (“multi Pomeron”) processes, shown in Figure 4 with their cross-sections as measured at Tevatron [9–12] and as predicted for LHC [5–8, 13–15]. Together with elastic scattering these processes represent about 50 % of the total cross-section. Many details of these processes with close ties to proton structure and low-energy QCD are still poorly understood. Majority of diffractive events (Figure 4) exhibits intact (“leading”) protons in the final state, characterized by their  $t$  and  $\xi$ . For large  $\beta^*$  (see Figure 2, right) most of these protons can be detected in the RP detectors. Already at an early stage, TOTEM will be able to measure  $\xi$ -,  $t$ - and mass-distributions in soft central and single diffractive events. The full structure of diffractive events with one or more sizeable rapidity gap in the particle distribution

(Figure 4) will be optimally accessible when the detectors of CMS and TOTEM will be combined for common data taking with an unprecedented rapidity coverage, as discussed in [2].

Figure 3 (right) shows the predicted central diffractive mass distribution [15] together with the acceptance corrected distributions for three different optics. With high and intermediate  $\beta^*$  optics, all diffractive mass values are observable. For low  $\beta^*$  optics on the other hand, the acceptance starts at  $\sim 250$  GeV but higher statistics for high masses will be collected due to the larger luminosity. By combining data from runs at low  $\beta^*$  with data from high or intermediate  $\beta^*$  runs, the differential cross-section as function of the central diffractive mass can be measured with good precision over the full mass range.

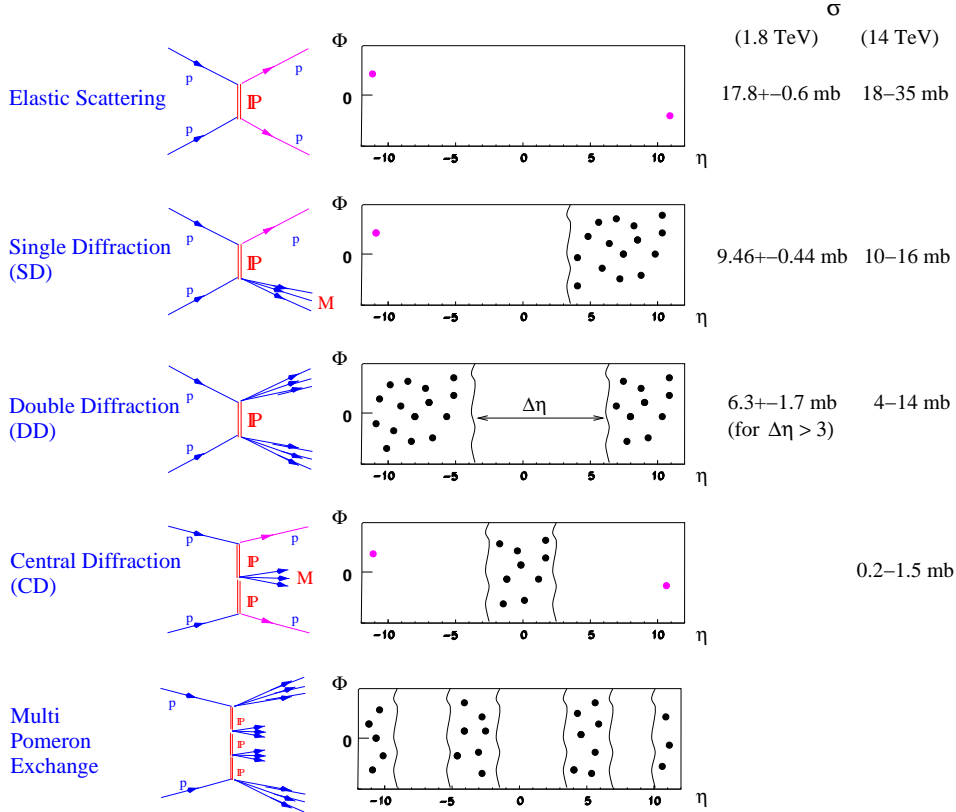


Fig. 4: Different classes of diffractive processes and their cross-sections as measured at Tevatron and as estimated for the LHC.

### 3.2 Total $pp$ cross-section

The optical theorem relates the total  $pp$  cross-section  $\sigma_{tot}$  and the luminosity  $\mathcal{L}$  to the differential elastic counting-rate  $dN_{el}/dt$  at  $t = 0$  and the total elastic  $N_{el}$  and inelastic  $N_{inel}$  rates as:

$$\sigma_{tot} = \frac{16\pi}{1 + \rho^2} \cdot \frac{dN_{el}/dt|_{t=0}}{N_{el} + N_{inel}} \quad \text{and} \quad \mathcal{L} = \frac{1 + \rho^2}{16\pi} \cdot \frac{(N_{el} + N_{inel})^2}{dN_{el}/dt|_{t=0}}. \quad (3)$$

The parameter  $\rho = \mathcal{R}[f_{el}(0)]/\mathcal{I}[f_{el}(0)]$ , where  $f_{el}(0)$  is the forward nuclear elastic amplitude, has to be taken from theoretical predictions. Since  $\rho \sim 0.14$  enters only as a  $1 + \rho^2$  term, its impact is small. The extrapolation of existing  $\sigma_{tot}$  measurements to LHC energies leaves a wide range for the expected value of  $\sigma_{tot}$  at LHC, typically between 85 and 120 mb, depending on the model used for the extrapolation. TOTEM aims at a 1 %  $\sigma_{tot}$  measurement. Hence the quantities to be measured are the following:

- the inelastic rate  $N_{inel}$  consisting of both non-diffractive minimum bias events and diffractive events, which can almost completely be measured by T1, T2 and the RP detectors;
- the total nuclear elastic rate  $N_{el}$  measured exclusively by the RP system;
- $dN_{el}/dt|_{t=0}$ : the nuclear part of the elastic cross-section extrapolated to  $t = 0$ .

A summary of the uncertainties on  $\sigma_{tot}$  at different high  $\beta^*$  optics configurations is given in Table 3. Here only the main uncertainties are described. The extrapolation procedure and uncertainty estimates are described in more detailed in Ref. [3]. At  $\beta^* = 90$  m, protons with  $|t| > 0.03$  GeV<sup>2</sup> are observed, whereas  $|t|_{min} = 10^{-3}$  GeV<sup>2</sup> at  $\beta^* = 1540$  m, leading to a significantly smaller uncertainty contribution due to  $N_{el}$ , 0.1 % compared to 2 %, and to the extrapolation of  $dN_{el}/dt$  to  $t = 0$ , 0.2% compared to 4%.

Uncertainty	$\beta^* = 90$ m	$\beta^* = 1540$ m
Extrapolation of $dN_{el}/dt$ to $t = 0$	$\pm 4$ %	$\pm 0.2$ %
Elastic rate $N_{el}$	$\pm 2$ %	$\pm 0.1$ %
Inelastic rate $N_{inel}$	$\pm 1$ %	$\pm 0.8$ %
$\rho$ parameter	$\pm 1.2$ %	$\pm 1.2$ %
Total $\sigma_{tot}$	$\pm 4\text{--}5$ %	$\pm 1\text{--}2$ %

Table 3: Relative uncertainty on the total  $pp$  cross-section  $\sigma_{tot}$  measurement estimated at different high  $\beta^*$  optics configurations. Note that the total uncertainty takes into account the correlations between the uncertainties, notably the strong correlation between the extrapolation of the differential elastic counting-rate  $dN_{el}/dt$  to  $t = 0$  and the elastic rate  $N_{el}$ .

The largest contribution to the uncertainty on  $\sigma_{tot}$  at  $\beta^* = 90$  m comes from the extrapolation of  $dN_{el}/dt$  to  $t = 0$ ; mainly due to systematics in the  $t$ -measurement from uncertainties in  $L$  and  $v$  (see Eq.1). This contribution will be reduced to 0.1 % at  $\beta^* = 1540$  m requiring, however, an improved knowledge of  $L$  and  $v$  and a RP alignment precision of better than 50  $\mu\text{m}$ . The dominating uncertainty, 0.2 %, will then be due to the model-dependent extrapolation procedure. For  $\beta^* = 1540$  m, the largest contribution to the  $\sigma_{tot}$  uncertainty will most likely come from  $N_{inel}$ , mainly from trigger losses in single and double diffractive events. The lost events, corresponding to  $\sim 3$  mb, have very low diffractive mass  $M$  (below  $\sim 10$  GeV/c<sup>2</sup>). As a consequence, all particles have pseudo-rapidities beyond the T2 acceptance and hence escape detection of the single arm trigger. To obtain the total inelastic rate, the fraction of events lost due to the incomplete angular coverage is estimated by extrapolating the reconstructed  $1/M^2$  distribution. The uncertainty on  $N_{inel}$  after corrections is estimated to be 0.8 and 1 % for  $\beta^* = 1540$  and 90 m optics, respectively. The uncertainty on the  $\rho$  parameter as estimated from lower energy measurement [16] gives a  $\sigma_{tot}$  uncertainty of 1.3 %. A reduction is expected when  $\rho$

is measured at the LHC via the interference between Coulomb and nuclear contributions to the elastic scattering cross-section [17].

At an early stage in 2009 with non-optimal beams and  $\beta^* = 90$  m, TOTEM will measure  $\sigma_{tot}(\mathcal{L})$  with a 4–5 % (7 %) relative precision. After having understood the initial measurements and with improved beams at  $\beta^* = 1540$  m, a final relative precision on  $\sigma_{tot}(\mathcal{L})$  of 1 % (2%) should be achievable.

#### 4 Early physics with TOTEM

The early runs at the LHC start will be characterized by low  $\beta^*$  beams with a reduced number of bunches and a lower number of protons per bunch. Under these conditions diffractive protons in the  $\xi$  range of 0.02 - 0.2 will be within the acceptance of RP220 giving TOTEM ample opportunities to make first soft diffractive studies. The early physics programme of TOTEM in stand-alone runs will concentrate on measurements of individual cross-sections and event topologies for the following processes:

- central diffractive events with diffractive masses between  $\sim 250$  GeV and  $\sim 2.8$  TeV;
- single diffractive events with diffractive masses between  $\sim 2$  TeV and  $\sim 6$  TeV;
- elastic scattering events with  $|t|$  values between  $\sim 2$  GeV<sup>2</sup> and  $\sim 10$  GeV<sup>2</sup>;
- forward charged particle multiplicity of inelastic  $pp$  events in the  $3.1 \leq |\eta| \leq 6.5$  region.

The cross-sections for the above processes are large ( $\gtrsim 5 \mu\text{b}$ ) even if the TOTEM acceptance is included, with the exception of high- $|t|$  elastic scattering. As an example, the BSW model [6] predicts an integrated elastic cross-section of  $\sim 60$  nb for  $|t| > 2$  GeV<sup>2</sup>. This prediction, together with the predictions of Ref. [13–15], imply that for an integrated luminosity of  $\sim 10 \text{ pb}^{-1}$ , TOTEM would collect more than  $10^7$  central and  $10^8$  single diffractive events, together with  $\sim 10^5$  high- $|t|$  elastic events allowing a first test of the validity of different models as discussed in section 3.1. The main background to diffractive events at low  $\beta^*$  is either due to two overlapping  $pp$  collisions, like e.g. two overlapping single diffractive events for central diffraction, or one  $pp$  collision overlapping with beam induced proton background. Hence the event purity will depend strongly on the average number of  $pp$  collisions per bunch crossing, which should be significantly smaller than one. The beam induced proton background not due to  $pp$  collisions in IP5 will be studied in bunch crossings where normal bunches meet "empty" bunches. The interest in the forward charged particle multiplicity is two-fold: first as a basic measurement of  $pp$  interaction at LHC energies and secondly as valuable input to the modeling of very high energy cosmic rays [2].

The installation schedule of the TOTEM detectors depends crucially on the CMS installation schedule as well as on the LHC commissioning schedule. The full experiment is planned to be installed for the 2009 LHC running. The focus in the early LHC runs will be to understand the performance of the detectors and other vital parts like trigger and data acquisition, especially the approach of the RP detectors to the beam. The feasibility and time scale of the early physics programme will critically depend on the LHC performance in terms of luminosity and beam induced background in the TOTEM detectors.



## 5 Diffractive proton detection at IP3

It has been suggested that the central exclusive diffractive process

$$pp \rightarrow p + X + p, \quad (4)$$

where a "+" denotes a rapidity gap, could complement the standard methods of searching and studying new particles ("X") at LHC, see e.g. Ref. [18]. The main advantage is that the mass of the centrally produced particle  $X$  can be reconstructed from the measured  $\xi$  values of the outgoing protons as shown in Eq. 2. Provided that the two  $\xi$  values can be determined with sufficient precision, peaks corresponding to particle resonances may appear in the reconstructed diffractive mass distribution independent of the particles' decay modes. These measurements should be performed with high luminosity optics since the cross-sections are expected to be small. The work presented here aims to find the best detector locations at LHC in terms of  $\xi$  acceptance and resolution for the proton measurement in central diffractive events.

The diffractive proton acceptance of near beam detectors is determined by the ratio  $D_x/\sigma_x$  between horizontal dispersion and beam width. With larger  $D_x$  the protons are deflected further away from the beam center, while the closest safe approach of a detector to the beam is given by a multiple – typically 10 to 15 – of  $\sigma_x$ . By construction, the LHC region where  $D_x$  and  $D_x/\sigma_x$  are maximized and hence the sensitivity to particle  $X$ , is the momentum cleaning insertion in IP3, where off-momentum beam protons are intercepted. The idea is to install proton detectors pairs with a lever arm of several tens of meters close to IP3 to detect diffractive protons in both beams just before they are absorbed by the momentum cleaning collimators. In addition to promising perspectives in diffraction, the placement of detectors in front of the collimators has advantages for accelerator diagnostics and protection. The technical aspects of placing proton detectors at IP3 is being worked out together with the LHC collimation group.

The proton acceptance and resolution of an experiment with detectors at the TOTEM RP220 location and at IP3 have been studied [19] by fully tracking the protons along the LHC ring with the MAD-X [20] program using standard LHC high luminosity  $\beta^* = 0.55$  optics. The detector acceptance at IP3 for protons originating from diffractive scattering in IP5 is  $0.0016 \leq \xi \leq 0.004$  and  $0.0016 \leq \xi \leq 0.01$  for protons turning clockwise ("B1") and anticlockwise ("B2") in the LHC, respectively. This complements well the  $0.02 \leq \xi \leq 0.20$  acceptance of RP220 for both beams. The IP3 acceptance for B1 protons is reduced since these protons have to pass through the aperture limiting betatron cleaning insertion at IP7. In case of central diffraction [15], this gives access to diffractive masses from 25 GeV to 2.8 TeV as shown in Fig. 5 (left). A  $\xi$  resolution  $\leq 10^{-4}$  for protons detected at IP3 is obtained in the study implying that the resolution will be limited by the beam energy spread of  $1.1 \cdot 10^{-4}$ . Combined with protons detected at RP220, this leads to a relative mass resolution ranging between 1 and 5 % for central diffractive events over the whole mass range as shown in Fig. 5 (right). The mass resolution depends on the ratio  $\xi_1/\xi_2$ , where  $\xi_1$  and  $\xi_2$  are the  $\xi$  value of the clockwise and anticlockwise turning proton, respectively.

The protons detectors at IP3 would in fact see diffractive protons with similar acceptance from all LHC interaction points (IP) and could by measuring the difference of the proton arrival times determine at which IP the event occurred. This way the low mass central diffractive spectrum could be determined independently for each IP and be used as means of an inter-experimental luminosity calibration.

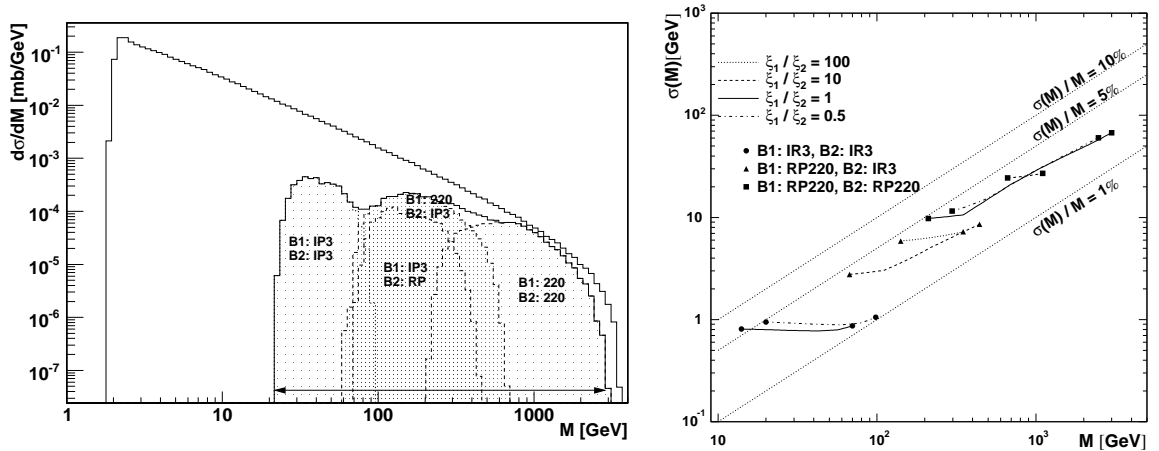


Fig. 5: Left: predicted diffractive mass distribution for central diffractive events with events indicated that have both protons within the acceptance of different combinations of the IP3 and RP220 detectors. Right: mass resolution for central diffractive events for some  $\xi_1/\xi_2$  ratios. B1 and B2 refers to protons turning clockwise and anticlockwise, respectively, in the LHC.

## 6 Summary

The TOTEM physics program aims at a deeper understanding of the proton structure by measuring the total and elastic  $pp$  cross sections and by studying a comprehensive menu of diffractive processes. TOTEM will run under all LHC beam conditions to maximize the coverage of the studied processes. Special high  $\beta^*$  runs are needed for the total  $pp$  cross section measurement with the luminosity-independent method and for soft diffraction with large forward proton acceptances. At an early stage with non-optimal beams and an intermediate  $\beta^*$ , TOTEM will measure  $\sigma_{tot}$  with a 4–5 % precision. With improved understanding of the beams and  $\beta^* = 1540$  m, a precision on  $\sigma_{tot}$  of 1% should be achievable. The measurement of elastic scattering in the range  $10^{-3} < |t| < 10 \text{ GeV}^2$  will allow to distinguish among a wide range of predictions according to current theoretical models. Early low  $\beta^*$  runs will provide first opportunities for measurements of soft diffraction for masses above  $\sim 250$  GeV and  $\sim 2$  TeV in central and single diffractive events, respectively, as well as studies of the forward charged multiplicity in inelastic  $pp$  events. Having proton detectors at IP3 would highly extend the diffractive mass acceptance of TOTEM for high luminosity runs giving e.g. a continuous mass acceptance from 25 GeV to 2.8 TeV for central diffractive events. Finally, hard diffraction as well as many forward physics subject will be studied in collaboration with CMS taking advantage of the unprecedented rapidity coverage for charged and neutral particles.

## References

- [1] TOTEM Coll., V. Berardi et al.: TOTEM: Technical Design Report CERN-LHCC-2004-002; addendum: CERN-LHCC-2004-020 (2004).

- [2] CMS and TOTEM diffractive and forward working group: Prospects for Diffractive and Forward Physics at the LHC, CERN-LHCC-**2006-039**, CMS Note-**2007/002**, TOTEM Note **06-5** (2006).
- [3] TOTEM Coll., G. Anelli et al.: The TOTEM experiment at the CERN Large Hadron Collider, JINST **3**, S08007 (2008).
- [4] H. Niewiadomski: Reconstruction of proton tracks in the TOTEM Roman Pot detectors at the LHC, PhD Thesis, University of Manchester, U.K. (2008).
- [5] M. M. Islam, R. J. Luddy and A. V. Prokudin, Int. J. Mod. Phys. **A 21**, S08007 (2006).
- [6] C. Bourrely, J. Soffer, and T. T. Wu, Eur. Phys. J. **C 28**, 97 (2003).
- [7] V. A. Petrov, E. Predazzi and A. Prokudin, Eur. Phys. J. **C 28**, 525 (2003).
- [8] M. M. Block, E. M. Gregores, F. Halzen and G. Pancheri, Phys. Rev. **D 60**, 054024 (1999).
- [9] CDF Coll., F. Abe et al., Phys. Rev. **D 50**, 5550 (1994).
- [10] E811 Coll., C. Avila et al., Phys. Lett. **B 445**, 419 (1999).
- [11] CDF Coll., F. Abe et al., Phys. Rev. **D 50**, 5535 (1994).
- [12] CDF Coll., T. Affolder et al., Phys. Rev. Lett. **87**, 141802 (2001).
- [13] M.G. Ryskin, A.D. Martin and V.A. Khoze, Eur. Phys. J. **C54**, 199 (2008).
- [14] E. Gotsman, E. Levin, U. Maor and J.S. Miller, TAUP-2878-08; arXiv:0805.2799 [hep-ph] (2008).
- [15] R. Engel: PHOJET manual (program version 1.05c, June 1996), available from: <http://www-ik.fzk.de/~engel/phojet.html> (LHC predictions are based on program version 1.12).
- [16] COMPETE Coll., J.R. Cudell et al., Phys. Rev. Lett. **89**, 201801 (2002).
- [17] TOTEM Coll., G. Anelli et al.: TOTEM physics, Proceedings of 17th Rencontre de Blois: 11th International Conference on Elastic and Diffractive Scattering, Château de Blois, France (2005).
- [18] V.A. Khoze, A.D. Martin and M.G. Ryskin, Eur. Phys. J. **C23**, 311 (2002).
- [19] K. Eggert on behalf of TOTEM Coll.: TOTEM, a different LHC experiment, CERN seminar February 2008, <http://indico.cern.ch/conferenceDisplay.py?confId=29356>; paper in preparation.
- [20] The MAD-X program, Methodical Accelerator Design, <http://www.cern.ch/mad>.

# The ALFA Detector and Physics Program

*K. Hiller<sup>a</sup>, H. Stenzel<sup>b</sup>*

<sup>a</sup> DESY Zeuthen, Platanenallee 6, D-15738 Zeuthen, Germany

<sup>b</sup> University of Giessen, II. Physikalisches Institut, Heinrich-Buff Ring 16, D-35444 Giessen, Germany

## Abstract

The ALFA detector is dedicated to obtaining a precise absolute calibration for luminosity measurements at the ATLAS experiment. Fiber trackers are installed in Roman Pots at a distance of 240m from the interaction point on both sides of the detector. In special runs with high  $\beta^*$  optics the pots approach the beam to distances of order a millimeter, allowing elastically scattered protons to be detected at extremely small angles. Extracting the differential cross section in the corresponding Coulomb-Nuclear interference kinematic region as a function of the squared four-momentum transfer  $t$  leads to luminosity measurements with a precision of 3%.

## 1 Introduction

The luminosity relates event rates to cross sections - the main observable quantity of all accelerator-based experiments. Its value is defined by the machine parameters: beam currents, transverse beam widths and revolution frequency. A good measurement of the luminosity is required to ensure precise cross section measurements and to give fast feedback for beam tuning and monitoring for optimal operation of the LHC.

ATLAS follows a number of different approaches to measure the luminosity [1]. The first method is based on direct calculation based on the knowledge of LHC machine parameters. A precision of around 20% - 30% is envisaged at the LHC startup. After some years of dedicated machine studies, 5% accuracy seems to be the end point of this method. The second type of luminosity measurement involves counting the rate of a process with a well-known cross-section. For example, the production of lepton pairs via the QED two-photon process can be precisely calculated and used as in luminosity measurements. However the QED cross sections are small and resulting event rates are at the statistical limit, especially in the low luminosity phase. The QCD production of W and Z bosons is a more promising process with a large cross section and a clean signature. It is one of the best known QCD cross sections and the main uncertainty comes from the PDFs. Including the experimental uncertainties a total luminosity error of 10% seems feasible. The PDFs may become more constrained when LHC data are available and the luminosity error from this method might reach 5% after some years of LHC running.

The third method is related to the elastic proton scattering process. This rate is linked to the total interaction rate through the optical theorem and will provide several additional options to determine the luminosity. The standard approach combines the total interaction rate  $R_{tot}$  and

the forward elastic rate  $R_{el}(t = 0)$  via the optical theorem and determines the luminosity as

$$L = \frac{1}{16\pi} \frac{R_{tot}^2(1 + \rho^2)}{dR_{el}/dt(t = 0)} .$$

Here  $\rho$  is the ratio of the real to the imaginary part of the elastic forward scattering amplitude, which lies in the range 0.13-0.14 at LHC energies [2]. Small-angle elastic scattering has traditionally been used to get a handle on the luminosity calibration at hadron colliders via equation 1. This generally requires a precise knowledge of the inelastic rate over the full rapidity range, in contrast to the limited rapidity coverage of real detectors such as ATLAS. However, if very small scattering angles, corresponding to very small momentum transfers  $t$ , can be covered, the cross section becomes sensitive to the electromagnetic scattering. Via the precisely known Coulomb interaction, a calibration can then be performed without measurement of the inelastic rate. This option is pursued by the ATLAS collaboration, for which the ALFA detector [3] is currently under construction. In order to reach the Coulomb-Nuclear interference region where the electromagnetic and strong interaction amplitudes are of similar size, scattering angles of about  $3.5 \mu\text{rad}$  must be covered, corresponding to  $|t| = 0.00065 \text{ GeV}^2$ . To reach the Coulomb region is a very challenging task, since the tracking detectors have to be moved to a very close distance of about 1.5 mm from the circulating beams. If this can be managed, a luminosity error of 3% seems to be feasible.

Some details of tracking detectors in the Roman Pots, the Monte Carlo estimates for the luminosity determination and the present status of the main ALFA components are described in the next chapters. This can only be achieved with special beam optics with a very high  $\beta^* = 2625 \text{ m}$  yielding a parallel-to-point focusing and a low normalised emittance  $\epsilon_N = 1 \mu\text{rad m}$ . In addition, the detector has to be operated very close to the beam at a distance of about 1.5 mm, corresponding to  $12 \sigma$  of the beam width. Dedicated runs are foreseen at low luminosity with these special beam conditions for measurement with ALFA, which can accumulate in 100 hours of beam time sufficient statistics to achieve a luminosity calibration with an accuracy of 3%, including systematic uncertainties [6].

## 2 The ALFA detector

Roman Pot stations equipped with two vertically movable Roman Pots housing the detectors will be installed in the LHC on both sides of the interaction point at a distance of 240 m. There will be two stations separated by 4 m on each side, thus in total 8 pots will be instrumented with ALFA detectors. Figure 1 shows an ALFA Roman Pot station in relation to the beampipe. Each unit consists of the Pots housing the detectors and the support and moving mechanics such as bellows, roller screws, motor drives, positioning sensors etc. To minimize the amount of material in front of the detectors the pots have thin  $80 \mu\text{m}$  windows. The interior of the Pot will be in a secondary vacuum of about 1 mbar to avoid deformations induced by the LHC primary vacuum. The 4m separation of the pairs of pots on either side of the interaction point ensures precise tracking. The positioning precision due to the Pot moving system is expected to be  $10 \mu\text{m}$ . The position of the Pot in respect to the circulating beam will be determined by LVDTs with a precision of  $\pm 20 \mu\text{m}$ . The Roman Pots are considered as machine elements and their movement is included in the LHC collimator control system.

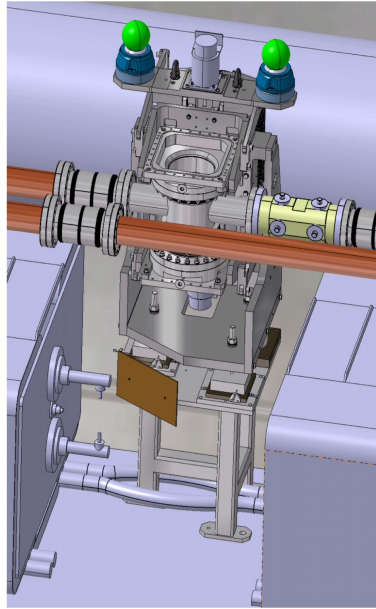


Fig. 1: Schematic drawing of the ALFA Roman Pot station.

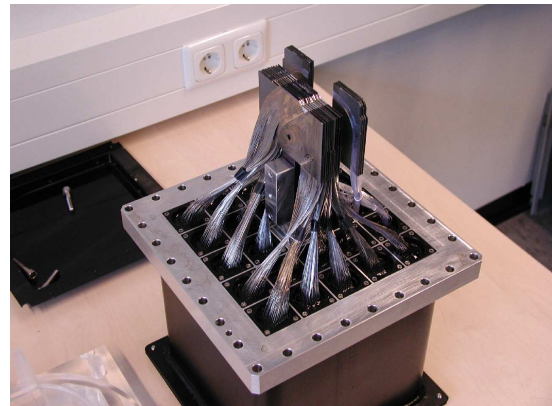
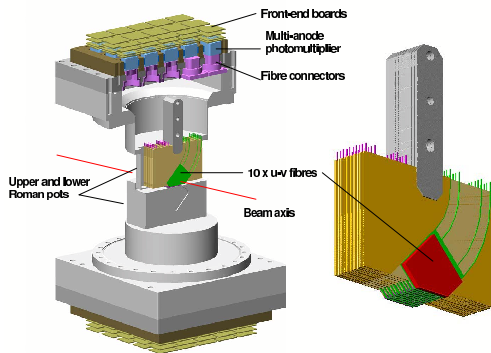


Fig. 2: Conceptual design of the ALFA tracker with multi-layer fiber detectors inserted and a photograph of a full-size prototype.

The design of the ALFA tracker is shown in Fig. 2. The tracking detectors are multi-layer scintillating fiber structures as illustrated in fig. 2. Layers of two times 64 KURARAY SCSF-78 single cladding fibers of square  $0.5 \times 0.5 \text{ mm}^2$  cross section are glued in stereo geometry on a Titanium substrate. Ten of such substrates, staggered by  $71 \mu\text{m}$ , are precisely assembled on a support structure. The ultimate resolution of such a detector arrangement is  $14 \mu\text{m}$  and in previous test beam measurements values of  $25 \mu\text{m}$  have been achieved [4, 5]. The spacing of the planes in beam direction is  $2.5 \text{ mm}$  results in an inclination of the staggered fibers by  $28 \text{ mrad}$  relative to the beam axis. Hence not to benefit from the staggering the detector axis should be

aligned with the beam axis with an precision around 3mrad.

As visible in fig. 2 the most fiber ends are cut at the lower edge under  $45^\circ$ . Apart from these cuts the fibers are aluminized to increase the light yield. For fibers with  $90^\circ$  ends the gain is about 75%, while for  $45^\circ$  ends about 50% of the light undergoes a reflection at the uncoated edge. The fibers are routed over 25cm distance to a connector flange. All 64 fibers of a plane are grouped into a  $8 \times 8$  matrix to be coupled to the photo-cathode of the Multi Anode Photo-Multiplier Tube (MAPMT) Hamamatsu H7546B. This device has a gain around  $10^6$  at the maximum voltage of 1000V. The cross talk between adjacent channels is at the level of 2-3 %.

To ensure an exact positioning of the fiber detectors in respect to the LHC beam, which can vary from fill to fill, each Roman Pot is equipped with a pair of overlap detectors. These detectors move with the Pots and measure the relative vertical positions of the upper and lower tracking detectors. The measurement principle is the common tracking of halo particles in both overlap detectors. These detectors consist of 3 planes of 30 horizontally arranged fibers staggered by  $166\mu\text{m}$  to each other. The achievable precision depends mainly on the statistics of accumulated halo tracks. A positioning precision of  $10\mu\text{m}$  of the upper and lower detectors are needed to keep the contribution to the luminosity error below 2%. All 180 fibers of the overlap detectors in a Pot are read out by 3 MAPMTs H7546B.

Both main and overlap detectors are equipped with corresponding trigger counters which cover the active area. For the main detectors two trigger tiles of fast plastic scintillator BICRON BC-408 are used in coincidence. The overlap detectors are covered by a single trigger tile. The light signals from the scintillators are guided by bundles of clear 0.5mm round double cladding KURARAY fibers to the photo-multipliers. To amplify the trigger signals 4 single channels photo-multipliers R7401P with Bi-alkali photo-cathode or the new type R9880U with Super-Bi-alkali photo-cathode and enhanced quantum efficiency around 35% are foreseen.

A proton traversing a 0.5 mm scintillating fiber gives on average a light signal of 4 photo-electrons. The MAPMT H7546B with a typical gain of  $0.5 - 1.0 \times 10^6$  leading therefore to signals charge of 0.3-0.6 pC at the amplifier input. The readout electronics is a stack of printed circuit boards, named PMF, located on top of each MAPMT. The MAPMT signals are fed into the MAROC2 readout chip, which performs amplification and shaping. The signals are compared to a threshold and the resulting digital data serially transmitted to the motherboard. The motherboard serialize the data from 23 PMF units and send them via an optical link to the central ATLAS data acquisition system.

### 3 The Measurement Principle

The detectors have to approach the circulating beams between 1 and 2mm distance, which requires well collimated beams under special optics. This optics at high  $\beta^* = 2625\text{m}$  and  $90^\circ$  phase advance yields a parallel-to-point focusing i.e. a linear relation between the track position in the fiber detectors and the scattering angle at the IP.

The expected detector performance was estimated by Monte Carlo simulation of elastic pp-scattering [6]. A modified version of PHYTIA6.4, to include the Coulomb-term and the real part of the nuclear elastic scattering amplitude, plus the beam transport program MADX were used for this purpose [7,8]. Accepted events are requested to fulfill the left-right trigger condition

and have a space point reconstructed in 4 fiber detectors. The resulting hit pattern in the ALFA fiber detectors is shown in fig. 3.

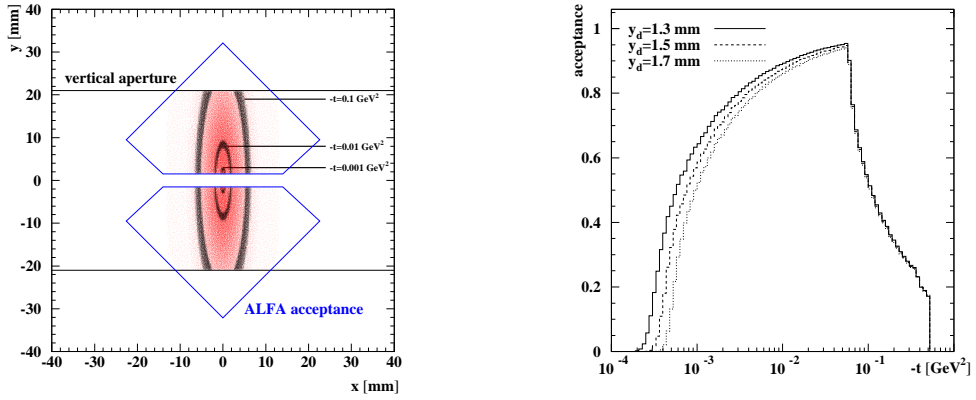


Fig. 3: Hit pattern of protons and acceptance in dependence on  $t$ .

Also shown in fig. 3 is the geometrical acceptance in dependence on  $t$ . The distance of closest approach to the beam centers is assumed between 10 and 20  $\sigma_{beam}$ , depending on the halo conditions. For a distance of 1.5 mm about 67% of all events in the  $t$ -range  $0.5 \cdot 10^{-5}$  to  $0.5 \text{ GeV}^2$  are accepted.

The absolute luminosity is obtained from a fit of the elastic scattering cross section formula to the reconstructed and corrected  $t$ -spectrum. Apart from the luminosity  $L$ , the nuclear slope  $b$ , the ratio of real and imaginary scattering amplitude  $\rho$  and the total cross section  $\sigma_{tot}$  are determined.

$$\frac{dN}{dt} = \pi L \left| -\frac{2\alpha}{|t|} + \frac{\sigma_{tot}}{4\pi} (i + \rho) e^{-b|t|/2} \right|^2$$

Out of 10 million generated elastic events 6.6 million with an acceptance above 50% are used for the luminosity fit. The simulated and reconstructed  $t$ -spectrum with a linear scale for the rate is shown in fig. 4. The large total cross section ensures the collection of enough events to keep the statistical error small. For 6.6 million events the statistical errors of the luminosity and the total cross section are 1.8% and 0.9%, respectively. Some systematic uncertainties which are not taken into account in the fit procedure are: the beam divergence and crossing angle at the IP (0.3%, 0.2%), the uncertainties in the knowledge of the optical functions and phase advance to convert the hit points into a scattering angle at the IP (0.6%, 1.0%), detector resolution and alignment (0.3%, 1.3%), and finally statistical fluctuations in the background subtraction (1.2%). These values combined with the statistical error result in a total error of 3% [6].

Based on this Monte Carlo study about 100 hours running at a low luminosity of  $1.0 \times 10^{27} \text{ cm}^{-2} \text{ s}^{-1}$  are necessary to collect the used data sample [3].



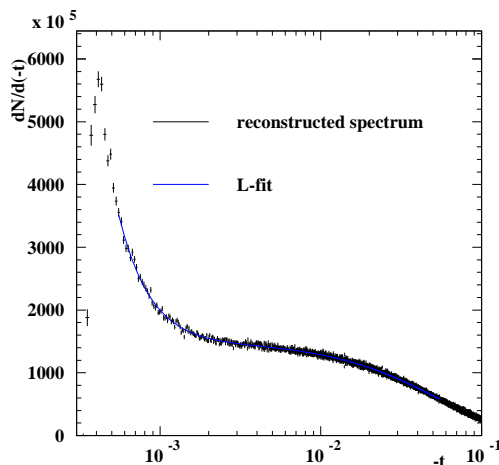


Fig. 4: Reconstructed  $t$ -spectrum for detectors placed at 1.5 mm distance.

#### 4 The Status of ALFA Components

This chapter gives a brief review about the production status of the main components in summer 2008: the fiber detectors, the electronics, and the mechanics.

To enlarge the light yield and to reduce the optical cross talk all fibers are coated by a thin Aluminum layer. The gain is about 75% for fibers cutted by  $90^\circ$  and 50% for the  $45^\circ$  fibers. The far end of the fibers are coated by sputtering technology in LIP Lisbon, followed by the side coating via vacuum evaporation at CERN. All fibers for detector production can be ready at the end of 2008. The fibers are glued on precise Titanium substrates which were produced by electro-erosion in HU Berlin. These substrates have precision holes and edges to ensure the staggering of the fiber layers. This production step is finished and the 3D measurements confirmed an accuracy below  $10\mu\text{m}$ . In the next step the fiber detectors are produced by capillary gluing at JLU Giessen. After that the assembling of the complete detector insert is performed, the routing of all fibers to the MAPMT connectors, the gluing and milling of the connectors. A prototype-1 detector has been produced for installation issues in the tight environment of the Roman pot. Another prototype-2 detector is ready for use in a test beam measurement in summer 2008. To benefit from the staggering all fiber positions are measured by microscope at DESY Hamburg. The fiber positions are described by straight lines, which are stored in a data base and used for the track reconstruction. The precise positioning is limited due to some inherent conditions: the RMS of the fiber diameter, defects from the Aluminum coating, the precision of approaching the edges due to dust particles and the bending force on the fibers, and more. In some substrates of the prototype-2 deviations of about  $100\mu\text{m}$  from the nominal staggering have been observed. This results in a reduced resolution of  $40\mu\text{m}$ , while  $25\mu\text{m}$  has been measured in the 2006 test beam campaign for a detector with 16 fibers per layer [4, 5]. Presently we investigate possible reasons for the staggering deviations to ensure that all detectors have similar quality close to the

demands of the design. The detector insert is completed by corresponding trigger substrates. The essential demand for these substrates is a good light yield to guarantee 100% trigger efficiency. The test beam campaign 2007 in a DESY 6 GeV electron beam has shown a sufficient light yield between 30 and 40 photo-electrons using clear fiber bundles as flexible light guides. The fibres are coupled by optical connectors through the vacuum flange to multi-anode PMTs (MAPMT) with 64 pixels. The MAPMTs are connected through a stack of PCBs to the MAROC read-out chip, which performs amplification, shaping, gain equalisation and discrimination of the signals. Signals from MAROC are further processed by a FPGA which samples the signals at 40 MHz, stores the data for the L1 latency and transmits the buffer serially to the motherboard in case of a positive trigger signal. All signals of a single ALFA detector with 23 MAPMTs are collected by the motherboard which transmits the signals via optical link to the ATLAS DAQ. The connection to the central ATLAS trigger processor is also done via optical link, while the control of the motherboard and connected components is achieved by an ELMB module. The scintillation signals from the individual fibers are amplified in the 64 channel MAPMTs H7546B. The gain and uniformity measurements to correct differences in the subsequent front-end electronics are performed for each device at DESY Hamburg. The front-end electronics consists of a so-called PMFs which are 3-layer-stacks of PCBs close to the MAPMTs. Each PMF contains a MAROC2 read-out chip, which performs amplification, shaping, gain equalisation and discrimination of the signals. Signals from MAROC2 are further processed by a FPGA which samples the signals at 40 MHz, stores the data for the L1 latency and transmits the buffer serially to the motherboard. For the test beam campaign with prototype-2 32 PMFs were produced in LAL Orsay. The S-curve measurements have shown very good quality in terms of homogeneity, linearity and sensitivity to expected fiber light signal of 4 to 5 photo-electrons.

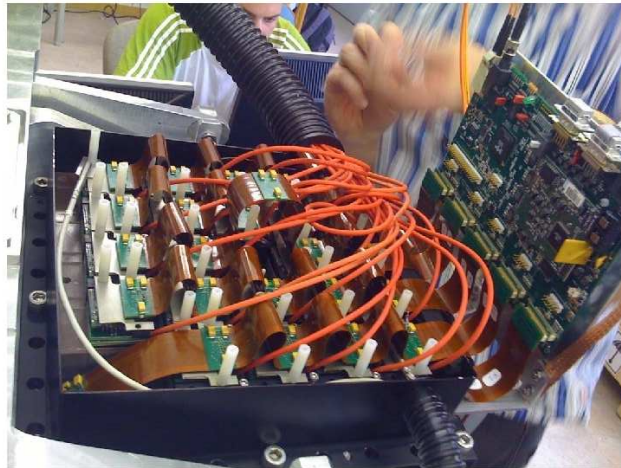


Fig. 5: Front-end electronics: Kapton cables each connected to 5 PMFs sitting on top of the MAPMTs.

The Roman Pot mechanics has to fulfill high demands on precision and positioning reproducibility. Mechanical and optical position measurements have been performed with a pre-

prototype. Some front-back and left-right distortions up to  $200\mu\text{m}$  have been observed in extreme positions. However their contribution to the total luminosity error is uncritical below 0.2%. In addition the stiffness of the slides keeping the pots have been improved replacing the Aluminum by Steel slides. The mechanical components for all stations received from Prague and are now assembled at CERN.

In summer 2008 a full Roman Pot was tested in the CERN test beam H8. A telescope of silicon strip detectors has been used for tracking. The data analysis is underway and will be published as internal ATLAS note. The schedule of the ALFA installation depends on the LHC machine status. A possible scenario is the installation of the mechanics in spring 2009. The pots itself are machined at CERN and should be installed together with the station mechanics to avoid another break of the LHC vacuum. The production of fiber detectors could be finished 2009 and their installation completed in the shut down 2009/2010.

## References

- [1] ATLAS Coll., ATLAS Detector and Physics Performance Technical Design Report, ATLAS TDR 014, CERN/LHCC/1999-014, 1999.
- [2] UA4 Coll., D.Bernard et al., Phys.Lett. 89 (2002) 1801.
- [3] ATLAS Coll., ATLAS Forward Detectors for Measurement of Elastic Scattering and Luminosity, ATLAS TDR 018, CERN/LHCC/2008-004, 2008.
- [4] S.Ask et al., Nucl.Instr. and Meth. A568 (2006) 588.
- [5] F.Anghinolfi et al., JINST 2, 07004, 2007.
- [6] H. Stenzel, Luminosity Calibration from Elastic Scattering, ATL-LUM-PUB-2007-001, 2007.
- [7] T.Sjostrand et al., PHYTIA 6.4 Physics and Manual, JHE05 026, 2006.
- [8] MADX homepage: <http://madox.web.cern.ch/madox>.

# Diffraction Physics in ALICE

*R. Schicker*

Physikalisches Inst., Philosophenweg 12, 69120 Heidelberg

## Abstract

The ALICE detector at the Large Hadron Collider (LHC) consists of a central barrel, a muon spectrometer and neutron calorimeters at  $0^\circ$ . Additional detectors for event classification and for trigger purposes are placed on both sides of the central barrel. Such a geometry allows the definition of a diffractive gap trigger by requiring no activity in the additional detectors. I discuss some physics topics which become accessible by this gap trigger.

## 1 The ALICE Experiment

The ALICE experiment is presently being commissioned at the Large Hadron Collider (LHC) [1, 2]. The ALICE experiment consists of a central barrel covering the pseudorapidity range  $-0.9 < \eta < 0.9$  and a muon spectrometer in the range  $-4.0 < \eta < -2.4$ . Additional detectors for trigger purposes and for event classification exist in the range  $-4.0 < \eta < 5.0$ . The ALICE physics program foresees data taking in pp and PbPb collisions at luminosities up to  $\mathcal{L} = 5 \times 10^{30} \text{ cm}^{-2} \text{ s}^{-1}$  and  $\mathcal{L} = 10^{27} \text{ cm}^{-2} \text{ s}^{-1}$ , respectively. An asymmetric system pPb will be measured at a luminosity of  $\mathcal{L} = 10^{29} \text{ cm}^{-2} \text{ s}^{-1}$ .

### 1.1 The ALICE Central Barrel

The detectors in the ALICE central barrel track and identify hadrons, electrons and photons in the pseudorapidity range  $-0.9 < \eta < 0.9$ . The magnetic field strength of 0.5 T allows the measurement of tracks from very low transverse momenta of about 100 MeV/c to fairly high values of about 100 GeV/c. The tracking detectors are designed to reconstruct secondary vertices resulting from decays of hyperons, D and B mesons. The granularity of the central barrel detectors is chosen such that particle tracking and identification can be achieved in a high multiplicity environment of up to 8000 particles per unit of rapidity. The main detector systems for these tasks are the Inner Tracking System, the Time Projection Chamber, the Transition Radiation Detector and the Time of Flight array. These systems cover the full azimuthal angle within the pseudorapidity range  $-0.9 < \eta < 0.9$  and are described below. Additional detectors with partial coverage of the central barrel are a PHOTon Spectrometer (PHOS), an electromagnetic calorimeter (EMCAL) and a High-Momentum Particle Identification Detector (HMPID).

#### 1.1.1 The Inner Tracking System

The Inner Tracking System (ITS) consists of six cylindrical layers of silicon detectors at radii from 4 cm to 44 cm. The minimum radius is determined by the beam pipe dimensions whereas the maximum radius chosen is determined by the necessity of efficient track matching with the outer detectors in the central barrel. The innermost layer extends over the range  $-2 < \eta < 2$

such that there is continuous overlap with event classification detectors outside of the central barrel. Due to the high particle density of up to 80 particles/cm<sup>2</sup> and in order to achieve the required tracking resolution, pixel detectors have been chosen for the first two layers. Silicon drift detectors are located in the middle two layers whereas double sided silicon strip detectors are in the outer two layers.

### 1.1.2 The Time Projection Chamber

The Time Projection Chamber (TPC) is the main tracking detector in the central barrel. The inner and outer radii of the active volume are 84.5 cm and 246.6 cm, respectively. The full radial track length is measured in the pseudorapidity range  $-0.9 < \eta < 0.9$  whereas tracks with at least one third of nominal radial length are covered in the pseudorapidity range  $-1.5 < \eta < 1.5$ . Particle identification is achieved by measuring the specific ionization loss. The chosen geometry results in a drift time of about 90  $\mu$ s. This long drift time is the factor limiting the proton-proton luminosity to the value mentioned above.

### 1.1.3 The Transition Radiation Detector

The principal goal of the Transition Radiation Detector (TRD) is to provide electron identification in the momentum range larger than 1 GeV/c. In this range, the electron identification by energy loss in the TPC is no longer sufficient. Since the TRD is a fast tracker, the TRD information can be used for an efficient trigger on high transverse momentum electrons. In addition, the position information from the TRD system improves the tracking performance of the central barrel.

### 1.1.4 The Time of Flight Detector

The Time-Of-Flight (TOF) array is located at a radial distance from 3.7 m to 4.0 m. The TOF information is used for particle identification in the range  $0.2 \text{ GeV/c} < p_T < 2.5 \text{ GeV/c}$ . For this detector, the Multi-gap Resistive-Plate (MRPC) technology was chosen. A strip with an active area of  $120 \times 7.4 \text{ cm}^2$  consists of pads of 3.5 cm length and 2.5 cm width.

### 1.1.5 The Central Barrel Performance

The ITS, TPC and TRD detectors described above are the main tracking detectors in the central barrel. With the information from these detectors, particles with momenta as low as 100 MeV/c can be tracked.

Fig.1 shows the transverse momentum resolution as expected from simulations. The TPC alone achieves a resolution of approximately 3% at a transverse momentum of  $p_T = 10 \text{ GeV/c}$ . Adding the information from ITS and TRD on the inner and outer side, respectively, improves the resolution considerably due to the increased leverage. The combined transverse momentum resolution from the ITS, TPC and TRD detector is expected to be about 3% at a transverse momentum of  $p_T = 100 \text{ GeV/c}$ .

Particle identification is achieved in the central barrel by different methods. The specific energy loss is measured by the TPC, the TRD and the strip and drift detectors of the ITS. Fig.2 shows the combined particle identification capability by  $dE/dx$  measurement as a function of

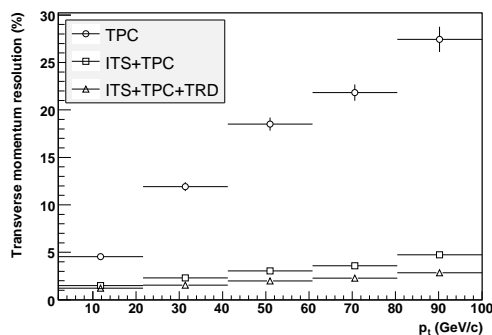


Fig. 1: Central barrel tracking resolution

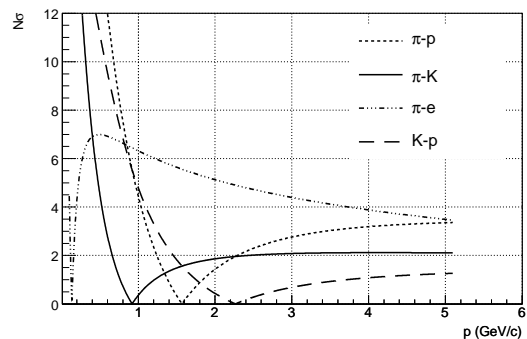


Fig. 2: Particle identification by dE/dx measurement

momentum. The separation of different particle species is shown in units of the resolution of the dE/dx measurement. The electron-pion separation at high momenta is significantly improved by the information of the TRD system.

## 1.2 The ALICE Zero Degree Neutron Calorimeter

The Zero Degree Neutron Calorimeters (ZDC) are placed on both sides of the interaction point at a distance of 116 m [3]. The ZDC information can be used to select different diffractive topologies. Events of the type  $pp \rightarrow ppX$  do not deposit energy in these calorimeters, events  $pp \rightarrow pN^*X$  will have energy in one of the calorimeters whereas events  $pp \rightarrow N^*N^*X$  will have energy deposited in both calorimeters. Here, X denotes a centrally produced diffractive state from which the diffractive L0 trigger is derived as described below.

## 2 The ALICE diffractive gap trigger

Additional detectors for event classification and trigger purposes are located on both sides of the ALICE central barrel. First, an array of scintillator detectors (V0) is placed on both sides of the central barrel. These arrays are labeled V0A and V0C on the two sides, respectively. Each of these arrays covers a pseudorapidity interval of about two units with a fourfold segmentation of half a unit. The azimuthal coverage is divided into eight segments of  $45^\circ$  degrees hence each array is composed of 32 individual counters. Second, a Forward Multiplicity Detector (FMD) is located on both sides of the central barrel. The pseudorapidity coverage of this detector is  $-3.4 < \eta < -1.7$  and  $1.7 < \eta < 5.1$ , respectively.

Fig.3 shows the pseudorapidity coverage of the detector systems described above. The geometry of the ALICE central barrel in conjunction with the additional detectors V0 and FMD is well suited for the definition of a rapidity gap trigger. The ALICE trigger system consists of a Central Trigger Processor (CTP) and is designed as a multi-level scheme with L0,L1 and L2 levels and a high-level trigger (HLT). A rapidity gap trigger can be defined by the requirement of signals coming from the central barrel detectors while V0 and FMD not showing any activity. Such a scheme requires a trigger signal from within the central barrel for L0 decision. The pixel detector of the ITS system is suited for delivering such a signal [4]. Alternatively, this L0 signal can be derived from the TOF detector.

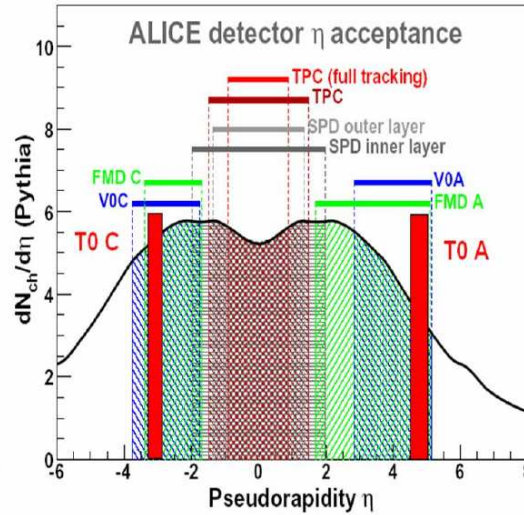


Fig. 3: Pseudorapidity coverage of trigger detectors and of detectors in central barrel

The high level trigger HLT has access to the information of all the detectors shown in Fig.3 and will hence be able to select events with rapidity gaps in the range  $-4 < \eta < -1$  and  $1 < \eta < 5$ . These gaps extend over seven units of pseudorapidity and are hence expected to suppress minimum bias inelastic events by many orders of magnitude.

In addition to the scheme described above, the ALICE diffractive L0 trigger signal can be generated from the Neutron ZDC if no central state is present in the reaction. A L0 signal from ZDC does, however, not arrive at the CTP within the standard L0 time window. A L0 trigger from ZDC is therefore only possible during special data taking runs for which the standard L0 time limit is extended. The possibility of such data taking is currently under discussion.

### 3 ALICE diffractive physics

The tracking capabilities at very low transverse momenta in conjunction with the excellent particle identification make ALICE an unique facility at LHC to pursue a long term physics program of diffractive physics. The low luminosity of ALICE as compared to the other LHC experiments restricts the ALICE physics program to reactions with cross section at a level of a few nb per unit of rapidity.

Fig.4 shows the transverse momentum acceptance of the four main LHC experiments. Not shown in this figure is the acceptance of the TOTEM experiment which has a physics program of measurements of total cross section, elastic scattering and soft diffraction [5]. The acceptance of the TOTEM telescopes is in the range of  $3.1 < |\eta| < 4.7$  and  $5.3 < |\eta| < 6.5$ . The CMS transverse momentum acceptance of about 1 GeV/c shown in Fig.4 represents a nominal value. The CMS analysis framework foresees the reconstruction of a few selected data samples to values as low as 0.2 GeV/c [6].

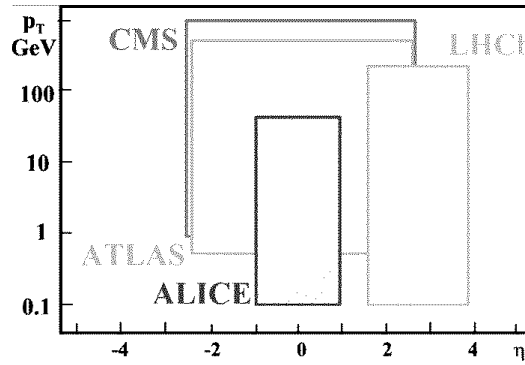


Fig. 4: Rapidity and transverse momentum acceptance of the LHC experiments

#### 4 Signatures of the Pomeron

The geometry of the ALICE experiment is suited for measuring a centrally produced diffractive state with a rapidity gap on either side. Such a topology can result, among other, from double Pomeron exchange with subsequent hadronization of the central state. It is expected that the secondaries from Pomeron-Pomeron fusion events show markedly different characteristics as compared to secondaries from inelastic minimum bias events.

First, it is expected that the production cross section of glueball states in Pomeron fusion is larger as compared to inelastic minimum bias events. It will therefore be interesting to study the resonances produced in the central region when two rapidity gaps are required [7].

Second, the slope  $\alpha'$  of the Pomeron trajectory is rather small:  $\alpha' \sim 0.25 \text{ GeV}^{-2}$  in DL fit and  $\alpha' \sim 0.1 \text{ GeV}^{-2}$  in vector meson production at HERA [8]. These values of  $\alpha'$  in conjunction with the small t-slope ( $< 1 \text{ GeV}^{-2}$ ) of the triple Pomeron vertex indicate that the mean transverse momentum  $k_t$  in the Pomeron wave function is relatively large  $\alpha' \sim 1/k_t^2$ , most probably  $k_t > 1 \text{ GeV}$ . The transverse momenta of secondaries produced in Pomeron-Pomeron interactions are of the order of this  $k_t$ . Thus the mean transverse momenta of secondaries produced in Pomeron-Pomeron fusion is expected to be larger as compared to inelastic minimum bias events.

Third, the large  $k_t$  described above corresponds to a large effective temperature. A suppression of strange quark production is not expected. Hence the  $K/\pi$  ratio is expected to be enhanced in Pomeron-Pomeron fusion as compared to inelastic minimum bias events [9]. Similarly, the  $\eta/\pi$  and  $\eta'/\pi$  ratios are expected to be enhanced due to the hidden strangeness content and due to the gluon components in the Fock states of  $\eta, \eta'$ .

#### 5 Signatures of Odderon

The Odderon was first postulated in 1973 and is represented by color singlet exchange with negative C-parity [10]. Due to its negative C-parity, Odderon exchange can lead to differences between particle-particle and particle-antiparticle scattering. In QCD, the Odderon can be a three gluon object in a symmetric color state. Due to the third gluon involved in the exchange, a suppression by the coupling  $\alpha_s$  is expected as compared to the two gluon Pomeron exchange.



However, finding experimental signatures of the Odderon exchange has so far turned out to be extremely difficult [11]. A continued non-observation of Odderon signatures would put considerable doubt on the formulation of high energy scattering by gluon exchange [12]. The best evidence so far for Odderon exchange was established as a difference between the differential cross sections for elastic  $pp$  and  $p\bar{p}$  scattering at  $\sqrt{s} = 53$  GeV at the CERN ISR. The  $pp$  cross section displays a dip at  $t = -1.3$  GeV<sup>2</sup> whereas the  $p\bar{p}$  cross section levels off. Such a behaviour is typical for negative C-exchange and cannot be due to mesonic Reggeons only.

### 5.1 Signatures of Odderon Cross Sections

Signatures of Odderon exchanges can be looked for in exclusive reactions where the Odderon (besides the Photon) is the only possible exchange. Diffractively produced C-even states such as pseudoscalar or tensor mesons can result from Photon-Photon, Photon-Odderon and Odderon-Odderon exchange. Any excess measured beyond the well understood Photon-Photon contribution would indicate an Odderon contribution.

Diffractively produced C-odd states such as vector mesons  $\phi$ ,  $J/\psi$ ,  $\Upsilon$  can result from Photon-Pomeron or Odderon-Pomeron exchange. Any excess beyond the Photon contribution would be indication of Odderon exchange.

Estimates of cross section for diffractively produced  $J/\psi$  in  $pp$  collisions at LHC energies were first given by Schäfer et al [13]. More refined calculations by Bzdak et al result in a  $t$ -integrated photon contribution of  $\frac{d\sigma}{dy} \big|_{y=0} \sim 15$  nb and a  $t$ -integrated Odderon contribution of  $\frac{d\sigma}{dy} \big|_{y=0} \sim 1$  nb [14]. These two numbers carry large uncertainties, the upper and lower limit of these numbers vary by about an order of magnitude. This cross section is, however, at a level where in  $10^6$  s of ALICE data taking the  $J/\psi$  can be measured in its  $e^+e^-$  decay channel at a level of 4% statistical uncertainty.

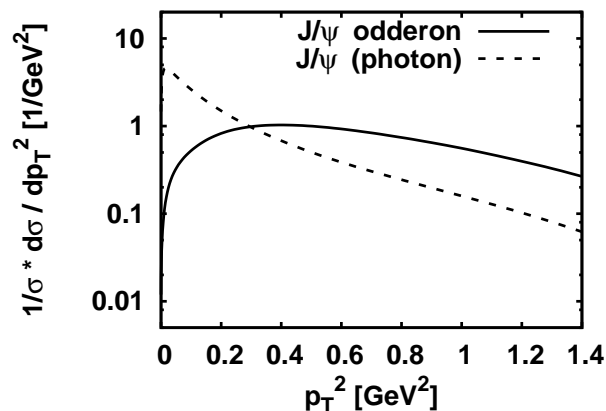


Fig. 5: The  $J/\psi$  transverse momentum distribution for the photon and Odderon contributions

Due to the different  $t$ -dependence, the Photon and Odderon contribution result in different transverse momentum distribution  $p_T$  of the  $J/\psi$ . The photon and Odderon contributions

are shown in Fig.5 by the dotted and solid lines, respectively. A careful transverse momentum analysis of the  $J/\psi$  might therefore allow to disentangle the Odderon contribution.

## 5.2 Signatures of Odderon Interference Effects

If the diffractively produced final state is not an eigenstate of C-parity, then interference effects between photon-Pomeron and photon-Odderon amplitudes can be analyzed.

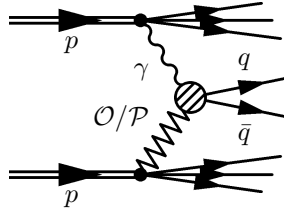


Fig. 6: photon-Pomeron and photon-Odderon amplitudes

Fig.6 shows the photon-Pomeron and the photon-Odderon amplitudes for  $q\bar{q}$  production. A study of open charm diffractive photoproduction estimates the asymmetry in fractional energy to be on the order of 15% [15]. The forward-backward charge asymmetry in diffractive production of pion pairs is calculated to be on the order of 10% for pair masses in the range  $1 \text{ GeV}/c^2 < m_{\pi^+\pi^-} < 1.3 \text{ GeV}/c^2$  [16, 17].

## 6 Photoproduction of heavy quarks

Diffractive reactions involve scattering on small- $x$  gluons in the proton. The number density of gluons at given  $x$  increases with  $Q^2$ , as described by the DGLAP evolution. Here,  $Q^2$  and  $x$  denote the kinematical parameters used in deep inelastic ep scattering. The transverse gluon density at a given  $Q^2$  increases with decreasing  $x$  as described by the BFKL evolution equation. At some density, gluons will overlap and hence reinteract. In this regime, the gluon density saturates and the linear DGLAP and BFKL equation reach their range of applicability. A saturation scale  $Q_s(x)$  is defined which represents the breakdown of the linear regime. Nonlinear effects become visible for  $Q < Q_s(x)$ .

Diffractive heavy quark photoproduction represents an interesting probe to look for gluon saturation effects at LHC. The inclusive cross section for  $Q\bar{Q}$  photoproduction can be calculated within the dipole formalism. In this approach, the photon fluctuates into a  $Q\bar{Q}$  excitation which interacts with the proton as a color dipole. The dipole cross section  $\sigma(x,r)$  depends on  $x$  as well as on the transverse distance  $r$  of the  $Q\bar{Q}$  pair. A study of inclusive heavy quark photoproduction in pp collisions at LHC energy has been carried out [18]. These studies arrive at differential cross sections for open charm photoproduction of  $\frac{d\sigma}{dy} \big|_{y=0} \sim 1.3 \mu\text{b}$  within the collinear pQCD approach as compared to  $\frac{d\sigma}{dy} \big|_{y=0} \sim 0.4 \mu\text{b}$  within the color glass condensate (CGC). The cross sections are such that open charm photoproduction seems measurable with good statistical

significance. The corresponding numbers for the cross section for bottom photoproduction are  $\frac{d\sigma}{dy}|_{y=0} \sim 20$  nb and 10 nb, respectively.

Diffraction photoproduction is characterized by two rapidity gaps in the final state. In the dipole formalism described above, the two gluons of the color dipole interaction are in color singlet state. Diffractive heavy quark photoproduction cross sections in pp, pPb and PbPb collisions at LHC have been studied [19]. The cross sections for diffractive charm photoproduction are  $\frac{d\sigma}{dy}|_{y=0} \sim 6$  nb in pp,  $\frac{d\sigma}{dy}|_{y=0} \sim 9 \mu\text{b}$  in pPb and  $\frac{d\sigma}{dy}|_{y=0} \sim 11$  mb in PbPb collisions. The corresponding numbers for diffractive bottom photoproduction are  $\frac{d\sigma}{dy}|_{y=0} \sim 0.014$  nb in pp,  $\frac{d\sigma}{dy}|_{y=0} \sim 0.016 \mu\text{b}$  in pPb and  $\frac{d\sigma}{dy}|_{y=0} \sim 0.02$  mb in PbPb collisions.

Heavy quarks with two rapidity gaps in the final state can, however, also be produced by central exclusive production, i.e. two Pomeron fusion. The two production mechanisms have a different  $t$ -dependence. A careful analysis of the transverse momentum  $p_T$  of the  $Q\bar{Q}$  pair might therefore allow to disentangle the two contributions.

### Acknowledgments

I thank Otto Nachtmann and Carlo Ewerz for illuminating discussions and Leszek Motyka for preparing and communicating Figure 5.

### References

- [1] F. Carminati et al, ALICE Collaboration, 2004, J.Phys. G: Nucl. Part. Phys. **30** 1517
- [2] B. Alessandro et al, ALICE Collaboration, 2006, J.Phys. G: Nucl. Part. Phys. **32** 1295
- [3] R. Arnaldi et al, Nucl. Instr. and Meth. A **564** (2006) 235
- [4] The ALICE collaboration, K. Aamodt et al., The ALICE experiment at the CERN LHC, 2008\_JINST\_3\_S08002.
- [5] K. Eggert, TOTEM a different LHC experiment, CERN colloquium, feb 21,2008
- [6] D. d’Enterria et al, Addendum CMS technical design report, J. Phys. G34:2307-2455, 2007
- [7] F. Close, A. Kirk, G. Schuler, Phys.Lett. B **477** (2000) 13
- [8] A. Donnachie, P. Landshoff, Phys.Lett. B**595** (2004) 393
- [9] T. Åkesson et al, Nucl. Phys. B **264** (1986) 154
- [10] L. Lukaszuk, B. Nicolescu, Lett. Nuovo Cim. **8** (1973) 406
- [11] C. Ewerz, Proceedings XII Rencontres de Blois (2005) 377
- [12] S. Donnachie, G. Dosch, P.V. Landshoff, O. Nachtmann, Pomeron physics and QCD, Cambridge University Press (2002) 297

- [13] A. Schäfer, L. Mankiewicz, O. Nachtmann, Phys.Lett. B **272** (1991) 419
- [14] A. Bzdak, L. Motyka, L. Szymanowski, J.R. Cudell, Phys.Rev. D **75** (2007) 094023
- [15] S.J. Brodsky, J. Rathsman, C. Merino, Phys.Lett. B **461** (1999) 114
- [16] P. Hägler, B. Pire, L. Szymanowski, O.V. Teryaev, Phys.Lett. B **535** (2002) 117
- [17] I.F. Ginzburg, I.P. Ivanov, N.N. Nikolaev, Eur.Phys.J. C **5** (2003) 02
- [18] V.P. Goncalves, M.V. Machado, Phys.Rev.D **71** (2005) 014025
- [19] V.P. Goncalves, M.V. Machado, Phys.Rev.D **75** (2007) 031502

# Physics with forward FP420/FP220 tagging systems.

Peter Bussey<sup>1\*</sup> and Pierre Van Mechelen<sup>2</sup>

<sup>1</sup> Department of Physics and Astronomy, Faculty of Physical Sciences, University of Glasgow, U.K

<sup>2</sup> Department of Physics, Universiteit Antwerpen, Belgium

## Abstract

We discuss selected physics topics in relation to proposals to upgrade the ATLAS and CMS detectors by the installation of forward silicon detector systems close to the beam line at distances of approximately 220 m and 420 m from the respective interaction points. The physics motivation and some of the aspects of the apparatus and its performance are briefly described.

## 1 Introduction

An important part of the physics programme at HERA has been the measurement of diffractive processes, in which the proton exchanges a colourless object, commonly referred to as the pomeron, with the incoming virtual photon. Two types of process here are of particular interest: the production of exclusive final states such as vector mesons, and hard processes in which the photon interacts with partonic components of the structure of the pomeron, which can be modelled in various ways. The hard processes can be induced by photons of varying virtuality, ranging from quasi-real photons to highly virtual photons that give deep inelastic scattering off the partons associated with the pomeron.

In a similar way, high energy photon-photon physics has been exploited at LEP, with processes that can be categorised in a similar manner. There is also an active program of diffractive physics at the Tevatron.

At the LHC, much higher energies are available than at HERA and LEP, enabling these physics programmes to be extended into areas where new physics can be discovered or studied. This is the subject of the present section. We outline first the physical setup that is envisaged, in which new detector systems will be installed close to the beam line at suitable locations downstream of the interaction points. We then present a summary of some of the new processes that should become open to investigation, and finally return to discuss the physical apparatus in further detail with an outline of its capabilities.

## 2 The basic proposal for forward detectors

Figure 1 illustrates the configuration of the LHC beamline on one side of an interaction point, showing the separate incoming and outgoing beams and the form of the particle trajectories on entering and leaving the interaction region. At distances greater than 260 m, the beam is dominated by the main bending magnets and is in the form of an irregular arc, which has been straightened

---

\*Royal Society of Edinburgh / Scottish Executive Support Research Fellow 2008

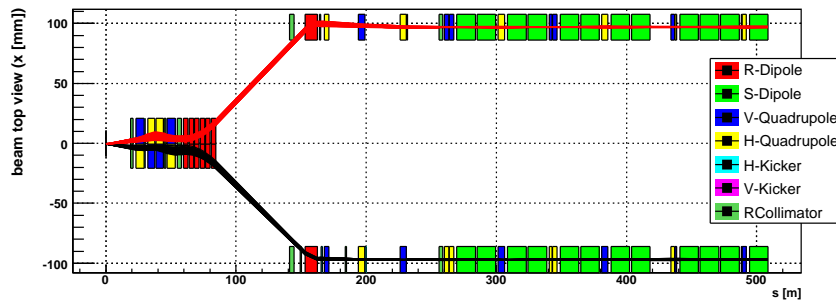


Fig. 1: Schematic representation of the LHC beamline on one side of an intersection point. The ATLAS or CMS detector is located at the origin of coordinates, and the incoming and outgoing beamlines are indicated, with the main bends straightened out for illustrative convenience.

out in the Figure. At two regions, namely around 220 m and 420 m from the interaction point, there are intervals in the beamline that are not occupied by magnets. Each of these regions provides approximately ten metres of clear space within which physics detectors can be stationed. It is proposed to install sets of silicon detectors in these regions, allowing them to be positioned as closely as possible to the outgoing beam. These detectors will detect diffractively scattered outgoing protons.

One or both protons in a  $pp$  collision may be scattered diffractively. In such a case, the fractional energy loss  $\xi$  suffered by the proton is typically small, as is the angle of scatter. These protons will continue to travel along the beam line, but in due course they will no longer be contained by the beam optics and will be bent either into a collimator or out of the beam line altogether. It is found that protons that have lost a few tens of GeV in the initial collision emerge out of the beam typically in the 420 m regions, and those that have lost a few hundreds of GeV emerge in the 220 m regions. By installing detector systems in these regions, we can identify the double diffractive production of exclusive centrally produced states whose mass is above a minimum value of the order of  $100 \text{ GeV}/c^2$ , provided that the state itself records a suitable signature in the central detector allowing its identification. Figure 2 illustrates the kind of process that we are interested in for the case of a Higgs particle denoted as  $H$ . A measurement of the energies of the outgoing protons makes possible a good determination of the mass of the centrally produced object, and in most cases this has better resolution than the measurement made in the central detector.

### 3 Central exclusive production

The central exclusive production of a Standard Model Higgs at the LHC has been the subject of a number of calculations. The cross section is strongly dependent on the gluon distributions that are assumed in the proton, and the detected cross section depends on the ability to trigger the process in the apparatus. Here we are faced with the difficulty that the present trigger electronics in ATLAS and CMS do not allow a first-level trigger to be based on the detection of a proton at 420 m, since the signal arrives too late. This forces the detection of a  $120 \text{ GeV}/c^2$  central state to

be based on central detector triggers, which are not highly efficient in the case of a SM Higgs at this mass. In our favour is that the background of quark-antiquark jets is suppressed dynamically relative to the signal by the  $J_z = 0$  selection rule [1]. An exclusive double-diffractively produced state is constrained to have  $J^{PC} = 0^{++}$ , so that if a Higgs or other particle is seen at all in this process, we have a good determination of its quantum numbers which may be hard to determine unambiguously by central detector measurements alone.

Recently the CDF Collaboration has observed for the first time the existence of central exclusive dijet production in hadronic collisions [2]. Exclusive production of the charmonium state  $\chi_c$  has also been reported [3], with a cross section of the predicted magnitude. These are major milestones, since the central exclusive production of known final states can be used as “standard candles” to confirm mechanisms and extract cross sections with small model uncertainties. Establishing the potential experimental dijet background is an important item in the search for new particles such as the Higgs.

From Fig. 3 (left) it is clear that measurements of the proton structure at HERA and the Tevatron have a strong relevance to predicting the strength of a possible SM Higgs signal in double diffraction at LHC. With the set-up that is currently envisaged, the prospects seem rather marginal. However there are additional opportunities if the Higgs occurs within a supersymmetric framework. There are two particularly important parameters of the SUSY scenario, denoted as  $m_A$  and  $\tan \beta$ , within whose parameter space a number of the features of the theory can be illustrated. Figure 3 (right) illustrates the enhancements to the SM Higgs cross section that might be obtained for the lighter of the two neutral SUSY Higgs particles, denoted as  $h$ , and showing also some contours of different  $h$  masses, taken from Heinemeyer et al. [4].

On this basis, the quantity of LHC luminosity needed for  $3\text{-}\sigma$  evidence and  $5\text{-}\sigma$  discovery of neutral SUSY Higgs in the exclusive double-diffractive mode can be estimated, as illustrated for the heavier SUSY Higgs  $H$  in Fig. 4 [5]. Contour plots of this kind have been presented by these authors for the  $h$  and  $H$  in a variety of related situations. This gives improved hope of being able to make Higgs studies with forward detectors at the LHC, although there is no advance guarantee that the values of the SUSY parameters will be favourable and the integrated luminosity needed might be substantial.

More cleverly thought-out triggers and cuts may improve the situation. Figure 5 illustrates some studies carried out by Pilkington et al [6]. The mass of the central object has been reconstructed using modelled measurements of the forward proton trajectories at 420 m, with

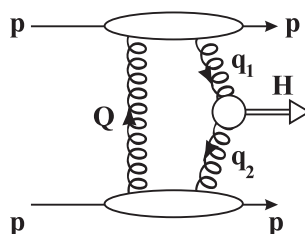


Fig. 2: Double diffractive production of a centrally produced object, denoted as  $H$ , by a colourless exchange modelled in terms of gluons.

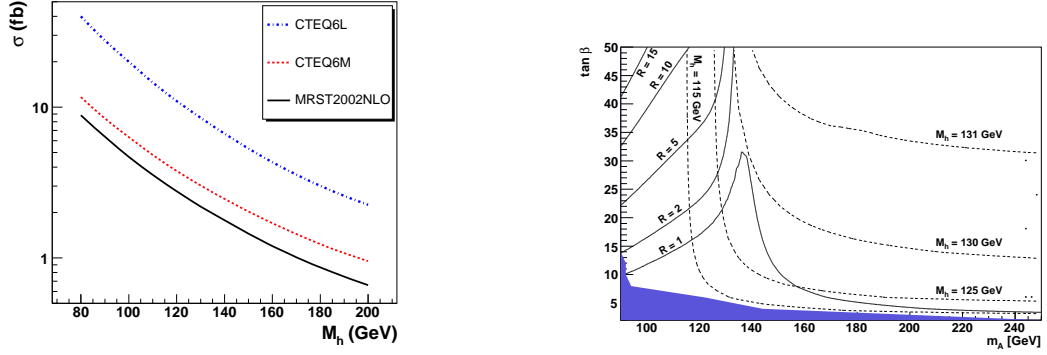


Fig. 3: Left: Variation of Higgs cross section with some parton models of the proton. Right: Contours for the ratio of signal events in the MSSM to those in the SM in the  $h \rightarrow b\bar{b}$  channel in the  $m_A$ - $\tan\beta$  plane. The ratio is shown in the  $M_h^{\max}$  benchmark scenario (with  $\mu = +200$  GeV). The values of the mass of the light Higgs boson,  $M_h$ , are indicated by dashed contour lines. The CMS acceptance was approximately modelled.

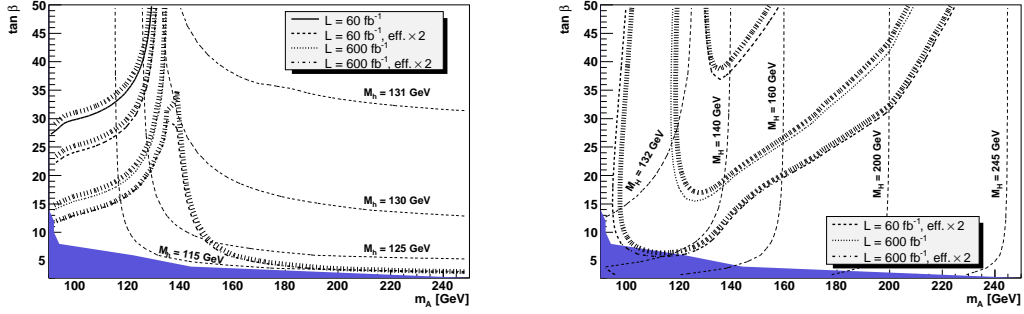


Fig. 4: Contours for 3- $\sigma$  evidence (left) and 5- $\sigma$  discovery (right) for the  $h$  and  $H$  SUSY Higgs in the scenario discussed in the text (S. Heinemeyer et al.)

estimated backgrounds from other processes included. During the first years of running, a measurement using  $60 \text{ fb}^{-1}$  seems a reasonable target and could produce evidence indicated by the first illustrated histogram. Higher luminosities will clearly assist, but will generate combinatorial backgrounds from overlapping events (“pile-up”). If these can be removed, as is envisaged, using precise timing measurements to isolate the event of interest, a signal might be seen giving a 5- $\sigma$  discovery with  $100 \text{ fb}^{-1}$  of running.

Particular attention was given during the workshop to the study of event pile-up at the LHC (Taševský, Pilkington). By exploiting the difference between particle multiplicities in central exclusive and non-diffractive processes, a further reduction of the pile-up background may be possible. Here, only tracks from the primary vertex associated with the hard-scale event are relevant. Additional reduction factors of 10 to 100 may be possible; at present there are uncertainties here due to model dependence, soft underlying event tune dependence and track selection criteria.



#### 4 Photoproduction processes.

TeV-energy protons are surprisingly efficient at radiating high energy photons. Single photoproduction off the second proton, and photon-photon processes are both of interest at LHC. Kinetically, photoproduction resembles diffractive scattering but with the tendency to a smaller transverse momentum transfer to the proton. The  $\gamma\gamma$  cross sections are harder than the pomeron-pomeron processes, overtaking the latter in cross section at  $W_{\gamma\gamma} \approx 1$  TeV. Since diffraction produces mainly gluon jets and photoproduction produces quark jets, there is little interference between the processes.

Single photoproduction will be of interest at the LHC in the production of electroweak particles. There are possibilities for the associated production of Higgs bosons and for the production of anomalous single top via FCNC. These processes are tagged by a single forward proton, but must be triggered and identified in the central detectors, and there will be potential difficulties at high luminosities since the use of timing to associate the forward protons with a central vertex requires two such forward protons. A number of generic cross sections are indicated in Fig. 6 (left), together with the forward detection system that will tag in different  $W_{\gamma p}$  ranges.

The  $\gamma\gamma$  process is capable of inducing the production of any type of charged particle-antiparticle pair. Of particular interest here is the possible production of charged SUSY particles, such as charginos and sleptons, whose signatures in the central detector will be high transverse energy leptons and missing energy carried by neutrinos or the lightest SUSY particle (LSP) if it is neutral. Figure 6 (right) shows cross sections for producing fermion and scalar charged particle pairs, compared to that for  $W^+W^-$  production, which is likely to be a very prolific background.  $ZZ$  production is possible only by anomalous couplings. The dimuon process is seen as good for the calibration of the forward detectors and even for LHC luminosity monitoring.

There are many possible SUSY mass scenarios. The possibilities that have been studied here are in terms of the so-called LM1 scenario, which involves a light LSP and light sleptons and charginos. This type of scenario will give the most favourable set of cross sections. The most natural variable to plot in order to separate SUSY signals from  $WW$  background would be the  $W_{\gamma\gamma}$  value reconstructed from the forward protons (Fig. 7a)) However the background is

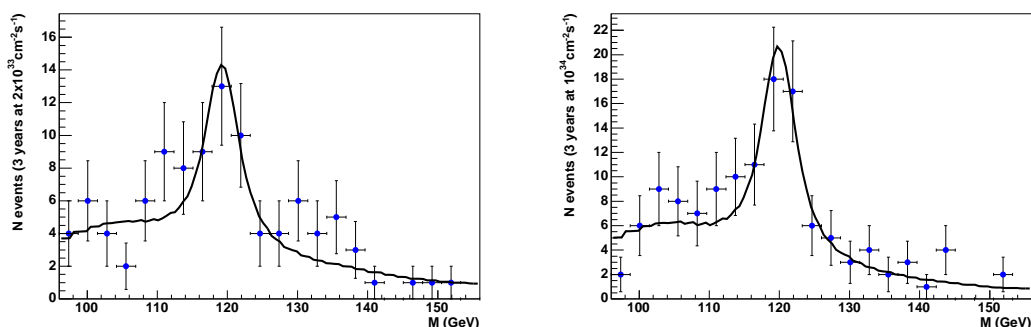


Fig. 5: Example analyses of an MSSM SUSY signal calculated with  $\tan \beta = 40$  and  $m_A = 120$  GeV (A. Pilkington).

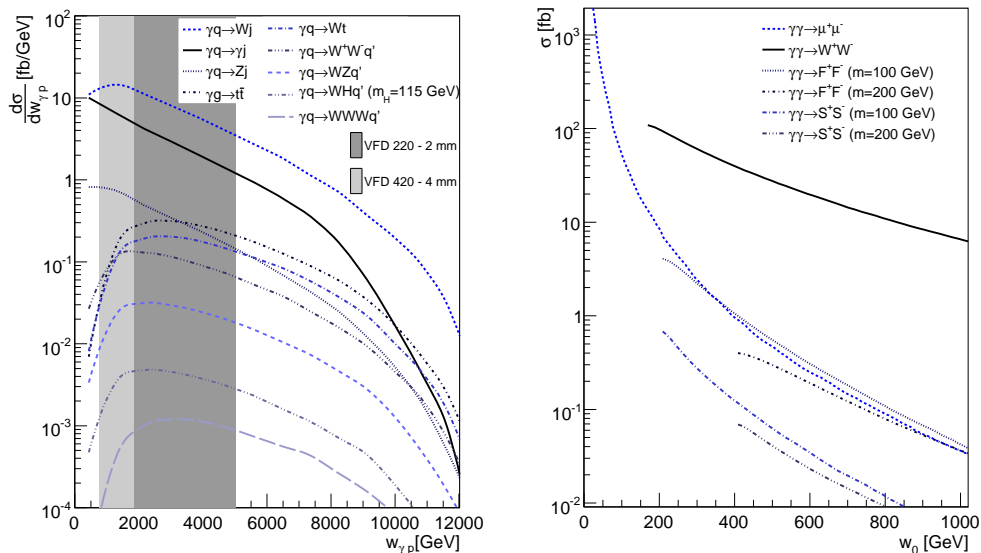


Fig. 6: Cross sections for various single photoproduction processes at LHC (left), as a function of photon-proton mass, and for various generic double photoproduction processes (right).

much more tractable when the variable  $W_{miss} = \sqrt{E_{miss}^2 - P_{miss}^2}$  is plotted (Fig. 7b), where the missing energy and momentum are calculated from the forward protons and the kinematics of the observed final state particles. Combinations of  $W_{\gamma\gamma}$  and  $W_{miss}$  give even more power (Fig. 7c) and can generate a distribution (Fig. 7d) that might give a 5- $\sigma$  discovery with only 25  $\text{fb}^{-1}$  of integrated luminosity.

## 5 Other physics processes

An intriguing example of completely new physics has been proposed by A. White in which a new SU(5) gauge theory obviates the need for a Higgs particle and gives remarkable experimental signatures for which pomeron physics may be an essential diagnostic tool [8]. An extended range of SUSY processes may also be accessible. One study made during this workshop has been the detection of pairs of long-lived gluinos in central exclusive processes [9]. Such particles can occur in split-SUSY models, where the sfermions have masses far above the TeV scale. The gluinos are lighter and therefore long lived, and may form bound states with gluons or quarks called *R*-hadrons. These will mimic the behaviour of muons and may be detected in muon chambers. For 300  $\text{fb}^{-1}$  approximately 10 events are expected for gluino masses up to 350 GeV. The advantage of using proton detectors lies again in the excellent accuracy for the reconstruction of the mass of the centrally produced object. The forward detectors at 220m and 420 m give access to the wide range of masses that such particle pairs may have.

Present space permits no more than a brief mention of other items in the range of physics processes that will be made observable by the use of forward tagging systems at LHC. The work initiated at HERA on hard pomeron scattering and structure can be continued by means of

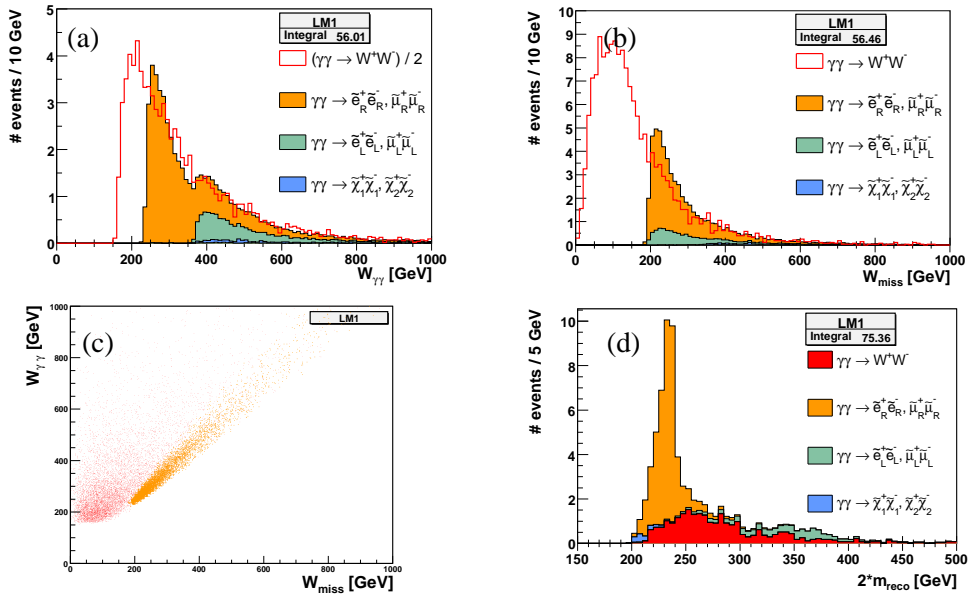


Fig. 7: Examples of the analysis of the double photoproduction of SUSY particles, as a function of the parameters  $W_{\gamma\gamma}$  and  $W_{miss}$ , to illustrate a possible way to isolate a clean SUSY signal [7].

photon-pomeron and pomeron-pomeron processes. It should be noted that the  $q\bar{q}$  final state is suppressed in the pomeron-pomeron process at low quark masses, assisting in the identification of potential new physics processes. There will be extended opportunities for further studies of the nature of the pomeron. In the early stages, at low LHC luminosities, the study of rapidity-gap survival will be interesting and important, generalised gluon distributions can be studied, and a variety of QCD effects can be investigated; a recent review by Khoze, Martin and Ryskin gives more details here [10].

## 6 The proposed apparatus

Traditionally, forward detection systems have consisted of relatively small installations mounted at suitable locations such that the detector systems can be moved towards the beam within localised structures known as Roman Pots. This idea has been expanded in the proposals for LHC so that there is planned to be an entire section of beam pipe that is movable, the so-called ‘‘Hamburg Pipe’’ scheme. It will be necessary to replace the cryostat connection between the portions of the beamline either side of the 420 m installations. Sets of silicon detectors will be mounted in the Hamburg Pipe. The best performance is envisaged if two sets of detectors are installed in each pipe, separated by approximately 10 m to make full use of the available space, so that the position and angle of the trajectory of an emerging proton can be measured. In the horizontal plane, precisions of approximately 10  $\mu\text{m}$  in position and 1  $\mu\text{rad}$  in angle should be obtainable. The vertical plane is less critical, and less good precisions in the vertical measurements will be accepted. The silicon detectors are of a recent ‘‘edgeless’’ technology to allow the sensitive area

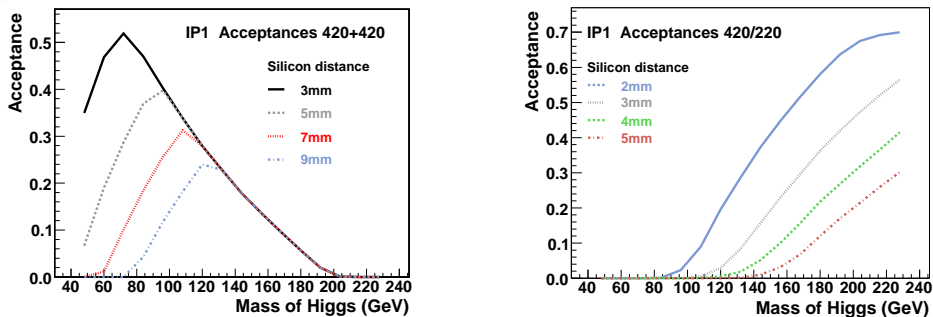


Fig. 8: Acceptance of the forward tagging systems as a function of the mass of the centrally produced system, taken here as a Higgs.

to be moved as close as possible to the main outgoing proton beam.

To perform the tracking of the protons into the relevant detector regions, two programs (FPtrack and Hector) have been written for ATLAS and CMS respectively [11]. They enable us to evaluate the acceptance of the apparatus under various conditions; this is illustrated in Fig. 8. The 420 m systems used on their own provide substantial acceptance for exclusively produced masses up to approximately 150 GeV/c<sup>2</sup>, and even if the silicon can be moved only to 7 mm from the beam, the acceptance at the critical region of 120 GeV/c<sup>2</sup> is not affected. By using the 420 m systems in conjunction with those at 220 m, a greatly extended mass range is achieved with excellent acceptances.

Figure 9(a) illustrates the distribution of the outgoing protons at 420 m in position, horizontally and vertically. The vertical beam spread is small and The mass  $M_X$  of an exclusively produced final state can be evaluated if the momenta of the forward protons can be reconstructed; this is achievable by means of polynomial-based formulae in terms of the horizontal position and angle in the detector regions. The value of  $M_X$  is then  $2\sqrt{p_0 - p_1}(p_0 - p_2)$  for an incoming beam momentum  $p_0$  and outgoing proton momenta  $p_1, p_2$ . Various uncertainties smear out this calculation, notably the intrinsic spread on  $p_0$ . Figure 9(b) shows the mass uncertainty that can be achieved under reasonable assumptions. In nearly all cases this is more precise than the direct measurement in the central detector. An exception to this is when the central state consists of two photoproduced muons. This promises to be a key process which can be used to calibrate the proton momentum measurements.

## 7 Summary

Forward tagging opens up a wide range of diffraction and photoproduction processes at LHC. Following from the HERA experiences, we hope to study these mechanisms at high energy, in which a number of new processes should be observable. There is discovery potential in some cases, while in others, known processes can be studied in more depth. This is a major new area of physics for the LHC.

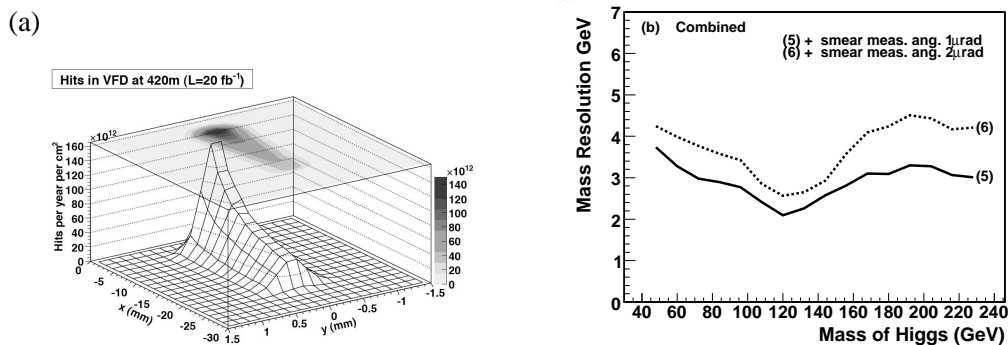


Fig. 9: (a) Typical distribution of a forward proton in a detector system at 420 m (X. Rouby). (b) Mass resolution using 420 m and/or 220 m detector systems if the resolution on the angular measurement is 1  $\mu\text{rad}$  or 2  $\mu\text{rad}$ . (PJB)

## Acknowledgements

Many people have contributed to the work of this part of these Proceedings, through talks and discussion in this Workshop and elsewhere. We would especially mention T. Coughlin, B. Cox, M. Grothe, V. Khoze, A. Pilkington, X. Rouby, C. Royon, M. Taševský and S. Watts, whose presentations at the various meetings have helped to shape much of what is presented in this section.

## References

- [1] V. A. Khoze, A. D. Martin and M. G. Ryskin, *Eur. Phys. J. C* **19**, 477 (2001), [Erratum-ibid. C **20**, 599 (2001)] .
- [2] T. Aaltonen et al., *Phys. Rev. D* **77**, 052004 (2008) .
- [3] T. Aaltonen et al., arXiv: 0902.1271v1 (hep-ex) (2009) .
- [4] S. Heinemeyer et al., *Eur. Phys. J. C* **53**, 231 (2008) .
- [5] S. Heinemeyer et al., arXiv: 0811.4571v1 (hep-ph) (2008) .
- [6] B. E. Cox, F. K. Loebinger and A. D. Pilkington, *JHEP* **10** 090 (2007) .
- [7] N. Schul and K. Piotrkowski, arXiv: 0806.1097v1 (hep-ph) (2008) .
- [8] A. White, arXiv: 0708.1306v1 (2007), 0803.1151v1 (2008) (hep-ph) .
- [9] P. J. Bussey, T. D. Coughlin, J. R. Forshaw, A. D. Pilkington, *JHEP* **0611** 027 (2006) .
- [10] V. A. Khoze, A. D. Martin and M. G. Ryskin, *Eur. Phys. J. C* **55**, 363 (2008) .
- [11] P. J. Bussey, <http://ppewww.physics.gla.ac.uk/~bussey/FPTRACK/>  
J. de Favereau, X. Rouby and K. Piotrkowski, *JINS* **2** (2007) P09005 .

## Chapter 5

# Working Group Cosmic Rays, HERA and the LHC

### Convenors:

*C. Diaconu (DESY and CPPM, Marseille),  
Ch. Kiesling (MPI Munich)  
T. Pierog (FZ Karlsruhe)*

# Introduction

*A. Bunyatyan*<sup>1,2</sup>, *A. Cooper-Sarkar*<sup>3</sup>, *C. Diaconu*<sup>4,5</sup>, *R. Engel*<sup>6</sup>, *C. Kiesling*<sup>7</sup>, *K. Kutak*<sup>4</sup>,  
*S. Ostapchenko*<sup>8,9</sup>, *T. Pierog*<sup>4</sup>, *T.C. Rogers*<sup>10</sup>, *M.I. Strikman*<sup>10</sup>, *T. Sako*<sup>11</sup>.

<sup>1</sup> MPI, Heidelberg, Germany

<sup>2</sup> Yerevan Physics Institute, Armenia

<sup>3</sup> Oxford University, Dept of Physics, Oxford, UK

<sup>4</sup> DESY, Hamburg, Germany

<sup>5</sup> CPPM, Marseille, France

<sup>6</sup> Forschungszentrum Karlsruhe, Institut für Kernphysik, Karlsruhe, Germany

<sup>7</sup> Max-Planck-Institute for Physics, München, Germany

<sup>8</sup> Institutt for fysikk, NTNU Trondheim, Norway

<sup>9</sup> D. V. Skobeltsyn Institute of Nuclear Physics, Moscow State University, Russia

<sup>10</sup> Pennsylvania State University, United States

<sup>11</sup> Solar-Terrestrial Environment Laboratory, Nagoya University, Nagoya, Japan

## Abstract

When particle physics started, cosmic rays were used as source of new particles. Nowadays particle physics is a fundamental key to understand the nature of the very high energy cosmic rays. Above  $10^{14}$  eV, primary cosmic rays are detected via air showers whose development strongly rely on the physics of the forward region of hadronic interactions as tested in the HERA and LHC experiments. After an introduction on air shower phenomenology, we will review how HERA and LHC can constrain the physics used both in hadronic interaction model, or for photon or neutrino primaries.

## 1 Physics questions and problems

One of the central questions of astroparticle physics is that of the sources and propagation of cosmic rays. Even more than 90 years after the discovery of cosmic rays we still don't know their elemental composition at high energy and also the information on the energy spectrum is very limited [1–6]. Knowing the cosmic-ray composition is the key to understanding phenomena such as the *knee*, a change in the power-law index of the cosmic ray flux at about  $3 \times 10^{15}$  eV, the transition from galactic to extra-galactic cosmic rays, and the implications of the existence of ultra-high energy cosmic rays with  $E > 10^{20}$  eV. In particular, composition information is essential for confirming or ruling out models proposed for the sources of ultra-high energy cosmic rays, many of which postulate new particle physics [7, 8].

The flux of cosmic rays is shown in Fig. 1 in the energy range from  $10^{12}$  eV up to the highest energies. It has been scaled by  $E^{2.5}$  to make the characteristic features of the spectrum clearly visible. In addition the equivalent energies of colliders, referring to proton-proton collisions, are indicated by arrows.

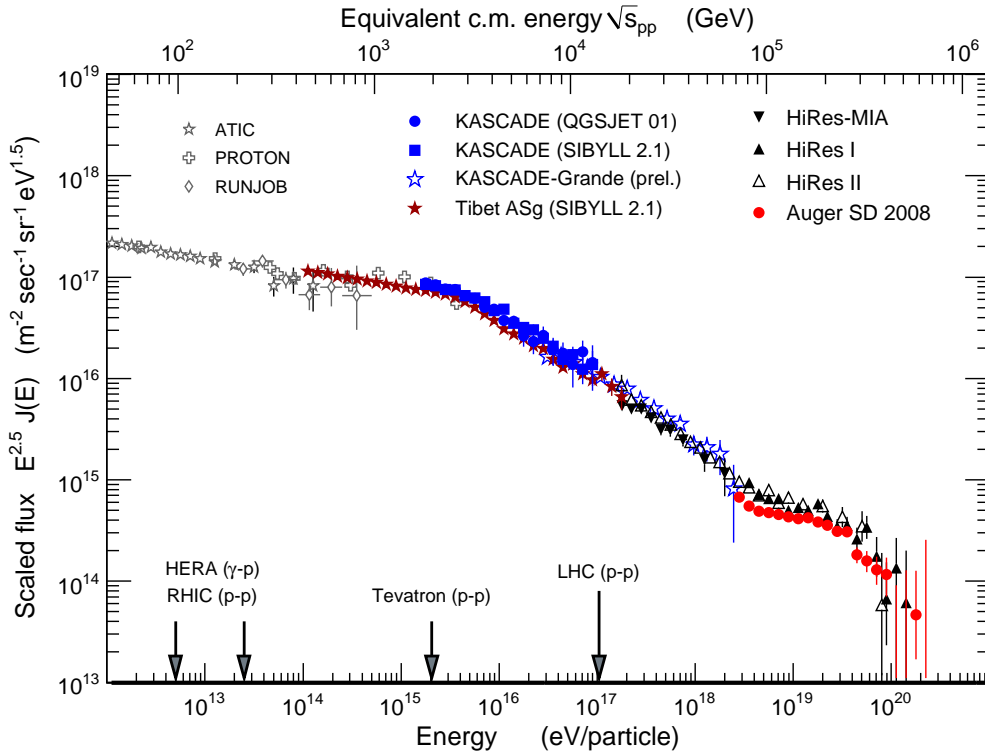


Fig. 1: All-particle flux of cosmic rays as obtained by direct measurements above the atmosphere by the ATIC [9], PROTON [10, 11], and RUNJOB [12] as well as results from air shower experiments. Shown are Tibet AS $\gamma$  results obtained with SIBYLL 2.1 [13], KASCADE data (interpreted with two hadronic interaction models) [14], preliminary KASCADE-Grande results [15], and Akeno data [16, 17]. The measurements at high energy are represented by HiRes-MIA [18, 19], HiRes I and II [20], and Auger [21].

The all-particle spectrum can be approximated by a broken power law  $\propto E^\gamma$  with a spectral index  $\gamma = -2.7$  below  $E_k \approx 4 \times 10^{15}$  eV. At the *knee*, the spectral index changes to  $\gamma \approx -3.1$ . The power law index changes again at about  $10^{18.5}$  eV, a feature that is called the *ankle*. At the very high end of the spectrum there seems to be a suppression of the flux. None of these features of the energy spectrum of cosmic rays is understood so far. In the following some of the related theoretical questions and models are presented for illustration.

- **Knee.** At the knee, the cosmic ray spectrum changes in a way that is very difficult to understand in models with a superposition of different sources, each producing a power-law flux. The knee could be feature of the acceleration process, it could be the result of propagation effects from the sources to Earth (leakage from the Galaxy), or it could be caused by new particle physics. Knowing the change of the elemental composition of cosmic rays through the knee energy region will help to distinguish some of the possible scenarios. Acceleration and propagation models of the knee predict that the spectra of individual elements should each exhibit a knee, however at an energy that is scaled by the



charge of the particle due to the coupling to astrophysical magnetic fields (for example, [22]). In contrast, models postulating new interaction physics (for example, [23]) and the *cannon ball* model [24] predict a scaling proportional to the number of nucleons of the nucleus (i.e. mass number). A review of the different scenarios and their predictions can be found in, for example, [25].

- **Ankle.** The ankle is often regarded as a signature of the transition from Galactic to extragalactic cosmic rays. Such a transition is expected in this energy range because of the strength of the Galactic magnetic fields being of the order of  $3 \mu\text{G}$  [26]. Particles with energies above  $10^{19}$  eV are not confined to the Galaxy. The exact energy of the transition is not known [27]. In the dip model the ankle is a result of the propagation of ultra-high energy cosmic rays through the microwave background radiation [28,29]. Within this model, ultra-high energy cosmic rays have to be dominated by protons. Other models of the ankle explain the feature in the spectrum by the superposition of different power laws from Galactic and extragalactic sources [4, 30, 31]. In such a scenario the composition would most likely be mixed with contributions from both light and heavy elements, i.e. in the range from protons to iron nuclei.
- **Upper end of the spectrum.** A strong suppression of the particle flux above  $E = 7 \times 10^{19}$  eV is expected from the interaction of cosmic rays with the cosmic microwave background radiation, the Greisen-Zatsepin-Kuzmin (GZK) effect [32, 33]. Both protons and nuclei suffer significant energy losses when propagating over distances larger than  $\sim 100$  Mpc. On the other hand, the sources could have reached their upper limit of acceleration or injection power and we would be mistaken by attributing the observations just to the GZK suppression. In any case the sources of such high energy particles have to be rather exotic [34]. One would have to build the LHC with a circumference of the length of the orbit of the planet Mercury to reach the same energy with the currently available technology. Particles of such energies also probe Lorentz invariance at extreme energies [35, 36] and hence allow to search for space-time fluctuations (for example, see [37, 38]).

To solve these questions, multi-messenger and multi-observable measurements are needed. First of all, the flux, composition and arrival direction distribution of cosmic rays will have to be measured with high statistics and precision. Secondly, complementary information obtained from observing secondary particle fluxes (gamma-rays and neutrinos) will greatly help to disentangle different source and propagation scenarios [39, 40].

At energies above  $10^5$  GeV, the flux of cosmic rays is so low that it cannot be measured directly using particle detectors. Therefore all cosmic-ray measurements of higher energy are based on analyzing the secondary particle showers, called extensive air showers, which they produce in the atmosphere of the Earth. To interpret the characteristics of extensive air showers in terms of primary particle type and energy, detailed modeling of the various interaction and decay processes of the shower particles is needed (for example, see [41, 42]). In particular, the elemental composition of the cosmic-ray flux reconstructed from air shower data depends very much on the assumptions on hadronic multiparticle production.

## 2 Air shower phenomenology and hadronic interactions

A commonly employed technique to observe air showers is the measurement of secondary particles (electrons, photons and muons) reaching the ground [2]. Using an array of particle detectors (for example, sensitive to  $e^\pm$  and  $\mu^\pm$ ), the arrival direction and information on mass and energy of the primary cosmic ray can be reconstructed. The main observables are the number and the lateral and temporal distributions of the different secondary particles. At energies above  $\sim 10^{17}$  eV, the longitudinal profile of a shower can be directly observed by measuring the fluorescence light induced by the charged particles traversing the atmosphere [43]. Two main observables can be extracted from the longitudinal shower profile: the energy deposit or the number of particles,  $N_{\max}$ , at the shower maximum and  $X_{\max}$ , the atmospheric depth of the maximum. Again, these quantities can be used to estimate the energy and mass of the primary particles. Shower-to-shower fluctuations of all observables make it impossible to derive the mass of the primary particle on a shower-to-shower basis. On the other hand, these fluctuations provide very useful and complementary composition information.

To qualitatively understand the dependence of the air shower development on some basic parameters of particle interaction, decay, and production, a very simple toy model can be used. Although initially developed for electromagnetic (EM) showers [44] it can also be applied to hadronic showers [45].

First we consider a simplified electromagnetic shower of only one particle type. A particle of energy  $E$  produces in an interaction two new particles of the same type with energies  $E/2$ , after a fixed interaction length of  $\lambda_e$ . With  $n$  being the number of generations (consecutive interactions), the number of particles at a given depth  $X = n \cdot \lambda_e$  follows from

$$N(X) = 2^n = 2^{X/\lambda_e}, \quad (1)$$

with the energy  $E$  per particle for a given primary energy  $E_0$  being

$$E(X) = \frac{E_0}{2^{X/\lambda_e}}. \quad (2)$$

Defining the critical energy  $E_c$  ( $\sim 85$  MeV in air) as the energy below which continuous energy loss processes (i.e. ionization) dominate over particle production, one can make the assumption that the shower maximum is reached at a depth at which the energy of the secondary particles is degraded to  $E_c$ . Then two main shower observables are given by

$$N_{\max} = \frac{E_0}{E_c} \quad \text{and} \quad X_{\max}^e(E_0) \sim \lambda_e \cdot \ln \left( \frac{E_0}{E_c} \right). \quad (3)$$

Of course, this very simplified picture does not reproduce the detailed behavior of an EM shower, but two important features are well described: the number of particles at shower maximum is proportional to  $E_0$  and the depth of shower maximum depends logarithmically on the primary energy  $E_0$ .

Generalizing this idea, a hadronic interaction of a particle with energy  $E$  is assumed to produce  $n_{\text{tot}}$  new particles with energy  $E/n_{\text{tot}}$ , two third of which being charged particles  $n_{\text{ch}}$  (charged pions) and one third being neutral particles  $n_{\text{neut}}$  (neutral pions). Neutral particles decay

immediately into em. particles ( $\pi^0 \rightarrow 2\gamma$ ), feeding the em. shower component. After having traveled a distance corresponding to the mean interaction length  $\lambda_{\text{ine}}$ , charged particles re-interact with air nuclei as long as their energy exceeds some typical decay energy  $E_{\text{dec}}$ .

In the end, most of the energy of an air shower is carried by em. particles ( $\sim 90\%$  for  $n = 6$ ). The depth of shower maximum is given by that of the em. shower component,  $X_{\text{max}}^e$ . As the first hadronic interaction produces em. particles of energy  $\sim E_0/n_{\text{tot}}$  one gets

$$X_{\text{max}}(E_0) \sim \lambda_{\text{ine}} + X_{\text{max}}^e(E_0/n_{\text{tot}}) \quad (4)$$

$$\sim \lambda_{\text{ine}} + \lambda_e \cdot \ln \left( \frac{E_0}{n_{\text{tot}} E_c} \right), \quad (5)$$

where  $\lambda_{\text{ine}}$  is the hadronic interaction length. This simplified expression for the shower depth of maximum neglects the em. sub-showers initiated by hadrons of later generations. The inclusion of higher hadronic generations does not change the structure of Eq. (5), see [46].

Following [45], we assume that all charged hadrons decay into muons when their energy reaches  $E_{\text{dec}}$ . By construction, charged particles will reach the energy  $E_{\text{dec}}$  after  $n$  interactions

$$E_{\text{dec}} = \frac{E_0}{(n_{\text{tot}})^n}. \quad (6)$$

Since one muon is produced in the decay of each charged particle, we get for the number of muons in an hadronic shower

$$N_\mu = n_{\text{ch}}^n = \left( \frac{E_0}{E_{\text{dec}}} \right)^\alpha, \quad (7)$$

with  $\alpha = \ln n_{\text{ch}} / \ln n_{\text{tot}} \approx 0.82 \dots 0.95$  [46, 47]. The number of muons produced in an air shower depends not only on the primary energy and air density, but also on the charged and total particle multiplicities of hadronic interactions.

In case of showers initiated by nuclei, one can use the superposition model to deduce the expectation value for inclusive observables [48]. In this model, a nucleus with mass  $A$  and energy  $E_0$  is considered as  $A$  independent nucleons with energy  $E_h = E_0/A$ . This leads to

$$N_{\text{max}}^A \approx A \cdot \frac{E_h}{E_c} = \frac{E_0}{E_c} = N_{\text{max}} \quad (8)$$

$$X_{\text{max}}^A \approx X_{\text{max}}(E_0/A) \quad (9)$$

$$N_\mu^A \approx A \cdot \left( \frac{E_0/A}{E_{\text{dec}}} \right)^\alpha = A^{1-\alpha} \cdot N_\mu. \quad (10)$$

There is no mass dependence of the number of charged particles at shower maximum. The number of muons and the depth of maximum depend on the mass of the primary particle. The heavier the shower-initiating particle the more muons are expected for a given primary energy. For example, an iron-induced shower has about 1.4 times more muons than a proton shower of the same energy.

There are several code packages available for performing Monte Carlo simulations of extensive air showers. The more frequently used programs are AIRES [50], CORSIKA [51],

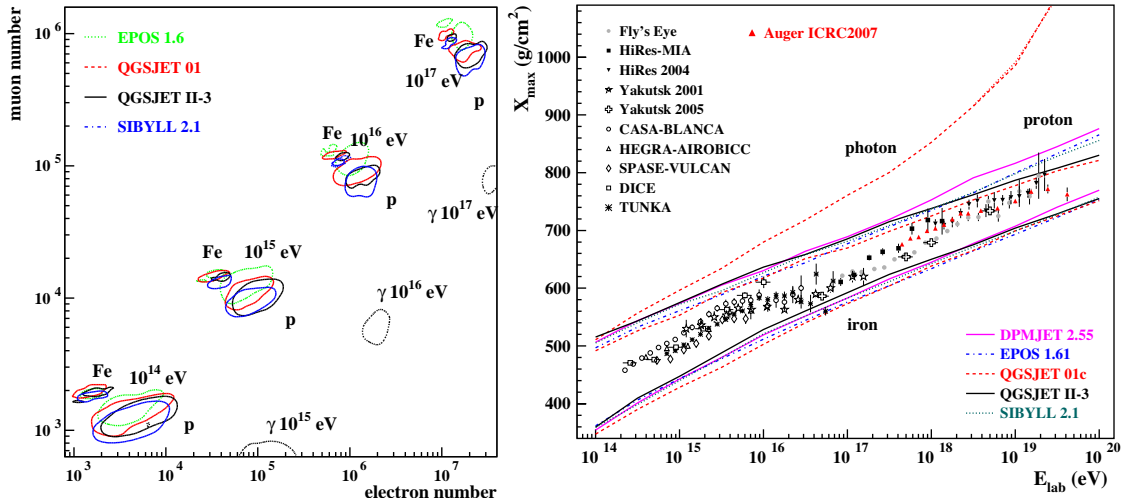


Fig. 2: Predictions for air shower observables for proton-, iron- and photon-induced showers. Left panel: Shown are the correlation between the number of electrons and muons at ground as expected with different hadronic interaction models (see text) [49]. Right panel: compilation of data of the mean depth of shower maximum and model predictions [49].

CONEX [52], SENECA [53], MOCCA [54], and COSMOS [55]. These packages provide either self-made hadronic interaction models that cover the full energy range from the particle production threshold to the highest energies or employ external models for the simulation of these interactions. Due to the different methods of modeling, external hadronic interaction models are typically optimized for low- or high-energy interactions.

Low-energy models describe hadronic interactions in terms of intermediate resonances (for example, the isobar model) and parametrizations of data. They are applicable in the energy range from the single particle production threshold up to several hundred GeV. Models that are often applied in simulations are FLUKA (which is a complete cascade simulation package that includes both low- and high-energy models) [56], GHEISHA [57], UrQMD [58], and the more specialized code SOPHIA [59]. Low-energy models are typically well-tuned to the large number of data sets from fixed target measurements. Still the differences between the model predictions are significant and can lead to very different muon densities in air shower simulations [60, 61].

High-energy interaction models are typically very complex models and based on Regge theory [62], Gribov's Reggeon calculus [63], and perturbative QCD. Central elements of these models are the production of QCD minijets and the formation of QCD color strings that fragment into hadrons. The most frequently used models are QGSJET 01 [64, 65] and II [66, 67], SIBYLL 2.1 [48, 68, 69], EPOS 1.6 [70, 71] and DPMJET II [72] and III [73, 74]. The extrapolation of these models to very high energy depends on the internal structure of the model and the values of the tuned model parameters and is, in general, rather uncertain. Different extrapolations obtained within one model by varying the parameters can be found in [75, 76] and represent only a lower limit to the uncertainty of the predictions.

Monte Carlo models typically applied in high energy physics are not used for air shower

simulations. Most of these models do not allow the simulation of particle production with air nuclei as target or are applicable in a rather limited energy range (however, see [77] for a study with HIJING [78]).

Detailed numerical simulations of extensive air showers confirm the overall functional relations between the shower energy, depth of shower maximum, and number of electrons and muons that have been derived within the simple Heitler-Matthews model. The expected correlation between the number of electrons and muons at a surface detector at sea level is shown in Fig. 2. The simulations were made for vertical showers with the air shower simulation package CORSIKA [51]. The predictions obtained for the interaction models QGSJET 01, QGSJET II.03, SIBYLL 2.1, and EPOS 1.6 are compared. While there is a reasonable discrimination power at low energy, the model-induced uncertainties do not allow us to discriminate between even the most extreme composition assumptions at ultra-high energy if only the number of muons and electrons is measured. The situation seems to be a somewhat better in case of the mean depth of shower maximum, but the model uncertainties are still very large.

It can be concluded from both simple cascade models of air showers and numerical studies [54,75,76,79] that the following characteristics of hadronic interactions are of central importance to air shower predictions

- Inelastic cross section for proton-air and pion/kaon-air interactions,
- Ratio between neutral and charged secondary particles (in other words,  $\pi^0$  and all other particles),
- Energy distribution of the most energetic secondary particles,
- Multiplicity of high energy secondary particles,
- Scaling or scaling violation of secondary particle distributions,
- Cross section for diffractive dissociation (i.e. low-multiplicity events).

It is clear that hadronic interactions at both high and low energies are influencing the model predictions for air showers. Low-energy interactions do not influence the depth of shower maximum very much but are of direct relevance to the muon density at large lateral distance from the shower core, see [60,61,80].

### 3 Limitations of air shower simulations

Before discussing shortcomings of air shower simulations it has to be emphasized that modern simulation packages provide a very good overall description of air shower observables. The situation has very much improved in comparison to the early days of air shower simulation [81].

Modern cosmic-ray detectors like KASCADE [82] and the Pierre Auger Observatory [83] measure several observables for each shower. By choosing different observables, the model dependence of the reconstructed energy and primary particle mass can be estimated. Studies show that the uncertainty in interpreting the data from these experiments is dominated by the uncertainty in predicting hadronic multi-particle production in extensive air showers. In the following we will discuss some representative examples that illustrate the limitations of currently available hadronic interaction models and air shower simulation tools.

The KASCADE Collaboration analyzed the measured number of electrons and muons at detector level to derive the primary energy and composition of the showers in the knee energy

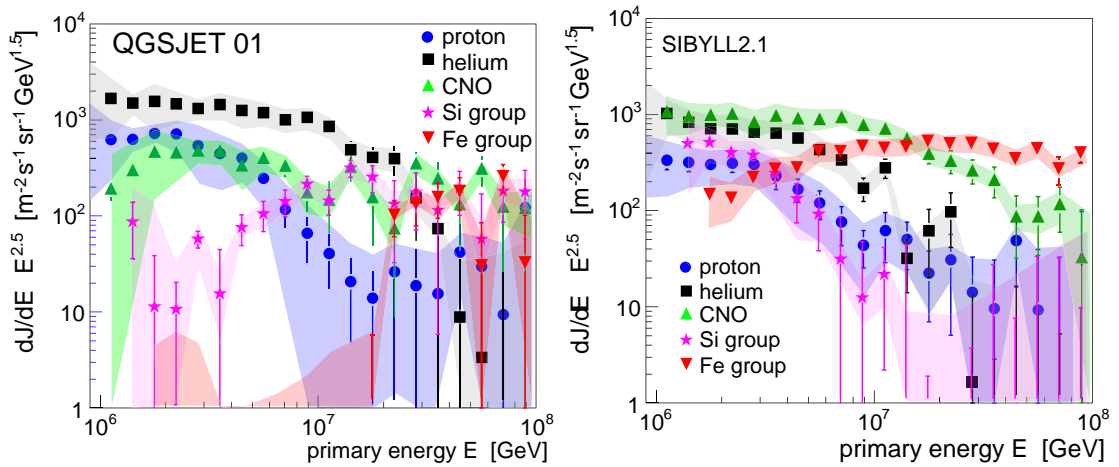


Fig. 3: Cosmic-ray flux for five elemental groups in the knee energy range as derived from KASCADE data using the hadronic interaction models QGSJET 01 (left panel) and SIBYLL 2.1 (right panel) [82].

region. Having collected more than 40 million showers it is still not possible to obtain a clear picture of the elemental composition [14]. Applying different hadronic interaction models leads to significantly different fluxes for the elemental groups considered in the analysis, see Fig. 3. In particular, the fundamental question of having a mass- or charge-dependent scaling of the knee positions of the individual flux components cannot be answered. Moreover, in an earlier study the KASCADE Collab. showed that selecting different observables gives inconsistent composition results even if the same hadronic interaction model is employed in the analysis [84].

A comparison of the world data set on electron-muon based and  $X_{\max}$  based composition measurements, using the same hadronic interaction models, shows a systematic inconsistency between composition results based on surface detector data and that based on the measurement of the mean depth of shower maximum [85]. Analysis of the surface detector data indicate a heavier primary composition than one would expect from  $\langle X_{\max} \rangle$  data. This is most clearly found in experiments that measure both  $X_{\max}$  and an observable related to the number of muons. For example, the prototype experiment HiRes-MIA [86] studied showers in the energy range from  $10^{17}$  to  $10^{18.5}$  eV. The measured muon densities at 600 m from the core could only be interpreted as iron-dominated composition, but the mean  $X_{\max}$  indicated a transition to a proton-dominated composition [19].

The analysis of Auger data with QGSJET II [87] leads to a similar discrepancy at an energy of about  $10^{19}$  eV. Using universality features of very high energy showers  $E > 10^{18}$  eV, one can relate the electromagnetic shower size at a lateral distance of 1000 m to the shower energy and the depth of shower maximum [88, 89]. The employed universality features are the same for showers simulated with the interaction models QGSJET II and SIBYLL 2.1. Considering showers at different angles and employing the independently measured depth of shower maximum, the observed muon signal can be set in relation to the predicted muon signal as shown in Fig. 4. Adopting the nominal energy scale of the Auger fluorescence detectors, the number of muons at 1000 m from the core is found to be twice as large as predicted by simulations with proton

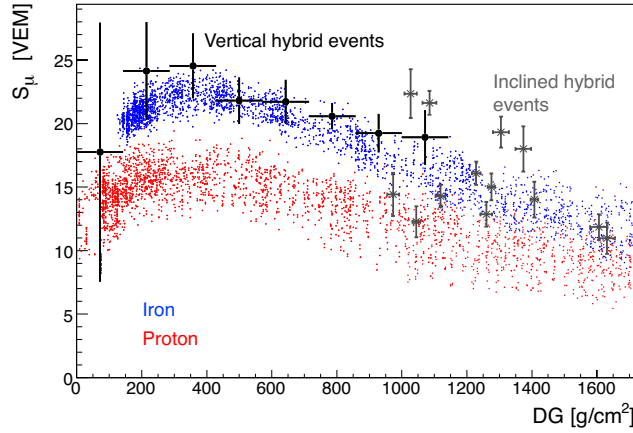


Fig. 4: Simulated and derived muon density as function of the detector depth relative to the depth of shower maximum, DG. The muon density is derived from Auger data at a distance of 1000 m from the shower core. The points show the prediction of simulations with QGSJET II and an energy increased by 30% relative to the reconstructed nominal shower energy, for details see [87].

showers. This number should be compared to that of iron-induced showers for which one expects a muon number increased by the factor 1.38 (QGSJET II) or 1.27 (SIBYLL 2.1). Increasing the energy scale by 30% as the constant intensity cut analysis of the data suggests and assuming a iron dominated composition seems to bring the surface detector data almost into agreement with the model predictions. On the other hand, the measured  $\langle X_{\max} \rangle$  data is at variance with an iron-dominated composition hypothesis at  $10^{19}$  eV.

#### 4 Main sources of model uncertainties

In the foreseeable future soft multi-particle production will not be calculable within QCD. Therefore the modeling of cosmic-ray interactions will continue to strongly depend on the input from accelerator experiments. There are two principal types of input needed for model building. First of all, data on cross sections, secondary particle distributions and multiplicities, as well as parton densities form the basis for tuning the parameters of the models. Secondly, guidance from further development and experimental verification of theoretical and phenomenological concepts and ideas will be crucial for model development.

At the current stage even the most fundamental question of scaling of secondary particle distributions in the forward phase space region cannot be answered<sup>1</sup>. Within some models very strong scaling violation of the distribution of leading particles is expected [90]. So far there is no experimental proof of such a scenario. If realized in nature, the implications will be profound and most of the very high energy cosmic ray data will have to be interpreted in terms of a light composition. The lack of data on hadron production in forward direction, with the exception of HERA measurements, is one of the main source of model uncertainties. The HERA measure-

<sup>1</sup>Feynman scaling is, of course, violated for central particle production.

ments of leading proton and neutron distributions are the only high energy data available and indicate surprisingly small scaling violations [91]. It has to be expected that the leading particle distribution is correlated with the centrality of the interaction, as found in heavy ion collisions. LHC data from the big experiments [92] and LHCf [93] will be of decisive importance in this respect.

The energy fraction transferred in an interaction to particles of very short lifetime, that decay to photons and electrons, is of direct relevance to air shower simulations. Currently the particle distribution of neutral pions is derived indirectly from the distributions of charged secondaries. With the exception of the UA7 [94], no high energy data of secondary  $\pi^0$  and photon distributions exist.

The extrapolation of the total and inelastic cross sections is currently hampered by the discrepant measurements from Tevatron experiments. Extrapolating the model cross section based on the CDF data [95] gives different air shower predictions than using the E710 [96] and E811 [97] data [76]. The measurement of the proton-proton cross section at LHC will reduce this uncertainty very much. Related to this cross section is, of course, the question of pion-proton and kaon-proton cross sections. The highest energy data available for the pion-nucleus cross section is that of SELEX [98]. There is no generally accepted theoretical model of how to extrapolate the ratio between proton-proton and meson-proton cross sections.

One further source of uncertainty stems from the fact that hadronic cross sections and secondary particle distributions are needed for the interaction with light nuclei in air shower simulations. At high energy, the calculation of such nuclear cross sections and particle distributions is not straightforward. At low energy, the Glauber approximation [99] is known to work remarkably well. Already the low-energy data indicates, however, the need for inelastic screening corrections for the calculation of which no reliable framework exists. For example, cross sections estimates based on air shower data indicate smaller particle production cross sections than current model extrapolations (see compilation in [100]).

One of the central theoretical questions that has to be addressed in all hadronic interaction models is that of the range of applicability of perturbative QCD. At high energy, most hadrons are produced in the fragmentation of minijets. It is of great importance to understand the correlations between individual parton-parton interactions, to which degree they can be considered independent from each other, their kinematic and color flow link to the remnants of the incoming hadrons, and the minimum momentum transfer for which such a picture can be applied. Closely related to this question is the modeling of non-linear effects in the low- $x$  parton evolution and possible saturation or high-density shadowing effects. HERA data is of direct relevance in this respect as are RHIC measurements too. A high density of partons can also influence string fragmentation and modify particle yields relative to those measured at low energy. There are different model predictions that address this point (see, for example, [70, 101–103]) but the experimental data are not conclusive.

## References

- [1] S. P. Swordy *et al.*, *Astropart. Phys.* **18**, 129 (2002), [astro-ph/0202159](#).
- [2] A. Haungs, H. Rebel, and M. Roth, *Rept. Prog. Phys.* **66**, 1145 (2003).



- [3] R. Engel and H. Klages, *Comptes Rendus Physique* **5**, 505 (2004).
- [4] A. M. Hillas, *J. Phys.* **G31**, R95 (2005).
- [5] K.-H. Kampert, *Nucl. Phys. Proc. Suppl.* **165**, 294 (2007),  
arXiv:astro-ph/0611884.
- [6] K.-H. Kampert, *J. Phys. Conf. Ser.* **120**, 062002 (2008), arXiv:0801.1986  
[astro-ph].
- [7] P. Bhattacharjee and G. Sigl, *Phys. Rev.* **D51**, 4079 (1995), astro-ph/9412053.
- [8] D. F. Torres and L. A. Anchordoqui, *Rept. Prog. Phys.* **67**, 1663 (2004),  
astro-ph/0402371.
- [9] ATIC-2 Collaboration, H. S. Ahn *et al.* Prepared for 28th International Cosmic Ray  
Conference (ICRC 2003), Tsukuba, Japan, 31 Jul - 7 Aug 2003, 1853-1856.
- [10] N. L. Grigorov *et al.*, *Yad. Fiz.* **11**, 1058 (1970).
- [11] N. L. Grigorov *et al.* Proc. of 12th Int. Cosmic Ray Conf. (Hobart), vol. 2, p. 206, 1971.
- [12] RUNJOB Collaboration, V. A. Derbina *et al.*, *Astrophys. J.* **628**, L41 (2005).
- [13] Tibet AS $\gamma$  Collaboration, M. Amenomori *et al.*, *Astrophys. J.* **678**, 1165 (2008),  
arXiv:0801.1803 [hep-ex].
- [14] KASCADE Collaboration, T. Antoni *et al.*, *Astropart. Phys.* **24**, 1 (2005),  
astro-ph/0505413.
- [15] A. Haungs *et al.* To appear in Proc. of XIV ISVHECRI 2006, Weihai, China, 2006.
- [16] M. Nagano *et al.*, *J. Phys.* **G10**, 1295 (1984).
- [17] M. Nagano *et al.*, *J. Phys.* **G18**, 423 (1992).
- [18] HiRes-MIA Collaboration, T. Abu-Zayyad *et al.*, *Astrophys. J.* **557**, 686 (2001),  
astro-ph/0010652.
- [19] HiRes-MIA Collaboration, T. Abu-Zayyad *et al.*, *Phys. Rev. Lett.* **84**, 4276 (2000),  
astro-ph/9911144.
- [20] HiRes Collaboration, R. Abbasi *et al.*, *Phys. Rev. Lett.* **100**, 101101 (2008),  
arXiv:astro-ph/0703099.
- [21] Pierre Auger Collaboration, J. Abraham *et al.*, *Phys. Rev. Lett.* **101**, 061101 (2008),  
arXiv:0806.4302 [astro-ph].
- [22] E. G. Berezhko and H. J. Voelk (2007), arXiv:0704.1715 [astro-ph].
- [23] A. A. Petrukhin, *Nucl. Phys. Proc. Suppl.* **151**, 57 (2006).

- [24] A. Dar and A. De Rujula, Phys. Rep. **466**, 179 (2006), arXiv:hep-ph/0606199.
- [25] J. R. Hoerandel, Astropart. Phys. **19**, 193 (2003), arXiv:astro-ph/0210453.
- [26] J. L. Han, Nucl. Phys. Proc. Suppl. **175-176**, 62 (2008).
- [27] C. De Donato and G. A. Medina-Tanco (2008), arXiv:0807.4510 [astro-ph].
- [28] V. S. Berezhinsky, S. I. Grigorieva, and B. I. Hnatyk, Astropart. Phys. **21**, 617 (2004), astro-ph/0403477.
- [29] R. Aloisio *et al.*, Astropart. Phys. **27**, 76 (2007), astro-ph/0608219.
- [30] T. Wibig and A. W. Wolfendale, J. Phys. **G31**, 255 (2005), astro-ph/0410624.
- [31] D. Allard, E. Parizot, and A. V. Olinto, Astropart. Phys. **27**, 61 (2007), astro-ph/0512345.
- [32] K. Greisen, Phys. Rev. Lett. **16**, 748 (1966).
- [33] G. T. Zatsepin and V. A. Kuzmin, J. Exp. Theor. Phys. Lett. **4**, 78 (1966).
- [34] A. M. Hillas, Ann. Rev. Astron. Astrophys. **22**, 425 (1984).
- [35] S. R. Coleman and S. L. Glashow, Phys. Rev. **D59**, 116008 (1999), hep-ph/9812418.
- [36] W. Bietenholz (2008), arXiv:0806.3713 [hep-ph].
- [37] F. R. Klinkhamer (2007), arXiv:0710.3075 [hep-ph]. Invited talk at 3rd Mexican Meeting on Mathematical and Experimental Physics, Mexico City, Mexico, 10-14 Sep 2007.
- [38] S. T. Scully and F. W. Stecker (2008), arXiv:0811.2230 [astro-ph].
- [39] W. Hofmann, J. Phys. Conf. Ser. **120**, 062005 (2008).
- [40] J. K. Becker, Phys. Rept. **458**, 173 (2008), arXiv:0710.1557 [astro-ph].
- [41] J. Knapp, D. Heck, S. J. Sciutto, M. T. Dova, and M. Risse, Astropart. Phys. **19**, 77 (2003), arXiv:astro-ph/0206414.
- [42] L. Anchordoqui *et al.*, Ann. Phys. **314**, 145 (2004), hep-ph/0407020.
- [43] Fly's Eye Collaboration, R. M. Baltrusaitis *et al.*, Nucl. Instrum. Meth. **A240**, 410 (1985).
- [44] W. Heitler, *The Quantum Theory of Radiation*, third edition<sup>th</sup> edn. Oxford University Press, London, 1954.
- [45] J. Matthews, Astropart. Phys. **22**, 387 (2005).
- [46] J. Alvarez-Muniz, R. Engel, T. K. Gaisser, J. A. Ortiz, and T. Stanev, Phys. Rev. **D66**, 033011 (2002), astro-ph/0205302.

- [47] T. Pierog, R. Engel, and D. Heck, Czech. J. Phys. **56**, A161 (2006), [arXiv:astro-ph/0602190](#).
- [48] J. Engel, T. K. Gaisser, T. Stanev, and P. Lipari, Phys. Rev. **D46**, 5013 (1992).
- [49] D. Heck. Talk given at CORSIKA School 2008, see <http://www-ik.fzk.de/corsika/corsika-school2008/> and private communication, 2008.
- [50] S. J. Sciutto (1999), [astro-ph/9911331](#).
- [51] D. Heck, J. Knapp, J. Capdevielle, G. Schatz, and T. Thouw, *CORSIKA: a Monte Carlo code to simulate extensive air showers* (unpublished). Wissenschaftliche Berichte FZKA 6019, Forschungszentrum Karlsruhe, 1998.
- [52] T. Bergmann *et al.*, Astropart. Phys. **26**, 420 (2007), [astro-ph/0606564](#).
- [53] H.-J. Drescher and G. R. Farrar, Phys. Rev. **D67**, 116001 (2003), [astro-ph/0212018](#).
- [54] A. M. Hillas, Nucl. Phys. Proc. Suppl. **52B**, 29 (1997).
- [55] K. Kasahara *et al.*, *COSMOS* (unpublished). [Http://cosmos.n.kanagawa-u.ac.jp/cosmosHome](http://cosmos.n.kanagawa-u.ac.jp/cosmosHome).
- [56] F. Ballarini *et al.*, J. Phys. Conf. Ser. **41**, 151 (2006).
- [57] H. Fesefeldt. Preprint PITHA-85/02, RWTH Aachen, 1985.
- [58] M. Bleicher *et al.*, J. Phys. G: Nucl. Part. Phys. **25**, 1859 (1999).
- [59] A. Mücke, R. Engel, J. P. Rachen, R. J. Protheroe, and T. Stanev, Comput. Phys. Commun. **124**, 290 (2000), [astro-ph/9903478](#).
- [60] H.-J. Drescher, M. Bleicher, S. Soff, and H. Stoecker, Astropart. Phys. **21**, 87 (2004), [astro-ph/0307453](#).
- [61] C. Meurer, J. Bluemer, R. Engel, A. Haungs, and M. Roth, Czech. J. Phys. **56**, A211 (2006), [arXiv:astro-ph/0512536](#).
- [62] P. D. B. Collins, *An Introduction to Regge Theorie & High Energy Physics*,. Cambridge University Press,, Cambridge, 1977.
- [63] V. N. Gribov, Sov. Phys. JETP **26**, 414 (1968).
- [64] N. N. Kalmykov and S. S. Ostapchenko, Phys. Atom. Nucl. **56**, 346 (1993).
- [65] N. N. Kalmykov, S. S. Ostapchenko, and A. I. Pavlov, Nucl. Phys. Proc. Suppl. **52B**, 17 (1997).
- [66] S. Ostapchenko, Phys. Rev. **D74**, 014026 (2006), [arXiv:hep-ph/0505259](#).

- [67] S. Ostapchenko, Phys. Lett. **B636**, 40 (2006), arXiv:hep-ph/0602139.
- [68] R. S. Fletcher, T. K. Gaisser, P. Lipari, and T. Stanev, Phys. Rev. **D50**, 5710 (1994).
- [69] R. Engel, T. K. Gaisser, T. Stanev, and P. Lipari. Prepared for 26th International Cosmic Ray Conference (ICRC 99), Salt Lake City, Utah, 17-25 Aug 1999.
- [70] K. Werner, F.-M. Liu, and T. Pierog, Phys. Rev. **C74**, 044902 (2006), arXiv:hep-ph/0506232.
- [71] T. Pierog and K. Werner, Phys. Rev. Lett. **101**, 171101 (2008), arXiv:astro-ph/0611311.
- [72] J. Ranft, Phys. Rev. **D51**, 64 (1995).
- [73] S. Roesler, R. Engel, and J. Ranft, *The Monte Carlo event generator DPMJET-III at cosmic ray energies* (unpublished). Prepared for 27th International Cosmic Ray Conference (ICRC 2001), Hamburg, Germany, 7-15 Aug 2001, p. 439.
- [74] F. W. Bopp, J. Ranft, R. Engel, and S. Roesler, Phys. Rev. **C77**, 014904 (2008), hep-ph/0505035.
- [75] M. Zha, J. Knapp, and S. Ostapchenko (2003). Prepared for 28th International Cosmic Ray Conference (ICRC 2003), Tsukuba, Japan, 31 Jul - 7 Aug 2003, p. 515-518.
- [76] R. Engel, Nucl. Phys. Proc. Suppl. **122**, 40 (2003).
- [77] V. Topor Pop, M. Gyulassy, and H. Rebel, Astropart. Phys. **10**, 211 (1999), nucl-th/9809014.
- [78] M. Gyulassy and X.-N. Wang, Comput. Phys. Commun. **83**, 307 (1994), arXiv:nucl-th/9502021.
- [79] R. Luna, A. Zepeda, C. A. Garcia Canal, and S. J. Sciutto, Phys. Rev. **D70**, 114034 (2004), hep-ph/0408303.
- [80] H.-J. Drescher and G. R. Farrar, Astropart. Phys. **19**, 235 (2003), hep-ph/0206112.
- [81] T. K. Gaisser, R. J. Protheroe, K. E. Turver, and T. J. L. McComb, Rev. Mod. Phys. **50**, 859 (1978).
- [82] KASCADE Collaboration, T. Antoni *et al.*, Nucl. Instrum. Meth. **A513**, 490 (2003).
- [83] Pierre Auger Collaboration, J. Abraham *et al.*, Nucl. Instrum. Meth. **A523**, 50 (2004).
- [84] KASCADE Collaboration, T. Antoni *et al.*, Astropart. Phys. **16**, 245 (2002), astro-ph/0102443.
- [85] J. R. Hörandel, J. Phys. **G29**, 2439 (2003), astro-ph/0309010.
- [86] HiRes Collaboration, T. Abu-Zayyad *et al.*, Nucl. Instrum. Meth. **A450**, 253 (2000).

- [87] Pierre Auger Collaboration, R. Engel (2007), [arXiv:0706.1921 \[astro-ph\]](#).
- [88] Pierre Auger Collaboration, A. S. Chou *et al.* Proc. of 29th Int. Cosmic Ray Conference (ICRC 2005), Pune, India, 3-11 Aug 2005, p. 319.
- [89] F. Schmidt, M. Ave, L. Cazon, and A. S. Chou, *Astropart. Phys.* **29**, 355 (2008), [arXiv:0712.3750 \[astro-ph\]](#).
- [90] H. J. Drescher, A. Dumitru, and M. Strikman, *Phys. Rev. Lett.* **94**, 231801 (2005), [arXiv:hep-ph/0408073](#).
- [91] R. Engel, *Nucl. Phys. B (Proc. Suppl.)* **75A**, 62 (1999), [astro-ph/9811225](#).
- [92] M. Albrow *et al.*, *Prospects for diffractive and forward physics at the LHC* (unpublished). CERN-LHCC-2006-039, CMS Note-2007/002, TOTEM Note 06-5.
- [93] T. Sako *et al.*, *Nucl. Instrum. Meth.* **A578**, 146 (2007).
- [94] UA7 Collaboration, E. Pare *et al.*, *Phys. Lett.* **B242**, 531 (1990).
- [95] CDF Collaboration, F. Abe *et al.*, *Phys. Rev.* **D50**, 5550 (1994).
- [96] E710 Collaboration, N. A. Amos *et al.*, *Phys. Rev. Lett.* **63**, 2784 (1989).
- [97] E811 Collaboration, C. Avila *et al.*, *Phys. Lett.* **B445**, 419 (1999).
- [98] SELEX Collaboration, U. Dersch *et al.*, *Nucl. Phys.* **B579**, 277 (2000), [arXiv:hep-ex/9910052](#).
- [99] R. J. Glauber and G. Matthiae, *Nucl. Phys.* **B21**, 135 (1970).
- [100] R. Ulrich, J. Blümer, R. Engel, F. Schüssler, and M. Unger (2007), [arXiv:0709.1392 \[astro-ph\]](#). In Proc. of 12th Int. Conf. on Elastic and Diffractive Scattering, Hamburg, May 21 - 25, 2007.
- [101] C. Pajares, D. Sousa, and R. A. Vazquez, *Phys. Rev. Lett.* **86**, 1674 (2001), [arXiv:astro-ph/0005588](#).
- [102] J. Dias de Deus, M. C. Espirito Santo, M. Pimenta, and C. Pajares, *Phys. Rev. Lett.* **96**, 162001 (2006), [arXiv:hep-ph/0507227](#).
- [103] J. Alvarez-Muniz *et al.*, *Astropart. Phys.* **27**, 271 (2007), [hep-ph/0608050](#).

# Experimental Results

*A. Bunyatyan, A. Cooper-Sarkar, C. Diaconu, R. Engel, C. Kiesling, K. Kutak, S. Ostapchenko, T. Pierog, T.C. Rogers, M.I. Strikman, T. Sako*

## 1 From HERA to LHC and Cosmic Rays

There seem to be two prime motivations for discussing HERA data in connection with the future running at the LHC and the physics of cosmic rays. First of all, HERA provides a precise picture of the structure of the proton, which are the scattering partners at the LHC. Concerning cosmic ray physics, the electron-proton ( $ep$ ) reactions at HERA can be viewed as collisions of ultra-high-energy photons - emitted by the electron - with nuclear matter. Comparing to the cosmic ray energy spectrum impinging on the earth's atmosphere, the HERA collider provides a photon beam equivalent to 50 TeV on a stationary proton target, lying about half way on a logarithmic scale, at about almost  $10^{14}$  eV, between the intensity maximum at 1 GeV and the “ankle” of the cosmic ray energy spectrum. Such high energy photon-proton collisions are of utmost importance for observational astrophysics, in particular for the understanding of the interactions of ultra-high-energy cosmic photons with our atmosphere which usually serves as the target in the cosmic ray experiments.

High energy photon interactions with hadronic matter are governed mainly by the strong interaction, which can be successfully described by quantum chromodynamics (QCD) as long as some “hard scale” of order several GeV is present in the reactions under study. Owing to the photon in the initial state, the overall size of the cross sections, however, is small, being proportional to the square of the fine-structure constant  $\alpha$ . In view of the LHC, the HERA data give direct information on quantities related to QCD, most importantly the parton distribution functions (pdfs) within the nucleon, and the running strong coupling  $\alpha_s$ , determining the overall strength of the partonic branching processes. These quantities, among others, are important ingredients to the Monte Carlo programs simulating cosmic ray showers in the atmosphere. There is, however, another interesting area in cosmic ray research, where HERA can provide important information, namely ultra-high energy neutrino scattering, which can be inferred from  $ep \rightarrow \nu X$  reactions at HERA. Also here, the neutrino energy accessible at HERA is equivalent to about 50 TeV on a stationary proton target.

In the following we will briefly summarize the data on the total photoproduction cross section from HERA and present some recent results on inclusive scattering, discussing the extraction of the parton distribution functions from a combined data set of the two collider experiments H1 and ZEUS. We will then discuss jet final states with emphasis on the phase space near the forward (proton) direction. These data shed light on the parton evolution models and also enable a unique measurement of the running strong coupling, providing new insight into QCD dynamics at very low values of the Bjorken variable  $x$ . We finally mention the relevance of the HERA charged current cross sections for the expectation of ultra-high energy neutrino nucleon cross sections, which will be elaborated in more detail in section 3.

**The HERA Physics Mission** One of the most successful tools for unraveling the structure of hadrons, most importantly of the nucleons, is deep-inelastic scattering (DIS) using charged leptons as probes. The HERA collider at the Deutsches Elektronen-Synchrotron DESY in Hamburg has provided the highest available center-of-mass energies for the collision of electrons and positrons with protons. HERA has been running from 1992 until mid 2007, accumulating a total of about  $500 \text{ pb}^{-1}$  for each of the two colliding beam experiments H1 [1] and ZEUS [2]. The data taking was divided into two phases, separated by a massive luminosity upgrade program in the years 2001-2002. As a further benefit of the upgrade, HERA also provided longitudinally polarized electron and positron beams, giving access to sensitive tests of the electroweak theory and allowing to carry out unique searches for the production of new heavy particles. While the electroweak sector was tested in electron-quark scattering at an unprecedented level, the hope for discovering “New Physics” at HERA did not materialize.

**Photoproduction at HERA** Measuring the total hadronic photoproduction cross section at high center-of-mass energies gives access to the asymptotic behavior of cross sections in general. The energy dependences of the total cross sections for  $pp$ ,  $\bar{p}p$ ,  $Kp$  and  $\pi p$  are well described by Regge theory [3]. Phenomenological fits based on this (non-perturbative) theory are successfully parameterizing all the hadronic cross sections in the full energy range (above the  $s$ -channel resonance region) using the common form

$$\sigma_{\text{tot}} = A \cdot s^{\epsilon} + B \cdot s^{-\eta},$$

where  $s$  is the square of the center-of-mass energy and  $A$  and  $B$  are constants. The parameter  $\epsilon$  describes the weak energy dependence at high energies ( $1 + \epsilon$  is the “Pomeron intercept”, which is about 1.09).

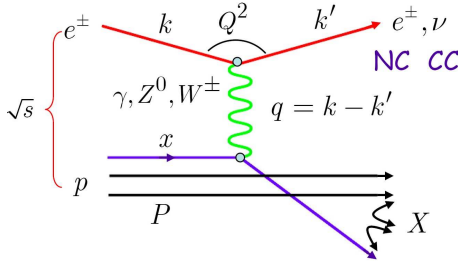


Fig. 1: Lowest order Feynman diagram for deep-inelastic electron-proton scattering in the parton picture, showing the relevant kinematic quantities characterizing inclusive DIS reactions and photoproduction (see text). The hadronic final state “fragmented” from the scattered and spectator partons is indicated by  $X$ .

The photon-proton total cross section is measured in the process  $ep \rightarrow e\gamma p \rightarrow eX$ , where the initial state electron has radiated a photon, which is then absorbed by the proton, producing a hadronic final state  $X$ . The event kinematics (see fig. 1 for a general lowest order Feynman diagram) is best described in terms of the Lorentz-invariant photon virtuality  $Q^2$ , and the event inelasticity  $y$ , both defined as

$$Q^2 = -q^2 = -(k - k')^2$$

and

$$y = \frac{p \cdot q}{p \cdot k}.$$

The square of the photon-proton center-of-mass energy  $W$ , i.e. the mass squared of the hadronic system  $X$ , is given by

$$W^2 = (q + p)^2 = 4E_e E_p y.$$

The photon virtuality has a kinematic minimum due to the finite electron mass  $m_e$ , and is given by

$$Q_{\min}^2 = \frac{m_e^2 y^2}{1 - y}.$$

The photoproduction cross section is related to the double differential electroproduction cross section (which is actually observed experimentally) by the equivalent photon approximation [4], which can be written as

$$\frac{d^2 \sigma^{ep}}{dy dQ^2} = \frac{\alpha}{2\pi Q^2} \left[ \left( \frac{1 + (1 - y)^2}{y} - \frac{2(1 - y)}{y} \frac{Q_{\min}^2}{Q^2} \right) \cdot \sigma_T^{\gamma p}(y, Q^2) + \frac{2(1 - y)}{y} \cdot \sigma_L^{\gamma p}(y, Q^2) \right],$$

where  $\sigma_T^{\gamma p}$  ( $\sigma_L^{\gamma p}$ ) is the cross section for transversely (longitudinally) polarized photon on protons. Since the virtuality of the photon is small by excluding deep inelastic scattering events ( $Q_{\max}^2 \sim 0.02 \text{ GeV}^2$ ), the longitudinal cross section is expected to be small. Integrating over  $Q^2$  gives the total  $\gamma p$  cross section in terms of the single  $ep$  differential cross section:

$$\sigma_{\text{tot}}^{\gamma p}(y) = \frac{2\pi}{\alpha} \left[ \frac{1 + (1 - y)^2}{y} \ln \frac{Q_{\max}^2}{Q_{\min}^2} - \frac{2(1 - y)}{y} \left( 1 - \frac{Q_{\min}^2}{Q_{\max}^2} \right) \right]^{-1} \cdot \frac{d\sigma^{ep}(y)}{dy}$$

The event inelasticity  $y$  is given by the acceptance of the electron tagging systems and can be integrated over, so that  $\sigma_{\text{tot}}^{\gamma p}(W)$  can be determined. The results of the measurements from HERA [5, 6] are shown in fig 2, together with the low energy data [7] and a phenomenological Regge fit [8] using hadron data, marked as “DL98”. The compatibility of the photoproduction cross section with the hadronic data supports the universal energy dependence of all total cross sections at asymptotic energies.

**Quantum Chromodynamics in the HERA Regime** Quantum Chromodynamics (QCD) is expected to describe the strong interactions between quarks and gluons. At distances small compared to the nucleon radius, or equivalently large momentum transfer  $Q^2$  where the strong coupling  $\alpha_s$  is small, perturbative QCD (pQCD) gives an adequate quantitative account of hadronic processes. The total cross sections, however, are dominated by long range forces (“soft interactions”), where a satisfactory understanding of QCD still remains a challenge. This is most importantly so also for all transitions of partons to hadrons in the final state (“fragmentation process”). In addition, non-perturbative effects govern the DIS kinematics through the momentum distribution (“parton distribution functions”, or “pdfs”) of the initial partons, interacting with the electrons via photon or  $Z^0$  exchange (see fig.1). The latter is important only at very large  $Q^2$ , i.e. around or beyond the mass of the  $Z^0$ . The division between the non-perturbative and the perturbative regimes is defined by the factorization scale, which should be sufficiently large ( $\mathcal{O}(\text{few GeV}^2)$ ) to hope for a convergent perturbative expansion in the strong coupling constant  $\alpha_s$ .



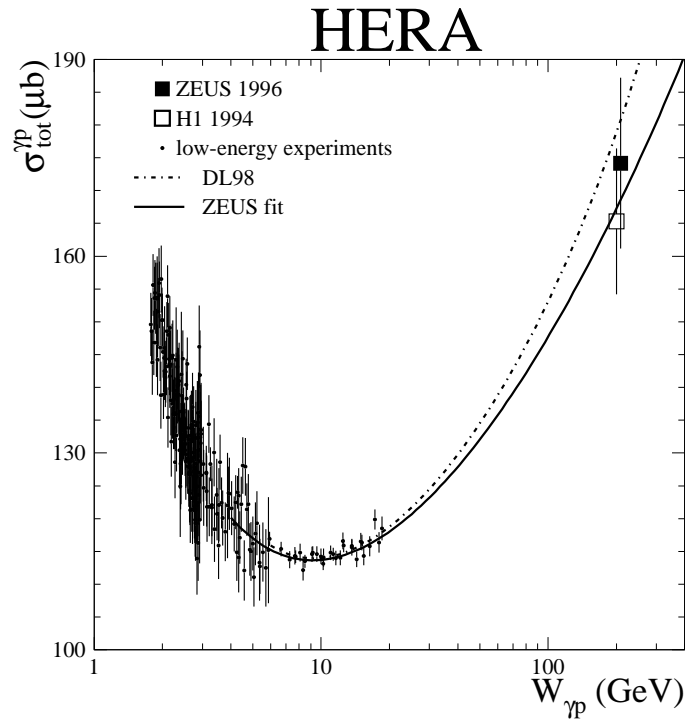


Fig. 2: Measurements of the total photoproduction cross section  $\sigma_{\gamma p}$  for positron-proton scattering from early measurements of H1 [5] and ZEUS [6].

Within the framework of perturbative QCD, the DIS cross section at the parton level is generically given by

$$\sigma = \sum_i \sigma_{\gamma^* i}(Q^2) \otimes x f_i(x, Q^2), \quad (1)$$

where  $Q^2$  is the virtuality of the exchanged boson (here: the virtual photon  $\gamma^*$ ),  $x$  is the momentum fraction (Bjorken  $x$ ) of the incoming parton, and  $\sigma_{\gamma^* i}$  is the total virtual photon-parton cross section. In this expression the factorization theorem of QCD [9] has been used, separating the cross section into a hard scattering part between the exchanged virtual photon and the incoming parton  $i$ , convoluted with a part (including a non-perturbative contribution) describing the momentum distribution  $x f_i(x, Q^2)$  of parton  $i$  within the proton. In eq.(1) one recognizes the incoherent summing of quark contributions, which is justified by the property of asymptotic freedom. Asymptotic freedom states that the interaction between the partons within the proton, characterized by the strong coupling constant  $\alpha_s$  become weak at large  $Q^2$  ( $\alpha_s \rightarrow 0$  as  $Q^2 \rightarrow \infty$ ). In this way the scattering process of the electron with the partons of the proton can be treated incoherently.

Figure 1 also indicates the kinematics in the HERA regime. Here,  $s$  is the square of the total  $ep$  center of mass energy. The four-momentum transfer squared  $Q^2$  is given by the scattered electron alone, the Bjorken variable  $x$  and the inelasticity  $y$  (equal to the energy fraction transferred from the electron to the virtual photon in the proton rest frame, see above), with  $x$

given by

$$x = \frac{Q^2}{2 P \cdot q}. \quad (2)$$

Only two of the three quantities in eq. (2) are independent, they are related via  $Q^2 = sxy$ . Another interesting quantity is the total mass  $M_X$  of the hadronic final state, given by

$$M_X^2 \equiv W^2 = (q + P)^2 = \frac{Q^2(1-x)}{x} \quad (3)$$

This relation shows that low  $x$  reactions correspond, at fixed  $Q^2$ , to large values of  $W^2$ , i.e. large invariant masses of the hadronic final state. Due to the high colliding beam energies (protons at 920 GeV, electrons at 27.6 GeV), HERA provided a large range of exploration for  $x$  and  $Q^2$ , extending the reach of previous fixed target experiments by more than 2 orders of magnitude in  $x$  and  $Q^2$ .

The double differential cross section for  $ep$  scattering is written in terms of structure functions as (see, e.g. [10] )

$$\frac{d^2\sigma(e^\pm p)}{dx dQ^2} = \frac{2\pi\alpha^2}{xQ^4} Y_+ \left[ F_2 - \frac{y^2}{Y_+} F_L \mp \frac{Y_-}{Y_+} xF_3 \right], \quad (4)$$

where the functions  $Y_\pm$  are given by  $Y_\pm = 1 \pm (1-y)^2$ , and the structure functions, apart from coupling constants, are combinations of the parton distribution functions. For the case of pure photon exchange, valid at low  $Q^2$ , one obtains

$$F_2(x, Q^2) = \sum_{i=u,d,\dots} e_i^2 x f_i(x, Q^2). \quad (5)$$

where the sum extends over all partons within the proton of charge  $e_i$ . As indicated in fig. 1, all reactions with neutral boson exchange are called “neutral current (NC)” reactions, those with  $W^\pm$  exchange (here the final state lepton is a neutrino) are called “charged current (CC)” reactions.

The non-perturbative parton distribution functions  $f_i(x)$  cannot be calculated from first principles and have therefore to be parameterized at some starting scale  $Q_0^2$ . Perturbative QCD predicts the variation of  $f_i$  with  $Q^2$ , i.e.  $f_i = f_i(x, Q^2)$  via a set of integro-differential evolution equations, as formulated by Altarelli and Parisi (“DGLAP” equations, see [11]). The predicted  $Q^2$  dependence (“scaling violations”) of the structure function  $F_2$ , see eq. (5), are nicely supported by the data from HERA [12].

**Low  $x$  Physics and the Parton Distribution Functions** At distances small compared to the nucleon radius, or equivalently large momentum transfer  $Q^2$  between the incoming and outgoing leptons, perturbative QCD (pQCD) gives an adequate quantitative account of hadronic processes in DIS. The most “elementary” observable in electron-proton scattering is the inclusive DIS cross section, where basically only the 4-vectors of the scattered lepton or the produced hadronic final state are measured.

Inclusive  $ep$  scattering can be divided into two distinct classes: Neutral current (NC) reactions ( $ep \rightarrow eX$ ), and Charged Current (CC) reactions ( $ep \rightarrow \nu X$ ). In NC reactions, a photon or

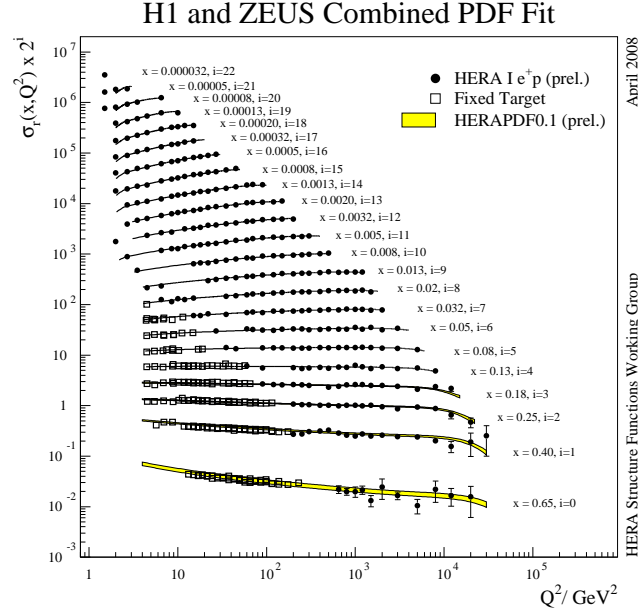


Fig. 3: Measurements of the reduced cross section  $\sigma_r(x, Q^2)$  for positron-proton scattering, based on the combined data of H1 and ZEUS [12]. The data show clear evidence for scaling violations, as expected from gluon emission of the initial quarks participating in the hard scattering process. The scaling violations are very well described by pQCD NLO fit HERAPDF 0.1 [13]. At low  $Q^2$ , the data from some fixed target experiments are also shown.

a  $Z^0$  is exchanged between the electron and a quark emitted from the proton. The corresponding double-differential cross section  $d^2\sigma/dxdQ^2$ , or the so-called “reduced” cross section  $\sigma_r$  factorizing out known kinematic terms, can be written in the following way (similar expressions also hold for the CC reactions):

$$\sigma_r(x, Q^2) \equiv \left( \frac{xQ^4}{2\pi\alpha^2 Y_+} \right) \frac{d^2\sigma(e^\pm p)}{dx dQ^2} = F_2 - \frac{y^2}{Y_+} F_L \mp \frac{Y_-}{Y_+} xF_3 \quad (6)$$

Here, the three (positive definite) structure functions  $F_2$ ,  $F_L$  and  $xF_3$  depend both on  $x$  and  $Q^2$ , and contain the (non-perturbative) parton distribution functions (pdfs). The structure function  $F_2$  contains contributions from quarks and antiquarks ( $\sim x(q + \bar{q})$ ),  $F_L$  is dominated by the gluon distribution ( $\sim xg$ ), and  $xF_3$  is sensitive to the valence quarks ( $\sim x(q - \bar{q})$ ).

At low  $Q^2$  and low  $y$  the structure functions  $xF_3$  (from  $Z^0$  exchange) and  $F_L$  (suppressed by the factor  $y^2$ ) can be safely neglected. Residual (small) contributions from  $F_L$  can also be modeled using pQCD. In this case the structure function  $F_2$  can be extracted at each point of  $x$  and  $Q^2$  from the “reduced” cross section  $\sigma_r$  (see eq. (6)). Measurements of  $\sigma_r$  from the combined H1 and ZEUS data [12] are shown in fig. 3. The data, most importantly their  $Q^2$  dependence, are very well described by NLO pQCD.

Figure 4 shows the pdfs resulting from the NLO pQCD fit HERAPDF 0.1 to the combined NC and CC double-differential cross sections from both HERA experiments [13]. The

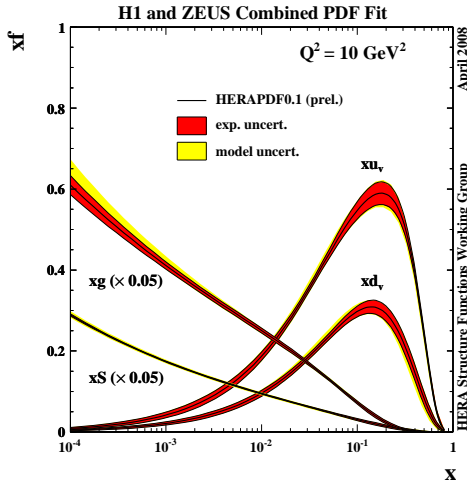


Fig. 4: The parton distribution functions from QCD fits to the HERA data on NC and CC inclusive reactions, using the combined data from H1 and ZEUS (HERAPDF 0.1) [13].

resulting uncertainties of the pdfs have drastically shrunk due to the combination of the HERA data. It should also be noted that the pdfs for the gluon and the sea quarks, even at the lowest values of Bjorken  $x$ , and for all values of  $Q^2$ , keep rising with decreasing  $x$ . This means that parton saturation has not been observed within the kinematic range of HERA - assuming that the parameterisation used in the fits would be flexible enough to allow the observation of such behaviour.

From fig. 4 one clearly sees that the gluon distribution is dominating the low  $x$  behavior of the DIS cross sections. At low  $x$ , the structure function  $F_2$  can be satisfactorily parameterized as being proportional to  $x^{-\lambda}$ . Figure 5 shows the values of  $\lambda$  as function of  $Q^2$ . One can observe a clear decrease of  $\lambda$  with decreasing  $Q^2$ , touching the hadron-hadron limit (and also photoproduction, see the left-most data point) at a photon virtuality around  $1 \text{ GeV}^2$ .

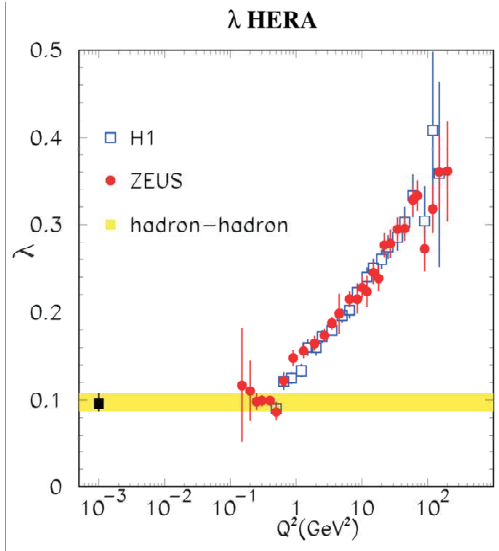


Fig. 5: Measurements of the slope of  $F_2$  for deep inelastic scattering as function of  $Q^2$ . To the far left, the photoproduction point  $\epsilon \equiv \lambda$  is also drawn. .

**Jet Production** Collimated bundles of particles (“jets”) are carrying the kinematic information of the partons emerging from DIS reactions at HERA and other high  $p_t$  colliding beam experiments. The study of jet production is therefore a sensitive tool to test the predictions of perturbative QCD and to determine the strong coupling constant  $\alpha_s$  over a wide range of  $Q^2$ .

Several algorithms exist to cluster individual final state hadrons into jets, but most commonly used at HERA is the so-called  $k_T$  clustering algorithm [14]. The jet finding is usually executed in the hadronic center of mass system, which is, up to a Lorentz boost, equivalent to the Breit frame. At the end of the algorithm, the hadrons are collected into a number of jets.

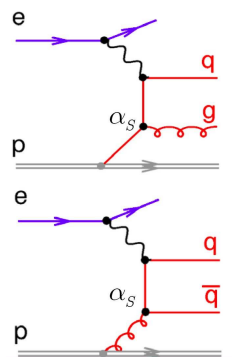


Fig. 6: Feynman diagrams for LO jet production. The upper subgraph is called “QCD Compton”, the lower subgraph is called “boson-gluon fusion”. Both graphs contribute to two-jet final states. Events with three jets can be interpreted as a di-jet process with additional gluon radiation from one of the involved quark lines, or as a gluon splitting into a quark-antiquark pair. These processes are of order  $\mathcal{O}(\alpha_s^2)$  (NLO).

At leading order (LO) in  $\alpha_s$ , di-jet production (see fig. 6) proceeds via the QCD Compton process ( $\gamma^* q \rightarrow qg$ ) and boson-gluon fusion ( $\gamma^* g \rightarrow q\bar{q}$ ). The cross section for events with three jets is of  $\mathcal{O}(\alpha_s^2)$ . These events can be interpreted as coming from a di-jet process with additional gluon radiation or gluon splitting (see caption of fig. 6), bringing the QCD calculation to next-to-leading order (NLO).

In jet physics, two different “hard” scales can be used to enable NLO (and higher) calculations: the variable  $Q$ , and the transverse energy  $E_T$  of the jets. Figure 7 shows the differential cross sections for inclusive jet production at high  $Q^2$  as measured by the ZEUS Collaboration [15], both with respect to  $Q^2$  and  $E_T$ . The data are compared to NLO calculations, using the renormalization and factorization scales as indicated in the figure. Both schemes are able to describe the data very well, indicating the validity of the choice of any of the two hard scales. Given the experimental and theoretical uncertainties at these large scales, no higher order (beyond NLO) corrections seem necessary.

**Forward Jets** All of the analyses regarding the observables mentioned in the previous chapters rest on the DGLAP  $Q^2$  evolution scheme for the pdfs involved. Potential deviations observed in certain regions of phase space (low  $x$ , low  $Q^2$ ) are usually attributed to the limited order of the presently computed QCD matrix elements (LO, NLO, sometimes NNLO). Especially for low  $x$  ( $\approx 10^{-4}$ ), but sufficiently large  $Q^2$  ( $>$  a few  $\text{GeV}^2$ ), there has been a vivid debate about the validity of the DGLAP approach. In this kinematic regime the initial parton in the proton can induce a QCD cascade, consisting of several subsequent parton emissions, before eventually an interaction with the virtual photon takes place (see fig. 8). QCD calculations based on the “direct” interaction between a point-like photon and a parton from the evolution chain, as given

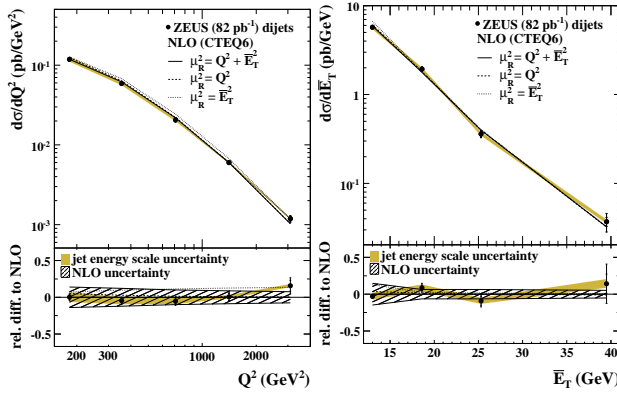


Fig. 7: Differential cross sections for inclusive jet production from the ZEUS experiment [15]. Also shown are the predictions from next-to-leading order QCD calculations, which give a good description of the data.

by the DGLAP approach, are very successful in describing, e.g. the unexpected rise of  $F_2$  with decreasing  $x$  over a large range in  $Q^2$  [16].

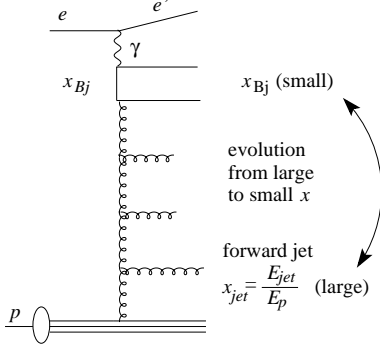


Fig. 8: Schematic diagram of  $ep$  scattering producing a forward jet. The evolution in the longitudinal momentum fraction  $x$ , from large  $x_{\text{jet}}$  to small  $x_{Bj}$ , is indicated.

For low values of  $x$ , there is, however, a technical reason to question the validity of the DGLAP evolution approach: Since it resums only leading  $\log(Q^2)$  terms, the approximation may become inadequate for very small  $x$ , where  $\log(1/x)$  terms become important in the evolution equations. In this region the BFKL scheme [17] is expected to describe the data better, since in this scheme terms in  $\log(1/x)$  are resummed.

The large phase space available at low  $x$  (see eq.(3)) makes the production of forward jets (in the angular region close to the proton direction) a particularly interesting topic for the study of parton dynamics, since jets emitted in this region lie well away in rapidity from the photon end of the evolution ladder (see fig. 8). Concerning the forward jets there is a clear dynamic distinction between the DGLAP and BFKL schemes: In the DGLAP scheme, the parton cascade resulting from hard scattering of the virtual photon with a parton from the proton is ordered in parton virtuality. This ordering along the parton ladder implies an ordering in transverse energy  $E_T$  of the partons, so that the parton participating in the hard scatter has the highest  $E_T$ . In the BFKL scheme there is no strict ordering in virtuality or transverse energy. The BFKL evolution therefore predicts that a larger fraction of low  $x$  events will contain high- $E_T$  forward jets than is predicted by the DGLAP evolution.

Both ZEUS [18] and H1 [19] have studied forward jet production, where “forward” typically means polar emission angles less than about 20 degrees relative to the proton direction. As

a first example, the single differential cross sections  $d\sigma/dx$  from H1 are shown in fig. 9. The data are compared to LO and NLO QCD calculations [20] (a), and several Monte Carlo models (b and c). The NLO calculation in (a) is significantly larger than the LO calculation. This reflects the fact that the contribution from forward jets in the LO scenario is kinematically suppressed. Although the NLO contribution opens up the phase space for forward jets and considerably improves the description of the data, it still fails by a factor of 2 at low  $x$ . In fig. 9b the predictions from the CASCADE Monte Carlo program [21] is shown, which is based on the CCFM formalism [22]. The CCFM equations provide a bridge between the DGLAP and BFKL descriptions by resumming both  $\log(Q^2)$  and  $\log(1/x)$  terms, and are expected to be valid over a wider  $x$  range. The model predicts a somewhat harder  $x$  spectrum, and fails to describe the data at very low  $x$ . In part (c) of the figure, the predictions (“RG-DIR”) from the LO Monte Carlo program RAPGAP [23] is shown, which is supplemented with initial and final state parton showers generated according to the DGLAP evolution scheme. This model, which implements only direct photon interactions, gives results similar to the NLO calculations from part (a), and falls below the data, particularly at low  $x$ . The description is significantly improved, if contributions from resolved virtual photon interactions are included (“RG-DIR+RES”). However, there is still a discrepancy in the lowest  $x$  bin, where a possible BFKL signal would be expected to show up most prominently. The Color Dipole Model (CDM) [24], which allows for emissions non-ordered in transverse momentum, shows a behavior similar to RG-DIR+RES.

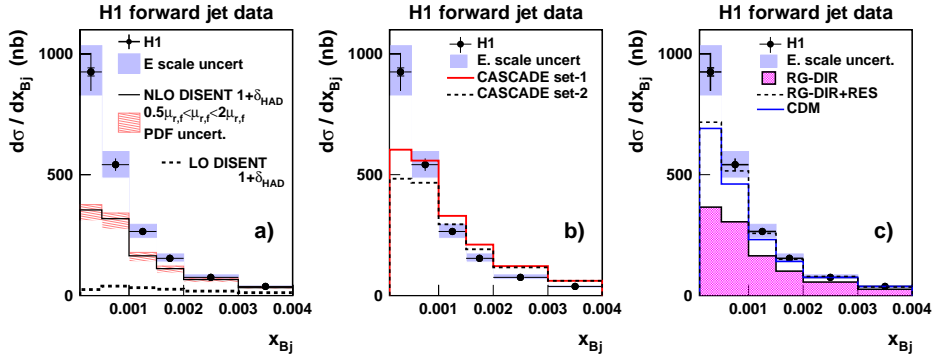


Fig. 9: Single differential cross sections for forward jets as functions of  $x$  from the H1 experiment [19], compared to NLO predictions [20] in (a), and QCD Monte Carlo models [23, 24] in (b) and (c). The dashed line in (a) shows the LO contribution.

For a more detailed study the forward jet sample was divided into bins of  $p_{t,\text{jet}}^2$  and  $Q^2$ . The triple differential cross section  $d^3\sigma/dxdQ^2dp_{t,\text{jet}}^2$  versus  $x$  is shown in fig. 10 for several regions in  $Q^2$  and  $p_{t,\text{jet}}^2$ . In addition, the expectations from the above mentioned QCD models are presented. Using the ratio  $r = p_{t,\text{jet}}^2/Q^2$ , various regimes can be distinguished: For  $p_{t,\text{jet}}^2 < Q^2$  ( $r < 1$ ) one expects a DGLAP-like behavior, dominated by direct photon interactions (see fig. 10 c). Due to the large bin sizes, however, the ranges of  $r$  can be quite large, so that  $r$  in this bin can assume values up to 1.8 due to admixtures from events with  $p_{t,\text{jet}}^2 > Q^2$ . This may explain why the DGLAP direct model (RG-DIR), although closer to the data in this bin than in any other, does not quite give agreement with the data except at the highest  $x$ -bin. In the region

$p_{t,\text{jet}}^2 \approx Q^2$  ( $r \approx 1$ , see fig. 10 b and f), DGLAP suppresses parton emission, so that BFKL dynamics may show up. However, the DGLAP resolved model (RG-DIR+RES) describes the data reasonably well.

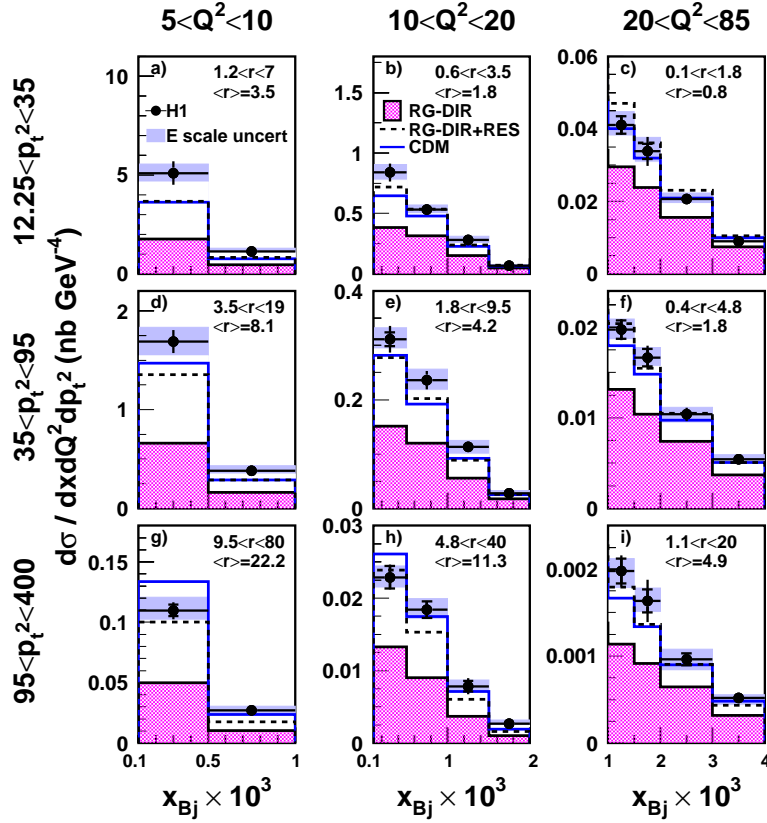


Fig. 10: Triple differential cross sections for forward jet production as function of  $x$  in bins of  $Q^2$  and  $p_{t,\text{jet}}^2$ , compared to various Monte Carlo calculations (see text).

The regime of  $p_{t,\text{jet}}^2 > Q^2$  ( $r > 1$ , see fig. 10 d, g and h), is typical for processes where the virtual photon is resolved, i.e. the incoming parton from the proton vertex interacts with a parton from the photon. As expected, the DGLAP resolved model (RG-DIR+RES) provides a good overall description of the data, again similar to the CDM model. However, it can be noted that in regions where  $r$  is largest and  $x$  is small, CDM shows a tendency to overshoot the data. DGLAP direct (RG-DIR), on the other hand, gives cross sections which are too low. Although the above analysis tries to isolate “BFKL regions” from “DGLAP regions”, the conclusion on underlying dynamics cannot be reached, most importantly since the “BFKL region” ( $r \approx 1$ ) is apparently heavily contaminated by “DGLAP-type” events. In addition, the two “different” evolution approaches, RG-DIR+RES (“DGLAP”) and CDM (“BFKL”), give similar predictions.

In a further step, the parton radiation ladder (see fig. 8) is examined in more detail by looking also at jets in the region of pseudorapidity,  $\eta = -\ln \tan(\theta/2)$ , between the scattered electron ( $\eta_e$ ) and the forward jet ( $\eta_{\text{forw}}$ ). In this region a “2-jet + forward” sample was selected,



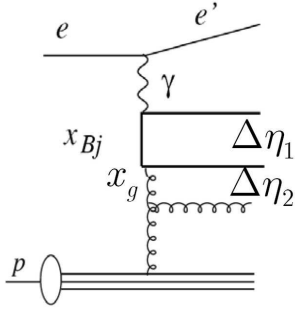


Fig. 11: Kinematic regions for the event sample “2jets + forward” (see text). The quarks in the photon-gluon fusion process are  $q_1$  (upper solid line) and  $q_2$  (lower solid line). The rapidity gap between  $q_1$  and  $q_2$  is denoted by  $\Delta\eta_1$ , the gap between  $q_2$  and the forward jet is denoted by  $\Delta\eta_2$ .

requiring at least 2 additional jets, with  $p_{t,\text{jet}} > 6$  GeV for all three jets, including the forward jet. In this scenario, evolution with strong  $k_t$  ordering is obviously disfavored. The jets are ordered in rapidity according to  $\eta_{\text{forw}} > \eta_{\text{jet2}} > \eta_{\text{jet1}} > \eta_e$ . Two rapidity intervals are defined between the two additional jets and the forward jet (see fig. 12):  $\Delta\eta_1 = \eta_{\text{jet2}} - \eta_{\text{jet1}}$  is the rapidity interval between the two additional jets, and  $\Delta\eta_2 = \eta_{\text{forw}} - \eta_{\text{jet2}}$  is the interval between jet 2 and the forward jet. If the di-jet system originates from the quark line coupling to the photon (see fig. 12), the phase space for evolution in  $x$  between the di-jet system and the forward jet is increased by requiring that  $\Delta\eta_1$  is small and that  $\Delta\eta_2$  is large: Requiring  $\Delta\eta_1 < 1$  will favor small invariant masses of the di-jet system. As a consequence,  $x_g$  will be small, leaving the rest for additional radiation. When, on the other hand,  $\Delta\eta_1$  is required to be large ( $\Delta\eta_1 > 1$ ) BFKL-like evolution may then occur between the two jets from the di-jet system or, when both  $\Delta\eta_1$  and  $\Delta\eta_2$  are small, between the di-jet system and the hard scattering vertex. Note that the rapidity phase space is restricted only for the forward jet.

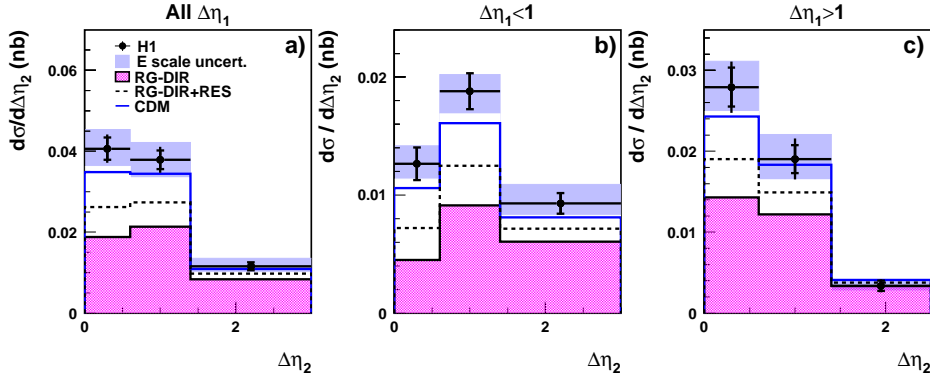


Fig. 12: Cross section for events with a reconstructed high transverse momentum di-jet system and a forward jet from the H1 experiment [19], as function of  $\Delta\eta_2$  for two regions of  $\Delta\eta_1$ . The data are compared to predictions of “DGLAP-like (RG-DIR+RES) and “BFKL-like” (CDM) Monte Carlo models (see text).

As argued above, this study disfavors evolution with strong ordering in  $k_t$  due to the common requirement of large  $p_{t,\text{jet}}$  for the three jets. Radiation which is not ordered in  $k_t$  may occur at any location along the evolution chain, depending on the values of  $\Delta\eta_1$  and  $\Delta\eta_2$ . Figure 12 show the measured cross sections as function of  $\Delta\eta_2$  for all data, and separated into the two regions of  $\Delta\eta_1$  discussed above. One can see that here the CDM model is in good agreement with

the data in all cases, while the DGLAP models predict cross sections which are too low, except when both  $\Delta\eta_1$  and  $\Delta\eta_2$  are large. For this topology all models (and the NLO calculation, not shown) agree with the data, indicating that the available phase space for evolution is exhausted.

It is important to realize that the “2+forward jet” sample indeed seems to differentiate between the CDM and DGLAP resolved models, in contrast to the more inclusive samples (see fig. 10). The conclusion is that additional breaking of the  $k_t$  ordering, beyond what is included in the resolved photon model, is required by the data, pointing towards some evidence for BFKL dynamics. It is, however, not excluded that such effects may also be described by higher order DGLAP calculations, which may become available in the future. Further investigations using forward particle emission will be discussed below (see section 2).

**The Strong Coupling Constant** One of the most important measurements using multi-jet final states is the determination of the strong coupling constant  $\alpha_s$ . At HERA, this measurement is particularly interesting, since  $\alpha_s$  can be determined in a single experiment over a large range of  $Q$  or  $E_T$ . Observables which are sensitive to  $\alpha_s$  come from various sources, such as inclusive jets, jet ratios (number of three jets relative to the number of two jets), and event shape variables (thrust, jet masses, angles between jets etc.). A recent compilation of  $\alpha_s$  determinations [25] from the two HERA experiments H1 and ZEUS, using various jet observables and the HERA I data set, is shown in fig. 13. An NLO fit to these data yields a combined value of  $\alpha_s(M_Z) = 0.1198 \pm 0.0019(\text{exp.}) \pm 0.0026(\text{th.})$ . The dominating theoretical error arises from the uncertainty due to terms beyond NLO, which is estimated by varying the renormalization scale by the “canonical” factors 0.5 and 2. A recent preliminary result obtained by the H1 Collaboration using the full HERA data set and based on multiple observables in inclusive and multi-jet events displays an experimental error below 1% [26]:  $\alpha_s = 0.1182 \pm 0.0008(\text{exp})_{-0.0031}^{+0.0041}(\text{th.}) \pm 0.0018$ . This illustrates the potential for a very precise measurement of the strong coupling using the full HERA data set.

**Ultra-High Energy Neutrino Reactions** With the era of high energy neutrino astrophysics approaching, it is interesting to review our knowledge about the neutrino-nucleon cross section at ultra-high energies beyond  $\mathcal{O}(10 \text{ TeV})$ . Such energies can indeed be reached with the HERA collider, as was discussed in the introduction. Looking at the charged current reaction  $ep \rightarrow \nu X$  measured at HERA, a cut in the transverse neutrino momentum of  $p_\perp > 25 \text{ GeV}$  is necessary for a clean separation of CC events from the background. The extrapolation to  $p_\perp = 0$  can be done within the Standard model, yielding a cross section for  $\nu N$  on a stationary target of about 200 pb at 50 TeV neutrino energy. Figure 14 shows the measurements from fixed target experiments and the HERA point. Also given are the linear extrapolation (corresponding to  $M_W = \infty$ ) and the prediction of the Standard Model ( $M_W = 80 \text{ GeV}$ ). As one can see, the neutrino nucleon cross section shows no anomaly, as could, for example, be expected by electroweak instanton effects proposed [27] as a source of possible cosmic ray events beyond the GZK cutoff. While the evidence for such events has become weaker recently [28,29], the search for instanton effects at HERA [30] has also been inconclusive so far. More details on the expectations of neutrino cross sections at asymptotic energies are presented further below (see section 3).

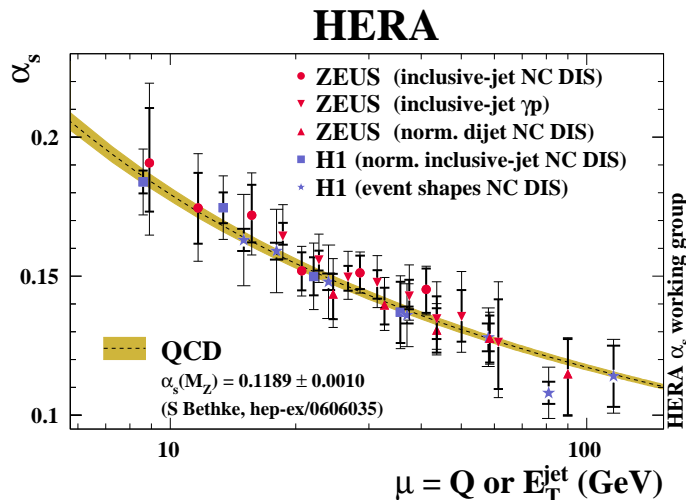


Fig. 13: Compilation of  $\alpha_s(\mu)$  measurements from H1 and ZEUS [25], based on jet variables as indicated. The dashed line shows the two loop solution of the renormalization group equation, evolving the 2006 world average for  $\alpha_s(M_Z)$ . The band denotes the total uncertainty of the prediction.

## 2 Forward particles from HERA to LHC

**Forward Particles at HERA** In  $ep$  scattering at HERA, a significant fraction of events contains a low-transverse momentum baryon carrying a large fraction of the incoming proton energy. Although the production mechanism of these leading baryons is not completely understood, exchange models [31] give a reasonable description of the data (Fig. 15). In this picture, the incoming proton emits a virtual particle which undergoes the deep inelastic scattering process with the incoming beam electron.

To measure the very forward particles, both the H1 and the ZEUS experiments have been equipped with the Forward Proton Spectrometers (LPS, FPS and VFPS) and the Forward Neutron Calorimeters (FNC). The Forward Proton Spectrometers are several Roman Pot detectors placed at different positions along the beamline in the direction of proton beam, between 24 and 220 m from the interaction point. They measure the energy and momentum of the protons which are scattered through the very small angles and keep a momentum fraction of the initial proton between 0.4 and 1.

The Forward Neutron Calorimeters were installed at  $\theta = 0^\circ$  and at 106 m from the interaction point in the proton beam direction. These are lead-scintillator sandwich calorimeters with energy resolution  $\sigma(E)/E = 70\%/\sqrt{E}$  for the ZEUS-FNC and  $\sigma(E)/E = 63.4\%/\sqrt{E} \oplus 3\%$  for the H1-FNC. The size and weight of the FNC are defined by the space available in the HERA tunnel. The detectors are about 2m long with  $\sim 70 \times 70 \text{ cm}^2$  transverse size. Below the H1 and ZEUS-FNC calorimeters are briefly described.

The general view of the H1-FNC is shown in Fig. 16(left). It consists of the Main Calorimeter and the Preshower. In addition, two layers of veto counters situated at the distance of 2m in front of Preshower are used to veto charged particles. The Preshower is  $\sim 40\text{cm}$  ( $\sim 1.5\lambda$ )

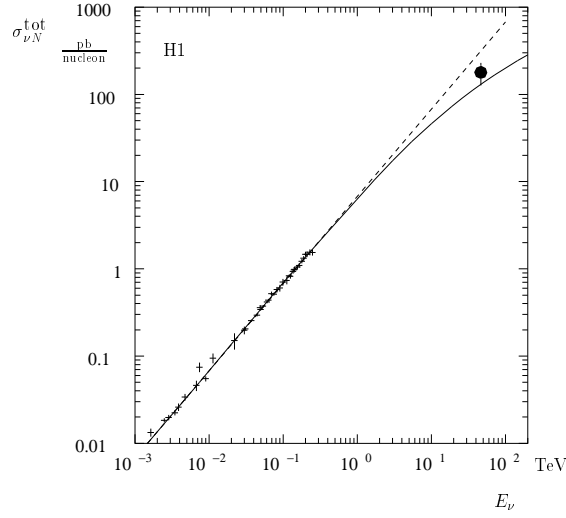


Fig. 14: Measurement of the neutrino nucleon total cross section inferred from the HERA charged current data (full circle), and various fixed target neutrino experiments (crosses).

long lead–scintillator sandwich calorimeter, it is placed in front of the Main Calorimeter. The electromagnetic showers completely develop in Preshower, while the hadronic showers leave in Preshower  $\sim 40\%$  of their energy (electromagnetic component). So the position resolution for the showers started in Preshower are defined by the electromagnetic component of the shower. Constructively the Preshower consists of two sections: the electromagnetic and the hadronic ones, each of them is composed of 12 planes. The transverse size of the scintillating plates is  $26 \times 26 \text{ cm}^2$ . Each scintillating plate has 45 grooves where 1.2mm wavelength shifters are glued in. In order to obtain a good spatial resolution, the orientation of fibres is changed in turn from horizontal to vertical for alternating planes. On each plate the fibres are combined by five into nine strips. Longitudinally the strips are combined in 9 vertical and 9 horizontal towers. The energy resolution for electromagnetic showers is  $\sim 20\%/\sqrt{E [\text{GeV}]}$  and the spatial resolution

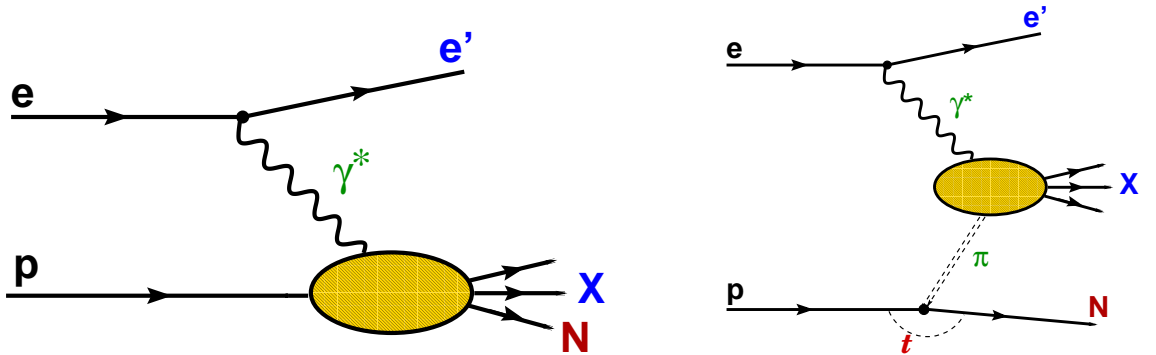


Fig. 15: (left) HERA  $ep$  scattering event with the final state baryon in the proton fragmentation system, (right) Leading baryon production via an exchange process.

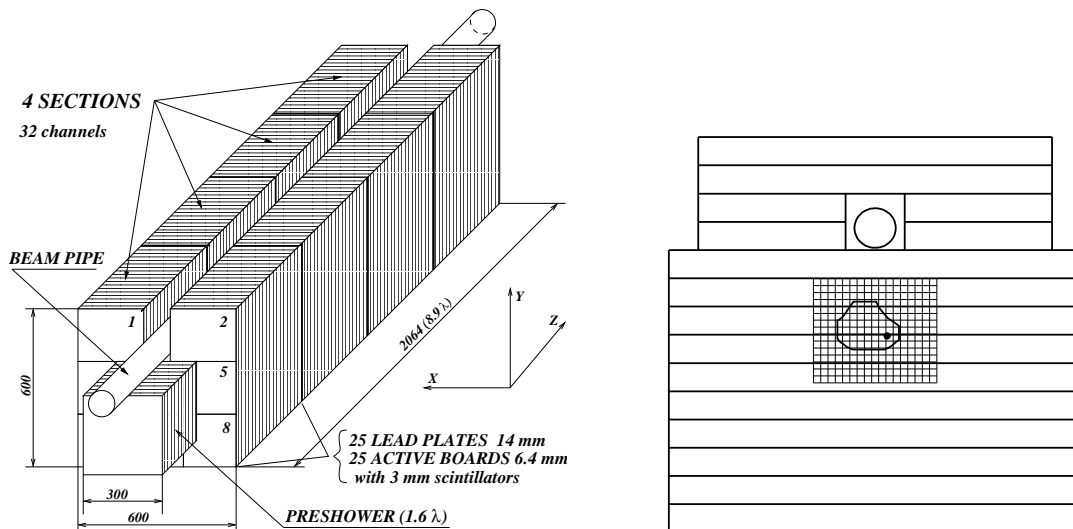


Fig. 16: General view of the H1-FNC calorimeter (left) and ZEUS-FNC calorimeter (right).

is  $\sim 2$  mm. Apart from improvement of the energy and position resolution the Preshower provides efficient separation of electromagnetic and hadronic showers. The Main Calorimeter of H1-FNC is a sandwich-type calorimeter consisting of four identical sections with transverse dimensions  $60 \times 60 \text{ cm}^2$  and length of 51.5 cm. Each section consists of 25 lead absorber plates 14 mm-thick, and 25 active boards with 3 mm scintillators. Each active board is made of 8 scintillating tiles with the transverse size of  $20 \times 20 \text{ cm}$  or  $20 \times 26 \text{ cm}$ . The 25 tiles of one section with the same transverse position form a “tower”. All together there are 32 towers in all four sections. In the top part of the calorimeter there is a opening for the proton beam vacuum pipe which is going through the calorimeter as seen from Fig. 16. The total length of the Main FNC calorimeter is 206.5 cm.

The structure of the ZEUS-FNC calorimeter is shown in Fig. 16(right). It is a finely segmented, compensating, sampling calorimeter with 134 layers of 1.25cm-thick lead plates as absorber and 2.6mm-thick scintillator plates as the active material. The scintillator is read out on each side with wavelength-shifting light guides coupled to photomultiplier tubes. It is segmented longitudinally into a front section, seven interaction-lengths deep, and a rear section, three interaction-lengths deep. The front section is divided vertically into 14 towers, each 5cm high. Inside the calorimeter at a depth of one interaction length a forward neutron tracker (FNT) is installed. It is a scintillator hodoscope designed to measure the position of neutron showers. Each scintillator finger is 16.8cm long, 1.2cm wide and 0.5cm deep; 17 are used for  $X$  position reconstruction and 15 for  $Y$ . The position of the FNT hodoscope in the FNC is indicated in Fig. 16.

The acceptance of the FNC calorimeters is defined by the aperture of the HERA beam line magnets and is limited to neutron scattering angles of  $\theta_n < 0.8 \text{ mrad}$  with approximately 30% azimuthal coverage (see Fig. 17). Thus the transverse momenta of neutrons are limited to  $p_{T,n}^{max} = 0.656 \cdot x_L$  for proton beam energy of 920 GeV. The overall acceptance of the FNC,

taking account of beam-line geometry, inactive material, beam tilt and angular spread, as well as the angular distribution of the neutrons, is  $\sim 20\%$  at low  $x_L$ , where the  $p_{T,n}$  range covered is small, but increases monotonically, exceeding 30% at high  $x_L$ .

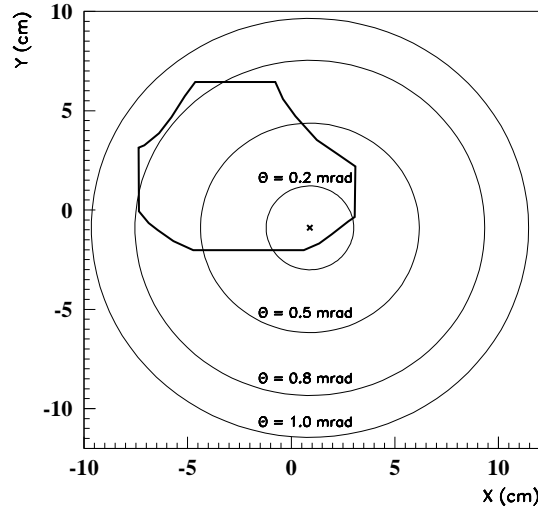


Fig. 17: The geometrical acceptance of FNC calorimeter defined by the aperture of the HERA beam-line elements.

**Physics with Leading Neutrons** The main goal of the FNC calorimeters is to measure the energy and angles of fast neutrons from the reaction  $ep \rightarrow e' + X + n$  (see Fig. 15). The H1 and ZEUS Collaborations provided many results on leading neutron production in DIS, photo-production, in events containing jets or charm in the final state [32]. The results are successfully interpreted within the approach that at high  $x_L = E_n/E_p$  and low  $p_{T,n}$  the dominant mechanism of forward neutron production is the  $\pi^+$ -exchange.

An example of the observed neutron energy and the transverse momentum distributions for the deep-inelastic scattering (DIS) events is shown in Fig. 18 and compared with the Monte Carlo simulation [33]. The distribution is well described by the pion exchange Monte Carlo simulation (RAPGAP) with some admixture of the standard DIS Monte Carlo simulation (DJANGO).

Based on the assumption that at high  $x_L$  the leading neutron production is dominated by the pion exchange mechanism, the measurement of DIS cross sections in events with leading neutrons can provide an important information about the pion structure. The quark and gluon distributions of the pion have previously been constrained using Drell–Yan data and direct photon production data obtained by  $\pi p$  scattering experiments and are limited to high  $x$  ( $x > 0.1$ ) values. Figure 19 shows  $F_2^{LN(3)}/\Gamma_\pi$  as a function of  $\beta$  for fixed values of  $Q^2$ . Here,  $F_2^{LN(3)}$  is the measured semi-inclusive structure function for leading neutron production,  $\Gamma_\pi$  is the integrated pion flux, and  $\beta = x/(1-x_L)$  is a Bjorken scaling variable for the virtual pion. Thus,  $F_2^{LN(3)}/\Gamma_\pi$  can be interpreted as a pion structure function  $F_2^\pi$  and can distinguish between the different parameterisations of the pion structure function (Fig. 19). Moreover, using the measured rate

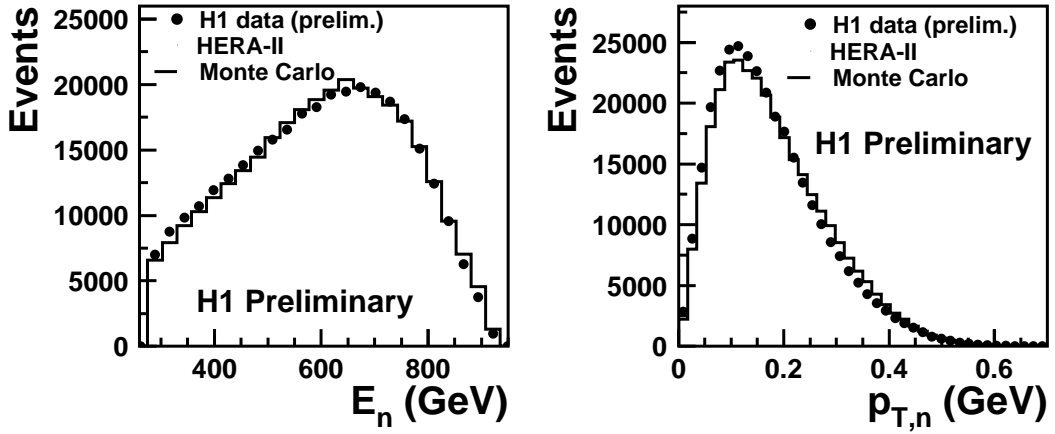


Fig. 18: The observed neutron energy spectrum and the transverse momentum  $p_T$  distribution from the DIS interactions. The data distribution is compared with the Monte Carlo simulation, which is the mixture of RAPGAP with pion exchange and the DJANGO models.

of leading neutron production in DIS, the total probability of  $p \rightarrow n\pi^+$  fluctuation in DIS of 16–25% was estimated [34].

In exchange models, neutron absorption can occur through rescattering. Absorption is a key ingredient in calculations of gap-survival probability in  $pp$  interactions at the LHC, critical in interpreting hard diffractive processes, including central exclusive Higgs production. In the processes with leading neutron production, due to the rescattering the neutron may migrate to lower  $x_L$  and higher  $p_T$  such that it is outside of the detector acceptance. The rescattering can also transform the neutron into a charged baryon which may also escape detection. Since the size of the virtual photon is inversely related to  $Q^2$ , more neutron rescattering would be expected for photoproduction ( $Q^2 \approx 0$ ) than for deep inelastic scattering. The size of the  $n\pi$  system is inversely proportional to the neutron  $p_T$ , so rescattering removes neutrons with large  $p_T$ . Thus rescattering results in a depletion of high  $p_T$  neutrons in photoproduction relative to DIS: a violation of vertex factorization. Figure 20 shows the ratio of the  $x_L$  distributions for photoproduction and DIS. In the range  $0.2 < x_L < 0.4$ , the ratio drops slightly but rises for higher  $x_L$  values, exceeding unity for  $x_L > 0.9$ . The deviation of the ratio from unity is a clear violation of vertex factorization. The dashed and solid curves in Fig. 20 are the expectation for the suppression of leading neutrons in photoproduction relative to DIS from a model of pion exchange with neutron absorption [35]. Within the normalization uncertainty the data are well described by the absorption model. Also shown in Fig. 20 is another model [36] which employs the optical theorem together with multi-Pomeron exchanges to describe all possible rescattering processes of the leading hadron, resulting in absorptive effects. With the correction for different  $W$  dependences, the prediction is close in magnitude to the data.

$$F_2^{\text{LN}(3)}(x_L = 0.73)/\Gamma_\pi, \Gamma_\pi = 0.131$$

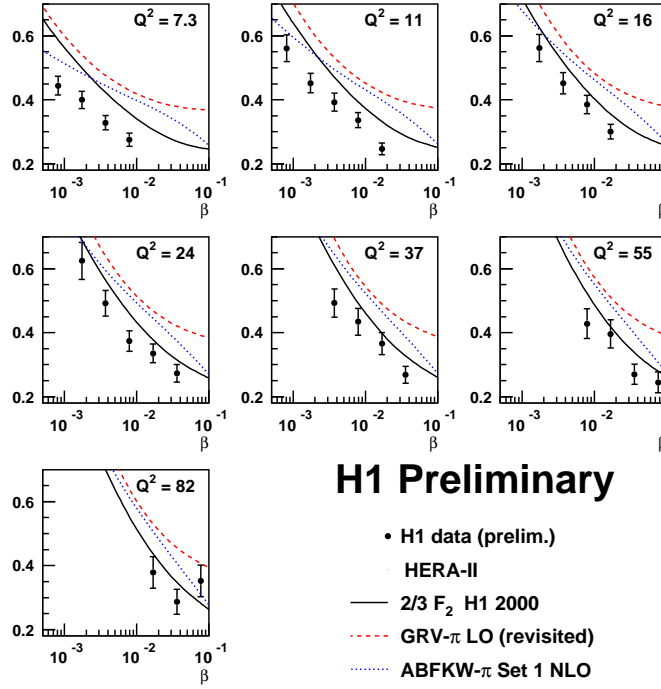


Fig. 19:  $F_2^{\text{LN}(3)}/\Gamma_\pi$  at  $x_L = 0.73$  plotted as a function of  $\beta$  for fixed values of  $Q^2$ . The quantity  $\Gamma_\pi$  is the  $p_T$  integrated pion flux factor.

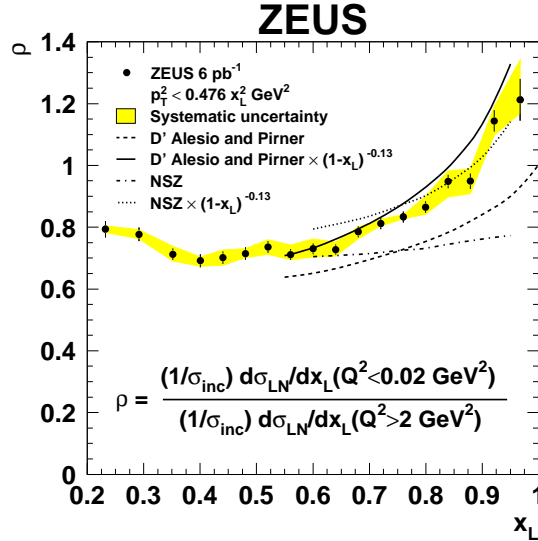


Fig. 20: Ratio of photoproduction and DIS  $x_L$  distributions, compared to the different rescattering models (see text)



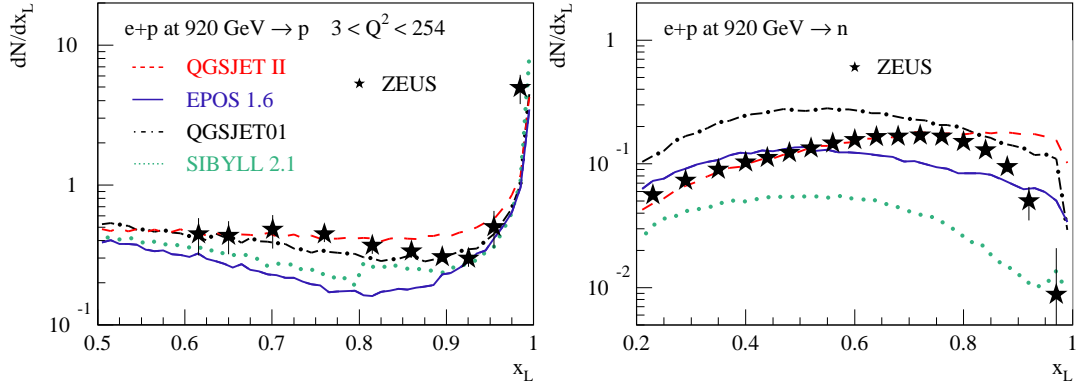


Fig. 21: Comparison of the leading proton and the leading neutron spectra measured at HERA (ZEUS [37]) with the predictions of the models used for cosmic ray analyses.

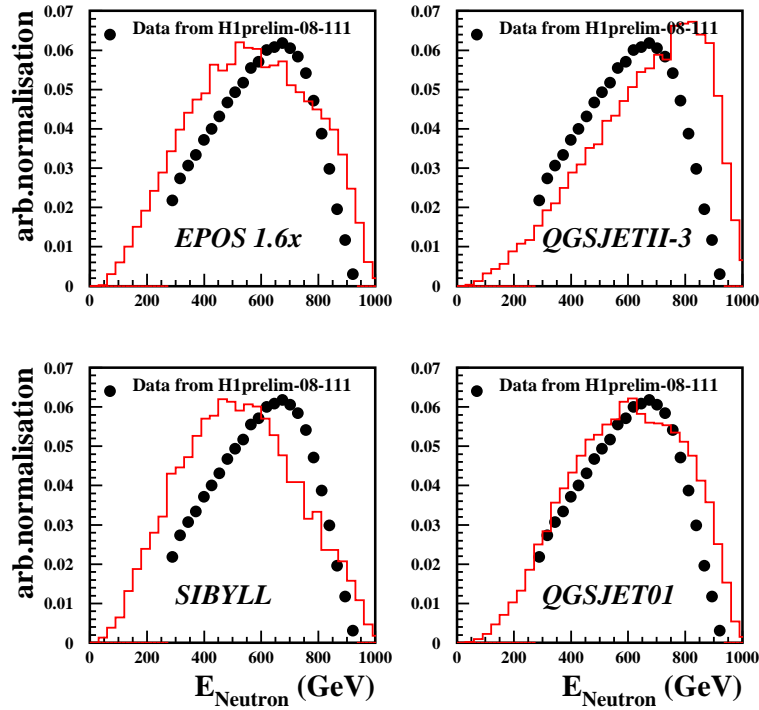


Fig. 22: Comparison of the leading neutron energy spectra measured at HERA (H1 [33]) with the predictions of the models used for cosmic ray analyses. The distributions are normalised to compare the shapes.

**Forward Particles at HERA and Cosmic Rays** The measurements of forward particles at HERA may provide valuable information for the physics of ultra-high energy cosmic rays. Despite the huge difference between the energy ranges accessible in the cosmic rays and the colliders, we may assume that the hadron production in the proton fragmentation region doesn't depend much on the energy and the type of interacting particle. The longitudinal segmentation of the FNC calorimeters at HERA allows to separate signals from the neutrons from that of photons, thus the experiments can measure the differential distributions of  $x_L$  and  $p_T$  for the neutrons and the photons. Moreover, the measurements can be made also for the different proton beam energies (we recall that the last three months the HERA collider was running at lower proton beam energies). The cosmic ray models can make predictions for these measurements and be tuned accordingly.

Comparison of the leading proton and the leading neutron spectra measured at HERA with the predictions of the models used for cosmic ray analyses are shown in Figs. 21 and 22. Here, the comparison is made before the detailed tunings of the models. It demonstrates that the HERA measurements are indeed sensitive to the differences between the models and can be used for the tuning of model parameters.

To summarise, the HERA experiments provide a wealth of measurements of leading baryon production. These measurements give an important input for an improved theoretical understanding of the proton fragmentation mechanism. The HERA data on forward particle production can help to reduce the uncertainty in the model predictions for very high energy cosmic ray air showers.

**Forward Particles at LHC** At the LHC, the collision energy of protons,  $\sqrt{s}=14$  TeV, corresponds to  $10^{17}$  eV in the laboratory system. So the measurements at the LHC are important to constrain the interaction models used in the cosmic-ray studies. The LHC is also capable of colliding different kind of ions. Measurements of ion collisions especially to simulate the interactions between cosmic-rays and atmosphere are also valuable. In the collider experiments, most of the collision energy flows into the very forward direction that is not covered by the general purpose detectors like ATLAS and CMS in case of the LHC. Dedicated experiments to cover these high rapidity region are necessary for the cosmic-ray studies. Fig. 23 shows the energy flux in 14 TeV collisions as a function of pseudo-rapidity  $\eta$ . Two independent experiments LHCf, TOTEM, and sub-detectors of the big experiments ZDCs are capable of measuring very forward particles. Coverage of each experiment in pseudo-rapidity is also indicated in Fig. 23 by arrows. Because each experiment has different capability (charged or neutral particle measurement, hadron or electromagnetic calorimeter, calorimeter or tracker, infinite or finite pseudo-rapidity coverage, aperture, position/energy resolutions), they provide complementary data for total understanding of the very forward particles.

LHCf (LHC forward) is an experiment dedicated to solve the cosmic-ray problems [38]. The experiment is a kind of ZDC (Zero Degree Calorimeter) but optimized to discriminate the interaction models used in the cosmic-ray studies. In LHC, at 140 m away from IP1 the beam pipe makes a transition from a common beam pipe facing the IP to two separate beam pipes joining to the arcs of LHC (the Y vacuum chamber). LHCf has installed two detectors in this 96 mm gap between two pipes at either side of IP1 and will measure the neutral particles of

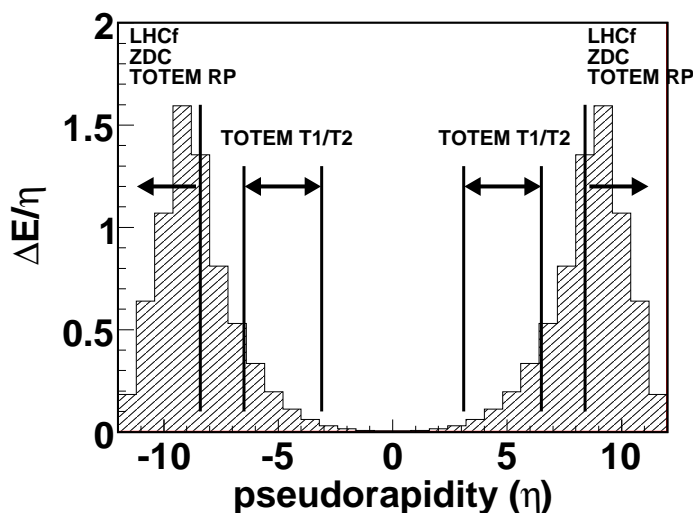


Fig. 23: pseudo-rapidity distribution at LHC

$\eta > 8.4$ . Each detector has two sampling calorimeter towers with  $44 X_0$  made of plastic scintillators and tungsten. The transverse cross-section of the calorimeters ranges from  $20 \text{ mm} \times 20 \text{ mm}$  to  $40 \text{ mm} \times 40 \text{ mm}$ . One detector has Scifi and MAPMT, and the other has silicon strip tracker for position measurements. The detectors can measure the energy and  $P_T$  distributions of gamma-rays and neutrons. Small double-tower configuration enables analysis of  $\pi^0$  mass reconstruction by measuring the energies and positions of decayed gamma-ray pairs, consequently the determination of the  $\pi^0$  energy spectrum. With the energy resolution better than 5% for gamma-rays and 30% for hadrons, and position resolution better than 0.2 mm, major models used in the CR studies can be discriminated as shown in Fig. 24. A comparison study considering some recent models has also predicted large variation from model to model that can be confirmed by the LHCf measurements [39]. LHCf can also study the Landau-Pomeranchuk-Migdal (LPM) effect in detail. In the tungsten calorimeter, electromagnetic showers of  $> \text{TeV}$  energy show  $> 10\%$  deviation from the non-LPM expectation. LHCf is planning to take data in the early stage of the LHC commissioning.

TOTEM is an experiment to measure the total cross section in the proton collisions at IP5 in the LHC [38]. TOTEM measures the numbers of the proton elastic scattering using the Roman Pot detectors and inelastic scattering using the so-called telescopes surrounding the beam pipe. The RP detectors also measure the position of the elastically scattered protons to determine  $dN_{el}/dt$  at  $t=0$  extrapolation. Combining these measurements and the optical theorem, TOTEM will determine the total cross section with  $\pm 1 \text{ mb}$  error.

ZDCs are the sub detectors of the ATLAS, CMS and ALICE experiments. Except a part of the ALICE ZDC (ZP), all ZDCs are installed in the place where the beam pipe is separated into two as was the case of LHCf. The prime motivation of the ZDCs is to determine the energy

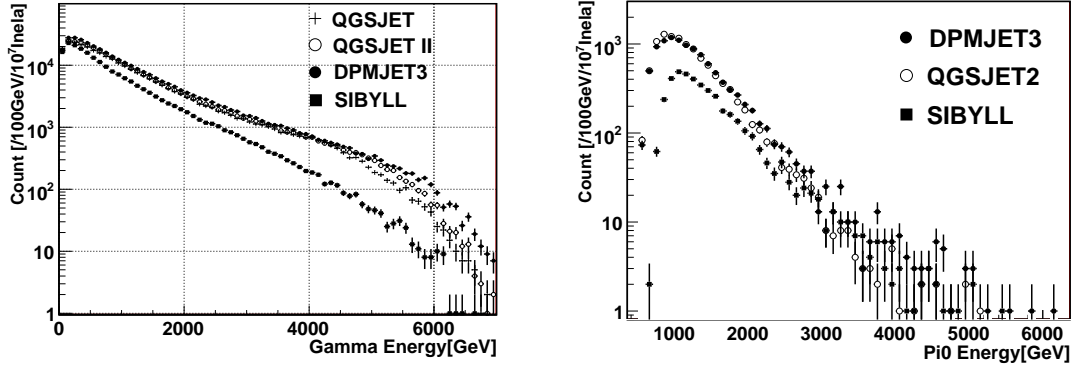


Fig. 24: Energy spectra of single  $\gamma$ -rays and  $\pi^0$ 's expected in the LHCf measurement using different interaction models.

carried by the spectator nucleons in ion collisions. For this purpose, ZDCs have as wide aperture as possible in the limited volume and as thick material as possible to measure the energy flow of the nucleons.

In summary, the LHC gives an unprecedented opportunity to constrain the interaction models used in the cosmic-ray studies. The integration of the data from not only the experiment dedicated for the cosmic-ray science (LHCf) but also the others, especially the forward experiments introduced above is important to constrain the interaction models used in the cosmic-ray studies.

### 3 Neutrino cross section and uncertainties

Predictions of neutrino cross-sections at high energies have sizeable uncertainties which derive largely from the measurement uncertainties on the parton distribution functions (PDFs) of the nucleon. In the framework of the quark-parton model, high energy scattering accesses very large values of  $Q^2$ , the invariant mass of the exchanged vector boson, and very small values of Bjorken  $x$ , the fraction of the momentum of the incoming nucleon taken by the struck quark. Thus when evaluating uncertainties on high energy neutrino cross-sections it is important to use the most up to date information from the experiments at HERA, which have accessed the lowest- $x$  and highest  $Q^2$  scales to date. The present paper outlines the use of the ZEUS-S global PDF fit formalism [40], updated to include *all* the HERA-I data. Full details are given in [41].

Conventional PDF fits use the Next-to-leading-order (NLO) Dokshitzer-Gribov-Lipatov-Altarelli-Parisi (DGLAP) formalism of QCD to make predictions for deep inelastic scattering (DIS) cross-sections of leptons on hadrons. At low- $x$  where the gluon density is rising rapidly it is probably necessary to go beyond the DGLAP formalism in order to resum  $\ln(1/x)$  diagrams, or even to consider non-linear terms which describe gluon recombination. Such approaches are beyond the scope of the present discussion, which is concerned with the more modest goal of estimating the uncertainties on high energy neutrino cross-sections which are compatible with

the conventional NLO DGLAP formalism. As a corollary, if cross-sections much outside the uncertainty bands presented here are observed, it would be a clear signal of the need for extensions to conventional formalism.

This work provide an update on the neutrino cross-sections in the literature [42] which used PDF sets which no longer fit modern data from HERA and an *ad hoc* procedure for estimating PDF uncertainties. There are several improvements on previous work. Firstly, a recent PDF analysis which includes data from all HERA-I running [40] is used. Secondly, a consistent approach to PDF uncertainties – both model uncertainties and, more importantly, the uncertainties which derive from the correlated systematic errors of the input data sets is used. Thirdly, NLO rather than LO calculations are used throughout. Fourthly, a general-mass variable flavour number scheme [43] is used to treat heavy quark thresholds.

The PDF fit formalism of the published ZEUS-S global PDF analysis [40] is used, but this fit is updated as follows. First, the range of the calculation has been extended up to  $Q^2 = 10^{12} \text{ GeV}^2$  and down to  $x = 10^{-12}$ . Second, *all* inclusive cross-section data for neutral and charged current reactions from ZEUS HERA-I running (1994–2000) are included in the fit. Third, the parametrization is extended from 11 to 13 free parameters, input at  $Q_0^2 = 7 \text{ GeV}^2$ .

The most significant source of uncertainties on the PDFs comes from the experimental uncertainties on the input data. The PDFs are presented with full accounting for uncertainties from correlated systematic errors (as well as from statistical and uncorrelated sources) using the conservative OFFSET method. The uncertainty bands should be regarded as 68% confidence limits. The PDF central values and uncertainties from this updated ZEUS-S-13 fit are comparable to those on the published ZEUS-S fit [40], as well as the most recent fits of the CTEQ [44] and MRST [45] groups.

Previous work [42] treated heavy quark production by using a zero-mass variable flavour number scheme, with slow-rescaling at the  $b$  to  $t$  threshold. The exact treatment of the  $b \rightarrow t$  threshold is not very important for the estimation of high energy neutrino cross-sections since the contribution of the  $b$  is suppressed, but the correct treatment of heavy quark thresholds is important in determining the PDFs for lower  $Q^2$  ( $\lesssim 5000 \text{ GeV}^2$ ) and middling  $x$  ( $5 \times 10^{-5} \lesssim x \lesssim 5 \times 10^{-2}$ ) and this is a kinematic region of relevance to the present study.

The results of this study show that the PDF uncertainty on the neutrino (and antineutrino) charged current (CC) cross-sections remains modest ( $< 15\%$ ) even at the highest energies considered here:  $s = 10^{12} \text{ GeV}^2$ . The reason for this is that the high energy ( $E_\nu > 10^7 \text{ GeV}$ )  $\nu N$  and  $\bar{\nu} N$  cross-sections are dominated by sea quarks produced by gluon splitting  $g \rightarrow q\bar{q}$  and, although the PDF uncertainty on the sea quarks is large at low- $x$  and low  $Q^2$ , the dominant contributions to the cross-sections do *not* come from very low  $Q^2$  values. The dominant contributions come from the kinematic region  $50 \lesssim Q^2 \lesssim 10^4 \text{ GeV}^2$  (where the exact region moves up gradually with  $s$ ). The contribution of higher  $Q^2$  ( $Q^2 > M_W^2$ ) is suppressed by the  $W$ -propagator. Furthermore, there is a restriction on the lowest value of  $x$  probed for each  $Q^2$  value due to the kinematic cut-off ( $y < 1$  and since  $x = Q^2/sy$ , we must have,  $x > Q^2/s$ ). This kinematic cut-off ensures that higher  $Q^2$  values do not probe very low- $x$  until the neutrino energies are very high indeed. For example, at  $E_\nu = 1.9 \times 10^7 \text{ GeV}$ , the important range is  $10^{-6} \lesssim x \lesssim 10^{-3}$ , while for  $E_\nu = 5.3 \times 10^9 \text{ GeV}$ , this moves down to  $10^{-8} \lesssim x \lesssim 10^{-4}$ . Full details on the PDF uncertainties and the predictions for the neutrino and antineutrino double

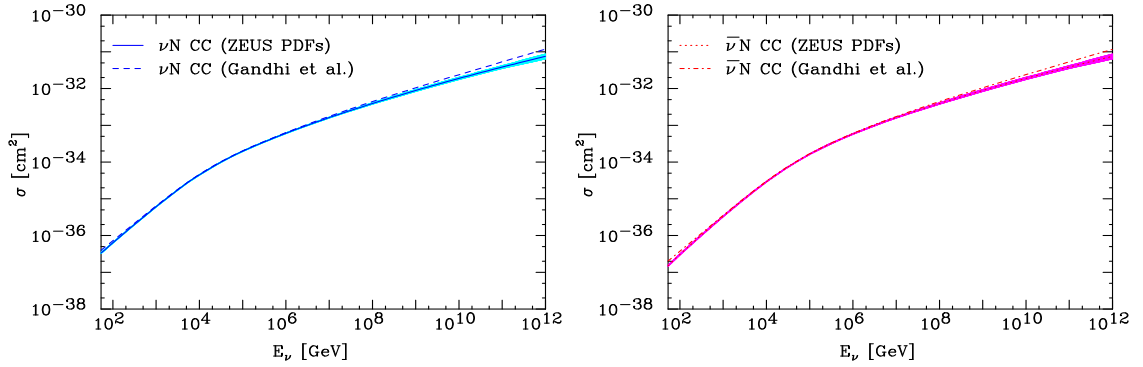


Fig. 25: The total CC cross-section at ultra high energies for neutrinos (left) and antineutrinos (right) along with the  $\pm 1\sigma$  uncertainties (shaded band), compared with the previous calculation by Gandhi *et al.*

differential cross-sections are given in reference [41].

The total CC cross-sections are obtained by integrating the predicted double differential cross-sections  $d^2\sigma/dxdy$ . These cross-sections are illustrated in Fig. 25 together with their uncertainties due to the PDFs, including both model uncertainties and the experimental uncertainties of the input data sets. The trend of the PDF uncertainties at high neutrino energy can be understood by noting that as one moves to higher and higher neutrino energies one also moves to lower and lower  $x$  where the PDF uncertainties are increasing. At lower neutrino energies ( $10^2 < E_\nu < 10^7$  GeV) the high- $x$  region becomes important and the neutrino and antineutrino cross-sections are *different* due to the valence PDF contribution. The onset of the linear dependence of the cross-section on  $s$  for  $s < M_W^2$  can be seen. The trend of the PDF uncertainties in the low energy region can be understood as follows: as one moves to lower neutrino energies one moves out of the very low- $x$  region such that PDF uncertainties decrease. These uncertainties are smallest at  $10^{-2} \lesssim x \lesssim 10^{-1}$ , corresponding to  $s \sim 10^5$ . Moving to yet lower neutrino energies brings us into the high- $x$  region where PDF uncertainties are larger again.

Figure 25 also compares our CC cross-section to the widely used leading-order calculation of Gandhi *et al* [42]. The present results show a less steep rise of the cross-section at high energies, reflecting the fact that more recent HERA cross-section data display a less dramatic rise at low- $x$  than the early data.

In conclusion, the charged current neutrino cross-section at NLO have been calculated in the Standard Model using the best available DIS data along with a careful estimate of the associated uncertainties. If cross-sections much outside the uncertainty bands presented here are observed at UHE cosmic neutrino detectors, it would be a clear signal of the need for extensions to conventional QCD DGLAP formalism.

## References

- [1] H1 Collaboration, I. Abt *et al.*, Nucl. Instrum. Meth. **A386**, 310 (1997).

- [2] ZEUS Collaboration, U. e. ZEUS-Collab., Holm, Status Report (unpublished), <http://www-zeus.desy.de/bluebook/bluebook.html> (1993).
- [3] P. D. B. Collins. Cambridge 1977, 445p.
- [4] V. N. Gribov, V. M. Shekhter, V. A. Kolkunov, and L. B. Okun, Sov. Phys. JETP **14**, 1308 (1962).
- [5] H1 Collaboration, S. Aid *et al.*, Z. Phys. **C69**, 27 (1995), [arXiv:hep-ex/9509001](#).
- [6] ZEUS Collaboration, S. Chekanov *et al.*, Nucl. Phys. **B627**, 3 (2002), [arXiv:hep-ex/0202034](#).
- [7] D. O. Caldwell *et al.*, Phys. Rev. Lett. **40**, 1222 (1978);  
HERA and COMPAS Groups Collaboration, S. I. Alekhin *et al.* CERN-HERA-87-01.
- [8] A. Donnachie and P. V. Landshoff, Phys. Lett. **B437**, 408 (1998), [arXiv:hep-ph/9806344](#).
- [9] J. C. Collins and D. E. Soper, Ann. Rev. Nucl. Part. Sci. **37**, 383 (1987).
- [10] F. Halzen and A. D. Martin. New York, Usa: Wiley ( 1984) 396p.
- [11] V. N. Gribov and L. N. Lipatov, Sov. J. Nucl. Phys. **15**, 438 (1972);  
G. Altarelli and G. Parisi, Nucl. Phys. **B126**, 298 (1977);  
Y. L. Dokshitzer, Sov. Phys. JETP **46**, 641 (1977).
- [12] H. Collaboration, Preliminary Result H1prelim 07-007 (2007);  
Z. Collaboration, Preliminary Result ZEUS-prel 07-026 (2007).
- [13] H. Collaboration, Preliminary Result H1prelim 08-045 (2008);  
Z. Collaboration, Preliminary Result ZEUS-prel 08-003 (2008).
- [14] S. D. Ellis and D. E. Soper, Phys. Rev. **D48**, 3160 (1993), [arXiv:hep-ph/9305266](#).
- [15] ZEUS Collaboration, S. Chekanov *et al.*, Nucl. Phys. **B765**, 1 (2007), [arXiv:hep-ex/0608048](#).
- [16] H1 Collaboration, C. Adloff *et al.*, Eur. Phys. J. **C13**, 609 (2000), [arXiv:hep-ex/9908059](#);  
ZEUS Collaboration, S. Chekanov *et al.*, Eur. Phys. J. **C21**, 443 (2001), [arXiv:hep-ex/0105090](#).
- [17] E. A. Kuraev, L. N. Lipatov, and V. S. Fadin, Sov. Phys. JETP **44**, 443 (1976);  
I. I. Balitsky and L. N. Lipatov, Sov. J. Nucl. Phys. **28**, 822 (1978).
- [18] ZEUS Collaboration, S. Chekanov *et al.*, Eur. Phys. J. **C52**, 515 (2007), [arXiv:0707.3093 \[hep-ex\]](#).

- [19] H1 Collaboration, A. Aktas *et al.*, Eur. Phys. J. **C46**, 27 (2006),  
arXiv:hep-ex/0508055.
- [20] S. Catani and M. H. Seymour, Nucl. Phys. **B485**, 291 (1997),  
arXiv:hep-ph/9605323.
- [21] H. Jung and G. P. Salam, Eur. Phys. J. **C19**, 351 (2001), arXiv:hep-ph/0012143;  
H. Jung, Comput. Phys. Commun. **143**, 100 (2002), arXiv:hep-ph/0109102.
- [22] M. Ciafaloni, Nucl. Phys. **B296**, 49 (1988);  
S. Catani, F. Fiorani, and G. Marchesini, Nucl. Phys. **B336**, 18 (1990).
- [23] H. Jung, Comp. Phys. Commun. **86**, 147 (1995).
- [24] L. Lonnblad, Comput. Phys. Commun. **71**, 15 (1992).
- [25] H. Collaboration, Preliminary Result H1prelim 07-132 (2007);  
Z. Collaboration, Preliminary Result ZEUS-prel 07-025 (2007).
- [26] H. Collaboration, Preliminary Result H1prelim 08-031 (2008).
- [27] Z. Fodor, S. D. Katz, A. Ringwald, and H. Tu, Phys. Lett. **B561**, 191 (2003),  
arXiv:hep-ph/0303080.
- [28] HiRes Collaboration, R. Abbasi *et al.*, Phys. Rev. Lett. **100**, 101101 (2008),  
arXiv:astro-ph/0703099.
- [29] K.-H. Kampert, J. Phys. Conf. Ser. **120**, 062002 (2008), arXiv:0801.1986  
[astro-ph].
- [30] H1 Collaboration, C. Adloff *et al.*, Eur. Phys. J. **C25**, 495 (2002),  
arXiv:hep-ex/0205078;  
ZEUS Collaboration, S. Chekanov *et al.*, Eur. Phys. J. **C34**, 255 (2004),  
arXiv:hep-ex/0312048.
- [31] J. D. Sullivan, Phys. Rev. **D5**, 1732 (1972);  
H. Holtmann, G. Levman, N. N. Nikolaev, A. Szczurek, and J. Speth, Phys. Lett.  
**B338**, 363 (1994);  
B. Kopeliovich, B. Povh, and I. Potashnikova, Z. Phys. **C73**, 125 (1996),  
arXiv:hep-ph/9601291;  
M. Przybycien, A. Szczurek, and G. Ingelman, Z. Phys. **C74**, 509 (1997),  
arXiv:hep-ph/9606294;  
A. Szczurek, N. Nikolaev, and J. Speth, Phys. Lett. **B428**, 383 (1998),  
arXiv:hep-ph/9712261.
- [32] H1 Collaboration, C. A. e. a. H1 Coll., Eur. Phys. J. **C6**, 587 (1999),  
arXiv:hep-ex/9811013;  
ZEUS Collaboration, J. B. e. a. ZEUS Coll., Nucl. Phys. **B596**, 3 (2001),



- arXiv:hep-ex/0010019;  
 ZEUS Collaboration, S. C. e. a. ZEUS Coll., Nucl. Phys. **B637**, 3 (2002),  
 arXiv:hep-ex/0205076;  
 ZEUS Collaboration, S. C. e. a. ZEUS Coll., Phys. Lett. **B590**, 143 (2004),  
 arXiv:hep-ex/0401017;  
 ZEUS Collaboration, S. C. e. a. ZEUS Coll., Phys. Lett. **B610**, 199 (2005),  
 arXiv:hep-ex/0404002;  
 H1 Collaboration, A. A. e. a. H1 Coll., Eur. Phys. J. **C41**, 273 (2005),  
 arXiv:hep-ex/0501074;  
 ZEUS Collaboration, S. C. e. a. ZEUS Coll., Nucl. Phys. **B776**, 1 (2007),  
 arXiv:hep-ex/0702028;  
 F. A. e. a. H1 Coll., *Leading Neutron Production in DIS at HERA* . H1prelim-08-111,  
 presented at ICHEP-08, Philadelphia, 2008.
- [33] H1 Collaboration, *Leading Neutron production in DIS at HERA* . H1-Preliminary-08-111,  
 presented at ICHEP-2008, Philadelphia, 2008.
- [34] A.Bunyatyan and B.Povh, Eur. Phys. J. **A27**, 359 (2006), arXiv:hep-ph/0603235.
- [35] U. D'Alesio and H. J. Pirner, Eur. Phys. J. **A7**, 109 (2000), arXiv:hep-ph/9806321.
- [36] N. Nikolaev, J. Speth, and B. G. Zakharov, *Absorptive corrections to the one pion exchange and measurability of the small-x pion structure function at HERA*. Preprint KFA-IKP(TH)-1997-17, 1997. arXiv:hep-ph/9708290.
- [37] ZEUS Collaboration, S. C. e. a. ZEUS Coll., Nucl. Phys. **B658**, 3 (2003),  
 arXiv:hep-ex/0210029.
- [38] LHCf Collaboration, O. Adriani *et al.*, JINST **3**, S08006 (2008).
- [39] H.-J. Drescher, Phys. Rev. **D77**, 056003 (2008), arXiv:0712.1517 [hep-ph].
- [40] ZEUS Collaboration, S. Chekanov *et al.*, Phys. Rev. **D67**, 012007 (2003),  
 arXiv:hep-ex/0208023.
- [41] A. Cooper-Sarkar and S. Sarkar, JHEP **01**, 075 (2008), arXiv:0710.5303 [hep-ph].
- [42] R. Gandhi, C. Quigg, M. H. Reno, and I. Sarcevic, Phys. Rev. **D58**, 093009 (1998),  
 arXiv:hep-ph/9807264.
- [43] R. S. Thorne and R. G. Roberts, Phys. Rev. **D57**, 6871 (1998),  
 arXiv:hep-ph/9709442;  
 R. S. Thorne, Phys. Rev. **D73**, 054019 (2006), arXiv:hep-ph/0601245.
- [44] J. Pumplin *et al.*, JHEP **07**, 012 (2002), arXiv:hep-ph/0201195;  
 W. K. Tung *et al.*, JHEP **02**, 053 (2007), arXiv:hep-ph/0611254.

- [45] A. D. Martin, R. G. Roberts, W. J. Stirling, and R. S. Thorne, Eur. Phys. J. **C23**, 73 (2002), [arXiv:hep-ph/0110215](#);  
A. D. Martin, W. J. Stirling, R. S. Thorne, and G. Watt, Phys. Lett. **B652**, 292 (2007), [arXiv:0706.0459 \[hep-ph\]](#).

# Model predictions for HERA, LHC and cosmic rays

*A. Bunyatyan, A. Cooper-Sarkar, C. Diaconu, R. Engel, C. Kiesling, K. Kutak, S. Ostapchenko, T. Pierog, T.C. Rogers, M.I. Strikman, T. Sako*

## 1 Hadron production

**Min-bias model comparison** The simple approach of section [1] allows us to extract the main observables which lead the air shower development, namely:

- cross section
- multiplicity
- forward spectra (inelasticity)
- (anti)baryon production

We will compare the commonly used hadronic interaction models for air shower simulations at HERA and LHC energies for these observables.

**Hadronic interaction models** There are several hadronic interaction models commonly used to simulate air showers. For high energy interactions ( $E_{\text{lab}} \gtrsim 100$  GeV), the models studied here are EPOS 1.6 [2,3], QGSJET 01 [4], QGSJET II [5,6], and SIBYLL 2.1 [7–9]. The physics models and assumptions are discussed in, for example, [10]. All the high-energy interaction models reproduce accelerator data reasonably well but predict different extrapolations above  $E_{\text{cms}} \sim 1.8$  TeV ( $E_{\text{lab}} \sim 10^{15}$  eV) that lead to very different results at high energy [11,12]. The situation is different at low energy where several measurements from fixed target experiments are available [13]. There one of the main problems is the extrapolation of measurements to the very forward phase space region close to the beam direction and the lack of measurements of pion-induced interactions. Both HERA and LHC can help to constrain these models.

**Cross section** As seen a previous section, the cross section is very important for the development of air showers and in particular for the depth of shower maximum. As a consequence, the number of electromagnetic particles at ground is strongly correlated to this observable (if the shower maximum is closer to ground, the number of particle is higher).

The proton-proton scattering total cross section is usually used as an input to fix basic parameters in all hadronic interaction models (see paragraph on total cross section below). Therefore, as shown Fig. 1 lefthand-side, the  $p$ - $p$  total cross section is very well described by all the models at low energy, where data exists. And then it diverges above 2 TeV center-of-mass (cms) energy because of different model assumption. Thanks to the TOTEM experiment, the cross section will be measured accurately at LHC energy allowing a strong reduction of the model uncertainty ( $\sim 20\%$ ). In all the figures of this subsection EPOS 1.6 is represented by a full (blue) line, QGSJET II by a dashed (red) line, QGSJET 01 by a dash-dotted (black) line and SIBYLL 2.1 by a dotted (green) line.

From  $p$ - $p$  to proton-air interactions, the Glauber model is used in all models but with different input parameters depending on nuclear effects (none in SIBYLL 2.1, strong in QGSJET II).

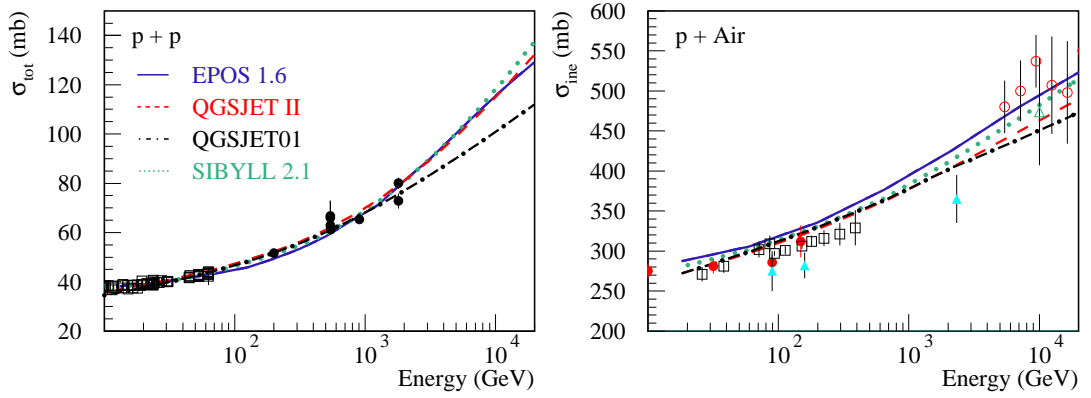


Fig. 1: Total cross section of  $p$ - $p$  collision (lefthand-side) and inelastic proton-air cross section (righthand-side) as calculated with EPOS 1.6 (full line), QGSJET II (dashed line), QGSJET 01 (dash-dotted line) and SIBYLL 2.1 (dotted line). Points are data from accelerator [14] and cosmic ray experiment [15].

So comparing the models to each other (Fig. 1 righthand-side), differences appear even at low energy where the  $p$ - $p$  cross section are similar. And at high energy the spread is again larger. Furthermore, the simulated cross sections seem all to increase faster than the measured one, even at low energy ( $< 1$  TeV) where direct measurement of single hadrons from cosmic rays can be done at ground [15] (almost accelerator like measurement since proton flux is known). Proton-Carbon interactions at LHC would be very helpful to solve this problem.

**Multiplicity** According to Sec. [1], the multiplicity plays a similar kind of role as the cross section, but with a weaker dependence (log). On the other hand, the predictions from the models have much larger differences. As shown Fig. 2, going from the multiplicity of charged particles with  $|\eta| < 3$  for nondiffractive collisions at 900 GeV cms energy (lefthand-side), where models agree with the UA5 data [16], to the multiplicity of charged particles (minimum bias) at 14 TeV (LHC) (righthand-side), the discrepancy can be larger than a factor of 2 in the tail of the distribution (and the shape is different). The EPOS model predicts much smaller multiplicity than QGSJET II.

The multiplicity distribution of charged particles is a very good test of the fundamental property of the hadronic interaction models and it should be one of the first result of the LHC experiments.

**Forward spectra** Forward particle distributions are crucial for air shower development because most of the energy is carried by these particles (and not the ones in the central region). The forward spectra have been measured in fixed target experiment at energies of few hundreds of GeV (few tens of GeV in cms energy) and the models reproduce this data correctly since they are used to fix some model parameters.

At higher energy, hadron collider experiments could not measure particles in the very

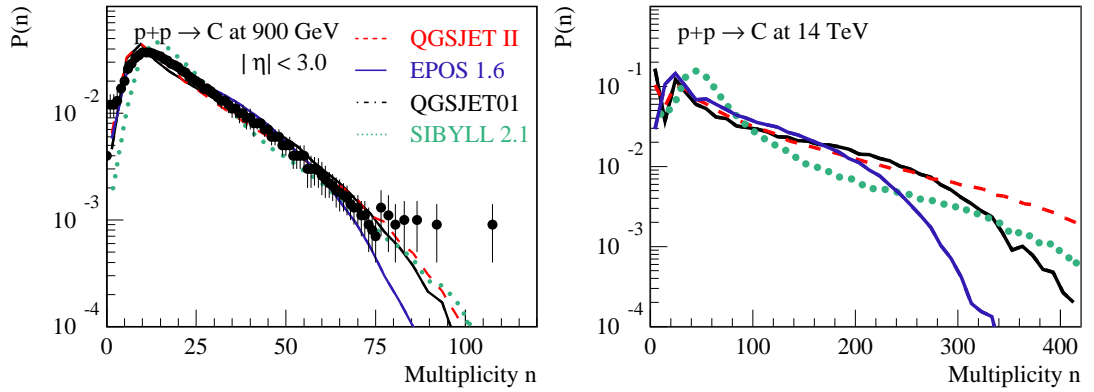


Fig. 2: Multiplicity distribution of  $\bar{p}$ - $p$  collision at 900 GeV cms energy (lefthand-side) and 14 TeV (righthand-side) as calculated with EPOS 1.6 (full line), QGSJET II (dashed line), QGSJET 01 (dash-dotted line) and SIBYLL 2.1 (dotted line). Points are data [16].

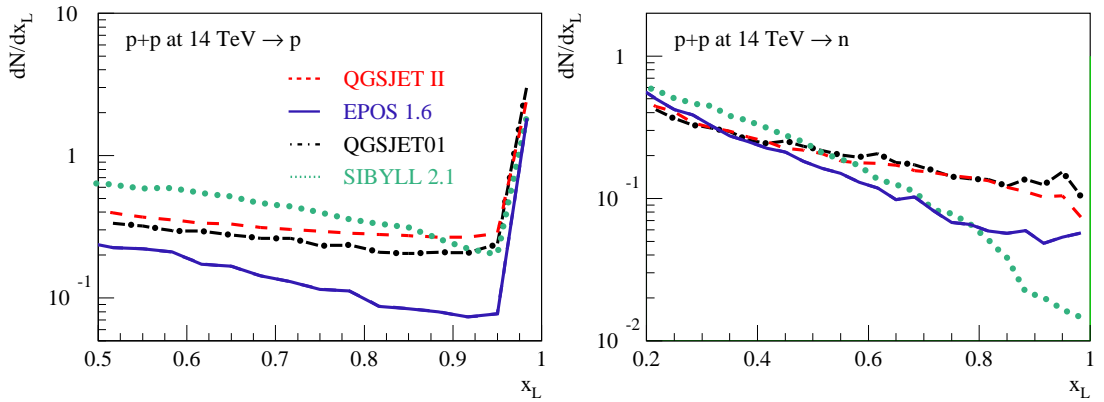


Fig. 3: Longitudinal  $x_L = p_L/P_{Beam}$  distribution from  $p$ - $p$  collision at 14 TeV cms energy for proton (lefthand-side) and neutron (righthand-side) as calculated with EPOS 1.6 (full line), QGSJET II (dashed line), QGSJET 01 (dash-dotted line) and SIBYLL 2.1 (dotted line).

forward region. But we can test the models thanks to the electron-proton HERA collider where proton or neutron production on the proton side can be measured up to very high longitudinal momentum. Results are shown Fig. [17]. While the models agree on  $x_L$  distributions at low energy, we can observe differences between them at HERA energy and in particular for EPOS 1.6 which seems to have a too strong proton dissociation in the forward region compared to the ZEUS experiment [18].

Various experiments at LHC (cf sec. [19]) should provide very usefull new data in this kinematic region, where we can see on Fig. 3, that the discrepancy between the models is very large.

**(Anti)Baryon production** In the forward region, the number of (anti)baryons is very important for the number of muons produced in air shower. The process is well described in [20], where it is also shown that the number of antiprotons on the projectile side of  $\pi$ -carbon collision can only be reproduced correctly by the EPOS model. This is due to a more sophisticated remnant treatment in this model which allows baryon number transfer from the inner part of the collision to the forward (or backward) region.

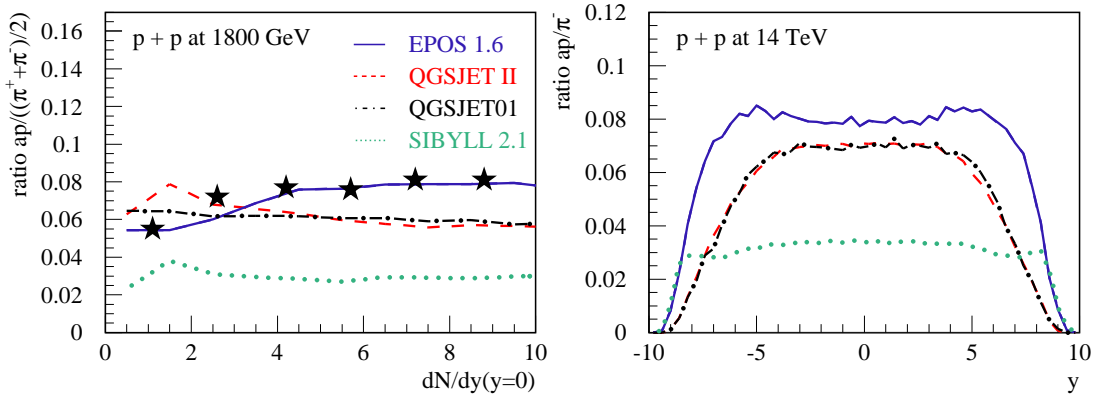


Fig. 4: Ratio of anti-proton over pion in  $\bar{p}$ - $p$  scattering at 1.8 TeV cms energy as a function of the plateau height (lefthand-side) and rapidity distribution of this ratio for  $p$ - $p$  interactions at LHC as calculated with EPOS 1.6 (full line), QGSJET II (dashed line), QGSJET 01 (dash-dotted line) and SIBYLL 2.1 (dotted line). Points are data [21, 22].

Another particularity of the (anti)baryons is that their production increase faster with the energy that the pion production. In other words, the ratio  $\bar{p}/\pi$  increase with energy. At the highest measured energy (TEVATRON [22]), we can see on the lefthand-side of Fig. 4, that only EPOS describes correctly this ratio as a function of the event multiplicity. Other models are too low.

Extrapolating to LHC, the difference between the models appears clearly on the rapidity distribution of the  $\bar{p}/\pi^-$  as shown Fig. 4 on the righthand-side. This ratio at midrapidity seems to saturate since the values at LHC are similar to the ones at TEVATRON, but the shape is really different comparing the models. Because of its remnant structure, EPOS predicts much more antiproton in the forward region of non-diffractive events ( $|y| \sim 7$ ).

This explain why air showers simulated with EPOS contain more muons. Measurement of (anti)-baryon distributions at LHC will be very important to constrain muon number in air showers.

**Total cross section** Among the most important quantities relevant for hadronic model applications to cosmic ray (CR) physics is the total hadron-hadron cross section  $\sigma^{\text{tot}}$ . The reason for that is twofold. First of all, the knowledge of the total cross section implies the knowledge of the corresponding elastic scattering amplitude, taken the optical theorem relation between the two quantities. Hence, one is able to calculate the corresponding inelastic cross section and, using the Glauber formalism, to generalize these results to hadron-nucleus collisions. In turn, inelastic hadron-air cross sections are crucial quantities for the description of CR-induced nuclear-electromagnetic cascades in the atmosphere, so-called extensive air showers (EAS).

Secondly, with the total cross section being the sum of partial contributions of all possible final states for a given reaction, optical theorem allows one, within a particular model approach, to establish a correspondence between various contributions to the elastic scattering amplitude and partial probabilities of particular configurations of the interaction. Thus, available experimental information on the energy dependence of  $\sigma_{pp}^{\text{tot}}$  may significantly constrain model predictions for basic characteristics of hadron production in the high energy asymptotics.

In particular, such a mapping is provided by the Gribov's Reggeon Field Theory (RFT) [23], where elastic hadron-hadron scattering is described by multiple exchanges of composite objects – Pomerons. Correspondingly, inelastic cross section may be obtained as a sum of contributions of certain unitarity cuts of elastic scattering diagrams, applying the Abramovskii-Gribov-Kancheli (AGK) cutting rules [24]. There, partial contributions to  $\sigma_{ad}^{\text{inel}}$  correspond to configurations of the interaction with a given number of 'elementary' production processes, the latter being described as 'cut Pomerons'. In fact, the essence of the AGK rules is that there is no interference between final states with different numbers of 'cut Pomerons', thanks to the fact that they occupy different regions of the phase space.

The described scheme takes an especially simple form if one assumes eikonal vertices for Pomeron-hadron coupling. However, one has to take into consideration contributions of multi-particle intermediate states for the projectile and target hadrons, 'between' Pomeron exchanges. The latter give rise to the diffraction dissociation and inelastic screening, the two phenomena being closely related to each other. Restricting oneself with low mass intermediate states only, one can develop a scheme of Good-Walker type, considering Pomeron-hadron coupling to be a matrix, whose elements correspond to transitions between hadronic elastic scattering eigenstates, and to obtain for total and absorptive (non-diffractive) hadron  $a$  - hadron  $d$  cross sections [25]

$$\sigma_{ad}^{\text{tot}}(s) = 2 \sum_{i,j} C_{i/a} C_{j/d} \int d^2b \left( 1 - e^{-\lambda_{i/a} \lambda_{j/d} \chi_{ad}^{\text{P}}(s,b)} \right) \quad (1)$$

$$\sigma_{ad}^{\text{abs}}(s) = \sum_{i,j} C_{i/a} C_{j/d} \int d^2b \left( 1 - e^{-2 \lambda_{i/a} \lambda_{j/d} \chi_{ad}^{\text{P}}(s,b)} \right) \quad , \quad (2)$$

where the Pomeron exchange eikonal  $\chi_{ad}^{\text{P}}(s, b)$  is the imaginary part of the corresponding amplitude in the impact parameter representation (the small real part can be neglected in high energy

asymptotics) and  $C_{i/a}$ ,  $\lambda_{i/a}$  are relative weights and relative strengths of elastic scattering eigenstates for hadron  $a$ .

Apart from the very possibility of introducing diffraction dissociation, the above-described treatment has two important differences from the purely eikonal scheme. First, both total and inelastic cross sections are reduced, the effect being enhanced for a scattering on a nuclear target. Predictions of cosmic ray interaction models for  $\sigma_{h\text{--air}}^{\text{inel}}$  sizably differ, depending on whether or not the inelastic screening corrections are taken into account and being in contradiction with available data in the latter case, see Fig. 1. Secondly and even more importantly, one obtains significantly bigger fluctuations of multiplicity of produced particles and of numbers of 'wounded' nucleons in hadron-nucleus and nucleus-nucleus interactions, which has a strong impact on specifying the 'centrality' of nuclear collisions in collider applications. It is worth stressing, however, that the described quasi-eikonal scheme can not treat high mass multi-particle intermediate states which give rise to high mass diffraction processes and result in additional screening contributions. The solution of the problem is provided by taking into consideration so-called enhanced diagrams corresponding to Pomeron-Pomeron interactions [5, 26, 27].

In hadronic interaction models, the Pomeron eikonal  $\chi_{ad}^P$  is usually split into two parts, corresponding to partial contributions of 'soft' and 'semi-hard' parton cascades to elementary scattering process [4, 28]:

$$\chi_{ad}^P(s, b) = \chi_{ad}^{\text{Psoft}}(s, b) + \chi_{ad}^{\text{Psh}}(s, b) \quad (3)$$

In particular, in the 'mini-jet' approach [28] the 'semi-hard' eikonal is expressed as the product of the corresponding inclusive cross section  $\sigma_{ad}^{\text{jet}}(s, p_{t,\text{cut}})$  for the production of parton jets with transverse momentum exceeding some cutoff  $p_{t,\text{cut}}$  and the hadron overlap function  $A(b)$  (convolution of hadronic form factors):

$$\chi_{ad}^{\text{mini-jet}}(s, b) = \sigma_{ad}^{\text{jet}}(s, p_{t,\text{cut}}) A(b), \quad (4)$$

where the inclusive jet cross section is given by a convolution of parton distribution functions (PDFs)  $f_{i/a}(x, Q^2)$  with the parton scatter cross section  $d\sigma_{ij}^{2\rightarrow 2}/dp_t^2$ :

$$\sigma_{ad}^{\text{jet}}(s, p_{t,\text{cut}}) = \sum_{i,j} \int dx^+ dx^- dp_t^2 f_{i/a}(x^+, p_t^2) f_{j/d}(x^-, p_t^2) \frac{d\sigma_{ij}^{2\rightarrow 2}}{dp_t^2} \Theta(p_t^2 - p_{t,\text{cut}}^2) \quad (5)$$

However, when realistic PDFs are employed, the steep energy rise of  $\sigma_{pp}^{\text{jet}}$  leads to a contradiction between the predicted and measured  $\sigma_{pp}^{\text{tot}}$ . To overcome the problem, one usually assumes that the low- $x$  rise of hadronic PDFs is strongly damped by parton saturation effects which are often mimicked via using an energy-dependent  $p_t$ -cutoff:  $p_{t,\text{cut}} = p_{t,\text{cut}}(s)$  [29]. Recently, one attempted to derive constraints on the required  $p_{t,\text{cut}}(s)$  dependence, based on the ansatz (4) [30]. Nevertheless, the situation remains puzzling: on one hand, one needs significant saturation effects in order to damp the quick energy rise of  $\sigma_{pp}^{\text{tot}}$ , on the other – no such a strong saturation has been observed in DIS experiments at HERA. A possible solution is that the factorization ansatz (4) for the semi-hard eikonal becomes invalid when non-linear corrections to parton dynamics are taken into account [6]. The latter is easy to understand when bearing in mind that the QCD



factorization applies to fully inclusive quantities only, an example being the inclusive jet cross section (5), while being inapplicable for calculations of hadronic cross sections and of partial probabilities of particular final states. As was shown in [6], the semi-hard eikonal still can be cast in the form similar to (4-5), however, with the usual PDFs  $f_{i/a}(x, Q^2)$  being replaced by reaction-dependent ones. Unlike the usual PDFs measured in DIS, those describe parton evolution *during the interaction process*, which is thus influenced by parton re-scattering on the partner hadron, as depicted in Fig. 5.

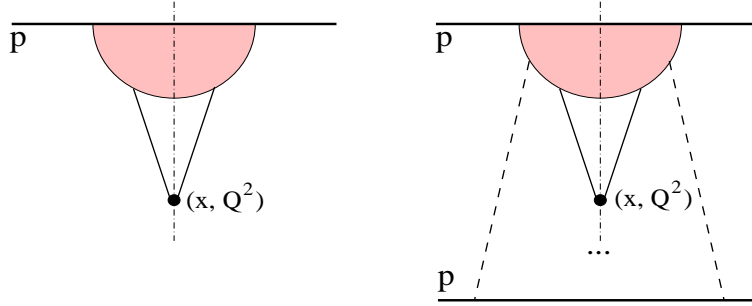


Fig. 5: Schematic view of parton distributions as “seen” in DIS (left) and in proton-proton collision (right). Low  $x$  parton (sea quark or gluon) originates from the initial state “blob” and interacts with a highly virtual “probe”. In proton-proton interaction the initial “blob” itself is affected by the collision process – due to additional soft re-scatterings on the target, indicated by dashed lines.

**Screening and saturation effects in MC models** Crucial differences between present hadronic MC generators are related to how they treat nonlinear interaction effects emerging in the high parton density regime. The latter appear naturally when considering hadron-hadron and, especially, nucleus-nucleus scattering in the limit of high energies and small impact parameters, where a large number of parton cascades develops in parallel, being closely packed in the interaction volume. In the QCD framework, the corresponding dynamics is described as merging of parton ladders, leading to the saturation picture: at a given virtuality scale the parton density can not exceed a certain value; going to smaller momentum fractions  $x$ , further parton branching is compensated by merging of parton cascades [31]. Importantly, at smaller  $x$ , the saturation is reached at higher and higher virtuality scale  $Q_{\text{sat}}^2(x)$ . The approach has been further developed in the large  $N_c$ -based color glass condensate (CGC) framework, where detailed predictions for the  $Q_{\text{sat}}^2(x)$  behavior have been derived [32].

In MC generators, one usually attempts to mimic the saturation picture in a phenomenological way. Standard method, employed, e.g., in the SIBYLL model [7–9], is to treat the virtuality cutoff  $Q_0^2$  between soft and semihard parton processes as an effective energy-dependent saturation scale:  $Q_0^2 = Q_{\text{sat}}^2(s)$  and to neglect parton (and hadron) production at  $|q^2| < Q_0^2(s)$ . The parameters of the corresponding  $Q_0^2(s)$  parametrization are usually tuned together with the other model parameters by fitting the measured proton-proton cross section.

A more sophisticated procedure has been applied in the EPOS model [3], where effective

saturation effects, being described by a set of parameters, depend on energy, impact parameter, types of interacting hadrons (nuclei). The corresponding mechanism influences not only the configuration of the interaction (how many processes of what type occur) but also the energy partition between multiple scattering processes and the hadronization procedure, the relevant parameters being fitted both with cross section and with particle production data.

An alternative approach has been employed in the QGSJET II model [5, 6], providing a microscopic treatment of nonlinear effects in the RFT framework: describing the latter by means of enhanced diagrams [26], corresponding to Pomeron-Pomeron interactions. In particular, the procedure proposed in [5] allowed one to resum contributions of dominant enhanced graphs to the scattering amplitude to all orders in the triple-Pomeron coupling. Furthermore, to treat secondary particle production, the unitarity cuts of the corresponding diagrams have been analyzed and a procedure has been worked out to resum the corresponding contributions for any particular final state of interest [27], which allowed one to implement the algorithm in the MC generator and to sample various configurations of the interaction in an iterative fashion. The main drawback of the approach is the underlying assumption that Pomeron-Pomeron coupling is dominated by soft ( $|q^2| < Q_0^2$ ) parton processes. Thus, in contrast to the perturbative CGC treatment, the model has no dynamical evolution of the saturation scale: the saturation may only be reached at the  $Q_0^2$  scale; at  $|q^2| > Q_0^2$  parton evolution is described by purely linear DGLAP formalism.

**Fragmentation of hadrons at ultra high energies** Currently practically no experimental information is available on production of leading hadrons ( $x_F \geq 0.1$ ) in the hadron - hadron collisions at the collider energies. At fixed target energies production of leading hadrons involves several partons of the projectile. For example, production of baryons in  $x_F \geq 0.4$  predominantly involves at least two valence quarks of the proton, which did not experience a significant inelastic interaction, leading to a rather flat distribution in  $x_F$ . Similarly, the spectrum of the leading pions is much harder than the one corresponding to the fragmentation of one quark of the proton.

At high energies a novel situation emerges since a parton of the projectile with a given  $x_{pr}$  can resolve partons in the target with smaller and smaller  $x_T \geq 4k_t^2/(x_{pr}s_{NN})$ . Here  $k_t$  is typical parton transverse momentum in the interaction. The cross section of inelastic interaction is proportional to the gluon density at  $x = x_T$ ,  $Q^2 \sim 4k_t^2$ . For  $x_{pr} = 0.3$ ,  $k_t = 1$  GeV/c at LHC (GZK) energies  $x$  down to  $\sim 10^{-7}(10^{-10})$  are resolved. As a result, probability of inelastic interaction for a parton passing at a fixed distance  $\rho$  from the center of the other nucleon grows with energy roughly as  $s^n$ ,  $n \geq 0.25$  until it reaches values close to one - the black disk regime (BDR). For example, at LHC energies, at  $\rho = 1$  fm the interaction is black for the leading quarks with  $p_t^2 \leq 1$  (GeV/c)<sup>2</sup> and for leading gluons with  $p_t^2 \leq 2$  (GeV/c)<sup>2</sup>, see [33] for the review. Between LHC and GZK energies the strength of interaction for fixed  $\rho$ , and given virtuality is expected to increase by at least a factor of five extending further the region of  $\rho$  where interaction remains black up to large virtualities. The range of  $\rho$  where interaction is black grows as a power of energy, while soft diffusion changes the radius of strong interaction logarithmically. Hence the fraction of peripheral inelastic collisions in which leading partons of the nucleon remain spectators should decrease with energy. (Obviously the effect is even stronger for the cosmic ray interactions with air ( $\langle A \rangle \sim 14$ ).)

In the BDR two effects modify fragmentation. One is that interaction selects configura-

tions in the colliding hadrons with large transverse momenta comparable to the scale of the BDR for given  $x_{pr}, \rho$ . This effectively results in the fractional energy losses [34,35]. The second effect is the loss of coherence between the leading partons as they receive large transverse momenta and cannot fragment jointly to the same leading hadron. As a result, the projectile becomes “shattered”: The leading partons with  $x \sim 0.2$  fragment independently into minijets with transverse momenta of few GeV and rapidities

$$y_{\text{minijet}} = y_{\text{max}} + \ln x - \ln(p_{\text{t BDR}}/m_N), \quad (6)$$

where  $y_{\text{max}} = \ln(p_N/m_N)$ . Production of hadrons from these minijets proceeds independently over a range of rapidities determined by condition that transverse momentum of hadrons in the jets due to primordial transverse momentum of a parton is larger than the soft transverse momentum scale  $p_{\text{t soft}} \sim 0.4 \text{ GeV}/c$ . In the fragmentation process the transverse momentum of the primary parton is shared by produced partons in proportion of their light cone fractions. Hence, one can estimate the range of fractions,  $z$ , of the jet momentum where fragmentation of partons can be treated as independent:

$$z = p_{\text{t soft}}/p_{\text{t BDR}}. \quad (7)$$

For  $p_{\text{t BDR}} \sim 1 \text{ GeV}/c$  and  $x \sim 0.2 \div 0.25$  this corresponds to  $x_F \geq 0.1$ . With increase of energy the range where independent fragmentation is valid should expand.

In the central  $p(\pi)A$  collisions where nucleus edge effects can be neglected the differential multiplicity of leading hadrons, integrated over  $p_{\perp}$ , is approximately given by the convolution of the nucleon parton density,  $f_a$ , with the corresponding parton fragmentation function,  $D_{h/a}$ , at the scale  $Q_{\text{eff}}^2 = 4p_{\text{t BDR}}^2$  [34,36–38]:

$$\frac{1}{N} \left( \frac{dN}{dx_F} \right)^{p+A \rightarrow h+X} = \sum_{a=q,g} \int_{x_F}^1 dx x f_a(x, Q_{\text{eff}}^2) D_{h/a}(x_F/x, Q_{\text{eff}}^2), \quad (8)$$

where  $N$  is total number of inelastic events. Eq.8 leads to a much steeper decrease of the forward spectrum with  $x_F$  than the one observed in soft collisions, and, in particular, to the  $\pi/N$  ratio  $\gg 1$  for  $x_F \geq 0.2$ . Hence the large  $x_F$  inclusive spectrum is likely to be dominated by very peripheral collisions which constitute progressively smaller fraction of the collisions with increase of energy. Hence one expects that the forward multiplicity will decrease with energy. Another manifestation of this mechanism is broadening of the transverse distribution of the forward hadrons which essentially reflects transverse momenta of the forward jets [36].

First studies of these effects for GZK energies were performed in [36]. It was found that a strong increase of the gluon densities at small  $x$  leads to a steeper  $x_F$ -distribution of leading hadrons as compared to low energy collisions and results in a significant reduction of the position of the shower maximum,  $X_{\text{max}}$ . Account of this effect in the models currently used for the interpretation of the data may shift fits of the composition of the cosmic ray spectrum near the GZK cutoff towards lighter elements.

In the near future it will be possible to test experimentally these prediction in the central deuteron - gold collisions at RHIC. Another possibility is to study  $pp$  collisions at the LHC with special centrality triggers [39]. At the same time such measurements would not test dynamics

of fragmentation in ultra high-energy pion - nucleus collisions which constitute the bulk of the air showers. The interaction which is most similar to  $\pi A$  interactions (especially for low  $p_t$ ) and could be studied at the collider energies in ultraperipheral heavy ion collisions is  $\gamma A$  collisions. In such collisions nuclei collide at large impact parameters where one nucleus effectively serves as a source of the Weizsacker-Williams photons. At the LHC one can probe a wide range of energies  $W_{\gamma N} \leq 1$  TeV [40]. For  $W_{\gamma N} \leq 200$  GeV it will be possible to compare forward spectra to the HERA data on the  $\gamma p$  collisions. It will be also possible to study forward spectrum as a function of  $W_{\gamma N}$ .

## 2 Ultra-high energy photons and s-channel unitarity

**Photon cross sections at ultra-high energies** Extrapolations of  $\gamma p$  and  $\gamma A$  cross sections to extremely high energies are frequently used in studies of ultra-high energy (UHE) cosmic rays. In particular, the UHE photon cross section is related to the cosmic ray air shower maximum,  $X_{max}$  (see [41] and references therein for a recent review). Furthermore, the identity of the primary particle affects the shape of the resulting air-shower.

At UHE energies, the incident photon interacts with the hadron target by first fluctuating into a virtual hadronic state a large distance ahead of the target. Probability of such interaction may become comparable to the probability of the electromagnetic interactions in the media, see review in [42]. Each of the virtual hadronic states interacts with the target with a strength characterized by its transverse size (which is inversely related to the state's virtuality). As the center-of-mass energy increases, there is an increasingly large contribution to the photon wavefunction from very small size quark-antiquark pairs.

It can be argued on the basis of general assumptions that the asymptotic energy dependence of photon cross sections is a power of  $\ln s$  somewhere between 2 and 3 [43, 44]. An important point is that one cannot directly apply the Froissart bound,  $\sigma_{tot} \sim \sigma_{\pi N} \propto \ln^2 s$ , to photon-hadron interactions because the incident photon wavefunction is non-normalizable – there is an ultra-violet divergent contribution coming from small size configurations. Furthermore, a model based on the combined contributions of a hard Pomeron and a soft Pomeron [45] badly violates unitarity in the asymptotic limit because of the power-law behavior of the cross section. (This is true even if eikonalization is used to enforce  $s$ -channel unitarity, because the power-law growth of the basic cross section leads to a power-law growth of the radius of the interaction in impact parameter space.) See [46] and references therein for a review of the different types of energy dependence for the  $\gamma p$  cross section predicted from various models.

Constraints on the growth of the photon cross section can be obtained by enforcing  $s$ -channel unitarity in impact parameter space for each individual hadronic state in the photon wavefunction. The method that we focus on here is the one used in [47] to address the unitarity limit in HERA data, and extended to the UHE real photon case in [43]. In this approach, the large size configurations have cross sections that grow at a rate typical of hadron-hadron interactions, while small size configurations have cross sections that grow according to leading twist (LT) pQCD. Intermediate sizes are obtained by extrapolating between these two regions. Configurations that grow according to LT pQCD quickly become too large to be realistic and violate  $s$ -channel unitarity. The approach in [43] is simply to allow this rapid growth, but to cut off

impact parameter dependent cross sections at their maximum possible values when they start to violate unitarity. The advantage of this approach is that it provides a conservative upper bound on the  $\gamma p$  cross section. The main disadvantage is that it does not address the details of the higher-twist dynamical effects and/or non-perturbative effects that tame the cross section and are ultimately responsible for enforcing unitarity.

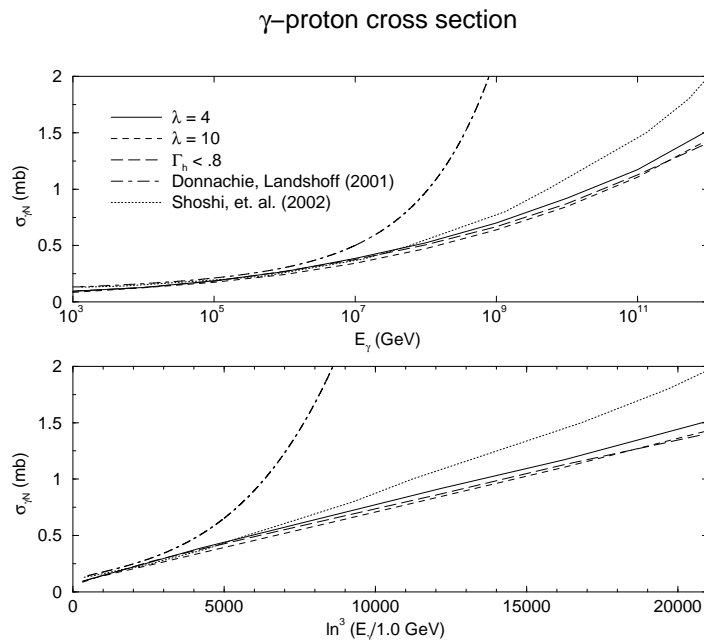


Fig. 6: The solid line is the dependence obtained the lower dashed lines show the sensitivity to variations in model parameters.

Figure 6 is taken from [43] and compares the unitarity-corrected model with models that allow a violation of  $s$ -channel unitarity. It should also be noted that the model of [43] is consistent with other extrapolations (see, e.g., [48]) based on logarithmic energy growth. Note that, although the unitarity corrections in [43] provide a conservative amount of taming, it still leads to a cross section that is less than what is predicted from parameterizations that use a power-law behavior for the basic cross section.

**Charm contribution** The framework in the previous section also allows for an estimate of the contribution to the photon cross section from charmed mesons.

The contribution of charm in the photon wavefunction is generally suppressed by the mass of the charm quark. However, at extremely high energies, there are large contributions from highly virtual quark-antiquark fluctuations, and for these fluctuations the suppression from the charm mass becomes negligible. If the energy is high enough that the  $\gamma p$  cross section is entirely dominated by these very small quark-antiquark pairs, then we expect a full recovery of flavor SU(4) symmetry. In other words, we could expect up to 40% of the cross section to be due to charm quarks. An analysis of this type was performed in [43] and shows that a significant contribution, around 25% of the cross section, is due to charm quarks. See also recent work in [49].

The enhancement of the charm production in the fragmentation region in the high gluon density regime should occur also for the hadron induced cascades. It should lead to an enhancement of the production of ultra-high energy muons in the cores of air showers with energies comparable with the GZK cutoff.

**Nuclear targets** For  $\gamma A$  interactions, a natural expectation is that one can directly extend the analysis for the proton target discussed in the previous section to the nuclear case by replacing the impact parameter dependent parton distribution function of the proton with the corresponding distribution function for a nucleus. However, allowing the full disk of the nuclear target to grow black yields cross sections that are even larger than what one expects from a naive extension of a Glauber type model of photon-nucleus cross sections. In a more realistic treatment, therefore, we can simply use the  $\gamma p$  cross section from section 2 in a Glauber-Gribov treatment of the interaction with a nuclear target. A large value of the  $\sigma_{diff}^{\gamma N}/\sigma_{tot}^{\gamma N} \sim 1/2$  results in a large nuclear shadowing and hence slower increase of the  $\gamma - A$  cross section with energy than in the  $\gamma p$  case. The resulting cross section from [43] is shown in Fig. 7.

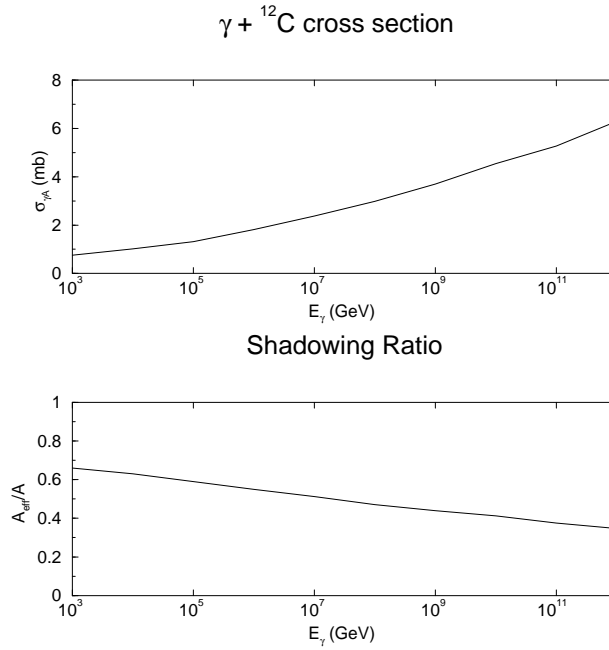


Fig. 7: The upper plot shows the cross section for a photon to scatter off Carbon using the basic cross section from section (2). The lower plot shows the corresponding shadowing ratio.

### 3 Extrapolation of neutrino cross section

Extrapolation of neutrino cross-section towards very high energy is needed if we want to estimate flux of ultrahigh energy neutrinos of extragalactic sources like Active Galactic Nuclei. Such estimation might be useful for Ice Cube experiment which can detect neutrinos of energy  $10^{12}$  GeV and higher. The dominant interaction with matter at such energies is Deep Inelastic Scattering on

nucleons and in particular with the gluonic component. This gluonic system is probed roughly at  $x = 10^{-8}$ . In order to be consistent with unitarity bound which states that total cross-section should grow not faster than  $\log^2 1/x$  one has to allow for gluon recombination effects which reduce the rate of growth of gluon density. The most suitable approach to calculate the UHE neutrino nucleon cross-section is the  $k_t$  factorisation approach (high energy factorisation). Within this scheme in order to calculate the neutrino cross-section one performs convolution of transverse momentum dependent hard matrix element (which in this case is weak boson-gluon fusion) with unintegrated gluon distribution which takes into account high energy effects. The evolution equation which introduces a large part of recombination effects in lepton-nucleon scattering is the Balitsky-Kovchegov [50] equation. This equation generalizes the BFKL [51] equation. It consists of a linear term which accounts for fast growth of gluon density at moderate values of  $x$  and nonlinear term which comes with negative sign which tames the growth of gluon density at low  $x$ . In reference [52] the calculation of  $F_2(x, Q^2)^{CC,NC}$  using the BK equation (with subleading corrections) was performed and the UHE neutrino-nucleon cross-section was calculated. This calculation shows (see Fig. 8 (right)) that nonlinear effects reduce cross-section roughly by a factor of two as compared to approach based on linear evolution equation (BFKL with subleading corrections). In the calculation it was assumed that gluons are uniformly distributed in the nucleon. A more realistic initial distribution would increase slightly the cross section as compared to obtained from uniformly distributed gluons.

## References

- [1] A. Bunyatyan et al, *Introduction*. These proceedings.
- [2] H. J. Drescher, M. Hladik, S. Ostapchenko, T. Pierog, and K. Werner, Phys. Rept. **350**, 93 (2001), arXiv:hep-ph/0007198.
- [3] K. Werner, F.-M. Liu, and T. Pierog, Phys. Rev. **C74**, 044902 (2006), arXiv:hep-ph/0506232.
- [4] N. N. Kalmykov, S. S. Ostapchenko, and A. I. Pavlov, Nucl. Phys. Proc. Suppl. **52B**, 17 (1997).
- [5] S. Ostapchenko, Phys. Lett. **B636**, 40 (2006), arXiv:hep-ph/0602139.
- [6] S. Ostapchenko, Phys. Rev. **D74**, 014026 (2006), arXiv:hep-ph/0505259.
- [7] R. S. Fletcher, T. K. Gaisser, P. Lipari, and T. Stanev, Phys. Rev. **D50**, 5710 (1994).
- [8] J. Engel, T. K. Gaisser, T. Stanev, and P. Lipari, Phys. Rev. **D46**, 5013 (1992).
- [9] R. Engel, T. K. Gaisser, T. Stanev, and P. Lipari. Prepared for 26th International Cosmic Ray Conference (ICRC 99), Salt Lake City, Utah, 17-25 Aug 1999.
- [10] S. Ostapchenko, Czech. J. Phys. **56**, A149 (2006), arXiv:hep-ph/0601230.
- [11] J. Knapp, D. Heck, S. J. Sciutto, M. T. Dova, and M. Risse, Astropart. Phys. **19**, 77 (2003), arXiv:astro-ph/0206414.

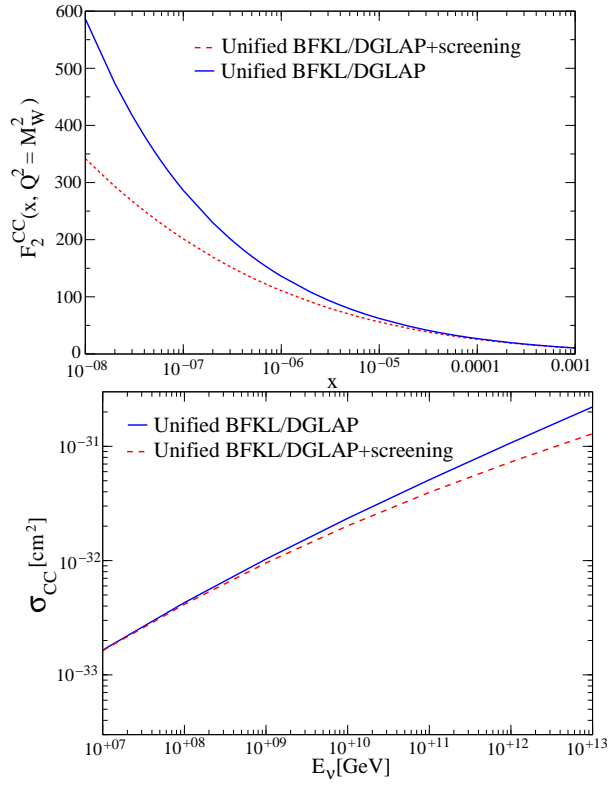


Fig. 8: (left) Charged current  $F_2^{CC}(x, Q^2)$  structure function, (right) neutrino cross-section obtained from BK (with subleading corrections) and from BFKL (with subleading corrections)



- [12] R. Engel and H. Rebel, *Acta Phys. Polon.* **B35**, 321 (2004).
- [13] C. Meurer, J. Bluemer, R. Engel, A. Haungs, and M. Roth, *Czech. J. Phys.* **56**, A211 (2006), [arXiv:astro-ph/0512536](#).
- [14] Particle Data Group Collaboration, C. Caso *et al.*, *Eur. Phys. J.* **C3**, 1 (1998).
- [15] H. H. Mielke, M. Foeller, J. Engler, and J. Knapp, *J. Phys.* **G20**, 637 (1994);  
G. b. Yodh, S. c. Tonwar, T. k. Gaisser, and R. w. Ellsworth, *Phys. Rev.* **D27**, 1183 (1983);  
M. Honda *et al.*, *Phys. Rev. Lett.* **70**, 525 (1993);  
R. M. Baltrusaitis *et al.*, *Phys. Rev. Lett.* **52**, 1380 (1984).
- [16] UA5 Collaboration, R. E. Ansorge *et al.*, *Z. Phys.* **C43**, 357 (1989).
- [17] A. Bunyatyan et al, *Experimental results (see fig 6)*. These proceedings.
- [18] ZEUS Collaboration, S. C. e. a. ZEUS Coll., *Nucl. Phys.* **B658**, 3 (2003),  
[arXiv:hep-ex/0210029](#).
- [19] A. Bunyatyan et al, *Experimental results*. These proceedings.
- [20] T. Pierog and K. Werner, *Phys. Rev. Lett.* **101**, 171101 (2008),  
[arXiv:astro-ph/0611311](#).
- [21] NA49 Collaboration, T. Susa, *Nucl. Phys.* **A698**, 491 (2002).
- [22] E735 Collaboration, T. Alexopoulos *et al.*, *Phys. Rev.* **D48**, 984 (1993).
- [23] V. N. Gribov, *Sov. Phys. JETP* **26**, 414 (1968);  
V. N. Gribov, *Sov. Phys. JETP* **29**, 483 (1969).
- [24] V. A. Abramovsky, V. N. Gribov, and O. V. Kancheli, *Yad. Fiz.* **18**, 595 (1973).
- [25] A. B. Kaidalov, *Phys. Rept.* **50**, 157 (1979).
- [26] J. L. Cardy, *Nucl. Phys.* **B75**, 413 (1974);  
A. B. Kaidalov, L. A. Ponomarev, and K. A. Ter-Martirosian, *Yad. Fiz.* **44**, 722 (1986).
- [27] S. Ostapchenko, *Phys. Rev.* **D77**, 034009 (2008), [arXiv:hep-ph/0612175](#).
- [28] L. Durand and P. Hong, *Phys. Rev. Lett.* **58**, 303 (1987);  
X.-N. Wang, *Phys. Rept.* **280**, 287 (1997), [arXiv:hep-ph/9605214](#);  
F. M. Liu, H. J. Drescher, S. Ostapchenko, T. Pierog, and K. Werner, *J. Phys.* **G28**, 2597 (2002), [arXiv:hep-ph/0109104](#).
- [29] F. W. Bopp, R. Engel, D. Pertermann, and J. Ranft, *Phys. Rev.* **D49**, 3236 (1994).
- [30] T. C. Rogers, A. M. Stasto, and M. I. Strikman, *Phys. Rev.* **D77**, 114009 (2008),  
[arXiv:0801.0303 \[hep-ph\]](#).
- [31] L. V. Gribov, E. M. Levin, and M. G. Ryskin, *Phys. Rept.* **100**, 1 (1983).

- [32] J. Jalilian-Marian, A. Kovner, A. Leonidov, and H. Weigert, Nucl. Phys. **B504**, 415 (1997), [arXiv:hep-ph/9701284](#);  
E. Iancu, A. Leonidov, and L. D. McLerran, Nucl. Phys. **A692**, 583 (2001), [arXiv:hep-ph/0011241](#).
- [33] L. Frankfurt, M. Strikman, and C. Weiss, Ann. Rev. Nucl. Part. Sci. **55**, 403 (2005), [arXiv:hep-ph/0507286](#).
- [34] L. Frankfurt, V. Guzey, M. McDermott, and M. Strikman, Phys. Rev. Lett. **87**, 192301 (2001), [arXiv:hep-ph/0104154](#).
- [35] L. Frankfurt and M. Strikman, Phys. Lett. **B645**, 412 (2007).
- [36] A. Dumitru, L. Gerland, and M. Strikman, Phys. Rev. Lett. **90**, 092301 (2003), [arXiv:hep-ph/0211324](#).
- [37] A. Berera, M. Strikman, W. S. Toothacker, W. D. Walker, and J. J. Whitmore, Phys. Lett. **B403**, 1 (1997), [arXiv:hep-ph/9604299](#).
- [38] F. Gelis, A. M. Stasto, and R. Venugopalan, Eur. Phys. J. **C48**, 489 (2006), [arXiv:hep-ph/0605087](#).
- [39] H. J. Drescher and M. Strikman, Phys. Rev. Lett. **100**, 152002 (2008).
- [40] K. Hencken *et al.*, Phys. Rept. **458**, 1 (2008), [arXiv:0706.3356 \[nucl-ex\]](#).
- [41] R. A. Vazquez, Nucl. Phys. Proc. Suppl. **175-176**, 487 (2008).
- [42] S. Klein, Rev. Mod. Phys. **71**, 1501 (1999), [arXiv:hep-ph/9802442](#).
- [43] T. C. Rogers and M. I. Strikman, J. Phys. **G32**, 2041 (2006), [arXiv:hep-ph/0512311](#).
- [44] V. N. Gribov, Zh. Eksp. Teor. Fiz. **57**, 1306 (1969). SLAC-TRANS-0102;  
L. B. Bezrukov and E. V. Bugaev, Yad. Fiz. **33**, 1195 (1981);  
E. Gotsman, E. M. Levin, and U. Maor, Eur. Phys. J. **C5**, 303 (1998), [arXiv:hep-ph/9708275](#).
- [45] A. Donnachie and P. V. Landshoff, Phys. Lett. **B518**, 63 (2001), [arXiv:hep-ph/0105088](#).
- [46] E. V. Bugaev, Nucl. Phys. Proc. Suppl. **175-176**, 117 (2008).
- [47] M. McDermott, L. Frankfurt, V. Guzey, and M. Strikman, Eur. Phys. J. **C16**, 641 (2000), [arXiv:hep-ph/9912547](#).
- [48] M. M. Block and F. Halzen, Phys. Rev. **D70**, 091901 (2004), [arXiv:hep-ph/0405174](#).

- [49] V. P. Goncalves and M. V. T. Machado, JHEP **04**, 028 (2007),  
arXiv:hep-ph/0607125.
- [50] I. Balitsky, Nucl. Phys. **B463**, 99 (1996), arXiv:hep-ph/9509348;  
Y. V. Kovchegov, Phys. Rev. **D60**, 034008 (1999), arXiv:hep-ph/9901281.
- [51] E. A. Kuraev, L. N. Lipatov, and V. S. Fadin, Sov. Phys. JETP **45**, 199 (1977).
- [52] K. Kutak and J. Kwiecinski, Eur. Phys. J. **C29**, 521 (2003), arXiv:hep-ph/0303209.

## Summary

*A. Bunyatyan, A. Cooper-Sarkar, C. Diaconu, R. Engel, C. Kiesling, K. Kutak, S. Ostapchenko, T. Pierog, T.C. Rogers, M.I. Strikman, T. Sako*

Since their beginning the studies of cosmic ray and elementary particle physics have always be closely related and it has been demonstrated that the very high energy cosmic ray puzzle can not be solved without the results of the HERA or LHC experiments.

Using a simple cascade model, it is possible to find the main parameters of hadronic interactions that influence air shower predictions. These parameters, namely the inelastic cross sections, the secondary particle multiplicity, the inelasticity, and the ratio of charged to neutral hadrons, depend of the hadronic interaction model. As a consequence, realistic simulations of hadron induced air-showers are model-dependent, leading to theoretical uncertainties in the analysis of experimental data. For a ground based detector, the model-related systematic error on energy estimation can be as large as about 20% at  $10^{19}$  eV if the mass of the primary particle is unknown. The theoretical uncertainties of the energy reconstruction are much smaller for fluorescence light detectors (less than 5% even for unknown primary particle mass). The model dependence of the primary mass estimation is crucial and currently the mass composition can only be derived for a given hadronic model. As a consequence, the models have to be carefully tested at the highest energy reached in experiments and especially in the forward region where HERA and LHC can provide crucial informations.

The data on the total photoproduction cross section and jet final states with emphasis on the phase space near the forward (proton) direction from HERA have been summarized, discussing the extraction of the parton distribution functions from a combined data set of the two collider experiments H1 and ZEUS. These data shed light on the parton evolution models and also enable a unique measurement of the running strong coupling, providing new insight into QCD dynamics at very low values of the Bjorken variable  $x$ .

In addition, the HERA experiments provide a wealth of measurements of leading baryon production. These measurements give an important input for an improved theoretical understanding of the proton fragmentation mechanism. As shown, the HERA data on forward particle production can help to reduce the uncertainty in the model predictions for very high energy cosmic ray air showers.

In the near future, the integration of the data from not only the LHC experiment dedicated for the cosmic ray science (LHCf) but also the others, especially the forward experiments introduced in [1] will be important to constrain the interaction models used in the cosmic-ray studies.

The charged current neutrino cross-section at NLO have been calculated in the Standard Model using the best available DIS data along with a careful estimate of the associated uncertainties. If cross-sections much outside the uncertainty bands presented here are observed at UHE cosmic neutrino detectors, it would be a clear signal of the need for extensions to conventional QCD DGLAP formalism.

Finally the extrapolation of photoproduction and neutrino cross-section towards very high energy is needed if we want to estimate flux of ultrahigh energy photons and neutrinos of ex-

tragalactic sources like Active Galactic Nuclei. Such estimation might be useful for the Pierre Auger Observatory to set a proper limit on the photon flux and Ice Cube experiment which can detect neutrinos of energy  $10^{12}$  GeV and higher. Here again, the best constrains are given by both HERA and LHC experiments.

**Acknowledgments** The research of M.S. was supported by the United States Department of Energy. S.O. would like to acknowledge the support of the European Commission under the Marie Curie IEF Programme (grant 220251).

## References

[1] A. Bunyatyan et al, *Experimental results*. These proceedings.

## Chapter 6

# Working Group Monte Carlo and Tools

### Convenors:

*P. Bartalini (Taiwan, CMS),  
S. Chekanov (Argonne, ZEUS),  
F. Krauss (IPP Durham),  
S. Gieseke (U. Karlsruhe),*

# Introduction

*P. Bartalini<sup>a</sup>, S. Chekanov<sup>b</sup>, S. Gieseke<sup>c</sup> and F. Krauss<sup>d</sup>*

<sup>a</sup> National Taiwan University, Taiwan

<sup>b</sup> HEP Division, Argonne National Laboratory, USA

<sup>c</sup> Institut für Theoretische Physik, Universität Karlsruhe, Germany

<sup>d</sup> Department of Physics, Durham University, UK

As for the previous HERA-LHC workshop, the main goals of the WG5 working group during 2006–2008 were: 1) To examine and improve Monte Carlo models for the LHC data using the experience and ideas from the HERA experiments; 2) To develop analysis frameworks to be used to tune and validate Monte Carlo models; 3) To review and further develop data analysis tools, common interfaces and libraries, which have their origin at HERA and can be useful for studies at the LHC.

Over the past few years, the working group has covered various aspects of data analysis tools and Monte Carlo models, from the conceptually simple ideas through technically detailed projects. Below we will briefly discuss several topics covered by the participants of the WG5 working group.

## 1 Monte Carlo event generators

There has been considerable progress in the development of Monte Carlo event generators during this workshop. In the working group, we had a very broad coverage of almost all existing Monte Carlo event generators which are expected to be used at the LHC. We have particularly discussed the developments of ALPGEN, PYTHIA8, HERWIG++, CASCADE, MC@NLO, THEPEG and Forward Physics Monte Carlo (FPMC) [1, 2]. A lot of progress has been made in different areas of simulation.

On the perturbative level, the matching of parton showers with high order matrix elements was discussed and developed extensively. The matching of high jet multiplicity matrix elements with multiple parton shower emissions was discussed as well as matching parton showers with complete next-to-leading order calculations.

The most important question for this workshop was whether we had the necessary tools for the LHC era and whether there was something that HERA could still contribute. Several new Monte Carlo event generators, such as PYTHIA 8, HERWIG++ and SHERPA, are completely new programs, all written in C++, that partly aim to be the successors of the FORTRAN event generators that had already been widely used at HERA. These Monte Carlo models are not just simple rewrites of the existing codes: as was discussed, in many respects, the simulation of the underlying physics in such Monte Carlo models is more sophisticated than in the previous FORTRAN-based versions. New parton shower models, new models for the underlying event and a more sophisticated simulation of the non-perturbative hadronization was discussed. A lot of emphasis has been put on the discussion of underlying event physics as some progress in understanding was expected from the latest HERA results. Details will be discussed in the following section.

In addition to a pure technical description of the progress made in the development of such models, we had several studies showing the relevance and importance of these models to the LHC physics, especially for the direct photons ( $\gamma$ +jet), top-pair production,  $Wt$  and the forward-jet physics [2, 3]. We have learned that the current event generators work satisfactorily for the description of HERA data, but the LHC experiments will substantially increase the demands on the physics models implemented in such models.

## 2 Multiple Parton Interactions in Monte Carlo generators

In the years '80, the evidence for Double Scattering (DS) phenomena in the high- $p_T$  phenomenology of hadron colliders [4] suggested the extension of the same perturbative picture to the soft regime, giving rise to the first implementation of the Multiple Parton Interaction (MPI) processes in a QCD Monte Carlo model [5] which was very successful in reproducing the UA5 charged multiplicity distributions [6].

On top of the general Minimum Bias (MB) observables these MPI models turn out to be particularly adequate to describe the Underlying Event (UE) physics at Tevatron [7], in particular they partly account for the pedestal effect (i.e. the enhancement of the Underlying Event activity with the energy scale of the interaction) as the effect of an increased probability of multiple partonic interactions in case a hard collision has taken place. A second important effect that can contribute to the pedestal effect is the increase in initial state radiation associated to the presence of a hard scattering.

Examples of MPI models are implemented in the general purpose simulation programs PYTHIA [8], HERWIG/JIMMY [9, 10] and SHERPA [11]. Other successful descriptions of UE and MB at hadron colliders are achieved by alternative approaches like PHOJET [12], which was designed to describe rapidity gaps and diffractive physics (relying on both perturbative QCD and Dual Parton Models). The most recent PYTHIA versions [13] adopt an optional alternative description of the colliding partons in terms of correlated multi-parton distribution functions of flavours, colors and longitudinal momenta.

From the contributions to the MC and multi-jet working groups of this HERA/LHC workshop, it is clear that the MPI are currently experiencing a growing popularity and are presently widely invoked to account for observations that would not be explained otherwise.

While preparing the ground for the traditional DS, MB and UE measurements at the LHC along the Tevatron experience (also complemented with the recent UE HERA results), new feasibility studies are proposed which in perspective will constitute a challenge to the performances of the MPI models: the usage of jet clustering algorithms providing an automated estimation of the UE activity, the investigation of the mini-jet structure of the MB events, the estimation of large pseudo-rapidity activity correlations, the connection between the partonic cross sections and the rapidity gap suppression in the hard diffractive events.

At the same time, the implementation of the MPI effects in the Monte Carlo models is quickly proceeding through an increasing level of sophistication and complexity that has already a deep impact on the analysis strategies at the LHC. For example new MC tools like PYTHIA8 and HERWIG++ can now be used in order to estimate complementary Standard Model backgrounds to searches coming from DS.



Further progress in the description of the MPI might be achieved with the introduction of a dynamical quantum description of the interacting hadrons, providing also a modeling of the diffractive interactions in the same context.

### 3 Introduction to Monte Carlo validation and analysis tools

The RIVET library, a successor to the successful HERA-oriented generator-analysis library, HZ-TOOL, is getting to be popular at the LHC for validating the performance of event generator and tuning [14]. Unlike FORTRAN-based HZTOOL, RIVET is written in object-oriented C++, and it is primarily a library which can be used from within any analysis framework.

For Monte Carlo tuning, the so-called PROFESSOR system [14] was recently successfully used for PYTHIA6 tuning. This led to a substantial improvement on the existing default tune, thus it can greatly aid the setup of new generators for LHC studies.

In this working group, we have moved beyond Monte Carlo specific validation tools. As an example, jHepWork analysis framework [15] presented at this working group can be considered as a multi-platform alternative to ROOT since it was written in Java. The framework can be useful for both experimentalists and theorists.

### 4 Conclusions

The presented proceedings describe the results of the work performed in the WG5 working group over several years between 2006–2008. Hopefully, we have provided a correct balance between experimental and theoretical results. As conveners of this working group, we were impressed by the quality and diversity of the presented results. The high quality of the presentations stimulated lively discussions often leading to new ideas and insights into the working group topics.

We would like to thank all participants for their work. We also thank all the organizers for the excellent organization of this workshop.

## References

- [1] L. Lenzi, *Alpgen and SHERPA in  $z/\gamma^* + \text{jets}$  at the LHC (these proceedings)*;  
M. Bähr *et al.*, *Herwig++ status report (these proceedings)*;  
T. Sjöstrand, *PYTHIA 8 status report (these proceedings)*;  
M. Deak, H. Jung, and K. Kutak, *Cascade (these proceedings)*.
- [2] C. White, *Single top production in the  $wt$  mode with MC@NLO (these proceedings)*;  
L. Lonnblad, *Toolkit for high energy physics event generation (these proceedings)*;  
M. Boonekamp, V. Juránek, O. Kepka, and C. Royon, *FORWARD PHYSICS MONTE CARLO (these proceedings)*.
- [3] S. Albino, *Perturbative description of inclusive single hadron production at hera (these proceedings)*;  
R. Blair, S. Chekanov, G. Heinrich, A. Lipatov, and N. Zotov, *Direct photon production at HERA, the TEVATRON and the LHC (these proceedings)*;  
R. Chierici, *Generator comparison for top-pair production (these proceedings)*;  
P. Stephens and A. van Hameren, *Propagation of uncertainty in a parton shower (these proceedings)*.
- [4] Axial Field Spectrometer Collaboration, T. Akesson *et al.*, *Z. Phys.* **C34**, 163 (1987);  
UA2 Collaboration, J. Alitti *et al.*, *Phys. Lett.* **B268**, 145 (1991);  
CDF Collaboration, F. Abe *et al.*, *Phys. Rev.* **D47**, 4857 (1993).
- [5] T. Sjostrand and M. van Zijl, *Phys. Lett.* **B188**, 149 (1987).
- [6] UA5 Collaboration, G. J. Alner *et al.*, *Z. Phys.* **C33**, 1 (1986).
- [7] CDF Collaboration, A. Affolder *et al.*, *Phys. Rev.* **D65**, 092002 (2002);  
CDF Collaboration, D. Acosta *et al.*, *Phys. Rev.* **D70**, 072002 (2004).
- [8] T. Sjostrand *et al.*, *Comput. Phys. Commun.* **135**, 238 (2001). [hep-ph/0010017](#).
- [9] G. Corcella *et al.*, *JHEP* **101**, 010 (2001). [hep-ph/0011363](#).
- [10] J. M. Butterworth, J. R. Forshaw, and M. H. Seymour, *Z. Phys.* **C72**, 637 (1996).  
[hep-ph/9601371](#).
- [11] T. Gleisberg *et al.*, *JHEP* **02**, 056 (2004). [hep-ph/0311263](#).
- [12] F. W. Bopp, R. Engel, and J. Ranft (1998). [hep-ph/9803437](#).
- [13] T. Sjostrand *et al.*, *JHEP* **05**, 026 (2006). [hep-ph/0603175](#).
- [14] A. Buckley, *Tools for event generator tuning and validation (these proceedings)*.
- [15] S. Chekanov, *JHEPWORK - JAVA object-oriented data analysis framework (these proceedings)*.

# A multi-channel Poissonian model for multi-parton scatterings

*Daniele Treleani*

Dipartimento di Fisica Teorica dell'Università di Trieste,  
INFN and ICTP, Trieste, I 34014 Italy

## Abstract

Multiple parton interactions are typically implemented in Montecarlo codes by assuming a Poissonian distribution of collisions with average number depending on the impact parameter. A possible generalization, which links the process to hadronic diffraction, is shortly discussed.

## 1 The simplest Poissonian model

A standard way to introduce multiple parton interactions in Montecarlo codes is to assume a Poissonian distribution of multiple parton collisions, with average number depending on the value of the impact parameter. The motivations were discussed long ago in several articles [1] [2] [3]: One introduces the three dimensional parton density  $D(x, b)$ , namely the average number of partons with a given momentum fraction  $x$  and with transverse coordinate  $b$  (the dependence on flavor and on the resolution of the process is understood) and one makes the simplifying assumption  $D(x, b) = G(x)f(b)$ , with  $G(x)$  the usual parton distribution function and  $f(b)$  normalized to one. The inclusive cross section for large  $p_t$  parton production  $\sigma_S$  may hence be expressed as

$$\sigma_S = \int_{p_t^c} G(x)\hat{\sigma}(x, x')G(x')dx dx' = \int_{p_t^c} G(x)f(b)\hat{\sigma}(x, x')G(x')f(b-\beta)d^2b d^2\beta dx dx' \quad (1)$$

where  $p_t^c$  is a cutoff introduced to distinguish hard and soft parton collisions and  $\beta$  the hadronic impact parameter. The expression allows a simple geometrical interpretation, given the large momentum exchange which localizes the partonic interaction inside the overlap volume of the two hadrons.

Neglecting all correlations in the multi-parton distributions, the inclusive cross section for a double parton scattering  $\sigma_D$  is analogously given by

$$\begin{aligned} \sigma_D &= \frac{1}{2!} \int_{p_t^c} G(x_1)f(b_1)\hat{\sigma}(x_1, x'_1)G(x'_1)f(b_1-\beta)d^2b_1 dx_1 dx'_1 \times \\ &\quad \times G(x_2)f(b_2)\hat{\sigma}(x_2, x'_2)G(x'_2)f(b_2-\beta)d^2b_2 dx_2 dx'_2 d^2\beta \\ &= \int \frac{1}{2!} \left( \int_{p_t^c} G(x)f(b)\hat{\sigma}(x, x')G(x')f(b-\beta)d^2b dx dx' \right)^2 d^2\beta \end{aligned} \quad (2)$$

which may be readily generalized to the case of the inclusive cross section for  $N$ -parton scatterings  $\sigma_N$ :

$$\sigma_N = \int \frac{1}{N!} \left( \int_{p_t^c} G(x) f(b) \hat{\sigma}(x, x') G(x') f(b - \beta) d^2 b dx dx' \right)^N d^2 \beta \quad (3)$$

The cross sections are divergent for  $p_t^c \rightarrow 0$ . The unitarity problem is solved by normalizing the integrand which, being dimensionless, may be understood as the probability to have a  $N$ th parton collision process in a inelastic event:

$$\int_{p_t^c} G(x) f(b) \hat{\sigma}(x, x') G(x') f(b - \beta) d^2 b dx dx' \equiv \sigma_S F(\beta), \quad \frac{(\sigma_S F(\beta))^N}{N!} e^{-\sigma_S F(\beta)} \equiv P_N(\beta) \quad (4)$$

here  $P_N(\beta)$  the probability of having  $N$  parton collisions in a hadronic interaction at impact parameter  $\beta$ . By summing all probabilities one obtains the hard cross section  $\sigma_{hard}$ , namely the contribution to the inelastic cross section due to all events with *at least* one parton collision with momentum transfer greater than the cutoff  $p_t^c$ :

$$\sigma_{hard} = \sum_{N=1}^{\infty} \int P_N(\beta) d^2 \beta = \sum_{N=1}^{\infty} \int d^2 \beta \frac{(\sigma_S F(\beta))^N}{N!} e^{-\sigma_S F(\beta)} = \int d^2 \beta [1 - e^{-\sigma_S F(\beta)}] \quad (5)$$

Notice that  $\sigma_{hard}$  is finite in the infrared limit, which allows to express the inelastic cross section as  $\sigma_{inel} = \sigma_{soft} + \sigma_{hard}$  with  $\sigma_{soft}$  the soft contribution, the two terms  $\sigma_{soft}$  and  $\sigma_{hard}$  being defined through the cutoff in the momentum exchanged at parton level,  $p_t^c$ .

An important property is that the single parton scattering inclusive cross section is related to the average number of parton collisions. One has:

$$\langle N \rangle \sigma_{hard} = \int d^2 \beta \sum_{N=1}^{\infty} N P_N(\beta) = \int d^2 \beta \sum_{N=1}^{\infty} \frac{N [\sigma_S F(\beta)]^N}{N!} e^{-\sigma_S F(\beta)} = \int d^2 \beta \sigma_S F(\beta) = \sigma_S \quad (6)$$

and more in general one may write:

$$\begin{aligned} \frac{\langle N(N-1) \dots (N-K+1) \rangle}{K!} \sigma_{hard} &= \int d^2 \beta \sum_{N=1}^{\infty} \frac{N(N-1) \dots (N-K+1)}{K!} P_N(\beta) \\ &= \int d^2 \beta \frac{1}{K!} [\sigma_S F(\beta)]^K = \sigma_K \end{aligned} \quad (7)$$

One should stress that the relations between  $\sigma_S$  and  $\langle N \rangle$  and between  $\sigma_K$  and  $\langle N(N-1) \dots (N-K+1) \rangle$  do not hold only in the case of the simplest Poissonian model. It can be shown that the validity is indeed much more general [4] [5].

## 2 The multi-channel Poissonian model

An implicit assumption in the Poissonian model is that the hadron density is the same in each interaction. On the other hand the hadron is a dynamical system, which fluctuates in different configurations in a time of the order of the hadron scale, much longer as compared with the time of a hard interaction. Interactions may hence take place while hadrons occupy various configurations, even significantly different as compared with the average hadronic configuration. A measure of the size of the phenomenon is given by hadronic diffraction.

The multichannel eikonal model [6] allows a simple description of hadronic diffraction. In the multichannel model the hadron state  $\psi_h$  is represented as a superposition of eigenstates  $\phi_i$  of the  $T$ -matrix, while the interaction is described by eikonalized multi-Pomeron exchanges.

$$\psi_h = \sum_i \alpha_i \phi_i \quad (8)$$

The eigenstates of the  $T$ -matrix can only be absorbed or scatter elastically and the cross sections of the physically observed states  $\psi_h$  can be expressed by the combinations of the cross sections between the eigenstates  $\phi_i$  and  $\phi_j$  as shown below:

$$\begin{aligned} \sigma_{tot} &= \sum_{i,j} |\alpha_i|^2 |\alpha_j|^2 \sigma_{tot}^{ij} \\ \sigma_{el} + \sigma_{sd} + \sigma_{dd} &= \sum_{i,j} |\alpha_i|^2 |\alpha_j|^2 \sigma_{el}^{ij} \\ \sigma_{in} &= \sum_{i,j} |\alpha_i|^2 |\alpha_j|^2 \sigma_{in}^{ij} \end{aligned}$$

In a single Pomeron exchange, one may distinguish between hard and soft inelastic interactions, according with the presence or absence of large  $p_t$  partons in the final state. One may thus write:

$$\sigma^{ij} = \sigma_J^{ij} + \sigma_S^{ij} \quad (9)$$

where the labels  $J$  or  $S$  correspond to the presence or absence of large  $p_t$  partons in the final state. One hence obtains the following expression of the hard cross section [7]:

$$\begin{aligned} \sigma_{hard} &= \sum_{i,j} |\alpha_i|^2 |\alpha_j|^2 \sigma_{hard}^{ij} = \sum_{i,j} |\alpha_i|^2 |\alpha_j|^2 \int d^2\beta \left[ 1 - e^{-\sigma_J^{ij}(\beta)} \right] \\ &= \sum_{i,j,N} |\alpha_i|^2 |\alpha_j|^2 \int d^2\beta \frac{(\sigma_J^{ij}(\beta))^N}{N!} e^{-\sigma_J^{ij}(\beta)} \end{aligned} \quad (10)$$

which, being a superposition of Poissonians, represents the natural generalization of the result of the simplest Poissonian model.

The easiest implementation of the multi-channel eikonal model is in the case of two eigenstates:

$$\psi_h = \frac{1}{\sqrt{2}}\phi_1 + \frac{1}{\sqrt{2}}\phi_2 \quad (11)$$

One obtains:

$$\sigma_{hard} = \frac{1}{4}\sigma_{hard}^{11} + \frac{1}{2}\sigma_{hard}^{12} + \frac{1}{4}\sigma_{hard}^{22} \quad (12)$$

while the  $N$ -parton scattering inclusive cross section  $\sigma_N$  is given by:

$$\sigma_N = \frac{\sigma_S^N}{N!} \left\{ \frac{1}{4} \int [F_{11}(\beta)]^N d^2\beta + \frac{1}{2} \int [F_{12}(\beta)]^N d^2\beta + \frac{1}{4} \int [F_{22}(\beta)]^N d^2\beta \right\} \quad (13)$$

where  $F_{ij}$  are the superpositions of the parton densities of the different eigenstates  $\phi_i$  and  $\phi_j$ . The case of gaussian parton densities is particularly simple. One has

$$F_{ij}(\beta) = \frac{1}{\pi(R_i^2 + R_j^2)} \times \exp\left(\frac{-\beta^2}{R_i^2 + R_j^2}\right) \quad (14)$$

One may take for the radii of the two parton densities  $R_1^2 = R^2/2$  and  $R_2^2 = 3R^2/2$ , in such a way that  $R^2$  is the average hadron size. With this choice the variance of the distribution is  $\omega_\sigma = 1/4$ , in agreement with the analysis of [8]. The explicit expression of the inclusive cross section  $\sigma_N$  is:

$$\sigma_N = \frac{\sigma_S^N}{NN!(\pi R^2)^{N-1}} \left\{ \frac{1}{4} \left( \frac{1}{\frac{1}{2} + \frac{1}{2}} \right)^{N-1} + \frac{1}{2} \left( \frac{1}{\frac{1}{2} + \frac{3}{2}} \right)^{N-1} + \frac{1}{4} \left( \frac{1}{\frac{3}{2} + \frac{3}{2}} \right)^{N-1} \right\} \quad (15)$$

In the figure the relative weights of the overlaps between the various configurations are shown for different inclusive cross sections  $\sigma_N$ . In the case of a single collision all four different configurations contribute with the same weight. When  $N$  grows the contribution of the overlap between the most compact and dense configurations becomes increasingly important and, for  $N=5$ , it accounts for almost 90% of the cross section.

Notice that the result obtained in the multi-channel eikonal model is *very different* with respect to the result obtained when terms with various transverse sizes are introduced directly in the hadronic parton density of the simplest Poissonian model. In PYTHIA [2] [9] the hadron density is represented by the sum of two gaussians with same weight and different size. The overlap function is hence given by

$$\frac{1}{4}F_{11}(\beta) + \frac{1}{2}F_{12}(\beta) + \frac{1}{4}F_{22}(\beta) \quad (16)$$

where  $F_{ij}$  are given by Eq.14, with  $R_1$  and  $R_2$  the radii of the two gaussians used to construct the actual hadronic parton density. The resulting expression of the inclusive cross sections is

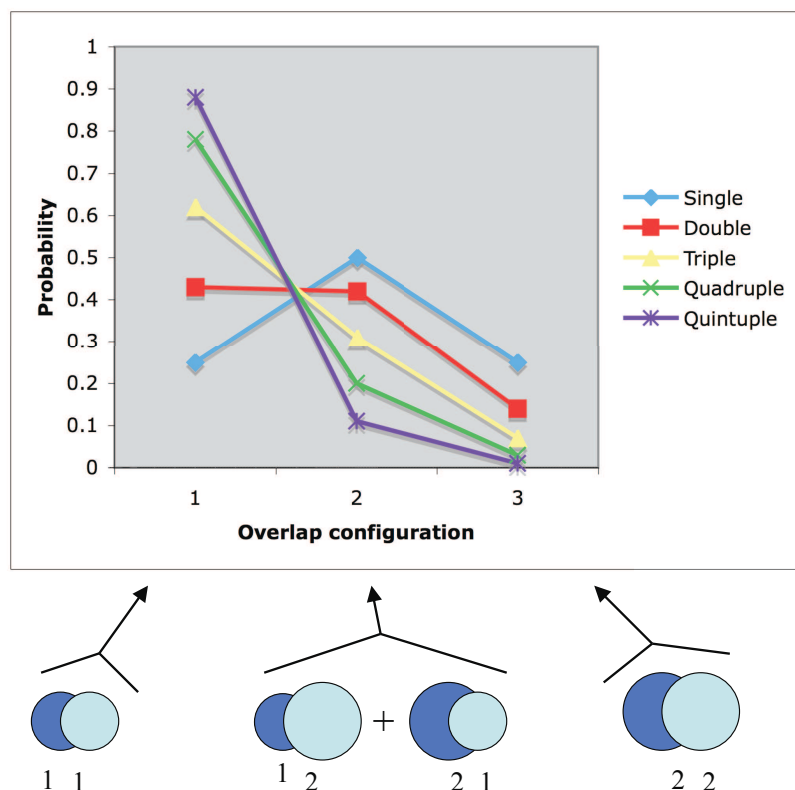


Fig. 1: Relative contributions to the inclusive cross section  $\sigma_N$  of the overlaps between the different hadronic configurations for  $1 \leq N \leq 5$

$$\sigma_N = \frac{\sigma_S^N}{N!} \int \left[ \frac{1}{4} F_{11}(\beta) + \frac{1}{2} F_{12}(\beta) + \frac{1}{4} F_{22}(\beta) \right]^N d^2 \beta \quad (17)$$

which should be compared with the inclusive cross section derived in the two-states eikonal model (expression in Eq.13).

### 3 Concluding remarks

In the present note it has been shown how the importance of small size hadronic configurations is emphasized by geometry in the multi-parton inclusive cross sections  $\sigma_N$  at large  $N$ . Here one has assumed that the transverse fluctuations of the hadron do not affect its parton content. In the two-states-model of hadronic diffraction one needs however to enhance the strength of the

Pomeron coupling between diffractive eigenstates with small radii, in order to fit the available data on elastic, inelastic, single and double diffractive cross sections [10], which corresponds to an increase of the parton content when the hadron occupies a configuration with small transverse size. In the analysis [8] hadronic diffraction is on the contrary fitted in a model where the number of partons decreases when the hadron occupies small size configurations. While in the former case the enhanced role of small transverse size configurations in multiparton collisions is amplified [7], in the latter it is on the contrary reduced [11].

The study of hadronic diffraction and of multiparton scatterings at the LHC may hence provide non trivial informations on the correlation between the parton content of the hadron and its transverse size. In addition to the measurements of hadronic diffraction and of multi-jets cross sections in hadron-hadron collisions, an important handle, to gain a better insight into this aspect of the hadron structure, may be represented by the measurement of multi-jets cross sections in hadron-nucleus collisions, where a model independent separation of the longitudinal and transverse parton correlations is, in principle, possible [12].

## References

- [1] Capella, A. and Tran Thanh Van, J. and Kwiecinski, J., Phys. Rev. Lett. **58**, 2015 (1987).
- [2] Sjostrand, T. and van Zijl, M., Phys. Rev. **D36**, 2019 (1987).
- [3] Ametller, L. and Treleani, D., Int. J. Mod. Phys. **A3**, 521 (1988).
- [4] Calucci, G. and Treleani, D., Int. J. Mod. Phys. **A6**, 4375 (1991).
- [5] Calucci, G. and Treleani, D., Phys. Rev. **D57**, 503 (1998).
- [6] Gotsman, E. and Levin, E. and Maor, U., Phys. Lett. **B452**, 387 (1999).
- [7] Treleani, Daniele, Phys. Rev. **D76**, 076006 (2007).
- [8] Blaettel, B. and Baym, G. and Frankfurt, L. L. and Heiselberg, H. and Strikman, M., Phys. Rev. **D47**, 2761 (1993).
- [9] Sjostrand, T. and Mrenna, S. and Skands, P., JHEP **05**, 026 (2006).
- [10] Gotsman, E. and Levin, E. and Maor, U. (2007).
- [11] Frankfurt, L. and Strikman, M. and Treleani, D. and Weiss, C. (2008).
- [12] Strikman, M. and Treleani, D., Phys. Rev. Lett. **88**, 031801 (2002).



# Underlying events in Herwig++<sup>\*</sup>

*Manuel Bähr<sup>1</sup>, Stefan Gieseke<sup>1</sup> and Michael H. Seymour<sup>2</sup>*

<sup>1</sup> Institut für Theoretische Physik, Universität Karlsruhe,

<sup>2</sup> Physics Department, CERN, and  
School of Physics and Astronomy, University of Manchester.

## Abstract

In this contribution we describe the new model of multiple partonic interactions (MPI) that has been implemented in Herwig++. Tuning its two free parameters is enough to find a good description of CDF underlying event data. We show extrapolations to the LHC and compare them to results from other models.

## 1 Introduction

With the advent of the Large Hadron Collider (LHC) in the near future it will become increasingly important to gain a detailed understanding of all sources of hadronic activity in a high energy scattering event. An important source of additional soft jets will be the presence of the underlying event. From the experimental point of view, the underlying event contains all activity in a hadronic collision that is not related to the signal particles from the hard process, e.g. leptons or missing transverse energy. The additional particles may result from the initial state radiation of additional gluons or from additional hard (or soft) scatters that occur during the same hadron–hadron collision. Jet measurements are particularly sensitive to the underlying event because, although a jet’s energy is dominated by the primary hard parton that initiated it, jet algorithms inevitably gather together all other energy deposits in its vicinity, giving an important correction to its energy and internal structure.

In this note, based on Ref. [1], we want to focus on the description of the hard component of the underlying event, which stems from additional hard scatters within the same proton. Not only does this model give us a simple unitarization of the hard cross section, it also allows to give a good description of the additional substructure of the underlying events. It turns out that most activity in the underlying event can be understood in terms of hard minijets. We therefore adopt this model, based on the model JIMMY [2], for our new event generator Herwig++ [3].

An extension to this model along the lines of [4], which also includes soft scatters is underway and will most probably be available for the next release of Herwig++. Covering the entire  $p_t$  range will also allow us to describe minimum bias interactions. We have examined the parameter space of such models at Tevatron and LHC energies in Ref. [5]. Existing measurements and the possible range of LHC measurements are used there to identify the maximally allowed parameter space.

---

<sup>\*</sup>to appear in the proceedings of the HERA and the LHC workshop.

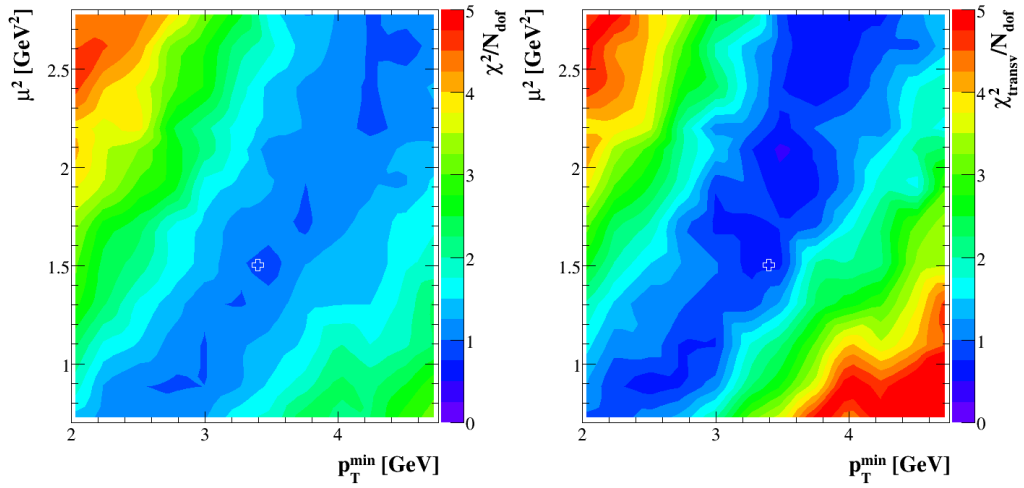


Fig. 1: Contour plots for the  $\chi^2$  per degree of freedom of all discussed observables (left) and only the ones from the transverse region (right). The cross indicates the location of our preferred tune.

## 2 Tevatron results

We have performed a tune of the model by calculating the total  $\chi^2$  against the jet data ( $p_t^{\text{jet}} > 20$  GeV) from Ref. [6]. For this analysis each event is partitioned into three parts, the **towards**, **away** and **transverse** regions. These regions are equal in size in  $\eta - \phi$  space and classify where particles are located in this space with respect to the hardest jet in the event. We compare our predictions to data for the average number of charged particles and for the scalar  $p_t$  sum in each of these regions.

The parameter space for this tune is two dimensional and consists of the  $p_t$  cutoff  $p_t^{\text{min}}$  and the inverse hadron radius squared,  $\mu^2$ . In Fig. 2 we show the  $\chi^2$  contour for describing all six observables and especially those from the transverse region, which is particularly sensitive to the underlying event. For these, and all subsequent plots, we have used Herwig++ version 2.2.1 and the built-in MRST 2001 LO [7] PDFs. All parameters, apart from the ones we were tuning, were left at their default values.

The description of the Tevatron data is truly satisfactory for the entire range of considered values of  $p_t^{\text{min}}$ . For each point on the  $x$ -axis we can find a point on the  $y$ -axis to give a reasonable fit. Nevertheless an optimum can be found between 3 ... 4 GeV. The strong and constant correlation between  $p_t^{\text{min}}$  and  $\mu^2$  is due to the fact that a smaller hadron radius will always balance against a larger  $p_t$  cutoff as far as the underlying event activity is concerned. As a default tune we use  $p_t^{\text{min}} = 3.4$  GeV and  $\mu^2 = 1.5$  GeV<sup>2</sup>, which results in an overall  $\chi^2/N_{\text{dof}}$  of 1.3.

## 3 LHC extrapolation

We start the discussion of our predictions for the LHC with the plot in Fig. 2. The plot shows the mean charged multiplicity as a function of pseudorapidity,  $\eta$ . We show Herwig++ with and without MPI. We used QCD jet production with a minimal  $p_T$  of 20 GeV as signal process. The

MPI parameters were left at their default values, i.e. the fit to Tevatron CDF data. The effect of MPI is clearly visible, growing significantly from the Tevatron to the LHC.

For calculating the LHC extrapolations we left the MPI parameters at their default values, i.e. the fit to Tevatron CDF data. In Ref. [8] a comparison of different predictions for an analysis modelled on the CDF one discussed earlier was presented. As a benchmark observable the charged particle multiplicity in the transverse region was used. We show this comparison in Fig. 3 together with our simulation. All expectations reached a plateau in this observable for  $p_t^{\text{lj}et} > 10$  GeV. Our prediction for this observable also reached a roughly constant plateau within this region. The height of this plateau can be used for comparison. In Ref. [8] PYTHIA 6.214 [9] ATLAS tune reached a height of  $\sim 6.5$ , PYTHIA 6.214 CDF Tune A of  $\sim 5$  and PHOJET 1.12 [10] of  $\sim 3$ . Our model reaches a height of  $\sim 5$  and seems to be close to the PYTHIA 6.214 CDF tune, although our model parameters were kept constant at their values extracted from the fit to Tevatron data.

We have seen already in the previous section that our fit results in a flat valley of parameter points, which all give a very good description of the data. We will briefly estimate the spread of our LHC expectations, using only parameter sets from this valley. The range of predictions that we deduce will be the range that can be expected assuming no energy dependence on our main parameters. Therefore, early measurements could shed light on the potential energy dependence of the input parameters by simply comparing first data to these predictions. We extracted the average value of the two transverse observables for a given parameter set in the region  $20 \text{ GeV} < p_t^{\text{lj}et} < 30 \text{ GeV}$ . We did that for the best fit points at three different values for  $p_t^{\text{min}}$ , namely 2 GeV, 3.4 GeV and 4.5 GeV, and found an uncertainty of about 7 % for the multiplicity and 10 % for the sum of the transverse momentum.

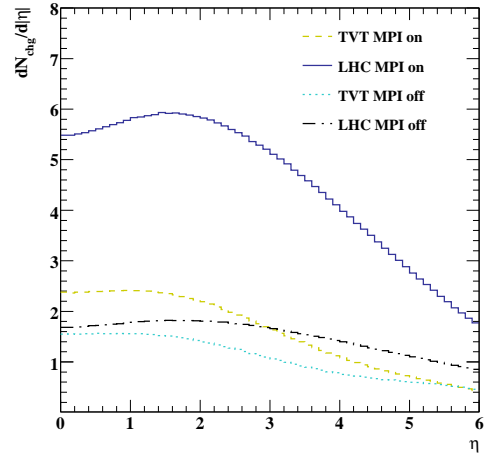


Fig. 2: Differential multiplicity distribution with respect to  $|\eta|$ . The different data sets are: Tevatron with MPI off, LHC with MPI off, Tevatron with MPI on and LHC with MPI on.

LHC predictions	$\langle N_{\text{chg}} \rangle^{\text{transv}}$	$\langle p_t^{\text{sum}} \rangle^{\text{transv}} [\text{GeV}]$
TVT best fit	$5.1 \pm 0.3$	$5.0 \pm 0.5$

Table 1: LHC expectations for  $\langle N_{\text{chg}} \rangle$  and  $\langle p_t^{\text{sum}} \rangle$  in the transverse region. The uncertainties are obtained from varying  $p_t^{\text{min}}$  within the range we considered. For  $\mu^2$  we have taken the corresponding best fit (Tevatron) values.

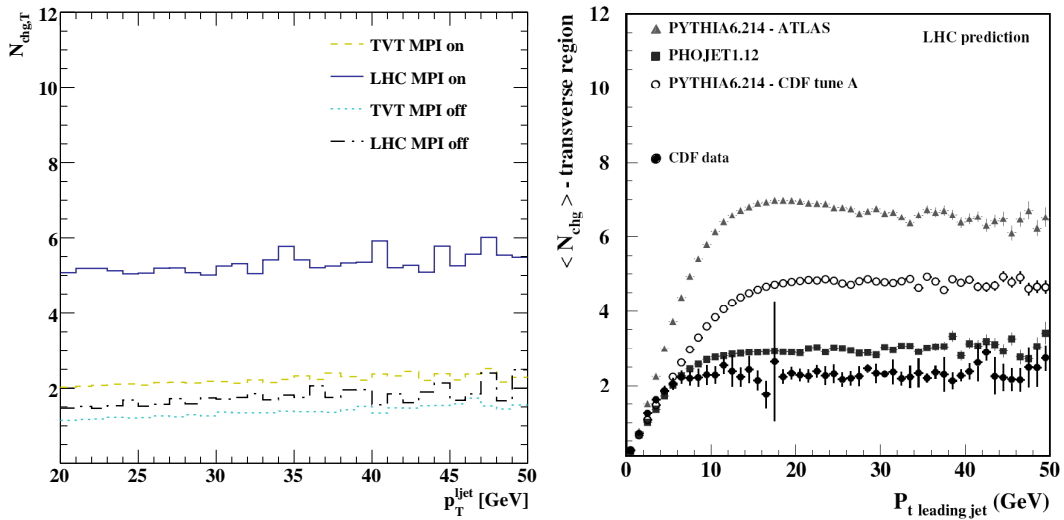


Fig. 3: Multiplicity in the transverse region for LHC runs with Herwig++ (left) and the same observable for several other generators (right), taken from Ref. [8]. The different data sets for the left plot are (from bottom to top): Tevatron with MPI off, LHC with MPI off, Tevatron with MPI on and LHC with MPI on.

## Acknowledgements

We would like to thank our collaborators on the Herwig++ project for many useful discussions. We wish to thank the organisers of the workshop for a very pleasant atmosphere. This work was supported in part by the European Union Marie Curie Research Training Network MCnet under contract MRTN-CT-2006-035606 and the Helmholtz–Alliance “Physics at the Terascale”. MB was supported by the Landesgraduiertenförderung Baden–Württemberg.

## References

- [1] M. Bähr, S. Gieseke, and M. H. Seymour, *Simulation of multiple partonic interactions in Herwig++*, *JHEP* **07** (2008) 076, [arXiv:0803.3633].
- [2] J. M. Butterworth, J. R. Forshaw, and M. H. Seymour, *Multi-Parton Interactions in Photoproduction at HERA*, *Z. Phys.* **C72** (1996) 637–646, [hep-ph/9601371].
- [3] M. Bähr *et. al.*, *Herwig++ Physics and Manual*, arXiv:0803.0883.
- [4] I. Borozan and M. H. Seymour, *An eikonal model for multiparticle production in hadron hadron interactions*, *JHEP* **09** (2002) 015, [hep-ph/0207283].
- [5] M. Bähr, J. M. Butterworth, and M. H. Seymour, *The Underlying Event and the Total Cross Section from Tevatron to the LHC*, arXiv:0806.2949.
- [6] **CDF Collaboration**, A. A. Affolder *et. al.*, *Charged jet evolution and the underlying event in  $p\bar{p}$  collisions at 1.8 TeV*, *Phys. Rev.* **D65** (2002) 092002.

- [7] A. D. Martin, R. G. Roberts, W. J. Stirling, and R. S. Thorne, *MRST2001: Partons and  $\alpha(s)$  from precise deep inelastic scattering and Tevatron jet data*, *Eur. Phys. J.* **C23** (2002) 73–87, [hep-ph/0110215].
- [8] S. Alekhin *et. al.*, *HERA and the LHC - A workshop on the implications of HERA for LHC physics: Proceedings Part A*, hep-ph/0601012.
- [9] T. Sjöstrand, L. Lönnblad, and S. Mrenna, *PYTHIA 6.2: Physics and manual*, hep-ph/0108264.
- [10] R. Engel, *Photoproduction within the two component dual parton model. 1. Amplitudes and cross-sections*, *Z. Phys.* **C66** (1995) 203–214.

# Multiple Interactions at HERA

*H. Jung<sup>a</sup>, Ll. Martí<sup>a</sup>, T. Namssoo<sup>a</sup>, S. Osman<sup>b</sup>*

<sup>a</sup> DESY, Hamburg, Germany

<sup>b</sup> Physics Department, University of Lund, Lund, Sweden

## Abstract

The study of Multiple Parton Interactions (MPI) has been an important subject at hadron colliders. In lepton-hadron collisions at HERA, the photon can interact as a point-like particle or as a composite hadron-like system. Event samples with an enriched direct- or resolved-photon component can be selected by choosing events with high or low  $x_\gamma$  or  $Q^2$  values. This was done in the three measurements presented here, which were conducted at HERA by the H1 and ZEUS collaborations. Two measurements in photoproduction are presented. The first looks at three- and four-jet events and the second, at the charged particle multiplicity in dijet events. Also presented is a measurement of the multiplicity of low  $p_T$  jets in inclusive one-jet deep inelastic scattering events. In all three analyses possible effects of MPI were found.

## 1 Introduction

In  $ep$  collisions at HERA the mediator boson was a virtual photon<sup>1</sup> which can be characterized by two variables namely, the photon virtuality,  $Q^2$ , and the inelasticity,  $y$ . The life-time of an  $e\gamma$ -state is of the order  $\sim 1/Q^2$ . Within this life-time the photon can develop  $q\bar{q}$ -fluctuations. The life-time of these fluctuations are constant as a function of the characteristic  $p_T$  of the interacting partons and are of the order  $\sim 1/p_T^2$ . Therefore, these fluctuations are important only if  $Q^2 \ll p_T^2$ . In this case, the photon can fluctuate into a  $q\bar{q}$  pair or even more complicated states and these events have similar characteristics to hadron-hadron collisions.

QCD Monte Carlo programs (MC) simulate  $ep$  collisions at leading order in  $\alpha_s$ ,  $\mathcal{O}(\alpha\alpha_s)$ , with a 2-to-2 parton scattering. The events are simulated with initial as well as final parton state radiation and the contributions from the break up of the proton. Finally, hadronisation models are applied so that colourless particles are produced. In this picture, the primary two hard partons lead to two jets. The underlying event is defined as everything except the lowest order process. Ideally, the lowest order process is not affected by the underlying event but experimentally contributions from the underlying event are present in these jets and cannot be disentangled. The underlying event is therefore the initial and final state radiation and the remnant-remnant interactions as well as re-scatters off the remnants. These two last contributions are referred to as multiple parton interactions (MPI). In perturbative Quantum Chromodynamics (pQCD), the AGK cutting rules [1–3] can be used to relate the different contributions to  $ep$  scattering, diffraction and single or multiple scattering, via multiple exchange of BFKL Pomerons.

---

<sup>1</sup>For the photon virtuality range considered in these analyses.

Remnant-remnant interactions can only be present if the interacting particles have a composite structure via multi-parton exchange. In lepton-proton collisions this is only possible if the photon is resolved. The fraction of the photon energy entering in the hard scattering  $x_\gamma$  may be used to select enriched samples by resolved or point-like (direct) photons. Thus, at LO parton level,  $x_\gamma = 1$  for direct processes whereas in the resolved case,  $x_\gamma < 1$ . Experimentally, the variable  $x_\gamma^{obs}$  is used. It is defined in terms of the two hardest jets,  $Jet_1$  and  $Jet_2$ , and the hadronic final state (HFS) as:

$$x_\gamma^{obs} = \frac{\sum_{h \in Jet_1} (E - P_z) + \sum_{h \in Jet_2} (E - P_z)}{\sum_h (E - P_z)}, \quad (1)$$

where the sums in the nominator run over the hadrons in  $Jet_1$  and  $Jet_2$ , while the sum in the denominator runs over all hadrons in the entire HFS.

In the past, the underlying event was studied at HERA in the photoproduction regime [4,5] but not in deep inelastic scattering (DIS). The next sections are organized as follows. Firstly, a three- and four-jet cross section measurement in photoproduction is presented. Then two different analyses with similar strategies are shown, in which four regions in the azimuthal angle  $\phi$  are defined with respect to the leading jet, i.e. that with the highest  $E_T$  in the event. The first of these analyses is a charged particle multiplicity measurement in dijet photoproduction. The second is a mini-jet multiplicity measurement in DIS, where a mini-jet refers to a jet with low transverse momentum.

## 2 Three- and four-jet events in photoproduction

The leading order for an  $n$ -jet event, via a single chain exchange, is  $\mathcal{O}(\alpha\alpha_s^{n-1})$ . However,  $n$ -jet events can also be generated via MPI, where several chains are present. Moreover, even soft MPI may affect the distribution of multi-jet events by adding or redistributing the energy flow generated by a primary process.

The ZEUS collaboration studied the multi-jet production in the photoproduction regime [6], where  $Q^2 < 1 \text{ GeV}^2$  and  $0.2 < y < 0.85$ . Three- and four-jet events, where the jets were defined with the  $k_T$  clustering algorithm [7] and require to have transverse energies  $E_T^{jets} > 6 \text{ GeV}$ , were studied in the pseudorapidity range  $|\eta^{jets}| < 2.4$ . Furthermore, these events were studied in two different  $n$ -jet invariant mass regions, namely,  $25 < M_{n-jets} < 50 \text{ GeV}$  and  $M_{n-jets} > 50 \text{ GeV}$ , referred to as the low- and high-mass regions, respectively. The cross sections of the three- and four-jet low- and high-mass samples were measured differentially.

The data were compared to predictions from two  $\mathcal{O}(\alpha\alpha_s)$  matrix element MC programs supplemented with parton showers, HERWIG 6.505 [8–10] and PYTHIA 6.206 [11], both with and without MPI. In the case of HERWIG, MPI events were simulated via an interface to JIMMY 4.0 [12], which is an impact parameter dependent model. For PYTHIA, MPI were generated using the so-called "simple model" [13].

In addition, the three-jet sample was compared to the fixed order ( $\mathcal{O}(\alpha\alpha_s^2)$ ) calculation by Klasen, Kleinwort und Kramer [14]. This calculation corresponds to the three-jet LO and, at the time, was the highest order prediction available in photoproduction. Thus, no calculation was available for the four-jet sample.

The three- and four-jet cross sections are shown as a function of  $M_{n-jets}$  in figure 1. In general, both cross sections decrease exponentially with increasing  $M_{n-jets}$ . The HERWIG and PYTHIA predictions with and without MPI are also shown. They are normalized to the high invariant  $n$ -jets mass region ( $M_{n-jets} > 50$  GeV), i.e. they are scaled to describe the high  $M_{n-jets}$  cross section. Both HERWIG and PYTHIA without MPI fail to describe the cross section dependence. When MPI are included, however, they are in quite good agreement with data. The discrepancy is larger in the four-jet case. The PYTHIA model was run using its default setting whereas the JIMMY model was tuned to the presented data [6].

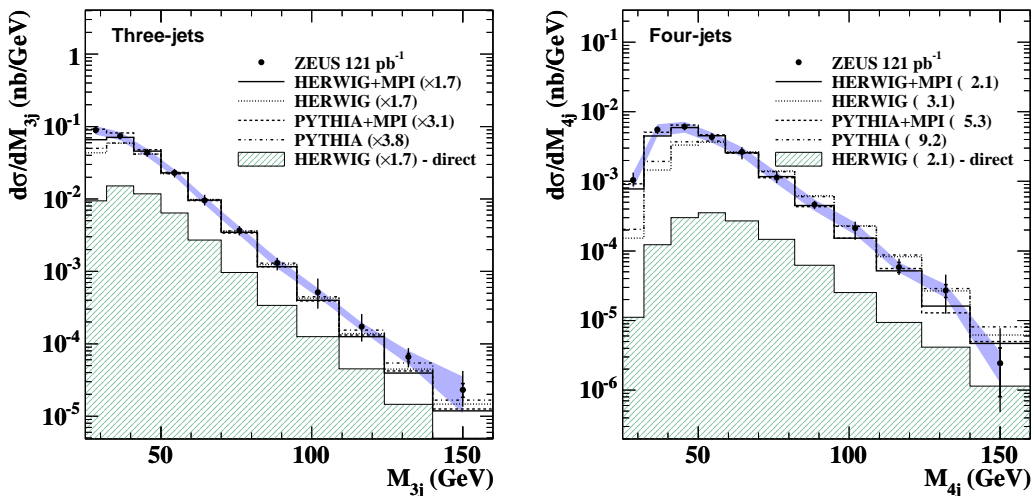


Fig. 1: Measured cross section as a function of (a)  $M_{3-jets}$  and (b)  $M_{4-jets}$  (solid circles). The inner and outer error bars and the shaded band represent the statistical, the statistical and the systematic added in quadrature and the calorimeter energy scale uncertainties, respectively.

Shown in Fig. 2a) is the measured three-jet cross section as a function of  $M_{3-jets}$ , compared to the fixed LO calculation for this process,  $\mathcal{O}(\alpha_s^2)$ . This calculation was corrected for hadronisation effects and MPI. The hadronisation and MPI corrections and their estimated uncertainties are shown in 2b). The hadronisation corrections are constant in  $M_{3-jets}$ , while MPI corrections increase towards low  $M_{3-jets}$ . The theoretical uncertainties on both the MPI corrections and the pQCD predictions are large. The magnitude and the shape of the calculation is consistent with the data within the large theoretical uncertainties. This is best seen in Fig. 2c) where the ratio data over theory is shown. Without the large MPI corrections the theoretical description would be far much worse at low  $M_{3-jets}$ .

### 3 Charged particle multiplicity in photoproduction

As described above, in quasi-real photoproduction ( $Q^2 \sim 0$ ) the photon can develop a hadronic structure, where remnant-remnant interactions may be present and therefore the particle production can be enhanced. However, the actual particle multiplicity depends not only on the number of multiple parton scatterings but also on the hadronisation and on the colour connections between



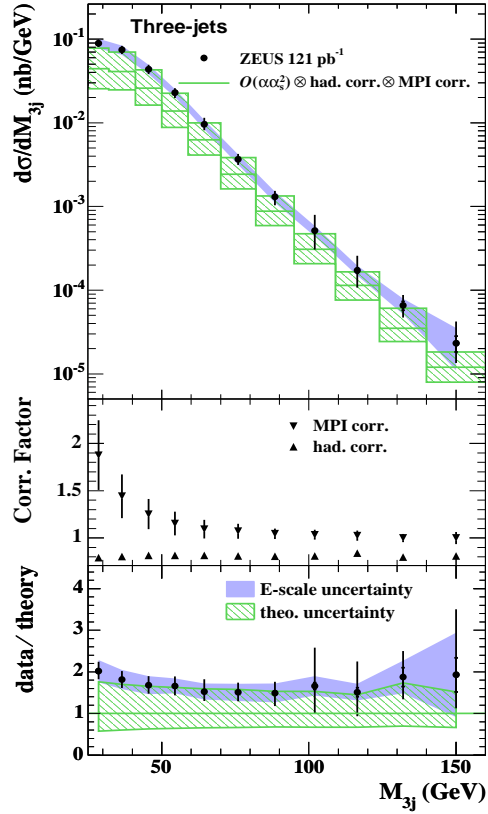


Fig. 2: (a) Measured three-jets cross section as a function of  $M_{3-jets}$  compared with an  $\mathcal{O}(\alpha_s^2)$  prediction, corrected for hadronisation and MPI effects. (b) The hadronisation and MPI correction factors as a function of  $M_{3-jets}$ . (c) The ratio of the  $M_{3-jets}$  cross section divided by the theoretical prediction. The theoretical uncertainty is represented by shaded bands.

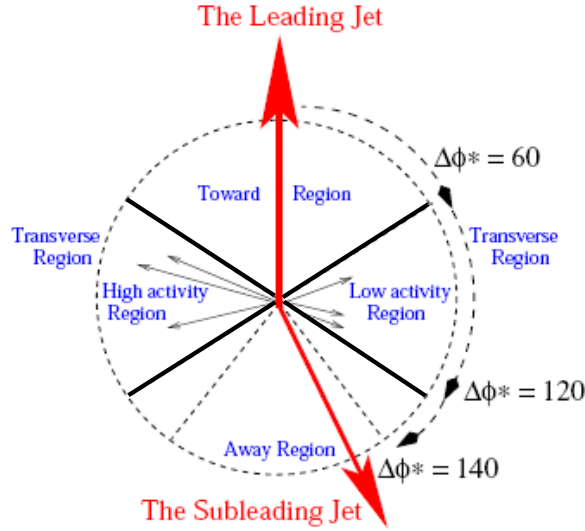


Fig. 3: Definition of the four azimuthal regions. The toward region is defined by the leading jet and by this means defines the away and transverse regions. The scalar sum of the transverse momenta  $P_t^{sum} = \sum_i^{tracks/HFS} P_T^i$  calculated in each transverse region defines the high and low activity region eventwise in the charged particle multiplicity and mini-jet analyses, respectively.

the multiple parton scatterings and the remnants. Within the model used [15], different colour connection scenarios are possible. Two scenarios are studied. In the first scenario, each hard scattering is independent of the other and therefore is connected only to the remnants, which gives long colour strings. In the second scenario, the colour strings are rearranged in order to provide shorter strings, i.e. the hard scatterings are colour connected with each other, which compared with the first scenario produces fewer particles.

This was studied in the H1 collaboration by using a dijet photoproduction sample, where  $Q^2 < 0.01 \text{ GeV}^2$  and  $0.3 < y < 0.65$ , looking at charged particles with transverse energies  $P_T^{track} > 150 \text{ MeV}$  in the pseudorapidity range  $|\eta^{track}| < 1.5$ . The jets were defined using the  $k_T$  clustering algorithm [7] and were required to have transverse momentum  $P_T^{jets} > 5 \text{ GeV}$  and  $|\eta^{jets}| < 1.5$ .

Four regions in the azimuthal angle,  $\phi$ , were then defined with respect to the leading jet as indicated in Fig. 3 in analogy to the CDF collaboration [16]. The leading jet ( $Jet_1$ ) defines the toward region, whereas the subleading jet, the jet with the next highest  $P_T^{jet}$ , is usually in the away region, although not necessarily. The transverse regions are less effected by the hard interaction and thus, expected to be more sensitive to the MPI. For each event, the hemisphere which has the highest scalar sum of the transverse momenta,  $P_t^{sum} = \sum_i^{tracks} P_T^i$ , is referred to as the high-transverse-activity hemisphere. The other is referred to as the low-transverse-activity hemisphere.

The average track multiplicity,  $\langle N_{charged} \rangle$ , is shown in figures 4 and 5 as a function of  $P_T^{Jet_1}$  for resolved photon enriched events,  $x_\gamma^{obs} < 0.7$  (left) and direct photon enriched events,  $x_\gamma^{obs} > 0.7$  (right). In the toward and away regions, the average track multiplicity increases with

$P_T^{Jet_1}$  as shown in figure 4. In the  $x_\gamma^{obs} > 0.7$  region (right) the measurements are reasonably well described by the simulation containing only one hard interaction with parton showers and hadronisation, whereas in the region  $x_\gamma^{obs} < 0.7$  (left) this is clearly not enough, especially at the lower values of  $P_T^{Jet_1}$ . MPI contributes as a pedestal and brings the prediction to a good agreement with the measurement.

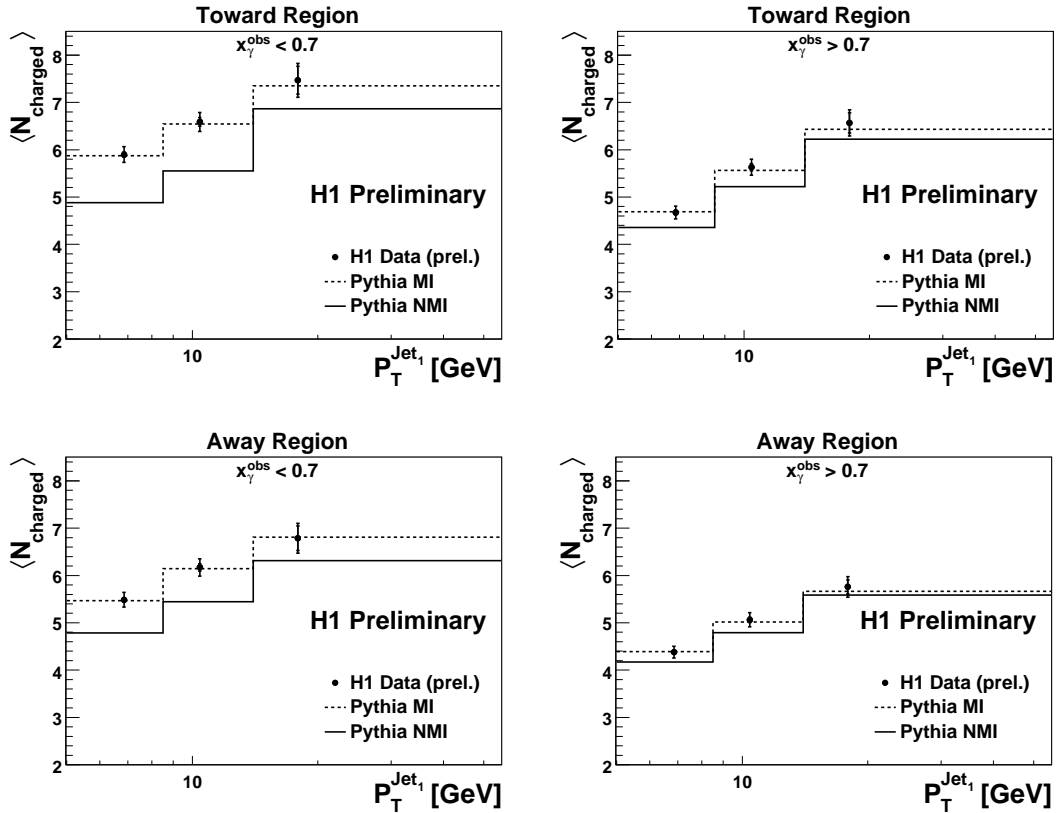


Fig. 4: Charged particle multiplicity for  $x_\gamma^{obs} < 0.7$  (left) and for  $x_\gamma^{obs} > 0.7$  (right). The leading jet ( $Jet_1$ ) is contained in the toward region, whereas the subleading jet, the second jet with highest  $P_T^{jet}$ , is usually in the away region, although not necessarily. Data is compared to PYTHIA with and without MPI.

In the transverse regions, shown in figure 5, the measured average track multiplicity decreases with  $P_T^{Jet_1}$ . At high  $x_\gamma^{obs}$  (right) the predicted average charged particle multiplicity with and without MPI also decreases with  $P_T^{Jet_1}$ , although only PYTHIA with MPI describes data. At low  $x_\gamma^{obs}$  (left) the PYTHIA prediction without MPI tends to increase with  $P_T^{Jet_1}$  while PYTHIA with MPI decreases with  $P_T^{Jet_1}$  giving the best description of the data.

We studied<sup>2</sup> also the different colour string scenarios in Fig. 6 where the transverse regions are shown. In the present simulation the long string configuration is preferred.

<sup>2</sup>This is done in PYTHIA by the parameters  $PARP(86) = 0.66$  and  $PARP(85) = 0.33$ , giving the probability that an additional interaction gives two gluons and the probability that an additional interaction gives two gluons with colour

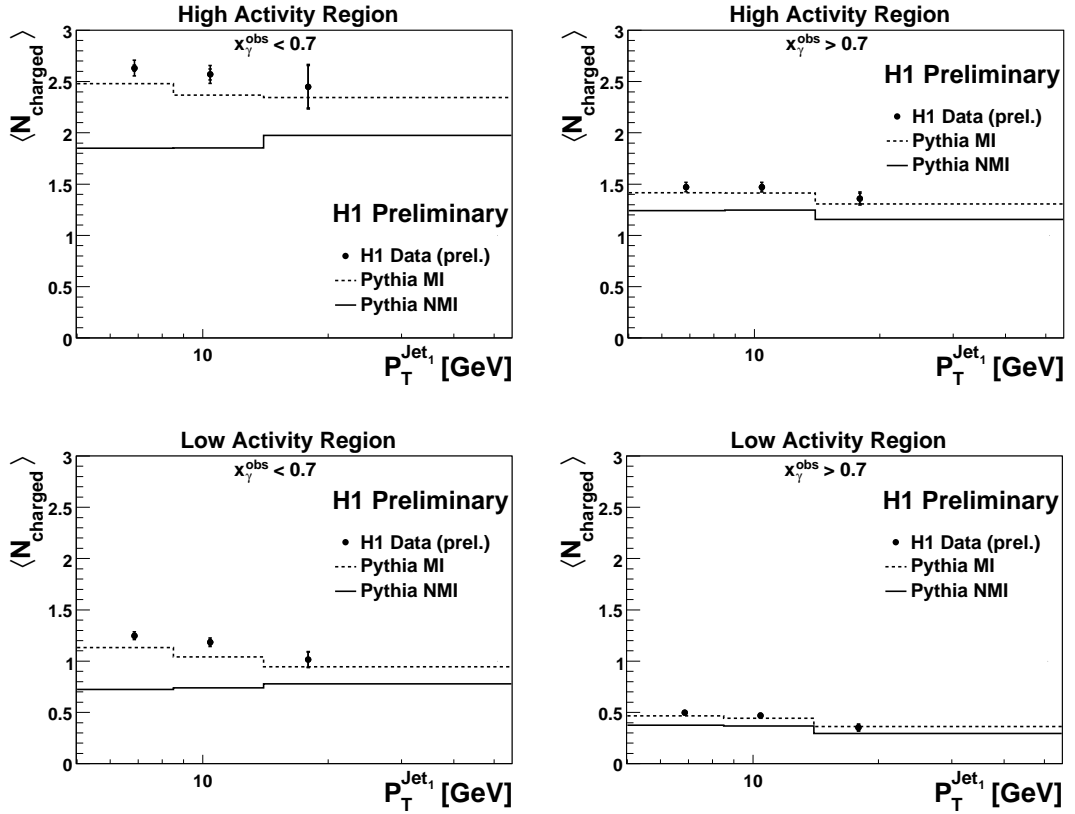


Fig. 5: Charged particle multiplicity for  $x_\gamma^{obs} < 0.7$  (left) and for  $x_\gamma^{obs} > 0.7$  (right). The transverse high activity regions, upper plots, are defined as the transverse region with a higher  $P_t^{sum}$  compared to the low activity regions, down. Data is compared to PYTHIA with and without MPI.

#### 4 Mini-jet multiplicity in DIS

The photon is more likely to develop a hadronic structure before interacting with the proton in photoproduction than in DIS. In DIS, the characteristic interaction time scales like  $\sim 1/Q^2$  and at high  $Q^2$ , it is too short for the fluctuations to occur. At HERA diffraction plays an important role at low  $x_{Bj}$ , and also at high  $Q^2$ . These events can be explained by the exchange of Pomerons. The AGK cutting rules relates the different contributions from diffraction and single or multiple parton scattering. Thus, it is interesting to study if evidence for multiple parton scattering can be seen within the data.

The H1 collaboration studied events in the kinematic region  $5 < Q^2 < 100 \text{ GeV}^2$  and  $0.1 < y < 0.7$ . Events with at least one jet with  $E_T^{jet} > 5 \text{ GeV}$  and in the laboratory pseudorapidity range  $-1.7 < \eta^{jet} < 2.79$  were selected<sup>3</sup> using the  $k_T$  clustering algorithm [7]. The HFS was required to have an invariant mass  $W > 200 \text{ GeV}$ .

connections to nearest neighbours, respectively.

<sup>3</sup>Applied both in the hadronic centre-of-mass frame (HCM) and in the laboratory frames.

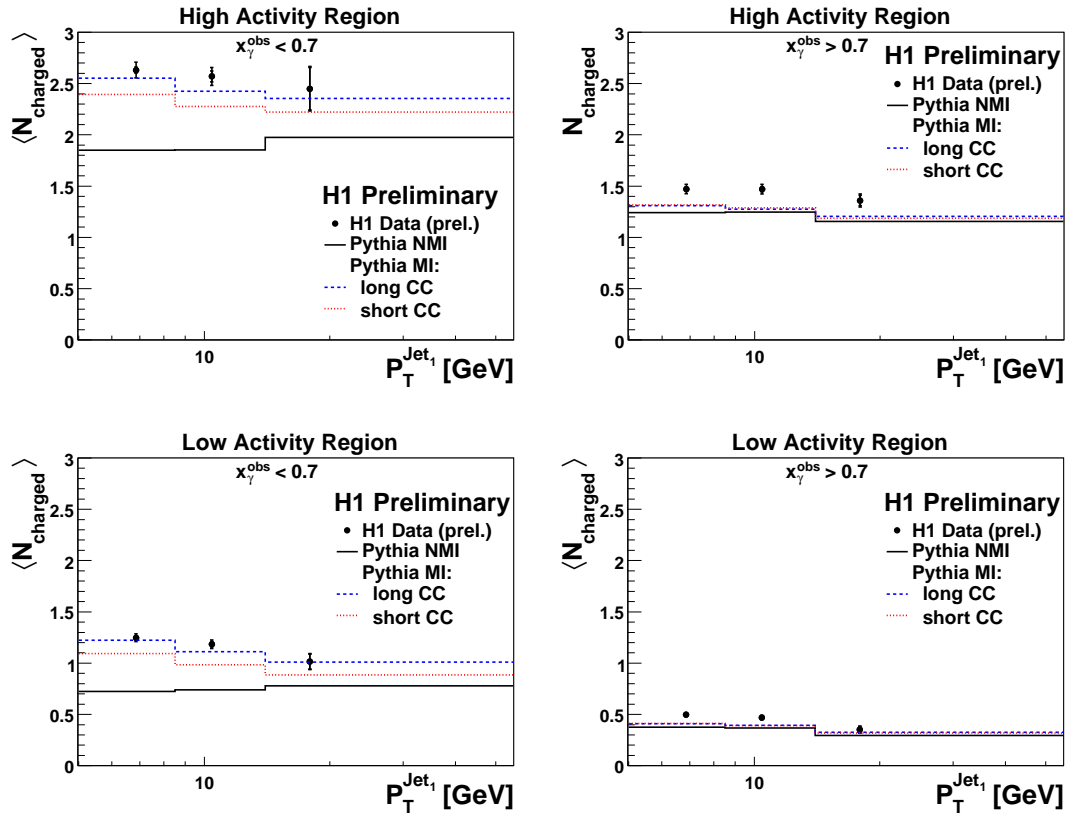


Fig. 6: Charged particle multiplicity for  $x_{\gamma}^{obs} < 0.7$  (left), and for  $x_{\gamma}^{obs} > 0.7$  (right). The transverse high activity regions, upper plots, are defined as the transverse region with a higher  $P_t^{sum}$  compared to the low activity regions, down. Here data is compared to PYTHIA without MPI and PYTHIA with MPI and high probability for long colour string connections, long CC, and short colour string connections, short CC.

The leading jet defines a toward, an away and two transverse regions (Fig. 3). The average multiplicity of jets with  $E_T^{mini} > 3$  GeV, the so-called mini-jets, was measured,  $\langle N_{mini-jet} \rangle$  in the range  $-1.7 < \eta < 2.79$  for the four  $\Delta\phi^*$  regions. A possible signature of MPI would be an increased value of  $\langle N_{mini-jet} \rangle$ , especially in the less populated high- and low-activity transverse regions and for the lower  $Q^2$  values.

In Figure 7 the measured average mini-jet multiplicity is shown as a function of the transverse momentum of the leading jet in the hadronic centre-of-mass (HCM) frame,  $P_{T,1j}^*$ . The data are compared to the predictions of RAPGAP [17], ARIADNE [18] and PYTHIA. The former two do not include MPI whereas PYTHIA was run both with and without MPI.

The toward region data are reasonably well described by all four MC. While RAPGAP and PYTHIA marginally underestimate  $\langle N_{mini-jet} \rangle$  at low  $P_{T,1j}^*$  in the lowest  $Q^2$  bin ARIADNE slightly overestimates the data. The PYTHIA description is improved by the introduction of MPI at low  $Q^2$ .

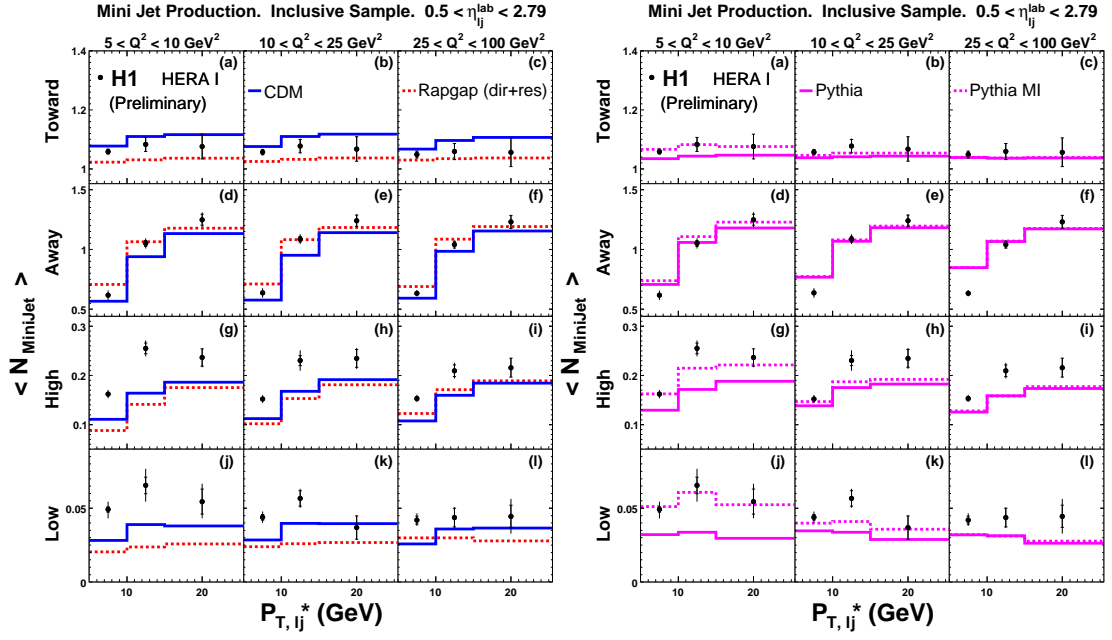


Fig. 7: The  $\langle N_{mini jet} \rangle$  data, in all four azimuthal regions, as a function of  $P_{T,1j}^*$  in three  $Q^2$  bins. Also shown are the predictions from four MC models.

The overall description in the away region is good. The PYTHIA model predicts the away region to be the least sensitive to MPI. In the low and high activity transverse regions all the MC that do not include MPI underestimate the data in all  $P_{T,1j}^*$  and  $Q^2$  bins. This is more pronounced at low  $P_{T,1j}^*$  and  $Q^2$  values. The introduction of MPI in PYTHIA certainly aids in the description of the low  $Q^2$  data. However, at large  $Q^2$  the effect of MPI is very small according to the simulation and so PYTHIA underestimates the  $Q^2$  data.

## 5 Conclusions

In all three analyses, both in photoproduction and in DIS, contributions from MPI are suggested. The three- and four-jet photoproduction cross sections shapes cannot be described by the  $\mathcal{O}(\alpha\alpha_s)$  plus parton shower calculations. In the three-jet case the LO pQCD calculation needs to include the estimated hadronisation and MPI effects to describe data, where the latter has a large contribution towards low  $M_{3-jets}$ .

Both the charged particle and the mini-jet multiplicities are larger than predicted by MCs not including MPI. More specifically, the charged particle multiplicity as a function of  $P_T^{Jet1}$  predictions have a different shape depending on whether MPI is included or not in the transverse regions for low  $x_{\gamma}^{obs}$  values as seen by PYTHIA. The multiplicity can be only described in all regions properly when MPI are included. In the mini-jet analysis, the measured multiplicity is larger than the predictions by the parton shower and colour dipole model MCs. MPI, as predicted by PYTHIA, helps to describe the distributions at low  $Q^2$  values but does not contribute at higher virtualities.

Higher partonic activity than predicted by standard MC is seen by all three analyses. These effects are also seen in DIS and at low and moderate  $Q^2$  can be reasonably well described by including MPI.

## References

- [1] Abramovsky, V. A. and Gribov, V. N. and Kancheli, O. V., *Yad. Fiz.* **18**, 595 (1973).
- [2] Bartels, J. and Salvadore, M. and Vacca, G. P., *Eur. Phys. J.* **C42**, 53 (2005).
- [3] Bartels, J. Prepared for Gribov-75: Memorial Workshop on Quarks, Hadrons, and Strong Interactions, Budapest, Hungary, 22-24 May 2005.
- [4] Derrick, M. and others, *Phys. Lett.* **B348**, 665 (1995).
- [5] Aid, S. and others, *Z. Phys.* **C70**, 17 (1996).
- [6] Namsoo, T., *Three- and Four-Jet States in Photoproduction at HERA*. Ph.D. Dissertation, Bristol University, September 2005.
- [7] Catani, S. and Dokshitzer, Yuri L. and Seymour, M. H. and Webber, B. R., *Nucl. Phys.* **B406**, 187 (1993).
- [8] Corcella, G. and others, *JHEP* **01**, 010 (2001).
- [9] Corcella, G. and others (2002).
- [10] Marchesini, G. and others, *Comput. Phys. Commun.* **67**, 465 (1992).
- [11] Sjostrand, Torbjorn and Lonnblad, Leif and Mrenna, Stephen (2001).
- [12] Butterworth, J. M. and Forshaw, Jeffrey R. and Seymour, M. H., *Z. Phys.* **C72**, 637 (1996).
- [13] Sjostrand, Torbjorn and Mrenna, Stephen and Skands, Peter, *JHEP* **05**, 026 (2006).
- [14] Klasen, Michael, *Eur. Phys. J.* **C7**, 225 (1999).
- [15] Sjostrand, Torbjorn and van Zijl, Maria, *Phys. Rev.* **D36**, 2019 (1987).
- [16] Acosta, Darin E. and others, *Phys. Rev.* **D65**, 072005 (2002).
- [17] Jung, Hannes, *Comp. Phys. Commun.* **86**, 147 (1995).
- [18] Lonnblad, Leif, *Comput. Phys. Commun.* **71**, 15 (1992).

# Modeling the underlying event: generating predictions for the LHC

*Arthur Moraes*

University of Glasgow, UK

## Abstract

This report presents tunings for PYTHIA 6.416 and JIMMY 4.3 to the underlying event. The MC generators are tuned to describe underlying event measurements made by CDF for  $p\bar{p}$  collisions at  $\sqrt{s} = 1.8$  TeV. LHC predictions for the underlying event generated by the tuned models are also compared in this report.

## 1 Introduction

Over the last few years, the Tevatron experiments CDF and D0 have managed to reduce uncertainties in various measurements to a level in which the corrections due to the underlying event (UE) have become yet more relevant than they were in Run I analyses. Studies in preparation for LHC collisions have also shown that an accurate description of the underlying event will be of great importance for reducing the uncertainties in virtually all measurements dependent on strong interaction processes. It is therefore very important to produce models for the underlying event in hadron collisions which can accurately describe Tevatron data and are also reliable to generate predictions for the LHC.

The Monte Carlo (MC) event generators PYTHIA [1] and HERWIG [2] are largely used for the simulation of hadron interactions by both Tevatron and LHC experiments. Both generators are designed to simulate the event activity produced as part of the underlying event in proton-antiproton ( $p\bar{p}$ ) and proton-proton (pp) events. HERWIG, however, needs to be linked to dedicated package, named “JIMMY” [3, 4], to produce the underlying event activity.

PYTHIA 6.2 has been shown to describe both minimum bias and underlying event data reasonably well when appropriately tuned [5–7]. Major changes related to the description of minimum bias interactions and the underlying event have been introduced in PYTHIA 6.4 [1]. There is a new, more sophisticated scenario for multiple interactions, new  $p_T$ -ordered initial- and final-state showers (ISR and FSR) and a new treatment of beam remnants [1].

JIMMY [4] is a library of routines which should be linked to the HERWIG MC event generator [2] and is designed to generate multiple parton scattering events in hadron-hadron events. JIMMY implements ideas of the eikonal model which are discussed in more detail in Ref. [3, 4].

In this report we present a tuning for PYTHIA 6.416 which has been obtained by comparing this model to the underlying event measurements done by CDF for  $p\bar{p}$  collisions at 1.8 TeV [8, 9]. We also compare the ATLAS tune for HERWIG 6.510 with JIMMY 4.3 to these data distributions [10].



## 2 MC predictions vs. UE data

Based on the CDF analysis [9], the underlying event is defined as the angular region in  $\phi$  which is transverse to the leading charged particle jet.

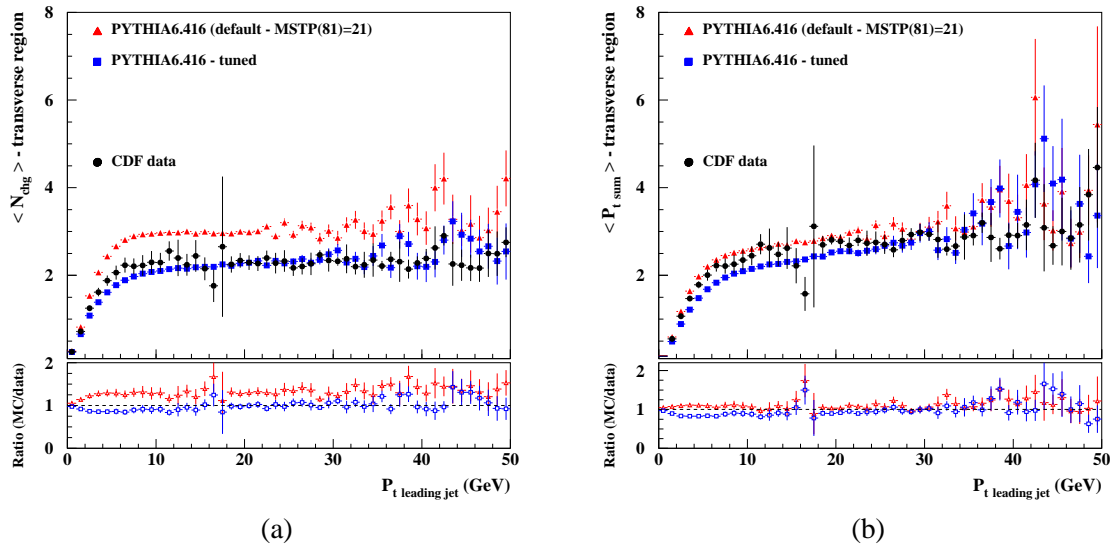


Fig. 1: PYTHIA 6.416 predictions for the underlying event compared to the  $\langle N_{chg} \rangle$  (a) and  $\langle p_T^{SUM} \rangle$  (b).

Figure 1 shows the PYTHIA 6.416 predictions for the underlying event compared to the CDF data for the average charged particle multiplicity,  $\langle N_{chg} \rangle$  (charged particles with  $p_T > 0.5$  GeV and  $|\eta| < 1$ ) and average sum of charged particle's transverse momentum,  $\langle p_T^{sum} \rangle$  in the underlying event [9]. Two MC generated distributions are compared to the data in these plots: one generated with all default settings in PYTHIA 6.416 except for the explicit selection of the new multiple parton interaction and new parton shower model, which is switched on by setting MSTP(81)=21 [1], and a second distribution with a tuned set of parameters. This particular PYTHIA 6.416 - tune was prepared for use in the 2008 production of simulated events for the ATLAS Collaboration. The list of tuned parameters is shown in table 1.

The guiding principles to obtain the parameters listed in Table 1 were two: firstly the new multiple parton interaction model with interleaved showering and colour reconnection scheme was to be used and, secondly, changes to ISR and FSR parameters should be avoided if at all possible.

In order to obtain a tuning which could successfully reproduce the underlying event data, we have selected a combination of parameters that induce PYTHIA to preferably chose shorter strings to be drawn between the hard and the soft systems in the hadronic interaction. We have also increased the hadronic core radius compared to the tunings used in previous PYTHIA versions, such as the ones mentioned in Ref. [6, 7]. As can be seen in fig. 1 PYTHIA 6.416 - tuned describes the data.

Default [1]	PYTHIA 6.416 - tuned	Comments
MSTP(51)=7 CTEQ5L	MSTP(51)=10042 MSTP(52)=2 CTEQ6L (from LHAPDF)	PDF set
MSTP(81)=1 (old MPI model)	MSTP(81)=21 (new MPI model)	multiple interaction model
MSTP(95)=1	MSTP(95)=2	method for colour reconnection
PARP(78)=0.025	PARP(78)=0.3	regulates the number of attempted colour reconnections
PARP(82)=2.0	PARP(82)=2.1	$p_{T_{\min}}$ parameter
PARP(83)=0.5	PARP(83)=0.8	fraction of matter in hadronic core
PARP(84)=0.4	PARP(84)=0.7	hadronic core radius

Table 1: PYTHIA 6.416 - tuned parameter list for the underlying event.

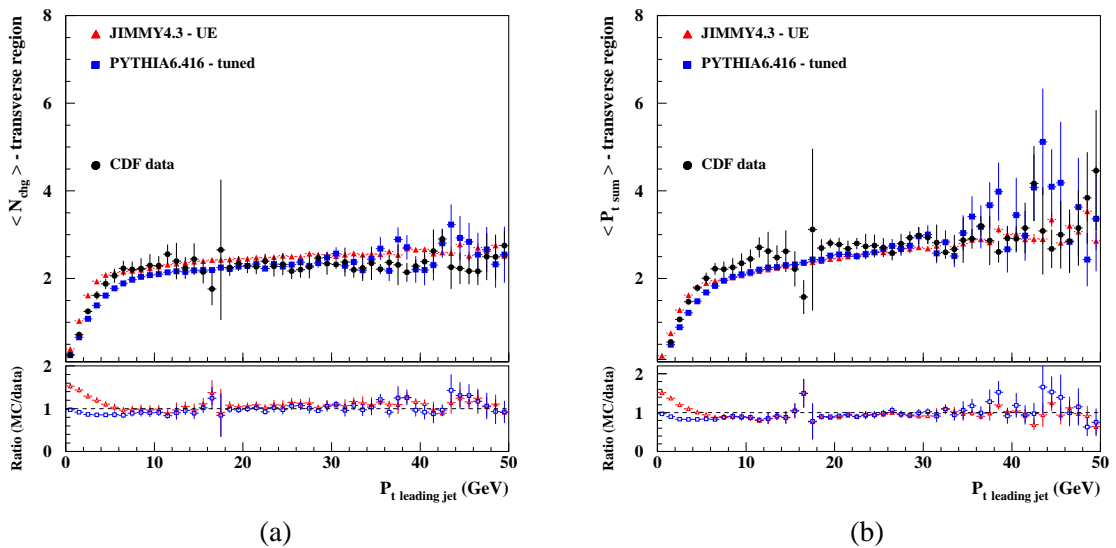
Fig. 2: PYTHIA 6.416 - tuned and JIMMY 4.3 - UE predictions for the underlying event compared to the  $\langle N_{chg} \rangle$  (a) and  $\langle p_T^{SUM} \rangle$  (b).

Figure 2 shows PYTHIA 6.416 - tuned and JIMMY4.3 - UE [10] predictions for the underlying event compared to the CDF data for  $\langle N_{chg} \rangle$  and  $\langle p_T^{sum} \rangle$ . Both models describe the data reasonably well. However, as shown in fig. 3, the ratio  $\langle p_T^{sum} \rangle / \langle N_{chg} \rangle$  is better de-

scribed by PYTHIA 6.416 - tuned. This indicates that charged particles generated by JIMMY4.3 - UE are generally softer than the data and also softer than those generated by PYTHIA 6.416 - tuned.

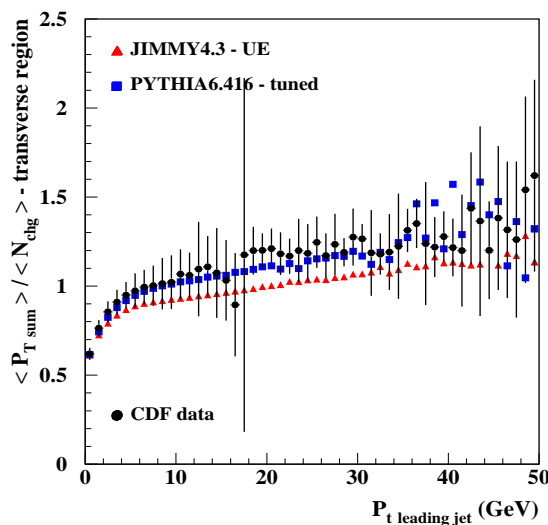


Fig. 3: PYTHIA 6.416 - tuned and JIMMY 4.3 - UE predictions for the underlying event compared to the ratio  $\langle p_T^{SUM} \rangle / \langle N_{chg} \rangle$ .

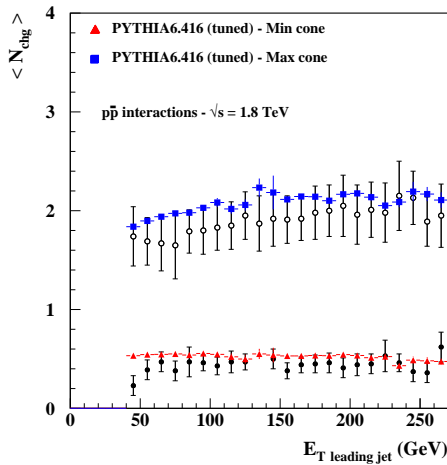
Another CDF measurement of the underlying event event was made by defining two cones in  $\eta - \phi$  space, at the same pseudorapidity  $\eta$  as the leading  $E_T$  jet (calorimeter jet) and  $\pm\pi/2$  in the azimuthal direction,  $\phi$  [8]. The total charged track transverse momentum inside each of the two cones was then measured and the higher of the two values used to define the “MAX” cone, with the remaining cone being labelled “MIN” cone.

Figure 4 shows PYTHIA 6.416 - tuned predictions for the underlying event in  $p\bar{p}$  collisions at  $\sqrt{s} = 1.8$  TeV compared to CDF data [8] for  $\langle N_{chg} \rangle$  and  $\langle P_T \rangle$  of charged particles in the MAX and MIN cones. PYTHIA 6.416 - tuned describes the data reasonably well. However, we notice that the  $\langle P_T \rangle$  in the MAX cone is slightly harder than the data.

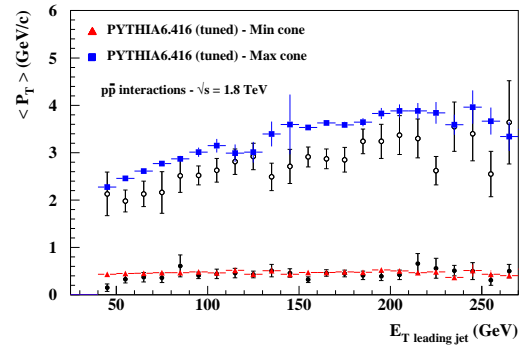
### 3 LHC predictions for the UE

Predictions for the underlying event in LHC collisions (pp collisions at  $\sqrt{s} = 14$  TeV) have been generated with PYTHIA 6.416 - tuned and JIMMY 4.3 - UE. Figure 5 shows  $\langle N_{chg} \rangle$  and  $\langle p_T^{SUM} \rangle$  distributions for the region transverse to the leading jet (charged particles with  $p_T > 0.5$  GeV and  $|\eta| < 1$ ), as generated by PYTHIA 6.416 - tuned (table 1) and JIMMY 4.3 - UE [10]. The CDF data ( $p\bar{p}$  collisions at  $\sqrt{s} = 1.8$  TeV) for the underlying event is also included in Fig. 5 for comparison.

A close inspection of predictions for the  $\langle N_{chg} \rangle$  in the underlying event given in fig.

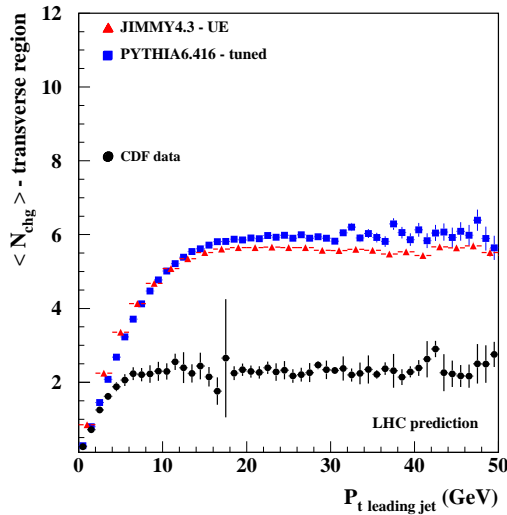


(a)

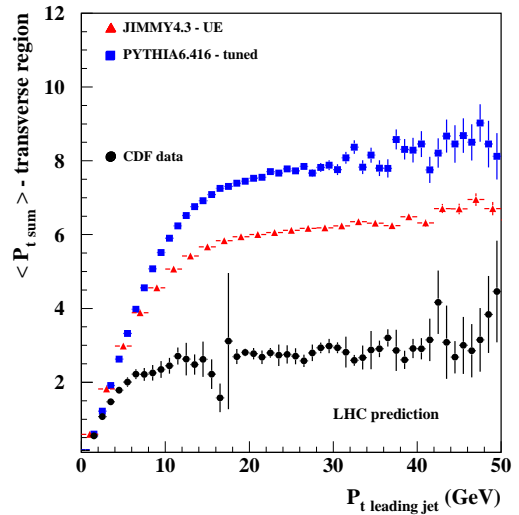


(b)

Fig. 4: (a) Average charged particle multiplicity,  $\langle N_{chg} \rangle$ , in MAX (top distributions) and MIN (bottom distributions) cones; (b) average total  $P_T$  of charged particles in MAX and MIN cones.



(a)



(b)

Fig. 5: PYTHIA 6.416 - tuned and JIMMY4.3 - UE predictions for the underlying event in pp collisions at  $\sqrt{s} = 14$  TeV for (a)  $\langle N_{chg} \rangle$  and (b)  $\langle p_T^{SUM} \rangle$ .

5(a), shows that the average charged particle multiplicity for events with leading jets with  $P_{t, \text{jet}} > 15$  GeV reaches a plateau at  $\sim 5.5$  charged particles according to both PYTHIA 6.416 - tuned and JIMMY4.3-UE. This corresponds to a rise of a factor of  $\sim 2$  in the plateau of  $\langle N_{chg} \rangle$  as

the colliding energy is increased from  $\sqrt{s} = 1.8$  TeV to  $\sqrt{s} = 14$  TeV.

The  $\langle p_T^{SUM} \rangle$  distributions in Fig. 5(b) show that PYTHIA 6.416 - tuned generates harder particles in the underlying event compared to JIMMY 4.3-UE. This is in agreement with the results shown in fig. 3, although for the LHC prediction the discrepancy between the two models is considerably larger than the observed at the Tevatron energy.

The difference between the predictions for the charged particle's  $p_T$  in the underlying event is a direct result of the tuning of the colour reconnection parameters in the new PYTHIA 6.4 model. This component of the PYTHIA model has been specifically tuned to produce harder particles, whereas in JIMMY4.3 - UE this mechanism (or an alternative option) is not yet available.

## 4 Conclusions

In this report we have compared tunings for PYTHIA 6.416 1 and JIMMY4.3 [10] to the underlying event. Both models have shown that, when appropriately tuned, they can describe the data.

In order to obtain the parameters for PYTHIA 6.416 - tuned, we have deliberately selected a combination of parameters that generate shorter strings between the hard and the soft systems in the hadronic interaction. We have also increased the hadronic core radius compared to the tunings used in previous PYTHIA versions (see Refs. [6, 7] for example).

We have noticed that PYTHIA 6.416 - tuned and JIMMY 4.3 - UE generate approximately the same densities of charged particles in the underlying event. This is observed for the underlying event predictions at the Tevatron and LHC energies alike.

However, there is a considerable disagreement between these tuned models in their predictions for the  $p_T$  spectrum in the underlying event, as can be seen in figs. 3 and 5(b). PYTHIA 6.416 - tuned has been calibrated to describe the ratio  $\langle p_T^{sum} \rangle / \langle N_{chg} \rangle$ , which has been possible through the tuning of the colour reconnection parameters in PYTHIA. JIMMY4.3 - UE has not been tuned to this ratio.

As a final point, we would like to mention that this is an “ongoing” study. At the moment these are the best parameters we have found to describe the data, but as the models are better understood, the tunings could be improved in the near future.

## References

- [1] T. Sjostrand, S. Mrenna and P. Skands, *JHEP* **05**, 026 (2006).
- [2] Corcella, G. et al, *JHEP* **01**, 010 (2001).
- [3] Butterworth, J. M. and Forshaw, J. R. and Seymour, M. H., *Z. Phys. C* **72**, 637 (1996).
- [4] J. M. Butterworth and M. H. Seymour, *JIMMY4: Multiparton Interactions in Herwig for the LHC*, October 2004.
- [5] Sjostrand, T. and Zijl, M. van, *Phys. Rev. D* **36**, 2019 (1987).

- [6] A. Moraes, C. Buttar and I. Dawson, Eur. Phys. J. C **50**, 435 (2007).
- [7] R. Field, *Min-Bias and the Underlying Event at the Tevatron and the LHC*, October 2002. (talk presented at the Fermilab ME/MC Tuning Workshop, Fermilab).
- [8] D. Acosta, et al, Phys. Rev. **D70**, 072002 (2004).
- [9] T. Affolder, et al, Phys. Rev. **D65**, 092002 (2002).
- [10] C. Buttar, et al, *Physics at Tev Colliders 2005 - QCD, EW and Higgs Working Group: Summary Report*, April 2006.

# Measurement of the Underlying Event in Jet Topologies using Charged Particle and Momentum Densities

*F. Ambroglini<sup>a</sup>, P. Bartalini<sup>b</sup>, F. Bechtel<sup>c</sup>, L. Fanò<sup>d</sup>, R. Field<sup>e</sup>*

*a) University of Trieste, Italy. b) National Taiwan University, Taiwan. c) Hamburg University, Germany. d) University of Perugia, Italy. e) University of Florida, USA.*

## Abstract

A study of Underlying Events with the CMS detector under nominal and start-up conditions is discussed. Using charged particle densities in charged particle jets, it will be possible to discriminate between QCD models with different multiple parton interaction schemes, which correctly reproduce Tevatron data but give different predictions when extrapolated to the LHC energy. This will permit improving and tuning Monte Carlo models at LHC start-up, and opens prospects for exploring QCD dynamics in proton-proton collisions at 14 TeV.

## 1 Introduction

From a theoretical point of view, the underlying event (UE) in a hadron-hadron interaction is defined as all particle production accompanying the hard scattering component of the collision. From an experimental point of view, it is impossible to separate these two components. However, the topological structure of hadron-hadron collisions can be used to define physics observables which are sensitive to the UE.

The ability to properly identify and calculate the UE activity, and in particular the contribution from Multiple Parton Interactions – MPI [1], has direct implications for other measurements at the LHC.

This work is devoted to the analysis of the sensitivity of UE observables, as measured by CMS, to different QCD models which describe well the Tevatron UE data but largely differ when extrapolated to the LHC energy. MPI are implemented in the PYTHIA simulations [2], for which the following tunes are considered: tune DW (reproducing the CDF Run-1  $Z$  boson transverse momentum distribution [3]), tune DWT (with a different MPI energy dependence parametrization [4]) and tune S0 (which uses the new multiple interaction model implemented in PYTHIA [5]). In addition, an Herwig [6] simulation has also been performed, providing a useful reference to a model without multiple interactions.

## 2 Analysis strategy

Significant progress in the phenomenological study of the UE in jet events has been achieved by the CDF experiment at the Tevatron [7, 8]. In the present work, plans are discussed to study the topological structure of hadron-hadron collisions and the UE at the LHC, using only charged particle multiplicity and momentum densities in charged particle jets. A charged particle jet

(referred to as a *charged jet* from now on) is defined using charged particles only, with no recourse to calorimeter information. Different integrated luminosity scenarios are considered: 1, 10 and 100 pb<sup>-1</sup>. The foreseen start-up CMS tracker alignment precision is applied in the case of 1 pb<sup>-1</sup>.

The direction of the leading charged jet, which in most cases results from the hard scattering, is used to isolate different hadronic activity regions in the  $\eta - \phi$  space and to study correlations in the azimuthal angle  $\phi$ . The plane transverse to the jet direction is where the 2-to-2 hard scattering has the smallest influence and, therefore, where the UE contributions are easier to observe.

In order to combine measurements with different leading charged jet energies, events are selected with a Minimum Bias (MB) trigger [9] and with three triggers based on the transverse momentum of the leading calorimetric jet ( $P_T^{calo} > 20, 60$  and 120 GeV/c).

Charged jets are reconstructed with an iterative cone algorithm with radius  $R = 0.5$ , using charged particles emitted in the central detector region  $|\eta| < 2$ . Two variables allow evaluating charged jet performances: the distance  $\Delta R = \sqrt{\Delta\phi^2 + \Delta\eta^2}$  between the leading charged jet and the leading calorimetric jet, and the ratio of their transverse momenta  $P_T$  (transverse momenta are defined with respect to the beam axis). The transverse momentum of the leading charged jet is used to define the hard scale of the event.

Figure 1 presents, for the four trigger streams, the density  $dN/d\eta d\phi$  of the charged particle multiplicity and the density  $dp_T^{sum}/d\eta d\phi$  of the total charged particle transverse momentum  $p_T^{sum}$ , as a function of the azimuthal distance to the leading charged jet. Enhanced activity is observed around the jet direction, in the “toward” region ( $\simeq 0$  degrees from the jet direction), together with a corresponding rise in the “away” region ( $\simeq 180$  degrees), due to the recoiling jet. The “transverse” region ( $\simeq \pm 90$  degrees) is characterized by a lower activity and almost flat density distributions, as expected.

### 3 UE observable measurement

#### 3.1 Data samples

The data samples used for the present analysis are based on the DWT PYTHIA tune. MB and QCD dijet event samples, generated in bins of the transverse momentum  $\hat{p}_T$  of the hard process, were reweighted according to their cross sections, the dijet events being merged into a single stream called hereafter *JET*. On that sample the calorimetric thresholds are applied in order to obtain the different trigger streams considered in the presented analysis. The samples were reweighted according to the integrated luminosities corresponding to the different scenarios studied below, with consistent statistical precision in the relevant figures.

#### 3.2 Tracking

Tracks of charged particles with  $P_T > 0.9$  GeV/c are reconstructed in CMS following the procedure described in [10]. The possibility to build the UE observables using tracks with  $p_T > 0.5$  GeV/c enhances sensitivity to the differences between the models. The standard CMS tracking algorithm was, thus, adapted to a 0.5 GeV/c threshold, by decreasing the  $p_T$  cut of the seeds and of the trajectory builder, and adapting other parameters of the trajectory reconstruction to optimize performance.



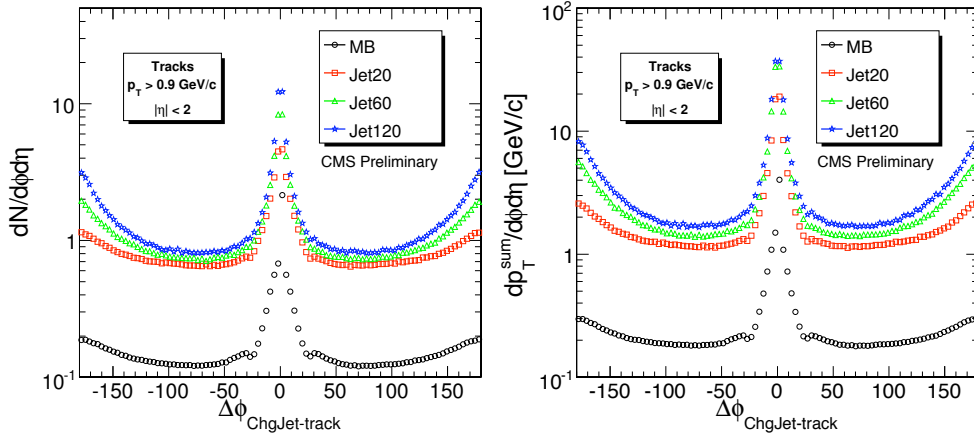


Fig. 1: Densities  $dN/d\eta d\phi$  of charged particle multiplicity (*left*) and  $dp_T^{sum}/d\eta d\phi$  of total charged transverse momentum (*right*), as a function of the azimuthal distance to the leading charged jet direction.

### 3.3 Results on density measurements

The corrected densities  $dN/d\eta d\phi$  of charged particle multiplicity and  $dp_T^{sum}/d\eta d\phi$  of charged transverse momentum are presented in Figure 2 for the transverse region. The data, corresponding to an integrated luminosity of  $10 \text{ pb}^{-1}$ , are reported at the reconstruction level, using the DWT tune. The average corrections for both the  $P_T$  scale and the UE observables are found to be independent from the particular model used for the simulations.

Two contributions to the hadronic activity can be identified: a fast saturation of the UE densities for charged jets with  $P_T < 20 \text{ GeV}/c$ , and a smooth rise for  $P_T > 40 \text{ GeV}/c$ . The former is due to the MPI contribution while the latter is due to initial and final state radiation, which keeps increasing with the hard scale of the event.

The statistical precision and the alignment conditions correspond to those achieved with an integrated luminosity of  $100 \text{ pb}^{-1}$ . The curves represent the predictions of the different PYTHIA (DW, DWT and S0 tunes) and HERWIG simulations.

With respect to the standard  $0.9 \text{ GeV}/c$  scenario, lowering the  $P_T$  threshold for track reconstruction to  $0.5 \text{ GeV}/c$  turns out to lead to an increase of about 50% of the charged particle multiplicity and of about 30% of the charged transverse momentum density, slightly enhancing the discrimination power between the different models in the charged jet  $P_T$  region below  $40 \text{ GeV}/c$ .

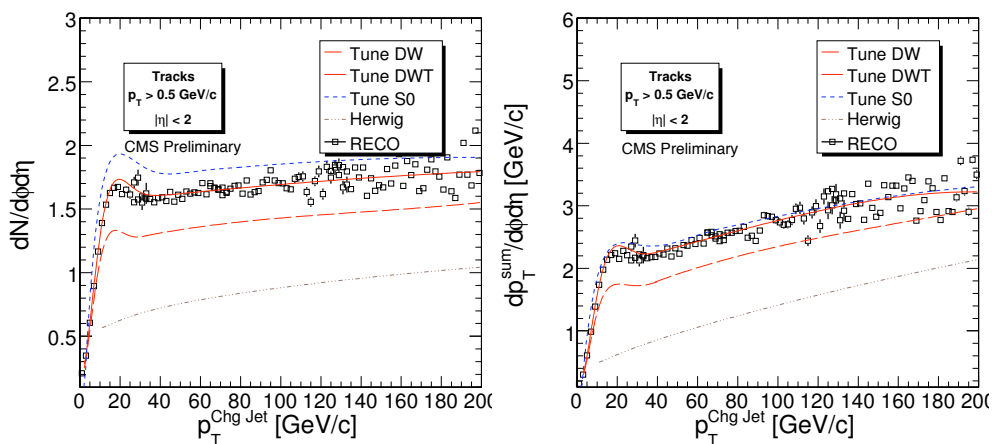


Fig. 2: Densities  $dN/d\eta d\phi$  (left) and  $dp_T^{sum}/d\eta d\phi$  (right) for tracks with  $p_t > 0.5$  GeV/c, as a function of the leading charged jet  $P_T$ , in the transverse region, for an integrated luminosity of  $100 \text{ pb}^{-1}$  (corrected distributions).

### 3.4 Results using observable ratios

The ratios between (uncorrected) UE density observables in the transverse region, for charged particles with  $p_T > 0.9$  GeV/c and with  $p_T > 1.5$  GeV/c, are presented in Figure 3, for an integrated luminosity of  $100 \text{ pb}^{-1}$ . Ratios are shown here as obtained after track reconstruction, without applying additional reconstruction corrections; given the uniform performance of track reconstruction, the ratios presented here at detector level are similar to those at generator level. These ratios show a significant sensitivity to differences between different MPI models, thus providing a feasible (and original) investigation method.

## 4 Start-up conditions

The CMS tracking performance at the LHC start-up, with an integrated luminosity of the order of  $1 \text{ pb}^{-1}$ , will be affected by imperfect knowledge of detector element alignment. This additional error to the reconstructed positions of charged particle hits in the tracker system is taken into account by the *alignment position error* (APE) tool [11] [12] [13].

Figure 4 compares the tracker performance between the case of an ideally aligned detector and the case of a misaligned detector, before and after using the APE tool. The track reconstruction efficiency is seriously degraded by the mis-alignment, but it can be completely recovered using the APE tool, thanks to an increase in the spatial window used to find compatible hits during the trajectory building. The larger search window recovers many good hits which would otherwise be lost, at the expense of significantly increasing the rate of fake tracks. The relative

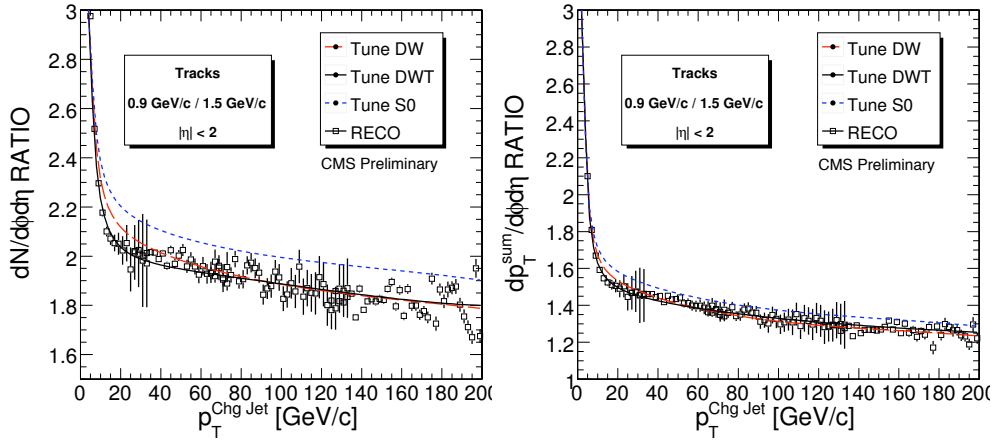


Fig. 3: Ratio of the UE event observables, computed with track transverse momenta  $p_T > 1.5$  GeV/c and  $p_T > 0.9$  GeV/c: densities  $dN/d\eta d\phi$  (left) and  $dp_T^{sum}/d\eta d\phi$  (right), as a function of the leading charged jet  $P_T$ , in the transverse region, for an integrated luminosity of  $100 \text{ pb}^{-1}$  (uncorrected distributions).

$p_T$  resolution, also shown in Figure 4, is seen to be almost fully recovered after correcting the misalignment.

## 5 Conclusions

The predictions on the amount of hadronic activity in the region transverse to the jets produced in proton-proton interactions at the LHC energies are based on extrapolations from lower energy data (mostly from the Tevatron). These extrapolations are uncertain and predictions differ significantly among model parameterisations. It is thus important to measure the UE activity at the LHC as soon as possible, and to compare those measurements with Tevatron data. This will lead to a better understanding of the QCD dynamics and to improvements of QCD based Monte Carlo models aimed at describing “ordinary” events at the LHC, an extremely important ingredient for “new” physics searches.

Variables well suited for studying the UE structure and to discriminate between models are the densities  $dN/d\eta d\phi$  of charged particle multiplicity and  $dp_T^{sum}/d\eta d\phi$  of total charged particle transverse momentum  $p_T^{sum}$ , in charged particle jets. An original approach is proposed, by taking the ratio of these variables for different charged particle  $p_T$  thresholds.

At LHC start-up, the first  $\text{pb}^{-1}$  of collected data will be mainly intended to calibrate the analysis tools. Even with such a low integrated luminosity, it will be possible to perform a first measurement of the UE activity in charged jet events. With  $10 \text{ pb}^{-1}$  and a partially calibrated de-

tector, it will be possible to control systematic uncertainties on the UE observables, to keep them at the level of the statistical errors and to perform a first discrimination between UE models. Extending the statistics to  $100 \text{ pb}^{-1}$  and exploiting the uniform performance of track reconstruction for  $p_T > 1.5 \text{ GeV}/c$  and  $p_T > 0.9 \text{ GeV}/c$ , the ratio of observables will probe more subtle differences between models.

## References

- [1] T. Sjostrand and M. van Zijl, Phys. Lett. **B188**, 149 (1987).
- [2] T. Sjostrand *et al.*, JHEP **05**, 026 (2006). [hep-ph/0603175](#).
- [3] CDF Collaboration, F. Abe *et al.*, Phys. Rev. Lett. **67**, 2937 (1991).
- [4] CMS Collaboration, D. Acosta *et al.*, CERN CMS-NOTE-2006-067 (2006).
- [5] P. Skands and D. Wicke, Eur. Phys. J. **C52**, 133 (2007). [hep-ph/0703081](#).
- [6] G. Corcella *et al.*, JHEP **101**, 010 (2001). [hep-ph/0011363](#).
- [7] CDF Collaboration, A. Affolder *et al.*, Phys. Rev. **D65**, 092002 (2002).
- [8] CDF Collaboration, D. Acosta *et al.*, Phys. Rev. **D70**, 072002 (2004).
- [9] CMS Collaboration, R. Hollis *et al.*, Physics Analysis Summary **PAS**, QCD (2007).
- [10] CMS Collaboration, W. Adam *et al.*, CERN CMS-NOTE-2006-041 (2006).
- [11] CMS Collaboration, P. Vanlaer *et al.*, CERN CMS-NOTE-2006-029 (2006).
- [12] CMS Tracker Collaboration, CERN CMS-NOTE- in preparation.
- [13] CMS Collaboration, G. Bayatian *et al.*, J. Phys. **G34**, 995 (2007).

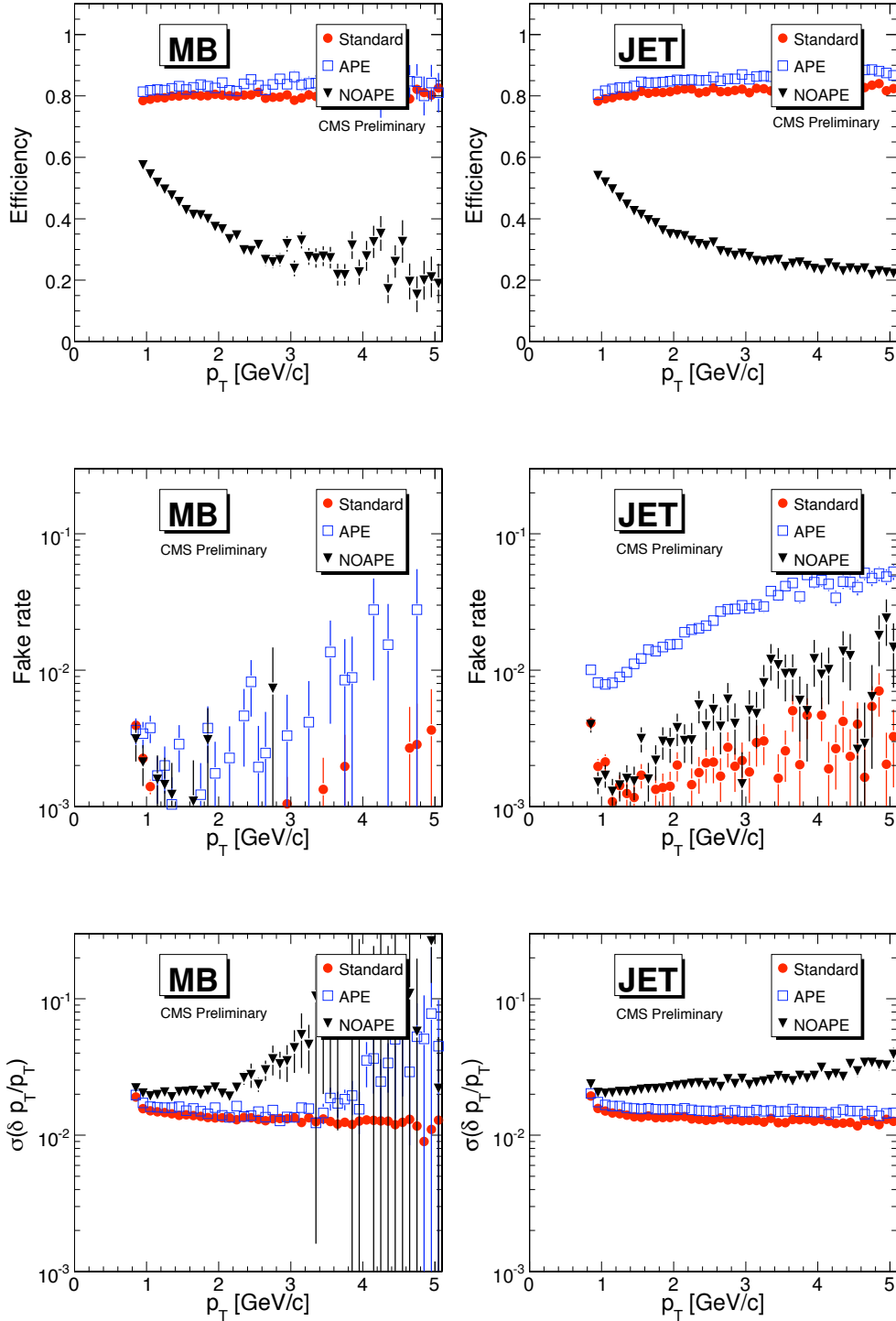


Fig. 4: Tracking performance for an ideal tracker (*circles*), for a misaligned tracker as expected at start-up (*triangles*) and for a misaligned tracker with use of the APE tool (*squares*), for charged particles with  $p_T > 0.9$  GeV/c from the MB (*left*) and JET (*right*) samples: track reconstruction efficiency, fake track rate and relative  $p_T$  resolution, as a

# Double-Parton-Scattering in Photon-Three-Jet Final States at the LHC

Florian Bechtel  
Hamburg University

## Abstract

The possible detection of double-parton-scattering in final states with one photon and three jets at the LHC is discussed. We study suitable variables to discriminate double-parton-scattering from shower contributions. Predictions of two event generators with different multiple interaction models are compared.

## 1 Direct Observation of Multiple Parton Interactions

There are good reasons to expect that multiple parton-parton scatterings will occur in most  $pp$  collisions at the LHC. For one, including multiple interactions in event generators greatly improves the description of the *underlying event* at the Tevatron. But hadronic event generators have many ingredients, making it difficult to conclude unambiguously the observation of multiple scattering.

Instead, a direct observation of multiple interactions involving final states accessible to a perturbative treatment would rule out other interpretations of the underlying event data. Four high- $p_T$  jets from two independent scatters in the same  $pp$  or  $p\bar{p}$  collision (*double-parton-scattering*, *DPS*) is the most prominent process. A four-jet-signature with two pairs of jets where the members of each pair have equal and opposite transverse momentum has been searched for by the AFS experiment [1] at CERN ISR, by the UA2 experiment [2] at CERN SppS and most recently by the CDF experiment [3] at the Tevatron.

Despite the large jet cross sections, the above searches had to face significant backgrounds as there are three possible ways to group four jets into two pairs. On top, the jet energy measurement is best at large energies where the cross section for double-parton scattering is small. Lowering the jet  $E_T$  threshold complicates the identification of an  $E_T$ -balanced pair as the measured jet  $E_T$ 's deviate from their true value.

In a new approach to detect DPS, the CDF experiment studied final states with one photon and three jets [4] looking for pairwise balanced photon-jet and dijet combinations. The data sample was selected with CDF's inclusive photon trigger, hence allowing to search for jets down to low energies. Measuring the photon's transverse energy more precise than the jet's transverse energy helps to identify an  $E_T$ -balanced pair.

## 2 Simulation of Double-Parton-Scattering

We present generator-level studies with version 8.108 of the PYTHIA [5] event generator program and with version 2.2.0 of the HERWIG++ [6] program. Both event generators model the underlying event including additional interactions, which are described in the context of perturbative QCD [7, 8].

Photon	$E_T(\gamma) \geq 20 \text{ GeV}$ $ \eta(\gamma)  \leq 2.5$
Jets	$E_T(\text{jet}) \geq 20 \text{ GeV}$ $E_T(\text{jet } 2)/E_T(\text{jet } 1) < 0.8$ $ \eta(\text{jet})  \leq 5$ $\Delta R(\gamma, \text{jet}) \geq 0.2$
Missing normalized $p_T$	$ \sum_i \vec{p}_{Ti}  / \sum_i  \vec{p}_{Ti}  \leq 0.1, i \in \{\gamma, 1, 2, 3\}$

Table 1: Kinematic selection of photon-three-jet combinations.

We compare PYTHIA default, shower-only, multiple-interactions-only and HERWIG++ default. Prompt-photon events were simulated in 5 GeV-bins of  $\hat{p}_T$  for PYTHIA,  $E_T(\gamma)$  for HERWIG++, of 100000 events each starting at  $\hat{p}_T = 10 \text{ GeV/c}$  and going up to  $100 \text{ GeV/c}$ . Additional jets come from multiple interactions or from parton showers. The respective samples were normalized to the total prompt photon production cross section. Note that this will give unphysical normalizations for the PYTHIA settings with one or several options switched off, but helps to identify phase space regions with enhanced contributions from multiple interactions.

### 3 Event Selection and Background Discrimination

A longitudinally invariant  $k_T$ -jet algorithm [9] with  $R = 0.4$  was run after the hadronization step on all stable particles, except neutrinos. Kinematic selections on photon and jets are summarized in Table 1.

The polar acceptances of the CMS electromagnetic and hadronic calorimeter are reflected in pseudorapidity cuts of  $|\eta(\gamma)| \leq 2.5$  and  $|\eta(\text{jet})| \leq 5$ , respectively. Photons and jets are required to have transverse energies above 20 GeV, corresponding to the reconstruction threshold [10]. Fig. 1 illustrates the three-jet thresholds for the various generator settings: The minimal jet transverse momentum is shown for the softest jet in the photon-three-jet-system. Jets from multiple interactions are softer in  $p_T$  than jets from initial state radiation: A balance has to be found between selecting a jet  $p_T$  threshold where jet reconstruction is of sufficient quality and a  $p_T$  threshold that still allows multiple interactions to contribute significantly to the final state. PYTHIA predicts more photon-three-jet combinations with one jet having a transverse momentum smaller than 25 GeV/c while at large transverse momenta, HERWIG++ and PYTHIA agree (Fig. 1 right).

In double-parton-scattering events, both scatterings are supposed to be uncorrelated in scale and direction. To test this assumption, AFS and CDF investigated azimuthal correlations between pairs (Fig. 2). Both chose to study the azimuthal difference between  $p_T$ -vectors representing each of the pairs. AFS constructed said  $p_T$ -vector from the vector difference between the two objects (upper), while CDF constructed the pair's  $p_T$  from the vector sum (lower). As the pair  $p_T$  must not be zero in order to compare its direction to the other pair's  $p_T$ , both methods fail for specific configurations: The AFS method fails for objects going in the same direction, while the CDF method fails for perfectly balanced objects. Both event generators predict similar shapes for the selected phase space, but PYTHIA's total cross section prediction is larger than HERWIG++'s, corresponding to a prediction of more photon-three-jet topologies in the detector

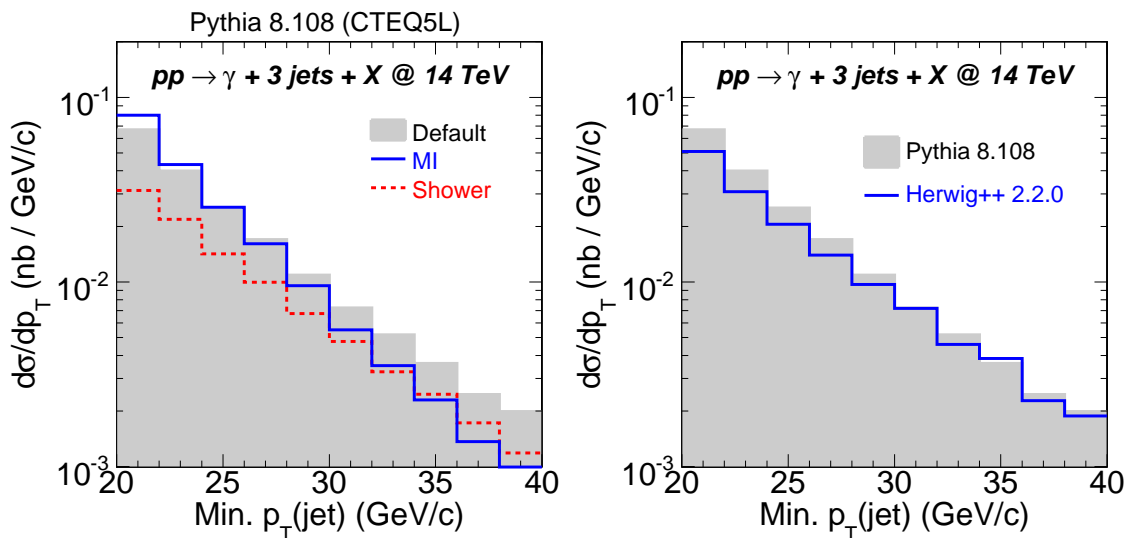


Fig. 1: Minimal jet  $p_T$  in photon-three-jet combinations. Comparison between three PYTHIA and default HERWIG prediction.

acceptance.

#### 4 Conclusions

We studied predictions of two event generators for the production of prompt photons accompanied by three jets at the LHC. This final state is sensitive to detecting multiple interactions in double-parton-scattering events.

Detecting double-parton-scattering in photon-three-jet final states requires jet reconstruction in a region of phase space where multiple interactions contribute significantly to the photon-three-jet cross section, i. e. at small transverse energies. A promising approach might be the reconstruction of jets from tracks which have been demonstrated to give a reasonable response down to small transverse energies [11]. It will also be beneficial to reconsider double-parton-scattering processes in clean final states, such as double-Drell-Yan production of four muons.

#### Acknowledgements

The author acknowledges financial support by the Marie Curie Fellowship program for Early Stage Research Training, by MCnet (contract number MRTN-CT-2006-035606) and by the German Federal Ministry of Education and Research (BMBF).

#### References

- [1] Akesson, T. and others, Z. Phys. **C34**, 163 (1987).
- [2] Alitti, J. and others, Phys. Lett. **B268**, 145 (1991).



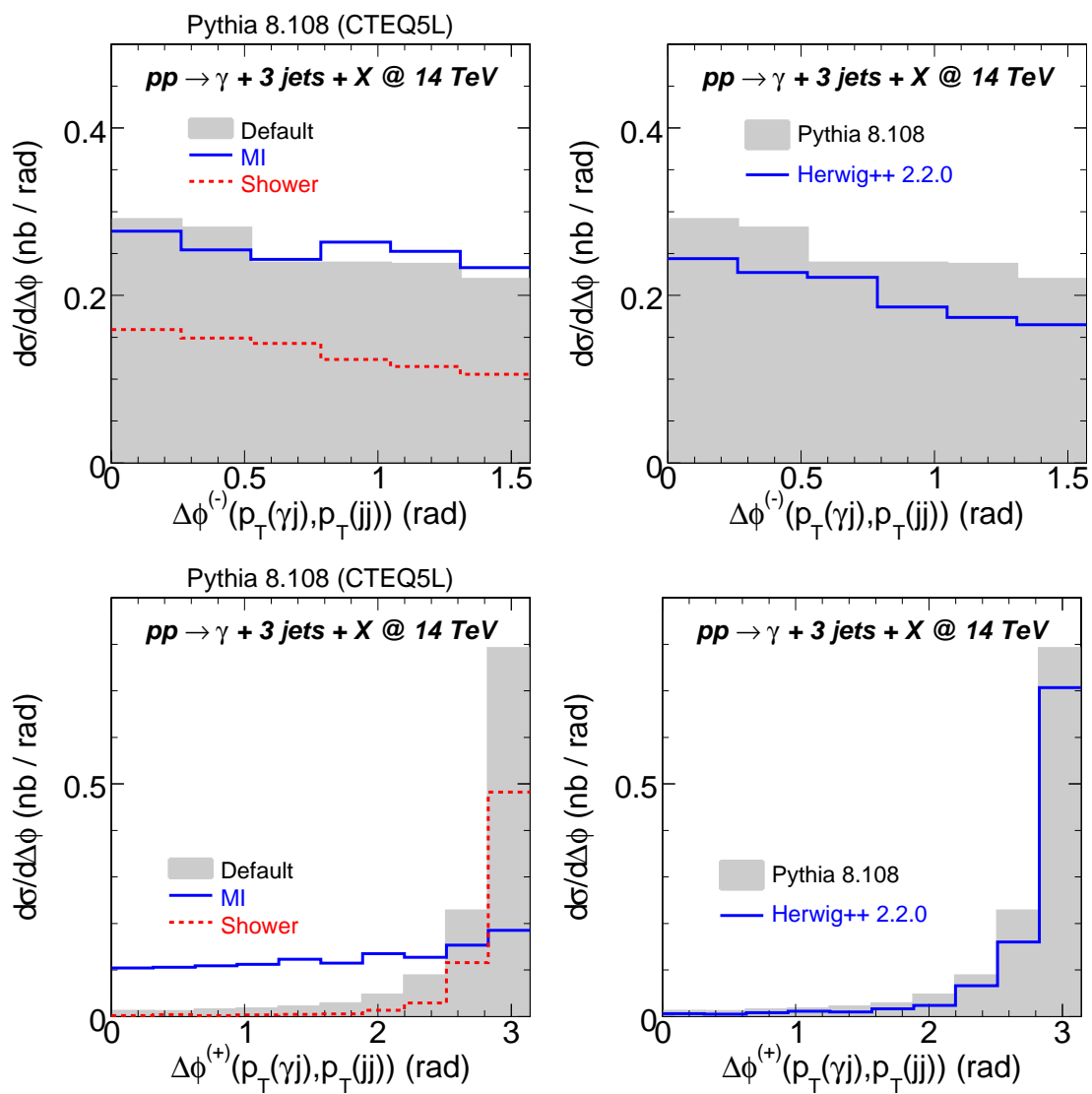


Fig. 2: Event shape variables for the photon-three-jet system.

- [3] Abe, F. and others, Phys. Rev. **D47**, 4857 (1993).
- [4] Abe, F. and others, Phys. Rev. **D56**, 3811 (1997).
- [5] Sjostrand, Torbjorn and Mrenna, Stephen and Skands, Peter, JHEP **05**, 026 (2006);  
Sjostrand, Torbjorn and Mrenna, Stephen and Skands, Peter, Comput. Phys. Commun. **178**, 852 (2008).
- [6] Bahr, M. and others (2008).
- [7] Sjostrand, Torbjorn and van Zijl, Maria, Phys. Lett. **B188**, 149 (1987);  
Sjostrand, T. and Skands, P. Z., JHEP **03**, 053 (2004);  
Sjostrand, T. and Skands, P. Z., Eur. Phys. J. **C39**, 129 (2005).
- [8] Bahr, Manuel and Gieseke, Stefan and Seymour, Michael H., JHEP **07**, 076 (2008).
- [9] Catani, S. and Dokshitzer, Yuri L. and Seymour, M. H. and Webber, B. R., Nucl. Phys. **B406**, 187 (1993);  
Ellis, Stephen D. and Soper, Davison E., Phys. Rev. **D48**, 3160 (1993).
- [10] Bayatian, G. L. and others. CERN-LHCC-2006-001.
- [11] Bayatian, G. L. and others, J. Phys. **G34**, 995 (2007).

# Underlying Event Studies with CASTOR in the CMS Experiment

Zuzana Ruriková<sup>a</sup>, Armen Bunyatyan<sup>b</sup>

<sup>a</sup> DESY, Hamburg

<sup>b</sup> MPI-K, Heidelberg and YerPhI, Yerevan

Multi-parton interactions (MI) play a significant role in soft and high  $p_T$  processes. Especially in case of LHC where the proton beams collide at very large energies, the understanding of MI is becoming crucial for the high precision measurements. Up to now various Monte Carlo (MC) models have been tuned to describe the Tevatron data [1], exploiting mainly the charged particle multiplicities and particle energy flows in the central  $\eta$  region. In the near future the full angular coverage of the CMS detector from the central to the most forward region ( $0 < \eta < 6.6$ ) will allow to study MI over a large rapidity range, which was not possible before.

Since the multi-parton interactions occur between the remnant partons of the colliding particles, the energy flow in the very forward region covered by the CASTOR calorimeter [2] ( $5.2 < \eta < 6.6$ ) is expected to be strongly affected and hence ideal for the MI model tuning. In addition one can study the long range correlations (correlation between activity in central and forward region) which were observed already at HERA and UA5 [3].

Results shown here are based on a generator level analysis of inclusive QCD processes<sup>1</sup> with PYTHIA MC 6.4.14, using several widely used MI tunes, such as Rick Field's tune A, Sandhoff-Skands tune S0 and also extreme scenario with MI being switched off.

In order to study the long range correlations the triggering on energy deposit in CASTOR  $\eta$  region is performed. Four energy ranges in the CASTOR ( $E_{\text{CAST}}$ ) are investigated. For each  $E_{\text{CAST}}$  bin the charged particle multiplicities as well as particle energy flow in central rapidity region are investigated (see figure 1). In order to mimic the detection threshold effects a minimum energy cut of 1 GeV is applied to all stable generated particles.

One can see that in case without MI no long range correlations are observed, i.e. charge particle multiplicities look the same for all  $E_{\text{CAST}}$  energy bins, as one would expect. On the other hand, when MI are included there is a clear correlation, larger energies in CASTOR region imply higher charged particle multiplicities and particle energy flow in the central region. Furthermore triggering on CASTOR enhances the differences between various MI tunes, and thus may contribute to better understanding of multi-parton interaction picture.

Study of multi-parton interactions within the hard processes, such as top production, is becoming extremely interesting since they are one of the major items of the LHC physics program. Therefore charged particle multiplicities (Fig.2 - upper plots) and particle energy flow observables were studied for the top processes<sup>2</sup> and were compared with the distributions for inclusive QCD processes (Fig.1). No selection cuts for top-quark reconstruction were applied. Besides much higher charged particle multiplicities and energy flow in central rapidity region in case of top production, which is due to the presence of hard scale, there is clearly more underlying event activity than in QCD processes. This can be easily seen for example by comparing the MC pre-

---

<sup>1</sup>PYTHIA parameters: MSEL= 1 (hard QCD processes), CKIN(3) = 5GeV (min.  $\hat{p}_\perp$  for hard process).

<sup>2</sup>PYTHIA parameters: MSEL= 6 ( $t\bar{t}$  production).

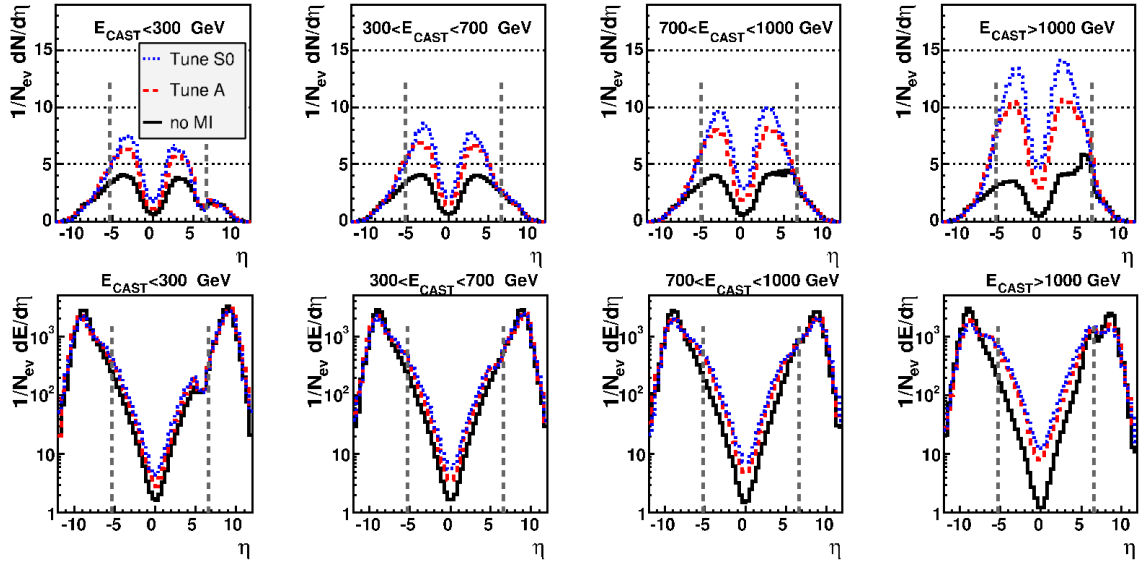


Fig. 1: Charged particle multiplicities (upper plots) and particle energy flow (lower plots) as function of  $\eta$  for four different CASTOR energy bins. Shown is PYTHIA MC prediction for inclusive QCD processes. The dashed vertical lines indicate the acceptance of the CMS detector.

diction with and without MI for inclusive QCD processes and for top processes separately. The differences amount to 2-5 particles per rapidity bin (Fig.2 - middle plots).

This suggests that a naive approach of subtracting underlying event contribution as determined for inclusive QCD processes from the top events would not work. As already seen from CDF measurements [1] the underlying event depends strongly on the collision centrality. The harder the collision is, the more underlying event activity one expects to see. This feature is also implemented into PYTHIA MC which is used in this analysis. After demanding a hard scale for inclusive QCD events in form of  $E_T^{\text{jet}} > 40$  GeV the differences between underlying event in QCD and in top events do almost disappear (Fig.2 - bottom plots).

Understanding of underlying event is essential also for all kind of measurements which involve high  $E_T$  jets in the final state. As the hadronic jets are the direct products of the parton hadronisation, the jet measurements give a look inside the dynamics of hard interaction. However, the underlying event produces additional energy in the available phase space which is largely uncorrelated with the partons originating from the hard interaction. This additional 'pedestal' energy is added by the jet reconstruction algorithms to the 'true' jet energy, thus spoiling the relation of the 'jets to the partons. However, as shown below, it is possible to estimate the 'pedestal' energy from the measurements in the forward calorimeters and subtract it from the reconstructed jet energy.

The analysis is done using the PYTHIA simulation using the different options for multi-parton interactions as well as without multi-parton interactions. Events are selected in which the jets are reconstructed by the inclusive  $k_\perp$  algorithm with transverse energies above 10 GeV and the jet axis at the central pseudorapidities ( $-3 < \eta^{\text{jet}} < 3$ ). Figure 3 shows the transverse energy

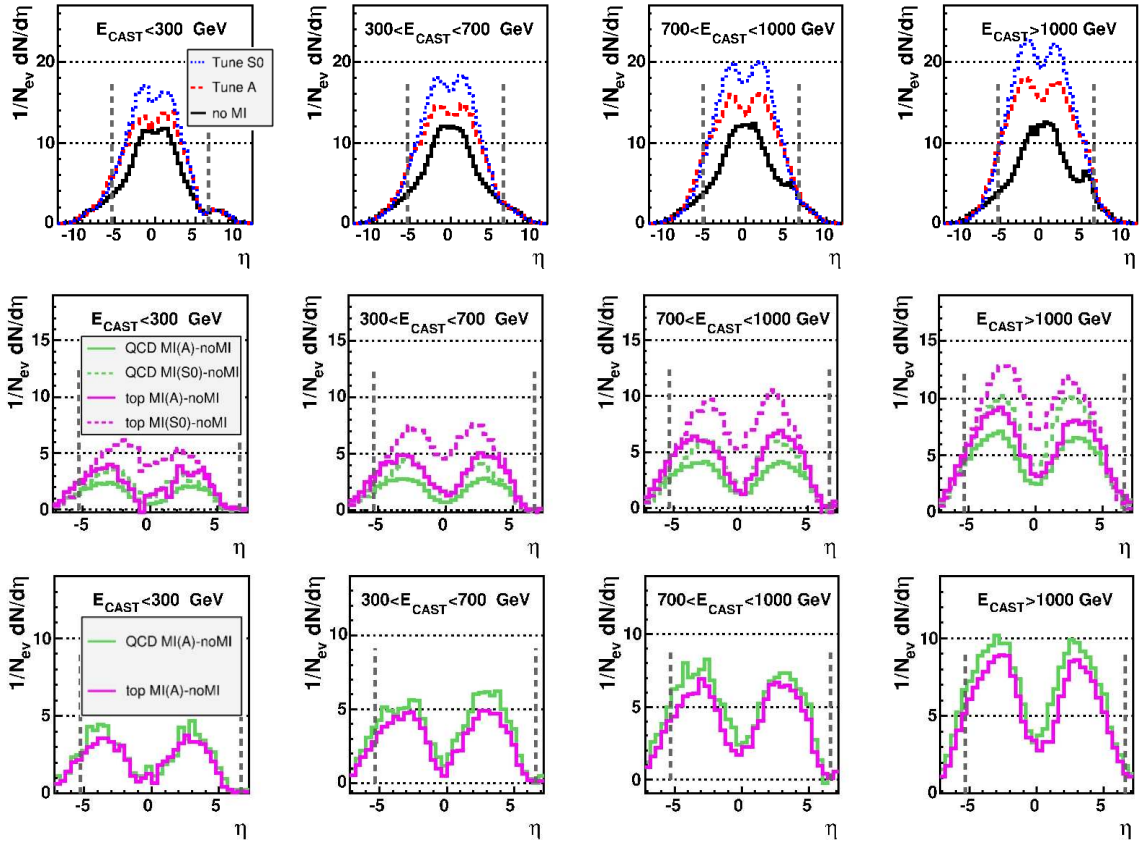


Fig. 2: Upper plots: charged particle multiplicities as a function of  $\eta$  for four different CASTOR energy bins. Shown is PYTHIA MC prediction for top processes. Middle plots: the charged particle multiplicities due to underlying event activity (MC with MI - MC without MI) as a function of  $\eta$  in top as well as inclusive QCD processes. Bottom plots: the charged particle multiplicities due to underlying event activity as a function of  $\eta$  in top and in inclusive QCD processes after demanding a presence of a hard jet  $E_T^{\text{jet}} > 40$  GeV in the central rapidity region  $|\eta| < 2.5$ . The dashed vertical lines indicate the acceptance of the CMS detector.

flow around the jet as a function of pseudorapidity. The different lines correspond to the different ranges of jet pseudorapidities ( $[-3, -2.5]$ ,  $[-1.5, -1]$ ,  $[0, 0.5]$ ,  $[1, 1.5]$ ,  $[2, 2.5]$ ), and two different jet transverse energy ranges ( $[10-20$  GeV],  $[20-30$  GeV]). Only transverse energies within one radian in azimuth of the jet are included. The left plot corresponds to the simulation without multi-parton interaction and the right plot for simulation with multi-parton interaction. The plots clearly show the effect of the underlying event pedestal when the multi-parton interactions are simulated. It is also observed that the level of pedestal doesn't depend on the jet pseudorapidity, but it gets higher for higher jet energies, i.e. it depends on the hardness of the interaction.

The idea of the method to determine and subtract the pedestal energy within the jet is demonstrated in the Fig.4. In the left upper figure the jet profile as a function of pseudorapidity is shown for the PYTHIA simulation which includes multi-parton interaction. For this figure the events are used which contain a jet with transverse energy above 10 GeV in the pseudorapidity

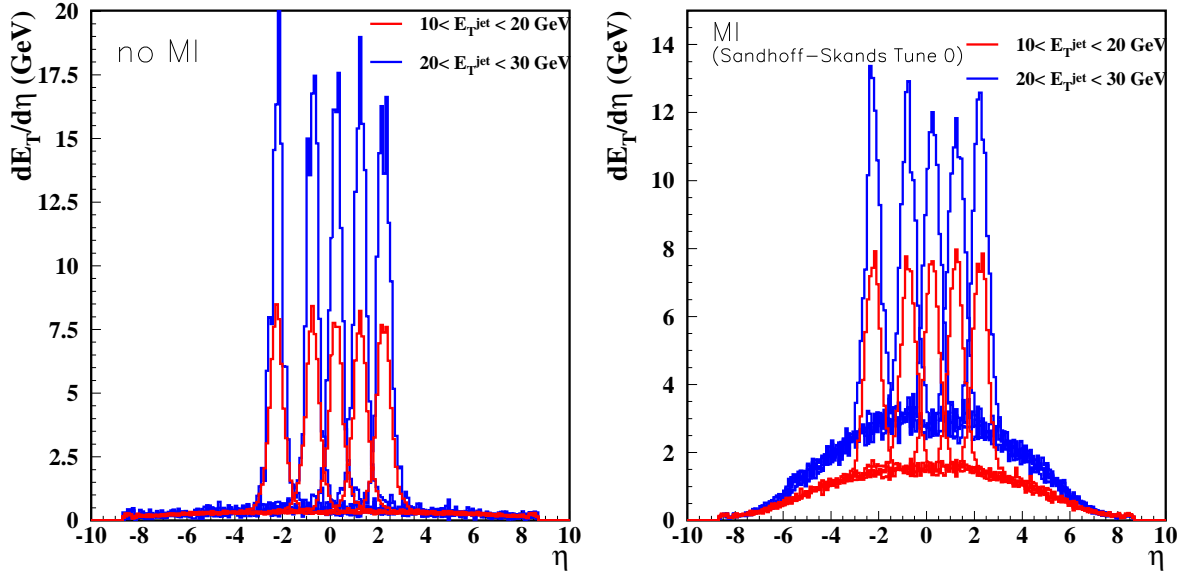


Fig. 3: The transverse energy distributions around the jets (jet profile) as a function of pseudorapidity. The left plot is obtained from the PYTHIA simulation without multi-parton interactions, while the right plot is for PYTHIA with multi-parton interactions. The different lines represent the different pseudorapidity ranges of the jets ( $[-3, -2.5]$ ,  $[-1.5, -1]$ ,  $[0, 0.5]$ ,  $[1, 1.5]$ ,  $[2, 2.5]$ ) and the different transverse energy ranges of the jets ( $[10-20 \text{ GeV}]$ ,  $[20-30 \text{ GeV}]$ ).

range  $0 < \eta^{\text{jet}} < 0.5$ . The transverse energy measured in the acceptance range of the CASTOR calorimeter ( $5.2 < \eta < 6.6$ ) is also shown by the red hatched area. The blue hatched area below the jet cone is the contribution of pedestal to the jet energy measurement determined with the method described here.

As the underlying event pedestal seem to be independent on the position of the jet in the central detector, we may attempt to describe the pedestal by a simple function. The possible function can be

$$f(\eta) = \frac{A}{1 + B \cdot e^{|\eta|-4}} \quad (1)$$

This function depends on two free parameters  $A$  and  $B$  and seems to describe the pedestals for the different models of multi-parton interactions and for the different cuts on jet transverse energies and pseudorapidities. The two free parameters could be the measured energies in the forward calorimeters, like CASTOR, which are away from the central region and don't get contribution from the energy of hard interaction. The function doesn't contain direct dependence on the  $E_T$  of the jet, because there are strong correlations of  $E_T^{\text{jet}}$  with the energy of pedestal and, correspondingly, with the energy in the forward calorimeters (see Fig.3). Therefore the  $E_T^{\text{jet}}$  dependence can be absorbed in the  $A$  and  $B$  parameters. In principle, the parameters  $A$  and  $B$  in eq.1 are strongly correlated, thus even the single energy measurement in the CASTOR can already provide the estimate of the pedestal under the jet. An example of the the fit of pedestal by this function is shown in Fig.4 (right) and the level of pedestal under the jet determined by

this method is shown in the Fig.4 (left) as a blue hatched histogram. As is seen, this approach gives reasonable result and can be developed further and used in analyses.

It should be noted, that presented studies have been done using the Lund fragmentation mechanism in PYTHIA. In principle, using another Monte Carlo or fragmentation models (CASCADE, ARIADNE, etc.) may lead to the different energy distribution of the underlying event. This may require the optimisation of the function of eq.1. The reliability of this method can be also improved by using an additional measurements of forward energy (in addition to the CASTOR), for example from the HF calorimeter.

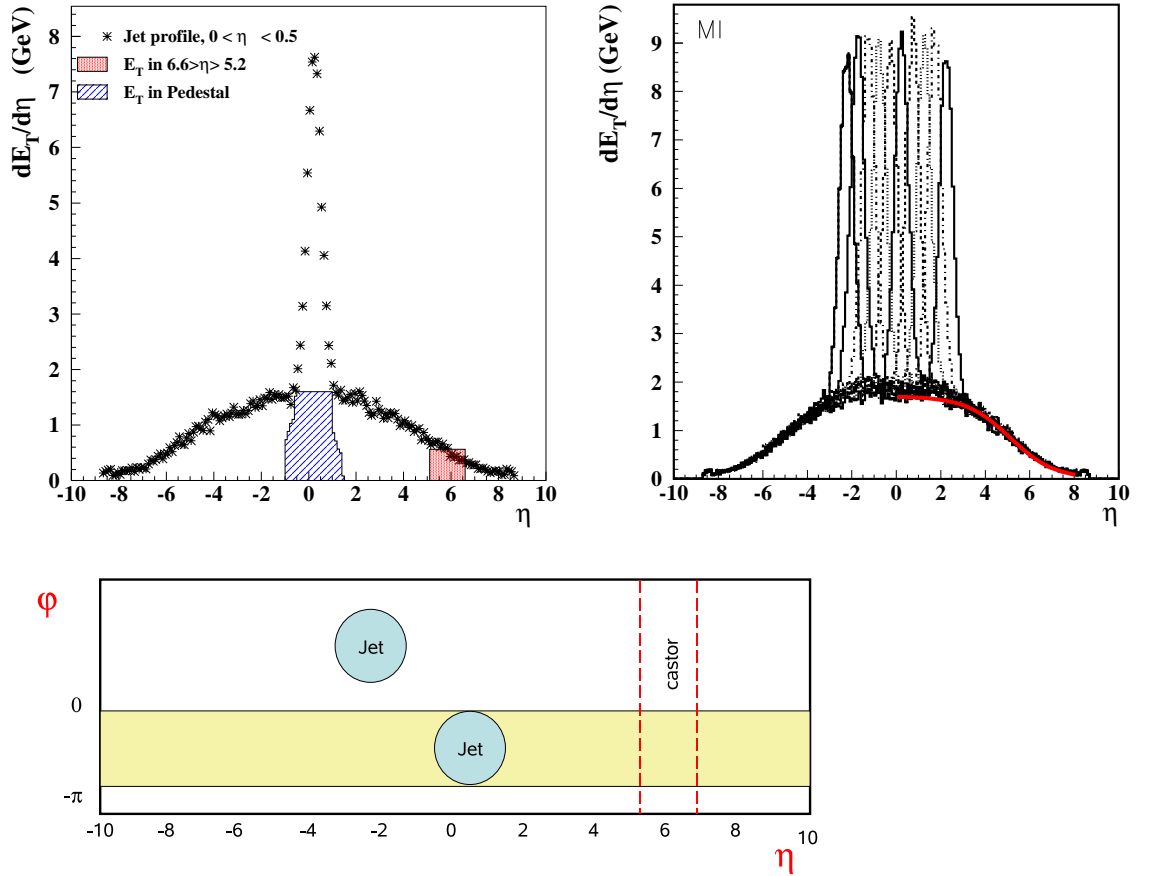


Fig. 4: (left) The transverse energy distributions around the jets (jet profile) as a function of pseudorapidity for the jets with  $0 < \eta^{\text{jet}} < 0.5$  and  $10 < E_T^{\text{jet}} < 20$  GeV. The red hatched histogram is the level of transverse energy in the pseudorapidity range of the CASTOR ( $5.2 < \eta < 6.6$ ). The blue hatched histogram below the jet area is the pedestal level determined from the method described in this report. (right) The jet profile as a function of pseudorapidity for jets with  $10 < E_T^{\text{jet}} < 20$  GeV. The different lines correspond to the different ranges of the jet pseudorapidity. The solid line on the right tail of distribution shows the result of the fit of pedestal by a function of eq.1.

In conclusion, the studies presented here show that the forward region is very sensitive to the multi-parton interactions. The measurements in the forward calorimeters, such as CASTOR,

can be used to discriminate between the various MI models and to improve the jet reconstruction in the central region. Nevertheless further studies with detailed simulation of detector response are essential. Simple smearing of particle energies in  $\eta$  CASTOR region according to the resolution as measured in test beam 2007 has already been tried, and leads to similar results.

## References

- [1] [CDF Collaboration], Phys. Rev. D **70** (2004) 072002.
- [2] CASTOR web page, [http : //cmsdoc.cern.ch/castor](http://cmsdoc.cern.ch/castor).
- [3] T. Sjostrand and M. van Zijl, *A multiple-interaction model for the event structure in hadron collisions*, Phys. Rev. D **36** (1987) 2019-2041.



# Direct photon production at HERA, the Tevatron and the LHC

R. E. Blair <sup>a</sup>, S. Chekanov <sup>a</sup>, G. Heinrich <sup>b</sup>, A. Lipatov <sup>c</sup> and N. Zotov <sup>c</sup>

<sup>a</sup> HEP Division, Argonne National Laboratory, 9700 S.Cass Avenue, Argonne, IL 60439, USA

<sup>b</sup> Institute for Particle Physics Phenomenology, Department of Physics,  
University of Durham, Durham, DH1 3LE, UK

<sup>c</sup> SINP, Moscow State University, 119991 Moscow, Russia

## Abstract

We review several most recent prompt-photon measurements at HERA and the Tevatron and discuss their implication for future measurements at the LHC. A comparison to Monte Carlo models, as well as to NLO QCD predictions based on the standard DGLAP and the  $k_T$ -factorization approaches is discussed. Effects from renormalization and factorization scale uncertainties, as well as uncertainties on the gluon density distribution inside a proton are discussed.

## 1 Introduction

Events with an isolated photon are an important tool to study hard interaction processes since such photons emerge without the hadronization phase. In particular, final states of  $ep$  and  $pp$  collisions with a prompt photon together with a jet are more directly sensitive to the underlying QCD process than inclusive prompt photon measurements.

The results on prompt-photon production provided by HERA are important for the interpretation of the LHC data. Unlike  $pp$  collisions,  $ep$  collisions involve a point-like incoming lepton, which leads to some simplification in the description of the prompt-photon production in  $ep$  compared to  $pp$ . At HERA, the quark content of the proton is probed through the elastic scattering of a photon by a quark,  $\gamma q \rightarrow \gamma q$  (see Fig. 1). Such QED events are significantly simpler than lowest-order compton-like  $qg \rightarrow q\gamma$  events which are dominant in  $pp$  collisions (see Fig. 2, left figure). The latter process has direct sensitivity to the strong coupling constant and requires much better understanding of the gluon structure function inside both incoming protons than for the lowest-order diagram in  $ep$  collisions.

Despite the difference between  $ep$  and  $pp$  collisions concerning certain lowest-order diagrams, a large class of partonic contributions are similar between  $ep$  and  $pp$  collisions, due to the hadronic nature of the resolved photon. In particular, a contribution to prompt-photon events from the  $gq \rightarrow q\gamma$  process in photoproduction, in which the photon displays its hadronic structure [1–4], leads to significant

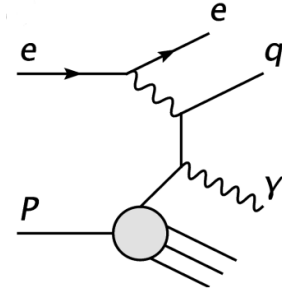


Fig. 1: Lowest-order diagram (Compton scattering) for  $\gamma$ +jet events in  $ep$  collisions

sensitivity to the gluon structure function as is the case in  $pp$  collisions (see Fig. 2, the two figures on the right). Therefore, analysis of HERA data can make a bridge between a better understood  $ep$  case and the less understood  $pp$  case, since apart from the convolution with different structure functions, photoproduction diagrams  $ep$  collisions involving a resolved photon are essentially the same as diagrams in  $pp$  collisions.

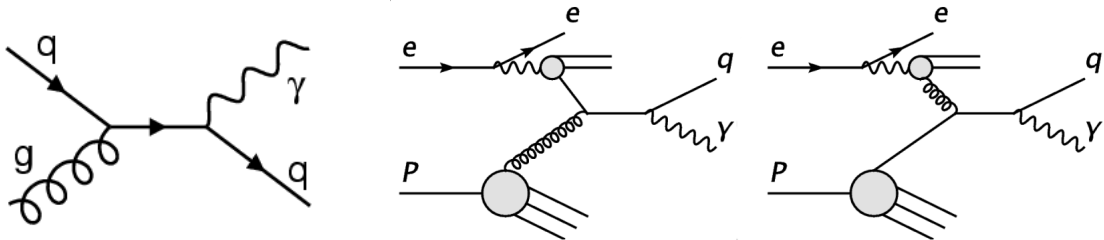


Fig. 2: The dominant diagram for prompt-photon events in  $pp$  collisions (left figure) compared to two resolved photon diagrams in  $ep$  photoproduction (see Section 2 for more details).

Prompt-photon events in  $ep$  collisions can constrain both quark and gluon parton densities (PDFs). In addition, differences between collinear factorization and  $k_T$  factorization in the description of the underlying hard subprocesses can be studied in detail. This is important not only for a better understanding of QCD dynamics, but also has direct implications for searches of exotic physics at the LHC, in which prompt-photon production is the main background. A number of QCD predictions [2–6] can be confronted with the data and some of them will be described in more detail below.

## 2 Photoproduction of prompt photons at NLO

In the photoproduction  $ep$  scattering processes, the electron is scattered at small angles, emitting a quasi-real photon which scatters with the proton. The spectrum of these photons can be described by the Weizsäcker-Williams approximation [7]. The photons will take part in the hard interaction either directly, or through their “partonic” content, in which case a parton stemming from the *resolved* photon participates in the hard subprocess. Similarly, a photon in the final state can either originate directly from the hard interaction or from the fragmentation of a parton. Therefore, one can distinguish four categories of subprocesses: 1) direct direct, 2) direct fragmentation, 3) resolved direct and 4) resolved fragmentation. Examples of leading order diagrams of each class are shown in Fig. 3. Beyond leading order, this distinction becomes ambiguous. For example, the NLO corrections to the direct part involve final state collinear quark-photon pairs which lead to divergences which are absorbed into the fragmentation function, such that only the sum of these contributions has a physical meaning. The complete NLO corrections to all four parts have been calculated in [4] for inclusive prompt photons and in [8] for photon plus jet final states. A public program EPHOX, written as a partonic event generator, is available from [9]. The NLO corrections to the direct-direct part also have been calculated in [3, 10] for the inclusive and photon plus jet final state.

The  $\gamma$ - $p$  scattering processes are of special interest since they are sensitive to both the partonic structure of the photon as well as of the proton. They offer the possibility to constrain

the (presently poorly known) gluon distributions in the photon, since in a certain kinematic region the subprocess  $qg \rightarrow \gamma q$ , where the gluon is stemming from a resolved photon, dominates [5].

Working within the framework of collinear factorization, i.e. assuming that the transverse momenta of the partons within the proton can be neglected and other non-perturbative effects can be factorized from the hard interaction at high momentum transfers, the cross section for  $ep \rightarrow \gamma X$  can symbolically be written as a convolution of the parton densities for the incident particles (respectively fragmentation function for an outgoing parton fragmenting into a photon) with the partonic cross section  $\hat{\sigma}$ :

$$d\sigma^{ep \rightarrow \gamma X}(P_p, P_e, P_\gamma) = \sum_{a,b,c} \int dx_e \int dx_p \int dz F_{a/e}(x_e, M) F_{b/p}(x_p, M_p) D_{\gamma/c}(z, M_F) d\hat{\sigma}^{ab \rightarrow cX}(x_p P_p, x_e P_e, P_\gamma/z, \mu, M, M_p, M_F), \quad (1)$$

where  $M, M_p$  are the initial state factorization scales,  $M_F$  the final state factorization scale,  $\mu$  the renormalization scale and  $a, b, c$  run over parton types. In the NLO calculations shown in Fig. 4, all these scales are set equal to  $p_T$  and varied simultaneously. The functions  $F_{b/p}(x_p, M_p)$  are the parton distribution functions in the proton, obeying DGLAP evolution. Note that including initial state radiation at NLO in the partonic calculation means that the partons taking part in the hard interaction can pick up a nonzero transverse momentum. In certain cases, this additional “ $k_T$ -kick” seems to be sufficient to describe the data well. For example, a study of the effective transverse momentum  $\langle k_T \rangle$  of partons in the proton has been made by ZEUS [11]. Comparing the shapes of normalized distributions for  $\langle k_T \rangle$ -sensitive observables to an NLO calculation, it was found that the data agree well with NLO QCD without extra intrinsic  $\langle k_T \rangle$  [8].

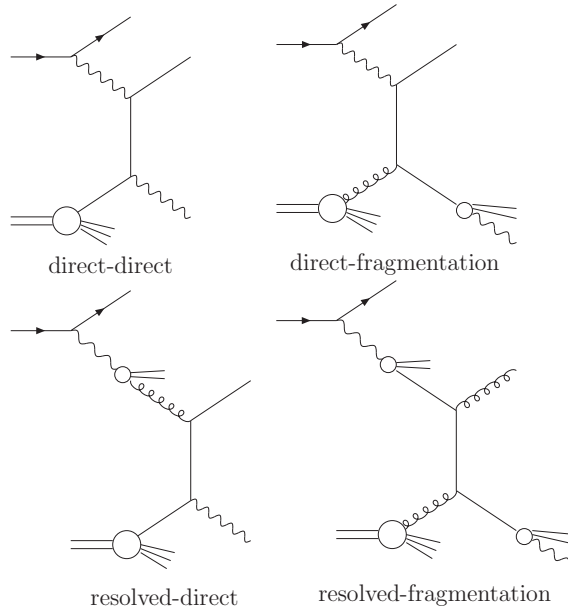


Fig. 3: Examples of contributing subprocesses at leading order to each of the four categories in  $ep$  collisions.

The “resolved” contributions are characterized by a resolved photon in the initial state where a parton stemming from the photon instead of the photon itself participates in the hard subprocess. In these cases,  $F_{a/e}(x_e, M)$  is given by a convolution of the Weizsäcker-Williams spectrum  $f_\gamma^e(y)$  with the parton distributions in the photon:

$$F_{a/e}(x_e, M) = \int_0^1 dy dx_\gamma f_\gamma^e(y) F_{a/\gamma}(x_\gamma, M) \delta(x_\gamma y - x_e). \quad (2)$$

The cases with “direct” attributed to the initial state photon correspond to  $a = \gamma$ , so  $F_{a/\gamma} = \delta(1 - x_\gamma)$  and  $F_{a/e}$  in eq. (2) collapses to the Weizsäcker-Williams spectrum. The cases “direct-direct” and “resolved-direct” correspond to  $c = \gamma$ , so  $D_{\gamma/c}(z, M_F) = \delta_{c\gamma} \delta(1 - z)$  in (1), i.e. the prompt photon is produced directly in the hard subprocess and not from the fragmentation of a hard parton.

If additional jets are measured, eq. (1) also contains a jet function, which defines the clustering of the final state partons other than the photon into jets. Prompt photon production in association with a jet offers more possibilities to probe the underlying parton dynamics. It allows for the definition of observables that provide information about the longitudinal momentum fractions  $x^\gamma, x^p$  carried by the particles taking part in the hard interaction. The partonic  $x^\gamma, x^p$  are not observable, but one can define the observables

$$\begin{aligned} x_{obs}^\gamma &= \frac{p_T^\gamma e^{-\eta^\gamma} + p_T^{\text{jet}} e^{-\eta^{\text{jet}}}}{2E^\gamma}, \\ x_{obs}^p &= \frac{p_T^\gamma e^{\eta^\gamma} + p_T^{\text{jet}} e^{\eta^{\text{jet}}}}{2E^p}, \end{aligned} \quad (3)$$

which, for direct photons in the final state, coincide with the partonic  $x^\gamma, x^p$  at leading order. Unique to photoproduction processes is the possibility to “switch on/off” the resolved photon by suppressing/enhancing large  $x^\gamma$ . As  $x^\gamma = 1$  corresponds to direct photons in the initial state, one can obtain resolved photon enriched data samples by placing a cut  $x_{obs}^\gamma \leq 0.9$ . Another possibility to enhance or suppress the resolved photon component is to place cuts on  $p_T$  and rapidity. From eq. (3) one can easily see that  $x_{obs}^\gamma$  is small at low  $p_T^{\text{jet}}$  values and large rapidities. Small  $x^\gamma$ -enriched data samples could be used to further constrain the parton distributions in the real photon, in particular the gluon distribution, as investigated e.g. in [5]. Similarly, one can suppress the contribution from the resolved photon to probe the proton at small  $x^p$  by direct  $\gamma$ - $p$  interactions [5].

In order to single out the prompt photon events from the background of secondary photons produced by the decays of light mesons, isolation cuts have to be imposed on the photon signals in the experiment. A widely used isolation criterion is the following: A photon is isolated if, inside a cone centered around the photon direction in the rapidity and azimuthal angle plane, the amount of hadronic transverse energy  $E_T^{\text{had}}$  deposited is smaller than some value  $E_{T,\text{max}}$ :

$$\text{for } \begin{aligned} (\eta - \eta_\gamma)^2 &+ (\phi - \phi_\gamma)^2 \leq R, \\ E_T^{\text{had}} &\leq E_{T,\text{max}}. \end{aligned} \quad (4)$$

HERA experiments mostly used  $E_{T,\text{max}} = \epsilon p_T^\gamma$  with  $\epsilon = 0.1$  and  $R = 1$ . Isolation not only reduces the background from secondary photons, but also substantially reduces the contribution

from the fragmentation of hard partons into high- $p_T$  photons. When comparing the result of partonic calculation to data, photon isolation is a delicate issue. For example, a part of the hadronic energy measured in the cone may come from the underlying event; therefore even the direct contribution can be cut by the isolation condition if the latter is too stringent.

### 3 $k_T$ -factorization approach

A complementary description is offered by the  $k_T$ -factorization approach [12], which relies on parton distribution functions where the  $k_T$ -dependence has not been integrated out.

In the framework of  $k_T$ -factorization approach the treatment of  $k_T$ -enhancement in the inclusive prompt photon suggests a possible modification of the above simple  $k_T$  smearing picture. In this approach the transverse momentum of incoming partons is generated in the course of non-collinear parton evolution under control of relevant evolution equations. In the papers [6, 13] the Kimber-Martin-Ryskin (KMR) formalism [14] was applied to study the role of the perturbative components of partonic  $k_T$  in describing of the observed  $E_T$  spectrum at HERA and Tevatron. The proper off-shell expressions for the matrix elements of the partonic subprocesses and the KMR-constructed unintegrated parton densities obtained independently were used in [13] to analyze the Tevatron data.

### 4 Comparison with HERA results

Recently published [15] ZEUS differential cross sections as functions of  $E_T$  and  $\eta$  for the prompt-photon candidates and for the accompanying jets have revealed some difference with both Monte Carlo predictions and the next-to-leading order (NLO) calculations based on the collinear factorization and the DGLAP formalism [3, 4], as shown in Fig. 4. The data are compared to QCD calculations performed by Krawczyk and Zembruski (KZ) [3], by Fontannaz, Guillet and Heinrich (FGH) [4], by A. Lipatov and N. Zotov (LZ) [6] and PYTHIA 6.4 [16] and HERWIG 6.5 [17] Monte Carlo models. The MC differential cross sections do not rise as steeply at low  $E_T^\gamma$  as do the data. It should be pointed out that no intrinsic transverse momentum of the initial-state partons in the proton was assumed for these calculations. The QCD calculation [6] based on the  $k_T$ -factorization [12] and the Kimber-Martin-Ryskin (KMR) prescription [14] for unintegrated quark and gluon densities, gives the best description of the  $E_T$  and  $\eta$  cross sections.

In the photon-rapidity distribution of Fig. 4, the data lying above the NLO theory prediction at low values of  $\eta^\gamma$  could be explained by the fact that in this region,  $x_{obs}^p$  is small, as can be seen from Eq. (3), and therefore  $k_T$ -effects may be important. On the other hand, this is not corroborated by the jet rapidity distribution, which has a problem at high  $\eta^{\text{jet}}$ , corresponding to small  $x_{obs}^\gamma$ . Indeed, a direct measurement [15] of  $x_{obs}^\gamma$  shows that the differences with NLO are mainly at low values of the  $x_{obs}^\gamma$  distribution. In this region, resolved photon events dominate, which may indicate that resolved photon remnants could have lead to an increase in the number of jets which have passed the experimental cuts, while these events are not accounted for in the partonic calculation.

The inclusive prompt photon data [18, 19] lie above the NLO theory prediction in the whole rapidity range, except for the bin of largest rapidity, where the agreement is good after hadronization corrections, see Fig. 5.

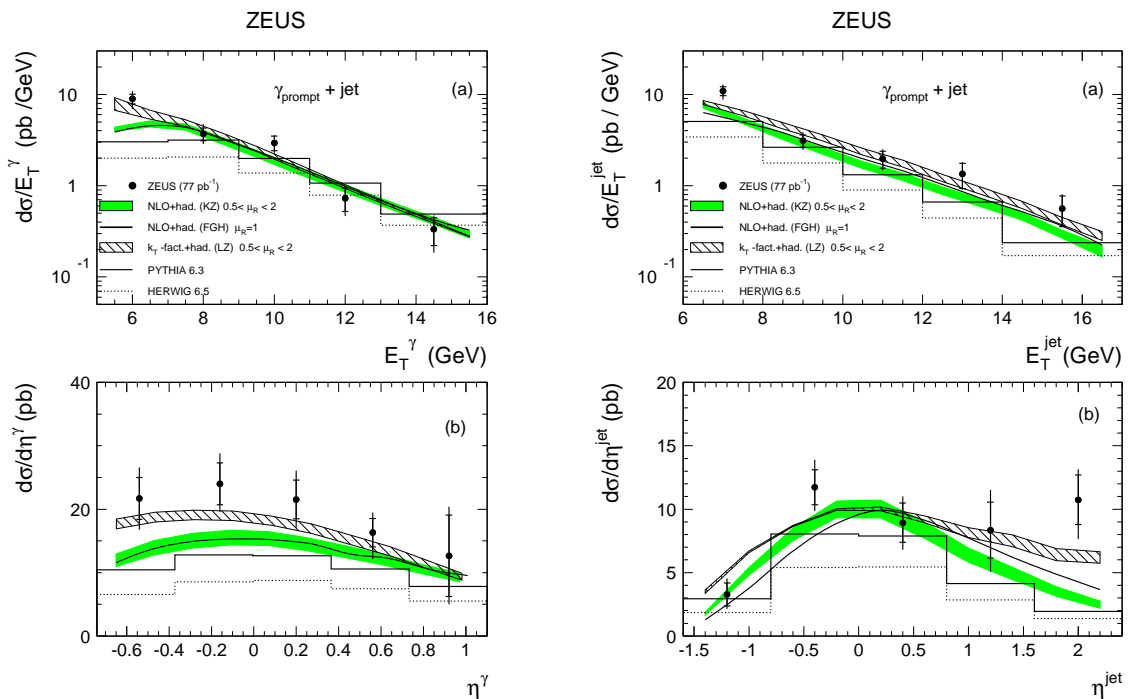


Fig. 4: The differential  $\gamma$ +jet cross sections as functions of  $E_T$  and  $\eta$  of the prompt photon and the jet. The data are compared to QCD calculations and Monte Carlo models as described in the text. The shaded bands correspond to a typical scale uncertainty which was obtained by changing the renormalization and factorization scales simultaneously by a factor of 0.5 and 2 respectively.

Interestingly, ZEUS investigated what happens if the minimum transverse energy of the prompt photon is increased to 7 GeV, and found that in this case, the NLO calculations are in good agreement [15], which suggests that non-perturbative effects may produce the discrepancy. See [20] and references therein for more details.

The H1 experimental data in photoproduction [18] are shown in Figs. 5 and 6. Both inclusive and  $\gamma$ +jet cross sections were compared to the FGH NLO calculations after hadronization corrections. The H1 data [18] referred to the kinematic region defined by  $5 < E_T^\gamma < 10$  GeV,  $-1 < \eta^\gamma < 0.9$  and  $0.2 < y < 0.7$ , which is rather similar to the ZEUS measurement shown in Fig. 4. Similar to the ZEUS case, MC predictions were found to underestimate the H1 cross sections, while NLO QCD gives a much better description. After taking into account hadronization and multiple interaction effects, NLO calculations predict somewhat smaller cross sections compared the measurements [18].

The H1 experimental data in photoproduction [18] were also compared to the  $k_T$ -factorization approach [6]. Comparison with the  $k_T$  factorization approach indicates somewhat better agreement, as shown in Fig. 7 (see [6] for details). One can see that the measured distributions are reasonably well described except the moderate  $E_T^\gamma$  region and in the pseudorapidity region

$-0.4 \leq \eta^\gamma \leq 0.9$  only. For  $-1 \leq \eta^\gamma \leq -0.4$  the  $k_T$ -factorization predictions are mostly below the experimental points. The discrepancy between data and theory at negative  $\eta^\gamma$  is found to be relatively strong at low values of the initial photon fractional momentum  $y$ . The effect of scale variations in transverse energy distributions is rather large: the relative difference between results for  $\mu = E_T^\gamma$  and results for  $\mu = E_T^\gamma/2$  or  $\mu = 2E_T^\gamma$  is about 15% within the  $k_T$ -factorization approach, which is due to missing higher order corrections. The scale dependence of the NLO QCD calculations in the collinear factorization approach is below the 10% level.

The individual contributions from the direct and resolved production mechanisms to the total cross section in the  $k_T$ -factorization approach is about 47% and 53%, respectively. The contributions of single resolved processes

$$q(k_1) + g(k_2) \rightarrow \gamma(p_\gamma) + q(p'),$$

$$g(k_1) + q(k_2) \rightarrow \gamma(p_\gamma) + q(p'),$$

$$q(k_1) + q(k_2) \rightarrow \gamma(p_\gamma) + g(p').$$

account for 80%, 14% and 6% respectively.

The transverse energy  $E_T^\gamma$  and pseudorapidity  $\eta^\gamma$  distributions for  $\gamma$ +jet events measured by H1 are compared to the  $k_T$ -factorization predictions in Fig. 8 (see also Ref. [6]). In contrast to the inclusive case, one can see that the  $k_T$ -factorization predictions are consistent with the data in most bins, although some discrepancies are present. The theoretical results are lower than the experimental data at negative  $\eta^\gamma$  and higher at positive  $\eta^\gamma$ . The scale variation as it was described above changes the estimated cross sections by about 10%. Note that such disagreement between predicted and measured cross sections has also been observed for the NLO QCD calculations in the collinear factorization approach, see Fig. 6.

Figure 9 shows the  $x_{obs}^\gamma$  and  $x_{obs}^p$  distributions (see Eq. 3) measured by H1. One can see that  $k_T$  factorization predictions reasonably well agree with the experimental data. The NLO calculations [3, 4] without corrections for hadronization and multiple interactions give similar results.

The H1 Collaboration [21] also has performed  $\gamma$ +jet measurements in DIS for  $Q^2 > 4 \text{ GeV}^2$ . The NLO calculations [22], which are only available for  $\gamma$ +jet final state, failed to describe normalization of the cross sections, although the agreement in shape was found to be reasonable (Fig. 10). No  $k_T$  factorization prediction available for DIS.

In summary, some differences with NLO QCD were observed in both photoproduction and DIS. Differences at low  $P_T^\gamma$  can be due to the treatment of the fragmentation contribution in NLO calculations. Further, it would be interesting to see the effect of calculations beyond NLO QCD. The approach based on the  $k_T$  factorization has better agreement with the data, but such calculations have larger theoretical uncertainties.

## 5 Comparison with Tevatron results

Isolated photons in  $p\bar{p}$  collisions at Tevatron have been measured recently by the CDF [23, 24] and D0 [25–28] Collaborations.

Measurements of  $p\bar{p} \rightarrow \gamma + \text{jet} + X$  for  $30 \text{ GeV} \leq p_T^\gamma \leq 300 \text{ GeV}$  have very recently been published by D0 [28]. The comparison to theory is done separately for different regions in rapidity of the photon and the jet. The NLO partonic Monte Carlo program JETPHOX [9, 29] was used to compare the data to theory at next-to-leading order. It was shown that the NLO calculations are not sufficient to describe the shape of  $P_T^\gamma$  distributions in different rapidity regions, as can be seen in Figure 11. At present, the comparison with the  $k_T$ -factorization prediction is in progress.

Differences with the collinear factorization approach have been seen previously as well. Both CDF [23] and D0 [26] cross sections were found to be above<sup>1</sup> NLO predictions at low  $P_T^\gamma$ . However, RHIC has also measured prompt photon production in  $pp$  collisions at  $\sqrt{s} = 200 \text{ GeV}$  and found good agreement with NLO theory in the collinear factorization approach [20, 30].

The same data were compared to the  $k_T$  factorization approach in [13]. Figures 12 and 13 show the CDF [23] and D0 [26] measurements for the  $d\sigma/dE_T^\gamma d\eta^\gamma$  cross sections calculated at  $\sqrt{s} = 630$  and  $1800 \text{ GeV}$  in central and forward kinematic regions together with the  $k_T$  factorization predictions. One can see that theoretical predictions agree with the experimental data within the scale uncertainties. However, the results of the calculation with the default scale tend to underestimate the data in the central kinematic region and agree with the D0 data in the forward  $\eta^\gamma$  region. The collinear NLO QCD calculations give a similar description of the data: generally there is a residual negative slope in the ratio of the data over the prediction as a function of  $E_T^\gamma$ . The scale dependence of the  $k_T$  factorization results is rather large (20 – 30%), due to the fact that these are leading order calculations.

The double differential cross sections  $d\sigma/dE_T^\gamma d\eta^\gamma$  are usually the most difficult observables to describe using QCD predictions. Yet, as it can be seen from Fig. 13, the  $k_T$ -factorization predictions agree well with D0 [25] and CDF [23] data both in shape and normalization. There are only rather small overestimations of the data at low  $E_T^\gamma$  values in Figs. 13 in the forward region. Again, the scale dependence of our calculations is about 20–30%. The theoretical uncertainties of the collinear NLO predictions are smaller (about 6% [25]), which is to be expected as inclusion of higher order terms reduces the scale uncertainty.

One can conclude that the results of calculations in the  $k_T$ -factorization approach in general agree well with Tevatron experimental data, within a large scale uncertainty.

## 6 Prompt photons at LHC

The direct photon production at LHC has significantly higher cross sections compared to the ones measured at Tevatron and HERA. The prompt-photon cross section at LHC is more than a factor of hundred higher than that at Tevatron and a factor of  $10^5$  larger than that for photoproduction at HERA, assuming a similar kinematic range ( $|\eta^\gamma| < 2$ ), as shown in Fig. 14. This will allow to explore the TeV energy scale already in a few years of data taking.

Figure 15 shows the comparison between PYTHIA and HERWIG Monte Carlo models and JETPHOX LO and NLO calculations. The cross sections for  $\gamma + \text{jet}$  events were calculated for  $|\eta^\gamma| < 2$ ,  $P_T^\gamma > 100 \text{ GeV}$  and  $P_T^{\text{jet}} > 105 \text{ GeV}$ . The cuts on the transverse momenta are asymmetric to avoid instabilities in the NLO calculations. An isolation requirement  $E_T^\gamma >$

<sup>1</sup>For D0, the difference was mainly concentrated in the central rapidity region.



$0.9 E_T^{tot}$  was imposed, where  $E_T^{tot}$  is the total energy of the jet which contains prompt photon. Jets were reconstructed with the longitudinally-invariant  $k_T$  algorithm in inclusive mode [31].

The NLO QCD calculation is 30–40% higher than that predicted by PYTHIA. On the other hand, PYTHIA is 20% above HERWIG. It is interesting to observe that the level of discrepancy between PYTHIA and HERWIG is about the same as that observed at HERA at much lower transverse momenta (for example see Fig. 4). However, there is no significant difference between NLO and PYTHIA at  $P_T^\gamma > 10$  GeV for  $ep$ , while at the LHC energy range the difference between NLO and PYTHIA is rather significant. Certainly, the overall normalization of Monte Carlo programs like PYTHIA or HERWIG has to be adjusted, as these programs cannot account for contributions from loop corrections at higher orders.

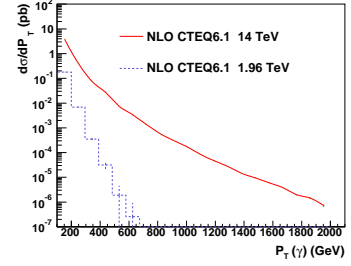


Fig. 14: The  $P_T^\gamma$  cross section for  $\gamma$ +jet events predicted by NLO QCD for the Tevatron and the LHC kinematic range.

Scale uncertainties were estimated by changing the renormalization and factorization scales in the range  $0.5 < \mu_f, \mu_R < 2$ . The relative difference between predicted cross sections is shown in Fig. 16. To make quantitative statements on scale uncertainties with the present level of statistical errors in calculations using JETPHOX, a linear fit was performed to determine the trend of the relative differences with increase of  $P_T^\gamma$ . As it can be seen, the scale uncertainty is about 10% and slowly increases with  $P_T^\gamma$ .

To estimate the uncertainty associated with the gluon density, the calculations have been performed using two CTEQ6.1M sets (15 and 30) which correspond to two extremes in the gluon density at large  $x$  [32]. Fig. 17 shows the relative difference between those two sets as a function of  $P_T^\gamma$ . It is seen that the gluon uncertainty is almost a factor of two larger compared to the scale uncertainty estimated above. No statistically significant difference has been observed between the cross sections calculated using CTEQ6.1M and MRST04. This is not totally surprising as both sets have similar input data for the global fit analysis.

The predictions for the  $k_T$  factorization approach were obtained for a wider pseudorapidity range, for both central and forward pseudo-rapidities  $\eta^\gamma$ . As a representative example, we will define the central and forward kinematic regions by the requirements  $|\eta^\gamma| < 2.5$  and  $2.5 < |\eta^\gamma| < 4$ , respectively. The transverse energy  $E_T^\gamma$  distributions of the inclusive prompt photon production in different  $\eta^\gamma$  ranges at  $\sqrt{s} = 14$  TeV are shown in Figs. 18. One can see that variation in scale  $\mu$  changes the estimated cross sections by about 20–30%. However, as it was already discussed above, there are additional theoretical uncertainties due to the non-collinear parton evolution, and these uncertainties are not well studied up to this time. Also the extrapolation of the available parton distribution to the region of lower  $x$  is a special problem at the LHC energies. In particular, one of the problem is connected with the correct treatment of saturation effects in small  $x$  region. Therefore, more work needs to be done until these uncertainties will be reduced.

Thus, the calculation based on the  $k_T$  factorization approach shows a larger scale uncertainty compared to the collinear factorization approach: for  $P_T^\gamma \sim 100$  GeV, the overall uncertainty for the NLO calculations is expected to be around 10%, while it reaches 20–30% for the

$k_T$ -factorization calculations for the same  $P_T^\gamma$  range, due to the fact that the latter are at leading order in  $\alpha_s$ . As the residual scale dependence of missing higher order terms resides in logarithms involving ratios of  $P_T^2$  and scales  $\mu^2$ , the effect becomes more dramatic at the LHC energy.

## 7 Summary

In this review, we have attempted to summarize recent progress in the description of prompt photon production at HERA, the Tevatron and the LHC. At HERA, some differences with NLO were observed in both photoproduction and DIS. The deficiencies at low  $P_T^\gamma$  values may indicate that non-perturbative effects at small  $P_T^\gamma$  play a non-negligible role. Also, one should expect that adding high-order corrections to the collinear-factorization approach should improve the description. Similar conclusions can be drawn for the Tevatron data which, as in the HERA case, has differences with NLO in the lowest  $P_T^\gamma$  region. Recently, significant differences with NLO were observed by the Tevatron for the shapes of  $P_T^\gamma$  distributions differential in  $\eta^\gamma$ . On the other hand, RHIC observes good agreement with NLO QCD. Considering the fact that RHIC uses a photon isolation method which is different from the usual cone isolation, the differences mentioned above may also have to do with isolation criteria acting differently in a partonic calculation than in the full hadronic environment of the experiment.

An alternative approach based on the  $k_T$  factorization generally improves the description of the HERA and the Tevatron data, but it has larger theoretical uncertainties. As for NLO, high-order corrections to the  $k_T$ -factorization approach should improve the description of the data. The applicability of the  $k_T$  factorization to the LHC data will be tested with the arrival of the first LHC data, but it is already evident that significant theoretical uncertainties are expected for the description of prompt-photon cross sections at LHC. Using the the collinear factorization approach, uncertainties of NLO calculations are expected to be 10–20% at about 1 TeV photon transverse momenta, and significantly larger for the  $k_T$ -factorization calculations. These uncertainties have to be reduced in the future for detailed comparison of the LHC data with the QCD predictions.

In all cases, PYTHIA and HERWIG predictions fail to describe prompt-photon cross sections, both in shape and normalization. Generally, HERWIG is significantly below PYTHIA. This could have a direct impact on the future LHC measurements, in particular for exotic searches which often rely on Monte Carlo predictions for estimations of rates for background events.

**Acknowledgments.** This work supported in part by the U.S. Department of Energy, Division of High Energy Physics, under Contract DE-AC02-06CH11357.

## References

- [1] J. F. Owens, *Rev. Mod. Phys.* **59**, 465 (1987).
- [2] L. Gordon and W. Vogelsang, *Phys. Rep.* **D52**, 58 (1995).
- [3] M. Krawczyk and A. Zembrzusi, *Phys. Rev.* **D64**, 14017 (2001).
- [4] M. Fontannaz, J. P. Guillet, and G. Heinrich, *Eur. Phys. J.* **C21**, 303 (2001).
- [5] M. Fontannaz and G. Heinrich, *Eur. Phys. J.* **C 34**, 191 (2004).
- [6] A. Lipatov and N. Zotov, *Phys. Rev.* **D72**, 054002 (2005).
- [7] C. F. von Weizsacker, *Z. Phys.* **88**, 612 (1934).  
E. J. Williams, *Phys. Rev.* **45**, 729 (1934).
- [8] M. Fontannaz, J. P. Guillet, and G. Heinrich, *Eur. Phys. J.* **C 22**, 303 (2001).
- [9] PHOX programs. Available at [http://lappweb.in2p3.fr/lapth/phox\\_family/main.html](http://lappweb.in2p3.fr/lapth/phox_family/main.html).
- [10] A. Zembrzusi and M. Krawczyk, Photoproduction of isolated photon and jet at the DESY HERA, 2003, hep-ph/0309308.
- [11] ZEUS Collaboration, S. Chekanov *et al.*, *Phys. Lett.* **B511**, 19 (2001).
- [12] E. M. Levin *et al.*, *Sov. J. Nucl. Phys.* **53**, 657 (1991).  
S. Catani, M. Ciafaloni, and F. Hautmann, *Nucl. Phys.* **B366**, 135 (1991).  
J. Collins and R. Ellis, *Nucl. Phys.* **B360**, 3 (1991).
- [13] A. V. Lipatov and N. P. Zotov, *J. Phys.* **G34**, 219 (2007).
- [14] M. A. Kimber, A. D. Martin, and M. G. Ryskin, *Phys. Rev.* **D63**, 114027 (2001).  
G. Watt, A. D. Martin, and M. G. Ryskin, *Eur. Phys. J.* **C31**, 73 (2003).
- [15] ZEUS Collaboration, S. Chekanov *et al.*, *Eur. Phys. J.* **C49**, 511 (2007).
- [16] T. Sjostrand, S. Mrenna, and P. Skands, *JHEP* **05**, 026 (2006).
- [17] G. Corcella *et al.*, *JHEP* **01**, 010 (2001).  
G. Corcella *et al.*, (2002), hep-ph/0210213.
- [18] H1 Collaboration, A. Aktas *et al.*, *Eur. Phys. J.* **C38**, 437 (2005).
- [19] ZEUS Collaboration, J. Breitweg *et al.*, *Phys. Lett.* **B472**, 175 (2000).
- [20] G. Heinrich, Proceedings of the International Conference Photon2007, Paris, France (2007).
- [21] H1 Collaboration, F. D. Aaron *et al.*, *Eur. Phys. J.* **C54**, 371 (2008).

- [22] A. Gehrmann-De Ridder, G. Kramer, and H. Spiesberger, Nucl. Phys. **B578**, 326 (2000).
- [23] CDF Collaboration, D. E. Acosta *et al.*, Phys. Rev. **D65**, 112003 (2002).
- [24] CDF Collaboration, D. E. Acosta *et al.*, Phys. Rev. **D70**, 074008 (2004).
- [25] D0 Collaboration, B. Abbott *et al.*, Phys. Rev. Lett. **84**, 2786 (2000).
- [26] D0 Collaboration, V. M. Abazov *et al.*, Phys. Rev. Lett. **87**, 251805 (2001).
- [27] D0 Collaboration, V. M. Abazov *et al.*, Phys. Lett. **B639**, 151 (2006).
- [28] D0 Collaboration, V. M. Abazov *et al.*, (2008), hep-ex/0804.1107.
- [29] P. Aurenche, M. Fontannaz, J.-P. Guillet, E. Pilon, and M. Werlen, Phys. Rev. **D73**, 094007 (2006).
- [30] PHENIX Collaboration, S. S. Adler *et al.*, Phys. Rev. Lett. **98**, 012002 (2007).
- [31] S. Ellis and D. Soper, Phys. Rev. **D48**, 3160 (1993).  
S. Catani *et al.*, Nucl. Phys. **B406**, 187 (1993).
- [32] D. Stump *et al.*, JHEP **310**, 46 (2003).

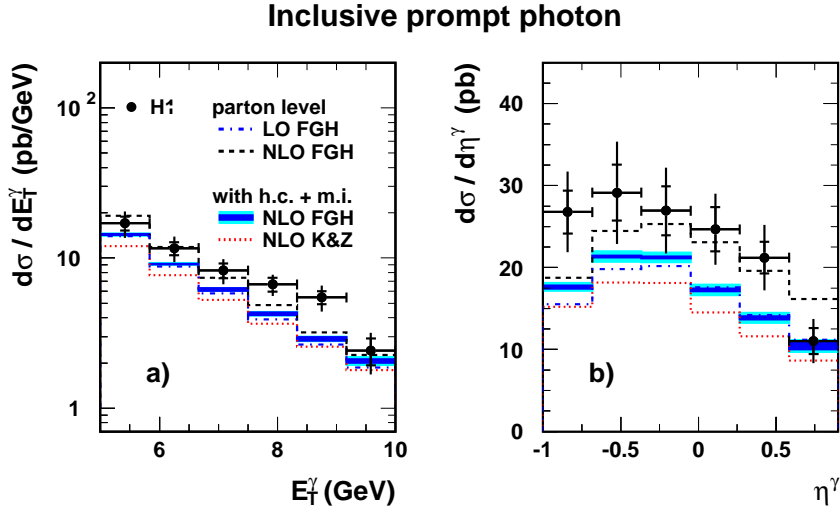


Fig. 5: The differential cross section  $d\sigma/dE_T$  and  $d\sigma/d\eta^\gamma$  as functions of  $E_T^\gamma$  and  $\eta^\gamma$  of the inclusive prompt photon photoproduction calculated at  $-0.7 < \eta^\gamma < 0.9$  and  $0.2 < y < 0.9$ . The data are compared to two different NLO calculations.

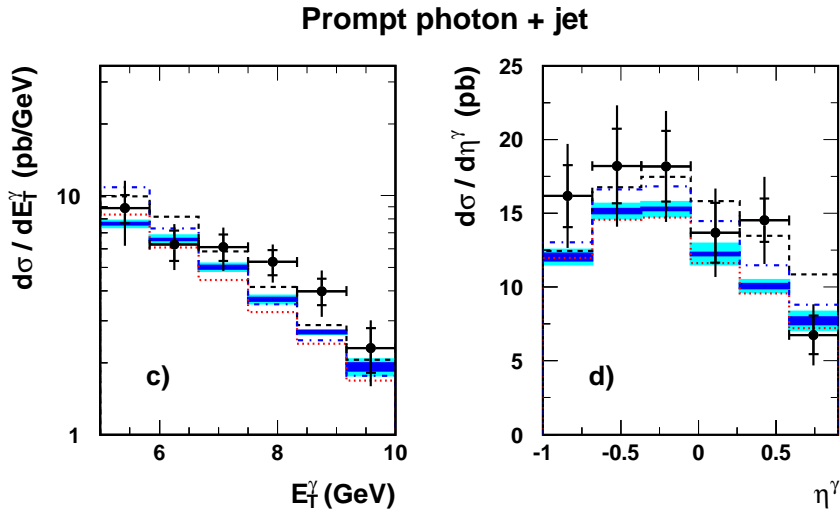


Fig. 6: Same as in Fig. 5, but for  $\gamma$ +jet events with the additional jet cuts:  $-1 < \eta^{\text{jet}} < 2.3$  and  $E_T^{\text{jet}} > 4.5$  GeV.

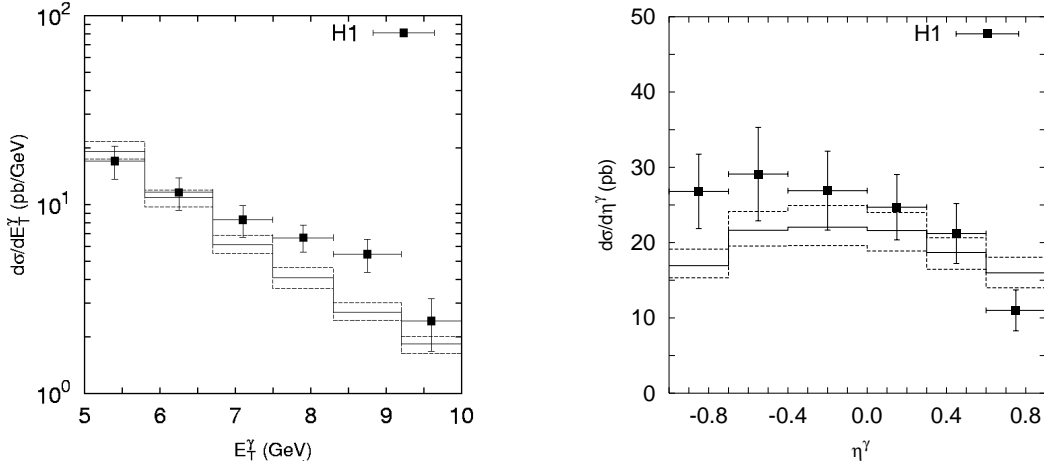


Fig. 7: The differential cross section  $d\sigma/dE_T$  and  $d\sigma/d\eta^\gamma$  as functions of  $E_T^\gamma$  and  $\eta^\gamma$  of the inclusive prompt photon photoproduction calculated at  $-0.7 < \eta^\gamma < 0.9$  and  $0.2 < y < 0.9$ . The data are compared to the  $k_T$ -factorization calculations. The bands correspond to a typical renormalization scale uncertainty which was obtained by changing  $\mu_R$  by a factor of 0.5 and 2.

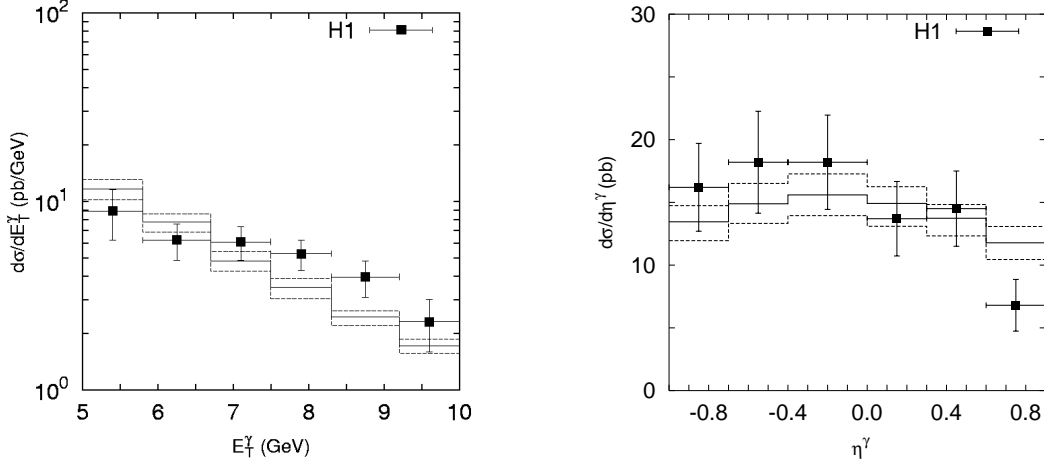


Fig. 8: Same as Fig. 7, but for  $\gamma$ +jet events with the additional jet cuts:  $-1 < \eta^{\text{jet}} < 2.3$  and  $E_T^{\text{jet}} > 4.5$  GeV.

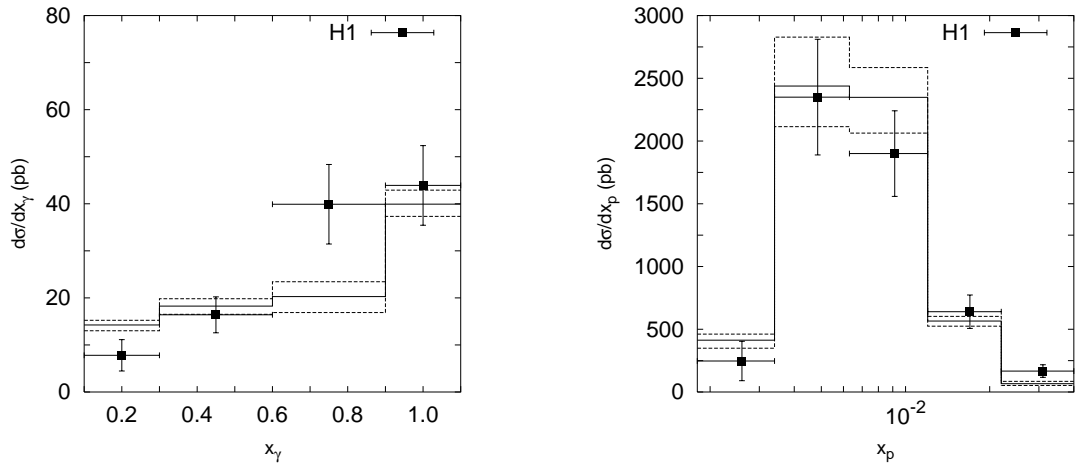


Fig. 9: The differential cross section  $d\sigma/dx_\gamma$  and  $d\sigma/dx_p$  of prompt photon + jet production calculated at  $5 < E_T^\gamma < 10$  GeV and  $0.2 < y < 0.7$  with an additional jet requirement  $-1 < \eta^{\text{jet}} < 2.3$  and  $E_T^{\text{jet}} > 4.5$  GeV.

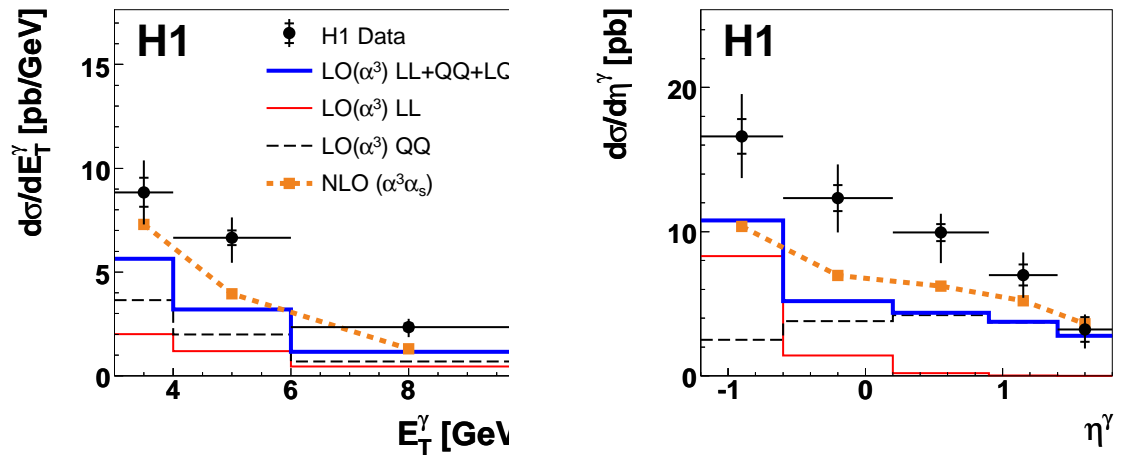


Fig. 10: The differential  $\gamma$ +jet cross sections as functions of  $E_T$  and  $\eta$  of the prompt photon in DIS. The data are compared to LO and NLO calculations.

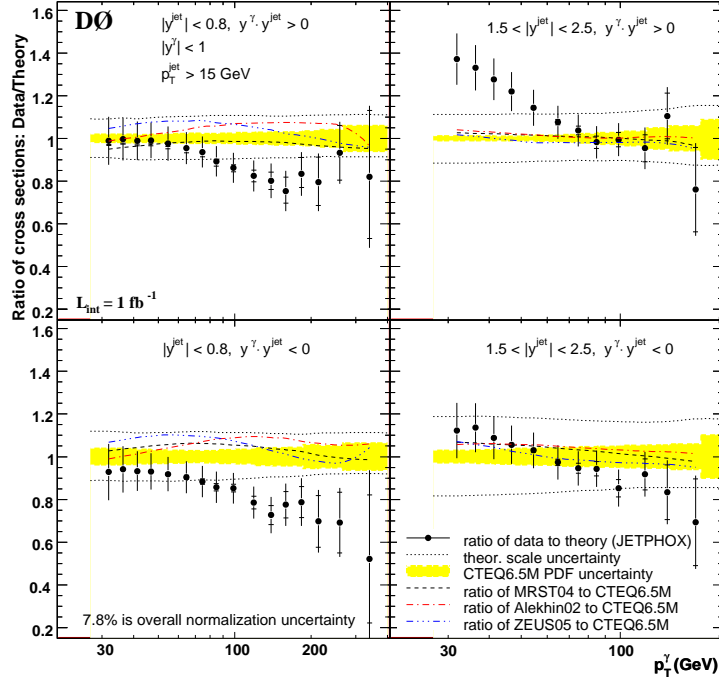


Fig. 11: The ratios of the triple-differential cross section measured by D0 compared to the NLO QCD prediction using JETPHOX. See details in Ref. [28].

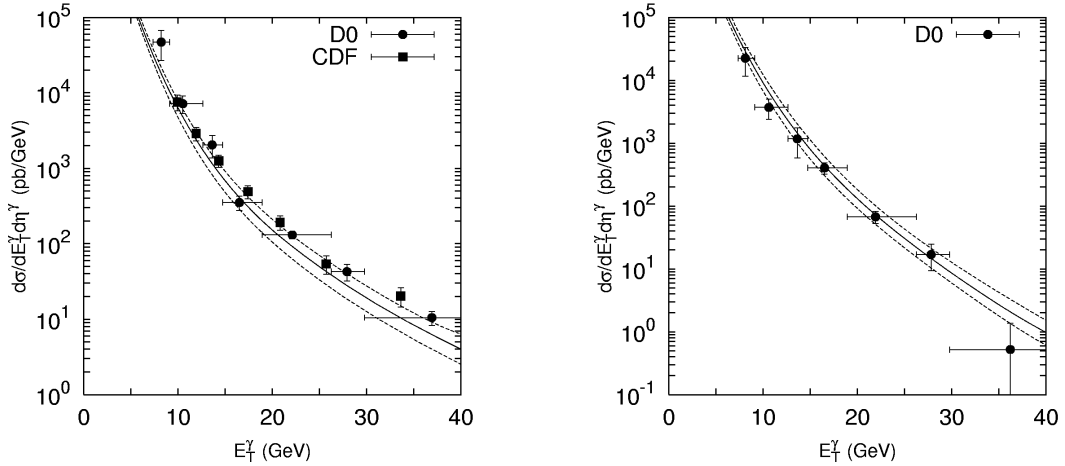


Fig. 12: The double differential cross section  $d\sigma/dE_T^\gamma d\eta^\gamma$  of inclusive prompt photon production at  $\sqrt{s} = 630$  GeV and  $|\eta^\gamma| < 0.9$  (left plot) and  $1.6 < |\eta^\gamma| < 2.5$  (right panel). The solid line corresponds to the default scale  $\mu = E_T^\gamma$  of the  $k_T$  factorization predictions, whereas upper and lower dashed lines correspond to the  $\mu = E_T^\gamma/2$  and  $\mu = 2E_T^\gamma$ .



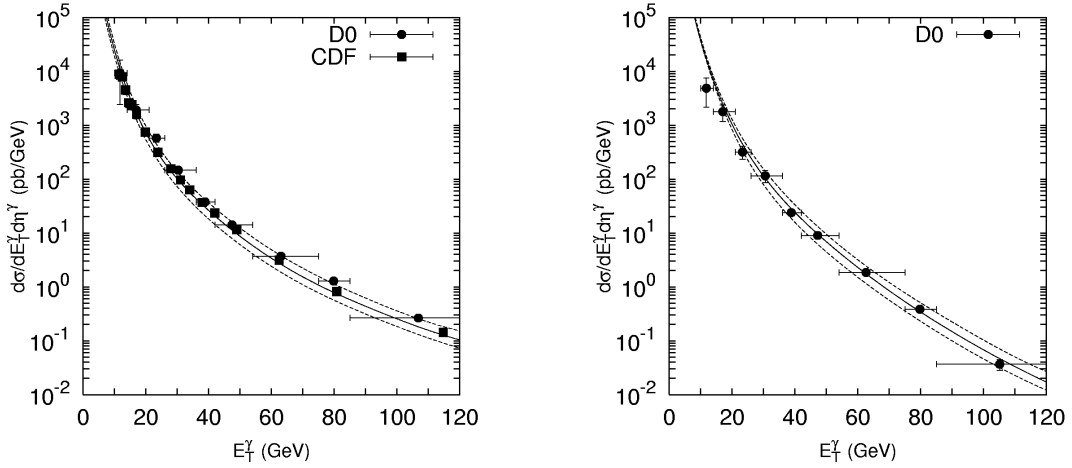


Fig. 13: The double differential cross section  $d\sigma/dE_T^\gamma d\eta^\gamma$  of inclusive prompt photon production at  $\sqrt{s} = 1800$  GeV and  $|\eta^\gamma| < 0.9$  (left plot) and  $1.6 < |\eta^\gamma| < 2.5$  (right plot). The solid line corresponds to the default scale  $\mu = E_T^\gamma$ , whereas upper and lower dashed lines correspond to the  $\mu = E_T^\gamma/2$  and  $\mu = 2E_T^\gamma$  for the  $k_T$  factorization calculations.

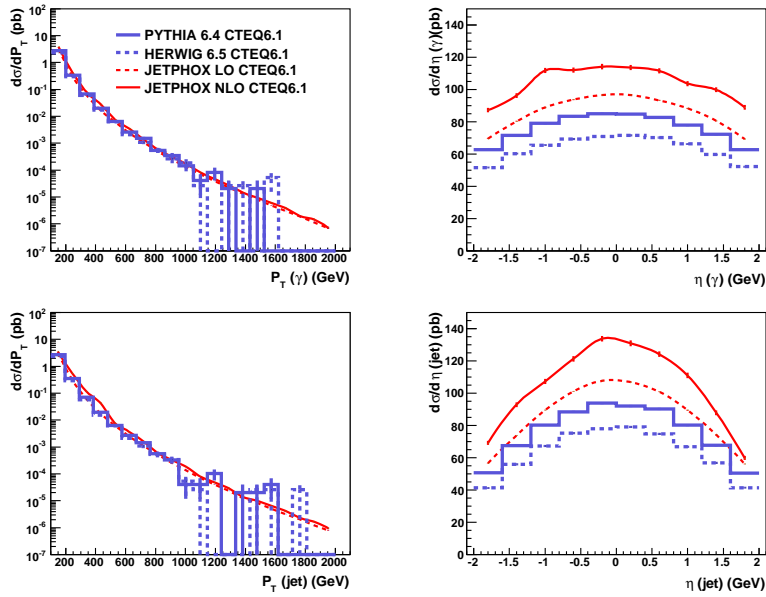


Fig. 15: Comparisons of Monte Carlo models with LO and NLO calculations as implemented in JETPHOX.

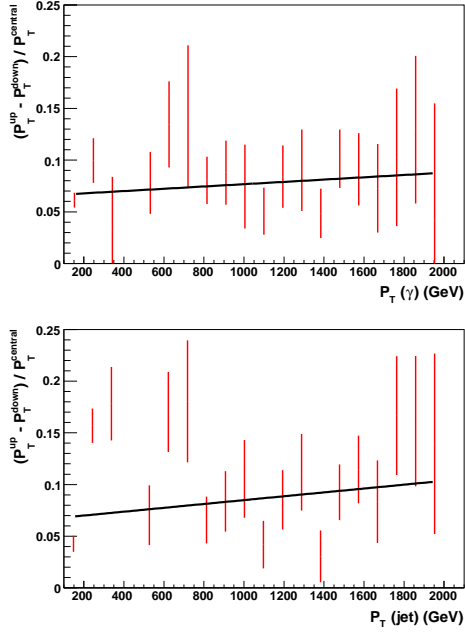


Fig. 16: Relative difference between the cross section estimated with  $\mu = 0.5$  ( $P_T^{up}$ ) and  $\mu = 2$  ( $P_T^{down}$ ) as a function of  $P_T$  for gamma and jet. The line represents a linear fit.

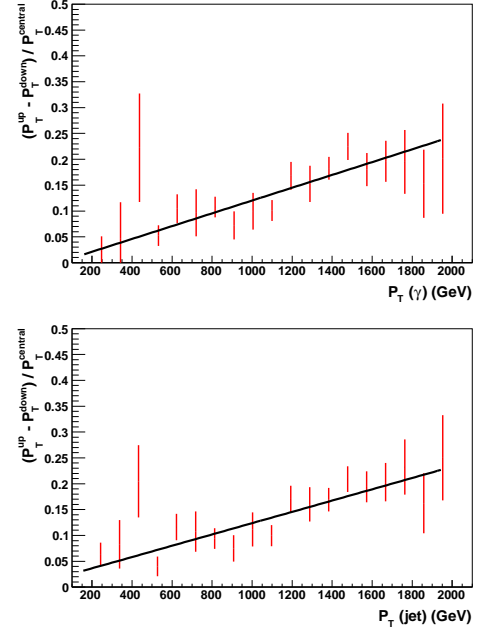


Fig. 17: Relative difference between the cross section estimated with CTEQ6.1M set=-15 ( $P_T^{up}$ ) and set=15 ( $P_T^{down}$ ) as a function of  $P_T$  for gamma and jet. The line represents a linear fit.

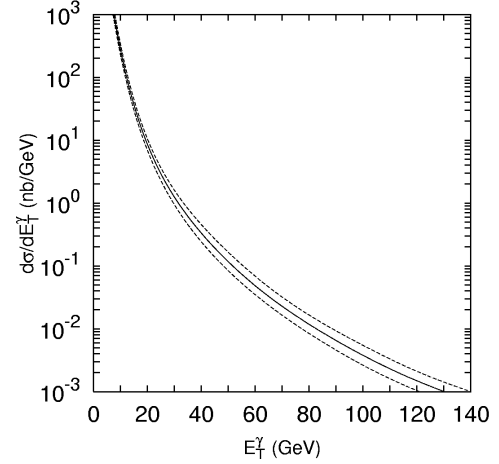
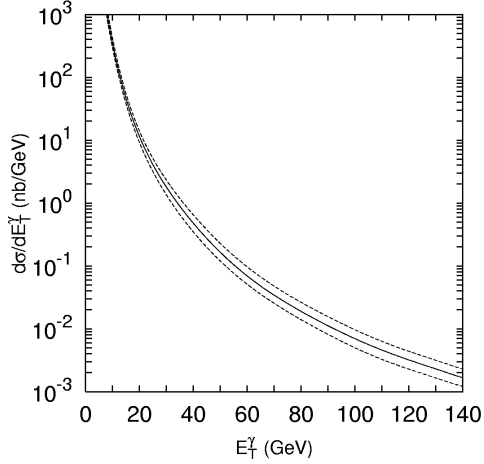


Fig. 18: Left plot: The  $k_T$  factorization predictions for differential cross sections  $d\sigma/dE_T^\gamma d\eta^\gamma$  at  $\sqrt{s} = 14$  TeV GeV and  $|\eta^\gamma| < 2.5$  (left plot); at  $2.5 < \eta^\gamma < 4.0$  (right plot). The solid line corresponds to the default scale  $\mu = E_T^\gamma$ , whereas upper and lower dashed lines correspond to the  $\mu = E_T^\gamma/2$  and  $\mu = 2E_T^\gamma$ .

# Propagation of Uncertainty in a Parton Shower\*

*Philip Stephens<sup>†</sup> and André van Hameren<sup>‡</sup>*

<sup>†</sup>Kennesaw State University, Department of Physics, 1000 Chastain Road, Kennesaw, GA 30144, USA

<sup>‡</sup>The H. Niewodniczański Institute of Nuclear Physics, Polish Academy of Sciences, Radzikowskiego 152, 31-342 Kraków, Poland

## Abstract

Presented here is a technique of propagating uncertainties through the parton shower by means of an alternate event weight. This technique provides a mechanism to systematically quantify the effect of variations of certain components of the parton shower leading to a novel approach to probing the physics implemented in a parton shower code and understanding its limitations. Further, this approach can be applied to a large class of parton shower algorithms and requires no changes to the underlying implementation.

## 1 Introduction

As we enter a new era of particle physics, precise knowledge of quantum chromodynamics (QCD) will become increasingly important in order to understand the physics beyond the standard model. Currently, one of the most useful tools for studying QCD is the parton shower approximation. This tool provides a mechanism to connect few-parton states to the real world of high-multiplicity hadronic final states while retaining the enhanced collinear and soft contributions to all orders.

Use of parton shower Monte Carlos (MC) has become common-place. Often, when one needs an estimate of the uncertainty of a MC prediction several different MC programs are used and the differences between them is considered the error [1]. Though this technique of estimating the error of the MC is generally acceptable, it does little to provide insight into the physics. It has been shown [2] that the uncertainties in both the perturbative expansion and the parton distribution functions indeed can lead to effects of the order of ten percent. We propose here a technique in which the known uncertainties of the physics can be propagated through the parton shower framework. This technique provides alternate weights to an event generated by a MC without having to change the basic structure of the MC program. We feel this technique could be valuable when determining how various improvements in the parton shower will impact the MC predictions. Furthermore, this gives a more satisfactory description of the errors in a MC prediction.

---

This work is partly supported by the EU grant mTkd-CT-2004-510126 in partnership with the CERN Physics Department and by the Polish Ministry of Scientific Research and Information Technology grant No 620/E-77/6.PRUE/DIE 188/2005-2008.

## 2 Variation of Parton Shower

In many parton showers [3–6] one starts with the fundamental probability density (for one emission) defined as

$$\mathcal{P} = f_R(\vec{y}) \exp \left( - \int^{\xi(\vec{y})} d^n \vec{y}' f_V(\vec{y}') \right). \quad (1)$$

Here the function  $f_R(\vec{y})$  is the distribution of the real emission while  $f_V(\vec{y})$  is the virtual contribution. In both cases the precise definition of  $\vec{y}$  is specific to the implementation. Furthermore, the limits of integration in the virtual component are also specific to the implementation: how the infra-red limit is treated, the definition of resolvable versus unresolvable emissions and the ordering of variables. For a time-like shower  $f_R = f_V$  and is given by

$$f_R(\vec{y}) = \frac{\alpha_S(g(\vec{y}))}{2\pi} P(\vec{y}), \quad (2)$$

where  $g(\vec{y})$  is some abstract function used to determine the scale of the running coupling. We find a similar result for the constrained MC [5]; for a space-like shower using the backward evolution algorithm we find  $f_R = f_V f(x, \vec{y})$  and

$$f_V(\vec{y}; x) = \frac{\alpha_S(g(\vec{y}))}{2\pi} \frac{f(x/z, \vec{y})}{f(x, \vec{y})} P(\vec{y}), \quad (3)$$

where  $f(x, \vec{y})$  is the PDF at energy fraction  $x$  and scale given by some combination of the components of  $\vec{y}$ . We can explicitly see that one of the components of  $\vec{y}$  is  $z$ , a momentum fraction.

In the forward (time-like) evolution algorithm, as well as the non-Markovian algorithm,  $P(\vec{y})$  is just the Alteralli-Parisi [7] splitting function divided by the scale. In the numerical results here we consider only the forward evolution algorithm; in the last section we propose a use for this technique in a backward evolution algorithm for CCFM.

We now define a functional to represent our functions  $f_R(\vec{y})$  and  $f_V(\vec{y})$

$$F_R[\varphi(\vec{y})] = f_R(\vec{y}); \quad F_V[\varphi(\vec{y})] = f_V(\vec{y}). \quad (4)$$

Here  $\varphi(\vec{y})$  are the functional components of  $F_{R/V}$  which we want to vary (e.g. the running coupling or the kernel). This defines the distribution of one branching as

$$\mathcal{P}[\varphi(\vec{y})] = F_R[\varphi(\vec{y})] \exp \left( - \int^{\xi(\vec{y})} d^n \vec{y}' F_V[\varphi(\vec{y}')] \right). \quad (5)$$

We can find the variation of this by

$$\delta \mathcal{P} = \mathcal{P}[(\varphi + \delta \varphi)(\vec{y})] - \mathcal{P}[\varphi(\vec{y})]. \quad (6)$$

If we define

$$\delta F_{R/V} = F_{R/V}[(\varphi + \delta \varphi)(\vec{y})] - F_{R/V}[\varphi(\vec{y})], \quad (7)$$

then

$$\delta \mathcal{P} = \mathcal{P} \left( 1 + \frac{\delta F_R}{F_R} \right) \exp \left( - \int^{\xi(\vec{y})} d^n \vec{y}' \delta F_V \right) - \mathcal{P}, \quad (8)$$

from which we have a weight

$$w \equiv \frac{\mathcal{P} + \delta\mathcal{P}}{\mathcal{P}} = \left(1 + \frac{\delta F_R}{F_R}\right) \exp\left(-\int^{\xi(\vec{y})} d^n \vec{y}' \delta F_V\right). \quad (9)$$

The weights defined in eqn. (9) are relative to the original probability density for one emission. To get the total weight for the full event, we must consider

$$\mathcal{P}_E[\varphi, \{\vec{y}_i\}] = \prod_i \mathcal{P}[\varphi(\vec{y}_i)], \quad (10)$$

and thus

$$\delta\mathcal{P}_E = \mathcal{P}_E[\varphi + \delta\varphi, \{\vec{y}_i\}] - \mathcal{P}_E[\varphi, \{\vec{y}_i\}]. \quad (11)$$

This leads to a total event weight given by

$$w_E \equiv \frac{\mathcal{P}_E + \delta\mathcal{P}_E}{\mathcal{P}_E} = \prod_i w_i. \quad (12)$$

### 3 Example Parton Shower Kinematics

For the examples given here we will use as a model bremsstrahlung emissions from one quark line. For the numerical results presented in the following sections we use a concrete implementation of the kinematics of the Herwig++ parton shower [3, 8]. In terms of those, we have

$$F_R[\varphi(\vec{y})] = F[(\alpha_S, P_{qq})(z, \tilde{q}^2)] = \frac{1}{2\pi\tilde{q}^2} \alpha_S(z, \tilde{q}^2) P_{qq}(z, \tilde{q}^2), \quad (13)$$

where  $P_{qq}$  is the splitting kernel,  $z$  is the splitting variable, and  $\tilde{q}^2$  is the evolution variable.

### 4 Kernel Variations

Varying the structure of the splitting kernel may be an interesting example. For example, one could start with the collinear splitting kernels and vary them by the mass dependent quasi-collinear kernels to see whether such changes introduce dramatic effects on a set of observables. The benefit to the procedure presented here is that there is no need to change the fundamental structure of a given MC. In fact one could add an option to their code to keep track of the alternate weights, without changing at all their basic MC program logics and structures. One caveat is that though this method will give an accurate estimate of the variations given, this is only true for regions of phase space in which the original MC fills. If some regions of phase space are empty, or rarely entered, the changes in that region due to the variation will still lack significant statistics.

The collinear kernel is simply

$$P_{qq}(z) = \frac{1 + z^2}{1 - z}. \quad (14)$$

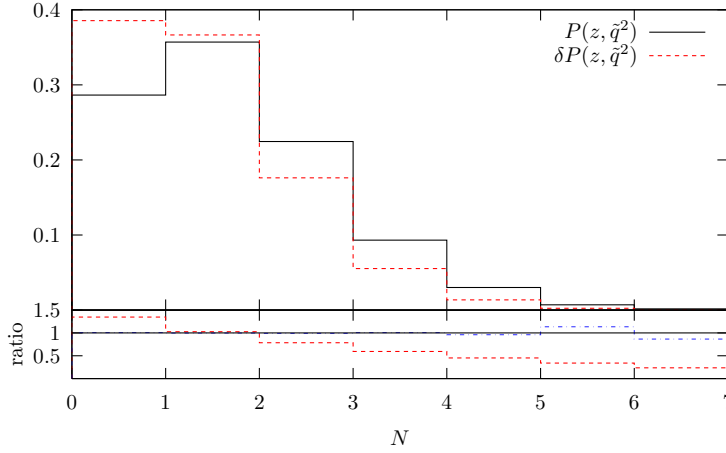


Fig. 1: The distribution of the number of emissions for the collinear kernel and the quasi-collinear kernel for  $m^2 = (175 \text{ GeV})^2$  and  $\tilde{q}^2 = (1 \text{ TeV})^2$ . The solid line shows the result when the quasi-collinear kernel is used, the dashed line shows the result when the variation in eqn. (15) is applied and the events are weighted. Again, the second panel shows the ratio of the varied to the unvaried MC.

To obtain the quasi-collinear kernel, we must define a variance of

$$\delta P_{qq}(z, \tilde{q}^2) = -\frac{2m^2}{z(1-z)\tilde{q}^2}. \quad (15)$$

With this variance we find the alternate weight, for the  $i$ th emission, is given by

$$w_{P_i} = \left(1 + \frac{\delta P_{qq}(z_i, \tilde{q}_i^2)}{P_{qq}(z_i, \tilde{q}_i^2)}\right) \exp \left( - \int_{\tilde{q}_i^2}^{\tilde{q}_{i-1}^2} \frac{d\tilde{q}^2}{\tilde{q}^2} \int_{z_i^-}^{z_i^+} dz \alpha_S [z^2(1-z)^2 \tilde{q}^2] \delta P_{qq}(z, \tilde{q}^2) \right), \quad (16)$$

and the total weight due to the kernel variation is the product of the weight for each emission. This weight is normalized to a weight 1 event with no variations.

We now show the result of this variation when showering a top quark with mass 175 GeV from an initial scale of 1 TeV. In figure 1 we show the effect that the quasi-collinear variation has on the distribution of the number of emissions. As would be expected, for larger masses we have fewer emissions. Figure 2 shows the  $p_\perp^2$  spectrum of the outgoing quark. The figures are divided into two panels. The top panel shows the results while the bottom panel shows the ratio of the reweighted MC vs. the unweighted one. In figure 1 the ratio panel also includes the ratio of the reweighted MC vs. an alternate MC sample created by changing the kernel in the MC to the quasi-collinear kernel. We see that this ratio is 1 with small variations.

#### 4.1 Combining Kernel with Running Coupling

Another potential variation that may be of interest is to vary the kernel by a term proportional to the running coupling. Such a variation could be used to introduce some NLO effects into the kernel. If we consider only the lowest order in the variations, then

$$\delta F \approx \delta \alpha_S P_{qq}^{(1)} + \alpha_S \delta P_{qq}^{(1)} + \alpha_S^2 \delta P_{qq}^{(2)}. \quad (17)$$

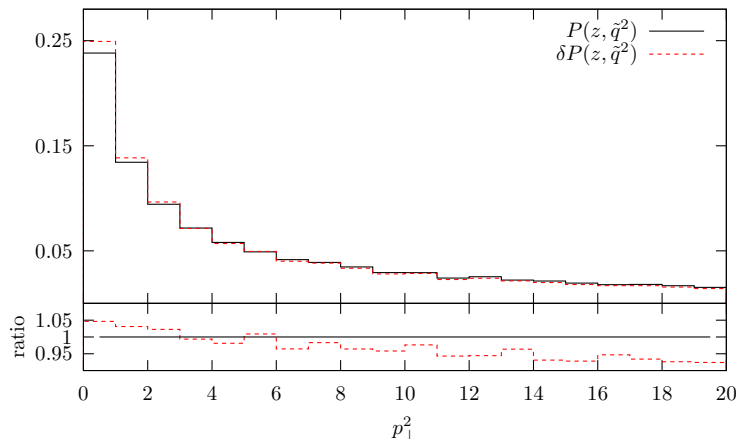


Fig. 2: The distribution of the  $p_{\perp}^2$  of the outgoing quark for the collinear and quasi-collinear cases under the same conditions as figure 1.

We choose the form of  $\delta P_{qq}^{(2)}(z)$  according to full NLO kernel [9, 10]. This is composed of two parts, the flavour singlet (S) and non-singlet (V) contributions

$$\delta P_{qq}^{(2)}(z, \tilde{q}^2) = P_{qq}^{S(2)}(z) + P_{qq}^{V(2)}(z), \quad (18)$$

We choose  $\delta P^{(1)} = 0$  and  $\delta\alpha = 0$  for these examples.

Figure 3 shows the effect on the number of emissions and figure 4 shows the effect on the  $p_{\perp}^2$ -spectrum of the outgoing quark line. We see that the number of emissions is slightly higher with a harder spectrum.

The construction of a next-to-leading log (NLL) parton shower has the problem of negative values for the splitting kernels. These destroy the probabilistic interpretation of the Sudakov form factors. Naively, one would assume that this will destroy any meaningful results for the NLL weights. In our case, this is not true. We are reweighting the total density according to the NLL corrections. These may introduce large or negative weights to the reweighted shower, but this is necessary as this correctly describes the density. In the inclusive picture, these negative weights are integrated over and pose no problem; exclusively, these negative weights must be treated correctly in the analysis.

## 5 Variation of Kinematics

We now consider another use of the alternate weights. Here we wish to use these weights to transform one parton shower into another. This, of course, is not an exact transformation. This requires additional knowledge about the structure of the alternate parton shower.

The idea is to use the variables generated by one shower and reshape the distribution to give the results if an alternate shower was used. In this section we discuss the intrinsic kinematical definitions.

Consider a new kinematics, similar to the one used in Pythia [4]. Here we wish to order the parton shower in virtuality ( $Q^2$ ). This requires a mapping from  $\tilde{q}^2$  into  $Q^2$ . Furthermore,

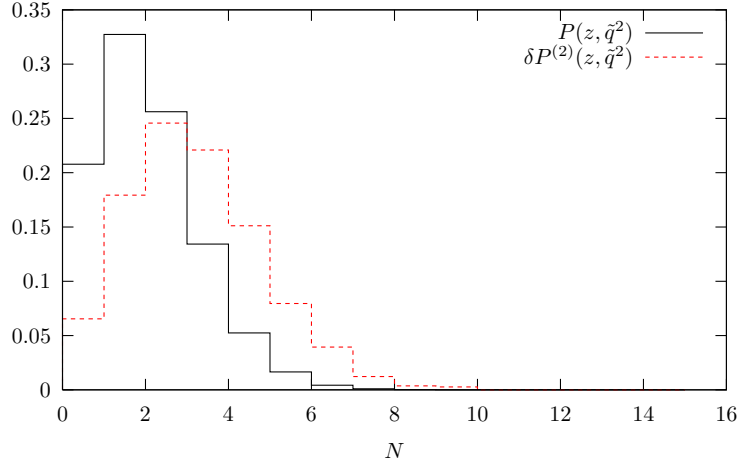


Fig. 3: The distribution of the number of emissions using the collinear kernel at  $\mathcal{O}(\alpha_S)$  and applying the variation discusses in the text at  $\mathcal{O}(\alpha_S^2)$ .

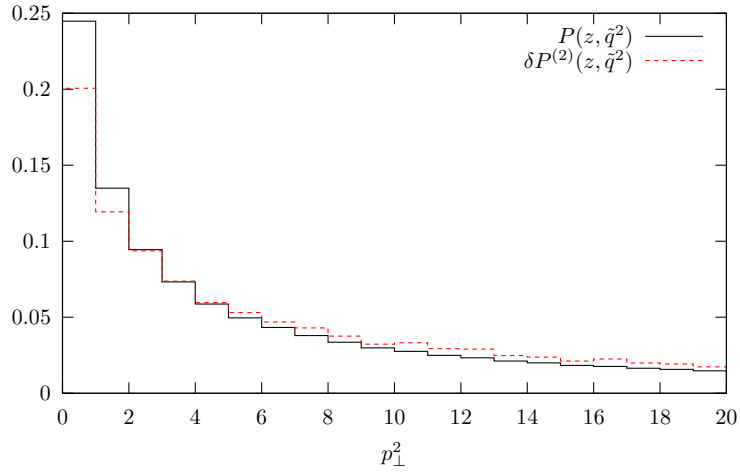


Fig. 4: The  $p_\perp^2$  distribution of the outgoing quark under the same conditions as figure 3.



there is a different interpretation of the meaning of the momentum fraction  $z$  in the Pythia-like and Herwig-like shower; they have the same distribution, however. We compensate for this by constructing the full four-momentum from the Herwig-like shower and deconstructing the associated variables for each emission. The weights can then be computed from this. This method has the additional benefit that the four momentum configuration is identical in both cases; thus hadronization effects and hadron decays are identical. We define our variations such that

$$\bar{F}[(\alpha_S, P_{qq})(\bar{z}, Q^2)] = F[(\alpha_S, P_{qq})(z, \tilde{q}^2)] + \delta F, \quad (19)$$

where the left-hand side refers to the Pythia-like shower. From this we find

$$\delta F = \bar{F}[(\alpha_S, P_{qq})(\mathcal{T}(z, \tilde{q}^2))]\mathcal{J}(\bar{z}, Q^2) - F[(\alpha_S, P_{qq})(z, \tilde{q}^2)], \quad (20)$$

where  $\mathcal{J}$  is the Jacobian factor for the coordinate transformation  $\mathcal{T}(z, \tilde{q}^2)$  from the Herwig-variables to the Pythia variables. At this point we can exploit the analytic structure of the Sudakov form factor,

$$\Delta(t; t_0) = \Delta(t; t_1)\Delta(t_1; t_0). \quad (21)$$

This allows the separation of the weights into the real and the Sudakov components and to calculate the Sudakov components over the full evolution scale, rather than just the scales between each emission. This gives

$$w_\Delta = \frac{\Delta_P(Q_{ini}^2; Q_0^2)}{\Delta_H(\tilde{q}_{ini}^2, \tilde{q}_0^2)}. \quad (22)$$

The total weight is given simply as

$$w = w_\Delta \prod_{i=1}^N w_i^{(R)}, \quad (23)$$

where the  $w_i^{(R)}$  refer to the weights for the real emissions.

The question now is what does the weighted shower physically give us? This gives us the weight, relative to the unweighted original shower, of producing the kinematical configuration via the other shower. For our example here this means that it will weight our Herwig-like shower to be that of the Pythia-like construction. Our weighted shower will produce events that are both ordered in virtuality and in angle. Comparing the weighted results versus an independent implementation of the full Pythia-like shower would illustrate, for any observable, the effect of the different limits in phase-space inherent in each implementation. Furthermore, it could be used to illustrate the effects of alternate choices of ordering; e.g. colour connections between jets.

To illustrate this technique we use as a model  $e + e^-$  annihilation into a  $q\bar{q}$  pair. This pair then undergoes final state radiation, but the subsequent emissions do not. We reconstruct the kinematics of the event and, in order to conserve  $\sqrt{s}$ , we rescale each jet by a common factor,  $k$ , such that

$$\sqrt{s} = \sum_{i=1}^N \sqrt{q_i^2 + k\mathbf{p}_i^2}, \quad (24)$$

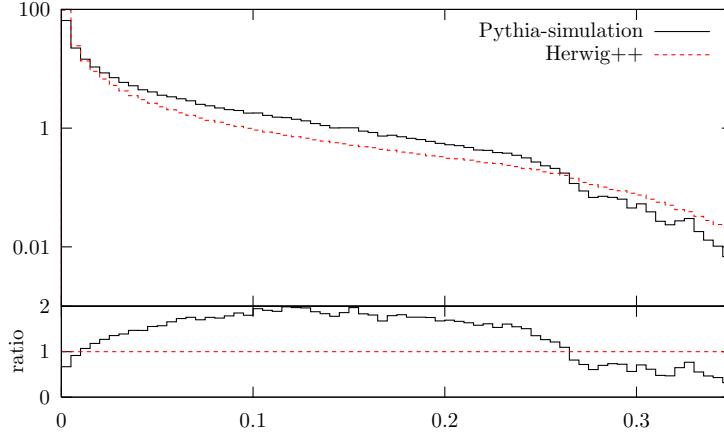


Fig. 5:  $1 - T$  for the Herwig-like shower and reweighted to a Pythia-like shower, as described in the text. These differences are due to the different kinematics definitions used in each shower. The bottom panel shows the ratio of the Pythia-like vs. Herwig-like.

where  $q_i^2$  is the virtuality of jet  $i$ . To illustrate the reweighting between the Herwig-like and Pythia-like shower we study the thrust observable. This is given by

$$T = \max_{\mathbf{n}} \frac{\sum_{i=1}^N |\mathbf{p}_i \cdot \mathbf{n}|}{\sum_{i=1}^N |\mathbf{p}_i|}. \quad (25)$$

This observable was chosen as the thrust has a strong correlation to the hardest emission, but also is effected by subsequent emissions. As we don't shower the emitted gluons, studying an observable which have a strong dependence on 2 or more emissions is not as illustrative.

Figure 5 shows the result for  $\sqrt{s} = 1$  TeV. We can see the deviations, and as expected they are not too large. As these are not the result of a full event generation it is not useful to compare these to data.

## 6 Uncertainty in Unintegrated Parton Distribution Functions

In the last example we show how to apply the technique to compute the effect of uncertainties in the unintegrated parton distribution function (updf) for the backwards evolution algorithm of CASCADE [11]. In this algorithm the updfs are taken from the outputs of an alternate Monte Carlo algorithm, based on SMALLX [11–13]. This leads to large uncertainties in the updfs. Additionally, in order to fit the initial conditions of the updf MC, based on SMALLX, one must match the output of CASCADE to data. The ability to take the uncertainty of the updf MC into account will allow for better fits overall. Figure 6 shows a schematic of this procedure.

We present here the formula needed to compute the effect of the updf uncertainties in the CASCADE algorithm. We do not endeavor here to implement these weights in the CASCADE program, nor suggest the ideal treatment of this information. This is left as future exercises for the authors of CASCADE.

The CCFM equation describes the gluonic structure of the proton. The variables of this

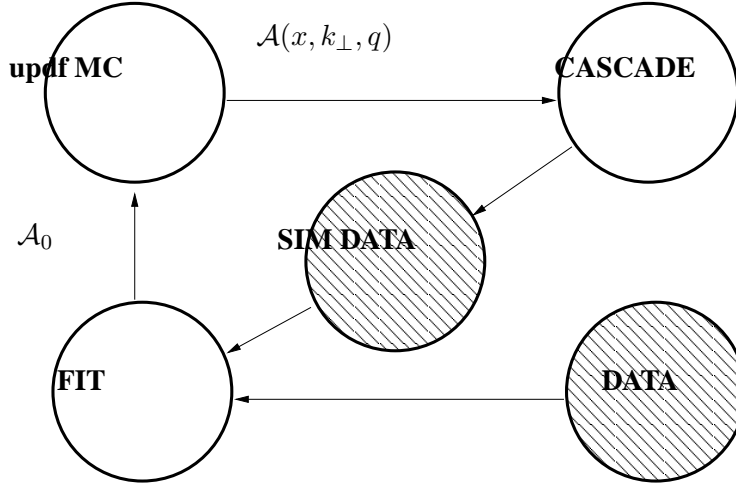


Fig. 6: Schematic of the flow of the fitting procedure using CASCADE and updf MC. As the output of the updf MC is not directly fitted, rather that of CASCADE, tracking uncertainties from the updf MC through CASCADE can prove useful in the fits.

evolution are a scale,  $q$ , the momentum fraction,  $x$ , and the transverse components,  $k_\perp$ . In CASCADE, given a step in the evolution terminates at  $q, x$  and  $k_\perp$ , the probability of evolving to a new  $\bar{q}, x/z$  and  $k'_\perp = |(1-z)/z \mathbf{q} + \mathbf{k}_\perp|$  is

$$\begin{aligned} \mathcal{P}(\bar{q}, z, \phi, k'_\perp; q, x, k_\perp) &= \frac{\tilde{P}(z, \bar{q}/z, k_\perp)}{2\pi z q^2} \mathcal{A}(x/z, k'_\perp, \bar{q}/z) \\ &\times \exp\left(-\int_q^{\bar{q}} \frac{dq'^2}{q'^2} \int \frac{dz d\phi}{z 2\pi} \tilde{P}(z, q'/z, k_\perp) \frac{\mathcal{A}(x/z, k'_\perp, q'/z)}{\mathcal{A}(x, k_\perp, q')}\right), \end{aligned} \quad (26)$$

where  $\tilde{P}$  is the kernel including the non-sudakov form factor and  $\mathcal{A}$  is the updf. In contrast to the previous examples, here the real and virtual contributions are clearly different. When we propagate the variance of the updf in the real function we find

$$\frac{\delta F_R[\varphi]}{F_R[\varphi]} = \frac{\delta \mathcal{A}(x/z, k'_\perp, q'/z)}{\mathcal{A}(x/z, k'_\perp, q'/z)}. \quad (27)$$

In the virtual case this is more complex. Here we find

$$\delta F_V[\varphi] = \frac{\tilde{P}(z, q'/z, k_\perp)}{2\pi z q'^2} \left( \frac{B + \delta B}{A + \delta A} - \frac{B}{A} \right) \approx \frac{\tilde{P}(z, q'/z, k_\perp)}{2\pi z q'^2} \frac{1}{A} \left( \delta B - B \frac{\delta A}{A} \right), \quad (28)$$

where

$$A \equiv \mathcal{A}(x, k_\perp, q') ; B \equiv \mathcal{A}(x/z, k'_\perp, q'/z). \quad (29)$$

These formulae can be used to give the weight associated with the uncertainty due to the updf. Of course, implementation of this weight in the CASCADE framework requires still some work. Once complete, however, use of this alternate weight during the fitting procedure should help improve overall predictions of the model.

## 7 Conclusion

We have presented a new approach to understanding the errors associated with a MC prediction. This approach can be added to almost all currently existing MC programs without changing the physics or the behaviour of the code. Instead, we have provided a method to track alternate weights for events. These alternate weights provide the tool to reshape MC predictions to see what such a prediction would be if various pieces of the MC were altered.

Though this technique is quite successful, it cannot compensate for all possible alterations. As this algorithm provides an alternate weight for an event generated by a MC it cannot provide events which cannot be generated by the original MC. This means that some of the physical limitations of an already existing code cannot be overcome through this method. We don't see this as a drawback, however. The purpose of this technique is to understand the physics and the limitations inherent in a MC implementation. To this end, such limitations of this technique can provide valuable insight.

This paper has provided numerical examples of a toy parton shower model based on the real MC behaviour of Herwig++ [3, 8]. It may be quite illustrative to apply this method to a fully featured general purpose MC, including hadronization and hadron decay, to see how much variation exists in such a parton shower implementation. With such an implementation one may be able to check the accuracy of many MC predictions and to understand the limitations of these predictions.

### *Acknowledgment*

The authors would like to thank S. Jadach and Z. Was for many useful discussions. Additionally, PS would like to thank H. Jung for suggesting the use of this method for the CASCADE fitting procedure.

## References

- [1] Grunewald, Martin W. and others (2000).
- [2] Gieseke, Stefan, JHEP **01**, 058 (2005).
- [3] Gieseke, S. and Ribon, A. and Seymour, M. H. and Stephens, P. and Webber, B., JHEP **02**, 005 (2004).
- [4] Sjostrand, Torbjorn and others, Comput. Phys. Commun. **135**, 238 (2001).
- [5] Jadach, S. and Skrzypek, M., Comput. Phys. Commun. **175**, 511 (2006).
- [6] Gleisberg, Tanju and others, JHEP **02**, 056 (2004).
- [7] Altarelli, G. and Parisi, G., Nucl. Phys. **B126**, 298 (1977).
- [8] Gieseke, S. and Stephens, P. and Webber, B., JHEP **12**, 045 (2003).
- [9] Furmanski, W. and Petronzio, R., Phys. Lett. **B97**, 437 (1980).

- [10] Curci, G. and Furmanski, W. and Petronzio, R., Nucl. Phys. **B175**, 27 (1980).
- [11] Jung, H. and Salam, G. P., Eur. Phys. J. **C19**, 351 (2001).
- [12] Marchesini, G. and Webber, B. R., Nucl. Phys. **B386**, 215 (1992).
- [13] Marchesini, G. and others, Comput. Phys. Commun. **67**, 465 (1992).

# Perturbative description of inclusive single hadron production at HERA

*S. Albino*

II. Institute for Theoretical Physics, University of Hamburg,  
Luruper Chaussee 149, 22761 Hamburg, Germany

## Abstract

Light charged hadron production data in the current fragmentation region at HERA are calculated using next-to-leading order perturbative calculations and fragmentation functions obtained from similar data from  $e^+e^-$  reactions. General good agreement is found at large photon virtuality  $Q^2$  and intermediate momentum fraction  $x_p$ , consistent with fragmentation function universality. The description of the small  $x_p$  and  $Q^2$  region is improved by incorporating hadron mass effects.

## 1 Introduction

Unpolarized quark fragmentation functions (FFs) for charge-sign unidentified light charged hadrons  $h^\pm = \pi^\pm, K^\pm$  and  $p/\bar{p}$  have been well constrained by data from  $e^+e^- \rightarrow h^\pm + X$  using calculations at next-to-leading order (NLO) accuracy. Due to universality in the factorization theorem, such FFs can be used to calculate the similar measurements of  $ep \rightarrow e + h^\pm + X$ . This contribution summarizes the main results of [1] comparing  $ep$  reaction data in the current fragmentation region from the H1 [2] and ZEUS [3] collaborations at HERA with calculations using FFs extracted from  $e^+e^-$  reactions.

The kinematic degrees of freedom are chosen to be the centre-of-mass energy  $\sqrt{s}$  of the initial state  $ep$  system, the magnitude of the hard photon's virtuality  $Q^2 = -q^2$ , the Bjorken scaling variable  $x = Q^2/(2P \cdot q)$  and the scaled detected hadron momentum  $x_p = 2p_h \cdot q/q^2$ . The normalized cross section (with the  $s$  dependence omitted for brevity) takes the form

$$F^{\text{proton } h^\pm}(\text{cuts}, x_{pA}, x_{pB}) = \frac{\int_{\text{cuts}} dQ^2 dx \int_{x_{pA}}^{x_{pB}} dx_p \frac{d\sigma^{\text{proton } h^\pm}}{dx_p dx dQ^2}(x, x_p, Q^2)}{\int_{\text{cuts}} dQ^2 dx \frac{d\sigma^{\text{proton}}}{dx dQ^2}(x, Q^2)}, \quad (1)$$

where “cuts” refers to a specified region in the  $(x, Q^2)$  plane, and where  $x_{pA(B)}$  is the lower (upper) edge of the  $x_p$  bin. The cross section and the kinematic variables are frame invariant, and are measured in the Breit frame, defined to be the frame where the photon energy vanishes. In this frame the target fragmentation region ( $x_p < 0$ ) contains the proton remnants, while the struck parton fragments into the current fragmentation region ( $x_p > 0$ ), and the latter process is equivalent to the fragmentation of a parton into an event hemisphere in  $e^+e^-$  reactions. The factorization theorem dictates that, at leading twist, the highly virtual photon undergoes hard scattering with a parton in the proton moving in the same direction and carrying away an energy / momentum fraction  $y$ . One of the partons produced in this scattering undergoes fragmentation to the observed hadron  $h^\pm$  moving in the same direction and carrying away an energy / momentum

fraction  $z$ . In other words, after the change of integration variables  $z \rightarrow x_p/z$  and  $y \rightarrow x/y$ , the factorized cross section in the numerator of Eq. (1) takes the form

$$\begin{aligned} \frac{d\sigma^{\text{proton } h^\pm}}{dx_p dx dQ^2}(x, x_p, Q^2) &= \int_{x_p}^1 \frac{dz}{z} \int_x^1 \frac{dy}{y} \sum_{ij} \frac{d\sigma^{ij}}{dz dy dQ^2} \left( y, z, \frac{Q^2}{\mu^2}, a_s(\mu^2) \right) \\ &\times f_i^{\text{proton}} \left( \frac{x}{y}, \mu^2 \right) D_j^{h^\pm} \left( \frac{x_p}{z}, \mu^2 \right), \end{aligned} \quad (2)$$

where  $f_i^{\text{proton}}$  is the parton distribution function (PDF) of parton  $i$  in the proton,  $D_j^{h^\pm}$  the FF of parton  $j$  to  $h^\pm$ ,  $d\sigma^{ij}$  the equivalent factorized partonic observable given to NLO in Ref. [4],  $\mu$  the factorization / renormalization scale which distinguishes the soft from the hard subprocesses and  $a_s(\mu^2) = \alpha_s(\mu)/(2\pi)$ .

## 2 Comparisons with data

At leading order in  $a_s$ , eq. (1) becomes

$$F^{\text{proton } h^\pm}(\text{cuts}, x_{pA}, x_{pB}) = \frac{\int_{x_{pA}}^{x_{pB}} dx_p \sum_I e_{q_I}^2(Q^2) G_I(Q^2) x_p D_I^{h^\pm}(x_p, Q^2)}{\sum_J e_{q_J}^2(Q^2) G_J(Q^2)}, \quad (3)$$

where the parton labels  $I, J$  are restricted to (anti)quarks  $q_I$  only, which have electric charges  $e_{q_I}$ , and  $G_I(Q^2) = \int_{\text{cuts}} dx x f_I^{\text{proton}}(x, Q^2)$ . In the limit that the  $G_I$  become independent of  $I$ , the numerator of Eq. (3) is equal to the equivalent LO result for  $e^+e^- \rightarrow h^\pm + X$ , and therefore the two types of observables are distinguished only by the  $G_I$ . If this discrepancy is small, a good description of HERA data is expected using FFs obtained from fits to  $e^+e^-$  data, such as the AKK [5], Kretzer [6] and KKP [7] FF sets<sup>1</sup> if universality and fixed order (FO) perturbation theory are reliable. Calculations using these sets for the H1 data are shown in Fig. 1, using the CTEQ6M PDF set [9] and the CYCLOPS program [10] here and throughout this work, unless otherwise stated. The strong disagreement between the FF sets at large  $x_p$  most likely arises from large experimental errors on the FFs due to poor constraints from  $e^+e^-$  reaction data at large momentum fraction. At high  $Q^2$ , the calculation for all 3 FF sets agrees well with the data. Therefore, the disagreements at large and small  $x_p$  values found with the lower  $Q^2$  data may be due to effects beyond the FO approach at leading twist. For example, resummation of soft gluon emission logarithms that become large at small and large  $x_p$  may be necessary to improve the calculation here. This is illustrated in Fig. 2 (left) by the effect of scale variation on the calculation, being largest at small and large  $x_p$ . The effect of the observed hadron's mass  $m_h$  is also important at small  $x_p$  for low  $Q^2$  values. For non-zero hadron mass, one has to distinguish between momentum, energy, light cone momentum etc., which are all equal when the hadron mass is negligible. According to the factorization theorem, the ‘‘momentum’’ fraction  $z$  appearing in eq. (2) is the fraction of light cone momentum carried away from the fragmenting parton by the observed hadron in a frame in which the spatial momenta of the virtual photon and the detected hadron are parallel, and  $x_p = \xi_p(1 - m_h^2/(Q^2\xi_p^2))$  should be replaced by the ratio of

<sup>1</sup>Since this work was completed, 3 further sets [8] have been extracted using improved theoretical and experimental input.

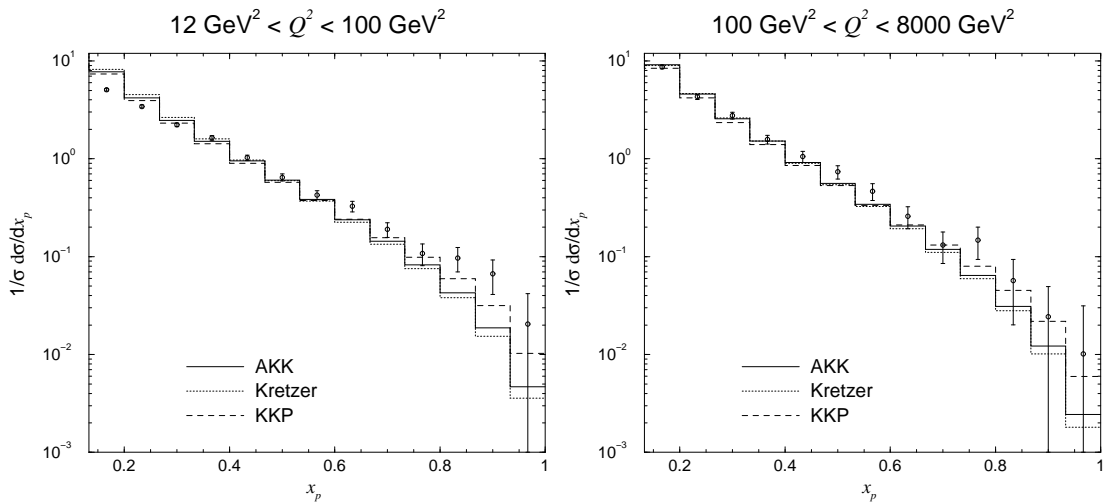


Fig. 1: Comparisons of theoretical predictions using the AKK, Kretzer and KKP FF sets with the  $x_p$  distributions from H1 [2].

the hadron's to the virtual photon's light cone momentum,  $\xi_p$ . Using this approach [1], one finds that the experimentally measured quantity  $d\sigma^{\text{proton } h^\pm}/dx_p dx dQ^2$  is related to the calculated quantity  $d\sigma^{\text{proton } h^\pm}/d\xi_p dx dQ^2$  by

$$\frac{d\sigma^{\text{proton } h^\pm}}{dx_p dx dQ^2}(x, x_p, Q^2) = \frac{1}{1 + \frac{m_h^2}{Q^2 \xi_p^2(x_p)}} \frac{d\sigma^{\text{proton } h^\pm}}{d\xi_p dx dQ^2}(x, \xi_p(x_p), Q^2), \quad (4)$$

which shows clearly that hadron mass effects become important at small  $x_p$  and low  $Q^2$ . According to Fig. 2, this correction improves the description in this region, if we compare the results of this figure with the low  $Q^2$  results of Fig. 1. The choice  $m_h = 0.5$  GeV represents an “average” mass for the light charged hadrons. We do not incorporate mass effects for the proton of the initial state, since this effect is expected to partially cancel between the numerator and denominator of eq. (1). By redoing the calculation with the MRST2001 PDF set [11], we see that the dependence on the choice of PDF set is small, particularly at small  $x_p$ , most likely because these quantities are well constrained but also because any variations in them are partially canceled between the numerator and denominator of eq. (1). As for  $e^+e^-$  reactions, the dependence on the gluon FF is small, particularly at large  $x_p$ .

To further verify these observations and inferences, we perform similar calculations for the ZEUS data. The different FF sets lead to similar results and good agreement with the data at large  $Q^2$  and intermediate  $x_p$  (Fig. 3). The scale variation (Fig. 4, top) generally decreases with increasing  $Q^2$ , and is largest for small  $x_p$ . Both hadron mass effects and gluon fragmentation are most important at low  $Q^2$  and small  $x_p$  (Fig. 4, bottom).



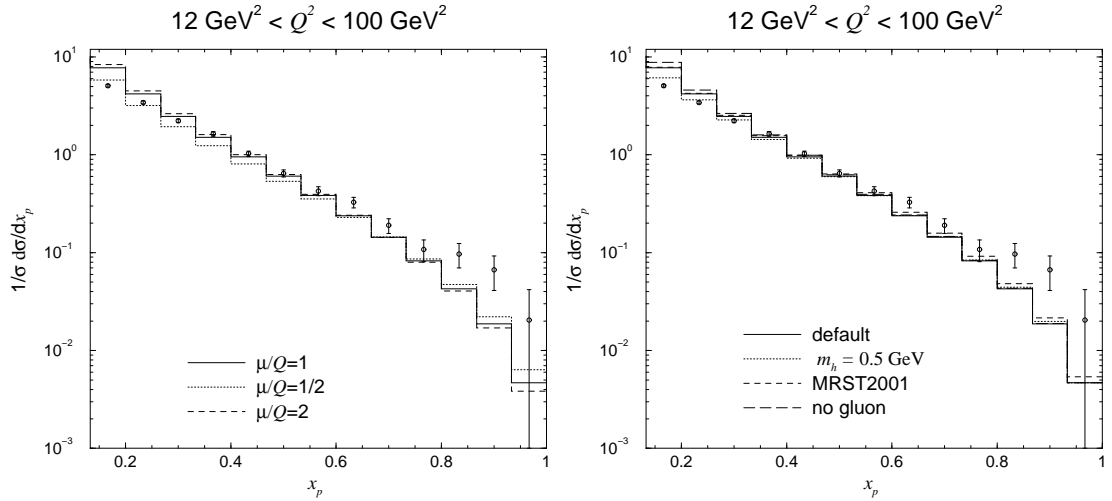


Fig. 2: As in Fig. 1, using only the AKK FF set. Left: The modifications arising from scale variation. Right: The modifications to the default predictions (solid line) arising from the replacement of the CTEQ6M PDF set by the MRST2001 PDF set of Ref. [11], from the removal of the evolved gluon, and from the incorporation of the hadron mass effect are shown.

### 3 Conclusions

High  $Q^2$  measurements of inclusive single hadron production at HERA are well described by perturbative QCD in the framework of the factorization theorem using available FF sets. Although some disagreement is found with data at lower  $Q^2$ , we note that there is significant room for improvement in the theory in this region, such as hadron mass effects studied in this work, but also resummation of the FO series at small and large  $x_p$ , higher twist effects and quark mass effects. Whether such effects are in fact relevant can be better verified by the effect of incorporating such data into global fits of FFs. More importantly, such data may also provide valuable information on the FFs' quark flavour components not constrained by  $e^+e^-$  reaction data, particularly since these type of HERA measurements may now be made very precisely [12]. However, in order to constrain FFs for each hadron species individually, and to ensure that the data is not contaminated by light charged particles other than  $\pi^\pm$ ,  $K^\pm$  and  $p/\bar{p}$ , the hadron species of the HERA data need to be identified.

### Acknowledgments

The author thanks Bernd A. Kniehl, Gustav Kramer and Carlos Sandoval for collaboration.

### References

- [1] S. Albino, B. A. Kniehl, G. Kramer and C. Sandoval, Phys. Rev. D **75**, 034018 (2007).
- [2] C. Adloff *et al.* [H1 Collaboration], Nucl. Phys. B **504**, 3 (1997).

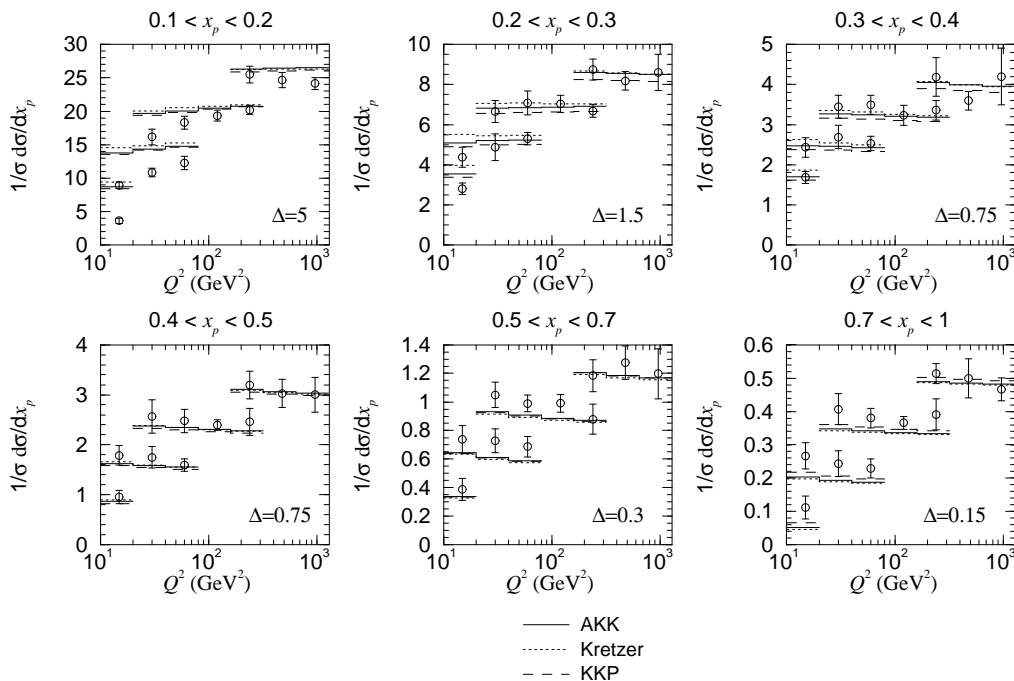


Fig. 3: As in Fig. 1, but for the ZEUS data [3]. Each data set is measured in a specific  $x_p$ -bin and, together with its predictions, is shifted upward relative to the one below by the indicated value for  $\Delta$ .

- [3] J. Breitweg *et al.* [ZEUS Collaboration], Phys. Lett. B **414**, 428 (1997).
- [4] G. Altarelli, R. K. Ellis, G. Martinelli, and S. Y. Pi, Nucl. Phys. B **160**, 301 (1979).
- [5] S. Albino, B. A. Kniehl, and G. Kramer, Nucl. Phys. B **725**, 181 (2005).
- [6] S. Kretzer, Phys. Rev. D **62**, 054001 (2000).
- [7] B.A. Kniehl, G. Kramer, and B. Pötter, Nucl. Phys. B **582**, 514 (2000).
- [8] M. Hira, S. Kumano, T. H. Nagai and K. Sudoh, Phys. Rev. D **75** (2007) 094009; D. de Florian, R. Sassot and M. Stratmann Phys. Rev. D **75** 114010 (2007); Phys. Rev. D **76** 074033 (2007); S. Albino, B. A. Kniehl and G. Kramer, Nucl. Phys. B **803** (2008) 42.
- [9] J. Pumplin, D. R. Stump, J. Huston, H. L. Lai, P. Nadolsky, and W. K. Tung, JHEP **0207**, 012 (2002).
- [10] D. Graudenz, Fortsch. Phys. **45**, 629 (1997).
- [11] A. D. Martin, R. G. Roberts, W. J. Stirling, and R. S. Thorne, Eur. Phys. J. C **23**, 73 (2002).
- [12] F. D. Aaron *et al.* [H1 Collaboration], Phys. Lett. B **654**, 148 (2007); B. Brzozowska [ZEUS Collaboration], prepared for the 15th International Workshop on Deep-Inelastic Scattering and Related Subjects (DIS2007), Munich, Germany, April 2007.

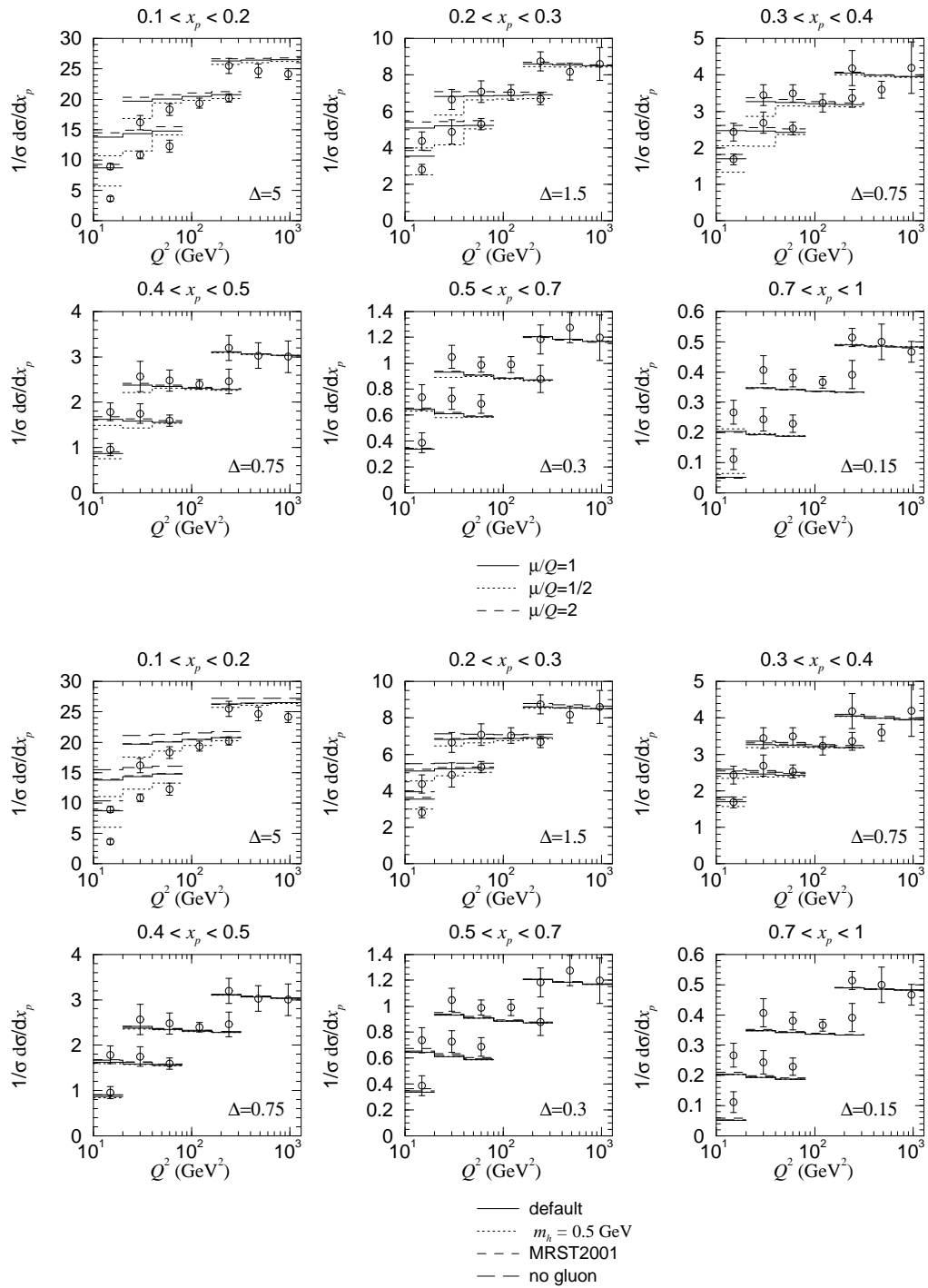


Fig. 4: As in Fig. 2, but for the ZEUS data [3].

# Non-perturbative corrections from an s-channel approach

*F. Hautmann*

Department of Theoretical Physics, University of Oxford, Oxford OX1 3NP

## Abstract

We report on studies of multi-parton corrections from nonlocal operator expansion. We discuss relations between eikonal-line matrix elements and parton distributions, and present an illustration for initial-state collinear evolution.

## 1 Introduction

Non-perturbative dynamics affects the structure of LHC events even for high momentum transfer, through hadronization, soft underlying scattering, multiple hard interactions. Models for these processes are necessary, for instance, for Monte Carlo generators to produce realistic event simulations.

The treatment of multiple parton interactions in QCD will require methods that go beyond the local operator expansion, and likely involve fully unintegrated parton correlation functions [1]. Besides the relevance for event generators, this should also provide a natural framework for the investigation at the LHC of possible new strong-interaction effects at very high energies, including parton saturation [2].

This report is based on the analysis [3] of nonlocal operator expansion, investigating corrections from graphs with multiple gluon exchange. The point of view in this study is to connect the treatment of multi-gluon contributions with formulations in terms of standard partonic operators, and in this respect it can be seen as deriving from the approach of [4]. We present an illustration for the case of structure functions. This case is also treated in the analyses of [5]. More discussion may be found in [6]. The formulation discussed below trades parton distribution functions for moments of eikonal-line correlators. We expect this formulation to be useful also for the treatment of the associated final-state distributions.

## 2 From parton distribution functions to eikonal-line matrix elements

The analysis [3] starts with the quark distribution function, defined as

$$f_q(x, \mu) = \frac{1}{4\pi} \int dy^- e^{ixP^+y^-} \langle P | \bar{\psi}(0) Q(0) \gamma^+ Q^\dagger(y^-) \psi(0, y^-, \mathbf{0}) | P \rangle_c \quad (1)$$

where  $\psi$  is the quark field,  $Q$  is the gauge link, and the subscript  $c$  is the instruction to take connected graphs. The matrix element (1) can be rewritten as the real part of a forward scattering amplitude [3], in which we think of the operator  $Q^\dagger \psi$  as creating an antiquark plus an eikonal line in the minus direction, starting at distance  $y^-$  from the position of the target.

Next, supposing that  $x$  is small, we treat the evolution of the antiquark-eikonal system in a hamiltonian framework (see [3] and references therein) which allows us to express the evolution operator in the high-energy approximation as an expansion in Wilson-line matrix elements. The leading term of this is (“dipole” term)

$$\Xi(z, \mathbf{b}) = \int [dP'] \langle P' | \frac{1}{N_c} \text{Tr} \{ 1 - F^\dagger(\mathbf{b} + \mathbf{z}/2) F(\mathbf{b} - \mathbf{z}/2) \} | P \rangle , \quad (2)$$

where  $F$  is the eikonal operator

$$F(\mathbf{r}) = \mathcal{P} \exp \left\{ -ig \int_{-\infty}^{+\infty} dz^- \mathcal{A}_a^+(0, z^-, \mathbf{r}) t_a \right\} , \quad (3)$$

$\mathbf{z}$  is the transverse separation between the eikonals in (2), and  $\mathbf{b}$  is the impact parameter.

In this representation the quark distribution (1) is given by the coordinate-space convolution

$$xf_q(x, \mu) = \int d\mathbf{b} dz u(\mu, \mathbf{z}) \Xi(\mathbf{z}, \mathbf{b}) - UV . \quad (4)$$

In [3] the explicit result is given for the function  $u(\mu, \mathbf{z})$  at one loop in dimensional regularization and for the counterterm  $-UV$  of  $\overline{\text{MS}}$  renormalization. The  $\overline{\text{MS}}$  result can also be recast in a physically more transparent form in terms of a cut-off on the  $\mathbf{z}$  integration region, as long as the scale  $\mu$  is sufficiently large compared to the inverse hadron radius:

$$xf_q(x, \mu) = \frac{N_c}{3\pi^4} \int d\mathbf{b} \frac{d\mathbf{z}}{z^4} \theta(z^2 \mu^2 > a^2) \Xi(\mathbf{z}, \mathbf{b}) , \quad (5)$$

where  $a$  is a renormalization scheme dependent coefficient given in [3].

The Wilson-line matrix element  $\Xi(\mathbf{z}, \mathbf{b})$  receives contribution from both long distances and short distances. At small  $\mathbf{z}$  it may be treated by a short distance expansion. At large  $\mathbf{z}$  it should be parameterized consistently with bounds from unitarity and saturation [2] and determined from data.

### 3 An algebraic relation for eikonal operators

A general relation between fundamental and adjoint representation for  $\Xi$ , valid for any distance  $\mathbf{z}$ , is given in [3], based on the algebraic relation

$$\begin{aligned} \frac{1}{N_c^2 - 1} \text{Tr} [1 - U^\dagger(\mathbf{z}) U(\mathbf{0})] &= \frac{C_A}{C_F} \frac{1}{N_c} \text{Re Tr} [1 - V^\dagger(\mathbf{z}) V(\mathbf{0})] \\ &- \frac{1}{2} \frac{C_A}{C_F} \frac{1}{N_c^2} |\text{Tr} [1 - V^\dagger(\mathbf{z}) V(\mathbf{0})]|^2 \end{aligned} \quad (6)$$

with  $V = F_{\text{fund.}}$ ,  $U = F_{\text{adj.}}$ .

From this one can obtain small- $\mathbf{z}$  relations connecting  $\Xi$  to the gluon distribution. For instance, for the fundamental representation at small  $\mathbf{z}$  this yields

$$\Xi(\mathbf{b}, \mathbf{z}) = z^2 \frac{\pi^2 \alpha_s}{2N_c} xG(x, \mu) \phi(\mathbf{b}), \quad (7)$$

where by  $xG$  we denote the gluon distribution (either the  $x_c$ -scale or weighted-average expressions in [3]), and  $\phi(\mathbf{b})$  obeys

$$\int d\mathbf{b} \phi(\mathbf{b}) = 1. \quad (8)$$

The result for  $\Xi$  in the fundamental representation corresponds directly to the one for the dipole cross section in the saturation model [2]. Results in the fundamental and adjoint cases are relevant to discuss quark saturation and gluon saturation.

#### 4 Power-suppressed contributions

In the s-channel framework of [3] contributions to hard processes suppressed by powers of the hard scale are controlled by moments of  $\Xi$ ,

$$\mathcal{M}_p = \frac{2^{2p} p}{\Gamma(1-p)} \int \frac{dz}{\pi z^2} (z^2)^{-p} \int d\mathbf{b} \Xi(z, \mathbf{b}) , \quad (9)$$

analytically continued for  $p > 1$ . Models for the dipole scattering function including saturation are reviewed in [2]. In this case the moments (9) are proportional to integrals over impact parameter of powers of the saturation scale. Higher moments are obtained from derivatives with respect to  $p$ ,

$$\mathcal{M}_{p,0} \simeq \int d\mathbf{b} [Q_s^2(\mathbf{b})]^p , \quad \mathcal{M}_{p,k} \simeq (-1)^k \frac{d^k}{dp^k} \mathcal{M}_{p,0} . \quad (10)$$

As an illustration, we determine the  $C_A/x$  part of the coefficients of the first subleading power correction from the s-channel for transverse and longitudinal structure functions  $F_T, F_L$ . Denoting the  $Q^2$  derivative by  $\dot{F}_j = dF_j/d\ln Q^2$  for  $j = T, L$ , and its leading-power contribution by  $F_{j,lead.}$ , one has

$$\dot{F}_j - \dot{F}_{j,lead.} = b_{j,0} \mathcal{M}_{2,0}/Q^2 + b_{j,1} \mathcal{M}_{2,1}/Q^2 + \dots \quad (11)$$

Structure functions can be analyzed in the same way [3] as described in Sec. 2 for the quark distribution function. The main difference compared to the case of the quark distribution (1) is that the ultraviolet region of small  $z$  is now regulated by the physical scale  $Q^2$  rather than requiring, e.g.,  $\overline{\text{MS}}$  renormalization. Saturation is reobtained [3] within the dipole approximation [2]. By the analysis based on (6),(7) the saturation scale  $Q_s(\mathbf{b})$  for a dipole in the fundamental representation is

$$Q_s^2(\mathbf{b}) = \frac{2\pi^2\alpha_s}{N_c} xG(x, \mu) \phi(\mathbf{b}). \quad (12)$$

To study the expansion in powers of  $1/Q^2$  it is convenient to go to Mellin moment space by representing  $\Xi$  via the Mellin transform

$$\Xi(z, \mathbf{b}) = z^2 \int_{a-i\infty}^{a+i\infty} \frac{du}{2\pi i} (z^2)^{-u} \tilde{\Xi}(u, \mathbf{b}) , \quad (13)$$

$0 < a < 1$ . Then the structure functions  $F_{T,L}$  have the representation

$$xF_{T,L} = \int d\mathbf{b} \int_{a-i\infty}^{a+i\infty} \frac{du}{2\pi i} \tilde{\Xi}(u, \mathbf{b}) \Phi_{T,L}(u) , \quad (14)$$

where  $\Phi_{T,L}(u)$  can be read from [7] and are given by

$$\Phi_T(u) = \langle e_a^2 \rangle \frac{N_c}{4^{u+2}\pi^2} (Q^2)^u \frac{\Gamma(3-u)\Gamma(2-u)\Gamma(1-u)}{\Gamma(5/2-u)\Gamma(3/2+u)} (1+u) \Gamma(u), \quad (15)$$

$$\Phi_L(u) = \langle e_a^2 \rangle \frac{N_c}{4^{u+2}\pi^2} (Q^2)^u \frac{[\Gamma(2-u)]^3}{\Gamma(5/2-u)\Gamma(3/2+u)} 2 \Gamma(1+u), \quad (16)$$

with  $\Gamma$  the Euler gamma function. The expansion in  $1/Q^2$  of (14) is controlled by the singularity structure of the integrand in the  $u$ -plane [3, 5, 6]. Eqs. (15),(16) show that longitudinal  $\Phi_L$  has no pole at  $u = 0$ , so that the leading singularity is given by the  $u = 0$  pole in  $\Xi$ , while the first subleading pole  $u = -1$  is absent in transverse  $\Phi_T$  due to the numerator factor  $(1+u)$ , so that the answer for the transverse case at next-to-leading level is determined by the singularity in  $\Xi$ , with  $\Phi$  contributing to the coefficient of the residue.

It can be verified that contributions to (14) in the lowest  $p = 1$  moments in Eq. (10) correctly reproduce the small- $x$  gluon part of renormalization-group evolution,

$$\begin{aligned} \dot{F}_{T,lead.} &= \langle e_a^2 \rangle \frac{\alpha_s}{2\pi} \int_x^1 dz \frac{[z^2 + (1-z)^2]}{z} f_g\left(\frac{x}{z}, Q\right) + \text{quark term} \\ &\simeq \langle e_a^2 \rangle \frac{\alpha_s}{2\pi} \frac{1}{3} G + \text{quark term} , \end{aligned} \quad (17)$$

using (8),(12) and the gluon distribution  $G$  evaluated at the average [3]  $x \simeq x_c$ , with the lowest  $x$ -moment of the gluon  $\rightarrow$  quark splitting function

$$\int_0^1 dz P_{qg}(z) = \int_0^1 dz [z^2 + (1-z)^2]/2 = 1/3 . \quad (18)$$

Beyond leading power, the first subleading corrections read

$$\dot{F}_T - \dot{F}_{T,lead.} = -\langle e_a^2 \rangle \frac{C_A}{20\pi^3 x} \frac{1}{Q^2} \int d\mathbf{b} [Q_s^2(\mathbf{b})]^2 + \dots , \quad (19)$$

$$\begin{aligned} \dot{F}_L - \dot{F}_{L,lead.} &= -\langle e_a^2 \rangle \frac{C_A}{15\pi^3 x} \left[ \frac{14}{15} + \psi(1) \right] \frac{1}{Q^2} \int d\mathbf{b} [Q_s^2(\mathbf{b})]^2 \\ &+ \langle e_a^2 \rangle \frac{C_A}{15\pi^3 x} \frac{1}{Q^2} \int d\mathbf{b} [Q_s^2(\mathbf{b})]^2 \ln[Q^2/Q_s^2(\mathbf{b})] + \dots . \end{aligned} \quad (20)$$

That is, the  $b$  coefficients in (11) are given by

$$\begin{aligned} b_{T,0} &= -\langle e_a^2 \rangle C_A / (20\pi^3 x) , & b_{T,1} &= 0 , \\ b_{L,0} &= -\langle e_a^2 \rangle C_A [14/225 + \psi(1)/15] / (\pi^3 x) , & b_{L,1} &= \langle e_a^2 \rangle C_A / (15\pi^3 x) , \end{aligned} \quad (21)$$

with  $\psi$  the Euler psi function.

Via process-dependent coefficients analogous to those in (11), the eikonal-operator moments (9) will also control power-like contributions to the associated jet cross sections due to multi-parton interactions in the initial state. At present these processes are modeled by Monte Carlo, which point to their quantitative significance for the proper simulation of hard events at the LHC. The above discussion also suggests the potential usefulness in this context of analyzing jet and structure function data by trading parton distribution functions for s-channel correlators defined according to the method of Sec. 2.

## References

- [1] T.C. Rogers, Phys. Rev. **D78**, 074018 (2008);  
T.C. Rogers, arXiv:0712.1195 [hep-ph] (2007).
- [2] L. Motyka, K. Golec-Biernat and G. Watt, arXiv:0809.4191 [hep-ph] (2008).
- [3] F. Hautmann and D.E. Soper, Phys. Rev. **D75**, 074020 (2007);  
F. Hautmann, Phys. Lett. **B643**, 171 (2006).
- [4] A.P. Bukhvostov, G.V. Frolov, L.N. Lipatov and E.A. Kuraev, Nucl. Phys. **B258**, 601 (1985).
- [5] J. Bartels, C. Bontus and H. Spiesberger, arXiv:hep-ph/9908411 (1999);  
J. Bartels and C. Bontus, Phys. Rev. **D61**, 034009 (2000);  
J. Bartels, K. Golec-Biernat and K. Peters, Eur. Phys. J. **C17**, 121 (2000).
- [6] F. Hautmann, arXiv:0802.1178 [hep-ph] (2008).
- [7] S. Catani and F. Hautmann, Nucl. Phys. **B427**, 475 (1994);  
S. Catani, M. Ciafaloni and F. Hautmann, Nucl. Phys. **B366**, 135 (1991);  
S. Catani, M. Ciafaloni and F. Hautmann, Phys. Lett. **B242**, 97 (1990).



# Single top production in the $Wt$ mode with MC@NLO

Chris D. White

Nikhef, Kruislaan 409, 1058AG Amsterdam, The Netherlands

## Abstract

We consider whether it is possible to isolate single top production in the  $Wt$  mode as a process at the LHC. A precise definition of this mode becomes problematic beyond leading order due to interference with  $t\bar{t}$  production. We give two definitions of the  $Wt$  mode whose difference mainly measures this interference, and implement both in the MC@NLO program. Comparison of the results allows us to conclude that is indeed feasible to try to separate the  $t\bar{t}$  and  $Wt$  processes, subject to adequate cuts.

## 1 Introduction

Single top physics is of great interest at the Tevatron and LHC both within and beyond the Standard Model. Firstly, it allows detailed scrutiny of the electroweak interactions of the top quark e.g. a direct measurement of  $V_{tb}$ . Secondly, the fact the mass of the top quark lies around the electroweak scale means that the top sector could be a sensitive probe of new physics. In the Standard Model, there are three ways to produce a single top quark. The least well understood of these is the  $Wt$  mode, in which the final state top quark is accompanied by a  $W$  boson. Although rather too small to be observed at the Tevatron, the cross-section is significant at the LHC (i.e. about 20% of the total single top cross-section).

At LO, the  $Wt$  mode has a well-defined cross-section, which is much smaller than that of  $t\bar{t}$  production. At NLO, however, a problem arises due to the real emission contributions shown in Fig. 1. These essentially consist of  $t\bar{t}$  production at LO, followed by the decay of the antitop, and result in a very large correction to the LO  $Wt$  cross-section. This large NLO contribution results from regions of the phase space where the invariant mass  $m_{bW}$  of the  $W\bar{b}$  pair becomes equal to the top mass i.e. when the antitop propagator becomes resonant. The question then arises as to whether it is still possible to define the  $Wt$  mode in such a way that it can be measured independently of top pair production at the LHC. This issue can only be fully addressed in the MC@NLO framework, in which a NLO matrix element is matched with a parton shower, due

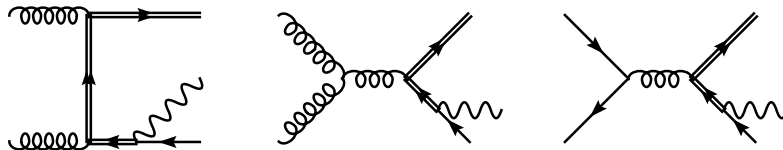


Fig. 1: Doubly resonant contributions to the  $Wt$  mode.

to the fact that the interference problem manifests itself at NLO and beyond. Furthermore, it is only in the presence of initial and final state showers that one has sufficiently realistic final states, which one may be reasonably confident of having an experimental applicable definition.

It could be argued that instead of isolating the  $Wt$  mode by itself, one should consider sums of processes with a given final state (in this case  $W^+W^-b(\bar{b})$ ), as was done in the present context in [1]. However, such approaches are problematic given that NLO QCD corrections cannot be included. One knows, for example, that NLO corrections to  $t\bar{t}$  production are large. This casts doubt on the accuracy of more inclusive approaches. Furthermore, it is unduly pessimistic to assume that interference with  $t\bar{t}$  prevents the practical definition of the  $Wt$  mode. It is phenomenologically desirable to isolate this process, and if it can be done then this should be investigated fully. Furthermore, a suitable definition allows full NLO QCD corrections to be implemented, thus leads to the most accurate description.

The problem of isolating  $Wt$  production has been considered before in the literature, as it is necessary in any calculation beyond LO. Previous ideas for solving the interference problem include restricting  $m_{bW}$  directly so as to lie away from the top mass [2], or implementing a global subtraction term to remove the resonant  $t\bar{t}$  contribution [3]. These methods were defined at the total cross-section level. A fully differential NLO definition was given in [4]. There, a transverse momentum veto was implemented on the  $b$  quark which did not originate from the top, if such a  $b$  was present. Harder  $b$  quarks tend to have originated from a  $\bar{t}$  decay, thus such a veto can be used to filter out the  $t\bar{t}$  contribution. Also in [4], some matrix elements with problematic initial states were removed ( $\bar{q}q$  in all cases, and  $gg$  if the factorisation scale was equal to the transverse momentum veto).

Whilst these solutions work well at the purely NLO level, they are not immediately applicable beyond this e.g. in a real experiment it is not possible to ascertain which decay products originated from a given particle in the hard matrix element. The removal of particular initial states is also theoretically problematic. Firstly, it violates renormalisation group invariance - thus invalidating one of the main motivations for going to NLO (i.e. reduced scale dependence). Secondly, removal of particular initial states is not meaningful in the presence of initial state showers, which mix different partonic subchannels. Nevertheless, we will see that some of the preceding ideas can be generalised in order to suitably define the  $Wt$  mode at the MC@NLO level.

## 2 Two definitions of the $Wt$ mode

We have given two independent definitions of the  $Wt$  mode, both of which are applicable locally in phase space and to all orders in the perturbation expansion. By comparing results from the two definitions, we can be confident that theoretical ambiguities in each definition are under control. Our two definitions are named as follows:

1. **DIAGRAM REMOVAL (DR)**. Here one simply removes double resonant diagrams from the  $Wt$  amplitude.
2. **DIAGRAM SUBTRACTION (DS)**. Here one modifies the naïve  $Wt$  cross-section with a subtraction term, which removes the  $t\bar{t}$  resonant contribution locally in phase space.

The difference between the definitions arises from the fact that the subtraction is carried out at the amplitude and cross-section levels respectively. Thus, the difference between DR and DS mainly measures the interference term between the  $Wt$  and  $t\bar{t}$  production modes.

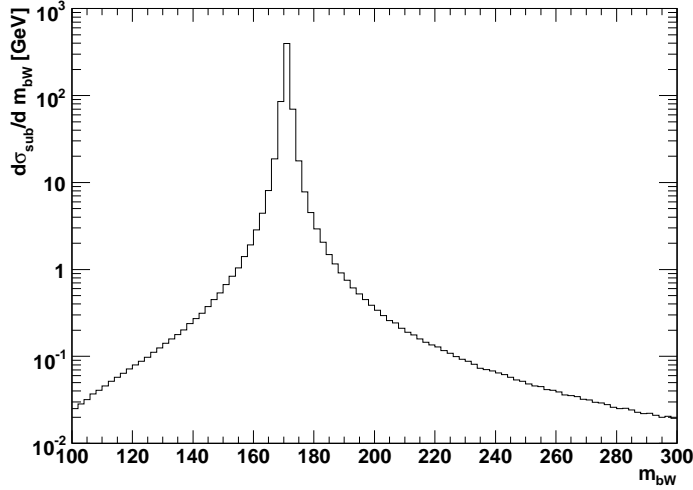


Fig. 2: The subtraction term used to form the DS cross-section, as a function of the invariant mass  $m_{bW}$  of the  $W\bar{b}$  pair.

Each of the approaches has some theoretical difficulty. DR, for example, violates QCD gauge invariance. We performed detailed checks in a number of gauges to establish that this is not a problem in practice. In DS, there are some ambiguities in how one forms the subtraction term. All one ultimately requires is that it be strongly peaked when  $m_{bW} \simeq m_t$ , and that it falls away quickly as  $m_{bW}$  moves away from the top mass. We thus use a local subtraction term:

$$d\sigma_{sub} = |\tilde{A}(tW\bar{b})_{t\bar{t}}|^2 \times \frac{f_{BW}(m_{bW})}{f_{BW}(m_t)}. \quad (1)$$

Here  $\tilde{A}(tW\bar{b})_{t\bar{t}}$  is the amplitude for  $tW\bar{b}$  production coming from  $t\bar{t}$ -like diagrams, where the kinematics are reshuffled to place the  $\bar{t}$  on-shell. This is then damped by a ratio of Breit-Wigner functions  $f_{BW}$  when the invariant mass  $m_{bW}$  lies away from the top mass  $m_t$ . For more details see [5]. A plot of our subtraction term is shown as a function of  $m_{bW}$  in Fig. 2. One can see that it is indeed strongly peaked when  $m_{bW} \rightarrow m_t$ , and falls off quickly for other values of  $m_{bW}$ . It cannot be zero for  $m_{bW} \neq m_t$  without violating gauge invariance, as happens in the DR definition. Having given two definitions of the  $Wt$  mode which are directly applicable in an all orders calculation, we have implemented both of them in the MC@NLO package of [6]. This required the recalculation of the  $Wt$  cross-section in the subtraction formalism of [7], and now completes the description of single top production modes in MC@NLO, as the  $s$  and  $t$ -channel modes have already been included [8]. Spin correlations of decay products were implemented for the DR cross-section using the method of [9].

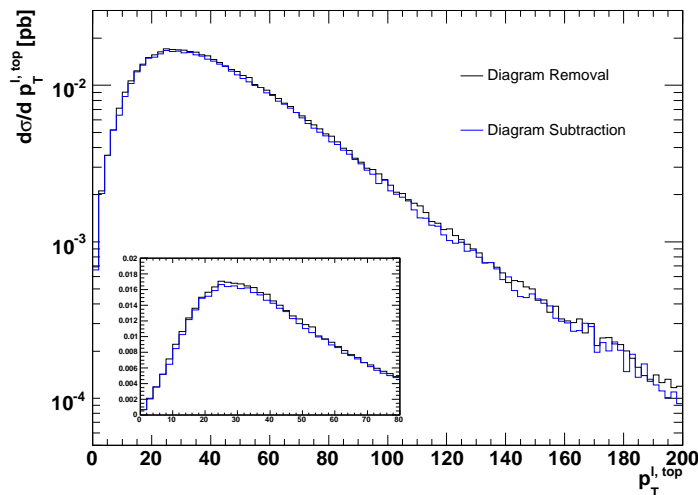


Fig. 3: Transverse momentum spectrum of the lepton from the top decay in both the DR and DS approaches, for  $p_{t,veto} = 50\text{GeV}$ .

### 3 Results

We considered example results in which all final state heavy particles decay leptonically. Furthermore, in order to address in more detail the issue of separation of the  $t\bar{t}$  and  $Wt$  processes, we implemented a transverse momentum veto on the second hardest  $B$  hadron by analogy with [4]. That is, events are *not* accepted if they contain a second hardest  $B$  hadron whose pseudo-rapidity satisfies  $|\eta| < 2.5$  and which has a transverse momentum  $p_t^b < p_{t,veto}$ . This then acts to reduce the interference term between  $Wt$  and  $t\bar{t}$ , due to the fact that harder  $b$  quarks tend to originate from a top decay.

We studied a number of observables, and compared the results from the DS and DR definitions of the  $Wt$  mode for various choices of  $p_{t,veto}$ . As a worst case scenario among the observables studied, we present results for the transverse momentum spectrum of the lepton from the top decay in Fig. 3. The results from the two definitions agree closely, except for at very high transverse momenta. However, the cross-section is small here. We also examined the effect of spin correlations, and of varying renormalisation and factorisation scales. These latter effects were larger than that arising from the difference between the DR and DS definitions in all cases.

### 4 Conclusion

QCD corrections threaten to undermine the definition of the  $Wt$  mode beyond LO due to interference with  $t\bar{t}$  production. However, it is of clear phenomenological interest to be able to separate the former process in its own right. We have given two workable definitions of this process, implemented in the MC@NLO framework, such that the difference between the definitions mostly measures the interference between  $Wt$  and  $t\bar{t}$  production.

Comparison of results obtained from the two definitions suggests that they agree closely subject to adequate cuts, and thus that it seems feasible to attempt to isolate  $Wt$  production at the LHC. Although further phenomenological analysis is needed to determine whether the  $t\bar{t}$  background itself can be sufficiently reduced, the resulting MC@NLO codes nevertheless represent the state of the art description of the  $Wt$  mode.

### Acknowledgements

This work was done in collaboration with S. Frixione, E. Laenen, P. Motylinski and B. Webber. CDW is supported by the Dutch National Foundation for Fundamental Physics Research (FOM).

### References

- [1] Kersevan, Borut Paul and Hinchliffe, Ian, *JHEP* **09**, 033 (2006).
- [2] Belyaev, A. S. and Boos, E. E. and Dudko, L. V., *Phys. Rev.* **D59**, 075001 (1999).
- [3] Tait, Tim M. P., *Phys. Rev.* **D61**, 034001 (2000).
- [4] Campbell, John and Tramontano, Francesco, *Nucl. Phys.* **B726**, 109 (2005).
- [5] Frixione, Stefano and Laenen, Eric and Motylinski, Patrick and Webber, Bryan R. and White, Chris D., *JHEP* **07**, 029 (2008).
- [6] Frixione, Stefano and Webber, Bryan R., *JHEP* **06**, 029 (2002).
- [7] Frixione, S. and Kunszt, Z. and Signer, A., *Nucl. Phys.* **B467**, 399 (1996).
- [8] Frixione, Stefano and Laenen, Eric and Motylinski, Patrick and Webber, Bryan R., *JHEP* **03**, 092 (2006).
- [9] Frixione, Stefano and Laenen, Eric and Motylinski, Patrick and Webber, Bryan R., *JHEP* **04**, 081 (2007).

# PYTHIA 8 Status Report

*Torbjörn Sjöstrand*

Department of Theoretical Physics, Lund University

## Abstract

PYTHIA 8, the C++ rewrite of the commonly-used PYTHIA event generator, is now available in a first full-fledged version 8.1. The older PYTHIA 6.4 generator in Fortran 77 is still maintained, for now, but users are strongly recommended to try out and move to the new version as soon as feasible.

## 1 Introduction

The “Lund Monte Carlo” family of event generators started in 1978 with the JETSET program. PYTHIA was begun a few years later, and the two eventually were joined under the PYTHIA label. Over the last 25 years the PYTHIA/JETSET program has been widely used to help understand the physics of high-energy collisions.

The program was from the onset written in Fortran 77, up to the current version 6.4 [1]. However, following the move of the experimental community to C++, a corresponding restart and rewrite was made for PYTHIA in 2004 – 2007, with most aspects cleaned up and modernized.

The first production quality release, PYTHIA 8.100, appeared towards the end of 2007 [2]. It was paced to arrive in time for LHC and therefore does not yet cover some physics topics. It has not yet caught on in the LHC experimental collaborations, however, and thus the older Fortran code is still maintained, even if at a reduced level.

## 2 Physics summary

Here follows a brief summary of the key physics aspects of PYTHIA 8.1, by topic.

**Hard processes:** The built-in library contains many leading-order processes, for the Standard Model almost all  $2 \rightarrow 1$  and  $2 \rightarrow 2$  ones and a few  $2 \rightarrow 3$ , beyond it a sprinkling of different processes, but not yet Supersymmetry or Technicolor. Parton-level events can also be input from external matrix-element-based generators, e.g. using Les Houches Event Files [3]. Also runtime interfaces are possible, and one such is provided to PYTHIA 6.4 for the generation of legacy processes. Resonance decays are included, often but not always with full angular correlations.

**Parton showers:** Transverse-momentum-ordered showers are used both for initial- and final-state radiation, the former based on backwards evolution. Implemented branchings are  $q \rightarrow qg$ ,  $g \rightarrow gg$ ,  $g \rightarrow q\bar{q}$ ,  $f \rightarrow f\gamma$  ( $f$  is a quark or lepton) and  $\gamma \rightarrow f\bar{f}$ . Recoils are handled in a dipole-style approach, but emissions are still associated with one emitting parton. Many processes include matching to matrix elements for the first (= hardest) emission; this especially concerns gluon emission in resonance decays.

**Underlying events and minimum-bias events:** PYTHIA implements a formalism with multiple parton-parton interactions, based on the standard QCD matrix elements for  $2 \rightarrow 2$

processes, dampened in the  $p_{\perp} \rightarrow 0$  limit. The collision rate is impact-parameter-dependent, and collisions are ordered in decreasing  $p_{\perp}$ . Multiple interactions (MI) are therefore combined with initial- and final-state radiation (ISR and FSR) in one common sequence of decreasing transverse momenta  $p_{\perp 1} > p_{\perp 2} > p_{\perp 3} \dots$ ,

$$\begin{aligned} \frac{d\mathcal{P}}{dp_{\perp}} \Big|_{p_{\perp}=p_{\perp i}} &= \left( \frac{d\mathcal{P}_{\text{MI}}}{dp_{\perp}} + \sum \frac{d\mathcal{P}_{\text{ISR}}}{dp_{\perp}} + \sum \frac{d\mathcal{P}_{\text{FSR}}}{dp_{\perp}} \right) \\ &\times \exp \left( - \int_{p_{\perp}}^{p_{\perp i-1}} \left( \frac{d\mathcal{P}_{\text{MI}}}{dp'_{\perp}} + \sum \frac{d\mathcal{P}_{\text{ISR}}}{dp'_{\perp}} + \sum \frac{d\mathcal{P}_{\text{FSR}}}{dp'_{\perp}} \right) dp'_{\perp} \right), \end{aligned}$$

using the “winner takes all” Monte Carlo strategy. This leads to a competition, in particular between MI and ISR, for beam momentum. The beam remnants are colour-connected to the interacting subsystems, with a detailed modelling of the flavour and momentum structure, also for the parton densities to be used at each successive step. The framework also contains a model for colour reconnection, likely the least well understood aspect of this physics area, and therefore one that may require further development.

**Hadronization:** The Lund model for string fragmentation is used to describe the transition from coloured partons to colour singlet hadrons. Subsequent hadronic decays are usually described isotropic in phase space, but in some cases matrix-element information is inserted. It is also possible to link to external decay packages, e.g. for  $\tau$  or  $B$  decays. A model for Bose–Einstein effects is included, but is off by default.

### 3 Program evolution

The above physics description largely also applies to PYTHIA 6.4. There are some differences to be noted, however.

Many old features have been definitely removed. Most notably this concerns the framework for independent fragmentation (a strawman alternative to string fragmentation) and the older mass-ordered showers (that still are in use in many collaborations, but do not fit so well with the new interleaved MI/ISR/FSR description).

Features that have been omitted so far, but should appear when time permits, include  $ep$ ,  $\gamma p$  and  $\gamma\gamma$  beam configurations and a set of SUSY and Technicolor processes.

New features, relative to PYTHIA 6.4 include

- the interleaved MI/ISR/FSR evolution (6.4 only interleaved MI and ISR),
- a richer mix of underlying-event processes, no longer only QCD jets but also prompt photons, low-mass lepton pairs and  $J/\psi$ ,
- possibility to select two hard processes in an event,
- possibility to use one PDF set for the hard process and another for MI/ISR, and
- updated decay data.

Major plans for the future include a new model for rescattering processes in the MI machinery, and new facilities to include matrix-element-to-parton-shower matching.

In addition minor improvements are introduced with each new subversion. Between the original 8.100 and the current 8.108 the list includes

- possibility to have acollinear beams, beam momentum spread and beam vertex spread,
- updated interfaces to several external packages,
- improved possibility to run several `Pythia` instances simultaneously,
- code modifications to compile under gcc 4.3.0 with the `-Wshadow` option, and
- some minor bug fixes.

## 4 Program structure

The structure of the `PYTHIA 8` generator is illustrated in Fig. 1. The main class for all user interaction is called `Pythia`. It calls on the three classes

- `ProcessLevel`, for the generation of the hard process, by sampling of built-in matrix elements or input from an external program,
- `PartonLevel`, for the additional partonic activity by MI, ISR, FSR and beam remnants, and
- `HadronLevel`, for the transition from partons to hadrons and the subsequent decays.

Each of these, in their turn, call on further classes that perform the separate kinds of physics tasks.

Information is flowing between the different program elements in various ways, the most important being the event record, represented by the `Event` class. Actually, there are two objects of this class, one called `process`, that only covers the few partons of the hard process above, and another called `event`, that covers the full story from the incoming beams to the final hadrons. A small `Info` class keeps track of useful one-of-a-kind information, such as kinematical variables of the hard process.

There are also two incoming `BeamParticles`, that keep track of the partonic content left in the beams after a number of interactions and initial-state radiations, and rescales parton distributions accordingly.

The process library, as well as parametrisations of total, elastic and diffractive cross sections, are used both by the hard-process selection machinery and the MI one.

The `Settings` database keeps track of all integer, double, boolean and string variables that can be changed by the user to steer the performance of `PYTHIA`, except that `ParticleDataTable` is its own separate database.

Finally, a number of utilities can be used just about anywhere, for Lorentz four-vectors, random numbers, jet finding, simple histograms, and for a number of other “minor” tasks.

## 5 Program usage

When you want to use `PYTHIA 8` you are expected to provide the main program. At least the following commands should them be used:

- `#include "Pythia.h"` to gain access to all the relevant classes and methods,
- `using namespace Pythia8;` to simplify typing,
- `Pythia pythia;` to create an instance of the generator,



- `pythia.readString("command");` (repeated as required) to modify the default behaviour of the generator (see further below), or alternatively
- `pythia.readFile("filename");` to read in a whole file of commands, one per line,
- `pythia.init();` to initialize the generator, with different optional arguments to be used to set incoming beam particles and energies,
- `pythia.next();` to generate the next event, so this call would be placed inside the main event generation loop,
- `pythia.statistics();` to write out some summary information at the end of the run.

The `pythia.readString(...)` and `pythia.readFile(...)` methods are used to modify the values stored in the databases, and it is these that in turn govern the behaviour of the program. There are two main databases.

- Settings come in four kinds, boolean flags, integer modes, double-precision parms, and string words. In each case a change requires a statement of the form `task:property = value`, e.g. `TimeShower:pTmin = 1.0`.
- `ParticleDataTable` stores particle properties and decay tables. To change the former requires a statement of the form `id:property = value`, where `id` is the identity code of the particle, an integer. The latter instead requires the form `id:channel:property = value`, where `channel` is a consecutive numbering of the decay channels of a particle.

Commands to the two databases can be freely mixed. The structure with strings to be interpreted also allows some special tricks, like that one can write `on` instead of `true` and `off` instead of `false`, or that the matching to variable names in the databases is case-insensitive.

Information about all settings and particle data can be found in the online manual, which exists in three copies. The `xml` one is the master copy, which is read in when an instance of the generator is created, to set up the default values that subsequently can be modified. The same information is then also provided in a copy translated to more readable `html` format, and another copy in `php` format. The interactivity of the latter format allows a primitive graphical user interface, where a file of commands can be constructed by simple clicking and filling-in of boxes.

The online manual contains more than 60 interlinked webpages, from a program overview to some reference material, and in between extensive descriptions how to set up run tasks, how to study the output, and how to link to other programs. In particular, all possible settings are fully explained.

## 6 Trying it out

If you want to try out PYTHIA 8, here is how:

- Download `pythia8108.tgz` (or whatever is the current version when you read this) from <http://www.thep.lu.se/~torbjorn/Pythia.html>

- `tar xvfz pythia8108.tgz` to unzip and expand.
- `cd pythia8108` to move to the new directory.
- `./configure ...` is only needed to link to external libraries, or to use options for debug or shared libraries, so can be skipped in the first round.
- `make` will compile in 1 – 3 minutes (for an archive library, same amount extra for a shared one).
- The `htmldoc/pythia8100.pdf` file contains A Brief Introduction [2].
- Open `htmldoc/Welcome.html` in a web browser for the full manual.
- Install the `phpdoc/` directory on a webserver and open `phpdoc/Welcome.php` in a web browser for an interactive manual.
- The `examples` subdirectory contains > 30 sample main programs: standalone, link to libraries, semi-internal processes, ...
- These can be run by `make mainNN` followed by `./mainNN.exe > outfile`.
- A Worksheet contains step-by-step instructions and exercises how to write and run main programs.

Note that PYTHIA is constructed so it can be run standalone, and this is the best way to learn how it works. For an experimental collaboration it would only be a piece in a larger software puzzle, and so a number of hooks has been prepared to allow various kinds of interfacing. The price to pay for using them is a more complex structure, where e.g. the origin of any errors is less easy to hunt down. Several aspects, such as the access to settings and particle data, should remain essentially unchanged, however.

## 7 Outlook

PYTHIA 6.4 is still maintained, with a current version 6.418 that weighs in at over 77,000 lines of code (including comments and blanks) and has a 580 page manual [1], plus update notes and sample main programs. No further major upgrades will occur with this program, however, and we intend to let it gradually die.

Instead PYTHIA 8.1 should be taking over. Currently it is smaller than its predecessor, with “only” 53,000 lines of code and a puny 27 page manual [2], but with much further online documentation and a big selection of sample main programs. It already contains several features not found in 6.4, and will gradually become the obvious version to use.

The LHC collaborations are strongly encouraged to accelerate the transition from 6.4 to 8.1, e.g. by serious tests with small production runs, to find any remaining flaws and limitations.

## Acknowledgements

The PYTHIA 8 program was made possible by a three-year “sabbatical” with the SFT group at CERN/EP. This unwavering support is gratefully acknowledged. Mikhail Kirsanov and other members of the GENSER group has provided further help with Makefiles and other technical tasks. The work was supported in part by the European Union Marie Curie Research Training Network MCnet under contract MRTN-CT-2006-035606.

**References**

- [1] Sjöstrand, T. and Mrenna, S. and Skands, P., JHEP **05**, 026 (2006).
- [2] Sjöstrand, T. and Mrenna, S. and Skands, P., Comput. Phys. Commun. **178**, 852 (2008).
- [3] Alwall, J. and others, Comput. Phys. Commun. **176**, 300 (2007).

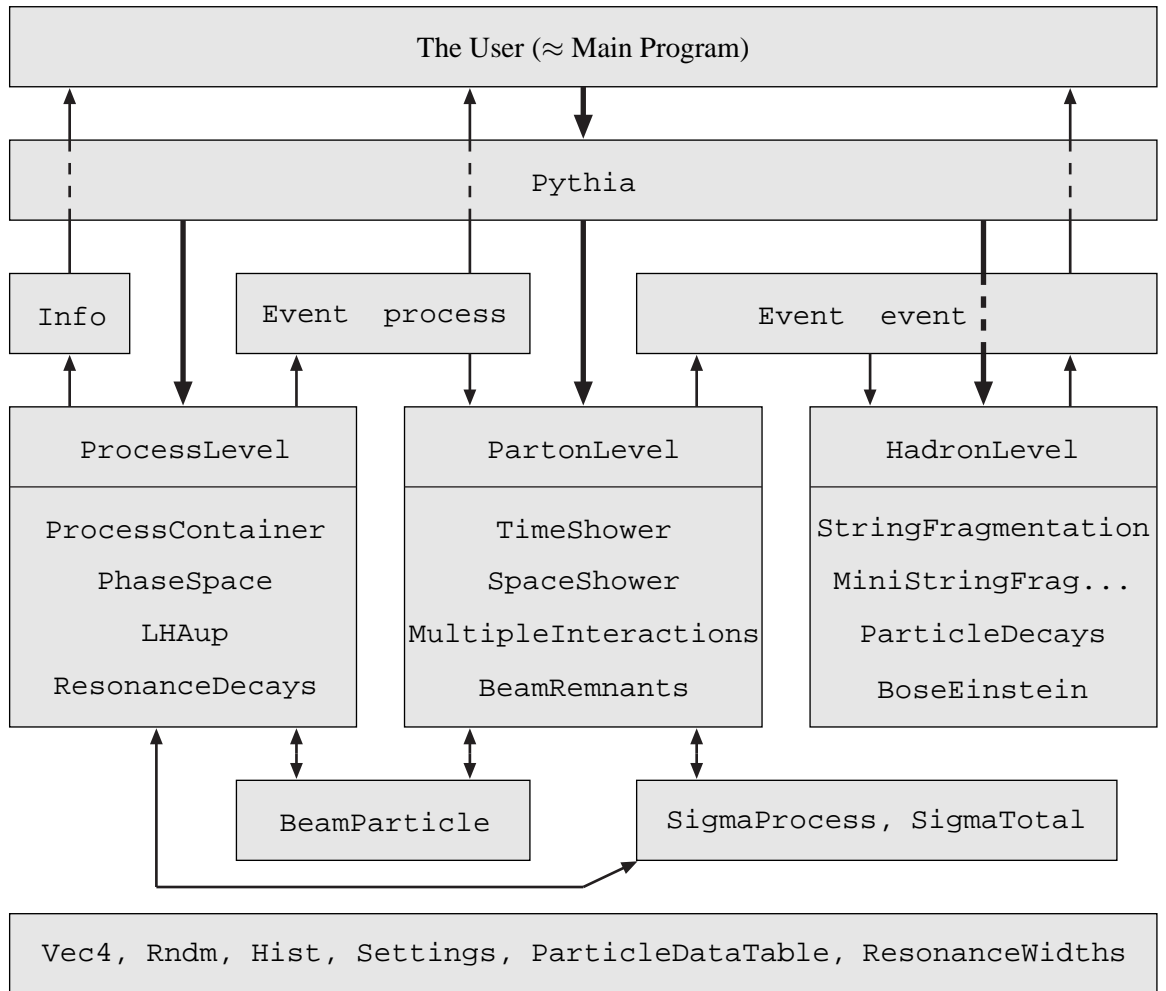


Fig. 1: The relationship between the main classes in PYTHIA 8. The thick arrows show the flow of commands to carry out different physics tasks, whereas the thinner show the flow of information between the tasks. The bottom box contains common utilities that may be used anywhere. Obviously the picture is strongly simplified.

# THEPEG

## Toolkit for High Energy Physics Event Generation

*Leif Lönnblad*

Department of Theoretical Physics, Lund University, Sweden

### Abstract

I present the status of the THEPEG project for creating a common platform for implementing C++ event generators. I also describe briefly the status of the new version of ARIADNE implemented using this framework.

## 1 Introduction

Monte Carlo Event Generators have developed into essential tools in High Energy Physics. Without them it is questionable if it at all would be possible to embark on large scale experiments such as the LHC. Although the current event generators work satisfactorily, the next generation of experiments will substantially increase the demands both on the physics models implemented in the event generators and on the underlying software technology.

Below is a very brief description of the THEPEG [1] project for designing a general framework in C++ for implementing event generator models, and also the ARIADNE program which uses THEPEG to implement the underlying dipole cascade model. Also HERWIG++ [2] is implemented in the THEPEG framework, but this program is described elsewhere in these proceedings.

## 2 Basic structure

THEPEG is a general platform written in C++ for implementing models for event generation. It is made up from the basic model-independent parts of PYTHIA7 [3, 4], the original project of rewriting the Lund family of event generators in C++. When the corresponding rewrite of the HERWIG program [5] started it was decided to use the same basic infrastructure as PYTHIA7 and therefore the THEPEG was factorized out of PYTHIA7 and is now the base of both PYTHIA7 and HERWIG++ [2]. Also the coming C++ version of ARIADNE [6] is using THEPEG. It should be noted, however, that the new C++ version of PYTHIA, called PYTHIA8 is not built on THEPEG.

THEPEG implements a number of general utilities such as smart pointers, extended type information, persistent I/O, dynamic loading, a system for handling physical units and some extra utilities for kinematics, phase space generation etc.

The actual event generation is then performed by calling different *handler* classes for hard partonic sub-processes, parton densities, QCD cascades, hadronization etc. To implement a new model to be used by THEPEG, the procedure is then to write a new C++ class inheriting from a corresponding handler class and implement a number of pre-defined virtual functions. Eg. a class for implementing a new hadronization model would inherit from the abstract `HadronizationHandler` class, and a new parton density parameterization would inherit

from the `PDFBase` class. These classes communicate with each other and with the underlying framework using pre-defined virtual function definitions and a highly structured `Event` object.

To generate events with THEPEG one first runs a setup program where an `EventGenerator` object is set up to use objects implementing different models for different steps of the generation procedure. All objects to be chosen from are stored in a *repository*, within which it is also possible to modify switches and parameters of the implemented models in a standardized fashion, using so called *interface* objects. Typically the user would choose from a number of pre-defined `EventGenerator` objects and only make minor changes for the specific simulation to be made. When an `EventGenerator` is properly set up, it is saved persistently to a file which can then be read into a special run program to perform the generation, in which case special `AnalysisHandler` objects may be specified to analyze the resulting events. Alternatively, the `EventGenerator` can be read into eg. a detector simulation program or a user supplied analysis program, where it can be used to generate events.

### 3 Status

THEPEG version 1.2 is available [1] and is working. As explained above, it contains the basic infrastructure for implementing and running event generation models. It also contains some simple physics models, such as some  $2 \rightarrow 2$  matrix elements, a few parton density parameterizations (and an interface to LHAPDF [7]) and a near-complete set of particle decays. However, these are mainly in place for testing purposes, and to generate realistic events, the PYTHIA7 and/or HERWIG++ programs are needed.

Currently the program only works under Linux and MacOS using the `gcc` compiler. This is mainly due to the use of dynamic linking of shared object files, which is inherently platform-dependent. However, the build procedure uses the `libtool` facility [8], which will hopefully allow for easy porting to other platforms in the future.

Although THEPEG includes a general structure for implementing basic fixed-order matrix element generation to produce the initial hard subprocesses in the event generation, a general procedure for reading such parton level events from external programs using the Les Houches accord [9, 10] is included.

The documentation of THEPEG is currently quite poor. The code itself is documented using the Doxygen format [11], which provides some technical documentation. The lack of documentation means that there is currently a fairly high threshold for a beginner to start using and/or developing physics modules for THEPEG. However, THEPEG has a well worked through low-level interface to be able to set parameter and switches, etc. in classes introduced to the structure from the outside. This means that the running of THEPEG does not require a C++ expert, but can be handled through a simple command-line facility or through a Java-based graphical user interface.

Among the recent developments in THEPEG one can note that there is now an option to do compile-time checking of units in all mathematical expressions. Also a number of helicity classes for construction of matrix elements has been imported from HERWIG++. Furthermore, the dependence on CLHEP [12] has been dropped and the only dependence on external packages is the GNU scientific library [13], which is a standard package in all Linux distributions.

### 3.1 ARIADNE

The reimplementaion of the ARIADNE [6] program using the framework of THEPEG has started but is not yet publically available. Although this is mainly a pure rewrite of the fortran version of ARIADNE, it will contain some improvements, such as CKKW matching [14, 15]. In addition, an improved version of the LDCMC [16] is planned.

ARIADNE is supposed to be used together with Lund string fragmentation, and for that purpose an interface of relevant parts of the PYTHIA8 program to the THEPEG framework is planned. Meanwhile there is already a simplified implementation of string fragmentation in the PYTHIA7 program [4] which was the first attempt to reimplement PYTHIA into C++.

## 4 Conclusions

THEPEG can now be considered to be a stable piece of software. Several improvements can be expected in the future, but the basic structure is fixed and has been working well for all models which have been implemented so far.

## References

- [1] Leif Lönnblad and others, *THEPEG program*. <http://www.thep.lu.se/ThePEG>.
- [2] Bahr, M. and others (2008).
- [3] Bertini, Marc and Lönnblad, Leif and Sjöstrand, Torbjörn, *Comput. Phys. Commun.* **134**, 365 (2001).
- [4] Leif Lönnblad and others, *PYTHIA7 program*. <http://www.thep.lu.se/Pythia7>.
- [5] Corcella, G. and others, *JHEP* **01**, 010 (2001).
- [6] Lönnblad, Leif, *Comput. Phys. Commun.* **71**, 15 (1992).
- [7] Giele, W. and others (2002).
- [8] Gord Matzigkeit and others, *The libtool program*. <http://www.gnu.org/software/libtool>.
- [9] Boos, E. and others (2001).
- [10] Alwall, J. and others, *Comput. Phys. Commun.* **176**, 300 (2007).
- [11] Dimitri van Heesch, *The doxygen documentation system*. <http://www.doxygen.org>.
- [12] Lönnblad, Leif, *Comput. Phys. Commun.* **84**, 307 (1994).
- [13] M. Galassi and others, *The gnu scientific library*. <http://www.gnu.org/software/gsl>.
- [14] Catani, S. and Krauss, F. and Kuhn, R. and Webber, B. R., *JHEP* **11**, 063 (2001).

- [15] Lönnblad, Leif, JHEP **05**, 046 (2002).
- [16] Kharraziha, Hamid and Lönnblad, Leif, JHEP **03**, 006 (1998).



# CASCADE

Michal Deák<sup>1</sup>, Hannes Jung<sup>1,2</sup>, Krzysztof Kutak<sup>1</sup>

<sup>1</sup> Deutsches Elektronen-Synchrotron DESY Hamburg, FRG

<sup>2</sup> University of Antwerp, Belgium

CASCADE is a full hadron level Monte Carlo event generator for  $ep$ ,  $\gamma p$ ,  $pp$  and  $p\bar{p}$  processes, which uses the unintegrated parton distribution functions convoluted with off - mass shell matrix elements for the hard scattering. The CCFM [1] evolution equation is an appropriate description valid for both small and moderate  $x$  which describes parton emission in the initial state in an angular ordered region of phase space. For inclusive quantities it is equivalent to the BFKL and DGLAP evolution in the appropriate asymptotic limits. The angular ordering of the CCFM description makes it directly applicable for Monte Carlo implementation.

A detailed description of CASCADE is given in [2], the source code of CASCADE and a manual can be found under: <http://www.desy.de/~jung/cascade/>. A description and discussion of the CCFM unintegrated gluon densities used in CASCADE can be found in [3,4] The unintegrated gluon density  $x\mathcal{A}_0(x, k_\perp, \bar{q})$  is a function of the longitudinal momentum fraction  $x$  the transverse momentum of the gluon  $k_\perp$  and the factorization scale  $\bar{q}$ . A general discussion of unintegrated gluon densities is given in [5–8].

The matrix elements for heavy quark [9, 10] and Higgs [11] production in  $k_t$ -factorization are available since long. The  $k_\perp$ -factorisation approach can be used all the way up to high transferred-momentum scales. As an illustration in Fig. 1 we present a numerical calculation for the transverse momentum spectrum of top-antitop pair production at the LHC [5]. Small- $x$  effects are not large in this case. Rather, this process illustrates how  $k_\perp$ -factorisation works in the region of finite  $x$  and large virtualities of the order of the top quark mass. It is interesting to note that even at LHC energies the transverse momentum distribution of top quark pairs calculated from  $k_\perp$ -factorisation is similar to what is obtained from a full NLO calculation (including parton showers, MC@NLO [12]), with CASCADE giving a somewhat harder spectrum, Fig. 1.

However, to use CASCADE for standard processes at the LHC,  $g^*g^* \rightarrow W/ZQ\bar{Q}$  production [13, 14] and quark induced processes [15] ( $q^*g \rightarrow qg$ ) needed to be calculated in the  $k_t$ -factorization approach. First results from these calculations are given in [16].

The QCD-Compton process needs special attention: First, we are dealing with light partons, and collinear and soft regions have to be avoided. This is done by applying a cut on the transverse momentum  $p_t^{cm}$  of any of the outgoing  $q$  or  $g$  in the laboratory frame. Secondly, unintegrated quark distributions had to be determined. Since the aim is mainly to cover the forward or backward region at LHC, only the valence quarks are considered, avoiding any complication with double counting of sea-quarks and gluon contributions. The unintegrated quark density is obtained from a full CCFM evolution of valence quarks (taken at  $Q_0$  from CTEQ 5 [17]) treating correctly the full kinematics during the evolution. Only the  $q \rightarrow qg$  splitting functions were included, which are finite for small  $x$ .

For all processes, the initial state parton shower is obtained from a deconvolution of the CCFM unintegrated parton densities, obeying the angular ordering constraint. The angular ordering is essential for the  $x$  dependence of the unintegrated parton densities. However, during

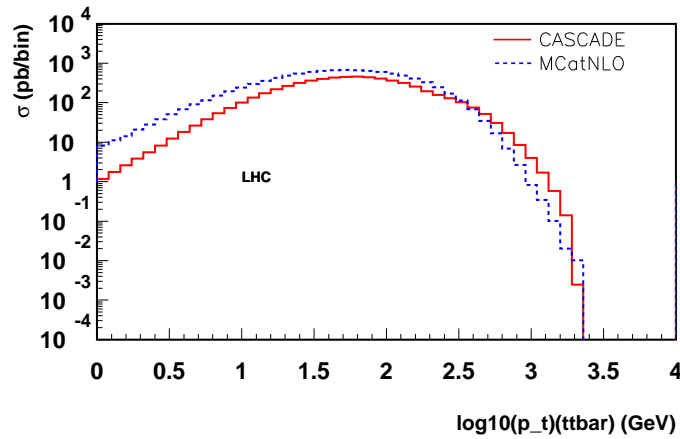


Fig. 1: Comparison of transverse momentum distribution of  $t\bar{t}$  pairs calculated from CASCADE with the NLO calculation MC@NLO at LHC energies.

the initial state cascade, the emitted parton can also undergo a further time-like cascade. This time-like showering is now included, where the maximum virtuality of the showering partons is set by the transverse momentum of the parent parton. The time-like cascade follows again angular ordering, but it does not change (except from kinematics) the angular ordering of the initial state cascade, which is constrained by the unintegrated parton density.

New developments to properly model the dense partonic system have lead to the introduction of an absorptive boundary simulating effectively the saturation effect coming from non-linear evolution equations. The absorptive boundary at small  $x$  suppresses the small  $k_t$  region of the unintegrated gluon density. The initial parameters for these uPDFs have to be determined from fits to measurements [18] and yield a similarly good  $\chi^2$ . These uPDFs are available in CASCADE (version 2.0.2), allowing the study of saturation effects with final state observables.

## References

- [1] M. Ciafaloni, Nucl. Phys. **B 296**, 49 (1988);  
S. Catani, F. Fiorani, and G. Marchesini, Phys. Lett. **B 234**, 339 (1990);  
S. Catani, F. Fiorani, and G. Marchesini, Nucl. Phys. **B 336**, 18 (1990);  
G. Marchesini, Nucl. Phys. **B 445**, 49 (1995).
- [2] H. Jung, Comp. Phys. Comm. **143**, 100 (2002).  
<http://www.desy.de/~jung/cascade/>.
- [3] M. Hansson and H. Jung, *Towards precision determination of uPDFs*, 2007.  
arXiv:0707.4276 [hep-ph].
- [4] H. Jung, A. V. Kotikov, A. V. Lipatov, and N. P. Zotov, *Towards precision determination of unintegrated parton density functions*, 2006. arXiv:hep-ph/0611093.
- [5] F. Hautmann and H. Jung, JHEP **10**, 113 (2008), arXiv:0805.1049 [hep-ph].

- [6] Small x Collaboration, J. R. Andersen *et al.*, Eur. Phys. J. **C48**, 53 (2006), [arXiv:hep-ph/0604189](#).
- [7] Small x Collaboration, J. R. Andersen *et al.*, Eur. Phys. J. **C35**, 67 (2004), [hep-ph/0312333](#).
- [8] Small x Collaboration, B. Andersson *et al.*, Eur. Phys. J. **C25**, 77 (2002), [hep-ph/0204115](#).
- [9] S. Catani, M. Ciafaloni, and F. Hautmann, Nucl. Phys. **B 366**, 135 (1991).
- [10] A. V. Lipatov and N. P. Zotov, Eur. Phys. J. **C27**, 87 (2003);  
S. P. Baranov and N. P. Zotov, J. Phys. **G29**, 1395 (2003);  
S. P. Baranov, Phys. Rev. **D66**, 114003 (2002).
- [11] F. Hautmann, Phys. Lett. **B535**, 159 (2002), [hep-ph/0203140](#).
- [12] S. Frixione, P. Nason, and B. R. Webber, JHEP **08**, 007 (2003), [arXiv:hep-ph/0305252](#).
- [13] M. Deak and F. Schwennsen, JHEP **09**, 035 (2008), [arXiv:0805.3763 \[hep-ph\]](#).
- [14] S. P. Baranov, A. V. Lipatov, and N. P. Zotov, Phys. Rev. **D77**, 074024 (2008), [arXiv:0708.3560 \[hep-ph\]](#).
- [15] M. Deak, H. Jung, and K. Kutak, *Valence quarks and  $k_T$  factorisation*, 2008. [arXiv:0807.2403 \[hep-ph\]](#).
- [16] S. Baranov et al,  *$k_T$ -factorization and  $uPDFs$  at HERA and the LHC*, 2008. These proceedings.
- [17] CTEQ Collaboration, H. L. Lai *et al.*, Eur. Phys. J. **C12**, 375 (2000), [arXiv:hep-ph/9903282](#).
- [18] K. Kutak and H. Jung (2008), [arXiv:0812.4082 \[hep-ph\]](#).

# AlpGen and SHERPA in $Z/\gamma^* + jets$ at LHC

Piergiulio Lenzi

Università degli Studi di Firenze and INFN Sez. Firenze

## Abstract

A study of **AlpGen** and **SHERPA** event generators in the production of  $Z/\gamma^* + jets$  events at LHC is presented. Both generators implement a combined use of multi-parton tree level matrix element calculations and parton shower, but the prescriptions used to match the two approaches are different. We will show a collection of lepton and jet observables and how they change as the parameters that steer the matching prescription are altered. We will also show a comparison between the two algorithms when run with the default parameter choice. The study has been done using the Rivet analysis framework.

## 1 Introduction

The characterization of  $Z/\gamma^* + jets$  production at LHC, with the vector boson decaying leptonically, will be one of the goals of the early LHC physics analyses; the rather clear leptonic signature will make these events easy to identify, and the vector boson kinematics will be reconstructed quite well even with a not perfectly calibrated/aligned detector: these signals will be very useful, for example, for the calibration of the calorimeter response using the balancing of the jets with the recoiling vector boson. Z bosons will be produced at the LHC with unprecedented rates, thus allowing a very precise determination of the vector boson mass and width; besides  $Z/W + jets$  events represent a background for many new physics searches, such as SUSY.

For all these reasons it's extremely important to understand the different characteristics of the event generators that can produce these events, to understand the theoretical uncertainties connected to residual dependence on parameters such as the scale choice and to spot how the differences among the event generators on the market translate into the observables reconstructed in the experiments.

Several event generators exist that can produce  $Z/\gamma^* + jets$  events. The **PYTHIA** [1] and **HERWIG** [2] event generators implement the LO calculation of the hard  $2 \rightarrow 2$  process and then continue the evolution with the parton shower technique.

A different approach, which proved quite effective in describing Tevatron data, consists of the combination of matrix element (ME) tree level calculations for up to several partons in the final state and subsequent parton shower (PS), with care not to double count configurations that can be produced both from the matrix element and from the parton shower. **AlpGen** [3] and **SHERPA** [4] both implement this approach, but with significant differences.

## 2 Matching prescriptions

**CKKW:** The **SHERPA** event generator comes with its own ME calculator, called **AMEGIC++** [5] (A Matrix Element Generator In C++), and with its own PS, called **APACIC++** [6] (A Parton

CAScade in C++). In this event generator the CKKW prescription for matching ME and PS is implemented in full generality.

The CKKW prescription was originally proposed for  $e^+e^-$  collision [7], then it was extended to hadron collisions [8]. It's based on a separation of the phase space in a region for jet production, handled by the ME and a region for jet evolution, handled by the PS. The separation is determined using a  $k_\perp$  measure; a configurable  $k_\perp$  cutoff,  $y_{cut} = Q_{cut}^2/E_{CM}^2$ , is used to define the separation of the two regions;  $Q_{cut}$  is the only parameter of this matching prescription.

The first step of the CKKW matching prescription is the calculation of the ME cross sections for all the parton multiplicities we want to enter the final state. In this calculation  $y_{cut}$  is used to cutoff divergences: the cross section is calculated for parton configurations such that the minimum  $k_\perp$  distance between two partons is above  $y_{cut}$ . In the ME cross section estimation a fixed value for  $\alpha_S$ ,  $\alpha_S^{ME}$ , is used.

The problem with ME calculation is that they are inclusive, so one cannot simply add ME cross sections for different final state parton multiplicities.

In the CKKW approach events produced according to the ME cross sections are reweighted with a Sudakov form factor weight. This makes ME cross sections exclusive. To calculate the Sudakov weight final state partons arising from the ME calculations are clustered back with a  $k_\perp$  clustering till the core  $2 \rightarrow 2$  process. In this way a series of splittings is reconstructed, that represent the splittings that would occur in a PS description of that final state. On this basis the Sudakov weight is calculated. An  $\alpha_S$  correction is also applied to take into account that the splittings happened at scales different from  $Q_{cut}$ , as originally imposed in the ME calculation.

Below the scale  $y_{cut}$  the evolution is described by the PS alone, but with a veto to avoid emission above  $y_{cut}$ , that has been taken into account already in the ME.

**MLM:** The MLM prescription is implemented in **AlpGen**; it is similar to the CKKW prescription for what concerns the production of ME events and the reweighting of  $\alpha_S$  but implements the Sudakov reweighting and the veto on the PS in a different way.

In the MLM approach a conventional PS program (**PYTHIA** or **HERWIG**) is used to shower events emerging from the ME. The shower is performed without any constraint. Partons resulting from the PS are clustered into jets with a cone algorithm. If all the jets match to all the partons generated from the ME the event is kept otherwise it is discarded. A special treatment is then needed for the events produced by the highest multiplicity ME, where additional jets, softer than the matched ones are allowed.

In this way the MLM prescription both reproduces the effect of the Sudakov reweighting and vetoes additional hard emission from the shower.

### 3 Analysis framework

Both programs were run with up to three additional partons from the matrix element. In order to better identify the effect of the different matching prescriptions we switched off the underlying event simulation.

We setup an analysis in the Rivet [9] analysis framework. Rivet is interfaced to a number

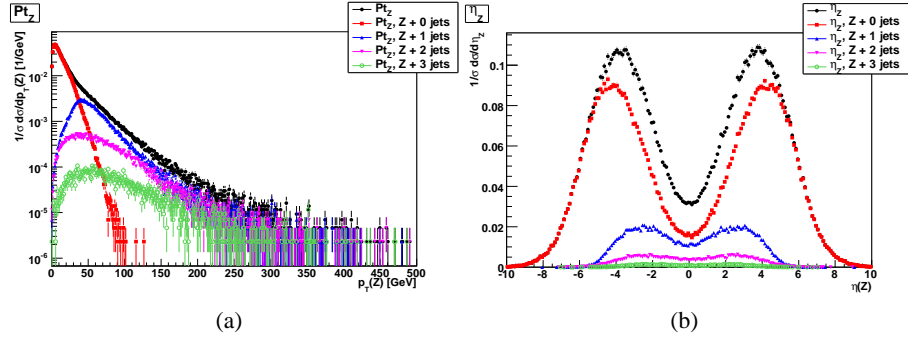


Fig. 1:  $p_T$  spectrum (a) and  $\eta$  distribution (b) for events produced with **SHERPA**. The contribution from different jet multiplicities is put into evidence in color.

of event generators through the **AGILE** package; this means that one can run both **SHERPA** and **AlpGen** within Rivet and run exactly the same analysis code on them. Rivet analyses are actually run on the **HepMC** [10] record as it is produced from the generator.

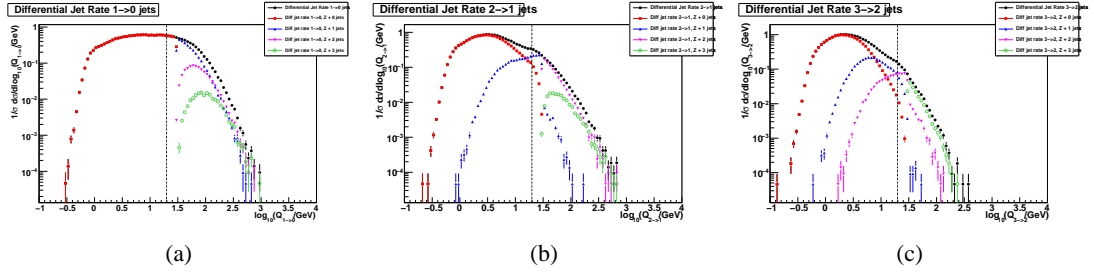
We run the analysis at hadron level, selecting final state particles with pseudorapidity  $\eta$  such that  $|\eta| < 5$ . We selected lepton pairs with an invariant mass between 66 GeV and 116 GeV. Jets were reconstructed with the longitudinally invariant  $k_\perp$  algorithm [11], as implemented in the **FastJet** package [12]. We set the pseudo-radius parameter of the  $k_\perp$  algorithm to 0.4 and we set a minimum  $p_T$  for jets of 30 GeV.

#### 4 Results for **SHERPA**

Fig. 1 shows the  $p_T$  (a) and  $\eta$  (b) distributions for the lepton pair produced in **SHERPA**. The contribution from different jet multiplicities is put into evidence in colour, while the overall contribution is in black. We observe that the high  $p_T$  tail of the distribution is due to the multiple jet contribution.

Fig. 2 shows differential jet rates in **SHERPA**. Differential jet rates are the distribution of the resolution parameter in the  $k_\perp$  clustering, that makes an  $n$  jet event turn into an  $n-1$  jet event. To compute differential jet rates one might think of running the  $k_\perp$  clustering in exclusive mode with different values of the resolution parameter, looking for the parameter that makes on jet disappear, thus leading to the transition  $n \rightarrow n-1$ . Actually this is done more efficiently simply looking at the relevant recombinations in the clustering sequence when running  $k_\perp$  clustering in inclusive mode. Those plots give a very detailed picture of how the phase space is filled. In particular one has to take care of what happens around the separation cut between the ME-filled region and the PS-filled region, marked with a vertical dashed line in the plots. The phase space above the line is filled by the ME, below by the PS. While the  $1 \rightarrow 0$  transition looks quite smooth, some structure around the separation cut is present in the  $2 \rightarrow 1$  and  $3 \rightarrow 2$  plots. The effect is anyway moderate, and is due to mismatches that can occur close to the cut, due to the way the PS modifies the ME kinematics.

Fig. 3 shows how the  $p_T$  and  $\eta$  distribution of the lepton pair change if the value of the parameter  $Q_{cut}$  that steers the matching is changed. As  $Q_{cut}$  is increased the  $p_T$  spectrum tends


 Fig. 2: Differential jet rates in **SHERPA**. (a)  $1 \rightarrow 0$ , (b)  $2 \rightarrow 1$  (c),  $3 \rightarrow 2$ 

to be softer and the  $\eta$  distribution less central. This is probably due to the reduced phase space available for the ME as  $Q_{cut}$  is increased. Since the ME is responsible for the hardest parton kinematics, an increase in  $Q_{cut}$  results in slightly softer spectra.

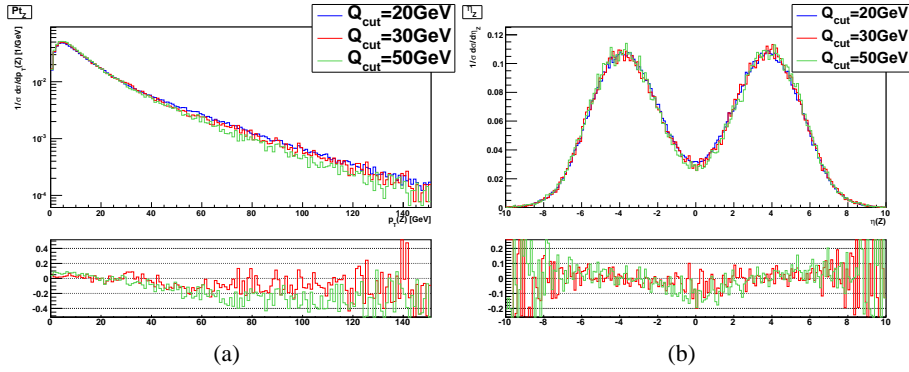
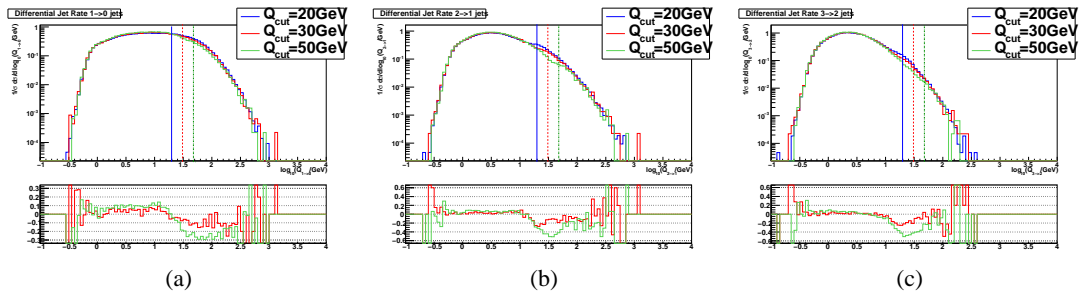

 Fig. 3:  $p_T$  distribution (a) and  $\eta$  distribution (b) for the lepton pair in **SHERPA** with three different values of  $Q_{cut}$ .

Fig. 4 shows the  $Q_{cut}$  dependency in differential jet rate plots. Differences are observed in the transition region around  $Q_{cut}$ . The difference with respect to the default 20 GeV is at most 40%.


 Fig. 4: Differential jet rates in **SHERPA** for three different values of  $Q_{cut}$ . (a)  $1 \rightarrow 0$ , (b)  $2 \rightarrow 1$  (c),  $3 \rightarrow 2$

## 5 Results for AlpGen

**AlpGen** sample has been showered using **PYTHIA**. We tried two different values for the minimum  $p_T$  in the cone algorithm that is used in **AlpGen** to steer the MLM matching: 25 GeV and 40 GeV.

Fig. 5 shows the effect of this change on the lepton pair  $p_T$  and  $\eta$  spectra. The effect is almost negligible.

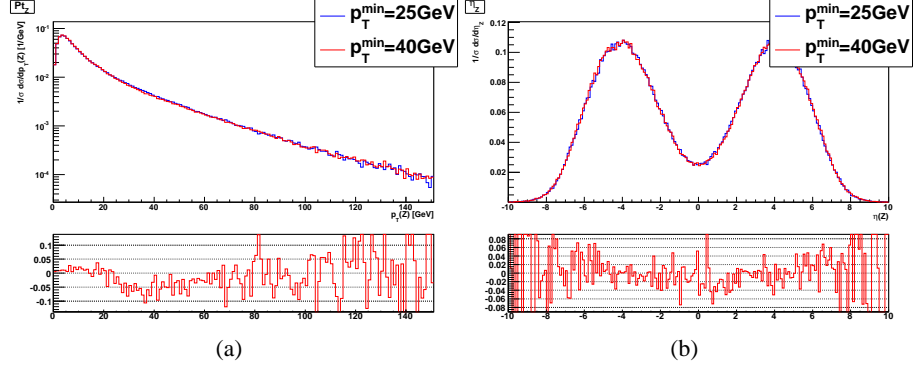


Fig. 5:  $p_T$  distribution (a) and  $\eta$  distribution (b) for the lepton pair with three different values of  $p_T^{min}$  in **AlpGen**.

Fig. 6 shows differential jet rate plots for **AlpGen** for the two values of the minimum  $p_T$  in the internal cone algorithm. Also in this case the differences are concentrated in the region around  $p_T^{min}$ , that is effectively the value used in **AlpGen** to separate the ME and PS regions.

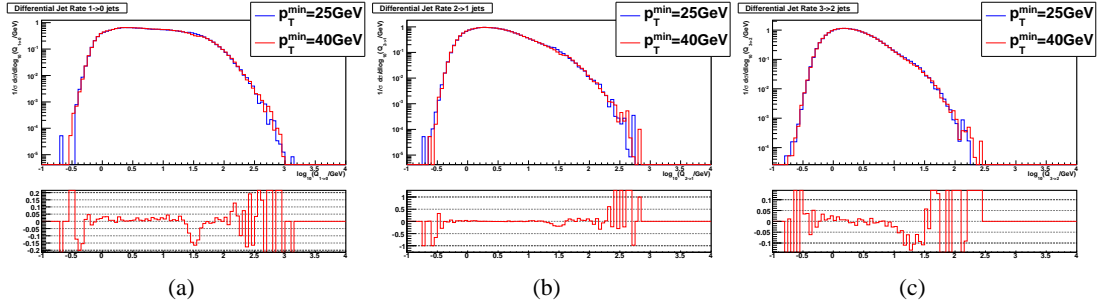


Fig. 6: Differential jet rates in **AlpGen**. (a)  $1 \rightarrow 0$ , (b)  $2 \rightarrow 1$  (c),  $3 \rightarrow 2$

## 6 A comparison between the two

We made a comparison between **AlpGen** and **SHERPA** when run with the default settings. For **AlpGen** we used both **PYTHIA** and **HERWIG** as parton showers. Fig. 7 shows the  $p_T$  spectrum and the  $\eta$  distribution of the lepton pair and the  $p_T$  spectrum of one of the two leptons. We observe that **SHERPA** shows the hardest spectrum both for the lepton pair and the single lepton, while **AlpGen**+**PYTHIA** is the softest. This translates into the  $\eta$  distribution, with **SHERPA** showing the most central boson, and **AlpGen**+**PYTHIA** the less central.



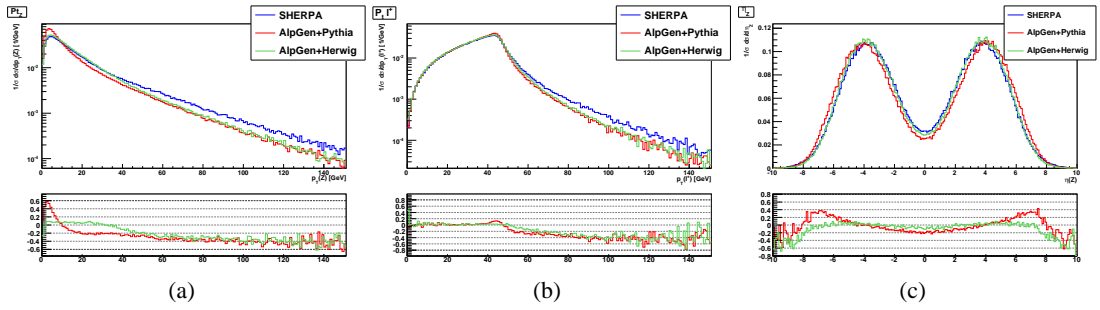


Fig. 7:  $p_T$  distribution of the lepton pair (a), of the positive lepton (b) and  $\eta$  distribution for the lepton pair (c) in **SHERPA**, **AlpGen+PYTHIA** and **AlpGen+HERWIG**. Relative difference plots are with respect to **SHERPA**.

Fig. 8 shows the jet multiplicity, the hardest and the second jet spectra. **SHERPA** shows a higher mean jet multiplicity; this is consistent with the harder leptonic spectra, given that the  $Z$  boson recoils against the jets. Also the leading jet  $p_T$  spectrum is harder in **SHERPA**, while the spectrum for the second jet is similar.

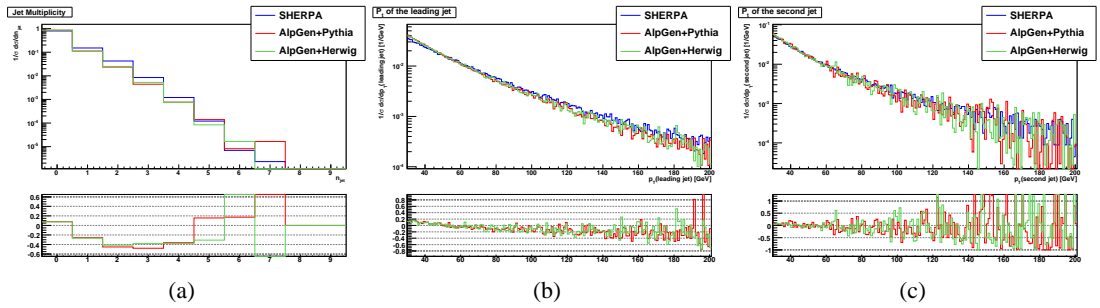


Fig. 8: Jet multiplicity (a) and  $p_T$  spectrum for the hardest (a) and second (b) jet in **SHERPA**, **AlpGen+PYTHIA** and **AlpGen+HERWIG**. Relative difference plots are with respect to **SHERPA**.

## 7 Conclusion

A study **AlpGen** and **SHERPA** for the production of  $Z/\gamma^* + jets$  has been done. A series of consistency checks have been performed with both generators to check the sensitivity to parameters that steer the matching prescription. No big dependencies were spotted. The two generators were compared when run with default settings. Some not negligible differences were spotted, both in the lepton and jet observables. **SHERPA** shows in general harder spectra, and also a higher mean jet multiplicity.

The analyses shown in this paper were performed with the Rivet Analysis framework.

## References

- [1] Sjostrand, Torbjorn and Mrenna, Stephen and Skands, Peter, JHEP **05**, 026 (2006).
- [2] Corcella, G. and others (2002).

- [3] Mangano, Michelangelo L. and Moretti, Mauro and Piccinini, Fulvio and Pittau, Roberto and Polosa, Antonio D., JHEP **07**, 1 (2003).
- [4] Gleisberg, Tanju and others, JHEP **02**, 56 (2004).
- [5] Krauss, F. and Kuhn, R. and Soff, G., JHEP **02**, 044 (2002).
- [6] Krauss, F. and Schalicke, A. and Soff, G., Comput. Phys. Commun. **174**, 876 (2006).
- [7] Catani, S. and Krauss, F. and Kuhn, R. and Webber, B. R., JHEP **11**, 63 (2001).
- [8] Krauss, F., JHEP **08**, 015 (2002).
- [9] Waugh, B. M. and others (2006).
- [10] Dobbs, Matt and Hansen, Jorgen Beck, Comput. Phys. Commun. **134**, 41 (2001).
- [11] Catani, S. and Dokshitzer, Yuri L. and Webber, B. R., Phys. Lett. **B285**, 291 (1992).
- [12] Cacciari, Matteo and Salam, Gavin P., Phys. Lett. **B641**, 57 (2006).

# Generator comparison for top-pair production at CMS

*Roberto Chierici*

Institut de Physique Nucleaire de Lyon, IN2P3-CNRS, Université Claude Bernard Lyon 1,  
Villeurbanne, France

## Abstract

This work presents a throughout comparison of some of the most popular generators for top-pair production at the LHC in the frame of the CMS software. The aim is to validate the physics contents after their integration in the experimental software and to give indications for the best possible choices of the generator set-up.

## 1 Introduction

The description of top-pair production at the LHC can be handled by different kind of generation tools. The most traditional approach, via leading order (LO) calculations (examples are generators like PYTHIA [1], TopRex [2]), is now accompanied by more modern tools allowing the inclusion of higher leading order (HLO) QCD terms, via the so-called matrix elements (ME) - parton shower (PS) matching [3] (examples are ALPGEN [4] or the recent version of MadGraph [5]). Also available are now next-to-leading-order (NLO) QCD generators like MC@NLO [6].

The aim of this work is to test the physics contents of the different generators in the domain of top physics and in the framework of the CMS software. This also allows a common environment for the comparisons. Studies at pure generator level are documented by several articles already [7]. This work should not be intended as a generator review.

## 2 Set-up and event reconstruction

In the following comparisons of event generators, performed for pp collisions at a centre-of-mass energy of 14 TeV, the pure PS part is described in a uniform way by the use of PYTHIA, with care to have the same input parameter settings in all conditions. Exception is MC@NLO, currently only interfaced to HERWIG. The scales and PDFs are also chosen to be as much as possible the same: exception to this is a slight difference in the scale definition in ALPGEN and MadGraph. The details of the input settings, as well as the numbers of events generated for this study, are reported in table 1. The validity of the choice of the tuning with new approaches for the description of the radiation goes beyond the scope of the present note; it is, on the contrary, relevant to maintain the input settings as uniform as possible.

The comparisons are made at the generator level, after radiation from PS. The variables are reconstructed from the quarks and leptons before their final state radiation, the shown variables are therefore sensitive to the description of initial or intermediate (from top) state radiation (ISR). All the plots shown in the following are normalised to unity for the sake of clarity.

Parameter	TopRex	MadGraph	ALPGEN	MC@NLO
PDFs	CTEQ5L	CTEQ5L	CTEQ5L	CTEQ5L
Renormalization scale	$m_T$	$m_t$	$m_T$	$m_T$
Factorization scale	$m_T$	$m_t$	$m_T$	$m_T$
$\Lambda_{QCD}$ in PYTHIA (PARP(61), PARP(62)) (GeV)	0.25	0.25	0.25	-
$Q_{max}^2$ PYTHIA switch (PARP(67))	2.5	2.5	2.5	-
Generated events	$1,5 \times 10^6$	$3 \times 10^6$	$2 \times 10^5$	$1 \times 10^6$

Table 1: Main generator input parameter settings, and total number of generated events for this study. The transverse mass  $m_T$  is defined as  $\sum_{tops} (m^2 + p_T^2)$ . The MC@NLO generator is only interfaced with the HERWIG hadronisation, so no direct comparison in the parameter settings can be made.

### 3 The importance of ME-PS matching

At the energy scale of the LHC the description of gluon radiation becomes crucial. Recent techniques for PS-ME matching allow to describe much better the hard gluon radiation, maintaining the parton shower approximation for low  $p_T$  emissions. In the following we have used TopReX as the LO reference, ALPGEN and MadGraph as examples of matched  $t\bar{t}$  event generations and MC@NLO as a NLO QCD description of the  $t\bar{t}$  process.

Differences in gluon radiation may manifest themselves in distortions of the top quark angular distributions and transverse variables. The most spectacular effect can be appreciated in the transverse momentum of the radiation itself, which equals the transverse momentum of the  $t\bar{t}$  system.

This is what is shown in figure 1 for two standard generations in comparison to the newly available matching scheme [8] of MadGraph: all the different contributions to a fixed ME order, ie  $t\bar{t}+0$ jets,  $t\bar{t}+1$ jets,  $t\bar{t}+2$ jets and  $t\bar{t}+3$ jets, are explicitly indicated. The matching scheme is such that there is no phase space double counting in the different samples: no matching is performed for the last sample to let the PS predict configurations at higher jet multiplicities. The samples are mixed together according to the respective cross-sections. In the same figure also the azimuthal difference between the two tops is shown.

From the picture it is evident that gluon production via ME predicts a much harder transverse spectrum. The difference in shape is impressive, reaching orders of magnitude in the ratio at very high  $p_T$ . The increased activity in hard gluon emission for the matched case also explains a decreased azimuthal distance between the two tops, as shown in the right-hand plot. The predicted average  $p_T$  of the radiation by MadGraph is 62 GeV/c (72 GeV/c with ALPGEN), with a 40% probability of having more than 50 GeV/c as gluon  $p_T$  in  $t\bar{t}$  events. This large gluon activity will have an impact in the capability of correctly reconstructing top quark events at the LHC, and in correctly interpreting radiation as a background for new physics searches.

Difference in differential distributions are visible not only in the transverse plane: having more radiation tends to increase the event transverse activity. Moreover, the two top quarks and the resulting decay products are more central and generally closer to each other. We believe the difference we see are important enough to motivate the choice of a matching generation for

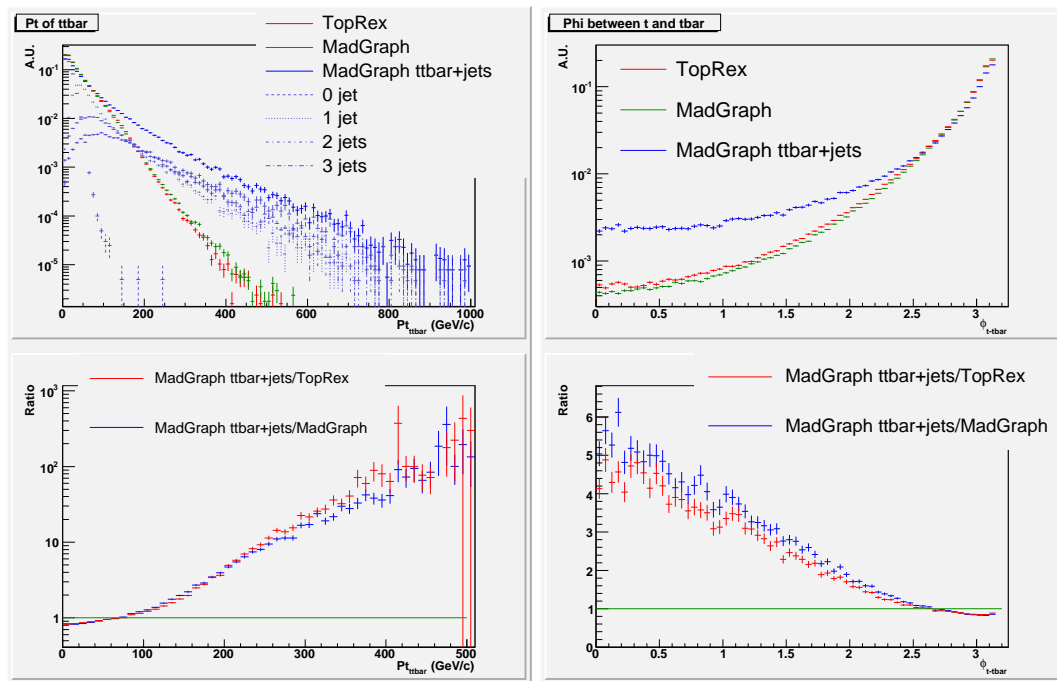


Fig. 1: Transverse momentum of the  $t\bar{t}$  system (left) and azimuthal difference between the top quarks (right) for TopRex, standard MadGraph and MadGraph with matching. The individual components  $tt+n$ jets are explicitly plotted in the left plot. The lower plots show the ratios of the histograms.

the description of any sufficiently hard SM process: this is particularly important when such processes are background to higher jet multiplicity configurations.

One important step in the validation of the physics contents of the matching in CMSSW is to compare two different approaches in the top sector. In figure 2 we present the ALPGEN predictions compared to MadGraph with ME-PS matching.

The blue and red curves represent the distributions for the matched samples of ALPGEN and MadGraph, respectively. For the  $p_T$  of the  $t\bar{t}$  system also the individual components are shown. The agreement is more than acceptable for the  $p_T$  and remarkable for the azimuthal difference between the top quarks. Especially in the tails of the distributions, corresponding to high radiation conditions, the disagreement reduces to a maximum discrepancy of 50%. To properly appreciate the difference between the two predictions we should, however, account for the theory errors as well. These errors come, mainly, from scale definitions, PDFs, PS tunings; a detailed study on the dependence of the results on these effects is desirable before any conclusion on residual discrepancies between the generators can be drawn.

The comparison showed very good agreement in many other distributions that are not shown here. We observed a slight difference in shape for the transverse momentum and an excellent agreement for angular variables, with difference typically below 5%. We believe that the two generators can equally well be used to describe environments with hard gluon emission

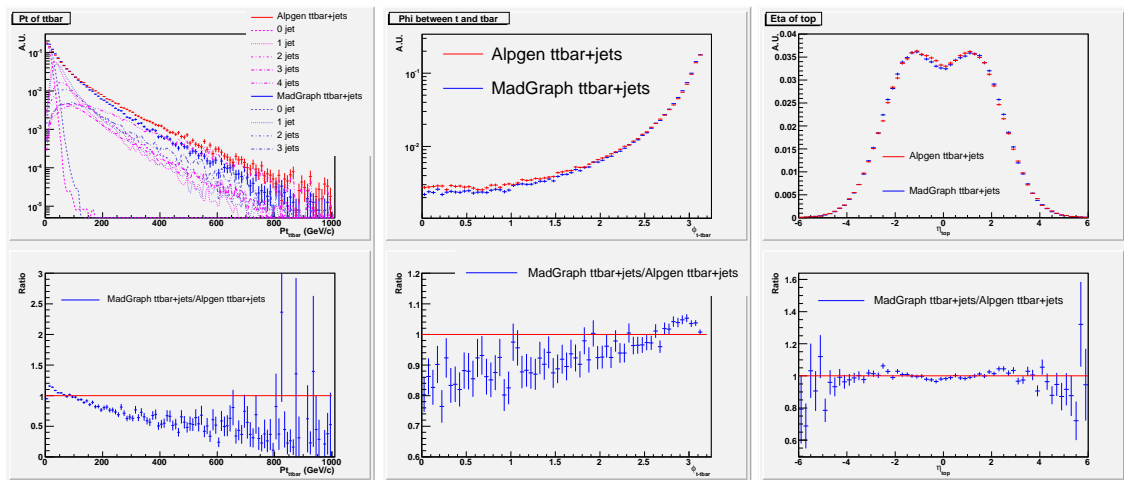


Fig. 2: Transverse momentum of the  $t\bar{t}$  system (left), azimuthal difference between the tops (center) and pseudo-rapidity of the tops (right) for ALPGEN matched and MadGraph matched. The individual components  $t\bar{t}+n$  jets are explicitly plotted in the left plot. The lower plots show the ratios of the histograms.

in the final state.

#### 4 Matched calculations versus NLO predictions

Another extremely important test comes by comparing ME-PS matched calculations with NLO QCD tools, especially for what concerns transverse variables. With the availability of MC@NLO as event generator this is now possible. Such comparison must be looked at with a grain of salt, since the hadronisation is performed with different tools and since inclusive NLO variables are compared with matched HLO quantities, typically at orders greater than the first. Nonetheless, in a throughout comparison of the kinematics of final state fermions and intermediate tops, a very good agreement was always found. Figure 3 shows the transverse momentum of the system, and excellent agreement in the high radiation tails is visible.

In this case discrepancies appear in the soft regime, where indeed the hadronisation with the PS plays an important role. There, a complete tuning of the PS models (with the respective externals MEs) needs to be made before performing a trustable comparison.

#### 5 Summary and outlook

We presented a throughout comparison, at parton level, of generator predictions in the top sector at the LHC energy. The tests were performed in the framework of the CMS software. A generation with matching PS-ME gives important differences in the description of the radiation and should be chosen as currently the best way to describe SM processes where the description of QCD radiation is important. This is even more relevant when such process is background to something else (SM or new physics). Matched calculations have also been tested versus NLO generators, with very good agreement in the prediction of transverse variables.

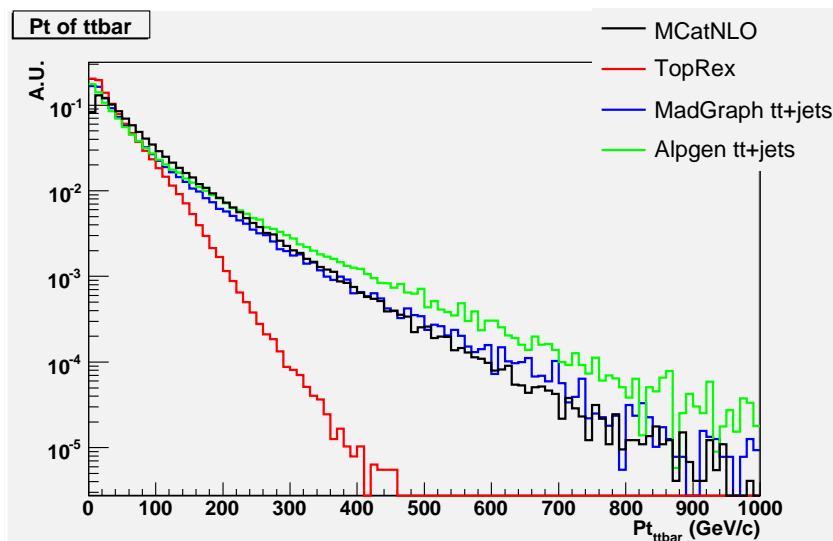


Fig. 3: Transverse momentum of the  $t\bar{t}$  system for ME-PS matched predictions and MC@NLO.

## References

- [1] T. Sjöstrand et al., Comput. Phys. Commun. 135 (2001) 238.
- [2] S.R. Slabospitsky, Comput. Phys. Commun. 148 (2002) 87.
- [3] S.Hoche et al., hep-ph/0602031.
- [4] M.L. Mangano et al., Journal of High Energy Physics **0307** (2003) 001.
- [5] F. Maltoni and T. Stelzer, hep-ph/0208156.
- [6] S. Frixione and B.R. Webber, Journal of High Energy Physics JHEP06 (2002) 029.
- [7] M. Mangano et al., CERN-PH-TH-2006-232  
J.Alwall et al., CERN-PH-TH-2007-066.
- [8] J.Alwall et al., CERN-PH-TH-2007-066.

# Herwig++ Status Report

*M. Bähr<sup>a</sup>, S. Gieseke<sup>a</sup>, M.A. Gigg<sup>b</sup>, D. Grellscheid<sup>b</sup>, K. Hamilton<sup>c</sup>, O. Latunde-Dada<sup>d</sup>,  
S. Plätzer<sup>a</sup>, P. Richardson<sup>b,e</sup>, M.H. Seymour<sup>e,f</sup>, A. Sherstnev<sup>d</sup>, J. Tully<sup>b</sup>, B.R. Webber<sup>d</sup>*

<sup>a</sup> Institut für Theoretische Physik, Universität Karlsruhe,

<sup>b</sup> IPPP, Department of Physics, Durham University,

<sup>c</sup> Centre for Particle Physics and Phenomenology, Université Catholique de Louvain,

<sup>d</sup> Cavendish Laboratory, University of Cambridge,

<sup>e</sup> Physics Department, CERN,

<sup>f</sup> School of Physics and Astronomy, University of Manchester. \*

## Abstract

Herwig++ is the successor of the event generator HERWIG. In its present version 2.2.1 it provides a program for full LHC event generation which is superior to the previous program in many respects. We briefly summarize its features and describe present work and some future plans.

## 1 Introduction

With the advent of the LHC era it was decided to completely rewrite the general purpose event generator HERWIG [1,2] in C++ under the name Herwig++, based on the package ThePEG [3,4]. The goal is not only to provide a simple replacement of HERWIG but to incorporate physics improvements as well [5]. From 2001 until now Herwig++ has been continuously developed and extended [6–10]. The current version is 2.2.1, cf. [11]. The physics simulation of the current version is more sophisticated than the one of Fortran HERWIG in many respects. In this report we will briefly summarize the status of the different aspects of the simulation. These are the hard matrix elements available, initial and final state parton showers, the hadronization, hadronic decays and the underlying event. We conclude with an outlook to planned future improvements.

## 2 Physics simulation steps

### 2.1 Matrix elements

The event generation begins with the hard scattering of incoming particles or partons in the case of hadronic collisions. We have included a relatively small number of hard matrix elements. These include  $e^+e^-$  annihilation to  $q\bar{q}$  pairs or simply to  $Z^0$  bosons and deep inelastic scattering. In addition there is the Higgsstrahlung process  $e^+e^- \rightarrow h^0 Z^0$ . For hadron–hadron collisions we have the QCD  $2 \rightarrow 2$  processes including heavy quark production. For colourless final states we have the following matrix elements,

$$hh \rightarrow (\gamma, Z^0) \rightarrow \ell^+ \ell^-, \quad hh \rightarrow W^\pm \rightarrow \ell^\pm \nu_\ell (\bar{\nu}_\ell), \quad hh \rightarrow h^0, \quad hh \rightarrow h^0 Z^0, \quad hh \rightarrow \gamma\gamma.$$

---

\*herwig@projects.hepforge.org



We also provide matrix elements for processes with additional jets in the final state, like

$$hh \rightarrow (\gamma, Z^0, W^\pm) + \text{jet} , \quad hh \rightarrow h^0 + \text{jet} .$$

In addition, there are matrix elements for perturbative decays of the top quark, which will be simulated including spin correlations (see below). There will be some more matrix elements added in future versions, e.g. for  $hh \rightarrow qqh^0$ . Despite the rather small number of matrix elements, there is no real limitation to the processes that may be simulated with Herwig++. In practice, one may use any matrix element generator to generate a standard event file [12] which in turn can be read and processed by Herwig++.

For processes with many legs in the final state we follow a different strategy. When the number of legs becomes large — typically larger than 6–8 particles in the final state — it will be increasingly difficult to achieve an efficient event generation of the full matrix element. For these situations we have a generic framework to build up matrix elements for production and decays of particles in order to approximate any tree level matrix element as a simple production process with subsequent two or three body decays. This is a good approximation whenever the widths of the intermediate particles are small. The spin correlations among these particles can be restored with the algorithm described in [13]. Also finite width effects are taken into account [14]. The full simulation of several processes of many models for physics beyond the standard model (MSSM, UED, Randall–Sunrum model) is thus possible in Herwig++ [15]. Here, all necessary matrix elements for production and decay processes are constructed automatically from a model file.

## 2.2 Parton Showers and matching with matrix elements

After the hard process has been generated, typically at a large scale  $\sim 100 \text{ GeV}$ – $1 \text{ TeV}$ , the coloured particles in the process radiate a large number of additional partons, predominantly gluons. As long as these are resolved by a hard scale of  $\sim 1 \text{ GeV}$  this is simulated with a coherent branching algorithm, as outlined in [16] which generalizes the original algorithm [17–19] used in HERWIG. The main improvements with respect to the old algorithm are boost invariance along the jet axis, due to a covariant formulation, and the improved treatment of radiation off heavy quarks. We are using mass-dependent splitting functions and a description of the kinematics that allows us to dynamically generate the dead-cone effect. In addition to initial and final state parton showers there are also parton showers in the decay of heavy particles, the top quark in our case.

When extrapolating to hard, wide-angle emissions, the parton shower description is not sufficiently accurate in situations where observables depend on large transverse momenta in the process. In these cases we supply so-called hard matrix element corrections that describe the hardest parton emission, usually a hard gluon, with the full matrix element for the process that includes that extra parton. In order to consistently describe the whole phase space one has to apply soft matrix element corrections. Matrix element corrections are available for Drell–Yan type processes, Higgs production in  $gg$  fusion and  $e^+e^-$  annihilation to  $q\bar{q}$ -pairs. In addition, we apply a matrix element correction in top-quark decays [20].

From the point of view of perturbation theory, the hard matrix element correction is only one part of the next-to-leading order (NLO) correction to the Born matrix element. The full NLO

calculation also includes the virtual part with the same final state as the Born approximation. When trying to match NLO calculations and parton shower algorithms systematically, we have to avoid double counting of the real emission contributions. Two systematic approaches are being successfully discussed and applied in event generators: MC@NLO [21–23] and the POWHEG approach [24, 25]. In Herwig++ we have included working examples of matching in both approaches. The MC@NLO method, adopted to Herwig++ is described in [26]. Whereas the POWHEG method has already been applied for several processes in  $e^+e^-$  annihilation [27, 28] and also for Drell–Yan production [29]. Parts of these implementations will become available in future releases.

Another viable possibility to improve the description of QCD radiation in the event generation is the matching to multiple tree–level matrix elements, that describe the radiation of  $n$  additional jets with respect to the Born level. Theoretically most consistent is the CKKW approach [30] which has been studied in the context of an angular ordered parton shower in [31].

### 2.3 Hadronization and decays

The hadronization model in Herwig++ is the cluster hadronization model which has not been changed much from its predecessor in HERWIG. After the parton shower, all gluons are split nonperturbatively into  $q\bar{q}$  pairs. Then, following the colour history of the parton cascade, all colour triplet–antitriplet pairs are paired up in colourless clusters which still carry all flavour and momentum information of the original partons. While these are heavier than some threshold mass they will fission into lighter clusters until all clusters are sufficiently light. These light clusters will then decay into pairs of hadrons.

The hadrons thus obtained are often heavy resonances that will eventually decay on time-scales that are still irrelevant for the experiment. These hadronic decays have been largely rewritten and are modeled in much greater detail in Herwig++. While in HERWIG they were often simply decayed according to the available phase space only, we now take into account more experimental information, like form factors, that allow for a realistic modeling of decay matrix elements [32, 33]. In a major effort, a large fraction of the decay channels described in the particle data book [34] have been included into Herwig++.

### 2.4 Underlying event

The underlying event model of Herwig++ is a model for multiple hard partonic interactions, based on an eikonal model, similar to JIMMY [35]. In addition to the signal process there are a number of additional QCD scatters, including full parton showers, that contribute to the overall hadronic activity in the final state and eventually also give rise to a (relatively soft) jet substructure in the underlying event. The model has two important parameters, one parameter  $\mu$ , describing the spatial density of partonic matter in the colliding protons. Secondly, there is one cut off parameter  $p_{\perp, \min}$  that gives a lower bound on the differential cross section for QCD  $2 \rightarrow 2$  jet production. The model has been carefully tuned to Tevatron data [36]. Further possible bounds on the model parameters have been studied in [37]. An alternative modeling of the underlying event on the basis of the UA5 model [38] is also available for historic reasons.

Currently, the multiple partonic interaction model is limited to hard scattering while a soft

component is simply not present. For a realistic simulation of minimum bias events a soft component is, however, very important. An extension into the soft region, allowing us the simulation of minimum bias events is currently being studied and is likely to be included in the next release of Herwig++.

### 3 Availability

The latest version of Herwig++ is always available from hepforge:

`http://projects.hepforge.org/herwig`

There one can also find wiki pages to help with questions concerning installation, changing particular parameters and other frequently asked questions. The installation process is straightforward on any modern variant of linux. The physics details of the program are now documented in great detail in our manual [33]. The pdf version of the manual contains additional links to the online documentation of the code. All important parameters have been carefully tuned to a wealth of available data and the code is shipped with default parameters that give the best overall description of the data that we have tuned to. Details of the tune can also be found in the manual [33].

### Acknowledgments

This work has been supported in part by the EU Marie Curie Research and Training Network MCnet under contract MRTN-CT-2006-035606.

### References

- [1] G. Corcella *et. al.*, *HERWIG 6: An event generator for hadron emission reactions with interfering gluons (including supersymmetric processes)*, *JHEP* **01** (2001) 010, [[hep-ph/0011363](#)].
- [2] G. Corcella *et. al.*, *HERWIG 6.5 release note*, [hep-ph/0210213](#).
- [3] L. Lönnblad, *ThePEG, Pythia7, Herwig++ and Ariadne*, *Nucl. Instrum. Meth.* **A559** (2006) 246–248.
- [4] M. Bertini, L. Lönnblad, and T. Sjöstrand, *Pythia version 7-0.0: A proof-of-concept version*, *Comput. Phys. Commun.* **134** (2001) 365–391, [[hep-ph/0006152](#)].
- [5] S. Gieseke, *Event generators: New developments*, [hep-ph/0210294](#).
- [6] S. Gieseke, A. Ribon, M. H. Seymour, P. Stephens, and B. Webber, *Herwig++ 1.0: An event generator for  $e^+e^-$  annihilation*, *JHEP* **02** (2004) 005, [[hep-ph/0311208](#)].
- [7] S. Gieseke *et. al.*, *Herwig++ 2.0 beta release note*, [hep-ph/0602069](#).
- [8] S. Gieseke *et. al.*, *Herwig++ 2.0 release note*, [hep-ph/0609306](#).

- [9] M. Bähr *et. al.*, *Herwig++ 2.1 Release Note*, arXiv:0711.3137.
- [10] M. Bähr *et. al.*, *Herwig++ 2.2 Release Note*, arXiv:0804.3053.
- [11] <http://projects.hepforge.org/herwig>.
- [12] J. Alwall *et. al.*, *A standard format for Les Houches event files*, *Comput. Phys. Commun.* **176** (2007) 300–304, [hep-ph/0609017].
- [13] P. Richardson, *Spin correlations in Monte Carlo simulations*, *JHEP* **11** (2001) 029, [hep-ph/0110108].
- [14] M. A. Gigg and P. Richardson, *Simulation of Finite Width Effects in Physics Beyond the Standard Model*, arXiv:0805.3037.
- [15] M. Gigg and P. Richardson, *Simulation of beyond standard model physics in Herwig++*, *Eur. Phys. J.* **C51** (2007) 989–1008, [hep-ph/0703199].
- [16] S. Gieseke, P. Stephens, and B. Webber, *New formalism for QCD parton showers*, *JHEP* **12** (2003) 045, [hep-ph/0310083].
- [17] G. Marchesini and B. R. Webber, *Simulation of QCD Jets Including Soft Gluon Interference*, *Nucl. Phys.* **B238** (1984) 1.
- [18] B. R. Webber, *A QCD Model for Jet Fragmentation Including Soft Gluon Interference*, *Nucl. Phys.* **B238** (1984) 492.
- [19] G. Marchesini and B. R. Webber, *Monte Carlo Simulation of General Hard Processes with Coherent QCD Radiation*, *Nucl. Phys.* **B310** (1988) 461.
- [20] K. Hamilton and P. Richardson, *A simulation of QCD radiation in top quark decays*, *JHEP* **02** (2007) 069, [hep-ph/0612236].
- [21] S. Frixione and B. R. Webber, *Matching NLO QCD computations and parton shower simulations*, *JHEP* **06** (2002) 029, [hep-ph/0204244].
- [22] S. Frixione, P. Nason, and B. R. Webber, *Matching NLO QCD and parton showers in heavy flavour production*, *JHEP* **08** (2003) 007, [hep-ph/0305252].
- [23] S. Frixione and B. R. Webber, *The MC@NLO 3.3 event generator*, hep-ph/0612272.
- [24] P. Nason, *A new method for combining NLO QCD with shower Monte Carlo algorithms*, *JHEP* **11** (2004) 040, [hep-ph/0409146].
- [25] S. Frixione, P. Nason, and C. Oleari, *Matching NLO QCD computations with Parton Shower simulations: the POWHEG method*, *JHEP* **11** (2007) 070, [arXiv:0709.2092].
- [26] O. Latunde-Dada, *Herwig++ Monte Carlo At Next-To-Leading Order for  $e+e-$  annihilation and lepton pair production*, *JHEP* **11** (2007) 040, [arXiv:0708.4390].

- [27] O. Latunde-Dada, S. Gieseke, and B. Webber, *A positive-weight next-to-leading-order Monte Carlo for  $e^+e^-$  annihilation to hadrons*, *JHEP* **02** (2007) 051, [hep-ph/0612281].
- [28] O. Latunde-Dada, *Applying the POWHEG method to top pair production and decays at the ILC*, arXiv:0806.4560.
- [29] K. Hamilton, P. Richardson, and J. Tully, *A Positive-Weight Next-to-Leading Order Monte Carlo Simulation of Drell-Yan Vector Boson Production*, arXiv:0806.0290.
- [30] S. Catani, F. Krauss, R. Kuhn, and B. R. Webber, *QCD matrix elements + parton showers*, *JHEP* **11** (2001) 063, [hep-ph/0109231].
- [31] S. Plätzer, *Diploma Thesis*, . Universität Karlsruhe, 2006.
- [32] D. Grellscheid and P. Richardson, *Simulation of Tau Decays in the Herwig++ Event Generator*, arXiv:0710.1951.
- [33] M. Bähr *et. al.*, *Herwig++ Physics and Manual*, arXiv:0803.0883.
- [34] **Particle Data Group** Collaboration, C. Amsler *et. al.*, *Review of particle physics*, *Phys. Lett.* **B667** (2008) 1.
- [35] J. M. Butterworth, J. R. Forshaw, and M. H. Seymour, *Multiparton interactions in photoproduction at HERA*, *Z. Phys.* **C72** (1996) 637–646, [hep-ph/9601371].
- [36] M. Bähr, S. Gieseke, and M. H. Seymour, *Simulation of multiple partonic interactions in Herwig++*, *JHEP* **07** (2008) 076, [arXiv:0803.3633].
- [37] M. Bähr, J. M. Butterworth, and M. H. Seymour, *The Underlying Event and the Total Cross Section from Tevatron to the LHC*, arXiv:0806.2949.
- [38] **UA5** Collaboration, G. J. Alner *et. al.*, *The UA5 High-Energy anti- $p$   $p$  Simulation Program*, *Nucl. Phys.* **B291** (1987) 445.

# Forward Physics Monte Carlo

*M. Boonekamp<sup>1</sup>, V. Juránek<sup>2</sup>, O. Kepka<sup>1,2,3</sup>, C. Royon<sup>1</sup>*

<sup>1</sup> CEA/IRFU/Service de physique des particules, 91191 Gif-sur-Yvette cedex, France

<sup>2</sup> Center for Particle Physics, Institute of Physics, Academy of Science, Prague

<sup>3</sup> IPNP, Faculty of Mathematics and Physics, Charles University, Prague

## Abstract

We give a short description of the Forward Physics Monte Carlo (FPMC) which is intended for studies of diffractive physics and two-photon exchanges at the LHC.

The Forward Physics Monte Carlo (FPMC) was developed to cover a variety of physics processes that can be detected with very forward proton spectrometers. The detectors are currently being proposed to ATLAS and CMS collaborations and soon will enable studies of single and double diffractive production, central exclusive production (CEP), two-photon exchange etc. Implementing all of these processes into a single FPMC program has the advantage of a quick data-to-model comparison and easier interfacing with the detector simulation framework. The latest version of the generator is available at [www.cern.ch/project-fPMC](http://www.cern.ch/project-fPMC).

In this report we shortly summarize the structure and usage of the FPMC program before presenting a few results coming directly from the generator.

## 1 The FPMC program

The FPMC is a stand-alone generator which generates events, treats particle decays and hadronization as in HERWIG. The forward physics processes are based on an exchange of pomerons, photons, or gluons in case of double pomeron exchange, two-photon production and central exclusive production, respectively. In FPMC, the radiation of a mediating particle of the incoming proton is described in terms of fluxes, probabilities that the incoming proton emits a mediating particle of a given energy. A selection of a specific flux therefore leads to a generation of a particular physics processes. In the following we briefly mention the most important switches of the program which are tabulated in Table 1. The detailed description of the program can be found in the complete manual [1].

- TYPEPR - switches between exclusive (“EXC”) and inclusive processes (“INC”), for example between the Higgs diffractive production in completely exclusive mode or in the inclusive one when there are pomeron remnants present.
- TYPINT - selects the QCD (“QCD”) or photon (“QED”) processes.
- NFLUX - as mentioned above, it specifies the mechanism of the exchange: 9 (factorized model, double pomeron exchange), 10 (factorized model, double reggeon exchange), 15 (two-photon exchange based Budnev photon flux [2]), 16 (exclusive KMR model, two gluon exchange [3]). Other non-default fluxes like Papageorgiou photon flux [4] or photon flux for heavy ions [5] are also present.

- IPROC - the process number, specifies what final state will be produced of the exchanged particles, some possible values are listed in Table 2. For illustration: IPROC=19999, NFLUX=16, TYPEPR=“QCD” generates exclusive Higgs production with all decay channels open following the KMR prediction or IPROC=16010, NFLUX=15, TYPEPR=“QED” produces exclusive  $WW$  two-photon production.
- ISOFTM - with this parameter, the survival probability factor [6] can be turned on (1) and off (0). It is of the order of 0.03 for LHC (0.1 for Tevatron) for QCD (double pomeron exchange, CEP) and 0.9 for QED two-photon exchange processes.
- IFITPDF - specifies a set of the parton density functions in the pomeron/reggeon. The common parameters are 10 or 20 which correspond to the most recent H1 and ZEUS fits of the densities, respectively [7].

Parameter	Description	Default
TYPEPR	Select exclusive 'EXC' or inclusive 'INC' production	'EXC'
TYPINT	Switch between QED and QCD process	'QCD'
NFLUX	Select flux	9
IPROC	Type of process to generate	11500
MAXEV	Number of events to generate	1000
ISOFTM	Turn survival probability factor on (1), off(0)	1
ECMS	CMS energy (in GeV)	14000
HMASS	Higgs mass ( $\text{GeV}/c^2$ )	115
PTMIN	Minimum $p_T$ in hadronic jet production	0
YJMIN	Minimum jet rapidity	-6
YJMAX	Maximum jet rapidity	+6
EEMIN	Minimum dilepton mass in Drell-Yan	10.0
IFITPDF	Diffraction PDF	10
NTNAME	Output ntuple name	'tmpntuple.ntp'

Table 1: Main FPMC parameters.

## 2 Examples of processes produced in FPMC

### 2.1 Inclusive diffraction

The first example we discuss is the inclusive diffraction. The starting point to predict inclusive diffraction at the LHC (or the Tevatron) is the measurement of gluon and quark densities in the pomeron performed at HERA [7]. Once these parton densities are known, it is straightforward to compute the diffractive production at the Tevatron or the LHC. The only assumption is that the factorization breaking between  $ep$  and hadron collisions is a soft process, independent of the hard process and it can be applied as a multiplicative factor to the cross section. In that sense, we call this model “factorized” model. In FPMC, we assume the survival probability to be 0.1 at the Tevatron and 0.03 for the LHC.

It will be important to remeasure the structure of the pomeron at the LHC and to study the factorization breaking of the cross section at high energies because inclusive diffraction also represents an important background for most of the processes to be studied at the LHC using forward detectors like exclusive Higgs production, studies of the photon anomalous coupling, SUSY particle production in two-photon exchange, etc.

In Figure 1, we give the dijet cross section as a function of minimum transverse jet momentum  $p_T^{min}$  for inclusive dijets, light quark jets and b-jets only. These cross sections were obtained using the process numbers IPROC=11500, 11701 and 11705 for  $gg$ , light quark and  $b$  jets processes, respectively. Other parameters were set NFLUX=9, TYPEPR='QCD', IFITPDF=10.

## 2.2 Central exclusive production / exclusive double pomeron exchange

In exclusive production, the full energy of the exchanged particles (pomerons, gluons) is used to produce a heavy object (Higgs boson, dijets, diphotons, etc.) in the central detector and no energy is lost in pomeron remnants as in inclusive case. There is an important kinematic consequence that the mass of the produced object can be computed using the proton momentum losses  $\xi_1, \xi_2$  measured in the forward detectors as  $M = \sqrt{\xi_1 \xi_2 s}$  (with  $s$  being the total center of mass energy of colliding protons). We can benefit from the good forward detector resolution on  $\xi$  to measure the mass of the produced object precisely. Moreover, since the CEP fulfill certain selection rules also other kinematic properties (spin and parity) of the produced object can be easily determined.

In Fig. 2 (left), we display the CEP cross sections of Higgs boson with its direct background of  $b$ -jet production as they are obtained directly from FPMC generator using the process numbers IPROC=19999 and 16005, respectively. Other parameters were set to NFLUX=16, TYPEPR='QCD'.

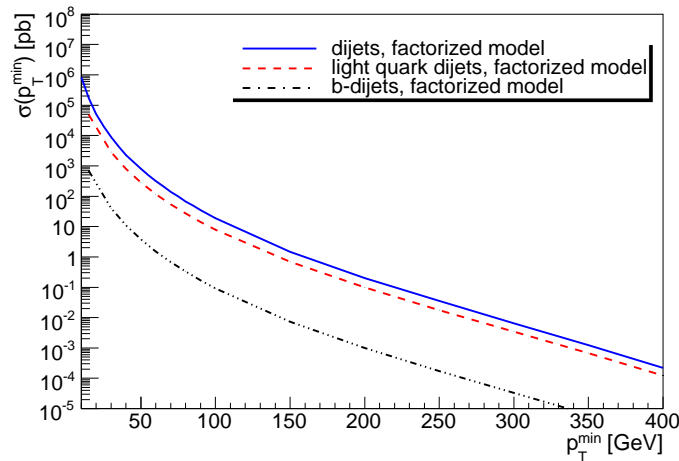


Fig. 1: Dijet cross section for inclusive dijets, light quark jets and b-jets only as a function of minimum transverse momentum of the two leading jets with  $p_T^{jet1}, p_T^{jet2} > p_T^{min}$  at  $\sqrt{s} = 14$  TeV.



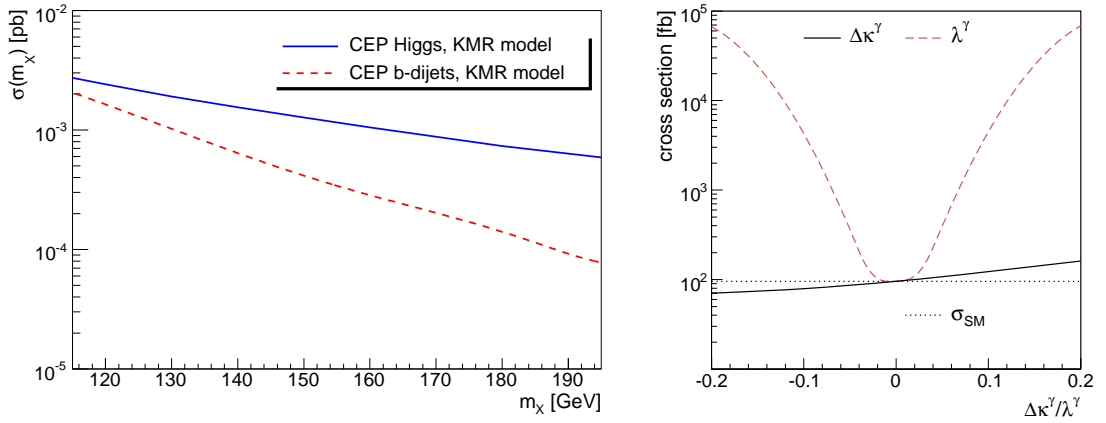


Fig. 2: *Left*: Higgs boson central exclusive production cross section for various masses of the Higgs boson  $m_X$  and  $b$ -jet production cross section as a function of the  $b\bar{b}$  invariant mass. *Right*: Cross section of the SM  $WW$  production through two-photon exchange as well as the effect of the  $\Delta\kappa^\gamma$  and  $\lambda^\gamma$  anomalous parameters.

### 2.3 $WW$ two-photon production

The two-photon production is described in terms of the photon flux. In FPMC one can study the dilepton, diboson, diphoton, and Higgs production. In the following we will discuss as an example the  $W$  pair production. The process number and other parameters for this process are IPROC=16010, TYPEPR='EXC', TYPINC='QED'.

Besides the SM production, FPMC was interfaced with O'Mega matrix element generator [8] to allow anomalous coupling studies [9]. Currently, the triple gauge boson  $WW\gamma$  effective Lagrangian is included which is parametrized with two anomalous parameters  $\Delta\kappa^\gamma$ ,  $\lambda^\gamma$ . The dependence of the total diboson production cross section in two-photon exchanges as a function of the two anomalous parameters is depicted in Fig. 2 on the right.

## 3 Conclusion

In this short report, we described the new Forward Physics Monte Carlo generator which allows to produce single and double pomeron exchanges, two-photon induced processes and Central Exclusive Production at hadron colliders. These processes are a heart of the forward physics program at the LHC. The main aim is to combine various available models into one interface to allow easy data-to-model comparisons.

## References

- [1] M. Boonekamp, V. Juranek, O. Kepka, M. Rangel. C. Royon, to appear; see <http://cern.ch/project-fPMC/>
- [2] V. M. Budnev, I. F. Ginzburg, G. V. Meledin and V. G. Serbo, Phys. Rept. **15** (1974) 181.

Process	IPROC	TYPEPR	TYPINC	NFLUX
Incl. $H$	11600+ID	INC	QCD	9,10,11
Excl. $H$	19900+ID	EXC	QCD	16
Excl. $H$	19900+ID	EXC	QED	12,13,14,15
Incl. $q\bar{q}$	11500	INC	QCD	9,10,11
Incl. $q\bar{q}$	11700+ID	INC	QCD	9,10,11
Excl. $q\bar{q}$	16000+ID	EXC	QCD	16
Incl. $W^+W^-$	12800	INC	QCD	9,10,11
Excl. $W^+W^-$	16010	EXC	QED	15
Incl. $\gamma\gamma$	12200	INC	QCD	9,10,11
Excl. $\gamma\gamma$	19800	INC	QCD	16
Excl. $\gamma\gamma$	19800	EXC	QED	12,13,14,15
Excl. $ll$	16006+IL	EXC	QED	12,13,14,15
Incl. $ll$	11350+IL	INC	QCD	9,10,11

Table 2: Setting of the FPMC for a number of physics processes. ID specif the decay products of a Higgs boson or a type of quarks produced. IL denote type of leptons in the final state. See manual for details [1].

- [3] V.A. Khoze, A.D. Martin, M.G. Ryskin, Eur. Phys. J. **C19** (2001) 477; Eur. Phys. J. **C24** (2002) 581; arXiv:0802.0177; Phys. Lett. B650 (2007) 41; A.B. Kaidalov, V.A. Khoze, A.D. Martin, M.G. Ryskin, Eur. Phys. J. **C33** (2004) 261; Eur. Phys. J. **C31** (2003) 387
- [4] E. Papageorgiu, Phys. Lett. **B250** (1990) 155 Phys. Lett. B **352** (1995) 394.
- [5] M. Drees, J. Ellis, D. Zeppenfeld, Phys. Lett. **B223** (1989) 454.
- [6] V. A. Khoze, A. D. Martin and M. G. Ryskin, Eur. Phys. J. C **23** (2002) 311.
- [7] H1 Collaboration, Eur. Phys. J. **C48** (2006) 715;  
C. Royon, L. Schoeffel, R. Peschanski, E. Sauvan, Nucl. Phys. **B746** (2006) 15;  
C. Royon, L. Schoeffel, S. Sapeta, R. Peschanski, E. Sauvan, Nucl. Phys. **B781** (2007) 1.
- [8] M. Moretti, T. Ohl and J. Reuter, arXiv:hep-ph/0102195.
- [9] O. Kepka, C. Royon, arXiv:0808.0322, in press in Phys. Rev. D.

# HEP data analysis using jHepWork and Java

*S. Chekanov*

HEP Division, Argonne National Laboratory, 9700 S.Cass Avenue, Argonne, IL 60439 USA

## Abstract

A role of Java in high-energy physics (HEP) and recent progress in development of a platform-independent data-analysis framework, jHepWork, is discussed. The framework produces professional graphics and has many libraries for data manipulation.

## 1 Introduction

Nowadays, the advantages of Java over C++ seem overwhelming. Being the most popular open-source programming language<sup>1</sup>, Java retains the C++ syntax, but significantly simplifies the language. This is (incomplete) list of advantages of Java over C++: 1) Java is multiplatform with the philosophy of "write once, run anywhere"; 2) Better structured, clean, efficient, simpler (no pointers); 3) Stable, robust and well supported: Java programs written (or compiled) many years from now can be compiled (or executed) without modifications even today. This is true even for JAVA source code with graphic widgets. In contrast, C++ programs always require continues time-consuming maintenance in order to follow the development of C++ compilers and graphic desktop environment; 4) Java has reflection technology, which is not present in C++. The reflection allows an application to discover information about created objects, thus a program can design itself at runtime. In particular, this is considered to be essential for building "intelligent" programs making decisions at runtime; 5) Free intelligent integrated-development environments (IDE), which are absolutely necessary for large software projects<sup>2</sup>; 6) Automatic garbage collection, i.e. a programmer does not need to perform memory management; 7) Extensive compile-time and run-time checking; 8) Programs written in Java can be embedded to the Web. This is important for distributed analysis environment (Java webstart, plugins, applets), especially when HEP data analysis tools are not localized in one single laboratory but scattered over the Web.

The importance of Java in HEP data analysis has been recognized since establishing the FreeHEP Java library and producing a first version of JAS (Java analysis studio) [1]. Presently, many elements of the grid software are written in Java. At LHC, Java is used for event displays and several other areas. While C++ language is remaining to be the main programming language at LHC, it lacks many features existing in Java, which makes the entire LHC software environment tremendously complicated. The lack of robustness and backward compatibility of C++ free compilers leads to various HEP-supported "scientific" flavors of Linux, with different architecture (32 bit or 64), which are all tightened to particular libraries and hardware. For example, the main computational platform for ATLAS is Scientific Linux 4.6. It will be used for future

---

<sup>1</sup>According to SourceForge.net and Freshmeat.net statistics, the number of open-source applications written in Java exceeds those written in C++.

<sup>2</sup>For example, the total number of lines of source code in ATLAS software is far higher than hundreds of thousands lines.

data taking, however, even now it is several generations behind the main-stream Linux modern distributions (Fedora, Ubuntu, Suse etc) and cannot be easily installed on modern laptops. Currently, the HEP community is required to support the entire computing chain, from hardware and operating systems, to the end-user programs, rather than concentrating on HEP-specific computational tasks. This is a significant difference from the initial concept, when HEP software could be run essentially on any platform and a vendor-supported operating system.

It should be pointed out that C+ has been chosen as the main programming language at LHC at the time when Java was still behind C++, lacking Just-in-time (JIT) compilers to convert parts of the bytecode to native code in order to improve execution time. At that time, Python [2], another portable programming language, also did not have enough power to be widely used in HEP. As Java, Python has also become increasingly popular programming language in science and engineering [3], since it is interactive, object-oriented, high-level, dynamic and portable. It has simple and easy to learn syntax which reduces the cost of program maintenance. While being portable, Python implemented in C (CPython) requires user-specific C/C++ libraries for high-performance computing, thus it cannot be considered a basis for a multiplatform data-analysis environment.

Jython [4] is an implementation of Python in Java and, as any Java application, is truly multiplatform. In contrast to CPython, Jython is fully integrated with the Java platform, thus Jython programs can make full use of extensive built-in and third-party Java libraries. Therefore, Jython programs have even more power than the standard Python implemented in C. Finally, the Jython interpreter is freely available for both commercial and non-commercial use.

jHepWork [5] is a full-featured object-oriented data analysis framework for scientists that takes advantage of the Jython language and Java. Jython macros are used for data manipulation, data visualization (plotting 1D and 2D histograms), statistical analysis, fits, etc. Data structures and data manipulation methods integrated with Java and JAIDA FreeHEP libraries [6] combine remarkable power with a very clear syntax. jHepWork Java libraries can also be used to develop programs using the standard JAVA, without Jython macros.

Programs written using jHepWork are usually rather short due the simple Python syntax and high-level constructs implemented in the core jHepWork libraries. As a front-end data-analysis environment, jHepWork helps to concentrate on interactive experimentation, debugging, rapid script development and finally on workflow of scientific tasks, rather than on low-level programming.

jHepWork is an open source product which is implemented 100 percent in Java. Since it is fully multiplatform, it does not require installation and can be run on any platform where Java is installed. It can be used to develop a range of data-analysis applications focusing on analysis of complicated data sets, histograms, statistical analysis of data, fitting. It offers a full-featured, extensible multiplatform IDE implemented in Java.

jHepWork is seamlessly integrated with Java-based Linear Collider Detector (LCD) software concept and it has the core based using FreeHEP libraries and other GNU-licensed packages. While jHepWork is mainly designed to be used in high-energy physics, it can also be used in any field, since all methods and classes are rather common in science and engineering.

Below we will discuss only the key features of jHepWork, without the coverage of all

available methods, which can easily be found using an extensive help system and the code completion feature of jHepWork. The main web page of jHepWork [5] contains the package itself, user manuals and about 50 examples with various macros. jHepWork consists of two major libraries: jeHEP (jHepWork IDE) and jHPlot (jHepWork data-analysis library). Both are licensed by the GNU General Public License (GPL).

## 2 Main differences with other data-analysis tools

Below we will compare jHepWork with two popular object-oriented packages currently used in high-energy physics: 1) JAS package [1], based on Java and FreeHEP libraries [6] and 2) C++ ROOT package [7].

### 2.1 Main differences with JAS

Compare to JAS, jHepWork:

- has a full-featured integrated development environment (IDE) with syntax highlighting, syntax checker, code completion, code analyser, an Jython shell and a file manager.
- contains powerful libraries to display data (including 3D plots) with a large choice for interactive labels and text attributes (subscripts, superscripts, overlines, arrows, Greek symbols etc.). jHepWork plots are more interactive than those written using FreeHEP JAIDA libraries linked with JAS. The plotting part is based on the jHPlot library developed for the jHepWork project and JaxoDraw Java application [8]. The latter can be used to draw Feynman diagrams in addition to standard plots;
- is designed to write short programs due to several enhancements and simpler class names. The classes written for jHepWork were designed keeping in mind simplicity of numerous high-level constructs enabling the user to write programs that are significantly shorter than programs written using JAS;
- includes high-level constructions for data manipulations, data presentations in form of tables, data input and output, calculations of systematical errors and visualization (plots, tables, spreadsheet, neural networks) which have no analogy in JAS;
- Essentially all jHepWok objects, including histograms, can be saved into files and restored using Java serialization mechanism. One can store collections of objects as well by using Jython maps or lists.
- includes an advanced help system with the code completion. For the core jHplot package, the code completion feature is complimented with a detailed API information on each method associated with certain class.

### 2.2 Main differences with the ROOT package

Compare to ROOT, jHepWork:

- is seamlessly integrated with Java-based Linear Collider Detector (LCD) software concept;
- is a Java-based program, thus it is fully multiplatform and does not require installation. This is especially useful for plugins distributed via the Internet in form of bytecode jar libraries;

- Java is very robust. Java source codes developed many years from now can easily be compiled without any changes even today. Even class libraries compiled many years from now can run on modern Java Virtual Machines. Therefore, the maintenance of jHepWork package is much less serious issue compared to ROOT;
- since jHepWork is 100% Java, it has automatic garbage collection, which is significant advantage over C++/C;
- has a full-featured IDE with syntax highlighting, syntax checker, code completion and analyser;
- can be integrated with the Web in form of applets, thus it is better suited for distributed analysis environment via the Internet. This is essential feature for modern large collaborations in high-energy physics and in other scientific fields;
- calculations based on Jython/Python scripts are typically 4-5 times shorter than equivalent C++ programs. Several examples are discussed in Ref. [5];
- calculations based on Jython scripts can be compiled to Java bytecode files and packed to jar class libraries without modifications of Jython scripts. In contrast, ROOT/CINT scripts have to be written using a proper C++ syntax, without CINT shortcuts, if they will be compiled into shared libraries;
- can access high-level Python and Java data structures;
- includes an advanced help system with a code completion based on the Java reflection technology. With increasingly large number of classes and methods in ROOT, it is difficult to understand which method belongs to which particular class. Using the jHepWork IDE, it is possible to access the full description of all classes and methods during editing Jython scripts;
- automatic updates which does not depend on particular platform. For ROOT, every new version has to be compiled from scratch;
- powerful and intelligent external IDEs (Eclipse, NetBean etc) can be used productivity in developing HEP analysis.

### 2.3 How fast it is?

Jython scripts are about 4-8 times slower than equivalent Java programs and about a factor five slower than the equivalent ROOT/CINT codes for operations on primitive data types (remember, all Jython data types are objects). This means that CPU extensive tasks should be moved to Java jar libraries.

jHepWork was designed for a data analysis in which program speed is not essential, as it is assumed that JHepWork scripts are used for operations with data and objects (like histograms) which have already been created by C++, Fortran or Java code. For such front-end data analysis, the bottleneck is mainly user input speed, interaction with a graphical object using mouse or network latency.

In practice, final results obtained with Jython programs can be obtained much faster than those designed in C++/Java, because development is so much easier in jHepWork that a user often winds up with a much better algorithm based on Jython syntax and jHepWork high-level objects

than he/she would in C++ or Java. In case of CPU extensive tasks, like large loops over primitive data types, reading files etc. one should use high-level structures of Jython and jHepWork or user-specific libraries which can be developed using the jHepWork IDE. Many examples are discussed in the jHepWork manual [5].

Acknowledgments. I would like to thanks many people for support, ideas and debugging of the current jHepWork version. This work supported in part by the U.S. Department of Energy, Division of High Energy Physics, under Contract DE-AC02-06CH11357.

## References

- [1] Java analysis studio.  
URL <http://jas.freehep.org/jas3/>
- [2] Python programming language – official website.  
URL <http://www.python.org/>
- [3] H. P. Langtangen, Python Scripting for Computational Science (Texts in Computational Science and Engineering), Springer-Verlag New York, Inc., Secaucus, NJ, USA, 2005.
- [4] The jython project.  
URL <http://www.jython.org/>
- [5] S. Chekanov, JHEPWORK - JAVA object-oriented data analysis framework.  
URL <http://projects.hepforge.org/jhepwork/>
- [6] FreeHEP java libraries.  
URL <http://java.freehep.org/>
- [7] R. Brun, F. Rademakers, P. Canal, M. Goto, ROOT status and future developments, ECONF C0303241 (2003) MOJT001.  
R. Brun, F. Rademakers, ROOT: An object oriented data analysis framework, Nucl. Instrum. Meth. A389 (1997) 81.  
URL <http://root.cern.ch/>
- [8] D. Binosi, L. Theussl, JaxoDraw: A graphical user interface for drawing feynman diagrams, Comp. Phys. Commun. 161 (2004) 76.  
URL <http://jaxodraw.sourceforge.net/>

# Tools for event generator tuning and validation

*Andy Buckley*

Institute for Particle Physics Phenomenology,  
Durham University, UK

## Abstract

I describe the current status of MCnet tools for validating the performance of event generator simulations against data, and for tuning their phenomenological free parameters. For validation, the Rivet toolkit is now a mature and complete system, with a large library of prominent benchmark analyses. For tuning, the Professor system has recently completed its first tunes of Pythia 6, with substantial improvements on the existing default tune and potential to greatly aid the setup of new generators for LHC studies.

## 1 Introduction

It is an inevitable consequence of the physics approximations in Monte Carlo event generators that there will be a number of relatively free parameters which must be tweaked if the generator is to describe experimental data. Such parameters may be found in most aspects of generator codes, from choices of  $\Lambda_{\text{QCD}}$  and  $p_{\perp}$  cutoff in the perturbative parton cascade, to the non-perturbative hadronisation process. These latter account for the majority of parameters, since the models are deeply phenomenological, typically invoking a slew of numbers to describe not only the kinematic distribution of  $p_{\perp}$  in hadron fragmentation, but also baryon/meson ratios, strangeness and  $\{\eta, \eta'\}$  suppression, and distribution of orbital angular momentum [1–4]. The result is a proliferation of parameters — of which between  $\mathcal{O}(10)$  and  $\mathcal{O}(30)$  may be of particular importance for physics studies.

Apart from rough arguments about their typical scale, these parameters are freely-floating: they must be matched to experimental data for the generator to perform well. Additionally, it is important that this tuning is performed against a wide range of experimental analyses, since otherwise parameters to which the selective analyses are insensitive will wander freely and may drive unconsidered observables to bad or even unphysical places. This requires a systematic and global approach to generator tuning: accordingly, I will summarise the current state of tools for systematically validating and tuning event generator parameters, and the first results of such systematic tunings.

## 2 Validation tools: Rivet

The Rivet library is a successor to the successful HERA-oriented generator analysis library, HZ-Tool [5]. Like its predecessor, the one library contains both a library of experimental analyses and tools for calculating physical observables. It is written in object-oriented C++ and there is strong emphasis on the following features:

- strict generator-independence: analyses are strictly performed on HepMC [6] event record objects with no knowledge of or ability to influence the generator behaviour;



- experimental reference data files are included for each standard analysis, and are used to ensure that analysis data binnings match their experimental counterparts as well as for fit comparisons;
- computational results are automatically cached for use between different analyses, using an infrastructure mechanism based on *projection* classes;
- clean, transparent and flexible programming interface: while much of the complexity is hidden, analyses retain a clear algorithmic structure rather than attempting to hide everything behind “magic” configuration files.

The “projection” objects used to compute complex observables are now a fairly complete set:

- various ways to obtain final state particles: all, charged only, excluding certain particles, with  $p_{\perp}$  and rapidity cuts, etc.;
- event shapes: sphericity, thrust, Parisi C & D parameters, jet hemispheres;
- jet algorithms: CDF and DØ legacy cones, Durham/JADE, and  $k_{\perp}$ , anti- $k_{\perp}$ , SISCONe, CDF “JETCLU” etc. from FastJet [7];
- miscellaneous: jet shapes, isolation calculators, primary and secondary vertex finders, DIS kinematics transforms, hadron decay finder, etc.

The set of standard analyses has also grown with time and is now particularly well-populated with analyses from the LEP and Tevatron experiments:

- LEP: ALEPH and DELPHI event shape analyses; ALEPH, DELPHI and PDG hadron multiplicities, strange baryons; DELPHI and OPAL b-fragmentation analyses;
- Tevatron: CDF underlying event analyses (from 2001, 2004 & 2008); CDF and DØ EW boson  $p_{\perp}$  analyses; CDF and DØ QCD colour coherence, jet decorrelation, jet shapes, Z+jets, inclusive jet cross-section;
- HERA: H1 energy flow and charged particle spectra; ZEUS dijet photoproduction.

In addition, users can write their own analyses using the Rivet projections without needing to modify the Rivet source, by using Rivet’s plugin system. We encourage such privately-implemented analyses to be submitted for inclusion in the main Rivet distribution, and would particularly welcome QCD analyses from HERA, b-factory and RHIC p-p experiments.

While Rivet is primarily a library which can be used from within any analysis framework (for example, it is integrated into the Atlas experiment’s framework), the primary usage method is via a small executable called *rivetgun*. This provides a frontend for reading in HepMC events from ASCII dump files and also for running generators “on the fly” via the AGILE interface library. This latter approach is particularly nice because there is no need to store large HepMC dump files and the corresponding lack of file I/O speeds up the analysis by a factor  $\sim \mathcal{O}(10)$ . In this mode, Rivet is ideal for parameter space scans, since generator parameters can be specified by name on the *rivetgun* command line and applied without recompilation. AGILE currently supports API-level interfaces to the Fortran HERWIG 6 [2] and Pythia 6 [1] generators (combined with the AlpGen [8] MLM multi-jet merging generator, the CHARYBDIS black hole generator [9], and the JIMMY hard underlying event generator [10] for HERWIG), plus the C++ generators Herwig++ [3], Sherpa [4] and Pythia 8 [11].

At the time of writing, the current version of Rivet is 1.1.0, with a 1.1.1 patch release pending. The main framework benefits of the 1.1.x series over 1.0.x are a safer and simpler mechanism for handling projection objects (massively simplifying many analyses), better compatibility of the AGILE loader with the standard LCG Genser packaging and a large number of new and improved analyses and projections. A “bootstrap” script is provided for easy setup. Anyone interested in using Rivet for generator validation should first visit the website <http://projects.hepforge.org/rivet/>.

Rivet is now a stable and powerful framework for generator analysis and we are looking forward to its increasing rôle in constraining generator tunings for background modelling in LHC high- $p_\perp$  physics. Future versions will see improvements aimed at high-statistics validation simulations, such as histogramming where statistical error merging is automatically correct, as well as the addition of more validation analyses.

### 3 Tuning tools: Professor

While Rivet provides a framework for comparing a given generator tuning to a wide range of experimental data, it provides no intrinsic mechanism for improving the quality of that tune. Historically, the uninspiring task of tuning generator parameters to data “by eye” has been the unhappy lot of experimental researchers, with the unsystematic nature of the study reflecting that significant improvements in quality of both life and tuning would have been possible. This call for an automated and systematic approach to tuning is taken up by a second new tool: Professor. This is written in Python code as a set of factorised scripts, using the SciPy numerical library [12] and an interface to rivetgun.

The rough formalism of systematic generator tuning is to define a goodness of fit function between the generated and reference data, and then to minimise that function. The intrinsic problem is that the true fit function is certainly not analytic and any iterative approach to minimisation will be doomed by the expense of evaluating the fit function at a new parameter-space point: this may well involve ten or more runs of the generator with 200k–2M events per run. Even assuming that such runs can be parallelised to the extent that only the longest determines the critical path, an intrinsically serial minimisation of  $\mathcal{O}(1000)$  steps will still take many months. This is clearly not a realistic strategy!

The Professor approach, which is the latest in a lengthy but vague history of such efforts [13, 14], is to parameterise the fit function with a polynomial. In fact, since the fit function itself is expected to be complex and not readily parameterisable, there is a layer of indirection: the polynomial is actually fitted to the generator response of each observable bin,  $\text{MC}_b$  to the changes in the  $n$ -element parameter vector,  $\vec{p}$ . To account for lowest-order parameter correlations, a second-order polynomial is used,

$$\text{MC}_b(\vec{p}) \approx f^{(b)}(\vec{p}) = \alpha_0^{(b)} + \sum_i \beta_i^{(b)} p'_i + \sum_{i \leq j} \gamma_{ij}^{(b)} p'_i p'_j, \quad (1)$$

where the shifted parameter vector  $\vec{p}' \equiv \vec{p} - \vec{p}_0$ , with  $\vec{p}_0$  chosen as the centre of the parameter hypercube. A nice feature of using a polynomial fit function, other than its general-purpose robustness, is that the actual choice of the  $\vec{p}_0$  is irrelevant: the result of a shift in central value is simply to redefine the coefficients, rather than change the functional form, but choosing a central value is numerically sensible.

The coefficients are determined by randomly sampling the generator from  $N$  parameter space points in an  $n$ -dimensional parameter hypercube defined by the user. Each sampled point may actually consist of many generator runs, which are then merged into a single collection of simulation histograms. A simultaneous equations solution is possible if the number of runs is the same as the number of coefficients between the  $n$  parameters, i.e.  $N = N_{\min}^{(n)} = (2 + 3n + n^2)/2$ . However, using this minimum number of runs introduces a systematic uncertainty, as we certainly do not expect the bin MC response to be a perfect polynomial. Here we are helped by the existence of the Moore–Penrose pseudoinverse: a generalisation of the normal matrix inverse to non-square matrices with the desirable feature that an over-constrained matrix will be inverted in a way which gives a least-squares best fit to the target vector. Even more helpful is that a standard singular value decomposition (SVD) procedure can be used to deterministically implement the pseudoinverse computation. Hence, we phrase the mapping on a bin-by-bin basis from coefficients  $C$  to generator values  $V$  as  $PC = V$ , where  $P$  is the parameter matrix to be pseudo-inverted. For a two parameter case, parameters  $\in \{x, y\}$ , the above may be explicitly written as

$$\underbrace{\begin{pmatrix} 1 & x_1 & y_1 & x_1^2 & x_1 y_1 & y_1^2 \\ 1 & x_2 & y_2 & x_2^2 & x_2 y_2 & y_2^2 \\ & & & \vdots & & \end{pmatrix}}_{P \text{ (sampled param sets)}} \underbrace{\begin{pmatrix} \alpha_0 \\ \beta_x \\ \beta_y \\ \gamma_{xx} \\ \gamma_{xy} \\ \gamma_{yy} \end{pmatrix}}_{C \text{ (coeffs)}} = \underbrace{\begin{pmatrix} v_1 \\ v_2 \\ \vdots \end{pmatrix}}_{V \text{ (values)}} \quad (2)$$

where the numerical subscripts indicate the  $N$  generator runs. Note that the columns of  $P$  include all  $N_{\min}^{(2)} = 6$  combinations of parameters in the polynomial, and that  $P$  is square (i.e. minimally pseudo-invertible) when  $N = N_{\min}^{(n)}$ . Then  $C = \tilde{I}[P] V$ , where  $\tilde{I}$  is the pseudoinverse operator.

Now that we have, in principle, a good parameterisation of the generator response to the parameters,  $\vec{p}$ , for each observable bin,  $b$ , it remains to construct a goodness of fit (GoF) function and minimise it. We choose the  $\chi^2$  function, but other GoF measures can certainly be used. Since the relative importance of various distributions in the observable set is a subjective thing — given 20 event shape distributions and one charged multiplicity, it is certainly sensible to weight up the multiplicity by a factor of at least 10 or so to maintain its relevance to the GoF measure — we include weights,  $w_{\mathcal{O}}$ , for each observable,  $\mathcal{O}$ , in our  $\chi^2$  definition:

$$\chi^2(\vec{p}) = \sum_{\mathcal{O}} w_{\mathcal{O}} \sum_{b \in \mathcal{O}} \frac{(f_b(\vec{p}) - \mathcal{R}_b)^2}{\Delta_b^2}, \quad (3)$$

where  $\mathcal{R}_b$  is the reference value for bin  $b$  and the total error  $\Delta_b$  is the sum in quadrature of the reference error and the statistical generator errors for bin  $b$  — in practise we attempt to generate enough data that the MC error is much smaller than the reference error for all bins.

The final stage of our procedure is to minimise this parameterised  $\chi^2$  function. It is tempting to think that there is scope for an analytic global minimisation at this order of polynomial, but not enough Hessian matrix elements may be calculated to constrain all the parameters and

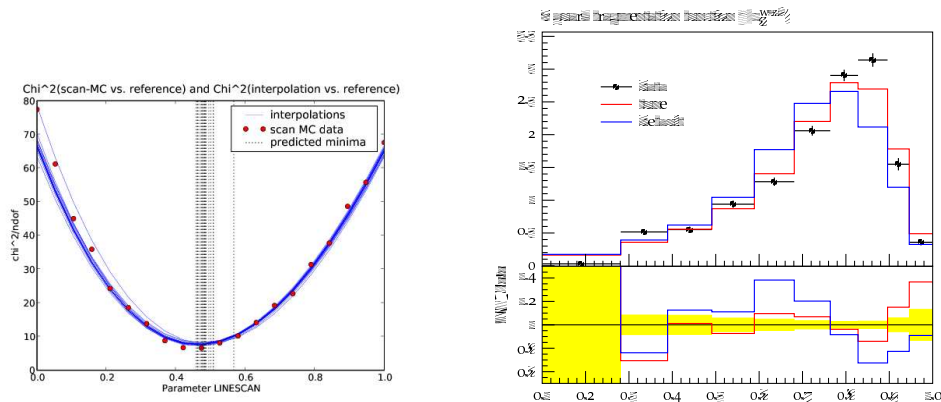


Fig. 1: (a) Parameter space line scan in  $\chi^2$ , showing the agreement between Professor’s predicted values (blue lines) and the true values (red dots). (b) Pythia 6 b-fragmentation functions, showing the improvements obtained using Professor (red) to tune the Bowler parameterisation against the default (blue).

hence we must finally resort to a numerical minimisation. We have implemented this in terms of minimisers from SciPy and also PyMinuit [15], with the latter’s initial parameter space grid scan making it our preferred choice.

Finally, on obtaining a predicted best tune point from Professor, it is prudent to check the result. This can be done directly with rivetgun, and Professor also has a line scan feature which allows scans along arbitrary straight lines in parameter space, which is useful to verify that the  $\chi^2$  behaves as interpolated and to explicitly compare default tunes to predicted tunes. Such a line scan can be seen in Fig. 1(a). We have explicitly checked the robustness of the polynomial and the random distribution of sampling points against various skewed test distributions and the behaviour is robust. We have also found it to be useful to over-sample by a considerable fraction, and then to perform the  $\chi^2$  minimisation for a large number of distinct run-combinations,  $N_{\min}^{(n)} < N_{\text{tune}} \leq N$ , which gives a systematic control on interpolation errors and usually a better performance than just using  $N_{\text{tune}} = N$ .<sup>1</sup>

The focus in testing and commissioning the Professor system has until recently been focused on Pythia 6 tunes against LEP data [16]. Here we were able to interpolate and minimise up to 10 parameters at a time for roughly 100 distributions, but beyond this the minimisation time became large and we were less happy with the minima. Eventually we decided to split the tuning into a two-stage procedure where flavour-sensitive fragmentation parameters were tuned first to provide a base on which to tune the semi-factorised kinematic parameters of the shower and hadronisation. The result has been a dramatic improvement of the Pythia 6 identified particle multiplicity spectra, without losing the event shape descriptions (originally tuned by DELPHI’s version of the same procedure), and a major improvement of the b-fragmentation function as seen in Fig. 1(b).<sup>2</sup> This tune will be adopted as the default parameter set for the next release of

<sup>1</sup>Note that the tuning runs need a significant degree of variation, i.e.  $N_{\text{tune}} \ll N$  for most of the tune run-combinations.

<sup>2</sup>Note that interpolation methods cannot deal with discrete settings such as the choice of functional form of b-fragmentation function. This required several parallel tunes with different values of the discrete parameter.

Pythia 6.

## 4 Conclusions

To conclude, the situation is looking positive for MC generator tuning at present: the Rivet and Professor tools are now in a state where they can be used to achieve real physics goals and the Pythia 6 tune described here (using both tools) has been a significant success. Development plans in the near future are very much aimed at getting the same tuning machinery to work for hadron collider studies, in particular initial state radiation (ISR) and underlying event (UE) physics. We aim to present tunes of C++ generators to LEP data shortly, along with first studies of interpolation-based tunes to CDF underlying event data. Finally, we are keen to constrain fragmentation and UE hadron physics for the LHC, using b-factory, RHIC and early LHC data.

## References

- [1] T. Sjostrand and S. Mrenna and P. Skands, *JHEP* **05**, 026 (2006), hep-ph/0603175.
- [2] B. Webber and others, *JHEP* **01**, 010 (2001), hep-ph/0011363, HERWIG Collaboration.
- [3] P. Richardson *et al.*, (2008), 0803.0883, Herwig++ Collaboration.
- [4] F. Krauss and others, *JHEP* **02**, 056 (2004), hep-ph/0311263, Sherpa Collaboration.
- [5] J. Bromley *et al.*, (1995), ZEUS and H1 Collaborations.
- [6] M. Dobbs and J. B. Hansen, *Comput. Phys. Commun.* **134**, 41 (2001).
- [7] M. Cacciari and G. Salam and G. Soyez, (2006), hep-ph/0607071.
- [8] M. Mangano *et al.*, *JHEP* **07**, 001 (2003), hep-ph/0206293.
- [9] C. Harris, P. Richardson, and B. Webber, *JHEP* **08**, 033 (2003), hep-ph/0307305.
- [10] J. Butterworth, J. Forshaw, and M. Seymour, *Z. Phys.* **C72**, 637 (1996), hep-ph/9601371.
- [11] T. Sjostrand, S. Mrenna, and P. Skands, *Comput. Phys. Commun.* **178**, 852 (2008), 0710.3820.
- [12] SciPy website: <http://www.scipy.org>.
- [13] DELPHI Collaboration, K. Hamacher *et al.*, *Z. Phys.* **C73**, 11 (1996).
- [14] K. Hamacher and M. Weierstall, (1995), hep-ex/9511011.
- [15] PyMinuit website: <http://code.google.com/p/pyminuit/>.
- [16] A. Buckley *et al.*, Professor Collaboration, in preparation.

# Prerequisites for the Validation of Experiment and Theory

*Lars Sonnenschein*

CERN and LPNHE Paris, Universités Paris VI, VII

## **Abstract**

In physics a better understanding of nature is achieved by a recursive interplay between experiment and theory. This requires a validation of both. On the theory side Monte-Carlo event generators can be validated by means of data from experiment. This data has to be corrected for detector effects to render an immediate comparison to event generators meaningful. A HepData database is available to retrieve published measurements including error correlation matrices from authors. Furthermore a validation framework Rivet is available in which authors are supposed to implement the necessary code to reproduce their published measurement exactly. To prevent any ambiguities this implementation should be accomplished at the time of publication. The constraints from published measurements are needed for further event generator development, of which experiments in turn will benefit in the next iteration.

## **1 Introduction**

In high energy physics the ultimate goal of experiment and theory is a better understanding of nature. While the theory needs input from experiment for the verification or falsification of concurrent models the experiment needs input from theory for the prediction of observables, the understanding of scattering processes/production rates and the discrimination of instrumental effects and background processes from (new) physics. A recursive interplay takes place between experiment and theory where the experiment probes the description of nature provided by the theory, as schematically depicted in fig. 1. The intersection point where experiment and theory meet is the cross section. But before measurements can be compared to theory, the measurements have to be corrected for detector effects on the one hand and the models in which the theory is embedded have to be simulated on the other hand. To render the comparison between theory

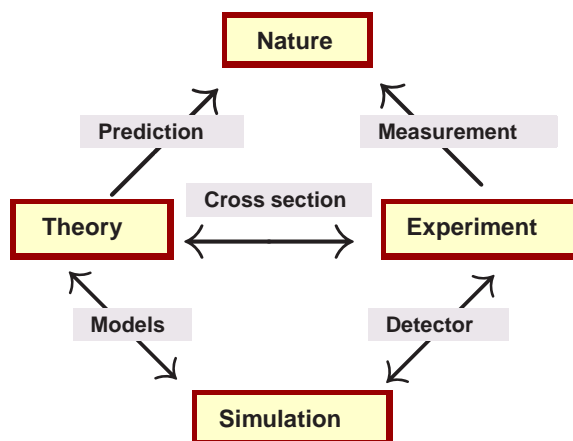


Fig. 1: Relations between theory, experiment, simulation and nature. The intersection point where experiment and theory meet is the cross section. While the theory makes predictions of nature and interfaces via models to the simulation the experiment measures nature and interfaces via the detector simulation or corrections obtained from data to the models.

and measurement meaningful the understanding (verification, validation and optimization) of Monte-Carlo event generation, simulation and experiment is crucial.

The need for the validation of experiment and theory is also documented by Sir Arthur Eddington's statement: "It is a good rule not to put overmuch confidence in a theory until it has been confirmed by observation. I hope I shall not shock the experimental physicists too much if I add that it is also a good rule not to put overmuch confidence in the observational results that are put forward *until they have been confirmed by theory*" (his italics).

## 2 Need for corrected data from experiment

The theory makes predictions to very few fixed orders (LO, NLO) plus resummation of radiation. More or less phenomenological models are needed for comparison with measurements. The models are implemented in Monte-Carlo event generators. They contain phenomenological parameters like e.g.:

- Parton shower termination parameters  $p_{\perp \text{ min}}, m_{\text{min}}$
- Lund string and cluster fragmentation parameters: string function parameters, mass
- Underlying event: primordial  $k_{\perp}$ , color reconnection parameters,
- Parton Distribution Functions (PDF's).

Therefore the models need to be validated and adjusted using real data from experiment. The data is coming from the HepData database [1] which is an archive of published HEP data from the last 30 years. It contains almost exclusively data which has been corrected for detector effects. Its focus is on cross section and similar measurements which makes the archive complementary to the Particle Data Group.

Authors who are publishing a measurement should remember to send their data to the HepData database. This data has to be corrected for detector effects (i.e. acceptance, efficiency

and instrumental background) which corresponds to a correction to the hadronic final state or particle level. It is important that the data is not corrected any further to prevent the introduction of model dependencies since the models are supposed to be tested with the data among others. Only if corrected in this way the data can be always compared to Monte-Carlo event generators and it will be useful any time in the future. Otherwise the published measurement will be obsolete sooner or later (typically rather soon).

### 3 Reproducibility of published analyses

Before a comparison of the theory and models via simulation to data can be accomplished the published analyses have to be implemented and they have to match the publications exactly. Phenomenologists spend an enormous amount of time to reproduce published data analysis in all details, e.g. jet algorithm details and how the algorithm has been applied exactly. The publication might seem unambiguous at the time of writing. Experience shows, that this is no longer the case later on. The solution is the validation tool Rivet [2] which contains the analysis code and provides the real data for comparison. Rivet can be directly interfaced by means of the standardised event record format HepMC [3] to various Monte-Carlo event generators, e.g. via the interface package AGILE [4]. Authors of published corrected measurements (see last section for details on the correction) should implement their analysis into the Rivet framework and this at the time of publication to prevent any ambiguities. Only in this way an exact reproduction is guaranteed.

Present and past collider centre-of-mass energies provide unique points of operation. Event generator authors (of Herwig++, Pythia8, Sherpa, etc.) appreciate very much corrected analyses from the electron positron collider LEP where the hadronisation corrections turned out to be larger than the detector corrections. Important constraints on fragmentation models have been provided by LEP analyses. The most important ones have already been implemented into the Rivet validation framework.

Another important item to be mentioned within the context of reproducibility is the correlation between errors in the measurement. The matrices of correlated errors are typically only provided by analyses accomplished in the QCD group of experiments. This information has to be obtained on an event by event basis and can therefore not be recovered from published plots containing measured distributions. Thus it is extremely important to document this information, too.

Constraints from new published data corrected for detector effects are needed for further Monte-Carlo event generator development, the more the better. Experiments will benefit from it in the next iteration.

### 4 Summary

An important prerequisite for the validation of experiment and theory is that experiments correct their data for detector effects. In this way the data can be used at a later time point, when different or new models and/or Monte-Carlo event generators have to be validated and optimised. In the case of correlated errors it is also important that the experiment provides the covariance matrix, since this information can not be recovered from published plots containing measured



distributions. Once a measurement is being published, the results should be send to the HepData database. The authors of the analysis should implement their analysis into the validation framework Rivet at the time of publication. In this way the usefulness of their measurement is guaranteed any time in the future. Experiments will benefit from the additional constraints imposed by their published analyses in the next iteration of event generator validation.

### **Acknowledgements**

This work has been supported by the Marie Curie Program, in part under contract number MRTN-CT-2006-035606 and the HEPtools EU Marie Curie Research Training Network under contract number MRTN-CT-2006-035505.

### **References**

- [1] HepData database, <http://projects.hepforge.org/hepdata>.
- [2] Validation framework Rivet, <http://projects.hepforge.org/rivet>.
- [3] M. Dobbs, J. B. Hansen, L. Garren, and L. Sonnenschein,  
[http://lcgapp.cern.ch/project/simu/HepMC/20400/HepMC2\\_user\\_manual.pdf](http://lcgapp.cern.ch/project/simu/HepMC/20400/HepMC2_user_manual.pdf).
- [4] A Generator Interface Library, <http://projects.hepforge.org/agile>.



## **Chapter 7**

# **List of Authors**

# List of Authors

Österberg, K., 527

Ajaltouni, Z.J., 331  
Albino, S., 710  
Altarelli, G., 8  
Ambroglini, F., 663  
Anderson, J., 106  
Antchev, G., 527  
Arneodo, M., 397  
Aspell, P., 527  
Avati, V., 527

Bähr, M., 641, 752  
Bacchetta, A., 129  
Bagliesi, M.G., 527  
Ball, R.D., 8, 54  
Banfi, A., 129, 155, 331  
Baranov, S., 129, 205, 331  
Bartalini, P., 631, 663  
Bartels, J., 129, 205  
Bechtel, F., 663, 670  
Berardi, V., 527  
Berretti, M., 527  
Beuf, G., 8  
Biasini, M., 296  
Bierenbaum, I., 331  
Blümlein, J., 331  
Blair, R.E., 681  
Bombonati, C., 296  
Boonekamp, M., 106, 758  
Bottigli, U., 527  
Boutle, S., 274  
Bozzo, M., 527  
Brücken, E., 527  
Bracinik, J., 274  
Bruni, A., 427  
Bruno, G.E., 296  
Buckley, A., 768  
Bunyatyan, A., 129, 421, 567, 675  
Burkhardt, H., 106  
Bussey, P., 557  
Buzzo, A., 527

Cacciari, M., 274  
Cafagna, F., 527

Calicchio, M., 527  
Caola, F., 8  
Catanesi, M.G., 527  
Catastini, P.L., 527  
Cecchi, R., 527  
Ceccopieri, F.A., 458  
Cerci, S., 516  
Chekanov, S., 631, 681, 763  
Chierici, R., 747  
Ciafaloni, M., 8  
Ciocci, M.A., 527  
Coco, V., 129, 182  
Colferai, D., 8  
Cooper-Sarkar, A., 75, 567  
Corcella, G., 129, 155, 331  
Czakon, M., 331

Dainese, A., 274  
Dasgupta, M., 129, 155  
Deák, M., 129, 205, 737  
Deile, M., 527  
Delsart, P.A., 129, 182  
Del Debbio, L., 54  
de Roeck, A., 126  
Diaconu, C., 567  
Diehl, M., 397  
Dimovasili, E., 527  
Dittmar, M., 106  
Dremin, I.M., 129, 257

Eggert, K., 527  
Engel, R., 567  
Eremin, V., 527  
Erhan, S., 516  
Ewerz, C., 510

Fanò, L., 663  
Feltesse, J., 54  
Ferrera, G., 331  
Ferro, F., 527  
Field, R., 663  
Forte, S., 54

Garcia, F., 527  
Geiser, A., 274

Geiser, A., 274  
 Gelis, F., 8  
 Giani, S., 527  
 Gieseke, S., 631, 641, 752  
 Gigg, M.A., 752  
 Glazov, A., 54, 75  
 Golec-Biernat, K., 471  
 Goulianos, K., 440  
 Grebenyuk, J., 75  
 Greco, V., 527  
 Grellscheid, D., 752  
 Grindhammer, G., 274  
 Grothe, M., 516  
 Guffanti, A., 54  
 Gwenlan, C., 129  
  
 Halyo, V., 106  
 Hamilton, K., 752  
 Hautmann, F., 129, 205, 716  
 Heino, J., 527  
 Heinrich, G., 681  
 Hildén, T., 527  
 Hiller, K., 540  
 Hollar, J., 516  
  
 Janssen, X., 427  
 Joseph, S., 129, 155  
 Jung, A.W., 274  
 Jung, H., 129, 205, 646, 737  
 Juránek, V., 758  
  
 Kašpar, J., 527  
 Kepka, O., 758  
 Khoze, V.A., 397, 482, 488  
 Kiesling, Ch., 567  
 Klasen, M., 448  
 Klein, S., 331  
 Kniehl, B.A., 331  
 Knutsson, A., 129, 205  
 Kopal, J., 527  
 Kramer, G., 331, 448  
 Krauss, F., 631  
 Kundrať, V., 527  
 Kurvinen, K., 527  
 Kutak, K., 129, 205, 567, 737  
  
 Lönnblad, L., 129, 733  
 Lami, S., 527  
 Latino, G., 527  
 Latorre, J.I., 54  
 Latunde-Dada, O., 752  
 Lauhakangas, R., 527  
 Lendermann, V., 75  
 Lenzi, P., 740  
  
 Li, G., 75  
 Likhoded, A., 331  
 Lipatov, A., 129, 205, 681  
 Lippmaa, E., 527  
 Lokajíček, M., 527  
 Lo Vetere, M., 527  
 Lucas Rodriguez, F., 527  
 Luisoni, G., 129, 155  
 Lytken, E., 296  
  
 Müller, K., 129, 240  
 Macrí, M., 527  
 Magazzù, G., 527  
 Majhi, A., 129  
 Majhi, S., 155  
 Marage, P., 427  
 Marti, L., 129, 646  
 Martin, A.D., 482, 488  
 Meucci, M., 527  
 Milstead, D.A., 331  
 Minutoli, S., 527  
 Mischke, A., 296  
 Moares, A., 656  
 Moch, S., 8  
 Motyka, L., 8, 471  
  
 Namssoo, T., 129, 646  
 Newman, P., 397, 401  
 Niewiadomski, H., 527  
 Nockles, C., 464  
 Noschis, E., 527  
 Notarnicola, G., 527  
 Nystrand, J., 503  
  
 Oliveri, E., 527  
 Oljemmark, F., 527  
 Orava, R., 527  
 Oriunno, M., 527  
 Osman, S., 129, 646  
 Ostapchenko, S., 567  
  
 Palazzi, P., 527  
 Pedreschi, E., 527  
 Pereira, A.V., 516  
 Perrey, H., 129, 240  
 Petäjäjärvi, J., 527  
 Petersen, T., 106  
 Piccione, A., 54  
 Pierog, T., 567  
 Pinfeld, J.L., 440  
 Piskounova, O.I., 331  
 Plätzer, S., 752  
  
 Quinto, M., 527

Rúriková, Z., 129, 274, 675  
Radermacher, E., 527  
Radescu, V., 54  
Radicioni, E., 527  
Ravotti, F., 527  
Rella, G., 527  
Richardson, P., 752  
Robutti, E., 527  
Rodrigo, G., 129  
Rodrigues, E., 129  
Rogal, M., 8  
Rogers, T.C., 567  
Rojo, J., 54, 129, 182  
Roloff, P., 274  
Ropelewski, L., 527  
Rosemann, C., 296  
Royon, Ch., 8, 205, 758  
Ruggiero, G., 527  
Rummel, A., 527  
Ruspa, M., 401  
Ryskin, M.G., 482, 488  
  
Sálek, D., 8  
Ślomiński, W., 412  
Saarikko, H., 527  
Sabio Vera, A., 129, 205  
Sako, T., 567  
Salam, G.P., 8  
Saleev, V.A., 331  
Sander, C., 129, 182  
Sanguinetti, G., 527  
Santroni, A., 527  
Schörner-Sadenius, Th., 129, 240  
Schicker, R., 548  
Schienbein, I., 331  
Schmidke, W.B., 421  
Schwennsen, F., 129, 205  
Scribano, A., 527  
Sette, G., 527  
Seymour, M.H., 641, 752  
Sherstnev, A., 752  
Sjöstrand, T., 726  
Snoeys, W., 527  
Somogyi, G., 129  
Sonnenschein, L., 774  
Soyez, G., 129, 182  
Spiesberger, H., 274, 331  
Spinella, F., 527  
Squillacioti, P., 527  
Staśto, A.M., 8  
Starodumov, A., 296  
Stenzel, H., 540  
Stephens, Ph., 699  
Ster, A., 527  
  
Stocco, D., 296  
Strikman, M., 129, 257, 495, 567  
  
Taylor, C., 527  
Teubner, T., 464  
Thorne, R.S., 8, 54, 331  
Trócsányi, Z., 129  
Treccani, M., 129  
Treleani, D., 129, 635  
Trentadue, L., 458  
Trummal, A., 527  
Tully, J., 752  
Tung, W.K., 331  
Turcato, M., 274  
Turini, N., 527  
  
Ubiali, M., 54  
  
Valkárová, A., 412  
van Hameren, A., 699  
Van Mechelen, P., 557  
Vermaseren, J.A.M., 8  
Vogt, A., 8  
  
Ward, B.F.L., 129, 155  
Watt, G., 54, 471  
Webber, B.R., 752  
Weiss, Ch., 495  
White, Ch., 8, 721  
Whitmore, J., 527  
Wolf, R., 296  
Wu, J., 527  
  
Yagües-Molina, A., 274  
Yost, S.A., 129, 155  
  
Zanderighi, G., 129, 331  
Zotov, N., 129, 205, 331, 681  
zur Nedden, M., 296

## **Chapter 8**

# **List of Participants**

# List of Participants

Adamczyk Leszek AGH- University of Science and Technology Cracow  
Adelodun Tesleem Alade University of Ibadan  
Adorisio Cristina Universita' della Calabria  
Ahmad, Ayaz Mohammad Aligarh Muslim University, Aligarh, India  
Ahmed Ijaz National Centre for Physics Islamabad  
Ajaltouni Ziad LHCB  
Akca Ali Riza TFI  
Akhundov Arif University of Valencia, Spain  
Albino Simon Hamburg University  
Alcaraz Maestre Juan CIEMAT - Madrid  
Alekhin Sergey Inst. for High Energy Physics (Protvino, Russia)  
Alessandro Bertolin INFN - Sez. di Padova  
Amelung Christoph CERN  
Anastasiou Anastasiou ETH  
Andersen Jeppe R. University of Cambridge  
Andreev Valeri UCLA  
Andreev Vladimir LPI, Moscow  
Anjos, Nuno LIP  
Antonio Zoccoli University and INFN - Bologna  
Arneodo Michele Universita' del Piemonte Orientale, Novara, Italy  
Arturo, Fernandez Tellez Universidad Autonoma de Puebla  
Asghar, Muhammad Irfan National Centre for Physics  
Aushev Vladimir KINR, Kiev/DESY  
Avati Valentina Helsinki University  
Avsar Emil Lund University  
Aybat, Mert ETH  
Bähr, Manuel University Karlsruhe  
Bacchetta Alessandro DESY  
Badelek Barbara Warsaw University  
Baghdasaryan Artem DESY/Yerevan  
Baines John RAL  
Ball Richard Edinburgh  
Bamberger Andreas University Freiburg  
Banerjee Sunanda Tata Institute of Fundamental Research  
Banfi Andrea Universita' degli Studi di Milano-Bicocca  
Baranov Sergey Lebedev Institute of Physics, Moscow  
Barbagli Giuseppe INFN - Firenze  
Bargiotti Marianne CERN  
Bartalini Paolo NTU  
Bartels Joachim Universitaet Hamburg  
Bechtel Florian Hamburg University  
Behera, Prafulla University of Iowa



Behnke Olaf Uni Heidelberg  
 Bel'kov Alexander Joint Institute for Nuclear Research, Dubna, Russia  
 Bellagamba Lorenzo INFN Bologna  
 Bellan Paolo Padova University - INFN  
 Bellan Riccardo Università degli Studi di Torino - INFN  
 Belov Sergey Joint Institute for Nuclear Research, Dubna, Russia  
 Bennaoum Malika theoretical physics  
 Beuf, Guillaume CEA / IPhT  
 Bierenbaum Isabella DESY, Zeuthen  
 Bluemlein Johannes DESY  
 Boettcher Helmut DESY Zeuthen  
 Bolzoni, Paolo DESY  
 Bombonati Carlo INFN & University of Padova  
 Bonato Alessio DESY / Hamburg University  
 Bondarenko Sergey Santiago de Compostela University  
 Boonekamp Maarten CEA/DAPNIA-Saclay  
 Boreskov Konstantin ITEP, Moscow  
 Bornheim Adolf CALTECH / CMS  
 Borrás Kerstin DESY  
 Botje Michiel NIKHEF  
 Bourilkov Dimitri University of Florida  
 Boutle, Sarah University College London  
 Bozzi, Giuseppe ITP Karlsruhe  
 Bozzo Marco CERN and INFN Genova  
 Bracinik Juraj MPI Munchen  
 Brock Ian University of Bonn  
 Brona, Grzegorz University of Warsaw  
 Bruni Alessia INFN Bologna  
 Bruno Giuseppe Università di Bari  
 Buchmueller Oliver CERN  
 Buckley Andy IPPP, Durham  
 Bunyatyan Armen MPI-Heidelberg / YerPhI  
 Buran, Torleiv dpt. of phys., univ. of oslo  
 Bussey, Peter University of Glasgow  
 Buttar Craig Sheffield University  
 Butterworth Jonathan UCL  
 Cacciari Matteo LPTHE, UPMC Paris  
 Cafarella, Alessandro NCSR Demokritos  
 Cakir, Orhan Ankara University  
 Caldwell Allen Max-Planck-Institut  
 Caola, Fabrizio Università di Milano and INFN-Milano  
 Capua Marcella University of Calabria and INFN  
 Carli Tancredi CERN  
 Caron Sascha NIKHEF  
 Catmore James Lancaster University, ATLAS  
 Ceccopieri, Federico Alberto Università di Parma  
 Cerminara Gianluca INFN - Università degli Studi di Torino  
 Chachamis Grigorios University of Hamburg  
 Chekanov Sergei ANL/DESY  
 Chekelian Vladimir MPI Munich  
 Chierici Roberto CNRS/IPNL  
 Chiochia Vincenzo University of Zurich  
 Cholewa Axel DESY

Coca Cornelia National Institute of Physics and Nuclear Engineering IFIN-HH, Bucharest  
 Coco, Victor LAPP-IN2P3-CNRS  
 Cole Jo University of Bristol  
 Colferai Dimitri Universita' di Firenze e INFN (Italy)  
 Collins John Penn State Univ  
 Collins-Tooth Christopher University of Glasgow, ATLAS  
 Cooper-Sarkar Amanda (Mandy) Oxford University, UK  
 Corcella Gennaro CERN  
 Corradi Massimo INFN Bologna  
 Corriveau Francois IPP / McGill University  
 Costa Marco University of Turin  
 Coughlin Tim The University of Manchester  
 Cox Brian University of Manchester  
 Czakon, Michal University of Wuerzburg  
 Czychula Zofia Jagiellonian University  
 d'Enterria David CERN  
 D'Orazio, Alessia Max-Planck-Institut f. Physik  
 Dainese Andrea INFN Legnaro  
 Daleo Alejandro ETH Zurich  
 Dasgupta Mrinal Manchester University  
 Daum Karin DESY/Uni Wuppertal  
 Davatz Giovanna CERN, EP  
 De Jesus Damiao, Dilson Universidade do Estado do Rio de Janeiro  
 De Roeck Albert CERN  
 Deak Michal DESY  
 Delenda Yazid University of Manchester  
 Delsart, Pierre-Antoine L.A.P.P (Annecy)  
 Derkach Denis DESY  
 Diaconu Cristinel CPPM/DESY  
 Dianna, Giovanni University of Milan - INFN  
 Diehl Markus DESY  
 Diez Carmen DESY  
 Dittmar Michael ETH Zurich  
 Dobur Didar INFN-Pisa  
 Drescher Hans-Joachim Frankfurt Institute for Advanced Studies  
 Drohan Janice UCL  
 Drozdetskiy Alexey University of Florida, Gainesville, USA  
 Eggert Karsten CERN  
 Eisele Franz Physikalisches Institut heidelberg  
 Eisenberg Yehuda Weizmann Institute  
 Ellis Keith Fermilab  
 Emelyanov, Valery MEPHI  
 Enberg Rikard Ecole Polytechnique  
 Engel Ralph Forschungszentrum Karlsruhe  
 Ewerz Carlo ECT\* Trento  
 Fabbri Fabrizio INFN Bologna - Italy  
 Fabris Daniela INFN Sezione di Padova - Italy  
 Falter Thomas Institut f. Theoretische Physik, Universitaet Giessen  
 Fano' Livio INFN - Perugia  
 Fawe Adewale Heritage international  
 Feltesse Joel DESY/HAMBURG/SACLAY  
 Felzmann Ulrich Institut für Experimentelle Kernphysik, University Karlsruhe  
 Ferrag Samir University of Oslo

Ferrera Giancarlo Univ. de Barcelona & Univ. de Granada, Spain  
 Ferro Fabrizio INFN Genova  
 Field Rick Florida/CDF  
 Filippo Ambroglini University of Perugia & INFN  
 Flossdorf Alexander DESY  
 Flucke Gero DESY  
 Forshaw Jeff Manchester University  
 Forte Stefano Milan University  
 Fuks Benjamin LPSC Grenoble  
 Gallinaro, Michele LIP  
 Gallo Elisabetta INFN Firenze  
 Gehrmann Aude ETH Zuerich  
 Geiser Achim DESY Hamburg  
 Geist Walter IReS/Strasbourg  
 Gelis, Francois CERN PH-TH  
 Ghazaryan Samvel Yerevan Physics Institute  
 Gieseke Stefan CERN/Uni Karlsruhe  
 Ginzburg Jonatan CERN  
 Gladilin Leonid Moscow State University  
 Glazov Alexandre DESY  
 Glover Nigel Durham U., IPPP  
 Gogitidze Nelly LPI, Moscow / DESY, Hamburg  
 Golec-Biernat, Krzysztof Institute of Nuclear Physics  
 Golutvin Igor JINR, CMS  
 Gotsman Eyal Tel Aviv University  
 Goulianos Konstantin Rockefeller University  
 Gouzevitch, Maxime Laboratoire LLR, Ecole Polytechnique  
 Grab Christoph ETH Zurich  
 Grebenyuk, Julia DESY, Hamburg  
 Greco Mario Univ. Rome III  
 Grindhammer Guenter Max-Planck-Institute for Physics, Munich  
 Grothe Monika Wisconsin/Turin  
 Groys Michael Tel Aviv university  
 Grzelinska, Agnieszka IFJ PAN, Cracow  
 Guernane Rachid LPC Clermont-Ferrand CNRS/IN2P3  
 Guffanti Alberto University of Edinburgh  
 Gustafson Gosta Lund University  
 Gutsche Oliver DESY / University of Hamburg  
 Guzey Vadim Ruhr-Universitaet Bochum  
 Gwenlan Claire UCL  
 Halyo, Valerie Princeton  
 Hansson Magnus Lund University  
 Harris Oliver UCL/ATLAS  
 Harrison Karl University of Cambridge  
 Hegner Benedikt DESY  
 Heinemann Beate University of California, Berkeley  
 Heister, Arno Boston University  
 Hinchliffe Ian Lawrence Berkeley National Lab  
 Hoeche Stefan TU Dresden  
 Hoepfner Kerstin RWTH Aachen, III.Phys.Inst.A  
 Hoeth Hendrik Lund University  
 Hoeth, Hendrik Lund University  
 Hollar, Jonathan Jason Lawrence Livermore Nat. Laboratory (LLNL)

Holzner Andre ETH Zuerich  
 Huston Joey Michigan State University  
 Iacobucci Giuseppe INFN Bologna  
 Illarionov Alexei INFN, Pisa & JINR, Dubna  
 Ingelman Gunnar Uppsala University  
 Ishikawa Akimasa KEK-IPNS  
 Jadach Stanislaw IFJ-PAN, Krakow  
 Janssen Xavier DESY  
 Javadi Khasraghi Atefeh Physics group of Alzahra university  
 Jechow Mirko Humboldt-University zu Berlin Dep. of Physics  
 Jung Hannes DESY  
 Jung, Andreas W. University of Heidelberg, KIP  
 Kahle Benjamin DESY  
 Kaidalov Alexei ITEP, Moscow  
 Kapishin Mikhail JINR, Dubna  
 Karshon Uri Weizmann Institute, Rehovot, Israel  
 Kaspar Jan Physical Institute, Czech Academy of Sciences, Prague  
 Kataoka Mayuko KEK, Nara Women's University  
 Katkov, Igor DESY  
 Kepka Oldrich Dapnia SPP, CEA, Saclay  
 Kharzeev Dmitri BNL  
 Khein Lev Moscow State University  
 Khoze Valeri IPPP, University of Durham  
 Kiesling Christian Max-Planck-Institut für Physik  
 Kirsanov Mikhail INR Moscow  
 Klanner Robert University of Hamburg  
 Klasen Michael LPSC Grenoble  
 Klein Max University of Liverpool  
 Klein Sebastian DESY Zeuthen  
 Kluge Thomas DESY  
 Knutsson Albert DESY  
 Kolhinen Vesa Univ. of Jyväskylä, Dept. of Physics  
 Kollar, Daniel MPI for Physics Munich  
 Korotkov, Vladislav IHEP  
 Kostka, Peter DESY  
 Kotanski Andrzej Jagellonian University, Cracow, Poland  
 Kotikov Anatoly Joint Institute for Nuclear Research  
 Kowalski Henri DESY  
 Kraan Aafke INFN Pisa  
 Kramer Gustav Hamburg University  
 Krastev Kaloyan DESY  
 Krauss Frank TU Dresden  
 Kretzer Stefan BNL / RBRC  
 Krueger Katja KIP, Uni Heidelberg  
 Kuhr Thomas CERN  
 Kulesza Anna DESY Theory  
 Kundrat Vojtech Institute of Physics ASCR, Prague, Czech Republic  
 Kurepin Alexey Institute for Nuclear Research, Moscow  
 Kusina, Aleksander Institute of Nuclear Physics PAN  
 Kutak Krzysztof DESY  
 Kyrieleis Albrecht University of Manchester  
 Lönnblad, Leif Lund University  
 Laenen Eric NIKHEF

Lagouri Theodota Aristotle University of Thessaloniki  
 Lami Stefano INFN Pisa  
 Latino Giuseppe Siena Univ. & Pisa INFN  
 Lavesson Nils Lund University  
 Lebedev Andrey LPI  
 Lehner Frank DESY  
 Lendermann Victor University of Heidelberg  
 Lenzi, Piergiulio Dipartimento di Fisica  
 Lessnoff Kenneth University of Bristol  
 Levchenko Boris SINP MSU  
 Levin Eugene Tel Aviv University  
 Levonian Sergey DESY  
 LI, Gang LAL  
 Likhoded Anatoly IHEP, Protvino, Russia  
 Lilley, Joseph University of Birmingham  
 Lipatov Artem SINP MSU  
 Lipatov Lev Hamburg University  
 Lipka Katerina University of Hamburg  
 Lippmaa Endel Estonian Academy of Sciences  
 Lippmaa Jaak HIP, Helsinki University  
 Livio Fano INFN Perugia  
 Loizides John University College London  
 Lola, Magda Univ. of Patras  
 Lublinsky Michael University of Connecticut  
 Luisoni, Gionata ITP University Zurich  
 Lukasik Jaroslaw DESY / AGH-UST Cracow  
 Lukina Olga Skobeltsyn Institute of Nuclear Physics, Moscow State University  
 Lunardon Marcello University and INFN Padova  
 Luszczak Agnieszka INF PAN KRAKOW  
 Lytken, Else CERN  
 Lytkin Leonid Dubna  
 Macri, Mario INFN Genova  
 Magill Stephen Argonne National Laboratory  
 Magnea Lorenzo University of Torino  
 Mangano Michelangelo CERN TH  
 Maor Uri Tel Aviv University  
 Marage, Pierre ULB - Universite Libre de Bruxelles  
 Marquet Cyrille CEA-Saclay SPHT  
 Marti-Magro Lluís Desy  
 Martin Alan IPPP, Durham  
 Martyn Hans-Ulrich RWTH Aachen & DESY  
 Martynov, Yevgen Bogolyubov Institute for Theoretical Physics  
 Marzani, Simone School of Physics  
 Mastroberardino Anna Calabria University  
 Matteuzzi Clara INFN and Universita Milano-Bicocca  
 Maxfield Stephen University of Liverpool  
 Mazumdar Kajari Tata Institute, Mumbai, India  
 Melzer-Pellmann Isabell-A. DESY Hamburg  
 Meyer Andreas Hamburg University  
 Michele Pioppi Univ. of Perugia  
 Miglioranza Silvia DESY  
 Milcewicz Izabela Institute of Nuclear Physics, Cracow  
 Milstead David Stockholm University

Mischke Andre Utrecht University  
 Mitov Alexander DESY  
 Moch Sven-Olaf DESY  
 Moenig Klaus DESY  
 Monk James University College London  
 Monteno, Marco INFN  
 Moraes Arthur University of Sheffield  
 Morando Maurizio University of Padova  
 Morsch Andreas CERN  
 Motyka Leszek DESY  
 Mozer Matthias IIHE  
 Mrenna Stephen Fermilab  
 Mueller Katharina Universitaet Zuerich  
 Munier Stephane Ecole polytechnique  
 Murray Michael University of Kansas  
 Nachtmann Otto Universitaet Heidelberg  
 Nadolsky, Pavel Michigan State University  
 Naftali Eran Tel Aviv University  
 Nagano Kunihiro KEK  
 Nagy, Zoltan DESY  
 Namsoo Tim Bristol  
 Naumann Sebastian Univ. Hamburg  
 Newman Paul University of Birmingham  
 Nick Brook Brook University of Bristol  
 Niewiadomski Hubert CERN  
 Nuncio Quiroz Elizabeth Hamburg University / DESY  
 Nystrand Joakim University of Bergen  
 Olivier, Bob Max Planck Institute for Physics  
 Olness, Fredrick SMU / CERN  
 Orava Risto University of Helsinki & Helsinki Institute of Physics  
 Osman Sakar Lund University  
 Ostapchenko Sergey University of Karlsruhe  
 Osterberg Kenneth University of Helsinki  
 Ozerov, Dmitry ITEP  
 Padhi Sanjay DESY  
 Panagiotou Apostolos UNIV. OF ATHENS, HELLAS  
 Panikashvili Natalia Technion , Israel  
 Passaleva Giovanni INFN-Firenze  
 Pavel Nikolaj Humboldt-University Berlin, Inst. for Physics  
 Perez Emmanuelle CERN  
 Peschanski Robi Service de Physique Theorique (Saclay)  
 Peters Krisztian DESY H1  
 Petersen, Troels CERN  
 Petrov Vladimir IHEP. Protvino  
 Petrov, Vladimir Institute for High Energy Physics  
 Petrucci Fabrizio INFN Roma III  
 Petrukhin, Alexey DESY/ITEP  
 Piccinini Fulvio INFN Sezione di Pavia  
 Piccione Andrea INFN Torino  
 Pierog Tanguy FZK,IK  
 Pilkington Andrew University of Manchester  
 Pinfold, James University of Alberta  
 Piotrkowski Krzysztof Louvain University

Pire Bernard CPhT Polytechnique, Palaiseau  
 Pirner Hans-Juergen Theoretical Physics, Heidelberg University  
 Pisano Cristian Vrije Universiteit Amsterdam  
 Piskounova Olga LPI, Moscow  
 Piskounova, Olga LPI  
 Plaätzer, Simon ITP, U Karlsruhe  
 Placzek Wieslaw Institute of Physics, Jagiellonian University, ul. Reymonta 4, 30-059 Cracow, Poland  
 Pokorski Witold CERN  
 Polesello Giacomo CERN/INFN Pavia  
 Price, Darren Lancaster University  
 Pukhaeva Nelli INFN Milano  
 Pumplun Jon Michigan State University  
 Qin Zhonghua DESY ATLAS GROUP  
 Rabbertz Klaus University of Karlsruhe  
 Radescu Voica DESY  
 Radescu Voica DESY  
 Ranieri Riccardo University of Firenze / INFN Firenze  
 Rathsmann Johan Uppsala University  
 Ravindran Vajravelu Visitor, DESY-Zeuthen, Associate Prof at Harish-Chandra Research Institute, India  
 Rebutti, Daniela MPI - Munich  
 Reisert Burkard Max-Planck-Institute for Physics, Munich  
 Renner, Dru DESY Zeuthen  
 Rezaeian, Amir Universidad Tecnica Federico Santa Marra  
 Reznicek, Pavel IPNP, Charles University  
 Richardson Peter IPPP, Durham  
 Richter-Was Elzbieta Jagellonian University & Institute of Nuclear Physics IFJ PAN, Cracow, Poland  
 Rioutine, Roman IHEP  
 Rislé Christiane DESY  
 Rizvi Eram QMUL  
 Robbe Patrick LAL Orsay  
 Rodrigo German CERN & IFIC Valencia  
 Rodrigues Eduardo NIKHEF  
 Rogal, Mikhail DESY, Zeuthen  
 Rojo-Chacon Juan LPTHE, Paris  
 Rolandi Gigi CERN  
 Roloff Philipp DESY  
 Roosen Robert Bruxelles  
 Rouby Xavier UC Louvain  
 Royon Christophe DAPNIA-SPP, CEA Saclay  
 Ruiz Hugo CERN  
 Ruiz Morales Ester UPM - Madrid  
 Rurikova, Zuzana DESY  
 Ruspa Marta Univ Piemonte Orientale  
 Ryan Patrick University of Wisconsin  
 Saarikko Heimo University of Helsinki  
 Sabio Vera Agustin CERN  
 Sacchi Roberto University of Torino  
 Sako, Takashi STE Labo. Nagoya University  
 Salam Gavin LPTHE, Univ Paris VI and VII and CNRS  
 Saleev Vladimir Samara State University  
 Saleh Rahimi Keshari MSc. student of Particle Physics, from Semnan Uni. ,Iran  
 Salek, David IPNP, Charles University, Prague  
 Salgado Carlos a Cern

Sander, Christian Institut fuer Experimentalphysik - Universitaet Hamburg  
 Savin Alexander University of Wisconsin-Madison  
 Sawicki Pawel Institute of Nuclear Physics, Krakow  
 Sbrizzi Antonio University of Bologna  
 Schicker Rainer Phys. Inst. Uni Heidelberg  
 Schienbein Ingo DESY  
 Schilling Frank-Peter CERN  
 Schmelling, Michael MPI for Nuclear Physics  
 Schmidke William MPI Munich  
 Schneider Anna Novgorod State University  
 Schneider Olivier EPFL, Lausanne (LHCb)  
 Schoerner-Sadenius Thomas Hamburg University  
 Schrempp Fridger DESY  
 Schultz-Coulon Hans-Christian Universitaet Heidelberg  
 Schumann Steffen ITP TU Dresden  
 Schwennsen Florian University Hamburg  
 Seymour Michael CERN  
 Sharafiddinov Rasulkhozha Institute of Nuclear Physics of Uzbekistan Academy of Sciences  
 Shaw Graham University of Manchester  
 Shcherbakova Elena II Inst. fr Theor. Phys. Hamburg Universit&t  
 Shears, Tara University of Liverpool  
 Shirmohammad Maryam Physics group, Alzahra University  
 Shulha Siarhei Joint Institute for Nuclear Research, Dubna, Russia  
 Siddiqui Rehan NCP/CERN  
 Siegert, Frank IPPP, University of Durham  
 Sigl Guenter Uni Hamburg  
 Sjöstrand Torbjörn CERN and Lund University  
 Skrzypek Maciej ifj-pan  
 Slabospitsky Sergey CMS Collaboration, IHEP  
 Sloan Terry Lancaster University  
 Smith John SUNY at Stony Brook, USA  
 Smizanska Maria Lancaster  
 Sobol Andrei IHEP, Protvino  
 Solano Ada Univ. of Torino and INFN Torino  
 Somogyi Gabor Institute of Nuclear Research of the Hungarian Academy of Sciences  
 Sonnenschein Lars CERN  
 Soper, Davison CERN/University of Oregon  
 Soyez Gregory University of Liege  
 Spiesberger Hubert Mainz University  
 Spiropulu Maria CERN  
 Sridhar Krishnamoorthy TIFR, Mumbai, India  
 Stamerra Antonio Universita' di Siena  
 Stanco Luca INFN Padova  
 Starodumov Andrey ETH Zurich  
 Starovoitov Pavel NC PHEP  
 Stasto Anna DESY  
 Staykova Zlatka DESY  
 Steinbrueck Georg Hamburg University  
 Stenzel Hasko University of Giessen  
 Stephens Philip IFJ-PAN  
 Stirling James University of Durham  
 Stocco Diego Universita' di Torino  
 Stockton, Mark University of Birmingham



Stoesslein Uta DESY Hamburg  
 Stopa Piotr Institute of Nuclear Physics Krakow Poland  
 Strikman Mark Penn State University  
 Sunar Deniz University of Antwerp  
 Sutton Mark University College London  
 Sykora Tomas UA Antwerp, MFF UK Prague  
 Szczypka Saul University of Bristol  
 Tapprogge Stefan Johannes Gutenberg Universitaet Mainz  
 Targett-Adams Christopher UCL  
 Tasevsky Marek Physics Institute, Prague  
 Tassi Enrico Universidad Autonoma de Madrid  
 Terron Juan Universidad Autonoma de Madrid  
 Teryaev Oleg JINR  
 Teubert Frederic CERN-PH  
 Teubner Thomas University of Liverpool  
 Thaeuder, Jochen KIP Uni Heidelberg  
 Thompson Paul Birmingham University  
 Thorne Robert University College London  
 Todorova Sharka ASCR Prague  
 Tokushuku Katsuo KEK, IPNS  
 Toll Tobias DESY  
 Tonazzo Alessandra University Roma Tre and INFN  
 Traynor Daniel Queen Mary, University of London  
 Treleani Daniele University of Trieste  
 Trentadue, Luca Universita' di Parma and INFN Milano - Gr. Pr  
 Tsirova, Natalia Samara State University  
 Tuning Niels NIKHEF LHCb  
 Turcato Monica Hamburg University  
 Turnau Jacek Institue of Nuclear Physics, PAN, Krakow  
 Turrisi Rosario University and INFN - Padova  
 Uwe Ulrich Physikalisches Institut Heidelberg  
 Vajravelu Ravindran Associate Professor  
 Valkarova, Alice Charles University, Insitute of Particle and Nuclear Physics  
 Vallee Claude CPPM Marseille / DESY  
 van Hameren Andreas IFJ-PAN Krakow  
 Van Mechelen Pierre Universiteit Antwerpen  
 Vasin Dmitry Samara State University / Hamburg University  
 Vazdik Iakov Lebedev Physical Institute, Moscow  
 Vazquez Acosta Monica CERN  
 Venugopalan Raju Brookhaven National Laboratory USA  
 Verducci Monica CERN  
 Vervink Kim EPFL  
 Vilela Pereira, Antonio University degli Studi di Torino/INFN Torino  
 Villa Mauro INFN Bologna  
 von Manteuffel Andreas Heidelberg  
 Voss Kai-Cristian Bonn University  
 Vulpescu Bogdan Physics Institute, University Heidelberg, Germany  
 Walsh Roberval McGill University  
 Ward Bennie Baylor University  
 Was Zbigniew IFJ PAN  
 Watt Graeme University College London  
 Waugh Ben University College London  
 Weinzierl Stefan University of Mainz

Weiser Christian University of Karlsruhe  
Weng Joanna CERN/University of Karlsruhe  
Whalley Mike IPPP, Durham  
White Chris NIKHEF  
Whitmore Jim Penn State Univ. and U.S. National Science Foundation  
Wing Matthew DESY/UCL  
Winter Jan CERN TH and TU Dresden  
Wobisch Markus Fermilab  
Wolf Roger Uni-Heidelberg  
Yagues Ana Humboldt University Berlin/ DESY  
Yamazaki Yuji KEK-IPNS  
Yokoya, Hiroshi CERN  
Yoshida Rik Argonne National Laboratory  
Yost Scott Baylor University  
Zanderighi Giulia University of Oxford  
Zapp Korinna Physikalisches Institut, Universität Heidelberg  
Zarubin Anatoly JINR, CMS  
Zenin Oleg IHEP, Russia  
Zotov Nikolai Skobeltsyn Institute of Nuclear Physics, MSU  
zur Nedden Martin Humboldt-Universität zu Berlin